frontiers | Research Topics

Advances in geomechanics research and application for deep unconventional reservoirs

Edited by
Peng Tan, Liuke Huang and Huiwen Pang

Coordinated by
Wenda Li

Published in
Frontiers in Energy Research
Frontiers in Built Environment



FRONTIERS EBOOK COPYRIGHT STATEMENT

The copyright in the text of individual articles in this ebook is the property of their respective authors or their respective institutions or funders. The copyright in graphics and images within each article may be subject to copyright of other parties. In both cases this is subject to a license granted to Frontiers.

The compilation of articles constituting this ebook is the property of Frontiers.

Each article within this ebook, and the ebook itself, are published under the most recent version of the Creative Commons CC-BY licence. The version current at the date of publication of this ebook is CC-BY 4.0. If the CC-BY licence is updated, the licence granted by Frontiers is automatically updated to the new version.

When exercising any right under the CC-BY licence, Frontiers must be attributed as the original publisher of the article or ebook, as applicable.

Authors have the responsibility of ensuring that any graphics or other materials which are the property of others may be included in the CC-BY licence, but this should be checked before relying on the CC-BY licence to reproduce those materials. Any copyright notices relating to those materials must be complied with.

Copyright and source acknowledgement notices may not be removed and must be displayed in any copy, derivative work or partial copy which includes the elements in question.

All copyright, and all rights therein, are protected by national and international copyright laws. The above represents a summary only. For further information please read Frontiers' Conditions for Website Use and Copyright Statement, and the applicable CC-BY licence.

ISSN 1664-8714
ISBN 978-2-8325-5651-1
DOI 10.3389/978-2-8325-5651-1

About Frontiers

Frontiers is more than just an open access publisher of scholarly articles: it is a pioneering approach to the world of academia, radically improving the way scholarly research is managed. The grand vision of Frontiers is a world where all people have an equal opportunity to seek, share and generate knowledge. Frontiers provides immediate and permanent online open access to all its publications, but this alone is not enough to realize our grand goals.

Frontiers journal series

The Frontiers journal series is a multi-tier and interdisciplinary set of open-access, online journals, promising a paradigm shift from the current review, selection and dissemination processes in academic publishing. All Frontiers journals are driven by researchers for researchers; therefore, they constitute a service to the scholarly community. At the same time, the *Frontiers journal series* operates on a revolutionary invention, the tiered publishing system, initially addressing specific communities of scholars, and gradually climbing up to broader public understanding, thus serving the interests of the lay society, too.

Dedication to quality

Each Frontiers article is a landmark of the highest quality, thanks to genuinely collaborative interactions between authors and review editors, who include some of the world's best academicians. Research must be certified by peers before entering a stream of knowledge that may eventually reach the public - and shape society; therefore, Frontiers only applies the most rigorous and unbiased reviews. Frontiers revolutionizes research publishing by freely delivering the most outstanding research, evaluated with no bias from both the academic and social point of view. By applying the most advanced information technologies, Frontiers is catapulting scholarly publishing into a new generation.

What are Frontiers Research Topics?

Frontiers Research Topics are very popular trademarks of the *Frontiers journals series*: they are collections of at least ten articles, all centered on a particular subject. With their unique mix of varied contributions from Original Research to Review Articles, Frontiers Research Topics unify the most influential researchers, the latest key findings and historical advances in a hot research area.

Find out more on how to host your own Frontiers Research Topic or contribute to one as an author by contacting the Frontiers editorial office: frontiersin.org/about/contact

Advances in geomechanics research and application for deep unconventional reservoirs

Topic editors

Peng Tan — CNPC Engineering Technology R & D Company Limited, China

Liuke Huang — Southwest Petroleum University, China

Huiwen Pang — China University of Petroleum, China

Topic coordinator

Wenda Li — Taiyuan University of Technology, China

Citation

Tan, P., Huang, L., Pang, H., Li, W., eds. (2024). *Advances in geomechanics research and application for deep unconventional reservoirs*. Lausanne: Frontiers Media SA. doi: 10.3389/978-2-8325-5651-1

Table of contents

07 Investigating fracture initiation and propagation in deep buried shale due to thermal shock: a numerical approach
Wei Wang, Peng Zhao, Yisha Liao, Yuelei Zhang, Jiao Peng, Hongyu Xian and Jun Liu

19 Research and performance optimization of carbon dioxide foam fracturing fluid suitable for shale reservoir
Song Li, Yu Fan, Tingting He, Jian Yang, Jinsui Li and Xi Wang

29 Evaluation method for reservoir damage of cementing slurry
Ji Li, Dapeng Wu, Ran Zhang, Chenguang Li and Qiang Zou

38 Three-peak evolution characteristics of supporting stress on a super-long working face in a thick coal seam
Hongbing Wang, Zhiheng Cheng, Jinhu Zhang, Liang Chen, Xin Luo, Meichen Li, Haoyi Chen and Yifei Xie

54 Research on dual lateral log simulation of shale bedding fractures under different influencing conditions
Naihui Wang, Kesai Li, Jiaqi Sun, Di Wang, Xianhong He, Zehou Xiang, Hui Liu and Pan Wang

65 Molecular dynamics simulation of surfactant induced wettability alteration of shale reservoirs
Debin Kong, Xianglong Meng, Jiadan Zhu and Wenning Zhou

76 A new type of high hardness coating for improving drill bit stability in unconventional oil and gas development
Lingchao Xuan and Jiangshuai Wang

84 *In-situ* stress prediction in ultra-deep carbonate reservoirs of Fuman Oilfield, Tarim Basin of China
Guoqing Yin, Kongyou Wu, Wei Ju, Yun Qin, Ziwei Qian, Ke Xu, Zhongyuan Lu, Peng Wang, Xiaobai Liang and Yan Liang

95 Study on mechanical properties and microscopic damage mechanism of tight sandstone reservoir under uniaxial compression
Jin Huang, Jiacheng Xing, Xingchuan Liao, Yixing Ren, Keer Ding and Jin Tan

109 Enhancing the benefit of slide steering drilling systems in horizontal wells of unconventional reservoirs
Hengzhi Chu, Chao Xiong, Kaili Hu, Yong Guo, Yucai Shi and Bo Zhang

116 Research on imbibition effect of surfactant fracturing fluid in offshore reservoirs with low permeability and high temperature
Yigang Liu, Jian Zou, Xitang Lan, Shang Gao, Liping Zhang and Xin He

125 True triaxial physics simulations and process tests of hydraulic fracturing in the Da'anzhai section of the Sichuan Basin tight oil reservoir
Song Li, Yu Fan, Yang Wang, Yuanshou Zhao, Zefei Lv, Zeng Ji, Weihua Chen and Jian Min

136 Deciphering the formation period and geological implications of shale tectonic fractures: a mini review and forward-looking perspectives
Hu Li

145 Regional outburst prevention technology of pre-drainage gas area in west well area of sihe coal mine
Peng Zhang

160 Energy evolution mechanism during rockburst development in structures of surrounding rocks of deep rockburst-prone roadways in coal mines
Zhongtang Xuan, Zhiheng Cheng, Chunyuan Li, Chaojun Fan, Hongyan Qin, Wenchen Li, Kai Guo, Haoyi Chen, Yifei Xie and Likai Yang

175 Prediction of natural fracture distribution characteristics in tight oil and gas reservoirs based on paleotectonic stress field
Lifei Lin, Mingwei Wang, Yanwei Wang, Yi Gao and Song Li

191 Fracturing fluid flow characteristics in shale gas matrix-fracture system based on NMR method
Jianfa Wu, Xuefeng Yang, Jiajun Li, Wenping Liu, Feng Chen, Shan Huang, Chuanxi Wang and Yongpeng Sun

200 Fracturing parameter optimization technology for highly deviated wells in complex lithologic reservoirs
Lihua Hao, Binxin Zhang, Beibei Chen, Hongwei Wang, Yuankun Wu, Liyan Pan and Yue Huang

215 Grouting solidification technology for fractured soft coal seams and its application in coalbed methane (coal mine gas) extraction
Zhang Guangbo, Zhang Suian, Jia Wei, Zhang Xiao, Zhang Yang, Lian Haoyu, Lian Xiaohua and Fang Huili

223 Geophysical exploration methods on bauxite reservoirs in L gasfield, Ordos Basin
Qi Yu, Li Dan, Yu Shanshan and Li Qixin

236 Identification of different lithofacies laminations in oil shale and their mechanical properties
Shizhong Cheng, Mao Sheng and Chao Deng

246 Study on multi-cluster fracturing simulation of deep reservoir based on cohesive element modeling
Jianfa Wu, Mingyang Wu, Yintong Guo, Haoyong Huang, Zhen Zhang, Guanghai Zhong, Junchuan Gui and Jun Lu

264 Study on the fracture propagation law of deep shale reservoir under the influence of different number of fracturing clusters
Bo Zeng, Mingyang Wu, Yuliang Su, Yintong Guo, Jiangrong Feng, Junchuan Gui and Jun Lu

284 Research and application of 'three zones' range within overlying strata in goaf of steep coal seam
Shouguo Yang, Ning Xu, Haoxin Liu, Xiaofei Zhang and Shuxin Mei

296 Numerical simulation study on evolution law of three-dimensional fracture network in unconventional reservoirs
Xiyu Chen, Yitao Huang, Yongming Li and Cheng Shen

313 Characteristics and controlling factors of tectonic fractures within the buried hill reservoirs from the Archaean metamorphic basement: a case study in the Bozhong 19–6 condensate gas field, Bohai Bay Basin
Zongbing Liu, Qi Cheng, Xinwu Liao, Lei Zhang, Wenchao Liu and Guanjie Zhang

325 The propagation of hydraulic fracture in layered coal seam: a numerical simulation considering the interface thickness based on the distinct element method
Hongye Gao, Baoshan Jia, Yun Lei, Yongxiang Zheng, Bin Shi, Haiyang Wei, Tongjing Zhang, Wei Wang and Qinghe Niu

342 Research on micro/nano scale 3D reconstruction based on scanning electron microscope
Huibao Dong, Hongliang Jia, Dahui Qin and Dawei Hu

353 Effect of disturbed coal pore structure on gas adsorption characteristics: mercury intrusion porosimetry
Yunpei Liang, Wanjie Sun, Zhaopeng Wu, Shuren Mao and Qican Ran

366 Research on geophysical response analysis and prediction technology of geostress in the shale gas area of the southern Sichuan Basin
Chang Wang, Cheng Yin, Xuewen Shi, Dongjun Zhang, Maojie Liao and Ruhua Zhang

381 The experimental and numerical analysis of elastic rock mechanical properties in tight conglomerate rock samples: a case study in Junggar Basin
Hongyan Qi, Danyang Li, Jun Zhao, Hailong Ma, Xueliang Wang, Xianhu Wang, Bolong Zhu, Jiaying Lin and Xiangyun Zhao

394 Numerical simulation and application of ground stress field in ultra-deep strike-slip faults—taking the FI12 fault zone in the Fuman Oilfield as an example
Yu Zhang, Ke Xu, Hui Zhang, Shujun Lai, Jingrui Liang and Ziwei Qian

407 Numerical study of hydraulic fractures propagation in deep fracture-cavity reservoir based on continuous damage theory
Hengjie Luan, Mingkang Liu, Qinglin Shan, Yujing Jiang, Bo Li, Changsheng Wang and Xianzhen Cheng

429 Two-dimensional spectrum characteristics and oil movability study of the shale oil reservoir
Changhong Cai, Li Wang, Rui Zhang, Qiang Kang, Qingxiu Zhang, Dan Zhao, Jingsu Guo, Manfei Chen, Hongbin Chen, Lei Lei, Ke Wang and Jiahuan He

437 Parametrical design and optimization of a reverse circulation drill bit for dust control
Liming Fan, Zhilin Li and Yongjiang Luo

frontiers | Frontiers in Energy Research

TYPE Original Research
PUBLISHED 14 July 2023
DOI 10.3389/fenrg.2023.1231958

Check for updates

OPEN ACCESS

EDITED BY
Peng Tan,
CNPC Engineering Technology R & D Company Limited, China

REVIEWED BY
Jie Chi,
China University of Petroleum (Huadong), China
Saipeng Huang,
University of Barcelona, Spain

*CORRESPONDENCE
Peng Zhao,
scu_zhaopeng@163.com

RECEIVED 31 May 2023
ACCEPTED 28 June 2023
PUBLISHED 14 July 2023

CITATION
Wang W, Zhao P, Liao Y, Zhang Y, Peng J, Xian H and Liu J (2023), Investigating fracture initiation and propagation in deep buried shale due to thermal shock: a numerical approach.
Front. Energy Res. 11:1231958.
doi: 10.3389/fenrg.2023.1231958

COPYRIGHT
© 2023 Wang, Zhao, Liao, Zhang, Peng, Xian and Liu. This is an open-access article distributed under the terms of the Creative Commons Attribution License (CC BY). The use, distribution or reproduction in other forums is permitted, provided the original author(s) and the copyright owner(s) are credited and that the original publication in this journal is cited, in accordance with accepted academic practice. No use, distribution or reproduction is permitted which does not comply with these terms.

Investigating fracture initiation and propagation in deep buried shale due to thermal shock: a numerical approach

Wei Wang[1,2], Peng Zhao[3]*, Yisha Liao[4], Yuelei Zhang[1,2], Jiao Peng[5], Hongyu Xian[5] and Jun Liu[1,2,6]

[1]Key Laboratory of Shale Gas Exploration, Ministry of Natural Resources, Chongqing Institute of Geology and Mineral Resources, Chongqing, China, [2]National and Local Joint Engineering Research Center of Shale Gas Exploration and Development, Chongqing Institute of Geology and Mineral Resources, Chongqing, China, [3]State Key Laboratory of Geohazard Prevention and Geoenvironment Protection, Chengdu University of Technology, Chengdu, China, [4]China Petroleum Xinan Oil & Gas Field Company Chongqing Gas Mine, Chongqing, China, [5]College of Environment and Civil Engineering, Chengdu University of Technology, Chengdu, China, [6]Institute of New Energy and Low-Carbon Technology, Sichuan University, Chengdu, China

As the burial depth of shale exploitation increases, it is challenge to form fracture networks through hydraulic fracturing technology. When cryogenic fluid contacts with hot rock, heat exchange process occurs and temperature gradient is generated at the rock surface, resulting in thermal stress. Once the thermal stress exceeds the tensile strength, the fractures are generated. To study the initiation and propagation of fractures induced by thermal shock, a thermal-mechanical (TM) coupled two-dimensional model is developed in the paper. To simulate the heat exchange process, the heat convective boundary is applied in the surface between the fluid and the rock. In addition, the initiation and propagation of fractures are described by the cohesive zone model. The accuracy and reliability of the numerical model is validated by an existing analytical solution. Under the thermal shock, the temperature at the contact surface drops quickly. The stress distribution is determined by the temperature variation. The variations of temperature and stress are greatly affected by the heat exchange coefficient. With the fractures embedded in the model, the initiation and propagation of fractures are analysed. The multi-fracture propagation induced by thermal shock exhibits competition effect. With the propagation of fractures, the stress distribution in the rock changes. The heat exchange coefficient has a significant effect on fracture initiation and propagation, presenting more fractures generation in the larger coefficient.

KEYWORDS

thermal shock, TM coupled model, distribution of temperature, stress initiation and propagation of fractures, heat exchange coefficient

1 Introduction

Shale gas is a type of clean and efficient energy resource. Through long-term research and engineering practice, the development technology of shale gas in middle-shallow layer (<3,500 m) is relatively mature. With the deepening of the exploration, the deep shale gas (with the buried depth of over 3,500 m) is a highly promising resource, which takes over 65% of the whole shale gas reserve in China. Currently, the development of deep shale gas has

made preliminary technical progress, but many challenges are reported in field, especially in the hydraulic fracturing as the key technique of shale gas efficiency development (Zhao et al., 2022).

Compared with shale gas in middle-shallow layer, the formation temperature and overburden pressure of deep shale increase, as well as the formation closure pressure, crustal stress difference, elastic modulus, failure strength and other mechanical parameters also increase in varying degrees (Guo et al., 2021). The reservoir characteristics listed above bring disadvantages to the hydraulic fracturing of deep shale gas, such as: (1) plasticity of shale is enhanced, which makes the fractures difficult to initiate and propagate; (2) it is challenge to improve the complexity of fractures and the volume of reservoir reconstruction; (3) the transportation of the proppant becomes difficult due to the narrow fracture width. At present, it is more realistic to form micro fractures with main fractures and relatively small extension ranges in deep shale hydraulic fracturing (Chang et al., 2022). It can be concluded that it is of great challenge to obtain an ideal fracturing region in deep shale reservoirs.

In addition to bearing external loads, rocks can also withstand thermal stress caused by internal temperature changes. Thermal crack is also an important factor in rock failure. Numerical simulation researches show that larger injecting fluid can effectively reduce the bottom hole temperature, with a maximum temperature drop of 80°C (well depth of 4,000 m) (Zhang et al., 2019). Field experiments and physical simulation experiments of enhanced geothermal extraction also indicate that reservoir permeability is improved by injecting cryogenic fluid into hot dry rocks (Garcia et al., 2015), (Rutqvist et al., 2015). Based on the above research conclusions, some researchers propose a type of fracturing method, namely, cryogenic fracturing technology (Tomac and Gutierrez., 2017). When cryogenic fluid is injected into a high-temperature formation, the temperature causes rock shrinkage and generate tensile stress. As the tensile stress is greater than the critical stress, fractures are generated in the rock (Enayatpour et al., 2018a). In addition, the cooling effect of cryogenic fluid can also effectively reduce the crustal stress and the critical value of fracture initiation or propagation, which is conducive to form a larger range of fracture network (Enayatpour et al., 2018b). Hence, a series of research on the cryogenic fracturing are conducted. For example, according to the experimental results, multiple cryogenic shocks could generate new fractures, increase the width of existing fractures, and rock characteristics would affect the generation of fractures (Cha et al., 2017; Wang et al., 2016; Enayatpour et al., 2018a; Enayatpour et al., 2018b) established a hydraulic fracturing model for shale reservoir under thermal shock (sharp thermal gradient). They analyzed the mechanism and effect of cryogenic fracturing, as well as the impact of rock thermophysical parameters and mechanical parameters. Based on the plane strain model for the initiation/propagation of secondary fractures, (Tran et al., 2012) discussed the effect of initial effective stress, elastic modulus, filtration loss, and temperature difference on the propagation of secondary fractures during cryogenic fracturing. (Bahr et al., 2010) found that the spacing between thermal shock fractures was proportional to the fracture length and inversely proportional to the propagation speed. Kim and Kemeny (Kim and Kemeny, 2009) analysed the effect of rapid cooling and unloading on rock damage by slowing heating and rapid cooling tests. (Dahi et al., 2014) investigated the effect of temperature on preexisting fractures and newly initiated fractures in the process of hydraulic fracturing. Generally, thermal shock has been recognized as an important type of fracturing.

Recently, liquid nitrogen (LN_2) or liquid carbon dioxide (LCO_2) is considered as fracturing fluid because of the strong thermal shock process. Many researches on the cryogenic fracturing are focused on LN_2 or LCO_2. (Cha et al., 2014) investigated the feasibility of fracture stimulation by using cryogenic fluids to create a strong thermal gradient surrounding a borehole. The experimental results showed that the material properties played a key role in the generation of fractures. (Han et al., 2020) found that after the immersion of cryogenic fluid nitrogen, shale rock exhibited obvious brittleness failure characteristics. In addition, (Wang et al., 2016; Qin et al., 2018; Zhang et al., 2016) and (Yang et al., 2019) conducted tri-axial fracturing experiments and the experimental phenomena indicated that larger complex fracture network can be obtained by cryogenic LN_2 fracturing. (Cai et al., 2014) analysed the properties of sandstone, marble and shale after liquid nitrogen cooling. (Yao et al., 2017) developed a numerical model to identify the influence of different confining stress, injection pressure and failure criteria on the cryogenic fracturing.

Numerical method is a feasible method to study the cryogenic fracturing technology. Generally, cryogenic fracturing involves complex physical processes, which includes thermal conduction/convection, rock deformation, fracture initiation/propagation, fluid flow and phase transition. Additionally, the material properties vary with the temperature (Burlayenko et al., 2016), (Trevisan et al., 2016), especially for the heterogeneity (Huang et al., 2019) (Huang et al., 2023). Actually, it is difficult to consider these processes in the numerical model simultaneously. Most researches focus on the thermal shock process (e.g., thermal/mechanical response and the fracturing process), and some factors can be discussed. Unlike conventional hydraulic fracturing, as the low-temperature fluid enters the main fracture, secondary fractures with alternate length on the surface of the main fracture are formed due to thermal shock (Tang et al., 2020; Tang et al., 2016). Understanding the competitive propagation of multiple fractures is very important. It is beneficial to improve the volume and complexity of the fracture network. Unfortunately, rare researches are conducted to study the non-uniform propagation of fractures along rock surface, as well as the influence factors.

This study develops a TM coupled two-dimensional model in ANSYS software. It should be noted that heat convective boundary, rather than the first temperature boundary, is considered in the model. The initiation and propagation of fractures are described by the cohesive zone model. The accuracy and reliability of the numerical model is validated by an existing analytical solution. Thereafter, under the thermal shock, the temperature and stress distribution are discussed in the elastic stage. With the fractures embedded in the model, the initiation and propagation of fractures are analysed, as well as the effect of the heat exchange coefficient. Generally, this work should help to analyse the thermal shock performance to enhance the reservoir stimulation.

2 Mathematical description of the TM model

2.1 Model assumptions

As cryogenic fracturing is a complex physical process, some assumptions are made to develop the numerical model (Tran et al., 2012; Tang et al., 2016; Tang et al., 2020).

(1) Only the thermal shock is considered in the model. Herein, the fluid flow in the fracture is ignored.
(2) The properties of rock keep constant with temperature change.
(3) Several fractures are preset in the model to simulate the competitive propagation of multiple fractures. Only the tension failure is considered.
(4) The rock matrix exhibits linear elastic mechanical behavior.
(5) The relationship between heat flux vector and thermal gradients obeys Fourier's law.

2.2 Governing equations

2.2.1 Thermalelasticity equations

Based on the assumptions expressed above, the governing equations of the thermalelasticity are as follows (Xu., 2016):

$$\{\varepsilon\} = [D]^{-1}\{\sigma\} + \{\alpha\}\Delta T \tag{1}$$

$$S = \{\alpha\}^T\{\sigma\} + \frac{\rho C_p}{T_0}\Delta T \tag{2}$$

where ε is the total strain vector; S is the entropy density; σ is the stress vector; $\triangle T$ ($=T\text{-}T_{ref}$) is the temperature change; T is the current temperature; T_{ref} is the reference temperature; T_0 is the absolute reference temperature; (D) is the elastic stiffness matrix; α is the vector of coefficients of thermal expansion; ρ is the density; and C_p is the specific heat at constant stress or pressure.

Using ε and $\triangle T$ as independent variables, and replacing the entropy density S in Eq. 2 by heat density Q using the second law of thermodynamics ($Q = T_0S$) for a reversible change, the following equation is obtained:

$$\{\sigma\} = [D]\{\varepsilon\} - \{\beta\}\Delta T \tag{3}$$

$$Q = T_0\{\beta\}^T\{\varepsilon\} + \rho C_v\Delta T \tag{4}$$

$$\{\beta\} = [D]\{\alpha\} \tag{5}$$

$$C_v = C_p - \frac{T_0}{\rho}\{\alpha\}^T\{\beta\} \tag{6}$$

where β is the vector of thermoelastic coefficients; and C_v is the specific heat at constant strain or volume.

2.2.2 Heat flow equations

The first law of thermodynamics states that thermal energy is conserved. Specializing this to a differential control volume, and the equation is written as (Zhao et al., 2023):

$$\rho C_v\left(\frac{\partial T}{\partial t} + \{v\}^T\{L\}T\right) + \{L\}^T\{q\} = q_0 \tag{7}$$

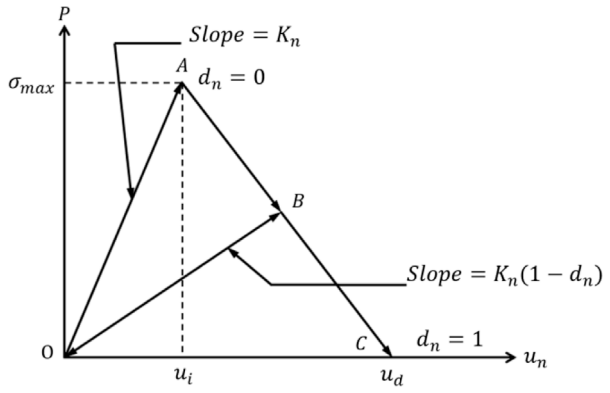


FIGURE 1
Constitutive relation of the cohesive zone model.

where L is the vector operator; v is the velocity vector for mass transport of heat; q is the heat flux vector; q_0 is the heat generation rate per unit volume.

Fourier's law is used to relate the heat flux vector to the thermal gradients:

$$\{q\} = -[K]\{L\}T \tag{8}$$

where $[K]$ is the conductivity matrix.

2.2.3 Coupled equation for TM model

Substituting the parameter Q in Eq. 4 into Eq. 7 produces the coupled equation of TH model.

$$\frac{\partial Q}{\partial t} = T_0\{\beta\}^T\frac{\partial\{\varepsilon\}}{\partial t} + \rho C_v\frac{\partial(\Delta T)}{\partial t} - [K]\nabla^2 T \tag{9}$$

2.3 Cohesive zone model

To avoid the stress singularity in the crack tip, the cohesive zone model is adopted to simulate the initiation and propagation of the fracture in the numerical model. The model is realized by interface element. Then, by defining the relationship between normal force and deformation, as well as tangential force and slip deformation, the mechanical behavior of the fracture is simulated. In this study, a bilinear traction-separation law is employed to describe the relationship, and the failure criterion is the maximum principal tensile stress criterion. The constitutive relation of the cohesive zone model is shown in Figure 1 (Tan et al., 2021).

In the numerical calculation, the relationship between the tensile stress and the gap between interface elements is described in the following equations:

$$P = K_n u_n(1 - d_n) \tag{10}$$

$$d_n = \begin{cases} 0 & u_n < u_i \\ \left(\frac{u_n - u_i}{u_n}\right)\left(\frac{u_d}{u_d - u_i}\right) & u_i \le u_n \le u_d \\ 1 & u_n > u_d \end{cases} \tag{11}$$

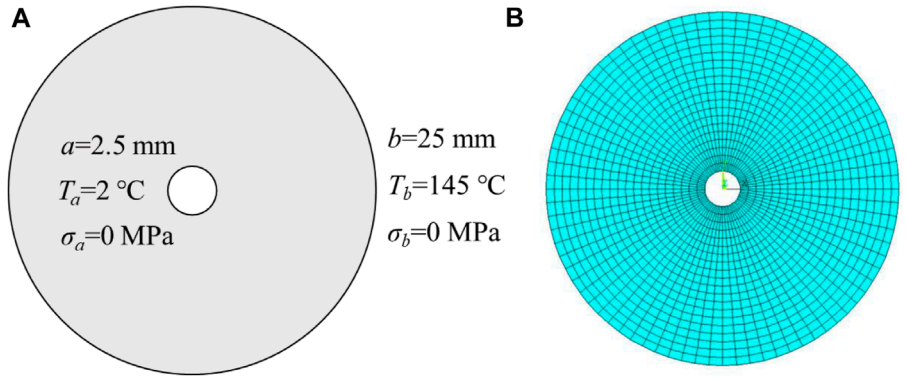


FIGURE 2
Description of the thick-walled cylinder model: **(A)** geometric modeling with initial boundary conditions; **(B)** finite element model.

where P is the tension stress; K_n is the normal stiffness of fracture surface; u_n is the gap between interface elements; u_i is the gap when P reaches to the maximum value; u_d is the gap when P is zero; d_n is the parameter which is used to describe the softening of material.

For rock, when $u_n < u_i$, the material is in the elastic stage; when $u_i \le u_n \le u_d$, damage occurs in the material and the degree is described by d_n; when $u_n > u_d$, macroscopic fracture is occurred in the material and there is no force between interface elements.

TABLE 1 Parameters of the thick-walled cylinder under thermal shock (Tang et al., 2020; Tang et al., 2016; Zhao et al., 2023).

Parameter	Value	Parameter	Value
Outer radius	25 (mm)	Inner radius	2.5 (mm)
Elastic modulus	20 (GPa)	Thermal conductivity	2 [W/(m·K)]
Poisson's ratio	0.25	Heat capacity	850 [J/(kg·K)]
Density	2,500 (kg/m^3)	Expansion coefficient	1e-5 [1/K]

3 Validation of the coupled TM model

To validate the coupled TM model developed in the paper, the analytical solution of thick-walled cylinder under thermal shock is adopted as simulation example. The two-dimensional model is described in Figure 2A. The outer and inner radius of the model are 25 mm and 2.5 mm, respectively. For the thermal boundary condition, the temperature of the external and inner walls is 2°C and 145°C, respectively. For the mechanical boundary condition, the axial stress of the external and inner walls is 0 MPa. In steady state condition, Xu (Xu, 2016) deduced the analytical solutions of the distribution of the temperature (T) and the hoop stress (σ_θ):

$$T = T_a \frac{\ln\frac{b}{r}}{\ln\frac{b}{a}} + T_b \frac{\ln\frac{a}{r}}{\ln\frac{a}{b}} \tag{12}$$

$$\sigma_\theta = -\frac{E\alpha(T_a - T_b)}{2(1-\mu)}\left(\frac{\ln\frac{b}{r} - 1}{\ln\frac{b}{a}} + \frac{\frac{b^2}{r^2}+1}{\frac{b^2}{a^2}-1}\right) \tag{13}$$

where b is the inner radius; a is the outer radius; T_a is the temperature at the inner wall; T_b is the temperature at the external wall; r represents the distance between any point and the centre of the circle; E is the elastic modulus; μ is the Poisson's ratio.

According to the description of the thick-walled cylinder model, the numerical model is developed (Figure 2B), and the relevant parameters are listed in Table 1.

The comparison between the analytical solution and the numerical results is shown in Figure 3. The results include the temperature and hoop stress at different positions. The results obtained from the numerical model are identical to the analytical solution (Figure 3). As the variable parameter r increases from 2.5 mm to 25 mm, the temperature increases nonlinearly (Figure 4A). The rate of change gradually decreases. For the stress induced by temperature gradient, with the increase of r, the hoop stress changes from tension stress to compress stress (Figure 4B). Consistent with the trend of temperature change, the rate of stress change is first fast and then slow. The maximum tension stress obtained from the analytical solution and the numerical result is 30.2 MPa and 29.4 MPa, respectively. The maximum compress stress obtained from the analytical solution and the numerical result is 7.9 MPa and 8.2 MPa, respectively. The error is less than 4%, which can be ignored. Thus, the accuracy of the coupled TM model is verified.

4 Thermal shock model

4.1 Description of the model

There are two cases developed in the paper: (1) Case 1: only the elastic behavior is considered. Then, the distribution of stress and temperature is discussed; (2) Case 2: the numerical model consists of matrix system and fracture system. Under thermal shock, the matrix is assumed to behave elastically and rock damage occurs in the fracture system.

For the two cases, a plate with the size of 50 mm × 25 mm is developed. The model is discretized into 20,000 coupled-field

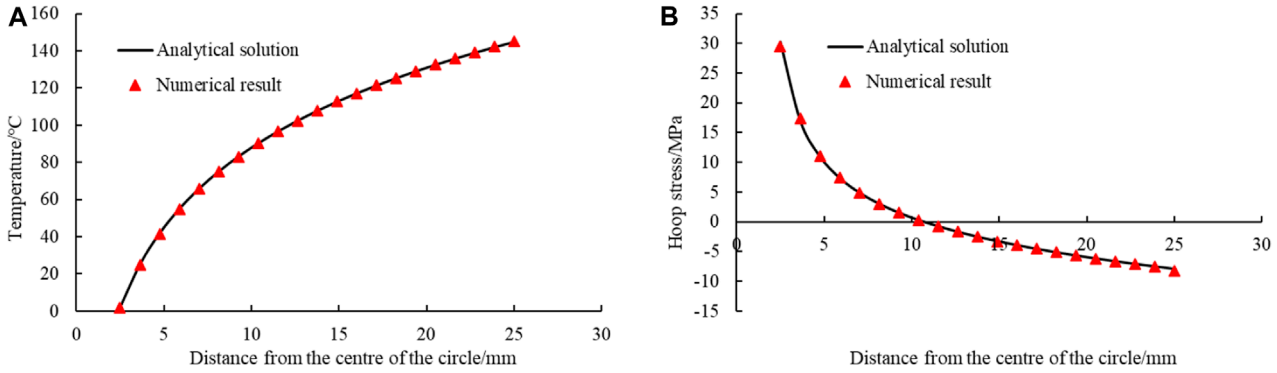


FIGURE 3
Variation in results at different positions: **(A)** temperature; and **(B)** hoop stress.

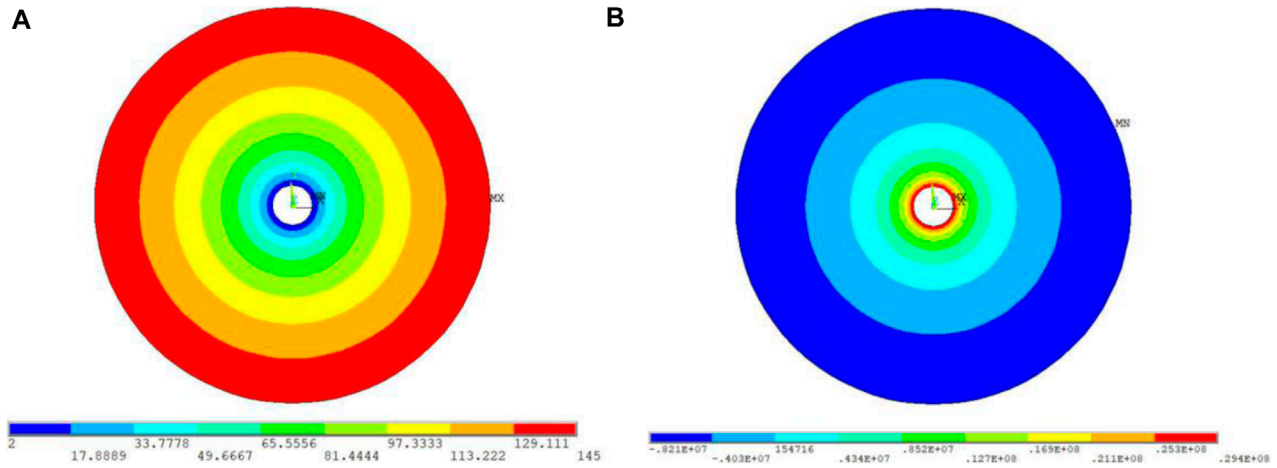


FIGURE 4
Distribution of the physical fields: **(A)** temperature; and **(B)** hoop stress.

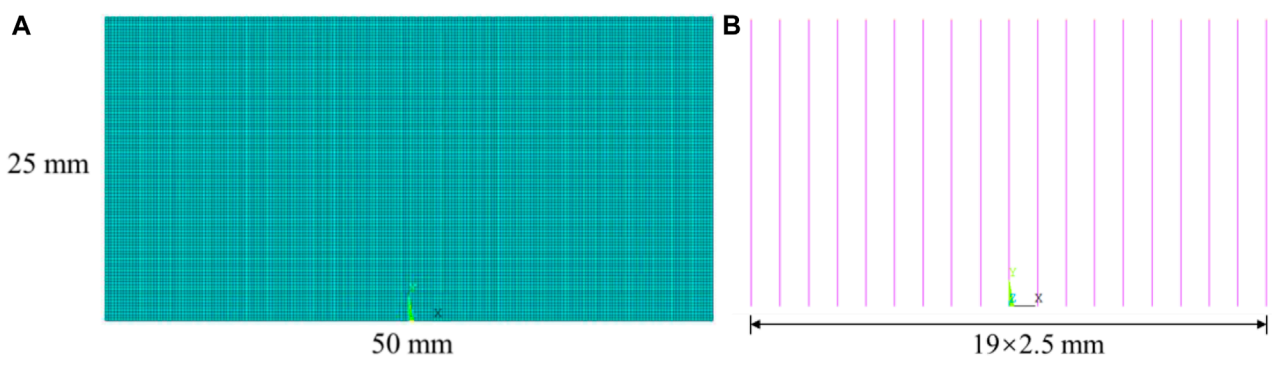


FIGURE 5
Conceptual model of thermal shock: **(A)** matrix system, and **(B)** fracture system.

TABLE 2 Physical properties (Tang et al., 2020; Tang et al., 2016; Zhao et al., 2023).

Parameter	Value	Parameter	Value
Elastic modulus	20e9 (Pa)	Heat exchange coefficient	1,000 [W/(m^2 K)]
Poisson's ratio	0.25	Tension stress	7 (MPa)
Heat capacity	850 [J/(kg K)]	Fracture normal stiffness	200 (GPa)
Thermal conductivity	2 [W/(m K)]	Expansion coefficient	1e-5 (1/K)

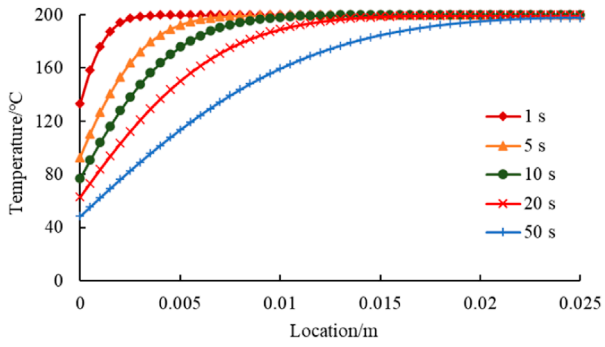


FIGURE 6
Temperature variation in the plate at different time.

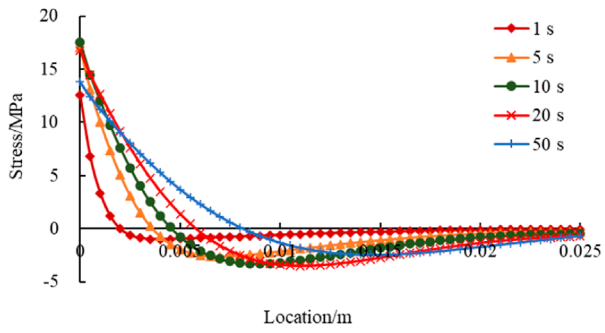


FIGURE 7
Stress variation in the plate at different time.

quadrilateral elements (Figure 5A). For the second case, to study the competitive propagation of multiple fractures induced by thermal shock, nineteen fractures are embedded in the model. The spacing between two fractures is 2.5 mm (Figure 5B). The fractures are simulated with the cohesive elements and the number of elements is 1900. The relevant physical parameters are listed in Table 2.

4.2 Initial and boundary conditions

The initial and boundary conditions of the TM model are listed as follows.

(1) Stress field. The bottom of the model is constrained along the y-direction, and the other surfaces are unconstrained.
(2) Temperature field. The initial temperatures of the rock and cryogenic fluid are 200°C and 20°C, respectively. The heat exchange occurs in the upper surface. In most studies, the boundary condition is defined as the first thermal boundary condition. For example, the upper surface is set by assuming that the temperature equals to that of cryogenic fluid, namely, 20°C. However, the definition ignores the process of heat exchange between hot rock and cryogenic fluid. The temperature of the rock surface in contact with cryogenic fluid does not immediately reach to 20°C. It is a heat convective boundary, rather than the first thermal boundary. The efficient of the heat exchange is described by the convective heat transfer coefficient between the fluid and the rock.

5 Results and discussion

5.1 Case 1

5.1.1 Temperature distribution induced by thermal shock

To describe the variation of the temperature at different time along the y direction, the nodes located in the middle of the plate (x = 0.025 m) are selected. With the distance from the upper surface increases from 0 m to 0.025 m, the temperature variations are shown in Figure 6. When the hot rock is subjected to thermal shock, it is a transient heat conduction process. The effect of the heat exchange cannot immediately occur in the whole rock. The efficient is determined by the thermal conductivity. Hence, the effect of the heat exchange time is an important factor when the temperature field is analysed. Generally, the temperature variation at different time is similar. As the heat exchange time continues, the temperature inside the rock gradually decreases. As shown in Figure 7, with the contact time between rock surface and cryogenic fluid increases, the temperature at the upper surface drops quickly. For example, when the time increases from 1 s to 50 s, the temperature drops from 133°C to 48°C. In a short period of time (e.g., t = 1 s, 5 s and 10 s), the process of the heat exchange only affects a certain distance from the upper surface, and the temperature of the region far away from the upper surface keeps constant. When the heat exchange time is 50 s, the temperature of larger region has dropped. With the location increases from 0 to 0.025 m, the variation rate of the temperature exhibits a characteristic of first fast and then slow. For the location

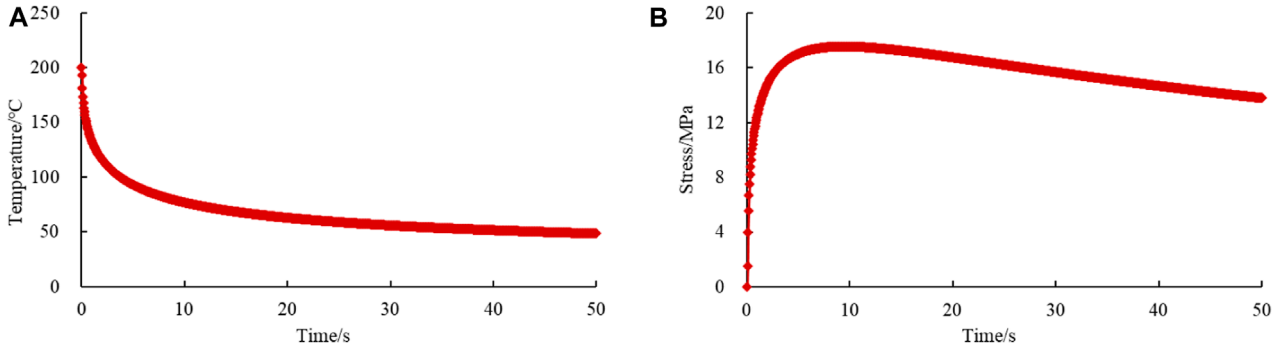


FIGURE 8
Variation of physical parameters with time at the upper surface (x = 0.025 m): **(A)** temperature; and **(B)** stress.

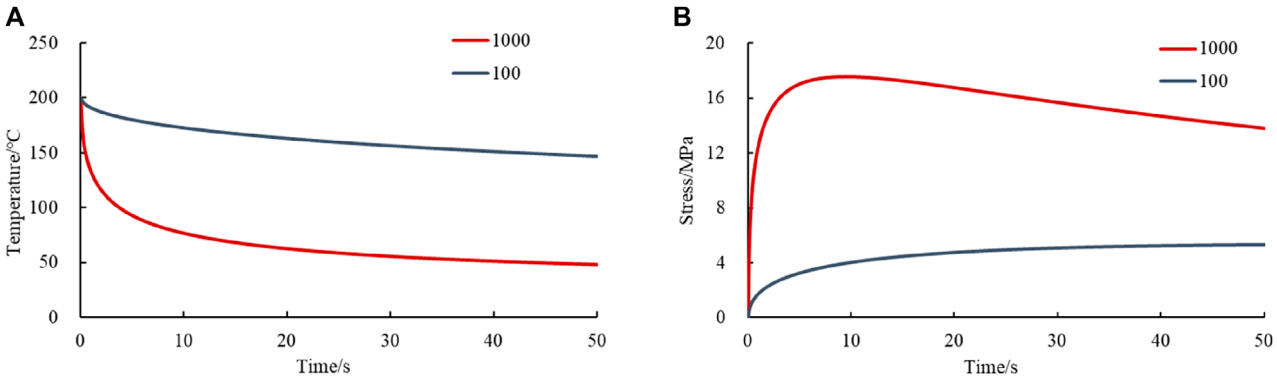


FIGURE 9
Effect of the heat exchange coefficient on the physical parameters at the upper surface (x = 0.025 m): **(A)** temperature, and **(B)** stress.

which is at 0.02 m from the upper surface, the temperature is 195°C and has only dropped by 5°C.

5.1.2 Stress distribution induced by thermal shock

During the process of heat exchange, the temperature distribution is non-uniform. Then, the temperature stress is induced by the temperature gradient. With the distance from the upper surface increases from 0 m to 0.025 m, the stress (along the x direction) variations are shown in Figure 7. At the thermal shock boundary, the temperature gradient is the highest. Hence, the maximum tensile stress (σ_t) occurs at the upper surface. When the heat exchange time is 1 s, σ_t is 12.5 MPa, which is greater than the tensile strength of shale. It can be seen that thermal shock in a short time is enough to generate damage in the rock. Similar with the temperature distribution, the stress occurs in the position which is near the upper surface. As the time of thermal shock increases, tensile stress is generated in a larger area inside the rock. With the location increases from 0 to 0.025 m, the stress quickly decreases, and the stress state transitions from tensile stress to compressive stress. Compare with the tensile area, the range of stress variation in the compressive area is relatively small.

5.1.3 Temperature and stress variation with time

5.1.3.1 Temperature variation

At the upper surface (x = 0.025 m), the variations of temperature with time are shown in.

Figure 8A. After the heat exchange of 50 s, the temperature decreases from 200°C to 50°C. The decline rate shows a trend of first fast and then slow (a) (b).

Figure 8A). In the first 5 s, the decrease of temperature can be up to 107°C. Over the next 5 s, the decrease of temperature is 16°C. Then, within the remaining 40 s, the temperature dropped by only 27°C. The decrease of temperature mainly occurs at the initial stage. For example, the temperature drop value in the first 5 s accounts for over 70% of the total decrease value. As the heat exchange continues, the temperature decreases slowly and tends to stabilize. According to the simulation results, it takes a time for the temperature at the boundary to decrease to the ambient temperature. More importantly, the efficiency of the thermal shock is determined by the heat exchange coefficient, and this parameter of different fluid varies greatly. Unfortunately, the first thermal boundary condition can not consider the effect of different fluid on the heat exchange. Applying this type of the boundary condition to the heat exchange

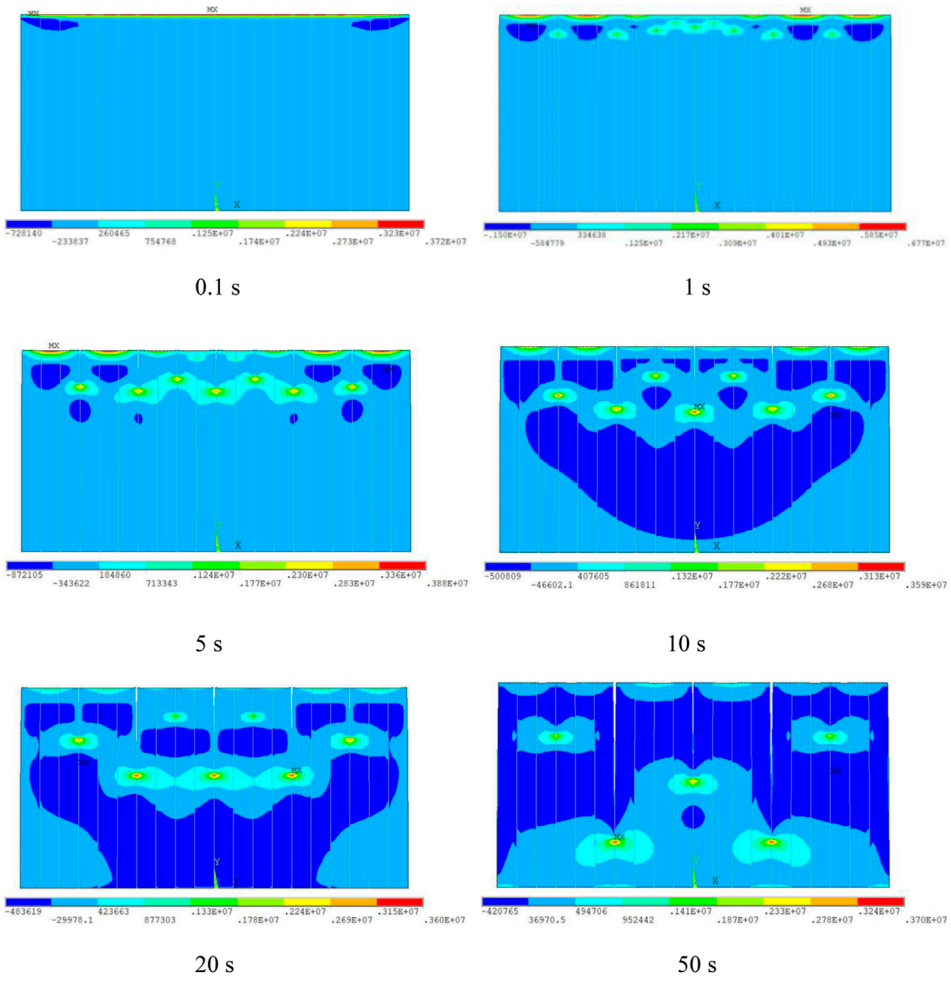


FIGURE 10
Propagation of fractures and stress distribution under thermal shock when heat exchange coefficient is 1,000 W/(m^{-2} K^{-1}).

surface is unreasonable. Otherwise, the effect of temperature stress will be overestimated.

5.1.3.2 Stress variation

At the upper surface (x = 0.025 m), the variations of stress with time are shown in Figure 8B. The stress variation is greatly determined by the temperature variation. Generally, the stress changes with time can be divided into three stages (a) (b).

Figure 8B firstly, the stress quickly increases to 12.5 MPa within 1 s. It corresponds to the stage of rapid decrease of temperature. Then, the stress slowly increases to the maximum stress, namely, 17.5 MPa, within the next 8.5 s. In the following heat exchange process, the stress decreases slowly. The final tensile stress value is 13 MPa. During the initial stage of thermal shock, the temperature of the heat exchange surface decreases rapidly and the cooling area is limited, which leads to a continuous increase in temperature gradient. Hence, the tensile stress generated at the heat exchange boundary continues to increase. Subsequently, due to the larger cooling area and the slow decrease rate of temperature at the upper surface, the temperature gradient gradually decreased, thereby reducing the tensile stress at the heat exchange boundary. Based on the stress variation with time, it can be concluded that once there is no damage occurred in the rock at the initial stage, there will be no damage in the later stage.

5.1.4 Effect of the heat exchange coefficient on the temperature and stress

The effect of the heat exchange coefficient on the variations of temperature and stress is shown in Figure 9. The heat exchange coefficient determines the decrease degree of the temperature. For example, when the values of the coefficient are 1000 W/(m^{-2} K^{-1}) and 100 W/(m^{-2} K^{-1}), the temperature drop is 150°C and 53°C, respectively. The difference is close to three times. Smaller heat exchange coefficient generates lower temperature gradient (Figure 9A). For the smaller coefficient of 100 W/(m^{-2} K^{-1}), the stress increases slowly during the whole thermal shock process (Figure 9B). After the thermal shock of 10 s, the stress is only 4 MPa, which is much lower than 18 MPa when the coefficient is 1000 W/(m^{-2} K^{-1}). Therefore, the heat exchange coefficient is an important parameter when selecting cryogenic fluid in thermal shock design.

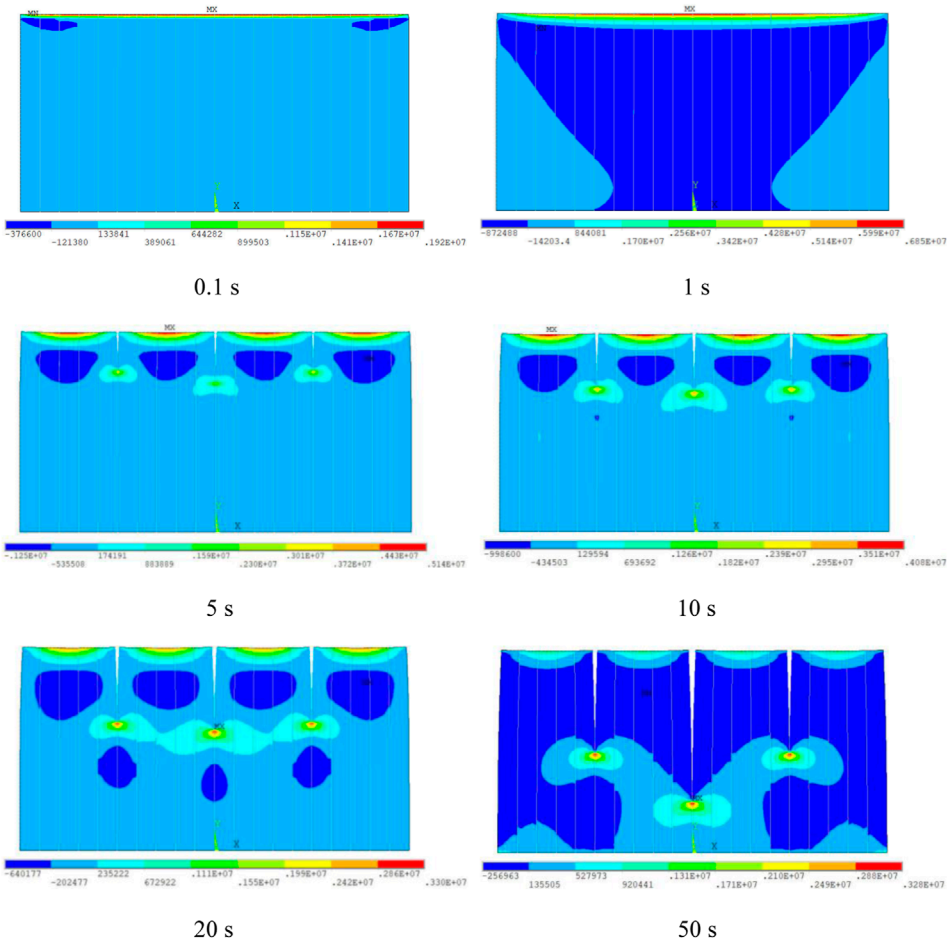


FIGURE 11
Propagation of fractures and stress distribution under thermal shock when heat exchange coefficient is 500 W/(m^{-2} K^{-1}).

5.2 Case 2

5.2.1 Propagation of fractures under thermal shock

When the tension stress exceeds the tensile strength, the fractures are generated in the rock. As the stress distribution is analysed above, the initiation of the fracture occurs at the upper surface, and the fractures propagate forward as the thermal shock continues. The initiation and propagation of multi-fracture is shown in Figure 10. In the initial stage (t = 0.1 s), the maximum tension stress is 3.7 MPa which is lower than the tension strength (7 MPa). Then, there is no fracture occurred in the upper surface. With thermal shock continues, the tension stress increases. Once the stress is greater than the tension stress, the rock is damaged. When t = 1 s, some fractures are generated and mainly concentrated in the middle area, which is determined by the stress distribution. The length of these fractures is relatively similar. Due to the small spacing between adjacent fractures, the propagation of a fracture inevitably affects the propagation of surrounding fractures. Hence, the multi-fracture propagation induced by thermal shock exhibits competition effect. During the subsequent thermal shock (t = 5–50 s), the competition effect is mainly manifested in three aspects: (1) there is difference in the fracture length; (2) the propagation rate of some fractures slows down, even being suppressed; and (3) some fractures change from the open state to the close state. After the thermal shock with 50 s, only two fractures keep propagating.

With the propagation of fractures, the stress distribution in the rock changes. When t = 0.1 s, the influence of thermal shock is mainly at the upper surface. The region is in a shrinkage state, and presents a tensile stress state. The interior of the rock is not affected by thermal shock and is in the compression state with low stress. With the heat exchange process continues (t = 1–5 s), the region surrounding the upper surface is affected by the fracture propagation. At the fracture tip, a stress concentration zone is formed. Because the temperature gradient is still high, the maximum tension stress occurs in the upper surface. When t = 10–20 s, the temperature gradient becomes small, and the maximum tension stress occurs in the fracture tip. It is noted that due to the stress release during fracture propagation, the maximum tension stress is small, which is lower than 4 MPa. In the interior of the rock, the influence of thermal shock is obvious gradually. The compressive stress decreases in the compression region. Finally, when t = 50 s, except for the region around the fracture tip, the other region in the rock is in a low stress zone.

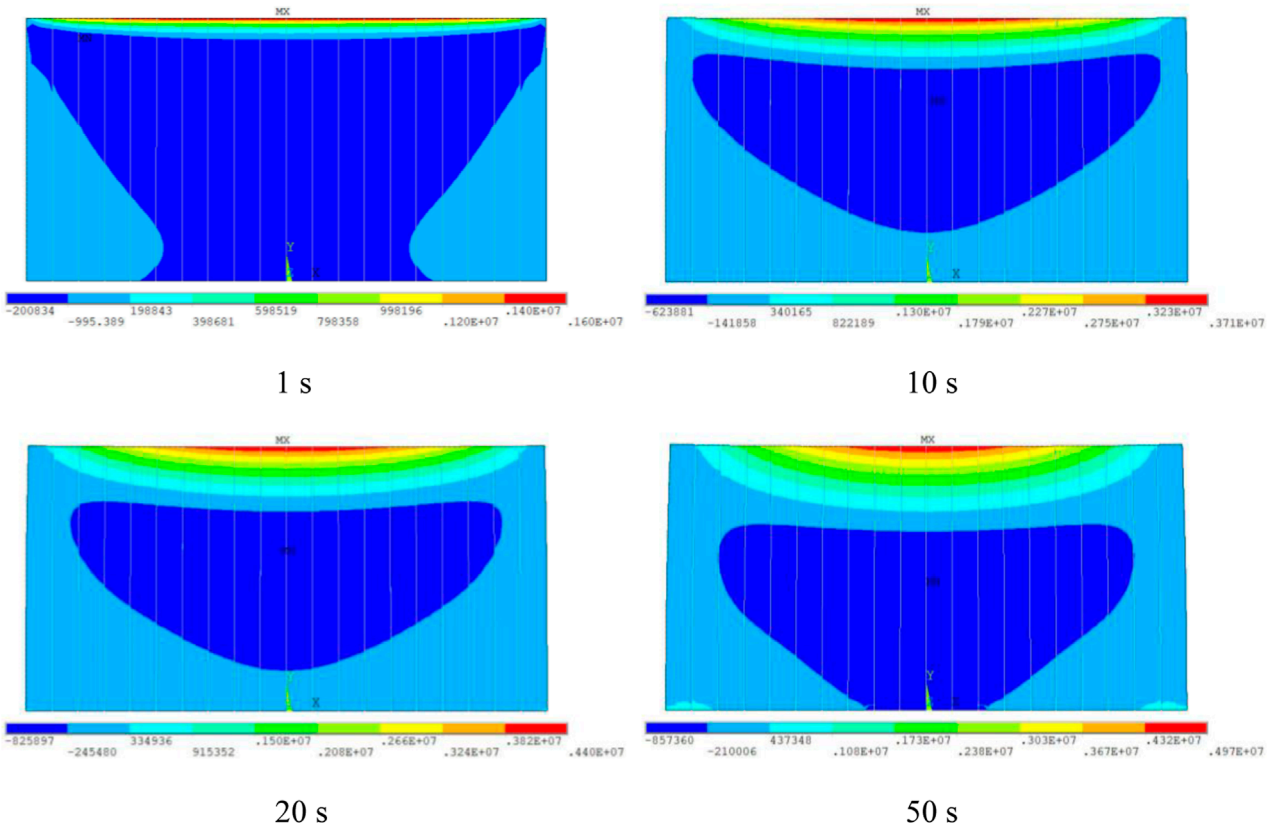


FIGURE 12
Stress distribution when the heat exchange coefficient is 100 W/(m^{-2} K^{-1}).

5.2.2 Effect of the heat exchange coefficient on the fracture propagation

When the heat exchange coefficient is 500 W/(m^{-2} K^{-1}), the propagation of fractures and stress distribution in the rock is shown in Figure 11. Unlike the former case, smaller coefficient induces lower temperature gradient. Then, the induced stress is also smaller. For example, when t = 1 s, the maximum stress in the upper surface is 6.8 MPa. During the period of thermal shock of 1 s, no fractures is generated in the rock. When t = 5 s, three fractures are generated. With thermal shock continues, the fractures propagate forward. However, there are no new fractures occurring. Generally, the characteristics is similar with the case with the coefficient of 1000 W/(m^{-2} K^{-1}).

When the heat exchange coefficient is 100 W/(m^{-2} K^{-1}), the stress distribution in the rock is shown in Figure 12. The maximum tension stress increases with the process of heat exchange. However, after the thermal shock of 50 s, the maximum tension stress is 5 MPa, which is lower than 7 MPa. Thus, there is no fractures generated in the rock.

Based on the analysis above, the heat exchange coefficient has a significant effect on fracture initiation and propagation. When the coefficient is small (e.g., 100 W/(m^{-2}·K^{-1})), there is no fracture generated in the rock. As the coefficient increases, the induced tension stress becomes high and lead to the fracture initiation. More important, the larger the coefficient, the more fractures are generated. Therefore, the fractures induced by thermal shock not only depend on the temperature difference between the hot rock and the cryogenic fluid, but also are determined by the heat exchange coefficient. By applying the heat convective boundary, the effect of the fracturing fluid on the fracture initiation and propagation can be further discussed.

6 Summary and conclusion

In this paper, a TH coupled model is developed to study the thermal shock process. The novel model considers the heat conductive boundary between the hot rock and the cryogenic fluid. Then, effect of the thermal shock on the distribution of the temperature and stress, as well as the initiation and propagation of fractures are analysed. The conclusions are summarized as follows:

(1) Once the thermal shock occurs, the temperature at the upper surface drops quickly. The temperature inside the rock gradually decreases. With the location increases from 0 to 0.025 m, the variation rate of the temperature exhibits a characteristic of first fast and then slow. Due to the temperature gradient, the stress occurs in the rock. With the location increases from 0 to 0.025 m, the stress quickly decreases, and the stress state translates from tensile stress to compressive stress.

(2) At the upper surface, the temperature decline rate shows a trend of first fast and then slow. The stress changes with time can be divided into three stages, which is very important to rock damage. Once there is no damage occurred in the rock at the initial stage, there will be no damage in the later stage. In addition, the variations of temperature and stress are greatly affected by the heat exchange coefficient.

(3) With thermal shock continues, the tension stress increases. As the stress is greater than the tension strength, the rock is damaged. The multi-fracture propagation induced by thermal shock exhibits competition effect. This process is very important to further fracturing. With the propagation of fractures, the stress distribution in the rock changes. The heat exchange coefficient has a significant effect on fracture initiation and propagation. The larger the coefficient, the more fractures are generated.

Data availability statement

The original contributions presented in the study are included in the article/supplementary material, further inquiries can be directed to the corresponding author.

Author contributions

All authors listed have made a substantial, direct, and intellectual contribution to the work and approved it for publication.

Funding

This study was financially supported by the major project of National Natural Science Foundation of China (Grant No. 52192622), the Key Laboratory of Shale Gas Exploration, Ministry of Natural Resources (Grant No. KLSGE-202103) the Science and Technology Department of Sichuan Province (Grant Nos. 2021YFH0118 and 2021YFH0048) and the Natural Science Foundation of Chongqing, China (Grant No. CSTB2022NSCQ-BHX0721).

Conflict of interest

Author YL was employed by the China Petroleum Xinan Oil & Gas Field Company Chongqing Gas Mine.

The remaining authors declare that the research was conducted in the absence of any commercial or financial relationships that could be construed as a potential conflict of interest.

Publisher's note

All claims expressed in this article are solely those of the authors and do not necessarily represent those of their affiliated organizations, or those of the publisher, the editors and the reviewers. Any product that may be evaluated in this article, or claim that may be made by its manufacturer, is not guaranteed or endorsed by the publisher.

References

Bahr, H. A., Hans-Jürgen, W., Bahr, U., Hofmann, M., Fischer, G., Lampenscherf, S., et al. (2010). Scaling behavior of thermal shock crack patterns and tunneling cracks driven by cooling or drying. *J. Mech. Phys. Solids* 58 (9), 1411–1421. doi:10.1016/j.jmps.2010.05.005

Burlayenko, V. N., Altenbach, H., Sadowski, T., and Dimitrova, S. D. (2016). Computational simulations of thermal shock cracking by the virtual crack closure technique in a functionally graded plate. *Comput. Mater. Sci.* 116, 11–21. doi:10.1016/j.commatsci.2015.08.038

Cai, C., Li, G., Huang, Z., Shen, Z., Tian, S., and Wei, J. (2014). Experimental study of the effect of liquid nitrogen cooling on rock pore structure. *J. Nat. Gas Sci. Eng.* 21, 507–517. doi:10.1016/j.jngse.2014.08.026

Cha, M., Alqahtani, N. B., Yin, X., Kneafsey, T. J., Yao, B., and Wu, Y. S. (2017). Laboratory system for studying cryogenic thermal rock fracturing for well stimulation. *J. Petroleum Sci. Eng.* 156, 780–789. doi:10.1016/j.petrol.2017.06.062

Cha, M. S., Yin, X. L., Kneafsey, T., Johanson, B., Alqahtani, N., Miskimins, J., et al. (2014). Cryogenic fracturing for reservoir stimulation - laboratory studies. *J. Nat. Gas Sci. Eng.* 124, 436–450. doi:10.1016/j.petrol.2014.09.003

Chang, X., Xu, E., Guo, Y. T., Yang, C. H., Hu, Z. W., and Guo, W. (2022). Experimental study of hydraulic fracture initiation and propagation in deep shale with different injection methods. *J. Petroleum Sci. Eng.* 216, 110834. doi:10.1016/j.petrol.2022.110834

Dahi, T. A., Ahmadi, M., Wang, W., and Olson, J. E. (2014). Thermal reactivation of microfractures and its potential impact on hydraulic-fracture efficiency. *SPE-180071-PA* 19, 761–770. doi:10.2118/163872-pa

Enayatpour, S., Van, O. E., and Patzek, T. (2018b). Thermal cooling to improve hydraulic fracturing efficiency and hydrocarbon production in shales. *J. Nat. Gas Sci. Eng.* 62, 184–201. doi:10.1016/j.jngse.2018.12.008

Enayatpour, S., Van, O. E., and Patzek, T. (2018a). Thermal shale fracturing simulation using the Cohesive Zone Method (CZM). *J. Nat. Gas Sci. Eng.* 55, 476–494. doi:10.1016/j.jngse.2018.05.014

Garcia, J., Hartline, C., Walters, M., Wright, M., Rutqvist, J., Dobson, P. F., et al. (2015). The northwest geysers EGS demonstration project, California- Part1: Characterization and reservoir response to injection. *Geothermics* 63, 97–119. doi:10.1016/j.geothermics.2015.08.003

Guo, J. C., Zhao, Z. H., Lu, Q. L., Yi, C. B., and Chen, C. G. (2021). Research progress in key mechanical theories of deep shale network fracturing. *Nat. Gas. Ind.* 41 (01), 102–117. doi:10.3787/j.issn.1000-0976.2021.01.009

Han, S. C., Gao, Q., Cheng, Y. F., Yan, C. L., Han, Z. Y., and Shi, X. (2020). Experimental study on brittle response of shale to cryogenic fluid nitrogen treatment. *J. Nat. Gas Sci. Eng.* 194, 107463. doi:10.1016/j.petrol.2020.107463

Huang, L. K., He, R., Yang, Z. Z., Tan, P., Chen, Z. W., Li, X., et al. (2023). Exploring hydraulic fracture behavior in glutenite formation with strong heterogeneity and variable lithology based on DEM simulation. *Eng. Fract. Mech.* 278, 109020. doi:10.1016/j.engfracmech.2022.109020

Huang, L., Liu, J., Zhang, F., Donstov, E., and Damjanac, B. (2019). Exploring the influence of rock inherent heterogeneity and grain size on hydraulic fracturing using discrete element modeling. *Int. J. Solids Struct.* 176, 207–220. doi:10.1016/j.ijsolstr.2019.06.018

Kim, K. M., and Kemeny, J. (2009). "Effect of thermal shock and rapid unloading on mechanical rock properties," in 43rd US Rock Mechanics Symposium and 4th US-Canada Rock Mechanics Symposium, Asheville, North Carolina, June - 1 July 2009 (American Rock Mechanics Association), 1–10.

Qin, L., Zhai, C., Liu, S., and Xu, J. (2018). Mechanical behavior and fracture spatial propagation of coal injected with liquid nitrogen under triaxial stress applied for coalbed methane recovery. *Eng. Geol.* 233, 1–10. doi:10.1016/j.enggeo.2017.11.019

Rutqvist, J., Jeanne, P., Dobson, P. F., Garcia, J., Hartline, C., Hutchings, L., et al. (2015). The northwest geysers EGS demonstration project, California-Part2: Modeling and interpretation. *Geothermics* 63, 120–138. doi:10.1016/j.geothermics.2015.08.002

Tan, P., Jin, Y., and Pang, H. W. (2021). Hydraulic fracture vertical propagation behavior in transversely isotropic layered shale formation with transition zone using XFEM-based CZM method. *Eng. Fract. Mech.* 248, 107707. doi:10.1016/j.engfracmech.2021.107707

Tang, S. B., Wang, J. X., and Chen, P. Z. (2020). Theoretical and numerical studies of cryogenic fracturing induced by thermal shock for reservoir stimulation. *Int. J. Rock Mech. Min. Sci.* 125, 104160. doi:10.1016/j.ijrmms.2019.104160

Tang, S. B., Zhang, H., Tang, C. A., and Liu, H. Y. (2016). Numerical model for the cracking behavior of heterogeneous brittle solids subjected to thermal shock. *Int. J. Solids Struct.* 80, 520–531. doi:10.1016/j.ijsolstr.2015.10.012

Tomac, I., and Gutierrez, M. (2017). Coupled hydro-thermo-mechanical modeling of hydraulic fracturing in quasi-brittle rocks using BPM-DEM. *J. Rock Mech. Geotechnical Eng.* 9 (1), 92–104. doi:10.1016/j.jrmge.2016.10.001

Tran, D., Settari, A., and Nghiem, L. (2012). "Initiation and propagation of secondary cracks in thermo-poroelastic media," in 46th U.S. Rock Mechanics/Geomechanics Symposium, Chicago, Illinois, June 2012 (American Rock Mechanics Association).

Trevisan, A., Borzi, G. P., Movchan, N. V., Movchan, A. B., and Brun, M. (2016). Thermal shock driven fracture in a structured solid: Dynamic crack growth and nucleation. *Int. J. Fract.* 202, 167–177. doi:10.1007/s10704-016-0118-6

Wang, L., Yao, B., Cha, M., Alqahtani, N. B., Patterson, T. W., Kneafsey, T. J., et al. (2016). Waterless fracturing technologies for unconventional reservoirs-opportunities for liquid nitrogen. *J. Nat. Gas Sci. Eng.* 35, 160–174. doi:10.1016/j.jngse.2016.08.052

Xu, Z. L. (2016). *Elastic mechanics*, 1. Beijing: Higher Education Press.

Yang, R. Y., Huang, Z. W., Shi, Y., Yang, Z. Q., and Huang, P. P. (2019). Laboratory investigation on cryogenic fracturing of hot dry rock under triaxial-confining stresses. *Geothermics* 79, 46–60. doi:10.1016/j.geothermics.2019.01.008

Yao, B. W., Wang, L., Yin, X. L., and Wu, Y. S. (2017). Numerical modeling of cryogenic fracturing process on laboratory-scale Niobrara shale samples. *J. Nat. Gas Sci. Eng.* 48, 169–177. doi:10.1016/j.jngse.2016.10.041

Zhang, X., Lu, Y., Tang, J., Zhou, Z., and Liao, Y. (2016). Experimental study on fracture initiation and propagation in shale using supercritical carbon dioxide fracturing. *Fuel* 190, 370–378. doi:10.1016/j.fuel.2016.10.120

Zhang, Z., Xiong, Y. M., Mao, L. J., Lu, J., Wang, M., and Peng, G. (2019). Transient temperature prediction models of wellbore and formation in well-kick condition during circulation stage. *J. Petroleum Sci. Eng.* 175, 266–279. doi:10.1016/j.petrol.2018.12.044

Zhao, J. Z., Ren, L., Jiang, T. X., Hu, D. F., Wu, L. Z., Wu, J., et al. (2022). Ten years of gas shale fracturing in China: Review and prospect. *Nat. Gas. Ind. B* 9 (2), 158–175. doi:10.1016/j.ngib.2022.03.002

Zhao, P., Liu, J., and Derek, E. (2023). Numerical study on a multifracture enhanced geothermal system considering matrix permeability enhancement induced by thermal unloading. *Renew. Energy* 203, 33–44. doi:10.1016/j.renene.2022.12.056

frontiers | Frontiers in Energy Research

TYPE Original Research
PUBLISHED 27 July 2023
DOI 10.3389/fenrg.2023.1217467

Check for updates

OPEN ACCESS

EDITED BY
Xiaojin Zheng,
Princeton University, United States

REVIEWED BY
Guodong Zhang,
Qingdao University of Science and Technology, China
Ying Zhong,
Chengdu University of Technology, China

*CORRESPONDENCE
Song Li,
lisong03011640@163.com

RECEIVED 05 May 2023
ACCEPTED 12 July 2023
PUBLISHED 27 July 2023

CITATION
Li S, Fan Y, He T, Yang J, Li J and Wang X (2023), Research and performance optimization of carbon dioxide foam fracturing fluid suitable for shale reservoir.
Front. Energy Res. 11:1217467.
doi: 10.3389/fenrg.2023.1217467

COPYRIGHT
© 2023 Li, Fan, He, Yang, Li and Wang. This is an open-access article distributed under the terms of the Creative Commons Attribution License (CC BY). The use, distribution or reproduction in other forums is permitted, provided the original author(s) and the copyright owner(s) are credited and that the original publication in this journal is cited, in accordance with accepted academic practice. No use, distribution or reproduction is permitted which does not comply with these terms.

Research and performance optimization of carbon dioxide foam fracturing fluid suitable for shale reservoir

Song Li[1,2]*, Yu Fan[1,2], Tingting He[1], Jian Yang[1,2], Jinsui Li[1] and Xi Wang[1]

[1]Engineering Technology Research Institute of PetroChina Southwest Oil & Gas Field Company, Chengdu, China, [2]National Energy R&D Center of High Sulfur Gas Exploitation, Guanghan, China

Compared to conventional fracturing techniques, foam fracturing has numerous advantages, including good shear resistance, strong sand carrying capacity, low fluid loss, low damage, and fast return rates. It is particularly suitable for stimulation in low pressure, low permeability, and water-sensitive formations. Specifically, CO_2 foam fracturing is crucial in energy savings and emission reductions, controlling the expansion of reservoir clay minerals, reducing crude oil viscosity, and improving the production of water-locked reservoirs. In this paper, we investigate the foam fracturing fluid and evaluate its performance. We selected thickeners with good foaming stability and foaming agents with excellent performance at low dosage levels, based on experimental evaluation. We finally determined the formulation of the foam fracturing fluid by analyzing the experimental data, such as foam half-life, foam mass, and viscosity. We experimentally evaluated the viscosity, static sand settling properties, and rheological properties of the fluid. After being tested on the reservoir core, the foam fracturing fluid has a viscosity of 2 mPas. Moreover, the residue content is 1.1 mg/L, the surface tension is 24.5 mN/m, and the interfacial tension is 1.5 mN/m. The fluid-carrying sand experiment of 40–70 mesh ceramic particles, commonly used in shale gas fracking, was evaluated. The sand-to-liquid ratio was set at 40% for the static sand-carrying experiment. The flow of the fluid-carrying sand was good, and the settling property was satisfactory for 3 h. We used shale reservoir cores from well W-1 to assess the rate of foam fracture, which was less than 19%. Under the experimental conditions of a shear rate of 170 S^{-1} and a temperature of 90°C, the viscosity of fracturing fluid was measured to be greater than 50 mPas, 90 min after shear, demonstrating the excellent temperature and shear resistance of the foam fracturing fluid. Using CO_2 foam fracturing fluid can significantly improve the reconstruction effect of low permeability hydrocarbon reservoirs (especially unconventional reservoirs) and solve problems related to water resources and environmental protection during the process of oil and gas reservoir development. It will be a major factor in improving construction impacts and addressing water and environmental concerns for low permeability hydrocarbon reservoirs, particularly unconventional ones that utilize CO_2 foam fracturing fluids.

KEYWORDS

shale gas reservoir, carbon dioxide, foam fracturing, foam quality, rheological property

1 Introduction

In recent years, with the rapid development of shale gas, the exploration and development of shale reservoirs have attracted more and more attention. The fracturing technology of shale reservoirs has become an important research area in the petroleum industry. China is rich in shale gas resources. The country's shale gas geological reserves are estimated at 134.42 trillion cubic meters, with a recoverable resource potential of 25.08 trillion cubic meters. This is roughly equivalent to the United States' technically recoverable reserves of 28 trillion cubic meters. Based on the US development experience, the key and core technology for efficient exploration and development of shale gas is horizontal well volume fracturing with slick water (Harris and Reidenbach, 1987; LIU et al., 2004; WANG et al., 2004; Yang et al., 2006; Tan et al., 2020; Tan et al., 2021; Huang et al., 2023). However, this development technique requires large amounts of water and can cause significant damage to the environment. According to the statistics of the US Environmental Protection Agency (EPA), a single shale gas well can consume approximately 0.76–2.39 ten thousand tons of water. While the United States is relatively water-rich and can roughly meet their development needs, China's relative lack of water resources makes it challenging to meet the huge demand for clean water (Reidenbach, 1986; Cawiezel, 1987; Harris and Heath, 1996; Zheng et al., 2020). In addition, the clay mineral content is relatively high in shale gas reservoirs in China, with terrestrial shale gas reservoirs having a clay mineral content of more than 60%. When conventional water-based fracturing fluids are used in these reservoirs, the clay minerals expand in contact with the water and cause significant permeability damage in shale reservoirs. Shale gas reservoirs in China are generally low in pressure and this may cause conventional water-based fracturing fluids to consume large amounts of water, thus causing significant damage to reservoirs, as well as having a low rate of return. Therefore, rather than simply copying other technologies, it is urgent to develop advanced fracturing technologies that use less water (or no water), are environmentally friendly, and cause relatively little damage to the reservoir (TUDOR et al., 1994; MAZZA and QUID, 2383; Luo XiangRong et al., 2014).

Foam fracturing fluids are a major achievement in liquid technology. They are liquid formations that disperse nitrogen or carbon dioxide as bubbles in water, acid, methanol/water mixtures, or hydrocarbon liquids. These fluids usually consist of 70%–80% gas (nitrogen or carbon dioxide) and water-based polymer. They can be considered as emulsions of gas-coated liquid, providing high viscosity and excellent proppant carrying capacity. Due to their low damage to oil and gas reservoirs, strong flowback capacity, small filtration loss, high fluid utilization efficiency, appropriate viscosity, and strong sand carrying capacity, foam fracturing fluids hold a significant position in frac fluid systems. As the world focuses more on carbon emissions and the demand for natural gas increases, the utilization of CO_2 will receive increased attention.

The properties of CO_2 foam fracturing fluid also have an impact on hydraulic fracture propagation. Several authors have reported the high performance of CO_2 foam due to its unique and favorable rheological characteristics (Barati and Liang, 2014; Sun et al., 2014; Li et al., 2015; Wanniarachchi et al., 2017; Ahmed et al., 2019; Ahmed S. et al., 2021). However, the flow behavior of foam, especially under operating conditions, is difficult to understand and model due to its complex nature. The versatility and uniqueness of foam can be attributed to its significantly higher viscosity compared to its base fluids, and the efficiency of foam fracturing is determined by its complex non-Newtonian behavior (Arezoo et al., 1858; Ahmed et al., 2017a; Jing et al., 2017; Verma et al., 2018; Wang et al., 2018; Ahmed Abdelaal et al., 2021). Numerous authors agree that foam rheology highly influences the design and overall performance of fracturing treatments (Luo X. et al., 2014; Edrisi and Kam, 2014; Gu and Mohanty, 2015; Ahmed et al., 2017b; Fei et al., 2017; Li et al., 2017; Verma et al., 2017; Kartini et al., 2021; Cong et al., 2022; Li et al., 2022; Wang et al., 2022; Gao et al., 2023). Currently, foam fracturing technology has reached a relatively mature stage in terms of indoor research, design, construction, and effectiveness assessment. From the development of foam fracturing fluid technology, it can be summarized into three processes. The first generation of foam fracturing fluids primarily consisted of water, brine, acid, alcohol, and crude oil as base fluids, and were prepared by mixing nitrogen and foaming agents with the base fluids. These fluids feature low filtration loss, strong sand carrying capacity, and fast flowback, but have low viscosity and short foam lifetime, making them only suitable for shallow wells and small-scale fracturing construction (Liu et al., 2020). The second generation of foam fracturing fluid is formed by adding linear glue, a foam stabilizer, to the first generation. In addition to the advantages of the first-generation fluids, the second-generation fluids have a longer foam lifetime, relatively higher viscosity, better sand carrying capacity, etc., making them suitable for frac construction in various wells (Feng et al., 2021). The third-generation foam fracturing fluid uses a delayed cross-linking gel as a foam stabilizer. It has a longer foam lifetime, higher viscosity, and stronger sand carrying capacity compared to the second-generation foam fracturing fluids.

The CO_2 foam fracturing fluid not only increases the viscosity of the fracturing fluid but also effectively controls the filtration of the fluid. In water-sensitive reservoirs, such as shale reservoirs, stable foam quality, low damage, good sand carrying capacity and reliability should also be considered to reduce water consumption.

The purpose of this research is to optimize the carbon dioxide foam fracturing fluid and to improve its applicability to shale reservoirs, so as to improve the fracturing effect and reduce the damage to the reservoir. This paper analyses the characteristics and advantages of carbon dioxide foam fracturing fluid and its applicability to shale reservoirs, and summarizes the research progress in this field. Therefore, we conducted experiments to optimize the thickening agent and foaming agent, to achieve good foaming stability, foaming power, and foaming stability at low dosage levels. We also developed a formulation for foaming fracturing fluid and evaluated its performance in reservoir damage and recovery feasibility. In conclusion, the research and optimization of carbon dioxide foam fracturing fluid suitable for shale reservoir has great theoretical and practical significance for the development of shale gas. By improving the fracturing effect and reducing the damage to the reservoir, it can contribute to the sustainable development of the petroleum industry and the protection of the environment.

2 Study on formula of foam fracturing fluid

Carbon dioxide foam fracturing fluid has the advantages of high viscosity and good carrying capacity, which can effectively reduce the damage of shale reservoirs during fracturing operations, and improve the production performance of shale gas wells. The selection of surfactants, crosslinking agents, and other components in the fluid formulation is an important factor affecting its performance in the field. The thickeners and foaming agents for foam fracturing fluids were experimentally evaluated. A thickener with good foaming properties and a foaming agent with good foaming strength and stability were selected in small amounts. The foam fracturing fluid formulation was developed and the performance of the developed formulation was assessed.

2.1 Experimental methods

The Waring Blender method was used to evaluate the foaming ability and foaming stability of the foaming agent, taking into consideration the characteristics of the foaming fracturing fluid (Dong et al., 2021; Zhu and Zheng, 2021; Ju et al., 2022). The properties of the foaming agent were determined using a high-speed agitator.

To evaluate the foaming ability and foaming stability of the foaming agent, 100 mL of the foaming agent solution (foaming agent + thickening agent + water) was poured into the mud cup and stirred at a specified high speed (>10000 r/min) for 60 s. The foam volume V0 (in mL) when stirring is stopped represents the foaming capacity, while the time (in minutes) when half of the liquid (50 mL) separates the foam represents the foam stability, also known as foam half-life.

2.2 Optimization of thickener

In order to select a thickener that can form a sand washing liquid with good foam stability at a lower dosage, the foam stability performance of the collected thickeners, such as hydroxypropyl guar gum (CT1, CT1WI), Instant solution carboxymethyl cellulose (CMC), carboxymethyl cellulose (CMC) and polyanionic cellulose (PAC), was evaluated and optimized. The evaluation process involved assessing the foam stability of each thickener, which can be seen in Table 1.

Firstly, the foam stability performance of hydroxypropyl guar gum (CT1, CT1WI) was evaluated. Next, the foam stability of Instant solution carboxymethyl cellulose (CMC) was examined. Then, the foam stability of carboxymethyl cellulose (CMC) was tested. Finally, the foam stability of polyanionic cellulose (PAC) was assessed. The purpose of this evaluation was to identify a thickener with excellent foam stability properties when used at a lower dosage.

In conclusion, the chosen thickeners were subjected to a comprehensive evaluation and optimization process to determine their foam stability. Table 1 provides a summary of the results.

CT1 thickener was selected as the thickener for foam fracturing fluid due to its superior foam stabilization performance compared to other available options, as indicated in Table 1. The data presented in the table illustrate that CT1 outperforms other thickeners in terms of foam stability, providing a reliable solution for foam fracturing fluid.

2.3 Optimization of foaming agent

The foaming capacity and half-life of various foaming agents, namely, CT1B, CT1S, sodium dodecyl benzene sulfonate (ABS), alkyl betaine (DSB), and CT1C, were evaluated in the thickener solution of CT1WII. Table 1 presents the results, where the foam quality is calculated using the formula $(V_0\text{-}100)/V_0$. After a

TABLE 1 Bubble stability evaluation of thickener.

Thickener	Regulator	Foaming agent	V_0, mL	Foam quality, %	Half-life of foam, hour
0.3% CT1	0.3% CT1U	0.3% CT1B	354	71.8	90
0.5% CT1WI			325	69.2	75
0.5% Hydroxypropyl guar gum			266	62.4	65
0.5% Instant solution CMC			266	62.4	16
0.5% CMC			262	61.8	27
0.5% PAC			269	62.8	14

TABLE 2 Evaluation of foaming power and foam stability of foaming agent.

Thickener	Foaming agent	V_0, mL	Foam quality, %	Half-life of foam, hour
0.5% CT1	0.3% CT1B	262	61.8	115
	0.3% CT1S	292	65.7	125
	0.3% DSB	288	65.3	105
	0.3% CT1C	292	65.7	110
	0.3% ABS	292	65.7	100

TABLE 3 Suspensibility of liquids at different temperatures (mm/s).

Dosage of CT1, %	Indoor temperature, °C				
	15	30	50	70	90
0.2	12.50	25.00	33.30	50.0	100.00
0.3	0.70	1.29	2.32	5.56	9.52
0.4	0.019	0.057	0.11	0.70	0.98
0.5	Almost stationary	Almost stationary	0.046	0.16	0.46

comprehensive analysis of the foaming power and stability data provided in Table 2, CT1S was chosen as the ideal foaming agent due to its excellent foaming power and stability. Consequently, CT1S was selected for use in foaming fracturing fluids.

2.4 Determination of dosage of thickening agent

2.4.1 Suspensibility of liquid with different thickening agent dosage

The settling rate of sand in the washing fluid with different dosage of thickening agent (0.2%, 0.3%, 0.4%, and 0.5%) was evaluated at temperatures ranging from 30°C to 90°C, and the results are presented in Table 3. As shown in Table 3, the settling velocity of sand in the liquid increases with increasing experimental temperature. When the dosage of thickening agent is 0.2% and the temperature is 90°C, the sustainability of the liquid is poor. When the dosage of thickening agent is increased to 0.3% or 0.4% and the temperature is 90°C, the sand settles at a rate of 1–10 mm/s. When the dose of the thickening agent was increased to 0.5%, the sand hardly sank.

After foam formation, the apparent viscosity of the liquid increases, which substantially enhances its ability to suspend and carry solid particles. The laboratory evaluation of foam sustainability shows that the sand particles are almost stationary when the dosage of thickening agent is 0.5% at a temperature of 90°C.

2.4.2 Foam stability under different thickening agent dosage

The stability, or half-life, of CT1S foam with foaming agents at 0.3% and thickening agents at 0.2%, 0.3%, 0.4%, and 0.5% were evaluated at temperatures ranging from 15°C to 90°C. As Table 4 shows, the foam half-life decreased as temperature increased. At 90°C, when the thickening agent dosage was 0.2%, the foam half-life was only 0.2 h. But when the dosage was at 0.3%–0.4%, the foam half-life increased to 1.3–2.3 h. Finally, when the dosage reached 0.5% and the temperature remained at 90°C, the foam stability reached a high of 4.1 h. Through a comprehensive analysis of the experimental data on viscosity, foam stability, and half-life, the optimum concentration of thickening agent for the foamed fracturing fluid was found to be 0.5%.

2.5 Determination of foaming agent dosage

To determine the appropriate amount of foaming agent required, a CT1S foaming agent at 0.5%, 1.0%, and 1.5% dosage was tested at 30 °C, while the CT1WII thickener was used at a dosage of 0.5%. The corresponding data obtained from the experiment is stated in Table 5.

According to Table 5, when the amount of CT1S foaming agent increases from 0.1% to 0.3% under the same experimental conditions, the foam half-life shows an increasing trend. Considering performance and cost factors, the amount of CT1S foaming agent was determined to be 0.3%.

2.6 Formula of foam fracturing fluid

To ensure the formulation of foam fracturing fluid meets the desired requirements, the experimental data on foam half-life, foam mass, and viscosity of individual agents, such as foaming and thickening agents, is analyzed. Subsequently, the formulation of the foam fracturing fluid is determined based on the analysis.

0.5% CT1 thickener +0.3% CT1S foaming agent +0.3% CT1D high temperature stabilizer +0.3% CT1U regulator.

3 Performance of foam fracturing fluid formulation

3.1 Preparation method of foam fracturing fluid

Preparation of the fracturing fluid base: Place the desired liquid mixture in a paddle mixer and adjust the mixer rotation speed until the mid-axis of the paddle blade is visible from the vortex. Next, add the regulator, temperature stabilizer, and potassium chloride

TABLE 4 Foam half-life at different temperatures.

CT1%	15°C		30°C		50°C		70°C		90°C	
	Foam quality, %	Half-life of foam, h	Foam quality, %	Half-life of foam, h	Foam quality, %	Half-life of foam, h	Foam quality, %	Half-life of foam, h	Foam quality, %	Half-life of foam, h
0.2	75.18	89.3	79.2	74	79.71	40.5	82.56	21	93.37	0.2
0.3	71.63	93	76.52	77	76.85	60.4	80.8	37.4	92.52	1.3
0.4	69.6	109.7	71.63	106.2	74.38	70	79.42	56.5	91.12	2.3
0.5	66.1	134	67.1	120	71.34	90.6	77.67	68.3	89.43	4.1

TABLE 5 Foam half-life with different amounts of CT1S.

Foaming agent	Thickener	V_0, mL	Foam quality, %	Half-life of foam, hour
0.1% CT1S	0.5% CT1WII	288	65.3	90
0.2% CT1S		292	65.7	110
0.3% CT1S		292	65.9	125



FIGURE 1
Configured CO_2 foam fracturing fluid.

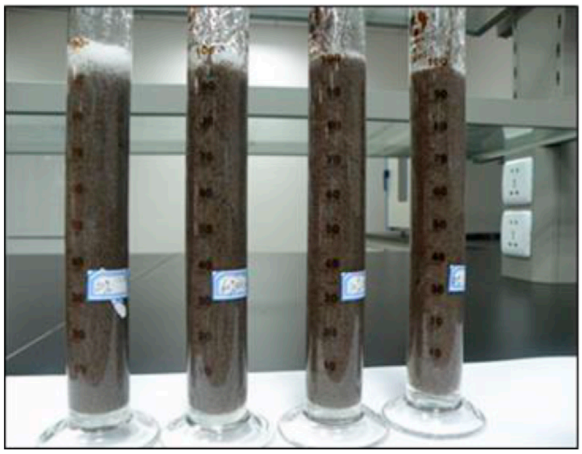


FIGURE 2
Evaluation of static sand settling performance of foam fracturing fluid.

to the water and stir until they are well mixed. Slowly pour in the thickener while stirring and stop once an even solution is formed. Pour the mixture into a beaker and let it swell for 4 hours to form the fracturing fluid base.

Preparation of the water-based fracturing fluid: Add the designed proportion of foaming agent to the fracturing fluid base and stir well to form water-based fracturing fluid without foaming. Preparation of the foaming fracturing fluid: Pour a certain volume of the base fluid of the fracturing fluid into a Waring blender, add the designed proportion of foaming fluid, and seal the blender. Inject CO_2 slowly into the solution and set the blender speed to 700 r/min. Stir for 5 min and stop once the desired froth volume is achieved. The prepared CO_2 foam fracturing fluid is shown in Figure 1, which was used to evaluate its performance in experiments.

3.2 Gel breaking performance of foam fracturing fluid

The residue content test of foam fracturing fluid is carried out according to the oil and gas industry standard SY/T5107-2005″Performance Evaluation Method of Water-based Fracturing Fluid". Firstly, the prepared 1,000 mL foam fracturing fluid was evenly divided into two groups. Then, 600 ppm of the gel breaking agent was added to each group. The gel was broken at 90 °C. After thorough gel fragmentation, centrifugal separation was performed. The separated residue was dried and weighed at 105°C ± 1°C to determine the content of residue in the fracturing fluid. The results of the tests are given in Table 6. The residue content of the gel breakup liquid is calculated as follows.

$$\eta = m/V \times 1000$$

η — Residue content in breaking liquid, mg/L. m — Residue quality, mg. V — Fracturing fluid volume, mL.

3.3 Static sand settling performance of foam fracturing fluid

The foam fluid used for fracturing (with 65% Q value) was prepared using the liquid preparation method. Specifically, 200 mL of the foam fluid was added to a beaker, which was then placed in a water bath at a temperature of 90°C for 20 min. During the steady-state water bath, the volume of clear liquid precipitated from the upper layer was recorded at regular intervals, and the results of the liquid static sand settling experiment are shown in Figure 2. The

TABLE 6 Gel breaking properties of foam fracturing fluid.

Viscosity of breaking liquid, mPa·s	Residue content, mg/L	Surface tension, mN/m	Surface tension, mN/m
2	1.1	1.5	24.5

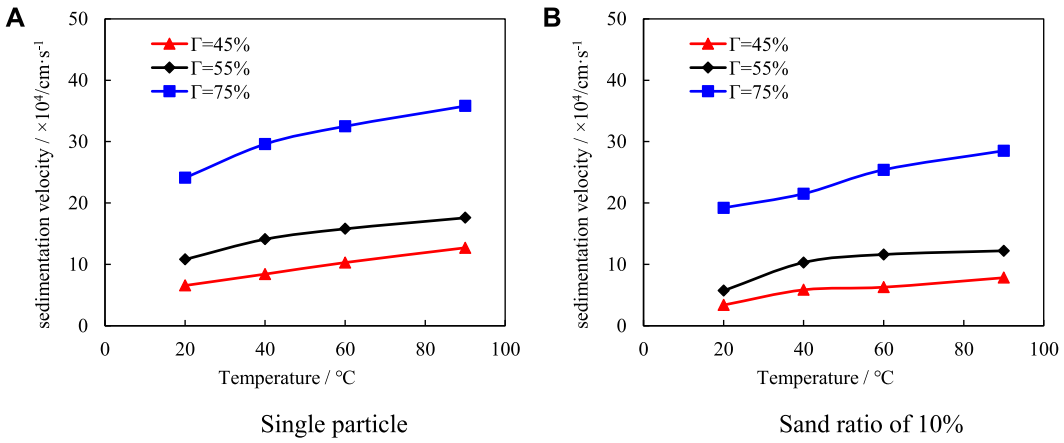


FIGURE 3
Comparison of proppant settling velocity under different temperatures and foam quality. **(A)** Single particle **(B)** Sand ratio of 10%.

experiments show that this property is uniformly dispersed within the foam after the formation of a stable foam in the fracturing fluid. Due to the interface between bubbles, the foam functions to wrap and support the sand particles used for propping open the induced fractures. As the temperature increases from room temperature to 90 °C, the sand mixture remains uniformly mixed for up to 3 h without showing any obvious delamination phenomena, indicating that the sand-carrying performance is good.

Figure 3 illustrates the relationship between the settling speed of proppant particles (single particle and sand ratio of 10%) and temperature under different temperatures and foam mass fractions. The temperature range is 20°C–90°C, the volume fraction of CO_2 is 45%–75%, and the pressure is 10 MPa. It can be inferred from the analysis of Figure 2 that the settling speed of proppant particles increases with temperature. This is attributed to the increased mobility of guar gum molecules, which consequently accelerates the thermal fracture of the hydrogen bond of linear guar gum in the liquid system, ultimately leading to the decrease of the effective viscosity of foam fracturing fluid. Meanwhile, the solution elasticity is also reduced to some extent, weakening the sand carrying performance. At the same experimental temperature, the settling velocity of the sand particles increases with the sand ratio. Moreover, the smaller the foam mass fraction is, the larger the particle settling speed is. This finding indicates that foam quality can suspend proppant and improve the sand carrying performance by increasing the foam mass fraction.

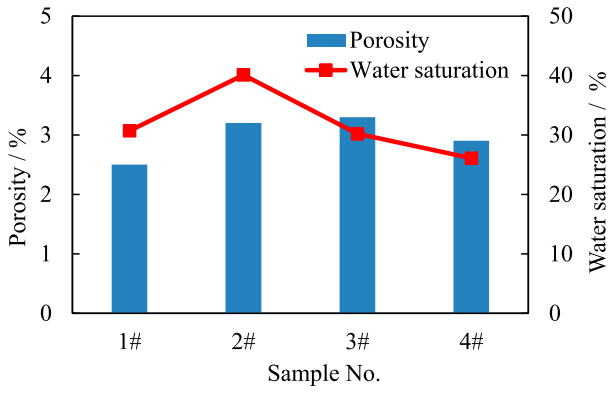


FIGURE 4
Experimental results of Well 1 reservoir physical properties.

3.4 Damage performance of foam fracturing fluid

3.4.1 Formation property characteristics of well 1

Figure 4 illustrates the results of a physical parameter analysis of the Longmaxi shale formation in Southwest China. The geological description of this particular section of the well is from 1963.0 to 1981.0 m. The shale is carbonaceous and locally calcareous with both dense and brittle characteristics. Additionally, there are localized pyrite deposits, with graptolites enriched in the section. The columnar bedding is horizontal and developed. Lastly, there are two total seams (both unfilled).

In conclusion, it is necessary for the author to more clearly express the main idea of each section of their writing. Moreover, the use of concise sentence structures can help to create more advanced and targeted expressions. By employing these techniques, the author can write more effectively and help readers more easily comprehend their intended message.

3.4.2 Damage experiment of foam fracturing fluid

After using the shale reservoir core from Well W1, we conducted experiments to evaluate the fracture properties of the foam fracturing fluid. The results of these tests are presented in Table 7. As seen in Table 7, the foam fracturing fluid caused little damage to the shale (less than 19%). In particular, the damage which was caused to the shale by the CO_2 foam fracturing fluid was weak.

TABLE 7 Experimental results of damage performance of foam fracturing fluid on core.

Sample No.	Gas phase permeability before fracturing fluid injection, $10^{-3}\mu m^2$	Gas phase permeability after fracturing fluid injection, $10^{-3}\mu m^2$	Injury rate, %	Average value, %
1#	0.12794	0.10711	16.44	13.76
2#	0.09686	0.08553	11.11	
3#	0.03665	0.02889	21.32	18.79
4#	0.02378	0.02002	16.25	

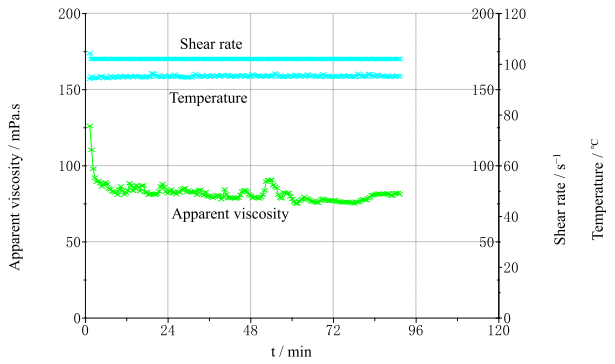


FIGURE 5
Evaluation result of rheological property of foam fracturing fluid.



FIGURE 6
Comparison of flowback liquid and clear water.

3.5 Rheological property of foam fracturing fluid

Foam fracturing fluid rheological properties evaluation method can be obtained by following these steps: Firstly, take 70 mL of base foam fracturing fluid and adjust its pH value to 5.8 by adding 0.3% volume ratio of a regulator. Secondly, add the foaming agent to the mixture as per the design proportion and stir thoroughly. Then, transfer the mixture to the RS6000 high-temperature rheometer closed system and access a carbon dioxide air source. Pressurize the system to 10 bars to ensure that the foam fracturing fluid is saturated with carbon dioxide, and then test its performance against temperature resistance and shear resistance. The results of these tests are shown in Figure 5.

According to the experimental results, the foam fracturing fluid has an apparent viscosity greater than 50 mPas, indicating strong spatial structure. The different formulations of the foam fracturing fluid can still maintain their apparent viscosity of more than 50 mPas after long-term shearing at 90°C, indicating excellent thermal and shear resistance.



FIGURE 7
Foam fracturing fluid base prepared by flowback fluid.

4 Reusability of foam fracturing fluid

Flowback fluid retrieved from shale gas fracking sites is used in recovery experiments. As shown in Table 8; Figures 6, 7, the viscosity of the foaming fracturing fluid prepared with the flowback

TABLE 8 Reusability of foam fracturing fluid.

Sample type	Viscosity of the foam fracturing fluid base, mPa·s	V_0, mL	Half-life of foam, hour
Foam fracturing fluid prepared with flowback fluid	24	410	32
Foam fracturing fluid prepared with clean water	66	356	90.5

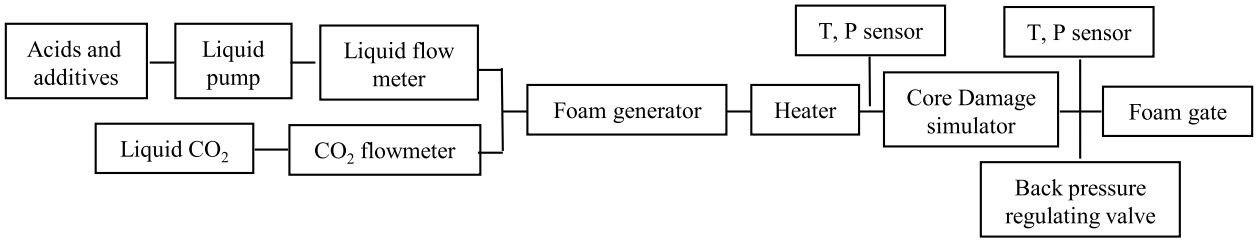


FIGURE 8
Recovery and treatment process of flowback CO_2 foam fracturing fluid.

fluid is only 24 mPas, much lower than that prepared with clean water. Additionally, the foaming fracturing fluid prepared with the flowback fluid has a shorter half-life of 32 h. This is due to the presence of metallic ions and other components in the flowback fluid, which affect the viscosity, half-life, and other properties of the fracturing fluid.

After hydraulic fracturing, the discharged flowback fluid from oil and gas wells must be replenished with liquid CO_2, foam stabilizer, and foaming agent after surface treatment. Please refer to Figure 8 for specific treatment procedures. Firstly, the flowback fluid is treated on the surface. Then, liquid CO_2, foam stabilizer, and foaming agent are added to replenish the fluid. Finally, the treated flowback fluid is ready to be reused. To improve the coherence of the article, more linking words and proper paragraph structures are necessary. It is also recommended to expand the vocabulary for smoother and more vivid expressions. Additionally, please double check for any grammar and syntax mistakes.

The process for treating and recovering backflow fluid from fracturing comprises several steps including solid-liquid separation, alkalization, chemical flocculation, oxidation, reverse osmosis, and biochemistry. These steps are aimed at removing different impurities found in the backflow fluid. In the final stage of treatment, dissolved total solids are removed using reverse osmosis membranes, while salts are recovered using methods such as evaporation and crystallization. In case of well sites with different situations, movable or fixed salt factories may be used. As a result of this full treatment process, the treated water is regarded as clean water, suitable for various construction purposes, hence achieving true zero discharge. In the process of application, the injection pressure, foam concentration, and foam quality are the main factors that affect the fracturing effect. Therefore, the performance optimization of carbon dioxide foam fracturing fluid should not only focus on component selection but also on technological innovation, supplemented by laboratory experiments and field trials.

5 Conclusion

(1) Through experimental evaluation and study on the performance of foam fracturing fluid, the formula of foam fracturing fluid which is suitable for shale gas reservoir fracturing has been developed. The formula includes 0.5% CT1 thickener, 0.3% CT1S foaming agent, 0.3% CT1D high-temperature stabilizer, and 0.3% CT1U regulator.

(2) The viscosity, static sand settling performance, and rheological properties of the foam fracturing fluid have been evaluated experimentally. The viscosity of the foam fracturing fluid is 2 mPa·s. The residue content is 1.1 mg/L, the surface tension is 24.5 mN/m, and the interfacial tension is 1.5 mN/m. Static sand settling experiments have been performed with 40–70 mesh ceramic particles which are commonly used in shale gas fracking. The sand-to-liquid ratio was set at 40% for the static sand-carrying experiment. The flow properties of the sand-carrying fluid were good, with no property settling within 3 h. Shale reservoir cores from well Wei-1 have been used to assess the rate of foam fracture, which was less than 19%. Under the experimental conditions of shear rate of 170 s-1 and temperature of 90°C, the viscosity of fracturing fluid was measured to be greater than 50 mPa·s, 90 min after shear, demonstrating the excellent temperature and shear resistance of the foam fracturing fluid.

(3) The fracturing flowback fluid retrieved from Changning H3 platform in Southwest China has been used for a recovery experiment. The viscosity of the fracturing fluid base prepared using the flowback fluid is only 24 mPas, which is much lower than the viscosity of the clean water preparation. At the same time, the foam fracturing fluid prepared with the flowback fluid has a shorter half-life of 32 h. The viscosity and half-life of foam fracturing fluids prepared with flowback fluid are worse than those prepared with clean water. The effluent needs to be treated until the treated water quality meets industry standards before it can be reused.

Data availability statement

The original contributions presented in the study are included in the article/Supplementary Material; further inquiries can be directed to the corresponding author.

Author contributions

SL: Conceptualization, resources, funding acquisition, writing—original draft and software. YF and JY: funding acquisition, project administration. TH: Data curation, formal analysis, methodology, project administration. JL: writing—original draft and writing—review and editing. XW: Project administration,

resources. All authors contributed to the article and approved the submitted version.

Funding

This work was supported by the 2021 Scientific Research Plan Project of PetroChina Southwest Oil and Gas Field Company: Research on the Transformation Technology of Permian Reservoir in the Middle Sichuan Paleo uplift (20220302-10).

Acknowledgments

The authors are grateful for the support of the Project of PetroChina Southwest Oil and Gas Field Company. Thanks to reviewers and editors for their careful review of this manuscript. We are grateful to Mr. Xiang Chao from the Natural Gas Research Institute of PetroChina Southwest Oil and Gas Field Company for providing reliable experimental data for the revision of our paper.

Conflict of interest

SL, YF, TH, JY, JL, and XW were employed by the Engineering Technology Research Institute of PetroChina Southwest Oil & Gas Field Company.

Publisher's note

All claims expressed in this article are solely those of the authors and do not necessarily represent those of their affiliated organizations, or those of the publisher, the editors and the reviewers. Any product that may be evaluated in this article, or claim that may be made by its manufacturer, is not guaranteed or endorsed by the publisher.

References

Ahmed, Abdelaal, Aljawad, Murtada. Saleh, Alyousef, Zuhair, and Muhammad, M. A. (2021b). A review of foam-based fracturing fluids applications: From lab studies to field implementations. *J. Nat. Gas Sci. Eng.* 95, 104236. doi:10.1016/j.jngse.2021.104236

Ahmed, S., Alameri, W., Ahmed, W. W., and Khan, S. A. (2021a). Rheological behavior of scCO$_2$-foam for improved hydrocarbon recovery: Experimental and deep learning approach. *J. Petroleum Sci. Eng.* 203, 108646. doi:10.1016/j.petrol.2021.108646

Ahmed, S., Elraies, K. A., Hanamertani, A. S., Hashmet, M. R., Shafian, S. R., and Hsia, I. C. "Investigation of carbon dioxide foam performance utilizing different additives for fracturing unconventional shales," in Proceedings of the 2019, Abu Dhabi International Petroleum Exhibition and Conference. Society of Petroleum Engineers, Abu Dhabi, UAE, November 2019.

Ahmed, S., Elraies, K. A., Hashmet, M. R., and Hanamertani, A. S. (2017a). Viscosity models for polymer-fre CO_2 foam fracturing fluid with the effect of surfactant concentration, salinity and shear rate. *Energies* 10 (12), 1970. doi:10.3390/en10121970

Ahmed, S., Elraies, K. A., Tan, I. M., and Hashmet, M. R. (2017b). Experimental investigation of associative polymer performance for CO_2 foam enhanced oil recovery. *J. Petrol. Sci. Eng.* 157, 971–979. doi:10.1016/j.petrol.2017.08.018

Arezoo, S. E., AhmedIbrahim, F., Hisham, A., and Nasr, E. D. "Mobility control using nanoparticle-stabilized CO2 foam as a hydraulic fracturing fluid," in Proceedings of the SPE-185863-MS, paper was prepared for presentation at the SPE Europec featured at 79th EAGE Conference and Exhibition held in Paris, Paris, France, June 2017.

Barati, R., and Liang, J. T. (2014). A review of fracturing fluid systems used for hydraulic fracturing of oil and gas wells. *J. Appl. Polym. Sci.* 131 (16). doi:10.1002/app.40735

Cawiezel, K. E. (1987). "*Rheological properties of foam fracturing fluids under downhole conditions*,". Dallas, Texas, United States, SPE 16191-MS (SPE).

Cong, Z. Y., Li, Y. W., Pan, Y. S., Liu, B., Shi, Y., Wei, J. G., et al. (2022). Study on CO_2 foam fracturing model and fracture propagation simulation. *Energy* 238, 121778. doi:10.1016/j.energy.2021.121778

Dong, Zhiyu, Liu, Shuo, Nie, Xin, Zhang, Yulong, Dong, Kaili, and Wang, Junfeng (2021). Experimental and molecular simulation research on the effect of metal ions on the stability of SDS foam. *Energy and Fuels* 36, 521–526. doi:10.1021/acs.energyfuels.1c03249

Edrisi, A., and Kam, S. I. (2014). A new foam model in pipes for drilling and fracturing applications. *SPE J.* 19 (4), 576–585. doi:10.2118/162709-pa

Fei, Y., Pokalai, K., Johnson, R., Gonzalez, M., and Haghighi, M. (2017). Experimental and simulation study of foam stability and the effects on hydraulic fracture proppant placement. *J. Nat. Gas. Sci. Eng.* 46, 544–554. doi:10.1016/j.jngse.2017.08.020

Feng, Chenchen, Ma, Xurui, and Jing, Zefeng (2021). Dynamic proppant-carrying performance of VES-CO_2 foam fracturing fluid in the pipeline and the fracture. *J. Petroleum Sci. Eng.* 210, 110034. doi:10.1016/j.petrol.2021.110034

Gao, C., Cheng, S., Wang, M., Wu, W., Gao, Z., Li, S., et al. (2023). Optimization of carbon dioxide foam fracturing technology for shale gas reservoir. *Geofluids* 23, 1–11. doi:10.1155/2023/6187764

Gu, M., and Mohanty, K. (2015). Rheology of polymer-free foam fracturing fluids. *J. Petrol. Sci. Eng.* 134, 87–96. doi:10.1016/j.petrol.2015.07.018

Harris, P. C., and Heath, S. J. (1996). Rheology of crosslinked foams. *SPE 28512-PA* 11 (2), 113–116. doi:10.2118/28512-pa

Harris, P. C., and Reidenbach, V. G. (1987). High-temperature rheological study of foam fracturing fluids. *SPE 13177-PA* 39 (5), 613–619. doi:10.2118/13177-pa

Huang, L. K., He, R., Yang, Z. Z., Tan, P., Chen, Z. W., Li, X. G., et al. (2023). Exploring hydraulic fracture behavior in glutenite formation with strong heterogeneity and variable lithology based on DEM simulation. *Eng. Fract. Mech.* 278, 109020. doi:10.1016/j.engfracmech.2022.109020

Jing, Z. F., Feng, C. C., Wang, S. Z., Xu, D. H., and Xu, G. X. (2017). Effect of foam quality on flow behavior of liquid CO_2-based foam fracturing fluid stabilized by hydrofluoroether. *J. Petrol. Sci. Eng.* 159, 710–716. doi:10.1016/j.petrol.2017.10.017

Ju, Shuang, Huang, Qiming, Wang, Gang, Li, Jun, Wang, Enmao, Qin, Cunli, et al. (2022). Rheological and morphological characteristics of foam fluid using hydroxypropyl guar and surfactant. *J. Petroleum Sci. Eng.* 211, 110124. doi:10.1016/j.petrol.2022.110124

Kartini, R., Kim, Y., and Lee, W. (2021). Evaluation of surfactant mixture for supercritical carbon dioxide foamed acid in carbonate matrix acidizing. *Energies* 14, 6567. doi:10.3390/en14206567

Li, C., Huang, Y. Q., Sun, X., Gao, R. M., Zeng, F. H., Tontiwachwuthikul, Paitoon, et al. (2017). Rheological properties study of foam fracturing fluid using CO_2 and surfactant. *Chem. Eng. Sci.* 170, 720–730. doi:10.1016/j.ces.2017.03.022

Li, Mingyang, Huang, Qiming, Yan, Yuting, and Chen, Kaipeng (2022). Influence of calcium chloride in coal on guar-based foam fracturing fluid rheological property: An experimental study. *Phys. Fluids* 34 (10), 103106. doi:10.1063/5.0115073

Li, Y., DiCarlo, D., Li, X., and Zang, J. (2015). An experimental study on application of nanoparticles in unconventional gas reservoir CO_2 fracturing. *J. Petrol. Sci. Eng.* 133, 238–244. doi:10.1016/j.petrol.2015.05.023

Liu, Shenggui, Huang, Jinkuang, Tang, Songlei, Shi, Shixiong, Wu, Xuan, and Liu, Xin (2020). Experimental study on the damage of artificial fracture permeability in coal during the flow back of guar-based fracturing fluid. *Geofluids* 2020, 1–13. doi:10.1155/2020/8302310

Liu, X., Cai, M., Cai, C., Jiang, X., Feng, Z., and Hu, J. (2004). Performance evaluation on CO_2 foam fracturing fluid. *Drill. Fluid Cem. Fluid* 21 (3), 1–15. doi:10.1016/j.ympev.2004.05.011

Luo, Xiang Rong, Wang, Shu Zhong, Jing, Ze Feng, Lv, Ming Ming, Wang, Zhi Guo, De Zhai, Zhen, et al. (2014a). A review of shale gas exploitation technology. *Appl. Mech. Mater.* 675-677, 1485–1489. doi:10.4028/www.scientific.net/amm.675-677.1485

Luo, X., Wang, S., Wang, Z., Jing, Z., and Lv, M. (2014b). Experimental research on rheological properties and proppant transport performance of GRF-CO_2 fracturing fluid. *J. Petrol. Sci. Eng.* 120, 154–162. doi:10.1016/j.petrol.2014.06.009

Mazza, R. L., and Quid, L. "Free CO_2/sand stimulations: An overlooked technology-production update," in Proceedings of the Paper SPE 72383 presented at the SPE Eastern Regional Meeting held in Canton, Ohio, United States, October 2001.

Reidenbach, V. G. (1986). "*Rheological study of foam fracturing fluids using nitrogen and carbon*,". SPE 12026-PADallas, Texas, United States, (SPE).

Sun, X., Liang, X. B., Wang, S. Z., and Lu, Y. (2014). Experimental study on the rheology of CO_2 viscoelastic surfactant foam fracturing fluid. *J. Petrol. Sci. Eng.* 119, 104–111. doi:10.1016/j.petrol.2014.04.017

Tan, P., Jin, Y., and Pang, H. W. (2021). Hydraulic fracture vertical propagation behavior in transversely isotropic layered shale formation with transition zone using XFEM-based CZM method. *Eng. Fract. Mech.* 248, 107707. doi:10.1016/j.engfracmech.2021.107707

Tan, P., Pang, H. W., Zhang, R. X., Jin, Y., Zhou, Y. C., Kao, J. W., et al. (2020). Experimental investigation into hydraulic fracture geometry and proppant migration characteristics for southeastern Sichuan deep shale reservoirs. *J. Petroleum Sci. Eng.* 184, 106517. doi:10.1016/j.petrol.2019.106517

Tudor, R., Vozniak, C., and Banks, M. L. "Technical advances in liquid CO2 fracturing," in Proceedings of the Paper CIM 94236, presented at the CIM Annual Technical Conference, Calgary, Canada, June 1994.

Verma, Amit, Chauhan, Geetanjali, Baruah, Partha Pratim, and Ojha, Keka (2018). Morphology, rheology and kinetics of nano-silica stabilized gelled foam fluid for hydraulic fracturing application. *Industrial Eng. Chem. Res.* 12, 13449–13462. doi:10.1021/acs.iecr.8b04044

Verma, Amit, Chauhan, Geetanjali, and Ojha, Keka (2017). Synergistic effects of polymer and bentonite clay on rheology and thermal stability of foam fluid developed for hydraulic fracturing. *Asia-Pac. J. Chem. Eng.* 12, 872–883. doi:10.1002/apj.2125

Wang, M., Wu, W., Chen, S., Li, S., Li, T., Ni, G., et al. (2022). Experimental evaluation of the rheological properties and influencing factors of gel fracturing fluid mixed with CO_2 for shale gas reservoir stimulation. *Gels* 8, 527. doi:10.3390/gels8090527

Wang, S. Z., Luo, X. R., and Jing, Z. F. (2018). Rheological properties of BCG-CO_2 fracturing fluid for shale gas. *Earth Environ. Sci.* 186, 012026. doi:10.1088/1755-1315/186/4/012026

Wang, Zhen-duo, Wang, Xiaoquan, and Lu, Yong-jun (2004). Application of carbon dioxide foam fracturing technology in low-permeability and low-pressure gas reservoir. *Oil Field Dev.* 25 (5), 66–70. doi:10.7623/syxb200403013

Wanniarachchi, W., Ranjith, P., and Perera, M. (2017). Shale gas fracturing using foam-based fracturing fluid: A review. *Environ. Earth Sci.* 76 (2), 91. doi:10.1007/s12665-017-6399-x

Yang, L. I., Weng, Dingwei, Yu, Yongbo, and Yin, Xiyong (2006). Study on foam fracturing and its field application. *DFCF* 23 (1), 51–54.

Zheng, Shichao, Kang, Zhongjian, Cui, Minghui, Nie, Yunliang, and Zhang, Anqi (2020). Improvement of shale gas reservoir based on plasma pulse shock and frequency resonance technology. *J. Nat. Gas Sci. Eng.* 80, 103403. doi:10.1016/j.jngse.2020.103403

Zhu, Wenxi, and Zheng, Xiuhua (2021). Study of an anti-hightemperature and salt-resistance alkyl glycine foaming agent and its foam stabilizing mechanism. *J. Dispersion Sci. Technol.* 44, 86–97. doi:10.1080/01932691.2021.1931282

frontiers | Frontiers in Energy Research

TYPE Original Research
PUBLISHED 08 August 2023
DOI 10.3389/fenrg.2023.1227981

Check for updates

OPEN ACCESS

EDITED BY
Xiaojin Zheng,
Princeton University, United States

REVIEWED BY
Sukru Merey,
Batman University, Türkiye
Zou Quanle,
Chongqing University, China

*CORRESPONDENCE
Ji Li,
tancai739919@163.com

RECEIVED 24 May 2023
ACCEPTED 28 July 2023
PUBLISHED 08 August 2023

CITATION
Li J, Wu D, Zhang R, Li C and Zou Q (2023), Evaluation method for reservoir damage of cementing slurry.
Front. Energy Res. 11:1227981.
doi: 10.3389/fenrg.2023.1227981

COPYRIGHT
© 2023 Li, Wu, Zhang, Li and Zou. This is an open-access article distributed under the terms of the Creative Commons Attribution License (CC BY). The use, distribution or reproduction in other forums is permitted, provided the original author(s) and the copyright owner(s) are credited and that the original publication in this journal is cited, in accordance with accepted academic practice. No use, distribution or reproduction is permitted which does not comply with these terms.

Evaluation method for reservoir damage of cementing slurry

Ji Li*, Dapeng Wu, Ran Zhang, Chenguang Li and Qiang Zou

The No. 2 Cementing Branch of PetroChina Bohai Drilling Engineering Company, Tianjin, China

The damage of cement slurry to the reservoir is directly related to the production of oil and gas wells, and is a problem that must be solved for the efficient and economic development of oil and gas reservoirs. According to the characteristics and field conditions of reservoir damage caused by cement slurry, this paper analyzes the main factors affecting the degree of reservoir damage, puts forward the technical index requirements of the evaluation device, and establishes the evaluation method of reservoir damage caused by cement slurry in case of loss of injection. The results show that the influence of temperature on the damage of the cement slurry layer is small, and the influence of pressure difference on the damage to the cement slurry layer is large; When the pressure difference is 22 Mpa, the penetration damage rate caused by cement slurry to the pore center without mud cake attachment is about 43%. After a day of core maintenance, the permeability damage rate will reach 61.2%; The damage of cement slurry to the pore micro-fractured core is very serious. After 1 day of maintenance, the damage to the core permeability after cement slurry solidification is as high as 83%, with an average of 76.5%; When the risk of leakage is low, the cement slurry system with low density and low water loss can be used for cementing operation. The filtrate of cement slurry should be better matched with the formation clay minerals, formation water, and drilling fluid filtrate. When the risk of leakage is high, high-density cement slurry, balanced pressure cementing, pressure control cementing, and other technologies to avoid leakage can be used for cementing operations. When the cementing conditions are more difficult, the cementing slurry system can be used to dissolve the cementing slurry system at a later stage. The research results provide theoretical data support for the study of reducing the damage of cement slurry to the reservoir.

KEYWORDS

reservoir damage, evaluation method, simulation device, cementing, cement slurry

Introduction

Reservoir damage refers to the situation that the output of reservoir oil and gas and the injection capacity of displacement fluid decrease due to various factors in the process of drilling, worker, stimulation, later transformation and development, and production of oil and gas (Yuan et al., 2014; Guo et al., 2020; Li et al., 2021). With the development of drilling and its supporting technologies in China, the drilling depth is also increasing, and the number of deep wells and ultra-deep wells in China is developing rapidly. In 2018, there were 160 wells drilled by China National Petroleum Corporation with a drilling depth of more than 6000 m. Different from conventional wells, deep wells have higher temperatures, pressure, and pressure difference, and there may be a regional formation pressure deficit (Sabins, 1990; Xi et al., 2021; Yang et al., 2022). With the continuous decrease of the original

formation pressure, the pressure difference between the wellbore and the reservoir will reach 30 Mpa when newly cementing, and a large amount of cement slurry filtrate may invade the reservoir, resulting in reservoir permeability damage. The difference between bottom hole pressure and formation pressure is called differential pressure. According to this method, wellbore pressure can be divided into overbalanced, underbalanced, and balanced. Overbalance (also called positive differential pressure) refers to the bottom hole pressure being greater than the formation pressure; Underbalanced (also called negative pressure difference) refers to the bottom hole pressure being less than the formation pressure; Balance refers to the condition that the bottom hole pressure is equal to the formation pressure. Near-balanced pressure drilling refers to overbalanced pressure drilling with the pressure difference within the specified range. In order to find out the severity of reservoir damage, to choose appropriate protection measures, at present, among the devices and methods for evaluating reservoir damage caused by cementing slurry, there is no device that can simulate the high-temperature and high-pressure downhole environment, no evaluation method for reservoir damage caused by lost cementing slurry, and no effective indoor research device and matching calculation method for invasion depth of slurry filtrate (Al-Jubori et al., 2009; Han et al., 2016; Du et al., 2021). Therefore, it is necessary to carry out the evaluation method of cementing slurry reservoir damage by simulating cementing conditions when conducting research.

At present, the research results on the evaluation device and experimental method of reservoir damage caused by cementing cement slurry have been relatively rich, and the evaluation methods of reservoir damage mainly include the evaluation method of static displacement damage evaluation and the evaluation method of dynamic damage evaluation device (Cellini et al., 2019; Lashof and Ahuja, 2019; Sha et al., 2019). When some researchers carry out the damage of cement slurry filtrate to the formation, they mainly focus on experimental research, using a water loss meter to make cement slurry filtrate, pass the filtrate through the damaged core of the static damage evaluation device, and using the core permeability as the main index to evaluate the damage law of cement slurry to the reservoir. Some researchers have used static cement slurry to evaluate the device for reservoir damage to conduct experiments on the dynamic damage of cement slurry filtrates of different components to the core and concluded that the chemical reactions of cement slurry filtrate and formation groundwater, clay minerals, and drilling fluid filtrates such as flocculation, expansion, and scaling are the most important factors causing reservoir damage, and external additives will also affect the chemical properties of cement slurry filtrate, reducing or aggravating harmful ion content to varying degrees (Bai et al., 2015; Shadravan et al., 2017; Wang et al., 2022). Some researchers use SW-II type core dynamic damage meter to evaluate the damage of cement slurry to the reservoir, the instrument mainly realizes the evacuation of the core, prepares saturated formation water, and measures the original permeability of the core, by soaking the drilling fluid filtrate for 24h, and comparing the dynamic reservoir damage of the drilling fluid under a pressure difference of 4.5Mpa and the dynamic damage of the drilling fluid to the core to form mud cake, by measuring the thickness of the mud cake, Core permeability and cement slurry dynamic damage core as well as the final permeability and total filter cake thickness, so as to calculate the damage rate of the permeability, while manually scraping off the outer mud cake and cleaning with clean water, cement slurry dynamic damage core measures the final permeability and filter cake thickness to calculate the permeability damage rate. Some researchers have proposed a set of damage evaluation methods for different reservoir types in view of the protection of dense clastic rock reservoirs in western Sichuan, and mainly carried out different indoor simulation evaluations: 1) the degree of blockage of filtrate containing polymer treatment agents on the width of the core joints by experimental simulation of the damage of the cores, and characterize the core permeability, and evaluate the cement slurry filtrate damage by static evaluation devices (Prohaska et al., 1995; Rongchao et al., 2007; Cui et al., 2021; Sahu et al., 2021); 2) The core is pretreated, and the gas permeability is measured after water and nitrogen displacement and saturation formation stabilization. The core is loaded into the core holder, and the core is damaged with room temperature and 3.5 MPa working fluid. The filter cake at both ends of the core is scraped to measure the gas permeability. The damage characteristics of water mud on the core are studied (Abimbola et al., 2016; Lian et al., 2020; Yin et al., 2021); 3) Through a series of experiments, the results show that the depth and degree of damage of cement slurry to the core are mainly positively related to the intrusion depth of its filtrate, and the evaluation of the double damage degree of drilling fluid and cement slurry to the reservoir is evaluated by calculating the filtrate depth (Barclay et al., 2001; Yue et al., 2018; Ahad et al., 2020). Some researchers have studied the evaluation method of cement slurry reservoir damage based on the proposed indoor evaluation method of drilling fluid and completion fluid damage. In order to make up for the shortcoming that this method can only evaluate the solid working fluid, the FDS-800-1000 formation damage evaluation system is used in the main experiment. In the experiment, vacuum and saturated formation water are pretreated by the core to measure its permeability, the mud cake of drilling fluid is formed through dynamic damage, and the external mud cake is scraped off. The permeability of the core is measured by scraping off the dynamic damage of the cement slurry and the filter cake. For cores with good cementation quality, the multi-point permeability measuring device is used to determine the damage depth. For the core with poor cementite quality, the damage depth is determined by the permeability of the fracture. Based on this, the degree of dual damage of drilling fluid and cement slurry to the reservoir is evaluated (Elkatatny, 2018; Cheng et al., 2022). Some scholars have analyzed the variation of coal seam permeability and the effect of enhanced recovery of coalbed methane, and calculated the degree of permeability damage caused by different factors. Studies have shown that burial depth, bottom hole pressure and dehydration rate have an effect on the effective stress acting on the coal reservoir, which in turn causes changes in permeability, productivity and other indicators. The elastic modulus of coal reflects the compressive capacity of coal: the higher the elastic modulus, the smaller the decline in permeability (Tao et al., 2012a). Some researchers have carried out FVS analysis on coal cores under different initial permeability, injection rate and injection intensity, and discussed the production response of coalbed methane wells to FVS at different drainage stages (Tao et al., 2017). Some scholars have studied the permeability damage of coalbed methane caused by increasing the pressure difference of displacement during the development of coalbed methane. The results show that in the development process, it is better to control the production pressure difference below the critical value of pressure drop (Tao et al., 2012b).

Oil and gas reservoir protection is subject to exploration, drilling, development, and downhole operations, and reducing

TABLE 1 Pressure coefficients of reservoir sections in the study area for different time periods.

Pound sign	Layer bits	Medium depth of air layer (m)	Formation pressure (MPa)	Pressure coefficient	Pressure measurement time
A-03	K(Cretaceous top sandstone)	5231.4	54.43	1.09	2010.12
A-08	E (Palaeoproterozoic basement sandstone)	4478.4	50.72	1.10	2012.5
A-09	E + K	4356.3	44.32	0.84	2014.3
A-13	E + K	3831.4	41.03	0.82	2016.9
A-16	E	3789.4	39.34	0.82	2018.6

the damage of cemented cement slurry to reservoirs during the cementing process is an important research topic (Ali et al., 2020; Bu et al., 2020). In this paper, taking the typical clastic rock reservoir of an oilfield in western China as the research object, according to the characteristics and site conditions of cementing cement slurry on reservoir damage, the main factors affecting reservoir damage are analyzed, the technical index requirements of the evaluation device are proposed, and the core damage and evaluation experiments are carried out to calculate the intrusion depth of cement slurry filtrate, so as to establish the damage evaluation method of the cement slurry to the reservoir when cementing leakage is lost, and provide theoretical data support for the study of reducing the damage of cemented cement slurry to the reservoir (McLeod, 1984).

Reservoir characteristics and cementing overview of the study area

Reservoir characteristics

In this paper, a typical clastic rock block of an oil field in western China is taken as the research object. The oil-bearing clastic rock reservoirs in the research area are mainly distributed in the Paleogene Kumglemu Formation, Cretaceous Bashi Kichik Formation, and Brazil Restructuring, among which the reservoir lithology of Paleogene Kumglemu Formation is mainly fine sandstone, silty mudstone, glutenite and argillaceous siltstone. The reservoir lithology of the Bashi Kichik Formation in the Cretaceous is mainly fine sandstone, mudstone, siltstone, argillaceous siltstone, and silty mudstone. The lithology of the reformed reservoirs in Cretaceous Brazil is mainly mudstone, fine sandstone, silty mudstone, and argillaceous siltstone, and there are obvious characteristics of upper mud and lower sand.

The temperature distribution of the stratum in study area A is as follows: the stratum temperature gradient is 1.98~2.21°C/100 m; The clastic rock reservoir section is generally buried within 4000~5000 m, and the temperature of the clastic rock reservoir section is about 100~120°C. After the oil and gas exploitation of the study area, there was a significant pressure deficit in the clastic rock reservoir section, and with the development of the mining progress, the pressure coefficient has dropped to below 1. The pressure coefficient is defined as the ratio of the measured formation pressure to the hydrostatic pressure at the same depth, which is a dimensionless quantity to measure the abnormal degree of the formation pressure (Singh and Roy, 2021). If the pressure coefficient is higher than 1.2, it is abnormally high pressure; If it is lower than 0.8, it is abnormally low pressure; Normal pressure is between 0.8 and 1.2. Table 1 gives the pressure measurement coefficient of the reservoir section of the study area in different time periods, which can be seen from the table: Due to the obvious pressure deficit, the pressure difference during cementing is as high as 15 Mpa above.

Through the investigation of the drilling core of the reservoir, it was found that the upper part of the clastic rock reservoir in the study area was subjected to less pressure on the overlying formation, resulting in a loose rock cementation structure, mainly forming a pore-type formation, the lower reservoir was subjected to a large pressure on the overlying formation, the cementation between the rocks was dense, and it was very easy to crack under the action of structural deformation and structural stress, forming a shrinkage joint or structural joint. Therefore, the permeability of the reservoir is better. This paper studies well A-16 in this block. Table 2 shows the statistics of core fractures. 8 of the 50 cores selected for the reservoir section of the well have structural fractures or shrinkage fractures, accounting for 16% of the fractures, and the maximum width of the structural fractures is 0.4 mm, penetration distance of 3 mm. The width of the shrinkage joint reaches 0.3 mm, and the crack width is still large, penetration distance of 1 mm. Therefore, when the cementing pressure difference is operated, the cement slurry can easily enter the reservoir directly through the fracture.

Overview of cementing

The cementing in the study area was mainly a 5-layer casing structure of 20"×13 3/8"× 7"× 5". The tailpipe cementing process is adopted, and the cement injection method is carried out at one time. Reduce the heat release, shrinkage and temperature change of concrete by adding fly ash and slag powder, and improve the crack resistance and durability of concrete. Through water reducers, coagulants and accelerators, it reduces the amount of cement used in concrete, improves fluidity and plasticity, reduces the viscosity of cement paste, delays the setting time of cement paste, and accelerates the setting and strength development of cement paste. The toughness, crack resistance and impact resistance of concrete can be increased by fiber materials, improving the durability and load bearing capacity of concrete. Table 3 shows the tailpipe cementing slurry formulation of a randomly selected well.

In this paper, the preparation of drilling fluid in the research area was investigated, and the reservoir section mainly adopted polysulfonite anti-collapse drilling fluid system, mainly using (wt%): bentonite (4%), caustic soda (0.4%), anti-high temperature filtration loss agent (3%),

TABLE 2 Core fracture statistics.

Pound sign	Well depth(m)	Construction seam width (mm)	Shrink seam width (mm)
A-16	4614.65	0.1	—
	4615.32	0.4	0.3
	4623.54	0.2	—
	4625.92	0.3	0.2
	4627.43	< 0.1	—
	4629.52	0.3	0.1
	4631.24	< 0.1	—
	4633.12	0.2	< 0.1
	4635.93	0.1	< 0.1

TABLE 3 Cementing cement slurry formulation.

Type	Grade G cement	Silicon powder	Water	Retarder	Dispersant	Water loss reducer	Defoamer
Increase (%)	100	35	32	2.9	1.4	3	0.3

sealing lubricant (2%), oil-soluble resin (3%), shielding temporary plugging agent type 1 (1%–2%), shielding temporary plugging agent type 2 (1~). 2%) and aggravators. The isolation liquid system used in cementing is a micro-fierce isolation liquid system, and the main materials are water, suspension agent (1%), retardant (3%) Dispersant (3%), aggravating agent (50%), defoamer (0.5%).

Reservoir rocks with higher porosity, permeability and toughness are more sensitive to the intrusion of fracturing fluid, which can easily cause reservoir damage, while the greater the depth of fracturing fluid intrusion, the more serious the degree of reservoir damage may be, and post-treatment measures such as cleaning, acidizing and sealing of fracturing fluid are conducive to mitigating and repairing the damage to the reservoir.In order to determine the depth of reservoir damage, the cement slurry filtrate was mixed with formation water at a certain volume ratio and placed in a wide-mouthed bottle, and then water bath maintenance was carried out after all the scaling phenomenon, which included granular crystals and flocculated precipitation.

Cementing slurry reservoir damage evaluation method

Influencing factors of reservoir damage

The causes of the damage to the cementing reservoir are often multifaceted, and the severity of the damage is also closely related to the physical properties of the reservoir, the performance of the cement slurry, the downhole environment, etc. The appearance is complex, but in the final analysis, the root cause of the damage is that the solid particles and liquid invading the formation are incompatible with the formation, resulting in damage to the reservoir. At the same time, there is no mud cake attached to the rock wall around the fractures, so the invasion of solid particles of the cement slurry will be larger and deeper than that attached to the mud cake on the well wall. Therefore, the damage depth of the cement slurry reservoir is mainly related to the extension and development of fractures, the damage degree, and the width of fractures, which can't be studied by indoor core experiments.

In this paper, in order to study the influencing factors of reservoir damage, the cement slurry contact core damage experiment is carried out, and the influencing factors of cementing leakage cement slurry on reservoir damage are analyzed. In the process of cementing leakage, the damage of cement slurry to the reservoir is mainly affected by temperature and pressure differences. In this paper, an experimental study of the damage of cement to the reservoir under temperature and pressure differences will be carried out.

The experimental equipment in this paper adopts a new cement slurry reservoir damage evaluation instrument, and the core selects a natural sandstone core with a diameter of 2.5 cm and a length of 5 cm, and the water of the saturated formation is treated by vacuum, and the formation water is treated with standard brine. The drilling fluid is formulated with KCI polymer drilling fluid, which has a wide range of uses, and the solid phase content and water loss of the drilling fluid are high. The isolation solution is made of water, GYW-201, GYW-301, and barite, the isolation liquid density is 1.75 g/cm^3, and the isolation fluid, drilling fluid, and cement slurry are mixed in a ratio of 50:25:25 for rheological experiments, and no chemical reactions such as flocculation and flash condensation occur. Cement paste is prepared from G grade cement, water loss reducing agent, dispersant, retarder and water. Water loss reducing agent improves the fluidity and plasticity of concrete, which contributes to the early hardening and curing of cement, dispersant improves the dispersibility of cement paste, which contributes to the uniform dispersion and early hardening of cement, and retarder slows down the setting time of cement paste. The density is 1.89 g/cm^3, the flow rate is 27 cm, and the API water loss is75 ml, the free liquid is less than 0.3%, the sedimentation stability is less than 0.02 g, the viscosity of cement slurry is 44 s and the thickening time is more than 200 min.

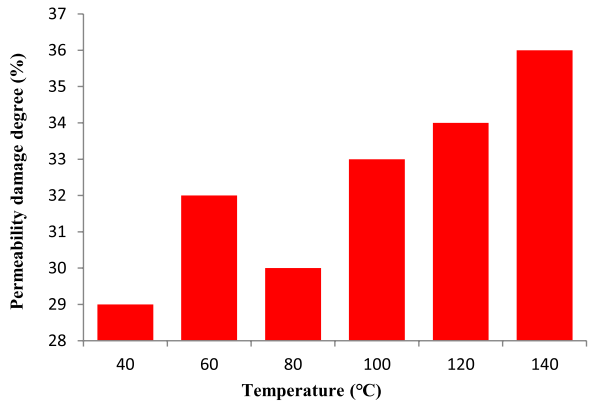


FIGURE 1
Degree of core permeability damage at different temperatures.

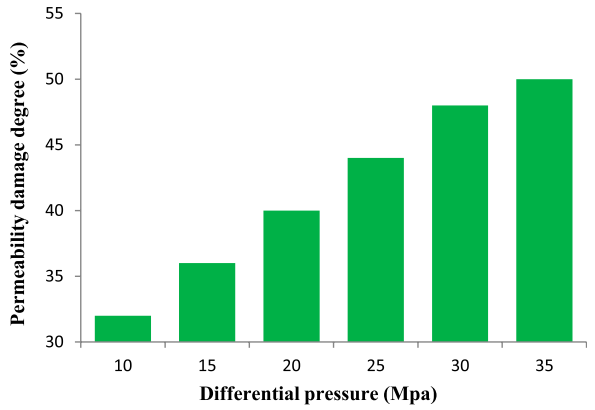


FIGURE 2
Degree of damage to core permeability by different pressure differences.

Test process: the surrounding pressure in the experiment is set to 15 Mpa, the core adopts the liquid permeability test method, and the cement slurry with different temperatures, 10 Mpa, 150rpm stirring speed, and fluid speed of about 0.5 m/s damage to the core is 1h, and the temperature is selected 40°C, 60°C, 80°C, 100°C, 120°C, Perform a comparative experiment at 140°C. Figure 1 shows the degree of core permeability damage at different temperatures, as can be seen from the figure: under the condition of maintaining the pressure difference and the shape of the mud cake, with the increase of temperature, the degree of core permeability damage does not change much, but the overall situation is still slowly increasing, the relationship between temperature and the degree of core penetration damage is 0.07%/°C.

The core temperature was selected for the test to be 100°C, the confining pressure was set to 15Mpa, and the core was measured by liquid permeability test method, and cement slurry with different temperatures, 10 Mpa, 150 rpm stirring speed and fluid speed of about 0.5 m/s was used to damage the core 1 h. Figure 2 shows the damage degree of different pressure differences on core permeability. It can be seen from the figure that the pressure difference increases from 10 Mpa to 35 Mpa and the damage rate of core permeability increases by about 18% while maintaining the same temperature and mud cake shape, the relationship between differential pressure and the degree of core infiltration damage is 0.72%/MPa. The pressure difference has a great impact on the damage to the cement slurry reservoir.

By analyzing the influence of temperature and pressure difference on the damage to the cement slurry reservoir, the temperature effect is small, and the pressure difference is large. Therefore, when establishing the damage evaluation method of the cement slurry reservoir, the influence of pressure difference needs to be considered according to the actual working conditions.

Cementing leakage grout reservoir damage evaluation method

(1) Preparation before the damage experiment: check that all instruments and utensils work properly and close the valves; Put a core containing saturated formation water into a core holder; The upper kettle cover and the lower kettle cover are connected in a sealed way through kettle body threads and connected to a magnetic stirrer; The nitrogen bottle is used to drive the formation water into the kettle body, and the emptying valve is opened until the whole kettle body is filled and the core is soaked in the formation water, and a uniform load is applied to make the core holder clamp the core.

(2) Cement slurry damage experiment process: loading the prepared cement slurry into a container; Open the drain valve to drain the formation water; Nitrogen drives cement slurry to completely replace the residual formation water and fill the upper kettle; Set the temperature and pressure of the upper and lower kettle bodies, manually set the pressure limiting value of the pressure limiting valve of the lower kettle body, and synchronously set the rotating speed of the stirrer; After the experiment started, the cement slurry began to damage the core, and the preset experimental temperature and pressure could be reached in about 15 min. At the same time, the time was started and the filtrate volume was measured. When the damage test reaches 60 min, stop heating and pressing, open the upper-pressure relief valve and discharge the high-pressure cement slurry; Close the pressure-limiting valve of the kettle body, measure the core permeability at constant pressure, finally close the experimental equipment and clean the kettle body and pipelines, and measure the core permeability again after curing the damaged core for 1 day.

Through the study of cementing leakage, the maximum depth of cement slurry damage to the reservoir is the depth of fracture and the depth of filtrate invasion into the porous reservoir. Because of the great difference in fracture development, the reservoir invasion depth under the condition of cementing loss is generally not considered in the evaluation method of reservoir damage.

Engineering applications

In this paper, the cores retrieved from a typical clastic reservoir in an oil field in western China are selected, and it



FIGURE 3
Core.

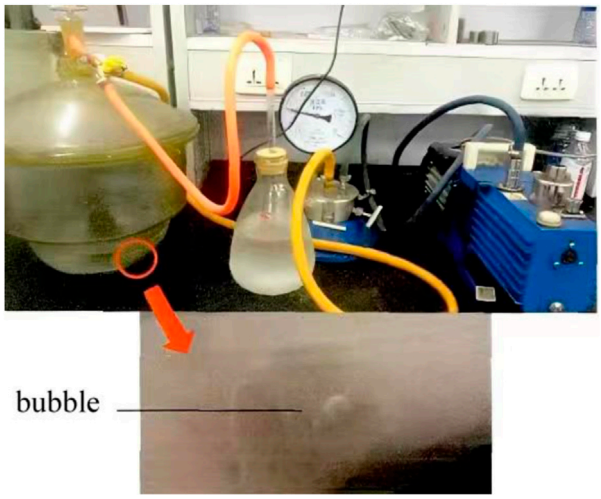


FIGURE 4
Core vacuum saturated formation water.

is found that the permeability values of the cores are quite different through measurement. In order to ensure the effectiveness of the experiment and the stability of the results, cores with similar permeability were grouped to reduce the variability between core samples, improve the reliability of the experiment and the comparability of the results, and more accurately study the interaction between formation water and rock (Figure 3). Core vacuum saturation with formation water was performed after grouping. In the experimental process of core vacuum saturated formation water, the core samples are put into the vacuum chamber and the air is extracted by the vacuum pump to form a vacuum environment, and the formation water is gradually injected into the core samples by means of injecting water or other liquids until the cores are completely saturated, and the saturation process of the water is more thorough in a vacuum environment, which can more accurately study the interactions between the formation water and the rocks, as shown in Figure 4.

Through the drilling fluid retrieved on-site, re-agitation is carried out before the experiment, heated to the experimental set temperature, and the performance of the drilling fluid is measured by a twelve-speed rotary viscometer to ensure that the drilling fluid is still within the validity period. If it fails, part of the drilling fluid material needs to be supplemented to meet the design requirements. Load the drilling fluid and the isolating fluid material retrieved on-site into an intermediate container for later use.

In the experiment, a well with cementing injection slurry leakage was selected to carry out the experiment, and the well number was A-45, the structure of the well was a three-open straight well, and the last opening was a drill bit with a diameter of 216 mm, and the depth of the well was 5230 m. The well uses a casing suspension cementing with a diameter of 178 mm, and the sealing section is up to 5134 m. The reservoir type of the well is clastic rock, the construction displacement of the cement slurry operation is 20 L/s, and the cement slurry density is 1.9 g/cm^3, drilling fluid density of 1.2 g/cm^3, isolation fluid density of 1.7 g/cm^3, maximum annular pressure of 75 Mpa. The liquid column pressure is 70 Mpa, the annular air pressure consumption is 3.5 Mpa, the formation pore pressure is 52KN, and the maximum pressure difference is 22 Mpa. In the cementing process, due to the excessive pressure difference, the pressure leakage formation appears, the cement slurry is lost by 3 m^3, and the core is taken by the proximity well. The development of microcracks in the core was found, and it can be determined that the microcracks were pressed open during cementing and caused leakage.

When evaluating reservoir damage experiments, it is mainly divided into damage experiments of ordinary pore-type core cement slurry and pore-micro-fracture core cement slurry. When ordinary cores are used to simulate larger fractures, the cement slurry causes damage to the porous reservoirs around the fracture due to the inflow into the fractures; When the pore-microcrack core is a man-made microcrack core in the room, the core is used to simulate the damage to the reservoir when the formation microcrack development causes small cement leakage analyses.

The test of reservoir damage caused by porous core cement slurry during cementing leakage is divided into two stages, that is, permeability damage caused by dynamic solid particles and filtrate invasion of cement injection operation, and permeability damage caused by hydration and consolidation of cement slurry solid particles in reservoir pores. After simulating the dynamic damage evaluation experiment of cement slurry, the core permeability is measured once, and after 1 day of maintenance in the high-temperature curing kettle, the permeability is measured again. During the experiment, the density of cement slurry was measured at 1.7 g/cm^3, the temperature was 110°C, and the differential pressure was taken 22 Mpa, the mixing speed of the leaf loading is set to 200 rpm, the dynamic damage time is set to 1 h, and the curing time for 1 day Figure 5 shows the experimental results of the leakage damage of the pore core cement slurry, which can be seen from the figure: when the pressure difference is at 22 Mpa, the permeability damage rate caused by the cement slurry to the core without mud cake attachment is about 43%, and when the

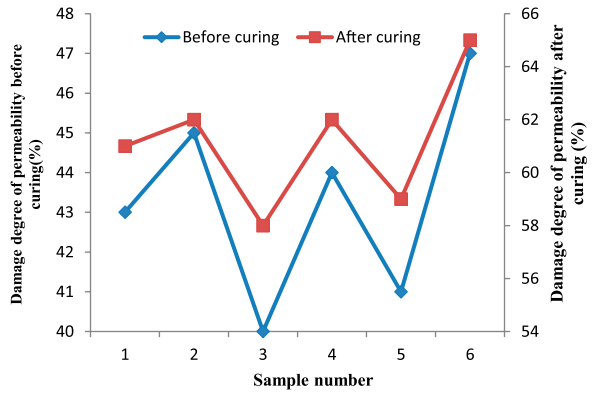


FIGURE 5
Experimental results of leakage damage of pore-type core cement slurry.

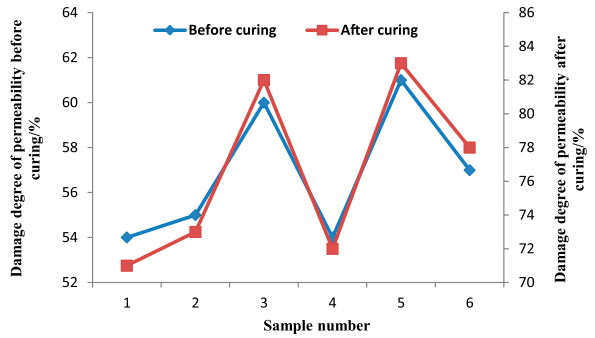


FIGURE 6
Experimental results of pore-microcracked cement slurry leakage damage.

damaged core is maintained for 1 day, the damage will be further aggravated, and the penetration damage rate will be reached 61.2%. Therefore, after damaging the core maintenance, the cross-sectional cement slurry filter cake and the solid phase particles that intrude into the core undergo hydration and consolidation, which will lead to the blockage of the pore throat, resulting in its penetration rate decreasing.

In the experiment on reservoir damage caused by porosity-microcrack cement slurry at the time of cementing leakage, the basic conditions set by the test are consistent with the pore core cement slurry. Figure 6 shows the experimental results of leakage damage of cement slurry with micro-cracks. It can be seen from the figure that the damage of cement slurry to the pore micro-fractured core is very serious, and after 1 day, the core permeability damage caused by cement slurry solidification can be as high as 83%, with an average of 76.5%. Therefore, when choosing a fractured core, you should choose a core with lower penetration, the crack must be the main seepage channel of the low permeability core, and the cement slurry enters the blocked fracture to cause the permeability sharp drop, even above 90%.

Through the evaluation test of cement slurry reservoir damage caused by cementing leakage, it can be concluded that the risk of lost circulation is higher and the formation pressure window is narrow. When low density cement slurry system is used for cementing operation, balanced pressure cementing or controlled pressure cementing technical measures shall be taken to avoid leakage and loss under the condition of limited cementing well conditions and high possibility of leakage, and the cement slurry that needs to be acid-soluble sealed in the later stage.

Conclusion

Oil and gas reservoir protection is affected by exploration, drilling, development, and downhole operations, and is a complex system engineering. In the cementing process, the high-pressure difference between the annular space and the formation, as well as the high filtration loss and high solid phase content of cementing cement slurry, how to reduce the damage of cemented cement slurry to the reservoir is the main research topic. At present, the evaluation of the damage of cement slurry to the reservoir includes the following problems: the evaluation device does not meet the application conditions of deep wells, and there is no evaluation method for the damage of cement slurry to the reservoir when the cement slurry is lost. In this paper, taking the typical clastic rock reservoir of an oilfield in western China as the research object, according to the characteristics of cementing cement slurry on reservoir damage, the main factors affecting reservoir damage are analyzed, and the damage evaluation method of the cement slurry to the reservoir when cementing is lost is established, to provide theoretical data support for the study of reducing the damage of cemented cement slurry to the reservoir. The main research results are.

(1) At present, the drilling depth is deepened, the pressure of the cementing fluid column is increased, the formation pore pressure is deficient in some blocks due to long-term exploitation, and the differential pressure between the well profile and the formation is even up to 30 MPa, but the existing evaluation device cannot achieve such high experimental conditions. In this paper, a cement slurry reservoir damage simulation and evaluation instrument are processed, and a cement slurry reservoir damage simulation device with a real simulation temperature of 200°C, pressure of 60 Mpa, and differential pressure of 35 Mpa is developed after several improvements. By analyzing the influence law of temperature and differential pressure on cement slurry reservoir damage, the temperature has less influence, while the differential pressure has greater influence.
(2) The permeability damage rate caused by the porosity core damaged by cementing leakage cement slurry reservoir is about 43%, and the permeability damage rate will reach 61.2% after 1 day of damage core maintenance; The damage of cement slurry to pore-micro-fissure cores is very serious, and after 1 day of maintenance, the damage to the core permeability caused by cement slurry curing can be as high as 83%, with an average of 76.5%; When the risk of leakage is small, cementing construction operations can use low-density, low-water loss cement slurry system and cement slurry filtrate should be

better proportioned with formation clay minerals, formation water and drilling fluid filtrate, etc. When the risk of leakage is large, cementing construction operations use low-density cement slurry, balanced pressure cementing and pressure-controlled cementing, and other technologies to avoid leakage, when cementing conditions are more difficult, the cementing cement slurry system can be used to dissolve the cementing cement slurry system in the later stage.

Data availability statement

The original contributions presented in the study are included in the article/Supplementary material, further inquiries can be directed to the corresponding author.

Author contributions

All authors listed have made a substantial, direct, and intellectual contribution to the work and approved it for publication.

Acknowledgments

The authors would like to show sincere thanks to those techniques who have contributed to this research.

Conflict of interest

Authors JL, DW, RZ, CL, and QZ were employed by The No 2 Cementing Branch of PetroChina Bohai Drilling Engineering Company.

Publisher's note

All claims expressed in this article are solely those of the authors and do not necessarily represent those of their affiliated organizations, or those of the publisher, the editors and the reviewers. Any product that may be evaluated in this article, or claim that may be made by its manufacturer, is not guaranteed or endorsed by the publisher.

References

Abimbola, M., Khan, F., and Khakzad, N. (2016). Risk-based safety analysis of well integrity operations. *Saf. Sci.* 84, 149–160. doi:10.1016/j.ssci.2015.12.009

Ahad, N. A., Jami, M., and Tyson, S. (2020). A review of experimental studies on sand screen selection for unconsolidated sandstone reservoirs. *J. Petroleum Explor. Prod. Technol.* 10 (4), 1675–1688. doi:10.1007/s13202-019-00826-y

Al-Jubori, A., Johnston, S., Boyer, C., Lambert, S. W., Bustos, O. A., Pashin, J. C., et al. (2009). Coalbed methane: Clean energy for the world. *Oilfield Rev.* 21 (2), 4–13.

Ali, J. A., Kalhury, A. M., Sabir, A. N., Ahmed, R. N., Ali, N. H., and Abdullah, A. D. (2020). A state-of-the-art review of the application of nanotechnology in the oil and gas industry with a focus on drilling engineering. *J. Petroleum Sci. Eng.* 191, 107118. doi:10.1016/j.petrol.2020.107118

Bai, M., Sun, J., Song, K., Li, L., and Qiao, Z. (2015). Well completion and integrity evaluation for CO2 injection wells. *Renew. Sustain. Energy Rev.* 45, 556–564. doi:10.1016/j.rser.2015.02.022

Barclay, I., Pellenbarg, J., Tettero, F., Pfeiffer, J., Slater, H., Staal, T., et al. (2001). The beginning of the end: A review of abandonment and decommissioning practices. *Oilfield Rev.* 13 (4), 28–41.

Bu, Y., Du, J., Guo, S., Liu, H., Liang, Y., Su, Z., et al. (2020). Effects of formation water influx on the bonding strength between oil well cement and the formation. *Constr. Build. Mater.* 251, 118989. doi:10.1016/j.conbuildmat.2020.118989

Cellini, S. R. N., Turner, N., and Ahuja, D. R. (2019). Gainfully employed? Assessing the employment and earnings of for-profit college students using administrative data. *J. Hum. Resour.* 54 (2), 342–370. doi:10.3368/jhr.54.2.1016.8302r1

Cheng, H., Yang, D., Lu, C., Qin, Q., and Cadasse, D. (2022). Intelligent oil production stratified water injection technology. *Wirel. Commun. Mob. Comput.* 2022, 1–7. doi:10.1155/2022/3954446

Cui, K. X., Jiang, G. C., Yang, L. L., Deng, Z. Q., and Zhou, L. (2021). Preparation and properties of magnesium oxysulfate cement and its application as lost circulation materials. *Petroleum Sci.* 18 (5), 1492–1506. doi:10.1016/j.petsci.2021.08.002

Du, X., Fang, H., Wang, S., Xue, B., and Wang, F. (2021). Experimental and practical investigation of the sealing efficiency of cement grouting in tortuous fractures with flowing water. *Tunn. Undergr. Space Technol.* 108, 103693. doi:10.1016/j.tust.2020.103693

Elkatatny, S. (2018). Application of artificial intelligence techniques to estimate the static Poisson's ratio based on wireline log data. *J. Energy Resour. Technol.* 140 (7). doi:10.1115/1.4039613

Guo, J., Zheng, Y., Li, W., Li, B., Yuan, B., and Xu, B. (2020). Design and application of well cementing technology based on the precise managed pressure balancing method in narrow pressure window hole sections. *Nat. Gas. Ind. B* 7 (3), 285–291. doi:10.1016/j.ngib.2019.11.004

Han, J., Cheng, H., Shi, Y., Wang, L., Song, Y., and Zhnag, W. (2016). Connectivity analysis and application of fracture cave carbonate reservoir in Tazhong. *Sci. Technol. Eng.* 16 (5), 147–152.

Lashof, D. A., and Ahuja, D. R. (2019). Relative contributions of greenhouse gas emissions to global warming. *Nature* 344 (6266), 529–531. doi:10.1038/344529a0

Li, J., Su, D., Tang, S., Li, Z., Wu, H., Huang, S., et al. (2021). Deformation and damage of cement sheath in gas storage wells under cyclic loading. *Energy Sci. Eng.* 9 (4), 483–501. doi:10.1002/ese3.869

Lian, W., Li, J., Tao, Q., Liu, G., Wang, W., and Ren, K. (2020). Sealing failure mechanism and control method for cement sheath during hydraulic fracturing. *Acs Omega* 5 (32), 19978–19994. doi:10.1021/acsomega.0c01326

McLeod, H. O. (1984). Matrix acidizing. *J. Petroleum Technol.* 36 (12), 2055–2069. doi:10.2118/13752-pa

Prohaska, M., Fruhwirth, R., and Economides, M. J. (1995). Modeling early-time gas migration through cement slurries. *SPE Drill. Complet.* 10 (03), 178–185. doi:10.2118/27878-pa

Rongchao, C., Ruihe, W., Huilian, C., Yuhuan, B., and Yuanfang, C. (2007). Development and evaluation of a new nanometer-based spacer NMS-I. *Petroleum Sci.* 4 (1), 49–54. doi:10.1007/bf03186573

Sabins, F. L. (1990). Problems in cementing horizontal wells. *J. petroleum Technol.* 42 (04), 398–400. doi:10.2118/20005-pa

Sahu, C., Kumar, R., and Sangwai, J. S. (2021). A comprehensive review on well completion operations and artificial lift techniques for methane gas production from natural gas hydrate reservoirs. *Energy Fuels* 35 (15), 11740–11760. doi:10.1021/acs.energyfuels.1c01437

Sha, F., Lin, C., Li, Z., and Liu, R. (2019). Reinforcement simulation of water-rich and broken rock with Portland cement-based grout. *Constr. Build. Mater.* 221, 292–300. doi:10.1016/j.conbuildmat.2019.06.094

Shadravan, A., Tarrahi, M., and Amani, M. (2017). Intelligent tool to design drilling, spacer, cement slurry, and fracturing fluids by use of machine-learning algorithms. *SPE Drill. Complet.* 32 (02), 131–140. doi:10.2118/175238-pa

Singh, J., and Roy, A. K. (2021). Numerical simulation of a conical roofed low-rise building to estimate the wind pressure coefficients. *Electron. J. Struct. Eng.* 21, 34–45. doi:10.56748/ejse.21289

Tao, S., Tang, D., Xu, H., Li, S., Geng, Y., Zhao, J., et al. (2017). Fluid velocity sensitivity of coal reservoir and its effect on coalbed methane well productivity: A case of baode block, northeastern ordos basin, China. *J. Petroleum Sci. Eng.* 152, 229–237. doi:10.1016/j.petrol.2017.02.021

Tao, S., Wang, Y. B., Tang, D. Z., Xu, H., and Lv, Y. M. (2012b). Coal permeability damage caused by production pressure difference. *Energy Sources, Part A Recovery, Util. Environ. Eff.* 34 (19), 1801–1807. doi:10.1080/15567036.2012.692756

Tao, S., Wang, Y., Tang, D., Xu, H., Lv, Y., He, W., et al. (2012a). Dynamic variation effects of coal permeability during the coalbed methane development process in the Qinshui Basin, China. *Int. J. Coal Geol.* 93, 16–22. doi:10.1016/j.coal.2012.01.006

Wang, M., Cheng, H., Wei, J., Zhang, K., Cadasse, D., and Qin, Q. (2022). High-temperature-resistant, clean, and environmental-friendly fracturing fluid system and performance evaluation of tight sandstone. *J. Environ. Public Health* 2022, 1–7. doi:10.1155/2022/5833491

Xi, Y., Li, J., Fan, L., Wang, W., and Zha, C. (2021). Mechanism and numerical simulation of a new device of bypass cementing device for controlling casing shear deformation induced by fault slipping. *J. Petroleum Sci. Eng.* 196, 107820. doi:10.1016/j.petrol.2020.107820

Yang, G., Liu, T., Zhu, H., Zhang, Z., Feng, Y., Leusheva, E., et al. (2022). Heat control effect of phase change microcapsules upon cement slurry applied to hydrate-bearing sediment. *Energies* 15 (12), 4197. doi:10.3390/en15124197

Yin, B., Li, B., Liu, G., Wang, Z., and Sun, B. (2021). Quantitative risk analysis of offshore well blowout using bayesian network. *Saf. Sci.* 135, 105080. doi:10.1016/j.ssci.2020.105080

Yuan, C. D., Pu, W. F., Jin, F. Y., Zhang, Y. C., Jia, H., and Zhao, T. H. (2014). Performance of oil-based cement slurry as a selective water-plugging agent in high-temperature and high-salinity cave-fractured carbonate reservoirs. *Industrial Eng. Chem. Res.* 53 (14), 6137–6149. doi:10.1021/ie4000129

Yue, Y., Wu, X., Zhang, Q., Zhao, H., and Jiang, W. (2018). Integration and scale application of shale gas exploration and development engineering technologies in Sichuan and Chongqing areas. *Nat. Gas. Ind. B* 5 (5), 523–532. doi:10.1016/j.ngib.2018.02.005

frontiers | Frontiers in Energy Research

TYPE Original Research
PUBLISHED 17 August 2023
DOI 10.3389/fenrg.2023.1238246

Check for updates

OPEN ACCESS

EDITED BY
Peng Tan,
CNPC Engineering Technology R&D Company Limited, China

REVIEWED BY
Li Qingmiao,
Chengdu University of Technology, China
Erlei Su,
Henan Polytechnic University, China
Chunshan Zheng,
Anhui University of Science and Technology, China

*CORRESPONDENCE
Zhiheng Cheng,
zh_cheng_2021@126.com
Jinhu Zhang,
jinhuzhang2021@126.com

RECEIVED 11 June 2023
ACCEPTED 02 August 2023
PUBLISHED 17 August 2023

CITATION
Wang H, Cheng Z, Zhang J, Chen L, Luo X, Li M, Chen H and Xie Y (2023), Three-peak evolution characteristics of supporting stress on a super-long working face in a thick coal seam.
Front. Energy Res. 11:1238246.
doi: 10.3389/fenrg.2023.1238246

COPYRIGHT
© 2023 Wang, Cheng, Zhang, Chen, Luo, Li, Chen and Xie. This is an open-access article distributed under the terms of the Creative Commons Attribution License (CC BY). The use, distribution or reproduction in other forums is permitted, provided the original author(s) and the copyright owner(s) are credited and that the original publication in this journal is cited, in accordance with accepted academic practice. No use, distribution or reproduction is permitted which does not comply with these terms.

Three-peak evolution characteristics of supporting stress on a super-long working face in a thick coal seam

Hongbing Wang[1], Zhiheng Cheng[2]*, Jinhu Zhang[3,4,5]*, Liang Chen[2], Xin Luo[6,7], Meichen Li[2], Haoyi Chen[1] and Yifei Xie[2]

[1]School of Civil and Resource Engineering, University of Science and Technology Beijing, Beijing, China, [2]School of Mining Safety, North China Institute of Science and Technology, Beijing, China, [3]CCTEG Coal Mining Research Institute, Beijing, China, [4]Coal Mining and Designing Department, Tiandi Science and Technology Co., Ltd., Beijing, China, [5]School of Energy and Mining Engineering, China University of Mining Technology-Beijing, Beijing, China, [6]School of Emergency Management and Safety Engineering, China University of Mining Technology-Beijing, Beijing, China, [7]School of Emergency Technology and Management, North China Institute of Science and Technology, Langfang, China

Increasing working face length is the development trend of intelligent and efficient longwall fully mechanized mining. By combining field measurement and theoretical calculation, change characteristics of the frequency, peak value, and range of weighting in a long working face in a 1000 m-deep shaft of Kouzidong Coal Mine (Fuyang City, Anhui Province, China) were studied. Based on the mechanical model of the hydraulic support group of the elastic independent support, force characteristics and posture change characteristics of the support in the 121304 working face of the mine were studied and analyzed. The supporting stress characteristics of the deep super-long working face were revealed, and the theoretical calculation was in good agreement with the actual measurement. Based on the aforementioned model, support parameters and control technology of the 140502 working face were studied. The results show that as the length of the working face increases, the supporting stress gradually transforms from a single peak to multiple peaks and expands to both ends of the working face. The weighting in different areas of the working face is characterized by an obvious time sequence and great difference in intensity. When the working face length is 300 m, the multi-peak characteristic of super-long working faces appears. The M-shaped three-peak characteristic can be used as the criterion for super-long working faces. A reasonable working face length should be determined by comprehensively considering occurrence conditions of coal seams, working face parameter, and equipment ability. According to the different attributes of hydraulic supports in space and function and combining with zonal characteristics of the long working face, the criterion for the super-long working face and the principle of zonal cooperative control of hydraulic support groups were revealed. In addition, a cooperative control method of equipment groups in the working face based on the state error and cost functions was put forward, and the three-level cooperative control strategy and implementation method were formulated. It can effectively guide the equipment group in the super-long fully mechanized working face in deep thick coal seams to achieve optimal coordinated control.

KEYWORDS
long working face, thick coal seam, supporting stress, three peaks, cooperative control

1 Introduction

With the development of efficient coal mining technologies (Wu et al., 2022; Li et al., 2023a), the spatial scale of fully mechanized working faces in coal mines in China constantly expands in three aspects: mining depth, horizontal scale (including the working face length and advance length), and vertical scale (mainly the mining height) (Liu et al., 2021; Zou et al., 2022a; Ye et al., 2022; Li et al., 2023b; Ma et al., 2023; Sun et al., 2023). In such context, the mining depth of coal increases at a speed of 10–25 m/a, and the working face length gradually increases from 100–200 m to 300–350 m, and even above 400 m in some cases (Li et al., 2021; Zou et al., 2022b; Zhang et al., 2023a; Su et al., 2023; Ye et al., 2023). The increases in the burial depth and working face length cause significant changes in strata behaviors (Zhang et al., 2022a; Liang et al., 2022; Ran et al., 2023a), and more pre-existing cracks are found in surrounding rocks of deep mines (Ran et al., 2023b; Zhang et al., 2023b; Zou et al., 2023). As a result, the weighting in working faces occurs more frequently with a smaller step, in different areas (Wang et al., 2019; He et al., 2022; Liang et al., 2023). Some scholars found the decrease in the lumpiness of broken rocks in the key strata of overburden with the increase in working face length, accompanied by weighting of the main key strata, through similar material simulation and field measurement (Zuo et al., 2021; Gao et al., 2022; Liu et al., 2022). A high-intensity working face (characterized by the large mining height, long working face, and fast advance speed) was simplified into a two-dimensional (2D) beam model (He et al., 2020; Behera et al., 2021; Lou et al., 2021). The research found that the height–length ratio of broken rocks in the main roof increases due to the growing thickness of the load-bearing layer, mining height, and working face length. In addition, rock blocks in the main roof are highly prone to sliding during the first weighting, which is the cause for intense strata behaviors during shallowly buried high-intensity mining. Based on bearing characteristics of hydraulic supports (Ren et al., 2022; Zhang et al., 2022b), some researchers (Xu and Wang, 2017; Xu et al., 2018; Chi et al., 2021; Zhang et al., 2022b) built the rock beam model for hydraulic support groups of the elastic independent support, deduced the matrix equation for the supporting stress field of hydraulic supports for the roof, and offered the corresponding simplified calculation method. Some established the three-dimensional (3D) numerical model for a fracture zone in overlying strata of deep stopes with thin bedrocks and thick unconsolidated layers (Zhang et al., 2015), based on the pressure arch, stress shell, and Platts theories (Ma and Wu, 2021; Wang et al., 2022). Then, influences of the working face length on the height of the fracture zone and support resistance were quantitatively analyzed. Numerical analysis and field measurement were also conducted to reveal that load-bearing arches can be formed in overlying strata of shallowly buried longwall faces (Ren and Qi, 2011). In addition, the working face has a critical length. Once exceeding the critical length, it exerts lowered influences on the stability of overlying strata. An energy model (Mohammad et al., 2015) fully considering the geometry of stopes and mechanical parameters of rocks was built and compared with the results of field measurement, the theoretical model, and the numerical model, revealing that the model is able to effectively predict the height of fracture zones in a stope. Previous research (Song and Wang, 2014; Wang and Ju, 2014) also found the W-shaped distribution characteristic of pressure in the dip direction of the working face by analyzing the strata behaviors in a 450 m super-long fully mechanized working face in Halagou Coal Mine (Shaanxi Province, China). Obviously, existing research on roof fracture along the length direction of working faces mainly summarized mine pressure using field measurements and analyzed its influencing factors combining numerical simulation (Chen et al., 2021; Zhao et al., 2021).

For further quantitative analysis, the research quantitatively analyzed the influencing factors of roof stability of a super-long working face buried about 1,000 m underground in Kouzidong Coal Mine (SDIC Xinji Energy Co., Ltd., Huainan, Anhui Province). Two working faces, 121304 and 140502, were observed, and mine pressure data were analyzed. On this basis, the distribution characteristics of supporting stress of hydraulic support groups and the weighting characteristics in the super-long fully mechanized working face in a deep thick coal seam were theoretically analyzed based on the model of the elastic independent support. In addition, the influencing factors of mine pressure in the super-long working face were revealed. According to distribution of the supporting stress in the super-long fully mechanized working face in the deep thick coal seam and combining the coupling characteristics of hydraulic supports and surrounding rocks, the principle, method, and control strategy of zonal cooperative control were proposed. The adaptability of hydraulic supports was improved through zonal cooperative control of hydraulic support groups in different areas, which provides a new method for roof control of intelligent working faces in similar coal mines.

2 Materials and methods

2.1 Overview of the deep super-long working face and model establishment

2.1.1 Overview of the coal mine

The coal seam of the 121304 working face in Kouzidong Coal Mine is buried 1,000 m underground and has a thickness of 2.2–6.7 m (5.18 m on average). The immediate roof of the working face is interbedding of mudstone and sandy mudstone with the thickness of 4.2–10.1 m and low hardness; the main roof is siliceous-cemented fine sandstone, with an average thickness of 5.0 m. The working face is 350 m long and excavated through full-seam mining with a large mining height. ZZ13000/27/60D four-leg shield hydraulic supports with a center-to-center distance of 1750 mm were used in the working face.

2.1.2 Model establishment

The supporting stress distribution of hydraulic support groups in the super-long working face can be analyzed using the elastic support model (Xu and Wang, 2017). As shown in Figure 1A (Xu et al., 2018), the model regards each support and the roadway walls

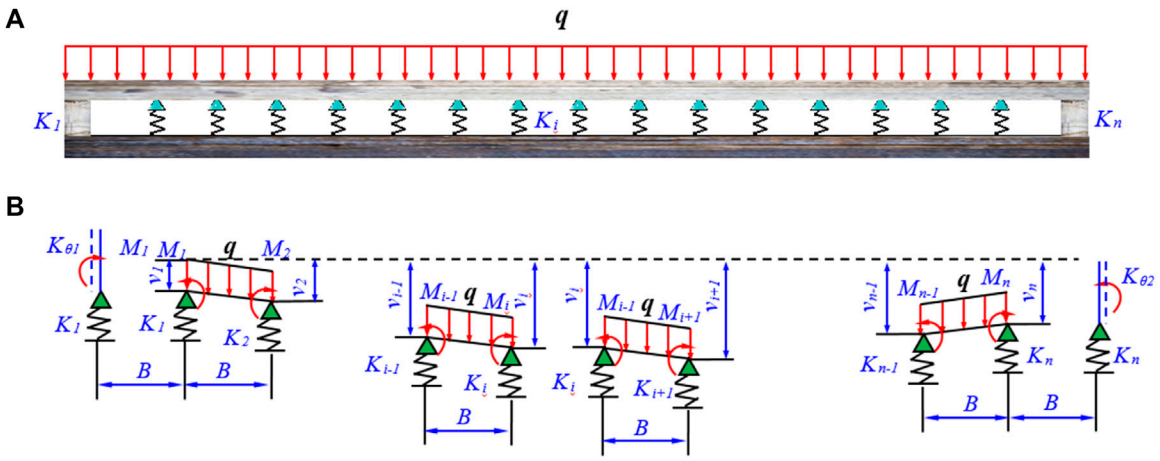


FIGURE 1
Model. **(A)** Hydraulic support groups regarded as an elastic support; **(B)** discrete single-span beam.

at both ends of the working face as elastomers of certain rigidity. Then, the relationship of the rigidity matrix $\{K\}$, moment of a single-span beam $\{M\}$, and load $\{Q\}$ of hydraulic supports is established based on the deformation compatibility condition of the rock beam (Xu and Wang, 2017).

As shown in Figure 1A a Cartesian system is established to analyze the stress field of the coal around a borehole: a linear pore elastic model and the coordinate transformation equation are used to convert the stress state distribution of the borehole in the natural spatial coordinate system to a stress model in *x*-, *y*-, and *z*-direction centered on the borehole to solve for the stress distribution around the borehole. The transformation equation is as follows:

$$\{K\}\{M\} = \{Q\}, \tag{1}$$

where K, M, and Q in are determined using the following equations:

$$K = \begin{bmatrix} a_{11} & a_{12} & a_{13} & & & & & 0 \\ a_{21} & a_{22} & a_{23} & a_{24} & & & & \\ a_{31} & a_{32} & a_{33} & a_{34} & a_{35} & & & \\ & a_{42} & a_{43} & a_{44} & a_{45} & a_{46} & & \\ & & & \ddots & \ddots & \ddots & & \\ & & & & a_{n-1n-3} & a_{n-1n-2} & a_{n-1n-1} & a_{n-1n} \\ 0 & & & & & a_{nn-2} & a_{nn-1} & a_{nn} \end{bmatrix},$$
$$M = \begin{bmatrix} M_1 \\ M_2 \\ M_3 \\ M_4 \\ \vdots \\ M_{n-1} \\ M_n \end{bmatrix}, Q = \begin{bmatrix} b_1 \\ b_2 \\ b_3 \\ b_4 \\ \vdots \\ b_{n+1} \\ b_{n+2} \end{bmatrix}, \tag{2}$$

where K is the symmetric matrix and the coefficient is $a_{ij} = a_{ji}$. If we convert Figure 1A into the discrete single-span beam in Figure 1B, values of the aforementioned parameters can be calculated. In the working face in the figure, n-2 hydraulic supports are erected, on which uniform load q is applied. The center-to-center distance of hydraulic supports is B; K_1 and K_n separately represent the rigidity of roadway walls, and K_i is the rigidity of hydraulic supports $(i = 2, 3, \cdots, n-1)$; $K_{\theta 1}$ and $K_{\theta 2}$ separately denote the rigidity of rock beams at both ends; M_i represents the bending moment at each elastic support; and v_i refers to the displacement of each support (Xu et al., 2018).

If the thickness of roof strata above the support does not change, the inertia moment of rock beams above the support is I, the bending moment at each support is M_i, and the subsidence of supports is v_i. The correlation coefficient of K and Q can be calculated according to Figure 1B (Zhang et al., 2022c).

$$\begin{cases} a_{11} = \dfrac{1}{K_{\theta 1}} + \dfrac{B}{3EI} + \dfrac{K_1 + K_2}{K_1 K_2 B^2} \\ a_{12} = \dfrac{B}{6EI} - \dfrac{1}{K_1 B^2} - \dfrac{2}{K_2 B^2} \\ a_{13} = \dfrac{1}{K_2 B^2} \\ a_{ii} = \dfrac{2B}{3EI} + \dfrac{1}{K_{i-1} B^2} + \dfrac{4}{K_i B^2} + \dfrac{1}{K_{i+1} B^2}, \\ a_{nn-2} = \dfrac{1}{K_{n-2} B^2} \\ a_{nn-1} = \dfrac{B}{6EI} - \dfrac{2}{K_{n-1} B^2} - \dfrac{1}{K_n B^2} \\ a_{nn} = \dfrac{1}{K_{\theta 2}} + \dfrac{B}{3EI} + \dfrac{K_{n-1} + K_n}{K_{n-1} K_n B^2} \end{cases} \tag{3}$$

$$\begin{cases} b_1 = \dfrac{qB^3}{24EI} - \dfrac{q}{2K_1} + \dfrac{q}{K_2} \\ b_2 = \dfrac{qB^3}{12EI} + \dfrac{q}{2K_1} - \dfrac{2q}{K_2} + \dfrac{q}{K_3} \\ b_i = \dfrac{qB^3}{12EI} + \dfrac{q}{K_{i-1}} - \dfrac{2q}{K_i} + \dfrac{q}{K_{i+1}} \\ b_{n-1} = \dfrac{qB^3}{12EI} + \dfrac{q}{K_{n-2}} - \dfrac{2q}{K_{n-1}} + \dfrac{q}{2K_n} \\ b_n = \dfrac{qB^3}{24EI} + \dfrac{q}{K_{n-1}} - \dfrac{q}{2K_n} \end{cases}. \tag{4}$$

The model parameters include a mining height of 5.5 m, support rigidity of 0.48 GN/m, thickness of roof strata of 15 m, bulk density of rocks of 27 kN/m^3, and elastic modulus of the roof of 40 GPa.

2.2 Conditions of the coal seam and determination method for supporting intensity in the working face

2.2.1 Conditions of the coal seam

The No. 5 coal seam, which has a simple structure and is mineable in the whole area, was mined in working face 140502. The average thickness of the coal seam is 6.56 m. The roof and floor are dominated by mudstone, with a small amount of fine sandstone, siltstone, and sandy mudstone. The immediate roof is composed of mudstone, with an average thickness of 2.81 m; the main roof consists of siltstone and sandstone, which are separately 7.65 and 13.85 m thick on average. The immediate floor mainly contains mudstone with an average thickness of 1.62 m. The main roof is interbedding of siltstone and sandstone and is 5.56 m thick on average. The dip angle of the coal seam is 8°–15° (14° on average), and the strike pitch in some areas of the working face is 17°.

2.2.2 Determination method of supporting intensity

The full-seam down-dip mining method was adopted in working face 140502, and the maximum mining height was 7 m. Because of the large burial depth, large mining height, and softness of the coal seam, reasonable selection of hydraulic supports is the key to safe and efficient mining of the working face. Considering the long-term usage in the Huainan Coal Mine area, four-leg shield hydraulic supports were adopted, which have been discussed in previous research (Wang et al., 2020), so it is not repeated here. The determination method for the reasonable supporting intensity required by the hydraulic supports was mainly introduced as follows. Previous research on the required supporting intensity in a working face buried 1,000 m underground in Tangkou Coal Mine (Xu et al., 2015) found that it is reasonable to use Eq. 5 to calculate the required supporting intensity of hydraulic supports in the deep working face.

$$P = (2.75 + \Psi)\frac{\gamma M}{K_p - 1}, \tag{5}$$

where P, γ, K_p, M, and Ψ denote the supporting intensity, bulk density, bulking coefficient of rocks, mining height, and coupling factor, respectively. The equation adds coupling factor Ψ to the formula for estimating the supporting intensity of hydraulic supports based on the bulk density of rock pillars equivalent to the mining height. Coupling factor Ψ can be calculated as

$$\Psi = \frac{11l}{\beta 8} + \frac{11\sqrt[4]{\eta}\left(E_c + 2\beta^3 EIM\right)(\alpha + 2)\cos \alpha l}{8E_c e^{\alpha l}}, \tag{6}$$

where l, η, E_c, EI, and M represent the length of top beams, ratio of rigidity of hydraulic supports to that of coal, elastic modulus of coal walls, flexural rigidity per unit width of rock beams in the roof, and mining height, respectively; $\alpha = \sqrt[4]{\frac{E_p}{4EIM}}$, and $\beta = \sqrt[4]{\frac{E_c}{4EIM}}$.

Obviously, coupling factor Ψ is a physical quantity related to the rigidity of hydraulic supports, lithology of the roof, and hardness of coal walls. If the supports and coal walls are regarded as rigid bodies, then $\Psi = 0$; that is, hydraulic supports are decoupled with surrounding rocks; if the supports and coal walls are elastomers, then $\Psi \neq 0$, which means that hydraulic supports are coupled with surrounding rocks. It is evident that Eq. 1 well describes the coupling relationship for the rigidity of hydraulic supports and surrounding rocks. The calculation parameters are set as follows (Pang et al., 2020): the elastic modulus of the coal seam is 30 GPa, the bulk density of rocks is 2.7 t/m^3, the bulking coefficient is 1.35, the maximum mining height is 7 m, the top beam is 5 m long, and the hydraulic supports have a center-to-center distance of 1.75 m. According to the coupling formula for the rigidity of hydraulic supports and surrounding rocks, the curve of the required supporting intensity of hydraulic supports is attained, as shown in Figure 2.

The blue straight line in the figure represents that the required supporting intensity of hydraulic supports is calculated to be 1.48 MPa according to the weight of rock pillars equivalent to nine times the mining height. The black curve in the figure is the required supporting intensity of hydraulic supports obtained based on the coupling theory of the rigidity of hydraulic supports and surrounding rocks. Obviously, the required supporting intensity of hydraulic supports is closely related to the lithology of roof, thickness of coal seams, and rigidity of supports, and the calculation result obtained using the traditional method is lower. Because the rigidity of hydraulic supports is lower than that of the coal seam (Xu, 2015; Xu et al., 2019), the required supporting intensity of hydraulic supports should not be lower than 1.7 MPa. Therefore, the supporting intensity of the ZZ18000/33/72D four-leg shield hydraulic supports is determined to be in the range of 1.73–1.78 MPa.

Because the supporting stress of hydraulic supports increases and the strata behaviors in working faces are intensified as the mining height grows, determining a reasonable working face length is a focus for studying working face 140502. Compared with working face 121304, the maximum mining height of working face 140502 is as large as 7 m, and the main roof of the working face is thicker. The calculation parameters include the mining height (7 m), rigidity of supports (0.6 GN/m), thickness of roof strata (21 m), and bulk density of rocks (27 kN/m^3).

3 Results and discussion

3.1 Characteristics of strata behaviors in the deep super-long working face

In the early mining period of the working face, a complete set of equipment including hydraulic supports was arranged in the working face and the roof was relatively stable. The overlying rock beam was interbedded in the strata and, therefore, can be regarded as rigidly fixed on the support (Figure 3). Under the condition, both the displacement and rotational angle at the

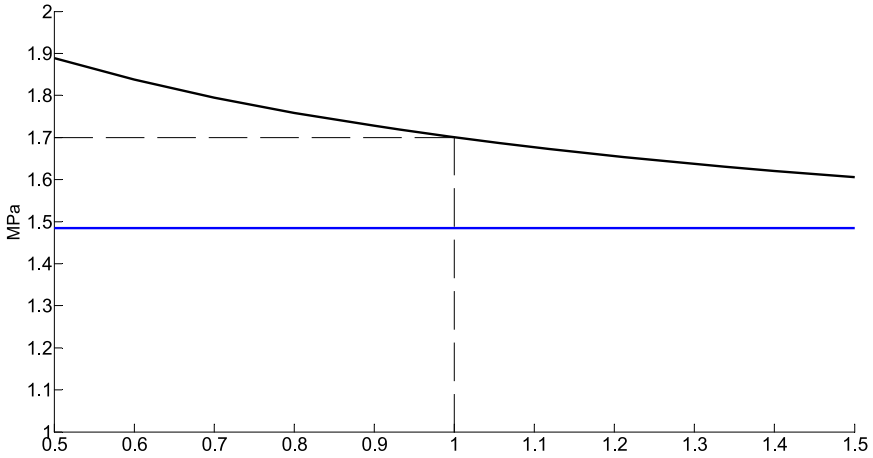


FIGURE 2
Required supporting intensity of hydraulic supports.

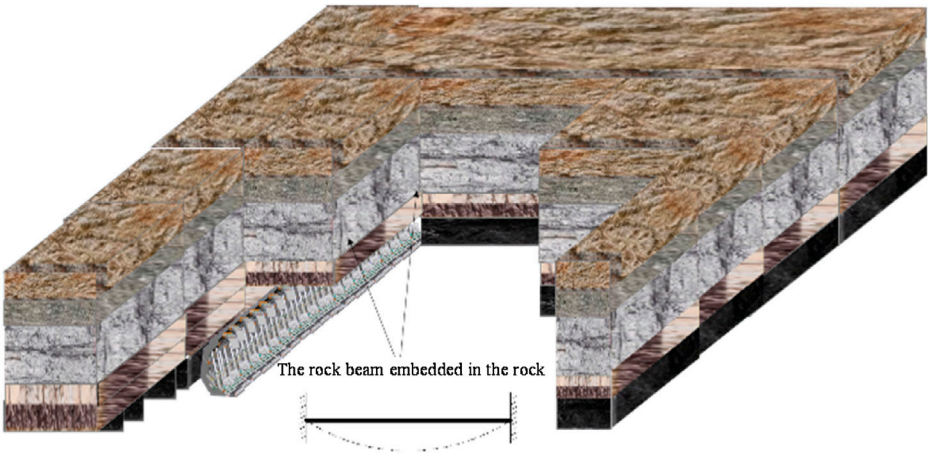


FIGURE 3
The roof is in a fixed support state after opening of the working face and at the initial stage of mining.

support were zero. Figures 4, 5 show the calculation results when considering roadway walls as rigid bodies (Figure 5 is the front view of the supporting stress of hydraulic support groups in the working face, that is, the projection of supporting stress in the working face onto the coal wall). It can be seen from the figures that the supporting stress has three peaks separately at points A, B, and C, which are located at 101 m, the middle, and 249 m of the working face, respectively. The supporting stress at points A and B is 1.3 MPa, and that at C is 1.26 MPa. Obviously, the peak values at points A and C are higher than that at B; that is, the peaks are high at both ends and low in the middle, forming a saddle shape seeming like the letter "M," so the phenomenon is collectively called three-peak M-like distribution.

To facilitate understanding of the distribution characteristics of the supporting stress of hydraulic support groups in the whole working face, the supporting force in Figure 4 is combined with the hydraulic support groups in the working face and data at each coordinate in Figure 4 are displayed to a certain scale. In this way, distribution characteristics of supporting stress of hydraulic support groups in the working face on each hydraulic support are obtained.

After opening the coal seam in the working face, overlying strata have a space to fracture, cave, and rotate, so the rock beam has corresponding migration along both strike and dip directions of the working face. In this case, several support modes, including simple support, elastic support, and elastic fixed end displayed in Figures 6, 7, are present in the working face.

When regarding roadway walls as elastomers with the rigidity of 30 GN/m while keeping other calculation parameters unchanged, distribution characteristics of the supporting stress of hydraulic support groups are shown in Figures 8–10. It can be seen from Figure 9 that points A, B, and C are separately located at 77 m, the middle, and 273 m of the working face, respectively.

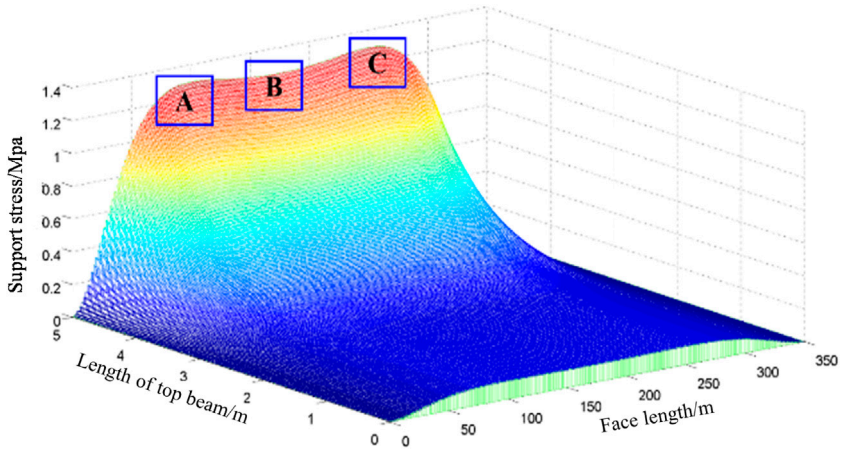


FIGURE 4
Supporting stress field of hydraulic supports.

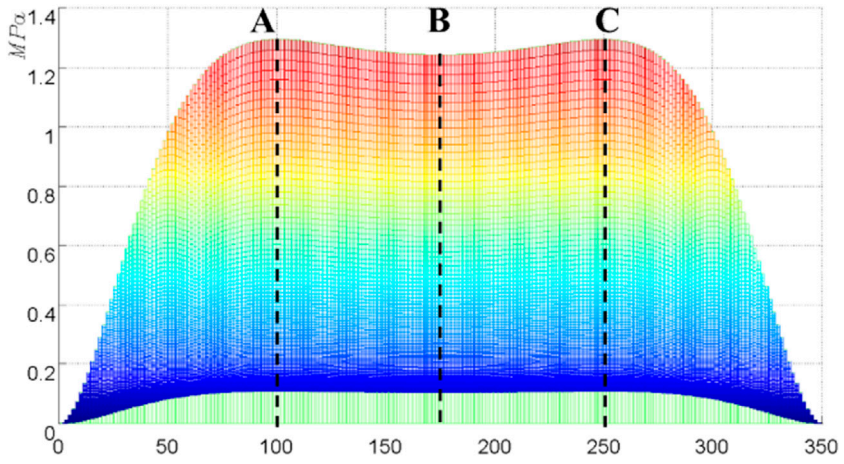


FIGURE 5
Front view of the supporting stress field.

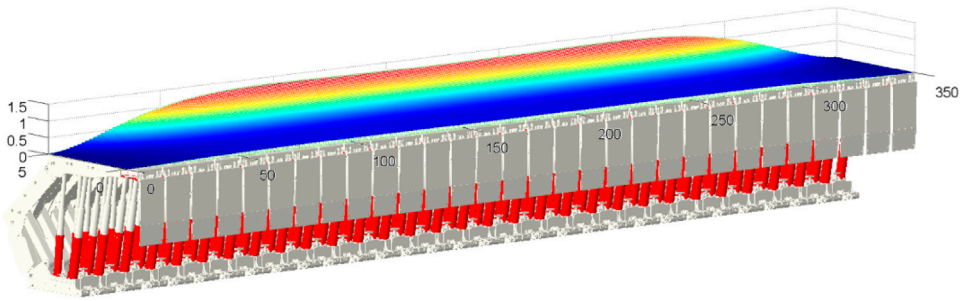


FIGURE 6
Supporting stress field of hydraulic support groups.

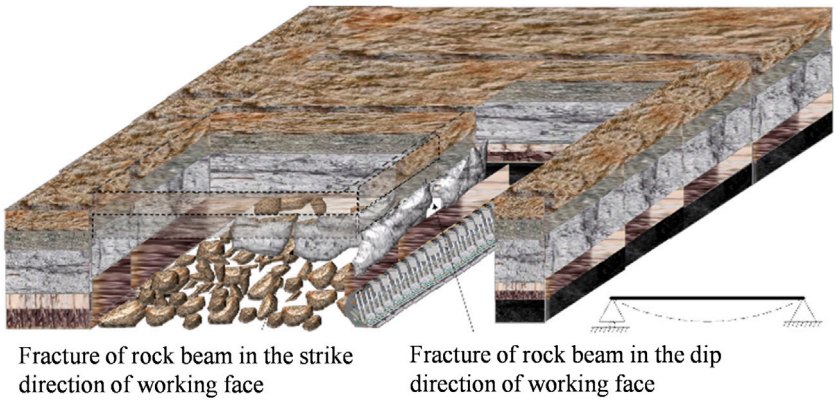


FIGURE 7
Roof collapse of the working face along the strike and dip directions in the normal mining stage.

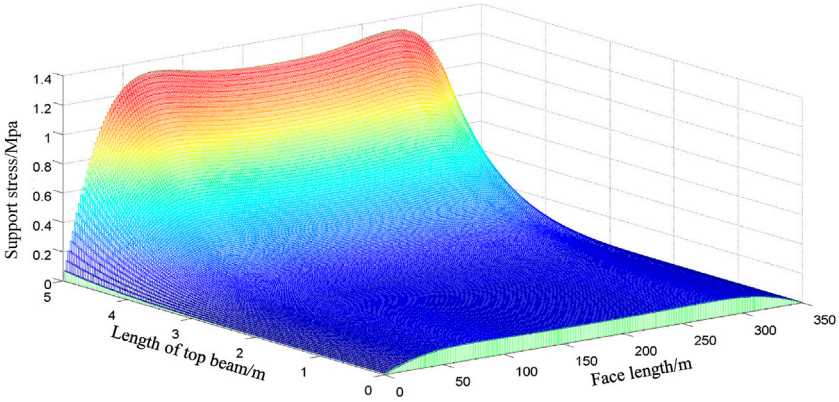


FIGURE 8
Supporting stress field of hydraulic supports.

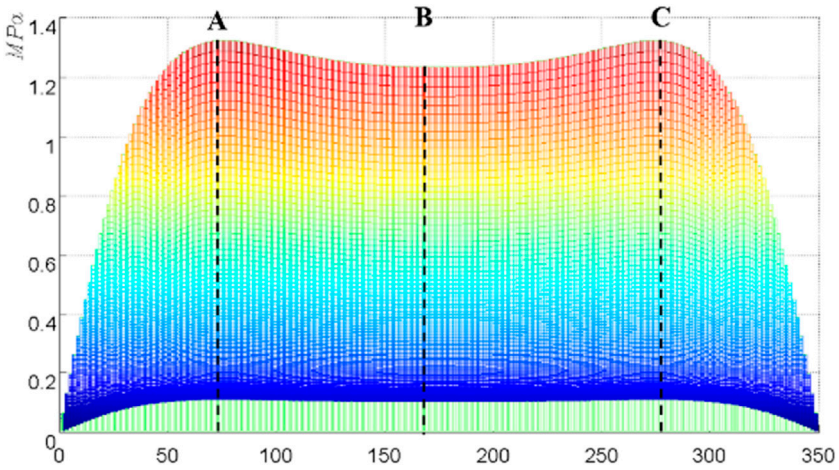


FIGURE 9
Front view of the supporting stress field.

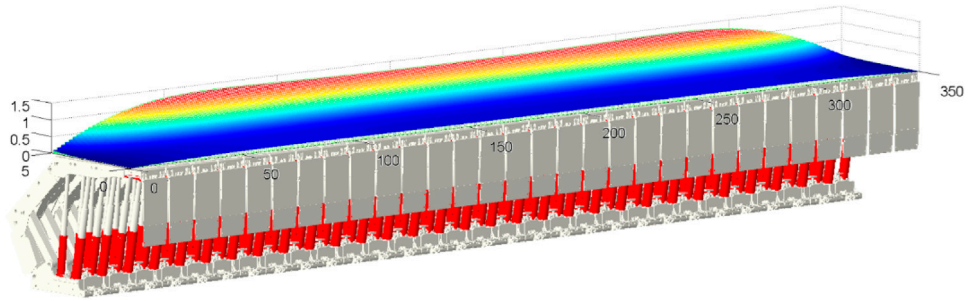


FIGURE 10
Distribution of the supporting stress of hydraulic support groups.

A comparison of Figures 5, 9 reveals that as the rigidity of roadway walls reduces, the maximum peak point A of the supporting stress shifts from the original location of 101 m–77 m in the working face; the maximum peak point B changes from the original location of 249 m–273 m; that is, the peak supporting stress of hydraulic supports shifts to both ends gradually and more supports in the working face are in the high-stress zones. Combined with Figures 3–10, the supporting stress of hydraulic supports in the super-long working face is distributed in a saddle shape with M-like three peaks, and large areas of hydraulic supports are in the high-stress zone.

3.2 Field-monitored support stress characteristics

The working resistance of hydraulic supports in working face 121304 was monitored online. Seven measuring lines were arranged separately along 9# and 189# supports on the upper and lower ends, 40# and 80# supports in the upper middle, 130# and 160# supports in the lower middle, and 100# support in the middle of the working face. Figure 11A shows the measured working resistance of hydraulic supports on the seven measuring lines along the advance direction of the working face; Figure 11B illustrates the measured values and distribution trends of working resistance of hydraulic supports on five profiles along the length direction of the working face under different advancing progresses. It can be seen from the figures that weighting in different areas of the working face shows obvious time sequences and different intensities, with a weighting step of 15–25 m and a smaller weighting step in the middle compared to the weighting step at both ends. Generally, weighting occurs first to the middle and lags behind in both ends of the working face. Particularly, the middle of the working face experiences weighting at a higher frequency with unobvious periodicity. Because the working face is long, the pressure on hydraulic supports in different areas varies significantly, showing a saddle-shaped distribution trend, which is in good agreement with the results of theoretical calculation.

Figures 12A–C separately show the supporting stress of hydraulic support groups when the working face length is 240, 300, and 350 m.

As shown in the figures, the supporting stress of hydraulic support groups begins to change from a single peak to multiple peaks with the increase in working face length. The supporting stress of hydraulic support groups has a single peak when the working face is 240 m long. The supporting stress begins to show the saddle-shaped three-peak M-like distribution when the working face length is 300 m. The saddle shape becomes more obvious when the working face is 350 m long, and the supporting stress begins to spread to both ends of the working face. It can be seen that the mining height exerts large influences on the distribution characteristics of the supporting stress of hydraulic support groups in the working face, so the working face length is determined to be 300 m.

3.3 Characteristics of the super-long working face in a deep thick coal seam

3.3.1 Relationship between the supporting stress and end conditions of the working face

Figure 13A shows the supporting stress of hydraulic support groups when changing roadway walls at two ends of the working face from rigid bodies to elastomers with a rigidity of 30 GN/m while keeping other conditions unchanged under the mining height and working face length separately of 7 and 240 m. The supporting stress of hydraulic support groups is distributed in the three-peak M-like pattern. Compared with Figure 12A, the supporting stress of hydraulic support groups begins to change from a single peak to three-peak M-like pattern as the rigidity of roadway walls at both ends of the working face reduces and more supports are located in the high-stress zone. It indicates that distribution of supporting stress in the working face is closely related to the condition of roadway walls at both ends. Obviously, the weaker the roadway walls are, the more likely it is for the supporting stress in the working face to show the three-peak M-like distribution under the same condition.

3.3.2 Relationship between the supporting stress in the working face and the lithology of the roof

Figure 13B shows the supporting stress of hydraulic support groups when the mining height and working face length are separately 7 and 300 m after adjusting the elastic modulus of the roof to 55 GPa while keeping other conditions unchanged. The

supporting stress only has a peak. Compared with Figure 12B, the supporting stress of hydraulic support groups begins to change from single-peak distribution to three-peak M-like distribution with the weakening of the roof, and more supports are located in the high-stress zone. The result suggests that the distribution of the supporting stress in the working face is closely related to the lithology of the overlying strata and roof. Obviously, the weaker the roof is, the more likely it is for the supporting stress in the working face to show the three-peak M-like distribution under the same conditions.

3.3.3 Relationship between the supporting stress in the working face and the thickness of the main roof

Figure 13C displays the supporting stress of hydraulic support groups when the mining height is 7 m and working face length is 300 m after increasing the thickness of the main roof from 21 m to 30 m while keeping other conditions unchanged. As shown, the supporting stress of hydraulic support groups only has a peak. A comparison with Figure 12B reveals that as the thickness of the main roof decreases, the supporting stress of hydraulic support groups starts to turn from single-peak distribution to three-peak distribution and more

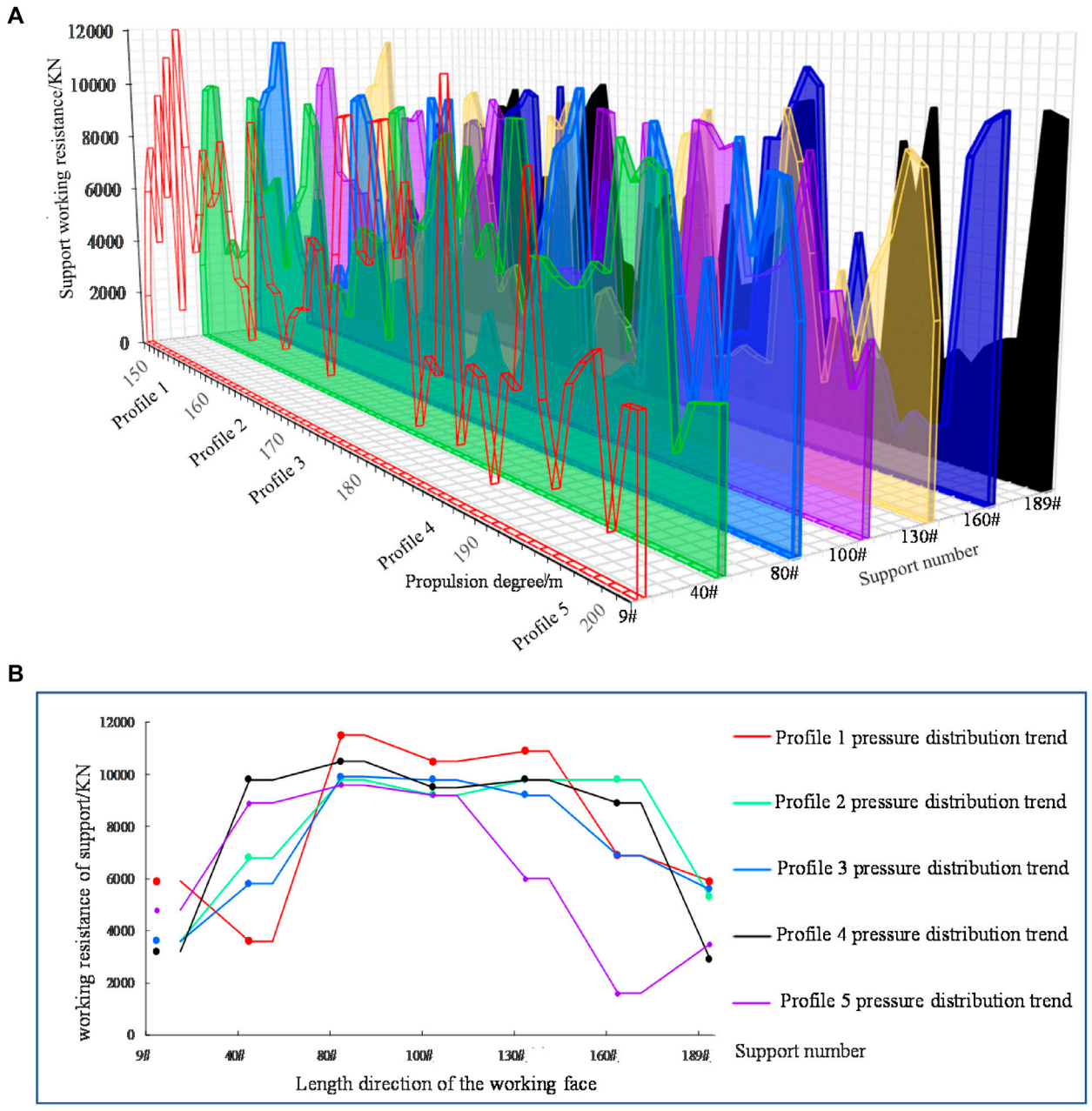


FIGURE 11
Curves of the measured working resistance of hydraulic supports. **(A)** Measured working resistance of hydraulic supports on the seven measuring lines along the advance direction of the working face; **(B)** measured values and distribution trends of working resistance of hydraulic supports on five profiles along the length direction of the working face under different advancing progresses.

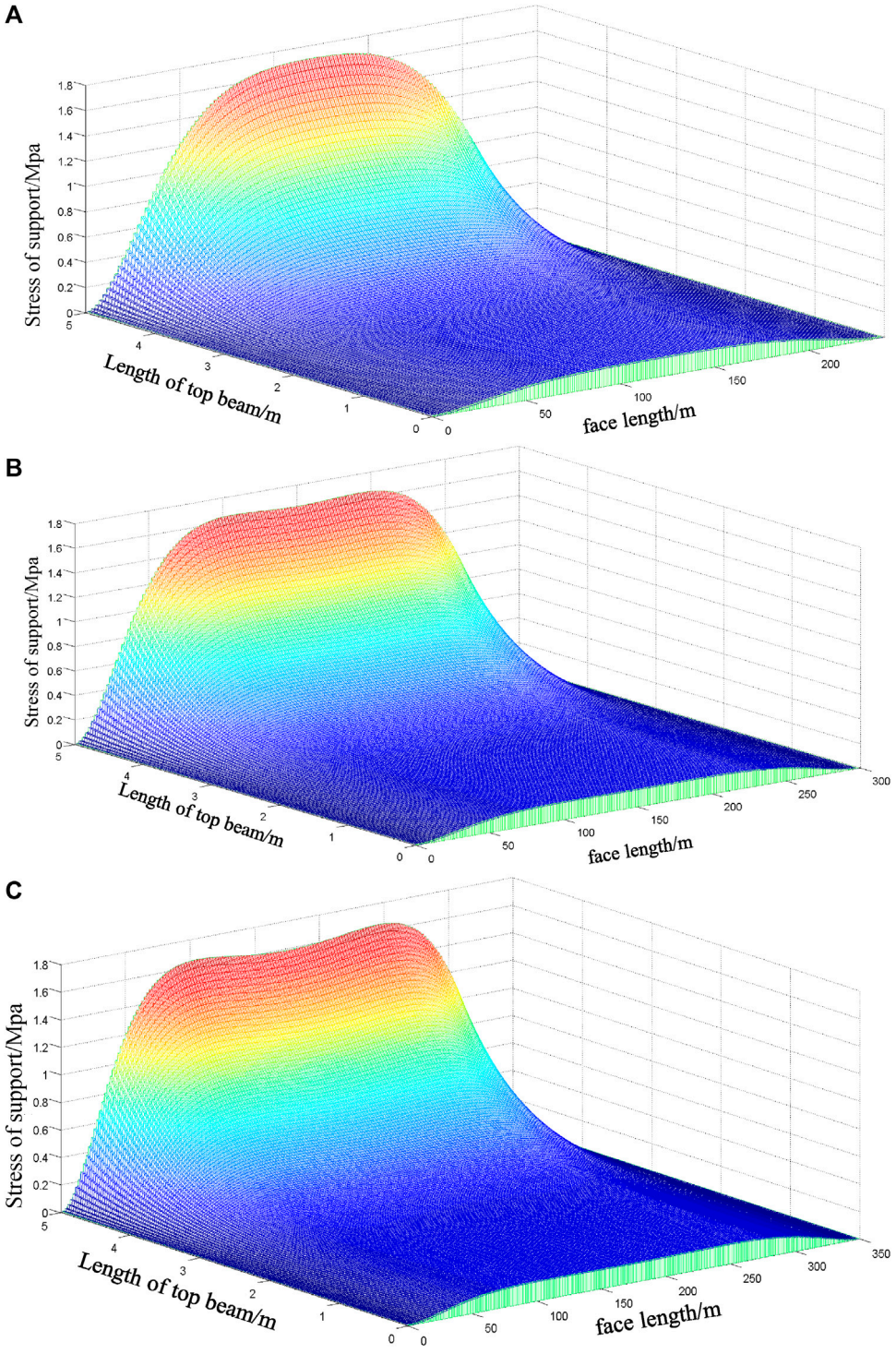


FIGURE 12
Supporting stress field of hydraulic support groups under different working face lengths. **(A)** The working face length is 240 m; **(B)** 300 m; **(C)** 350 m.

supports are found in the high-stress zone. The result indicates the close correlation between the distribution of the supporting stress in the working face and the thickness of the overlying bedrock. It is evident that the thinner the overlying bedrock is, the more likely it is for the supporting stress in the working face to show the three-peak M-like distribution under the same condition.

3.4 Criterion for the super-long working face

The presence of three-peak M-like distribution of the supporting stress in the working face is a characteristic first proposed in according to the measured pressure data in a 450 m super-long

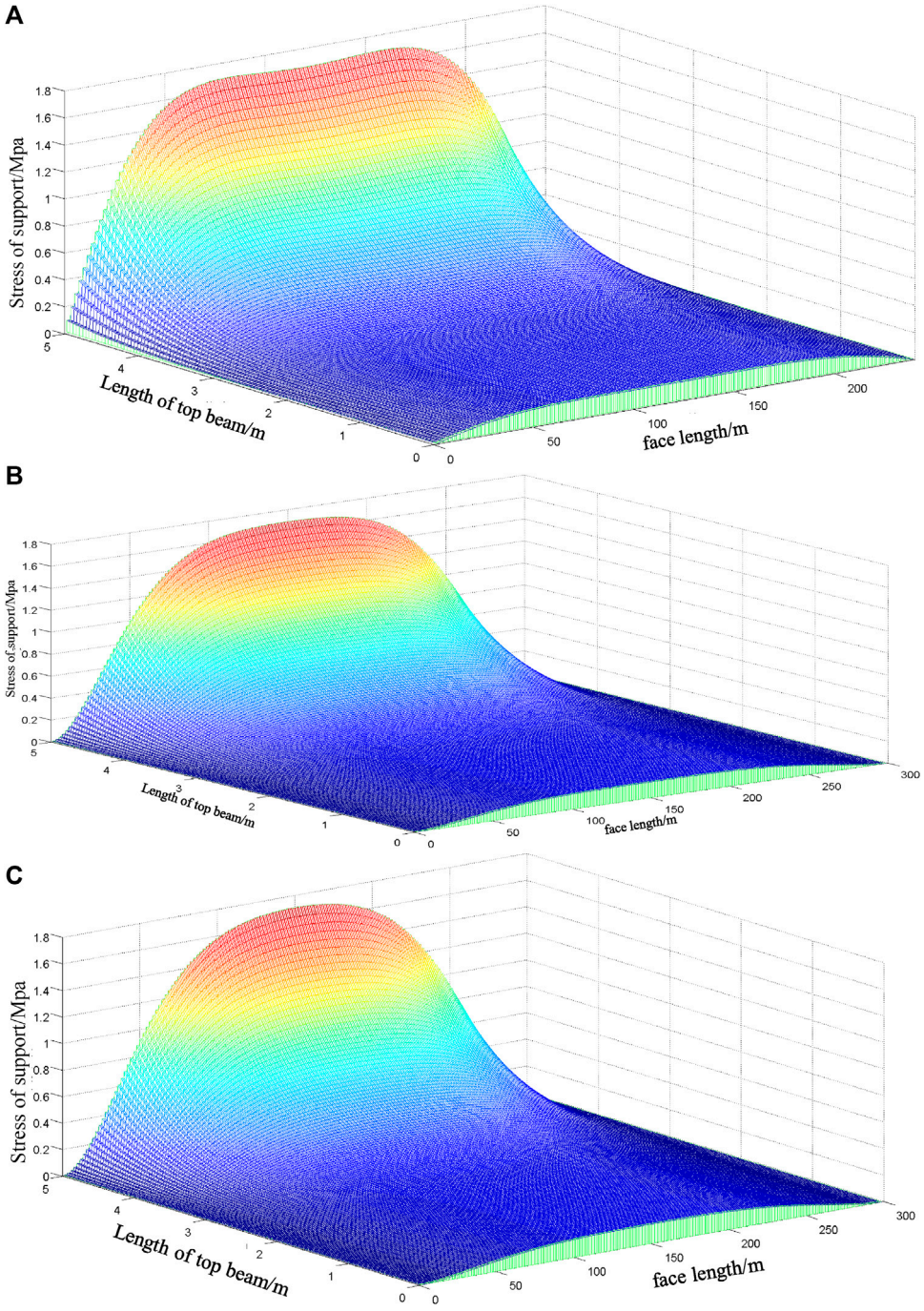


FIGURE 13
Supporting stress field of hydraulic supports. **(A)** The mining height and working face length separately of 7 and 240 m, bodies to elastomers with rigidity of 30 GN/m; **(B)** the mining height and working face length separately of 7 and 300 m, the elastic modulus of the roof to 55 GPa; **(C)** the mining height and working face length separately of 7 and 300 m, increasing the thickness of the main roof from 21 m to 30 m.

working face in Halagou Coal Mine (Song and Wang, 2014; Wang and Ju, 2014), which has also been studied in the work of Xu et al. (2018). According to the aforementioned analysis, the supporting stress of hydraulic support groups in the working face definitely turns from the single-peak distribution to three-peak M-like distribution with the increase in the working face length while keeping other conditions unchanged. After the occurrence of the three-peak M-like distribution, the phenomenon becomes more significant once the working face length is further increased, and the peaks shift to both ends of the working face.

The three-peak M-like distribution of the supporting stress in the working face is closely related to the working face length and it is bound to occur once the working face length exceeds a certain value. This reveals that the three-peak M-like distribution characteristic is

an attribute specific for super-long working faces. Therefore, whether the supporting stress of hydraulic support groups in the working face has the three-peak M-like distribution characteristic or not can be taken as a criterion for super-long working faces.

The main cause for the three-peak M-like distribution of the supporting stress in the super-long working face was analyzed as follows. The aforementioned analysis indicates that under the same condition, as the support conditions of roadway walls at the ends of working faces weaken, the supporting stress in the working face begins to change from one peak to three peaks. This suggests that the support conditions of roadway walls at ends of the working face greatly influence the distribution pattern of the supporting stress in the working face. The influences of conditions of roadway walls at the ends on the supporting stress can be used to explain the cause for the three peaks of the supporting stress in the super-long working face. With the increase in working face length, the support action of the roadway walls at both ends of the working face for the overlying strata in the middle weakens. Under the same support conditions, the subsidence of overlying strata in the middle gradually increases so that more supports are located in the high-stress zone, and therefore, the supporting stress has three peaks. Once further increasing the working face length after the occurrence of the three-peak distribution of the supporting stress, the support action of roadway walls at both ends of the working face for the middle further weakens. The range in the middle of the working face where subsidence of overlying strata increases begins to expand to both ends and more supports are in the high-stress zone, which is shown as a shift of the peak supporting stress to both ends of the working face. Obviously, the supporting stress in the working face shows three peaks, which is caused by the weakened action of the support conditions at the ends on the overlying strata in the middle of the working face. This is the primary cause for the three-peak M-like distribution of the supporting stress in the super-long working face.

The three-peak M-like distribution of the supporting stress in the working face is not only determined by a single parameter (working face length) but also related to many conditions, including the burial depth, mining height, working face length, roof lithology, bedrock thickness, and condition of roadway walls. The three-peak M-like distribution occurs to the 450 m-long working face in Halagou Coal Mine; the distribution pattern appears in the 350 m-long working face in Kouzidong Coal Mine when the mining height is 5.5 m; and the distribution characteristic occurs in working face 140502 under the working face length of only 300 m when the mining height is 7 m. For the fully mechanized working face with a large mining height in deep thick coal seams, its length has to be determined reasonably according to the concrete occurrence conditions of the coal seams. Particularly for deep working faces of a large mining height, thin bedrock, soft coal seam, and fractured roof, the aforementioned aspects need to be fully considered to determine a reasonable working face length.

3.5 Cooperative control of equipment groups in the working face based on the state error and cost functions

As mentioned previously, the typical characteristic of the supporting stress in a super-long working face in a deep thick coal seam is the occurrence of three-peak M-like distribution. The supporting stress of hydraulic supports varies across areas and its peak shits to both ends of the working face, and more hydraulic supports are located in the high-stress zone as the working face length increases. Because the roof pressure is large in the areas of the M-like three peaks, overlying strata in these areas are first fractured, followed by fracture of overlying strata at both ends bearing lower pressure. Roof weighting occurs first to the middle and then both ends of the working face, which is shown as asynchronized and frequent weighting in different areas of the working face. The three-peak M-like distribution of the supporting stress in the super-long working face well explains phenomena including weighting in different areas, frequent weighting, and multiple pressure peaks in working face 121304 of Kouzidong Coal Mine.

Aiming at the aforementioned phenomena, the key to improving the support capacity and adaptability of hydraulic supports in the super-long fully mechanized working face in the deep thick coal seam is to use the zonal cooperative control method; that is, different control strategies are used for hydraulic supports in different areas.

Due to changes in the distribution characteristics of stress in surrounding rocks of the super-long working face, hydraulic supports cannot be controlled using the consistent process parameters in their support and advance process. Otherwise, the consistent and continuous control of surrounding rocks and advance of equipment in the working face cannot be ensured. Therefore, how to automatically adjust mining parameters in different areas of the super-long working face to reach the optimal overall support effect and the highest advance efficiency has become a key problem to be solved. Here, a cooperative control method for equipment groups in the working face based on the state error and cost functions was proposed to realize the optimal coordinated control of equipment groups in the super-long fully mechanized working face in the deep thick coal seam.

As shown in Figure 14, the cooperative control method for equipment groups in the working face based on the state error and cost functions was established to realize the expected behaviors of equipment groups. These include four objectives for equipment groups: velocity consistency, desired trajectory and velocity tracking, aggregation, and collision avoidance. The state error is defined as follows:

$$\dot{\hat{X}} = A\hat{X} + B\widehat{U}, \tag{7}$$

where X, A, U, and B represent the aggregation stage of all objects in a system at a certain time, the state matrix, the control input of the system, and the control matrix, respectively.

The group problem is converted to an optimal control problem of aggregation containing three components of cost functions.

$$\begin{aligned} &\min: J = J_1 + J_2 + J_3, \\ &s.t. \dot{\hat{X}} = A\hat{X} + BU, \end{aligned} \tag{8}$$

where J_1 is the cost function to ensure velocity consistency; J_2 is the cost function to ensure desired trajectory and velocity tracking, aggregation, and collision avoidance; and J_3 is the cost function of the cost control.

3.5.1 Control of hydraulic support groups

The control system of hydraulic support groups deduces specific parameters of three-peak M-like distribution of supporting stress in the super-long working face based on the

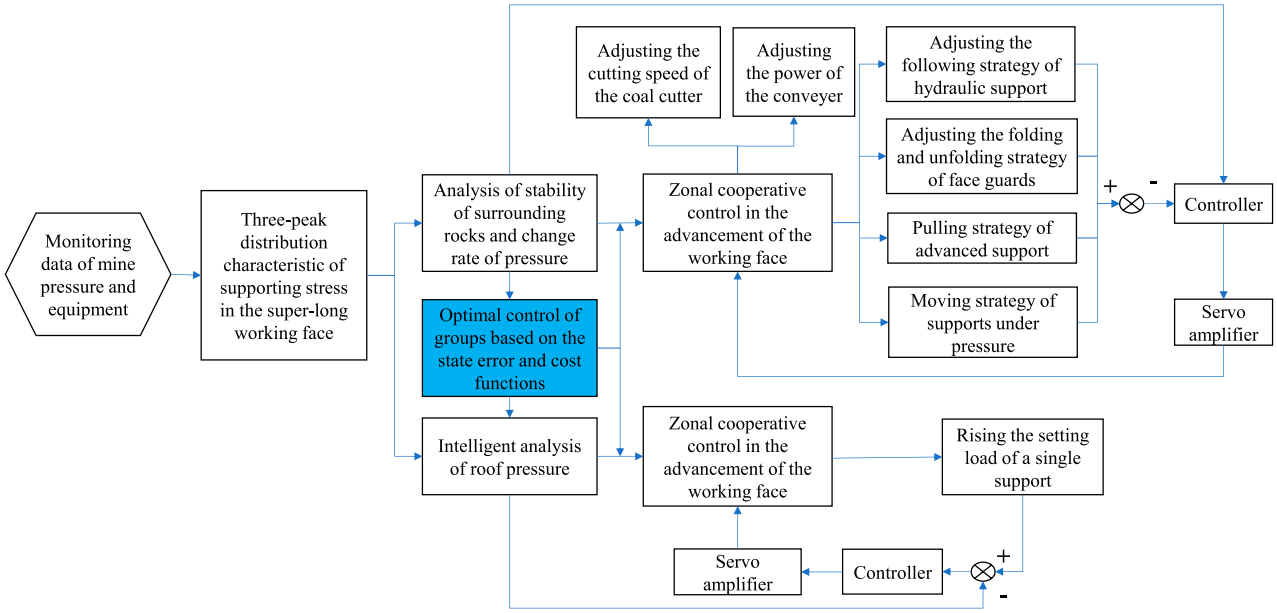


FIGURE 14
Method of group cooperative control of the working face.

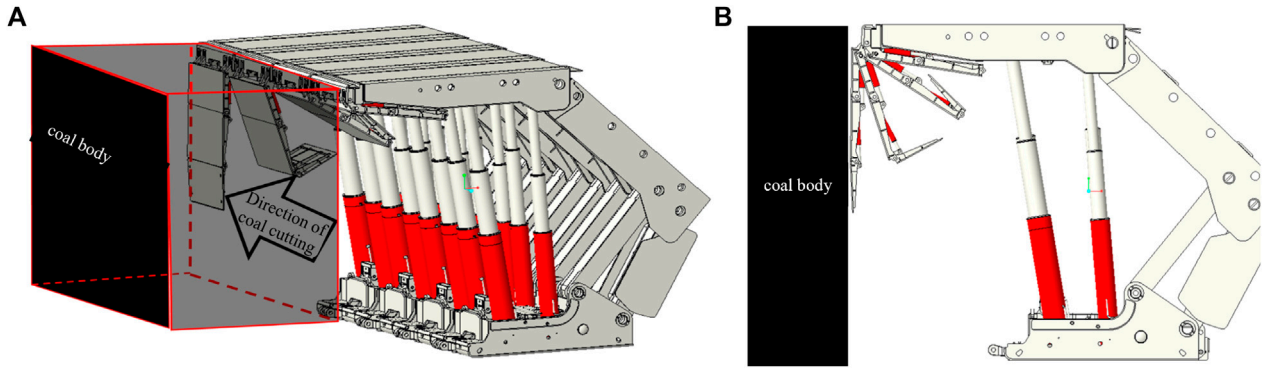


FIGURE 15
Cooperative control of three-level face guard mechanisms. **(A)** The area of five hydraulic supports along the advance direction of the coal cutter as the cooperative action zone of the face guard mechanism; **(B)** the real-time dynamic changes in the sequential control zone of the face guard mechanisms.

monitoring data of mine pressure and equipment. These parameters include the peak pressure, change rate, change period, maximum subsidence, and subsidence rate, which are separately input in control equation 8. In this way, the optimization model for the zonal adaptive control of supports and the zonal cooperative control of advancement of equipment for the working face is established. The adaptive control of supports means adaptive adjustment of the setting load of a single support; the cooperative control of advancement of equipment mainly refers to coordinated control of the hydraulic support, coal cutter, and scraper conveyer in areas of different pressures. The method is described in detail as follows: different control strategies are adopted in different areas according to pressure distribution characteristics in the working face; then, the three-level cooperative control strategy of "single-support control → multi-support control → group control" is used; the information acquisition module is used to acquire information including the advancing progress of the working face, roof weighting step, weighting frequency, shrinkage of support, pressure on props, and dip angle of the roof for decision making; the hydraulic support group is controlled to support the roadway actively to realize zonal cooperative control of the supporting intensity, rigidity, and stability of supports (Kang et al., 2018).

Based on perceptual information including the pressure, dip angle, and pushing of a single support, the 3D posture of the single

support is controlled along the vertical, horizontal, and strike directions using strategies including support in the vertical direction, collapse resistance in the horizontal direction, and pushing control in the strike direction. The posture of the single support is automatically controlled via precise support in the vertical direction, quantitative pushing in the strike direction, and prevention of deviation in the horizontal direction using a series of cooperative control methods. These methods include roof support, protection of roadway walls, pushing, bottom lifting, lateral pushing, and balance. Because down-dip mining was adopted in the working face, the setting load guarantee system was used for real-time monitoring and increasing the setting load of hydraulic supports during down-dip mining, as shown in Figure 14, to avoid difficulty in caving of the suspended roof in the overlying strata. This can realize the immediate caving and unloading of the roof after mining and avoids gas accumulation in the goaf, which is detrimental to production safety.

According to zonal roof caving of the working face and the sequential relationship of cooperative advancement, hydraulic support groups at the head, middle, and tail of the coal cutter were controlled separately based on control demands for the strength, rigidity, and stability and combining with the geological and production conditions in different areas. The middle of the working face is characterized by the high peak pressure, high probability to bear impact loads, and large proportion of opened safety valves. Considering this, the strength and rigidity adaptability of hydraulic support groups in the middle should be mainly improved. The pressure rises rapidly on hydraulic support groups in some areas on two sides of the middle, where the strata behaviors are more intense than in the conventional working face and the support bears offset loads. Therefore, the strength and rigidity adaptability of the hydraulic supports should be improved on the premise of ensuring the stability. At both ends of the working face, especially the head of the coal cutter, the cooperative advance relationship of the hydraulic support groups with the advanced support system is mainly coordinated, and the location relationship of the two should be controlled with particular attention.

The zonal weighting determines that the equipment is inevitably advanced asynchronized in the advancement of the working face. After several mining cycles, the pressure on the equipment in the working face is not uniform, so the group control strategy should be used; that is, the hydraulic support groups in the working face are taken as the research object to automatically align the working face using a straightening system of working faces, so as to manage the hydraulic support groups.

3.5.2 Control of ends of the working face and roadway walls

As mentioned previously, the stability of ends of the working face and the roadway walls has some influences on the distribution of the supporting stress of hydraulic support groups in the working face. Because the roadway roof is fractured in Kouzidong Coal Mine, the supports at the ends of working faces and roadway walls should be enhanced, so as to improve the support capacity and adaptability of hydraulic supports in the whole working face. At first, high-strength anchor cables, high-strength bolts, and anchor meshes were used for active high-strength support at the ends of the working face to improve stability of strata around the roadway. Then, high-strength face-end supports of high working resistance were adopted. On one hand, supports at the ends of the working face were stabilized, and on the other hand, the roof-cutting capacity of the face-end support was improved. Together with the automatic anchor withdrawal device, the pressure was relieved immediately at the ends of the working face. This avoids gas accumulation in the goaf and prevents the case that overlying strata of the roadway cannot cave and relieve pressure immediately after mining due to the high-strength support of roadway walls, otherwise causing gas accumulation in the goaf. Gas accumulation is very harmful for safe mining in the Huainan Coal Mine area of high gas content. The working face can be safely mined using the aforementioned method.

3.5.3 Cooperative control of protection of roadway walls

Most hydraulic supports in the middle of the working face are in a state of high supporting stress. According to the coupling of hydraulic supports and surrounding rocks, the coal wall is also under high pressure and, therefore, is prone to rib spalling. Because the maximum mining height is as large as 7 m, a three-level face guard mechanism was designed to realize the stable protection of coal walls. To ensure the cutting speed of the coal cutter and pushing of hydraulic supports in the working face, the area of five hydraulic supports along the advance direction of the coal cutter was determined as the cooperative action zone of the face guard mechanism. As shown in Figure 15A, the fifth support in front of the coal cutter for normal coal cutting needs to self-inspect the hydraulic system and move the extensible canopy before action, due to the sequential control in the cooperative action zone of the face guard mechanism of hydraulic supports. The fourth support in front of the coal cutter begins to move its face guard. The third-level face guard mechanism is withdrawn and folded, and the second- and first-level face guard mechanisms act simultaneously and the whole mechanisms are withdrawn to 25% of the completely withdrawal state. At the moment, the face guard mechanisms of the third and second hydraulic supports in front of the coal cutter have been withdrawn to 50% and 75% of the complete withdrawal state, while that of the first support that is adjacent to the coal cutter has been completely withdrawn. Under the condition, the face guard will not be cut when cutting coal to the first hydraulic support. The aforementioned process is repeated, and Figure 15B shows the real-time dynamic changes in the sequential control zone of the face guard mechanisms. Similar to this, after cutting coal using the coal cutter, the face guard mechanisms of hydraulic supports were unfolded, which act and support the coal wall, and hydraulic supports behind the coal cutter extend their extensible canopies and unfold their face guards successively. The automatic withdrawal and extension of face guards and extensible canopies in front of and behind the coal cutter, on one hand, prevent the cutting drum of the coal cutter from colliding and interfering with support beams, and on the other hand, this also achieves cooperative control of the action of hydraulic supports and the coal cutter, ensures stable control of coal walls and reliable support at the ends of working faces, and improves the efficiency of cooperative advancement of the coal cutter, scraper conveyer, and hydraulic supports in the working face.

4 Conclusion

The force characteristics and posture change characteristics of the support in the working face of the mine were studied and analyzed. The supporting stress characteristics of the deep super-long working face were revealed. Based on the aforementioned model, the support parameters and control technology of the working face were studied. The conclusions are shown as follows:

1) The studied working face in Kouzidong Coal Mine is a typical super-long working face in a deep thick coal seam. Strata behaviors in the working face show characteristics including an unobvious periodicity of weighting, an obvious time sequence, and greatly different intensities of weighting in different areas and the presence of many areas of peak pressure in the working face.
2) The presence of the three-peak M-like distribution of the supporting stress in the working face can be used as the criterion for a super-long working face. The three-peak distribution of the supporting stress in the super-long working face is a result of the weakened support action of support conditions in the roadway for the middle of the working face.
3) The three-peak M-like distribution of the supporting stress in the super-long working face is not only determined by a single parameter (working face length) but also related to many factors, including the burial depth, mining height, working face length, roof lithology, bedrock thickness, and condition of roadway walls. Therefore, the reasonable working face length should be determined according to the occurrence condition of the working face and coal seams in practical mining.
4) The zonal cooperative control for hydraulic support groups based on the state error and cost functions was used in the super-long deep working face, that is, the three-level cooperative control strategy of "single-support control → multi-support control → group control." The single-support control, multi-support control, and group control are an effective way to achieving safe and efficient support of super-long working faces in deep thick coal seams.

Data availability statement

Publicly available datasets were analyzed in this study. All data used during this research are available from the corresponding authors on reasonable request.

Author contributions

Conceptualization: ZC and JZ; methodology: HW; data curation: LC, ML, and HC; writing—original draft preparation: and HW and ZC; writing—review and editing: JZ, XL, and YX. All authors contributed to the article and approved the submitted version.

Funding

The authors acknowledge financial support provided by the National Natural Science Foundation of China (52074120, 52204133), and the Fundamental Research Funds for the Central Universities (3142019005, 3142017107).

Conflict of interest

Author JZ was employed by Tiandi Science and Technology Co., Ltd.

The remaining authors declare that the research was conducted in the absence of any commercial or financial relationships that could be construed as a potential conflict of interest.

Publisher's note

All claims expressed in this article are solely those of the authors and do not necessarily represent those of their affiliated organizations, or those of the publisher, the editors, and the reviewers. Any product that may be evaluated in this article, or claim that may be made by its manufacturer, is not guaranteed or endorsed by the publisher.

References

Behera, B., Yadav, A., Singh, G. S. P., and Sharma, S. K. (2021). Assessment of excavation damage and spalling potential at a mechanized longwall face A numerical modeling study. *Geomechanics Geophys. Geo-Energy Geo-Resources* 7 (4), 104. doi:10.1007/s40948-021-00299-6

Chen, J. C., Zhou, L., Xia, B. W., Su, X. P., and Shen, Z. H. (2021). Numerical investigation of 3D distribution of mining-induced fractures in response to longwall mining. *Nat. Resour. Res.* 30 (1), 889–916. doi:10.1007/s11053-020-09759-4

Chi, X. L., Yang, K., and Wei, Z. (2021). Breaking and mining-induced stress evolution of overlying strata in the working face of a steeply dipping coal seam. *Int. J. Coal Sci. Technol.* 8 (4), 614–625. doi:10.1007/s40789-020-00392-3

Gao, Y. N., Lan, D. H., Zhang, Y. D., Chang, X. Y., Xie, J., and Gao, M. Z. (2022). The strata movement and ground pressure under disturbances from extra thick coal seam mining A case study of a coal mine in China. *Geomechanics Geophys. Geo-Energy Geo-Resources* 8 (6), 199. doi:10.1007/s40948-022-00506-y

He, M. C., Sui, Q. R., Li, M. N., Wang, Z. J., and Tao, Z. G. (2022). Compensation excavation method control for large deformation disaster of mountain soft rock tunnel. *Int. J. Min. Sci. Technol.* 32 (5), 951–963. doi:10.1016/j.ijmst.2022.08.004

He, Z. Q., Xie, H. P., Gao, M. Z., Deng, G. D., Peng, G. Y., and Li, C. (2020). The fracturing models of hard roofs and spatiotemporal law of mining-induced stress in a top coal caving face with an extra-thick coal seam. *Geomechanics Geophys. Geo-Energy Geo-Resources* 7 (1), 2. doi:10.1007/s40948-020-00202-9

Kang, H. P., Wang, G. F., Jiang, P. F., Wang, J. C., Zhang, N., Jing, H. W., et al. (2018). Conception for strata control and intelligent mining technology in deep coal mines with depth more than 1 000 m. *J. China Coal Soc.* 43 (7), 1789–1800. doi:10.13225/j.cnki.jccs.2018.0634

Li, B., Yang, X., Yuan, Y., Liang, Y. P., Li, S. Q., Zhu, C. Q., et al. (2023a). Experimental research on the influence of different factors on the behaviour of broken coal and rock particles during compaction. *Constr. Build. Mater.* 367, 130127. doi:10.1016/j.conbuildmat.2022.130127

Li, X. L., Zhang, X. Y., Shen, W. L., Zeng, Q. D., Chen, P., Qin, Q. Z., et al. (2023b). Research on the mechanism and control technology of coal wall sloughing in the ultra-large mining height working face. *Int. J. Env. Res. Pub He* 20 (2), 868. doi:10.3390/ijerph20010868

Li, X. L., Chen, S. J., Wang, S., Zhao, M., and Liu, H. (2021). Study on *in situ* stress distribution law of the deep mine Taking linyi mining area as an example. *Adv. Mater. Sci. Eng.* 2021, 5594181–5594211. doi:10.1155/2021/5594181

Liang, Y. P., Kong, F. J., Zou, Q. L., and Zhang, B. C. (2023). Effect of strain rate on mechanical response and failure characteristics of horizontal bedded coal under quasi-

static loading. *Geomechanics Geophys. Geo-Energy Geo-Resources* 9 (1), 52. doi:10.1007/s40948-023-00587-3

Liang, Y. P., Ran, Q. C., Zou, Q. L., Zhang, B. C., and Hong, Y. (2022). Experimental study of mechanical behaviors and failure characteristics of coal under true triaxial cyclic loading and unloading and stress rotation. *Nat. Resour. Res.* 31 (2), 971–991. doi:10.1007/s11053-022-10022-1

Liu, B. G., Song, Y., and Chu, Z. F. (2022). Time-dependent safety of lining structures of circular tunnels in weak rock strata. *Int. J. Min. Sci. Technol.* 32 (2), 323–334. doi:10.1016/j.ijmst.2021.12.003

Liu, T., Lin, B. Q., Fu, X. H., Zhao, Y., Gao, Y. B., and Yang, W. (2021). Modeling coupled gas flow and geomechanics process in stimulated coal seam by hydraulic flushing. *Int. J. Rock Mech. Min. Sci.* 142, 104769. doi:10.1016/j.ijrmms.2021.104769

Lou, J. F., Gao, F. Q., Yang, J. H., Ren, Y. F., Li, J. Z., Wang, X. Q., et al. (2021). Characteristics of evolution of mining-induced stress field in the longwall panel Insights from physical modeling. *Int. J. Coal Sci. Technol.* 8 (5), 938–955. doi:10.1007/s40789-020-00390-5

Ma, K., and Wu, J. (2021). Analytical study on limit support pressure of working face in underground space exploitation based on improved 3D wedge-prism model. *Geomechanics Geophys. Geo-Energy Geo-Resources* 7 (1), 10. doi:10.1007/s40948-020-00204-7

Ma, T. F., Liu, H. H., Zou, Q. L., Kong, F. J., Ran, Q. C., and Wang, P. T. (2023). Damage evolution characteristics and deterioration mechanism of mechanical properties of sandstone subjected to drying-wetting cycles. *J. Mater. Res. Technol.* 23, 4591–4605. doi:10.1016/j.jmrt.2023.02.068

Mohammad, R., Mohammad, F. H., and Abbas, M. (2015). A time-independent energy model to determine the height of de-stressed zone above the mined panel in longwall coal mining. *Tunn. Undergr. Space Technol.* 47, 81–92. doi:10.1016/j.tust.2015.01.001

Pang, Y. H., Wang, G. F., and Li, B. B. (2020). Stress path effect and instability process analysis of overlying strata in deep stopes. *J. Rock Mech. Eng.* 39 (4), 682–694. doi:10.13722/j.cnki.jrme.2019.0622

Ran, Q. C., Liang, Y. P., Zou, Q. L., Hong, Y., Zhang, B. C., Liu, H., et al. (2023a). Experimental investigation on mechanical characteristics of red sandstone under graded cyclic loading and its inspirations for stability of overlying strata. *Geomechanics Geophys. Geo-Energy Geo-Resources* 9 (1), 11. doi:10.1007/s40948-023-00555-x

Ran, Q. C., Liang, Y. P., Zou, Q. L., Zhang, B. C., Li, R. F., Chen, Z. H., et al. (2023b). Characteristics of mining-induced fractures under inclined coal seam group multiple mining and implications for gas migration. *Nat. Resour. Res.* 32 (3), 1481–1501. doi:10.1007/s11053-023-10199-z

Ren, P. F., Wang, Q., Tang, D. Z., Xu, H., and Chen, S. D. (2022). *In situ* stress-coal structure relationship and its influence on hydraulic fracturing A case study in zhengzhuang area in qinshui basin, China. *Nat. Resour. Res.* 31 (3), 1621–1646. doi:10.1007/s11053-022-10036-9

Ren, Y. F., and Qi, Q. X. (2011). Study on characteristic of stress field in surrounding rocks of shallow coalface under long wall mining. *J. China Coal Soc.* 36 (10), 1612–1618. doi:10.13225/j.cnki.jccs.2011.10.022

Song, L. B., and Wang, Q. X. (2014). Study on safety technology of China first 450 m ultra long fully mechanized coal face. *Coal Eng.* 46 (3), 45–51.

Su, E. L., Liang, Y. P., Chen, X. J., Wang, Z. F., Ni, X. M., Zou, Q. L., et al. (2023). Relationship between pore structure and mechanical properties of bituminous coal under sub-critical and super-critical CO2 treatment. *Energy* 280, 128155. doi:10.1016/j.energy.2023.128155

Sun, X. Y., Ran, Q. C., Liu, H., Ning, Y. H., and Ma, T. F. (2023). Characteristics of stress-displacement-fracture multi-field evolution around gas extraction borehole. *Energies* 16 (6), 2896. doi:10.3390/en16062896

Wang, G. F., Hu, X. P., Liu, X. H., Yu, X., Liu, W. C., Lv, Y., et al. (2020). Adaptability analysis of four-leg hydraulic support for underhand working face with large mining height of kilometer deep mine. *J. China Coal Soc.* 45 (3), 865–875. doi:10.13225/j.cnki.jccs.SJ19.1516

Wang, J. C., Yang, S. L., Yang, B. G., Li, Y., Wang, Z. H., Yang, Y., et al. (2019). Roof sub-regional fracturing and support resistance distribution in deep longwall face with ultra-large length. *J. China Coal Soc.* 44 (1), 54–63. doi:10.13225/j.cnki.jccs.2018.5139

Wang, Q., Wang, Y., He, M. C., Li, S. C., Jiang, Z. H., Jiang, B., et al. (2022). Experimental study on the mechanism of pressure releasing control in deep coal mine roadways located in faulted zone. *Geomechanics Geophys. Geo-Energy Geo-Resources* 8 (2), 50. doi:10.1007/s40948-021-00337-3

Wang, Q. X., and Ju, J. F. (2014). Study on mine strata pressure behavior of 450 m ultra long fully-mechanized coal mining face. *Coal Sci. Technol.* 42 (3), 125–128. doi:10.13199/j.cnki.cst.2014.03.033

Wu, Q. F., Yu, M. G., and Zheng, K. (2022). Experimental investigation on the effect of obstacle position on the explosion behaviors of the non-uniform methane/air mixture. *Fuel* 320, 123989. doi:10.1016/j.fuel.2022.123989

Xu, G. (2015). Experimental and theoretical study on hydraulic support in working face and its relationship with roof subsidence. *J. China Coal Soc.* 40 (7), 1485–1490. doi:10.13225/j.cnki.jccs.2015.0220

Xu, Y. J., Li, D. Y., Liu, X. K., and Ma, D. Z. (2019). Theoretical analysis and testing of vertical stiffness of hydraulic support. *Coal Min. Technol.* 24 (1), 40–44+52. doi:10.13532/j.cnki.cn11-3677/td.2019.01.009

Xu, Y. J., Wang, G. F., and Ren, H. W. (2015). Theory of coupling relationship between surrounding rocks and powered sup-port. *J. China Coal Soc.* 40 (11), 2528–2533. doi:10.13225/j.cnki.jccs.2015.7023

Xu, Y. J., and Wang, G. F. (2017). Supporting principle and bearing characteristics of hydraulic powered roof support groups. *Chin. J. Rock Mech. Eng.* 36 (S1), 3367–3373. doi:10.13722/j.cnki.jrme.2016.0706

Xu, Y. J., Wang, G. F., Zhang, J. H., Ren, H. W., and Li, D. Y. (2018). Theory and application of supporting stress fields of hydraulic powered support groups in fully mechanized mining face with large mining height based on elastic supporting beam model. *Chin. J. Rock Mech. Eng.* 37 (5), 1226–1236. doi:10.13722/j.cnki.jrme.2017.1471

Ye, C. F., Xie, H. P., Wu, F., and Li, C. B. (2022). Nonlinear creep properties and time-to-failure prediction of sandstone under saturated and dry conditions. *Environ. Earth Sci.* 81, 545. doi:10.1007/s12665-022-10666-5

Ye, C. F., Xie, H. P., Wu, F., and Li, C. B. (2023). Study on the nonlinear time-dependent deformation characteristics and viscoelastic-plastic model of shale under direct shear loading path. *Bull. Eng. Geol. Environ.* 82 (5), 189. doi:10.1007/s10064-023-03170-y

Zhang, B. C., Liang, Y. P., Zhao, Z. Y., Zou, Q. L., Zheng, H. L., Ning, Y. H., et al. (2023a). Effect of stress amplitude on mechanical and acoustic emission of sandstone under constant–cyclic loading. *Bull. Eng. Geol. Environ.* 82, 284. doi:10.1007/s10064-023-03307-z

Zhang, B. C., Liang, Y. P., Zou, Q. L., Ding, L. Q., and Ran, Q. C. (2023b). Experimental investigation into the damage evolution of sandstone under decreasing-amplitude stress rates and its implications for coalbed methane exploitation. *Environ. Earth Sci.* 82, 208. doi:10.1007/s12665-023-10825-2

Zhang, D. P., Yan, J., and Zhao, Y. Z. (2022c). Comparative study on development of ship structural mechanics in China and Russia. *Mech. Electr. Eng. Technol.* 51 (12), 43–46+60.

Zhang, T. C., Zou, Q. L., Jia, X. Q., Liu, T., Jiang, Z. B., Tian, S. X., et al. (2022a). Effect of cyclic water injection on the wettability of coal with different SiO_2 nanofluid treatment time. *Fuel* 312, 122922. doi:10.1016/j.fuel.2021.122922

Zhang, T., Yuan, L., Zhao, Y. X., and Hao, X. J. (2015). Distribution law of working face pressure under the fracture zone distri-bution characteristic of deep mining. *J. China Coal Soc.* 40 (10), 2260–2268. doi:10.13225/j.cnki.jccs.2015.6006

Zhang, Y., Hou, S. H., Mei, S. H., Zhao, T. J., and Li, D. Y. (2022b). Experimental study of permeability-hydraulic fracturing characteristics of tight rocks. *Geomechanics Geophys. Geo-Energy Geo-Resources* 8 (6), 182. doi:10.1007/s40948-022-00499-8

Zhao, T., Gong, P. L., Yetilmezsoy, K., Bahramian, M., and Liu, C. Y. (2021). Dynamic failure and stability model analysis of thick and hard rock with wedge-structure immediate roof occurrence. *Geomechanics Geophys. Geo-Energy Geo-Resources* 7 (3), 80. doi:10.1007/s40948-021-00277-y

Zou, Q. L., Chen, Z. H., Cheng, Z. H., Liang, Y. P., Xu, W. J., Wen, P. R., et al. (2022a). Evaluation and intelligent deployment of coal and coalbed methane coupling coordinated exploitation based on Bayesian network and cuckoo search. *Int. J. Min. Sci. Technol.* 32 (6), 1315–1328. doi:10.1016/j.ijmst.2022.11.002

Zou, Q. L., Huo, Z. X., Zhang, T. C., Jiang, C. Z., and Liang, J. Y. (2023). Surface deposition characteristics of water-based SiO_2 nanofluids on coal. *Fuel* 340, 127489. doi:10.1016/j.fuel.2023.127489

Zou, Q. L., Zhang, T. C., Ma, T. F., Tian, S. X., Jia, X. Q., and Jiang, Z. B. (2022b). Effect of water-based SiO_2 nanofluid on surface wettability of raw coal. *Energy* 254, 124228. doi:10.1016/j.energy.2022.124228

Zuo, J. P., Yu, M. L., Li, C. Y., Sun, Y. J., Hu, S. Y., and Li, Z. D. (2021). Analysis of surface cracking and fracture behavior of a single thick main roof based on similar model experiments in Western Coal Mine, China. *Nat. Resour. Res.* 30 (1), 657–680. doi:10.1007/s11053-020-09735-y

frontiers | Frontiers in Energy Research

TYPE Original Research
PUBLISHED 22 August 2023
DOI 10.3389/fenrg.2023.1249985

Check for updates

OPEN ACCESS

EDITED BY
Peng Tan,
CNPC Engineering Technology R & D Company Limited, China

REVIEWED BY
Jun Liu,
Sichuan University, China
Chun Zhu,
Hohai University, China

*CORRESPONDENCE
Kesai Li,
l.k.s.2016@foxmail.com

RECEIVED 29 June 2023
ACCEPTED 07 August 2023
PUBLISHED 22 August 2023

CITATION
Wang N, Li K, Sun J, Wang D, He X, Xiang Z, Liu H and Wang P (2023), Research on dual lateral log simulation of shale bedding fractures under different influencing conditions.
Front. Energy Res. 11:1249985.
doi: 10.3389/fenrg.2023.1249985

COPYRIGHT
© 2023 Wang, Li, Sun, Wang, He, Xiang, Liu and Wang. This is an open-access article distributed under the terms of the Creative Commons Attribution License (CC BY). The use, distribution or reproduction in other forums is permitted, provided the original author(s) and the copyright owner(s) are credited and that the original publication in this journal is cited, in accordance with accepted academic practice. No use, distribution or reproduction is permitted which does not comply with these terms.

Research on dual lateral log simulation of shale bedding fractures under different influencing conditions

Naihui Wang[1,2,3], Kesai Li[4]*, Jiaqi Sun[4], Di Wang[1,2], Xianhong He[4], Zehou Xiang[4], Hui Liu[4] and Pan Wang[4]

[1]State Key Laboratory of Shale Oil and Gas Enrichment Mechanisms and Effective Development, Beijing, China, [2]National Energy Shale Oil Research and Development Center, Beijing, China, [3]School of Earth Resources, China University of Geosciences (Wuhan), Wuhan, China, [4]College of Energy, Chengdu University of Technology, Chengdu, China

Micro scale fractures play a crucial role in facilitating the migration of oil and gas in low permeability shale reservoirs. However, the identification of such fractures is a complex task. The efficacy of the dual lateral log physical field changes as a means of identifying shale micro fractures remains uncertain. To address this issue, a three-layer shale bedding fracture model was developed using the finite element method and core and conventional logging data from eight wells, which was based on different shale reservoirs within the Yanchang Formation in the Ordos Basin. The present study examines the dual lateral log response characteristics resulting from distinct characteristics of horizontal bedding fractures, with a focus on the response mechanism. The simulation of logging response characteristics of shale and siltstone combination were utilized by core statistical data for verification purposes. The results indicate that under the lithology combination of shale and siltstone, the magnitude of the difference between the resistivity of the filled fracture and the formation resistivity, the greater the formation resistivity of the shale itself, the wider the fracture width, and the greater the difference between the apparent resistivity and the real formation resistivity. Furthermore, the suitable conditions for the detection of shale bedding fracture characteristics by dual lateral log are clarified. In the presence of effective filling, the dual lateral log has the capability to identify shale fractures at the micron scale. The findings of our study establish a theoretical framework for the identification and assessment of shale fractures, and furnish technical assistance for the optimal selection of "sweet spots" within shale reservoirs and the precise evaluation of reservoirs. This study lays a theoretical foundation for the identification and evaluation of shale fractures, and provides technical support for the optimal "sweet spot" selection of shale reservoirs and the accurate evaluation of reservoirs.

KEYWORDS

Ordos basin, shale fractures, dual lateral log, simulation, applicable conditions

1 Introduction

Recent developments in shale oil and gas exploration in China have shown significant progress (Zou et al., 2023). Shale reservoirs are characterized by their high content of brittle minerals and the presence of multiple types of pores and fractures (Wang et al., 2016; Sun et al., 2022). Fractures serve as both reservoir spaces and seepage channels, enhancing the

physical properties of the reservoir and facilitating the extraction of oil and gas. The presence of such fractures plays a crucial role in determining the potential for shale oil enrichment (Zeng et al., 2007; George et al., 1968; Fu H. J. et al., 2022; Fu et al., 2007). The identification and assessment of fractures in shale formations present several technical challenges owing to the intricate nature of their origin and classification of shale fracture systems (Yin et al., 2021; Shi et al., 2022). Consequently, it is imperative to devise a precise, practical, and flexible methodology for the detection and evaluation of fractured shale reservoirs (Wang et al., 2021; Ren et al., 2023; Gan et al., 2023).

The logging method serves as a valuable instrument for the quantitative depiction of fracture characteristics. Various logging techniques exhibit limitations in identifying fractures, with acoustic logging being susceptible to "cycle-skipping" phenomena and neutron porosity indicating high values for gas bearing fractures (Fan et al., 2008). While these methods are cost-effective, their indirect nature may result in inconsistent responses to fractures across different regions. Imaging logging provides accurate representation of fracture characteristics, but its detection range is limited and lacks data (Hadi et al., 2016; Dong et al., 2020). High resolution array induction logging struggles to interpret complex intrusion profiles (Tang, 2015). The cross dipole with high accuracy is only applicable to vertical fractures or high angle fractures near the wellbore (Wen et al., 2018). While new logging techniques have emerged that can extract detailed formation information, their widespread use is restricted by cost and application scope limitations (Wang et al., 2005; Tang et al., 2012; Xie et al., 2020; Lu, 2018; Liu, 2022; Liu et al., 2022). Nevertheless, the dual lateral log's unique instrument structure, featuring a strong focusing effect, enables the detection of deeper formations. The fractured intervals' logging response characteristics are distinctly apparent, as evidenced by the amplitude disparity between deep and shallow lateral resistivity curves. The positive difference is observed in the high dip angle fracture and vertical fracture, while the low dip angle fracture and horizontal fracture generally exhibit negative difference (Chen et al., 2005). Furthermore, the invasion difference ratio parameters, in conjunction with the response characteristics of dual lateral log, can aid in fracture identification (Zhou and Yang, 2003). The dual lateral log technology is an effective method for identifying fractures, characterized by good longitudinal continuity, moderate detection scale, low cost, and accurate description of fracture characteristics. Drawing upon the primary controlling factors of fractures, including lithology, structural, and stress control, geological data such as formation lithology and thickness are interpreted through logging curves to anticipate areas conducive to fracture development. The finite element numerical simulation method, a semi-quantitative approach to fracture prediction, amalgamates the benefits of other numerical simulation algorithms and can be implemented in complex 3D strata. (Zhang and Wang, 1996; Tan et al., 2007; Yang et al., 2009; Gao et al., 2010; Um et al., 2015; Tang et al., 2016; Huang et al., 2019; Xue et al., 2021; Yin et al., 2022). Scholars have conducted pertinent research on reservoirs utilizing the logging finite element method. Sibbit and Faivre (1985) developed a two-dimensional fracture model to simulate the dual lateral log response of fractures and assess fracture characteristics in vertical wells. Pezard and Anderson (1990) subsequently derived the relationship between fracture dip angle and dual lateral log response using a plate fracture model. Shi et al. (2004) computed the correlation between the dual lateral response of fractured formations and fracture porosity, mud resistivity, fracture dip angle, and bedrock resistivity. Deng et al. (2012); Zhao et al. (2015) simulated the dual lateral log response of fracture-cave formations. Subsequently, Tan et al. (2014); Su et al. (2015) gradually applied dual lateral log response simulation technology to shale fracture evaluation. Yong et al. (2022) used finite element to characterize nano scale shale fractures.

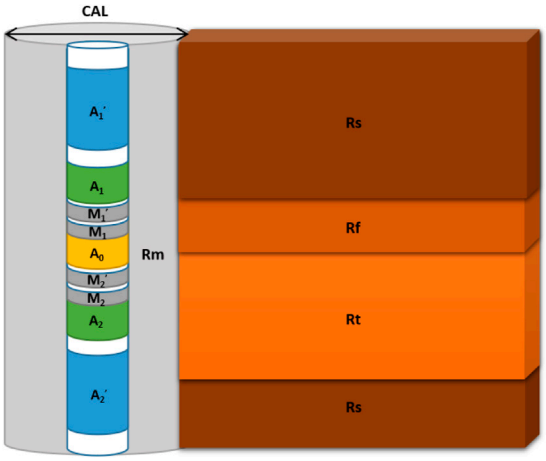


FIGURE 1
Horizontal fracture model of the dual lateral log.

Currently, the identification and evaluation of fractures rely primarily on the analysis of curve changes and actual logging data calculations. The suitability of dual lateral logs cannot be assessed through the response mechanism based on physical field alterations. Additionally, there is a dearth of logging response simulations for shale fracture formation, resulting in a lack of theoretical foundation for the identification and evaluation of shale fractures through logging. Hence, utilizing logging data from eight wells and considering the prevailing formation conditions, a sophisticated wellbore-formation model of horizontal fractures is formulated. The logging response mechanism is scrutinized in light of the impact of fractures on electric field distribution under varying fracture conditions. To obtain more accurate fracture information, the fracture types and logging correction conditions that can be identified by dual lateral log are elucidated.

2 Methods

2.1 Establishment of the wellbore model of the fracture instrument

The dual lateral log tool comprises nine electrodes, consisting of a main electrode (A_0), two sets of monitoring electrodes (M_1, M_2 and M_1', M_2'), and two sets of shielding electrodes (A_1, A_2 and A_1', A_2'). The instrument has a diameter of 0.089 m, with the main electrode situated at the center. The remaining electrode pairs of the same type are symmetrically distributed and connected via wires to form a short circuit with identical potential. During operation, the main electrode A_0 emits a constant current I_0 for deep lateral logging, while the shielding electrode emits a current with the same polarity as the primary electrode. This results in the main current flowing vertically through

the shielding electrode to the deeper formation, thereby obtaining an apparent resistivity that approximates the true resistivity of the formation. For shallow lateral log, the external shielding electrode is replaced by a loop electrode. The effect of the shielding current is reduced, the detection scale is reduced, so that the resistivity of the invasion zone can be measured. In order to obtain more accurate simulation experiment results, a fracture instrument wellbore model for horizontal fractures is established using the finite element interpolation method, based on the working principle of the dual lateral log tool and actual formation conditions. This model is depicted in Figure 1, where Rs represents wall rock resistivity, Rf represents fracture resistivity, Rt represents undisturbed formation resistivity, Rm represents mud resistivity and CAL represents the well diameter.

2.2 Dual lateral logging finite element method

The essence of the finite element method of dual lateral logging is the calculation of the steady current electric field in the formation. The potential value in the monitoring electrode can be decomposed into the superposition result of the partial electric field generated by multiple emission electrodes. First, the problem of determining solution is transformed into the problem of determining solution of objective universal function through the constraint of boundary conditions. Then, the target area is discretizated. Finally, the target area is interpolated, and the interpolation function is substituted into the function to solve the equations. So that the apparent resistivity value of dual lateral logging can be obtained from the perspective physical field changes.

The distribution of the electrostatic field electromotive force in the 3D cylindrical coordinate system of double lateral measurement should satisfy:

$$\frac{\partial}{\partial x}\left(\sigma\frac{\partial\phi}{\partial x}\right)+\frac{\partial}{\partial y}\left(\sigma\frac{\partial\phi}{\partial y}\right)+\frac{\partial}{\partial z}\left(\sigma\frac{\partial\phi}{\partial z}\right)=0 \tag{1}$$

In the context of dual lateral log numerical simulation, various boundary conditions are employed on the boundary and instrument surface in the x, y, z direction.

The first type of boundary condition is used for constant-pressure electrodes, where φ is a known constant.

The second boundary condition applies to the surface of the constant current electrode:

$$\int_{\Gamma}\sigma_m\frac{\partial\phi}{\partial n}\cdot\vec{n}d\tau=I_E \tag{2}$$

In the formula: Γ—the whole electrode surface; $\vec{n}$- Electrode direction; I_E - Electrode current; σ_m- Drilling fluid resistivity.

On the insulation boundary surface:

$$\frac{\partial\phi}{\partial n}=0 \tag{3}$$

The objective functional is constructed according to the above problem:

$$F=\frac{1}{2}\iiint_{\Omega}\sigma\left[\left(\frac{\partial\phi}{\partial x}\right)^2+\left(\frac{\partial\phi}{\partial y}\right)^2+\left(\frac{\partial\phi}{\partial z}\right)^2\right]dxdydz-\sum_E I_E\Phi_E \tag{4}$$

In the formula: Φ_E—Points on the electrode.

Thus, the problem of determining the definite solution is converted into an extreme value problem of the universal function. According to the boundary conditions obtained in the research process of dual lateral log, the universal function can be solved and the value to be solved can be obtained.

After discretization and interpolation of the objective function, we get:

$$\Phi^e=\frac{1}{2}\Phi^{eT}G^e\Phi^e \tag{5}$$

In the formula: Φ—vector to be solved; Ge—Stiffness matrix of elements.

Ge is a symmetric real matrix of or 4 × 4 or 10 × 10. According to Ge, the total conductance matrix is obtained:

$$\Phi=\sum_{i=1}^{M}\Phi_i=\frac{1}{2}{\Phi_i}^TG\Phi_i=\begin{Bmatrix}\phi_1\\\phi_2\\\vdots\\\phi_N\end{Bmatrix}^T\begin{pmatrix}G_{11}&\cdots&G_{1N}\\\vdots&\ddots&\vdots\\G_{N1}&\cdots&G_{NN}\end{pmatrix}\begin{Bmatrix}\phi_1\\\phi_2\\\vdots\\\phi_N\end{Bmatrix} \tag{6}$$

In the formula: M is the number of elements, N is the number of nodes, Φ is the vector at ϕ each node position to be solved, and G is the total Ge stiffness matrix obtained by N × N installation.

G is a large sparse symmetric matrix, and the matrix is a real number. Because of the extreme value of the functional, we must make each node satisfy the following conditions:

$$\frac{\partial F}{\partial\phi_i}=0 \tag{7}$$

That is:

$$G\Phi=I_E \tag{8}$$

The value of each node can be obtained by solving Formula (5). Use formula (9) to calculate the apparent resistivity.

$$R_a=k\frac{U_{M1}}{I_0} \tag{9}$$

It is important to note that multiple nodes will exist on each electrode after meshing, and each electrode can be treated as an equipotential body. Consequently, all nodes on the electrode possess the same electromotive force, and the electromotive force of all nodes on the boundary of the target area is also identical. The ratio of the electromotive force between the shielding electrodes A_1 and A_2 remains a fixed value, with a positive ratio observed in the deep lateral direction and a negative ratio in the shallow lateral direction. In the calculation of unknowns, the ratio of the electromotive force of the two shielding electrodes is positive, then the apparent resistivity is the deep lateral resistivity. If it is negative, then the apparent resistivity is the shallow lateral resistivity.

3 Analysis of fracture characteristics of typical shale oil reservoirs

Core samples and thin sections of 8 wells at Ordos basin were observed and samples were collected to study fracture typical growth and logging characteristics in Chang 9 shale. We statistics the Chang

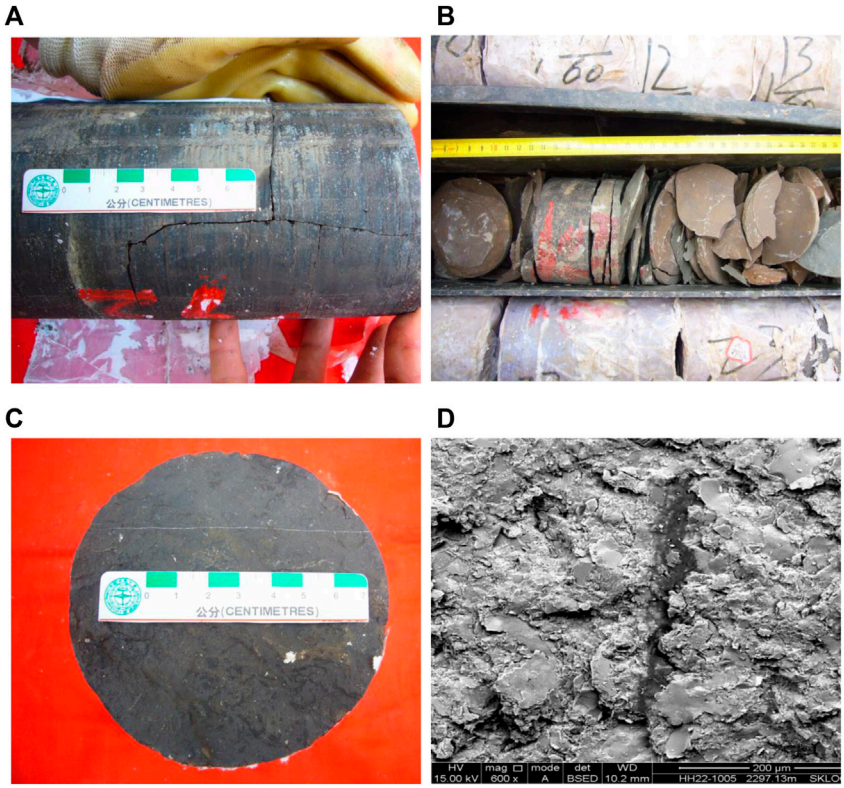


FIGURE 2
Typical fracture types and filling characteristics in shale oil reservoir of Chang-9 Member. **(A)** Structural fracture. Well YY7 1,304.05 m. **(B)** Bedding fractures. Well YY7 1,141.14–1,141.3 m. **(C)** Structural fracture with filled with calcite. Well YY7 1,143.7–1,143.82 m. **(D)** Micro fractures are filled with organic matter. Well HH22.

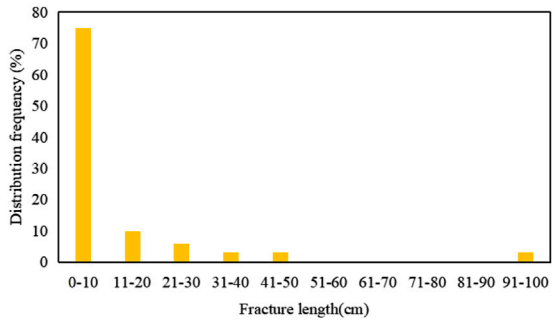


FIGURE 3
Statistical graph of fracture lengths in the Chang 9 section of 8 coring wells.

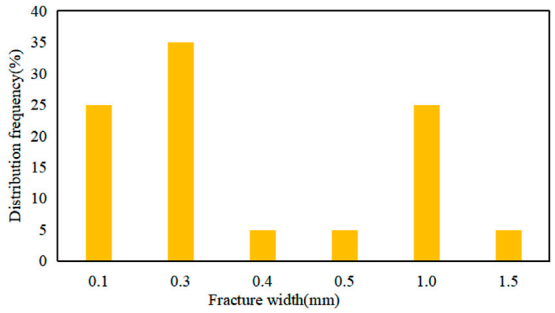


FIGURE 4
Statistical graph of fracture widths in the Chang 9 section of 8 imaging wells.

9 shale oil reservoir includes black oil shale, grey–black or black mud, silt-fine sandstone, sandstone and sand-mud interbeds. Based on the composition of sedimentary minerals and the characteristics of rock grain size, three types of lithological combinations, including shale and mudstone, shale and siltstone, and shale and sandstone, were divided. Five types of Structural fractures, including interlayer fractures, bedding fractures, and occasional abnormal fracturing fractures and reticular fractures were identified in work area, among which structural fractures (Figure 2A) and bedding fractures (Figure 2B) are dominant in mudstone (shale) fractures of 8 wells. Structural fractures are often developed in interlayer shales, and bedding fractures are often developed in bedding shale with high gas content (Gao et al., 2022). According to the mechanical causes, the structural fractures are divided into shear fracture and extension fracture (Gong et al., 2021). Shear fractures are the common ones in the Chang-9 Member mudstone (shale) fractures. Less extension fractures. The main length range of fracture observed by core is 0–10 cm, as shown in Figure 3, the main width

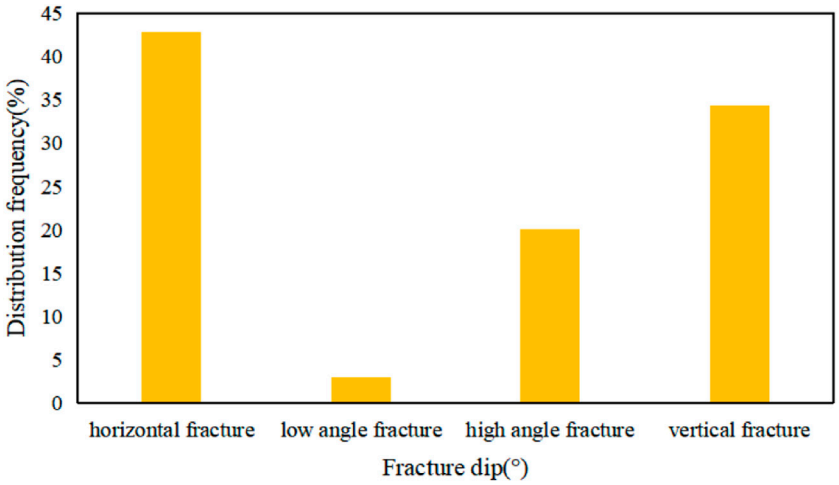


FIGURE 5
Statistical graph of fracture dips in the Chang 9 section of 8 coring wells.

range of fractures is mainly 0.1–1.5 mm, as shown in Figure 4. Calcite (Figure 2C), asphalt (Figure 2D) and carbon chip (Du et al., 2022) are seen in several of the fractures, unfilled fractures contain gas. As shown in Figure 5, vertical fractures and bedding fractures are the main ones. Horizontal bedding fracture is the most developed. Low angle fractures are not developed. Therefore, we mainly choose horizontal fractures for research. Through the analysis of conventional logging, the dual lateral log response characteristics of shale section in Ordos basin, the deep and shallow lateral resistivity almost coincide (Guo et al., 2023). When the fracture exists, the deep and shallow lateral resistivity will have amplitude difference (Wu, 2021).

4 Results

The measurement results of the instrument can be influenced by the borehole, formation, and fracture when the borehole passes through the formation. To investigate the impact of various horizontal fracture characteristics on the response results of dual lateral log, it is assumed that the fracture is free from mud invasion, the well diameter remains constant, and each formation is uniform. A three-layer formation model is established, with a mud resistivity of 1.0 Ω·m, a sampling spacing of 0.1 m, a borehole radius of 0.1016 m, and a surrounding rock formation resistivity of 20 Ω·m. Based on the above determination of formation conditions and resistivity parameters, combined with the vertical fracture and horizontal fracture instrument wellbore models, the corresponding model parameters are established. By altering the fracture parameters, one can analyze the impact of various fracture fillings, fracture width, shale resistivity, and the conditions under which dual lateral log is applicable. The response characteristics of dual lateral log with different lithology combinations were analyzed by fixed formation conditions, mud resistivity, borehole radius and sampling spacing. In the following, the resulting calculation outcomes represent the apparent resistivity under distinct fracture characteristics, which are influenced by multiple factors, including formation. The target layer resistivity represents the true formation resistivity, unaffected by extraneous factors.

4.1 Influence of fracture filling

In instances where the fracture fillings differ, the response mechanism of dual lateral log remains unclear. The information of shale fracture fillings cannot be effectively accurately to evaluate the effectiveness of fractures. Hence, it is imperative to investigate the influence mechanism of fracture fillings on dual lateral log response, drawing upon statistical findings of actual shale reservoir fractures in the study region. Based on the analysis of fracture characteristics aforementioned, the fractures are commonly categorized as asphalt-filling fractures, calcite-filling fractures, unfilled gas-containing fractures, and carbon chip-filling fractures. The deep lateral resistivity of asphalt filled fracture is 156.988 Ω·m, and the shallow lateral resistivity is 163.086 Ω·m. The deep lateral resistivity of calcite-filled fracture is 45.444 Ω·m, and the shallow lateral resistivity is 43.481 Ω·m. The deep lateral resistivity of unfilled gas-bearing fracture is 51.73 Ω·m, and the shallow lateral resistivity is 45.33 Ω·m. The lateral resistivity of the carbon chip filling fracture resistivity is 62.645 Ω·m, and the shallow lateral resistivity is 50.004 Ω·m. Without considering the influence of mud intrusion, three-layer formation models of asphalt filling, calcite filling, gas filling and carbon chip filling were established. Under the condition of vertical well, the resistivity of the upper and lower surrounding rocks is 20 Ω·m. The resistivity of the target formation is 30 Ω·m. The fracture scale is 0.5 m, and the resistivities of the fracture with gas filling, asphalt filling, calcite filling and carbon filling are 100 Ω·m, 444 Ω·m, 266 Ω·m and 5 Ω·m, respectively. The findings depicted in Figure 6 illustrate that the dual lateral log response exhibits an abnormal “M-shaped” trend due to the disparity in resistivity between the fracture fillings and the surrounding rock. The anomalous segment corresponds to the

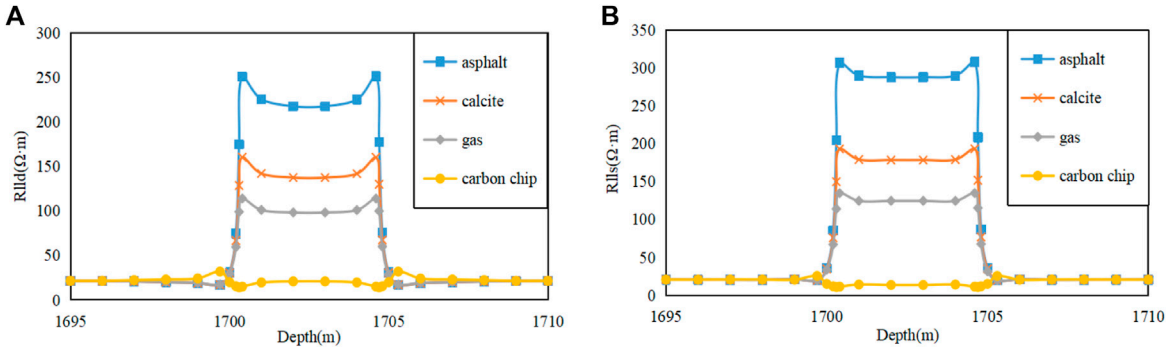


FIGURE 6
(A) Deep lateral response under different crack filling conditions; **(B)** Shallow lateral response under different crack filling conditions.

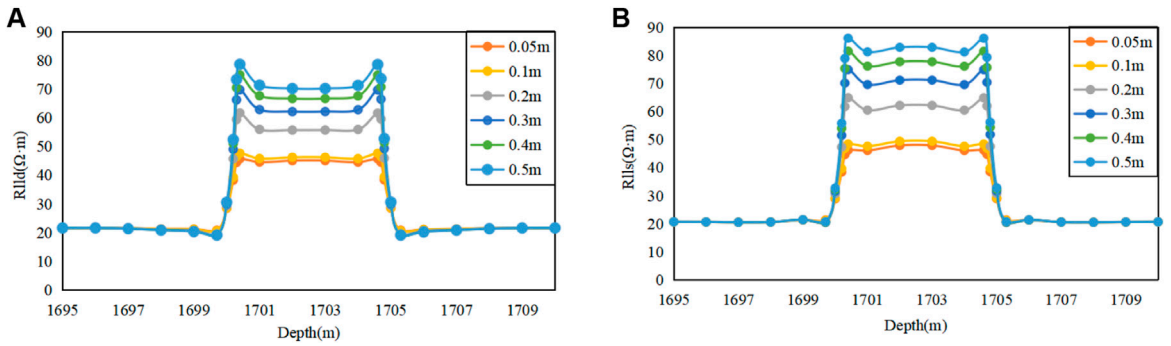


FIGURE 7
(A) Deep lateral response under different crack width conditions; **(B)** Shallow lateral response under different crack width conditions.

fracture section that is filled with diverse materials, and the depth section of this segment represents the thickness of the fractured reservoir. Notably, the resistivity of the asphalt-filled fracture is the highest, while the carbon chip-filled fracture exhibits the lowest resistivity. When the fracture is filled, the greater the difference between the resistivity and the formation resistivity, the greater the difference between the apparent resistivity and the real resistivity of the formation.

4.2 Influence of fracture scale

The impact of varying fracture scales on dual lateral log response remains uncertain, and the identification of micro-scale fractures is challenging. Consequently, it is imperative to investigate the influence of fracture scale on dual lateral log response by analysing statistical data on actual shale reservoir fractures in the study area. The scale of fractures within the work area undergoes a transition from centimeter to millimeter dimensions, with the primary range of fracture scales falling between 0.1 and 1.5 mm. When the fracture width is 0.01 m, the deep lateral resistivity is 35.917 Ω·m, and the shallow lateral resistivity is 40.75 Ω·m. When the fracture width is 0.03 m, the deep lateral resistivity is 34.454 Ω·m, and the shallow lateral resistivity is 37.402 Ω·m. Without considering the influence of mud invasion, a three-layer fracture width model is established: under the condition of a vertical well, the target formation resistivity is 45 Ω·m, and the fracture width is 0.05 m, 0.1 m, 0.2 m, 0.3 m, 0.4 m, and 0.5 m. Figure 7 illustrates that the resistivity of fractures differs from that of the surrounding rock due to variations in width. This discrepancy results in an anomalous dual lateral log response, with the abnormal portion representing the fracture section. The depth section of the abnormal part corresponds to the thickness of the fractured reservoir. The difference between the apparent resistivity and the real resistivity of the formation increases with the widening of fracture width. The shallow side is more affected than the deep side.

4.3 Influence of different shale resistivities

The dual lateral log response varies significantly when fractures occur in different shale reservoirs. The resistivity of the shale reservoirs within the study area is distributed between 20 Ω·m to 160 Ω·m. The deep lateral resistivity of the 1,383.75 m (mud) shale in Well X 45 is 20.29 Ω·m, and the shallow lateral resistivity is

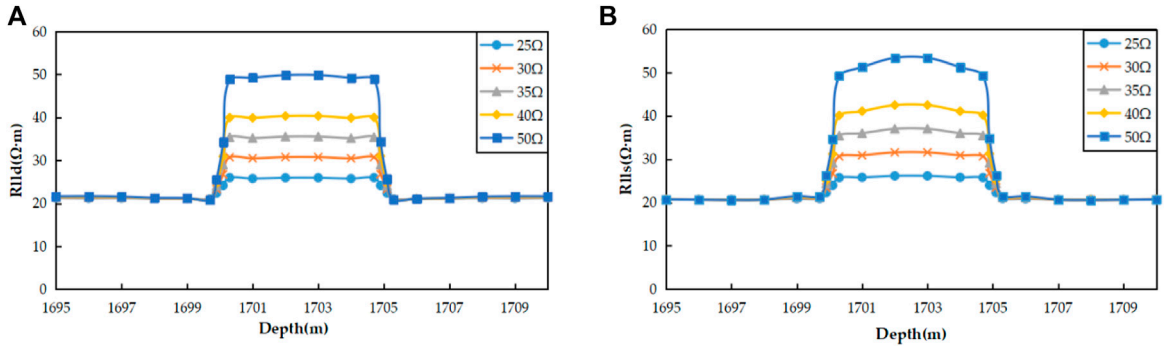


FIGURE 8
(A) Deep lateral response under different shale resistivity conditions; **(B)** Shallow lateral response under different shale resistivity conditions.

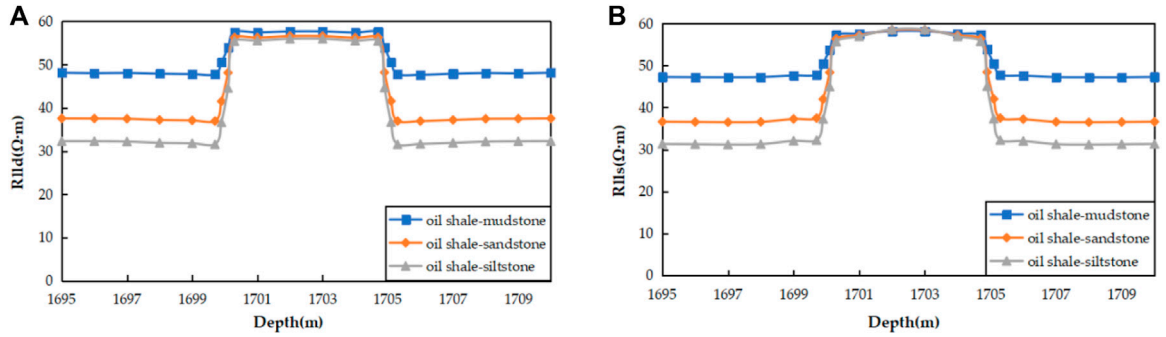


FIGURE 9
(A) Response characteristics of deep lateral logging under different lithologic combinations (oil shale); **(B)** Response characteristics of shallow lateral logging under different lithologic combinations (oil shale).

22.927 Ω·m. The deep lateral resistivity of the (mud) shale in the 1,684.52 m–1693.52 m of the LP 171 well is 24.415 Ω·m, and the shallow lateral resistivity is 33.254 Ω·m; the deep lateral resistivity of Well YY6 shale is 33.611 Ω m, and the shallow lateral resistivity is 34.002 Ω·m. The deep lateral resistivity of the 859.1–859.6 m (mud) shale in the C109 well is 35.817 Ω·m, and the shallow lateral resistivity is 40.75 Ω·m. LP171 well 1,678.82–1,679.82 m deep lateral resistivity is 39.922 Ω·m, shallow lateral resistivity is 55.165 Ω·m; the deep lateral resistivity of 1853.22–1853.62 m shale in LP171 well is 47.025 Ω·m, and the shallow lateral resistivity is 60.381 Ω·m. Without considering the influence of mud invasion, a three-layer model is established: under the condition of a vertical well, the fracture scale is 0.5 m. The target formation resistivities are 25 Ω·m, 30 Ω·m, 35 Ω·m, 40 Ω·m and 50 Ω·m. Figure 8 illustrates that the dual lateral log response is anomalous due to the disparity between the resistivity of the shale and that of the surrounding rock. The fracture section is identified as the abnormal section, and the thickness of the fractured reservoir corresponds to the depth of the anomalous part. The greater the formation resistivity of shale itself, the greater the difference between the apparent resistivity and the true formation resistivity. The shallow side is more susceptible to the effects of the fracture than the deep side.

4.4 Response mechanism of dual lateral log in different lithologic assemblages

The dual lateral log response exhibits significant variation when fractures develop under distinct lithology combination conditions, necessitating an exploration of the statistical results of actual shale reservoir fractures in the work area to establish a law. To this end, we categorized the shale reservoirs in the work area into two groups, namely oil shale reservoirs and low-resistivity shale reservoirs, and investigated the dual lateral log response of different lithology combinations (shale-mudstone combination, shale-sandstone and shale-siltstone combination) in each group. The deep lateral resistivity of high resistivity shale is 51.730 Ω·m, and the shallow lateral resistivity is 45.337 Ω·m. The deep lateral resistivity of low resistivity shale is 24.261 Ω·m, and the shallow lateral resistivity is 27.632 Ω·m; mudstone resistivity deep lateral resistivity 44.971 Ω·m, shallow lateral resistivity 56.183 Ω·m; the deep lateral resistivity of sandstone is 35.540 Ω·m, and the shallow lateral resistivity is 37.720 Ω·m. The deep lateral resistivity of siltstone is 30.892 Ω·m, and the shallow lateral resistivity is 38.698 Ω·m. Without considering the influence of mud invasion, a three-layer formation model is established: under the condition of a vertical well, the fracture scale is 0.5 m, the resistivity of the target layer of the

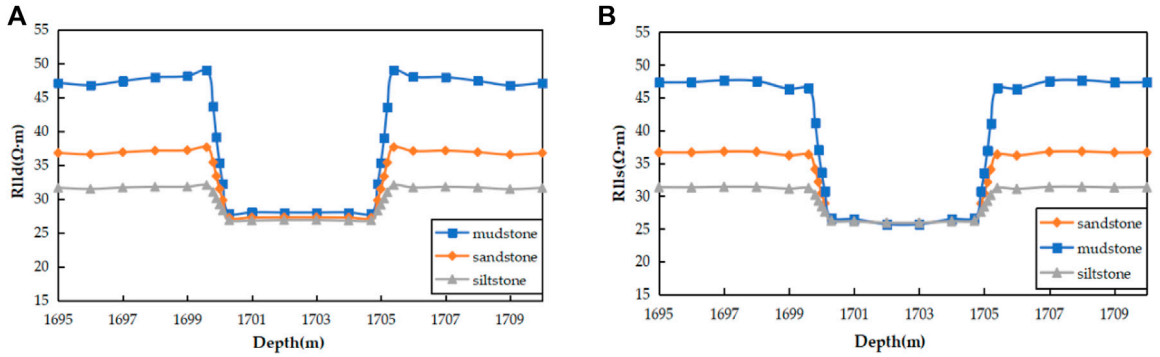


FIGURE 10
(A) Response characteristics of deep lateral logging under different lithologic combinations (low resistivity shale); **(B)** Response characteristics of shallow lateral logging under different lithologic combinations (low resistivity shale).

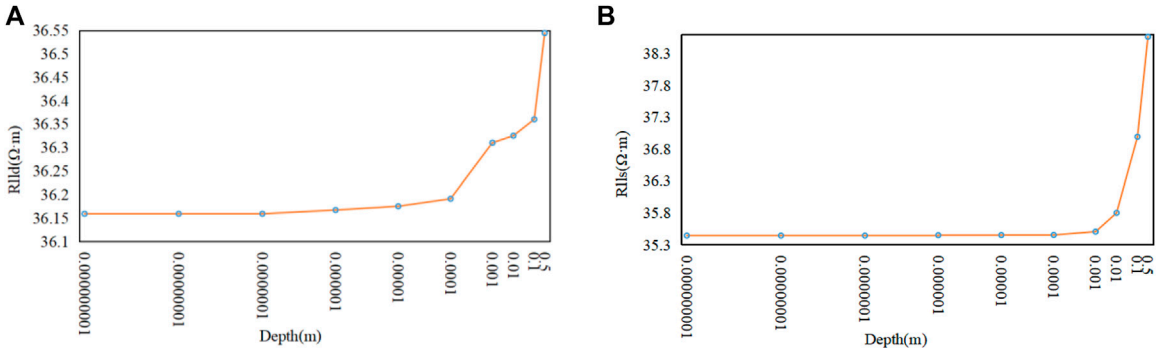


FIGURE 11
(A) Deep lateral response under effective filling conditions; **(B)** Shallow lateral response under effective filling conditions.

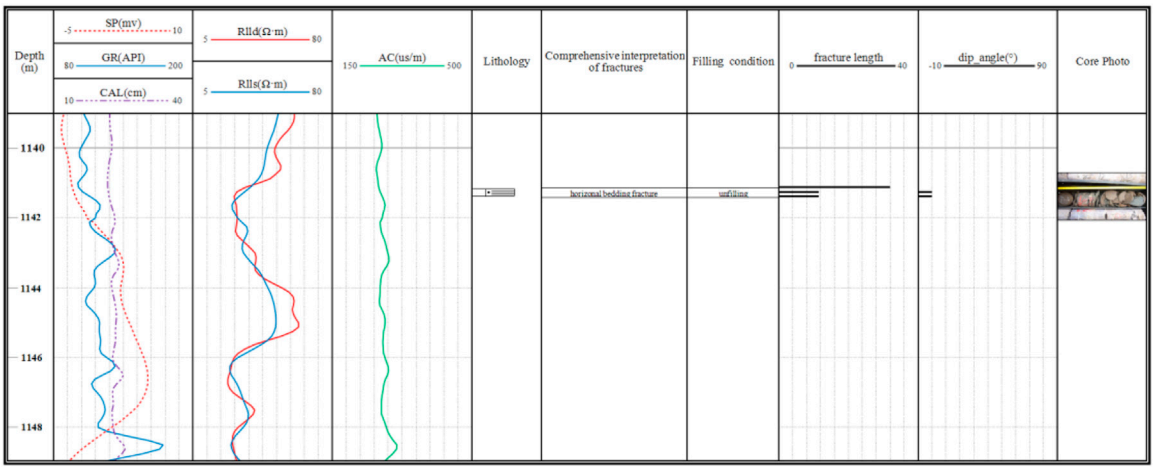


FIGURE 12
Comprehensive analysis of fractures in well section one139–1,149 m of the YY7 well.

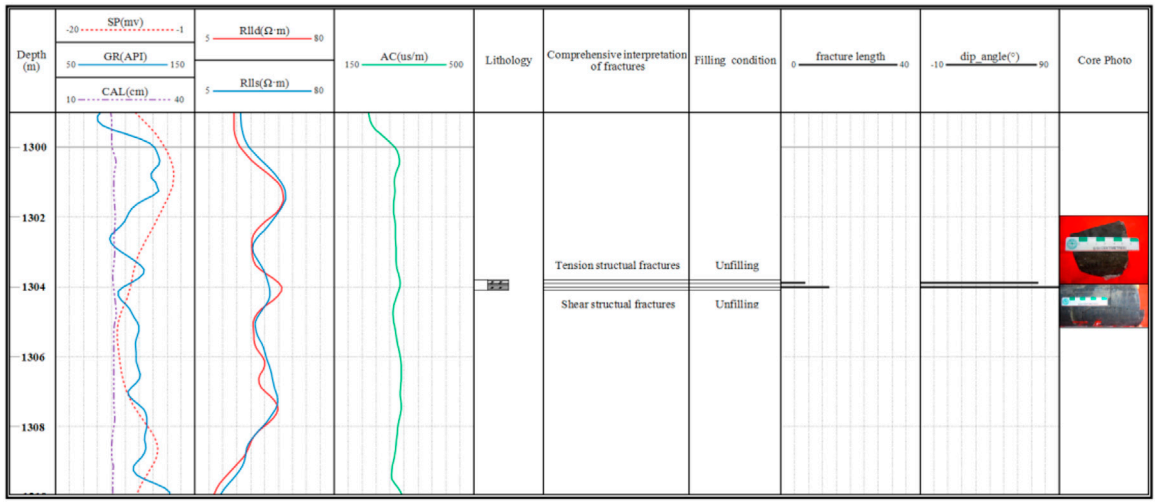


FIGURE 13
Comprehensive analysis of fractures in well section one299–1,310 m of the YY7 well.

oil shale reservoir is 55 Ω·m, and the resistivity of the target layer of the low resistivity shale reservoir is 25 Ω·m. The analysis of different lithological combinations is shown in Figures 9, 10. The dual lateral log response is disrupted in the fracture section due to the influence of surrounding rock alterations. The thickness of the fractured reservoir is indicated by the depth of the abnormal section. While the dual lateral log response is minimally impacted by different lithological combinations in oil shale and low-resistivity shale reservoirs, distinctions still exist. It can be seen that the greater the difference between shale and surrounding rock is, the greater the error between the apparent resistivity and the real formation resistivity. The shallow lateral resistivity remains largely unaffected by varying lithological combinations.

5 Discussion

5.1 Suitability analysis

In order to investigate the response properties of shale fractures containing effective filling, a three-layer model is constructed for a vertical well. The mud resistivity is 1 Ω·m. The resistivity of the upper and lower surrounding rocks is 20 Ω·m. The resistivity of the target layer is 35 Ω·m. The fracture width is 0.5 m–1 nm. As illustrated in Figure 11, it is apparent that fractures with a width of less than 0.1~1 μm exhibit a linear response in both deep and shallow lateral directions, rendering them indistinguishable. Thus, the minimum dimension of a fracture is 0.1–1 μm.

5.2 Application and effect

In order to validate the precision of the simulation, practical application was conducted using the measured data from Well YY7 in the work area, as depicted in Figures 12, 13. An unfilled horizontal bedding fracture section can be seen at a vertical depth of 1,139~1,149 m. The deep lateral resistivity of the fracture at 1,141.14~1,141.35 m is 38.531 Ω·m, and the shallow lateral resistivity is 32.729 Ω·m. The resistivity value of the dual lateral logging exhibits an overall decrease, while the core observation reveals the presence of horizontal bedding fractures, which is in agreement with the identification of fractures by lateral log. The response characteristics of the dual lateral log for vertical fractures are similar to those of horizontal fractures. To compare the difference of dual lateral log characteristics between horizontal and vertical fractures, two structural black oil shale fractures can be seen in the 1,299~1,310 m well section. The deep lateral resistivity of the fracture at 1,308.5 m is 50.3 Ω·m, and the shallow lateral resistivity is 43.806 Ω·m. The dual lateral log shows a positive difference, and the acoustic interval transit time does not change much, which indicate a high angle fracture. The core observation shows that it is a high-angle tensile structural fracture without filling. The deep lateral resistivity of the fracture at 1,304.5 m is 51.638 Ω·m, and the shallow lateral resistivity is 45.142 Ω·m. The dual lateral log shows positive difference, indicating a vertical fracture. The core observation indicates the presence of unfilled vertical fractures. The identification conclusion of the fracture dual lateral log is consistent with the core observation statistics.

6 Conclusion

Based on geological and logging data, our study proposes reasonable parameters for shale bedding fracture formation models. Additionally, the study clarifies the conditions for applying dual-lateral logging methods under varying fracture characteristics and analyzes the minimum scale of fractures that can be characterized by this method. These findings provide a foundation for identifying and evaluating shale fractures.

The work area exhibits predominantly horizontal bedding fractures, with fracture lengths primarily ranging from 0–10 cm

and widths ranging from 0.1 to 1.5 mm. Some fractures are filled with calcite, asphalt, and carbon chip.

The formation model with filling, fracture scale, different shale resistivity, and different lithological combinations is established and simulated in the forward direction. When the resistivity of the fracture is filled, the greater the difference between the resistivity and the formation resistivity, the greater the fracture scale, the greater the formation resistivity of the shale itself, the greater the difference between the resistivity of the surrounding rock and the target formation, and the greater the difference between the apparent resistivity value and the true resistivity value of the original formation. The horizontal fracture scale of shale identified by the dual lateral logging method under effective filling can reach the micron level or above.

In the future, it is recommended to conduct dual lateral log forward modelling of shale vertical fractures. On the basis of understanding the response law of forward simulation, combined with intelligent algorithm, the actual single well fracture identification is carried out, which lays a theoretical foundation for comprehensive reservoir evaluation.

Data availability statement

The original contributions presented in the study are included in the article/Supplementary material, further inquiries can be directed to the corresponding author.

Author contributions

Conceptualization, KL and NW; methodology, NW, KL, and JS; formal analysis, NW, JS, and HL; resources, KL; data curation, NW, JS, and HL; writing—original draft preparation, NW; writing—review and editing, NW, JS, KL, XH, ZX and PW; funding acquisition, KL and DW. All authors contributed to the article and approved the submitted version.

Funding

This research was funded by the State Key Laboratory of Shale Oil and Gas Enrichment Mechanism and Effective Development and the National Energy Shale Oil Research and Development Center, grant number 33550000-20-FW2099-0153. The research was also supported by Science and Technology Department of Sichuan Province, grant number 2023NSFSC0765 and 2020JDJQ0058.

Acknowledgments

The authors are grateful to the State Key Laboratory of Shale Oil and Gas Enrichment Mechanism and Effective Development and the National Energy Shale Oil Research and Development Center for their founding (Grant No. 33550000-20-FW2099-0153). The author are also grateful from Science and Technology Department of Sichuan Province (Grant No. 2020JDJQ0058 and 2023NSFSC0765). They appreciate the guidance and help from the teachers of the Chengdu University of Technology and the Skate Key Laboratory of Oil and Gas Reservoir Geology and Exploitation.

Conflict of interest

The authors declare that the research was conducted in the absence of any commercial or financial relationships that could be construed as a potential conflict of interest.

Publisher's note

All claims expressed in this article are solely those of the authors and do not necessarily represent those of their affiliated organizations, or those of the publisher, the editors and the reviewers. Any product that may be evaluated in this article, or claim that may be made by its manufacturer, is not guaranteed or endorsed by the publisher.

References

Chen, G. H., Wang, X. J., Wang, Y. G., Zhu, J. J., and Yang, H. X. (2005). Transversal prediction for reservoir parameters of fractured reservoirs in buried hills. *J. China Univ. Petroleum(Edition Nat. Sci.* (04), 26–29+34.

Deng, S. G., Mo, X. X., Lu, C. L., Zhang, Y., and Liu, L. L. (2012). Numerical simulation of the dual laterolog response to fractures and caves in fractured-cavernous formation. *Petroleum Explor. Dev.* 39 (06), 751–757. doi:10.1016/s1876-3804(12)60100-1

Dong, S. Q., Lyu, W. Y., Xia, D. L., Wang, S. J., Du, X. Y., Wang, T., et al. (2020). An approach to 3D geological modeling of multi-scaled fractures in tight sandstone reservoirs. *Oil Gas Geol.* 41 (03), 627–637. doi:10.11743/ogg20200318

Fan, C. H., Qin, Q. R., Guo, X. S., Hu, D. F., Zhou, J. L., and Fan, Z. H. (2008). *Fracture characterization and prediction of low permeability reservoir*. Beijing: science press.

Fu, H. J., Yan, D. t., Yao, C. P., Su, X. B., Wang, X. M., Wang, H., et al. (2022a). Pore structure and multi-scale fractal characteristics of adsorbed pores in marine shale: a case study of the lower silurian longmaxi shale in the sichuan basin, China. *J. Earth Sci.* 33 (05), 1278–1290. doi:10.1007/s12583-021-1602-0

Fu, X. F., Gong, L., Su, X. C., Liu, B., Gao, S., Yang, J. G., et al. (2022b). Characteristics and controlling factors of natural fractures in continental tight-oil shale reservoir. *Minerals* 12 (12), 1616. doi:10.3390/min12121616

Gao, J., Ke, S. Z., Wei, B. J., and Tan, M. J. (2010). Theoretical methods for identifying important functional genes in bacterial genomes. *Well Logging Technol.* 34 (01), 1–8. doi:10.1016/j.resmic.2009.10.007

Gao, L. J., Wu, P., Shi, X. F., Li, Y., Pang, J. D., and Yang, T. M. (2022). Logging interpretation and classification method of reservoir parameters of marine continental transitional shale based on source and reservoir type. *Nat. Gas. Geosci.* 33 (7), 1132–1143. doi:10.11764/j.issn.1672-1926.2022.01.007

Gong, L., Gao, S., Liu, B., Yang, J. G., Fu, X. F., Xiao, F., et al. (2021). Quantitative prediction of natural fractures in shale oil reservoirs. *Geofluids* 2021, 1–15. doi:10.1155/2021/5571855

Guo, H., Zhao, H. G., Li, Y., Lei, L. L., Wang, J., Li, J., et al. (2023). Fracture characteristics and hydrocarbon significance in the Chang 7 to Chang 9 members of triassic Yanchang Formation of gufengzhuang area, western Ordos Basin. *Petroleum Geol. Exp.* 45 (01), 109–121. doi:10.11781/sysydz202301109

Hadi, S. J., Morteza, D., Chen, Z. X., and Peyman, P. (2016). Comprehensive evaluation of fracture parameters by dual laterolog data. *J. Appl. Geophys.* 131, 214–221. doi:10.1016/j.jappgeo.2016.06.005

Huang, J. D., Hu, T. Y., Li, J. S., Li, Y. D., and Song, J. Y. (2019). *Comparison between discontinuous finite element method and finite difference method*. Beijing, China: Annual Meeting of Chinese Geoscience Union.

Jiang, B., Xin, Z. X., Zhang, X. F., Deng, Y. S., Wang, M. Z., Li, S. D., et al. (2023). Mechanical properties and influence mechanism of confined concrete arches in

high-stress tunnels. *Int. J. Min. Sci. Technol.* 33, 829–841. doi:10.1016/j.ijmst.2023.03.008

Li, G., Zhu, C., He, M. C., Zuo, Y. J., Gong, F. Q., Xue, Y. G., et al. (2023). Intelligent method for parameters optimization of cable in soft rock tunnel base on longitudinal wave velocity. *Tunn. Undergr. Space Technol.* 133, 104905. doi:10.1016/j.tust.2022.104905

Li, Y., Chen, J. Q., Elsworth, D., Pan, Z. J., and Ma, X. T. (2022). Nanoscale mechanical property variations concerning mineral composition and contact of marine shale. *Geosci. Front.* 13, 101405. doi:10.1016/j.gsf.2022.101405

Liu, S. Q., Shi, Q., Tang, J. Z., Liu, T. Y., Zhao, W. J., and Chen, P. (2022). Novel evaluation of fracture-type reservoir based on optimization inversion of Sphere-Fracture Model. *Chin. J. Geophys.* 65 (04), 1451–1460. doi:10.6038/cjg2022P0481

Liu, Y. J. (2022). Application of multi-resolution comprehensive evaluation of fracture logging to Asmari formation carbonate reservoir in a oilfield, southeastern Iraq. *Mineralogy Petrology* 42 (02), 101–111. doi:10.19719/j.cnki.1001-6872.2022.02.10

Murray, George H. (1968). Quantitative fracture study—sanish pool, mckenzie county, north Dakota. *AAPG Bull.* 52 (1), 57–65.

Pezard, P. A., and Anderson, R. N. (1990). "*In situ* measurements of electrical resistivity, formation anisotropy and tectonic context," in SPWLA 31st Annual Logging Symposiu, Lafayette, Louisiana, June 24-27, 1990.

Ren, F. Q., Zhu, C., He, M. C., Shang, J. L., Feng, G. L., and Bai, J. W. (2023). Characteristics and precursor of static and dynamic triggered rockburst: insight from multifractal. *Rock Mech. Rock Eng.* 56 (3), 1945–1967. doi:10.1007/s00603-022-03173-3

Shi, G., He, T., Wu, Y. Q., Liu, J. H., and Ma, Y. (2004). A study on the dual laterologo response to fracture using the forward numerical modeling. *Chin. J. Geophys.*, 359–363. doi:10.1002/cjg2.499

Shi, Z. S., Zhao, S. X., Zhao, Q., Sun, S. S., Zhou, T. Q., Cheng, F., et al. (2022). Fractures in cores from the Lower Paleozoic Wufeng-Longmaxi shale in southern Sichuan Basin and their implications for shale gas exploration. *Oil Gas Geol.* 43 (5), 1087–1101. doi:10.11743/ogg20220507

Sibbit, A. M., and Faivre, Q. (1985). "The dual laterolog response in fractured rocks," in SPWLA 26st Annual Logging Symposium, Texas: Dallax, June 1985.

Su, J. (2015). *Study on numerical simulation of dual laterolog using finite element method in shale gas reservoir*. Beijing, China: D. China University of Geosciences Beijing.

Sun, Z. L., Li, Z. M., He, C. C., Zhu, F., Shen, B. J., and Lu, L. F. (2022). Characteristics of connected pores and evaluation of shale oil mobility in the qianjiang formation, qianjiang sag, jianghan basin, China. *J. Earth Sci.*, 1–19.

Tan, M. J., Wang, P., Liu, Q., and Yang, Q. (2014). Numerical simulation and fracture evaluation method of dual laterolog in organic shale. *J. Appl. Geophys.* 100, 1–13. doi:10.1016/j.jappgeo.2013.10.006

Tan, M. J., Zhang, G. Y., Yun, H. Y., and Zhao, W. J. (2007). 3-D numerical mode-matching (NMM) method for resistivity logging responses in nonsymmetric conditions. *Chin. J. Geophys.* 50, 803–810. doi:10.1002/cjg2.1096

Tang, S. B., and Tang, C. A. (2012). Numerical studies on tunnel floor heave in swelling ground under humid conditions. *Int. J. Rock Mech. Min. Sci.* 55, 139–150. doi:10.1016/j.ijrmms.2012.07.007

Tang, S. B., Zhang, H., Tang, C. A., and Liu, H. Y. (2016). Numerical model for the cracking behavior of heterogeneous brittle solids subjected to thermal shock. *Int. J. Solids Struct.* 80, 520–531. doi:10.1016/j.ijsolstr.2015.10.012

Tang, X. M., Chen, X., and Xu, X. (2012). A cracked porous medium elastic wave theory and its application to interpreting acoustic data from tight formations. *Geophysics* 77 (6), 245–D252. doi:10.1190/geo2012-0091.1

Tang, X. Y. (2015). A review and perspective of logging evaluation technology for lower permeability reservoir. *Prog. Geophys.* 30 (02), 783–789.

Um, E. S., Commer, M., Newman, G. A., and Hoversten, G. M. (2015). Finite element modelling of transient electromagnetic fields near steel-cased wells. *Geophys. J. Int.* 202 (2), 901–913. doi:10.1093/gji/ggv193

Wang, J., Yang, C. C., Xyu, D. H., Chi, X. R., and Tan, M. J. (2005). Application and prospect of the formation microresistivity image well logging. *Prog. Geophys.* (02), 357–364.

Wang, R. Y., Ding, W. L., Zhang, Y. Q., Wang, Z., Wang, X. H., He, J. H., et al. (2016). Analysis of developmental characteristics and dominant factors of fractures in lower cambrian marine shale reservoirs: a case study of niutitang Formation in cen'gong block, southern China. *J. Petroleum Sci. Eng.* 138, 31–49. doi:10.1016/j.petrol.2015.12.004

Wang, R. Y., Hu, Z. Q., Dong, L., Gao, B., Sun, C. X., Yang, T., et al. (2021). Advancement and trends of shale gas reservior characterization and evaluation. *Oil Gas Geol.* 42, 54–65. doi:10.11743/ogg20210105

Wen, R., Ji, C. L., Li, D., Li, N., Wang, Z. T., and Luo, J. (2018). "Comprehensive evaluation of fracturing effect by borehole micro-seismic and dipole acoustic logging," in Proceedings of International Field Exploration and Development Conference, Xi'an, China, 18th September 2018.

Wu, F. (2021). *Research on fracture development and brittleness index of Chang 8 reservoir in Xiasiwan area*. Xi'an, China: D. Xi' an Shiyou University.

Wu, P., Gao, L. J., Li, Y., Wu, J. G., Shi, X. F., Kang, H. N., et al. (2022). An evaluation method for shale gas potential of marine–continent transitional facies with frequent interbedded lithology: a case study on the lower permian shanxi Formation in linxing block of the Ordos Basin. *Nat. Gas. Ind.* 42 (2), 28–39. doi:10.3787/j.issn.1000-0976.2022.02.004

Xie, Y., Liu, D. J., Li, C. F., Qyu, Y., and Sun, Y. (2020). Molecular mechanisms of the action of myricetin in cancer. *Pet. Drill. Tech.* 48 (02), 123–133. doi:10.2174/1389557519666191018112756

Xue, G. Q., Chang, J. H., Lei, K. X., and Chen, K. (2021). Review on three-dimensional simulations of transient electromagnetic field. *J. Earth Sci. Environ.* 43 (03), 559–567. doi:10.19814/j.jese.2020.11029

Yang, S. W., Wang, H. N., Chen, G. B., and Yao, D. H. (2009). The 3-D finite difference time domain (FDTD) algorithm of response of multi-component electromagnetic well logging tool in a deviated and layered anisotropic formation. *Chin. J. Geophys.* 52 (03), 833–841+257. doi:10.1002/CJG2.1368

Yin, Q., Wu, J. Y., Jiang, Z., Zhu, C., Su, H. J., Jing, H. W., et al. (2022). Investigating the effect of water quenching cycles on mechanical behaviors for granites after conventional triaxial compression. *Geomechanics Geophys. Geo-Energy Geo-Resources* 8 (2), 77. doi:10.1007/s40948-022-00388-0

Yin, Q., Wu, J. Y., Zhu, C., He, M. C., Meng, Q. X., and Jing, H. W. (2021). Shear mechanical responses of sandstone exposed to high temperature under constant normal stiffness boundary conditions. Geomechanics Geophys. Geo-Energy Geo-Resources 7, 35. doi:10.1007/s40948-021-00234-9

Zeng, L. B., Li, X. Z., Shi, C. E., Wang, Z. G., Zhao, J. Y., and Wang, Y. K. (2007). Characteristics and origin of fractures in the extra low-permeability sandstone reservoirs of the upper triassic Yanchang Formation in the Ordos Basin. *Acta Geol. sin.* 2, 174–180. doi:10.3321/j.issn:0001-5717.2007.02.005

Zhang, G. J., and Wang, H. M. (1996). Numerical pattern matching solution of common resistivity logging. *J. China Univ. Petroleum(Edition Nat. Sci.* (02), 23–29.

Zhao, J., Wang, D., and Gu, H. W. (2015). Numerical simulation of dual laterolog in cavernous carbonatite reservoir. *J. Coast. Res.* 73, 758–762. doi:10.2112/si73-130.1

Zhou, C. C., and Yang, C. D. (2003). Contributing factor of sandstone fracture and its intgrated identifying technology for reugulae logging data. *Oil Geophys. Prospect.* 4, 425–430+462+9+98+100. doi:10.13810/j.cnki.issn.1000-7210.2003.04.016

Zou, C. N., Ma, F., Pan, S. Q., Zhang, X. S., Wu, S. T., Fu, G. Y., et al. (2023). Formation and distribution potential of global shale oil and the developments of continental shale oil theory and technology in China. *Earth Sci. Front.* 30 (01), 128–142. doi:10.13745/j.esf.sf.2022.8.29

frontiers | Frontiers in Energy Research

TYPE Original Research
PUBLISHED 05 September 2023
DOI 10.3389/fenrg.2023.1272132

Check for updates

OPEN ACCESS

EDITED BY
Peng Tan,
CNPC Engineering Technology R&D Company Limited, China

REVIEWED BY
Qitao Zhang,
The Pennsylvania State University (PSU), United States
Yi Zhang,
Dalian University of Technology, China

*CORRESPONDENCE
Debin Kong,
kongdb@ustb.edu.cn
Wenning Zhou,
wenningzhou@ustb.edu.cn

RECEIVED 03 August 2023
ACCEPTED 24 August 2023
PUBLISHED 05 September 2023

CITATION
Kong D, Meng X, Zhu J and Zhou W (2023), Molecular dynamics simulation of surfactant induced wettability alteration of shale reservoirs.
Front. Energy Res. 11:1272132.
doi: 10.3389/fenrg.2023.1272132

COPYRIGHT
© 2023 Kong, Meng, Zhu and Zhou. This is an open-access article distributed under the terms of the Creative Commons Attribution License (CC BY). The use, distribution or reproduction in other forums is permitted, provided the original author(s) and the copyright owner(s) are credited and that the original publication in this journal is cited, in accordance with accepted academic practice. No use, distribution or reproduction is permitted which does not comply with these terms.

Molecular dynamics simulation of surfactant induced wettability alteration of shale reservoirs

Debin Kong[1,2]*, Xianglong Meng[1,3], Jiadan Zhu[4] and Wenning Zhou[4]*

[1]State Key Laboratory of Shale Oil and Gas Enrichment Mechanisms and Effective Development, Beijing, China, [2]School of Civil and Resources Engineering, University of Science and Technology Beijing, Beijing, China, [3]Research Institute of Exploration and Production, Beijing, China, [4]School of Energy and Environmental Engineering, University of Science and Technology Beijing, Beijing, China

Shale oil has recently received considerable attention as a promising energy source due to its substantial reserves. However, the recovery of shale oil presents numerous challenges due to the low-porosity and low-permeability characteristics of shale reservoirs. To tackle this challenge, the introduction of surfactants capable of modifying wettability has been employed to enhance shale oil recovery. In this study, we perform molecular dynamics simulations to investigate the influence of surfactants on the alteration of wettability in shale reservoirs. Firstly, surfaces of kaolinite, graphene, and kerogen are constructed to represent the inorganic and organic constituents of shale reservoirs. The impact and underlying mechanisms of two types of ionic surfactants, namely, the anionic surfactant sodium dodecylbenzene sulfonate (SDBS) and cationic surfactant dodecyltrimethylammonium bromide (DTAB), on the wettability between oil droplets and surfaces are investigated. The wettability are analyzed from different aspects, including contact angle, centroid ordinates, and self-diffusion coefficient. Simulation results show that the presence of surfactants can modify the wetting characteristics of crude oil within shale reservoirs. Notably, a reversal of wettability has been observed for oil-wet kaolinite surfaces. As for kerogen surfaces, it is found that an optimal surfactant concentration exists, beyond which the further addition of surfactant may not enhance the efficiency of wettability alteration.

KEYWORDS

shale oil, surfactant, wettability alteration, enhanced oil recovery, molecular dynamics simulation

1 Introduction

With the rapid advancement of society and economy, traditional oil and gas resources cannot meet the increasing demand (Zheng et al., 2022; Sun et al., 2023). Hence, it is of great significance to enhance oil and gas production through advanced technologies. Despite recent great breakthroughs in untraditional oil exploration, a substantial amount of shale oil remains trapped within shale reservoirs due to their low-porosity and low-permeability characteristics, resulting in relatively low recovery rates (Zou et al., 2019; Tang et al., 2020; Sun C. et al., 2021). During oil extraction operations, residual oil gets trapped in the nanopores of shale reservoirs after water injection, presenting a significant challenge to the oil recovery process (Dang et al., 2022; Guo et al., 2022). In recent years, several enhanced oil recovery (EOR) techniques have been developed (Rezaei et al., 2018; Zhao et al., 2021; Yang

et al., 2023), with surfactant flooding emerging as one of the most effective technologies for oil recovery enhancement (Liu et al., 2019a; Sun Y.-P. et al., 2021; Larestani et al., 2022). Surfactants exhibit diverse and unique physical and chemical properties, thereby offering considerable potential for optimizing oil recovery under varying conditions, including geological conditions, reservoir compositions, brine salinities, etc. (Tang et al., 2019)

From a macroscopic perspective, the deformability and mobility of oil droplets play a crucial role in determining the ease of detaching oil droplets from the rock surface of oil reservoirs, ultimately leading to enhanced oil recovery (Zhang et al., 2010; Pei et al., 2012). A Previous researchers have conducted extensive experimental and theoretical studies, which have elucidated two primary mechanisms through which surfactants enhance oil recovery. Firstly, surfactants reduce the interfacial tension between oil and water, thereby improving the fluidity of crude oil (Liu et al., 2022; Zhou et al., 2022). Secondly, they alter the wettability of reservoirs from lipophilic to hydrophilic, facilitating the release of more residual oil and enhancing oil recovery (Mirchi et al., 2015; Kubelka et al., 2021; Okunade et al., 2021). Currently, research on the influence of different wettability conditions on the adsorption and diffusion behaviors of shale reservoirs is still in its early stages. Scholars hold different views on shale wettability due to differences in tectonic features and mineral compositions. Shale surface wettability is a critical factor in shale oil recovery as it directly affects the distribution of oil within shale reservoirs, the injection of oil displacement agents into the formation, and the effectiveness of oil displacement (Zhao and Jin, 2021; Shi et al., 2022).

The wettability of reservoir rocks can be influenced by external conditions. Despite extensive research efforts made by scholars worldwide to understand the mechanisms underlying reservoir wettability, a consensus has not yet been reached. Since reservoir rocks are formed in water environments, most of the component minerals are hydrophilic (Guo et al., 2012). Consequently, the initial state of the reservoir rock surface is hydrophilic, characterized by the presence of a water film on the surface. However, the generation and migration of oil and gas within the reservoir typically result in a transition from hydrophilic to lipophilic wettability (Su et al., 2018; Zhang et al., 2020). Furthermore, the wettability of reservoirs can be further modified by drilling fluids and various oil displacement agents such as water, chemicals, and CO_2 (Al Mahrouqi et al., 2017; Yao et al., 2021; Deng et al., 2020; Zhang et al., 2022; Afekare et al., 2021; Qin et al. 2022). These modifications in wettability are often desirable since altering the distribution of reservoir fluids within the pore network through the introduction of oil displacement agents can enhance shale oil recovery.

Researchers have conducted experimental investigations to study the impact of surfactants on enhancing shale oil recovery. Mirchi et al. (Mirchi et al., 2015) investigated the dynamic interfacial tensions and contact angles in two brine/oil/shale systems in the presence of surfactants using the rising/captive bubble technique. They reported that anionic surfactants exhibit higher adsorption on shale compared to nonionic surfactants. SalahEldin Hussien et al. (SalahEldin Hussien et al., 2019) studied the effects of surfactants on fracturing fluid performance by measuring surface tension using the pendant drop technique. Their results revealed that surfactants significantly influenced the wettability of shale rock, rendering it more water-wet. Liu et al. (Liu et al., 2019b) utilized nuclear magnetic resonance (NMR) to evaluate the wettability of shales. Their results indicated that anionic surfactants are more effective compared to nonionic and cationic surfactants in altering the wettability of clay surfaces. Although certain quantitative results can be obtained, it remains challenging to observe the underlying mechanisms and microscopic processes solely through macroscopic experiments (Roshan et al., 2016).

With the rapid development of computer technology, molecular dynamic (MD) simulation is becoming an effective tool for unravelling the underlying mechanisms governing complex processes and behaviors at the microscale level (Zhou et al., 2019a; Zhou et al., 2019b; Zhou et al., 2020; Chen et al., 2023). Researchers have applied extensive MD simulations on investigating the wettability behaviors of shale reservoir for EOR. Chai et al. (2009) examined the wettabilities of surfaces of hydroxylated and silylated amorphous silica. They claimed that the fully silylated silica surface

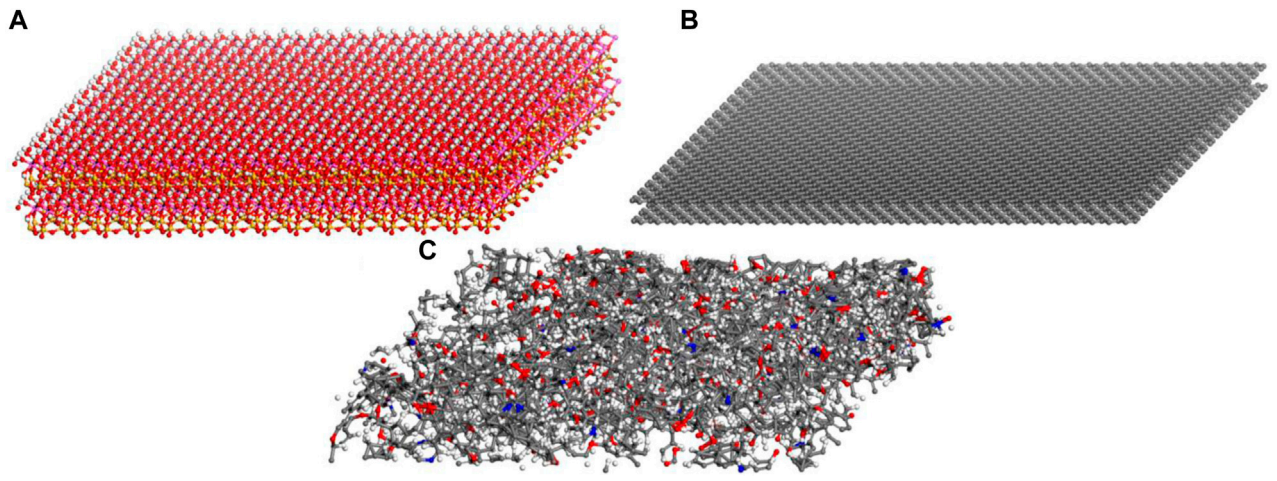


FIGURE 1
Different surface models: **(A)** kaolinite; **(B)** graphene; **(C)** kerogen. Red, white, yellow, purple, grey, and blue atoms represent oxygen, hydrogen, silicon, aluminium, carbon, and nitrogen, respectively.

TABLE 1 Annealing process for developing kerogen surface model.

Ensemble	T (K)	P (bar)	*t* (ns)
NVT	900		0.2
NPT	900	10	0.2
NPT	900→700	10	0.1
NPT	700	10	0.2
NPT	700→500	10	0.1
NPT	500	10	0.2
NPT	500→365	10	0.1
NPT	365	10	0.2
NPT	365	10→275	0.2
NPT	365	275	0.5
NPT	1,000→365	275	1.0
NPT	365	275	1.0

exhibit higher hydrophobicity, while the fully hydroxylated amorphous silica surface display greater hydrophilicity. Jagadisan and Heidari. (2022) conducted MD simulations to explore the influences of thermal maturity and reservoir temperature on the wettability performances of organic kerogen surfaces. Their simulation results indicated that the formed air/water/kerogen contact angle is maximal on type III and minimal on type II kerogen surfaces.Bai et al. (2020) utilized MD simulation to examine the correlation between molecular charge distribution and the efficiency of wettability reversal of quaternary ammonium type cationic surfactants on calcite surfaces. Their results revealed that the charge distribution on the hydrogen atoms within the methylene group of the quaternary ammonium moiety plays a critical role in determining the surfactants' ability to modify wettability. By employing MD simulations, Chen et al. (2015) studied various functional groups on the silica surface. Their results suggested that the presence of different functional groups exhibit a significant impact on the surface contact angle of silica, leading to substantial changes in wettability. Kubelka and his co-workers (Kubelka et al., 2021) investigated the altered wettability of oil-wet calcite by surfactants through MD simulations. They claimed that cationic surfactants demonstrated greater efficiency in separating organic carboxylates and wettability alteration compared to brine.

Although many efforts have been devoted on investigating wettability alteration of oil reservoirs, studies on insightful mechanism and the effects of surfactant type, concentration, and surface properties on wettability of shale reservoirs are still limited. In the present work, we perform MD simulations to investigate the effects of different surfactants and reservoir properties on wettability alteration of shale reservoirs, taking into account their diverse constituents. The obtained results are expected to provide valuable insights and guidance for the development of effective surfactant flooding strategies for enhancing shale oil recovery.

2 Models and simulation methods

2.1 Physical models and force field

In this study, three types of surfaces, i.e., kaolinite, graphene, and kerogen surfaces are constructed to characterize the structures of

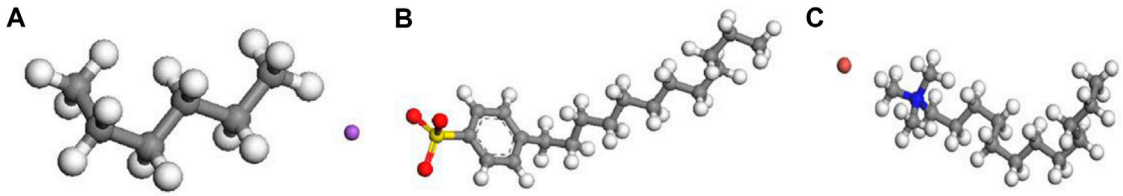


FIGURE 2
Molecular models of **(A)** n-hexane, **(B)** sodium dodecylbenzene sulfonate, and **(C)** dodecyltrimethylammonium bromide. Grey, white, red, yellow, purple, earthy yellow, and blue represent carbon, hydrogen, oxygen, sulphur, sodium, bromine, and nitrogen, respectively.

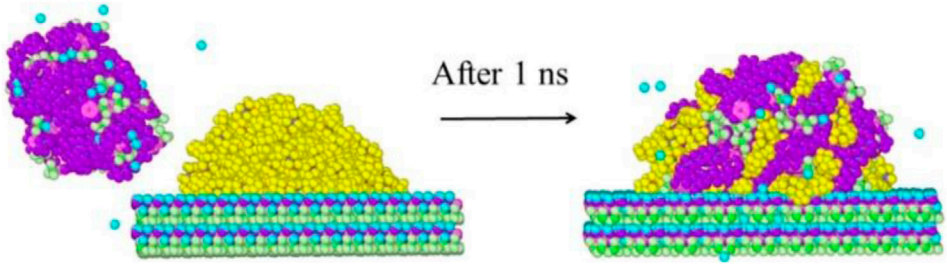


FIGURE 3
Snapshots of the surface/oil/water/surfactant system.

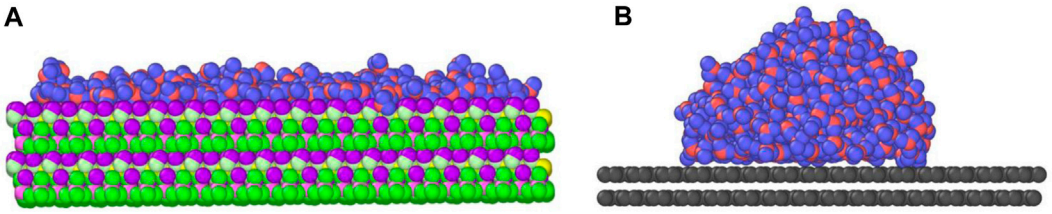


FIGURE 4
Wetting behaviors of water droplet on the **(A)** kaolinite and **(B)** graphene surfaces.

inorganic, simplified organic, and organic surfaces in shale reservoirs, respectively. The Silica-Face-to-Gibbsite-Face (SG-FF) manner is used to construct the {0 0 1} octahedral surface model with dimensions of 81 × 78 × 14 Å^3 of kaolinite, as shown in Figure 1A (Šolc et al., 2011; Tenney and Cygan, 2014; Sun H.-m. et al., 2021). A 33 × 18 × 2 supercell of the graphene unit cell structure with the size of 74 × 77 × 4 Å^3 is built for the graphene surface model, as displayed in Figure 1B. The kerogen surface model is developed based on the relaxation process proposed by Michalec and Lisaĺ (Michalec and Lísal, 2017) and the modification by Yu et al. (2021) Firstly, 40 III-A type kerogen molecules are randomly inserted into a cuboid simulation box with an initial system density of approximately 0.05 g/cm^3. Subsequently, the annealing process is performed following the relaxation protocol outlined in Table 1. After 12 cycles, a kerogen surface model with the size of 63.6 × 63.6 × 22.7 Å^3 is obtained, as presented in Figure 1C. The final density of the model is 1.259 g/cm^3, which is in good agreement with the experimental result of 1.28 ± 0.3 g/cm^3 (Stankiewicz et al., 2015).

In this study, the shale oil model is simplified with n-hexane, as depicted in Figure 2A. The oil molecules are parameterized using the polymer consistent force field (PCFF) (Sun et al., 1994; Plimpton, 1995; Chen et al., 2006; Cui et al., 2022), which has proven to be capable to accurately predict the structural and thermodynamic properties of oil components (Tang et al., 2019). The surfactants utilized in this study are the anionic surfactant sodium dodecylbenzene sulfonate (SDBS) and the cationic surfactant dodecyltrimethylammonium bromide (DTAB), as illustrated in Figures 2B,C. These surfactants are widely used in oil recovery experiments due to their commonality and ready availability. In this study, all molecular models are constructed using the Materials Studio package (version 2017).

2.2 Simulation details

Firstly, 120 n-hexane molecules are randomly placed onto a surface within a simulation box. Following geometrical optimization, the alkane molecules are superimposed on the surface forming an oil droplet. The system is then immersed in water and equilibrated in a canonical (NVT) ensemble at 330 K for 1 ns (Tang et al., 2019). This equilibration stage allows for the determination of the competitive adsorption of oil and water on the surfaces, resulting in different wettability behaviors. After equilibration, water is removed and surfactants are placed on the left side of the system. The water in the simulation is controlled to redissolve the generated shale surface/oil/water/surfactant system. Finally, the shale surface/oil/water/surfactant system is simulated at 330 K for 1 ns, as illustrated in Figure 3. In this work, the time step for the simulations is 1 fs and periodic boundary conditions are adopted (Kubelka et al., 2021). The extended simple point charge (SPC/E) model is used for characterizing water molecules (Taylor et al., 1996). All molecular dynamics simulations in this study are performed on the Large-scale Atomic/Molecular Massively Parallel Simulator (LAMMPS) (Plimpton, 1995). The simulation results are visualized using OVITO software.

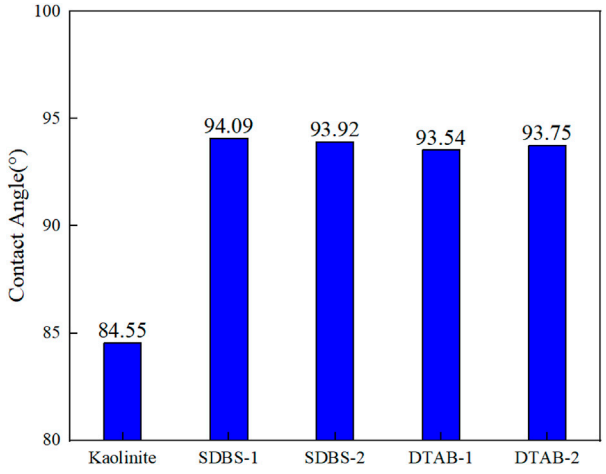


FIGURE 5
Comparison of contact angles on kaolinite surfaces with different surfactants.

3 Results and discussion

3.1 Model validation

In this study, the contact angles of water droplets on the kaolinite and graphite surfaces are first simulated to validate the accuracy of the physical model and force field, as displayed in Figure 4. The simulation results demonstrate that the droplet spreads on the kaolinite surface, forming an incomplete monomolecular layer with a contact angle close to zero. This indicates an extremely hydrophilic nature of kaolinite surface,

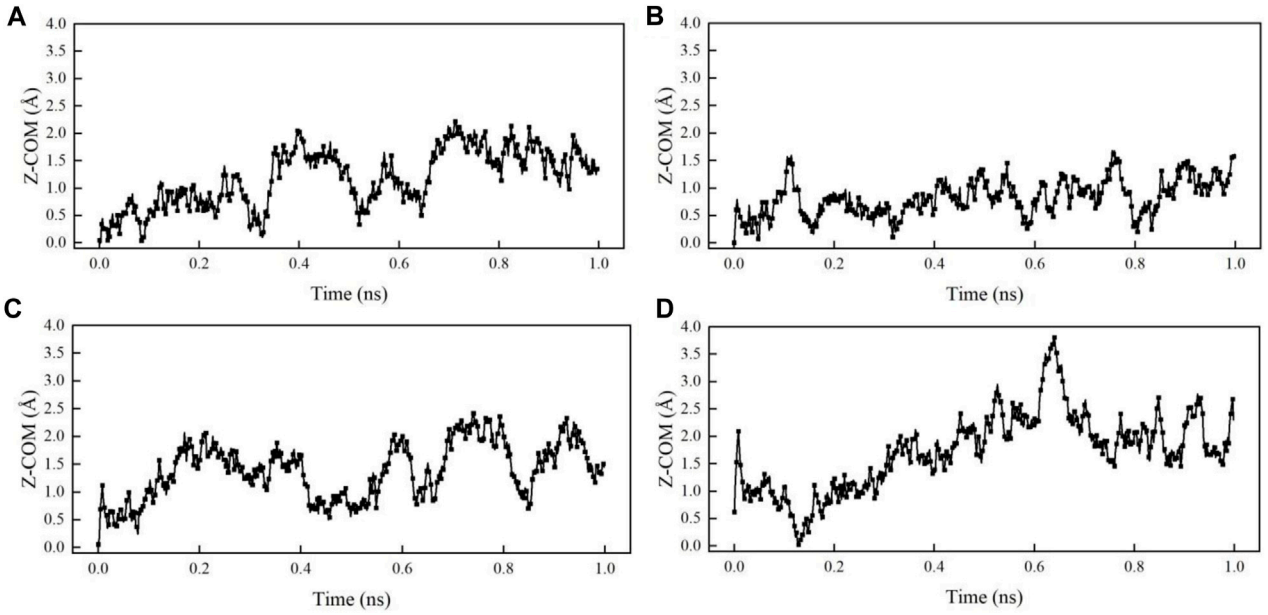


FIGURE 6
Variations of centroid ordinates in different systems: **(A)** SDBS-1; **(B)** SDBS-2; **(C)** DTAB-1; **(D)** DTAB-2.

which is consistent with the results obtained by Šolc et al. (Šolc et al., 2011) The simulated contact angle of water droplet on the graphene surface is 94.2°, which is in good agreement with the simulation result of 99.1° obtained by Xiong et al. (Xiong et al., 2022) In this work, the contact angles of droplets are determined by:

$$\theta = \arcsin\left(\frac{2hr}{h^2 + r^2}\right) \quad (h < R) \tag{1}$$

$$\theta = 90° + \arcsin\left(\frac{2hr}{h^2 + r^2}\right) \quad (h > R) \tag{2}$$

where θ denotes the wetting contact angle, h is the droplet height, r is the radius of the circular contact surface between the droplet and the surface, and R is the radius of the droplet.

3.2 Effect of surfactants on the wettability of inorganic kaolinite surfaces

In order to examine the effects of different types and concentrations of surfactants on the wettability of n-hexane oil droplets on a kaolinite surface, a series of MD simulations are performed. Specifically, two sets surfactants, namely, SDBS-1/DTAB-1 (consisting of 25 surfactant molecules) and SDBS-2/DTAB-2 (consisting of 40 surfactant molecules) are examined.

3.2.1 Comparison of contact angle

To quantitatively describe the contact angles of oil droplets composed of 120 n-hexane molecules on the shale surface, we assume that the oil mass in equilibrium is a part of an ideal sphere. It should be noted that the mentioned contact angles hereinafter are measured with oil droplet on different surfaces.

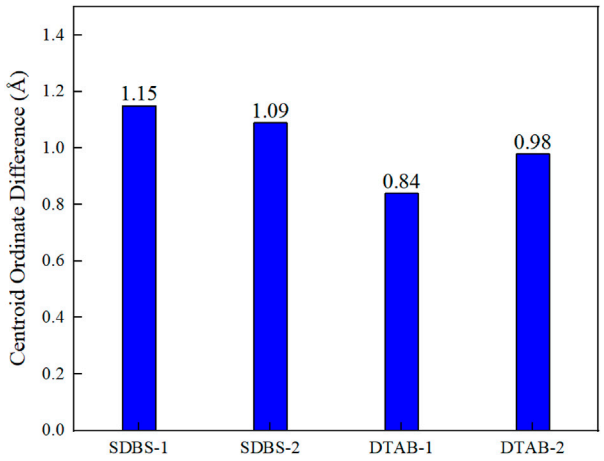


FIGURE 7
Comparison of centroid ordinate differences in different kaolinite systems with different surfactants.

Figure 5 presents the variations in contact angle for the kaolinite/oil/water/surfactant system with different concentrations of SDBS and DTAB. In the SDBS-1 model group, the contact angle of n-hexane oil droplets increases from 84.55° to 94.09° after 1 ns of simulation calculations, while 93.92° for SDBS-2 system. The contact angle increase from 84.55° to 93.54° in DTAB-1 system, while 93.75° for DTAB-2 system. It is concluded that wettability alteration from intermediate-oleophilic to intermediate-oleophobic can be observed for both SDBS and DTAB. However, the concentration of surfactants indicates slight influences on the degree of wettability alteration.

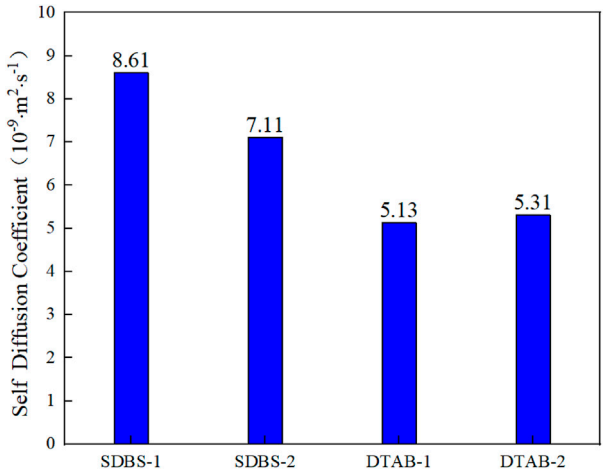


FIGURE 8
Comparison of self-diffusion coefficients in different kaolinite systems with different surfactants.

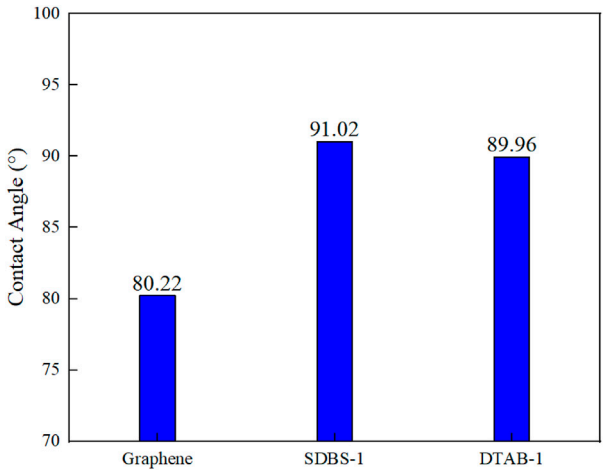


FIGURE 9
Comparison of contact angle on different graphene surfaces with different surfactants.

3.2.2 Comparison of centroid ordinates

The vertical distance between the centroid of the oil droplet and kaolinite surface, i.e., the centroid ordinates of the oil droplet, is calculated by the COM (centre of mass) command in LAMMPS, and the centroid ordinates of the oil droplets in the Z direction are recorded every 2000 steps to observe the trend of oil droplets. Figure 6 shows the comparison of centroid ordinate differences in kaolinite system. The rise in the centroid ordinates indicates that the oil droplets have a tendency to move upwards away from the kaolinite surface due to the action of the surfactant. After 1 ns of simulation, the centroid ordinates of n-hexane oil droplets in SDBS-1 system increases by 1.15 Å, while 1.09 Å for SDBS-2 system. The COM trajectory of DTAB-1 system with the cationic surfactant also shows that the volume of oil droplet increases after the addition of DTAB, and the centroid ordinate in the Z direction rises by 0.84 Å. The centroid ordinates increase by 0.98 Å in the DTAB-2 system, as can be seen in Figure 7. It can be observed that n-hexane aggregates move much faster in the Z direction due to the interaction with SDBS. However, this effect decreases with the increasing concentration. Under the action of DTAB, the aggregates move faster with higher concentrations.

3.2.3 Comparison of self-diffusion coefficients

The self-diffusion coefficient can fully reflect the diffusion and migration ability of n-hexane molecules on the shale surface. The self-diffusion coefficient of n-hexane molecules needs to be calculated to describe their movement and changes on the shale surface. The calculation formula can be written as:

$$MSD = \langle |R(t) - R(0)|^2 \rangle \tag{3}$$

$$D = \frac{1}{2N} \lim_{t\to\infty} \frac{d}{dt} \langle |R(t) - R(0)|^2 \rangle \tag{4}$$

where D is the self-diffusion coefficient of the n-hexane molecule, $R(t)$ is the position of the n-hexane molecule at time t, and $R(0)$ is the initial position of the n-hexane molecule. First, the mean square displacement of n-hexane molecules is obtained using the MSD command in LAMMPS. Then, the self-diffusion coefficient can be calculated.

Figure 8 shows the comparison of self-diffusion coefficients of the oil droplets. The self-diffusion coefficient of oil droplets in the SDBS-1 and SDBS-2 model are 8.61×10^{-9} and 7.11×10^{-9} m^2 · s^{-1}, respectively. The self-diffusion coefficients in the DTAB-1 and

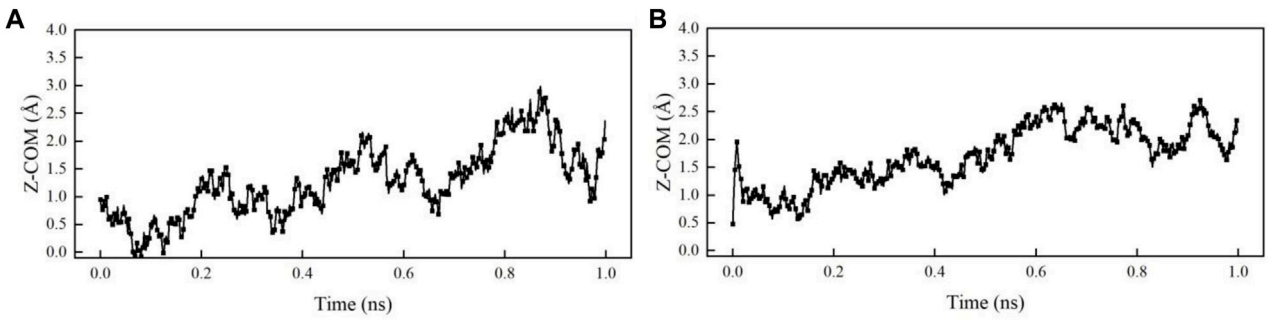


FIGURE 10
Variations of centroid ordinates in the systems: **(A)** SDBS-1; **(B)** DTAB-1.

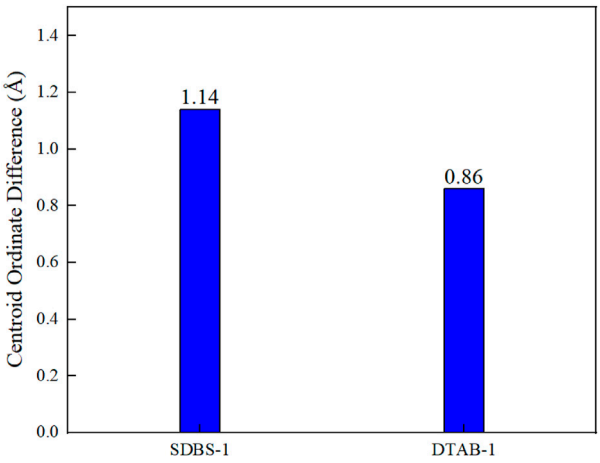


FIGURE 11
Comparison of centroid ordinate variations in different graphene systems with different surfactants.

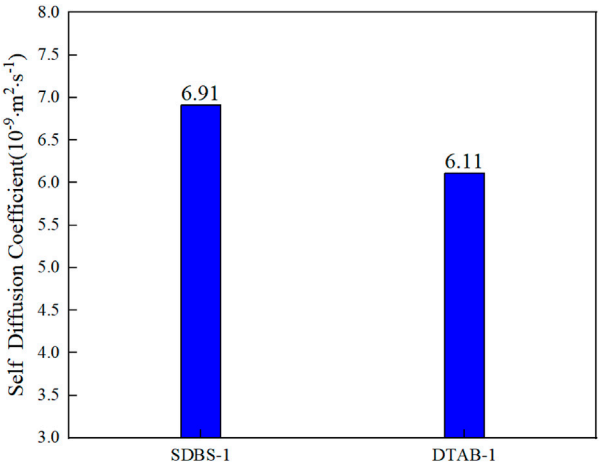


FIGURE 12
Comparison of self-diffusion coefficients in different graphene systems with different surfactants.

DTAB-2systems are 5.13×10^{-9} and 5.31×10^{-9} m$^2 \cdot$ s^{-1}, respectively. It indicates that the n-hexane aggregates diffuse to a greater extent due to the action of SDBS. Higher SDBS concentrations lead to smaller self-diffusion coefficients of n-hexane molecules. In contrast, the higher concentration in the DTAB group corresponds to a greater self-diffusion coefficient. With higher self-diffusion coefficients, oil molecules have greater movement speed, stronger escape ability, and easier detachment from the kaolinite surface.

The magnitudes of contact angle and self-diffusion coefficient and the centroid position variation of the oil droplets clearly indicate the different effects of different surfactants on the oil adsorption onto the kaolinite surface. According to the simulation results, SDBS has better oil displacement performance than DTAB. This difference in oil displacement performance of the two surfactants was attributed to the head group effect. The groups in SDBS have a stronger attraction for water molecules. As a result, the SDBS migrates faster over the oil aggregation surface, and the oil molecule deformation separation is faster.

Although the data are somewhat scattered, a clear correlation between the wettability index and surfactant concentration can be observed. At higher concentrations, SDBS has less effect on the wettability variation of oil droplets on the kaolinite surface and less wettability inversion effect. Meanwhile, DTAB shows the opposite trend. Therefore, the effect of DTAB is opposite to that of SDBS. At higher concentrations, DTAB has a better effect on the wettability variation of oil droplets on the kaolinite surface and a better wettability inversion effect.

3.3 Effect of surfactants on the wettability of graphene surfaces

In the section, the effects of surfactant on the wettability on the simplified graphene surfaces are focused. We develop the system models containing 25 surfactant molecules, denoted as SDBS-1 and DTAB-1, respectively. After 1 ns of simulation, the contact angle of n-hexane oil droplets in SDBS-1 increases from 80.22° to 91.02°, while that in DTAB-1 increases to 89.96°, as shown in Figure 9. The vertical distances between the centroid of the oil droplet and the graphene surface, i.e., the centroid ordinates of the oil droplet, are recorded every 2000 steps to observe the trend of the oil droplets, as shown in Figure 10.

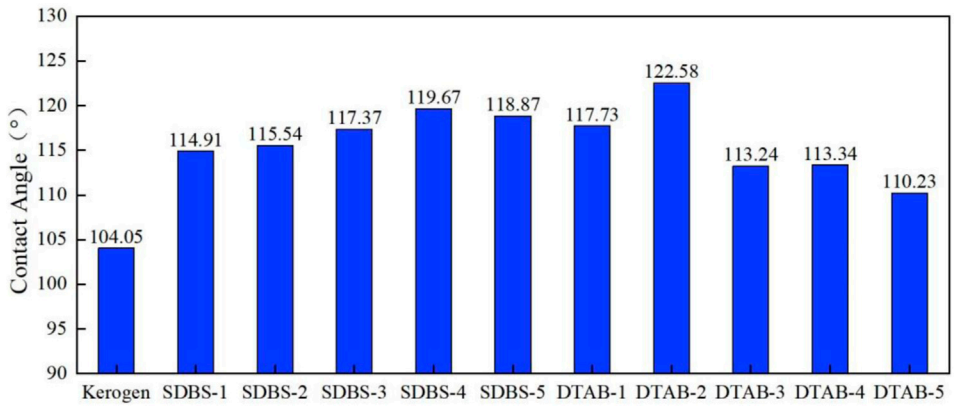


FIGURE 13
Comparison of contact angles on kerogen surfaces with different surfactants.

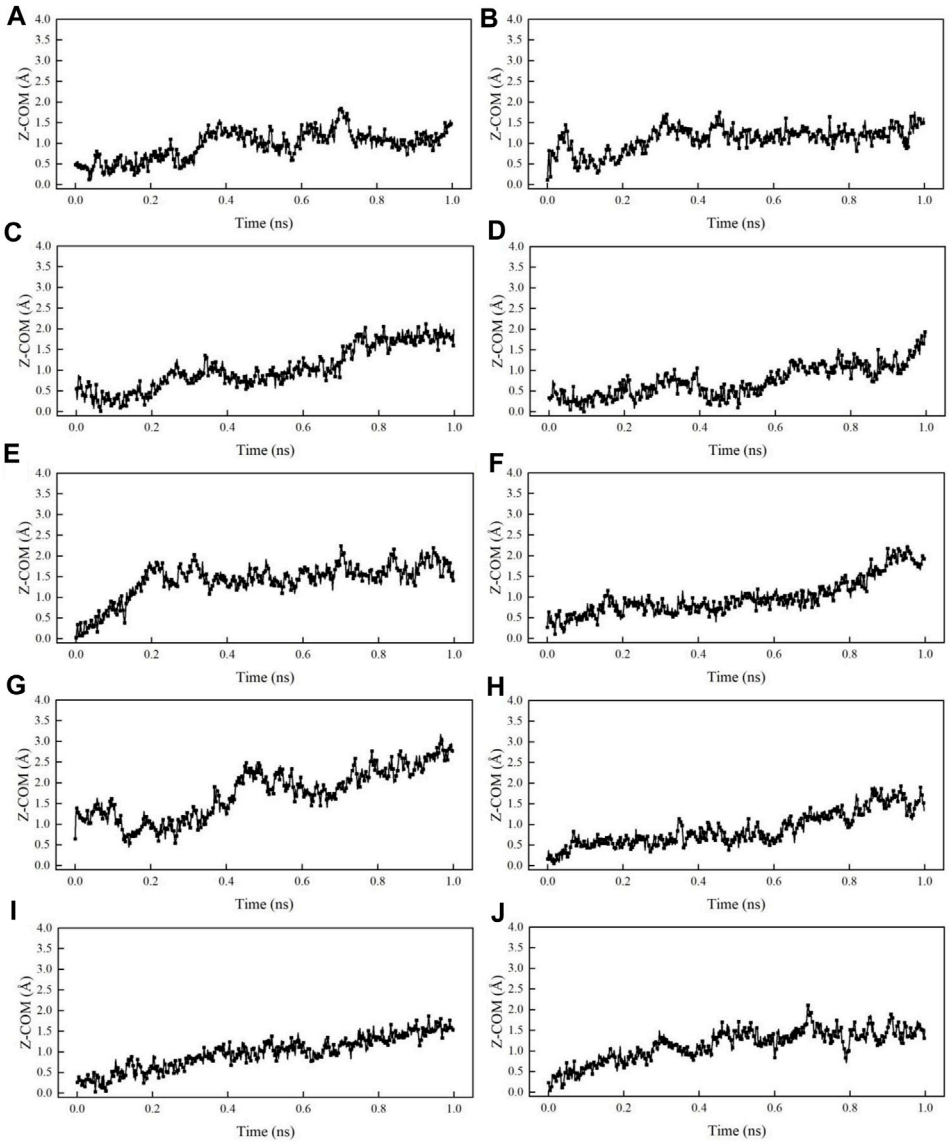


FIGURE 14
Variations of centroid ordinates in different systems: **(A)** SDBS-1; **(B)** SDBS-2; **(C)** SDBS-3; **(D)** SDBS-4; **(E)** SDBS-5; **(F)** DTAB-1; **(G)** DTAB-2; **(H)** DTAB-3; **(I)** DTAB-4; **(J)** DTAB-5.

After 1 ns of simulation calculation, the centroid ordinate of n-hexane oil droplets rises by 1.14 Å in SDBS-1 and 0.86 Å in DTSB-1, as shown in Figure 11. The diffusion coefficient can fully reflect the diffusion and migration ability of n-hexane molecules on the shale surface. The diffusion coefficient of n-hexane molecules needs to be calculated to describe their movement and changes on the shale surface. As shown in Figure 12, the diffusion coefficient is 6.91×10^{-9} $m^2 \cdot s^{-1}$ in SDBS-1 and 6.11×10^{-9} $m^2 \cdot s^{-1}$ in DTAB-1. The magnitudes of contact angle and diffusion coefficient and the centroid position variation of the oil droplets clearly indicate that the surfactants can alter the wettability of oil adsorbed onto the graphene surface. Meanwhile, the effect of SDBS is better than DTAB, which is consistent with the findings in the previous section. The reason may be that groups in SDBS have a stronger attraction for water molecules. As a result, the SDBS migrates faster over the oil aggregation surface, and the oil molecule deformation separation is faster. We can all see that SDBS is more effective than DTAB when compared to kaolinite systems with the same number of surfactants, but SDBS is slightly less effective in changing wettability in the graphene system than in the kaolinite system. DTAB, on the other hand, demonstrated the inverse trend, with a slightly better effect in the graphene system than in the kaolinite system. This could be due to the various properties of the shale surface.

3.4 Effect of surfactants on the wettability of kerogen surfaces

To examine the effects of surfactant on wettability alteration of organic matter in shale reservoirs, a realistic kerogen surface is also developed. Different surfactant concentrations of SDBS-1 and

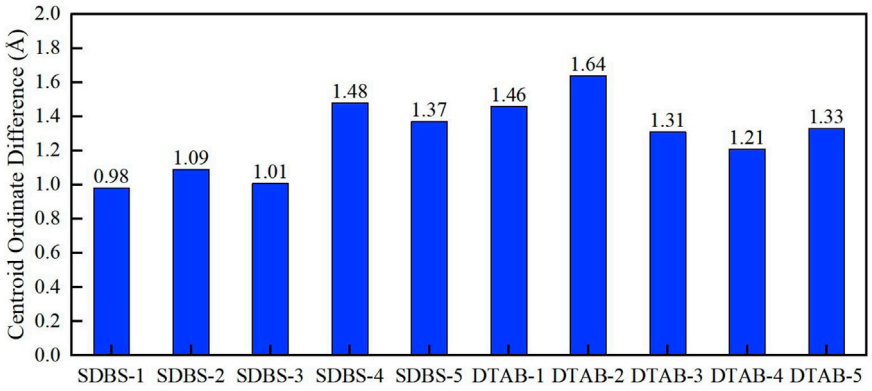


FIGURE 15
Comparison of centroid ordinate differences in different kerogen systems with different surfactants.

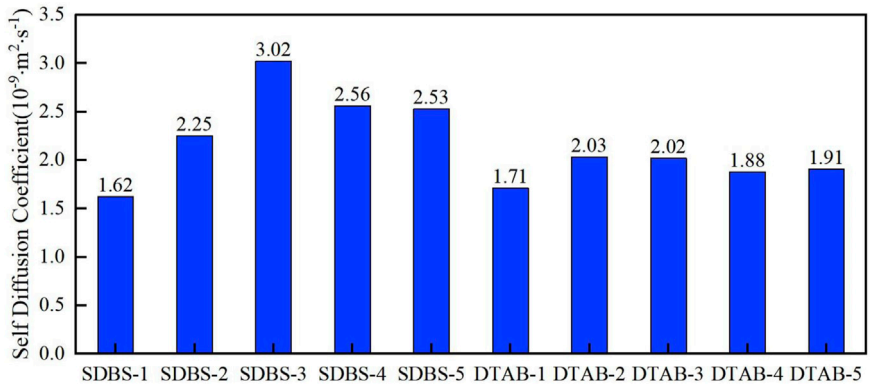


FIGURE 16
Comparison of self-diffusion coefficients in different kerogen systems with different surfactants.

DTAB-1 to SDBS-5 and DTAB-5 (20, 25, 30, 35, 40 surfactant molecules) are further designed.

3.4.1 Comparison of contact angles

Figure 13 shows the contact angle variation of the kerogen/oil/water/surfactant system with different concentrations of SDBS or DTAB. Without surfactant, the contact angle of the equilibrated oil droplet is 104.05°on the kerogen surface. With the increase of SDBS concentration, the contact angle of oil droplet increases from 114.91° to 119.67° and then shows a slight decrease to 118.87°. While for DTAB, a similar tendency is observed, with the contact angle increasing from 117.73° to 122.58° and declining to 110.23°. It indicates that there is an optimal concentration of surfactant for wettability alteration. It can be observed from Figure 13 that with 25 surfactant molecules, the interaction between DTAB and the oil/water interface is more intense, and the contact angle of n-hexane oil droplets changes more rapidly. While for SDBS, the contact angle changes more drastically with 35 surfactant molecules.

3.4.2 Comparison of centroid ordinates

Figure 14 shows the comparison of centroid ordinate differences in all kerogen systems. After 1 ns of calculation, the centroid ordinates of oil droplets in the system with SDBS increase by 0.98, 1.09, 1.01, 1.48 and 1.37 Å, respectively. The trajectory of the DTAB system also shows that the centroid ordinates in the Z direction increase by 1.46, 1.64, 1.31, 1.21 and 1.33 Å, respectively. Figure 15 shows a comparison of oil droplet centroid ordinate variations along the vertical direction. It is observed that the droplet move much faster in Z direction due to the interaction with DTAB. It is clear from the figure that there are optimal concentrations for both SDBS and DTAB in altering wettability of kerogen surface. The variation pattern of oil droplet centroid is consistent with that of contact angle.

3.4.3 Comparison of self-diffusion coefficients

Figure 16 shows the comparison of self-diffusion coefficients of oil droplets. It is found that the self-diffusion coefficients of oil

molecules increases and then decreases with the increment of the concentrations of SDBS and DTAB, which are consistent with earlier findings. It is observed that the effects of surfactant on the wettability of organic kerogen surfaces is significantly different from that on inorganic kaolinite surfaces. The difference is due to the different nature of the substrate. Different types of surfactants have different effects on the solution surface/interfacial tension. Surfactants significantly decrease the interfacial tension, but the extents of the decreases vary. As a water-bearing aluminosilicate, kaolinite is a clay mineral. Kerogen is a dispersed organic matter in sedimentary rocks insoluble in alkalis, non-oxidizing acids, and organic solvents. The differences in the structure and properties of kaolinite and kerogen lead to different effects of surfactants on their surfaces.

4 Conclusion

In the present work, molecular dynamics simulations have been adopted to investigate the effects of surfactant on wettability alterations on kaolinite, graphene, and kerogen surfaces in shale reservoirs. The following conclusions can be drawn.

(1) The changes of contact angle, centroid ordinates, and self-diffusion coefficients in the simulations indicate that surfactants can alter the wettability of oil droplets on the surfaces of kaolinite, graphene, and kerogen.
(2) For oil-wet kaolinite surfaces with contact angle of 84.55°, the wettability reversals have been observed for both SDBS and DTAB. However, compared with graphene and kerogen surfaces, the degree of wettability alteration is less sensitive to surfactant concentration.
(3) For organic graphene and kerogen surfaces, surfactants are found to be able to further improve the contact angels of oil droplets. However, for kerogen surfaces, there is an optimal surfactant concentration for both SDBS and DTAB, beyond which the further addition of surfactant could decrease the contact angel.
(4) The obtained results suggest that the effects of SDBS and DTAB on the surfaces of kaolinite, graphene, and kerogen are obviously different, which is due to the interactions between headgroups of surfactants and surfaces.

Data availability statement

The original contributions presented in the study are included in the article/Supplementary Material, further inquiries can be directed to the corresponding authors.

Author contributions

DK: Funding acquisition, Investigation, Project administration, Validation, Writing–review and editing. XM: Conceptualization, Data curation, Validation, Writing–review and editing. JZ: Data curation, Investigation, Visualization, Writing–original draft, WZ: Validation, Visualization, Writing–original draft, Writing–review and editing.

Acknowledgments

The authors acknowledge the financial support from the Natural Sciences for Youth Foundation of China (No. 42102163), the Fundamental Research Funds of the Central Universities (No. FRF-TP-20-006A1) and the Open Fund of State Key Laboratory of Shale Oil and Gas Enrichment Mechanisms and Effective Development (No. 33550000-21-FW2099-0166).

Conflict of interest

The authors declare that the research was conducted in the absence of any commercial or financial relationships that could be construed as a potential conflict of interest.

Publisher's note

All claims expressed in this article are solely those of the authors and do not necessarily represent those of their affiliated organizations, or those of the publisher, the editors and the reviewers. Any product that may be evaluated in this article, or claim that may be made by its manufacturer, is not guaranteed or endorsed by the publisher.

References

Afekare, D., Garno, J., and Rao, D. (2021). Enhancing oil recovery using silica nanoparticles: nanoscale wettability alteration effects and implications for shale oil recovery. *J. Petrol. Sci. Eng.* 203, 108897. doi:10.1016/j.petrol.2021.108897

Al Mahrouqi, D., Vinogradov, J., and Jackson, M. D. (2017). Zeta potential of artificial and natural calcite in aqueous solution. *Adv. Colloid Interface Sci.* 240, 60–76. doi:10.1016/j.cis.2016.12.006

Bai, S., Kubelka, J., and Piri, M. (2020). Relationship between molecular charge distribution and wettability reversal efficiency of cationic surfactants on calcite surfaces. *J. Mol. Liq.* 318, 114009. doi:10.1016/j.molliq.2020.114009

Chai, J., Liu, S., and Yang, X. (2009). Molecular dynamics simulation of wetting on modified amorphous silica surface. *Appl. Surf. Sci.* 255, 9078–9084. doi:10.1016/j.apsusc.2009.06.109

Chen, C., Zhang, N., Li, W., and Song, Y. (2015). Water contact angle dependence with hydroxyl functional groups on silica surfaces under CO_2 sequestration conditions. *Environ. Sci. Technol.* 49, 14680–14687. doi:10.1021/acs.est.5b03646

Chen, Y.-J., Xu, G.-Y., Yuan, S.-L., and Sun, H.-Y. (2006). Molecular dynamics simulations of AOT at isooctane/water interface. *Colloid Surf. A* 273, 174–178. doi:10.1016/j.colsurfa.2005.08.031

Chen, Z., Sun, J., Wu, P., Liu, W., Chen, C., Lang, C., et al. (2023). Cyclodextrin as a green anti-agglomerant agent in oil–water emulsion containing asphalt. *Fuel* 335, 127041. doi:10.1016/j.fuel.2022.127041

Cui, F., Jin, X., Liu, H., Wu, H., and Wang, F. (2022). Molecular modeling on Gulong shale oil and wettability of reservoir matrix. *Capillarity* 5 (4), 65–74. doi:10.46690/capi.2022.04.01

Dang, W., Nie, H., Zhang, J., Tang, X., Jiang, S., Wei, X., et al. (2022). Pore-scale mechanisms and characterization of light oil storage in shale nanopores: new method and insights. *Geosci. Front.* 13, 101424. doi:10.1016/j.gsf.2022.101424

Deng, X., Kamal, M. S., Patil, S., Hussain, S. M. S., and Zhou, X. (2020). A review on wettability alteration in carbonate rocks: wettability modifiers. *Energy fuels.* 34, 31–54. doi:10.1021/acs.energyfuels.9b03409

Guo, H., He, M., Sun, C., Li, B., and Zhang, F. (2012). Hydrophilic and strength-softening characteristics of calcareous shale in deep mines. *J. Rock Mech. Geotech. Eng.* 4, 344–351. doi:10.3724/sp.j.1235.2012.00344

Guo, Q., Yao, Y., Hou, L., Tang, S., Pan, S., and Yang, F. (2022). Oil migration, retention, and differential accumulation in "sandwiched" lacustrine shale oil systems from the Chang 7 member of the Upper Triassic Yanchang Formation, Ordos Basin, China. *Int. J. Coal Geol.* 261, 104077. doi:10.1016/j.coal.2022.104077

Jagadisan, A., and Heidari, Z. (2022). Molecular dynamic simulation of the impact of thermal maturity and reservoir temperature on the contact angle and wettability of kerogen. *Fuel* 309, 122039. doi:10.1016/j.fuel.2021.122039

Kubelka, J., Bai, S., and Piri, M. (2021). Effects of surfactant charge and molecular structure on wettability alteration of calcite: insights from molecular dynamics simulations. *J. Phys. Chem. B* 125, 1293–1305. doi:10.1021/acs.jpcb.0c10361

Larestani, A., Mousavi, S. P., Hadavimoghaddam, F., Ostadhassan, M., and Hemmati-Sarapardeh, A. (2022). Predicting the surfactant-polymer flooding performance in chemical enhanced oil recovery: cascade neural network and gradient boosting decision tree. *Alexandria Eng. J.* 61, 7715–7731. doi:10.1016/j.aej.2022.01.023

Liu, J., Sheng, J. J., and Huang, W. (2019b). Experimental investigation of microscopic mechanisms of surfactant-enhanced spontaneous imbibition in shale cores. *Energy fuels.* 33, 7188–7199. doi:10.1021/acs.energyfuels.9b01324

Liu, J., Sheng, J. J., Wang, X., Ge, H., and Yao, E. (2019a). Experimental study of wettability alteration and spontaneous imbibition in Chinese shale oil reservoirs using anionic and nonionic surfactants. *J. Petrol. Sci. Eng.* 175, 624–633. doi:10.1016/j.petrol.2019.01.003

Liu, X., Kang, Y., Yan, L., Tian, J., Li, J., and You, L. (2022). Implication of interfacial tension reduction and wettability alteration by surfactant on enhanced oil recovery in tight oil reservoirs. *Energy Rep.* 8, 13672–13681. doi:10.1016/j.egyr.2022.10.052

Michalec, L., and Lísal, M. (2017). Molecular simulation of shale gas adsorption onto overmature type II model kerogen with control microporosity. *Mol. Phys.* 115, 1086–1103. doi:10.1080/00268976.2016.1243739

Mirchi, V., Saraji, S., Goual, L., and Piri, M. (2015). Dynamic interfacial tension and wettability of shale in the presence of surfactants at reservoir conditions. *Fuel* 148, 127–138. doi:10.1016/j.fuel.2015.01.077

Okunade, O. A., Yekeen, N., Padmanabhan, E., Al-Yaseri, A., Idris, A. K., and Khan, J. A. (2021). Shale core wettability alteration, foam and emulsion stabilization by surfactant: impact of surfactant concentration, rock surface roughness and nanoparticles. *J. Petrol. Sci. Eng.* 207, 109139. doi:10.1016/j.petrol.2021.109139

Pei, H., Zhang, G., Ge, J., Tang, M., and Zheng, Y. (2012). Comparative effectiveness of alkaline flooding and alkaline–surfactant flooding for improved heavy-oil recovery. *Energy fuels.* 26, 2911–2919. doi:10.1021/ef300206u

Plimpton, S. (1995). Fast Parallel algorithms for short-range molecular dynamics. *J. Comput. Phys.* 117, 1–19. doi:10.1006/jcph.1995.1039

Qin, C., Jiang, Y., Zhou, J., Zuo, S., Chen, S., Liu, Z., et al. (2022). Influence of supercritical CO2 exposure on water wettability of shale: implications for co2 sequestration and shale gas recovery. *Energy* 242, 122551. doi:10.1016/j.energy.2021.122551

Rezaei, N., Zendehboudi, S., Chatzis, I., and Lohi, A. (2018). Combined benefits of capillary barrier and injection pressure control to improve fluid recovery at breakthrough upon gas injection: an experimental study. *Fuel* 211, 638–648. doi:10.1016/j.fuel.2017.09.048

Roshan, H., Al-Yaseri, A. Z., Sarmadivaleh, M., and Iglauer, S. (2016). On wettability of shale rocks. *J. Colloid Interface Sci.* 475, 104–111. doi:10.1016/j.jcis.2016.04.041

SalahEldin Hussien, O., Elraies, K. A., Almansour, A., Husin, H., Belhaj, A., and Ern, L. (2019). Experimental study on the use of surfactant as a fracking fluid additive for improving shale gas productivity. *J. Petrol. Sci. Eng.* 183, 106426. doi:10.1016/j.petrol.2019.106426

Shi, K., Chen, J., Pang, X., Jiang, F., Hui, S., Pang, H., et al. (2022). Effect of wettability of shale on CO2 sequestration with enhanced gas recovery in shale reservoir: implications from molecular dynamics simulation. *J. Nat. Gas. Sci. Eng.* 107, 104798. doi:10.1016/j.jngse.2022.104798

Šolc, R., Gerzabek, M. H., Lischka, H., and Tunega, D. (2011). Wettability of kaolinite (001) surfaces — molecular dynamic study. *Geoderma* 169, 47–54. doi:10.1016/j.geoderma.2011.02.004

Stankiewicz, A., Bennett, B., Wint, O., Ionkina, N., Motherwell, B., and Mastalerz, M. (2015). "Kerogen density revisited – lessons from the duvernay shale," in Unconventional Resources Technology Conference, San Antonio, Texas, 20-22 July 2015, 864–874. doi:10.15530/urtec-2015-2157904

Su, S., Jiang, Z., Shan, X., Zhu, Y., Wang, P., Luo, X., et al. (2018). The wettability of shale by NMR measurements and its controlling factors. *J. Petrol. Sci. Eng.* 169, 309–316. doi:10.1016/j.petrol.2018.05.067

Sun, C., Nie, H., Dang, W., Chen, Q., Zhang, G., Li, W., et al. (2021a). Shale gas exploration and development in China: current status, geological challenges, and future directions. *Energy fuels.* 35, 6359–6379. doi:10.1021/acs.energyfuels.0c04131

Sun, H.-m., Yang, W., Chen, R.-p., and Kang, X. (2021c). Microfabric characteristics of kaolinite flocculates and aggregates — insights from large-scale molecular dynamics simulations. *Appl. Clay Sci.* 206, 106073. doi:10.1016/j.clay.2021.106073

Sun, H., Mumby, S. J., Maple, J. R., and Hagler, A. T. (1994). An *ab initio* CFF93 all-atom force field for polycarbonates. *J. Am. Chem. Soc.* 116, 2978–2987. doi:10.1021/ja00086a030

Sun, J., Chen, Z., Wang, X., Zhang, Y., Qin, Y., Chen, C., et al. (2023). Displacement characteristics of CO_2 to CH_4 in heterogeneous surface slit pores. *Energy fuels.* 37, 2926–2944. doi:10.1021/acs.energyfuels.2c03610

Sun, Y.-P., Xin, Y., Lyu, F.-T., and Dai, C.-L. (2021b). Experimental study on the mechanism of adsorption-improved imbibition in oil-wet tight sandstone by a nonionic surfactant for enhanced oil recovery. *Pet. Sci.* 18, 1115–1126. doi:10.1016/j.petsci.2021.07.005

Tang, L., Song, Y., Jiang, S., Li, L., Li, Z., Li, Q., et al. (2020). Sealing mechanism of the roof and floor for the wufeng-longmaxi shale gas in the southern sichuan basin. *Energy fuels.* 34, 6999–7018. doi:10.1021/acs.energyfuels.0c00983

Tang, X., Xiao, S., Lei, Q., Yuan, L., Peng, B., He, L., et al. (2019). Molecular dynamics simulation of surfactant flooding driven oil-detachment in nano-silica channels. *J. Phys. Chem. B* 123, 277–288. doi:10.1021/acs.jpcb.8b09777

Taylor, R. S., Dang, L. X., and Garrett, B. C. (1996). Molecular dynamics simulations of the liquid/vapor interface of SPC/E water. *J. Phys. Chem.* 100, 11720–11725. doi:10.1021/jp960615b

Tenney, C. M., and Cygan, R. T. (2014). Molecular simulation of carbon dioxide, brine, and clay mineral interactions and determination of contact angles. *Environ. Sci. Technol.* 48, 2035–2042. doi:10.1021/es404075k

Xiong, J., Tang, J., Zhou, X., Liu, X., Liang, L., and Hou, L. (2022). Molecular dynamics simulation and experimental studies of the wettability behaviors of shales. *Energy fuels.* 36, 3526–3538. doi:10.1021/acs.energyfuels.1c04346

Yang, N., Yuan, R., Li, W., Tan, X., Liu, Z., Zhang, Q., et al. (2023). Magnetic-driving giant multilayer polyelectrolyte microcapsules for intelligent enhanced oil recovery. *Colloid Surf. A* 664, 131107. doi:10.1016/j.colsurfa.2023.131107

Yao, Y., Wei, M., and Kang, W. (2021). A review of wettability alteration using surfactants in carbonate reservoirs. *Adv. Colloid Interface Sci.* 294, 102477. doi:10.1016/j.cis.2021.102477

Yu, K. B., Bowers, G. M., Loganathan, N., Kalinichev, A. G., and Yazaydin, A. O. (2021). Diffusion behavior of methane in 3D kerogen models. *Energy fuels.* 35, 16515–16526. doi:10.1021/acs.energyfuels.1c02167

Zhang, H., Dong, M., and Zhao, S. (2010). *Energy fuels.* 24, 1829–1836. doi:10.1021/ef901310v

Zhang, L., Liao, H., and Cui, M. (2022). Effect of CO2 flooding in an oil reservoir with strong bottom-water drive in the Tahe Oilfield, Tarim Basin, Northwest China. *Energy Geosci.*, 100127. doi:10.1016/j.engeos.2022.08.004

Zhang, W., Huang, Z., Li, X., Chen, J., Guo, X., Pan, Y., et al. (2020). Estimation of organic and inorganic porosity in shale by NMR method, insights from marine shales with different maturities. *J. Nat. Gas. Sci. Eng.* 78, 103290. doi:10.1016/j.jngse.2020.103290

Zhao, M., Guo, X., Wu, Y., Dai, C., Gao, M., Yan, R., et al. (2021). Development, performance evaluation and enhanced oil recovery regulations of a zwitterionic viscoelastic surfactant fracturing-flooding system. *Colloid Surf. A* 630, 127568. doi:10.1016/j.colsurfa.2021.127568

Zhao, Y., and Jin, Z. (2021). Hydrocarbon mixture phase behavior in multi-scale systems in relation to shale oil recovery: the effect of pore size distributions. *Fuel* 291, 120141. doi:10.1016/j.fuel.2021.120141

Zheng, J., Feng, G., Ren, Z., Qi, N., Coffman, D. M., Zhou, Y., et al. (2022). China's energy consumption and economic activity at the regional level. *Energy* 259, 124948. doi:10.1016/j.energy.2022.124948

Zhou, W., Jiang, L., Liu, X., Hu, Y., and Yan, Y. (2022). Molecular insights into the effect of anionic-nonionic and cationic surfactant mixtures on interfacial properties of oil-water interface. *Colloid Surf. A* 637, 128259. doi:10.1016/j.colsurfa.2022.128259

Zhou, W., Wang, H., Yan, Y., and Liu, X. (2019a). Adsorption mechanism of CO_2/CH_4 in kaolinite clay: insight from molecular simulation. *Energy & Fuels* 33, 6542–6551. doi:10.1021/acs.energyfuels.9b00539

Zhou, W., Wang, H., Yang, X., Liu, X., and Yan, Y. (2020). Confinement effects and CO_2/CH_4 competitive adsorption in realistic shale kerogen nanopores. *Ind. Eng. Chem. Res.* 59, 6696–6706. doi:10.1021/acs.iecr.9b06549

Zhou, W., Wang, H., Zhang, Z., Chen, H., and Liu, X. (2019b). Molecular simulation of CO_2/CH_4/H_2O competitive adsorption and diffusion in brown coal. *RSC Adv.* 9, 3004–3011. doi:10.1039/c8ra10243k

Zou, C., Zhu, R., Chen, Z.-Q., Ogg, J. G., Wu, S., Dong, D., et al. (2019). Organic-matter-rich shales of China. *Earth Sci. Rev.* 189, 51–78. doi:10.1016/j.earscirev.2018.12.002

frontiers | Frontiers in Energy Research

TYPE Original Research
PUBLISHED 14 September 2023
DOI 10.3389/fenrg.2023.1277648

Check for updates

OPEN ACCESS

EDITED BY
Peng Tan,
CNPC Engineering Technology R&D Company Limited, China

REVIEWED BY
Yan Xi,
Beijing University of Technology, China
Chao Wang,
Yangtze University, China

*CORRESPONDENCE
Jiangshuai Wang,
wjs125126@163.com

RECEIVED 15 August 2023
ACCEPTED 04 September 2023
PUBLISHED 14 September 2023

CITATION
Xuan L and Wang J (2023), A new type of high hardness coating for improving drill bit stability in unconventional oil and gas development.
Front. Energy Res. 11:1277648.
doi: 10.3389/fenrg.2023.1277648

COPYRIGHT
© 2023 Xuan and Wang. This is an open-access article distributed under the terms of the Creative Commons Attribution License (CC BY). The use, distribution or reproduction in other forums is permitted, provided the original author(s) and the copyright owner(s) are credited and that the original publication in this journal is cited, in accordance with accepted academic practice. No use, distribution or reproduction is permitted which does not comply with these terms.

A new type of high hardness coating for improving drill bit stability in unconventional oil and gas development

Lingchao Xuan[1,2] and Jiangshuai Wang[1,3]*

[1]State Key Laboratory of Shale Oil and Gas Enrichment Mechanisms and Effective Development, Beijing, China, [2]Sinopec Research Institute of Petroleum Engineering Co. Ltd., Beijing, China, [3]School of Petroleum and Gas Engineering, Changzhou University, Changzhou, China

In deep unconventional oil and gas development, the problem faced is that PDC bits are eroded by solid-liquid high-speed fluids, resulting in damage. It has led to serious damage to the stability of the drill bit, a decrease in the service life of the drill bit, and an increase in the difficulty in efficient drilling. The essence is that the surface hardness and erosion resistance of the drill bit are not strong enough. Therefore, improving the stability of drill bits is a crucial and urgent problem to be solved. In this paper, Ni60A + 20% WC + 0.3% graphene composite coatings were prepared on a Q235 steel substrate, which is a new type of high hardness coating. Moreover, the effects of microstructure and microhardness of the composite coatings at different laser powers (800 W, 1200 W, 1600 W, and 2000 W) were investigated. The results show that the laser power can significantly affect the microstructure of the coating. The phase composition of the composite coatings is essentially the same at different laser powers. However, there are significant differences in the content of each phase. When the laser power is higher than 1200W, the content of $M_{23}C_6$, Cr_3C_2 and Fe_3C in the composite coating increases and the microhardness of the coating decreases. When the laser power is below 1200 W, the dilution rate of the substrate is low and a metallurgical bond cannot be formed between the composite coating and the substrate.

KEYWORDS

laser cladding, laser power, WC particles, Ni-based alloys, drill bit

1 Introduction

During the unconventional oil and gas high-speed well construction process (Tan et al., 2020; Wang et al., 2021), the stability of the drill bit is severely damaged, and the service life of the drill bit decreases (Dontsov, 2022; Wang et al., 2023a; Huang et al., 2023). Improving the stability of drill bits is a crucial and urgent issue to be addressed, especially in the development process of unconventional oil and gas resources such as deep shale oil and gas (Tan et al., 2021; Ma et al., 2022; Wang et al., 2023b). It is related to drilling speed, development efficiency, and national energy security issues. Laser cladding technology uses a high-energy laser beam to rapidly heat and cool a material surface for the preparation of protective coatings with properties such as high hardness, wear and corrosion resistance (Wang et al., 2022a; Chen et al., 2023; Wu et al., 2023). The protective coatings prepared by laser cladding technology are able to achieve metallurgical bonding with the metal substrate (Qunshuang et al., 2016). Furthermore, the coatings are characterized by a homogeneous microstructure, fine grain size and low dilution rates (Meng et al., 2022; Xu et al., 2022; Ren

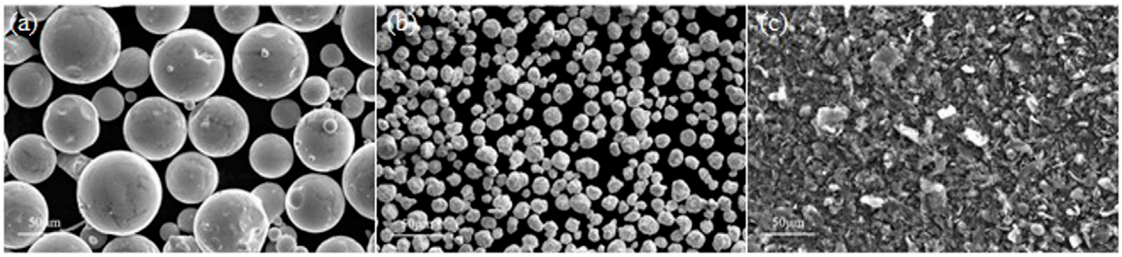


FIGURE 1
The SEM of the powder; **(A)** Ni60, **(B)** WC, **(C)** Graphene.

et al., 2023). The coatings prepared by laser cladding technology have excellent microstructural properties and mechanical properties. Moreover, these have received widespread attention in the fields of aerospace, industrial machinery, oil and gas chemicals (Jie et al., 2022; Kendall et al., 2023). Nickel-based alloy coatings are widely used for laser cladding due to their affordability and good self-lubricating properties and corrosion resistance (Zhang et al., 2023a; Li et al., 2023). Ceramic-based particles such as WC, TiC and SiC are often added to nickel-based alloy coatings as an additive phase to improve the mechanical properties of the coating (Hu et al., 2022; Chen et al., 2022; Wu et al., 2022; Zhang et al., 2023b).

Nickel-based alloy/WC coatings have been studied by a large number of academics for their excellent corrosion and wear resistance properties. Hu et al. (Hu et al., 2022b) found that grain refinement in the new WC coating increased with increasing WC content. In the process, the thermomechanical stability and hardness of the coating also increased. Li et al. (2022) found that the WC content in Ni60/WC coatings can influence the microstructure and phase components of the coatings. In detail, the WC content is positively correlated with the hardness and wear resistance of the coatings. Yao et al. (2018) found that the distribution of WC in Ni60/WC coatings can affect the mechanical properties of the coatings. And, the denser the WC is on the surface of the coating. There are the better the hardness and wear resistance of the coating. Wu et al. (2004) found that lower laser power would result in the deposition of WC towards the bottom of the coating. In addition, the interface between the Ni-based alloy and the WC particles would be the initiation point for cracks within the coating. Xu et al. (2014) found that the appearance of cracks in Ni-based alloy/WC coatings was related to the WC distribution. Chiang and Chen (2007) found that increasing the laser power facilitated WC decomposition and reduced the WC content in the coating. Wang et al. (2022b) and Wu et al. (2004) found that the preparation of gradient Ni-based alloy-WC coatings on the substrate surface was able to reduce the tendency of the coatings to crack. Due to its excellent toughness and self-lubricating properties, Xia et al. (2022) and Chang et al. (2023) found that the addition of graphene into metal matrix composite coatings, was beneficial in reducing the tendency of the coatings to crack. Therefore, appropriate melting power, WC content or the introduction of graphene are beneficial in reducing the cracking tendency of Ni-based alloy/WC coatings.

In the present work, graphene/Ni60/WC coatings were prepared on the surface of Q235 steel using pre-powdered laser melting. The effect of laser melting power on the microstructure, composition and coating hardness of the coatings was investigated.

TABLE 1 Chemical compositions of Q235 and Ni60A powder (wt.%).

	Fe	C	Si	Mn	Cr	Ni	Cu	O
Q235	Bal.	0.16	0.26	0.15	0.02	0.025	0.024	-
Ni60A	4.63	0.76	4.11	-	16.58	Bal.	-	0.03

2 Materials and experimental process

2.1 Material and sample preparation

The substrate material used for the laser cladding experiments was Q235 steel with a specimen size of 100 mm × 100 mm × 5 mm. The powder material used for laser cladding is a mixture of Ni60A + 20% WC + 0.3% graphene. The particle size range of Ni60A powder is 50 μm–150 μm and its microscopic morphology is shown in Figure 1A. The composition of Q235 steel and Ni60A powder are shown in Table 1. The WC powder particle size ranges from 15 μm to 45 μm and its microscopic morphology is shown in Figure 1B. The graphene is multilayer graphene and its microscopic morphology is shown in Figure 1C.

Sodium dodecylbenzene sulfonate was mixed with graphene in a ratio of 1:10. After adding an appropriate amount of alcohol, the dispersion of graphene was carried out using an ultrasonic shaker, followed by drying using a vacuum drying oven. The treated graphene, WC powder and Ni60A powder were proportionally configured to produce a Ni60A + 20% WC+0.3% graphene blend. The powder is dried for 2 h and then blended for 8 h using a planetary ball mill (DECO, type PBM-AD-4L) set at 300 r/min autogenous and 4 r/min metric.

The Q235 steel substrate is sanded with 60 grit sandpaper before the start of the pre-powdering process. Polyvinyl cellulose was used to prepare a polyvinyl alcohol solution (ratio 8:1000), which was mixed with Ni60A + 20% WC + 0.3% graphene mixed powder. The mixed powder is spread on the surface of the specimen to a thickness of 1.5 mm and the work is carried out using a laser cladding processing system. The laser cladding power was selected as 800 W, 1,200 W, 1,600 W, and 2,000 W respectively, with the remaining parameters shown in Table 2.

TABLE 2 Ni60A + 20% WC + 0.3% graphene mixed powder laser cladding process parameters.

Coatings	DepositedSpeed (m/min)	Overlapping ratio (%)	Spot diameter (g/min)	Shielding gas flow (L/min)
	0.35	50%	14.8	15

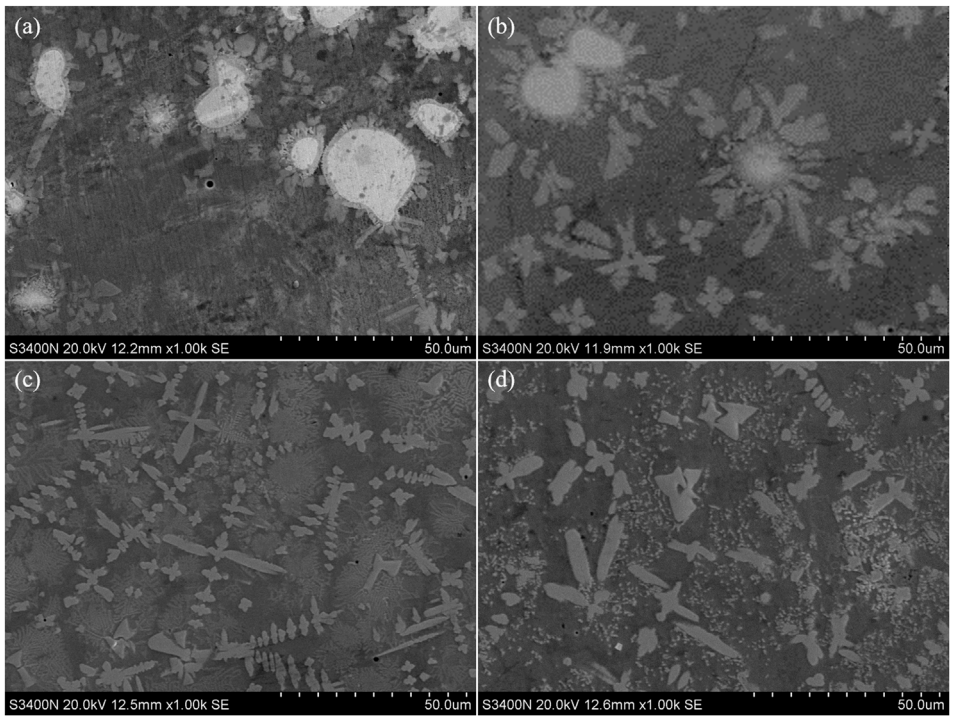


FIGURE 2
Cross-sectional morphology of the top of a Ni60A + 20% WC + 0.3% graphene composite coating by laser cladding at different laser powers: **(A)** 800 W, **(B)** 1,200 W, **(C)** 1,600 W, **(D)** 2,000 W.

2.2 Analysis methods

The morphology and elemental distribution of the cross-sections were analyzed at different locations using a Hitachi S-3400 N scanning electron microscope (SEM) and an energy spectrometer (EDS). X-ray diffraction (XRD) using a Bruker D8 X-ray diffractometer goniometer, Cu target K_α rays, voltage 40 kV, current 30 mA, diffraction angle 10°–90° scan speed 6°/min. The microhardness of the clad surface was tested using a micro-vickers hardness tester (HVS-1000A) with an applied load of 0.2 kg and a holding time of 15 s. The hardness was measured using a four-point measurement method.

3 Results and discussion

3.1 Cross-sectional morphological analysis

Figure 2 shows the cross-sectional morphology of the top of a Ni60A + 20% WC + 0.3% graphene composite coating by laser cladding at different laser powers. There are significant differences in the microstructure of the top part of the coating at different laser powers. At a laser power of 800 W, a large number of WC particles were present in the top part of the coating and decarburized at high temperatures to form W_2C, W atoms and C atoms (Liao et al., 2023). The W and C atoms expanded into the Ni-based alloy and reacted with it. New phases in the form of blocks and rods are formed around the WC particles. At 1,200 W, the decomposition of the WC particles is promoted by the increased heat input. The size of the WC particles in the top part of the coating decreases significantly and the precipitated phase is predominantly rod and snowflake shaped. When the laser power was 1,600 W, no WC particles were observed in the top part of the coating. It indicates that the WC particles had completely decomposed and that the precipitated phase in the top part of the coating was mainly in the form of flocculent and fishbone structures. This is due to the further elevation of the heat input promoting the dissolution of W and C atoms into the Ni-based alloy. In addition, small porous defects appear in the top part of the coating.

To further characterize the distribution of elements in the characteristic areas of the coating, a surface scan analysis was carried out on the top area of the coating with a laser power of 1,200 W. As shown in Figure 3, W and Si elements are enriched in WC particles and in the precipitation phase of rod and snowflake structures. There is a significant enrichment of Cr elements around the WC particles, and it can be assumed that the C atoms from the WC decomposition reacted with the Cr in the Ni-based alloy. The

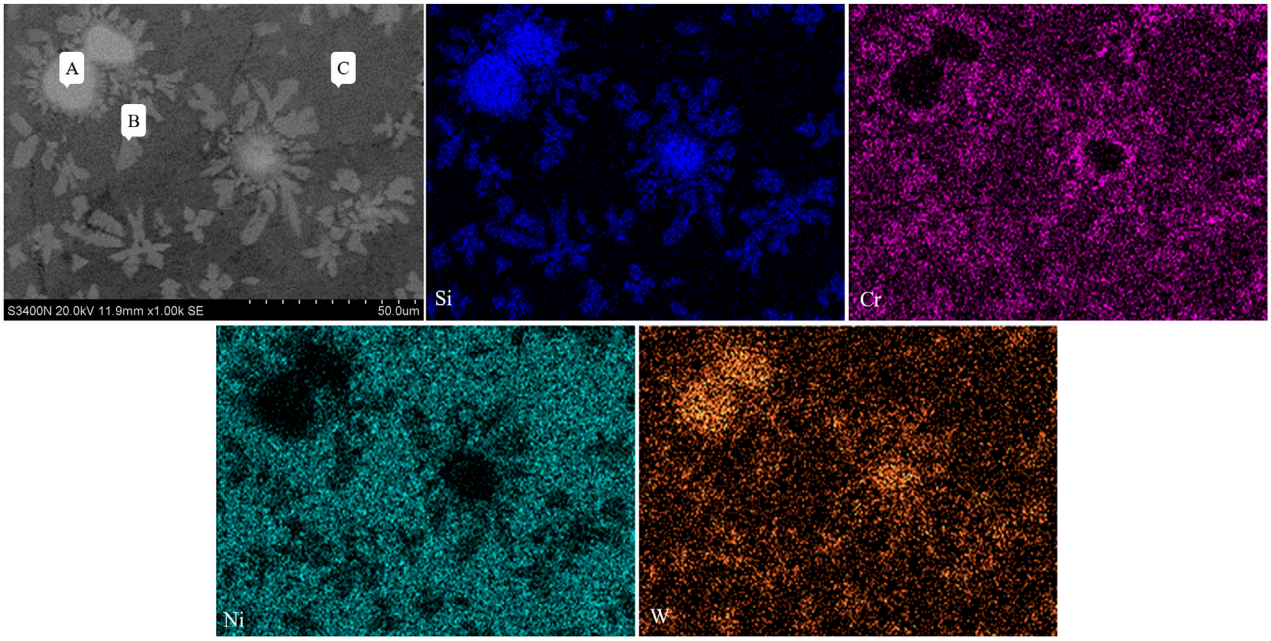


FIGURE 3
EDS map scanning results of the coating at a laser power of 1,200 W.

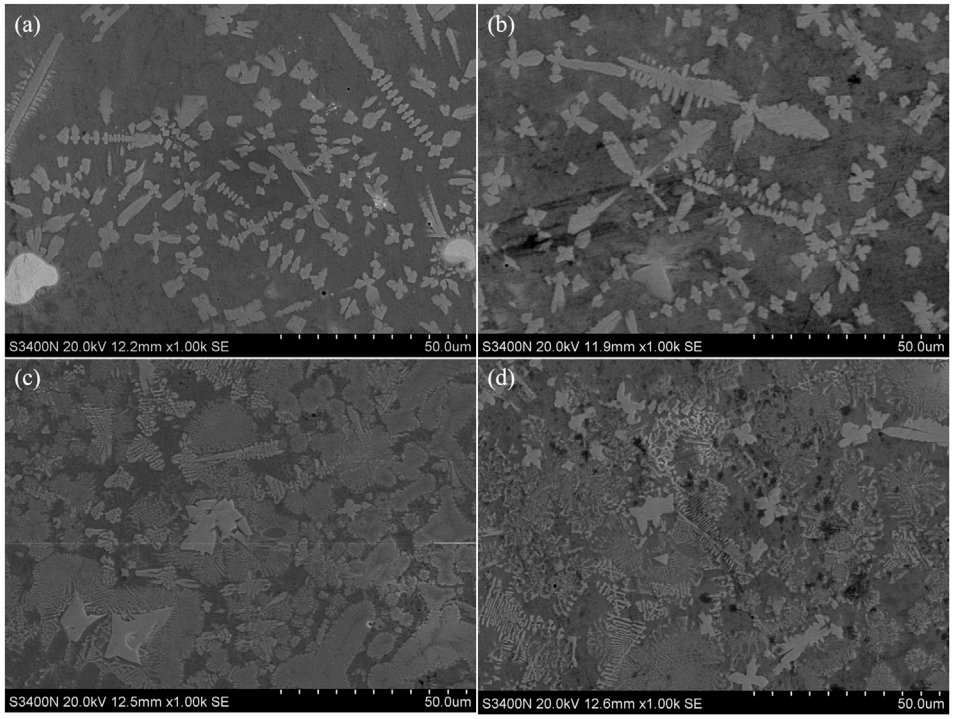


FIGURE 4
Cross-sectional morphology of the middle of a Ni60A + 20% WC + 0.3% graphene composite coating by laser cladding at different laser powers: **(A)** 800 W, **(B)** 1,200 W, **(C)** 1,600 W, **(D)** 2,000 W.

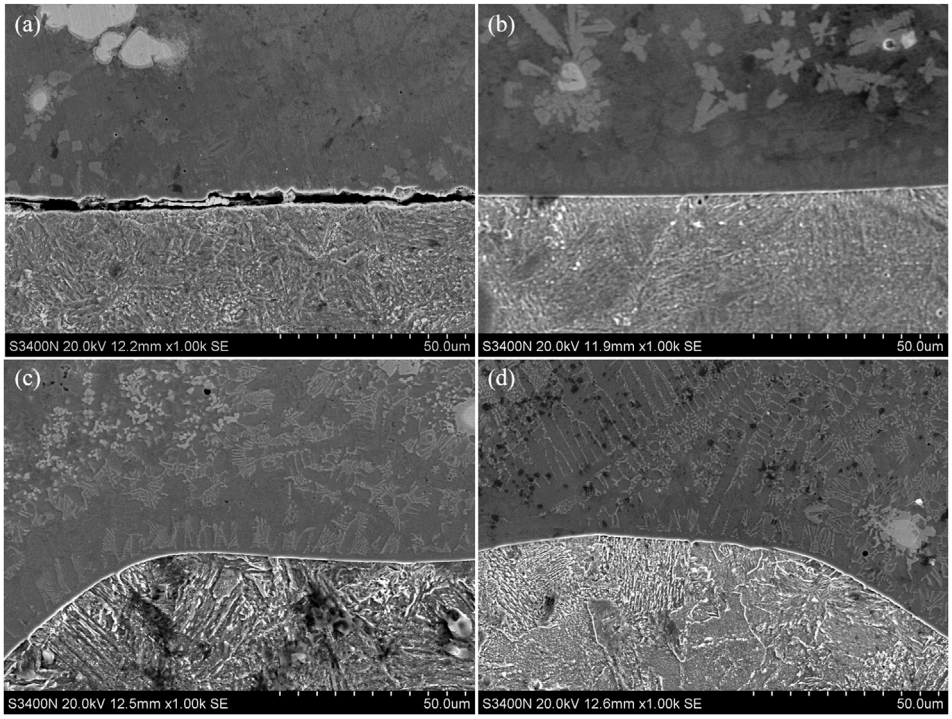


FIGURE 5
Cross-sectional morphology of the bottom of a Ni60A + 20% WC + 0.3% graphene composite coating by laser cladding at different laser powers: **(A)** 800 W, **(B)** 1,200 W, **(C)** 1,600 W, **(D)** 2,000 W.

element Ni is also present around the WC particles and in the precipitated phase positions of the rod and block structures. However, the Ni content is lower than in the Ni-based alloy region.

Figure 4 shows the cross-sectional morphology of the middle of a Ni60A + 20% WC + 0.3% graphene composite coating by laser cladding at different laser powers. At a laser power of 800 W, there are fewer WC particles in the middle of the coating and the precipitated phase is dominated by rod and fishbone structures. At a laser power of 1,200 W, the morphology of the middle part of the coating is similar to that at 800 W. At a laser power of 1,600 W, the predominantly flocculent and massive structure of the precipitated phase in the middle of the coating. In detail, there is difference between the top and the middle of the coating at 1,600 W. It is mainly due to the fact that the top part of the coating is in contact with air and dissipates heat at a faster rate. This fact favours nucleation so that the top precipitated phase of the coating appears as a fishbone structure (Ge et al., 2022). When the laser power is 2,000 W, the structure of the precipitated phase in the middle of the coating is similar to that of the 1,600 W condition.

Figure 5 shows the cross-sectional morphology of the bottom of a Ni60A + 20% WC + 0.3% graphene composite coating by laser cladding at different laser powers. When the laser power is 800 W, there is delamination at the interface between the coating and the substrate. This is due to the lower laser power, most of the input energy is absorbed by the coating powder above the substrate. It results in a very small dilution of the cladding layer, resulting in insufficient metallurgical bonding between the cladding layer and the substrate. The phenomenon is very easy to occur when the cladding layer is detached, manifesting itself as the separation of the substrate and the coating. At a laser power of 1,200 W, the metallurgical bonding between the substrate and the coating is metallurgical and the fusion line is relatively flat. At laser power levels of 1,600 W and 2,000 W, the heat input increases further resulting in a deeper melt pool and increased curvature of the fusion line. Large number of columnar crystal structures appear at the bottom of the coating due to slow heat dissipation at the bottom of the coating, a large temperature gradient and grain growth.

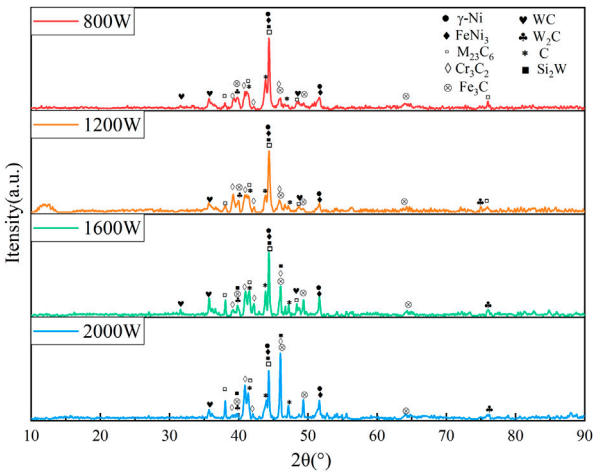


FIGURE 6
XRD results of a composite coating of Ni60A + 20% WC + 0.3% graphene by laser cladding at different laser powers.

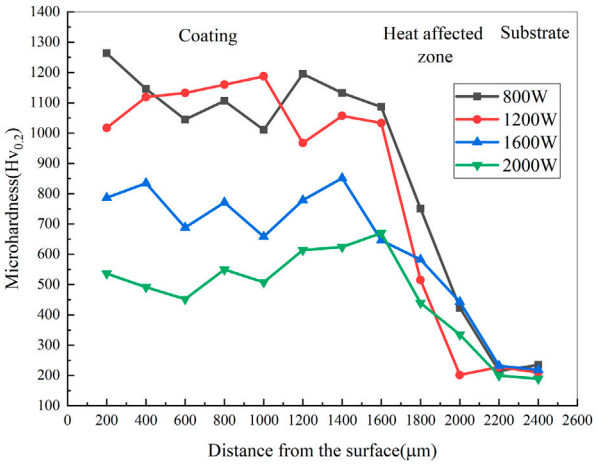


FIGURE 7
Microhardness distribution results of the composite coating of Ni60A + 20% WC + 0.3% graphene by laser cladding at different laser powers.

3.2 XRD analysis

Figure 6 shows the XRD results of the composite coating of Ni60A + 20% WC + 0.3% graphene by laser cladding at different laser powers. The composition of the coating phases at different powers does not differ significantly and consists mainly of γ-Ni, $FeNi_3$, $M_{23}C_6$ (M = Fe, Cr), Cr_3C2, Fe_3C, WC, W_2C, Si_2W and C. However, the intensity of the peaks corresponding to the different species can be judged to be significantly different. When the laser power is 1,600 W, a significant increase in the intensity of the corresponding peaks for $M_{23}C_6$, Cr_3C_2, and Fe_3C can be observed. When the laser power is further increased to 2,000 W, further enhancement of the corresponding peaks of $M_{23}C_6$, Cr_3C_2, and Fe_3C can be observed, and their intensity has surpassed the main peak of the pure Ni60A cladding at 1,200 W power.

3.3 Microhardness analysis

Figure 7 shows the Microhardness distribution results of the composite coating of Ni60A + 20% WC + 0.3% graphene by laser cladding at different laser powers. In Figure 7, the hardness distribution area can be divided into the cladding layer zone, fusion zone, and heat affected zone. The cladding layer zone has the highest hardness, while the fusion zone belongs to the transition zone, and the hardness begins to decrease. It can be seen that the hardness value of the cladding layer zone does not change much, while the hardness of the fusion zone rapidly decreases, indicating that the fusion zone is relatively narrow.

In addition, the average microhardness of the composite coatings at laser powers of 800 W–2,000 W were 1,046 HV, 1031.8 HV, 769.4 HV, and 559 HV respectively. The average hardness of the coating does not change significantly at laser powers of 800 W and 1,200 W. When the laser power exceeds 1,200 W, the hardness of the coating decreases as the laser power increases. When the laser power is 800 W and 1,200 W, there is still a distribution of WC particles on the upper surface of the coating. Although the size of WC particles decreases under 1,200 W conditions, the C and W formed by the decarburization reaction of WC promotes the formation of carbides and W-rich phases in the coating. It plays a role in solid solution strengthening (Chen et al., 2023). When the laser power is further increased, the WC particles on the substrate surface have been completely dissolved. The increased power of the laser causes more energy to enter the substrate resulting in the remelting of the Fe in the substrate and the formation of the Fe_3C phase with the C in the powder. Figure 6 XRD results can be observed that the intensity of the corresponding peaks of the phases of $M_{23}C_6$, Cr_3C_2, and Fe_3C are significantly increased at 1,600 W and 2,000 W. However, the hardness of the above phases is lower than that of WC, so the increase in their content will instead reduce the hardness of the cladding.

4 Conclusion

In this paper, a new type of high hardness coating for improving drill bit stability in unconventional oil and gas development was developed. The present work investigates the microstructure and microhardness of Ni60A + 20% WC + 0.3% graphene composite coatings by laser cladding at different powers, and the following conclusions were obtained:

(1) When the laser power is low, the WC particles do not dissolve sufficiently, the dilution rate of the substrate is low and the metallurgical bond between the coating and the substrate cannot be formed.
(2) Too high laser power leads to a decrease in the microhardness of the coating. When the laser power is 1,200 W, the overall performance is the best.
(3) There is no significant difference in the composition of the coating phases at different power levels, consisting mainly of γ-Ni, $FeNi_3$, $M_{23}C_6$, Cr_3C_2, Fe_3C, WC, W_2C, Si_2W, and C. The percentage of $M_{23}C_6$, Cr_3C_2, and Fe_3C in the coating increased with increasing laser power.

Data availability statement

The original contributions presented in the study are included in the article/Supplementary Material, further inquiries can be directed to the corresponding author.

Author contributions

LX: Conceptualization, Funding acquisition, Investigation, Methodology, Validation, Writing–review and editing. JW: Data curation, Formal Analysis, Writing–original draft.

Funding

The authors declare financial support was received for the research, authorship, and/or publication of this article. This work

was supported by the Open Fund of State Key Laboratory of Shale Oil and Gas Enrichment Mechanisms and Effective Development, and the General Project of Jiangsu Province University Basic Science (NATURAL SCIENCE) Research (grant no. 22KJD430001).

Conflict of interest

Author LX was employed by Sinopec Research Institute of Petroleum Engineering Co. Ltd.

The remaining author declares that the research was conducted in the absence of any commercial or financial relationships that could be construed as a potential conflict of interest.

Publisher's note

All claims expressed in this article are solely those of the authors and do not necessarily represent those of their affiliated organizations, or those of the publisher, the editors and the reviewers. Any product that may be evaluated in this article, or claim that may be made by its manufacturer, is not guaranteed or endorsed by the publisher.

References

Chang, W., Xiao, G., Zhang, H., Chen, H., Yi, M., Zhang, J., et al. (2023). Microstructure and properties of graphene reinforced co-based composite coating by laser cladding. *Surf. Coatings Technol.* 453, 129139. doi:10.1016/j.surfcoat.2022.129139

Chen, C., Feng, A., Wei, Y., Wang, Y., Pan, X., and Song, X. (2023). Effects of WC particles on microstructure and wear behavior of laser cladding Ni60 composite coatings. *Opt. Laser Technol.* 163, 109425. doi:10.1016/j.optlastec.2023.109425

Chen, L., Yu, T., Chen, X., Zhao, Y., and Guan, C. (2022). Process optimization, microstructure and microhardness of coaxial laser cladding TiC reinforced Ni-based composite coatings. *Opt. Laser Technol.* 152, 108129. doi:10.1016/j.optlastec.2022.108129

Chiang, K. A., and Chen, Y. (2007). Microstructural characterization and microscopy analysis of laser cladding Stellite12 and tungsten carbide. *J. Mater Process Technol.* 182, 297–302. doi:10.1016/j.jmatprotec.2006.08.007

Dontsov, E. V. (2022). Analysis of a constant height hydraulic fracture driven by a power-law fluid. *Rock Mech. Bull.* 1 (1), 100003. doi:10.1016/j.rockmb.2022.100003

Ge, T., Chen, L., Gu, P., Ren, X., and Chen, X. (2022). Microstructure and corrosion resistance of TiC/Inconel 625 composite coatings by extreme high speed laser cladding. *Opt. Laser Technol.* 150, 107919. doi:10.1016/j.optlastec.2022.107919

Hu, Y., Wang, Z., and Pang, M. (2022b). Effect of WC content on laser cladding Ni-based coating on the surface of stainless steel. *Mater. Today Commun.* 31, 103357. doi:10.1016/j.mtcomm.2022.103357

Hu, Z., Li, Y., Lu, B., Tan, N., Cai, L., and Yong, Q. (2022a). Effect of WC content on microstructure and properties of high-speed laser cladding Ni-based coating. *Opt. Laser Technol.* 155, 108449. doi:10.1016/j.optlastec.2022.108449

Huang, L. K., He, R., Yang, Z. Z., Tan, P., Chen, Z. W., Li, X. G., et al. (2023). Exploring hydraulic fracture behavior in glutenite formation with strong heterogeneity and variable lithology based on DEM simulation. *Eng. Fract. Mech.* 278, 109020. doi:10.1016/j.engfracmech.2022.109020

Jie, G., Yan, S., Kangning, W., Qiang, S., and Canming, W. (2022). Effect of Fe content on microstructure and corrosion resistance of Ni-based alloy formed by laser cladding. *Surf. Coatings Technol.* 446, 128761. doi:10.1016/j.surfcoat.2022.128761

Kendall, O., Abrahams, R., Paradowska, A., Reid, M., Qiu, C., Mutton, P., et al. (2023). Influence of multi-layer laser cladding depositions and rail curvature on residual stress in light rail components. *Eng. Fail. Anal.* 150, 107330. doi:10.1016/j.engfailanal.2023.107330

Li, S., Huang, K., Zhang, Z., Zheng, C., Li, M., Wang, L., et al. (2023). Wear mechanisms and micro-evaluation of WC + TiC particle-reinforced Ni-based composite coatings fabricated by laser cladding. *Mater. Charact.* 197, 112699. doi:10.1016/j.matchar.2023.112699

Li, W., Yang, X., Wang, S., Duan, D., Li, F., Qiao, Y., et al. (2022). The effect of WC content on the bonding strength and mechanical properties of WC/Ni60 coatings of brake disc. *Opt. Laser Technol.* 149, 107822. doi:10.1016/j.optlastec.2021.107822

Liao, Z., Huang, X., Zhang, F., Li, Z., Chen, S., and Shan, Q. (2023). Effect of WC mass fraction on the microstructure and frictional wear properties of WC/Fe matrix composites. *Int. J. Refract. Metals Hard Mater.* 114, 106265. doi:10.1016/j.ijrmhm.2023.106265

Ma, X., Zhang, S., Zhang, X., Liu, J., Jin, J., Cheng, W., et al. (2022). Lithology-controlled stress variations of Longmaxi shale–Example of an appraisal wellbore in the Changning area. *Rock Mech. Bull.* 1 (1), 100002. doi:10.1016/j.rockmb.2022.100002

Meng, L., Sheng, P., and Zeng, X. (2022). Comparative studies on the Ni60 coatings deposited by conventional and induction heating assisted extreme-high-speed laser cladding technology: formability, microstructure and hardness. *J. Mater. Res. Technol.* 16, 1732–1746. doi:10.1016/j.jmrt.2021.12.110

Qunshuang, M., Yajiang, L., Juan, W., and Kun, L. (2016). Microstructure evolution and growth control of ceramic particles in wide-band laser clad Ni60/WC composite coatings. *Mater. Des.* 92, 897–905. doi:10.1016/j.matdes.2015.12.121

Ren, M., Li, R., Zhang, X., Gu, J., and Jiao, C. (2023). Effect of WC particles preparation method on microstructure and properties of laser cladded Ni60-WC coatings. *J. Mater. Res. Technol.* 22, 605–616. doi:10.1016/j.jmrt.2022.11.120

Tan, P., Jin, Y., and Pang, H. W. (2021). Hydraulic fracture vertical propagation behavior in transversely isotropic layered shale formation with transition zone using XFEM-based CZM method. *Eng. Fract. Mech.* 248, 107707. doi:10.1016/j.engfracmech.2021.107707

Tan, P., Pang, H. W., Zhang, R. X., Jin, Y., Zhou, Y. C., Kao, J. W., et al. (2020). Experimental investigation into hydraulic fracture geometry and proppant migration characteristics for southeastern Sichuan deep shale reservoirs. *J. Petroleum Sci. Eng.* 184, 106517. doi:10.1016/j.petrol.2019.106517

Wang, J., Cai, C., Fu, P., Deng, S., and Tang, Z. (2023a). Study on simulation of cement plug-formation interface stripping failure and main influencing factors. *Front. Earth Sci.* 11, 1123620. doi:10.3389/feart.2023.1123620

Wang, J., and Cai, C. (2023b). The failure law of the cement plug-casing interface for direct plugging in the casing of old wells for salt cavern gas storage. *J. Adhesion Sci. Technol.*, 1–18. doi:10.1080/01694243.2023.2240594

Wang, J., Li, J., Liu, G., Liu, S., Ren, M., Luo, K., et al. (2021). Development and application of wellbore heat transfer model considering variable mass flow. *Undergr. Space* 6 (3), 316–328. doi:10.1016/j.undsp.2020.04.001

Wang, Q., Chen, F. Q., Li, Q., Zhang, L., Jin, H., and Zhang, J. W. (2022a). Microstructure and properties of Ni60 alloy coating prepared by electromagnetic compound field assisted laser cladding. *Mater. Chem. Phys.* 291, 126678. doi:10.1016/j.matchemphys.2022.126678

Wang, Q., Li, Q., Zhang, L., Chen, D. X., Jin, H., Li, J. D., et al. (2022b). Microstructure and properties of Ni-WC gradient composite coating prepared by laser cladding. *Ceram. Int.* 48, 7905–7917. doi:10.1016/j.ceramint.2021.11.338

Wu, P., Du, H. M., Chen, X. L., Li, Z. Q., Bai, H. L., and Jiang, E. Y. (2004). Influence of WC particle behavior on the wear resistance properties of Ni–WC composite coatings. *Wear* 257, 142–147. doi:10.1016/j.wear.2003.10.019

Wu, T., Shi, W., Xie, L., Gong, M., Huang, J., Xie, Y., et al. (2022). Effects of re-melting process parameters on the forming quality of the Stellite 6/WC laser cladding layer. *Optik* 269, 169887. doi:10.1016/j.ijleo.2022.169887

Wu, T., Shi, W., Xie, L., Gong, M., Huang, J., Xie, Y., et al. (2023). Study on the effect of Ni60 transition coating on microstructure and mechanical properties of Fe/WC composite coating by laser cladding. *Opt. Laser Technol.* 163, 109387. doi:10.1016/j.optlastec.2023.109387

Xia, J., Yu, Y., Chen, Z., Zhang, S., Guo, F., and Ma, X. (2022). Effect of graphite powder addition on the structure and properties of WC-reinforced Ni-based composite coatings. *Surf. Technol.*, 1–11.

Xu, J.-S., Zhang, X.-C., Xuan, F.-Z., Wang, Z.-D., and Tu, S.-T. (2014). Rolling contact fatigue behavior of laser cladded WC/Ni composite coating. *Surf. Coatings Technol.* 239, 7–15. doi:10.1016/j.surfcoat.2013.11.005

Xu, S., Cai, Q., Li, G., Lu, X., and Zhu, X. (2022). Effect of scanning speed on microstructure and properties of TiC/Ni60 composite coatings on Ti6Al4V alloy by laser cladding. *Opt. Laser Technol.* 154, 108309. doi:10.1016/j.optlastec.2022.108309

Yao, J., Zhang, J., Wu, G., Wang, L., Zhang, Q., and Liu, R. (2018). Microstructure and wear resistance of laser cladded composite coatings prepared from pre-alloyed WC-NiCrMo powder with different laser spots. *Opt. Laser Technol.* 101, 520–530. doi:10.1016/j.optlastec.2017.12.007

Zhang, K., Ju, H., Xing, F., Wang, W., Li, Q., Yu, X., et al. (2023b). Microstructure and properties of composite coatings by laser cladding Inconel 625 and reinforced WC particles on non-magnetic steel. *Opt. Laser Technol.* 163, 109321. doi:10.1016/j.optlastec.2023.109321

Zhang, W., Shang, X., Hu, M., He, X., Yang, B., Dai, K., et al. (2023a). Microstructure and corrosion-wear behaviors for laser cladding repaired martensitic stainless steels using Co-based and Ni-based powders. *Mater. Today Commun.* 35, 106287. doi:10.1016/j.mtcomm.2023.106287

frontiers | Frontiers in Energy Research

TYPE Original Research
PUBLISHED 14 September 2023
DOI 10.3389/fenrg.2023.1271377

Check for updates

OPEN ACCESS

EDITED BY
Peng Tan,
CNPC Engineering Technology R&D Company Limited, China

REVIEWED BY
Jingshou Liu,
China University of Geosciences Wuhan, China
Shuai Yin,
Xi'an Shiyou University, China

*CORRESPONDENCE
Wei Ju,
wju@cumt.edu.cn

RECEIVED 02 August 2023
ACCEPTED 04 September 2023
PUBLISHED 14 September 2023

CITATION
Yin G, Wu K, Ju W, Qin Y, Qian Z, Xu K, Lu Z, Wang P, Liang X and Liang Y (2023), *In-situ* stress prediction in ultra-deep carbonate reservoirs of Fuman Oilfield, Tarim Basin of China.
Front. Energy Res. 11:1271377.
doi: 10.3389/fenrg.2023.1271377

COPYRIGHT
© 2023 Yin, Wu, Ju, Qin, Qian, Xu, Lu, Wang, Liang and Liang. This is an open-access article distributed under the terms of the Creative Commons Attribution License (CC BY). The use, distribution or reproduction in other forums is permitted, provided the original author(s) and the copyright owner(s) are credited and that the original publication in this journal is cited, in accordance with accepted academic practice. No use, distribution or reproduction is permitted which does not comply with these terms.

In-situ stress prediction in ultra-deep carbonate reservoirs of Fuman Oilfield, Tarim Basin of China

Guoqing Yin[1,2], Kongyou Wu[1], Wei Ju[3]*, Yun Qin[2], Ziwei Qian[2], Ke Xu[2], Zhongyuan Lu[2], Peng Wang[2], Xiaobai Liang[3] and Yan Liang[3]

[1]School of Geosciences, China University of Petroleum, Qingdao, Shandong, China, [2]Tarim Oilfield Company, PetroChina, Korla, Xinjiang, China, [3]School of Resources and Geosciences, China University of Mining and Technology, Xuzhou, Jiangsu, China

The Fuman Oilfield in Tarim Basin has great potential for ultra-deep carbonate oil and gas resources, and is an important area for future storage and production increase. The present-day *in-situ* stress field is critical during the exploration and development. However, no systemic investigations have been carried out in this oilfield. Therefore, in this study, the present-day *in-situ* stress field in the Ordovician carbonate reservoir is predicted and analyzed based on well log calculation and geomechanical numerical modeling. The results indicate that, 1) NE-SW-trending is the dominant horizontal maximum principal stress (S_{Hmax}) orientation. The vertical principal stress is the maximum principal stress, showing the Ordovician reservoir is under a normal faulting stress regime. 2) The distribution of *in-situ* stresses in the Ordovician carbonate reservoir is heterogeneous, which is mainly controlled burial depth and fault/fracture development. High stress magnitudes in the Yingshan Formation are mainly in the southeastern part of Fudong area, Fuman Oilfield. The present-day horizontal differential stress mainly ranges from 27 MPa to 30 MPa in the Yingshan carbonate reservoir. iii) Natural fractures are generally stale under the present-day *in-situ* stress state. Fractures that parallel to the S_{Hmax} orientation with high fracture dip angle are easier to be reactivated. The results are expected to provide geomechanical references for further oil and gas development in the Fuman Oilfield of Tarim Basin.

KEYWORDS

geomechanical modeling, Fudong area, *in-situ* stress, Fuman Oilfield, mechanical earth model

1 Introduction

Carbonate formations are the most important type of hydrocarbon reservoirs (Kargarpour, 2020). Aljuboori et al. (2019) reported that 70% of conventional oil reserves in the Middle East lies in carbonate reservoirs. Commonly, in many cases, carbonate reservoirs are tight, hence, it is highly recommended to apply an efficient well stimulation, e.g., acid or hydraulic fracturing. The outcome of hydraulic fracturing largely depends on rock mechanical property, the presence of natural fractures, and most importantly, variations of present-day *in-situ* stresses. The orientation of horizontal maximum principal stress (S_{Hmax}) affects the propagation direction of hydraulic fractures, controls the aperture and permeability of natural fractures within reservoirs (Finkbeiner et al., 1997; Ju et al., 2020a). Besides, due to

the heterogeneity of stress field, wells may not be stimulated equally. As a result, many fields including unconventional oil and gas exploration and development, drilling and completion engineering, borehole stability assessment, optimal well trajectory determination, hydraulic fracturing stimulation plan, etc., benefit from a better understanding of the present-day *in-situ* stress state (Reynolds et al., 2003; Zoback, 2007; Pitcher and Davis, 2016; Rajabi et al., 2016; Ju et al., 2017; Ju et al., 2018; Ju et al., 2020b; Liu et al., 2017;

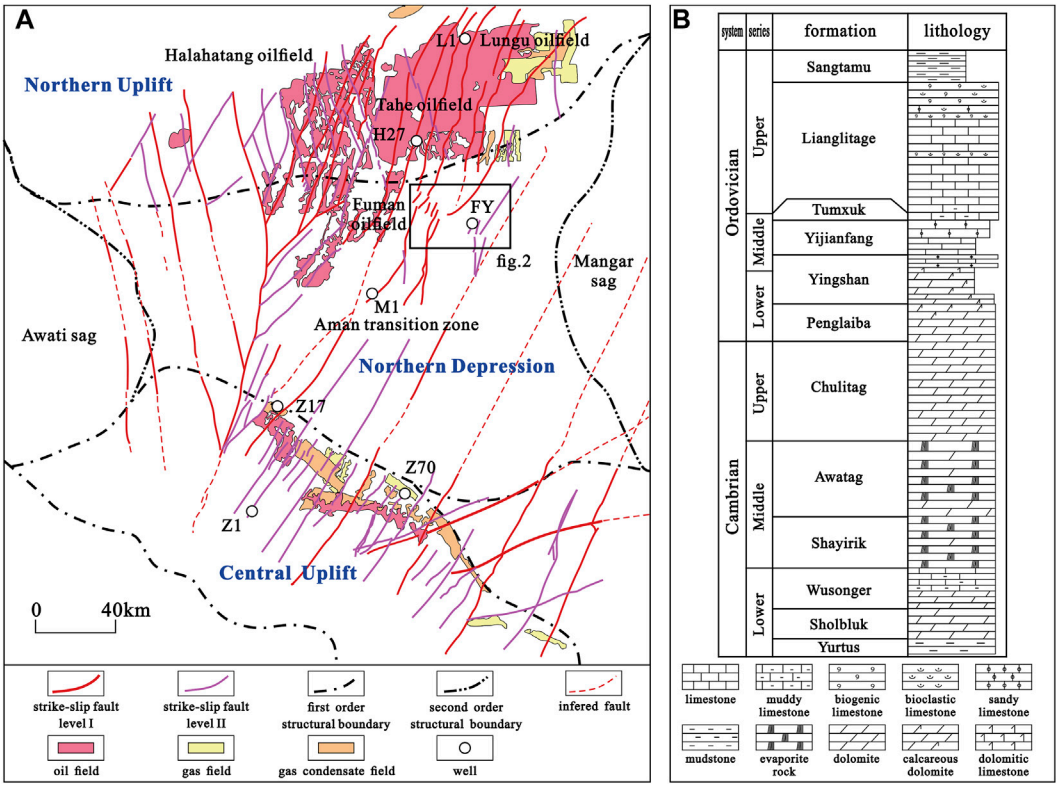


FIGURE 1
(A) The strike-slip fault system in the Ordovician carbonates of Tarim Basin; **(B)** the Cambrian-Ordovician stratigraphic column in the Tarim Basin (after Zhu et al., 2022).

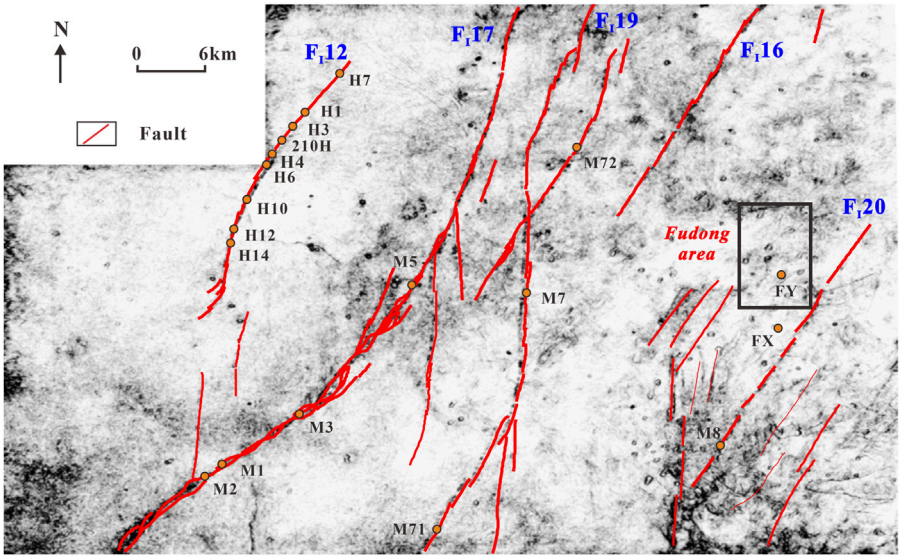


FIGURE 2
The coherent attribute and fault distribution in the Yingshan Formation third member of Fuman Oilfield.

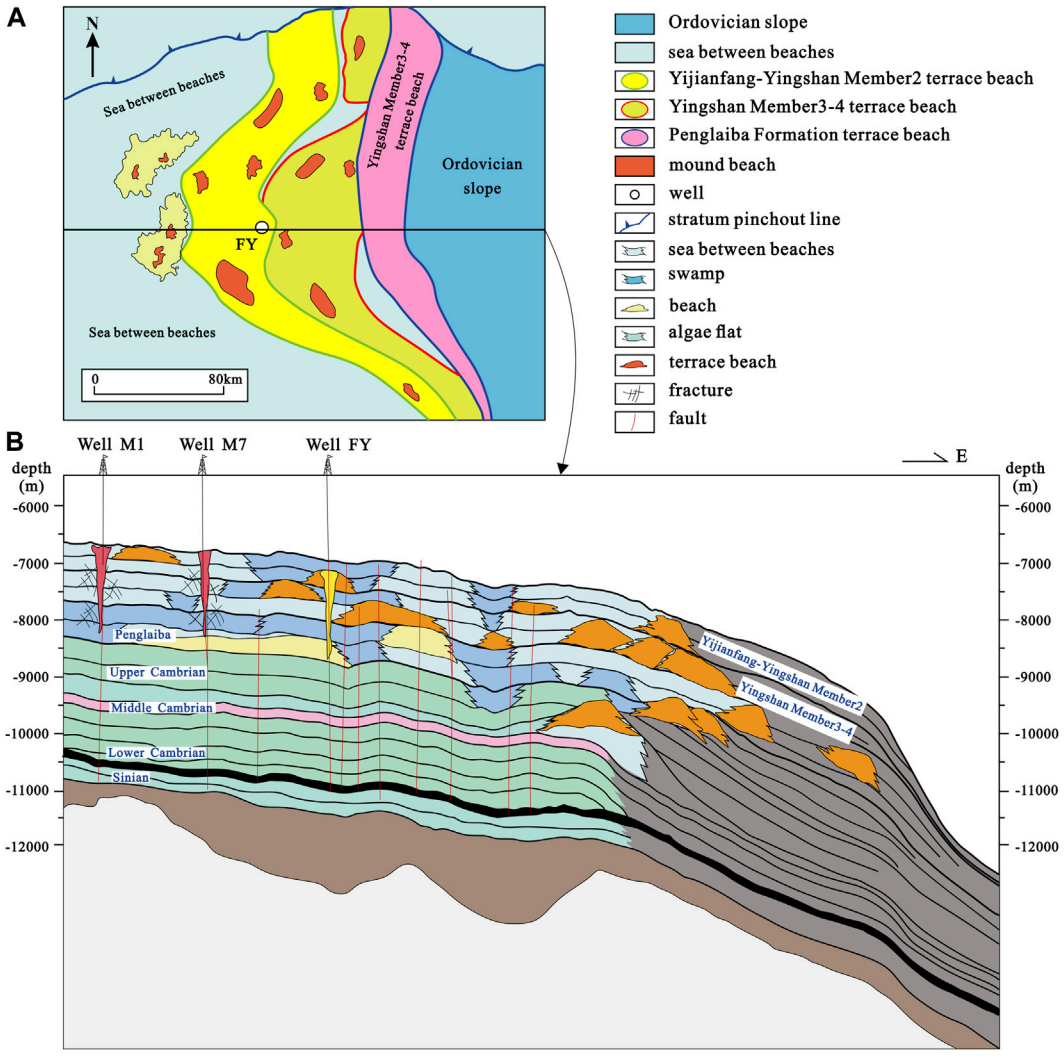


FIGURE 3
Superposition of high-energy platform marginal beach **(A)** and sedimentary microfacies map **(B)** in the Fudong area of Tarim Basin (after Wang et al., 2023).

Yin et al., 2019; Tan et al., 2021; Dontsov, 2022; Yong et al., 2022; Huang et al., 2023).

In-situ stress contains gravitational and tectonic stress. Commonly, in many sedimentary basins, *in-situ* stress can be expressed as three principal stresses, namely, the S_{Hmax}, vertical principal stress (S_v), and the horizontal minimum principal stress (S_{hmin}). Furthermore, based on the relative magnitude of S_{Hmax}, S_v and S_{hmin}, three types of stress regime can be divided (Anderson, 1951):

i, normal faulting stress regime, $S_v > S_{Hmax} > S_{hmin}$;
ii, strike-slip faulting stress regime, $S_{Hmax} > S_v > S_{hmin}$;
iii, reverse faulting stress regime, $S_{Hmax} > S_{hmin} > S_v$.

The deep Cambrian-Ordovician carbonate rocks in the Tarim Basin are enriched with hydrocarbon resources, which serves as a critical field for increasing oil and gas reserves and production (Yang et al., 2020; Ma et al., 2022). In the Tarim Basin, oil and gas resources in these carbonate reservoirs are estimated to be 70×10^8 tons, and are mainly controlled by strike-slip faults (Li et al., 2020; Jia et al., 2022). However, carbonate rocks in the Tarim Basin are deep and ultra-deep buried, generally form a tight reservoir, and hydrocarbon distributions are complicated, which limits the economic development (Zhu et al., 2022). With the improvement of technology and theory, since the year 2020, many large oil and gas discoveries have been successively made in carbonate reservoirs of Tarim Basin. Well M 1 is a discovery well of fault-controlled reservoir with high single well production. In the Ordovician Yijianfang Formation with a burial depth of over 7,535 m, the tested oil and gas production reach approximately 624 m^3/d and 37.13×10^4 m^3/d, respectively (Yang et al., 2020). Further, the exploration direction of ultra-deep carbonate oil and gas resources in the platform area turns to fracture-controlled and reef-beach type reservoirs, which have become a major drilling target. Recently, Well Fudong 1 was successfully drilled in the Fuman Oilfield, which confirms that the high-energy platform marginal shoal with secondary network faults has the capacities of reservoir development and hydrocarbon accumulation. This finding breaks through the exploration forbidden zone in ultra-deep high-energy shoal carbonate rocks with the burial depth of greater than 8,000 m, and

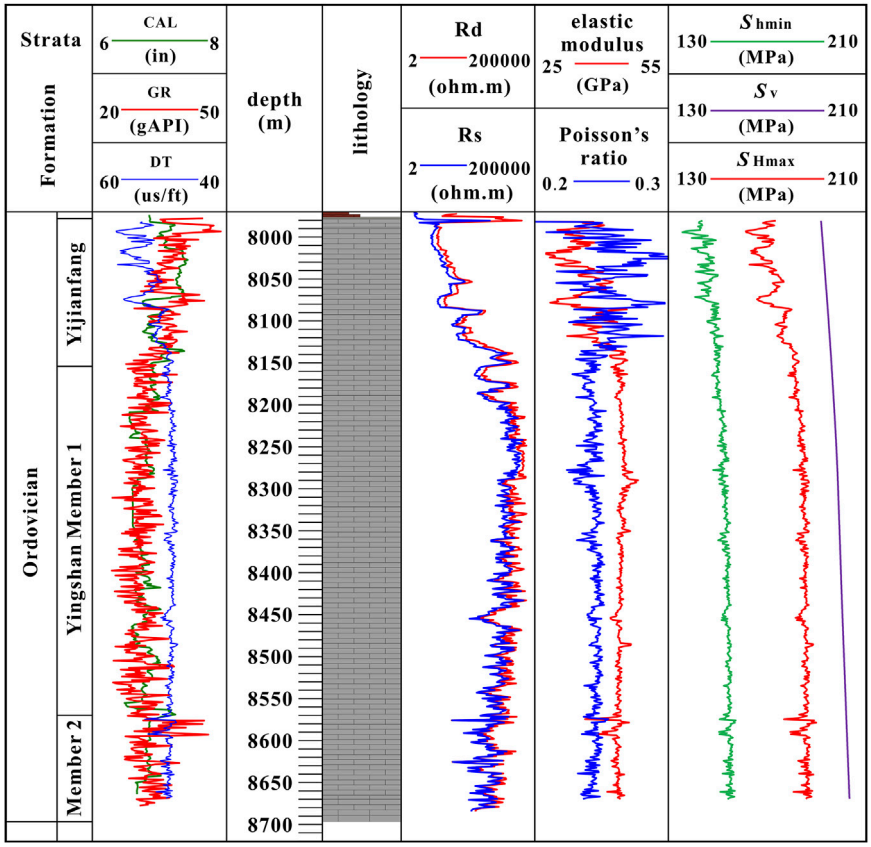


FIGURE 4
The 1D MEM in the Ordovician reservoir of Well FX.

expands the understanding on hydrocarbon accumulation pattern in carbonate reservoirs (Wang et al., 2023).

In the Tarim Basin, the carbonate reservoirs commonly show strong heterogeneity due to the development of strike-slip faults, fault-related natural fractures, caves and vugs. As a result, the development of this type of reservoir faces problems of large variation in single-well production capacity. Besides, complex present-day *in-situ* stress system and reservoir pressure cause difficult drilling operation and frequent incidents, and it is difficult to optimize effective measures for well completion (Yang et al., 2018). Understanding well of the *in-situ* stress field can help better deal with and solve the above problems (Zhao et al., 2020).

Prior to this analysis, distribution of present-day *in-situ* stress in ultradeep carbonate reservoirs of Fuman Oilfield, especially the Fudong area, has not been the subject of any systematical investigations, which limits the further development. Therefore, to improve the development efficiency, the present-day *in-situ* stress section was built, spatial distributions were predicted based on geomechanical models in this study. The results are expected to provide *in-situ* stress references for high-efficient development.

2 Geological setting

The Fuman Oilfield is located in the Northern Depression of Tarim Basin, between the Northern Uplift and Central Uplift (Figure 1A), which is the largest ultra-deep-sea facies fractured cave-type carbonate reservoir discovered in China. The petroleum geological reserves exceed 1×10^9 tons, and the annual oil production has more than 2×10^6 tons (Wang et al., 2021). The carbonate reservoirs in Fuman Oilfield are generally at ultra-depth of 7,500 m–10,000 m, and the main oil producing layer is the Ordovician Yijianfang Formation to Yingshan Formation (Figure 1B). The reservoir has huge exploration potential and development benefits. The largest thickness of the reservoir is 550 m, and the highest oil production is more than 1,600 m^3/d. Overall, it has the features of ultra-deep, ultra-high temperature, and ultra-high pressure that are rare in the world (Zhu et al., 2022; Wang et al., 2023). For the Fuman Oilfield, traditional oil and gas geology theories are basically "not applicable", conventional drilling techniques are basically "unsuccessful", and the exploration and development are extremely difficult.

The distributions of carbonate reservoirs in Fuman Oilfield are controlled by large strike-slip faults. During multiple tectonic movements, these faults have evolved into the current structure pattern through regeneration, inheritance, superposition, and transformation, showing the features of longitudinal stratification, planar zoning, and segmentation along the strike (Tian et al., 2021; Jia et al., 2022; Zhu et al., 2022; Figure 2).

The formation and internal configuration of strike-slip faults are affected by regional tectonic stress. Strike-slip faults in the Fuman Oilfield have experienced at least three stages, namely, the Middle Caledonian stage, the Late Caledonian stage, and the Middle-Late

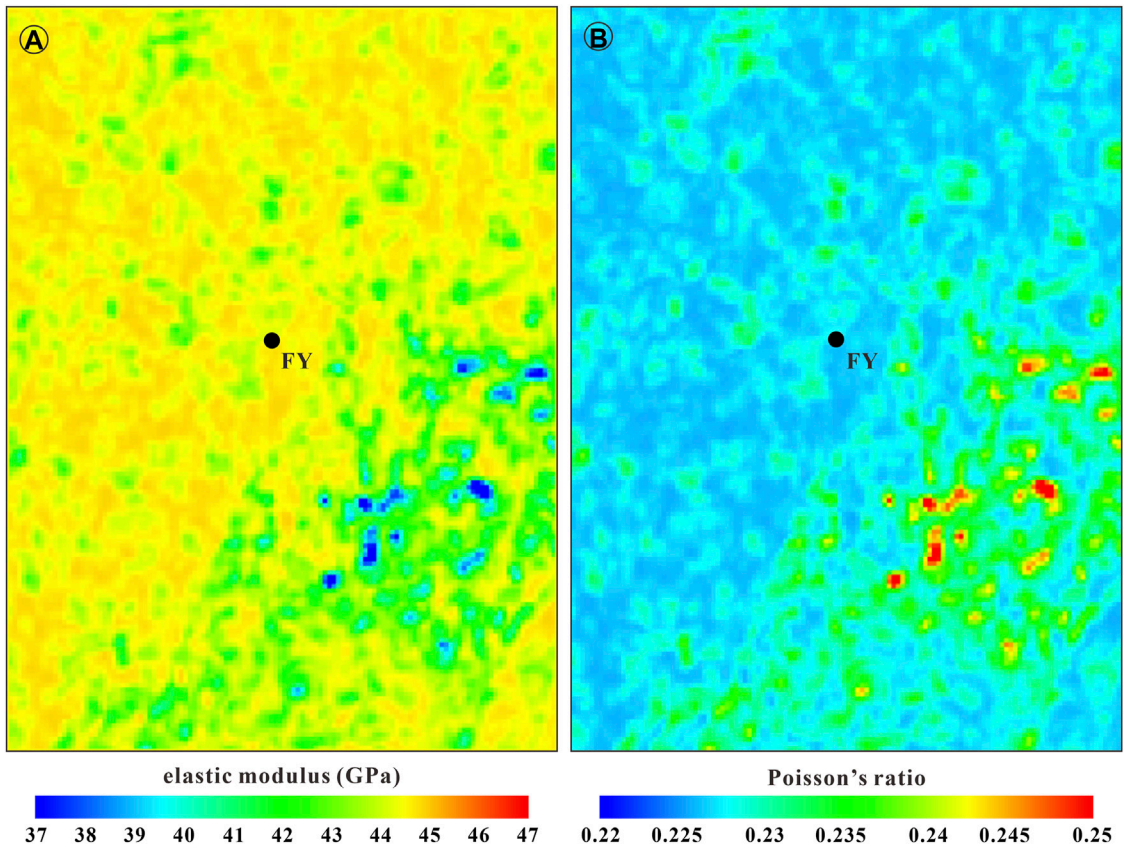


FIGURE 5
Mechanical properties used in the FE numerical model of Fudong area, Fuman Oilfield **(A)** elastic modulus; **(B)** Poisson's ratio.

Hercynian stage. Different fracture assemblages were formed due to the differences in the kinetic mechanisms underlying each active phase, which in turn controlled the differential oil and gas accumulation patterns (Jia et al., 2022; Wang et al., 2022).

In the Fuman Oilfield, the Fudong area is located within a platform margin high energy beach body (Figure 3). Structural paleo-geographical environment is also favorable for the development of platform margin high-energy shoals. Besides, the development of secondary network faults reforms the reservoir and provide favorable transport conditions. Taking Well Fudong 1 as an example, well testing shows that there are totally 13 layers with a thickness of 41.95 m in the Yijianfang Formation-Yingshan Formation. The second member of Yingshan Formation is extremely great. The estimated reservoir pressure is 175.21 MPa, pressure coefficient is approximately 2.1, which indicates an ultra-high pressure condensate gas reservoir.

3 Method and parameters

3.1 One dimensional (1D) mechanical Earth model (MEM)

Generally, the 1D MEM is built to analyze the variations of three principal stress magnitudes (S_v, S_{Hmax} and S_{hmin}) with burial depth. The S_v can be easily calculated and determined based on the integration of rock density from the ground surface to a specific depth (Eq.1; Zoback et al., 2003; Ju et al., 2017).

$$S_v = \int_0^z \rho(z) g \, dz \tag{1}$$

where S_v is the vertical principal stress, g is the gravitational acceleration, z is the burial depth from surface to a specific depth, $\rho(z)$ is the density of overburden as a function of burial depth.

Actually, no density logs and velocity data are obtained from the ground level during well log measurement. Hence, in this study, a S_v gradient of approximately 23,500 Pa/m was used from ground surface to the depth with the first density value.

In this study, magnitudes of S_{Hmax} and S_{hmin} are calculated using poroelastic stress equations (Thiercelin and Plumb, 1994; Eqs. 2, 3):

$$S_{Hmax} = \frac{\mu}{1-\mu}(S_v - \alpha P_o) + \alpha P_o + \frac{E}{(1-\mu)^2}(\varepsilon_{max} + \mu\varepsilon_{min}) \tag{2}$$

$$S_{hmin} = \frac{\mu}{1-\mu}(S_v - \alpha P_o) + \alpha P_o + \frac{E}{(1-\mu)^2}(\varepsilon_{min} + \mu\varepsilon_{max}) \tag{3}$$

where μ is the static Poisson's ratio, E is the static Young's modulus, ε_{max} is the strain in the maximum stress direction, ε_{min} is the strain in the minimum stress direction, P_o is the pore pressure, and α is the Biot's coefficient.

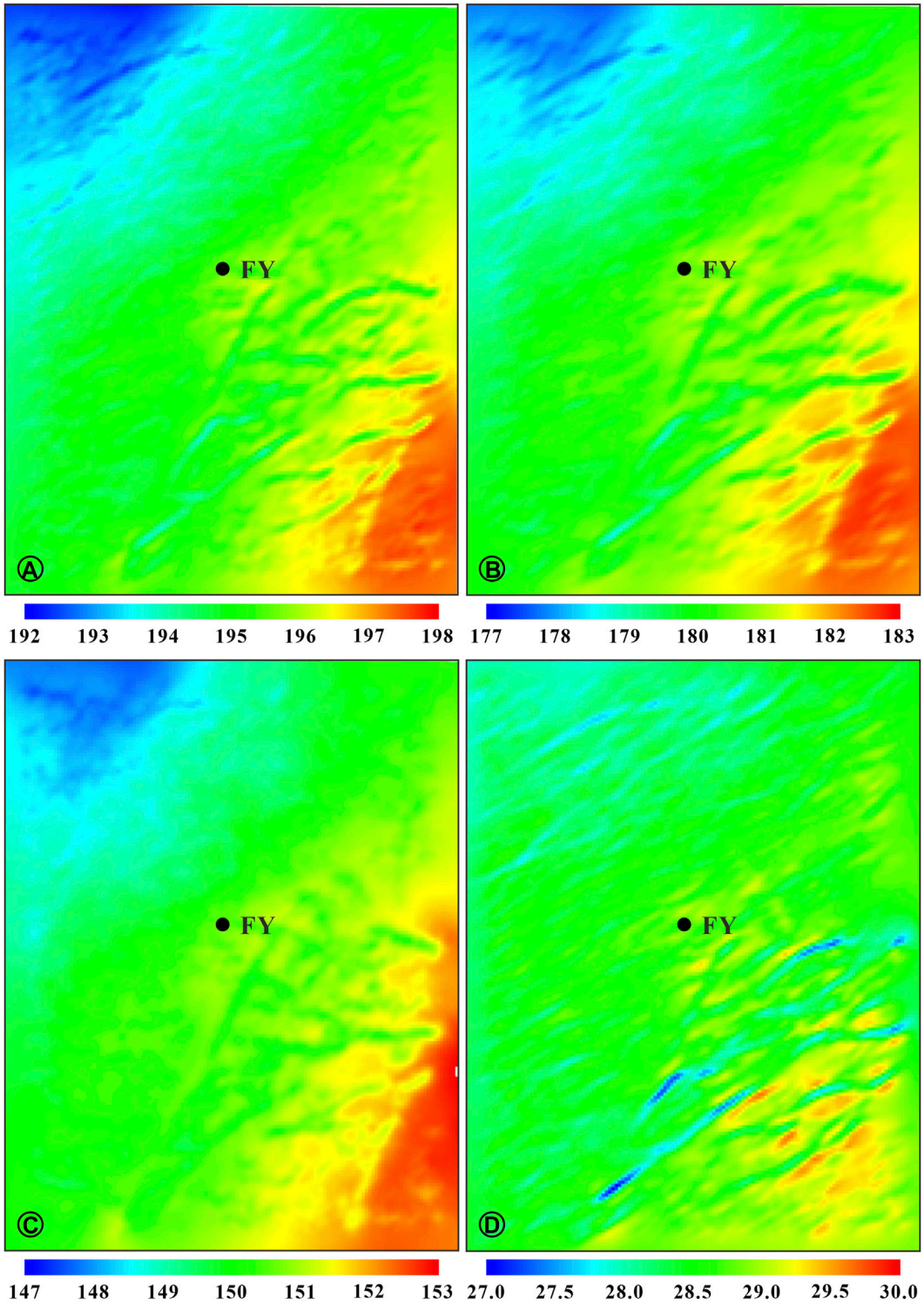


FIGURE 6
Stress spatial distribution in the Ordovician Yingshan Formation reservoir of Fudong area **(A)** S_v; **(B)** S_{Hmax}; **(C)** S_{hmin}; **(D)** horizontal stress difference; unit: MPa.

The α is calculated based on an empirical equation (Eq.4):

$$\alpha = 1 - \exp\left(7.5 \tan \frac{\varphi\pi}{2}\right) \quad (4)$$

where φ is the porosity of the rock, which can be obtained from laboratory experiments or well log calculations.

Commonly, the ε_{max} and ε_{min} are unable to be obtained directly. Parameters of the E, μ, P_o, and α can be measured from experiments or empirical formula. The S_{Hmax} and S_{hmin} magnitudes may be calculated based on hydraulic fracturing. Hence, in this study, parameters of ε_{max} and ε_{min} could be obtained inversely based on Eqs. 2, 3.

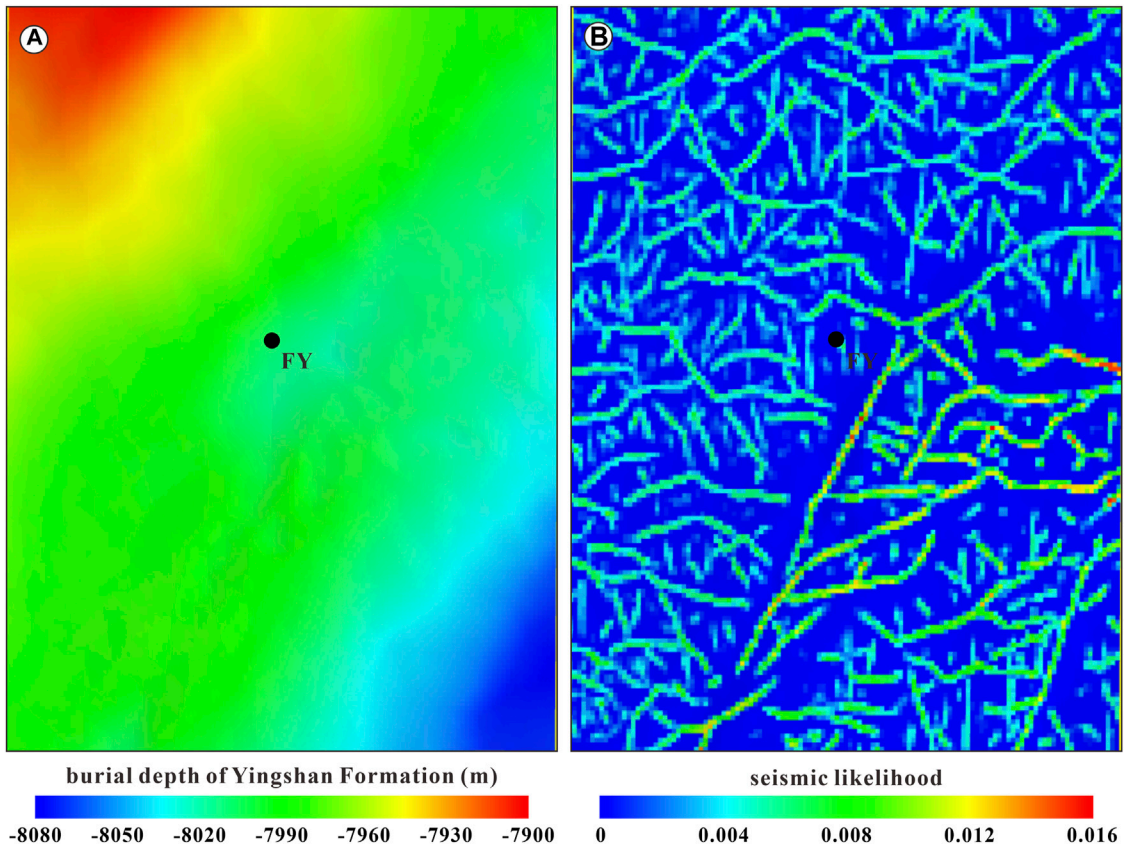


FIGURE 7
Burial depth **(A)** and seismic likelihood **(B)** of Yingshan Formation in the Fudong area of Fuman Oilfield.

3.2 *In-situ* stress finite element (FE) numerical modeling

In the study area, there are only three drilling wells, which limits the further understanding on spatial distribution of present-day *in-situ* stresses. Hence, the FE numerical modeling technique and FracMAN code are utilized to investigate the present-day *in-situ* stress distribution in the carbonate reservoirs of Fudong area.

During the FE numerical modeling, all geological bodies are discretized into finite continuous elements that are connected by nodes in accordance with the fundamental principle of the FE modeling approach. The entire region's field function is converted into a node function including fundamental variations in stress, strain, and displacement resulted from external forces (Ding et al., 2012; Liu et al., 2017).

Theoretically, based on the principle of virtual displacement, the relationship among nodal displacement, integral nodal load and integral stiffness follows Eq. 5.

$$[F] = [K][\delta] \tag{5}$$

where $[F]$ is the integral nodal load matrix, $[\delta]$ is the nodal displacement matrix for the integral structure of the examined elemental array, and $[K]$ is the integral stiffness matrix.

The matrix form can be derived as follows (Eq.6).

$$[\varepsilon] = [B][\delta] \tag{6}$$

where $[\delta]$ is the nodal displacement matrix, $[B]$ is the geometric matrix.

From the physical equation, stress and strain can be expressed as Eq. 7:

$$[\sigma] = [D][\varepsilon] \tag{7}$$

where $[D]$ is the elasticity matrix, σ is the stress, and ε is the strain.

The modeling process involves the following three steps: 1) determining the geometric shapes and characteristics of strata, 2) determining the spatial distributions of mechanical properties, and 3) determining the loading pattern for geological bodies within the model, and the associated boundary conditions.

4 Results

4.1 The 1D MEM in the Fuman Oilfield

Stress variations with burial depth are calculated and plotted in Figure 5. The S_v, S_{Hmax} and S_{hmin} magnitudes vary from 191.90 MPa to 198.98 MPa, 160.33 MPa–190.38 MPa, and 134.35 MPa–157.51 MPa, respectively, in the Yingshan carbonate reservoir. The S_{Hmax} and S_{hmin} magnitudes slightly change with depth, which may be influenced by factors of natural fracture development and bedding. Overall, the S_v and S_{hmin} are the maximum and minimum principal stress (Figure 4), following the relationship of $S_v > S_{Hmax} > S_{hmin}$, indicating a normal

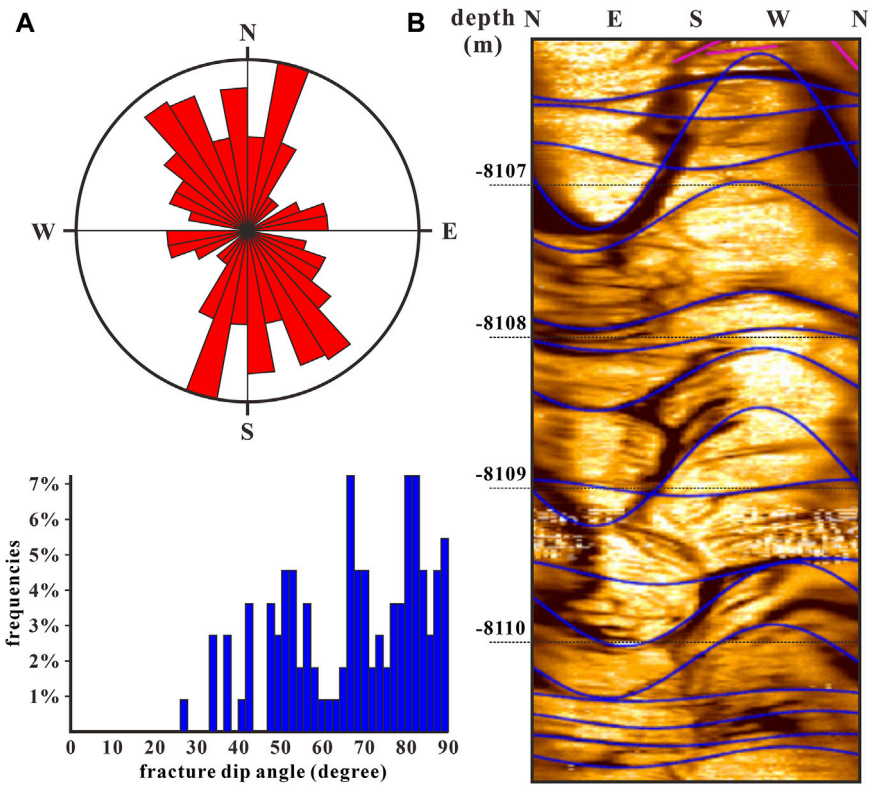


FIGURE 8
Characteristics of natural fractures in the carbonate reservoirs of Well M7 in Fuman Oilfield. **(A)** fracture strike and dip angle; **(B)** imaging log showing natural fractures.

faulting stress regime in the Yingshan carbonate reservoir of Fudong area.

4.2 Spatial distribution of present-day *in-situ* stresses

The initial three dimensional (3D) geometric model was built using the Petrel platform based on geological information obtained from seismic interpretation. The 3D reservoir grid was created using pillar gridding, makeup horizons and layering.

In this study, each element has the proper mechanical properties assigned to it (Figure 5). The elastic modulus in the Yingshan carbonate reservoir mainly ranges from 37 GPa to 47 GPa. The Poisson's ratio varies between 0.22 and 0.25 in the Yingshan Formation of Fudong area.

Generally, many methods can be used to determine the S_{Hmax} orientation, including interpretations from wellbore breakouts (BOs) and drilling-induced fractures (DIFs), focal mechanism analysis, etc. (Zoback et al., 2003; Heidbach et al., 2010; Rajabi et al., 2016; Ju et al., 2020a). In this study, the present-day S_{Hmax} orientation was analyzed from BOs and DIFs, which is approximately NE60° on average in the Yijianfang-Yingshan Formation of Fuman Oilfield. The orientation is consistent with the strike-slip fault direction. The Fuman Oilfield is controlled by the NE–SW horizontal tectonic compressive stress field.

It is unrealistic to place the loading conditions directly into each of the reservoir grid. Generally, there are three types of boundary conditions, namely, gravity, initialization and explicit initialization. In this study, the far field boundary condition was used for FE modeling with initialization method, which calculates the initial stress using the ratio of horizontal stresses and vertical stress. Based on calculated 1D MEM in the Ordovician reservoir of Fuman Oilfield, in the numerical model, the S_v gradient is 0.0235 MPa/m, the S_{Hmax}/S_v ratio is 0.921, and the S_{hmin}/S_v ratio is 0.769. The present-day S_{Hmax} orientation is set NE60°.

The results indicate that the S_v ranges from 192 MPa to 198 MPa, the S_{Hmax} magnitude is between 177 MPa and 183 MPa, the S_{hmin} magnitude varies from 147 MPa to 153 MPa (Figure 6). Their relationship follows $S_v > S_{Hmax} > S_{hmin}$, indicating a normal faulting stress regime. All the three principal stresses show similar distribution pattern, high and low stress magnitudes are mainly in the southeastern and northwestern part of Fudong area, respectively.

The overall distribution pattern is mainly controlled by burial depth. Larger depth produces higher stress magnitude (Figure 7A). Detailed variations of stress distribution commonly result from the development minor faults and natural fractures (Figure 7B).

5 Discussions

5.1 Horizontal stress difference

The commercial production of carbonate reservoir frequently requires hydraulic fracturing. The present-day *in-situ* stress state,

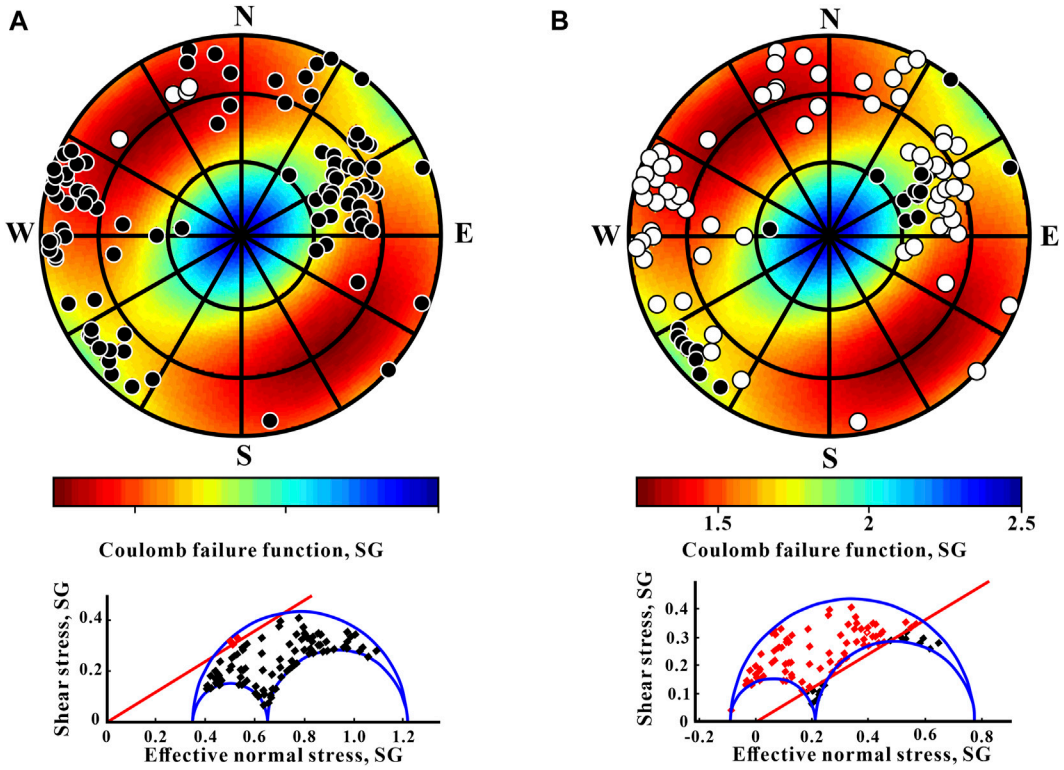


FIGURE 9
Lower hemisphere stereonet plots and three dimensional Mohr circles showing critically stressed natural fractures in the Ordovician carbonate reservoirs of Well M7, Fuman Oilfield **(A)** 1.29 MPa/100 m; **(B)** 1.73 MPa/100 m The fracture orientations are plotted as the pole of planes. The red colors show the high likelihood of fracture reactivation, while the blue colors indicate the low likelihood of reactivation for all possible fractures in the present-day stress state. Black and white dots in the stereonet plots are normal and critically stressed natural fractures, respectively. In the Mohr circles, black and red dots are normal and critically stressed natural fractures. SG is specific gravity.

rock mechanical property and natural fractures may influence the propagation of hydraulic fractures (Zoback, 2007; Ardakani et al., 2017; Ju et al., 2020a). Differential stress is widely used to analyze the propagation pattern of hydraulic fractures, and low stress difference can generate complex hydraulic fracture networks in most cases. Besides, high stress difference may easily cause rock failures, influencing wellbore stability.

Based on the above *in-situ* stress prediction, the present-day horizontal differential stress mainly ranges from 27 MPa to 30 MPa in the Yingshan reservoir. Relatively low values are located in the northwestern part of Fudong area (Figure 6D).

5.2 Coupling effect between *in-situ* stress and natural fracture

In-situ stress state is a significant factor that influences the transmitting ability of natural fractures (Zoback, 2007). When fracture orientations parallel to the present-day S_{Hmax} orientation, fluid flows in natural fractures well be greatly improved. Commonly, hydraulic fracturing process involves increasing the reservoir pressure by injecting high-pressure fluid into the target reservoir, which will cause many geomechanically-induced deformations, including fracture shear slip capacity improvement and natural fracture reactivation (Reynolds et al., 2003). This process plays a positive role in the transportation of oil and gas from the periphery of the well to the wellbore (Xu et al., 2022).

To quantitatively understand and analyze the coupling effect between *in-situ* stress and natural fractures, the "reactivation risk plot" that uses the Mohr's Circle Criterion (Mildren et al., 2002; Rajabi et al., 2016) are introduced to evaluate the risk of natural fracture reactivations in the Ordovician carbonate reservoir of Fuman Oilfield.

In this study, Well M7 is taken as an example, characteristics of natural fractures developed in the Ordovician carbonate rocks of Fuman Oilfield are analyzed based on imaging logs. Fracture strikes mainly range from NW-SE to NNE-SSW (Figure 8A), fracture dip angles are relatively high, the majority of them are higher than 50° (Figure 8B).

Analysis of the coupling effect between *in-situ* stress and natural fractures indicates that natural fractures are generally stable under the present-day *in-situ* stress state. With the injection of fluids into the carbonate rocks, reservoir pressure increases, causing the leftward movement of the Mohr's Circle (Figure 9). Furthermore, those fractures parallel to the S_{Hmax} orientation with high fracture dip angle are easier to be reactivated during the fluid injection process (Figure 9A). When the net bottom reservoir pressure is

1.29 MPa/100 m, four natural fractures are reactivated and become effective with the reactivation rate of 3.63% (Figure 9A). When the net bottom reservoir pressure is 1.73 MPa/100 m, the majority of natural fractures are reactivated, the reactivation rate is approximately 81.82% (Figure 9B).

6 Conclusion

In this study, the present-day *in-situ* stress field in the Ordovician carbonate reservoir of Fuman Oilfield, especially the Fudong area, was analyzed and predicted based on well calculation and geomechanical modeling. The results are expected to provide references in *in-situ* stress for subsequent efficient exploration and development.

The dominant S_{Hmax} orientation is NE-SW-trending (nearly 60°N) in the Yijianfang-Yingshan Formation of Fuman Oilfield. The S_v and S_{hmin} are the maximum and minimum principal stress, respectively, indicating that the Ordovician reservoir is under a normal faulting stress regime.

The present-day *in-situ* stress in the Ordovician reservoir is heterogeneously distributed, mainly controlled by burial depth, fault/natural fracture development and distribution. High stress magnitudes in the Yingshan Formation of Fudong area are mainly in the southeastern part of the study area. The present-day horizontal differential stress mainly ranges from 27 MPa to 30 MPa in the Yingshan carbonate reservoir. Relatively low values are located in the northwestern part of Fudong area.

The strikes of natural fracture in the Ordovician reservoir mainly range from NW-SE to NNE-SSW. Analysis of the coupling effect between *in-situ* stress and natural fractures indicates that natural fractures are generally stable under the present-day *in-situ* stress state. There is a critical value for fractures to be reactivated. Fractures parallel to the S_{Hmax} orientation with high fracture dip angle are easier to be reactivated.

Data availability statement

The raw data supporting the conclusion of this article will be made available by the authors, without undue reservation.

Author contributions

GY: Methodology, Writing–original draft. KW: Supervision, Writing–review and editing. WJ: Conceptualization, Writing–review and editing. YQ: Data curation, Writing–review and editing. ZQ: Data curation, Writing–review and editing. KX: Data curation, Writing–review and editing. ZL: Writing–review and editing, Resources. PW: Writing–review and editing, Resources. XL: Methodology, Writing–review and editing. YL: Methodology, Writing–review and editing.

Funding

The author(s) declare financial support was received for the research, authorship, and/or publication of this article. This study is supported by the Major Scientific and Technological Project of PetroChina Co., Ltd. (2018E-1803). The funder was not involved in the study design, collection, analysis, interpretation of data, the writing of this article, or the decision to submit it for publication.

Acknowledgments

Many thanks to the reviewers for improving this manuscript.

Conflict of interest

Authors GY, YQ, ZQ, KX, ZL, and PW were employed by Tarim Oilfield Company, PetroChina.

The remaining authors declare that the research was conducted in the absence of any commercial or financial relationships that could be construed as a potential conflict of interest.

Publisher's note

All claims expressed in this article are solely those of the authors and do not necessarily represent those of their affiliated organizations, or those of the publisher, the editors and the reviewers. Any product that may be evaluated in this article, or claim that may be made by its manufacturer, is not guaranteed or endorsed by the publisher.

References

Aljuboori, F. A., Lee, J. H., Elraies, K. A., and Stephen, K. D. (2019). Gravity drainage mechanism in naturally fractured carbonate reservoirs: review and application. *Energies* 12, 3699. doi:10.3390/en12193699

Anderson, E. M. (1951). *The dynamics of faulting and dyke Formation with applications to britain*. second edition. Edinburgh: Oliver, 206.

Ardakani, E. P., Urbancic, T., Baig, A. M., and Viegas, G. (2017). The influence of bedding-parallel fractures in hydraulic fracture containment. *First Break* 35 (4), 71–76. doi:10.3997/1365-2397.35.4.87844

Ding, W. L., Fan, T. L., Yu, B. S., Huang, X. B., and Liu, C. (2012). Ordovician carbonate reservoir fracture characteristics and fracture distribution forecasting in the Tazhong area of Tarim Basin, Northwest China. *J. Petroleum Sci. Eng.* 86-87, 62–70. doi:10.1016/j.petrol.2012.03.006

Dontsov, E. V. (2022). Analysis of a constant height hydraulic fracture driven by a power-law fluid. *Rock Mech. Bull.* 1 (1), 100003. doi:10.1016/j.rockmb.2022.100003

Finkbeiner, T., Barton, C. A., and Zoback, M. D. (1997). Relationships among *in-situ* stress, fractures and faults, and fluid flow: monterey formation, santa maria basin, California. *AAPG Bull.* 81, 1975–1999.

Heidbach, O., Tingay, M., Barth, A., Reinecker, J., Kurfeß, D., and Muller, B. (2010). Global crustal stress pattern based on the World Stress Map database release 2008. *Tectonophysics* 482, 3–15. doi:10.1016/j.tecto.2009.07.023

Huang, L. K., He, R., Yang, Z. Z., Tan, P., Chen, W. H., Li, X. G., et al. (2023). Exploring hydraulic fracture behavior in glutenite formation with strong heterogeneity and variable lithology based on DEM simulation. *Eng. Fract. Mech.* 278, 109020. doi:10.1016/j.engfracmech.2022.109020

Jia, C. Z., Ma, D. B., Yuan, J. Y., Wei, G. Q., Yang, M., Yan, L., et al. (2022). Structural characteristics, formation & evolution and genetic mechanisms of strizke–slip faults in the Tarim Basin. *Nat. Gas. Ind. B* 9 (1), 51–62. doi:10.1016/j.ngib.2021.08.017

Ju, W., Jiang, B., Miao, Q., Wang, J. L., Qu, Z. H., and Li, M. (2018). Variation of *in situ* stress regime in coal reservoirs, eastern yunnan region, south China: implications for coalbed methane production. *AAPG Bull.* 102 (11), 2283–2303. doi:10.1306/04241817376

Ju, W., Niu, X. B., Feng, S. B., You, Y., Xu, K., Wang, G., et al. (2020b). Predicting the present-day *in situ* stress distribution within the Yanchang Formation Chang 7 shale oil reservoir of Ordos Basin, central China. *Petroleum Sci.* 17, 912–924. doi:10.1007/s12182-020-00448-8

Ju, W., Niu, X. B., Feng, S. B., You, Y., Xu, K., Wang, G., et al. (2020a). Present-day *in-situ* stress field within the Yanchang Formation tight oil reservoir of Ordos Basin, central China. *J. Petroleum Sci. Eng.* 187, 106809. doi:10.1016/j.petrol.2019.106809

Ju, W., Shen, J., Qin, Y., Meng, S. Z., Wu, C. F., Shen, Y. L., et al. (2017). *In-situ* stress state in the linxing region, eastern ordos basin, China: implications for unconventional gas exploration and production. *Mar. Petroleum Geol.* 86, 66–78. doi:10.1016/j.marpetgeo.2017.05.026

Kargarpour, M. A. (2020). Carbonate reservoir characterization: an integrated approach. *J. Petroleum Explor. Prod. Technol.* 10, 2655–2667. doi:10.1007/s13202-020-00946-w

Li, H. Y., Liu, J., Gong, W., Huang, C., and Ren, L. D. (2020). Identification and characterization of strike-slip faults and traps of fault-karst reservoir in the Shunbei area, Tarim Basin. *China Pet. Explor.* 25 (3), 107–120. doi:10.3969/j.issn.1672-7703.2020.03.010 (in Chinese with English abstract)

Liu, J. S., Ding, W. L., Yang, H. M., Wang, R. Y., Yin, S., Li, A., et al. (2017). 3D geomechanical modeling and numerical simulation of *in-situ* stress fields in shale reservoirs: A case study of the lower cambrian niutitang Formation in the cen'gong block, south China. *Tectonophysics* 712-713, 663–683. doi:10.1016/j.tecto.2017.06.030

Ma, Y. S., Cai, X. Y., Yun, L., Li, Z. J., Li, H. L., Deng, S., et al. (2022). Practice and theoretical and technical progress in exploration and development of Shunbei ultra-deep carbonate oil and gas field, Tarim Basin, NW China. *Petroleum Explor. Dev.* 49 (1), 1–20. doi:10.1016/s1876-3804(22)60001-6

Mildren, S. D., Hillis, R. R., and Kaldi, J. (2002). Calibrating predictions of fault seal reactivation in the Timor Sea. *APPEA J.* 42, 187–202. doi:10.1071/aj01011

Pitcher, T., and Davis, T. L. (2016). Geomechanical analysis of *in-situ* stress and its influence on hydraulic fracturing at the Wattenberg field, Colorado. *First Break* 34 (3), 45–50. doi:10.3997/1365-2397.34.3.83974

Rajabi, M., Tingay, M., and Heidbach, O. (2016). The present-day state of tectonic stress in the darling basin, Australia: implications for exploration and production. *Mar. Petroleum Geol.* 77, 776–790. doi:10.1016/j.marpetgeo.2016.07.021

Reynolds, S., Hillis, R., and Paraschivoiu, E. (2003). *In situ* stress field, fault reactivation and seal integrity in the Bight Basin, South Australia. *Explor. Geophys.* 34, 174–181. doi:10.1071/eg03174

Tan, P., Jin, Y., and Pang, H. W. (2021). Hydraulic fracture vertical propagation behavior in transversely isotropic layered shale formation with transition zone using XFEM-based CZM method. *Eng. Fract. Mech.* 248, 107707. doi:10.1016/j.engfracmech.2021.107707

Thiercelin, M. J., and Plumb, R. A. (1994). Core-based prediction of lithologic stress contrasts in east Texas formations. *Soc. Petroleum Eng. Form. Eval.* 9 (4), 251–258. doi:10.2118/21847-pa

Tian, J., Yang, H. J., Zhu, Y. F., Deng, X. L., Xie, Z., Zhang, Y. T., et al. (2021). Geological conditions for hydrocarbon accumulation and key technologies for exploration and development in Fuman Oilfield, Tarim Basin. *Acta Pet. Sin.* 42 (8), 971–985. doi:10.7623/syxb202108001 (in Chinese with English abstract)

Wang, Q. H., Yang, H. J., Wang, R. J., Li, S. Y., and Deng, X. L. (2021). Discovery and exploration technology of fault-controlled large oil and gas fields of ultra-deep formation in strike-slip fault zone in Tarim Basin. *China Pet. Explor.* 26, 58–71. doi:10.3969/j.issn.1672-7703.2021.04.005 (in Chinese with English abstract)

Wang, Q. H., Yang, H. J., Zhang, Y. T., Li, Y., Yang, X. Z., Zhu, Y. F., et al. (2023). Great discovery and its significance in the ordovician in well Fudong 1 in fuman oilfield, Tarim Basin. *China Pet. Explor.* 28 (1), 47–58. doi:10.3969/j.issn.1672-7703.2023.01.005 (in Chinese with English abstract)

Wang, X. T., Wang, J., Cao, Y. C., Han, J., Wu, K. Y., Liu, Y., et al. (2022). Characteristics, formation mechanism and evolution model of Ordovician carbonate fault-controlled reservoirs in the Shunnan area of the Shuntuogole lower uplift, Tarim Basin, China. *Mar. Petroleum Geol.* 145, 105878. doi:10.1016/j.marpetgeo.2022.105878

Xu, K., Yang, H. J., Zhang, H., Ju, W., Li, C., Fang, L., et al. (2022). Fracture effectiveness evaluation in ultra-deep reservoirs based on geomechanical method, Kuqa Depression, Tarim Basin, NW China. *J. Petroleum Sci. Eng.* 215, 110604. doi:10.1016/j.petrol.2022.110604

Yang, H. J., Deng, X. L., Zhang, Y. T., Xie, Z., Li, Y., Li, S. Y., et al. (2020). Great discovery and its significance of exploration for Ordovician ultra-deep fault-controlled carbonate reservoirs of Well Manshen 1 in Tarim Basin. *China Pet. Explor.* 25 (3), 13–23. doi:10.3969/j.issn.1672-7703.2020.03.002 (in Chinese with English abstract)

Yang, H. J., Zhang, H., Yin, G. Q., and Han, X. J. (2018). Geomechanics-based geology-engineering integration boosting high-efficiency exploration of fractured-vuggy carbonate reservoirs: A case study on west yueman block, northern Tarim Basin. *China Pet. Explor.* 23 (2), 27–36. doi:10.3969/j.issn.1672-7703.2018.02.004 (in Chinese with English abstract)

Yin, S., Xie, R. C., Wu, Z. H., Liu, J. S., and Ding, W. L. (2019). *In situ* stress heterogeneity in a highly developed strike-slip fault zone and its effect on the distribution of tight gases: A 3D finite element simulation study. *Mar. Petroleum Geol.* 99, 75–91. doi:10.1016/j.marpetgeo.2018.10.007

Yong, R., Wu, J. F., Huang, H. Y., Xu, E. S., and Xu, B. (2022). Complex *in situ* stress states in a deep shale gas reservoir in the southern sichuan basin, China: from field stress measurements to *in situ* stress modeling. *Mar. Petroleum Geol.* 141, 105702. doi:10.1016/j.marpetgeo.2022.105702

Zhao, R., Zhao, T., Kong, Q. F., Deng, S., and Li, H. L. (2020). Relationship between fractures, stress, strike-slip fault and reservoir productivity, China Shunbei oilfield, Tarim Basin. *Carbonates Evaporites* 35, 84. doi:10.1007/s13146-020-00612-6

Zhu, Y. F., Zhang, Y. T., Zhao, X. X., Xie, Z., Wu, G. H., Li, T., et al. (2022). The fault effects on the oil migration in the ultra-deep Fuman Oilfield of the Tarim Basin, NW China. *Energies* 15, 5789. doi:10.3390/en15165789

Zoback, M. D., Barton, C. A., Brudy, M., Castillo, D. A., Finkbeiner, T., Grollimund, B. R., et al. (2003). Determination of stress orientation and magnitude in deep wells. *Int. J. Rock Mech. Min. Sci.* 40 (7-8), 1049–1076. doi:10.1016/j.ijrmms.2003.07.001

Zoback, M. D. (2007). *Reservoir geomechanics*. Cambridge: Cambridge University Press, 461.

frontiers | Frontiers in Energy Research

TYPE Original Research
PUBLISHED 19 September 2023
DOI 10.3389/fenrg.2023.1272086

Check for updates

OPEN ACCESS

EDITED BY
Peng Tan,
CNPC Engineering Technology R & D Company Limited, China

REVIEWED BY
Xiufeng Zhang,
Tongji University, China
Yanfang Gao,
Northwest University, China

*CORRESPONDENCE
Xingchuan Liao,
liaoxc1998@163.com

RECEIVED 03 August 2023
ACCEPTED 06 September 2023
PUBLISHED 19 September 2023

CITATION
Huang J, Xing J, Liao X, Ren Y, Ding K and Tan J (2023), Study on mechanical properties and microscopic damage mechanism of tight sandstone reservoir under uniaxial compression.
Front. Energy Res. 11:1272086.
doi: 10.3389/fenrg.2023.1272086

COPYRIGHT
© 2023 Huang, Xing, Liao, Ren, Ding and Tan. This is an open-access article distributed under the terms of the Creative Commons Attribution License (CC BY). The use, distribution or reproduction in other forums is permitted, provided the original author(s) and the copyright owner(s) are credited and that the original publication in this journal is cited, in accordance with accepted academic practice. No use, distribution or reproduction is permitted which does not comply with these terms.

Study on mechanical properties and microscopic damage mechanism of tight sandstone reservoir under uniaxial compression

Jin Huang[1], Jiacheng Xing[2], Xingchuan Liao[1,3]*, Yixing Ren[3], Keer Ding[3] and Jin Tan[3]

[1]Environment and Resources Institute of Southwest University of Science and Technology, Mianyang, Sichuan, China, [2]Downhole Operation Company, CNPC Xibu Drilling Engineering Co, Ltd, Karamay, Xinjiang, China, [3]School of Civil Engineering and Geomatics, Southwest Petroleum University, Chengdu, Sichuan, China

Due to the characteristics of low porosity, low permeability and serious anisotropy in tight reservoirs, it is difficult for conventional hydraulic fracturing theory to accurately guide the efficient exploitation of tight reservoirs. It has been shown that the reservoir rock mechanical properties are the key factor impacting the fracturing effect, but the current research on the damage properties of tight reservoir rocks is not comprehensive enough. Therefore, in order to improve the fracturing theory of tight reservoirs, this paper first explores the evolution mechanism of rock fractures through uniaxial compression experiments. Secondly, based on the particle discrete element method, the damage and failure process of tight sandstone under uniaxial compression is simulated from the microscopic scale. The test results show that the rock failure mainly includes tensile failure, shear failure, and tensile-shear failure; Internal micro-fractures will interconnect during rock destruction to form primary fractures through the rock mass, while secondary micro-fractures will also be generated. The numerical simulation results show that when the rock is subjected to tensile-shear failure, with the increase of load, tensile micro-fractures are mainly produced in the specimen, accompanied by a few shear fractures. Under the joint action of shear failure and tensile failure, V-shaped cracks are easily formed in rock. The tensile strength of rock is mainly affected by the microscopic tensile strength, and the cohesive force, modulus, stiffness ratio, friction coefficient and friction angle have significant effects on the compressive strength of rock. Therefore, a reasonable choice of microscopic parameters can realistically simulate the compression-tensile strength ratio of the rock. The research results of this paper can provide the theoretical basis of rock mechanics for the efficient exploitation of tight reservoirs.

KEYWORDS

tight reservoirs, uniaxial compression, damage mechanism, particle discrete elements, hydraulic fracturing

1 Introduction

Oil and natural gas as an important energy to promote the rapid development of the world, the demand is increasing year by year (He et al., 2023; Huang et al., 2022). With the depletion of conventional oil and gas resources, the effective development of unconventional reservoirs such as tight oil and tight gas is becoming a global trend (Huang et al., 2018; Huang et al., 2023; Zhang et al., 2022). Under the action of sedimentation, diagenesis and tectonic movement, the interior of this kind of low permeability reservoir is composed of irregularly shaped skeleton particles and cemented fill, accompanied by a large number of micro-fractures, so its interior presents typical characteristics such as discontinuity, anisotropy and heterogeneity (Bai et al., 2023; Huang et al., 2019; S; Huang et al., 2018; Li et al., 2022; Wang et al., 2022). Basic production capacity is basically not available after drilling, and it is necessary to achieve commercial development standards through hydraulic fracturing (Tan et al., 2021; Tan et al., 2017; Zhang et al., 2019). Hydraulic fracturing is a technical method to pump high pressure liquid into the rock to break the rock and increase the permeability of low permeability reservoir (Zhang et al., 2017; Huang et al., 2020; Dontsov, 2022). The effect of its reconstruction is influenced by many factors (Tan et al., 2020; Luo et al., 2022; Zheng et al., 2022). Previous studies have shown that the mechanical properties of reservoir rocks are the key to determining the fracturing effect except fracturing parameters and reservoir temperature (Detournay et al., 2022; Ji et al., 2015). Therefore, clarifying the mechanical properties of reservoir rock is the key to perfecting hydraulic fracturing technology.

The laboratory test can obtain the uniaxial tensile strength, uniaxial compressive strength and triaxial compressive strength of the rock. The stress-strain curve can be calculated to get the modulus of elasticity, Poisson's ratio, friction coefficient, as well as the cohesion of the rock and the angle of internal friction and other macro-mechanical parameters of the rock (Huang et al., 2022; Du et al., 2022). Previous studies have shown that the macroscopic mechanical parameters of rocks have an important influence on the study of rock mechanical properties. However, they cannot explain the internal fracture initiation, fracture extension and anisotropy characteristics of rocks, so it is essential to further study the characteristics of rocks from the micro-scale or mesoscale (Tian et al., 2022; Zhang et al., 2023). Microscale studies are not applicable to reservoirs in meters and kilometers (Liu et al., 2021). While the meso scale (micron to millimeter range) is the statistical performance of the mechanical properties at the micro scale, which can be better linked with the macro scale. Moreover, the particle size range of most rocks belongs to the mesoscale range, so studying the mechanical properties of rocks on the mesoscale can better reflect the complex mechanical characteristics of rocks and provide a basis for the macroscopic mechanical properties of rocks (Lai et al., 2023). In this paper, the evolution process of rock fractures is explored on the basis of uniaxial compression test, and flat-joint damage model is established based on particle discrete element method, which can effectively describe rock mesoscopic damage. The damage process of rock is studied from the mesoscale, and the sensitivity analysis of rock mesoscopic parameters is carried out.

2 Uniaxial compression experiment

2.1 Experimental method

In order to study the fracture evolution process of low permeability sandstone, uniaxial compression test combined with non-contact three-dimensional deformation measurement system is used to track the deformation and strain conditions of rock specimen surface, obtain the stress-strain curve of rock and analyze the fracture evolution of rock sample during deformation and failure. This uniaxial compression experiment adopts a microcomputer controlled electro-hydraulic servo universal testing machine (Figure 1A), which can exert a maximum pressure of 1,000 kN. The Aramis system (Figure 1B) is used to measure strain and deformation failure of the rock sample during uniaxial loading. The Aramis system consists of two high-resolution cameras (resolution: 2,448 × 2050 pixels, acquisition speed: 15 Hz), graphics workstation, controller and display. It has the advantages of high measurement accuracy, wide range and intuitive results, and can synchronize time, pictures and analog signals accurately. The sample size can be measured from 1 mm to 1,000 mm, the accuracy is 0.01%, and the measurement range is 0.01%–500%.

2.2 Analysis of experimental results

The rock samples used in this experiment are taken from the low permeability tight sandstone reservoir of Chang 6, Zhenying area, Ordos Basin. The rock samples in this area are mainly lithic feldspar sandstone and feldspar lithic sandstone. A total of 9 standard cores with a height of 50 mm and a diameter of 25 mm are taken from the low permeability tight sandstone reservoir at a depth of 900–1,600 m, and the loading rate is 0.01 mm/s during the experiment. Three representative cores with numbers A3, A6 and A7 are selected for results analysis in those experimental results.

Figure 2 and Figure 3 show the stress-strain curve and failure process of core A3. Corresponding feature points such as A, B, C and D can be found in the curve in Figure 2. The curve can be divided into four stages, namely, OA stage, AB stage, BC stage and CD stage. The OA stage is the pore and fracture compaction stage. The micro-fractures and structural planes in the core will gradually close under the action of external pressure. The deformation in this stage is nonlinear, showing an upward concave trend, and the stiffness of the sample will gradually increase. Phase AB is a linear elastic process, and the stress-strain curve is approximately straight line. It can be find that the stiffness of the specimen is basically kept constant. The BC stage is the unstable development stage of the fracture. With the increase of the external load of the rock, the stress concentration at the fractures and pores inside the rock becomes more and more obvious. The fracture changes from stable expansion to unstable expansion, and the energy inside the rock gathers rapidly. When it extends to the critical energy release point, the fracture develops rapidly into a macroscopic fracture. When it develops to a certain stage, the stress will reach the peak strength of 52.01 MPa, that is, point C. In the BC stage, shear fractures are formed at the end of the core and extended rapidly. With the increase of stress, new shear fractures are formed and quickly connected with the previous shear fractures. At this time, the surface of the sample remained intact and

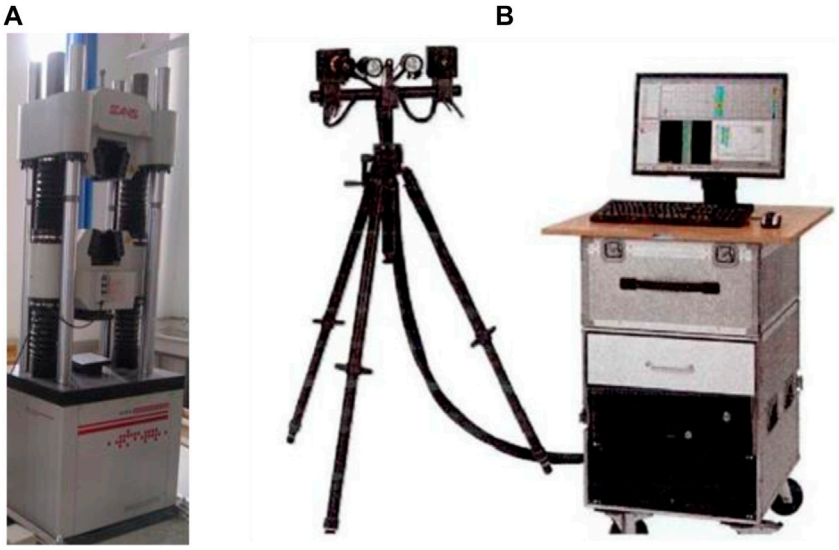


FIGURE 1
Monitoring system of rock uniaxial compression failure: **(A)** Universal testing machine; **(B)** ARAMIS strain measurement system.

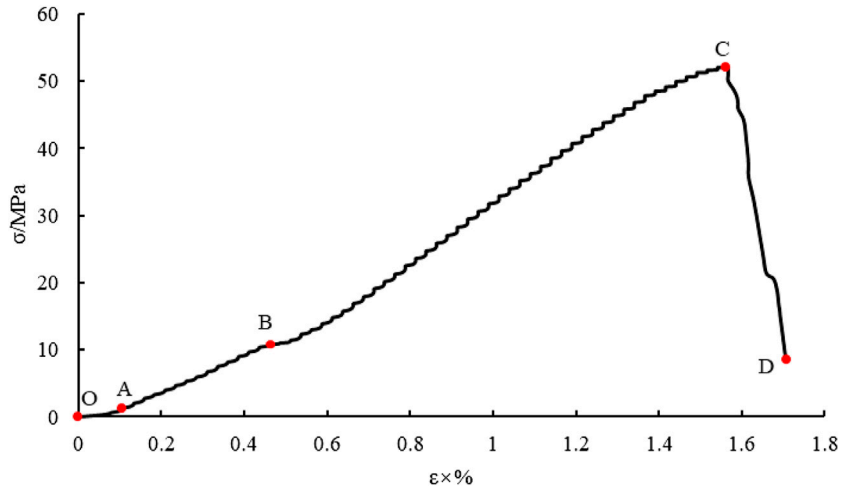


FIGURE 2
Stress-strain curve of core A3.

do not collapse, as shown in Figure 3. The CD stage is the post-rupture stage. Under the action of macroscopic cracks, the internal structure of the core is destroyed and continues to load. The macroscopic cracks penetrate through each other and form the macroscopic fracture surface.

Figure 4 and Figure 5 show the stress-strain curve and core failure process of A6 core. The stress-strain curve follows the O-A-B-C process, which is similar to the process of A3 core, including pore and fracture compaction stage, linear elastic stage and fracture unstable development stage. After the peak stress point C, the rock still has some residual strength, which is due to the core failure in the BC stage is split failure, in other words, a tensile fracture is produced. After the peak stress, there are new shear fractures and tensile fractures generated, when the internal fractures of the core have not yet penetrated the whole core. Following the redistribution of stresses within the core, the sample showed a certain increase in stress at point D and finally fell to point E. At this time, a number of tensile fractures and shear fractures occurred in the sample, and the internal structure of the sample is damaged, as shown in Figure 5.

Figure 6 shows the stress-strain curve of core A7, which has a double peak stress intensity, and the uniaxial compression process stage before point C is similar to that of core A3 and A6.

The first peak strength (29.07 MPa) at point C is due to shear fractures appearing at the top of the core with the increase of stress and strain in section BC, resulting in local fractures in the core. Local

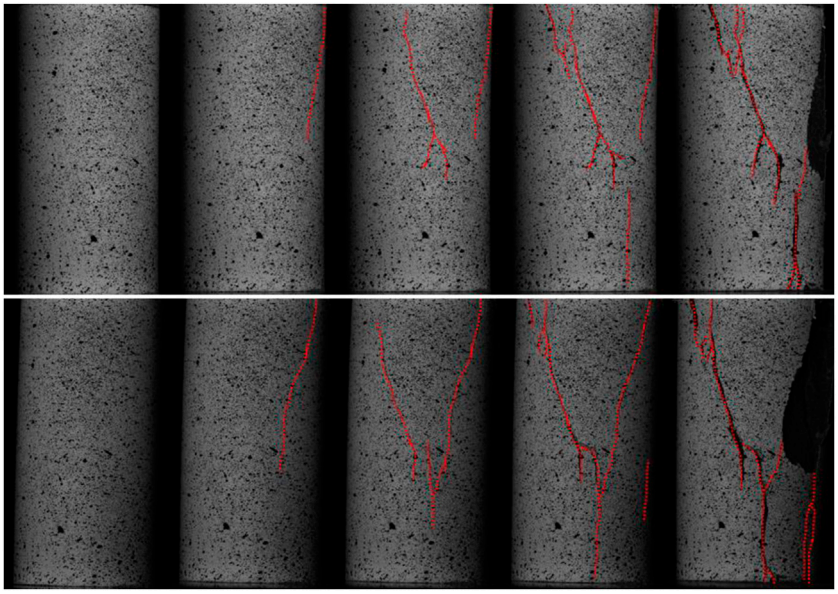


FIGURE 3
Failure process of core sample A3, the upper part is shot by the left camera, the lower part is shot by the right camera, and the red dotted line indicates the fracture.

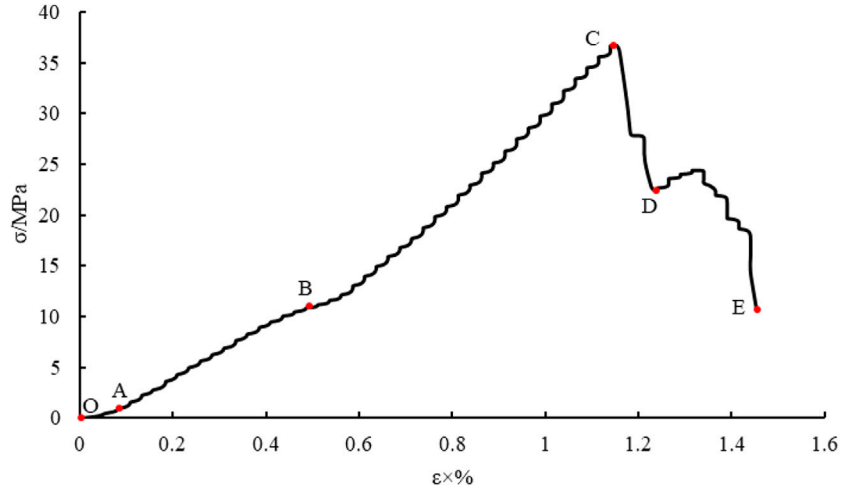


FIGURE 4
Stress-strain curve of core A6.

instability leads to the reduction of the core bearing capacity, but the overall structure of the core is not damaged, as shown in Figure 7. When the stress drops to a certain extent, the internal stress of the core is redistributed, and the ability of the core to withstand external loads increases. At the same time, the core cracked under the combined action of tension and shear, which expanded rapidly and the stress reached the second peak strength (28.94 MPa) at point D. Continuing to apply the load, the fracture penetrates the entire specimen, and the interior of the core is damaged, so that the stress falls rapidly to the E point, while the opening of the fracture increases.

3 Basic theory of particle discrete element method

Most of the large deformation in engineering is interpreted as the relative movement along various soft surfaces and contact zones. The deformation of these materials mainly comes from the slip and rotation of particles and the opening and locking of the contact interface, rather than from the deformation of a single particle itself. In order to obtain the internal mechanical properties of the rock, the rock can be regarded as a particle binder with complex shape, as shown in Figure 8A. Cundall proposed the

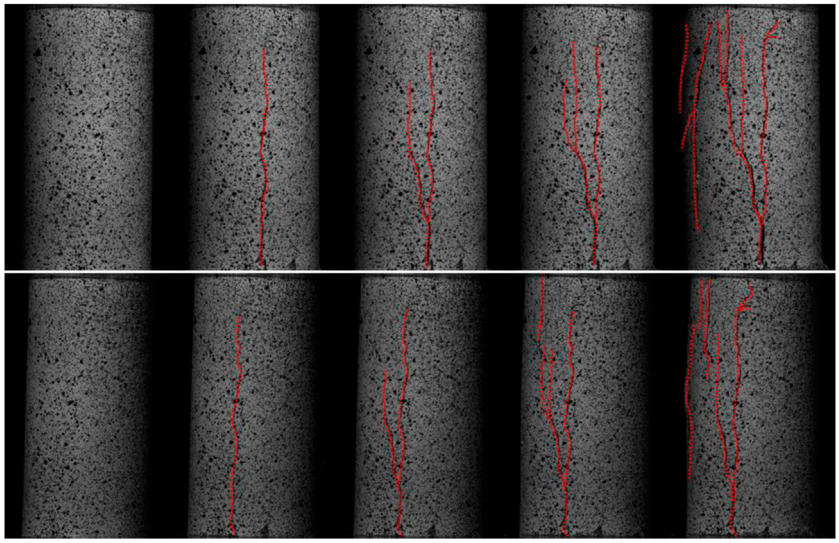


FIGURE 5
Failure process of core sample A6 the upper part is shot by the left camera, the lower part is shot by the right camera, and the red dotted line indicates the fracture.

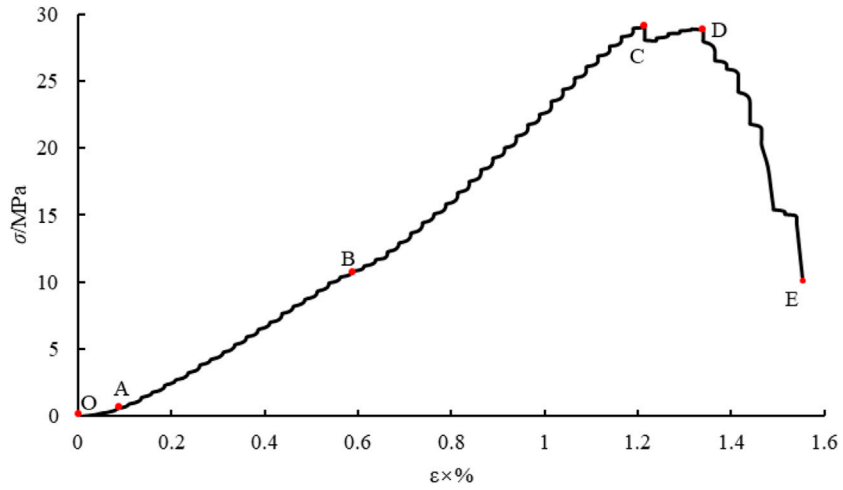


FIGURE 6
Stress-strain curve of core A7.

discrete element method in 1979, which is gradually developed into the block discrete element method and the particle discrete element method (Cundall and Strack, 1979). Particle discrete element method is used to simulate the motion and interaction of granular medium by circular (or polygon) discrete element method, which does not need to add other conditions to simulate the rock fracture process indirectly. The parallel bond model and parallel joint model proposed by Potyondy can directly simulate the rock fracture process with nonlinear (Potyondy and Cundall, 2004), heterogeneous and anisotropic characteristics, and this method can study the mechanical properties of rock at mesoscale. Therefore, the particle discrete element method is selected for simulation in this paper. The particle discrete element method makes the following assumptions in the simulation process.

(1) The particle unit is a rigid body.
(2) Contact occurs in a very small range, that is, point contact.
(3) The contact is flexible contact, and the contact is allowed to have a certain amount of “overlap".
(4) The amount of “overlap” is related to the contact force, and the amount of “overlap” is small compared with the particle size.
(5) The contact has a special connection strength.
(6) The particle unit is circular (or spherical).

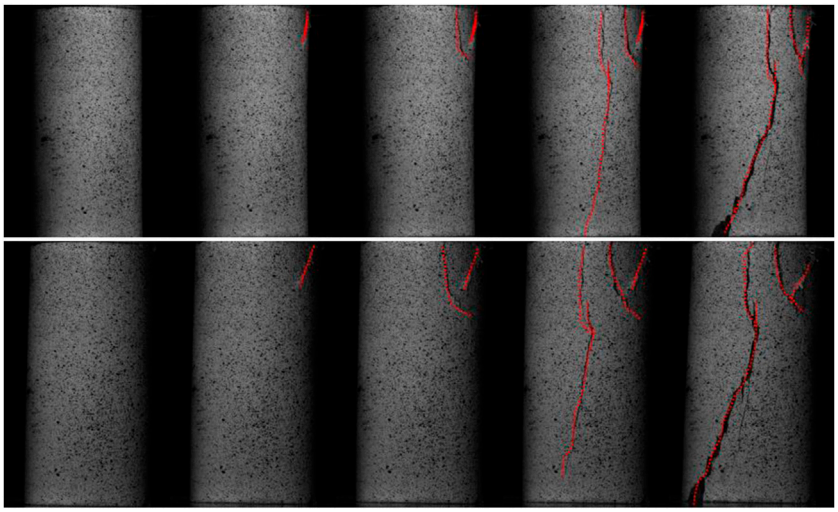


FIGURE 7
Failure process of core sample A7, the upper part is shot by the left camera, the lower part is shot by the right camera, and the red dotted line indicates the fracture.

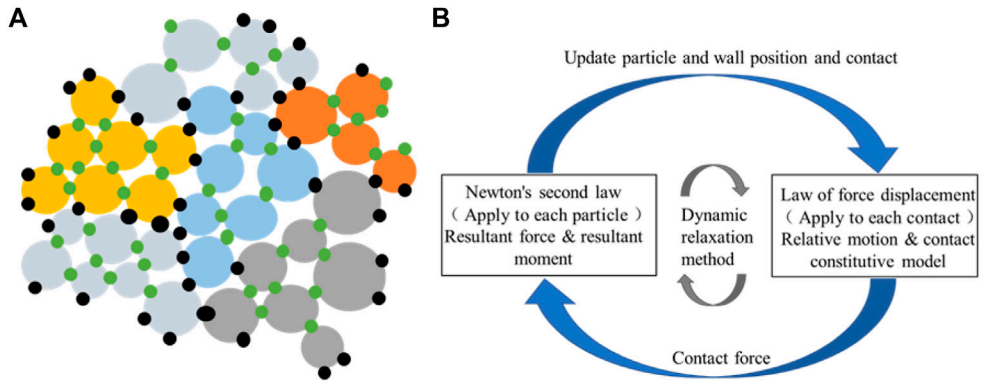


FIGURE 8
Particle discrete element method: **(A)** Rock mass model; **(B)** Calculating the cycle process (Potyondy, 2012).

The particle discrete element method uses the dynamic relaxation method to calculate and transforms the nonlinear statics problem into the dynamic problem to solve, which can reduce the computational storage and thus reduce the waste of computing resources. The cyclic process of particle discrete element method in calculation is shown in Figure 8B. The contact force and displacement between particles are updated according to the physical equation (force-displacement equation) and the equation of motion (Newton's second law). In calculation, the generation of fractures in the specimen is automatically judged by the constitutive model used and realized automatically within the program.

(1) Physical equations - force and displacement equations

The force-displacement equation describes the direct relationship between the contact force and the relative displacement at the contact point between particles. Assuming that the normal contact force at the contact is F_n N) and the relative displacement is u_n m), the tangential force at the contact is described by increment, that is, the tangential force increment at the contact is ΔF_s N) and the relative displacement is u_s m). The normal force and tangential forces-displacement equation at the contact is expressed by the following formula:

$$\begin{cases} F_n = k_n u_n \\ \Delta F_s = k_s \Delta u_s \end{cases} \quad (1)$$

Where k_n, k_s is the normal and tangential contact stiffness (N/m) respectively.

(2) Equations of motion - Newton's second Law

In the discrete element method, the particle is assumed to be a rigid body, and the contact force exists between the particle and the

particle. Under the action of external forces, the particles are in an unbalanced state, which will cause the particles to generate acceleration and velocity. At this time, the particles will produce rotation and dynamic behavior, and the contact force will be updated with the change of particle force and displacement. Assuming that at time t s), the resultant force of particles in the direction i is F_i, the bending moment is M_i (Nm), the mass of particles is m (kg), and the moment of inertia is I_i (kgm^2), then the translational acceleration $\ddot{u}_i$ (m/s^2) and rotational acceleration $\dot{\theta}_I$ (s^{-2}) of particles in the direction i are respectively as follows:

$$\begin{cases} \ddot{u}_i = F_i/m \\ \dot{\theta}_i = M_i/I_i \end{cases} \tag{2}$$

At $t+\Delta t/2$, the translational velocity and rotational velocity of the particle in the direction i are as follows:

$$\begin{cases} \dot{u}_{\mathrm{i}}^{(t+\Delta t/2)} = \dot{u}_i^{(t-\Delta t/2)} + \ddot{u}_i^{(t)}\Delta t \\ \theta_{\mathrm{i}}^{(t+\Delta t/2)} = \theta_i^{(t-\Delta t/2)} + \dot{\theta}_i^{(t)}\ \Delta t \end{cases} \tag{3}$$

where $\dot{u}_i^{(t-\Delta t/2)}$ is the translational velocity (m/s) of the particle in direction i at the moment t-$\Delta t/2$, with Δt being the calculated time step, and $\theta_{\mathrm{i}}^{(t-\Delta t/2)}$ is the rotation velocity (s^{-1}) of this particle in the i direction at the moment t-$\Delta t/2$.

At $t+\Delta t$, the displacement of the particle in the i direction is as follows:

$$u_{\mathrm{i}}^{(t+\Delta t)} = u_i^{(t)} + \dot{u}_i^{(t+\Delta t/2)}\Delta t \tag{4}$$

(3) Boundary conditions

In the discrete element method, the particle system can be loaded by assigning force or velocity to the particle, and the fixed edge particles can be used as the boundary constraint of the particle system. The boundary setting is flexible, and complex boundary conditions can be realized by writing functions.

(4) Constitutive model selection

In the particle discrete element method, the constitutive model of the material is defined by assigning the contact model to the contact between particles. It mainly includes four models: linear parallel bond model (Wu et al., 2021), flat-joint model (Potyondy, 2012), smooth-joint model (Fener et al., 2005) and soft-bond model (Huang et al., 2023). The flat-joint model is composed of rigid grains, and the grains are bonded by the contact of the flat-joint. The grains are composed of circular (2D) or spherical (3D) particles and notional surfaces. A grain surface can have multiple abstract surface units, and the abstract surface unit is rigidly connected with the corresponding grain. Therefore, the effective contact between the grains becomes the contact between the abstract surfaces. Flat-joint contact describes the behavior of the intermediate contact surface between abstract surfaces, as shown in Figure 9. In the two-dimensional model, the contact is a straight-line segment that can be discretized into several small units of equal length. In the three-dimensional model, the contact is a disc with a certain thickness, which can be discretized into a number of small units of equal volume from the radial and circular directions. Each element may be bonded, non-bonded with friction, so that the mechanism behavior of the intermediate contact surface may be bonded, non-bonded friction type, or vary along the contact surface. Compared with the linear parallel bonding model, this model can solve the problems such as low compression-tensile strength ratio, small internal friction angle and linear strength envelope. Compared with the linear parallel bond model, this model can solve problems such as low compression-tensile strength ratio, small internal friction angle, linear strength envelope and so on. The element failure at the bond adopts the constitutive relation curve of Figure 10. Since the contact in the flat-joint model contains multiple elements, the failure of each element remains independent, so the model can characterize the damage process in the failure of the specimen.

4 Numerical simulation of microscopic damage

4.1 Numerical model

The flat-joint model can well simulate the microscopic damage of rock, so this paper adopts the model to investigate the microscopic parameters and damage process of rock. Some scholars have carried out sensitivity analysis on the microscopic parameters such as modulus (E_c) stiffness ratio (K_n/K_s), tensile strength (σ_t), bond strength (C)l, friction coefficient μ) and friction angle Φ) in the flat-joint model, and proposed a fast parameter calibration method (Wu and Xu, 2016). Therefore, this chapter does not reiterate the parameter calibration method. The physical parameters of tight sandstone, shale and coal rock in low permeability reservoirs are quite different. On the basis of previous studies, this paper selects the relevant macro parameters, and calibrates the meso parameters for rock uniaxial compression experiment and numerical calculation. The macro and meso parameters of rock are shown in Table 1. The sample used for numerical simulation is 100 mm in height and 50 mm in width. The contact between particles contains two abstract surface elements. The maximum particle radius is 0.6 mm, while the ratio of maximum radius to minimum radius is 1.8, and the particle density ρ) is 2,500 kg/m^3.

The particle contact in the plane joint model can be divided into several abstract surface units, each of which can break separately. Therefore, it is assumed that the contact is broken only when the last broken abstract surface unit at the contact between particles is broken, and microcracks appear at this time. The abstract surface units that are broken before the contact are the damage of the contact. This model is defined in this paper as the flat-joint damage model. In the ordinary flat-joint model, if the abstract surface element at the contact is broken, there will be a micro-fracture. Hence, the results of the flat-joint damage model are consistent with those of the flat-joint model, but the number of micro-fractures produced is inconsistent.

Figure 11 shows the numerical simulation results of the sample. Figure 11A shows that rock failure is accompanied by the generation of multiple fragments. At this time, multiple shear fractures and tensile fractures appear in the rock macroeconomically, moreover,

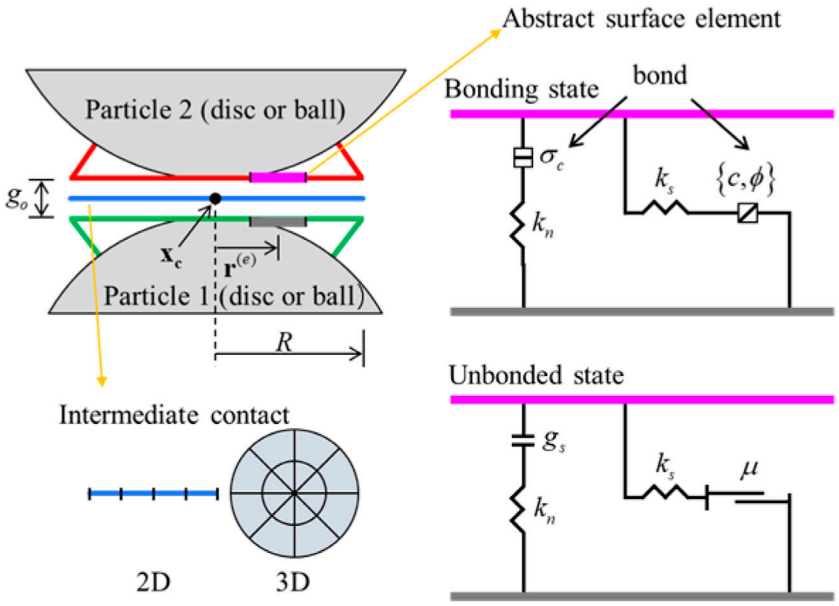


FIGURE 9
Schematic diagram of flat-joint model (Potyondy, 2012).

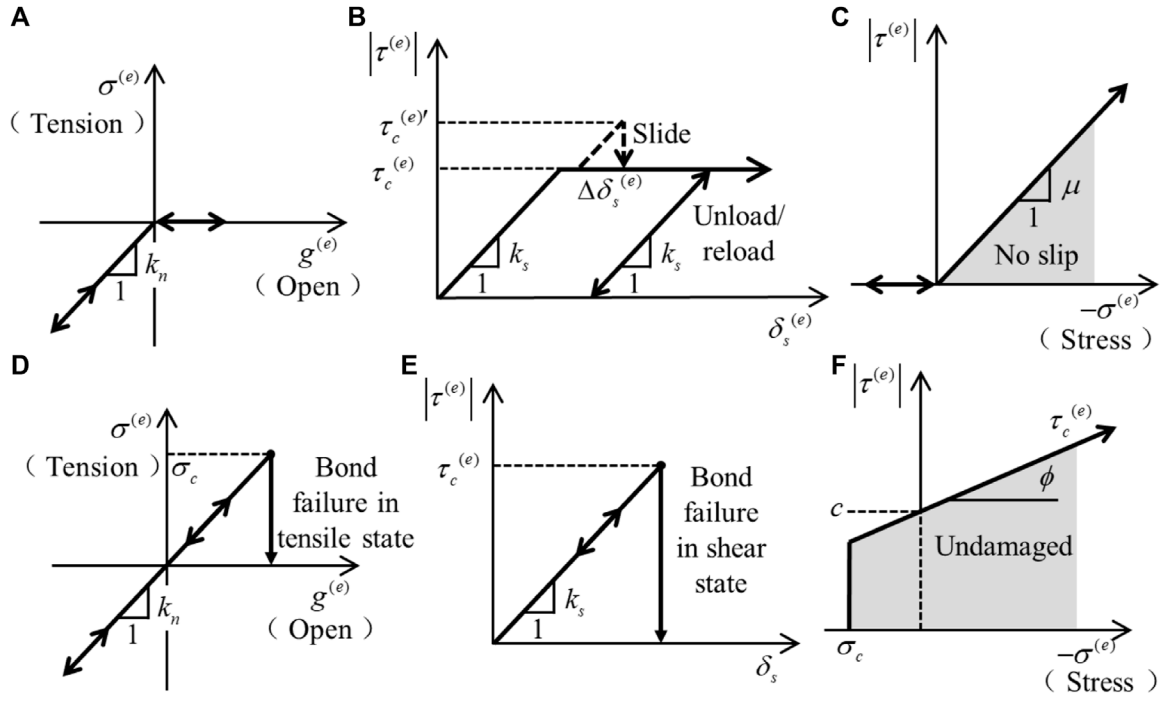


FIGURE 10
Constitutive relation curve of the flat-joint model, a-c Is the force-displacement curve of the unbonded flat-joint element, d-f Is the force-displacement curve of the flat-joint element in the bonded state: **(A)** Normal force and contact unit spacing curve; **(B)** Shear force and relative shear displacement curve; **(C)** Slip envelope; **(D)** Normal force and contact unit spacing curve; **(E)** Shear force and relative shear displacement curve; **(F)** Failure envelope.

the shear fractures run through the entire sample. Figure 11B shows the stress-strain curve of the specimen. There is a certain fluctuation in the initial stress increase of the curve, which is due to the stress change caused by the decrease of the porosity of the sample under compression and the densification of the particle structure. While the stress continues to increase, the stress-strain curves show linear

TABLE 1 Macro and microscopic parameters of rocks.

Microscopic parameter	E_c (GPa)	K_n/K_s	σ_t (MPa)	C (MPa)	μ
value	19.0	2.2	10	35	0.45
Microscopic parameter	Φ	fj_n	R_{max} (mm)	ρ(kg/m^3)	R_{max}/R_{min}
value	30	2	0.6	2,500	1.8
Macroscopic parameter	E_c (GPa)	Poisson's ratio	σ_c (MPa)	σ_t (MPa)	—
value	24.18	0.19	92.56	6.56	—

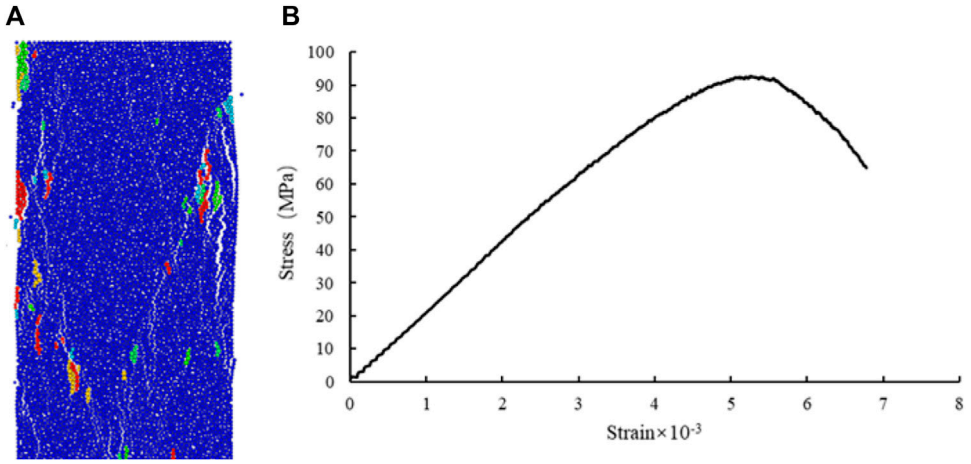


FIGURE 11
Numerical simulation of uniaxial compression, when the strength is 70% of the peak strength, the loading is stopped: **(A)** Failure pattern of specimens (multiple particles of the same color are rock fragments); **(B)** Stress-strain curve.

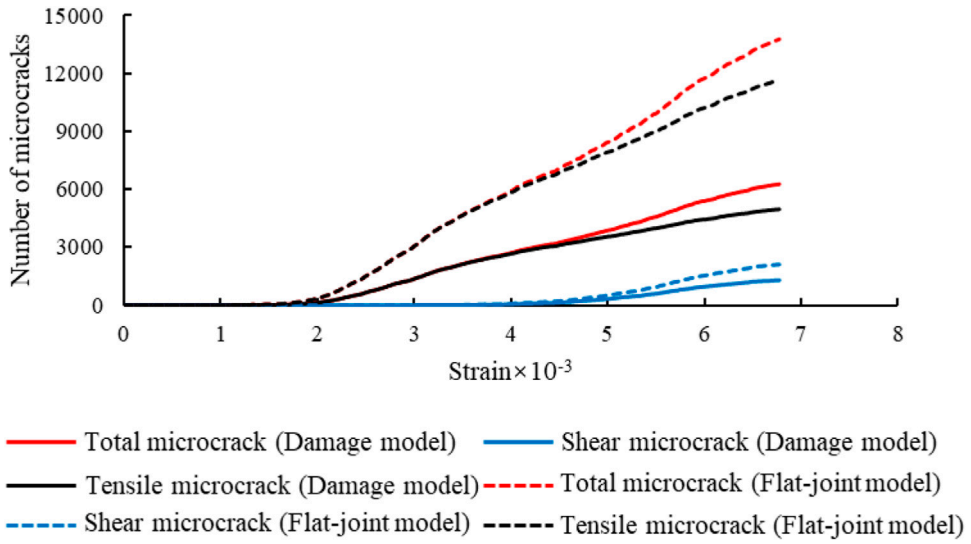


FIGURE 12
The variation curve of micro-fractures with strain during uniaxial compression failure of rock.

characteristics, and there are micro-fractures in the specimen. It can be seen from Figure 12 that the generated micro-fractures are mainly tensile failure micro-fractures. The number of tensile micro-fractures in the flat-joint damage model is significantly lower than that in the flat-joint model, that is, there are two failure modes between rock particles. With the increase of stress, the shear failure micro-fractures gradually appear in the sample. The comparison of tensile micro-fractures in two different models shows that the number of micro-fractures in contact damage and tensile failure continues to increase. When the stress reaches its peak, the shear failure micro-fractures increase rapidly, and the tensile failure micro-fractures increase linearly. When the strain exceeds the peak strength, the stress decreases, and the number of shear failure micro-fractures and tensile micro-fractures continues to increase. At this time, the rock sample is destroyed and a V-shaped shear fracture is formed. After stopping loading, a total of 6,265 micro-fractures are generated in the flat-joint damage model (including 4,968 tensile failure micro-fractures and 1,297 shear failure micro-fractures), and a total of 13,771 micro-fractures are generated in the flat-joint model (including 11,658 tensile failure micro-fractures and 2,113 shear failure micro-fractures). The number of tensile break micro-fractures in the flat-joint model is more than twice that of those in the flat-joint damage model. Therefore, in the process of core failure, there are two failure modes of shear failure and tensile failure at the contact, but the damage is mainly tensile failure. After reaching the peak stress, the shear micro-fractures appear rapidly and gradually form a V-shaped shear fracture throughout the whole specimen.

4.2 Influence of microscopic parameters on compression-tensile strength ratio and micro-fracture

Compressive strength, tensile strength and the compression and tension ratio are important factors affecting the mechanical properties of rock (Fener et al., 2005; Nazir et al., 2013). At the same time, the type of micro-fractures is an important factor affecting rock failure. Therefore, based on the above-mentioned uniaxial compression damage simulation research of rock, the numerical simulation of uniaxial compression and direct tension is further carried out to explore the influence of microscopic parameters on compressive strength, tensile strength, compression-tensile strength ratio and the change of fracture type.

(1) The effect of the microscopic modulus (E_c)

Figure 13 shows the influence curve of compressive strength and tensile strength with the change of microscopic parameter modulus. With the increase of microscopic modulus, the tensile strength changes little, the compressive strength increases rapidly at first and then slowly, while the compression-tensile strength ratio remains above 10, which is consistent with the trend of compressive strength. Therefore, the microscopic modulus has a small effect on the tensile strength and a great effect on the compressive strength, as well as a significant effect on the compression-tensile strength ratio.

(2) Influence of microscopic stiffness ratio (K_n/K_s)

Figure 14 shows the influence curve of the meso-parameter stiffness ratio on the strength. When the stiffness ratio is within the range of 1–2.4, the compressive strength fluctuates up and down to a certain extent. After the stiffness ratio is greater than 2.4, the tensile strength decreases with the increase of the stiffness ratio. The tensile strength decreases with the increase of microscopic stiffness ratio, while the compression-tensile strength ratio increases overall. Therefore, the variation of microscopic stiffness ratio has a definite effect on the compressive strength, tensile strength and compression-tensile strength ratio.

(3) The influence of microscopic friction coefficient μ) and microscopic friction angle Φ)

The friction coefficient μ) and the friction angle Φ) of the microscopic parameters have slight effect on the tensile strength, while the compressive strength and the compression-tensile strength ratio have some influence. As the microscopic coefficient of friction increases, the compressive strength and compression ratio increase, as shown in Figure 15 and Figure 16. The influence of microscopic friction angle on compressive strength and compression-tensile strength ratio is more significant than that of microscopic friction coefficient.

(4) Influence of microscopic tensile strength (σ_t)

Figure 17 shows the relationship between microscopic tensile strength and strength. When the microscopic tensile strength is in the range of 1–50 MPa, the compressive strength and tensile strength increase with the increase of microscopic tensile strength. However, the compression-tensile strength ratio is opposite. This is because as the inter-particle microscopic tensile strength increases, the resistance to tensile stress inside the specimen increases, and the proportion of tensile micro-fractures in all micro-fractures decreases, while the shear micro-fractures increase, as shown in Figure 18. When the inter-particle tensile strength increases to greater than the maximum shear stress inside the sample, there will be all shear micro-fractures inside the sample during the uniaxial compression test. That is to say, when the microscopic tensile strength increases from 50 MPa to 80 MPa, the compressive strength and tensile strength change little, at the same time, the ratio of compression-tensile strength also changes little. When the microscopic tensile strength exceeds 80 MPa, the compressive strength, tensile strength and compression-tensile strength ratio will remain unchanged.

(5) Effect of microscopic cohesion C)

Figure 19 shows the relationship between microscopic cohesion and strength. When the microscopic cohesion is within 5 MPa, the internal tensile strength of the sample is larger than the shear strength, so the micro-fractures of the sample are all shear micro-fractures (Figure 20). The tensile strength and compressive strength increase with the increase of microscopic cohesion, while the compression-tensile strength ratio decreases. When the microscopic cohesion is greater than 10 MPa, the compressive strength increases with the increase of the microscopic cohesion, the tensile strength remains unchanged, the compression-tensile strength ratio is consistent with the trend of the compressive strength, and the shear micro-fracture will decrease while the tensile micro-facture will increase.

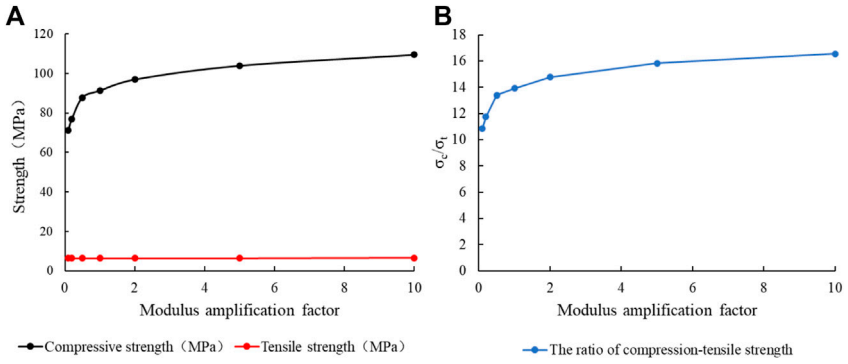


FIGURE 13
Relation curve between modulus (E_c) and strength: **(A)** Modulus (E_c); **(B)** Compression-tensile strength ratio.

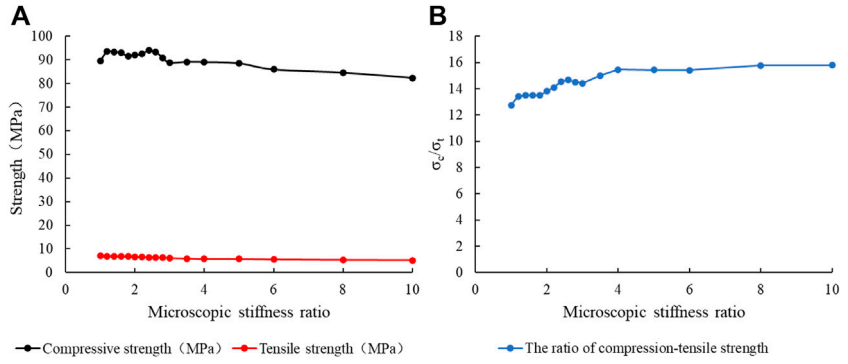


FIGURE 14
Relation curve between microscopic stiffness ratio and strength: **(A)** Microscopic stiffness ratio (K_n/K_s); **(B)** Compression-tensile strength ratio.

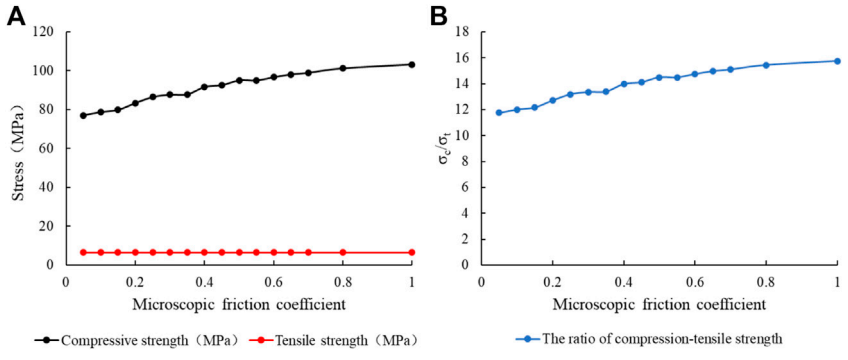


FIGURE 15
Relation curve between microscopic friction coefficient (μ) and microscopic strength: **(A)** Microscopic friction coefficient (μ); **(B)** Microscopic compression-tensile strength ratio.

5 Discussion

The microscopic parameters of rock are one of the important factors affecting the mechanical properties of rock. It is a key step to reveal the damage mechanism of rock by clarifying the change mechanism of rock properties under various parameters. The above research shows that, in addition to the tensile strength (microscopic), the rest of the rock meso-parameters change the ratio between the two micro-fractures by affecting the compressive strength of the rock. Under conventional conditions, the rock

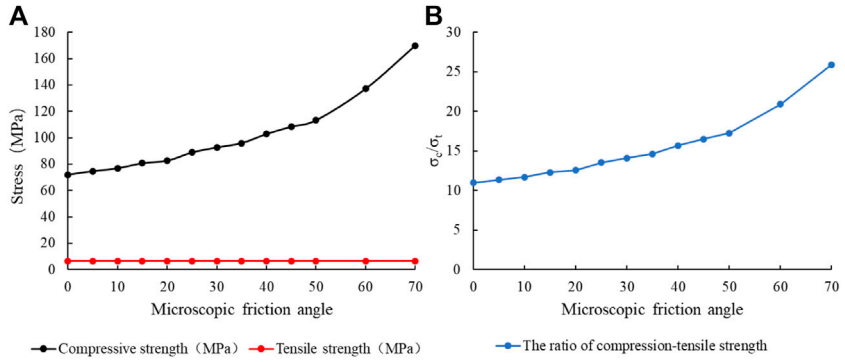


FIGURE 16
Relation curve between friction angle (Φ) and strength: **(A)** Friction angle (Φ); **(B)** Compression-tensile strength ratio.

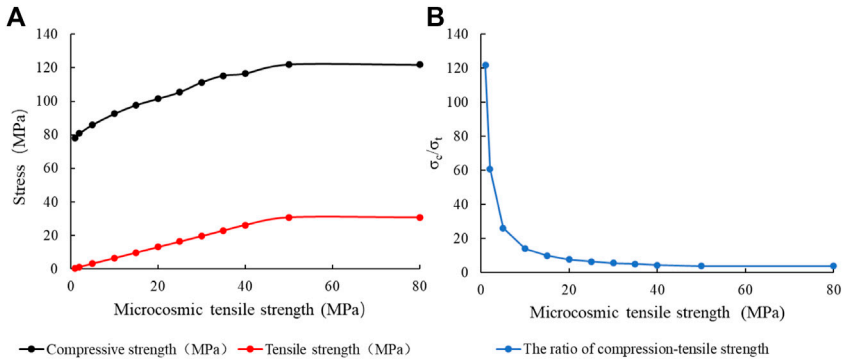


FIGURE 17
Relationship between microscopic tensile strength and strength: **(A)** Microscopic tensile strength (σ_t); **(B)** Compression-tensile strength ratio.

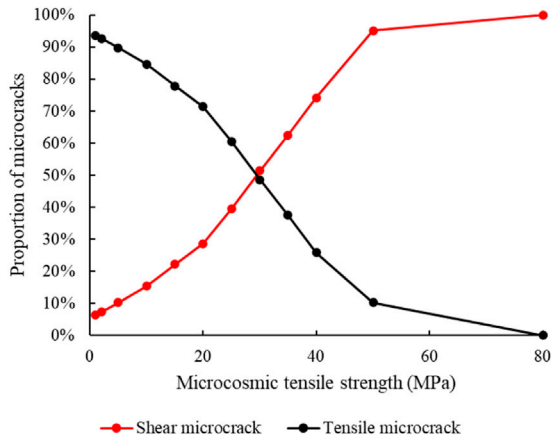


FIGURE 18
Influence curve of microscopic tensile strength (σ_c) on micro-fracture (UCS).

sample is squeezed from the height direction by uniaxial compression, and the two sides of the rock sample are continuously expanding outward under the action of internal force. Since the compressive strength of the rock is much greater than the tensile strength, the ability of the rock sample to withstand external expansion is much lower than the ability to withstand pressure. At this time, the inside of the rock sample slips downward while expanding to both sides, forming a large number of tensile micro-fractures, and the surface of the rock sample shows obvious V-shaped fractures. The compressive strength of the rock increases with the increase of rock microscopic parameters, but the tensile strength is almost unchanged. Compared with the normal condition, the vertical bearing capacity of the rock is greatly enhanced. Under the same pressure, the vertical displacement of the rock sample is smaller, but the outward expansion trend on both sides is almost unchanged, so it is difficult for the fracture to appear as a V-shape. However, the increase of pressure bearing capacity will inevitably lead to the accumulation of a large amount of pressure inside the rock, making the rock fracture more sudden and lack of buffer stage.

The absence of fracture buffer stage will make the rock fracture change from ductile failure to brittle failure, which is obviously unfavorable. In order to effectively identify the mechanism of rock failure, the ratio of compressive strength to tensile strength can be introduced to effectively predict the ratio of shear micro-fractures and tensile micro-fractures during rock failure, so as to determine the fracture mode of rock. However, how to accurately locate the transition point of rock fracture mechanism under compression-tensile strength ratio is still a difficult problem to be solved.

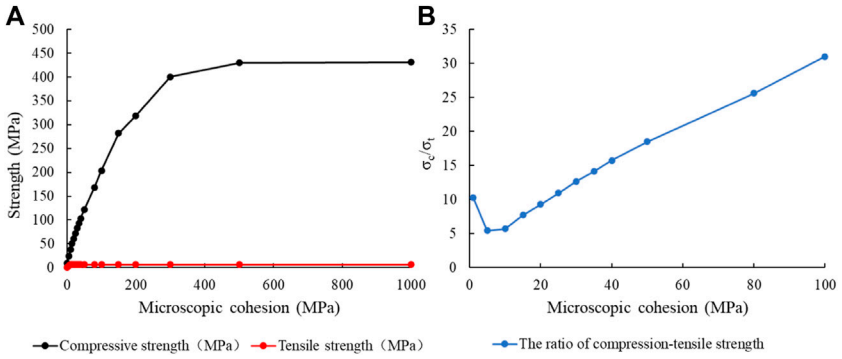


FIGURE 19
Relation curve between cohesion (C) and strength: **(A)** Microscopic cohesion (C); **(B)** Compression-tensile strength ratio.

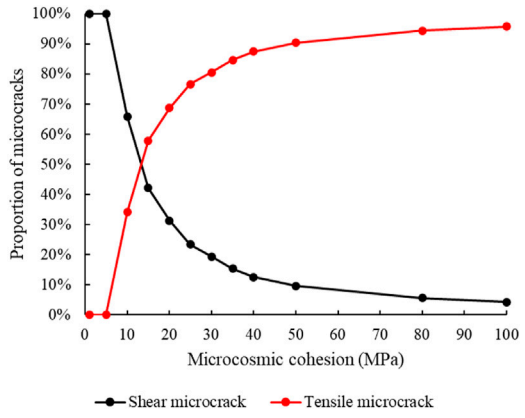


FIGURE 20
Influence curve of Microscopic cohesion (C) on micro-fracture (UCS).

6 Conclusion

In order to study the fracture evolution process of low permeability sandstone, a laboratory uniaxial compression experiment is conducted to investigate the failure mode and evolution process of rock. Secondly, using the discrete element method, the damage process of rock under uniaxial compression is simulated by the flat-joint model which can characterize the damage. The influence of various microscopic parameters on the strength of the sample and the type of micro-fractures are analyzed. The results show that.

(1) The fracture evolution is complex and varied, and the failure modes include tensile failure, shear failure, and tensile-shear failure;
(2) Internal micro-fractures will interconnect during rock destruction to form primary fractures through the rock mass, while secondary micro-fractures will also be generated;
(3) With the increase of external pressure, the rock mainly produces tensile micro-fractures accompanied by a few shear micro-fractures. When the rock damage reaches a certain extent, the shear micro-fractures and tensile micro-fractures increase rapidly. At this point, the micro-fractures interconnect with each other to form macroscopic main fractures and secondary fractures, and the rock presents V-shaped shear failure.
(4) Rock microscopic parameters mainly change the ratio between the two kinds of micro-fractures by affecting the compressive strength of the rock. The larger the microscopic parameters, the greater the compressive strength of the rock and the more tensile micro-fractures.

Data availability statement

The raw data supporting the conclusion of this article will be made available by the authors, without undue reservation.

Author contributions

JH: Data curation, Writing–original draft. JX: Software, Writing–original draft. XL: Project administration, Writing–review and editing. YR: Data curation, Writing–original draft. KD: Data curation, Writing–original draft. JT: Data curation, Investigation, Writing–original draft.

Funding

The author(s) declare financial support was received for the research, authorship, and/or publication of this article.

Acknowledgments

The authors acknowledge the support provided by the Ph.D. Programs Foundation of Southwest University of Science and Technology (19zx7104), Open Research Fund of State Key Laboratory of Geomechanics and Geotechnical Engineering, Institute of Rock and Soil Mechanics, Chinese Academy of Sciences (Grant No. Z020009), and natural science starting project of SWPU (No.2022QHZ009).

Conflict of interest

JX was employed by Downhole Operation Company, CNPC Xibu Drilling Engineering Co, Ltd.

The remaining authors declare that the research was conducted in the absence of any commercial or financial relationships that could be construed as a potential conflict of interest.

Publisher's note

All claims expressed in this article are solely those of the authors and do not necessarily represent those of their affiliated organizations, or those of the publisher, the editors and the reviewers. Any product that may be evaluated in this article, or claim that may be made by its manufacturer, is not guaranteed or endorsed by the publisher.

References

Bai, L., Huang, W., Qin, J., Zhang, Z., Ba, Z., Bai, Z., et al. (2023). Genesis and microscopic characteristics of tight reservoirs in the Fengcheng Formation, at the southern margin of the Mahu Sag. *Energy Geosci.* 4, 100162. doi:10.1016/j.engeos.2023.100162

Cundall, P. A., and Strack, O. D. (1979). A discrete numerical model for granular assemblies. *Geotechnique* 29, 47–65. doi:10.1680/geot.1979.29.1.47

Detournay, C., Damjanac, B., Torres, M., Cundall, P., Ligocki, L., and Gil, I. (2022). Heat advection and forced convection in a lattice code – implementation and geothermal applications. *Rock Mech. Bull.* 1, 100004. doi:10.1016/j.rockmb.2022.100004

Dontsov, E. V. (2022). Analysis of a constant height hydraulic fracture driven by a power-law fluid. *Rock Mech. Bull.* 1, 100003. doi:10.1016/j.rockmb.2022.100003

Du, K., Li, X., Su, R., Tao, M., Lv, S., Luo, J., et al. (2022). Shape ratio effects on the mechanical characteristics of rectangular prism rocks and isolated pillars under uniaxial compression. *Int. J. Min. Sci. Technol.* 32, 347–362. doi:10.1016/j.ijmst.2022.01.004

Fener, M., Kahraman, S., Bilgil, A., and Gunaydin, O. (2005). A comparative evaluation of indirect methods to estimate the compressive strength of rocks. *Rock Mech. Rock Eng.* 38, 329–343. doi:10.1007/s00603-005-0061-8

He, R., Yang, J., Li, L., Yang, Z., Chen, W., Zeng, J., et al. (2023). Investigating the simultaneous fracture propagation from multiple perforation clusters in horizontal wells using 3D block discrete element method. *Front. Earth Sci.* 11, 1–19. doi:10.3389/feart.2023.1115054

Huang, L., Dontsov, E., Fu, H., Lei, Y., Weng, D., and Zhang, F. (2022a). Hydraulic fracture height growth in layered rocks: perspective from DEM simulation of different propagation regimes. *Int. J. Solids Struct.* 238, 111395. doi:10.1016/j.ijsolstr.2021.111395

Huang, L., Tan, J., Fu, H., Liu, J., Chen, X., Liao, X., et al. (2023). The non-plane initiation and propagation mechanism of multiple hydraulic fractures in tight reservoirs considering stress shadow effects. *Eng. Fract. Mech.* 292, 109570. doi:10.1016/j.engfracmech.2023.109570

Huang, L., Liu, J., Ji, Y., Gong, X., and Qin, L. (2018). A review of multiscale expansion of low permeability reservoir cracks. *Petroleum* 4, 115–125. doi:10.1016/j.petlm.2017.09.002

Huang, L., Liu, J., Zhang, F., Dontsov, E., and Damjanac, B. (2019). Exploring the influence of rock inherent heterogeneity and grain size on hydraulic fracturing using discrete element modeling. *Int. J. Solids Struct.* 176–177, 207–220. doi:10.1016/j.ijsolstr.2019.06.018

Huang, L., Liu, J., Zhang, F., Fu, H., Zhu, H., and Damjanac, B. (2020). 3D lattice modeling of hydraulic fracture initiation and near-wellbore propagation for different perforation models. *J. Pet. Sci. Eng.* 191, 107169. doi:10.1016/j.petrol.2020.107169

Huang, Y., Yang, S., Tian, W., and Wu, S. (2022b). Experimental and DEM study on failure behavior and stress distribution of flawed sandstone specimens under uniaxial compression. *Theor. Appl. Fract. Mech.* 118, 103266. doi:10.1016/j.tafmec.2022.103266

Ji, Y., Wang, J., and Huang, L. (2015). Analysis on inflowing of the injecting Water in faulted formation. *Adv. Mech. Eng.* 7, 1–10. doi:10.1177/1687814015590294

Lai, Y., Zhao, K., He, Z., Yu, X., Yan, Y., Li, Q., et al. (2023). Fractal characteristics of rocks and mesoscopic fractures at different loading rates. *Geomech. Energy Environ.* 33, 100431. doi:10.1016/j.gete.2022.100431

Li, Q., Lu, H., Li, J., Wu, S., Wu, Y., Wen, L., et al. (2022). Characteristics and formation mechanism of the tight tuff reservoirs of the Upper Triassic Chang 7 member in the southern Ordos Basin, China. *Mar. Pet. Geol.* 139, 105625. doi:10.1016/j.marpetgeo.2022.105625

Liu, Y., Dong, X., Chen, Z., Hou, Y., Luo, Q., and Chen, Y. (2021). A novel experimental investigation on the occurrence state of fluids in microscale pores of tight reservoirs. *J. Pet. Sci. Eng.* 196, 107656. doi:10.1016/j.petrol.2020.107656

Luo, H., Xie, J., Huang, L., Wu, J., Shi, X., Bai, Y., et al. (2022). Multiscale sensitivity analysis of hydraulic fracturing parameters based on dimensionless analysis method. *Lithosphere* 2022. doi:10.2113/2022/9708300

Nazir, R., Momeni, E., Armaghani, D. J., and Amin, M. F. M. (2013). Correlation between unconfined compressive strength and indirect tensile strength of limestone rock samples. *Electron. J. Geotech. Eng.* 18 I, 1737–1746.

Potyondy, D. O. (2012). "A flat-jointed bonded-particle material for hard rock," in *46th US rock mech./geomech. Symp* (Chicago, Illinois: ACM), 1510–1519.

Potyondy, D. O., and Cundall, P. A. (2004). A bonded-particle model for rock. *Int. J. Rock Mech. Min. Sci.* 41, 1329–1364. doi:10.1016/j.ijrmms.2004.09.011

Tan, P., Jin, Y., Han, K., Hou, B., Guo, X., Gao, J., et al. (2017). Analysis of hydraulic fracture initiation and vertical propagation behavior in laminated shale formation. *Fuel* 206, 482–493. doi:10.1016/j.fuel.2017.05.033

Tan, P., Jin, Y., and Pang, H. (2021). Hydraulic fracture vertical propagation behavior in transversely isotropic layered shale formation with transition zone using XFEM-based CZM method. *Eng. Fract. Mech.* 248, 107707. doi:10.1016/j.engfracmech.2021.107707

Tan, P., Pang, H., Zhang, R., Jin, Y., Zhou, Y., Kao, J., et al. (2020). Experimental investigation into hydraulic fracture geometry and proppant migration characteristics for southeastern Sichuan deep shale reservoirs. *J. Pet. Sci. Eng.* 184, 106517. doi:10.1016/j.petrol.2019.106517

Tian, G., Deng, H., Xiao, Y., and Yu, S. (2022). Experimental study of multi-angle effects of micron-silica fume on micro-pore structure and macroscopic mechanical properties of rock-like material based on NMR and SEM. *Mater. (Basel)* 15, 3388. doi:10.3390/ma15093388

Wang, X., Song, Y., Guo, X., Chang, Q., Kong, Y., Zheng, M., et al. (2022). Pore-throat structure characteristics of tight reservoirs of the middle permian lucaogou formation in the jimsar sag, Junggar basin, northwest China. *J. Pet. Sci. Eng.* 208, 109245. doi:10.1016/j.petrol.2021.109245

Wu, M., Huang, R., and Wang, J. (2021). DEM simulations of cemented sands with a statistical representation of micro-bond parameters. *Powder Technol.* 379, 96–107. doi:10.1016/j.powtec.2020.10.047

Wu, S., and Xu, X. (2016). A study of three intrinsic problems of the classic discrete element method using flat-joint model. *Rock Mech. Rock Eng.* 49, 1813–1830. doi:10.1007/s00603-015-0890-z

Zhang, F., Damjanac, B., and Maxwell, S. (2019). Investigating hydraulic fracturing complexity in naturally fractured rock masses using fully coupled multiscale numerical modeling. *Rock Mech. Rock Eng.* 52, 5137–5160. doi:10.1007/s00603-019-01851-3

Zhang, F., Dontsov, E., and Mack, M. (2017). Fully coupled simulation of a hydraulic fracture interacting with natural fractures with a hybrid discrete-continuum method. *Int. J. Numer. Anal. Methods Geomech.* 41, 1430–1452. doi:10.1002/nag.2682

Zhang, F. S., Huang, L. K., Yang, L., Dontsov, E., Weng, D. W., Liang, H. B., et al. (2022). Numerical investigation on the effect of depletion-induced stress reorientation on infill well hydraulic fracture propagation. *Pet. Sci.* 19, 296–308. doi:10.1016/j.petsci.2021.09.014

Zhang, Z., Wang, E., Li, N., Zhang, H., Bai, Z., and Zhang, Y. (2023). Research on macroscopic mechanical properties and microscopic evolution characteristic of sandstone in thermal environment. *Constr. Build. Mater.* 366, 130152. doi:10.1016/j.conbuildmat.2022.130152

Zheng, Y., He, R., Huang, L., Bai, Y., Wang, C., Chen, W., et al. (2022). Exploring the effect of engineering parameters on the penetration of hydraulic fractures through bedding planes in different propagation regimes. *Comput. Geotech.* 146, 104736. doi:10.1016/j.compgeo.2022.104736

frontiers | Frontiers in Energy Research

TYPE Brief Research Report
PUBLISHED 29 September 2023
DOI 10.3389/fenrg.2023.1267228

Check for updates

OPEN ACCESS

EDITED BY
Xiaojin Zheng,
Princeton University, United States

REVIEWED BY
Chun Zhu,
Hohai University, China
Jun Yang,
Changzhou University, China

*CORRESPONDENCE
Yucai Shi,
shiyucai@upc.edu.cn
Bo Zhang,
zhangboupc@126.com

RECEIVED 26 July 2023
ACCEPTED 11 September 2023
PUBLISHED 29 September 2023

CITATION
Chu H, Xiong C, Hu K, Guo Y, Shi Y and Zhang B (2023), Enhancing the benefit of slide steering drilling systems in horizontal wells of unconventional reservoirs.
Front. Energy Res. 11:1267228.
doi: 10.3389/fenrg.2023.1267228

COPYRIGHT
© 2023 Chu, Xiong, Hu, Guo, Shi and Zhang. This is an open-access article distributed under the terms of the Creative Commons Attribution License (CC BY). The use, distribution or reproduction in other forums is permitted, provided the original author(s) and the copyright owner(s) are credited and that the original publication in this journal is cited, in accordance with accepted academic practice. No use, distribution or reproduction is permitted which does not comply with these terms.

Enhancing the benefit of slide steering drilling systems in horizontal wells of unconventional reservoirs

Hengzhi Chu[1], Chao Xiong[1], Kaili Hu[2], Yong Guo[1], Yucai Shi[3]* and Bo Zhang[4]*

[1]Engineering and Technology Research Institute, CNPC Xinjiang Oilfield Company, Karamay, Xinjiang, China, [2]Development Company, CNPC Xinjiang Oilfield Company, Karamay, Xinjiang, China, [3]School of Petroleum Engineering, China University of Petroleum (East China), Qingdao, Shandong, China, [4]CNPC Research Institute of Safety and Environment Technology, Beijing, China

The slide steering drilling system consisting of a bent positive displacement motor (PDM) and measurement while drilling (MWD) system is widely used to continuously implement all wellpath control operations by alternately applying the slide and compound drilling modes. Due to the large friction force on the drilling string during slide drilling in the horizontal section, there is a significant adverse impact on both the drilling speed and horizontal extension ability. To efficiently and economically drill long horizontal sections, it is essential to increase the compound drilling proportion and decrease the alternative times of the two drilling modes. According to the features of wavy or tortuous horizontal sections and wellpath calculation models, a prediction and control method for the compound drilling proportion of horizontal sections is first established, and subsequently, its influencing factors and laws are analyzed and verified using an example. Theoretical research and drilling practice have shown that the compound drilling proportion of the horizontal section depends on the build-up rate of slide drilling and the inclination and azimuth change rates of compound drilling and is independent of the target area parameters and wellpath fluctuation ratio. In order to increase the compound drilling proportion and reduce the slide drilling frequency in the horizontal section, it is necessary to increase the build-up rate of slide drilling properly and reduce the inclination and azimuth change rates of compound drilling to the greatest extent. This paper is helpful to enhance the benefit of slide steering drilling systems in horizontal wells of unconventional reservoirs.

KEYWORDS

slide steering drilling system, compound drilling, slide drilling, horizontal section, wellpath control, build-up rate, inclination change rate

1 Introduction

A horizontal well is an important method to develop unconventional reservoirs, like shale gas (Guo et al., 2019; Lu et al., 2021), tight oil, gas hydrate (Zhang et al., 2022a), and even deep reservoirs (Zhang et al., 2022b; Cao et al., 2022). The slide steering drilling system composed of a bent positive displacement motor (PDM) and measurement while drilling (MWD) system is widely used in horizontal wells. This system has two working modes, namely, slide drilling mode and compound drilling mode (Samuel et al., 2005;

Guan et al., 2021). By alternatively applying these two modes, it can continuously implement wellpath control operations without tripping operations. Currently, longer horizontal wells are being drilled to develop unconventional oil and gas (Guo et al., 2019; Lu et al., 2021; Yu et al., 2021; Ma et al., 2022). Because the drillstring does not rotate in the slide drilling mode, the friction force on the drillstring not only decreases the weight-on-bit transmission efficiency and causes low drilling speed but also influences the horizontal extension ability (Maidla and Haci, 2004; Samuel, 2010; Zhu et al., 2019).

Some researchers have pointed out that the actual wellpath of a horizontal section drilled by the slide steering drilling system is always in a wavy or tortuous shape, and the wellpath tortuosity influences the wellpath calculation, drag, and torque on the drillstring (Samuel et al., 2005; Samuel, 2010; Brands and Lowdon, 2012; Noshi and Schubert, 2019; Samuel et al., 2021). Some models have taken the wellpath tortuosity into account to enhance the calculation precision of the wellpath (Samuel et al., 2005; Noshi and Schubert, 2019) and the prediction precision of drag and torque on the drillstring (Samuel, 2010; Brands and Lowdon, 2012). Some researchers have realized that the wellpath tortuosity and drilling efficiency are influenced by the build-up rate of slide drilling and the inclination and azimuth change rates of compound drilling. Some models have been established to predict the build-up rate of slide drilling (Williams et al., 1989; Shi et al., 2017; Liu et al., 2019) or inclination and azimuth change rates of compound drilling (Peng and Di Qinfeng, 2000; Guo et al., 2013; Koulidis et al., 2021). Although it is well known that increasing the compound drilling proportion is the key to achieving fast and cost-effective drilling, the prediction and control method for the compound drilling proportion is still lacking.

In order to enhance the benefit of a slide steering drilling system, a prediction and control method for the compound drilling proportion of horizontal sections is established, and subsequently, its influencing factors and laws are analyzed.

2 Methods (compound drilling proportion of horizontal sections)

2.1 Wellpath description of the drilled horizontal section

As shown in Figure 1, the actual wellpath of the horizontal section drilled by a slide steering drilling system is always in a wavy or tortuous shape (Samuel et al., 2005; Noshi and Schubert, 2019). Because the inclination and azimuth commonly fluctuate slowly under compound drilling, the slide drilling must be alternated to decrease (or increase) the inclination and azimuth and control the wellpath within the target area once the drill bit is near the boundary lines of the horizontal target area. For a long horizontal section, two drilling modes may alternate multiple times. Then, the actual horizontal section has more control cycles. In one wavy cycle or control cycle, two drilling modes alternate once.

Suppose that the compound drilling tends to increase inclination and azimuth simultaneously, and then take the rectangular horizontal target area and the first wellpath control cycle as an example. The target half-width is set as a, and the target half-height is b; for the compound drilling interval, the starting point is No. 0 point, the lowest point on the vertical projection plot (the far left point on the horizontal plot) is No. 1 point, and the endpoint is No. 2 point; and for the slide drilling interval, the starting point is No. 2 point, the highest point (the far right point on the horizontal plot) is No. 3 point, and the last point is No. 4 point. To reduce the alternate times of slide and compound drilling, let the inclinations of the highest and lowest points on the vertical projection plot be equal

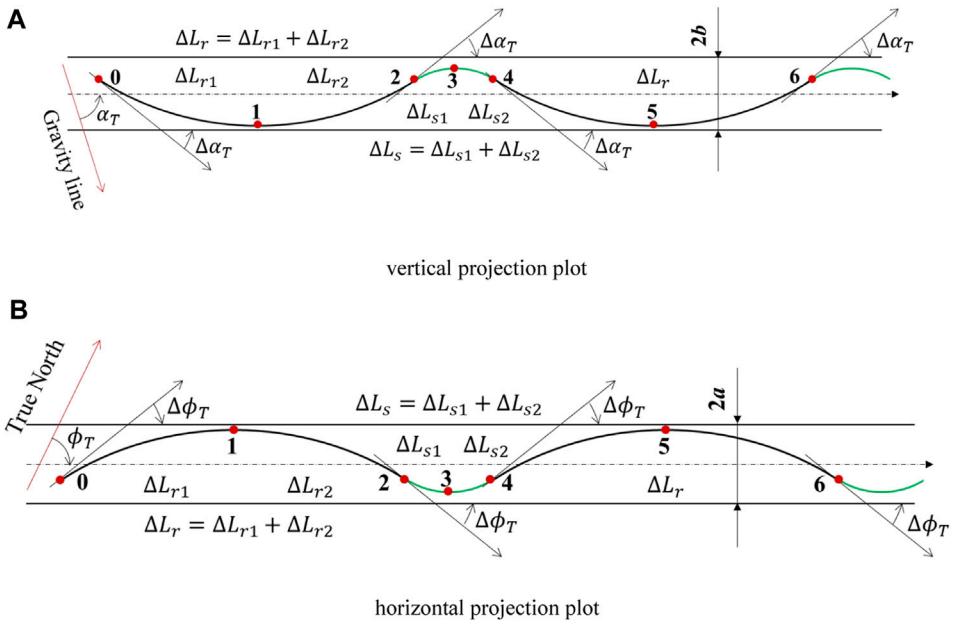


FIGURE 1
Actual wellpath of the horizontal section. **(A)** Vertical projection plot; **(B)** horizontal projection plot.

to the target inclination and the azimuths of the far left and right points on the horizontal plot be equal to the target azimuth. All node parameters of the actual horizontal section are presupposed and shown in Figure 1. For the compound drilling interval, the key parameters include the compound drilling length ΔL_r ($\Delta L_r = \Delta L_{r1} + \Delta L_{r2}$), the inclination change rate K_α, and azimuth change rate K_ϕ; for the slide drilling interval, the key parameters include the slide drilling length ΔL_s ($\Delta L_s = \Delta L_{s1} + \Delta L_{s2}$) and build-up rate K_s; and for these two intervals, the key parameters include the allowable inclination bias $\Delta\alpha_T$ and azimuth bias $\Delta\phi_T$.

2.2 Wellpath constraints of the drilled horizontal section

According to the wellpath calculation methods (Guan et al., 2021), the actual shapes of compound and slide drilling intervals are closest to the cylindrical spiral line and the inclined arc line, respectively. The cylindrical spiral method (curvature radius method) and inclined arc method (minimum curvature method) are applied alternatively to calculate all wellpath parameters of the actual horizontal section. According to the presupposed node parameters in Figure 1, the first wellpath control cycle from No. 0 point to No. 4 point can be divided into four intervals, and then all vertical depth increments ΔD_i (i = 1–4), N-coordinate increments ΔN_i (i = 1–4), E-coordinate increments ΔE_i (i = 1–4), and dog-leg angles γ_i can be calculated using Eqs 1–4, respectively:

$$\Delta D_i = \begin{cases} \frac{1}{K_\alpha}\left[\sin\alpha_i - \sin\alpha_{i-1}\right] & (i = 1, 2), \\ \frac{1}{K_s}\tan\frac{\gamma_i}{2}\left[\cos\alpha_{i-1} + \cos\alpha_i\right] & (i = 3, 4), \end{cases} \tag{1}$$

$$\Delta N_i = \begin{cases} \frac{1}{K_\phi \cdot \Delta\alpha_T}\left[\cos\alpha_{i-1} - \cos\alpha_i\right]\left[\sin\phi_i - \sin\phi_{i-1}\right] & (i = 1, 2), \\ \frac{1}{K_s}\tan\frac{\gamma_i}{2}\left[\sin\alpha_{i-1}\cos\phi_{i-1} + \sin\alpha_i\cos\phi_i\right] & (i = 3, 4), \end{cases} \tag{2}$$

$$\Delta E_i = \begin{cases} \frac{1}{K_\phi \cdot \Delta\alpha_T}\left[\cos\alpha_{i-1} - \cos\alpha_i\right]\left[\cos\phi_i - \cos\phi_{i-1}\right] & (i = 1, 2), \\ \frac{1}{K_s}\tan\frac{\gamma_i}{2}\left[\sin\alpha_{i-1}\sin\phi_i + \sin\alpha_i\sin\phi_i\right] & (i = 3, 4), \end{cases} \tag{3}$$

$$\cos\gamma_i = \cos\alpha_{i-1}\cos\alpha_i + \sin\alpha_{i-1}\sin\alpha_i\cos\left(\phi_i - \phi_{i-1}\right) \ (i = 1 \sim 4). \tag{4}$$

As shown in Figure 1, while drilling the horizontal section, the actual horizontal wellpath must be controlled within the target area, and then the actual wellpath of the horizontal section must meet the inequality constraint as follows:

$$\begin{cases} \left|\Delta D_2 + \Delta D_3\right|\sin\alpha_T \le 2b, \\ \left|\left(\Delta N_2 + \Delta N_3\right)\sin\phi_T + \left(\Delta E_2 + \Delta E_3\right)\cos\phi_T\right| \le 2a, \end{cases} \tag{5.a}$$

or

$$\begin{cases} \left|\Delta D_1 + \Delta D_4\right|\sin\alpha_T \le 2b, \\ \left|\left(\Delta N_1 + \Delta N_4\right)\sin\phi_T + \left(\Delta E_1 + \Delta E_4\right)\cos\phi_T\right| \le 2a. \end{cases} \tag{5.b}$$

If the designed target inclination $\alpha_T \neq 90°$ and/or target azimuth $\phi_T \neq 90°$, the next derivation process will be more complex. However, you can imagine that the horizontal section can be rotated in the horizontal direction on the vertical projection plot and in the east direction on the horizontal plot. After the rotation transformation, the shape of the actual horizontal section has not changed. Next, the node parameters in Figure 1 are substituted into Eqs 1–4 and then into Eq. 6. Finally, Eq. 6 can be deduced as follows:

$$\begin{cases} \frac{1-\cos\Delta\alpha_T}{K_\alpha} + \frac{\tan\frac{\gamma}{2}\sin\Delta\alpha_T}{K_s} \le 2b, \\ \frac{\sin\Delta\alpha_T\left[1-\cos\Delta\phi_T\right]}{K_\phi\cdot\Delta\alpha_T} + \frac{\tan\frac{\gamma}{2}\cos\Delta\alpha_T\sin\Delta\phi_T}{K_s} \le 2a, \\ \cos\gamma = \cos\Delta\alpha_T\cos\Delta\phi_T. \end{cases} \tag{6}$$

Considering the allowed inclination bias $\Delta\alpha_T$ and azimuth bias $\Delta\phi_T$, which are characterized by the parameters of the compound drilling interval (inclination change rate K_α, azimuth change rate K_ϕ, and length ΔL_r) and slide drilling interval (build-up rate K_s and length ΔL_s), Eq. 6 can be transformed into Eq. 7.

$$\begin{cases} \frac{1-\sin\left(K_\alpha\Delta L_r\right)}{K_\alpha} + \frac{\tan\frac{K_s\Delta L_s}{2}\sin\left(K_\alpha\Delta L_r\right)}{K_s} \le 2b, \\ \frac{\sin\left(K_\alpha.\Delta L_r\right)\left[1-\cos\left(K_\phi\Delta L_r\right)\right]}{K_\phi.K_\alpha.\Delta L_r} \\ \quad + \frac{\tan\frac{K_s\Delta L_s}{2}\cos\left(K_\alpha\Delta L_r\right)\sin\left(K_\phi\Delta L_r\right)}{K_s} \le 2a, \\ \cos\left(K_s\Delta L_s\right) = \cos\left(K_\alpha\Delta L_r\right)\cos\left(K_\phi\Delta L_r\right). \end{cases} \tag{7}$$

From Eqs 6, 7, it can be observed that

(1) Once the target half-width a and target half-height b are given, the maximum allowed inclination bias $\Delta\alpha_T$ and azimuth bias $\Delta\phi_T$ of the horizontal section, the maximum allowed compound drilling length ΔL_r, and slide drilling length ΔL_s in one wellpath control cycle depend on the build-up rate K_s of slide drilling and the inclination change rate $K_\alpha$and azimuth change rate K_ϕ of compound drilling.

(2) Once the build-up rate K_s of slide drilling and the inclination change rate K_α and the azimuth change rate K_ϕ of compound drilling are given, the maximum allowed inclination bias $\Delta\alpha_T$ and azimuth bias $\Delta\phi_T$ of the horizontal section can be solved using Eq. 6, and the maximum allowed compound drilling length ΔL_r and slide drilling length ΔL_s of the horizontal section in one wellpath control cycle can be solved using Eq. 7.

2.3 Compound drilling proportion of the horizontal section

In one wellpath control cycle of the horizontal section, the allowed compound drilling length is ΔL_r, the slide drilling length is ΔL_s, and the compound drilling proportion c_r is defined and calculated using Eq. 8.

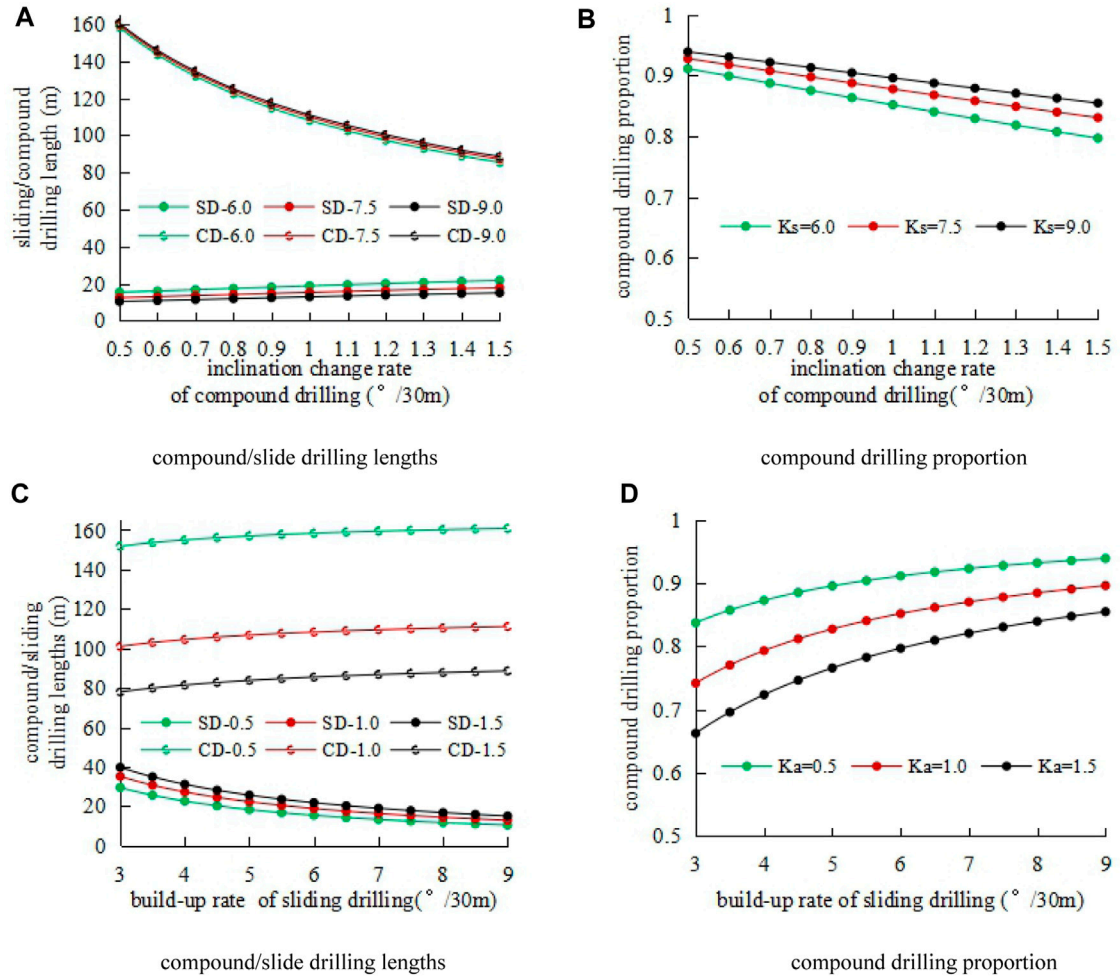


FIGURE 2
Compound drilling results vs. build-up rate. **(A)** Compound/slide drilling lengths; **(B)** compound drilling proportion; **(C)** compound/slide drilling lengths; **(D)** compound drilling proportion.

$$c_r = \frac{\Delta L_r}{\Delta L_r + \Delta L_s}. \tag{8}$$

If the build-up rate K_s of slide drilling and the inclination change rate K_α, and azimuth change rate K_ϕ of compound drilling are given, the maximum allowed compound drilling length ΔL_r and slide drilling length ΔL_s in one wellpath control cycle can be solved using Eq. 7. In fact, according to the last formula in Eq. 7, another relationship among these five characteristic parameters can be derived as follows:

$$\begin{cases} K_s \cdot \Delta L_s > |K_\alpha| \cdot \Delta L_r, \\ K_s \cdot \Delta L_s > |K_\phi| \cdot \Delta L_r. \end{cases} \tag{9}$$

According to Eq. 9, the upper limit of the compound drilling proportion c_r can be estimated as follows:

$$c_r = \frac{\Delta L_r}{\Delta L_r + \Delta L_s} < \min\left(\frac{K_s}{|K_\alpha| + K_s}, \frac{K_s}{|K_\phi| + K_s}\right). \tag{10}$$

Because the inclination change rate K_α and azimuth change rate K_ϕ of compound drilling may be positive (the inclination and azimuth increase) or negative (the inclination and azimuth decrease), these two values in Eqs 9, 10 must use their absolute values.

According to Eq. 10, it can be observed that the compound drilling proportion of the horizontal section depends on the build-up rate K_s of slide drilling and the inclination change rate K_α and azimuth change rate K_ϕ of compound drilling and is independent of the target parameters and wavy amplitude of the horizontal section. In order to enhance the compound drilling proportion for faster and more cost-effective drilling, the build-up rate K_s of slide drilling should be enhanced properly, and then the inclination change rate K_α and azimuth change rate K_ϕ of compound drilling should be reduced to the greatest extent.

3 Results (influencing factors and laws of the compound drilling proportion)

3.1 Inclination change rate of compound drilling

According to the actual horizontal drilling data, the target area is set at 1.0 m (target half-height) × 6.0 m (target half-width), and then the key parameters of slide and compound drilling are set as follows:

the build-up rates K_s = 6.0°–9.0°/30 m (6.0°/30 m for 1.0° bent PDM, 7.5°/30 m for 1.25° bent PDM, and 9.0°/30 m for 1.5° bent PDM), the inclination change rate K_α = 0.1°–1.5°/30 m, and azimuth change rate K_ϕ = 0.3°/30 m. The drilling results are estimated using Eqs 7, 8 and shown in Figures 2A, B. In the legend zone, "SD" and "CD" represent "slide drilling" and "compound drilling," respectively, and the numbers represent the build-up rate (unit: °/30 m) of slide drilling.

If the inclination change rate of compound drilling increases, the compound drilling length ΔL_r decreases significantly, but the slide drilling length ΔL_s increases slightly, and then the compound drilling proportion decreases obviously. For a given inclination change rate under compound drilling, if the build-up rate of slide drilling increases, the compound drilling length ΔL_r increases slightly, but the slide drilling length ΔL_s decreases obviously, and then the compound drilling proportion increases obviously. It is proved that increasing the build-up rate K_s of slide drilling and reducing the inclination change rate K_α and azimuth change rate K_ϕ of compound drilling contribute to increasing the compound drilling length and proportion of the horizontal section.

3.2 Build-up rate of slide drilling

Taking 1.25° bent PDM as an example, the build-up rate of slide drilling is set at 7.5°/30 m, the inclination change rate of compound drilling is set at 0.5°–1.5°/30 m, and the azimuth change rate is set at 0.3°/30 m, and then the drilling results are estimated using Eqs 7, 8 and shown in Figures 2C, D. In the legend zone, "SD" and "CD" represent "slide drilling" and "compound drilling," respectively, but the numbers represent the inclination change rates (unit: °/30 m) of compound drilling.

If the build-up rate of slide drilling increases, the compound drilling length ΔL_r increases slightly, but the slide drilling length ΔL_s decreases obviously, and then the compound drilling proportion increases obviously. For a given build-up rate under slide drilling, if the inclination change rate of compound drilling increases, the compound drilling length ΔL_r decreases significantly, but the slide drilling length ΔL_s increases slightly, and then the compound drilling proportion decreases obviously. It is proved again that increasing the build-up rate K_s of slide drilling and reducing the inclination change rate K_α and azimuth change rate K_ϕ of compound drilling contribute to increasing the compound drilling length and proportion of the horizontal section.

3.3 Case analysis

3.3.1 Drilling results

The LS3-3 horizontal well is located in China. The designed horizontal section is approximately 1200 m. The target area is 1.0 m (target half-height) × 6.0 m (target half-width). Target inclination is 88.15°, and target azimuth is 161.29°. Bottom-hole assembly (BHA) and drilling parameters are described as follows: BHA: φ152.4 mm PDC bit + φ127 mm bent PDM (1.25 for the first run and 1° for the second run) + float valve + Φ148 mm stabilizer + LWD + Φ96 mm non-magnetic drill pipe. Drilling parameters: weight on bit 30 kN, top drive speed 50 r/min, and drilling fluid flowrate 18 L/s.

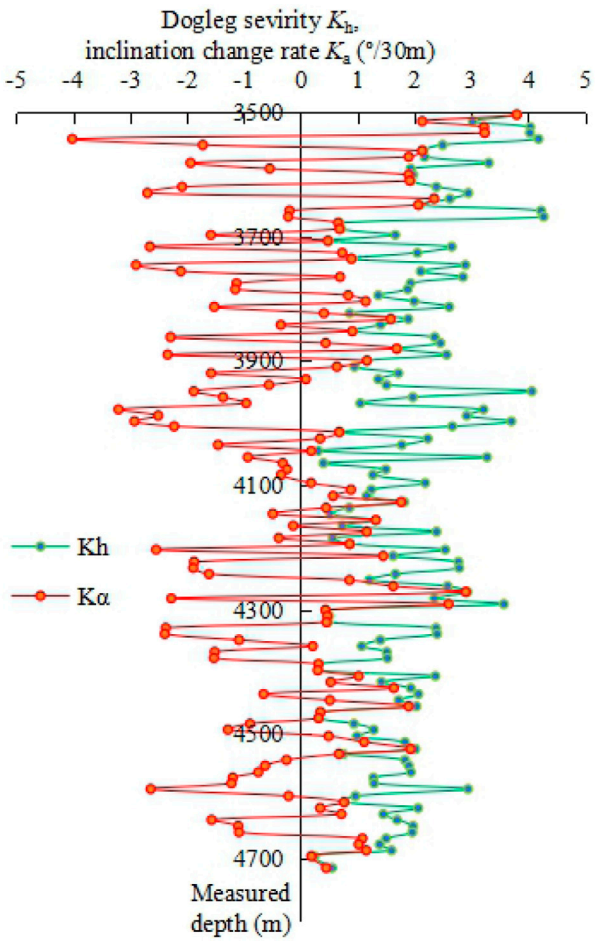


FIGURE 3
Dogleg severity and inclination change rate.

The statistical horizontal section length is 1,138.66 m, and the alternation time of two drilling modes is 58 in total. Wellbore curvature (dogleg severity) and inclination change rate are shown in Figure 3. For the compound drilling, the inclination mainly increases and the azimuth mainly maintains the same change rate; the average inclination and azimuth change rates are approximately 0.5°/30 m and 0.2°/30 m, respectively; the cumulative length is 1,036.9 m; the average interval length is 17.9 m/time; the maximum interval length is 66.5 m; and the compound drilling proportion is 91.1%. For slide drilling, the build-up rates are approximately 7.5°/30 m and 6.0°/30 m for the first and second runs, respectively; the cumulative length is 101.8 m; the average interval length is 1.8 m/time; the maximum interval length is 3.4 m; and the slide drilling proportion is 8.9%.

3.3.2 Verifying analysis

Based on the statistical results, the build-up rate of slide drilling is set at 6.0°–7.5°/30 m and the inclination and azimuth change rates of compound drilling are set at 0.5°/30 m and 0.2°/30 m, respectively; the wellbore fluctuation ratio (amplitude of fluctuation vs. target height) is set at 0.5–0.6. The drilling results of the horizontal section are estimated

TABLE 1 Prediction results of slide and compound drilling.

K_s (°/30 m)	c_f	ΔL_r (m)	ΔL_s (m)	c_r (%)
6.0	0.5	158.8	14.3	91.8 (92.3)
6.0	0.6	174.0	15.6	91.8 (92.3)
7.5	0.5	160.2	11.5	93.3 (93.8)
7.5	0.6	175.5	12.6	93.3 (93.8)

and shown in Table 1. Here, c_f is the wellbore fluctuation ratio equal to $\frac{\Delta D}{2b}$ (ΔD is the fluctuation amplitude along the wellbore axis on the vertical projection plot; b is the target half-height); the compound drilling proportions outside and inside brackets are estimated using Eqs 7, 10, respectively. Subsequently, the values outside brackets are set as the theoretical values; the values inside brackets are set as the estimated values.

Eq. 10 can estimate the compound drilling proportion. The theoretical prediction results show that the slide drilling length is approximately 11.5–15.6 m and the compound drilling length is approximately 158.8–175.5 m in one cycle. The compound drilling proportion is approximately 91.8%–93.3%. The actual drilling results show that the compound drilling length is approximately 17.9 m/time, the slide drilling length is approximately 1.77 m/time, and the compound drilling proportion is approximately 91.1%. The compound drilling proportion is in good agreement with the theoretical results, but the compound drilling and slide drilling lengths are less than the theoretical values. One reason is that the actual wellpath has a lagging effect while alternating compound or slide drilling modes (Su, 2000). Another reason is that the target half-height is only 1.0 m. As a result, the directional drilling engineer had to increase the wellpath adjustment frequency and shorten the interval lengths to avoid missing of the target.

3.3.3 Suggestions

The bottom-hole assembly and drilling parameters should be optimized totally to properly increase the build-up rate of slide drilling and reduce the inclination and azimuth change rates of compound drilling to the greatest extent. To achieve this purpose, BHA with two stabilizers (one stabilizer fixed near the drill bit and the other stabilizer fixed above the bent PDM) and medium weight-on-bit (WOB) are recommended (Peng and Di Qinfeng, 2000; Guo et al., 2013; Koulidis et al., 2021). At the same time, more attention should be paid to the formation. The lithology and mechanical properties of the pay zone also have a significant influence on drilling results (Yin et al., 2021; Zhu et al., 2021; Cao et al., 2022).

4 Conclusion

(1) The compound drilling proportion of the horizontal section is independent of the target parameters and the wellbore fluctuation amplitude but depends on the build-up rate of slide drilling and the inclination and azimuth change rates of compound drilling.
(2) The compound drilling proportion of the horizontal section can be estimated by the build-up rate of slide drilling and the inclination and azimuth change rates of compound drilling.
(3) To enhance the compound drilling proportion of the horizontal section and reduce the adjustment frequency of slide drilling, it is necessary to increase the build-up rate of slide drilling and reduce the inclination and azimuth change rates of compound drilling.

Data availability statement

The original contributions presented in the study are included in the article/Supplementary material; further inquiries can be directed to the corresponding authors.

Author contributions

HC: writing–original draft. CX: writing–review and editing. KH: writing–review and editing. YG: writing–original draft. YS: writing–original draft and funding acquisition. BZ: formal analysis and writing–review and editing.

Funding

The author(s) declare that financial support was received for the research, authorship, and/or publication of this article. This study was supported by the Major Project of National Science and Technology "Development of Rotary Steerable Drilling System (2016ZX05022-002)" and Major Project of China National Petroleum Corporation "Research and application of key technologies for exploration and development of medium and high maturity continental shale oil (2019E-2605)." The funder was not involved in the study design, collection, analysis, interpretation of data, the writing of this article, or the decision to submit it for publication. This research was also sponsored by Beijing Nova Program.

Conflict of interest

Authors HC, CX, and YG were employed by the company Engineering and Technology Research Institute, CNPC Xinjiang Oilfield Company. Author KH was employed by the company Development Company, CNPC Xinjiang Oilfield Company.

The remaining authors declare that the research was conducted in the absence of any commercial or financial relationships that could be construed as a potential conflict of interest.

Publisher's note

All claims expressed in this article are solely those of the authors and do not necessarily represent those of their affiliated organizations, or those of the publisher, the editors, and the reviewers. Any product that may be evaluated in this article, or claim that may be made by its manufacturer, is not guaranteed or endorsed by the publisher.

References

Brands, S., and Lowdon, R. (March 2012). Scaled tortuosity index: quantification of borehole undulations in terms of hole curvature, clearance and pipe stiffness. Proceedings of the IADC/SPE drilling conference and exhibition, San Diego, California, USA.

Cao, L., Sun, J., Zhang, B., Lu, N., and Xu, Y. (2022). Sensitivity analysis of the changing law of temperature profile in the production string of the high-pressure high temperature gas well considering the coupling relation among the gas flow friction, gas properties, temperature and pressure. *Front. Phys.* 10, 1050229. doi:10.3389/fphy.2022.1050229

Guan, Zhichuan, Chen, Tinggen, and Liao, Hualin (2021). *Theory and Technology of drilling engineering*. Singapore: Springer.

Guo, X., Li, Y., Li, J., Feng, M., and Duan, H. (2019). Discovery of fuling shale gas field and its prospects. *Front. Energy* 13 (2), 354–366. doi:10.1007/s11708-018-0581-z

Guo, Zonglu, Gao, Deli, and Zhang, Hui (2013). Analysis and optimization of holding-inclination capability of steerable assembly with single bend and two stabilizers. *Pet. Drill. Tech.* 41 (6), 19–24.

Koulidis, A., Kelessidis, V., and Ahmed, S., (May 2021). Exploitation of field drilling data with an innovative drilling simulator: highly effective simulation of rotating and sliding mode. Proceedings of the SPE/IADC Middle East drilling Technology conference and exhibition, Abu Dhabi, UAE.

Liu, H., Ma, T., Chen, P., Wang, X., and Wang, X. (2019). Mechanical behaviors of bottom hole assembly with bent-housing positive displacement motor under rotary drilling. *Arabian J. Sci. Eng.* 44, 6029–6043. doi:10.1007/s13369-017-2564-5

Lu, N., Zhang, B., Wang, T., and Fu, Q. (2021). Modeling research on the extreme hydraulic extension length of horizontal well: impact of formation properties, drilling bit and cutting parameters. *J. Petroleum Explor. Prod.* 11 (3), 1211–1222. doi:10.1007/s13202-021-01106-4

Ma, T., Liu, J., Fu, J., and Wu, B. (2022). Drilling and completion technologies of coalbed methane exploitation: an overview. *Int. J. Coal Sci. Technol.* 9 (1), 68. doi:10.1007/s40789-022-00540-x

Maidla, E., and Haci, M. (January 2004). Understanding torque: the key to slide-drilling directional wells. Proceedings of the IADC/SPE drilling conference, Dallas, Texas, USA.

Noshi, C. I., and Schubert, J. J. (March 2019). Calculating a tortuosity index metric using machine learning techniques, Proceedings of the SPE/IADC international drilling conference and exhibition, Hague, The Netherlands.

Peng, Guorong, and Di Qinfeng, (2000). Predication of steering ability of the slide steering assembly in compounding drilling mode. *Pet. Drill. Tech.* 28 (6), 4–5.

Robello, Samuel. (March 2010). Friction factors: what are they for torque, drag, vibration, bottom hole assembly and transient surge/swab analyses? Proceedings of the IADC/SPE drilling conference and exhibition, New Orleans, Louisiana, USA.

Robello, Samuel, Jonathan Dale, Lightfoot, and William, Turner. (September 2021). Mechanical and geometrical tortuosities: vanishing and appearing tortuosities. Proceedings of the SPE annual technical conference and exhibition, Dubai, UAE.

Robello, Samuel, Kaiwan, Bharucha, and Yuejin, Luo. (February 2005). Tortuosity factors for highly tortuous wells: A practical approach. Proceedings of the SPE/IADC drilling conference, Amsterdam, The Netherlands.

Shi, Yucai, Guan, Zhichuan, Zhao, Hongshan, and Huang, Genlu (2017). A new method for build-up rate prediction of bottom-hole assembly in well drilling. *J. China Univ. Petroleum* 41 (1), 85–89.

Su, Yinao (2000). *Wellpath control of horizontal well*. Beijing, China: Petroleum Industry Press.

Williams, J. B., Apostal, M. C., and Haduch, G. A. (October 1989). An analysis of predicted wellbore trajectory using a three-dimensional model of a bottomhole assembly with bent sub, bent housing, and eccentric contact capabilities. Proceedings of the SPE annual technical conference and exhibition, San Antonio, Texas.

Yin, Q., Wu, J., Jing, H., He, M., and Meng, Q. (2021). Shear mechanical responses of sandstone exposed to high temperature under constant normal stiffness boundary conditions. *Geomechanics Geophys. Geo-Energy Geo-Resources* 7, 35 doi:10.1007/s40948-021-00234-9

Yu, R., Guo, W., Ding, L., Wang, M., Cheng, F., Zhang, X., et al. (2021). Quantitative characterization of horizontal well production performance with multiple indicators: A case study on the weiyuan shale gas field in the sichuan basin, China. *Front. Earth Sci.* 15 (2), 395–405. doi:10.1007/s11707-021-0885-x

Zhang, B., Jiang, R., Sun, B., Lu, N., Hou, J., Bai, Y., et al. (2022a). Establishment of the productivity prediction method of Class III gas hydrate developed by depressurization and horizontal well based on production performance and inflow relationship. *Fuel* 308, 122006. doi:10.1016/j.fuel.2021.122006

Zhang, B., Lu, N., Guo, Y., Wang, Q., Cai, M., and Lou, E. (2022b). Modeling and analysis of sustained annular pressure and gas accumulation caused by tubing integrity failure in the production process of deep natural gas wells. *J. Energy Resour. Technol.* 144 (6), 063005. doi:10.1115/1.4051944

Zhu, C., He, M., Zhou, Y., Qin, X. z., and Yin, Q. (2021). Numerical investigation on the fatigue failure characteristics of water-bearing sandstone under cyclic loading. *J. Mt. Sci.* 18 (12), 3348–3365. doi:10.1007/s11629-021-6914-0

Zhu, Xiaohua, Li, Ke, and An, Jiawei (2019). Calculation and analysis of dynamic drag and torque of horizontal well strings. *Nat. Gas. Ind. B* 6, 183–190. doi:10.1016/j.ngib.2018.08.004

frontiers | Frontiers in Energy Research

TYPE Original Research
PUBLISHED 01 November 2023
DOI 10.3389/fenrg.2023.1297738

Check for updates

OPEN ACCESS

EDITED BY
Peng Tan,
CNPC Engineering Technology R & D Company Limited, China

REVIEWED BY
Mengfei Zhou,
The University of Texas at Austin, United States
Han Jia,
China University of Petroleum, China

*CORRESPONDENCE
Xitang Lan,
lanxitang522@163.com

RECEIVED 20 September 2023
ACCEPTED 02 October 2023
PUBLISHED 01 November 2023

CITATION
Liu Y, Zou J, Lan X, Gao S, Zhang L and He X (2023), Research on imbibition effect of surfactant fracturing fluid in offshore reservoirs with low permeability and high temperature.
Front. Energy Res. 11:1297738.
doi: 10.3389/fenrg.2023.1297738

COPYRIGHT
© 2023 Liu, Zou, Lan, Gao, Zhang and He. This is an open-access article distributed under the terms of the Creative Commons Attribution License (CC BY). The use, distribution or reproduction in other forums is permitted, provided the original author(s) and the copyright owner(s) are credited and that the original publication in this journal is cited, in accordance with accepted academic practice. No use, distribution or reproduction is permitted which does not comply with these terms.

Research on imbibition effect of surfactant fracturing fluid in offshore reservoirs with low permeability and high temperature

Yigang Liu[1], Jian Zou[1], Xitang Lan[1]*, Shang Gao[1], Liping Zhang[1] and Xin He[2]

[1]Tianjin Branch Research Institute, Tianjin, China, [2]Key Laboratory of Enhanced Oil and Gas Recovery of Ministry of Education, Northeast Petroleum University, Daqing, Heilongjiang, China

Surfactant imbibition can effectively improve the development effect of fracturing technique. In order to enhance oil recovery, a temperature resistant surfactant was selected using interfacial tension and contact angle testers based on the offshore reservoir conditions of high temperature and low permeability. Experiments on spontaneous and forced imbibition with artificial columnar cores were performed to optimize parameters of imbibition processes during fracturing in high temperature and low permeability reservoirs. Results show that among the three surfactants, amphoteric Gemini surfactant had a stable molecular structure with non-compressible hydrophobic groups which significantly reduced oil-water interfacial tension, enhanced rock wettability, and demonstrated good resistance to high temperatures The maximum recovery increase during amphoteric Gemini surfactant imbibition is 16.22%. The higher the core permeability, the higher the core inside pressure, and the longer the well shut-in time, the greater the forced imbibition effect. A proper well shut-in time and injection volume should be considered when using surfactant solution as fracturing liquid.

KEYWORDS

surfactants, imbibition effect, offshore oilfields, high temperature, low permeability, physical simulation

1 Introduction

China's demand for oil and gas resources increases annually and offshore oilfields occupy an important position in the oil and gas supply field. Continuous development in China's offshore oilfields has resulted in a greater proportion of crude oil reserves in low-permeability reservoirs, as well as increasing development difficulties (Cao et al., 2022; Han et al., 2022; Lin et al., 2022). Block Z of the Bohai Oilfield is characterized by high-temperature and low-permeability. Its oil has low density, low viscosity, low sulfur content, high wax content, and a high solidification point (Wei and Liu, 2019; Zhong et al., 2020; Xu et al., 2021). Besides, this reservoir is a structural layered reservoir with a complex oil-water relationship influenced by fault cutting, along with poor inter-well connectivity (Abbassi et al., 2022). During the initial stage of oil production, crude oil has good properties, a strong self-jet ability, a high production ability, and a long period of low water-cut (Dontsov, 2022;

Ma et al., 2022). But, when a well encounters water, its production capacity falls off significantly and quickly. A fracturing technique is an effective way to decrease the seepage resistance (Tan et al., 2023; Huang et al., 2023a), and then increase the production of low permeability oil wells (Tan et al., 2021; Huang et al., 2023b). However, hundreds of cubic meters of guar gum or gel fracturing fluid can not only supply the formation energy, but also reduce the matrix permeability near the fracture due to its wall building property. Therefore, the current offshore fracturing technique has limited oil-increasing effects because of reservoir physical properties. The method to use surfactant solution as fracturing liquid to enhance imbibition function has shown to be an effective strategy to further improve oil recovery.

Due to the effectiveness of imbibition of surfactant in the fracturing fluid to develop a low permeability reservoir, petroleum technology professionals have studied spontaneous imbibition extensively under the condition of unconnected wells. Wang et al. developed a static imbibition mathematical model for the numerical simulation of spontaneous imbibition, which considered the influence of imbibition driving forces such as capillary force and gravity on imbibition oil recovery (Wang et al., 2022; Marzhan et al., 2023). Through spontaneous imbibition experiments, Xu et al. investigated the mechanism of core imbibition oil displacement under different permeabilities, and concluded that better pore structure can enhance spontaneous imbibition (Xu and Ma, 2015). Li et al. used numerical modeling to explore the influence of fracturing fluid interfacial tension on spontaneous imbibition in low permeability reservoirs (Li et al., 2018). Based on low field nuclear magnetic resonance testing, Wang et al. carried out on-line scanning of core nuclear magnetic resonance under five boundary conditions. Zhu et al. studied the effects of different hydrophilic and hydrophobic structures on spontaneous imbibition in high temperature, high salinity and low permeability reservoirs (Zhu et al., 2021). Cai et al. analyzed the discriminant parameters of spontaneous imbibition mechanism including interfacial tension and wetting angle (Cai and Yu, 2012).

Currently, spontaneous imbibition is the main experimental technique used to explore imbibition in low-permeability cores, and the experiment temperature is often not more than 100°C. There are few studies considering external fluid pressure on the imbibition effect in high-temperature and low-permeability reservoirs (Gushchin et al., 2018; Bai et al., 2021; Liu et al., 2023). Therefore, in view of the characteristics of high temperature, insufficient productivity and disconnection between wells in Block Z of Bohai Oilfield, this paper studied the imbibition development effect of high temperature resistant surfactant through spontaneous and forced imbibition experiments. The type and concentration of imbibition agent suitable for target reservoir were optimized by static imbibition and forced imbibition physical simulation experiments. The influence mechanism of factors such as shut-in pressure, shut-in time and core permeability on the forced imbibition effect. The related study can provide theoretical basis for the practical construction in Block Z.

2 Experimental section

2.1 Experimental materials

Experimental agents include: lauryl alcohol sodium sulfate (anionic), effective content of 30%; lauric acid (anionic), effective content of 40%; Gemini surfactant (amphoteric), content of 40%; heavy water (D_2O), deuterium element could effectively shield nuclear magnetic signal, effective content of 99.9%.

The water used in spontaneous imbibition and forced imbibition is simulated injection water, and is prepared by using distilled water and heavy water, respectively. The ionic composition of injection water is shown in Table 1. The experimental oil was prepared by mixing degassed crude oil and light hydrocarbon in Bohai oilfield, with a viscosity of 5.0 mPa s at 138°C.

In this study, the effects of the surfactant imbibition ratio on spontaneous imbibition and forced imbibition were investigated using artificial hydrophilic columnar cores cemented by quartz sands (Ø2.5 × 5.0 cm) (Han et al., 2016; Xie et al., 2018). The permeabilities of these cores were approximately 20mD, 60mD, respectively, and their pore structures and permeabilities were comparable to reservoir cores in the Bohai oilfields. The procedures to prepare the artificial cores can be found in the Chinese patent "Quartz sand epoxy resin cementation heterogeneity model making method".

2.2 Experimental instruments

The IFT between the oil and water was measured at 138 °C using a TX500HP high temperature interfacial tension meter. The contact angle was measured at 138 °C with an OCA20 optical contact angle measuring instrument using a sessile drop method. Additionally, spontaneous imbibition recovery was measured using an imbibition cell made of high-temperature and pressure-resistant glass (as shown in Figure 1). The smallest division values of this imbibition cell were 0.005 mL. The forced imbibition test equipment mainly includes ISCO injection pump, confining pressure pump, intermediate vessels, pressure sensor and core online displacement nuclear magnetic resonance analyzer (MacroMr12-150H–I, Niumag Analytical Instrument, Suzhou, China), with the experimental temperature of 138 °C. The nuclear magnetic pictures of T_2 spectrum before and after forced imbibition were compared. Changes in T_2 spectrum are used to determine the relative content change of crude oil at different pores scales in the core. The experimental equipment and procedures are shown in Figure 2.

2.3 Experimental instruments

2.3.1 Spontaneous imbibition

1) The dried cores were weighed before and after being saturated with simulated injection water prepared by distilled water. The pore volume was calculated through measuring the weight difference of the core sample.
2) Each core was placed into the core holder, saturated with crude oil, and aged with crude oil at 138 °C for 24 h to prepare it for use.
3) For spontaneous imbibition, an oil-aged core was placed inside an imbibition cell at 138 °C. The imbibition cell was filled with a surfactant solution to a desired height.
4) The volume of produced oil was monitored and recorded as often as appropriate. The imbibition recovery was calculated based on the volume of produced oil.

TABLE 1 Ion composition of injection water (mg/L).

Cations			Anions				Total dissolved solids (TDS)
Ca^{2+}	Mg^{2+}	Na^{+}	CO_3^{2-}	HCO_3^{-}	Cl^{-}	SO_4^{2-}	
193.12	10.71	3196.54	0	846.51	4879.12	4.30	9130.30



FIGURE 1
Imbibition cell used in spontaneous imbibition.

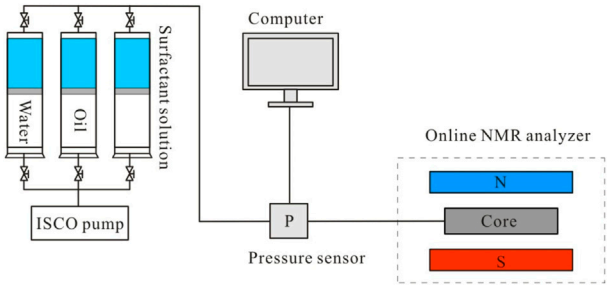


FIGURE 2
Schematic diagram of forced imbibition using on-line nuclear magnetic resonance.

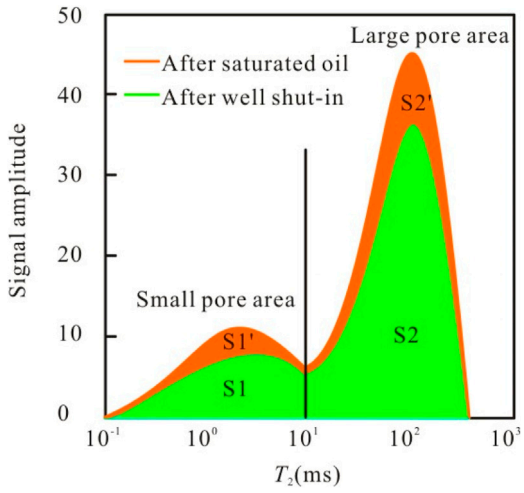


FIGURE 3
Schematic diagram of method for calculating oil imbibition recovery.

2.3.2 Forced imbibition

The specific experimental procedures of forced imbibition are as follows:

1) The dried core was weighed before and after being saturated with simulated water prepared by heavy water. The pore volume could be calculated by measuring the weight difference.
2) Core was placed into a core holder and was saturated with oil at reservoir temperature until it comes out at the outlet. The crude oil injection speed was 0.02 mL/min. After the oil saturation process, the core was aged with the crude oil at 138 ˚C for 24 h to prepare it for use. The core was placed into the core holder of NMR analyzer, and then the initial T_2 spectrum was tested;
3) The experimental surfactant solution prepared by heavy water was heated to the temperature of 80 ˚C in advance.
4) The surfactant solution was injected at 0.2 mL/min into the core holder, the outlet was shut at the same time. When the injection pressure reaches the set pressure, close the inlet for a designed shut-in time to simulate forced imbibition during well shut;
5) Outlet valve was opened until no liquid flows out after the shut-in time reached the designed time, the T_2 spectrum after forced imbibition was tested.
6) The forced imbibition effect of core was analyzed by comparing the change of T_2 spectrum in different size pore-throat.

2.3.3 Experimental theory

During NMR testing, the signal amplitude of transverse relaxation time T_2 spectrum reflects the relative saturation of residual oil in pores of different sizes. Additionally, the decreasing amplitude of the T_2 spectrum at various time intervals is used to quantify crude oil recovery. . . Regions with T_2 relaxation times less than 10 m are defined as small pores, and regions with T_2 relaxation times greater than 10 m are defined as large pores (Xie et al., 2022). The T_2 spectrum of the initial stage and stage after well shut was entered into a computer image recognition program. The relative movable oil of different size pores was obtained by comparing the area of T_2 spectrum between initial stage and stage after well shutting. According to Figure 3, the oil recovery can be calculated using following formula:

$$R_1 = \frac{S_1'}{(S_1 + S_1')} \quad (1)$$

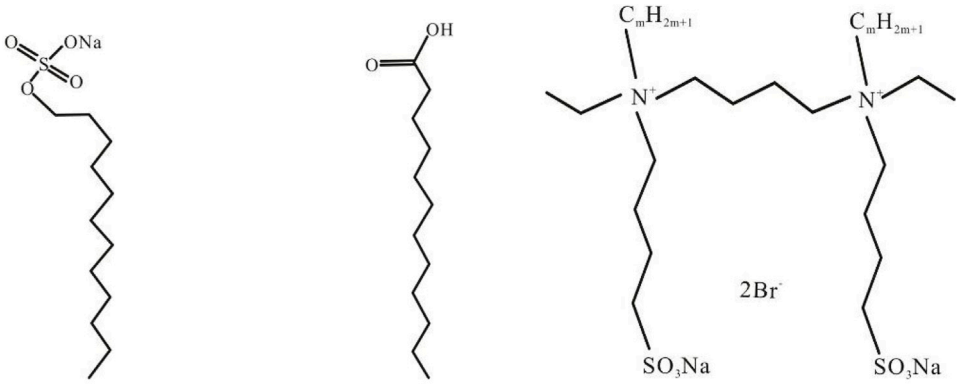


FIGURE 4
Structure of different surfactants.

TABLE 2 Interfacial tension test results (mN/m).

Surfactant type	Concentration (%)		
	0.1	0.2	0.3
Sodium lauryl alcohol sulfate	2.27×10^{-1}	1.89×10^{-2}	1.15×10^{-3}
Lauric acid	1.51×10^{-3}	1.33×10^{-3}	1.19×10^{-3}
Amphoteric Gemini surfactant	1.20×10^{-3}	9.70×10^{-4}	6.80×10^{-4}

$$R_2 = \frac{S_2'}{(S_2 + S_2')} \quad (2)$$

$$R = \frac{(S_1' + S_2')}{(S_1 + S_1' + S_2 + S_2')} \quad (3)$$

where R_1, R_2, R refers to the oil recovery of small pore, large pore, and total pore. S_1, S_1' refers to the final area of T_2 spectrum and differential area between beginning and ending time in small pore. S_2, S_2' refers to the final area of T_2 spectrum and differential area between beginning and ending time in small pore.

3 Results and discussion

3.1 Forced imbibition system performance evaluation

3.1.1 Interfacial tension

Three surfactants at concentrations of 0.1%, 0.2% and 0.3% were prepared using simulated injection water at 138°C reservoir temperature. Surfactant molecular structures and interfacial tension test results are shown in Figure 4 and Table 2 respectively.

As shown in Figure 4 and Table 2, the concentrations of the surfactant solutions and the interfacial tension are negatively correlated. At a concentration of 0.2%, the interfacial tension follows the trend: sodium lauryl alcohol sulfate > lauric acid > amphoteric Gemini surfactant. A greater oil-water interface layer results from a change in the structure of diffusion electric double layers due to high temperature, which also causes the hydrophobic group of chain structures to curl. As a result of the surfactants' low temperature tolerance, the interfacial tension rises. In contrast with the previous two surfactants, the amphoteric surfactant has a higher degree of hydrophobic chain branching and a more stable bond energy (C-C bond 332 kJ/mol). It also has a temperature-resistant sulfonic acid group ($-SO_3^{2-}$) in its hydrophobic chain. The surfactant's hydrophobic chain is capable of maintaining a stretch state at high temperatures due to its stable molecular structure. Additionally, the hydrophobic group is difficult to be compressed which is good for high temperature resistance.

3.1.2 Temperature resistance

The standing time of different surfactants of 0.3% concentration under the temperature of 138°C was changed, and then the interfacial tension between them and crude oil was tested by interfacial tension meter can be used in high temperature and high pressure. The test results are shown in Table 3.

As shown in Table 3, the standing time of the surfactant solutions at high temperature has an effect on the oil-water interfacial tension. After standing for 5 days, the interfacial tension of amphoteric Gemini surfactant can still obtain an oil-water interfacial tension of 10^{-3} mN/m, showing the best temperature resistance.

3.1.3 Wettability

Columnar cores with a permeability of 20 mD were cut into several thin slices of 2 mm thickness using a mechanical cutting machine, and the initial contact angle is 65.2° which means a weaker water-wet. The cores were immersed in three surfactants of 0.1%, 0.2% and 0.3% concentrations for 24 h at 138 °C. The variation of contact angle on the core surface in relation to the type and concentration of surfactant is shown in Table 4.

As shown in Table 4, the contact angle of the rock surface decreases with the increase of surfactant concentration. When the surfactant concentration is 0.2%, the contact angle shows the following trend: sodium lauryl sulfate > lauric acid > amphoteric

TABLE 3 Interfacial tension after different standing time (mN/m).

Type	Time(d)			
	0	1	3	5
Sodium lauryl sulfate	1.15×10^{-3}	2.30×10^{-3}	8.80×10^{-3}	2.33×10^{-2}
Lauric acid	1.19×10^{-3}	3.15×10^{-3}	3.25×10^{-3}	3.15×10^{-3}
Amphoteric Gemini surfactant	6.80×10^{-4}	2.22×10^{-3}	2.39×10^{-3}	2.46×10^{-3}

TABLE 4 Relationship between contact angle, contact angle difference and surfactant concentration (°).

Concentration (%)		Surfactant type		
		Sodium lauryl sulfate	Lauric acid	Amphoteric gemini surfactant
0.1	Before soaking	65.03	65.88	64.64
	After soaking	60.91	59.42	56.29
	Difference	4.12	6.46	8.35
0.2	Before soaking	65.03	65.88	64.64
	After soaking	47.55	42.65	38.03
	Difference	17.48	23.23	26.61
0.3	Before soaking	65.03	65.88	64.64
	After soaking	43.73	40.66	35.66
	Difference	21.30	25.22	28.98

TABLE 5 Core spontaneous imbibition recovery.

Surfactant type	Concentration (%)	Permeability K_g (mD)	Interfacial tension (mN/m)	Oil saturation (%)	Recovery (%)
Sodium lauryl sulfate	0.1	19	2.27×10^{-1}	62.70	7.69
	0.2	20	1.89×10^{-2}	61.94	14.22
	0.3	21	1.15×10^{-3}	62.89	10.65
Lauric acid	0.1	20	1.51×10^{-3}	62.42	8.78
	0.2	22	1.33×10^{-3}	62.83	15.33
	0.3	21	1.19×10^{-3}	62.86	11.34
Amphoteric Gemini surfactant	0.1	19	1.20×10^{-3}	62.97	10.36
	0.2	22	9.70×10^{-4}	62.62	16.22
	0.3	21	6.80×10^{-4}	62.74	12.74

Gemini surfactant. Compared with the two anionic surfactants sodium lauryl sulfate and lauric acid, amphoteric Gemini surfactant can effectively improve the wettability of the core surface and make the core surface more water-wet. .It is challenging to determine the imbibition effectiveness solely based on physicochemical properties since the influencing factors during the surfactant imbibition process are complex. Therefore, spontaneous imbibition experiments are used to further compare and optimize the types and concentrations of surfactants for offshore oilfields.

3.2 Optimization of technological parameters of forced imbibition system

3.2.1 Spontaneous imbibition

Columnar cores were immersed in the surfactant solution in the high temperature imbibition bottle placed in the temperature of 138°C. The results of core spontaneous imbibition recovery experiments are shown in Table 5.

In static spontaneous imbibition, amphoteric Gemini surfactant had the maximum oil recovery among the three surfactants, as

TABLE 6 Forced imbibition recovery under different core permeability.

Permeability K_g (mD)	Core inside pressure (MPa)	Shut-in time (h)	Oil saturation (%)	Recovery (%)		
				R_1	R_2	R
20	15	24	62.16	28.70	27.02	27.42
60			61.98	38.89	35.51	36.24

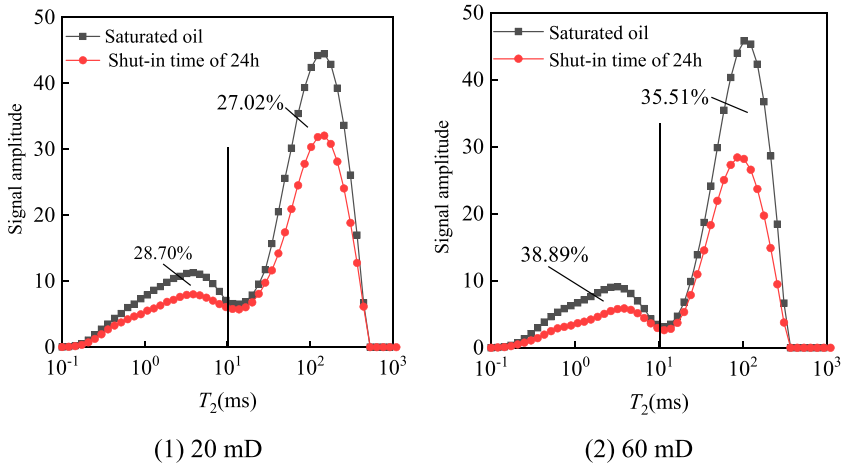


FIGURE 5
T_2 spectrum distribution under different core permeability.

indicated in Table 5. When the surfactant concentration was 0.2%, the oil recovery of the amphoteric Gemini surfactant solution was 16.22%. A mechanism study shows that improving imbibition oil recovery can be achieved by properly increasing the surfactant concentration and reducing interfacial tension. However, too low interfacial tension will limit the capillary force, which is detrimental for imbibition. In addition, when the surfactant concentration exceeds the critical micelle concentration, the effective concentration decreases and the imbibition effect deteriorates. Further analysis revealed that surfactants can change the wettability of the rock pore surface to more water-wet resulting in the reduction of the adhesion of oil phase on the rock surface. This causes an even force field to form around the oil droplets in the pore-throat, which facilitates the oil film's easier separation from the rock's surface and increases imbibition.On the other hand, surfactants have the ability to significantly lower the capillary resistance and adherence of the rock surface to oil droplets by lowering the interfacial tension between oil and water. This increases the number of capillaries, enhancing the deformability of oil droplets, improving the flow ability of the oil phase, and thus increasing the imbibition oil recovery. Based on the above results, 0.2% amphoteric Gemini surfactant is recommended for subsequent experimental studies taking into account the technical and economic factors.

3.2.2 Forced imbibition

1) Influence of core permeability

0.2% of amphoteric Gemini surfactant was prepared by simulated formation water using heavy water. The inlet was closed when the core inside pressure reached a pressure of 15MPa, and then outlet was opened after a shut-in time of 24 h. When the outlet has no fluid to flow, the T_2 spectrum was tested. The effect of core permeability on the forced imbibition and corresponding T_2 spectrum are shown in Table 6 and Figure 5.

As shown in Table 6 and Figure 5, as core permeability increases, the pore throat radius increases, oil has a lower flow resistance, more oil can be produced through imbibition under the function of capillary and displacement, and the forced imbibition recovery rate increases. According to the analysis, oil in large pore areas is primarily dependent on the displacement of surfactant, so the small pore area has a higher oil recovery than large pore areas, and the oil recovery in large pore areas decreases with the decrease of core permeability. The analysis also shows that small pore areas have a stronger capillary force, which is helpful to enhance imbibition function. Because the initial saturated oil volume is larger and the large pore area has a larger pore volume, oil recovery from the large area accounts for the majority of overall oil recovery.

2) Influence of core inside pressure

The reservoir inside pressure has an obvious effect on imbibition for it will influence the crossflow between large pore area and small pore area. Different volumes of fracturing fluid will lead to a different reservoir inside pressure. The core inside pressure was changed in the experiments to study the proper injection volume of fracturing fluid. A concentration of 0.2% amphoteric Gemini surfactant was prepared by simulated formation water using

TABLE 7 Forced imbibition recovery at different core inside pressure.

Core inside pressure (MPa)	Shut-in time (h)	Permeability K_g (mD)	Oil saturation (%)	Recovery (%)		
				R_1	R_2	R
5	24	21	61.83	17.53	12.36	13.50
10		20	61.94	22.01	18.37	19.21
15		21	62.16	28.70	27.02	27.42

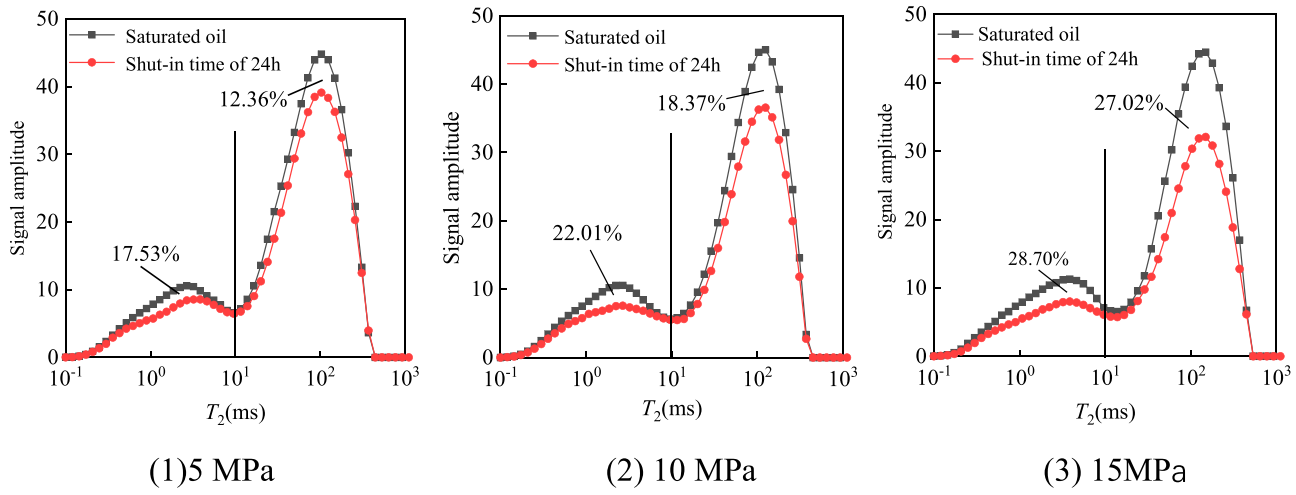


FIGURE 6
T_2 spectrum distribution under different core inside pressure.

heavy water. The inlet was closed when the core inside pressure reached a pressure of 5, 10 and 15MPa, and the outlet was opened after a shut-in time of 24 h. When the outlet had no fluid flowing, the T_2 spectrum was tested. The effects of core inside pressure on forced imbibition and corresponding T_2 spectrum are shown in Table 7 and Figure 6.

As shown in Table 7, the forced imbibition oil recovery increases with increasing core insidepressure. The forced imbibition recovery can reach 27.42% at a core inside pressure of 15 MPa. The analysis presents that the surfactant injection volume increases with the increase in core inside pressure. On the one hand, more pore volume is displaced and water-wet degree of more area is improved, more pores will happen imbibition, oil recovery in small pore area and large pore area becomes higher. On the other hand, a larger core inside pressure can supply more energy for fluid after shut-in time, which is helpful for overcoming flow resistance.

As shown in Figure 6, the T_2 spectrum following forced imbibition exhibits a declining tendency when compared to the T_2spectrum of the first stage. The decreasing amplitude becomes larger as the core inside pressure increases and as core inside pressure increases, surfactant solution volume injected into the core increases. Due to the strong connection between different pores in the large pore area and the displacement of the larger pore volume, the oil recovery from the large pore area is increased. Besides, as the core inside pressure rises, the imbibition area between the large and small pore throats will be stronger due to a higher core inside pressure, increasing the likelihood that oil will be recovered from the small pore area. Therefore, a proper reservoir pressure should be considered when designing surfactant solution injection volume.

3) Influence of shut-in time

When employing surfactant solution as the fracturing fluid, the well shut-in time affects the reservoir interior pressure, hence the shut-in period should be optimised. A concentration of 0.2% amphoteric Gemini surfactant was prepared by simulated formation water using heavy water. The inlet was closed when the core inside pressure reached a pressure of 15MPa, and the outlet was opened after a shut-in time of 24h, 48 and 72h, respectively. When the outlet had no fluid flowing, the T_2 spectrum was tested. The effects of core inside pressure on forced imbibition and the corresponding T_2 spectrum are shown in Table 8 and Figure 7.

The oil recovery via forced imbibition is obviously influenced by the well shut-in duration, as illustrated in Table 8 and Figure 7, respectively. As a well's shut-in duration increases, the rate of oil recovery rises. After a 72-h shut-in period, the forced imbibition oil recovery can reach 50.88%, which is higher than the forced imbibition recovery of 27.42% after a 24-h shut-in time. As the pressure diffuses during shut-in, surfactant solution can flow into more pore volume and displace the oil, causing crossflow between

TABLE 8 Forced imbibition recovery under different shut-in time.

Shut-in time (h)	Core inside pressure (MPa)	Permeability K_g (mD)	Oil saturation (%)	Recovery (%)		
				R_1	R_2	R
24	15	21	62.16	28.70	27.02	27.42
48		22	61.84	35.65	42.15	40.64
72		21	62.23	41.69	53.44	50.88

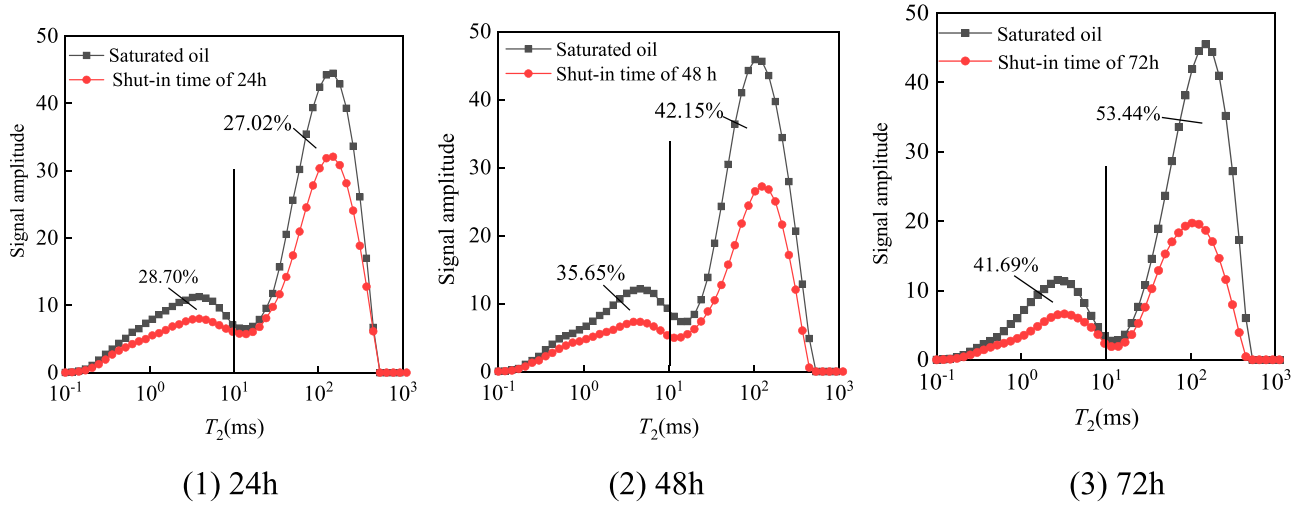


FIGURE 7
T_2 spectrum distribution under different shut-in time.

small and large pore areas. The oil recovery increasing amplitude of the big pore area is greater than that of the small pore area because the oil produced by displacement is more than the oil produced by imbibition. Therefore, a proper shut-in time should be considered when designing a well shut-in time.

4 Conclusion

The surfactant used in fracturing liquid can obviously improve the effect of increasing oil in offshore oilfields with low permeability and high temperature, the surfactant type, construction, spontaneous imbibition effect and forced imbibition effect should be considered at the same time.

1) As the concentration of the three surfactant increases, the IFT decreases, and the water-wet ability becomes stronger. Amphoteric Gemini surfactant has superior temperature resistance compared to sodium lauryl alcohol sulphate and lauric acid because of its stable molecular structure and the difficulty compressing its hydrophobic group.
2) In spontaneous imbibition, it was found that amphoteric Gemini surfactant showed by far the highest oil recovery of the three surfactants tested. At a concentration of 0.2% of the surfactant, amphoteric Gemini can achieve spontaneous oil recovery of 16.22% of the oil.
3) Imbibition oil recovery can be improved by appropriately increasing the surfactant concentration and decreasing interfacial tension, however, too low interfacial tension will limit the capillary force, which is undesirable for imbibition.
4) The forced imbibition effect is influenced by the core permeability, the core inside pressure and the well shut-in time. The high core permeabilities, high core inside pressures, and long well shut-in times results into better forced imbibition effect. When employing surfactant solutions as a fracturing liquid, proper well shut-in time and injection volume should be taken into account.

Data availability statement

The original contributions presented in the study are included in the article/supplementary material, further inquiries can be directed to the corresponding author.

Author contributions

YL: Conceptualization, Formal Analysis, Investigation, Methodology, Writing–original draft. JZ: Project administration,

Supervision, Writing–review and editing. XL: Conceptualization, Formal Analysis, Writing–original draft, Writing–review and editing. SG: Methodology, Writing–review and editing. LZ: Writing–review and editing. XH: Writing–review and editing.

Funding

The author(s) declare financial support was received for the research, authorship, and/or publication of this article. Project of Exploration and Research on Fracturing Technology of Enhancing Energy and Improving Efficiency in Bohai Oilfield (CCL2021TJT0NST2278). This work was supported by Tianjin Branch Research Institute.

Conflict of interest

The authors declare that the research was conducted in the absence of any commercial or financial relationships that could be construed as a potential conflict of interest.

Publisher's note

All claims expressed in this article are solely those of the authors and do not necessarily represent those of their affiliated organizations, or those of the publisher, the editors and the reviewers. Any product that may be evaluated in this article, or claim that may be made by its manufacturer, is not guaranteed or endorsed by the publisher.

References

Abbassi, F. T., Karrech, A., Islam, M. S., and Seibi, A. C. (2022). Poromechanics of fractured/faulted reservoirs during fluid injection based on continuum damage modeling and machine learning. *Nat. Resour. Res.* 32 (1), 413–430. doi:10.1007/s11053-022-10134-8

Bai, Y., Pu, C. S., and Liu, S. (2021). Carboxyl/alkyl composite silica-based amphiphilic nanoparticles enhanced imbibition of low spontaneous permeability sandstone at reservoir conditions. *Colloids Surfaces A Physicochem. Eng. Aspects* 2021, 629. doi:10.1016/j.colsurfa.2021.127504

Cai, J. C., and Yu, B. M. (2012). Advances in studies of spontaneous imbibition in porous media. *Adv. Mech.* 42 (6), 735–754. doi:10.6052/1000-0992-11-096

Cao, G. S., Wu, J. J., Zhang, N., Sui, Y., and Bai, Y. (2022). Study on migration characteristics of oil gas water three-phase interface and distribution law of remaining oil in gas cap edge water reservoir. *Energy Sources, Part A Reserv. Util. Environ. Eff.* 44 (3), 6362–6377. doi:10.1080/15567036.2022.2090642

Dontsov, E. V. (2022). Analysis of a constant height hydraulic fracture driven by a power-law fluid. *Rock Mech. Bull.* 1 (1), 100003. doi:10.1016/j.rockmb.2022.100003

Gushchin, P. A., AntonovS, V., Mishin, A. S., Khamidullina, V., Gushchina, Y. F., and Khlebnikov, V. N. (2018). Physicochemical mechanisms of light oil oxidation during extraction from high-temperature low-permeability oil reservoirs. *Chem. Technol. Fuels Oils* 54 (1), 64–71. doi:10.1007/s10553-018-0899-6

Han, D. W., Lu, X. G., Wang, T. T., et al. (2016). Difference of pore structure between artificial cores and natural cores and its influence on the seepage characteristics of oil displacement agent. *Petroleum Geol. Effic. Recovery* 23 (4), 82–87. doi:10.13673/j.cnki.cn37-1359/te.2016.04.013

Han, H. S., Chen, X. L., Ji, Z. M., Li, J., Lv, W., Zhang, Q., et al. (2022). Experimental characterization of oil/gas interface self-adjustment in CO_2-assisted gravity drainage for reverse rhythm reservoir. *Energies* 15 (16), 5860. doi:10.3390/en15165860

Huang, L. K., He, R., Yang, Z. Z., Tan, P., Chen, W., Li, X., et al. (2023b). Exploring hydraulic fracture behavior in glutenite formation with strong heterogeneity and variable lithology based on DEM simulation. *Eng. Fract. Mech.* 278, 109020. doi:10.1016/j.engfracmech.2022.109020

Huang, L. K., Tan, J., Fu, H. F., Liu, J., Chen, X., Liao, X., et al. (2023a). The non-plane initiation and propagation mechanism of multiple hydraulic fractures in tight reservoirs considering stress shadow effects. *Eng. Fract. Mech.* 292, 109570. doi:10.1016/j.engfracmech.2023.109570

Li, A. F., He, B. Q., and Lei, Q. H. (2018). Influence of interfacial tension on water-imbition in low-wet permeability reservoirs. *J. China Univ. Petroleum Ed. Nat. Sci.* 42 (4), 67–74. doi:10.1016/j.engfracmech.2022.109020

Lin, R. Y., Jia, Y., and Sun, L. (2022). Experimental study on the seepage characteristics of multilayer commingled production and influencing factors of the development effect in low-permeability tight sandstone gas reservoirs. *ACS omega* 7 (38), 34080–34088. doi:10.1021/acsomega.2c03273

Liu, Y., Yang, D., Liang, C., Li, Y., He, M., Jia, J., et al. (2023). A scientometric review on imbibition in unconventional reservoir: a decade of review from 2010 to 2021. . *Process.* 11 (3), 845. doi:10.3390/pr11030845

Ma, X., Zhang, S., Zhang, X., Liu, J., Jin, J., Cheng, W., et al. (2022). Lithology-controlled stress variations of Longmaxi shale–Example of an appraisal wellbore in the Changning area. *Rock Mech. Bull.* 1 (1), 100002. doi:10.1016/j.rockmb.2022.100002

Marzhan, K., Razieh, K., and Peyman, P. (2023). A review of wettability alteration by spontaneous imbibition using low-salinity water in naturally reservoirs. *Energies* 16 (5), 2373. doi:10.3390/en16052373

Tan, P., Fu, S. H., Chen, Z. W., and Zhao, Q. (2023). Experimental investigation on fracture growth for integrated hydraulic fracturing in multiple gas bearing formations. *Geoenergy Sci. Eng.* 2023, 212316. doi:10.1016/j.geoen.2023.212316

Tan, P., Jin, Y., and Pang, H. W. (2021). Hydraulic fracture vertical propagation behavior in transversely isotropic layered shale formation with transition zone using XFEM-based CZM method. *Eng. Fract. Mech.* 248, 107707. doi:10.1016/j.engfracmech.2021.107707

Wang, Q., Zhao, J. Z., and Hu, Y. Q. (2022). Numerical simulation of static spontaneous seepage at core scale. *J. Petroleum* 43 (6), 860–870. doi:10.7623/syxb202206010

Wei, R., and Liu, C. J. (2019). Techniques for low efficiency well management in complex formation of BZ34-5 oilfield. *Prospect. Eng. Geotech. Drill. Eng.* 46 (6), 47–52. doi:10.12143/j.tkgc.2019.06.009

Xie, K., Lu, X. G., Pan, H., Han, D., Hu, G., Zhang, J., et al. (2018). Analysis of dynamic imbibition effect of surfactant in microcracks of reservoir at high temperature and low permeability. *SPE Prod. Operations* 33 (03), 596–606. doi:10.2118/189970-pa

Xie, K., Mie, J., Cao, W. J., Cao, B., Yao, L., Zhang, B., et al. (2022). Improving oil mechanism of polymer gel fracturing fluid based on filtration displacement. *J. petroleum Sci. &engineering* 218, 111030. doi:10.1016/j.petrol.2022.111030

Xu, J. H., and Ma, L. L. (2015). Spontaneous imbibition in Efficitured low permeability reservoir. *Petroleum Geol. Recovery Reserv.* 22 (3), 111–114. doi:10.13673/j.cnki.cn37-1359/te.2015.03.020

Xu, K., Lu, Y. J., Chang, J., and Li, Y. (2021). Research progress of high temperature resistant fracturing fluid system. *J. Phys. Conf. Ser.* 2076 (1), 012039. doi:10.1088/1742-6596/2076/1/012039

Zhong, L. G., Zhu, T. Y., Hao, T. C., Zhang, X., Wang, X., and Zhang, L. (2020). Prediction method of formation pressure for the adjustment well in the reservoir with fault. *J. Phys. Conf. Ser.* 1707 (1), 012012. doi:10.1088/1742-6596/1707/1/012012

Zhu, W. Y., Zhao, C. Y., and Ma, Q. P. (2021). Effect of hydrophobic carbon chain length of alky betaine surfactant on spontaneous imbibition of low-permeability core. *Special Oil Gas Reservoirs* 28 (4), 102–107. doi:10.3969/j.issn.1006-6535.2021.04.014

frontiers | Frontiers in Energy Research

TYPE Original Research
PUBLISHED 02 November 2023
DOI 10.3389/fenrg.2023.1267782

Check for updates

OPEN ACCESS

EDITED BY
Peng Tan,
CNPC Engineering Technology R&D Company Limited, China

REVIEWED BY
Daobing Wang,
Beijing Institute of Petrochemical Technology, China
Mingjun Chen,
Southwest Petroleum University, China
Xiaopeng Yan,
Changzhou University, China

*CORRESPONDENCE
Song Li,
lisong03011640@163.com

RECEIVED 27 July 2023
ACCEPTED 24 August 2023
PUBLISHED 02 November 2023

CITATION
Li S, Fan Y, Wang Y, Zhao Y, Lv Z, Ji Z, Chen W and Min J (2023), True triaxial physics simulations and process tests of hydraulic fracturing in the Da'anzhai section of the Sichuan Basin tight oil reservoir.
Front. Energy Res. 11:1267782.
doi: 10.3389/fenrg.2023.1267782

COPYRIGHT
© 2023 Li, Fan, Wang, Zhao, Lv, Ji, Chen and Min. This is an open-access article distributed under the terms of the Creative Commons Attribution License (CC BY). The use, distribution or reproduction in other forums is permitted, provided the original author(s) and the copyright owner(s) are credited and that the original publication in this journal is cited, in accordance with accepted academic practice. No use, distribution or reproduction is permitted which does not comply with these terms.

True triaxial physics simulations and process tests of hydraulic fracturing in the Da'anzhai section of the Sichuan Basin tight oil reservoir

Song Li[1,2]*, Yu Fan[1,2], Yang Wang[1], Yuanshou Zhao[3], Zefei Lv[1], Zeng Ji[1], Weihua Chen[1] and Jian Min[1,2]

[1]Engineering Technology Research Institute of PetroChina Southwest Oil and Gas Field Company, Chengdu, China, [2]National Energy R&D Center of High Sulfur Gas Exploitation, Guanghan, China, [3]Qilin Gas Production Area of the Fourth Oil Production Plant of PetroChina Changqing Oilfield Company, Yulin, China

The limestone reservoir of the Da'anzhai section is the main production layer of Jurassic tight oil in central Sichuan, with tight and strongly heterogeneous reservoir rocks. In the early stages, small-scale plug removal and acidification techniques were mainly applied to the dacite section of the reservoir. However, using a single conversion method was not suitable for tight reservoirs with underdeveloped fractures. To address this challenge, we conducted large-scale real-world triaxial simulation test system experiments on hydraulic fracture propagation using samples from dense limestone outcrops. The aim was to elucidate the laws of hydraulic fracture propagation in dense limestone oil reservoirs. The L1 well in this area was selected to test the volumetric fracturing technology in order to achieve a breakthrough in test production and the reconstruction technology of the Da'anzhai section of the tight limestone reservoir. The experiments have shown that low stress differences, natural fracture development, and low viscosity slippery water are favorable factors for obtaining complex fracture morphology. In contrast to the construction parameters, the structural properties of the rock are the dominant factors in the formation of complex fracture morphologies. By optimizing the geological dessert and implementing targeted technological measures, bulk fracturing has been proven to be feasible for the dense limestone reservoir in the Da'anzhai section.

KEYWORDS

tight oil reservoir, Da'anzhai, true triaxial, volume fracturing, technology test

1 Introduction

Unconventional tight oil reservoirs are widely distributed in China. For example, the Chang 7 section of the Yanchang Formation in the Ordos Basin, the carbonate rock of the Shahejie lacustrine formation in Bohai Bay, the Cretaceous Marl of the Jiuquan Basin, the Permian Marl of the Junggar Basin, and the Lower Tertiary Marl of the Jianghan Basin are all unconventional tight oil reservoirs. In addition, the Jurassic oil resources in the central Sichuan Basin are estimated at 1.07 billion tons. After 50 years of development, 160 million tons of tertiary reserves have been acquired in central Sichuan, including 81.18 million tons

of proven reserves and 5.3603 million tons of technically recoverable reserves. However, the resource discovery rate is only 15% and the proved discovery rate is only 7.6%. Clearly, the central Sichuan region is rich in hydrocarbon sources and abundant resources, making it one of the largest oil-producing regions in China yet to be developed on a large scale. As a result, the development and utilization of low permeability tight oil and gas reservoirs will play an increasingly important role in increasing the reserves and production of oil and gas fields, especially with the advent of later stages of field development. This is of great practical importance to China.

Tight oil, or shale oil, is an important source of energy worldwide. The United States' Bakken and China's Yingtan are typical representatives of the commercial development of tight oil globally (Warpinski et al., 2009; Wei et al., 2013; Du et al., 2014; Yang et al., 2014; Yu et al., 2014). Currently, the domestic Changqing and Daqing oilfields are also making great progress in the exploration of tight oil (Li et al., 2015; Cao, 2022). The aforementioned blocks' tight sandstone reservoirs have all undergone volumetric fracturing using induced stress, which has been found to greatly affect the shape and size of the fracture network's contribution to well production (Mayerhofer et al., 2010; Wang et al., 2023a). A new parameter, "Reservoir Renovation Volume (SRV)," has been proposed to characterize the degree of impact on the production of a fracturing well after fracturing. The researchers also studied the initiation and extension patterns of multiple fractures in the vicinity of the borehole region. They have proposed a conceptual diagram of radial fracture network extension (Mcdaniel, 2010). In addition, using the step-by-step construction method, researchers have improved the connectivity between the natural and main fractures, thereby increasing the complexity and effectiveness of fracture network fracturing (Soliman et al., 2010; Hou et al., 2016; Hou et al., 2019) compared and evaluated the factors affecting the expansion of shale, limestone, and tight sandstone with the fracture expansion of rocks. They concluded that the initiation and expansion of hydraulic fractures in highly brittle rocks are mainly affected by fracture toughness. On the other hand, the formation of complex fracture networks in low-brittleness rocks is influenced by the use of low-viscosity fracturing fluid. In addition, Cai et al. (2022) conducted experiments on rock mechanics param of Gulong shale to investigate the impact on fracture expansion. They optimized the perforation mode, cluster spacing, proppant particle size combination, and shale oil reservoir type, as well as the fracturing construction control process. These improvements enhanced the combined volume fracturing technology for Gulong shale oil reservoirs. By establishing a three-dimensional fracture initiation and propagation model, taking into account the effects of fracturing parameters such as well completion method, *in situ* stress, natural fractures, cluster spacing, and displacement on the initiation and propagation of fracturing fractures, the difficulties of indoor conventional experiments limited by small rock and crack sizes and large boundary effects were overcome (Wang et al., 2020; Wang et al., 2020; Tan et al., 2020; Tan et al., 2021a). However, most of the rock and fracture mathematical models built were based on ideal assumptions, which were somewhat different from actual working conditions (Lin et al., 2020; Tang et al., 2021b; Li et al., 2021; Lucas et al., 2021; Li et al., 2022; Wang et al., 2022) conducted true triaxial

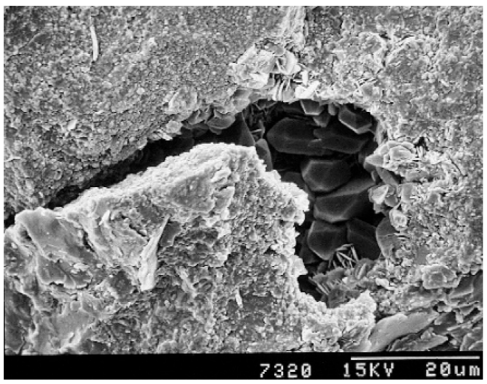


FIGURE 1
Scanning electron microscope of Da'anzhai section.

Fracking experiments on 30 cm and 50 cm cement cube rock mass with prefabricated natural fractures through concrete similar simulation experiments, respectively, and studied the effects of natural fracture development, dip angle and strike, and different stress differences on fracture propagation. Based on the characteristics of the reservoir and the simulation results of large-scale fracturing experiments, it is recommended to adopt a volume fracturing concept and process technology that focuses on "large liquid volume, large displacement, and expanded swept volume" to achieve the goal of transforming complex fracture networks. Wang et al. (2023b) conducted a temporary plugging agent sealing pressure test about multiscale temporary plugging fracturing shale oil reservoirs, which elucidated the effect of different types, combinations and concentrations of temporary plug agents on the sealing pressure. Based on the similarity criterion design of dimensional analysis method (π theorem) physical simulation experiments, Kong et al. (2023) conducted unconventional volume fracturing physical simulation experiments using an artificial sample system, simulating the equilibrium initiation and extension behavior of fracturing fractures under five unconventional volume fracturing processes: hydraulic pulse pretreatment, cluster temporary blocking, flow limiting method, cyclic loading and unloading, and pulse intermittent fracturing.

Despite years of progressive exploration and development of the central Sichuan basin's Jurassic oil reservoirs, it has been difficult to significantly increase their productivity scale and recovery factor, which has left central Sichuan's annual oil production inadequate to its resources and vast oil-bearing area. The shelly limestone reservoir of the Da'anzhai section is the main production layer of Jurassic tight oil in central Sichuan. In the early stages, the acidification process was mainly tested on different acid fluid systems, such as conventional acid, gelling acid, and drag-reducing acid, showing single-process and small-scale properties. Field tests have shown that the former process is not suitable for tight limestone reservoirs with underdeveloped fractures. Whether this type of reservoir can be learned from the successful experience of volumetric fracturing conversion in tight sandstone reservoirs at home and abroad is an urgent question to be answered. Physical simulations of true triaxle fracture have been performed with outcropping limestone samples to explore fracture propagation

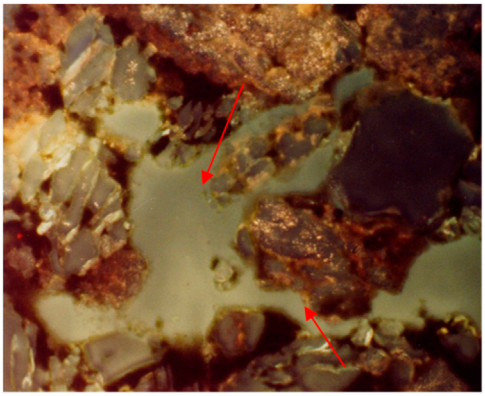


FIGURE 2
Micro pore structure of reservoir with a throat radius of approximately 25 μm × 100 μm.

laws in limestone reservoirs in terms of stress differences, natural fractures, and fluid types. Well L 2 was selected for testing of the volumetric fracturing technology and the results demonstrated that the tight limestone reservoir in the Da'anzhai section is viable for volumetric fracturing.

Simulations of realistic triaxle physics have demonstrated the influence of stress orientation and magnitude on fracture behavior in the Da'anzhai Section, a compact rock formation. Performance tests show that changes in fracture parameters can effectively control fracture propagation and enhance reservoir connectivity. The findings suggest that production of oil and gas from tight reservoirs can be significantly increased by optimizing fracture design. This study has successfully investigated the hydraulic fracturing process in the Da'anzhai Section of the Sichuan Basin tight reservoir through realistic triaxle physics simulations and process tests. The results demonstrate the importance of optimizing fracture design for enhanced reservoir connectivity and oil/gas production.

2 Reservoir characteristics of Da'anzhai section

The total thickness of the Da'anzhai reservoir ranges from 40 to 110 m. It is mostly composed of bioclastic limestone, which is mostly developed in the first and third sectors of the Da'anzhai Formation. Individual layers within the reservoir are typically 3–20 m thick, with cumulative thickness ranging from 5 to 40 m. Lianggaoshan has a layer thickness of 50–150 m. The reservoirs in the Liangshang section consist primarily of pale gray powdery to fine-grained quartz sandstone with lithic feldspar. The layers are generally 1–4 m thick, with cumulative thickness ranging from 10 to 20 m. The Shaximiao Formation is primarily located in the lower part of Shaximiao and consists of light gray fine to medium to coarse-grained lithic feldspar quartz sandstone ranging in thickness from 5 to 30 m. The reservoir exhibits significant vertical variability, including the presence of limestone and sandstone. Compared with shale oil reservoirs at home and abroad, the shale oil reservoirs in central Sichuan Basin are characterized by vertical lithologic interaction (shale, sandstone, limestone). There are major differences in rock mechanics and geostress properties in the vertical direction. In addition, the physical properties of the reservoir are poor, with porosity ranging from 1.4% to 4.5% and generally less than 2%, permeability ranging from 0.001 to 0.018 mD, water saturation from 15% to 50%, and TOC content ranging from 1.2% to 1.7%. Overall, it exhibits extremely low porosity and permeability. The original formation pressure coefficient of the reservoir is 0.8–1.7, the geothermal gradient is 2.07°C/m, the crude oil density is 0.6–0.8 g/cm^3, and the viscosity is 0.2–4.0 mPa·s.

2.1 Microstructural characteristics of reservoirs

The displacement pressure of the Da'anzhai section reservoir is 18.27 MPa, which belongs to the ultra-high displacement pressure. The median pressure is 75.85 MPa, which belongs to ultra-high

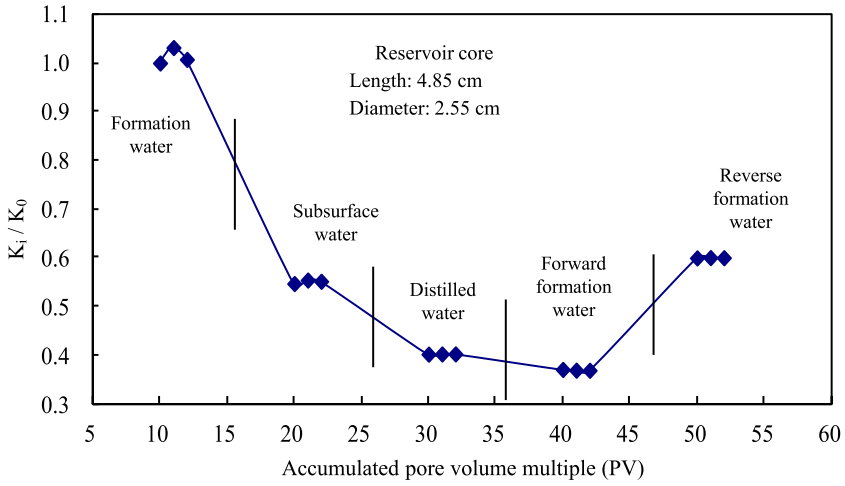


FIGURE 3
Water sensitivity test curve of rock samples from Da'anzhai section.

TABLE 1 Rock mechanics param of Da'anzhai reservoir.

Well No.	Rock density g/cm^3	Compressive strength MPa	Young's modulus × 10^{4}MPa	Poisson's ratio
G2	2.74	385.8	6.77	0.25
L1	2.70	324.2	5.46	0.24
L1	2.71	346.3	5.44	0.21
L2	2.72	367.8	5.79	0.22

TABLE 2 Ground stress and stress difference coefficient of Da'anzhai reservoir.

Well No.	Horizon	Well depth m	Triaxial principal stress MPa			Direction of geostress		Stress difference coefficient
			σ_H	σ_h	σ_v	σ_h	σ_H	
L 2	Da'anzhai	2,770	68.6	55.0	59.3	10°~15°	105°~115°	0.24

TABLE 3 Param of unconventional fracturing process simulation experiment.

Completion type	Sample No.	Perforation hole size/cm	Ground stress/ MPa $\sigma_v/\sigma_h/\sigma_H$	Fracturing fluid	Viscosity/ mPa·s	Pump displacement/ mL/min	Natural fractures
Open hole	1	—	55/40/48	Slick water	5	8	
Perforation	2	0.2	55/40/48	Slick water	5	8	
	3	0.2	55/40/48	Slick water	5	0→8→0 (5s) →8→0 (5s) →8	
	4	0.2	55/40/48	Crosslinked fluid	50	8	
	5	0.2	55/40/48	Slick water	5	8	
	6	0.2	55/40/48	Slick water	5	8	
	7	0.2	55/46/48	Slick water	5	8	
	8	0.2	55/40/48	Slick water	5	8	Development
	9	0.2	55/40/48	Slick water	5	8	No development
	10	0.2	55/40/48	Cross-linked fluid	50	8	Development

capillary pressure. The median radius of the pore throat is extremely small. The scanning electron microscope shows that the reservoir has developed pinholes, well-developed pores, and good connectivity. Crude oil is visible in the pores, and microfractures are developed (Figures 1, 2). Figure 2 shows a diameter of 2,468.56 m in Da'anzhai, where the intergranular dissolved pores and throat are filled with oil.

2.2 Mineral and sensitivity characteristics

The X-ray diffraction experiment shows that the mineral composition of the reservoir is mainly Calcite, containing a small amount of argillaceous, siliceous, erogenous clastic, organic matter and Pyrite. In clay minerals, Yimeng mixed bed, Pyrite and other sensitive mineral components are widespread, indicating that there is potential damage to the reservoir. The sensitivity experiment of the reservoir indicates that the reservoir has moderate to strong water sensitivity characteristics (Figure 3), which requires the liquid entering the well to have good anti swelling performance.

2.3 Reservoir space

The Da'anzhai limestone reservoir has a mainly microporous structure created by dissolution, structural fractures, and dissolution fractures. Meanwhile, the major reservoir spaces in the Lianggaoshan and Shaximiao sandstone reservoirs consist of intergranular and intergranular dissolution pores with small residual intergranular pores and structural microfractures. Although the fractures in Chung-guyok consist of a gentle overall



FIGURE 4
Large scale true triaxial simulation test system.



FIGURE 5
Sample drilling.

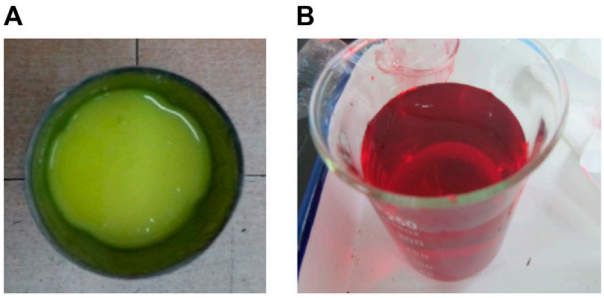


FIGURE 6
Crosslinking solution (Left) and smooth water (Right) after mixing dyes.

structure, there are weak stresses and strong heterogeneity in the development and distribution of the fractures. The fractures in the Da'anzhai reservoir are mainly characterized by low-sloping, horizontal, small, and microfractures. However, there are high-angle, large and medium-sized structural fractures that have not yet developed. Fractures are relatively developed in regions of strong stress, which include fault ends, structural axes, turning points, nasal protrusions, kinks, and steeply varying zones. The strike of the main fracture on the aircraft is generally consistent with a structural strike. The effects of fissures are manifested in the following ways:

Fractures are essential for achieving high production rates in oil wells, and the majority of high production wells are associated with fractures. Production capacity can vary significantly from well to well, often resulting in low, small or no production in the vicinity of high yield wells. In addition, there is often a discrepancy between the permeability of rock samples and the measured permeability of oil well production. To further develop this argument, more specific examples and thorough justification should be incorporated throughout the paper.

The measured permeability of a large number of cores from various Jurassic beds is generally less than 1.0 mD, reflecting the permeability of pores in the rock matrix. However, when it comes to high production industrial wells, the interpreted permeability at well test time often reaches tens or even hundreds of millers. This can be attributed to the percolation nature commonly found in typical fractured reservoirs. And the permeability of these wells can vary greatly depending on several key factors, such as the degree of fracturing, the pore structure, and the effect of any external forces that may occur. An in-depth analysis of fractured reservoirs is therefore essential to accurately interpret such data. In summary, the study of permeability in fractured reservoirs is a complex yet essential task that requires a holistic understanding of geological structures and processes. By implementing advanced techniques and tools, we can further improve our understanding of these reservoirs and pave the way for more effective management and utilization of our valuable resources.

2.4 Rock mechanics and *in situ* stress characteristics of reservoir

Rock mechanics experiment shows that the Young's modulus of the reservoir is high, ranging from (5.4–6.8) × 10^4MPa, while the Poisson's ratio is low, ranging from 0.21 to 0.25 (as shown in Table 1). This indicates that the reservoir's rock is strong and resistant to deformation, as well as more likely to respond elastically to stress. These properties make it a good candidate for oil and gas storage.

In order to provide a more specific explanation and relate this information to reservoir management, various factors need to be considered. The Young's modulus of a rock determines its elasticity under stress, while the Poisson's ratio measures deformations perpendicular to the applied force. Thus, a high Young's modulus implies that the reservoir can withstand high pressures, while a low Poisson's ratio implies that the reservoir is less susceptible to destructive changes in shape or volume under stress. Overall, these factors contribute to making the reservoir a desirable location for oil and gas storage. However, a thorough investigation of geological history, current market demand and future projections, among other things, is necessary for a complete understanding. In order to provide a more concrete explanation and relate this information to reservoir management, we need to consider several factors. The Young's modulus of a rock indicates its elasticity under stress, while the Poisson's ratio quantifies the deformation normal to the applied

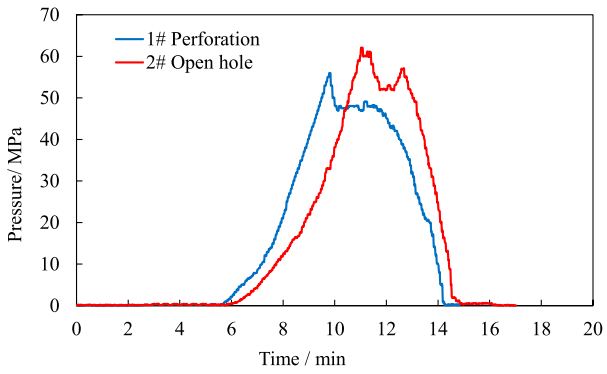


FIGURE 7
Pump pressure curves of samples 1 # and 2 # under different completion methods.



FIGURE 8
Fracturing results of sample 3 #.

force. Thus, a high Young's modulus implies that the formation is able to withstand high pressures, while a low Poisson's ratio implies a low value for the reservoir.

The maximum horizontal stress measured in the differential strain experiment was 68.6 MPa. In addition, the minimum horizontal and axial stresses of the specimen were recorded as 55.0 MPa and 59.3 MPa, respectively. By combining the differential strain and paleomagnetic experiments, the direction of maximum horizontal stress of the specimen was determined to be 114.4° (Table 2).

The high stress difference coefficient of the Da'anzhai reservoir makes it difficult to form complex fractures. It is necessary to maximize the net pressure inside the fracture to create the conditions for complex fracture formation. Moreover, techniques such as filling the fracture with a low-density liquid can be employed to increase the net pressure. Complex fracture formation has significant implications and applications, and further exploration of its effects and practical examples would be beneficial.

3 Physical simulation tests of fracturing

The hydraulic fracturing technique plays a crucial role in enhancing oil and gas production in tight reservoirs.

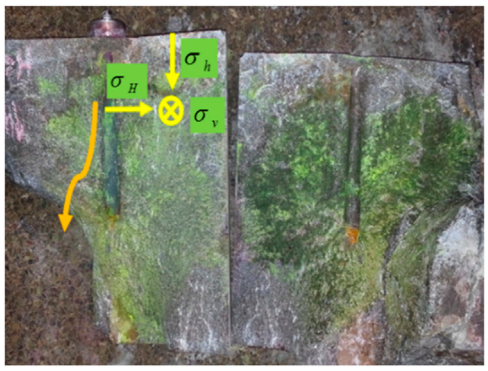


FIGURE 9
Schematic diagram of fracturing results for sample 4 #.

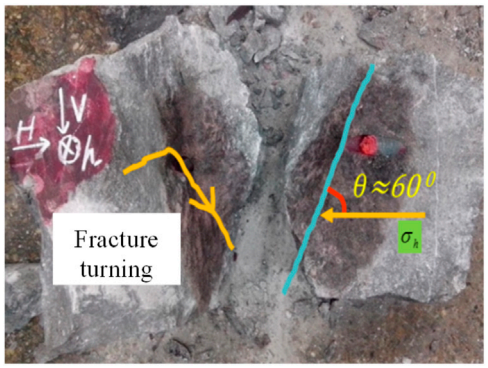


FIGURE 10
Schematic diagram of fracturing results for sample 5 #.

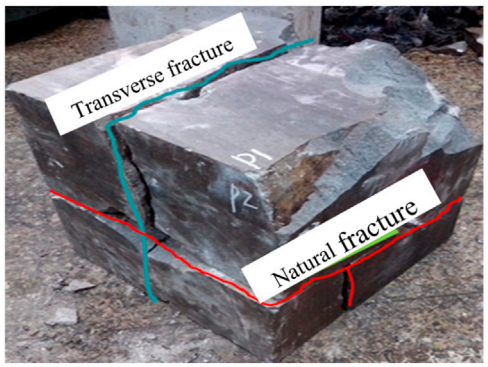


FIGURE 11
Fracturing results of test sample 6 #.

Understanding the fracturing mechanics and optimizing fracturing param are important for successful stimulation. This study focuses on the Da'anzhai section in the Sichuan Basin, aiming to explore the true triaxle physics simulations and process tests for hydraulic fracturing (Table 3).

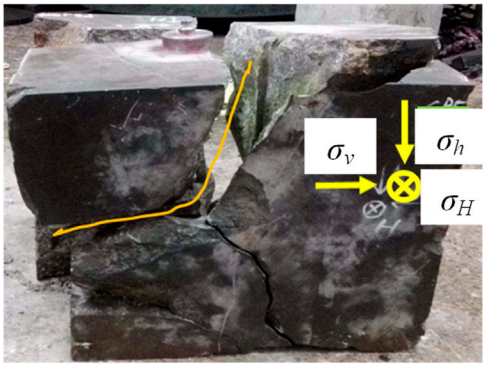


FIGURE 12
Schematic diagram of 7 # test sample fracturing results.

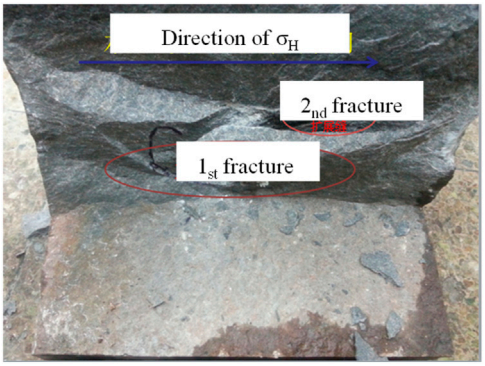


FIGURE 14
Schematic diagram of fracturing results for sample 9 #.

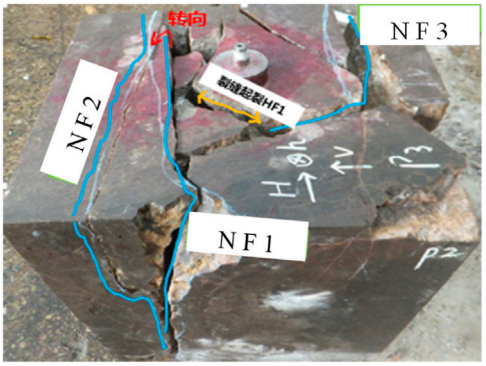


FIGURE 13
Schematic diagram of fracturing results for sample 8 #.

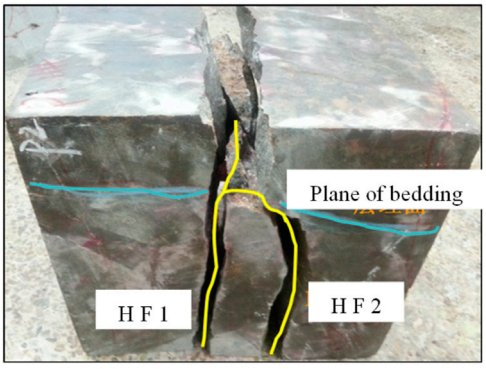


FIGURE 15
Schematic diagram of fracturing results for sample 10 #.

3.1 Large scale true triaxle simulation test system

The large-scale true triaxle simulation test system consists of a triaxle shear test rack, an MTS servo hydraulic pump, a Local-AT14 acoustic emission sensor, a power stabilizer, a water-oil isolator, and other auxiliary equipment. The overall structure is shown in Figure 4. An MTS servo booster pump was used to pump high-pressure liquid into the simulated borehole. The MTS Booster pump has a program controller that can pump liquid with constant or variable displacements. The MTS data collection system records param such as pressure and displacement of the fracturing fluid. A sliding sleeve oil-water separator is used in the thick-walled, cylindrical autoclave to separate the MTS working medium from the fracturing fluid. With a volume of 700 mL and a pressure-bearing capacity of 70 MPa, the system meets the requirements of a simulated fracture test.

3.2 Sample preparation and experimental methods

3.2.1 Sample preparation

The sample was taken from a dense limestone outcrop in the Da'anzhai section of central Sichuan. Using a rock cutting machine, the sample was cut into a cube rock block measuring 300 mm × 300 mm × 300 mm in size. A diamond core drill bit was used to drill a core on site, simulating a circular bore hole with a depth of 18 mm and 16 bore. We created 3 clusters of perforation simulations using a stainless-steel mold, where the simulated phase was a 90° spiral perforation, the perforation hole diameter was 2.0 mm, and the perforation depth was 40 mm. The sample is shown in Figure 5. To more clearly identify the geometry of fractures, we mixed dyes into the fracturing fluid (Figures 6A, B). After the experiment was completed, we knocked open the specimen with a hammer alone. The hole is then filled with filling material, glue is injected and the hole is finally sealed. To simulate the perforation, a stainless-steel mold was used to create 3 clusters of perforation simulations, with a simulated phase of 90° spiral perforation, a perforation hole diameter of 2.0 mm, and a perforation depth of 40 mm. The sample is shown in Figure 5. To more clearly trace the geometry of fractures, dyes were mixed into the fracturing fluid (Figure 6). After the experiment was completed, the fracturing fracture to observe the morphology of the fracture.

To ensure quasi-static fracture propagation and prevent rapid breaking through the outer surface of the specimen, the fracture tip propagation velocity was clamped by increasing the confining

TABLE 4 Basic parameters of the Daanzhai formation reservoir in Well L 2.

Layer	Well section/m	Thickness/m	Lithology	Porosity/%	Water saturation/%	Logging interpretation
Daanzhai	2,769.6–2,774.0	4.4	Brown gray shell limestone	4–6	30–45	Oil and gas layer

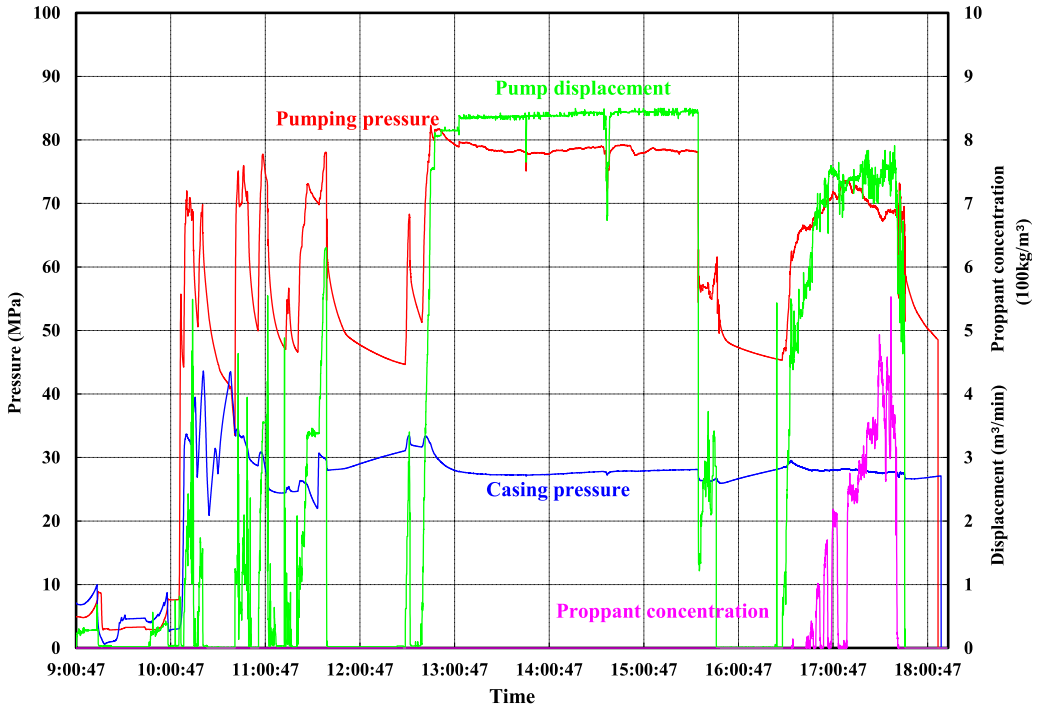


FIGURE 16
Sand fracturing construction curve for Da'anzhai section of Well L 2.

pressure. The sample was then placed in the press and the pressure plate and other components were installed. To ensure uniform loading, a rubber gasket was placed between the pressure plate and the specimen. After mounting, a three-way confining pressure was applied by a hydraulic pressure source before the fracturing fluid was pumped into the simulated wellbore at a predetermined displacement until the sample ruptured. Finally, the morphology of the formed fractures was observed and param such as pump injection pressure and displacement during fracture propagation were recorded using an MTS test machine.

3.2.2 Experimental parameter design

The simulated geomechanically environment in the experiment comprises an average formation temperature of 70°C, an average elastic modulus of 5.865×10^4 MPa, an average Poisson's ratio of 0.23, and an average compressive strength of 356.02 MPa. In the experimental triaxle stress design, the maximum horizontal principal stress is 55 MPa, the minimum horizontal principal stress is 40 MPa, and the vertical principal stress is 48 MPa. Various conditions such as different rock types, wellbore trajectories, and fluid types are used to model the morphology of fracture initiation and propagation.

3.3 Analysis of test results

We conducted 10 sets of indoor simulation tests to investigate the impact of completion method, type of fracturing fluid, *in situ* stress, and the observed greater increase in fracture length when using a low-viscosity fracturing fluid. Third, *in situ* stress conditions in the formation should be taken into account, as they have a significant effect on the orientation of the fracture. Finally, it is important to take into account pump displacements and specimen sizes, which have a direct effect on the fracture propagation pattern. Overall, the experimental findings suggest that the pattern of fracture elongation is determined by a combination of factors, namely, pump displacement, natural fracture, and specimen size.

3.3.1 Impact of completion methods

Sample 1 simulates open-hole completion, while sample 2 simulates perforation completion. From Figure 7, it can be seen that sample 1 # shows a break at 63 MPa, while sample 2 # shows a break at 56 MPa. Analyzing the highest experimental pump pressure values corresponding to the two completion methods in Figure 7, it is found that perforation completion is helpful for crack initiation.

Sample 3 was also subjected to simulated perforation completion, but repeated loading tests did not reveal any

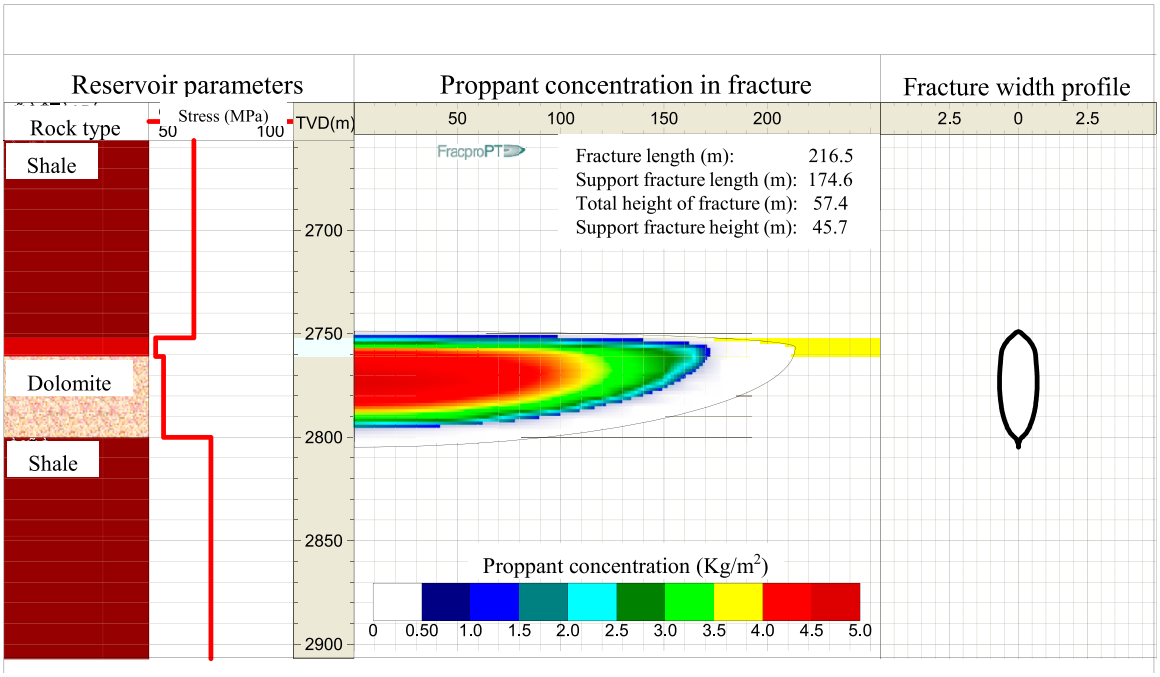


FIGURE 17
Simulated morphology of formed fracturing fractures for Da'anzhai section of Well L 2.

significant fractures. When the sample was pried open (Figure 8), it was observed that there was no fracture upon prying open the sample (Figure 8), it was found that the pre-drilled hole remained intact without fracturing. Indoor tests demonstrated that the fracture pressure of the open hole completion method was lower compared to the perforated completion method. This phenomenon can be attributed to the following reasons. First, the inability to create a complete perforation channel penetrating the wellbore indoors leads to increased energy loss at the simulated wellbore perforation point. Second, some holes are sealed by cementing fluid. Additionally, the open hole completion method ensures sufficient infiltration of fracturing fluid into the rock sample.

3.3.2 Impact of fracturing fluid type

Figure 9 illustrates the test results for a sample numbered 4 tested with a cross-linked fluid. Initially, the onset of fracture does not follow the direction of the maximum horizontal principal stress due to the presence of a natural fracture surface near the bore. However, after a certain amount of expansion, the effect of the 3D principal stress becomes dominant and, as a result, the fracture turns in the direction of the largest transverse principal stress. On the other hand, Figure 10 shows the test findings for a sample numbered 5 tested with pure water. In this case, hydraulic fractures also showed a turning angle, but there was a 60° angle between the turning line and the direction of the minimum horizontal principal stress. Moreover, the fracture surface exhibits kinks and tilts. The limited penetration of the cross-linked fluid into the strata reduces the likelihood of shear slip and expansion leading to degenerate fractures. In addition, pure water has the ability to propagate towards natural fractures more easily, which can result in a lower pressure drop of the flowing fluid within the fracture, thus increasing the probability of new fractures forming at the ends of natural fractures.

3.3.3 Influence of ground stress difference

Figure 11 illustrates the results of the test performed on sample 6 with a horizontal stress difference of 8 MPa. Similarly, Figure 12 shows the corresponding results for sample 7 with a level stress difference of 2 MPa. The fracture morphology of sample 6# after compression is relatively simple, exhibiting a single transverse main fracture that fully penetrates the natural fracture surface without any turning or dynamic bifurcation. In contrast, the fracture in sample 7 shows a tendency to turn in the direction of the natural fracture. Lateral stress differences play a significant role in fracture propagation in rocks. A larger transverse stress difference leads to a restricted fracture initiation and propagation direction, resulting in the formation of a simpler fracture morphology. In turn, when the transverse stress difference is small, fractures tend to turn and dynamically bifurcate, facilitating connections with natural fractures and eventually complex networks. Understanding the effect of transverse stress differences on fractures is therefore crucial for improving the accuracy of rock mechanics models.

3.3.4 Natural fracture impact

Experimental results show that natural fractures and bedding have a significant impact on the complexity of fracking. The photographs in Figures 13–15 demonstrate this effect by testing samples of different types of fractures with different fluids. Specifically, Figure 13 shows a test using smooth water on an 8 # sample with well-developed natural fractures. In contrast, Figure 14 shows a test using smooth water on sample 9 # with an underdeveloped natural fracture. In addition, Figure 15 illustrates

a test using a cross-linked liquid on a 10 # sample with well-developed natural fractures. When comparing and analyzing the 8 # and 9 # samples, we find that the more developed the natural fractures and bedding, the more complex the hydraulic fracture morphology becomes, resulting in a larger spreading of the fracture network. On the other hand, it is challenging to form complex fracture morphologies when using smooth water for hydraulic fracturing in underdeveloped natural fracture reservoirs (as demonstrated in the comparison between samples 9 # and 10 #). In contrast, the use of cross-linked fracturing can increase the complexity and diversity of hydraulic fractures in naturally fractured reservoirs.

Physical model experiments have shown that small stress differences, natural fracture development, and low viscosity water can promote the formation of complex fracture morphologies. The randomness of the direction of the fracture bifurcation is mainly related to factors such as the degree of natural fracture development and the local stress field. According to our analysis, the rock itself dominates the formation of complex fracture morphologies, rather than the building parameters.

4 Process testing

Located in central Sichuan of China, L 2 is an appraisal well consisting of brownish-gray crustal limestone in the Da'anzhai section. Conventional logging data indicates the development of reservoir fractures, and geological logging shows "oil and gas invasion" at 2,772.0–2,773.0 m, which is comprehensively interpreted as an oil and gas reservoir, and the specific physical parameters of the reservoir are shown in Table 4. In the initial stage of stimulation treatment, correlated transitions are performed on the trap-deceit cross section. 60.3 m^3 of conventional acid was injected with a displacement of 2.0–2.5 m^3/min and a pump pressure of 83–85 MPa. After acidification, a test gas volume of 600 m^3/d was obtained.

Since the desired results from the acidification process were not achieved, it was decided to conduct hydraulic fracturing tests based on the concept of "large liquid volume, large displacement, and expansion of affected volume". According to the geological characteristics of the reservoir and the engineering conditions of the L1 well, the feasibility of fracturing was demonstrated (Figure 16). A hybrid fracture pattern of a linear gel and a cross-linked fluid was used. Through the Φ114.0 mm oil well tubing, a net liquid volume of 2042.7 m^3 was injected into the formation with a flow rate of 7.5–8.4 m^3/min and a pump pressure of 72–78 MPa. After hydraulic fracturing process, the well achieved a breakthrough from "no production" to a production rate of 2 t/d for oil and 3,000 m^3/d for gas, demonstrating successful results.

The actual data from the fracture process of this well were analyzed using software to simulate and analyze the fracture morphology, which is depicted in Figure 17. The simulation results indicate a total fracture length of 216.5 m, an effective fracture length of 174.6 m, and a fracture height of 57.4 m at pressure. Longer range fracture transitions can be obtained by effectively controlling the fracture height. This analysis is important as it provides valuable insights into the efficiency and effectiveness of the fracturing process for this well.

Seismic monitoring revealed a fracture zone with a length of 200 m, a width of 170 m and a height of 64 m, successfully achieving the volumetric fracture target. The testing of Well L2 using volumetric fracturing represents a technological breakthrough in the development of compact limestone reservoirs in the Da'anzhai section of the Sichuan Basin.

5 Conclusion

(1) The reservoir rocks in the Da'anzhai section are dense and show varying degrees of water sensitivity, ranging from moderate to strong. In addition, these rocks exhibit heterogeneity, with variations in mineral composition and texture throughout the formation.
(2) Large scale physical model experiments have shown that complex fracture morphology can be achieved through a combination of factors, including low stress differences, the presence of natural fractures, and the low viscosity of fracking fluids. However, beyond the parameters of the fracture process itself, the structural properties of the reservoir rock play a dominant role in determining the final fracture pattern.
(3) On-site process tests have demonstrated that significant fracturing transformations can be achieved in the test well by optimizing geological parameters and adopting specific volume fracturing techniques. These methods are based on reservoir properties, including the need for a large liquid volume, displacement, and expansion of the affected region. Taken together, these findings suggest that bulk fracturing in dense limestone reservoirs in the Da'anzhai section of central Sichuan is a viable approach.

Data availability statement

The raw data supporting the conclusion of this article will be made available by the authors, without undue reservation.

Author contributions

SL: Conceptualization, Formal Analysis, Writing–original draft, Writing–review and editing. YF: Funding acquisition, Project administration, Supervision, Resources, Writing–review and editing. YW: Data curation, Formal Analysis, Software, Writing–original draft. YZ: Writing–review and editing. ZL: Methodology, Resources, Validation, Writing–original draft. ZJ: Data curation, Methodology, Supervision, Writing–review and editing. WC: Funding acquisition, Resources, Writing–review and editing. JM: Data curation, Methodology, Writing–review and editing.

Funding

The author(s) declare financial support was received for the research, authorship, and/or publication of this article. This work was supported by the scientific research project of PetroChina Southwest Oil and Gas Field Company in 2022: volume fracturing technology research of Shale oil in Lianggaoshan Formation of Sichuan Basin (No. 20220302-10).

Acknowledgments

The authors are grateful for the support of the scientific research project of PetroChina Southwest Oil and Gas Field Company. We are also grateful to Professor Bing Hou and his research team from China University of Petroleum (Beijing) for providing reliable experimental data for the revision of our paper.

Conflict of interest

SL, YF, YW, ZL, ZJ, WC, and JM were empolyed by the Engineering Technology Research Institute of PetroChina Southwest Oil and Gas Field Company and YZ was employed Qilin Gas Production Area of the Fourth Oil Production Plant of PetroChina Changqing Oilfield Company

Publisher's note

All claims expressed in this article are solely those of the authors and do not necessarily represent those of their affiliated organizations, or those of the publisher, the editors and the reviewers. Any product that may be evaluated in this article, or claim that may be made by its manufacturer, is not guaranteed or endorsed by the publisher.

References

Cai, M., Tang, P. F., Wei, X., Liu, Y., and Zhang, H. (2022). Optimization of composite volume fracturing technology for Gulong shale oil. *Petroleum Geol. Oilfield Dev. Daqing* 41 (3), 156–164. doi:10.19597/J.ISSN.1000-3754.202111084

Cao, B. G. (2015). Discussion on volume fracturing method of horizontal wells in tight reservoir of Ordos Basin. *Reserv. Eval. Dev.* 5 (5), 62–68. doi:10.13809/j.cnki.cn32-1825/te.2015.05.014

Du, J. H., He, H. Q., Li, J. Z., Yang, T., Huang, F. X., Guo, B. C., et al. (2014). Progress in China's tight oil exploration and challenges. *China Pet. Explor.* 19 (1), 1–9. doi:10.3969/j.issn.1672-7703.2014.01.001

Hou, B., Tan, P., Chen, M., Yuan, L., Xiong, Z. Y., and Xu, C. L. (2016). Experimental investigation on propagation geometry of hydraulic fracture in compact limestone reservoirs. *Chin. J. Geotechnical Eng.* 38 (2), 219–225. doi:10.11779/CJGE201602004

Hou, Z. K., Cheng, H. L., Sun, S. W., Chen, J., Qi, D. Q., and Liu, Z. B. (2019). Crack propagation and hydraulic fracturing in different lithologies. *Appl. Geophys.* 16 (2), 243–251. doi:10.1007/s11770-019-0764-3

Kong, X. W., Yan, R. T., Xu, H. X., and Li, S. (2023). Experiment on equilibrium initiation and extension of multiple clusters of fractures based on true triaxial physical simulation. *Nat. Gas. Geosci.* 34 (7), 1123–1136. doi:10.11764/j.issn.1672-1926.2023.03.010

Li, J. W., and Wu, K. (2022). Impact of horizontal weak interfaces on the hydraulic fracturing from height growth to lateral propagation. Proceedings of the Paper URTEC-3723910-MS, presented at the SPE/AAPG/SEG Unconventional Resources Technology Conference, Houston, Texas, USA, June 2022.

Li, S., Zhang, H. L., Wang, M., Zhang, X., and Zhou, C. L. (2021). Experimental evaluation and process optimization of temporary plugging to acid-frac in fractured carbonate reservoirs. *Chem. Eng. Oil Gas* 50 (3), 90–95. doi:10.3969/j.issn.1007-3426.2021.03.015

Li, Z. X., Li, J., Qu, X. F., Li, X. W., Lei, Q. H., and Fan, J. M. (2015). The experiment and recognition of the development of Chang 7 tight oil in Ordos basin. *Nat. Gas. Geosci.* 26 (10), 1932–1940. doi:10.11764/j.issn.1672-1926.2015.10.1932

Lin, B. T., Shi, C., Zhuang, L., You, H. J., and Huang, y. (2020). Study on fracture propagation behavior in ultra-heavy oil reservoirs based on true triaxial experiments. *Petroleum Explor. Dev.* 47 (3), 651–660. doi:10.1016/S1876-3804(20)60082-9

Lucas Wesley, B., Bruce Roman, M., and Tran, V. P. (2021). Innovative analysis of treatment well data determines cluster efficiency, assesses fracture complexity, and provides fracture geometry in unconventional reservoirs. *Seg. Glob. Meet. Abstr.*, 182–223. doi:10.15530/ap-urtec-2021-208315

Mayerhofer, M. J., Lolon, E. P., Warpinski, N. R., Cipolla, C. L., Walser, D., and Rightmire, C. M. (2010). What is stimulated reservoir volume. *SPE Prod. operations* 25 (1), 89–98. doi:10.2118/119890-pa

Mcdaniel, B. W. (2010). Horizontal wells with multistage fracs provide better economics for many lower permeability reservoirs. Proceedings of the Paper SPE 113427 prepared for the presentation at the SPE Asia Pacific Oil and Gas Conference and Exhibition. Brisbane. Queensland. Australia. 18–20. October 2010.

Soliman, M. Y., East, L. E., and Augustine, J. R. (2010). Fracturing design aimed at enhancing fracture complexity. *Soc. Petroleum Eng.* doi:10.2118/130043-MS

Tan, P., Jin, Y., and Pan, P. (2021a). Hydraulic fracture vertical propagation behavior in transversely isotropic layered shale formation with transition zone using XFEM-based CZM method. *Eng. Fract. Mech.* 248, 107707. doi:10.1016/j.engfracmech.2021.107707

Tan, P., Pan, P., Zhang, R. X., Jin, Y., Zhou, Y., Kao, J., et al. (2020). Experimental investigation into hydraulic fracture geometry and proppant migration characteristics for southeastern Sichuan deep shale reservoirs. *J. Petroleum Sci. Eng.* 184, 106517. doi:10.1016/j.petrol.2019.106517

Tang, P. F., Liu, Y., Qi, S. L., Deng, D. W., and Li, C. R. (2021b). Physical simulation experiment on hydraulic fracturing of large-scale tight sandstone outcrop. *Fault-Block Oil Gas Field* 28 (3), 397–402. doi:10.6056/dkyqt202103021

Wang, D. B., Zhou, F. J., Li, Y. P., Yu, B., Martyushev, D., Liu, X. F., et al. (2022). Numerical simulation of fracture propagation in Russia carbonate reservoirs during refracturing. *Petroleum Sci.* 19 (6), 2781–2795. doi:10.1016/j.petsci.2022.05.013

Wang, D. B., Zlotnik, S., Díez, P., Ge, H., Zhou, F. J., and Yu, B. (2020b). A numerical study on hydraulic fracturing problems via the proper generalized decomposition method. *Comput. Model. Eng. Sci.* 122, 703–720. doi:10.32604/cmes.2020.08033

Wang, D., Dong, Y., Sun, D., and Yu, B. (2020a). A three-dimensional numerical study of hydraulic fracturing with degradable diverting materials via czm-based fem. *Eng. Fract. Mech.* 237, 107251. doi:10.1016/j.engfracmech.2020.107251

Wang, Y., Fan, Y., and Wang, X. J. (2023a). Study on migration law of multiscale temporary plugging agent in rough fractures of shale oil reservoirs. *Front. Phys.* 11, 1228006. doi:10.3389/fphy.2023.1228006

Wang, Y., and Lv, Z. F. (2023b). Composite stimulation technology for improving fracture length and conductivity of unconventional reservoirs. *Front. Phys.* 11, 1181302. doi:10.3389/fphy.2023.1181302

Warpinski, N. R., Mayerhofer, M. J., Vincent, M. C., Cipolla, C. L., and Lolon, E. P. (2009). Stimulating unconventional reservoirs: maximizing network growth while optimizing fracture conductivity. *J. Can. Petroleum Technol.* 48 (10), 39–51. doi:10.2118/114173-MS

Wei, H. F., Fan, Z. Y., and Yuan, X. C. (2013). Review on new advances in foreign tight oil development technology and their enlightenment. *Petroleum Geol. Recovery Effic.* 20 (2), 62–66. doi:10.13673/j.cnki.cn37-1359/te.2013.02.014

Yang, H., Wang, R., Zhou, W., and Li, L. (2014). Beneficial effects of β-conglycinin on renal function and nephrin expression in early streptozotocin-induced diabetic nephropathy rats. *J. China Univ. Petroleum Ed. Nat. Sci.* 38 (6), 78–85. doi:10.1017/S0007114513001876

Yu, W., and Sepehrnoori, K. Optimization of well spacing for Bakken tight oil reservoirs. Proceedings of the Unconventional Resources Technology Conference. 2014, January 2014, Denver, Colorado, USA, doi:10.15530/urtec-2014-1922108

frontiers | Frontiers in Energy Research

TYPE Perspective
PUBLISHED 10 November 2023
DOI 10.3389/fenrg.2023.1320366

Check for updates

OPEN ACCESS

EDITED BY
Peng Tan,
CNPC Engineering Technology R&D Company Limited, China

REVIEWED BY
Fuhua Shang,
Inner Mongolia University of Technology, China
Shang Xu,
China University of Petroleum (East China), China
Ruyue Wang,
SINOPEC Petroleum Exploration and Production Research Institute, China

*CORRESPONDENCE
Hu Li,
lihu860628@126.com

RECEIVED 12 October 2023
ACCEPTED 02 November 2023
PUBLISHED 10 November 2023

CITATION
Li H (2023), Deciphering the formation period and geological implications of shale tectonic fractures: a mini review and forward-looking perspectives. *Front. Energy Res.* 11:1320366. doi: 10.3389/fenrg.2023.1320366

COPYRIGHT
© 2023 Li. This is an open-access article distributed under the terms of the Creative Commons Attribution License (CC BY). The use, distribution or reproduction in other forums is permitted, provided the original author(s) and the copyright owner(s) are credited and that the original publication in this journal is cited, in accordance with accepted academic practice. No use, distribution or reproduction is permitted which does not comply with these terms.

Deciphering the formation period and geological implications of shale tectonic fractures: a mini review and forward-looking perspectives

Hu Li[1,2,3,4]*

[1]Sichuan College of Architectural Technology, Chengdu, China, [2]Post-Doctoral Research Center, Southwest Petroleum University, Chengdu, China, [3]Shale Gas Evaluation and Exploitation Key Laboratory of Sichuan Province, Chengdu, China, [4]Natural Gas Geology Key Laboratory of Sichuan Province, Chengdu, China

In complex geological areas, the chronology of tectonic fracture formation is pivotal for the conservation and enhancement of shale gas reservoirs. These fractures, evolving over different geologic epochs, critically influence the modifications in hydraulic fracturing. The review sheds light on an integrated methodology that bridges conventional geological evaluations with experimental diagnostics to decipher the intricate evolution of such fractures in complex geological areas. Shale tectonic fractures, predominantly shear-induced, are delineated into four distinct levels (I, II, III, IV) based on observational scales. Understanding the geometric interplay across these scales provides insight into fracture distribution. Recognizing the constraints of isolated approaches, this study amalgamates macroscopic geological assessments, such as structural evolution and fault analysis, with microscopic techniques, including fluid inclusion studies, isotopic testing, rock AE experiments (U-Th)/He thermochronology, and AFT analysis, etc. This combined approach aids in accurately determining the tectonic fracture's genesis and its geological time. Future research endeavors should refine this framework, with an emphasis on enhanced geochemical profiling of fracture fillings.

KEYWORDS

tectonic fractures, formation timing, geochemistry, low-temperature thermochronology, fracture fillings, shale, complex structural areas

1 Introduction

Shale gas, recognized as a premier clean energy resource, has witnessed significant advancements in the Sichuan Basin, underpinned by a constellation of geological theories and innovative exploration and extraction methodologies (Wang et al., 2016a; Li et al., 2022; Li, 2022; 2023). The marine shale strata within the Wufeng-Longmaxi Formation are particularly noteworthy due to their elevated Total Organic Carbon (TOC) concentration, pronounced stratigraphic thickness, advanced maturity, inherent brittleness, and abundant gas content, solidifying their status as the prime locus for shale gas prospecting and extraction (Wang et al., 2018; 2022a). A testament to nearly a decade of relentless exploratory and developmental endeavors, successful shale gas fields have been commissioned in locales such as Fuling, Changning, Zhaotong, Weiyuan-Rongchang,

and Luzhou (Fan et al., 2020a; Xu et al., 2020a; He et al., 2022a; He et al., 2022b). The marine shale sequences in the Sichuan Basin have been subjected to myriad tectonic episodes, culminating in the genesis of intricate fracture network systems spanning various scales—tectonic fractures being particularly prevalent (Li J. et al., 2022; 2023; Zhu et al., 2023). The evolution and architecture of these fractures and faults are pivotal in shaping the efficacy of shale gas reservoirs (Fan et al., 2020b). Serving dual roles, they act as reservoir spaces and enhance reservoir connectivity by bridging pores and microfractures, thereby ameliorating pore-permeability dynamics (Hou et al., 2020; Fan et al., 2022; Zhu et al., 2023).

Additionally, the unique adsorption and storage mechanisms of shale gas within rocks dictate that the development of these reservoirs relies on large-scale hydraulic fracturing to achieve industrial gas production (Hui et al., 2022). The construction of tectonic fracture networks plays an important role in the formation and expansion of hydraulic fractures (Wang et al., 2016b; Xia and Lu, 2022; Huang et al., 2023; Tan et al., 2023). Over the years, scholars have made significant progress in understanding various aspects of shale fractures, including their development characteristics, quantitative characterization, identification methods, distribution patterns, controlling factors, and impact on gas content, etc (Gale et al., 2014; Wu et al., 2019; Xu et al., 2019; 2020b; Gong et al., 2021; Meng et al., 2021; Shan et al., 2021; Tan et al., 2021). The formation period of tectonic fractures is considered a challenging and crucial aspect in this research field. It is generally believed that tectonic fractures are controlled by regional or local stress in the geological mechanical environment. Determining the formation period reflects the evolution periods of shale gas preservation conditions and contributes to the coupled study of shale gas enrichment and migration (Feng et al., 2023). Additionally, it can indicate the formation periods of geological structures, such as folds and faults.

Various methods have been developed to determine the formation period of tectonic fracture. These methods include structural analysis, multi-scale fracture cutting relationships, fracture fillings analysis, and rock AE analysis. This paper summarizes the latest developments and the potential challenges it may face. It provides a systematic and intuitive perspective on fracture formation, development, and evolution in “sweet spot” shale layers. It is expected to be a reference and guide for research and practices on exploring shale fracturing mechanisms, optimizing hydraulic fracturing processes, and increasing and stabilizing shale gas production.

2 Characterization of types and development characteristics parameters of shale tectonic fractures

Over the years, many research efforts have yielded a comprehensive understanding of the development characteristics of tectonic fractures. This understanding is based on the outcrop, core, and thin slice observation, focusing on parameters such as fracture types, length, aperture, density, and fillings, etc. Shale tectonic fractures are primarily dominated by shear fractures, followed by tensile fractures (Li et al., 2019a; Li et al., 2021a). In field outcrops, shear fractures are particularly prevalent, characterized by straight and stable orientations, often occurring in groups, and exhibiting prominent crosscutting relationships. Based on the mutual relationship between shear fractures and rock layers, they can be further classified into plane and profile shear fractures (Figure 1A). Plane shear fractures typically form early, primarily when the rock layers have not undergone significant deformation (Figure 1A). These fractures have relatively flat fracture surfaces and often intersect with the rock layers at high angles, ranging from 45° to 75° or even vertically (75°–90°) (Figures 1B,C). Plane shear fractures often exhibit a multi-set “X" type conjugate relationship on the plane of the rock layer. In cross-section, they can result in a stepped blocky exposure of the rock. In contrast, profile shear fractures form later, typically after significant deformation of the rock layers has occurred (Figure 1A). The fracture surfaces may display scratch marks resulting from shear action and intersect the rock layer at low-angle obliquities, ranging from 15° to 45° (Figure 1D). Tensile fractures, on the other hand, are less developed, but due to surface weathering and erosion in exposed outcrops, their recognition can be challenging. They tend to have unstable orientations, and are often filled with calcite (Figure 1E).

Fractures in core samples are still primarily characterized by shear fractures, which exhibit features such as flat fracture surfaces, long extents, and penetrating the entire core (Li et al., 2021a; Li et al., 2021b). On one hand, shear fractures can cut across the entire core, resulting in relatively smooth fracture surfaces after the core is split (Figure 1F). On the other hand, in the cross-section of the core, multiple sets of fractures can be observed intersecting each other at certain angles (Figure 1G). Tensile fractures, in contrast, are characterized by rough fracture surfaces, shorter extents, and uneven apertures. They often intersect, forming a network-like pattern, and most are partial to fully filled by calcite (Figures 1H,I).

Tectonic microfractures encompass grain-boundary fractures (intergranular fractures) and mineral cleavage fractures (intragranular fractures). Among them, grain-boundary fractures primarily develop along mineral grain boundaries, exhibiting shapes and patterns that are in harmony with the morphology of mineral boundaries. Their orientations and dip angles are often variable, and the fracture apertures can vary significantly (Figure 1J). Mineral cleavage fractures, on the other hand, develop within mineral grains. They feature straight fracture surfaces, minimal curvature, and show no evidence of cement fillings. The grain size of the mineral particles controls the length of these microfractures. In addition to undergoing deformation and displacement, the mineral grains may exhibit internal lattice dislocation or failure phenomena (Figure 1K).

3 Determining the formation period of shale tectonic fractures

3.1 Geological analysis

Based on the fracture orientation data measured from field outcrops resembling the target geological formation, applying structural geological theories to invert the ancient tectonic stress field is essential for establishing stress-matching relationships. In general, the intersection lines of conjugate shear fractures are parallel to the intermediate principal stress axis σ_2. The

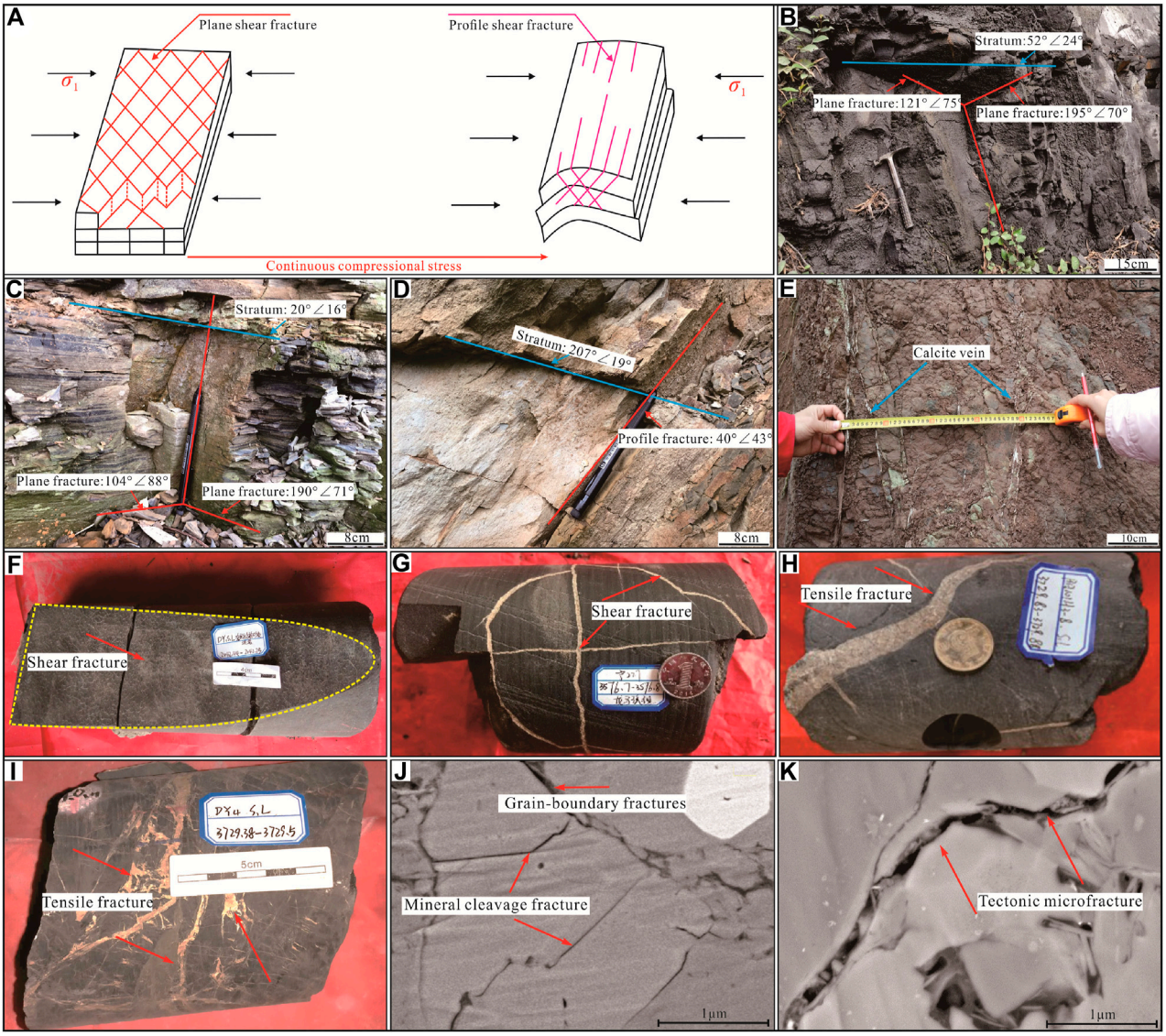


FIGURE 1
Tectonic fracture types and characteristics of the Longmaxi Formation shale in the Sichuan Basin (Zhong, 2019; Fan et al., 2020b). **(A)** Schematic diagram of the formation of plane shear fractures and profile shear fractures. **(B,C)** Plane shear fractures in Changning area (Fan et al., 2020b); **(D)** Profile shear fractures in Changning area; **(E)**. Tensile fractures in Dingshan area; **(F)** DY1, 2042.45–2042.75 m, shear fracture; **(G)** N227, 3,576.70–3,576.80 m, shear fracture; **(H)** Y101H3-8, 3,729.83–3,729.86 m, tensile fracture; **(I)** DY4, 3,729.38–3,729.50 m, multiple tensile fractures forming a network; **(J)** DY1, grain-boundary fractures and mineral cleavage fractures; **(K)** DY1, tectonic fracture.

maximum principal stress axis σ_1 and the minimum principal stress axis σ_3 are oriented along the angle bisectors of their acute and obtuse angles, respectively (Batayneh et al., 2012). This approach determines the maximum principal stress direction in the ancient tectonic stress regime. Utilizing image logging data for fracture orientation identification is currently one of the most accurate methods, particularly in areas where oriented core samples are unavailable. Based on the interpretation of fracture orientations from the imaging logging in the study area, generating a rose diagram of fracture orientations and analyzing the dominant orientations, combined with understanding the formation mechanisms of conjugate shear fractures, enables the accurate determination of the sequence of fracture formation.

Determining the sequence of fractures based on the crosscutting relationships observed between fractures in the outcrops, cores, thin slices, and other geological materials is one of the most fundamental and direct methods. In general, when determining the relative timing of fracture formation, the following principles are typically followed: If another fracture cuts a fracture, it forms earlier; If a fracture is truncated or terminated by another fracture, it forms later; If a fracture is not filled, it generally formed later. However, it is important to note that determining fracture sequences based on crosscutting relationships often represents only a portion of multiple-stage fractures in a single image. Comprehensive analysis is required to make accurate judgments.

Additionally, fault evolution and fracture development are controlled by the same regional structural stress field in the same geological region (Meier et al., 2015). They exhibit inheritance and consistency in terms of their origin and characteristics. Therefore, combining the fault characteristic can assist in analyzing the timing of tectonic fracture development. Generally, there is good correspondence between field outcrop analysis of similar exposures, multi-scale fracture crosscutting relationships, imaging log orientation analysis, and fault structural analysis.

3.2 Experimental testing analysis

In recent years, experimental testing has played a significant role in determining the timing of fracture formation. These experiments encompass a range of methods, including fluid inclusions, isotopes, AE, low-temperature thermochronology, and thermal history simulation, etc.

3.2.1 Experimental testing of fracture fillings

The minerals, such as calcite and quartz, found filling fractures in sedimentary rocks within oil and gas basins are the products of fluid migration, material transport, energy and substance exchange, and fluid-rock interactions during diagenesis. They represent the diagenetic response of these fractures to factors such as the geochemistry of diagenetic fluids, temperature-pressure conditions, and sources of materials at the time of their formation. Therefore, conducting experimental tests on fracture fillings can be utilized to analyze the timing of fracture formation. Additionally, it can provide insights into the dynamic evolution of temperature-pressure conditions and fluid redox environments during the burial and uplift processes of sedimentary strata within oil and gas basins.

3.2.1.1 Fluid inclusion testing

Fluid inclusions are portions of diagenetic or ore-forming fluids trapped within the lattice defects or cavities of minerals during their crystallization process. These inclusions remain sealed within the main mineral and have boundaries with the host mineral. They preserve geochemical information about the geological environment during their entrapment, including pressure, temperature, salinity, and more. Therefore, analyzing fluid inclusions can be employed to determine the timing of fracture formation, as they serve as valuable repositories of geological information related to the formation period (Fall et al., 2012).

Fluid inclusion temperature measurement is currently the most widely used non-destructive analysis method. Saltwater inclusions coexisting with oil and gas inclusions of different ages often have uniform temperatures, which can approximate the formation temperature of the reservoir at the time of inclusion trapping. Freeze-thaw analysis (freezing point depression) can be used to determine the original geological fluid type and salinity data preserved within these inclusions. Using the measured temperatures and referencing established fluid freezing point-salinity relationships, initial dissolution temperatures, and fluid type data, one can roughly infer the salinity and fluid type stored within the fluid inclusions. This information reflects different periods of fracture formation (Chen and Liu, 2021). However, it is important to note that there are limitations in this application, such as the difficulty in observing phase changes in some fluid inclusions during testing and the limited applicability range of empirical formulas for salinity-freezing point relationships.

3.2.1.2 Carbon and oxygen isotope testing

Fractures and faults in sedimentary rocks are crucial pathways for fluid movement in oil and gas basins. Under burial conditions, the formation of fractures allows underground saturated aquifer water to enter them first and flow along the fracture surfaces, resulting in the precipitation of mineral crystals on these surfaces. Different diagenetic environments and properties of diagenetic fluids during geological evolution lead to noticeable differences in the precipitated crystals' carbon and oxygen stable isotope values. After identifying the stages and sequences of fractures within rock cores and assigning them to different periods, carbon and oxygen isotope experiments can be conducted on the corresponding fracture fillings to determine the distribution range of isotope values (Zhang et al., 2016; Kontakiotis et al., 2020; 2021). Combining this data with oxygen isotope thermometry and burial history analysis allows for determining the timing of fracture formation.

3.2.2 Rock acoustic emission experiment analysis

AE phenomena occur during the process of material stress and deformation. The essence of rocks' AE phenomenon is derived from the expansion of internal micro-defects. Each time rocks are subjected to stress, their internal micro-fracture system, known as Griffith Microfracture, adapts to the magnitude and direction of the applied stress (Becker et al., 2014; Cai, 2020; Wang et al., 2022b). When rocks are subjected to stress below the threshold stress required to propagate pre-existing fractures or defects, there will be no further fracture development, and thus, no acoustic emission occurs. However, when the applied stress reaches or exceeds the threshold, the pre-existing fractures or defects will extend further, resulting in AE phenomena, known as the Kaiser effect. At this point, the stress value represents the paleo stress conditions during the previous fracture extension. Analyzing the number of Kaiser effect points on the AE response curve makes it possible to infer the stress-induced fracture periods and the paleo stress field strength that the rocks have experienced. In recent years, this method has been widely applied in studying fracture evolution history, fracture staging and correlation, and determining the stress field strength.

3.2.3 Low-temperature thermochronology analysis

In recent years, low-temperature thermochronology has been an important branch and cutting-edge field of geological dating research. It mainly involves two dating techniques: AFT and (U-Th)/He dating. The target minerals for this technique are primarily apatite, zircon, and titanite, with the first two being the most common. In sedimentary basins, the depth at which organic matter generates hydrocarbons corresponds to the partial annealing temperature zones of AFT and AHe systems. These systems exhibit a clear consistency, and a specific functional relationship (annealing sensitivity) exists between the length and density of mineral tracks and the sample's history of uplift, erosion, and thermal events (Deng et al., 2016). Therefore, low-temperature thermochronology can

effectively quantify a basin's thermal history and the uplift and erosion processes. Based on low-temperature thermochronology measurements, it is possible to determine the sequence of tectonic movements and geological time, which can assist in identifying the timing of tectonic fracture formation.

The fission track dating method is based on the spontaneous fission of ^{238}U in minerals and the resulting radiation damage to the host mineral. It involves analyzing the isotope ages that develop in minerals based on the spontaneous track density and the ^{238}U content. Unlike conventional organic geochemical analysis methods, fission track dating can effectively record paleotemperatures and the time spent at these temperatures during the geological evolution of a geological body. It can provide insights into the paleotemperature evolution process at depths of 3–5 km near the Earth's surface. (U-Th)/He dating, on the other hand, relies on the production of He through the decay of radioactive elements. In minerals, particularly apatite, the He primarily comes from the decay of ^{238}U, ^{235}U, and ^{232}Th.

4 Discussion

4.1 Comprehensive determination of the fracture formation period

As previously mentioned, there are generally three methods for studying the formation period of tectonic fractures. However, individual methods for determining the fracture formation period have their limitations. Therefore, a comprehensive method for determining the fracture formation period based on macroscopic geological analysis and experimental testing has been established (Li et al., 2020; Li et al., 2021a; Hu et al., 2023).

1) Quantitative characterization of fracture parameters: The study begins with the quantitative characterization of fundamental parameters associated with the development of fractures at various scales. This quantification is achieved through a combination of methods, including seismic interpretation, field outcrop investigations, core observations, thin slices, scanning electron microscopy, and CT scanning, etc. Geometric quantitative relationships for characteristic parameters of tectonic fractures at different scales (I-II-III-IV) are established. 2) Integration of macroscopic and microscopic analyses: Following this, a fusion of macroscopic geological analysis is undertaken, which encompasses tectonic evolution analysis, the evaluation of fault and fold structures, and the examination of matching and crosscutting relationships among multi-scale fracture orientations. This macroscopic analysis is complemented by microscopic experimental techniques, including fluid inclusion and carbon-oxygen isotope testing of fracture fillings, rock AE experiments, (U-Th)/He low-temperature thermochronology, and AFT analysis, etc. 3) Cross-Verification and comprehensive determination: Through the combination of these diverse methods, the study cross-verifies and comprehensively determines the formation periods and geological times of fractures formed under multi-stage tectonic stress conditions. This integrative approach overcomes the limitations of individual techniques, providing a more holistic understanding of the timing of tectonic fracture formation.

Figure 2 provides a good example of a comprehensive method for determining the formation periods of tectonic fractures of Dingshan area in Sichuan Basin. Tectonic fractures (faults) are the result of stress and can generally be divided into four stages, which we define as four different scales (I, II, III, IV) ranging from micro to macro. The matching and crosscutting relationships of multi-scale fracture orientations indicate the presence of two formation periods. The AE experiments reveal five periods, after removing the influence of current stress, it can be determined as four periods. In addition, the Indosinian movement in the study area is mainly characterized by ascending and descending movements, with almost no fracture formation. Therefore, the AE experiment can be determined as third stage periods (Xie et al., 2019a; 2019b). The fluid inclusion homogenization temperatures show three periods, and the carbon and oxygen isotope tests indicate three periods. By combining the analysis of tectonic evolution and thermal history, we ultimately determined three formation periods for tectonic fractures in this area (Figure 2).

4.2 Geological significance of the formation periods of shale tectonic fractures

The degree of fracture development is a crucial factor in the quality of shale gas reservoirs. Well-developed fractures can improve porosity and permeability by providing pathways for gas migration and storage near them in shale gas reservoirs that are not disrupted. The timing of tectonic fracture formation is of great significance for preserving and enriching shale gas. It forms the basis for analyzing the timing and evolution of shale gas accumulation (Li et al., 2019a; Li et al., 2019b).

Shale gas reservoir preservation is an intricate interplay of geological processes and is independent of the structural morphology. The post-formation dynamics of shale gas, particularly the timing and magnitude of subsequent structural uplifts, play a pivotal role in determining the reservoir's integrity and gas content. Intricately linked to this is the timing of shale tectonic fracture formation. The interrelation between the emergence of these fractures and the extent of structural uplift underscores the notion that fracture formation timing profoundly influences gas content (Ma et al., 2022; Wood, 2022). Delving into the historical geology of China's southern marine shale regions, two distinct phases emerge: an early phase dominated by continuous burial and a later phase characterized by consistent uplift (Li et al., 2019a; Wang et al., 2020). The extended deep burial in the initial phase acted as a catalyst for shale gas genesis. Contrarily, the subsequent structural evolution dictated the intensity and scope of shale gas migration. A notable consequence of stratigraphic uplift is the cessation of the hydrocarbon generation process within source rocks. Thus, the moment of this uplift is a key determinant in gauging potential gas losses from the reservoir. To elucidate, precocious uplifts would mean an extended exposure of shale gas reservoirs to late-stage geological alterations, culminating in a more intricate fracture network. This nuanced understanding of the temporal dynamics of uplift and burial offers invaluable insights for exploration strategies and reservoir management.

Post-uplift weathering and erosion decrease overlying strata pressure, upsetting the reservoir's formation-pore pressure

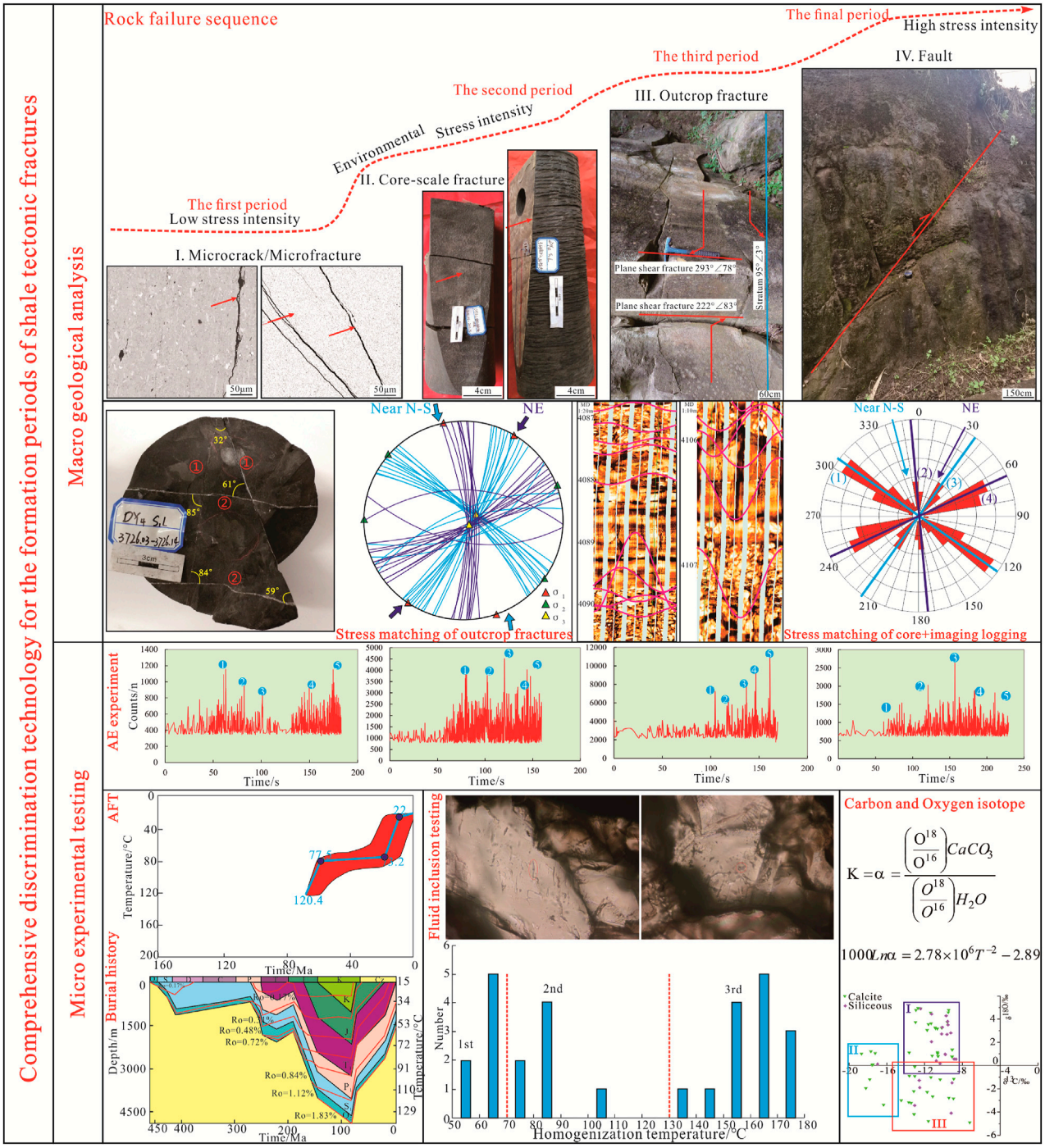


FIGURE 2
A comprehensive method for determining the formation periods of tectonic fractures in shale (Data sourced from Xie et al., 2019a; 2019b; Zhong, 2019; Xie, 2020).

balance. This shift can lead to the opening of deep underground fractures (Li et al., 2019c; Oliveira et al., 2021; Yuan et al., 2021). Reduced temperature and pressure increase rock brittleness, making them prone to complex fractures under tectonic compression. Consequently, areas with significant strata uplift have enhanced fracture development and increased shale gas dissipation. In contrast, regions with minimal uplift exhibit limited fractures, preserving the shale gas reservoir's overpressure (Li et al., 2019b). Tectonic fractures from different periods vary in orientation due to distinct tectonic stresses. The angle between fracture direction and the current maximum principal stress influences gas content. Large angles keep fractures mostly closed, preventing gas escape, while smaller angles or parallel alignments create open pathways for gas migration.

5 Conclusion and prospection

Shale tectonic fractures play a crucial role in the preservation and enrichment of shale gas, with fractures from different formation periods carrying distinct geological implications. Based on bibliometrics, this paper reviews the research techniques and methods associated with the formation periods of shale tectonic fractures. It establishes a comprehensive discrimination method for determining the formation period of these fractures, leading to the following conclusions and prospects.

(1) Tectonic fractures are the most important type of fractures in organic-rich shale, with predominant shear fractures. In field outcrops, they can be further divided into plane and profile shear fractures. Under microscopic examination, they mainly consist of grain-boundary fractures (intergranular fractures) and mineral joint fractures (intramineral fractures). Depending on the precision of observation, tectonic fractures can be categorized into four scales ranging from micro to macro, and establishing geometric quantitative relationships for I-II-III-IV level multi-scale fracture characteristics is of great significance for evaluating the distribution patterns of fractures.
(2) The analysis methods for determining the formation periods of tectonic fractures in shale primarily include field outcrop observations, core examinations, thin slice analysis, filling material analysis, and AE methods. However, each method has its own advantages and limitations when assessing the timing of fracture formation. Establishing a comprehensive determination approach based on macro-geological analysis and experimental testing often yields better results and is currently a mainstream method for studying the timing of tectonic fracture formation.
(3) The fracture formation period is paramount for preserving, enriching, and adjusting shale gas reservoirs. The formation of tectonic fractures often corresponds to tectonic uplift. Moderate uplift can promote the opening of I-II level fractures, improving the reservoir space and facilitating the desorption of adsorbed gas. However, excessive uplift can induce the formation and opening of III-IV level fractures, leading to shale gas loss and reducing the gas content of shale reservoirs. Additionally, the differences in fracture orientation at different periods, matching with the present maximum principal stress, can also impact the gas content of shale formations.
(4) Tectonic fractures are the smallest-scale features resulting from tectonic movements. Therefore, a comprehensive determination of the fracture formation period must rely on regional tectonic evolution as the fundamental constraint. Structural analysis plays a pivotal role in establishing when fractures form. This can be achieved through various methods, including field exposures, detailed seismic interpretation, low-temperature thermochronology, and the analysis of thermal evolution history (burial history and hydrocarbon generation history). These analyses help accurately assess the tectonic evolution history of the study area and determine the magnitude and direction of tectonic stress.

Data availability statement

The original contributions presented in the study are included in the article/Supplementary Material, further inquiries can be directed to the corresponding author.

Author contributions

HL: Conceptualization, Data curation, Formal Analysis, Funding acquisition, Investigation, Methodology, Project administration, Resources, Supervision, Visualization, Writing–original draft, Writing–review and editing.

Funding

The authors declare financial support was received for the research, authorship, and/or publication of this article. This study was financially supported by the Open funds of Shale Gas Evaluation and Exploitation Key Laboratory of Sichuan Province (Nos. YSK2023001 and YSK2022002) and Natural Gas Geology Key Laboratory of Sichuan Province (No. 2021trqdz05), the key R&D projects of the Deyang Science and Technology Plan (No. 2022SZ049), and the research project of Sichuan College of Architectural Technology (No. 2023KJ14).

Conflict of interest

The author declares that the research was conducted in the absence of any commercial or financial relationships that could be construed as a potential conflict of interest.

Publisher's note

All claims expressed in this article are solely those of the authors and do not necessarily represent those of their affiliated organizations, or those of the publisher, the editors and the reviewers. Any product that may be evaluated in this article, or claim that may be made by its manufacturer, is not guaranteed or endorsed by the publisher.

References

Batayneh, A., Ghrefat, H., and Diabat, A. (2012). Lineament characterization and their tectonic significance using gravity data and field studies in the Al-Jufr Area, southeastern Jordan Plateau. *J. Earth Sci.* 23 (6), 873–880. doi:10.1007/s12583-012-0298-6

Becker, D., Cailleau, B., Kaiser, D., and Dahm, D. (2014). Macroscopic failure processes at mines revealed by acoustic emission (AE) monitoring. *Bull. Seismol. Soc. Am.* 104 (4), 1785–1801. doi:10.1785/0120130286

Cai, M. F. (2020). Key theories and technonogies for surrounding rock stability and ground control in deep mining. *J. Min. Strata Control Eng.* 2 (3), 033037. doi:10.13532/j.jmsce.cn10-1638/td.20200506.001

Chen, S. W., and Liu, J. Z. (2021). Research progress and prospects of the stages, genesis and fluid evolution of micro-fracture veins in petroliferous basins. *Bull. Geol. Sci. Tech.* 40 (4), 81–92. doi:10.19509/j.cnki.dzkq.2021.0426

Deng, B., Yong, Z. Q., Liu, S. G., Li, Z. W., Zhao, G. P., Mise, Z. H., et al. (2016). Cenozoic mountain-building processes in the Daliangshan, southeastern margin of the Tibetan Plateau: evidence from low-temperature thermochronology and thermal modeling. *Chin. J. Geophys.-CH.* 59 (6), 2162–2175. doi:10.6038/cjg20160621

Fall, A., Eichhubl, P., Cumella, S. P., Bodnar, R. J., Laubach, S. E., and Becker, S. P. (2012). Testing the basin-centered gas accumulation model using fluid inclusion observations: southern Piceance Basin, Colorado. *AAPG Bull.* 96 (12), 2297–2318. doi:10.1306/05171211149

Fan, C. H., Li, H., Qin, Q. R., He, S., and Zhong, C. (2020a). Geological conditions and exploration potential of shale gas reservoir in Wufeng and Longmaxi Formation of southeastern Sichuan Basin, China. *J. Petrol. Sci. Eng.* 191, 107138. doi:10.1016/j.petrol.2020.107138

Fan, C. H., Li, H., Zhao, S. X., Qin, Q. R., Fan, Y., Wu, J. F., et al. (2020b). Formation stages and evolution patterns of structural fractures in marine shale: case study of the Lower Silurian Longmaxi Formation in the Changning area of the southern Sichuan Basin, China. *Energy Fuel* 34 (8), 9524–9539. doi:10.1021/acs.energyfuels.0c01748

Fan, C. H., Xie, H. B., Li, H., Zhao, S. X., Shi, X. C., Liu, J. F., et al. (2022). Complicated fault characterization and its influence on shale gas preservation in the southern margin of the Sichuan Basin, China. *Lithosphere* 2022 (S12), 8035106. doi:10.2113/2022/8035106

Feng, Q. Q., Qiu, N. S., Borjigin, T., Li, F., Ji, R. Y., Liu, X., et al. (2023). Effect of tectonic reworking on shale fracturing and gas preservation in the upper Yangtze block, south China. *Mar. Petrol. Geo.* 148, 106069. doi:10.1016/j.marpetgeo.2022.106069

Gale, J. F. W., Laubach, S. E., Olson, J. E., Eichhubl, P., and Fall, A. (2014). Natural fractures in shale: a review and new observations. *AAPG Bull.* 98 (11), 2165–2216. doi:10.1306/08121413151

Gong, L., Wang, J., Gao, S., Fu, X. F., Liu, B., Miao, F. B., et al. (2021). Characterization, controlling factors and evolution of fracture effectiveness in shale oil reservoirs. *J. Petrol. Sci. Eng.* 203, 108655. doi:10.1016/j.petrol.2021.108655

He, S., Qin, Q. R., Li, H., and Wang, S. L. (2022b). Deformation differences in complex structural areas in the southern Sichuan Basin and its influence on shale gas preservation: a case study of Changning and Luzhou area. *Front. Earth Sci.* 9, 818155. doi:10.3389/feart.2021.818155

He, S., Qin, Q. R., Li, H., and Zhao, S. X. (2022a). Deformation differences in complex structural areas in the southern Sichuan Basin and its influence on shale gas preservation: a case study of changning and Luzhou areas. *Front. Earth Sci.* 9, 818543. doi:10.3389/feart.2021.818534

Hou, E. K., Cong, T., Xie, X. S., and Wei, J. B. (2020). Ground surface fracture development characteristics of shallow double coal seam staggered mining based on particle flow. *J. Min. Strata Control Eng.* 2 (1), 013521. doi:10.13532/j.jmsce.cn10-1638/td.2020.01.002

Hu, X. F., Deng, H. C., He, J. H., Shen, Z. M., and Peng, X. F. (2023). Complex genesis of multiperiod fractures in the middle triassic leikoupo formation in the pengzhou gas field, western Sichuan Basin, China. *Petro. Sci.* 20 (1), 161–176. doi:10.1016/j.petsci.2022.10.001

Huang, L. K., Tan, J., Fu, H. F., Liu, J. J., Chen, X. Y., Liao, X. C., et al. (2023). The non-plane initiation and propagation mechanism of multiple hydraulic fractures in tight reservoirs considering stress shadow effects. *Eng. Fract. Mech.* 292, 109570. doi:10.1016/j.engfracmech.2023.109570

Hui, G., Chen, Z., Chen, S., and Gu, F. (2022). Hydraulic fracturing-induced seismicity characterization through coupled modeling of stress and fracture-fault systems. *Adv. Geo-Energy Res.* 6 (3), 269–270. doi:10.46690/ager.2022.03.11

Kontakiotis, G., Karakitsios, V., Cornée, J. J., Moissette, P., Zarkogiannis, S. D., Pasadakis, N., et al. (2020). Preliminary results based on geochemical sedimentary constraints on the hydrocarbon potential and depositional environment of a Messinian sub-salt mixed siliciclastic-carbonate succession onshore Crete (Plouti section, eastern Mediterranean). *Med. Geosc. Rev.* 2, 247–265. doi:10.1007/s42990-020-00033-6

Kontakiotis, G., Karakitsios, V., Maravelis, A. G., Zarkogiannis, S. D., Agiadi, K., Antonarakou, A., et al. (2021). Integrated isotopic and organic geochemical constraints on the depositional controls and source rock quality of the Neogene Kalamaki sedimentary successions (Zakynthos Island, Ionian Sea). *Med. Geosc. Rev.* 3, 193–217. doi:10.1007/s42990-020-00045-2

Li, H. (2022). Research progress on evaluation methods and factors influencing shale brittleness: a review. *Energy Rep.* 8, 4344–4358. doi:10.1016/j.egyr.2022.03.120

Li, H. (2023). Coordinated development of shale gas benefit exploitation and ecological environmental conservation in China: a mini review. *Front. Ecol. Evol.* 11, 1232395. doi:10.3389/fevo.2023.1232395

Li, H., Qin, Q. R., Zhang, B. J., Ge, X. Y., Hu, X., Fan, C. H., et al. (2020). Tectonic fracture formation and distribution in ultradeep marine carbonate gas reservoirs: a case study of the Maokou Formation in the Jiulongshan Gas Field, Sichuan Basin, southwest China. *Energy Fuel* 34 (11), 14132–14146. doi:10.1021/acs.energyfuels.0c03327

Li, H., Tang, H. M., Qin, Q. R., Zhou, J. L., Qin, Z. J., Fan, C. H., et al. (2019a). Characteristics, formation periods and genetic mechanisms of tectonic fractures in the tight gas sandstones reservoir: a case study of Xujiahe Formation in YB area, Sichuan Basin, China. *J. Petrol. Sci. Eng.* 178, 723–735. doi:10.1016/j.petrol.2019.04.007

Li, H., Tang, H. M., and Zheng, M. J. (2019b). Micropore structural heterogeneity of siliceous shale reservoir of the Longmaxi Formation in the southern Sichuan Basin, China. *Minerals* 9, 548. doi:10.3390/min9090548

Li, H., Tang, H. M., Qin, Q. R., Wang, Q., and Zhong, C. (2019c). Effectiveness evaluation of natural fractures in Xujiahe Formation of Yuanba area, Sichuan basin, China. *Arab. J. Geosci.* 12 (6), 194. doi:10.1007/s12517-019-4292-5

Li, H., Wang, Q., Qin, Q. R., and Ge, X. Y. (2021a). Characteristics of natural fractures in an ultradeep marine carbonate gas reservoir and their impact on the reservoir: a case study of the Maokou Formation of the JLS Structure in the Sichuan Basin, China. *Energy Fuel* 35 (16), 13098–13108. doi:10.1021/acs.energyfuels.1c01581

Li, H., Zhou, J. L., Mou, X. Y., Guo, H. X., Wang, X. X., An, H. Y., et al. (2022a). Pore structure and fractal characteristics of the marine shale of the Longmaxi Formation in the changning area, southern Sichuan Basin, China. *Front. Earth Sci.* 10, 1018274. doi:10.3389/feart.2022.1018274

Li, H. T., Peng, R., Du, W. S., Li, X. P., and Zhang, N. B. (2021b). Experimental study on structural sensitivity and intervention mechanism of mechanical behavior of coal samples. *J. Min. Strata Control Eng.* 3 (4), 043012. doi:10.1638/td.20210820.001

Li, J., Li, H., Yang, C., Ren, X. H., and Li, Y. D. (2023). Geological characteristics of deep shale gas and their effects on shale fracability in the Wufeng–Longmaxi Formations of the southern Sichuan Basin, China. *Lithosphere* 2023 (1), 4936993. doi:10.2113/2023/4936993

Li, J., Li, H., Yang, C., Wu, Y. J., Gao, Z., and Jiang, S. L. (2022b). Geological characteristics and controlling factors of deep shale gas enrichment of the Wufeng-Longmaxi Formation in the southern Sichuan Basin, China. *Lithosphere* 2022 (S12), 4737801. doi:10.2113/2022/4737801

Ma, J., Fang, D. Z., Zhang, P. X., Gu, H. T., Hu, C. F., and Lu, B. (2022). Characteristics and genesis of shale fractures in Wufeng-Longmaxi formations of Yangchungou structural belt in Southeast Chongqing. *Nat. Gas. Geosci.* 33 (7), 1117–1131. doi:10.11764/j.issn.1672-1926.2022.03.001

Meier, S., Bauer, J. F., and Philipp, S. L. (2015). Fault zone characteristics, fracture systems and permeability implications of Middle Triassic Muschelkalk in Southwest Germany. *J. Struct. Geo.* 70, 170–189. doi:10.1016/j.jsg.2014.12.005

Meng, Q. F., Hao, F., and Tian, J. Q. (2021). Origins of non-tectonic fractures in shale. *Earth Sci. Rev.* 222, 103825. doi:10.1016/j.earscirev.2021.103825

Oliveira, G. P., Rodrigues, T. N. E., and Lie, K.-A. (2021). GAWPS: a MRST-based module for wellbore profiling and graphical analysis of flow units. *Adv. Geo-Energy Res.* 6 (1), 38–53. doi:10.46690/ager.2022.01.04

Shan, S. C., Wu, Y. Z., Fu, Y. K., and Zhou, P. H. (2021). Shear mechanical properties of anchored rock mass under impact load. *J. Min. Strata Control Eng.* 3 (4), 043034. doi:10.13532/j.jmsce.cn10-1638/td.20211014.001

Tan, P., Fu, S. H., Chen, Z. W., and Zhao, Q. (2023). Experimental investigation on fracture growth for integrated hydraulic fracturing in multiple gas bearing formations. *Geoenergy Sci. Eng.* 231, 212316. doi:10.1016/j.geoen.2023.212316

Tan, P., Jin, Y., and Pang, H. W. (2021). Hydraulic fracture vertical propagation behavior in transversely isotropic layered shale formation with transition zone using XFEM-based CZM method. *Eng. Fract. Mech.* 248, 107707. doi:10.1016/j.engfracmech.2021.107707

Wang, R. Y., Ding, W. L., Zhang, Y. Q., Wang, Z., Wang, X. H., He, J. H., et al. (2016b). Analysis of developmental characteristics and dominant factors of fractures in Lower Cambrian marine shale reservoirs: a case study of Niutitang formation in Cen'gong block, southern China. *J. Petrol. Sci. Eng.* 138, 31–49. doi:10.1016/j.petrol.2015.12.004

Wang, R. Y., Gu, Y., Ding, W. L., Gong, D. J., Yin, S., Wang, X. H., et al. (2016a). Characteristics and dominant controlling factors of organic-rich marine shales with high thermal maturity: a case study of the Lower Cambrian Niutitang Formation in the Cen'gong block, southern China. *J. Nat. Gas. Sci. Eng.* 33, 81–96. doi:10.1016/j.jngse.2016.05.009

Wang, R. Y., Hu, Z. Q., Sun, C. X., Liu, Z. B., Zhang, C. C., Gao, B., et al. (2018). Comparative analysis of shale reservoir characteristics in the Wufeng-Longmaxi (O_3w-S_1l) and Niutitang (ϵ_1n) Formations: a case study of wells JY1 and TX1 in the southeastern Sichuan Basin and its neighboring areas, southwestern China. *Interpretation-J. Sub.* 6 (4), SN31–SN45. doi:10.1190/INT-2018-0024.1

Wang, R. Y., Nie, H. K., Hu, Z. Q., Liu, G. X., Xi, B. B., and Liu, W. X. (2020). Controlling effect of pressure evolution on shale gas reservoirs:A case study of the Wufeng–Longmaxi Formation in the Sichuan Basin. *Nat. Gas. Ind.* 40 (10), 1–11. doi:10.3787/j.issn.1000-0976.2020.10.001

Wang, X., Li, J., Jiang, W., Zhang, H., Feng, Y., and Yang, Z. (2022a). Characteristics, current exploration practices, and prospects of continental shale oil in China. *Adv. Geo-Energy Res.* 6 (6), 454–459. doi:10.46690/ager.2022.06.02

Wang, S. L., Li, H., Lin, L. F., and Yin, S. (2022b). Development characteristics and finite element simulation of fractures in tight oil sandstone reservoirs of Yanchang Formation in western Ordos Basin. *Front. Earth Sci.* 9, 823855. doi:10.3389/feart.2021.823855

Wood, D. A. (2022). Predicting brittleness indices of prospective shale formations from sparse well-log suites assisted by derivative and volatility attributes. *Adv. Geo-Energy Res.* 6 (4), 334–346. doi:10.46690/ager.2022.04.08

Wu, S., Li, T. T., Ge, H. K., Wang, X. Q., Li, N., and Zou, Y. S. (2019). Shear-tensile fractures in hydraulic fracturing network of layered shale. *J. Petrol. Sci. Eng.* 183, 106428. doi:10.1016/j.petrol.2019.106428

Xia, Y., and Lu, A. H. (2022). Analysis of the mechanical properties and damage characteristics of continuously graded high-strength cemented backfill. *J. Min. Strata Control Eng.* 5 (1), 013037. doi:10.13532/j.jmsce.cn10-1638/td.20221212.002

Xie, J. T. (2020). *Shale fractures in complex tectonic zones and their effects on shale gas preservation - a case study of Longmaxi Formation in Dongxi-Songkan area of southeast Sichuan*. PhD dissertation. Sichuan: Southwest Petroleum University. doi:10.27420/d.cnki.gxsyc.2020.000008

Xie, J. T., Qin, Q. R., and Fan, C. H. (2019a). Quantitative prediction of fracture distribution of the Longmaxi Formation in the Dingshan Area, China-using FEM numerical simulation. *Acta Geol. sin.-eng. Ed.* 93 (6), 1662–1672. doi:10.1111/1755-6724.13815

Xie, J. T., Qin, Q. R., and Fan, C. H. (2019b). Influencing factors of gas adsorption capacity of marine organic shale: a case study of Dingshan Area, southeast Sichuan. *J. Coast. Res.* 93, 507–511. doi:10.2112/SI93-066.1

Xu, S., Gou, Q. Y., Hao, F., Zhang, B. Q., Shu, Z. G., and Zhang, Y. Y. (2020b). Multiscale faults and fractures characterization and their effects on shale gas accumulation in the Jiaoshiba area, Sichuan Basin, China. *J. Petrol. Sci. Eng.* 189, 107026. doi:10.1016/j.petrol.2020.107026

Xu, S., Hao, F., Shu, Z. G., Zhang, A. H., and Yang, F. (2020a). Pore structures of different types of shales and shale gas exploration of the Ordovician Wufeng and Silurian Longmaxi successions in the eastern Sichuan Basin, South China. *J. Asian Earth Sci.* 193, 104271. doi:10.1016/j.jseaes.2020.104271

Xu, S., Liu, R., Hao, F., Engelder, T., Yi, J. Z., Zhang, B. Q., et al. (2019). Complex rotation of maximum horizontal stress in the Wufeng-Longmaxi Shale on the eastern margin of the Sichuan Basin, China: implications for predicting natural fractures. *Mar. Petrol. Geol.* 109, 519–529. doi:10.1016/j.marpetgeo.2019.06.008

Yuan, Y. Y., Li, H., Wang, Y., Xiang, H., Xu, G. H., and Bian, Y. Y. (2021). Study on the influence of lithofacies types on the formation and evolution of fracture: a case study of Longmaxi Formation in Northwest Guizhou. *Chin. J. Geol.* 56 (1), 82–97. doi:10.12017/dzkx.2021.006

Zhang, Q. Y., Liang, B., Qin, F. R., Cao, J. W., Dan, Y., and Li, J. R. (2016). Environmental and geochemical significance of carbon and oxygen isotopes of Ordovician carbonate paleokarst in Lunnan, Tarim Basin. *Enviorn. Earth .Sci.* 75 (14), 1074. doi:10.1007/s12665-016-5882-0

Zhong, C. (2019). *Characteristics of shale fractures in the Longmaxi Formation in the Dingshan area of southeastern Sichuan and their relationship with gas bearing properties*. MA Thesis. Sichuan: Southwest Petroleum University. doi:10.27420/d.cnki.gxsyc.2019.000349

Zhu, B. Y., Meng, J. H., Pan, R. F., Hu, H. Y., Song, C., Zhu, Z. P., et al. (2023). New insights into the evaluation criteria for high-quality deep marine shale gas reservoirs in the Longmaxi formation: evidence from organic matter pore development characteristics. *Front. Ecol. Evol.* 11, 1138991. doi:10.3389/fevo.2023.1138991

frontiers | Frontiers in Energy Research

TYPE Original Research
PUBLISHED 13 November 2023
DOI 10.3389/fenrg.2023.1296830

Check for updates

OPEN ACCESS

EDITED BY
Peng Tan,
CNPC Engineering Technology R & D Company Limited, China

REVIEWED BY
Li Qingmiao,
Chengdu University of Technology, China
Shixiang Tian,
Guizhou University, China

*CORRESPONDENCE
Peng Zhang,
bnzp123@sina.com

RECEIVED 19 September 2023
ACCEPTED 31 October 2023
PUBLISHED 13 November 2023

CITATION
Zhang P (2023), Regional outburst prevention technology of pre-drainage gas area in west well area of sihe coal mine.
Front. Energy Res. 11:1296830.
doi: 10.3389/fenrg.2023.1296830

COPYRIGHT
© 2023 Zhang. This is an open-access article distributed under the terms of the Creative Commons Attribution License (CC BY). The use, distribution or reproduction in other forums is permitted, provided the original author(s) and the copyright owner(s) are credited and that the original publication in this journal is cited, in accordance with accepted academic practice. No use, distribution or reproduction is permitted which does not comply with these terms.

Regional outburst prevention technology of pre-drainage gas area in west well area of sihe coal mine

Peng Zhang*

Ningxia Tiandi Benniu Industrial Group Co., Ltd., China

Coal and gas outburst is one of the main factors affecting the safe and efficient production of coal mines. With the increase of mining depth and mining speed, the dynamic phenomena of coal and gas outburst will become more and more serious. Through the study of various outburst prevention measures in the pre-drainage gas area such as surface drilling, bedding (directional) drilling, and cross-layer drilling, combined with the coal seam occurrence and mining technology of the West Mine Area, a feasible regional pre-drainage comprehensive outburst prevention mode suitable for the characteristics of the 3# coal seam in the West Mine Area has been obtained. This mode is based on pre-pumping of surface drilling first, directional long borehole along the reservoir and pre-pumping of cross-zone borehole, which provides reliable guarantee for safe and efficient production in outburst well area.

KEYWORDS

ground wells, bedding drilling, cross-layer drilling, outburst prevention measures, pre-drainage gas

1 Introduction

As one of the main energy sources supporting the development of China's national economy, coal is the "ballast stone" to ensure energy security (Liang et al., 2022; Sun X. Y. et al., 2023; Ma et al., 2023). Coal consumption will account for 56% of total energy consumption in 2021. And in the future for a long period of time, the status of coal as the main energy will not change (Liang et al., 2023; Su et al., 2023; Wu et al., 2023). In the process of coal mining, gas disaster is still one of the main disasters in coal mines, which is easy to cause large-scale casualties (Wu et al., 2022; Zou et al., 2023b). Coal and gas outburst is one of the typical gas disasters in coal mines (Cheng et al., 2022; Zheng et al., 2022; Zhao et al., 2023a), and with the mining operation of coal seam extending to the depth year by year (Xie et al., 2022; Ye et al., 2022; 2023; Xie et al., 2023), the permeability of coal seam gradually decreases with the increase of ground stress, gas pressure and temperature, which increases the risk of coal mine gas outburst (Liu and Li, 2016; Pan et al., 2020; Song et al., 2022). In recent years, although our defense technology has made remarkable progress, prominent security accidents still occur from time to time (Liu et al., 2021; Ran et al., 2023a; Zhang C. L. et al., 2023). At present, China has formed two "four-in-one" comprehensive anti-outburst technology systems, which are mainly regional measures and supplemented by local measures. Among them, the application of local anti-outburst technical measures such as hydraulic fracturing, hydraulic punching and coal seam water injection is limited due to the large engineering amount, long outburst elimination period and technical difficulty (Xiao

et al., 2022; Zhang et al., 2022; Zou et al., 2023a; Zhao et al., 2023b). Regional outburst prevention measures mainly include mining protective layer and pre-pumping coal seam gas. Mining the protective layer is conducive to improving the air permeability of coal, improving the gas extraction effect, and preventing outburst. Wang et al. (2014) discussed the key problem of determining the reasonable protection range in the mining protective layer, established the gas seepage field equation and the deformation field of coal and rock mass, and determined the pressure relief protection range in the mining of the upper protective layer by analyzing the example of Nantong mining area. Yuan and Xue. (2014) developed a method to reduce outburst range of protective layer according to the content of coal seam gas. Wang et al. (2013) analyzed the influence of factors such as coal seam inclination, coal seam spacing, pressure relief Angle and coal pillar on the mining of the protective layer, proposed solutions to the existing technical problems such as the mining scope of the protected work being greater than the protection scope of the protected layer, and verified the effectiveness of the proposed method with examples. However, due to the great difference of address in different regions of China, the occurrence conditions of coal seams are different, and the thickness of the protective layer of coal seams is not consistent, it is difficult to obtain the ideal effect (Wang et al., 2022; Zou et al., 2022).

The pre-extraction of coal seam gas is an effective method for controlling gas outburst disasters in coal mines and is currently the primary technical means used by the coal mining industry (Zhao et al., 2022; Liu S. M. et al., 2023; Zhang B. C. et al., 2023). This process involves drilling and extracting gas from the coal seam in advance of the excavation face production (Liao et al., 2021; Liu Y. B. et al., 2023). By pre-pumping the gas in the coal seam, the gas pressure and content within the coal seam can be reduced (Li et al., 2020; Chen et al., 2023). This allows the release elasticity of the coal body to achieve pressure relief and permeability improvement, thereby preventing coal and gas outbursts. In China, the main methods of gas pre-pumping include surface well pre-pumping, borehole pre-pumping, and borehole pre-pumping along stratum (Wang et al., 2023). Zhang Y. J. et al. (2023) combined the above - and underground gas extraction technologies, and proposed an up-and-down joint anti-outburst adaptation model of short - distance coal groups with “hole group cover-coordinated extraction” and long - distance coal groups with “enhanced anti-permeability - progressive extraction”. Han and Li. (2020) proposed an outburst prevention method in which the protection layer was drilled underground and the protected layer was extracted by surface Wells, and the method was successfully applied in Zhujixi Mine. By measuring gas parameters, theoretical analysis, numerical simulation and engineering practice, Wang et al. (2021) proposed a dual pressure relief anti-outburst model for the relief field of deep roadway, and verified that the model could achieve the effect of anti-outburst by drilling through strata and pumping gas from floor rock roadway through the application in Qujiang Coal Mine. In order to solve the poor outburst elimination effect of bedding drilling in coal mining face, Gao et al. (2019) took Xieqiao Coal Mine as the test object, and adopted the hydraulic fracturing technology of bedding drilling to improve the outburst elimination effect (Tan et al., 2021; Huang et al., 2023a). By considering the parameters such as hydraulic fracturing radius, drilling parameters, water injection pressure, water injection volume and holding time, the gas extraction efficiency was improved (Huang et al., 2023b; Tan et al., 2023).

In conclusion, while there has been extensive research on the technical measures of regional outburst prevention in pre-drainage coal seam gas from various perspectives, studies on the coordinated extraction of surface well drilling, cross-layer drilling, and bedding drilling to achieve regional outburst prevention are limited. It remains challenging to establish a comprehensive regional pre-drainage outburst prevention model that encompasses surface well pre-drainage, underground cross-layer drilling pre-drainage, and bedding drilling pre-drainage. Therefore, this paper focuses on the west well area of Sihe Mine. Through studying various pre-drainage gas regional outburst prevention measures such as surface drilling, bedding (directional) drilling, and cross-layer drilling, it aims to develop a comprehensive regional pre-drainage outburst prevention model to ensure the safe and efficient extraction of coalbed methane.

2 Overview of the research area

Sihe Mine, located in the northwest of Jincheng City, Shanxi Province, falls under the administrative jurisdiction of Jincheng City and spans Qinshui, Yangcheng, and Zezhou counties. The geographical coordinates are 35°30′51″N to 35°36′11″N and 112°27′07″E to 112°40′54″E. The western well area covers 56.27 km^2. The mine field comprises three layers: 3#, 9#, and 15#, with a total thickness of 10.32 m and a recoverable coal-bearing coefficient of 7.6%. The 3# coal seam is the primary seam, with a thickness ranging from 4.45 m to 8.75 m and an average of 6.31 m. The coal seam structure is relatively simple, and the entire area is stable and recoverable. The total geological coal reserves in the western well area amount to 690 million tons, including 450 million tons of 3# coal, 50 million tons of 9# coal, and 190 million tons of 15# coal. The total recoverable reserves are 370 million tons, including 220 million tons of 3# coal, 300 million tons of 9# coal, and 120 million tons of 15# coal.

The coal-bearing strata in this mine field belong to the Shanxi Formation of the Lower Permian System and the Taiyuan Formation of the Upper Carboniferous System. These strata contain between 11 and 21 layers of coal, with an average total coal seam thickness of 11.49–13.87 m. The stable mineable coal seams are the 3# and 15# seams, with the 9# seam being locally mineable. The dip angle of the 3# coal seam ranges from 2° to 10°, typically around 5°, and the average thickness of this coal seam is 6.31 m. The characteristics of mineable coal seams in the middle of the minefield are shown in Table 1. The 3# coal seam is anthracite with low-medium ash, ultra-low sulfur, medium phosphorus, high calorific value, high ash fusion temperature, and high strength. It has good thermal stability, strong slagging characteristics, good theoretical clean coal recovery, and high fixed carbon content.

The western well area employs a mechanical extraction partition ventilation mode. Currently, the mine has established independent ventilation systems in the eastern and western well areas. The total intake air volume in the western well area is approximately 24,645 m^3/min, while the total return air volume in the mine is about 25,320 m^3/min. The effective air volume in the mine is around 22,920 m^3/min, with an effective air volume rate of approximately 93%. The equal area hole measures 8.62 m^2.

TABLE 1 Main coal seam characteristics table of mine field.

Coal seam	Coal seam thickness	Coal seam distance	Texture of coal seam	Stability	Recoverable situation	Roof-floor lithology	
	(m)	(m)				Roof	Floor
	Minimum ~ maximum average	Minimum&~ maximum average					
3	5.04 ~ 7.16		plain	stabilization	recoverable	Mudstone, siltstone, silty mudstone	Siltstone, mudstone
	6.31	22.81~ 80.00					
9	0.32 ~ 1.90	48.95	plain	relatively stable	mostly recoverable	Mudstone, siltstone, silty mudstone	Siltstone, mudstone
	1.0	30.45 ~ 53.28					
15	0.30 ~ 6.17	40.04	plain	relatively stable	recoverable	Mudstone, calcium mudstone	mudstone
	3.21						

The gas content of raw coal in the 3# coal seam of the western well area ranges from 15.04 to 21 m^3/t, with a residual amount of 3.52 m^3/t. According to the mine gas level and carbon dioxide emission identification results from 2009, the absolute gas emission of the western well area is 342.27 m^3/min (with an air exhaust gas volume of 45.28 m^3/min and an underground gas drainage volume of 296.99 m^3/min). The gas drainage volume of the ground well in the western well area is 132 m^3/min. On 20 May 2007, an outburst occurred in the #6 contact roadway between Xihui and Xijiao in the western well area of Sihe Mine. The 3# coal seam in the western well area of Sihe Mine is an outburst coal seam, making the western well area an outburst mine.

Currently, a permanent ground drainage pumping station has been established in the Xifeng well industrial site in the western well area of Sihe Mine. The station is equipped with six CBF-710 A water ring vacuum pumps, all dedicated to pre-drainage of coal seam gas. With the four openings and two preparations, the extraction capacity can reach 400 N.m^3/min. At present, the extraction capacity has achieved 315.37 N.m^3/min. The absolute gas emission in the western well area of Sihe Mine is 363.07 m^3/min, and the gas drainage rate in the western well area is 86.86%.

3 Regional outburst prevention technology

The regional outburst prevention measures for pre-drainage coal seam gas in the western well area primarily involve two types of pre-drainage: surface and underground. Underground pre-drainage further includes three methods: bedding (directional) drilling, bedding (ordinary) drilling, and cross-layer drilling (Sun D. L. et al., 2023).

3.1 Gas extraction and outburst prevention technology in surface well area

In the Chengzhuang Mine, which is adjacent to the western well area, a study was conducted on the arrangement method of surface drilling wells. Through the use of Computational Fluid Dynamics (CFD) simulation technology, the gas flow and distribution law in the underground goaf were studied and understood. This knowledge was then used to determine a reasonable arrangement for surface drilling.

Figure 1 illustrates the Computational Fluid Dynamics (CFD) prediction of gas distribution in the goaf when ground drilling is not in operation. The simulation results reveal that a significant amount of oxygen enters the goaf, with the oxygen concentration exceeding 12% on the intake roadway side, 300 m behind the working face. Oxygen accumulation is observed 150 m behind the working face on the return air lane side, where the maximum gas concentration in the goaf can reach 80%. These findings suggest that high concentrations of goaf gas can be extracted by positioning ground goaf gas extraction boreholes 20–70 m from the return airway. This understanding is crucial for optimizing the design of ground goaf gas extraction boreholes, designing goaf gas extraction systems, and achieving improved extraction results (Ran et al., 2023b).

Figure 2 illustrates the predicted gas and oxygen flow field distribution in the goaf of the working face when a negative pressure of 40 kPa is applied to the surface borehole orifice under different borehole combinations. The distribution is completely opposite to the gas flow field distribution and oxygen distribution.

Based on the factors influencing regional outburst prevention and the results of CFD numerical simulation analysis, we have preliminarily determined the principles for selecting well locations and drilling spacing for outburst prevention in surface drilling areas.

1) Drilling location

Surface drilling should not only be arranged along the axis of the anticline and the wings of the anticline and syncline, but should also be organized within the geological structure zone. Additionally, ground wells should be considered for placement at distances ranging from 20 to 70 m from the return airway.

2) Drilling spacing

Based on the numerical simulation results and the analysis of surface drilling and drainage data in the eastern well field, we have preliminarily determined that the surface drilling spacing used for

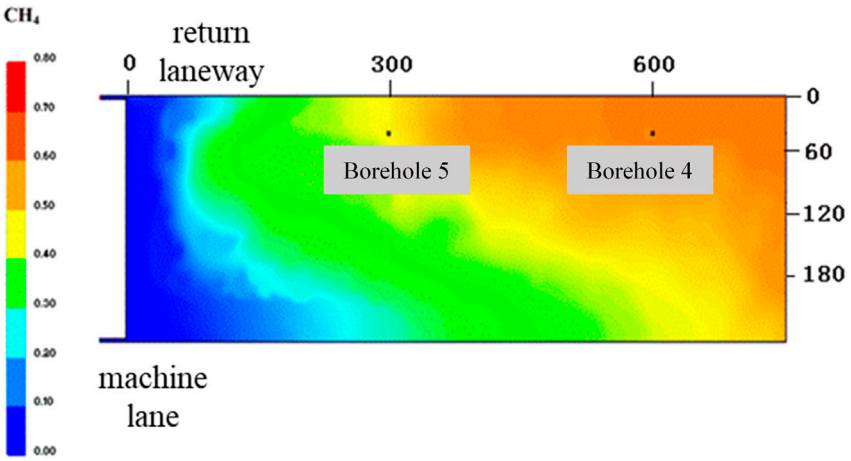


FIGURE 1
CFD simulation of gas distribution in goaf of working face.

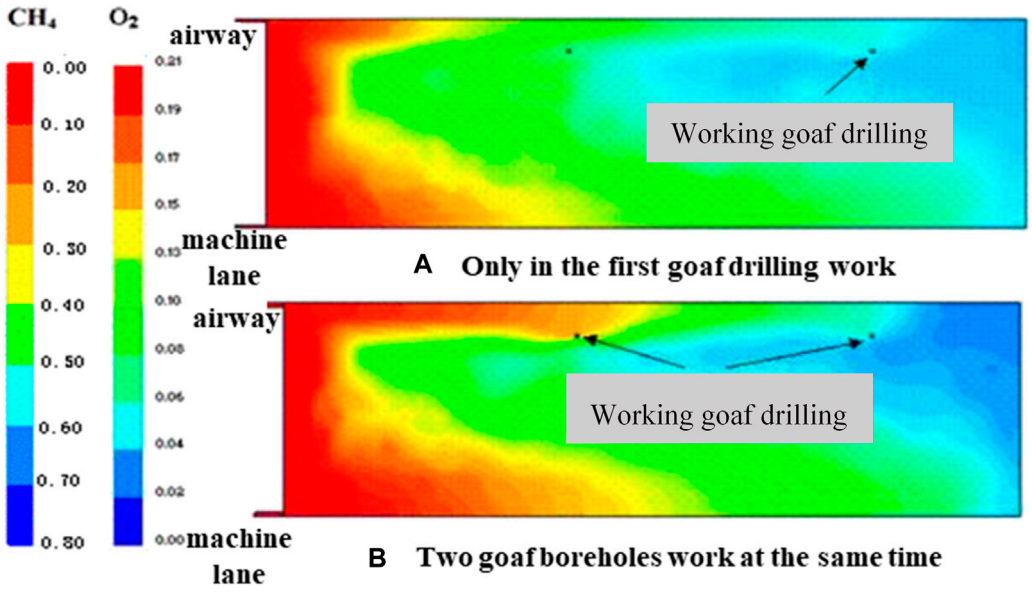


FIGURE 2
Gas distribution diagram of goaf under different extraction conditions in working face. **(A)** Only in the first goaf drilling work; **(B)** Two goaf boreholes work at the same time.

outburst prevention in the pre-drainage area in the normal area is 300 m × 300 m. Meanwhile, the surface drilling spacing in the geological structure zone is 150 m × 150 m.

3.2 Outburst prevention technology in pre-drainage gas area of bedding borehole

3.2.1 Bedding drilling pre-drainage gas area drilling design

The number of holes and the design depth for each drilling field should be determined based on the production connection and the length of the working face. Field tests suggest that the most economical design length for the extraction unit is between 300 and 400 m. The end of each borehole should extend beyond the roadway of the replacement working face or the replacement drilling field by at least 30 m. Each borehole is designed with 2–3 branches, with a horizontal vertical distance between branches of 12–15 m. The main hole depth for bedding drilling is generally within 400 m, as construction drilling speed slows significantly beyond this depth, leading to frequent sticking phenomena and low drilling efficiency. Figure 3 provides a schematic diagram of the bedding directional drilling arrangement in the western well area.

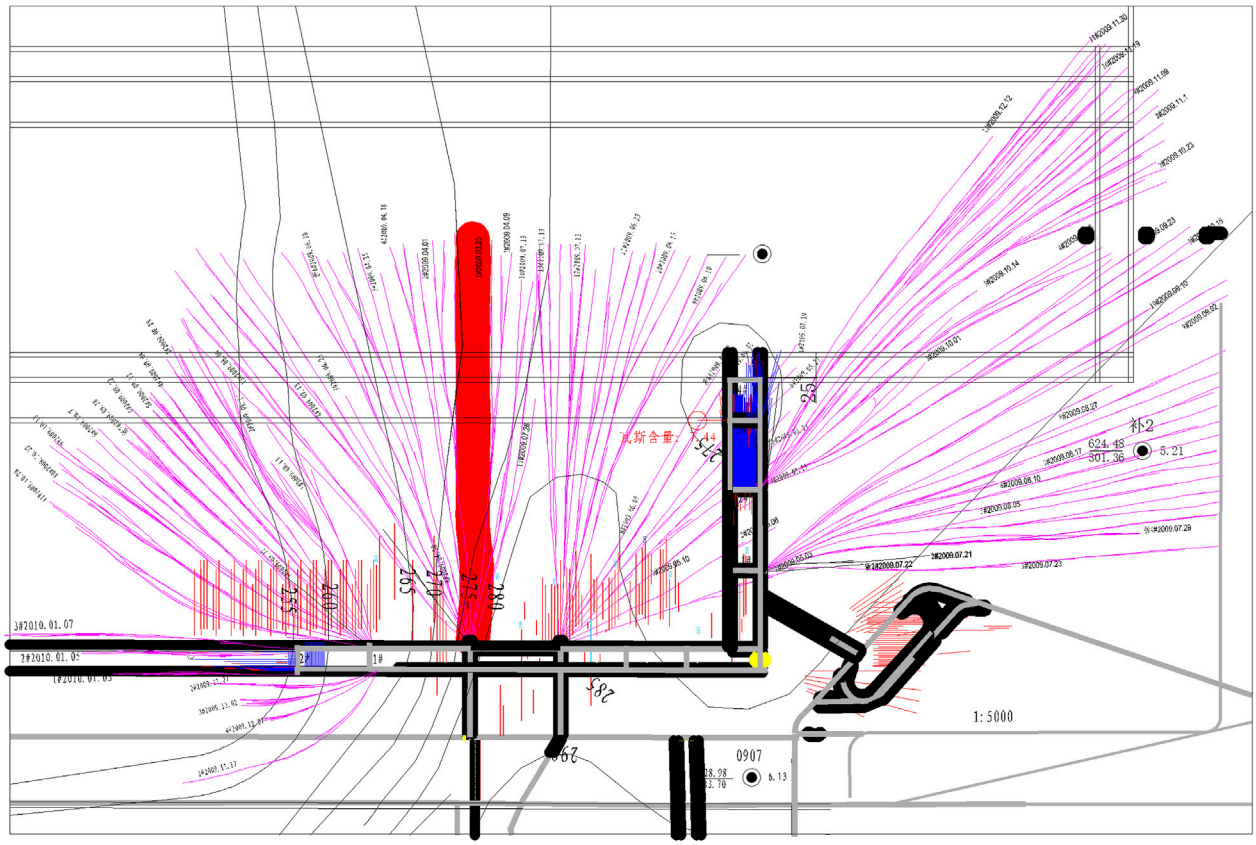


FIGURE 3
The schematic diagram of 0802 bedding directional drilling arrangement in west well area.

3.2.2 Outburst prevention technology of bedding drilling in heading face of coal roadway

1) Design of outburst prevention measures for pre-drainage boreholes in heading face

Preparation for excavation on the 1301 working face began in June 2006. The gas content of the coal seam in this area is between 18 and 20 m^3/t. To ensure safe excavation, the target residual gas content of the coal seam should be less than 8 m^3/t. In the early stage of excavation, an MK drilling rig was primarily used to construct strip drainage boreholes in the roadway of the first mining face. Later, extraction work was organized by combining bedding ordinary boreholes and directional boreholes. According to predictions from gas extraction numerical simulation software, when the borehole spacing is 1 m and the drilling footage per ton of coal is 0.11 m, the pre-drainage period can meet the standard within 12 months. To improve the efficiency of roadway excavation while ensuring safety, drilling hole parameters on the working face were designed as follows: drilling hole spacing is 1 m, with 12 holes arranged in three rows, and drilling footage per ton of coal is 0.33 m. In addition to head-on arrangement, construction was also carried out on both sides of the roadway to strengthen extraction from pre-drainage drilling fields, with drilling parameters in these fields matching those of head-on drilling. The design also requires pre-drainage drilling to extend 15 m beyond the roadway's contour line. According to predictions from gas extraction numerical simulation software, using the adjusted borehole design allows for a standard extraction time of 4 months.

2) Construction of outburst prevention measures for pre-drainage boreholes in heading face

The 1301 working face is the first mining face in the western well area. To reduce the gas content to less than 8 m^3/t and improve the pre-drainage time of the working face before mining, it is crucial to safely penetrate the working face as soon as possible. This allows for pre-drainage of the working face gas by drilling along the working face. Therefore, when excavating the test roadway, we enhanced the parameters of drilling holes based on the original design. The specific layout parameters for various boreholes are presented in Table 2, and a schematic diagram of the boreholes is shown in Figure 4.

3.2.3 Outburst prevention technology of bedding drilling in first mining face

Based on the previous analysis, it is clear that the 1301 working face of the first mining face can adopt pre-drainage drilling spacing of 1 m, 2 m, 3 m, and 5 m. To determine the optimal pre-drainage drilling arrangement, these four different drilling arrangements are analyzed individually. Before mining the working face, the gas content of the coal seam is reduced to less than 8 m^3/t and can

TABLE 2 Design and construction parameter table of outburst prevention engineering in bedding drilling area of heading face.

Bedding drilling form	Hole depth (m)	Drill-hole spacing (m)	Drilling hole amount (ind)	Height of opening (m)	Pre-pumping standard time	Drilling rig model
Heading, drilling field	150	0.5	18	Lower row 1.5 Upper row 1.7	March-June	MKD-5S
Advanced drilling						
13013–13012 Lane	65	1	60	Lower row 1.5 Upper row 1.7	March-June	MK-4
Hengchuan coal pillar drilling						
13012–13014 Lane	65	1	30	Lower row 1.5 Upper row 1.7	March-June	MK-4
Hengchuan coal pillar drilling						
13015–13011 Lane	65	1	30	Lower row 1.5 Upper row 1.7	March-June	MK-4
Hengchuan coal pillar drilling						
13013,13012,13014 Lane	60	1	——	Lower row 1.5 Upper row 1.7	March-June	MK-4
Roadway side drilling						
13012–13014 Lane	30	1	——	Lower row 1.5 Upper row 1.7	March-June	MK-4
Roadway side drilling						
13015–13011 Lane	30	1	——	Lower row 1.5 Upper row 1.7	March-June	MK-4
Roadway side drilling						
Directional drilling	>300	1	——	——	July-October	VLD-1000

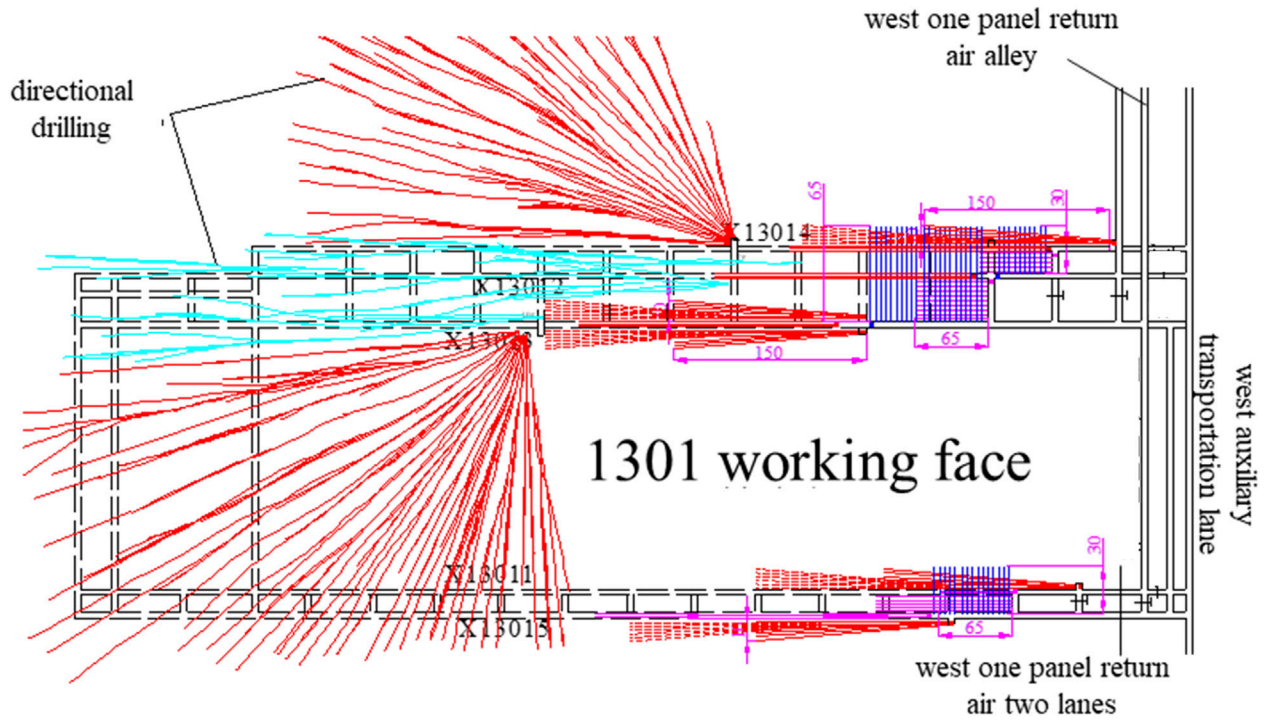


FIGURE 4
Drilling layout of pre-drainage outburst prevention measures in heading face.

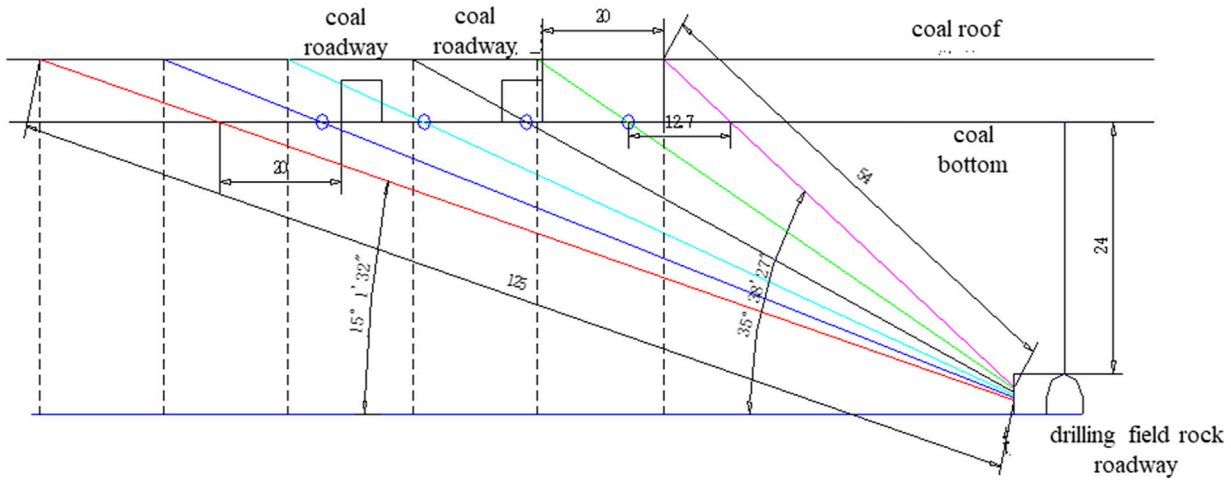


FIGURE 5
Cross-layer borehole design profile layout diagram.

meet the requirements of the annual output of the working face of 4 Mt/a. When the borehole spacing is 3 m and 5 m, it can meet the pre-drainage time of the working face for more than 17 months. Through comparison and selection, although the borehole engineering quantity is smallest when the borehole spacing is 5 m, considering the maximum reduction of coal seam gas content in the 1301 working face, a pre-drainage borehole is selected to be arranged with a spacing of 3 m.

3.3 Outburst prevention technology of pre-drainage gas area by cross-layer drilling

3.3.1 Drilling design of pre-drainage gas area of cross-layer drilling

Cross-layer boreholes in the western well area are arranged within the development roadway. The thickness of the rock roadway from the coal seam exceeds 24 m. Each drilling field is generally designed with three to six rows of boreholes, with each row containing 15–20 boreholes. The spacing between boreholes is 0.5 m, and boreholes are typically spaced 3–5 m apart. A drilling field is constructed every 30 m, with each drilling field covering the excavation range of 15 m coal roadways on both sides. The final hole of the drilling extends 20 m (horizontal projection distance) beyond the outer side of the design coal lane at the farthest end, controlling a coal body of 60 × 120 (m^2) and a control coal volume of approximately 64,000 t. Currently, there are 45 cross-layer drilling fields in the western well area. The borehole diameter is primarily 94 mm. The ratio of borehole coal to rock holes is usually 1:3. The length of borehole per ton of coal is 0.103 m/t, with the length of coal hole per ton of coal being about 0.026 m/t. The cross-layer drilling design profile is shown in Figure 5.

3.3.2 Application of outburst prevention in pre-drainage gas area of cross-layer drilling

In the western well area, outburst prevention measures in the pre-drainage gas area of the cross-layer borehole were tested and applied during the eastern excavation of the return air roadway. The measured original gas content in the uncovered coal area averages approximately 17.56 m^3/t, and the gas reserve is about 2.88 million m^3, indicating that it is an outburst-dangerous area.

To reduce the gas content to less than 8 m^3/t within 9 months, cross-layer drilling pre-drainage measures were implemented. Based on the predicted extraction effect of cross-layer drilling and the corresponding drilling engineering requirements, the 38# and 39# cross-layer drilling fields were arranged during construction when the distance from the uncovered coal was 37 m. The MKD-5 S drilling rig was used in the construction of cross-layer drilling. A total of 128 cross-layer drillings were designed and constructed, with a drilling quantity of 6600 m. The drilling control range extends 13 m outside the contour line of the roadway, starting from the coal uncovering point, and covers a range of 13 m to the east and west. The horizontal spacing of the final hole point of the borehole is 3 m, and the final hole point is located at 0.5 m in the roof of the 3# coal seam. The arrangement of boreholes for uncovering coal is shown in Figure 6, Figure 7, to Figure 8.

4 Application effect of regional outburst prevention

4.1 Outburst prevention effect of bedding borehole pre-drainage

Before each excavation, the measured gas content is used to evaluate the pre-drainage effect on the coal in front of the excavation face (0–150 m in front of the excavation and 8–10 m outside the roadway contour line). When evaluating the measured residual gas content, a content test point is arranged every 20–30 m, and it is required that each test point be equidistant from the surrounding boreholes. Using the 13013 roadway as an example, we explain the layout of the test hole, the test results of residual gas content, and the verification results of the first mining face. The arrangement

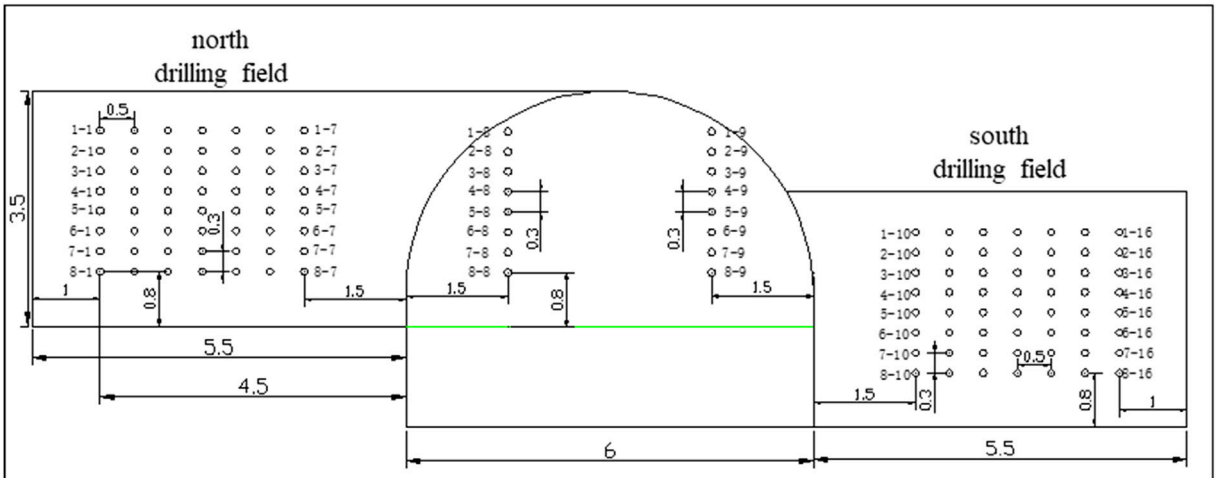


FIGURE 6
Schematic diagram of borehole section layout in east excavation of west return air roadway.

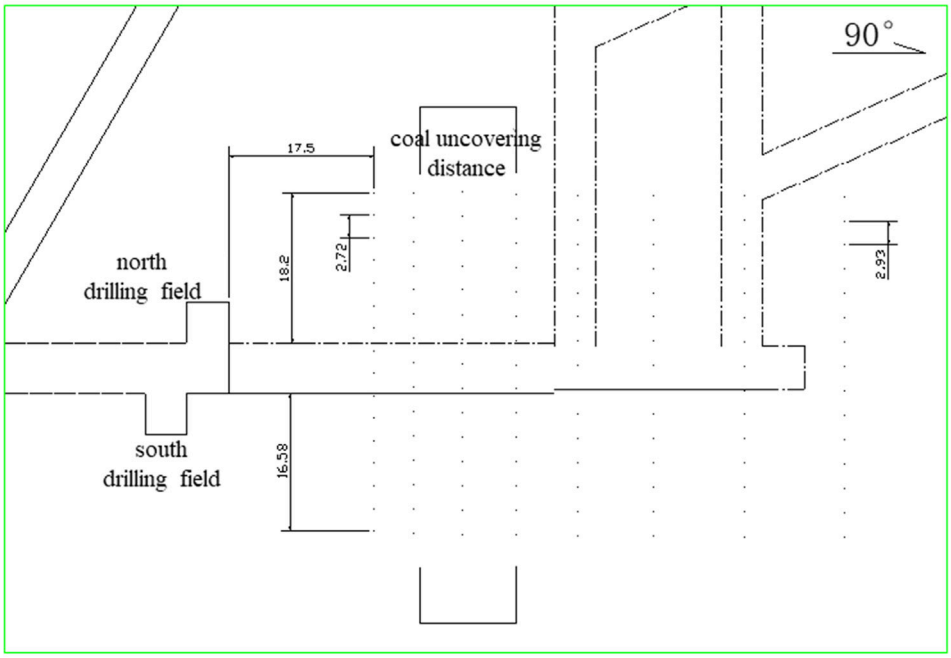


FIGURE 7
The schematic diagram of the final hole position of the east excavation coal uncovering borehole in the west return air roadway.

of pre-drainage effect content test boreholes in the excavation roadway of the first mining face is shown in Figure 9, and the measured results of residual gas content are presented in Table 3.

From the measured content data in Table 3, it can be seen that the residual gas content has been reduced to less than 8 m^3/t before each excavation. This indicates that the measures

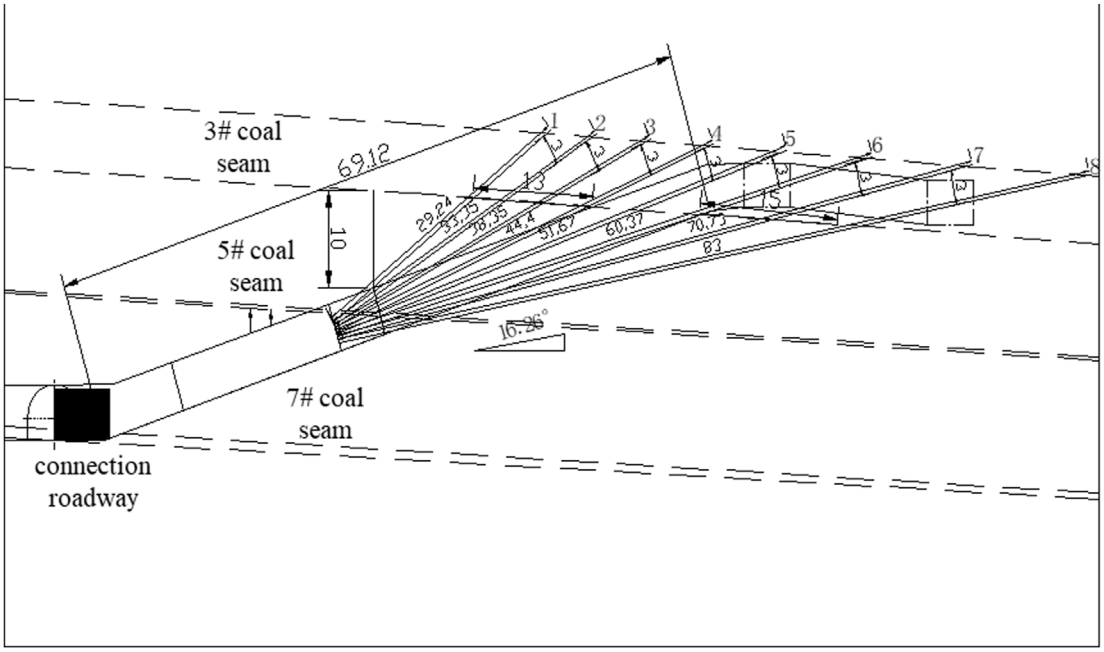


FIGURE 8
The schematic diagram of the borehole section of the east excavation of the west return air roadway.

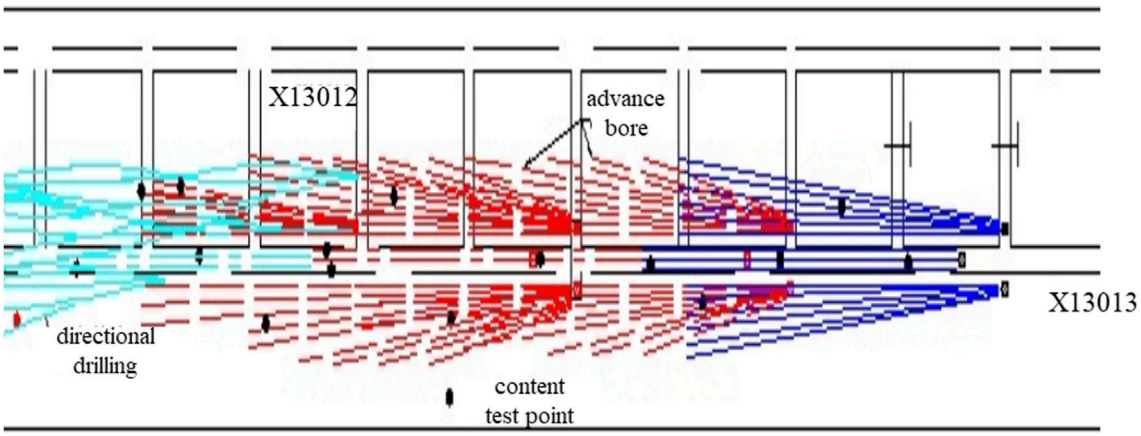


FIGURE 9
The measured content point layout diagram of 13013 roadway in west well area.

implemented in the gas extraction area of the excavation working face are effective.

Residual gas content tests show that during the excavation process of five roadways, such as 13013 and 13014 in the first mining face, a strip area of 150 m advanced drilling and roadway side drilling is typically adopted to enhance extraction. After 3–6 months, the residual gas content in the control area can be reduced to less than 8 m^3/t, thereby achieving the outburst prevention effect of the working face. After 7–10 months of pre-drainage, even under the condition of pre-drainage by directional drilling in the second half of the working face, the residual gas content of the coal roadway strip can also be reduced to less than 8 m^3/t. It has been verified that after pre-drainage, the 13013 roadway is a non-outburst danger zone.

After confirming the effectiveness of the pre-drainage in the 1301 first mining face, the first regional verification was conducted within a 10 m range of the 1301 first mining face. The specific method was as follows: 13 verification boreholes using the drilling cuttings method were arranged every 15 m along the working face (excluding 10 m at the upper and lower outlet sections of the working face). The boreholes were arranged as much as possible in the soft layer, parallel to the mining direction of the working face.

TABLE 3 13013 Lane effect test residual gas content measured results table.

Inspection point number	The depth of the test point from the working face (m)	Residual gas content (m^3/t)	Inspection point number	The depth of the test point from the working face (m)	Residual gas content (m^3/t)
1	20	7.303	21	20	6.765
2	50	6.527	22	50	7.67
3	80	6.012	23	80	7.012
4	100	6.57	24	20	7.487
5	20	7.33	25	50	5.637
6	50	7.67	26	80	6.334
7	80	7.29	27	20	5.67
8	100	6.89	28	50	6.08
9	30	7.52	29	30	5.437
10	60	5.56	30	60	6.48
11	80	6.303	31	90	7.37
12	30	5.67	32	30	5.45
13	60	6.052	33	60	7.7
14	80	6.437	34	30	7.38
15	20	7.563	35	60	6.453
16	50	7.79	36	90	5.83
17	80	7.60	37	30	5.2
18	100	5.012	38	60	7.85
19	30	6.47	39	90	6.9
20	60	5.36	40	30	6.47

Starting from a depth of 2 m in each borehole, the S value of all drilling cuttings in a 1 m section was measured for each 1 m drilling, and coal drilling cuttings with a particle size of 1–3 mm discharged from the orifice were collected for each 2 m drilling. The K_1 value of the gas desorption index of the drilling cuttings was measured. The critical value of the outburst verification index is: S = 6 kg/m, K_1 = 0.5 mL/g.$min^{1/2}$. The statistics of the verification index results at the incision are presented in Table 4.

Based on the results presented in Table 4, the maximum values of K1 and S in the 13 verification boreholes are below the critical value. Additionally, there were no significant risk omens observed during the drilling construction. Therefore, the regional verification indicates that there is no significant danger zone within 10 m of the first mining face.

4.2 Effect of pre-drainage and outburst prevention of cross-layer drilling

In the eastern excavation and coal uncovering area of the western return air roadway, after 10 months of pre-drainage, the cumulative drainage volume of the drilling field is 1.87 million m^3 according to the drainage volume statistics. The residual gas content is expected to be 6.16 m^3/t. Therefore, a residual gas content test was conducted in this area with 13 test points. The layout of the test points covered a range of 1–8 m on the upper, middle, and both sides of the uncovered coal area. The results are presented in Table 5 below.

5 Regional outburst prevention mode in west well area

5.1 Construction of regional outburst prevention mode

Considering the characteristics of the 3# coal seam in the western well area, such as stable overall occurrence, hard coal quality, good gas permeability, high gas content, and favorable hole forming conditions for bedding drilling, we have combined the applicable conditions of three regional outburst prevention measures and their respective extraction characteristics. We preliminarily propose the following regional outburst prevention modes: prioritize regional outburst prevention of ground wells, implement regional pre-drainage and outburst prevention measures of ground drilling as far as possible in the conditional area, and implement regional pre-drainage and outburst prevention measures of bedding boreholes after underground development is

TABLE 4 Statistical table of verification results of drilling cuttings method index in open-off cut area of 1301 first mining face.

Verification drilling	Verify indicators	Depth (m)									Maximum value of index	Safety or insecurity
		2	3	4	5	6	7	8	9	10		
1# verification hole	K_1 (mL/g.min$^{1/2}$)	0.08		0.13		0.21		0.17		0.25	0.25	Safety
	S (kg/m)	2.4	2.6	3	2.8	3.6	4.6	2.9	3.9	5.1	5.1	
2# verification hole	K_1 (mL/g.min$^{1/2}$)	0.18		0.03		0.42		0.19		0.35	0.42	Safety
	S (kg/m)	2.8	3	3	4.2	4.6	3.9	3.5	4.7	4.1	4.7	
3# verification hole	K_1 (mL/g.min$^{1/2}$)	0.11		0.15		0.08		0.24		0.13	0.24	Safety
	S (kg/m)	3.4	4.0	2.6	2.4	3.9	3.6	4.1	3.2	4.1	4.1	
4# verification hole	K_1 (mL/g.min$^{1/2}$)	0.14		0.19		0.11		0.16		0.12	0.19	Safety
	S (kg/m)	3.1	2.6	3.8	2.2	3.7	4.1	4.5	3.9	4.0	4.5	
5# verification hole	K_1 (mL/g.min$^{1/2}$)	0.21		0.19		0.34		0.18		0.27	0.34	Safety
	S (kg/m)	3.1	3.6	3.5	2.8	3.7	4.3	2.9	4.6	5.3	5.3	
6# verification hole	K_1 (mL/g.min$^{1/2}$)	0.21		0.27		0.13		0.33		0.35	0.35	Safety
	S (kg/m)	2.9	3.6	3	3.8	3.1	2.6	3.9	4.3	4.0	4.3	
7# verification hole	K_1 (mL/g.min$^{1/2}$)	0.07		0.23		0.12		0.25		0.45	0.45	Safety
	S (kg/m)	2.7	2.6	3.3	3.8	4.6	5.2	4.5	3.7	4.2	5.2	
8# verification hole	K_1 (mL/g.min$^{1/2}$)	0.15		0.05		0.21		0.34		0.16	0.34	Safety
	S (kg/m)	2.6	3.0	3.6	2.7	3.1	2.6	3.5	3.2	3.5	3.6	
9# verification hole	K_1 (mL/g.min$^{1/2}$)	0.14		0.12		0.08		0.06		0.09	0.12	Safety
	S (kg/m)	3.1	2.9	3.2	3.2	3.6	3.1	4.2	4.9	3.5	4.2	
10# verification hole	K_1 (mL/g.min$^{1/2}$)	0.09		0.26		0.14		0.38		0.27	0.38	Safety
	S (kg/m)	3.4	3.6	2.5	3.8	4.7	4.1	2.9	3.6	4.3	4.7	
11# verification hole	K_1 (mL/g.min$^{1/2}$)	0.25		0.07		0.33		0.41		0.31	0.41	Safety
	S (kg/m)	2.2	2.4	3.5	3.2	3.8	2.5	4.9	3.3	4.2	4.9	
12# verification hole	K_1 (mL/g.min$^{1/2}$)	0.07		0.23		0.12		0.25		0.45	0.45	Safety
	S (kg/m)	2.7	2.6	3.3	3.8	4.6	5.2	4.5	3.7	4.2	5.2	
13# verification hole	K_1 (mL/g.min$^{1/2}$)	0.15		0.25		0.26		0.31		0.09	0.31	Safety
	S (kg/m)	3.6	3.1	3.4	2.8	3.9	2.6	2.5	3.2	3.5	3.9	

TABLE 5 The measured content results of the east excavation and uncovering coal area of the west return air roadway.

Inspection point serial number	Residual gas content (m^3/t)	Inspection point serial number	Residual gas content (m^3/t)
1	7.013	8	5.87
2	6.492	9	7.43
3	5.23	10	7.885
4	6.542	11	7.142
5	5.4347	12	6.5293
6	7.42	13	6.942
7	7.672	——	——

revealed. In combination with the implemented regional measures of ground drilling, we ensure that the effect of regional outburst prevention measures before mining reaches the standard (directional drilling is mainly used in bedding drilling, supplemented by bedding ordinary long drilling in the blank area of directional drilling or areas where extraction and outburst prevention need to be strengthened). However, in the face of coal uncovering area and large geological structure area, when it is difficult to implement bedding drilling, we should adopt the outburst prevention measures of cross-layer drilling to carry out extraction and outburst prevention in the target area.

5.2 Comprehensive experimental study on regional outburst prevention measures

Based on the three measures of surface drilling, cross-layer drilling, and bedding drilling, three types of outburst prevention measures are comprehensively applied. These measures are tailored according to the specific pumping, excavation, mining time, and specific coal seam geological conditions in other working faces other than the first mining face in the first panel and the entire mining area in the second panel. This approach ensures that the advantages and characteristics of various measures are fully utilized. The specific performance is as follows:

1) In the 2301, 2302, and other working faces of the second panel, surface drilling is utilized in advance for coalbed methane mining and regional pre-drainage and outburst prevention. According to statistics, surface drilling in the western well area reduces the gas content by nearly 1 m^3/t each year. Therefore, after 4–6 years of pre-drainage, the gas content in most areas of the second panel will be reduced to 16 m^3/t or even less. This saves valuable time for the pre-drainage of bedding boreholes when later development and mining operations approach the area. At the same time, leveraging the 'one well multi-purpose' characteristic of ground drilling is conducive to preventing gas overrun accidents in the working face during mining.

For example, there are three surface drilling wells near the 2301 working face, and the pre-drainage time is 4–6 years on average. When the directional drilling pre-drainage is carried out in this area, the pre-drainage time of the bedding drilling is about 24 months, and the gas content can be reduced to less than 8 m^3/t, which realizes the safe and rapid excavation of the open-off cut roadway. Compared with the surrounding gas occurrence conditions are similar, but there is no ground drilling pre pumping area, bedding drilling pre pumping time is usually more than half a year or even longer. Therefore, the pre-pumping of surface drilling creates conditions for the pre-pumping effect of underground outburst prevention measures to reach the standard in a relatively short time, which is conducive to the safe and efficient production of the mine.

2) In the rock roadways arranged close to the mining face, such as the current air intake roadway of the first panel of the west, the bottom of the Sanshuigou well, and the auxiliary transportation roadway of the west, cross-layer boreholes are evenly arranged. These cross-layer boreholes are used to pre-drain gas in adjacent coal roadway strips (such as 23011 roadway and 23015 roadway) or gas in the cross-cut area that may be exposed by the pre-draining roadway (such as the air intake and return roadway of the second panel of the west, and the auxiliary transportation roadway of the second panel of the west). According to investigations, after completion of cross-layer drilling construction in a 60 × 120 (m^2) area in the western well area (where the gas content of raw coal is within 16 m^3/t), when the coal hole is 0.026 m/t, an average of 18 months of pre-drainage can ensure that extraction in the area meets standards. This effectively ensures coal seam safety and creates a breakthrough for implementing large-scale pre-drainage and outburst prevention in subsequent stages.

As of January 2008, cross-layer drilling has been used to cover a total of 2,000 m in lanes 23011 and 23015. Through the pre-drainage of cross-layer drilling, the first mining of the 2301 working face in the second panel has been safely exposed. In addition, drilling holes were evenly arranged from the auxiliary transportation roadway in the western area, covering and pre-draining the entire strip of the first and second lanes of the return air in the western area. This has enabled the safe excavation of the two lanes, thereby creating conditions for improving the ventilation system in the western area.

3) In the exposed coal seam roadway working face, such as the 13015 roadway, 13014 roadway, 2301 open-off cut, and 23011 roadway, a large number of directional boreholes were constructed using kilometer directional drilling rigs. This allowed for modular extraction in the subsequent mining replacement working face section. The directional drilling module extraction not only controls the entire coal mining area but also manages all the unexcavated crossheadings related to the replacement working face. The gas in the excavation and mining area is reduced to below the critical index of outburst risk before excavation, creating favorable conditions for the safety and efficiency of later excavation and mining. According to application investigations, in underground areas where the gas content of raw coal is within 16 m^3/t, the residual gas content in the area can typically be reduced to less than 8 m^3/t after an average pre-drainage of 24 months by directional drilling.

During the safe tunneling process of the 23011 and 23015 roadways, the K_1 verification index in this area did not exceed the standard even once, so no local supplementary measures were carried out.

5.3 Summary of complete set technology of regional outburst prevention measures in xixi well area

Through the extraction characteristics of three regional outburst prevention measures and the underground application research, we have gained an understanding of the applicable characteristics and field effects of various measures. Therefore, under the current coal seam gas occurrence conditions in the western well area, the

complete set of technologies for regional pre-drainage and outburst prevention measures suitable for the western well area are as follows:

1) In areas where the coal seam gas content is greater than or equal to 16 m^3/t, it is essential to implement surface drilling area pre-drainage and outburst prevention measures. This ensures that the coal seam gas content is less than 16 m^3/t during underground development. In other coal seam areas, it is advisable to implement surface drilling area pre-drainage and outburst prevention measures as much as possible.
2) In areas where the coal seam gas content is less than 16 m^3/t during development, it is advisable to implement bedding drilling area drainage outburst prevention measures underground. This should be done in conjunction with the implementation of surface drilling area measures to ensure that the mining area meets the standard for outburst prevention measures before mining. Bedding drilling, particularly directional drilling, should be prioritized. In areas where directional drilling is not possible or where drainage and outburst prevention need to be strengthened, ordinary long drilling can be used as a supplement.

When adopting progressive pre-drainage of bedding directional drilling, the drilling length should be at least 300–500 m, and the drilling field should move once every 300–500 m. The range of directional drilling cover control should include the front of the roadway excavation (>60 m), the entire block section of the succeeding coal mining face, and the three crossheading roadways on the other side of the succeeding working face. After reducing the coal body in the cover control range to 8 m^3/t, safe excavation and mining can be achieved. The same progressive layout should be implemented to the next mining replacement surface in the new excavation roadway on the other side of the working face. This approach ensures a reasonable connection of the entire mine mining face.

3) In areas where geological structures make drilling construction difficult during coal uncovering, and in the main roadway of the coal seam floor, pre-pumping outburst prevention measures should be used through the layer drilling area. This ensures that regional outburst prevention measures meet mining standards before mining begins.

Uncovering coal area: When the cross-cut uncovers the coal seam in the coal uncovering area, cross-layer drilling must be used to prevent regional outbursts. This should continue until the outburst risk in the uncovered coal area is eliminated.

Open up the roadway area:According to the mine design, main development roadways such as the auxiliary transportation roadway in the west area of the west well area, the belt conveyor roadway, the north belt conveyor roadway in the west area, the north auxiliary transportation roadway in the west area, and the north return air roadway in the west area will be arranged in the rock stratum. Therefore, these rock roadways that will be constructed should be used for adjacent working faces (such as W23011 roadway and W23015 roadway), adjacent panel concentrated coal roadways (such as the auxiliary transportation roadway in the west second panel), and construction of the working face mining area. Cross-layer drilling is used for strip and section pre-drainage and outburst prevention.

Working face crossheading area: Under normal geological conditions of a coal seam, long-distance and large-range bedding drilling can be used for pre-drainage in crossheadings or coal roadways. However, when encountering special areas such as large faults, collapse columns, or increased soft layer thickness, it becomes difficult to construct bedding drilling holes and meet the requirements of regional control range. In such cases, a temporary rock roadway or rock drilling field should be constructed in the roof or floor. Cross-layer drilling should be carried out in the special area above the rock roadway (drilling field). By relying on the rock stratum as a safety barrier, the gas content in the special area is reduced to less than 8 m^3/t, eliminating the regional outburst risk. Then, under the protection of local outburst prevention measures, return to the coal roadway to continue advancing until it is far from the influence range of special areas.

In summary, the application mode of regional outburst prevention measures in the west well area should be reasonably combined and fully utilized according to different gas content areas, different occurrence conditions, and different time and space requirements. This approach ensures that the regional outburst prevention measures in the west well area are more reliable, reasonable, and economical. It is more conducive to the balanced and coordinated development of 'pre-drainage outburst prevention, tunneling, and mining' under the existing production conditions, providing a strong guarantee for the efficient and safe production of the west well area.

6 Conclusion

Based on the mine conditions and relevant experience, this paper examines the outburst prevention measures of various pre-drainage gas areas such as surface drilling, bedding (directional) drilling, and cross-layer drilling. In conjunction with the coal seam occurrence and mining technology in the western well area, it is concluded that surface drilling pre-drainage is primary, underground bedding directional long drilling pre-drainage is the main approach, and cross-layer drilling pre-drainage is supplementary. This practical and feasible regional pre-drainage comprehensive outburst prevention mode, suitable for the characteristics of the 3# coal seam in the western well area, provides a reliable guarantee for the safe and efficient production of the outburst well area. The following conclusions are drawn:

1) In areas where the coal seam gas content is greater than or equal to 16 m^3/t and not open, surface drilling area pre-drainage outburst prevention measures must be implemented. This ensures that when the mine and mining area main roadway development is underway, the control area's coal seam gas content is reduced to 16 m^3/t or less. In other areas where the coal seam gas content is less than 16 m^3/t, surface drilling area pre-drainage outburst prevention measures should be implemented as far as possible. The surface drilling spacing for outburst prevention in the normal area is determined to be 300 m × 300 m, and in the geological structure zone, it is

150 m × 150 m. Other parameters are consistent with the CBM development of surface wells.

2) In the underground, regional outburst prevention measures are primarily implemented through the pre-drainage of gas using directional long boreholes along the bedding. These measures are combined with the implementation of surface drilling pre-drainage gas regional measures to ensure that the effect of regional outburst prevention measures meets mining standards before mining begins
3) During the excavation process of five roadways such as 13013 and 13014 in the first mining face, 150 m advance drilling and roadway side drilling are used to strengthen the extraction of the strip area. After 7–10 months of pre-drainage, the residual gas content of the coal roadway strip can also be reduced to less than 8 m^3/t. It is verified that the 13013 roadway is a non-outburst danger zone after pre-drainage, and the research has formed an outburst prevention mode for the pre-drainage area of the directional long borehole along the strata under different conditions. Through the arrangement of drilling cuttings method to verify the drilling, it is verified that there is no outburst danger zone within 10 m of the first mining face, and an outburst prevention mode for the pre-drainage area of the directional long drilling along the mining face under different parts is formed.
4) In the area where the rock roadway uncovers coal and geological structures cause difficulties in the construction of bedding drilling, as well as in the main roadway control area in the mining area located in the coal seam floor rock layer, cross-layer drilling area pre-drainage and outburst prevention measures should be adopted. This ensures that regional outburst prevention measures meet mining standards before mining begins in the extraction area.

Data availability statement

The original contributions presented in the study are included in the article/supplementary material, further inquiries can be directed to the corresponding author.

Author contributions

PZ: Writing–original draft, Writing–review and editing.

Funding

The author(s) declare that no financial support was received for the research, authorship, and of this article.

Conflict of interest

Author PZ was employed by Ningxia Tiandi Benniu Industrial Group Co., Ltd.

Publisher's note

All claims expressed in this article are solely those of the authors and do not necessarily represent those of their affiliated organizations, or those of the publisher, the editors and the reviewers. Any product that may be evaluated in this article, or claim that may be made by its manufacturer, is not guaranteed or endorsed by the publisher.

References

Chen, Z. H., Zou, Q. L., Gao, S. K., Zhan, J. F., Chen, C. M., Ran, Q. C., et al. (2023). Long-term evolution of overlying rock fractures in mined-out areas and its effect on gas flow conductivity. *Fuel* 353, 129213. doi:10.1016/j.fuel.2023.129213

Cheng, L., Xu, J., Peng, S. J., Qin, L., Yan, F. Z., Bai, Y., et al. (2022). Influence of different coal seam gas pressures and their pulse characteristics on coal-and-gas outburst impact airflow. *Nat. Resour. Res.* 31 (5), 2749–2767. doi:10.1007/s11053-022-10087-y

Gao, S., Mou, J. S., and Yang, H. M. (2019). Permeability enhancement technology of hydraulic fracturing of bedding drilling borehole in outburst coal seam. *Min. Saf. Environ. Prot.* 46 (04), 92–94. In Chinese.

Han, Q. S., and Li, S. Q. (2020). Engineering practice of combined outburst prevention for distant coalseam groups in west zhuiji coalmine. *Energy Technol. Manag.* 45 (04), 16–17. In Chinese.

Huang, L. K., He, R., Yang, Z. Z., Tan, P., Chen, W. H., Li, X. G., et al. (2023a). Exploring hydraulic fracture behavior in glutenite formation with strong heterogeneity and variable lithology based on DEM simulation. *Eng. Fract. Mech.* 278, 109020. doi:10.1016/j.engfracmech.2022.109020

Huang, L. K., Tan, J., Fu, H. F., Liu, J. J., Chen, X. Y., Liao, X. C., et al. (2023b). The non-plane initiation and propagation mechanism of multiple hydraulic fractures in tight reservoirs considering stress shadow effects. *Eng. Fract. Mech.* 292, 109570. doi:10.1016/j.engfracmech.2023.109570

Li, Q. M., Liang, Y. P., Zou, Q. L., and Li, Q. G. (2020). Acoustic emission and energy dissipation characteristics of gas-bearing coal samples under different cyclic loading paths. *Nat. Resour. Res.* 29 (2), 1397–1412. doi:10.1007/s11053-019-09508-2

Liang, Y. P., Kong, F. J., Zou, Q. L., and Zhang, B. C. (2023). Effect of strain rate on mechanical response and failure characteristics of horizontal bedded coal under quasi-static loading. *Geomechanics Geophys. Geo-Energy Geo-Resources* 9 (1), 52. doi:10.1007/s40948-023-00587-3

Liang, Y. P., Ran, Q. C., Zou, Q. L., Zhang, B. C., and Hong, Y. (2022). Experimental study of mechanical behaviors and failure characteristics of coal under true triaxial cyclic loading and unloading and stress rotation. *Nat. Resour. Res.* 31 (2), 971–991. doi:10.1007/s11053-022-10022-1

Liao, Z. W., Liu, X. F., Song, D. Z., He, X. Q., Nie, B. S., Yang, T., et al. (2021). Micro-structural damage to coal induced by liquid CO2 phase change fracturing. *Nat. Resour. Res.* 30 (2), 1613–1627. doi:10.1007/s11053-020-09782-5

Liu, S. M., and Li, X. L. (2016). Discussion on coupling disaster mechanism of coal and gas outburst and rock burst in deep coal mining. *Coal Technol.* 35 (09), 134–136. doi:10.13301/j.cnki.ct.2016.09.053

Liu, S. M., Sun, H. T., Zhang, D. M., Yang, K., Wang, D. K., Li, X. L., et al. (2023a). Nuclear magnetic resonance study on the influence of liquid nitrogen cold soaking on the pore structure of different coals. *Phys. Fluids* 35, 012009. doi:10.1063/5.0135290

Liu, T., Lin, B. Q., Fu, X. H., and Liu, A. (2021). Mechanical criterion for coal and gas outburst: a perspective from multiphysics coupling. *Int. J. Coal Sci. Technol.* 8, 1423–1435. doi:10.1007/s40789-021-00447-z

Liu, Y. B., Wang, E. Y., Jiang, C. B., Zhang, D. M., Li, M. H., Yu, B. C., et al. (2023b). True triaxial experimental study of anisotropic mechanical behavior and permeability evolution of initially fractured coal. *Nat. Resour. Res.* 32 (2), 567–585. doi:10.1007/s11053-022-10150-8

Ma, T. F., Liu, H. H., Zou, Q. L., Kong, F. J., Ran, Q. C., and Wang, P. T. (2023). Damage evolution characteristics and deterioration mechanism of mechanical properties of sandstone subjected to drying-wetting cycles. *J. Mater. Res. Technol.* 23, 4591–4605. doi:10.1016/j.jmrt.2023.02.068

Pan, J. F., Qi, Q. X., Liu, S. H., Wang, S. W., Ma, W. T., and Kang, X. C. (2020). Characteristics,types and prevention and control technology of rock burst in deep coal mining in China. *J. China Coal Soc.* 45 (01), 111–121. doi:10.13225/j.cnki.jccs.YG19.1638

Ran, Q. C., Liang, Y. P., Zou, Q. L., Hong, Y., Zhang, B. C., Liu, H., et al. (2023a). Experimental investigation on mechanical characteristics of red sandstone under graded cyclic loading and its inspirations for stability of overlying strata. *Geomechanics Geophys. Geo-Energy Geo-Resources* 9 (1), 11. doi:10.1007/s40948-023-00555-x

Ran, Q. C., Liang, Y. P., Zou, Q. L., Zhang, B. C., Li, R. F., Chen, Z. H., et al. (2023b). Characteristics of mining-induced fractures under inclined coal seam group multiple mining and implications for gas migration. *Nat. Resour. Res.* 32 (3), 1481–1501. doi:10.1007/s11053-023-10199-z

Song, M. Y., Li, Q. G., Hu, Q. T., Wu, Y. Q., Ni, G. H., Xu, Y. C., et al. (2022). Resistivity response of coal under hydraulic fracturing with different injection rates: a laboratory study. *Int. J. Min. Sci. Technol.* 32 (4), 807–819. doi:10.1016/j.ijmst.2022.06.004

Su, E. L., Liang, Y. P., Chen, X. J., Wang, Z. F., Ni, X. M., Zou, Q. L., et al. (2023). Relationship between pore structure and mechanical properties of bituminous coal under sub-critical and super-critical CO2 treatment. *Energy* 280, 128155. doi:10.1016/j.energy.2023.128155

Sun, D. L., Liang, Y. P., Huang, X. C., and Ran, Q. C. (2023a). Progress and prospects of coalbed methane development and utilization in coal mining areas with large dip angle and multiple coal groups in Xinjiang. *Coal Sci. Technol.* 51 (S1), 161–171. doi:10.13199/j.cnki.cst.mcq2022-1325

Sun, X. Y., Ran, Q. C., Liu, H., Ning, Y. H., and Ma, T. F. (2023b). Characteristics of stress-displacement-fracture multi-field evolution around gas extraction borehole. *Energies* 16 (6), 2896. doi:10.3390/en16062896

Tan, P., Fu, S. H., Chen, Z. W., and Zhao, Q. (2023). Experimental investigation on fracture growth for integrated hydraulic fracturing in multiple gas bearing formations. *Geoenergy Sci. Eng.* 231 (1), 212316. doi:10.1016/j.geoen.2023.212316

Tan, P., Jin, Y., and Pang, H. W. (2021). Hydraulic fracture vertical propagation behavior in transversely isotropic layered shale formation with transition zone using XFEM-based CZM method. *Eng. Fract. Mech.* 248, 107707. doi:10.1016/j.engfracmech.2021.107707

Wang, G. F., Ren, H. W., Zhao, G. R., Zhang, D. S., Wen, Z. G., Meng, L. Y., et al. (2022). Research and practice of intelligent coal mine technology systems in China. *Int. J. Coal Sci. Technol.* 9, 24. doi:10.1007/s40789-022-00491-3

Wang, H. F., Cheng, Y. P., Liu, G. J., Kong, S. L., and Zhang, R. (2013). Range extender of protection and continuous mining technology of protected seam. *J. Min. Saf. Eng.* 30 (04), 595–599. In Chinese.

Wang, H. T., Huang, G. L., Yuan, Z. G., Shu, C., and Hu, G. Z. (2014). Model of gas leak flow coupled solid and gas for exploiting of steep-inclined upper-protective layer and its protection scope. *Rock Soil Mech.* 35 (05), 1377–1382. doi:10.16285/j.rsm.2014.05.022

Wang, Z. H., Chen, B., Zhang, Y. J., Yang, H. M., and Cao, J. J. (2021). Research on dual pressure relief and outburst prevention model for deep floor rock roadways. *Arabian J. Geosciences* 14, 845. doi:10.1007/s12517-021-07118-y

Wang, Z. M., Liang, Y. P., Zou, Q. L., Zhang, B. C., and Ran, Q. C. (2023). Movement of overlying rock and deformation law of surface well under multiple mining with large dip angle. *Coal Sci. Technol.* 51 (04), 47–55. doi:10.13199/j.cnki.cst.2021-0827

Wu, Q. F., Han, S. X., Li, S. S., Yu, M. G., Zheng, K., Li, H. T., et al. (2023). Explosive characteristics of non-uniform methane-air mixtures in half-open vertical channels with ignition at the open end. *Energy* 284, 128687. doi:10.1016/j.energy.2023.128687

Wu, Q. F., Yu, M. G., and Zheng, K. (2022). Experimental investigation on the effect of obstacle position on the explosion behaviors of the non-uniform methane/air mixture. *Fuel* 320, 123989. doi:10.1016/j.fuel.2022.123989

Xiao, S. Q., Ren, Q. Y., Cheng, Y. G., Wang, H. Y., Zhang, L., Liao, Y., et al. (2022). Research and application of high-pressure water jets drilling and repairing failure drainage borehole for enhancing coalbed methane recovery in underground coal mines. *Geomechanics Geophys. Geo-Energy Geo-Resources* 8 (6), 191. doi:10.1007/s40948-022-00500-4

Xie, H. P., Lu, J., Li, C. B., Li, M. H., and Gao, M. Z. (2022). Experimental study on the mechanical and failure behaviors of deep rock subjected to true triaxial stress: a review. *Int. J. Min. Sci. Technol.* 32 (5), 915–950. doi:10.1016/j.ijmst.2022.05.006

Xie, Y. C., Hou, M. Z., and Li, C. B. (2023). Anisotropic characteristics of acoustic emission and the corresponding multifractal spectrum during progressive failure of shale under cyclic loading. *Int. J. Rock Mech. Min. Sci.* 165, 105364. doi:10.1016/j.ijrmms.2023.105364

Ye, C. F., Xie, H. P., Wu, F., and Li, C. B. (2022). Nonlinear creep properties and time-to-failure prediction of sandstone under saturated and dry conditions. *Environ. Earth Sci.* 81, 545. doi:10.1007/s12665-022-10666-5

Ye, C. F., Xie, H. P., Wu, F., and Li, C. B. (2023). Study on the nonlinear time-dependent deformation characteristics and viscoelastic-plastic model of shale under direct shear loading path. *Bull. Eng. Geol. Environ.* 82 (5), 189. doi:10.1007/s10064-023-03170-y

Yuan, L., and Xue, S. (2014). Defining outburst-free zones in protective mining with seam gas content-method and application. *J. China Coal Soc.* 39 (09), 1786–1791. doi:10.13225/j.cnki.jccs.2014.8019

Zhang, B. C., Liang, Y. P., Zhao, Z. Y., Zou, Q. L., Zheng, H. L., Ning, Y. H., et al. (2023a). Effect of stress amplitude on mechanical and acoustic emission of sandstone under constant–cyclic loading. *Bull. Eng. Geol. Environ.* 82, 284. doi:10.1007/s10064-023-03307-z

Zhang, C. L., Wang, P. Z., Wang, E. Y., Chen, D. P., and Li, C. (2023b). Characteristics of coal resources in China and statistical analysis and preventive measures for coal mine accidents. *Int. J. Coal Sci. Technol.* 10 (1), 22. doi:10.1007/s40789-023-00582-9

Zhang, T. C., Zou, Q. L., Jia, X. Q., Jiang, C. Z., and Niu, X. G. (2022). Effect of SiO2 nanofluid with different concentrations on the wettability of coal. *Fuel* 321, 124041. doi:10.1016/j.fuel.2022.124041

Zhang, Y. J., Zou, Q. L., Yuan, H. M., Chen, Z. H., Cao, J. J., and Cheng, Z. H. (2023d). Outburst coal seam group joint ground and underground gas extraction mode and its key technology. *J. China Coal Soc*. doi:10.13225/j.cnki.jccs.S022.1663

Zhao, C., Cheng, Z. H., Liu, Y. Q., Chen, L., Wu, B., Zhang, J. G., et al. (2022). A mathematical model for optimization and decision-making of the optimal scheme for coordinated exploitation of coal and coalbed methane. *Geomechanics Geophys. Geo-Energy Geo-Resources* 8 (4), 120. doi:10.1007/s40948-022-00419-w

Zhao, J. J., Tian, S. X., Li, P., Xie, H. G., and Cai, J. J. (2023a). Molecular dynamics simulation and experimental research on the influence of SiO2-H2O nanofluids on wettability of low-rank coal. *Colloids Surfaces A Physicochem. Eng. Aspects* 679, 132580. doi:10.1016/j.colsurfa.2023.132580

Zhao, J. J., Tian, S. X., Xie, H. G., and Zhang, X. (2023b). Study of time-varying laws of stability and wettability of SiO2–H2O nanofluids with different particle sizes. *Industrial Eng. Chem. Res.* 62, 13529–13540. doi:10.1021/acs.iecr.3c02110

Zheng, J., Huang, G., Cheng, Q., Jia, J. K., and Cai, Z. H. (2022). A novel experimental apparatus for evaluating coal-and-gas outburst risk. *Nat. Resour. Res.* 31 (1), 535–550. doi:10.1007/s11053-021-09994-3

Zou, Q. L., Chen, Z. H., Cheng, Z. H., Liang, Y. P., Xu, W. J., Wen, P. R., et al. (2022). Evaluation and intelligent deployment of coal and coalbed methane coupling coordinated exploitation based on Bayesian network and cuckoo search. *Int. J. Min. Sci. Technol.* 32 (6), 1315–1328. doi:10.1016/j.ijmst.2022.11.002

Zou, Q. L., Huo, Z. X., Zhang, T. C., Jiang, C. Z., and Liang, J. Y. (2023a). Surface deposition characteristics of water-based SiO2 nanofluids on coal. *Fuel* 340, 127489. doi:10.1016/j.fuel.2023.127489

Zou, Q. L., Ning, Y. H., Zhang, B. C., Tian, S. X., Jiang, Z. B., and An, Y. Q. (2023b). Mechanical properties and failure characteristics of sandstone under ramp loading paths. *Geomechanics Geophys. Geo-Energy Geo-Resources* 9 (1), 39. doi:10.1007/s40948-023-00574-8

frontiers | Frontiers in Energy Research

TYPE Original Research
PUBLISHED 16 November 2023
DOI 10.3389/fenrg.2023.1283079

Check for updates

OPEN ACCESS

EDITED BY
Peng Tan,
CNPC Engineering Technology R&D Company Limited, China

REVIEWED BY
Li Qingmiao,
Chengdu University of Technology, China
Shixiang Tian,
Guizhou University, China

*CORRESPONDENCE
Zhiheng Cheng,
zh_cheng_2021@126.com
Chunyuan Li,
lcy6055@163.com

RECEIVED 25 August 2023
ACCEPTED 30 October 2023
PUBLISHED 16 November 2023

CITATION
Xuan Z, Cheng Z, Li C, Fan C, Qin H, Li W, Guo K, Chen H, Xie Y and Yang L (2023), Energy evolution mechanism during rockburst development in structures of surrounding rocks of deep rockburst-prone roadways in coal mines. *Front. Energy Res.* 11:1283079. doi: 10.3389/fenrg.2023.1283079

COPYRIGHT
© 2023 Xuan, Cheng, Li, Fan, Qin, Li, Guo, Chen, Xie and Yang. This is an open-access article distributed under the terms of the Creative Commons Attribution License (CC BY). The use, distribution or reproduction in other forums is permitted, provided the original author(s) and the copyright owner(s) are credited and that the original publication in this journal is cited, in accordance with accepted academic practice. No use, distribution or reproduction is permitted which does not comply with these terms.

Energy evolution mechanism during rockburst development in structures of surrounding rocks of deep rockburst-prone roadways in coal mines

Zhongtang Xuan[1,2,3], Zhiheng Cheng[4]*, Chunyuan Li[5]*, Chaojun Fan[6], Hongyan Qin[7], Wenchen Li[4], Kai Guo[8], Haoyi Chen[8], Yifei Xie[4] and Likai Yang[4]

[1]Chinese Institute of Coal Science, Beijing, China, [2]China University of Mining and Technology (Beijing), Beijing, China, [3]China Coal Research Institute, Beijing, China, [4]School of Mining Safety, North China Institute of Science and Technology, Beijing, China, [5]Deep Mining and Rockburst Prevention Institute, China Institute of Coal Science, Beijing, China, [6]College of Mining, Liaoning Technical University, Fuxin, China, [7]School of Safety Engineering, North China Institute of Science and Technology, Beijing, China, [8]School of Civil and Resource Engineering, University of Science and Technology Beijing, Beijing, China

Influenced by the deep high-stress environment, geological structures, and mining disturbance in coal mines, the frequency of rockburst disasters in roadways is increasing. This research analyzed energy evolution characteristics during rockburst development in the elastic bearing zone and energy conversion in the plastic failure zone. The critical energy criteria for structural instability of roadway surrounding rocks were deduced. Numerical software was also applied to simulate the energy evolution during rockburst development in surrounding rocks of rockburst-prone roadways under conditions of different mining depths and coal pillar widths. The occurrence mechanism of rockburst deep in coal mines was analyzed from the perspective of energy in structures of deep roadway surrounding rock in coal mines. The research results show that the critical energy criteria are closely related to the elastic strain energy stored in deep roadway surrounding rocks and the energy absorbed by support systems. The impact energy in roadways is directly proportional to the square of the stress concentration factor k. Moreover, as the mining depth increases, the location of the peak point of maximum energy density gradually shifts to coal ahead of the working face. The larger the mining depth is, the more significantly the energy density is influenced by advanced abutment pressure of the working face and the wider the affected area is. With the increment of the coal pillar width, the distance from the peak point of energy density to the roadway boundary enlarges abruptly at first and then slowly, and the critical coal pillar width for gentle change in the distance is 30 m. Changes in the peak elastic energy density in coal pillars with the coal pillar width can be divided into four stages: the slow increase stage, abrupt increase stage, abrupt decrease stage, and slow decrease stage. The elastic energy density is distributed asymmetrically in deep roadway surrounding rocks in coal mines. Under the action of structures of roadway surrounding rocks, energy evolution in these structures differs greatly during rockburst development

under conditions of different coal pillar widths. This research provides an important theoretical basis for the support of rockburst-prone roadways during deep coal mining.

KEYWORDS

energy evolution mechanism, rockburst, deep coal mines, rockburst-prone roadways, structures of surrounding rocks

1 Introduction

Coal is the main energy source that supports the economic development in China (Wu et al., 2022; Sun D. L. et al., 2023; Su et al., 2023). In the recent decade, the raw coal yield in China has always been high (Tan P. et al., 2023; Zhang et al., 2023a; Wu et al., 2023), with huge annual output (Tan et al., 2021; Zhang et al., 2022; Ran et al., 2023a). However, the shallow coal resources are gradually exhausted, and the number of deep coal mines grows by years with the increase in the mining intensity (Zou et al., 2022b; Huang et al., 2023a; Zhao et al., 2023a; Sun X. Y. et al., 2023). Some coal mines that are originally not prone to rockburst have turned into rockburst-prone mines. In such context, rockburst has become and will continue to be one of the main disasters that restrict safe and efficient mining in China (Pan et al., 2013; Jiang et al., 2018; Liang et al., 2023). According to statistics, damage caused by 87% of rockburst is found in roadways, and rockburst disasters in roadways have become increasingly severe and frequent. Hence, rockburst disasters in roadways have become one of the main challenges that hinder safe production of coal mines (Xu et al., 2021; Dai et al., 2022; He and Wang, 2023; Wang et al., 2023). Rockburst in roadways may cause not only serious economic loss and casualties but also extremely negative social impact (Gong et al., 2022; Wang et al., 2022; Liu et al., 2023). In addition, the frequent occurrence of rockburst disasters in roadways in the coal industry is incompatible with the theme for harmonious and stable development of the current society (Zou et al., 2022a; Huang et al., 2023b), which restricts the further development of the coal industry (Tan Y. L. et al., 2023; Zhao et al., 2023b; Zhang C. L. et al., 2023).

The mining disturbance is an important factor that induces rockburst in roadways (Li et al., 2020; Ye et al., 2022). Litwiniszyn (2009) regarded rockburst as a result of an impact wave released by gravity-induced fractures of strata overlying a chamber. Li et al. studied the mechanical properties of hard rocks under dynamic-static loading by carrying out laboratory dynamic-static loading tests and simulated the rockburst induction mechanism by dynamic disturbances under high stress (Lei et al., 2005; Li et al., 2013). Lu et al. (2008) explored the impact failure law of roadway surrounding rocks under stress waves through numerical simulation and described the sudden failure process of spalled thin layers during rockburst in roadways. Afterward, Lu et al. (2008) investigated the formation process of spalling structures in roadway surrounding rocks under influences of disturbing stress waves, spalling failure phenomena in roadways induced by stress waves, and energy criteria for impact failure of roadways. Zhang et al. (2017) divided the coal wall into shallow plastic coal and deep subelastic coal along the vertical direction. The shallow plastic coal confines the subelastic coal. If the coal–rock contact surface is smooth enough, it is favorable for reducing the rockburst risk; if the contact surface is rough, it increases the rockburst risk. Characteristics of two focuses (mining-induced roof fracture and fault slip) and their influences on roadway surrounding rocks were studied (Wei et al., 2010; Hu et al., 2013). Aiming at characteristics of rockburst near faults, Cai et al. (2014) put forward a fault-induced rockburst mechanism characterized by one mining disturbance, two loads, interaction of three objects, and four failure modes. By studying typical rockburst cases, Pan et al. (2012) analyzed the rockburst evolution process, revealed three evolution stages (rockburst start-up, energy transfer, and rockburst occurrence), and obtained the material–structure dynamic failure mechanism for rockburst start-up. Linkov (1996) considered rockburst as the failure caused by softening and flowing deformation of coal–rock mass, and mining causes the coal–coal boundary, spatial structures of coal–rock mass, stress state, and elastic energy distribution to all change with time (Ran et al., 2023b; Zhang et al., 2023b; Chen et al., 2023; Zou et al., 2023). Therefore, the occurrence of rockburst has close temporal and spatial relationships with mining and is a result of the joint action of multiple temporal and spatial parameters. By carrying out microseismic tests, Gao et al. (2007) studied the energy attenuation factor during propagation of shock waves in different media and explored the fracture and failure mechanism of composite roof based on fracture mechanics and elastic–plastic mechanics. On this basis, three conditions related to the bearing capacity, deformation, and energy for impact failure of roadways were deduced, and the evolution process of six cracks (one horizontal and five vertical ones) in the roadway roof during rockburst under dynamic impact loads was expounded (Gao et al., 2017). Zhao et al. (2003) considered that huge elastic energy is accumulated in coal under triaxial stresses. The energy consumed by the failure of coal–rock mass under triaxial stresses is far larger than the energy needed for failure under uniaxial stress (Li et al., 2023; Ye et al., 2023). Once damage initiates in the coal–rock mass under triaxial stresses, the stress state of coal–rock mass is rapidly adjusted from biaxial to uniaxial stress states (Ma et al., 2023). The energy consumed by failure in the uniaxial stress state is the minimum energy needed for the failure of coal–rock mass, and the residual energy is the main energy factor that induces rockburst.

In summary, scholars in China and abroad studied the occurrence mechanism of rockburst mainly based on coal–rock properties, force sources, and mining (Du et al., 2022; He et al., 2022; Huang et al., 2022; Lou et al., 2023). However, there is little research conducted on energy evolution during rockburst development in deep roadway surrounding rocks under high static elastic energy. There is a lack of critical energy criteria for structural instability of surrounding rocks of rockburst-prone roadways, and the existing mechanism for controlling rockburst in roadways is ambiguous. In

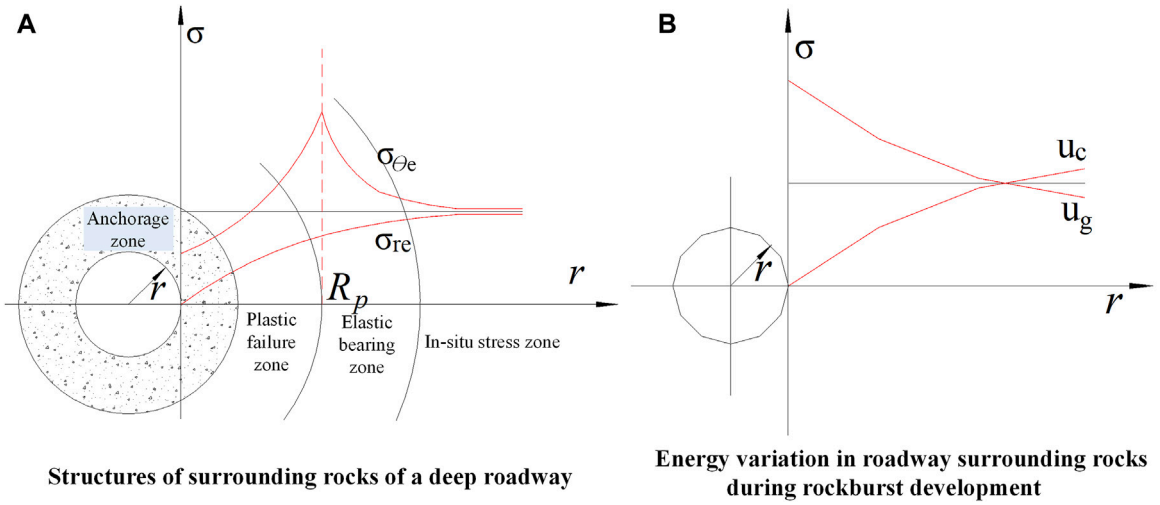


FIGURE 1
Structures and the energy evolution model of roadway surrounding rocks. **(A)** Structures of surrounding rocks of a deep roadway; **(B)** Energy variation in roadway surrounding rocks during rockburst development.

view of this, energy evolution during rockburst development in the elastic bearing zone and energy conversion characteristics in the plastic failure zone were studied based on the theory of elastic mechanics combining with structural characteristics of deep roadway surrounding rocks in coal mines. Influences of energy dissipation in coal–rock mass and support on the rockburst occurrence were analyzed combined with the state equation of rockburst. Based on the theory of rockburst start-up and the energy theory, critical energy criteria for structural instability of roadway surrounding rocks under static and dynamic loading were deduced. Using the FLAC^{3D} numerical simulation software, influences of the mining depth and coal pillar width on the elastic energy field in surrounding rocks of rockburst-prone roadways were revealed. Changes in the peak elastic energy density of roadway surrounding rocks and its peak point with the width of protective coal pillars in roadways and the asymmetric distribution of the elastic energy field in roadway surrounding rocks were analyzed. In this way, the occurrence mechanism of rockburst deep in coal mines was unveiled from the perspective of energy in structures of deep roadway surrounding rocks in coal mines.

2 Theoretical analysis of energy evolution in structures of deep roadway surrounding rocks during rockburst development

To analyze energy evolution in structures of deep roadway surrounding rocks during rockburst development, it is assumed that a roadway is located in a uniform stress field with the stress of σ0 before excavation; after excavation and support of the roadway, the surrounding rock structures are composed of four parts, namely, an anchorage zone, a plastic failure zone, an elastic bearing zone, and an *in situ* stress zone, as displayed in Figure 1.

2.1 Energy evolution during rockburst development in the elastic bearing zone

For the elastic bearing zone of the deep roadway, it is supposed that the minimum and maximum horizontal distances from the elastic bearing zone to the roadway boundary are separately R_p and l. The inner energy variation ΔU is solved directly using the elastic mechanics combined with the stress and displacement (Chen and Dou, 2008).

$$\Delta U = \frac{2\pi E}{1+\mu} R_p^2 u_{R_p} du_{R_p} \left(\frac{1}{R_p^2} - \frac{1}{l^2} \right), \tag{1}$$

where σ_{R0} and u_{Rp} represent the radial stress and displacement at the radius R_p of the plastic failure zone, respectively; μ and E denote the Poisson's ratio and elastic modulus of the roadway surrounding rocks, respectively.

According to Eq. 1, du_{Rp} is a linear function of dR_p. When dR_p = 0, the inner energy variation is 0 if the stress and support conditions of roadway surrounding rocks and the range of plastic failure zone remain unchanged; if $dRp > 0$, when changing the stress and support conditions of roadway surrounding rocks and enlarging the range of the plastic failure zone, the energy in the elastic bearing zone of roadway surrounding rocks begins to change. Therefore, energy is absorbed and accumulated in the elastic bearing zone when the coal–rock mass in the zone is affected by the mining disturbance.

Meanwhile, when not influenced by the mining disturbance, the roadway surrounding rocks in the elastic bearing zone are always stable and such state remains unchanged. That is, no energy is dissipated. Whereas, energy release from roadway surrounding rocks is a result of fracture propagation in the elastic bearing zone of surrounding rocks and accumulation of plastic deformation to a certain degree. Therefore, energy in the elastic bearing zone of roadway surrounding rocks can only change unidirectionally under external loads, that is, be absorbed. The following two energy-absorbing modes are mainly involved:

(1) When the roadway surrounding rocks are disturbed by mining, energy is absorbed and accumulated in the coal–rock mass in the elastic bearing zone, which serves as the propagation media of the external disturbance energy to transfer and release energy to shallow roadway sidewalls.
(2) With the enlarging radius of the plastic failure zone, the constraint changes for some coal–rock mass at the interface between the elastic bearing zone and plastic failure zone. The high tangential stress on the boundary is adjusted rapidly, and the energy accumulated in the elastic bearing zone is released instantaneously. This causes the energy released during roadway excavation to transfer to the deep space in the roadway and further induces energy accumulation in the coal–rock mass in the elastic bearing zone.

Similarly, when energy is released by the coal–rock mass in the *in situ* stress zone under the mining disturbance, coal–rock mass therein and in the elastic bearing zone both serve as the propagation media of external energy toward shallow roadway sidewalls and, thus, play a role in energy transfer.

2.2 Energy conversion characteristics in the plastic failure zone

Supposing that the roadway surrounding rocks are homogeneous, the elastic strain energy U_e accumulated in unit volume of coal–rock mass before excavation is calculated as follows:

$$U_e = \frac{3\sigma_0^2(1-2\mu)}{2E}. \tag{2}$$

After excavation, energy is accumulated in the shallow part of the roadway, where structures of the surrounding rocks are changed. Under the condition, the elastic strain energy U_P in unit volume of coal–rock mass in the plastic failure zone is calculated as follows:

$$U_P = \frac{\sigma_0^2\left[3(1-2\mu)+\frac{2(1+\mu)a^4}{r^4}\right]}{2E}, \tag{3}$$

where a is the roadway radius; r is the radius of the *in situ* stress zone of roadway surrounding rocks.

A comparison of Eqs. (2) and (3) shows that $U_P > U_e$. According to the triaxial compression tests, certain strain energy can be stored in coal–rock mass under the confining pressure (Liang et al., 2022). As the confining pressure increases, the ultimate strain energy U_P stored in the coal–rock mass ramps up; if the confining pressure is left unchanged, the harder or more intact the coal–rock mass is or the fewer the joints and fractures are in coal–rock mass, the higher the U_P. In the meantime, after excavating the roadway, the confining pressure is low in shallow surrounding rocks and is 0 around the roadway, and the ultimate strain energy stored in the fractured zone is low. As a result, the elastic strain energy that should be accumulated around the roadway is transferred to the deep coal–rock mass. With the growing distance from the roadway boundary, the elastic deformation energy stored in the deep coal–rock mass of the roadway gradually recovers to that before excavation again (elastic strain energy U_e). The energy release and transfer characteristics in roadway surrounding rocks during rockburst development are shown in Figure 1B.

In the near field of the roadway, mining induces redistribution of stress and energy in the rocks and causes energy transfer to the deep part, where coal–rock mass is plastically deformed. The stress state changes from triaxial to biaxial and even uniaxial one. According to the minimum energy principle, the energy needed for failure under uniaxial stress is far lower than that needed for failure under triaxial stresses. Therefore, the ultimate strain energy U_P declines abruptly. If the energy accumulated in the roadway surrounding rocks exceeds the energy dissipation U_k to overcome the failure, there is residual energy. Part of the residual energy is converted into kinetic energy for ejecting coal–rock mass, which can be further absorbed by the support or form kinetic energy; the other is converted into other dissipated energies such as acoustic energy and thermal energy. Assuming that the total energy input by the work done by external forces is U, its value is the deformation energy accumulated in all rock units in the rock system under triaxial stresses. Because other dissipated energies including acoustic energy are relatively low, if they are ignored, the state equation of rockburst of coal–rock mass is expressed as follows:

$$U = \frac{1}{2}mv^2 + U_k + U_c, \tag{4}$$

where m is the mass of the ejected coal–rock mass, v is the initial impact velocity of coal–rock mass, and U_c is the energy absorbed by the support.

According to Eqs. (3) and (4), the greater the energy accumulated in coal–rock mass after roadway excavation is, the higher the rockburst proneness will be. Enhancing the energy dissipation U_k of roadway surrounding rocks themselves and increasing the absorbed energy U_c of the support to some extent can limit the impact and ejection velocity of coal–rock mass, thus inhibiting the occurrence of rockburst.

Meanwhile, the energy in the elastic bearing zone and plastic failure zone of roadway surrounding rocks does not change in a certain time period after excavation, while it is affected by the disturbance of the external energy field. It is mainly shown as tremors induced by fracture of hard roofs and shear dislocation of faults, which disturb the near-field coal–rock mass in the roadway. The disturbances to structures of roadway surrounding rocks mainly include energy transfer, damage by stress waves, and weakening of support.

(1) Energy transfer: Energy is transferred outward from the focus to the surrounding area of the roadway. Under the effect of the transfer media, the energy is attenuated, and some energy is absorbed by the transfer media. Because the near-field structures of the roadway exert a small attenuation effect on the external disturbance energy, the energy is still high after attenuation. Rockburst may occur if Eq. 4 is satisfied.
(2) Damage by stress waves: Because external energy is applied to roadway surrounding rocks as compressed loading waves, which form reflected unloading waves in the pre-existing and secondary fractures in coal–rock mass and on the surface of roadway surrounding rocks, the reflected unloading waves are interacted with the compressed wave tail and reflected to form tensile stress waves. If the dynamic tensile–shear fracture criterion is met, fracture development is promoted so that the plastic zone of roadway surrounding rocks expands

abruptly, thus causing facture and ejection of coal–rock mass on the roadway surface to trigger rockburst.

(3) Weakening of support: Due to the interaction between support and surrounding rocks, disturbances of impact stress waves may result in fracture propagation in the structures of surrounding rocks. If the impact load is too large, the support fails when it absorbs energy that exceeds the allowable energy of deformation, thus failing to play its role in stably supporting the structures of roadway surrounding rocks. This triggers deep energy release and, therefore, rockburst disasters in the roadway.

2.3 Critical energy criteria for structural instability of roadway surrounding rocks

According to characteristics of energy sources that trigger rockburst in roadways, such rockburst can be divided into three types: the static load-type, dynamic load-type, and dynamic load-induced ones (Pan et al., 2012). Energy that causes static load-type rockburst in roadways sources from the static elastic energy stored in the elastic zone of roadway surrounding rocks during or after roadway excavation. For dynamic load-type rockburst in roadways, the elastic energy stored in the elastic zone of roadway surrounding rocks can be ignored, and the main energy source is the mining-induced external disturbance energy, which is non-steady and high. Part of energy causing dynamic load-induced rockburst in roadways sources from the elastic energy in the elastic zone of roadway surrounding rocks, and the other is the external disturbance energy. The two act together to induce rockburst in roadways. Under the condition, the dynamic energy is probably low and only functions as the starting condition for rockburst.

2.3.1 Critical energy characteristics in structures of roadway surrounding rocks under static loading

According to the theory of rockburst start-up, rockburst is composed of three stages, namely, rockburst start-up, energy transfer, and rockburst occurrence. The development of static elastic deformation energy is a necessary condition for the rockburst start-up stage. The energy density at any point in deep roadway surrounding rocks has a square relationship with the stress.

The occurrence of rockburst is a dynamic failure process, in which energy conversion follows the minimum energy principle for dynamic failure of rocks. That is to say, once damage initiates in rocks, the stress state of rocks changes rapidly from the triaxial to biaxial and finally uniaxial stress state. The failure criterion follows the uniaxial compression or shear failure criterion (Zou and Jiang, 2004):

(1) The failure criterion under uniaxial compression is $\sigma > \sigma_c$, and the energy consumption is $u_1 > \sigma_c^2/2E$, in which σ_c is the uniaxial compressive strength of rocks

(2) The failure criterion under uniaxial shear is $\tau > \tau_c$, and the energy consumption is $u_1 > \tau_c^2/2G$, in which τ_c and G are the shear strength and shear modulus of rocks, respectively

After rockburst start-up in the coal–rock mass, if energy release U_0 in the rockburst start-up zone is larger than energy consumption U' in the energy transfer and rockburst occurrence stages, then rockburst occurs, that is,

$$U_0\text{-}U' > 0. \tag{5}$$

The energy consumption in the energy transfer and rockburst occurrence stages mainly includes the energy for damaging coal–rock mass in the energy transfer process, refraction of stress waves, energy consumed by reflection, and energy absorbed by the support, that is,

$$U_0 = (u\text{-}u_1)V_0, U' = u_c V' + U'', V' = R_0 S, \tag{6}$$

where U_0 is the energy release in the rockburst start-up zone; U' is the energy consumption in the energy transfer process; u_1 is the energy density consumed in the rockburst start-up zone after start-up; V_0 is the volume of coal–rock mass that releases energy in the rockburst start-up zone; u_c is the average energy-dissipating capacity of coal–rock mass in the energy transfer process of rockburst; V' is the volume of coal–rock mass involved in energy dissipation in the energy transfer process of rockburst; U'' is the energy absorbed by the support system; R_0 is the distance from the rockburst start-up zone to the rockburst occurrence zone; and S is the average cross-sectional area of coal–rock mass involved in the energy transfer process of rockburst.

Therefore, under the joint action of the elastic strain energy stored in deep roadway surrounding rocks, energy release in the rockburst start-up zone, and energy in the energy transfer and consumption stages, the critical energy criterion for structural instability of structures of roadway surrounding rocks under static loading is given as follows:

$$\left\{\frac{k^2}{2E}\left[1 + {\lambda_x}^2 + {\lambda_y}^2 - 2\mu\left(\lambda_x + \lambda_y + \lambda_y\lambda_x\right)\right]\gamma^2 z^2 - \sigma_c^2\right\}V_0 - u_c R_0 S - U'' > 0. \tag{7}$$

If Eq. 7 is established, static load-type rockburst will occur in roadways.

The criterion was verified by an example. Rockburst occurred at 13 p.m. on 21 August 2008 when mining the lower roadway in the 21141 working face to 660 m in Qianqiu Coal Mine (Henan Province), and the damage range was 560–650 m to the opening of the roadway. The rockburst is a typical example of static load-type rockburst in roadways. When mining the lower roadway to 660 m, the stress concentration factor was large, and the static elastic energy was extremely high in the area due to tectonic influences. As the tunneling head advanced, the distance R0 from the mining space to the elastic zone with high static loads shortens, thus reaching the energy condition for occurrence of rockburst, which verifies the correctness of the criterion in Eq. 7.

According to Eqs. (3) and (7), rockburst in roadways can be prevented from three aspects when the burial depth of roadways and properties of coal–rock mass cannot be changed. The first is to reduce the stress concentration factor k. Because the impact energy is directly proportional to the square of the stress concentration factor k, reducing k can effectively decrease the impact energy. The second is to enlarge the distance from the rockburst start-up zone to the rockburst occurrence zone by taking artificial control measures. The third is to enhance the energy-absorbing capacity of the support, that is, improving U''.

2.3.2 Critical energy characteristics of structures of roadway surrounding rocks under dynamic loading

The energy sources for rockburst in roadways under dynamic loading include the elastic energy in the elastic zone of roadway surrounding rocks and the external disturbance energy. The two act together to trigger rockburst in roadways. After excavating a roadway, the stable static elastic deformation energy U_0 has been stored in the surrounding rocks, which, however, cannot meet the energy condition for rockburst start-up. With the advance of the working face, the disturbance energy $U_{\mathrm{d}}{}^0$ released at the moment of fracture of hard roof or fault slip and disturbance energy U_{d} transferred to the area with relatively stable and high elastic deformation energy density are superimposed with the relatively stable static elastic energy. As a result, the area becomes the rockburst start-up zone in the first stage of rockburst. The energy criterion for rockburst is expressed as follows:

$$U_0 + U_{\mathrm{d}}\text{-}U' > 0. \tag{8}$$

When the disturbance energy U_d^0 is transferred to the roadway surrounding rocks, the residual disturbance energy U_d is expressed as follows:

$$U_{\mathrm{d}} = \left(U_{\mathrm{d}}^0 \cdot d\right)^{-n}. \tag{9}$$

Combining with Eqs. (3) and (7), the critical energy criterion for structural instability of roadway surrounding rocks under dynamic loading is given as follows:

$$\left\{\frac{k^2}{2E}\left[1 + {\lambda_x}^2 + {\lambda_y}^2 - 2\mu\left(\lambda_x + \lambda_y + \lambda_y\lambda_x\right)\right]\gamma^2 z^2 - \sigma_{\mathrm{c}}^2\right\} V_0 + U_d^0 d^{-\eta} - u_c R_0 S - U'' > 0, \tag{10}$$

where d is the distance from the dynamic focus to the rockburst start-up zone and η is the disturbance energy attenuation factor.

If Eq. 10 is established, the dynamic load-type or dynamic load-induced rockburst will occur. The rockburst that occurred on 8 April 2018 in Menkeqing Coal Mine (the Inner Mongolia Autonomous Region) and on 9 June 2019 in Longjiabao Coal Mine (Jilin Province) both belong to dynamic load-induced rockburst.

3 Energy evolution in surrounding rocks of rockburst-prone roadways at different mining depths during rockburst development

In accordance with engineering and geological conditions of Menkeqing Coal Mine, FLAC^{3D} numerical simulation software was adopted to simulate energy evolution in surrounding rocks of rockburst-prone roadways at different mining depths during rockburst development. Considering the calculation accuracy and speed, the model with dimensions of 800 m × 800 m × 240 m (width × length × height) contained 1,394,200 grids and 1,522,018 nodes. The cross-sectional area of the driving roadway was 6.0 m × 5.0 m (width × height). The roadway was located in the center of the model. In static calculation, the displacements of left and right boundaries were fixed; the bottom was a boundary with fixed displacement, while uniform stress was applied onto the upper free boundary, on which loads of overlying strata were applied to simulate the elastic energy evolution at five mining depths, namely, 400, 600, 800, 1,000, and 1,200 m.

The Mohr–Coulomb model was used as the constitutive model. The mechanical parameters of coal–rock mass were converted from laboratory mechanical parameters of rocks. The elastic modulus, cohesion, and tensile strength were one-fifth to one-third of the laboratory test values, while Poisson's ratio is 1.2–1.4 times of the blocks. The physical and mechanical parameters used in the numerical simulation are listed in Table 1.

According to the aforementioned theoretical analysis and Eq. 12, the built-in FISH language of FLAC^{3D} was adopted to calculate the elastic deformation energy of elements.

If the principal stress is used to represent the principal strain and supposing that the coal–rock mass follows the generalized Hooke law, each principal stress in any element of coal–rock mass has the following relationship with the principal strain:

$$\begin{aligned}\varepsilon_1 &= \frac{1}{E}\left[\sigma_1 - \mu\left(\sigma_2 + \sigma_3\right)\right], \varepsilon_2 = \frac{1}{E}\left[\sigma_2 - \mu\left(\sigma_1 + \sigma_3\right)\right],\\ \varepsilon_3 &= \frac{1}{E}\left[\sigma_3 - \mu\left(\sigma_2 + \sigma_1\right)\right],\end{aligned} \tag{11}$$

where σ_1, σ_2, and σ_3 represent three principal stresses in the x-, y-, and z-direction, respectively; ε_1, ε_1, and ε_3 are strains corresponding to the three principal stresses, respectively; then,

$$u = \frac{\left[\sigma_1^2 + \sigma_2^2 + \sigma_3^2 - 2\mu\left(\sigma_1\sigma_2 + \sigma_1\sigma_3 + \sigma_3\sigma_2\right)\right]}{2E}. \tag{12}$$

To unveil influences of the mining depth on energy evolution in surrounding rocks of rockburst-prone roadways during rockburst development, the 3102 working face in Menkeqing Coal Mine was simulated. One side of the roadway in the working face was gob, and the width of the protective coal pillar was 30 m. The mining layout is displayed in Figure 2.

The post-processing software Tecplot was utilized to extract the strain energy density in roadway surrounding rocks. Combining with surfer software, cloud pictures for energy distribution and 3D cloud pictures for energy were drawn, as shown in Figure 3 and Figure 4, respectively.

Analysis of Figure 3 shows that as the mining depth increases, the energy density grows in the same zone of surrounding rocks. When the protective coal pillar is 30 m wide, the zone with large energy density is located in the roadway, and energy density is high in the retained coal pillar in the gob within a region 100 m behind the working face. The maximum energy density in entity coal in the working face is found at the end of the gob side near the 3101 working face. When the burial depth is 400 m, the maximum energy density is 280 kJ/m^3 in retained coal pillar in the gob within the region 100 m behind the gob, while it increases to 700, 1,500, 2,600, and 4,200 kJ/m^3 when the mining depths are 600, 800, 1,000, and 1,200 m, respectively. This indicates that as the burial depth of the roadway increases, the maximum energy density increases significantly and shows larger difference. Meanwhile, the energy density is only 190 kJ/m^3 in the region with the maximum energy density in surrounding rocks in the entity coal side of the working face at the burial depth of 400 m, while it grows to 500, 1,050, 1,900, and 2,800 kJ/m^3 when the mining depths are 600, 800, 1,000, and 1,200 m, respectively. Likewise, the deeper the

TABLE 1 Physical and mechanical properties used in numerical simulation.

Strata	Thickness/m	Density/kg.m^{-3}	Bulk modulus/GPa	Shear modulus/GPa	Poisson's ratio	Internal friction angle/°	Cohesion/MPa	Tensile strength/MPa
Silty mudstone	8	2,495	1.84	0.95	0.28	36	3.4	1.0
Sandy mudstone	8	2,430	1.15	0.47	0.32	36	3.0	0.8
Siltstone	7	2,495	1.84	0.95	0.28	36	3.4	1.0
Sandy mudstone	5	2,430	1.15	0.47	0.32	36	3.0	0.8
Siltstone	4	2,495	1.84	0.95	0.28	36	3.4	1.0
Sandy mudstone	5	2,430	1.15	0.47	0.32	36	3.0	0.8
Medium-grained sandstone	3	2,333	3.30	1.88	0.26	38	4.8	1.5
Siltstone	6	2,495	1.84	0.95	0.28	36	3.4	1.0
Sandy mudstone	5	2,430	1.15	0.47	0.32	36	3.0	0.8
Medium-grained sandstone	62.5	2,333	3.30	1.88	0.26	38	4.8	1.5
Siltstone	2	2,495	1.84	0.95	0.28	36	3.4	1.0
Sandy mudstone	5	2,430	1.15	0.47	0.32	36	3.0	0.8
Fine-grained sandstone	2	2,419	3.02	1.23	0.32	37	4.2	1.1
Siltstone	3	2,495	1.84	0.95	0.28	36	3.4	1.0
Fine-grained sandstone	18.5	2,419	3.02	1.23	0.32	37	4.2	1.1
Siltstone	4	2,495	1.84	0.95	0.28	36	3.4	1.0
3-1 coal	5	1,325	1.00	0.3	0.32	32	2.6	0.6
Sandy mudstone	10	2,430	1.84	0.95	0.28	36	3.4	1.0
Fine-grained sandstone	10	2,419	3.02	1.23	0.32	37	4.2	1.1

burial depth of the roadway is, the greater the difference in the maximum energy density will be. However, compared with energy density in the coal pillar, that in roadway surrounding rocks in the entity coal side of the working face is relatively small. Therefore, rockburst is likely to be triggered in the coal pillar in the deep gob-side roadway behind the stope, so retaining of coal pillars should be avoided during mining of the working face or pressure-relief measures should be taken to control energy accumulation in the coal pillar.

According to Figure 4, when retaining a protective coal pillar with the width of 30 m, the energy density is maximum in the coal pillar, and the larger the burial depth is, the more concentrated the energy accumulation will be. Figure 3 shows that the elastic energy density in the coal pillar is larger than that in the entity coal side of working face, and the elastic energy density in the coal pillar behind the working face is greater than that in the coal pillar ahead of the working face. The energy density is high in the retained coal pillar in the gob in the region 100 m behind the working face. The maximum elastic energy density in entity coal in the working face is found at the lower end of the working face, while it is lower than that in the coal pillar in the same region. Ahead of the working face, the elastic energy density gradually recovers to that in the *in situ* state beyond the range of advanced abutment pressure.

The energy density is high in the retained coal pillar in the region 100 m behind the stope, so rockburst is likely to occur in the region. However, even if rockburst occurs, it only slightly influences the safe production, so rockburst in the region is not discussed. When retaining a coal pillar of 30 m width, the energy density is high in the protective coal pillar in the range 50 m behind and 50 m ahead

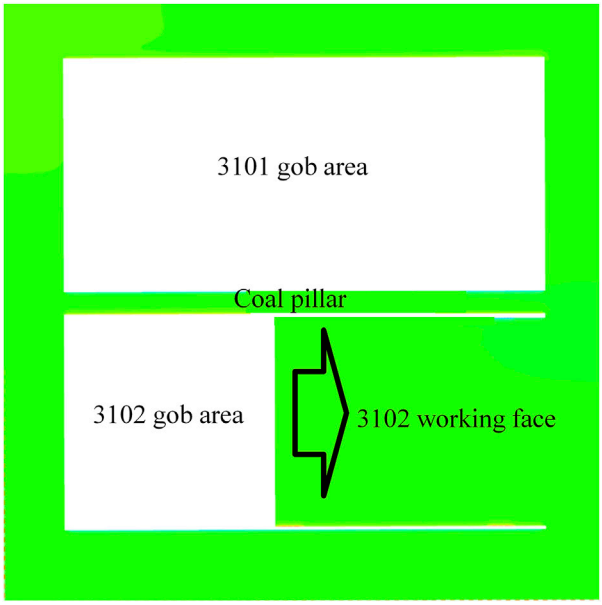


FIGURE 2
Schematic diagram of the simulated mining layout.

of the working face, so the region is most likely to experience rockburst according to the aforementioned analysis. For the protective coal pillar behind the working face, it can be damaged artificially to lose its bearing capacity so that elastic deformation energy cannot be stored therein. As a result, the energy cannot reach the condition for the occurrence of rockburst, which prevents the occurrence of rockburst. For the protective coal pillar ahead of the working face, its energy density is higher than that in the entity coal. The energy is distributed asymmetrically in roadway surrounding rocks, and the energy density is high in roadway surrounding rocks within the affected area of advanced abutment pressure, which gradually reduces to the value under conditions not being affected by the advanced abutment pressure. Therefore, the support technologies controlling structural stability of roadway surrounding rocks can be adopted according to energy characteristics in structures of surrounding rocks.

Additionally, the energy density in coal–rock mass ahead of the working face at different burial depths was extracted, and the changes are shown in Figure 5.

Analysis of Figure 5 shows that as the mining depth grows, the peak point of maximum energy density tends to shift to the coal ahead of the working face. As the mining depth varies from 400 m to 1,200 m, the peak point of maximum energy density gradually shifts inward from a position 5 m from the edge of the working face to a position 14 m from the working face. With the increase in burial depth, the energy density is more greatly influenced by the advanced abutment pressure of the working face, and the affected area is wider. With the increment in the mining depth, the maximum energy density in the affected area of advanced abutment pressure of the working face grows significantly. According to the critical energy criteria for structural instability of roadway surrounding rocks, the larger the mining depth is, the higher the proneness of coal–rock mass ahead of the working face to rockburst will be. This explains why the rockburst occurs more frequently with the increase in mining depth from the perspective of energy.

4 Energy evolution in surrounding rocks of rockburst-prone roadways during rockburst development under different coal pillar widths

To further study influences of the coal pillar width on energy evolution in surrounding rocks of rockburst-prone roadways during rockburst development, a roadway prototype with the gob in one side and the burial depth of 600 m in Menkeqing Coal Mine was taken as the background. Eight conditions with different widths of the protective coal pillar (4, 6, 8, 10, 15, 20, 30, and 60 m) were simulated, and the elastic energy density in roadway surrounding rocks was extracted and analyzed. According to Section 3, the rockburst is most likely to occur within and behind the affected area of advanced abutment pressure of the working face in the gob side. At the burial depth of 600 m, the peak point of elastic energy density in the entity coal in the working face is found at the position 10 m ahead of the working face. Therefore, the section mainly explores the distribution of elastic energy density in roadway surrounding rocks in the region 10 m ahead of the working face near the coal pillar side under different coal pillar widths.

The elastic energy density fields in roadway surrounding rocks under conditions of different widths of the protective coal pillar were extracted, as displayed in Figure 6. In the figure, positive values on the abscissa indicate the distance from the mining side of the roadway to a point inside entity coal in the working face, and the absolute values of negative values represent the distance from the coal pillar side to a point inside the coal pillar. This description is applied to similar cases below and not repeated.

Analysis of Figure 6 unveils that at the burial depth of 600 m, the peak elastic deformation energy density increases at first and then decreases with the increase in the width of the protective coal pillar. The energy density in the coal pillar gradually changes from one peak point to two, and the peak elastic energy density in the entity coal declines with the increase in coal pillar width.

To further clearly show changes in the elastic energy density field in roadway surrounding rocks under different widths of the protective coal pillar, change curves of energy under various coal pillar widths were obtained through pairwise comparison, as illustrated in Figure 7.

It is clearly seen from Figure 7A that when the protective coal pillar is 4 m wide, the peak elastic energy density in the coal pillar is very small (0.15×10^5 J/m^3), while that in the entity coal is 6.7×10^5 J/m^3. The peak point of elastic energy density in the entity coal is 9.5 m from the mining side of the roadway. When the width of the protective coal pillar is 6 m, the peak elastic energy densities in the coal pillar and entity coal are 0.32×10^5 and 6.3×10^5 J/m^3, respectively. Additionally, the peak point of elastic energy density in the entity coal is 10 m from the mining side of the roadway.

As displayed in Figure 7B, when the protective coal pillar is 8 m wide, the peak elastic energy densities in the coal pillar and entity coal are, respectively, 1.8×10^5 and 5.9×10^5 J/m^3, and the peak point is 10.5 m from the mining side of the roadway. If the protective coal pillar is 10 m wide, the peak elastic energy densities in the coal pillar

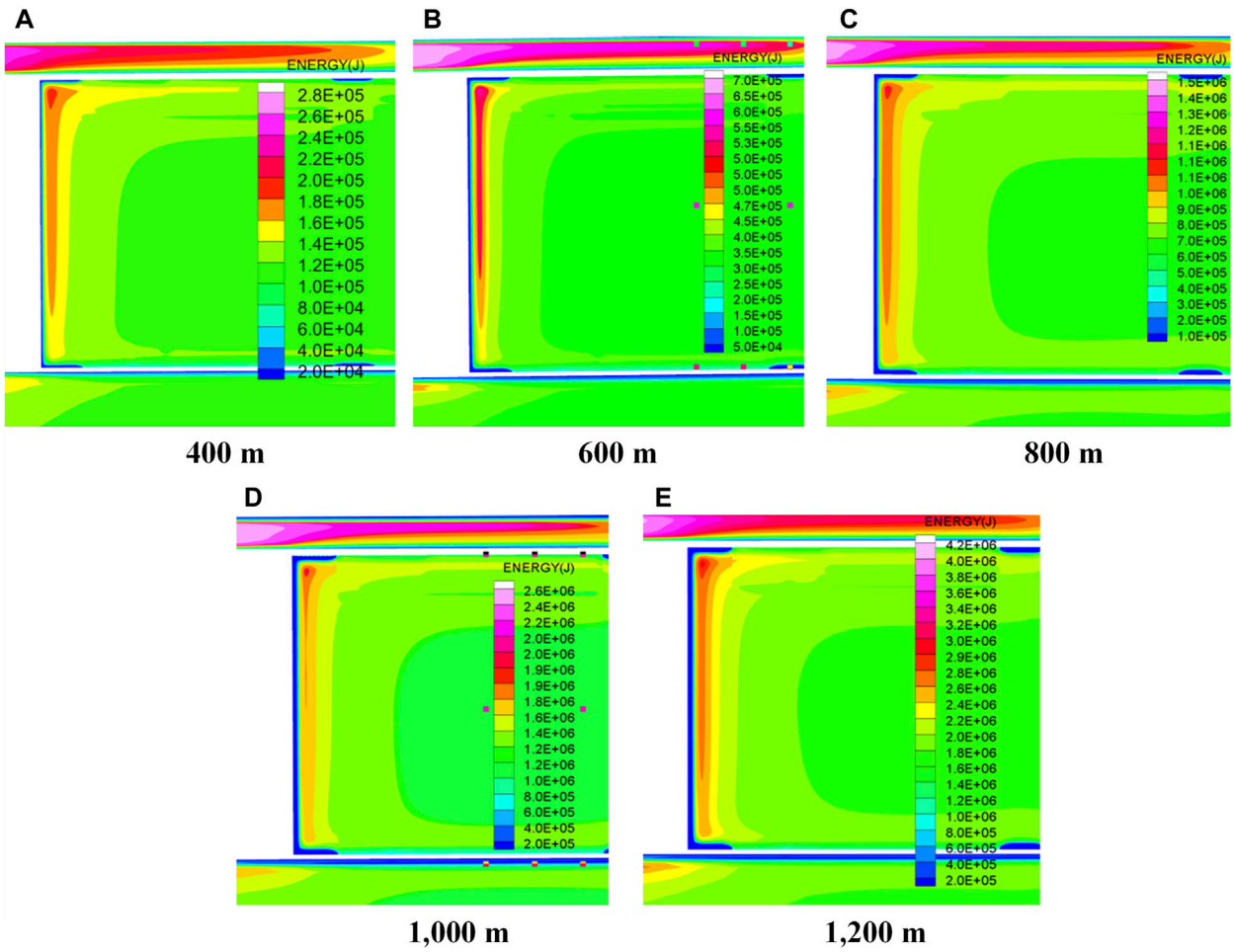


FIGURE 3
Cloud pictures for energy distribution in roadway surrounding rocks at different mining depths. **(A)** 400 m; **(B)** 600 m; **(C)** 800 m; **(D)** 1,000 m; **(E)** 1,200 m.

and entity coal are, respectively, 5.76×10^5 and 5.3×10^5 J/m^3, and the peak point of elastic energy density in the entity coal is 11 m from the mining side of the roadway.

According to Figure 7C, the peak elastic energy densities in the coal pillar and entity coal are, respectively, 7.1×10^5 and 5.14×10^5 J/m^3, and the peak point of elastic energy density in the entity coal is 12 m from the mining side of the roadway, when the protective coal pillar is 15 m wide. If the protective coal pillar is 20 m wide, the peak elastic energy densities in the coal pillar and entity coal are 6.0×10^5 and 4.7×10^5 J/m^3, respectively, and the peak point of elastic energy density in the entity coal is 12.5 m from the mining side.

It can be seen from Figure 7D that when the width of the protective coal pillar is 30 m, the peak elastic energy densities in the coal pillar and entity coal are 5.1×10^5 and 4.3×10^5 J/m^3, respectively, with the peak point of elastic energy density in the entity coal found at a position 13.5 m from the mining side of the roadway. When the protective coal pillar is 60 m wide, the elastic energy density in the coal pillar has two peaks: the one near the roadway side is small (3.77×10^5 J/m^3), while that near the gob side is large (4.40×10^5 J/m^3). The peak elastic energy density in the entity coal is 3.9×10^5 J/m^3, and its peak point is 15.5 m from the mining side.

As shown in Figure 6 and Figure 7, the energy field is asymmetrically distributed in roadway surrounding rocks, and its value and location of peak point are strongly correlated with the coal pillar width. On the whole, the wider the protective coal pillar, the lower the peak energy in the entity coal and the deeper the peak point shifts to the coal, which is more conducive to preventing rockburst. However, retaining a wide coal pillar may waste coal resources; if retaining a protective coal pillar narrower than 8 m, the elastic energy density is low in the coal pillar, while that is high in the entity coal. The peak energy density in the entity coal side of the roadway can be reduced by taking artificial control measures including drilling large-diameter boreholes for pressure relief and softening coal by water injection.

The peak points of elastic energy density and peak energy characteristics in the entity coal under different coal pillar widths are summarized in Figure 8.

As shown in Figure 8A, as the width of the protective coal pillar enlarges, the distance from the peak point of energy density to the roadway boundary enlarges abruptly at first and then slowly, with the critical coal pillar width for gentle change in the distance being 30 m. When the coal pillar width is 4 m, the peak point of elastic

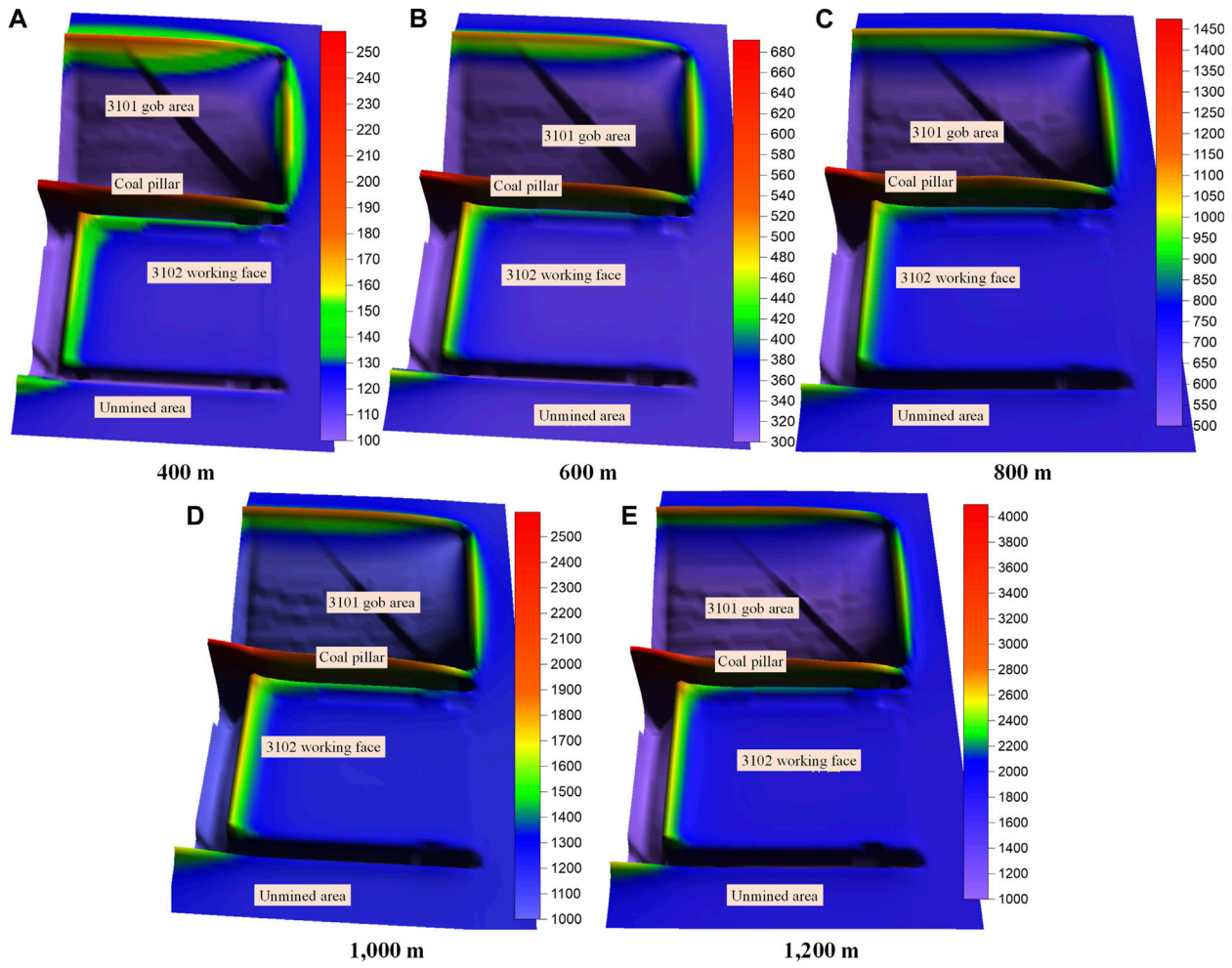


FIGURE 4
3D images for energy evolution in roadway surrounding rocks at different depths. **(A)** 400 m; **(B)** 600 m; **(C)** 800 m; **(D)** 1,000 m; **(E)** 1,200 m.

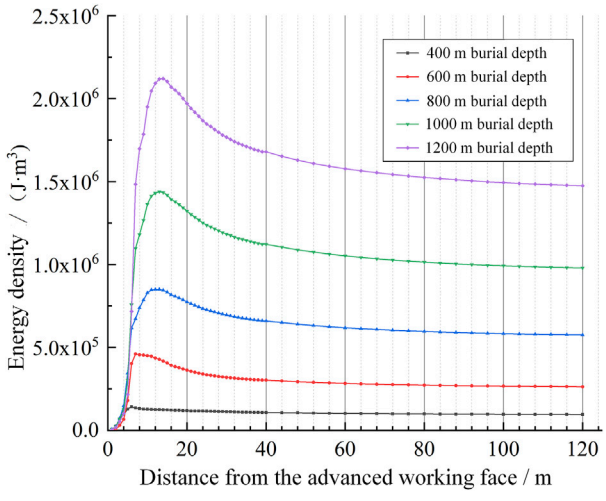


FIGURE 5
Inner elastic energy and density change curves of coal–rock mass ahead of the working face at different depths.

energy density in the entity coal is 9.5 m from the mining side of the roadway. As the width gradually enlarges to 60 m, the peak point gradually shifts to the position 15.5 m from the mining side. The change trend indicates that when the coal pillar width is smaller than 15 m, changes in the width significantly affect the location of peak point of elastic energy density in the entity coal, while the influence becomes gentle when the width is larger than 15 m.

Figure 8B depicts that when the width of the protective coal pillar is 4 m, the peak elastic energy density in the entity coal is 6.6×10^5 J/m^3, while it gradually declines to 3.90×10^5 J/m^3 when the width is 60 m. The change trend can be roughly divided into two stages: when the coal pillar width is smaller than 20 m, the peak energy density declines abruptly with the widening of the protective coal pillar; when the width is in the range of 20–60 m, reduction of the peak energy density flattens. It is predictable that the peak elastic energy density in the coal pillar will approximate to a value when the width of the protective coal pillar reaches a certain value.

In the meantime, changes in the elastic energy density in the coal pillar under conditions of different coal pillar widths were extracted, as displayed in Figure 9. It is evident that changes in the peak elastic energy density in the coal pillar with the coal pillar width can be roughly

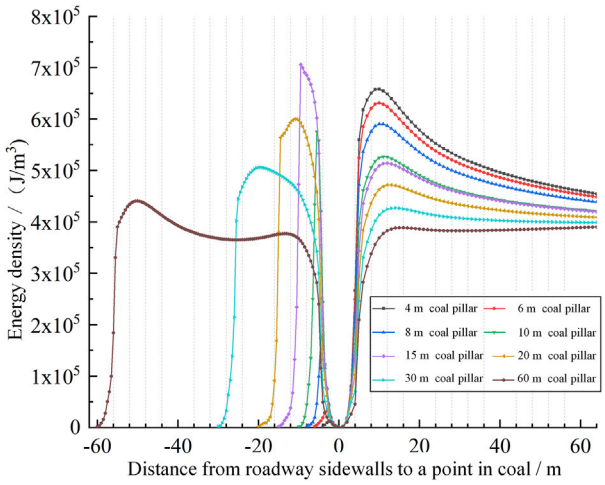


FIGURE 6
Variation law of elastic energy density fields in roadway surrounding rocks with different widths of protective coal pillar.

divided into four stages. The first is the slow increase stage of energy density: when the protective coal pillar is 4–6 m wide, the peak elastic energy density in the coal pillar increases slowly from the minimum (0.15×10^5 J/m^3) to 0.32×10^5 J/m^3. The second is the abrupt increase stage of energy density: when the width of the protective coal pillar is in the range of 6–13 m, the peak elastic energy density in the coal pillar grows abruptly from 0.32×10^5 to 7.70×10^5 J/m^3. The third is the abrupt decrease stage of energy density: when the coal pillar width is in the range of 13–20 m, the peak elastic energy density in the coal pillar reduces abruptly to 6.0×10^5 J/m^3. The fourth is the slow decrease stage of energy density: when the coal pillar width is larger than 20 m, the peak elastic energy density in the coal pillar declines slowly with the increase in width. It is predictable that the peak elastic energy density in the coal pillar may approximate to a value when the width of the protective coal pillar reaches a certain value.

Meanwhile, changes in the peak energy density in deep roadway surrounding rocks with the coal pillar width are summarized in Table 2.

As displayed in Table 2, the peak energy density in the entity coal gradually reduces from 6.6×10^5 to 3.9×10^5 J/m^3, and the distance from the peak point to the roadway boundary increases from 9.5 to

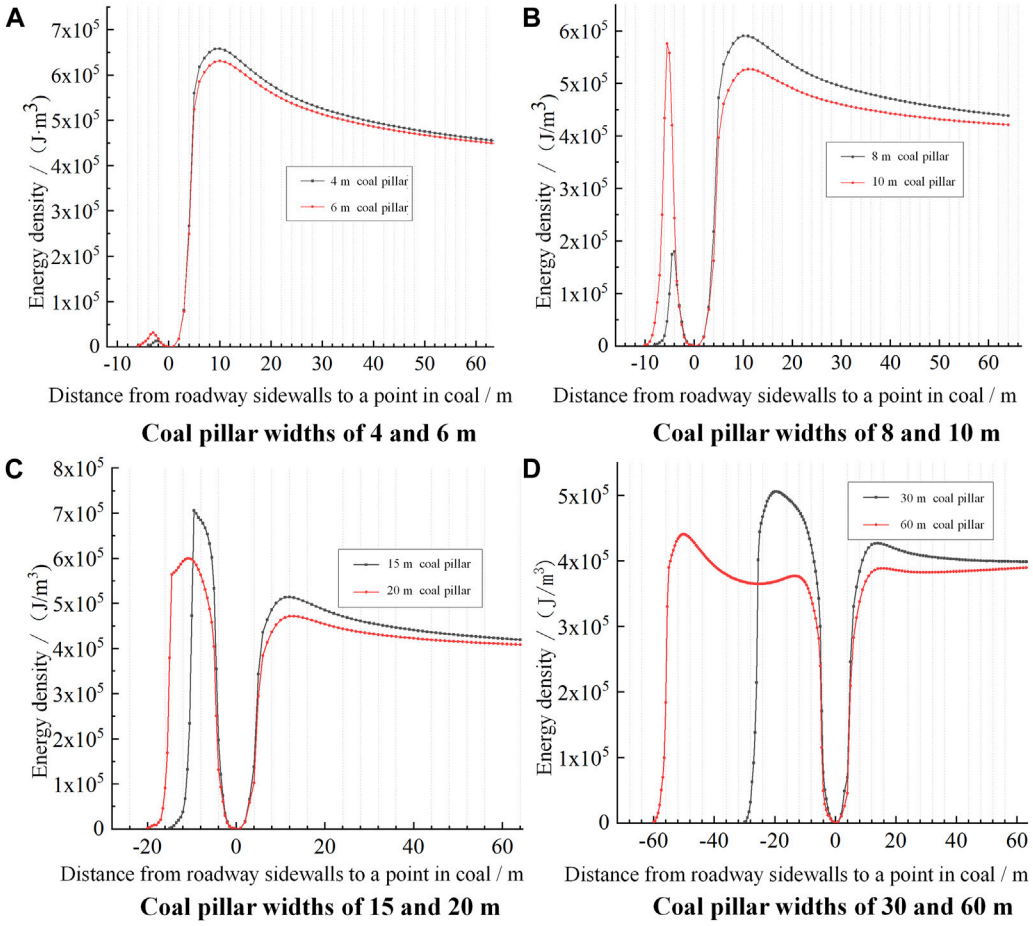


FIGURE 7
Variation law of elastic energy density fields in roadway surrounding rocks with different widths of protective coal pillar. **(A)** Coal pillar widths of 4 and 6 m; **(B)** Coal pillar widths of 8 and 10 m; **(C)** Coal pillar widths of 15 and 20 m; **(D)** Coal pillar widths of 30 and 60 m.

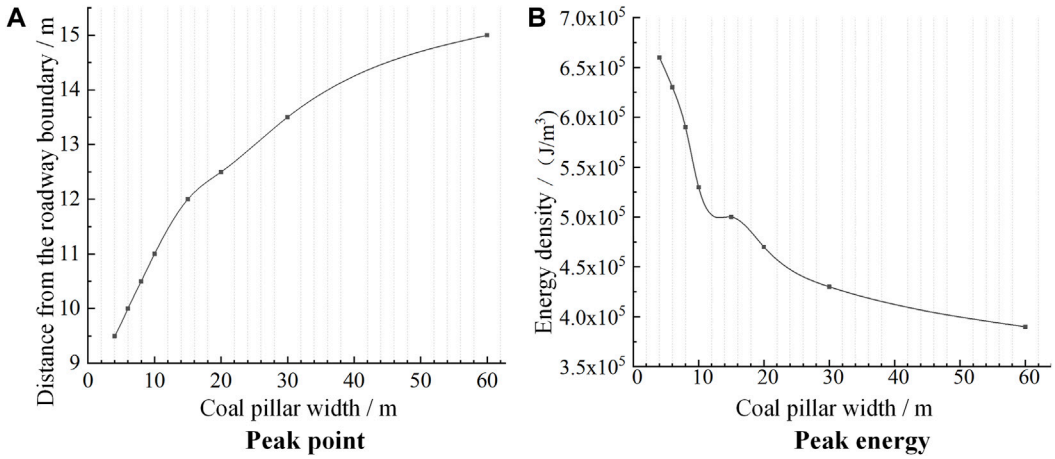


FIGURE 8
Peak point of inner elastic energy density in entity coal and the changes in peak energy.

TABLE 2 Peak energy density of deeply impacted roadway surrounding rocks with the coal pillar width.

Coal pillar width	4 m	6 m	8 m	10 m	15 m	20 m	30 m	60 m
Peak energy density in the entity coal/10^5J/m^3	6.6	6.3	5.9	5.3	5.14	4.70	4.30	3.90
Peak energy density in the coal pillar/10^5J/m^3	0.15	0.32	1.80	5.76	7.10	6.0	5.11	3.77
Distance from the peak energy density in entity coal to the coal wall/m	9.5	10.0	10.5	11.0	12.0	12.5	13.5	15.5

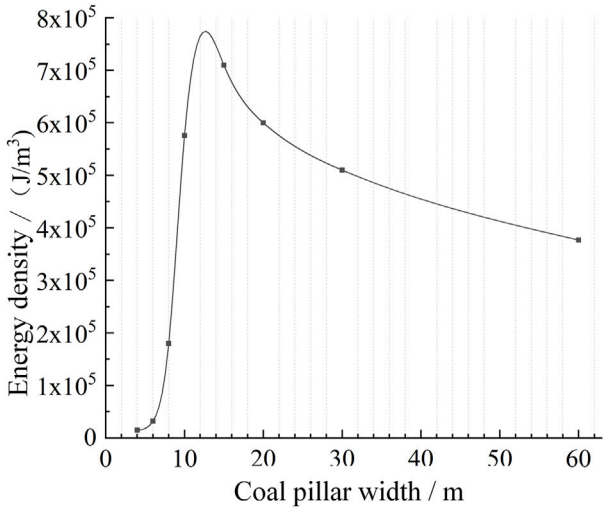


FIGURE 9
Variation law of the peak elastic energy density in coal pillars with the coal pillar width.

15.5 m with the increase in coal pillar width. On the contrary to changes in the peak energy density in the entity coal, the wider the coal pillar is, the higher the peak energy density in the coal pillar will be, which grows from 0.15 × 10^5 J/m^3 under the coal pillar width of 4 m to 3.77 × 10^5 J/m^3 when the width is 60 m.

Therefore, the elastic energy density is notably asymmetrically distributed in deep roadway surrounding rocks in the coal mine. Under action of structures of roadway surrounding rocks, the energy evolution during rockburst development in these structures differs remarkably under different coal pillar widths. To prevent rockburst in roadways, the support patterns suitable for deep rockburst-prone roadways should be proposed according to structural characteristics of deep roadway surrounding rocks and energy evolution characteristics during rockburst development in the coal mine.

5 Conclusion

The energy evolution characteristics during rockburst development in structures of deep roadway surrounding rocks were studied according to structural characteristics of deep roadway surrounding rocks in coal mines. FLAC3D numerical simulation software was utilized to analyze influences of the mining depth and coal pillar width on energy evolution in rockburst-prone roadways during rockburst development. The main conclusions include the following:

(1) Based on the theory of elastic mechanics, energy evolution during rockburst development in the elastic bearing zone and energy conversion characteristics in the plastic failure zone of roadway surrounding rocks were analyzed. According to the state equation of rockburst, influences of energy dissipation in coal–rock mass and support on rockburst were analyzed, and

disturbance characteristics of external energy on structures of roadway surrounding rocks were discussed. The research pointed out that with the enlargement of the affected area of the plastic failure zone, coal–rock mass in the elastic bearing zone only changes unidirectionally into energy absorption. Two energy-absorbing modes are involved, namely, energy absorption of propagation media of disturbance energy toward the roadway and energy transfer and accumulation for rockburst development. The coal–rock mass and stress state in the plastic failure zone change from the triaxial to biaxial and even uniaxial state, and the elastic strain energy reduces abruptly.

(2) Based on the theory of rockburst start-up and the energy theory, critical energy criteria for structural instability of roadway surrounding rocks under static and dynamic loading were deduced, taking energy release in the rockburst start-up zone larger than energy consumption during energy transfer and rockburst occurrence as the criterion. They are closely related to the elastic strain energy stored in deep roadway surrounding rocks and the energy absorbed by support systems. The impact energy in roadways is found to be directly proportional to the square of the stress concentration factor k. The occurrence of rockburst can be prevented by reducing the stress concentration factor, enlarging the distance from the rockburst start-up zone to the rockburst occurrence zone using artificial control measures, and enhancing the energy-absorbing capacity of the support.

(3) As the mining depth increases, the energy density in surrounding rocks grows in the same region. When the protective coal pillar is 30 m wide, the region with high energy density in the coal–rock mass is found in the roadway, and the energy density is high in the retained coal pillar in the gob in the region 100 m behind the working face. The maximum energy density in the entity coal in the working face is found at the end in the gob side near the previous working face. As the mining depth increases, the peak point of maximum energy density gradually shifts to the coal ahead of the working face. With increase in burial depth, the energy density is more remarkably affected by the advanced abutment pressure of the working face, and the larger the burial depth is, the wider the affected area will be. The maximum energy density in the coal–rock mass ahead of the working face exhibits an obvious increment with the increase in mining depth.

(4) At the same burial depth, the peak elastic energy density in the coal pillar increases at first and then decreases with the increase in coal pillar width. The energy density in the coal pillar changes from one peak point to two as the coal pillar width enlarges, and the peak elastic energy density in the entity coal decreases with the increase in width. As the coal pillar width enlarges, the distance from the peak point of energy density to the roadway boundary increases abruptly at first and then slowly, and the critical coal pillar width for the gentle change is 30 m. Changes in the peak elastic energy density in the coal pillar with the coal pillar width can be roughly divided into four stages: the slow increase stage, abrupt increase stage, abrupt decrease stage, and slow decrease stage of energy density. The elastic energy density in deep roadway surrounding rocks in the coal mine is obviously asymmetrically distributed. Under the action of structures of roadway surrounding rocks, the energy evolution during rockburst development differs greatly in these structures under different coal pillar widths.

Data availability statement

The original contributions presented in the study are included in the article/Supplementary Material; further inquiries can be directed to the corresponding authors.

Author contributions

ZX, ZC, and CL: writing–original draft and writing–review and editing. CF, HQ, WL, KG, HC, YX, and LY: data curation and writing–original draft.

Funding

The authors acknowledge financial support provided by the Science and Technology Development Fund Project of Coal Research Institute (Basic Fund), the National Natural Science Foundation of China (52074120, 52104131), and the Fundamental Research Funds for the Central Universities (3142019005, 3142017107).

Conflict of interest

The authors declare that the research was conducted in the absence of any commercial or financial relationships that could be construed as a potential conflict of interest.

Publisher's note

All claims expressed in this article are solely those of the authors and do not necessarily represent those of their affiliated organizations, or those of the publisher, the editors, and the reviewers. Any product that may be evaluated in this article, or claim that may be made by its manufacturer, is not guaranteed or endorsed by the publisher.

References

Cai, W., Dou, L. M., He, J., Liu, H. S., Li, Z. L., and Ding, Y. L. (2014). Mechanical genesis of Henan (China) Yima thrust nappe structure. *J. Central South Univ.* 21 (7), 2857–2865. doi:10.1007/s11771-014-2251-6

Chen, G. X., and Dou, L. M. (2008). Energy analysis of rock burst on excavated circular roadway under uniform pressure. *J. Min. Saf. Eng.* 25 (1), 27–31.

Chen, Z. H., Zou, Q. L., Gao, S. K., Zhan, J. F., Chen, C. M., Ran, Q. C., et al. (2023). Long-term evolution of overlying rock fractures in mined-out areas and its effect on gas flow conductivity. *Fuel* 353, 129213. doi:10.1016/j.fuel.2023.129213

Dai, J. H., Yang, J. H., Yao, C., Hu, Y. G., Zhang, X. B., Jiang, Q. H., et al. (2022). Study on the mechanism of displacement mutation for jointed rock slopes during blasting excavation. *Int. J. Rock Mech. Min. Sci.* 150, 105032. doi:10.1016/j.ijrmms.2021.105032

Du, F., Ma, J., Guo, X. F., Wang, T. F., Dong, X. H., Li, J. S., et al. (2022). Rockburst mechanism and the law of energy accumulation and release in mining roadway: a case study. *Int. J. Coal Sci. Technol.* 9 (1), 67. doi:10.1007/s40789-022-00521-0

Gao, M. S., Dou, L. M., Zhang, N., Mu, Z. L., Wang, K., and Yang, B. S. (2007). Experimental study on earthquake tremor for transmitting law of rockburst in geomaterials. *Chin. J. Rock Mech. Eng.* 26 (7), 1365–1371.

Gao, M. S., Liu, Y. M., Zhao, Y. C., Gao, X. J., and Wen, Y. Y. (2017). Failure mechanism of impact fracture of deep coal roadway roof and its dynamic manifestations. *J. China Coal Soc.* 42 (7), 1650–1655. doi:10.13225/j.cnki.jccs.2016.1464

Gong, F. Q., He, Z. C., and Jiang, Q. (2022). Internal mechanism of reducing rockburst proneness of rock under high stress by real-time drilling pressure relief. *Rock Mech. Rock Eng.* 55 (8), 5063–5081. doi:10.1007/s00603-022-02904-w

He, M. C., and Wang, Q. (2023). Rock dynamics in deep mining. *Int. J. Min. Sci. Technol.* 33 (9), 1065–1082. doi:10.1016/j.ijmst.2023.07.006

He, M. M., Zhao, J. R., Deng, B. Y., and Zhang, Z. Q. (2022). Effect of layered joints on rockburst in deep tunnels. *Int. J. Coal Sci. Technol.* 9 (1), 21. doi:10.1007/s40789-022-00489-x

Hu, S. B., Wang, E. Y., and Shen, R. X. (2013). Characteristics of dynamic disturbance response in deep coal and rock and its numerical analysis. *J. China Univ. Min. Technol.* 42 (4), 540–546.

Huang, L. K., He, R., Yang, Z. Z., Tan, P., Chen, W. H., Li, X. G., et al. (2023a). Exploring hydraulic fracture behavior in glutenite formation with strong heterogeneity and variable lithology based on DEM simulation. *Eng. Fract. Mech.* 278, 109020. doi:10.1016/j.engfracmech.2022.109020

Huang, L. K., Tan, J., Fu, H. F., Liu, J. J., Chen, X. Y., Liao, X. C., et al. (2023b). The non-plane initiation and propagation mechanism of multiple hydraulic fractures in tight reservoirs considering stress shadow effects. *Eng. Fract. Mech.* 292, 109570. doi:10.1016/j.engfracmech.2023.109570

Huang, L. Q., Si, X. F., Li, X. B., Gong, F. Q., and Luo, Y. (2022). Influence of maximum principal stress direction on the failure process and characteristics of D-shaped tunnels. *Int. J. Min. Sci. Technol.* 32 (5), 1125–1143. doi:10.1016/j.ijmst.2022.07.004

Jiang, F. X., Yang, G. Y., Wei, Q. D., Wang, C. W., Qu, X. C., and Zhu, S. T. (2018). Study and prospect on coal mine composite dynamic disaster real-time prewarning platform. *J. China Coal Soc.* 43 (2), 333–339. doi:10.13225/j.cnki.jccs.2017.4152

Lei, G. Y., Lu, A. H., and Mao, X. B. (2005). Numerical simulation on layered crack and failure of roadway under stress wave. *Rock Soil Mech.* 26 (09), 1477–1480.

Li, B., Yang, X., Yuan, Y., Liang, Y. P., Li, S. Q., Zhu, C. Q., et al. (2023). Experimental research on the influence of different factors on the behaviour of broken coal and rock particles during compaction. *Constr. Build. Mater.* 367, 130127. doi:10.1016/j.conbuildmat.2022.130127

Li, Q. M., Liang, Y. P., Zou, Q. L., and Li, Q. G. (2020). Acoustic emission and energy dissipation characteristics of gas-bearing coal samples under different cyclic loading paths. *Nat. Resour. Res.* 29 (2), 1397–1412. doi:10.1007/s11053-019-09508-2

Li, X. B., Yao, J. R., and Du, K. (2013). Preliminary study for induced fracture and non-explosive continuous mining in high-geostress hard rock mine-a case study of Kaiyang phosphate mine. *Chin. J. Rock Mech. Eng.* 32 (6), 1101–1111.

Liang, Y. P., Kong, F. J., Zou, Q. L., and Zhang, B. C. (2023). Effect of strain rate on mechanical response and failure characteristics of horizontal bedded coal under quasi-static loading. *Geomechanics Geophys. Geo-Energy Geo-Resources* 9 (1), 52. doi:10.1007/s40948-023-00587-3

Liang, Y. P., Ran, Q. C., Zou, Q. L., Zhang, B. C., and Hong, Y. (2022). Experimental study of mechanical behaviors and failure characteristics of coal under true triaxial cyclic loading and unloading and stress rotation. *Nat. Resour. Res.* 31 (2), 971–991. doi:10.1007/s11053-022-10022-1

Linkov, A. M. (1996). Rockbursts and the instability of rock masses. *Int. J. Rock Mech. Min. Sci. Geomechanics Abstr.* 33 (7), 727–732. doi:10.1016/0148-9062(96)00021-6

Litwiniszyn, J. (2009). Rarefaction shock waves, out bursts and consequential coal damage. *Int. J. Rock Mech. Min. Sci. Geomechanics Abstr.* 27 (6), 535–540. doi:10.1016/0148-9062(90)91004-Q

Liu, C. Y., Zhao, G. M., Xu, W. S., Meng, X. R., Liu, Z. X., Cheng, X., et al. (2023). Experimental study on failure characteristics of single-sided unloading rock under different intermediate principal stress conditions. *Int. J. Min. Sci. Technol.* 33 (3), 275–287. doi:10.1016/j.ijmst.2022.12.005

Lou, J. F., Gao, F. Q., Li, J. Z., Yuan, G. Y., and Sharifzadeh, M. (2023). Effect of dynamic loading conditions on the dynamic performance of MP1 energy-absorbing rockbolts: insight from laboratory drop test. *Int. J. Min. Sci. Technol.* 33 (2), 215–231. doi:10.1016/j.ijmst.2022.09.023

Lu, A. H., Yu, S. L., Qin, H., and Mao, X. B. (2008). Stability of layered crack structure in roadway surrounding rock under stress wave. *J. China Univ. Min. Technol.* 37 (6), 769–775.

Ma, T. F., Liu, H. H., Zou, Q. L., Kong, F. J., Ran, Q. C., and Wang, P. T. (2023). Damage evolution characteristics and deterioration mechanism of mechanical properties of sandstone subjected to drying-wetting cycles. *J. Mater. Res. Technol.* 23, 4591–4605. doi:10.1016/j.jmrt.2023.02.068

Pan, J. F., Mao, D. B., Lan, H., Wang, S. W., and Qi, Q. X. (2013). Study status and prospects of mine pessure bumping control Technology in China. *Coal Sci. Technol.* 41 (06), 21–25+41. doi:10.13199/j.cst.2013.06.27.panjf.012

Pan, J. F., Ning, Y., Mao, D. B., Lan, H., Du, T. T., and Peng, Y. W. (2012). Theory of rockburst start-up during coal mining. *Chin. J. Rock Mech. Eng.* 31 (3), 586–596.

Ran, Q. C., Liang, Y. P., Zou, Q. L., Hong, Y., Zhang, B. C., Liu, H., et al. (2023a). Experimental investigation on mechanical characteristics of red sandstone under graded cyclic loading and its inspirations for stability of overlying strata. *Geomechanics Geophys. Geo-Energy Geo-Resources* 9 (1), 11. doi:10.1007/s40948-023-00555-x

Ran, Q. C., Liang, Y. P., Zou, Q. L., Zhang, B. C., Li, R. F., Chen, Z. H., et al. (2023b). Characteristics of mining-induced fractures under inclined coal seam group multiple mining and implications for gas migration. *Nat. Resour. Res.* 32 (3), 1481–1501. doi:10.1007/s11053-023-10199-z

Su, E. L., Liang, Y. P., Chen, X. J., Wang, Z. F., Ni, X. M., Zou, Q. L., et al. (2023). Relationship between pore structure and mechanical properties of bituminous coal under sub-critical and super-critical CO2 treatment. *Energy* 280, 128155. doi:10.1016/j.energy.2023.128155

Sun, D. L., Liang, Y. P., Huang, X. C., and Ran, Q. C. (2023a). Progress and prospects of coalbed methane development and utilization in coal mining areas with large dip angle and multiple coal groups in Xinjiang. *Coal Sci. Technol.* 51 (S1), 161–171. doi:10.13199/j.cnki.cst.mcq2022-1325

Sun, X. Y., Ran, Q. C., Liu, H., Ning, Y. H., and Ma, T. F. (2023b). Characteristics of stress-displacement-fracture multi-field evolution around gas extraction borehole. *Energies* 16 (6), 2896. doi:10.3390/en16062896

Tan, P., Fu, S. H., Chen, Z. W., and Zhao, Q. (2023a). Experimental investigation on fracture growth for integrated hydraulic fracturing in multiple gas bearing formations. *Geoenergy Sci. Eng.* 231 (1), 212316. doi:10.1016/j.geoen.2023.212316

Tan, P., Jin, Y., and Pang, H. W. (2021). Hydraulic fracture vertical propagation behavior in transversely isotropic layered shale formation with transition zone using XFEM-based CZM method. *Eng. Fract. Mech.* 248, 107707. doi:10.1016/j.engfracmech.2021.107707

Tan, Y. L., Ma, Q., Liu, X. L., Liu, X. S., Elsworth, D., Qian, R. P., et al. (2023b). Study on the disaster caused by the linkage failure of the residual coal pillar and rock stratum during multiple coal seam mining: mechanism of progressive and dynamic failure. *Int. J. Coal Sci. Technol.* 10 (1), 45. doi:10.1007/s40789-023-00603-7

Wang, T. A., Zhai, Y., Gao, H., Li, Y. B., and Zhao, R. F. (2023). A novel binary effective medium model to describe the prepeak stress-strain relationship of combined bodies of rock-like material and rock. *Int. J. Min. Sci. Technol.* 33 (5), 601–616. doi:10.1016/j.ijmst.2022.11.007

Wang, X., Li, J. C., Zhao, X. B., and Liang, Y. (2022). Propagation characteristics and prediction of blast-induced vibration on closely spaced rock tunnels. *Tunn. Undergr. Space Technol.* 123, 104416. doi:10.1016/j.tust.2022.104416

Wei, M. Y., Wang, E. Y., Liu, X. F., Song, D. Z., and Zhang, Y. (2010). Numerical simulation of roof fracture induced by dynamic disturbance. *J. Min. Saf. Eng.* 27 (04), 532–536.

Wu, Q. F., Han, S. X., Li, S. S., Yu, M. G., Zheng, K., Li, H. T., et al. (2023). Explosive characteristics of non-uniform methane-air mixtures in half-open vertical channels with ignition at the open end. *Energy* 284, 128687. doi:10.1016/j.energy.2023.128687

Wu, Q. F., Yu, M. G., and Zheng, K. (2022). Experimental investigation on the effect of obstacle position on the explosion behaviors of the non-uniform methane/air mixture. *Fuel* 320, 123989. doi:10.1016/j.fuel.2022.123989

Xu, L., Gong, F. Q., and Luo, S. (2021). Effects of pre-existing single crack angle on mechanical behaviors and energy storage characteristics of red sandstone under uniaxial compression. *Theor. Appl. Fract. Mech.* 113, 102933. doi:10.1016/j.tafmec.2021.102933

Ye, C. F., Xie, H. P., Wu, F., and Li, C. B. (2022). Nonlinear creep properties and time-to-failure prediction of sandstone under saturated and dry conditions. *Environ. Earth Sci.* 81, 545. doi:10.1007/s12665-022-10666-5

Ye, C. F., Xie, H. P., Wu, F., and Li, C. B. (2023). Study on the nonlinear time-dependent deformation characteristics and viscoelastic-plastic model of shale under direct shear loading path. *Bull. Eng. Geol. Environ.* 82 (5), 189. doi:10.1007/s10064-023-03170-y

Zhang, B. C., Liang, Y. P., Zhao, Z. Y., Zou, Q. L., Zheng, H. L., Ning, Y. H., et al. (2023a). Effect of stress amplitude on mechanical and acoustic emission of sandstone under constant–cyclic loading. *Bull. Eng. Geol. Environ.* 82, 284. doi:10.1007/s10064-023-03307-z

Zhang, B. C., Liang, Y. P., Zou, Q. L., Ding, L. Q., and Ran, Q. C. (2023b). Experimental investigation into the damage evolution of sandstone under decreasing-amplitude stress rates and its implications for coalbed methane exploitation. *Environ. Earth Sci.* 82, 208. doi:10.1007/s12665-023-10825-2

Zhang, C. G., Ismet, C., Faham, T., and Bruce, H. (2017). Assessment of energy release mechanisms contributing to coal burst. *Int. J. Min. Sci. Technol.* 27 (1), 43–47. doi:10.1016/j.ijmst.2016.09.029

Zhang, C. L., Wang, P. Z., Wang, E. Y., Chen, D. P., and Li, C. (2023c). Characteristics of coal resources in China and statistical analysis and preventive measures for coal mine accidents. *Int. J. Coal Sci. Technol.* 10 (1), 22. doi:10.1007/s40789-023-00582-9

Zhang, T. C., Zou, Q. L., Jia, X. Q., Jiang, C. Z., and Niu, X. G. (2022). Effect of SiO2 nanofluid with different concentrations on the wettability of coal. *Fuel* 321, 124041. doi:10.1016/j.fuel.2022.124041

Zhao, J. J., Tian, S. X., Li, P., Xie, H. G., and Cai, J. J. (2023a). Molecular dynamics simulation and experimental research on the influence of SiO2-H2O nanofluids on wettability of low-rank coal. *Colloids Surfaces A Physicochem. Eng. Aspects* 679, 132580. doi:10.1016/j.colsurfa.2023.132580

Zhao, J. J., Tian, S. X., Xie, H. G., and Zhang, X. (2023b). Study of time-varying laws of stability and wettability of SiO2–H2O nanofluids with different particle sizes. *Industrial Eng. Chem. Res.* 62, 13529–13540. doi:10.1021/acs.iecr.3c02110

Zhao, Y. S., Feng, Z. C., and Chang, Z. X. (2003). Least energy priciple of dynamical failure of rock mass. *Chin. J. Rock Mech. Eng.* 11, 1781–1783.

Zou, D. Y., and Jiang, F. X. (2004). Research of energy storing and gestation mechanism and forecasting of rockburst in the coal and rock mass. *J. China Coal Soc.* 29 (2), 159–163.

Zou, Q. L., Chen, Z. H., Cheng, Z. H., Liang, Y. P., Xu, W. J., Wen, P. R., et al. (2022a). Evaluation and intelligent deployment of coal and coalbed methane coupling coordinated exploitation based on Bayesian network and cuckoo search. *Int. J. Min. Sci. Technol.* 32 (6), 1315–1328. doi:10.1016/j.ijmst.2022.11.002

Zou, Q. L., Ning, Y. H., Zhang, B. C., Tian, S. X., Jiang, Z. B., and An, Y. Q. (2023). Mechanical properties and failure characteristics of sandstone under ramp loading paths. *Geomechanics Geophys. Geo-Energy Geo-Resources* 9 (1), 39. doi:10.1007/s40948-023-00574-8

Zou, Q. L., Zhang, T. C., Ma, T. F., Tian, S. X., Jia, X. Q., and Jiang, Z. B. (2022b). Effect of water-based SiO2 nanofluid on surface wettability of raw coal. *Energy* 254, 124228. doi:10.1016/j.energy.2022.124228

frontiers | Frontiers in Energy Research

TYPE Original Research
PUBLISHED 24 November 2023
DOI 10.3389/fenrg.2023.1324934

Check for updates

OPEN ACCESS

EDITED BY
Peng Tan,
CNPC Engineering Technology R & D Company Limited, China

REVIEWED BY
Yongpeng Sun,
China University of Petroleum (East China), China
Jiajia Bai,
Changzhou University, China

*CORRESPONDENCE
Mingwei Wang,
tougaozhongwen@163.com

RECEIVED 20 October 2023
ACCEPTED 13 November 2023
PUBLISHED 24 November 2023

CITATION
Lin L, Wang M, Wang Y, Gao Y and Li S (2023), Prediction of natural fracture distribution characteristics in tight oil and gas reservoirs based on paleotectonic stress field.
Front. Energy Res. 11:1324934.
doi: 10.3389/fenrg.2023.1324934

COPYRIGHT
© 2023 Lin, Wang, Wang, Gao and Li. This is an open-access article distributed under the terms of the Creative Commons Attribution License (CC BY). The use, distribution or reproduction in other forums is permitted, provided the original author(s) and the copyright owner(s) are credited and that the original publication in this journal is cited, in accordance with accepted academic practice. No use, distribution or reproduction is permitted which does not comply with these terms.

Prediction of natural fracture distribution characteristics in tight oil and gas reservoirs based on paleotectonic stress field

Lifei Lin[1], Mingwei Wang[2]*, Yanwei Wang[3], Yi Gao[1] and Song Li[4]

[1]Shaanxi Yanchang Petroleum (Group) Co., Ltd., Yan'an, China, [2]School of Oil and Natural Gas Engineering, Southwest Petroleum University, Chengdu, China, [3]Changqing Downhole Technology Operation Company of Chuanqing Drilling Engineering Co., Ltd., Xi'an, China, [4]Engineering Research Institute of PetroChina Southwest Oil and Gas Field Company, Chengdu, China

The production of fractured oil and gas reservoirs in the world accounts for more than half of total oil and gas production and is one of the important fields for increasing oil and gas storage and production in the 21st century. The key to characterizing fractured oil and gas reservoirs is the distribution pattern of natural fractures. The distribution of natural fractures is dominated by structural deformations and fractures. Therefore, analytical and structural simulations of the tectonic stress field in geological structural systems play a crucial role in obtaining fracture distribution patterns. In this paper we have developed a description of the distribution of natural fractures based on finite element numerical simulations of the paleotectonic stress field. The study focused on the Chang 7 and Huangjialing Chang 8 reservoirs in the underground Siwan region of the Ordos Basin in China. First, an experimental assessment of the rock mechanics of the reservoir was completed, and the values of the paleotectonic stresses obtained from the tests were used as inversion criteria for the stress field simulations. Based on the geology, a refined geological model has been developed to study the structure of the Chang 7 and Chang 8 oil reservoirs in the block. The simulated paleotectonic stress fields for natural fractures in the Indosinian period are as follows: maximum principal stress of 94.67 MPa, minimum principal stress of 21.58 MPa, and vertical stress of 28.07 MPa. The direction of maximum principal stress remains essentially in the NE-SW direction, with the largest differential stress occurring in the Chang 8 oil layer group in Huangjialing, while the differential stress is relatively uniform in the Chang 7 oil layer group in Xiasiwan. It predicts the relative density of natural fractures in the Chang 7 and Chang 8 reservoirs, and finds high-to-low plane heterogeneity in the Huangjialing Chang 8 reservoir group and the Xiasiwan Chang 7 reservoir group, respectively. The paper reveals the pattern of development of reservoir fractures in both vertical and horizontal directions, providing an important geological basis for efficient and rational exploitation of oil and gas resources in the study area and improving oil recovery.

KEYWORDS

fractured oil and gas reservoirs, natural fracture, paleotectonic stress, rock mechanics, finite element simulation, fracture development pattern

1 Introduction

As the world's conventional oil and gas resources are increasingly depleted, their production is gradually declining, which conflicts with increasing demand. As a result, unconventional oil and gas resources such as low permeability tight oil and gas are gradually gaining attention. Among them, tight oil and gas, due to its wide distribution, abundant resource reserves and long extraction life, has gradually become a hot research area among relevant scholars worldwide and a hot direction for oil and gas exploration and development (Song et al., 2001; Gong et al., 2019; Li, 2021; Tan et al., 2023).

In recent years, methods for predicting fractures can be roughly divided into three methods: using tectonic stress fields to predict fracture development, using logging data to predict fracture development, and using seismic methods to predict fractures (Zhang et al., 2022a; Hu, 2022). Many scholars have studied the relationship between tectonic stress field and the development and distribution of fractures in oil and gas reservoirs, and have obtained many important insights, which have effectively guided oil and gas exploration (Li and Zhang, 1997; Wang et al., 1997; Qin et al., 2004; Zhang et al., 2022b; Liu et al., 2023). Therefore, tectonic stress field simulation can predict the development and distribution of tectonic fractures. Rouchet, (1981) proposed that "stress field is the key to oil and gas migration," breaking the common understanding that formation water migration is the key factor determining oil and gas migration, and fundamentally revealing the mechanism of oil and gas migration. The crucial role of tectonic stress field in the exploration and exploitation of fractured oil and gas resources (Wu et al., 2022a). Under the action of regional tectonic stress, fractures and fractures are formed in the rock, so the distribution and characteristics of fractures are closely related to all the tectonic movements, stress field sizes and directions experienced in the region (Wang, 2013; Lou et al., 2020; Tan et al., 2020). Murry, (1977) studied and established the relationship between the main curvature of the structure and the degree of fracture development. Zobock (Zobock et al., 1985; Zobock and Peska, 1995) measured the magnitude of ground stress using hydraulic fracturing, Haimson and Herrick, (1985) and Peska and Zoback, (1995) studied the magnitude and direction of the corresponding stress field using wellbore collapse method, and Jaeger et al. (2007) conducted systematic experimental research on the stress field using rock group method, The research results obtained through these experimental testing methods have played an important role in the exploration and development of oil and gas fields.

Currently, fractures are mainly studied with a focus on mechanical causes, and fractures are evaluated by simulating the tectonic stress field using different methods. Some researchers analyze rock mechanical parameters for different lifetimes through lithographic segmentation, construct geological models, and convert geological models into rock mechanical models for stress-field simulations (Ding et al., 2016). Some researchers also use finite element software to conduct mechanical analysis of rock layers and establish *in situ* stress models (Hu et al., 1994; Guo et al., 2016; Xu et al., 2017; Tan et al., 2021; Wu et al., 2022b; Wang et al., 2022) to obtain the spatial distribution characteristics of *in situ* stress, and based on this, predict fractures. Wei and Sun, (2016) believed that structural fractures in low-permeability reservoirs are important storage spaces for oil and gas, which can significantly improve reservoir permeability. They used a three-dimensional finite element model (3D-FEM) to simulate the Himalayan paleotectonic stress field, estimated rock failure criteria (RFC) and comprehensive fracture rate (CRR), and quantitatively determined the development and distribution of structural fractures in low-permeability reservoirs of the Xiagou formation. Khair et al. (2015) used image log fractures and fault network within an iterative boundary element method (iBEM3D) to predict the paleo-tectonic events and the fracture network in the Cooper Basin. Their methodology was able to predict only the major tectonic events that occurred after the deposition of the Cooper Basin sediments and contributed to the formation of the natural fractures. Wu et al. (2017) established a reasonable geological, mechanical, and mathematical model for the study area based on the fault system interpreted by seismic data, fracture characteristics of drilling data, uniaxial and triaxial compression tests, and rock acoustic emission tests. They overlaid multiple stages of ancient tectonic stress fields and predicted the distribution of reservoir structural fractures. Feng et al. (2019) used a finite element based on geomechanical modeling method to infer the degree of fracture development based on stress-strain curves, establish a mathematical model for fracture development, and quantitatively predict fracture development and distribution. Li et al. (2021) took Halahatang Oilfield in the north of Tarim basin as the research object, comprehensively used outcrop observation, drilling core, thin section, logging and seismic data, simulated the structural stress field of deep carbonate reservoir in three different tectonic movement periods based on finite element method, and quantified the spatial distribution characteristics of multi-stage fractures with fracture density as the evaluation parameter. Huang et al. (2019) studied the effect of inherent anisotropy and particle size distribution of rock on the initiation and propagation of hydraulic fractures under different propagation mechanisms through two-dimensional discrete element simulation. Ren et al. (2019) determined the characteristics of tectonic fractures parameters based on the data of formation core and imaging logging. The paleo tectonic stress field of two key fracture periods and current stress field in Hetian river gas field were simulated by combining 3 D element numerical simulation method, and the fracture linear density and aperture formulas were established to calculate the distribution of tectonic fractures in different periods. Huang et al. (2023) proposed a mathematical method for the generation of irregular polygonal gravels, and established the hydraulic fracturing model of glutenite with different gravel characteristics utilizeing 2D particle discrete element method.

Finite-element numerical simulations of the paleotectonic stress field to predict fracture are one of the effective methods for semi-quantitative characterization of fracture development in reservoirs. This approach was first evaluated experimentally in rock mechanics, where values of protective stresses obtained from rock mechanics experiments were used as inversion criteria for stress field simulations. At the same time, an objective fine-grained geological model of the structure of the oil reservoir is developed on a geological basis, and the two are combined to model the paleotectonic stress field during the main formation period of the natural fracture. The fracture rate is

calculated by analyzing the ancient tectonic stress field and then predicting the extent of structural fracture in the reservoir. The finite element numerical simulation method can not only restore the distribution of reservoir structural stress field during the formation period of structural fractures, but also predict the distribution and development degree of reservoir structural fractures based on geological mechanics theory, providing technical support for the exploration and development of fractured oil and gas reservoirs. Therefore, in this paper we numerically simulate the paleotectonic stress field in the studied region and predict the relative density of natural fractures in the studied region.

2 Analysis of paleostress during the formation of fractures

2.1 Principles of acoustic emission experiment

The process of measuring *in situ* stresses using the acoustic emission Kessel effect method involves indoor loading tests on rocks taken from underground sites. Acoustic emission instruments are used to measure acoustic signals emitted from the interior of the rock during loading. According to the Kessel effect principle, when the stress on a rock reaches its historical maximum, the acoustic signal generated by the rock will suddenly increase. Based on this, it is possible to obtain stress values for the test rock below ground. Due to the 3D forces acting on the subsurface rock, it was necessary to carry the core in different directions for testing. Generally, when re coring rock cores taken from the site indoors, at least one vertical and three horizontal directions (each separated by 45°) of rock samples should be taken. Based on the results of the tests performed on the four rock samples described above, the primary geostress of the three formations at the depth of the well in which the rock is located can be fully determined using the following formula:

$$\sigma_{\mathrm{v}} = \sigma_{\perp} + \alpha \mathrm{P_P} - \mathrm{KP}_c \tag{1}$$

$$\sigma_{\mathrm{H}} = \frac{\sigma_{0^\circ} + \sigma_{90^\circ}}{2} + \frac{\sigma_{0^\circ} - \sigma_{90^\circ}}{2}\left(1 + \mathrm{tg}^2 2\alpha\right)^{\frac{1}{2}} + \alpha \mathrm{P_P} - \mathrm{KP}_c \tag{2}$$

$$\sigma_h = \frac{\sigma_{0^\circ} + \sigma_{90^\circ}}{2} + \frac{\sigma_{0^\circ} + \sigma_{90^\circ}}{2}\left(1 + \mathrm{tg}^2 2\alpha\right)^{\frac{1}{2}} + \alpha \mathrm{P_P} - \mathrm{KP}_c \tag{3}$$

Where,

$$tg2a = \frac{\sigma_{0^\circ} + \sigma_{90^\circ} - \sigma_{45^\circ}}{\sigma_{0^\circ} - \sigma_{90^\circ}}$$

σ_v, σ_H, σ_h—respectively refer to the overlying strata pressure, horizontal maximum and minimum horizontal geostress, MPa. P_P—Pore pressure, MPa. α—Effective stress coefficient, Dimensionless. $\sigma_\perp$—Vertical Kessel point stress of rock core under confining pressure, MPa. $\sigma_{0^\circ}, \sigma_{45^\circ}, \sigma_{90^\circ}$ is the Kessel point stress under the confining pressure of the rock core in three horizontal directions of 0°, 45°, and 90°, respectively, MPa. P_c—is the confining pressure borne by the rock core in the high-pressure wellbore, MPa. K—the confining pressure correction coefficient, Dimensionless.



FIGURE 1
Core sample of reservoir core in Xin 118 well.

2.2 Acoustic emission experimental results

In this experiment, ten representative samples from the target layer were selected for lithography. As an example, experimental procedures and data processing were performed on samples taken from 1,568.00 to 1,568.63 m underground in Well Xin 118. Firstly, manually set a reference line on the sample and take four column samples along the 0°, 45°, 90°, and vertical directions (Figure 1).

An acoustic emission experiment was subsequently performed using the experimental core sample. The experimental results showed that the stress value corresponding to the 0° direction was 112.4 MPa, the stress value corresponding to the 45° direction was 112.5 MPa, the stress value corresponding to the 90° direction was 29.1 MPa, and the stress value corresponding to the vertical direction was 48.2 MPa. Further combining the log and production data, we obtain the relevant parameters. Based on Eq., it can be calculated that the maximum principal stress of the experimental rock sample during the period of most severe geological activity and fracture formation is 106.6 MPa, the minimum principal stress is 18.4 MPa, and the vertical stress is 28.3 MPa.

2.3 Paleostress analysis

According to the above method, the other 9 samples were tested sequentially and the paleotectonic stress results of 10 samples were calculated (Table 1).

From Table 1, it can be seen that there is not much difference between the measurements in this region. Considering that the ten samples underwent similar tectonic evolution processes and experimental errors, the average of the measured results for these samples was taken to be the paleostress of the region during the period of most intense geological activity and fracture formation. Thus, during that period, the maximum principal stress in layer 7 was 95.48 MPa, the minimum principal stress was 21.92 MPa, and the vertical stress was 28.10 MPa. The maximum principal stress of the 8th layer is 101.26 MPa, the minimum principal stress is 25.36 MPa, and the vertical stress is 28.82 MPa.

TABLE 1 Paleostress and main stress data during the main fracturing period in the study area.

Layer	Rock sample number	Horizontal maximum principal stress (MPa)	Horizontal minimum principal stress (MPa)	Vertical stress (MPa)
Chang 8	1	103.6	26.7	29.3
	2	102.5	26.1	28.9
	3	100.8	25.4	28.8
	4	100.5	25.2	28.9
	5	98.9	23.4	28.2
Chang 7	6	98.4	24.7	28.5
	7	92.7	19.4	28.0
	8	91.4	18.9	28.1
	9	99.1	25.1	28.3
	10	95.8	21.5	27.6



FIGURE 2
Experimental setup diagram.

3 Rock mechanics parameter testing

3.1 Experimental equipment and steps

The uniaxial and triaxial strength testing equipment used in this experiment (Figure 2) consists of five main parts: a high-temperature and high-pressure triaxial chamber, a confining pressure system, an axial pressure system, a heating and constant temperature system, and a data acquisition and control system. The design of the triaxial chamber is based on a confining pressure of 100 MPa and a diameter of 50 mm to accommodate rock samples. The internal design of the high-pressure kettle has a compensation function for the confining pressure of the system during loading, which can self-offset the upward force on the plunger due to the confining pressure. Thus, in triaxial experiments, the longitudinal pressure exerted by the press on the rock sample is equal to the differential pressure exerted on the rock sample, making the operation and use of the press very convenient. The confining pressure and axial pressure of the triaxial chamber are controlled and pressured by electro-hydraulic servos. In the experiments, the axial and transverse strains and axial loads of the rock samples were measured by sensors mounted in a high-pressure kettle, and the data signals were transmitted to a computerized automated collection and control system. It enables automatic data collection, storage, processing and plotting of stress-strain curves.

The experimental steps are as follows:

(1) The processed rock sample is placed in a high-pressure vessel.
(2) Open the computer data collection system, adjust the program, and everything is in a ready state; During uniaxial testing, the hydraulic press is directly turned on to apply axial load to the sample, and the data collection system collects and records the stress and strain of the rock sample during the loading process until the rock sample is damaged and loading stops. During triaxial testing, a high-pressure pump is used to apply confining pressure to a certain value, and then a hydraulic press is turned on to apply axial load to the sample. The data collection system collects and records the stress and strain of the rock sample during the loading process, until the rock sample is damaged and loading stops.
(3) At the end of the experiment, a computer data acquisition system is used to draw the stress-strain curve, which can be saved as a file or printed out by a printer.

3.2 Calculation of rock mechanics parameters

The experimental data collected by the testing machine can be processed by a computer to obtain a stress-strain curve, and the elastic modulus can be calculated using the following formula:

$$E = \frac{\Delta\sigma_a}{\Delta\varepsilon_a} \tag{4}$$

Where, E is elastic modulus, MPa. $\Delta\sigma_a$ is axial stress increment, MPa. $\Delta\varepsilon_a$ is axial strain increment.

The calculation formula for Poisson's ratio of rocks:

$$\nu = \frac{\Delta\varepsilon_r}{\Delta\varepsilon_a} \tag{5}$$

TABLE 2 Experimental data results of mechanical properties of samples in the study area.

Work area	Rock type	Young's modulus (GPa)	Poisson's ratio
Xiasiwan	Type I	20.23	0.32
	Type II	25.46	0.24
	Type III	40.51	0.19
	Type IV	49.63	0.17
	Surrounding rock	35.08	0.20
Huangjialing	Type I	15.73	0.33
	Type II	22.43	0.28
	Type III	34.16	0.23
	Type IV	47.51	0.18
	Surrounding rock	33.86	0.21

Where, v is Poisson's ratio, Dimensionless. $\Delta\varepsilon_a$ is the axial strain increment, Dimensionless. $\Delta\varepsilon_r$ is the radial strain increment, Dimensionless.

From the triaxial compressive strength test, the failure strength of the specimens under different confining pressures can be obtained. The Mohr Coulomb criterion is used to regress the experimental data, and the internal friction angle and cohesion of the specimens can be obtained.

3.3 Experimental results of rock mechanics

This experiment will divide the samples obtained in each study area into four categories based on sand mud ratio and sedimentary facies. At the same time, the average mechanical properties of the samples obtained near the edge of each study area will be used as a representative of the mechanical properties of the surrounding rocks in the study area. After experiments, as shown in Table 2.

4 Numerical simulations of paleotectonic stress field in reservoirs

4.1 Principles of finite element numerical simulation

The finite element method (FEM) is widely used to solve mathematical, physical, and engineering problems, also known as finite element numerical simulation. The basic principle of finite element method is to solve boundary value problems of partial differential equations through variational methods. The overall idea is to subdivide the large problem into smaller finite element elements. As the large solving model is subdivided, each small element has a single and simple form, which is easy to solve. Each element is connected by nodes, and algebraic methods are introduced to associate the nodes with the internal solution quantity of the element. Then, the simple equation finite element modeling generated by a single element is integrated into a total system of equations to model the entire problem. Finally, the variational method in the variational principle is used to minimize the relevant error function and obtain the optimal solution.

As a type of complex material unit, geological bodies can be divided into individual small, homogeneous, and simple form units using finite element method. By dividing a large number of fine and simple structural units and accumulating the units, close to the actual geological conditions can be obtained, and reasonable results can be obtained. Analyzing the distribution pattern of ground stress in reservoirs through finite element numerical simulation is helpful in understanding the structural morphology of oil and gas bearing basins, analyzing the migration patterns of oil and gas, and most importantly, predicting the distribution of fractures in reservoirs.

4.2 Finite element numerical simulation of paleostress field

The *in situ* stress field is the fundamental cause of structural fractures in reservoirs. Therefore, the study of structural *in situ* stress is crucial for analyzing and studying fractures. In order to quantitatively simulate the stress state of each point in the study area, this paper uses numerical simulation methods to study the tectonic stress field. In this numerical simulation, the geological body data obtained from reservoir modeling is mainly relied on, and on the basis of mainly considering the shale content, the stress effect inside the reservoir and the main factors controlling the distribution of fractures are comprehensively considered for numerical simulation. Because the fractures in the underground Siwan and Huangjialing work areas of the Ordos Basin were mainly formed during the Indosinian tectonic geological movement. Therefore, this article uses the finite element numerical simulation method and relevant software to conduct a study on the Indosinian *in situ* stress finite element numerical simulation of the Chang 7 and Chang 8 reservoirs in the study area.

The process of finite element numerical simulation mainly includes the establishment of geological models, mechanical models, and digital models. Among them, the establishment of geological models is the key to finite element numerical simulation, the establishment of mechanical models is the key to converting geological models into numerical calculations, and the

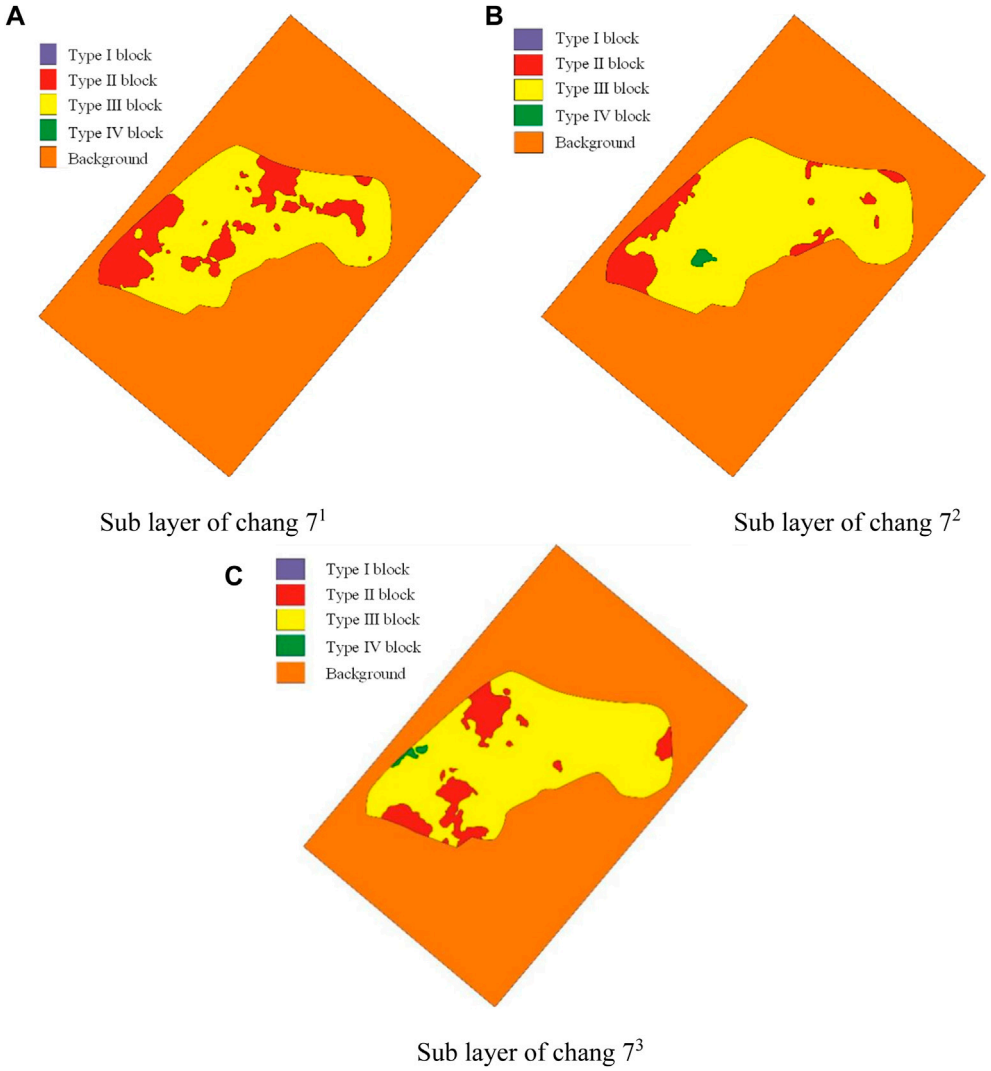


FIGURE 3
Geological models of each sub layer of Xiasiwan Chang 7. **(A)** Sub layer of chang 7¹ **(B)** Sub layer of chang 7² **(C)** Sub layer of chang 7³.

establishment of mathematical models is the process of quantitative prediction of fractures in the research area.

The establishment of this research model mainly considers the following four points:

(1) The clarity of studying bulk unit materials indicates that different materials undergo different deformations under stress.
(2) The selection and limitation of geological isolation bodies.
(3) The zoning of geological bodies has different rock mechanics parameters in different regions.
(4) Determination and experimental analysis of rock mechanical parameters in different attribute areas. The dynamic mechanical parameters obtained from rock mechanics experiments and the static mechanical parameters calculated from logging data are converted to obtain the rock mechanics parameters of the entire area, such as Young's modulus, Poisson's ratio, cohesion, internal friction angle, etc. The key is the selection of rock mechanics parameters, which greatly affects the accuracy of the simulation. The simulated rock mechanics parameters were obtained through acoustic emission experiments.

4.2.1 Geological model of the work area

Geological models should accurately reflect the surface structure and sedimentary environment of ancient geological periods. In order to develop a geological model, it is necessary to consider in a comprehensive way the sedimentary microstructure, the sand-to-soil ratio, the structural evolution history, and the logging data of the study area. Combined with experimental data on indoor rock mechanics, a geological model of the actual work area should be divided into zones. Each zone has different rock mechanics parameters, that is, different compressive and stabilizing forces corresponding to stress effects. In geological models, the main parameters used are the Young's modulus and the Poisson's ratio.

Based on the actual tectonic movement in the study area, through the observation of outcrop structural deformation (including joints, folds, faults, etc.) in the Ordos Basin and the

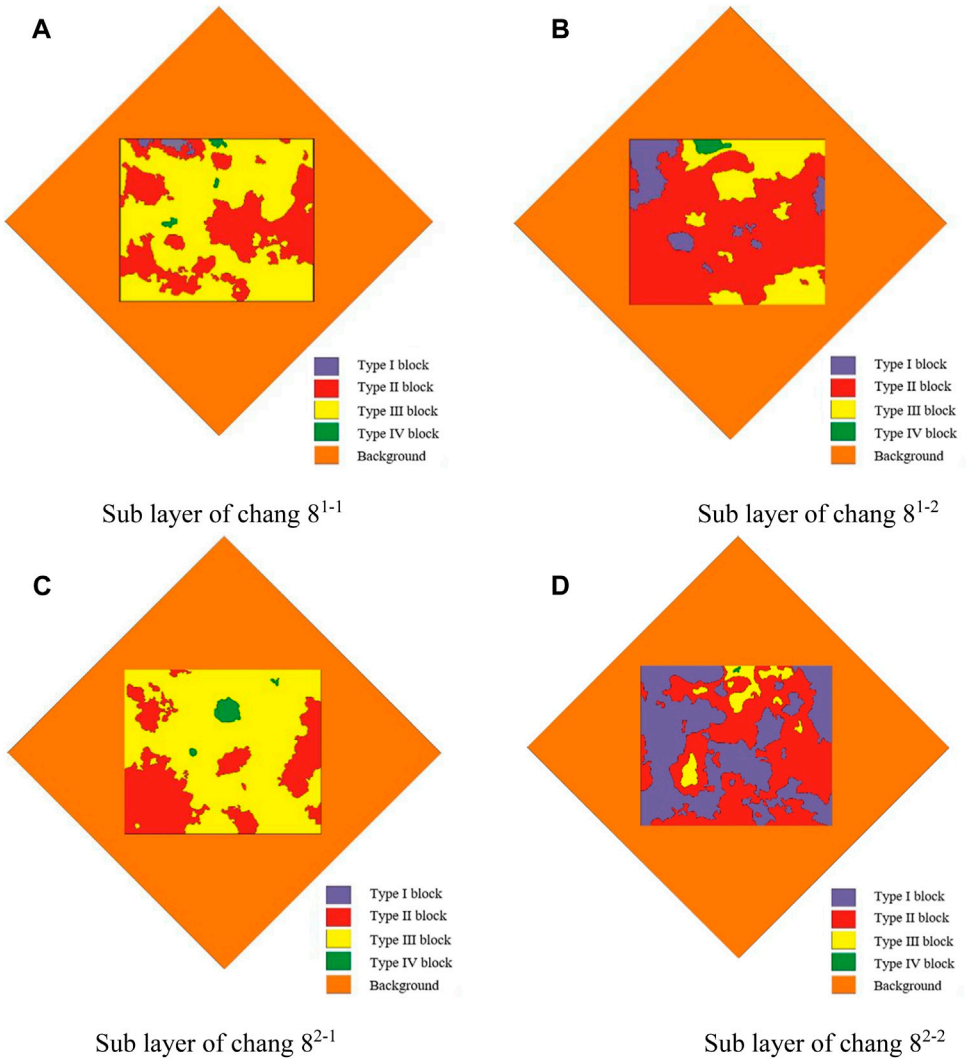


FIGURE 4
Geological models of each sub layer of Chang 8 in Huangjialing. **(A)** Sub layer of chang 8^{1-1} **(B)** Sub layer of chang 8^{1-2} **(C)** Sub layer of chang 8^{2-1} **(D)** Sub layer of chang 8^{2-2}.

establishment of structural formation sequences, it can be concluded that since sedimentation, the main period of fracture formation in the study area has been the Indosinian ancient tectonic movement. Thus, the data obtained from acoustic emission can be identified as representing the ancient stress state of the Indosinian period. Based on the results of acoustic emission experiments, numerical simulation calculations of the Indosinian period were conducted on the main source rocks in the area (Figures 3, 4). Due to the monoclinic structure of the study area, which is relatively simple in structure, there was no significant tectonic movement during the geological history period. Therefore, in this simulation, the current stratigraphic structure map approximately represents the ancient topography during the formation of the two stages of fracture.

As shown in the above Figure 4, based on the ratio of structural highs to sand content, combined with the degree of structural deformation, and taking into account geological factors, the geological bodies in the work area were classified into attributes, and geological models were established for their main production layers. Each work area is divided into 5 different attribute units, and the mechanical properties of the same class of attribute units within each work area are the same. The mechanical properties of the same class of attribute units vary between work areas. Different attribute units have been selected to test their rock mechanical properties, and the conclusions can be found in the rock mechanical experiments mentioned above.

4.2.2 Mechanical and mathematical models of the work area

The mechanical model is built on top of a geological model whose stress conditions and boundary constraints are mainly determined by combining the actual situation in the studied region with the main stress conditions studied during each phase of the orogeny. Based on field outcrop and core observation research, the mechanical model in this numerical model adopts the method of adding maximum principal stress in the NE-SW direction (2,200 m), adding minimum principal stress in the NW-NE direction, and without

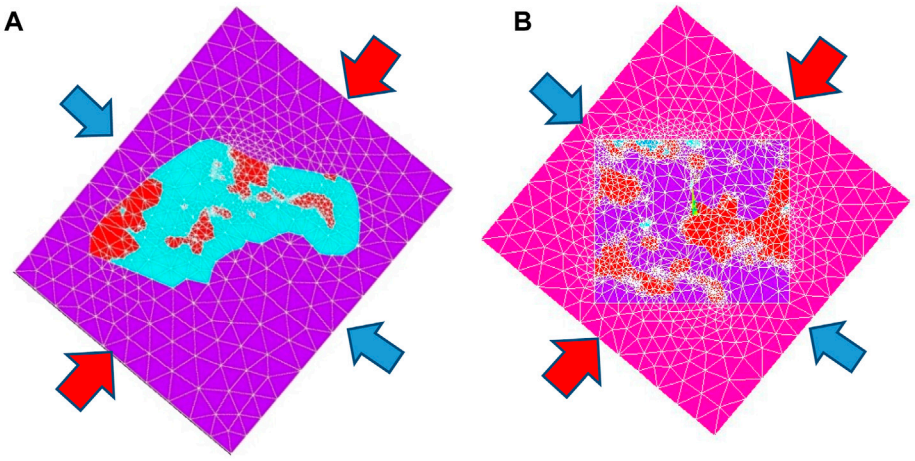


FIGURE 5
Schematic diagram of small layer mechanical model and grid division. **(A)** Irregular shape of the work area (Sub layer of chang 7^1 in Xiasiwan) **(B)** Rectangular work area (Sub layer of chang 8^{1-1} Huangjialing).

any constraints around (Figure 5A). This can effectively remove boundary effects and provide model prediction accuracy. The mathematical model mainly solves differential equations under the control of the physical properties of the reservoir. It is built on geological and mechanical models, and different computational and grid partitioning schemes can be chosen based on the actual geological features and accuracy requirements. This study comprehensively considers the complexity of stratigraphic zoning and adopts the triangulation method for calculation (Figure 5B).

4.3 Finite element numerical simulation results of paleostress field

4.3.1 Direction of principal stress

Numerical simulation shows that during the Indosinian period, the direction of rock mechanical properties in different blocks and layers in a single work area changed slightly, but due to the absence of faults, the structure was relatively simple and the overall direction remained unchanged (as shown in Figures 6, 7). The yellow arrow represents the minimum principal stress direction, while the blue arrow represents the maximum principal stress direction. It can be seen that the maximum principal stress directions of the four work areas in the entire research area remain basically in the NE-SW direction.

4.3.2 Distribution of differential stress magnitude

Through numerical simulation, it was found that the distribution range of differential stress varies slightly among different research layers due to differences in their internal structural morphology and rock composition, but the overall difference is not significant (Table 3).

In the same research horizon, the distribution of differential stress during the Indosinian period is controlled by multiple factors, among which the mechanical properties of rocks and the direction of principal stress have a significant impact. In areas with low Poisson's ratio and high Young's modulus, the differential stress is generally higher. At the same time, the distribution of differential stress is patchy and banded, with the extension direction of the band parallel to the maximum principal stress direction (Figures 8, 9).

By comparing the differential stress distribution map with the lithological distribution maps obtained in the other sections, it is found that the differential stress shows a significant increase in areas with high sand content and a significant decrease in areas with high mud content. There is a good correspondence between lithology and the magnitude of differential stress. The reason for this is that lithology largely controls the mechanical properties of the mechanical units, which are the main factors governing the distribution of differential stresses. Moreover, there is a good correlation between the distribution of the lithology and the differential stress.

5 Comprehensive evaluation of the plane development law of natural fractures

5.1 Evaluation principle of reservoir fracture plane development law

Underground rock masses can rupture and create fractures under *in situ* stress. According to the theory of elastic mechanics, the elastic strain energy accumulates inside a solid during deformation and its magnitude can be measured by the strain energy density. The strain of elastic materials follows the

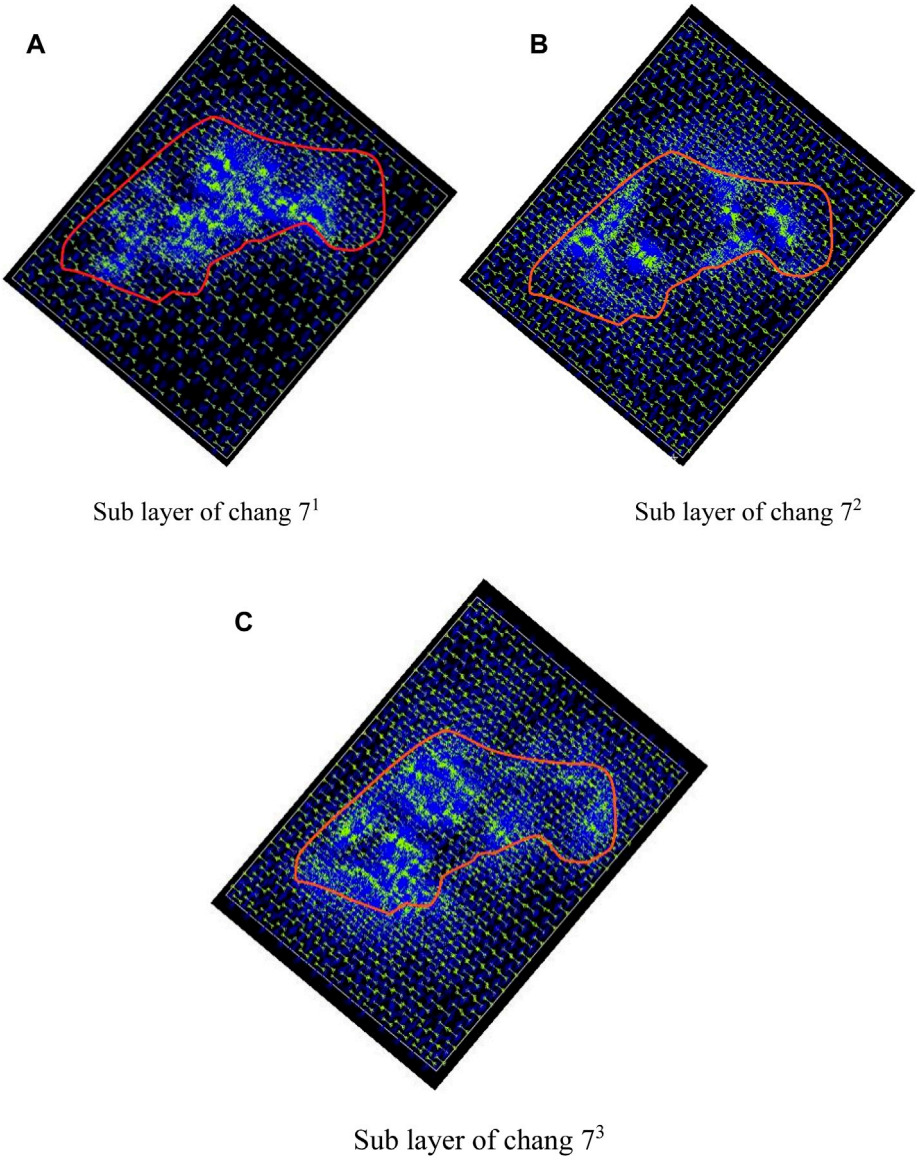


FIGURE 6
Schematic diagram of main stress directions for each small layer of Xiasiwan Chang 7. **(A)** Sub layer of chang 7^1 **(B)** Sub layer of chang 7^2 **(C)** Sub layer of chang 7^3.

generalized Hooke's law, so that the elastic strain energy of a rock can be calculated in terms of stress and strain. According to maximum strain energy density theory and maximum tensile stress theory in brittle fracture mechanics, fracture occurs when the release rate of elastic strain energy accumulated within the rock is equal to the energy required to generate a fracture surface per unit area. In this way, we can fully evaluate the planar development law of reservoir fracture based on the ancient stress field, provided we obtain the mechanical properties of the rock.

When a rock fractures, some of the strain energy released is used to offset the surface energy required for the newly added fracture surface area, while the rest is released in the form of elastic waves (cross-sectional energy). For fractures, the elastic wave energy is very small and negligible, so the partial strain energy released within the unit is equal to the energy required for the newly added fracture surface area. If ω_f is considered as the remaining strain energy density after subtracting the elastic strain energy density f that must be overcome to generate fractures from the current strain energy density of the unit, the calculation formula for fracture volume density ω_e is:

$$D_{vf} = \frac{S_f}{V} = \frac{\omega_f}{J} = \frac{\omega - \omega_e}{J} = \frac{1}{2EJ}\left[\sigma_1^2 + \sigma_2^2 + \sigma_3^2 - 2\mu\left(\sigma_1\sigma_2 + \sigma_2\sigma_3 + \sigma_1\sigma_3\right)\right] - \frac{\omega_e}{J} \quad (6)$$

Where, D_{vf} is the volume density of fractures within a unit, which is the ratio of the total surface area of the fracture body to the volume of the unit body, m^2/m^3. S_f is the new fracture surface area, m^2. V represents the volume of the characterized unit, m^3;ω_f is the strain energy density required for the newly added fracture

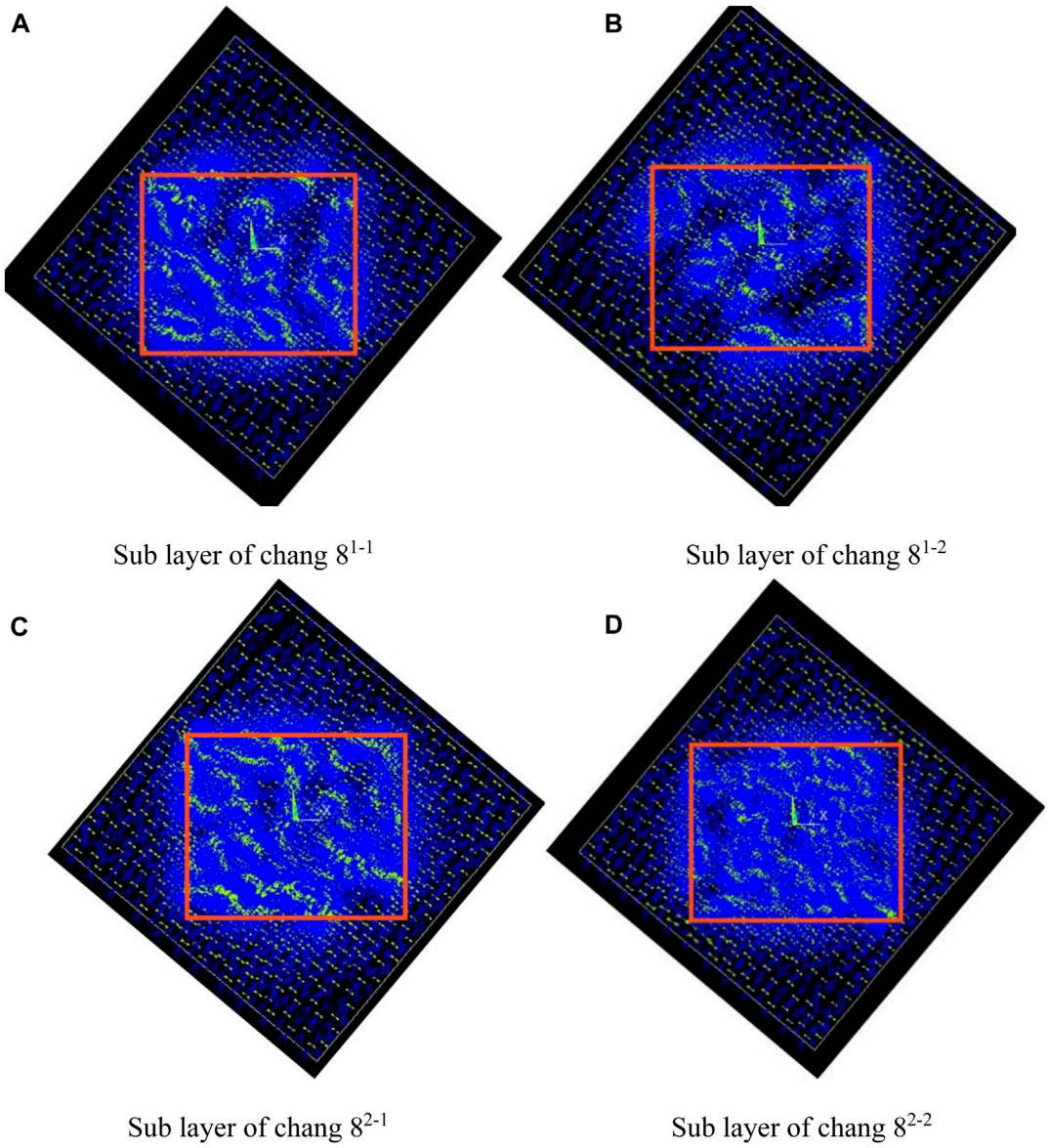


FIGURE 7
Schematic diagram of main stress directions for each sub layer of Huangjialing Chang 8. **(A)** Sub layer of chang 8^{1-1} **(B)** Sub layer of chang 8^{1-2} **(C)** Sub layer of chang 8^{2-1} **(D)** Sub layer of chang 8^{2-2}.

TABLE 3 Distribution of differential stress in the study area.

Work area	Layer	Distribution range of ancient differential stress (MPa)
Xiasiwan	Chang 7^1	57.88–95.29
	Chang 7^2	49.21–106.67
	Chang 7^3	55.30–105.57
Huangjialing	Chang 8^{1-1}	51.56–126.23
	Chang 8^{1-2}	48.52–115.75
	Chang 8^{2-1}	52.67–114.12
	Chang 8^{2-2}	34.89–125.38

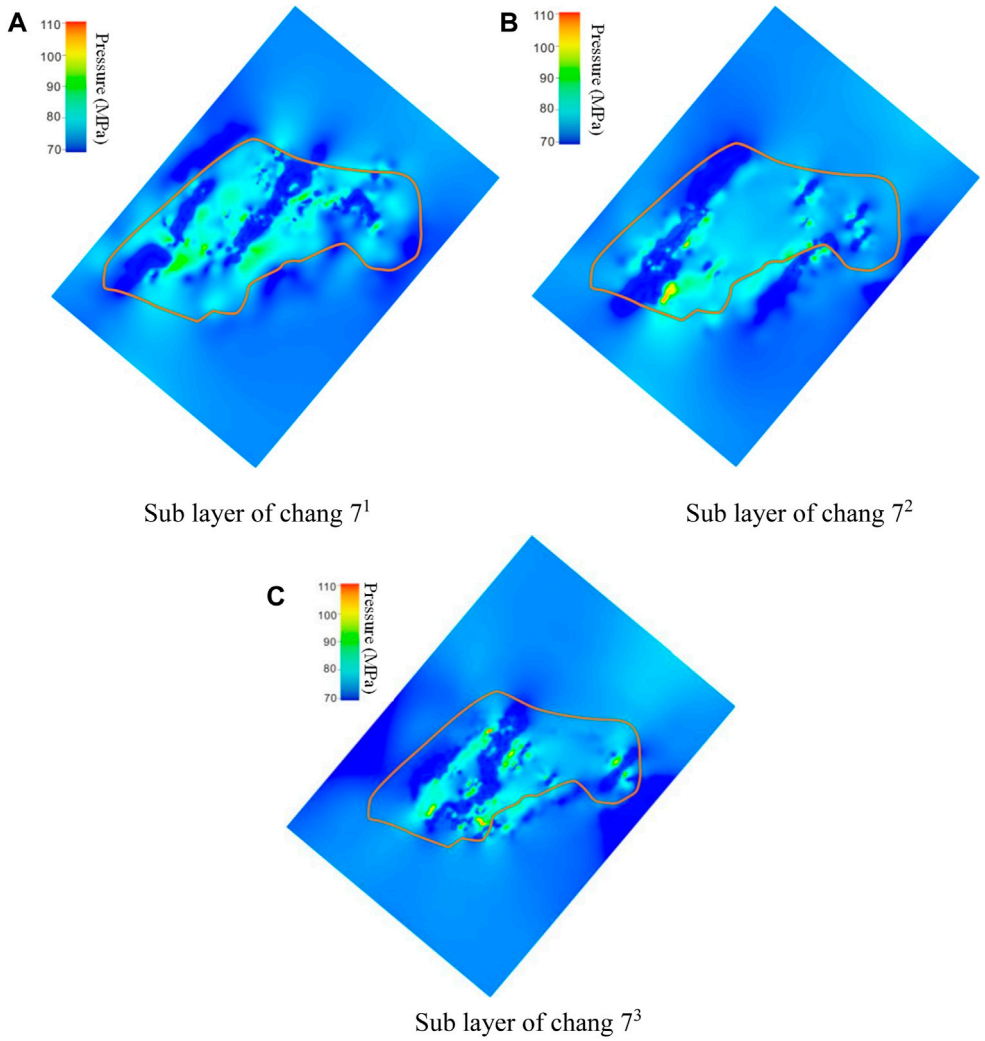


FIGURE 8
Distribution of differential stress in different layers of Xiasiwan Chang 7. **(A)** Sub layer of chang 7^1 **(B)** Sub layer of chang 7^2 **(C)** Sub layer of chang 7^3.

surface area, J/m³. *J* is the energy required to generate fractures per unit area, J/m². ω is the strain energy density, J/m ³;ω_e is the elastic strain energy density that must be overcome to generate fractures, J/m³. *E* is the elastic modulus, MPa. μ is the stiffness coefficient, N/m. σ_1, σ_2, σ_3 are the maximum principal stress, intermediate principal stress, and minimum principal stress, MPa.

Due to the different mechanical properties of brittle elastic rocks under compressive stress and tensile stress, it is necessary to analyze the various *in situ* stress states that actually exist. In fact, the vast majority of the geostress field in the region is a three-dimensional non-uniform compressive stress field dominated by horizontal stress, with two principal stress directions approximately horizontal (σ_H and σ_h) An approximate vertical (σ_v) It can be divided into three types and four types of geostress: the maximum principal stress direction of Class I geostress is vertical, and $\sigma_V > \sigma_H > \sigma_h$. The minimum principal stress direction of Class II ground stress is vertical, and $\sigma_H > \sigma_h > \sigma_v$. The middle principal stress direction of Class III geostress is vertical, and $\sigma_H > \sigma_v > \sigma_h$. Type I geostress can be further divided into two types: type I_a geostress and type I_b geostress $\sigma_v > \sigma_H > \sigma_h > 0$; Type I_b geostress $\sigma_v > 0$, σ_H or σ_h has a value less than zero or both. Therefore, Type I_a, Type II, and Type III geostress are in a triaxial compressive geostress state, while Type I_b geostress is in a geostress state with tensile stress present.

When the local stress type is type I_a, type II, or type III ground stress, the rock is in a three-dimensional compressive stress state, and the fracture of the rock is mainly shear and compressive shear. The Coulomb Mohr fracture criterion can be used as the fracture criterion. If the minimum principal stress σ If σ_3 is known, the minimum value of the maximum principal stress for rock fracture is:

$$\sigma_p = \frac{2C_0 \sin 2\theta + (1 + \cos 2\theta)\sigma_3}{1 - \cos 2\theta} \tag{7}$$

The shear failure rate σ_P is the stress on the fracture surface (σ_p) The shear strength of the rock, i.e., the ability to resist failure under

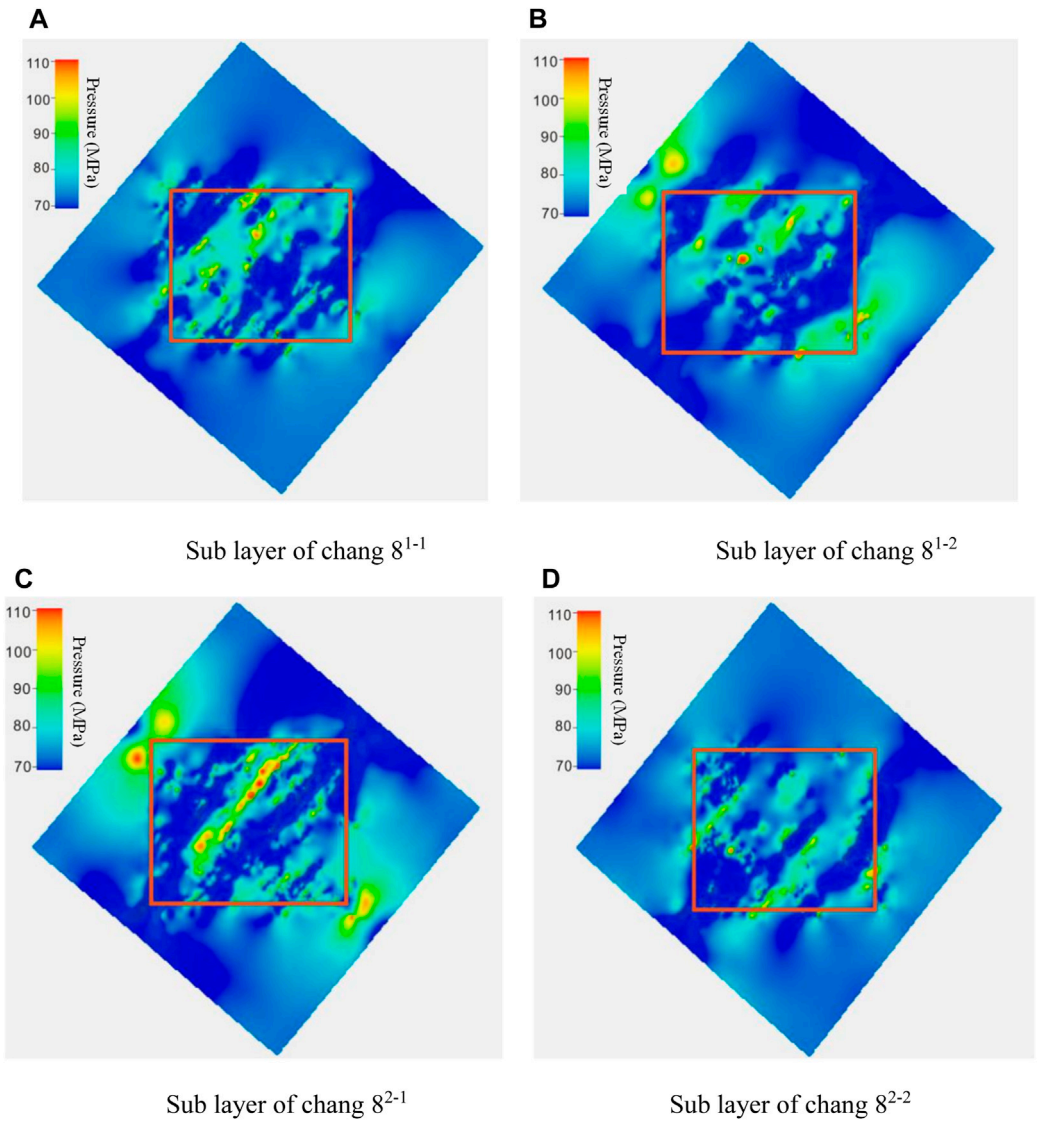


FIGURE 9
Distribution of differential stress in different sub layers of Huangjialing Chang 8. **(A)** Sub layer of chang 8^{1-1} **(B)** Sub layer of chang 8^{1-2} **(C)** Sub layer of chang 8^{2-1} **(D)** Sub layer of chang 8^{2-2}.

shear $[\sigma_p]$ The ratio of is usually taken as a positive value, and its expression is:

$$P = \left| \frac{\sigma_p}{[\sigma_p]} \right| \tag{8}$$

When the local stress type is type I_b, if there is tensile stress on the protruding side of the rock layer under longitudinal bending folding and the overall rock layer under transverse bending, the rock fracture is mainly tensile fracture and shear fracture. The Coulomb Moore criterion is no longer applicable, and the Griffith criterion is used for fracture judgment. It can be used to determine whether rocks undergo irreversible deformation and tensile fracture when subjected to external stress. The mathematical expression is as follows:

$$\sigma_t = \frac{(\sigma_1-\sigma_2)^2 + (\sigma_2-\sigma_3)^2 + (\sigma_1-\sigma_3)^2}{24(\sigma_1+\sigma_2+\sigma_3)} \text{ (When } \sigma_1 + 3\ \sigma_3 > 0) \tag{9}$$

$$\sigma_t = \sigma_1 \text{ (When } \sigma_1 + 3\ \sigma_3 < 0) \tag{10}$$

The tensile fracture rate T is the ratio of the stress on the fracture surface and tensile strength of the rock, i.e., the ability to resist failure under tension $[(\sigma_t)]$, shear stress refers to the force under shear, usually taken as a positive value, and its expression is:

The tensile fracture rate T is the ratio of the stress (σ_t) on the fracture surface to the tensile strength of the rock $[(\sigma_t)]$, which is the resistance to failure under tension. Shear stress refers to the force when subjected to shear, usually taken as a positive value, and its expression is:

$$T = \left| \frac{\sigma_t}{[\sigma_t]} \right| \tag{11}$$

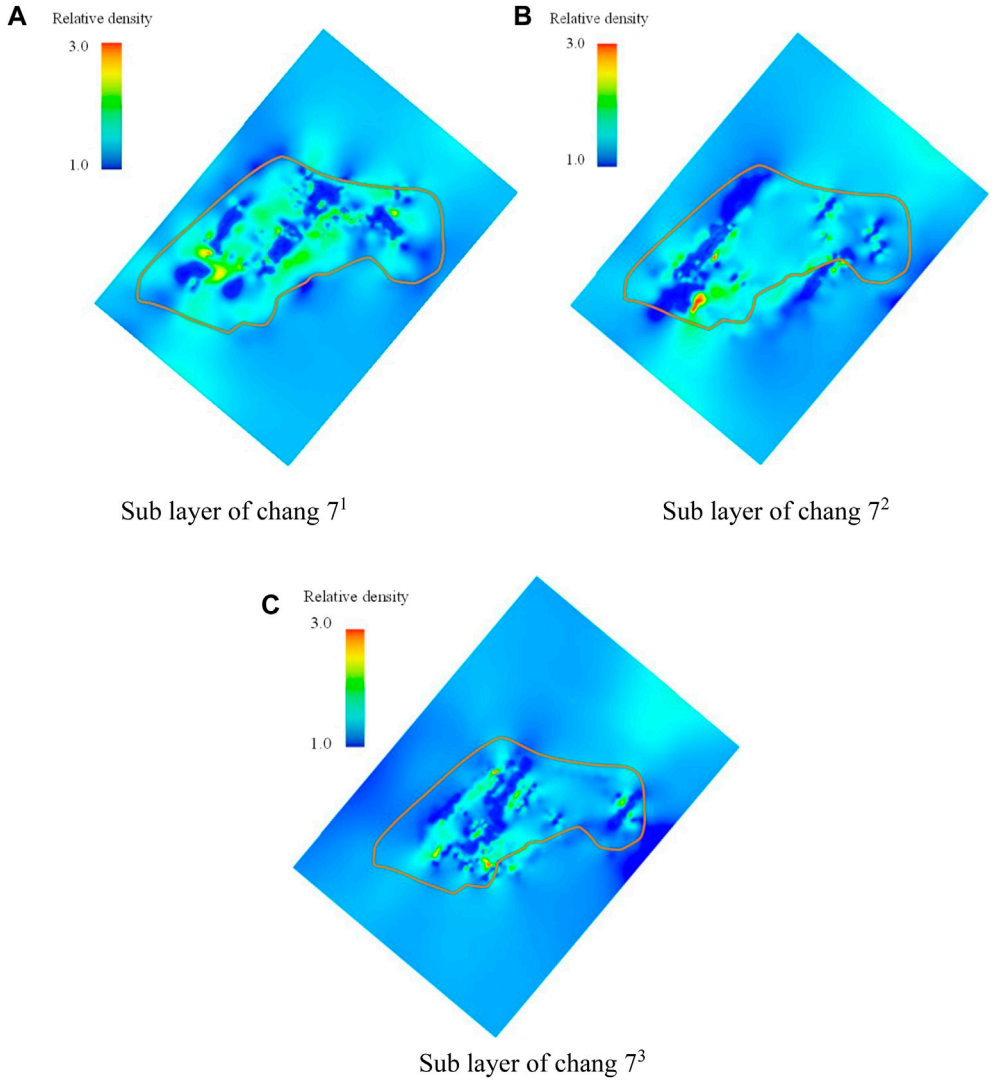


FIGURE 10
Distribution of relative density of fractures in various small layers of Xiasiwan Chang 7. **(A)** Sub layer of chang 7^1 **(B)** Sub layer of chang 7^2 **(C)** Sub layer of chang 7^3.

The fracture coefficients *P* and *T* of tension and shear can qualitatively characterize the degree of fracture development. When a rock layer ruptures, the degree of fracture is positively correlated with the fracture coefficient. In this fracture simulation, the relative size of the fracture rate is used as the "relative fracture density" to qualitatively describe the distribution of fractures.

5.2 Comprehensive evaluation of reservoir fracture development

Based on the results of numerical simulation of ancient stress, a comprehensive evaluation was conducted on the distribution of relative density of the study layers in each work area (Figures 10, 11). In general, the distribution of the relative density corresponds to, or differs from, the distribution of the differential pressure, and is generally governed by the mechanical properties of the rock within the attribute cell, and also by the relative position of the attribute cell. In areas with high sand content, the relative density of fractures is high. The fracture zone has continuity and is distributed in strips whose extension direction is parallel to the direction of maximum principal stress. Plane heterogeneities due to fractures in the studied regions were found sequentially from top to bottom in the Huangjialing Chang 8 layer and the Xiasiwan Chang 7 layer.

In terms of comparison between research areas, by observing the relative density of fractures in each work area, it can be found that the distribution of fractures in the Xiasiwan Chang 7 oil layer group is the most uniform, while the Huangjialing Chang 8 oil layer group is more uniform.

6 Conclusion

(1) The maximum principal stress, minimum principal stress, and vertical stress of the study block during the most intense

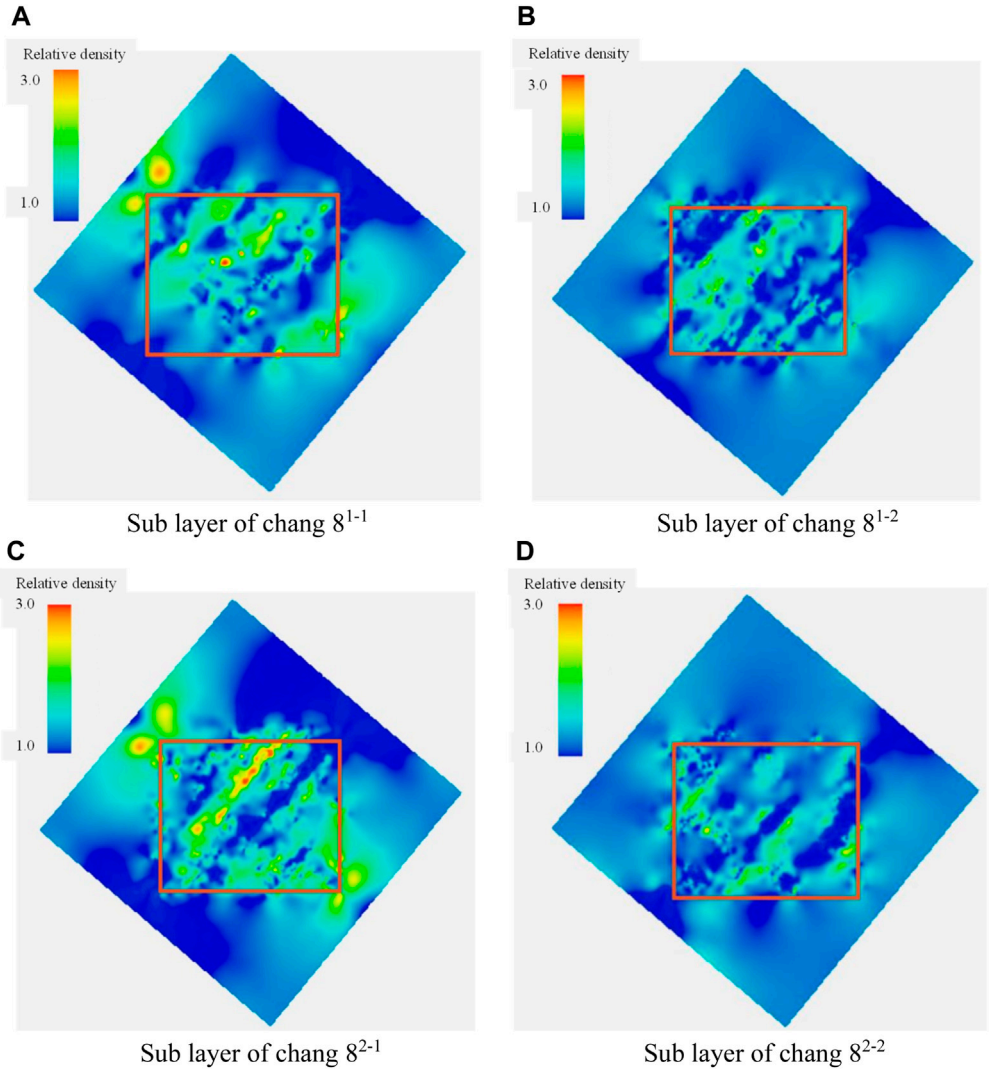


FIGURE 11
Distribution of relative density of fracks in each sub layer of Chang 8 in Huangjialing. **(A)** Sub layer of chang 8^{1-1} **(B)** Sub layer of chang 8^{1-2}. **(C)** Sub layer of chang 8^{2-1} **(D)** Sub layer of chang 8^{2-2}.

geological activity and fracture formation period were 94.67 MPa, 21.58 MPa, and 28.07 MPa, respectively. During this period, there is a slight change in the direction of the principal stress within a single work area, while the overall direction remains the same. The direction of maximum principal stress remains essentially in the NE-SW direction.

(2) The numerical simulation of stress field shows that due to the absence of faults and relatively simple structure, during the Indosinian period, the ancient stress direction of the Chang 7 and Chang 8 oil layers remained generally unchanged, and the maximum principal stress direction remained basically in the NE-SW direction. In particular, however, within small layers, the direction of the paleostress varies slightly in different blocks and layers around the NE-SW direction due to changes in the mechanical properties of the rock.

(3) During the Indosinian period, the differential stress of the ancient stress field between the Chang 7 and Chang 8 oil layers gradually increased with the deepening of the layer depth, and the overall difference was not significant. The maximum differential stress occurs in the Chang 8 oil layer in Huangjialing. In contrast to the other work zones, the differential stress is most uniform in the Chang 7 oil layer group at Xiasiwan. The distribution of differential stresses is controlled by a variety of factors, among which the mechanical properties of the rock and the direction of the principal stress have a significant influence. In regions with low Poisson ratio and high Young's modulus, the differential stress is generally higher. The distribution of the differential stress has continuity and is distributed in strips whose extension direction is parallel to the direction of maximum principal stress.

(4) The distribution of relative density and differential pressure of natural fractures in the Chang 7 and Chang 8 oil layers in the study area are influenced by the dual effects of rock mechanical properties and the relative position of mechanical units. Based on the mechanical analysis, it can be concluded that the planar heterogeneity due to fractures in the studied regions is from high

to low in the Huangjialing Chang 8 layer group and the Xiasiwan Chang 7 layer group, respectively.

Data availability statement

The raw data supporting the conclusion of this article will be made available by the authors, without undue reservation.

Author contributions

LL: Conceptualization, Data curation, Investigation, Methodology, Writing–original draft, Writing–review and editing. MW: Data curation, Formal Analysis, Methodology, Project administration, Supervision, Writing–original draft. YW: Methodology, Project administration, Supervision, Validation, Writing–original draft. YG: Investigation, Methodology, Supervision, Visualization, Writing–original draft. SL: Writing–original draft, Writing–review and editing.

Funding

The author(s) declare financial support was received for the research, authorship, and/or publication of this article. This work was supported by the National Natural Science Foundation of China: Study of the dynamic characteristics of methane/carbon dioxide in shale heterogeneous reservoirs under multi-field coupling (Program No. 41772150).

Acknowledgments

The authors are grateful for the support of the Shaanxi Yanchang Petroleum (Group) Co., Ltd.

Conflict of interest

Authors LL and YG were employed by Shaanxi Yanchang Petroleum (Group) Co., Ltd. Author YW was employed by Changqing Downhole Technology Operation Company of Chuanqing Drilling Engineering Co., Ltd. Author SL was employed by Engineering Research Institute of PetroChina Southwest Oil and Gas Field Company.

The remaining author declares that the research was conducted in the absence of any commercial or financial relationships that could be construed as a potential conflict of interest.

Publisher's note

All claims expressed in this article are solely those of the authors and do not necessarily represent those of their affiliated organizations, or those of the publisher, the editors and the reviewers. Any product that may be evaluated in this article, or claim that may be made by its manufacturer, is not guaranteed or endorsed by the publisher.

References

Ding, W. L., Zeng, W. T., Wang, R. Y., et al. (2016). Method and application of tectonic stress field simulation and fracture distribution prediction in shale reservoir. *Earth Sci. Front.* 23 (2), 63–74. doi:10.13745/j.esf.2016.02.008

Feng, J., Shi, S., Zhou, Z., Li, X., and Luo, P. (2019). Characterizing the influence of interlayers on the development and distribution of fractures in deep tight sandstones using finite element method. *J. Struct. Geol.* 123, 81–95. doi:10.1016/j.jsg.2019.03.009

Gong, L., Su, X., Gao, S., Fu, X., Jabbari, H., Liu, B., et al. (2019). Characteristics and formation mechanism of natural fractures in the tight gas sandstones of Jiulongshan gas field, China. *J. Petroleum Sci. Eng.* 175, 1112–1121. doi:10.1016/j.petrol.2019.01.021

Guo, P., Yao, L., and Ren, D. (2016). Simulation of three-dimensional tectonic stress fields and quantitative prediction of tectonic fracture within the Damintun Depression, Liaohe Basin, northeast China. *J. Struct. Geol.* 86, 211–223. doi:10.1016/j.jsg.2016.03.007

Haimson, B. C., and Herrick, C. G. (1985). *In-situ* stress evaluation from borehole breakouts: experimental studies. *Proc. 26th U. S. Symposium Rock Mech.*, 1207–1218.

Hu, L. (2022). A review of mechanical mechanism and prediction of natural fracture in shale. *Arabian J. Geosciences* 15 (6), 474. doi:10.1007/s12517-022-09786-w

Hu, Z. S., Peng, D. J., and Dai, D. S. (1994). Numerical simulation of fault stress and fracture distribution within Lower Permian local structures in southern Sichuan. *Xinjiang Pet. Geol.* 15 (2), 158–162.

Huang, L., He, R., Yang, Z., Tan, P., Chen, W., Li, X., et al. (2023). Exploring hydraulic fracture behavior in glutenite formation with strong heterogeneity and variable lithology based on DEM simulation. *Eng. Fract. Mech.* 278, 109020. doi:10.1016/j.engfracmech.2022.109020

Huang, L., Liu, J., Zhang, F., Dontsov, E., and Damjanac, B. (2019). Exploring the influence of rock inherent heterogeneity and grain size on hydraulic fracturing using discrete element modeling. *Int. J. Solids Struct.* 176, 207–220. doi:10.1016/j.ijsolstr.2019.06.018

Jaeger, J. C., Cook, N. G. W. W., and Zimmerman, R. W. (2007). *Fundamentals of rock mechanics*. Malden, MA, USA: Blackwell Publishing Ltd.

Khair, H. A., Cooke, D., and Hand, M. (2015). Paleo stress contribution to fault and natural fracture distribution in the Cooper Basin. *J. Struct. Geol.* 79, 31–41. doi:10.1016/j.jsg.2015.07.007

Li, H. (2021). Quantitative prediction of complex tectonic fractures in the tight sandstone reservoirs: a fractal method. *Arabian J. Geosciences* 14, 1986–2016. doi:10.1007/s12517-021-08344-0

Li, H., Lin, C. Y., Ren, L. H., Zhang, G. Y., Chang, L. J., and Dong, C. M. (2021). Quantitative prediction of multi-period tectonic fractures based on integrated geological-geophysical and geomechanics data in deep carbonate reservoirs of Halahatang oilfield in northern Tarim Basin. *Mar. Petroleum Geol.* 134, 105377. doi:10.1016/j.marpetgeo.2021.105377

Li, Z. M., and Zhang, J. Z. (1997). *Ground stress and oil and gas exploration and development*. Beijing, China: Petroleum Industry Press, 138–140.

Liu, S., Feng, J., Osafo, J. A., Li, G., and Li, G. (2023). Quantitative prediction of multistage fractures of ultra-deep tight sandstone based on the theory of minimum energy dissipation. *Front. Earth Sci.* 10, 1036493. doi:10.3389/feart.2022.1036493

Lou, Y., Wu, Z., Sun, W., Yin, S., Wang, A., Liu, H., et al. (2020). Study on failure models and fractal characteristics of shale under seepage-stress coupling. *Energy Sci. Eng.* 8 (5), 1634–1649. doi:10.1002/ese3.621

Murray, G. H., Jr (1977). Quantitative fracture study—sanish pool, mckenzie county, north Dakota. *AAPG Bull.* 52 (1), 57–65. doi:10.1306/5D25C293-16C1-11D7-8645000102C1865D

Peska, P., and Zoback, M. D. (1995). Compressive and tensile failure of inclined well bores and determination of *in situ* stress and rock strength. *J. Geophys. Res. Solid Earth* 100 (B7), 12791–12811. doi:10.1029/95JB00319

Qin, Q. R., Zhang, L. H., Deng, H., Su, P. D., and Wang, Z. Y. (2004). Determination of magnitude of palaeo-tectonic stress and application to tectonic geological modeling. *Chin. J. Rock Mech. Eng.* 23 (23), 3979–3983.

Ren, Q. Q., Jin, Q., Feng, J. W., and Li, M. P. (2019). Simulation of stress fields and quantitative prediction of fractures distribution in upper Ordovician biological limestone formation within Hetianhe field, Tarim Basin, NW China. *J. Petroleum Sci. Eng.* 173, 1236–1253. doi:10.1016/j.petrol.2018.10.081

Rouchet, J. D. (1981). Stress fields, a key to oil migration. *AAPG Bull.* 65 (1), 74–85. doi:10.1306/2f919774-16ce-11d7-8645000102c1865d

Song, H. Z., Jia, C. z., Ou, Y. J., et al. (2001). *Theory and methods of fractured reservoir research*. Beijing, China: Petroleum Industry Press, 288–304.

Tan, P., Fu, S. H., Chen, Z. W., and Zhao, Q. (2023). Experimental investigation on fracture growth for integrated hydraulic fracturing in multiple gas bearing formations. *Geoenergy Sci. Eng.* 231, 212316. doi:10.1016/j.geoen.2023.212316

Tan, P., Jin, Y., Pang, H. W., et al. (2021). Hydraulic fracture vertical propagation behavior in transversely isotropic layered shale formation with transition zone using XFEM-based CZM method. *Eng. Fract. Mech.* 248, 107707. doi:10.1016/j.engfracmech.2021.107707

Tan, P., Pang, H. W., Zhang, R. X., Jin, Y., Zhou, Y., Kao, J., et al. (2020). Experimental investigation into hydraulic fracture geometry and proppant migration characteristics for southeastern Sichuan deep shale reservoirs. *J. Petroleum Sci. Eng.* 184, 106517. doi:10.1016/j.petrol.2019.106517

Wang, S., Li, H., Lin, L., and Yin, S. (2022). Development characteristics and finite element simulation of fractures in tight oil sandstone reservoirs of Yanchang formation in western Ordos basin. *Front. Earth Sci.* 9, 823855. doi:10.3389/feart.2021.823855

Wang, X. S., Li, J. C., Wang, S. M., and Song, H. Z. (1997). Oil and gas accumulation and structural stress field in Tarim basin. *Acta Pet. Sin.* 18 (1), 23–27. doi:10.7623/syxb199701004

Wang, Y. (2013). *Research on prediction methods and applications of fractured oil and gas reservoirs*. Wuhan, China: China University of Geosciences.

Wei, J., and Sun, W. (2016). Tectonic fractures in the lower cretaceous Xiagou formation of Qingxi oilfield, Jiuxi Basin, NW China part one: characteristics and controlling factors. *J. Petroleum Sci. Eng.* 146, 617–625. doi:10.1016/j.petrol.2016.07.042

Wu, Y., Liu, C., Zang, Q., Awan, R. S., Li, G., Wu, Y., et al. (2022a). Simulation of tectonic stress field and prediction of tectonic fractures in shale reservoirs: a case study of the Ansai area in the Ordos Basin, China. *Interpretation* 10 (3), SJ15–SJ28. doi:10.1190/INT-2021-0181.1

Wu, Z., Tang, M., Zuo, Y., Lou, Y., Wang, W., Liu, H., et al. (2022b). Acoustic emission-based numerical simulation of tectonic stress field for tectoclase prediction in shale reservoirs of the northern Guizhou area, China. *Energy Geosci.* 3 (4), 436–443. doi:10.1016/j.engeos.2021.10.005

Wu, Z., Zuo, Y., Wang, S., Chen, J., Wang, A., Liu, L., et al. (2017). Numerical study of multi-period palaeotectonic stress fields in lower cambrian shale reservoirs and the prediction of fractures distribution: a case study of the Niutitang formation in Feng'gang No. 3 block, South China. *Mar. Petroleum Geol.* 80, 369–381. doi:10.1016/j.marpetgeo.2016.12.008

Xu, Y. F., Zuo, Y. J., Wu, Z. H., and Sun, W. J. B. (2017). Numerical simulation of tectonic stress field and fracture prediction of Yanshan period in Fenggang area. *Coal Technol.* 36 (7), 128–130.

Zhang, D., Tang, J., Chen, K., Wang, K., Zhang, P., He, G., et al. (2022a). Simulation of tectonic stress field and prediction of tectonic fracture distribution in Longmaxi Formation in Lintanchang area of eastern Sichuan Basin. *Front. Earth Sci.* 10, 1024748. doi:10.3389/feart.2022.1024748

Zhang, H., Xu, G., Zhan, H., Li, X., and He, J. (2022b). Simulation of multi-period paleotectonic stress fields and distribution prediction of natural Ordovician fractures in the Huainan coalfield, Northern China. *J. Hydrology* 612, 128291. doi:10.1016/j.jhydrol.2022.128291

Zoback, M. D., Moos, D., Mastin, L., and Anderson, R. N. (1985). Wellbore breakouts and *in situ* stress. *J. Geophys. Res. Solid Earth* 90 (B7), 5523–5530. doi:10.1029/JB090iB07p05523

Zoback, M. D., and Peska, P. (1995). *In-situ* stress and rock strength in the GBRN/DOE pathfinder well, south eugene island, gulf of Mexico. *J. Petroleum Technol.* 47 (7), 582–585. doi:10.2118/29233-PA

frontiers | Frontiers in Energy Research

TYPE Original Research
PUBLISHED 24 November 2023
DOI 10.3389/fenrg.2023.1321114

Check for updates

OPEN ACCESS

EDITED BY
Peng Tan,
CNPC Engineering Technology R&D Company Limited, China

REVIEWED BY
Chaohua Guo,
China University of Geosciences Wuhan, China
Muchen Sun,
University of Arkansas, United States
Kai Gao,
University of Twente Enschede, Netherlands in collaboration with reviewer MS

*CORRESPONDENCE
Jiajun Li,
lijj_2021@petrochina.com.cn
Yongpeng Sun,
sunyongpeng@upc.edu.cn

RECEIVED 13 October 2023
ACCEPTED 13 November 2023
PUBLISHED 24 November 2023

CITATION
Wu J, Yang X, Li J, Liu W, Chen F, Huang S, Wang C and Sun Y (2023), Fracturing fluid flow characteristics in shale gas matrix-fracture system based on NMR method. *Front. Energy Res.* 11:1321114. doi: 10.3389/fenrg.2023.1321114

COPYRIGHT
© 2023 Wu, Yang, Li, Liu, Chen, Huang, Wang and Sun. This is an open-access article distributed under the terms of the Creative Commons Attribution License (CC BY). The use, distribution or reproduction in other forums is permitted, provided the original author(s) and the copyright owner(s) are credited and that the original publication in this journal is cited, in accordance with accepted academic practice. No use, distribution or reproduction is permitted which does not comply with these terms.

Fracturing fluid flow characteristics in shale gas matrix-fracture system based on NMR method

Jianfa Wu[1], Xuefeng Yang[1], Jiajun Li[1]*, Wenping Liu[2], Feng Chen[2], Shan Huang[1], Chuanxi Wang[3] and Yongpeng Sun[3]*

[1]Shale Gas Research Institute of PetroChina, Southwest Oil&Gas Field Company, Chengdu, Sichuan, China, [2]PetroChina Southwest Oil&Gas Field Company, Chengdu, Sichuan, China, [3]Key Laboratory of Unconventional Oil & Gas Development, China University of Petroleum (East China), Ministry of Education, Qingdao, China

To understand the occurrence state of fracturing fluid in shale gas matrix-fracture system, an experimental method for evaluating fracturing fluid flow characteristics in matrix-fracture system was established. By using Nuclear Magnetic Resonance method, the flow characteristics of fracturing fluid were investigated from three processes of filtration, well shut-in and flowback. The T2 spectrum of fracturing fluid flow process and fracturing fluid saturation in matrix-fracture core model were clarified. The results demonstrate that the peak area of T2 spectra increases gradually during the filtration process, and the fracturing fluid quickly fills the fractures and matrix pores. During the well shut-in process, the fracturing fluid gradually flows from the fracture space to the matrix pores, and the signal of the matrix pores increases by 50.5%. During the flowback process, fracturing fluid flows out of the matrix and fracture. And when it reaches a stable state, the peak signal in the fracture decreases by 64.5% and the matrix signal reduces by 18.8%. The better the porosity and permeability characteristics of the core, the more likely the fracturing fluid is to stay in the formation and cannot be discharged. This paper would contribute to basic parameters for shale gas fracturing design and production strategy optimization.

KEYWORDS

shale gas, matrix-fracture system, fracturing fluid, occurrence characteristics, flow behavior

1 Introduction

As a kind of efficient and clean unconventional energy, shale resources account for 80% of global oil and gas resources and have broad development prospects (Jiang et al., 2016; Zou et al., 2016; He et al., 2021). Vigorously developing shale resource exploitation technology is also of strategic significance for alleviating the contradiction between energy supply and demand and solving the problem of energy security, and is the key field for increasing and stabilizing oil and gas resources in the future (Dehghanpour et al., 2012; Sun et al., 2018).

Shale reservoir is characterized by low porosity and low permeability, which is far lower than the permeability of conventional rock reservoir. At present, shale reservoir is mainly exploited by hydraulic fracturing technology (Dehghanpour et al., 2013; Huang et al., 2023a; Tan et al., 2023). Through continuous injection of fracturing fluid into the reservoir, fracture continue to expand with the migration of fracturing fluid, and a complex fracture network

TABLE 1 Formation water mineral composition.

Ingredient	Content/(mg·L^{-1})
NaCl	18,837
KCl	201.19
$CaCl_2$	650.29
$MgCl_2$	230.92
$NaHCO_3$	2,170.91
$NaSO_4$	2,986.35
Total	25,076.66

will be established in the reservoir (Huang et al., 2019; Tan et al., 2021). Shale reservoir has complex pore network, fluid flow characteristics in shale reservoir are affected by fluid-solid interaction, physical and chemical properties, adsorption and dissolution properties, etc (Huang et al., 2023b).

The flow characteristics of fluids in pores have been studied extensively (Driskill et al., 2013; Ren et al., 2015; Bi, 2018). You et al. studied the flow rule of nC8 in quartz pores under the condition of water film through molecular dynamics, and found that layered structures were formed on the surface of quartz pores and liquid-liquid slip occurred at the oil-water interface, revealing the migration mechanism of oil in quartz pores under the condition of water film (Zhou et al., 2017; Liu et al., 2019). By analyzing a variety of cationic surfactants, Yang et al. studied their adsorption mechanism on the quartz surface and found that a double-layer structure was formed at the critical micelle concentration, indicating that the surfactant affected the properties of the cationic adsorption film on the quartz surface (Wu et al., 2017; Su et al., 2019; Hou, 2020). Wang et al. investigated the flow pattern of oil-water two phases in calcite pores through molecular dynamics and found that liquid-liquid slip existed at the oil-water interface (Yang, 2016; You et al., 2018). Tong et al. used molecular dynamics to study the fluid behavior and flow in clay pores and concluded that the fluid properties in clay pores would affect the efficiency of oil recovery, indicating that diffusion, viscosity reduction and other factors are the main mechanisms affecting enhanced oil recovery (Tong et al., 2021; Wang et al., 2021). Shale fracturing has formed a complex porous - fracture dual medium, in which the fluid flow state is still unclear (Ma, 2018; Ma et al., 2019; Zhai, 2021).

In this paper, the basic physical properties of the shale core such as porosity and permeability are tested first, and the parameters such as the viscosity and surface tension of the fracturing fluid are tested after the fracturing fluid is configured. A matrix-fractured shale core model was developed, and the T2 spectrum characteristics of fracturing fluid in the process of filtration, well shut-in and flowback were tested by means of low-field nuclear magnetic resonance experiment. The saturation characteristics of fracturing fluid in matrix and fracture were analyzed, and the flow characteristics of fracturing fluid in shale core were compared under different porosity and permeability parameters. In this paper, the flow characteristics of fracturing fluid in shale matrix-fracture are defined, which provides basic parameters for shale gas fracturing design and production capacity construction.

2 Experimental method

2.1 Experimental material

The experimental cores were shale cores from wells X9 and X7 of the Wufeng Formation and Longmaxi Formation in the Yongchuan area of southern Sichuan, both of which were processed into cylindrical specimens with a length of 3 cm and a diameter of 2.5 cm.

The experimental fluid was the slick water fracturing fluid provided by the fracturing site of PetroChina Southwest Oil and Gas Field Company, and was prepared by adding 0.025% drag reducer and 0.25% flowback additives to the formation water. The mineral composition of the formation water is shown in Table 1.

2.2 Experimental instrument

Smart-Perm Pulse Decay gas permeability measuring instrument (ULP-613, Yineng, Beijing, China), Helium porosity measuring instrument (PMI-100, Yineng, Beijing, China), Core Cutting machine (D24000, Dewalt, Maryland, United States), Nuclear Magnetic Resonance Online Analysis system (MacroMR12-150H-I, Niumag, Suzhou, China), High temperature and high pressure interface rheometer (TRACKER-S, Teclis, Auvergne, France), Rheometer (Haake MARS60, Thermo Scientific, Massachusetts, United States).

2.3 Experimental method

2.3.1 Core porosity and permeability parameters

Because the permeability of shale is generally at the Nano Darcy level, the pressure pulse Decay method is generally used to measure the permeability of shale. The shale cores from Wells X7 and X9 were selected and processed into 2.5–3 cm long core sections. After drying in the 110°C oven for 48 h, the permeability and porosity were measured by Smart-Perm pulse decay gas permeability measuring instrument and helium porosity measuring instrument.

2.3.2. Fracturing fluid basic property

According to the industry standard Shale Gas Fracturing Fluids Part 3: Performance Index and Evaluation Method of Continuous Mixing fracturing Fluid (NB/T14003.3-2017). After preparation of fracturing fluid, the surface tension of fracturing fluid was measured by Teclis Tracker high temperature and high pressure interfacial rheometer, and the viscosity of fracturing fluid at 170 s^{-1} was measured by HaakeMARS60 rheometer.

2.3.3 Fracturing fluid flow test

Because the permeability of shale is generally at the Nano Darcy level, the pressure pulse Decay method is generally used to measure the permeability of shale. The shale cores from Wells X7 and X9 were selected and processed into 2.5–3 cm long core sections. After drying in the 110°C oven for 48 h, the permeability and porosity were measured by Smart-Perm pulse decay gas permeability measuring instrument and helium porosity measuring instrument.

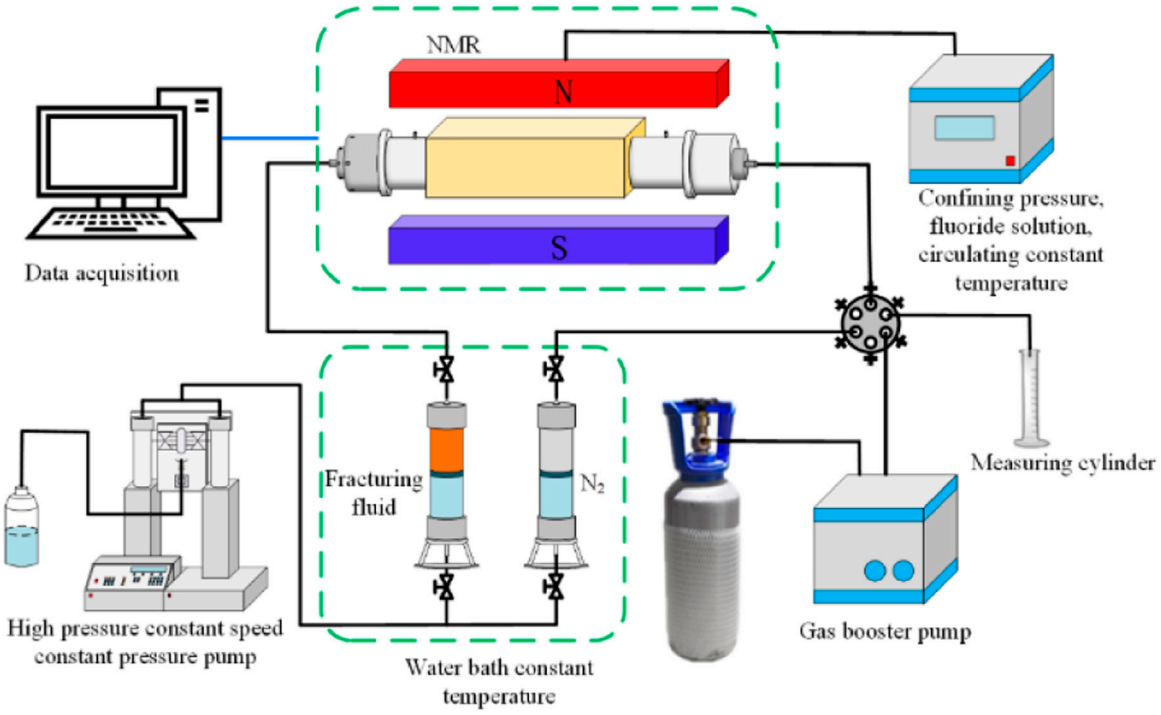


FIGURE 1
Flow chart of NMR on-line displacement evaluation system.

2.3.3.1 filtration process

① Open the heating device so that the temperature of the core holder rises to the set value and remains stable, and open the cold slot for coil cooling; ② Open the NMR measurement and analysis software, put the standard sample into the core holder, connect the experimental pipeline, and load the constant confining pressure; ③ Click cumulative sampling, measure the base signal of the core holder, and set a collection plan with an interval of 15 min; ④ Open the ISCO pump, set the constant pressure 6,895 kPa, click the execution plan, and start displacing at the same time; ⑤ Stop the experiment when the sampling trend line is stable, click on the inversion data, and obtain the T2 curve.

2.3.3.2 well shut-in process

① After the filtration curve is stable, turn off the ISCO pump and close both ends of the core holder; ② Set a new well shut-in acquisition plan, set acquisition sequence, sampling interval and sampling frequency; ③ Click the execution plan and start sampling; ④ Stop the experiment when the sampling trend line is stable, click on the inversion data, and obtain the T2 curve.

2.3.3.3 flowback process

① After the curve of the well shut-in process is stabilized, open both ends of the core holder and set a new flowback process acquisition plan; ② Fill the target pressure of nitrogen into the middle container with the help of the gas cylinder; ③ Set backflow displacement parameters and turn on the pump for constant pressure displacement; ④ Reduce the confining pressure so that the liquid in the annulus of the core and the core holder flows out, and then increase the confining pressure to the target value; ⑤ Stop the experiment when the sampling trend line is stable, click the inversion data to obtain the T2 curve, turn off the heating device, relieve the confining pressure, turn off the instrument, and end the experiment.

The flow chart of the experimental device is shown in Figure 1.

TABLE 2 Core porosity parameters of Wells X7 and X9.

Well number	Layer number	Porosity/ %	Permeability/ mD
Well X7	2	5.31–5.65	0.0022–0.0028
Well X7	3	5.30	0.00241
Well X7	4	5.44–5.52	0.00257–0.00265
Well X9	1	7.33–7.62	0.0167–0.0215
Well X9	2	8.45–10.12	0.0188–0.0258
Well X9	3	8.32–9.06	0.0206–0.0284

3 Results and analysis

3.1 Basic properties of core samples and fracturing fluid

The permeability and porosity were measured by Smart-Perm Pulse Decay gas permeability measuring instrument and helium porosity measuring instrument. The results are shown in Table 2.

As can be seen from Table 2: The core permeability of well X7 ranges from 0.0022 to 0.0028 mD, and the porosity ranges from

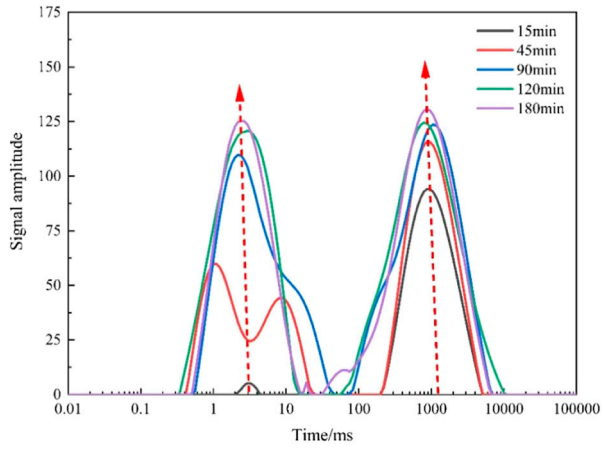


FIGURE 2
T2 spectrum during filtration process of layer 1 in well X9.

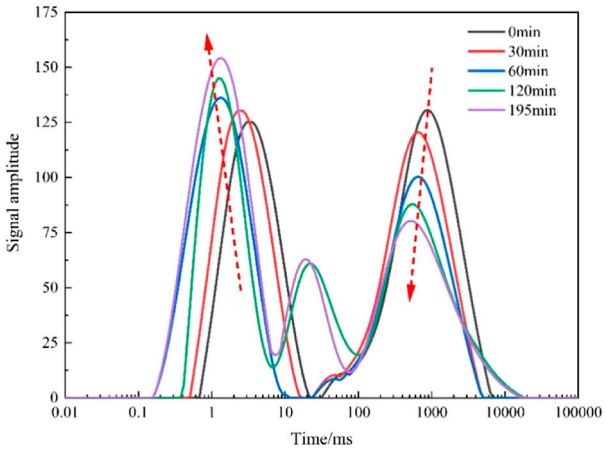


FIGURE 3
T2 spectrum during well shut-in process of layer 1 in well X9.

5.30% to 5.65%; the core permeability of well X9 ranges from 0.0167 to 0.0284 mD, and the porosity ranges from 7.33% to 10.12%, which can provide basic data for the analysis of subsequent experimental results.

The surface tension of fracturing fluid was 44.5 mN/m by means of Teclis Tracker high temperature and high pressure interfacial rheometer. The rheometer was used to test the rheological property of fracturing fluid. The viscosity of fracturing fluid was 2.38 mPa·s at 170 s^{-1}. Fracturing fluid surface tension and viscosity parameters meet the requirement of industry standards.

3.2 T2 spectrum characteristics of fracturing fluid flow in shale matrix-fracture system

3.2.1 T2 spectrum characteristics during filtration process

In the process of fracturing, it is sometimes difficult to avoid a large amount of fracturing fluid loss to the formation. Selecting a shale core of layer 1 in well X9 to make a matrix-fracture core model. In the experiment, 2.7 MPa filtration pressure difference was used to simulate the fracturing fluid filtration process, and T2 spectrum signals were collected every 15 min until the signals were stable. The spectrum diagram of typical T2 signals during the fracturing fluid loss process is shown in Figure 2.

It can be seen from Figure 2 that in the process of fracturing fluid filtration process, the T2 signal features obvious left and right peaks, with the left peak corresponding to semaphores in small matrix pores and the right peak corresponding to semaphores in fractures. Both matrix and fracture signals gradually increase with the increase of filtration time. The right fracture signal increases rapidly after the start of filtration process, and basically reaches the highest peak after 45 min of filtration process, and becomes completely stable after 180 min of filtration process, with the amplitude of fracture signal reaching 146.6 after stabilization. The left stromal signal rose slowly, but it was basically stable after 180 min, when the stromal signal amplitude was 126.8. During the filtration process, fracturing fluid gradually percolates into fractures and matrix pores under the action of filtration pressure difference, resulting in the rise of the T2 spectrum signal. The fracture space is larger than the matrix pores, and fracturing fluid is easier to flow in the fracture, so the fracture is quickly filled with fracturing fluid at the beginning of filtration process, and the corresponding fracture T2 spectrum on the right side increases rapidly with time. The pores of shale matrix are small, and the fracturing fluid flows slowly in the matrix, so the corresponding matrix T2 spectrum signal on the left side rises slowly. When fracturing fluid flows through the matrix, it preferentially fills large pores, and then gradually flows into small pores. Therefore, the T2 peak signal on the left side shows a trend of gradually shifting to the left.

3.2.2 T2 spectrum characteristics during well shut-in process

After fracturing is completed, the well is usually closed for a period of time to restore formation pressure. After the completion of the filtration test, to simulate the flow of fracturing fluid during the well shut-in process, both ends of the core holder were closed and the well shut-in period was 2.5 h, during which T2 signals were collected every 15 min. The typical T2 signal variation spectrum during the well shut-in process is shown in Figure 3.

As can be seen from Figure 3, during the well shut-in process, the signal quantity in the right fracture gradually decreases with the well shut-in time. After the well shut-in process is over, the fracture signal amplitude decreases by 16.1%. The left matrix signal increased significantly and gradually shifted to the left with the time of well shut-in. After 195 min of well shut-in, the increase of matrix pore signal value was as high as 50.5% compared with that after the end of filtration process. The results show that the fracturing fluid in the fracture will gradually flow into the matrix during the well shut-in process, causing the signal value in the right fracture to decrease, and the signal value in the left matrix pore to increase gradually. Fracturing fluid will preferentially invades into the matrix with larger pores, and then gradually permeate into smaller micropores. Therefore, the semaphore of fracturing fluid in the left pore will gradually increase while it will show a trend of deviation to the left. The matrix signal changes obviously during the well shut-in process, fracturing fluid enters the matrix space in large quantities, and

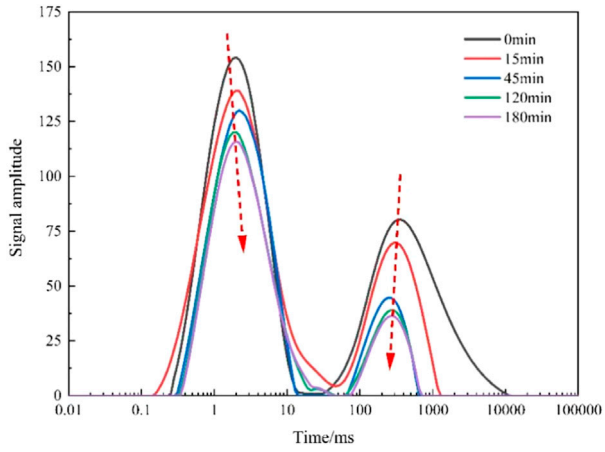


FIGURE 4
T2 spectrum during filtration process of layer 1 in well X9.

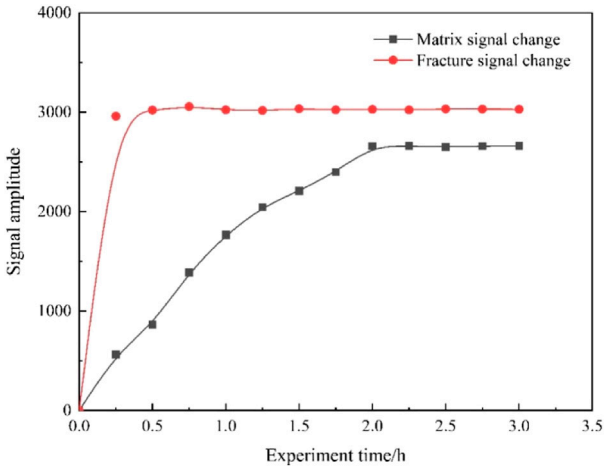


FIGURE 5
The accumulated signal during filtration process of layer 1 in well X9.

fracturing fluid utilization of the matrix is significantly improved after well shut-in closure.

3.2.3 T2 spectrum characteristics during filtration process

After the completion of well shut-in process, both ends of the core holder were opened, the flowback pressure difference of 1.3 MPa was adopted, and nitrogen was reverted into the core model from the outlet of the core holder to simulate the flowback process until the T2 spectrum signal was stable. The spectrum diagram of typical T2 signals during the flowback process is shown in Figure 4.

As can be seen from Figure 4, during the flowback process of fracturing fluid, the signals in both matrix and fracture decreased significantly, and the fracture signal decreased rapidly. The signal in fracture basically decreased to the lowest value 45 min after the flowback process began, and after the flowback reached a stable state, the peak signal in the right fracture decreased by as much as 64.5% compared with the end of well shut-in process. The left matrix signal decreased slowly and uniformly, and the decrease was smaller after stabilization, which decreased by 18.8% compared with the peak matrix signal after the completion of well shut-in process. Due to good fracture permeability, flowback fluid preferentially enters larger pores with a small pressure gradient, forming advantageous channels. During the filtration process, fracturing fluid mainly flowback from fractures, and the degree of matrix utilization is low. Therefore, the T2 signal of fractures decreases significantly, while the matrix signal decreases only slightly, so it is difficult to flowback fracturing fluid in shale reservoirs.

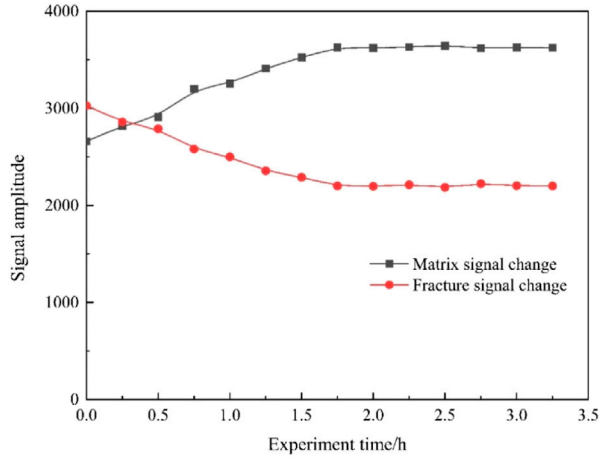


FIGURE 6
The accumulated signal during well shut-in process of layer 1 in well X9.

3.3 Fracturing fluid saturation characteristics in shale matrix-fracture system

3.3.1 Saturation characteristics during filtration process

According to the experimental results of T2 spectrum characteristics of fracturing fluid flow, the signal amplitudes of filtration process were calculated, and the variation curves of matrix and fracture signal amplitudes over time were plotted, respectively. The results are shown in Figure 5.

It can be seen from Figure 5 that both matrix and fracture signal amplitudes increase with the increase of filtration time. The fracture signal amplitude increases rapidly at the beginning, and reaches a stable state 0.5 h after the filtration process begins. The amplitude of the matrix signal rose slowly, rising at a constant rate during 0–2 h of filtration process, and then reached a stable state. At the beginning of filtration loss, because the fracture permeability is good, the fracture is quickly filled with fracturing fluid, and the corresponding signal amplitude rises rapidly. When the fracture is completely filled with fracturing fluid, it reaches a stable state. The flow of fracturing fluid into the matrix is a slow percolation, so the signal amplitude in the matrix

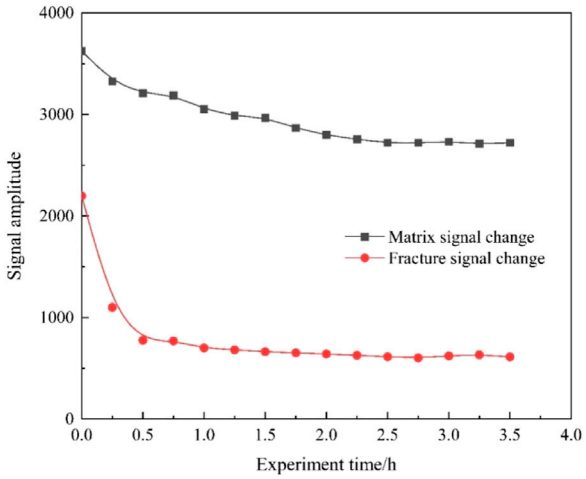


FIGURE 7
The accumulated signal during flowback process of layer 1 in well X9.

rises slowly. When the fracturing fluid enters the limiting small pores, the matrix-fracture model approaches the saturation state, and the matrix and fracture signal do not change.

3.3.2 Saturation characteristics during well shut-in process

The variation curves of matrix and fracture signal amplitudes over time during well shut-in process were plotted respectively, and the experimental results are shown in Figure 6.

It can be seen from Figure 6 that the fracture signal gradually decreases during the well shut-in process and becomes basically stable 2 h after the start of well shut-in process. After stabilization, the fracture signal decreases by 27.3% compared with the initial value. The matrix signal gradually increased and reached a stable state after 2 h, and the matrix signal increased by 36.3%. Due to the closure of the two ends of the core holder, the core model is that the fluid is isolated from the outside world and the fracturing fluid is restricted to flow in the matrix and fracture space during well shut-in process. Under the action of capillary force, the fracturing fluid in the fracture invades into the matrix pores, and fluid exchange occurs in the fracture and matrix. In the absence of foreign fluid intrusion or fracturing fluid outflow, the fracturing fluid in the fracture is less and less, and the fracturing fluid in the matrix gradually increases. The fracturing fluid volume reduced in the fracture is the increased fracturing fluid volume in the matrix pores.

3.3.3 Saturation characteristics during flowback process

The signal amplitudes of flowback process were calculated, and the variation curves of matrix and fracture signal amplitudes over time were plotted, respectively. The results are shown in Figure 7.

It can be seen from Figure 7 that both matrix and fracture signal amplitudes decrease with the increase of flowback time during the flowback process. The fracture signal amplitude decreased rapidly. The signal basically reached a stable state 1 h after the start of flowback process, and the signal after stability decreased by 55.1% compared with that at the end of the well shut-in process. The matrix signal amplitude decreased slowly during 0–2.5 h of flowback process, and then became basically stable, and the matrix signal amplitude decreased by 24.8%. During the flowback process, fracture permeability is high, which is the main body of fracturing fluid flowback, so the flowback rate is high, and the flowback is rapid, and the signal amplitude decreases and reaches the stable state faster. Due to the capillary force, fracturing fluid in the matrix is difficult to be driven out by nitrogen, so the matrix signal decreases slowly and the matrix flowback rate is low.

TABLE 3 The core porosity and permeability.

Core number	Porosity/%	Permeability/mD
X7-4	4.5	0.00157
X7-2	5.3	0.00224
X9-4	8.3	0.0284

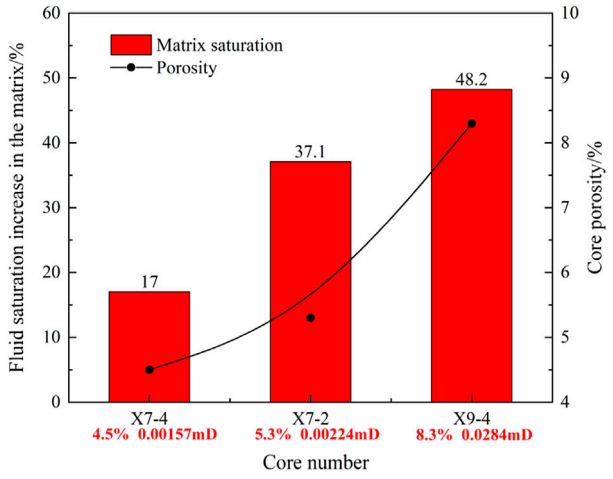


FIGURE 8
Comparison of matrix saturation during filtration process of different layers in well X7.

3.4 Comparison of fracturing fluid saturation in different porous cores

The difference in porosity and permeability parameters of shale reservoir is large, which will directly affect the flow behavior of fracturing fluid. In order to explore the influence of different porosity and permeability parameters on fracturing fluid flow behavior, three cores with different porosity and permeability parameters were selected for experiments. The selected cores simulated the three processes of fracturing fluid filtration, well shut-in and flowback, respectively, and calculated matrix saturation through T2 signal spectrum data. The core porosity and permeability parameters are shown in Table 3.

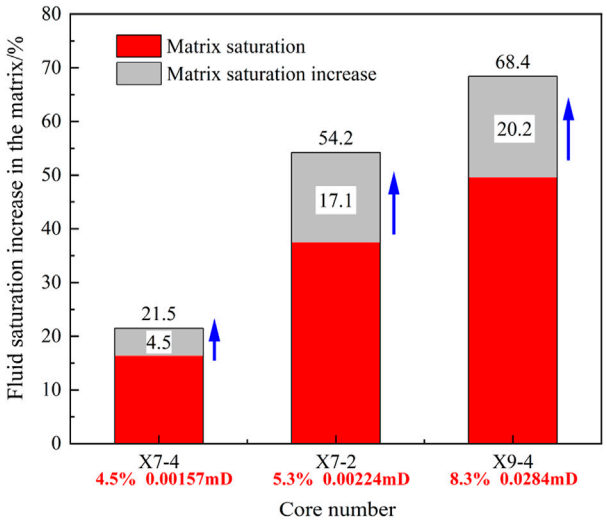


FIGURE 9
Comparison of matrix saturation during well shut-in process of different layers in well X7.

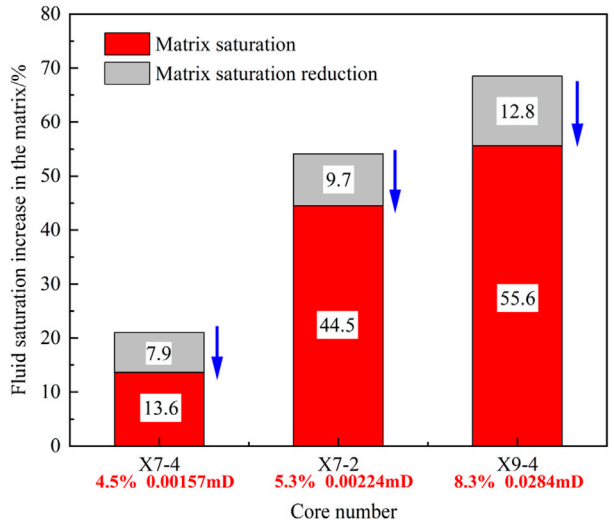


FIGURE 10
Comparison of matrix saturation during flowback process of different layers in well X7.

3.4.1 Matrix saturation characteristics during filtration process

Under the same fracturing technology (experimental conditions), the porosity and permeability of the core itself will also affect the flow behavior of fracturing fluid. The histogram of changes in matrix saturation with core porosity and the curve of core porosity are drawn, and the experimental results are shown in Figure 8.

It can be seen from Figure 8 that after the filtration process, the matrix saturation gradually increases with the improvement of the porosity and permeability of the core, that is, the larger the porosity and permeability of the core, the more likely the fracturing fluid is to filter out and enter the matrix, and the higher the filtration loss of the fracturing fluid. Core X9-4 has the best porosity and permeability properties. Compared with core X7-4, which has the worst porosity and permeability, the porosity of core X9-4 increases by 0.84 times and the permeability increases by 170.9 times. Therefore, the matrix saturation of core X9-4 after the end of filtration process is 31.2% higher than that of core X7-4. The analysis shows that the larger the porosity of the core, the more sufficient the pore space, the greater the permeability of the core, the better the connectivity between the pores, and the stronger the fluid passing ability. Therefore, the core with more pores and larger pore volume is more prone to fracturing fluid filtration. However, when the core matrix pores are small and the pore space connectivity is poor, it is more difficult for fracturing fluid to flow in them, and it is more difficult for fracturing fluid loss to occur.

3.4.2 Matrix saturation characteristics during well shut-in process

After the completion of the simulated fracturing fluid filtration process, the well shut-in process was continued to be simulated, and the changes of the T2 spectrum were monitored in real-time during the experiment until the spectrum signal was stable. The change of matrix saturation was calculated and a histogram of core matrix saturation change was drawn. The experimental results are shown in Figure 9.

As can be seen from Figure 9, the matrix water saturation of core models with different porosity and permeability properties increased after the completion of the well shut-in experiment, and the better the core porosity and permeability properties, the greater the matrix saturation increase. Core X7-4 has low porosity and low permeability, and has the worst porosity and permeability parameters. Even after well shut-in process, the increase of matrix saturation is still small, only 4.5%. Core X9-4 has the best porosity and permeability properties, and the final matrix saturation reaches 68.4% after well shut-in process completion, 2.2 times higher than that of core X7-4, and 20.2% higher than that of core X7-4 after completion of filtration process. The analysis shows that there is no foreign fluid entering during the well shut-in process, fracturing fluid flows in the matter-fracture system, and fracturing fluid will spontaneously enter the matrix pores through the fractures. When the porosity and permeability of the core are good, fracturing fluid makes it easier to enter the matrix. In the process of restoring formation pressure after pressurization, the formation matrix with better porosity and permeability conditions is more likely to enter more fracturing fluid, and a large amount of fracturing fluid will invade into the matrix space from the fracture channel, which may cause fracturing retention and cannot be excluded.

3.4.3 Matrix saturation characteristics during flowback process

After the well shut-in process, high-purity nitrogen was reverted into the back end of the core holder to simulate the fracturing fluid flowback process in the production process. After the stability of the experimental T2 spectrum, the change of matrix saturation was calculated and a histogram of the change of core matrix saturation was drawn. The experimental results are shown in Figure 10.

As can be seen from Figure 10, the matrix water saturation of the three core models with different porosity and permeability

parameters all decreased to a certain extent after the flowback experiment, and the reduction amplitude gradually increased with the increase of core porosity and permeability, and the better the core porosity and permeability properties, the higher the matrix residual saturation after the flowback experiment. Core X7-4 has the worst porosity parameters, and after the end of well shut-in process, the residual matrix saturation is only 13.6, which is 7.9% lower than that after the well shut-in test. Core X9-4 has the best porosity and permeability properties, and loses the most fracturing fluid in the filtration process, with a loss volume of 12.8%. However, its matrix residual saturation after flowback is still as high as 55.6%, which is 3.1 times higher than that of core X7-4. The analysis shows that, in the post-pressure production process, the core with better porosity and permeability parameters is more prone to fracturing fluid flowback, but due to sufficient pore space, a large amount of fracturing fluid still exists in the matrix after flowback process, while the matrix with poor properties is not prone to a large amount of fracturing fluid retention. Therefore, in the process of post-pressure production, there is a large amount of fracturing fluid retention in the formation matrix with good porosity and permeability conditions, which is more likely to cause formation damage and pollution, and more attention should be paid to the countermeasures for fracturing fluid damage.

4 Conclusion

(1) The fracture system has a fast filtration rate and is basically stabilized 45 min after filtration. The filtration in matrix is slow, and it takes 2 h to reach a stable state for our samples. In the process of filtration, fracturing fluid gradually percolates into fractures and matrix pores under the action of filtration pressure drop. It first fills the fracture space rapidly, and then enters the matrix pores slowly.

(2) Fluid exchange occurs in between fractures and matrix during the well shut-in process, and fracturing fluid in fractures migrates into matrix pores. 2 h after well shut-in, the matrix and fracture signals reached a stable state, and the fracture signal decreased by 27.1% and the matrix signal increased by 40.9% compared with the initial state.

(3) During the flowback process, the amplitude of fracture signal and matrix signal decreased rapidly. The fracturing fluid fluxed out of the fracture and matrix space. The fluid signal decreased by 55.1% in fracture and 24.8% in matrix, compared with the end of the well shut-in process. Some fracturing fluids are difficult to discharge from the matrix and fractures.

(4) The better the porosity and permeability parameters of the core, the easier the fracturing fluid is to filtrate into the core matrix. Core X9-4 has the best porosity and permeability, and the matrix residual saturation after filtration is as high as 55.6%, which is 3.1 times higher than that of core X7-4. At the same time, fracturing fluid with good porosity and permeability parameters is more likely to be retained, and more attention should be paid to fracturing fluid retention damage during hydraulic fracturing.

Data availability statement

The original contributions presented in the study are included in the article/Supplementary material, further inquiries can be directed to the corresponding author.

Author contributions

JW: Conceptualization, Writing–review and editing. XY: Data curation, Methodology, Writing–review and editing. JL: Investigation, Validation, Writing–original draft. WL: Methodology, Project administration, Resources, Writing–review and editing. FC: Data curation, Methodology, Writing–review and editing. SH: Investigation, Resources, Validation, Writing–review and editing. CW: Conceptualization, Investigation, Writing–review and editing. YS: Funding acquisition, Project administration, Writing–review and editing.

Funding

The author(s) declare financial support was received for the research, authorship, and/or publication of this article. This research was funded by Shandong Provincial Natural Science Foundation (ZR2023ME016) and Open Fund (YSK2022001) of Shale Gas Evaluation and Exploitation Key Laboratory of Sichuan Province.

Acknowledgments

The authors thank the editor, the associate editor, and the reviewers for their constructive comments, which improved this paper.

Conflict of interest

Authors JW, XY, JL, and SH were employed by Shale Gas Research Institute of PetroChina, Southwest Oil&Gas Field Company. Authors WL and FC were employed by PetroChina Southwest Oil&Gas field Company.

The remaining authors declare that the research was conducted in the absence of any commercial or financial relationships that could be construed as a potential conflict of interest.

Publisher's note

All claims expressed in this article are solely those of the authors and do not necessarily represent those of their affiliated organizations, or those of the publisher, the editors and the reviewers. Any product that may be evaluated in this article, or claim that may be made by its manufacturer, is not guaranteed or endorsed by the publisher.

References

Bi, W. (2018). *Study on influence factors of propping fractures conductivity in shale formation*. China: China University of Petroleum.

Dehghanpour, H., Lan, Q., Saeed, Y., Fei, H., and Qi, Z. (2013). Spontaneous imbibition of brine and oil in gas shales: effect of water adsorption and resulting microfractures. *Energy & Fuels* 27 (6), 3039–3049. doi:10.1021/ef4002814

Dehghanpour, H., Zubair, H. A., Chhabra, A., and Ullah, A. (2012). Liquid intake of organic Shales. *Energy & Fuels* 26 (9), 5750–5758. doi:10.1021/ef3009794

Driskill, B., Walls, J., Sinclair, S. W., et al. (2013). "Micro-scale characterization of the Eagle Ford formation using SEM methods and digital rock modeling," in Unconventional Resources Technology Conference, Denver, Colorado, August, 2013.

He, X., Li, W., Dang, L., et al. (2021). Key technological challenges and research directions of deep shale gas development. *Nat. Gas. Ind.* 41 (1), 118–124. (ISSN 1000-0976; In Chinese). doi:10.3787/j.issn.1000-0976.2021.01.010

Hou, P. (2020). *Research on the proppant uneven distribution and conductivity of complex fracture network in shale gas reservoir*. Beijing, China: China University of Petroleum.

Huang, L., He, R., Yang, Z., Tan, P., Chen, W., Li, X., et al. (2023b). Exploring hydraulic fracture behavior in glutenite formation with strong heterogeneity and variable lithology based on DEM simulation. *Eng. Fract. Mech.* 278, 109020. doi:10.1016/j.engfracmech.2022.109020

Huang, L., Liu, J., Zhang, F., Dontsov, E., and Damjanac, B. (2019). Exploring the influence of rock inherent heterogeneity and grain size on hydraulic fracturing using discrete element modeling. *Int. J. Solids Struct.* 176, 207–220. doi:10.1016/j.ijsolstr.2019.06.018

Huang, L., Tan, J., Fu, H., Liu, J., Chen, X., Liao, X., et al. (2023a). The non-plane initiation and propagation mechanism of multiple hydraulic fractures in tight reservoirs considering stress shadow effects. *Eng. Fract. Mech.* 292, 109570. doi:10.1016/j.engfracmech.2023.109570

Jiang, Z., Wang, F., Duan, Y., and Zhou, J. (2016). China's gas market under new situations: trends and countermeasures-Taking Sichuan and Chongqing gas provinces as an example. *Nat. Gas. Ind.* 36 (4), 187–194. (ISSN 1000-0976; In Chinese). doi:10.1016/j.ngib.2016.05.002

Liu, Y., Gao, D., Li, Q., et al. (2019). Mechanical frontiers in shale-gas development. *Adv. Mech.* 49, 201901. doi:10.6052/1000-0992-17-020

Ma, D. (2018). *Study on fluid-solid coupling in multiple medium and its influence on seepage law for shale gas reservoirs*. Beijing, China: University of Science and Technology Beijing.

Ma, L., Zhang, C., Liu, D., et al. (2019). Preliminary study on the well-soaking adaptability after fracturing in fuling shale gasfield. *Special Oil Gas Reservoirs* 26 (1). doi:10.3969/j.issn.1006-6535.2019.01.026

Ren, K., Ge, H., Yang, L., et al. (2015). Imbibition experiment of shale and its application in flowback analysis. *Sci. Technol. Eng.* 15, 1671–1815. doi:10.3969/j.issn.1671-1815.2015.30.019

Su, J., Dong, W., Luo, H., et al. (2019). Quantitative test and analysis of clay surface hydration water based on low-field nuclear; magnetic resonance technology. *Acta Pet. Sincia* 40 (4), 468–474. doi:10.7623/syxb201904008

Sun, Z., Wang, Y., Wu, B., et al. (2018). Chemical reactions and effects of slick water fracturing fluid on the pore structures of shale reservoirs in different deposition environments. *J. Univ. Chin. Acad. Sci.* 35 (5), 712–719. doi:10.7523/j.issn.2095-6134.2018.05.019

Tan, P., Fu, S., Chen, Z., and Zhao, Q. (2023). Experimental investigation on fracture growth for integrated hydraulic fracturing in multiple gas bearing formations. *Geoenergy Sci. Eng.* 231, 212316. doi:10.1016/j.geoen.2023.212316

Tan, P., Jin, Y., Pang, H., et al. (2021). Hydraulic fracture vertical propagation behavior in transversely isotropic layered shale formation with transition zone using XFEM-based CZM method. *Eng. Fract. Mech.* 248, 107707. doi:10.1016/j.engfracmech.2021.107707

Tong, H., Liu, Z., Zhang, H., et al. (2021). Theory and method of temporary macrofracture plugging to prevent casing deformation in shale gas horizontal wells. *Nat. Gas. Ind.* 41 (5), 92–100. (ISSN 1000-0976; In Chinese). doi:10.3787/j.issn.1000-0976.2021.05.010

Wang, F., Ruan, Y., Chen, Q., and Zhang, S. (2021). A pressure drop model of post-fracturing shut-in considering the effect of fracturing-fluid imbibition and oil replacement. *Petroleum Explor. Dev.* 48 (6), 1440–1449. doi:10.1016/s1876-3804(21)60300-2

Wu, W., Kakkar, P., Zhou, J., et al. (2017). "An Experimental investigation of the conductivity of unpropped fractures in shales," in SPE Hydraulic Fracturing Technology Conference and Exhibition, The Woodlands, Texas, USA, January, 2017.

Yang, L. (2016). *Fracturing fluid imbibition into gas shale and its impact on engineering*. Beijing, China: China University of Petroleum.

You, L., Xie, B., Yang, J., et al. (2018). Mechanism of fracture damage induced by fracturing fluid flowback in shale gas reservoirs. *Nat. Gas. Ind.* 38 (12), 61–69. (ISSN 1000-0976; In Chinese). doi:10.3787/j.issn.1000-0976.2018.12.007

Zhai, L. (2021). *Study on the initiation and extension mechanism of hydraulic fracturing in the perforated oil shale horizontal well*. Changchun, China: Jilin University.

Zhou, T., Zhang, S., Yang, L., et al. (2017). Experimental study on surface softening law of fracturing fracture in shale reservoirs. *J. Xi'an Shiyou Univ. Sci. Ed.* 32 (1), 1. doi:10.3969/j.issn.1673-064X.2017.01.009

Zou, C., Zhao, Q., Zhang, G., and Xiong, B. (2016). Energy revolution: from a fossil energy era to a new energy era. *Nat. Gas. Ind.* 36 (1), 1–11. (ISSN 1000-0976 ;In Chinese). doi:10.1016/j.ngib.2016.02.001

frontiers | Frontiers in Energy Research

TYPE Methods
PUBLISHED 07 December 2023
DOI 10.3389/fenrg.2023.1303521

Check for updates

OPEN ACCESS

EDITED BY
Xiaojin Zheng,
Princeton University, United States

REVIEWED BY
Tianshou Ma,
Southwest Petroleum University, China
Jianhua He,
Chengdu University of Technology, China

*CORRESPONDENCE
Binxin Zhang,
zbx721@126.com

RECEIVED 28 September 2023
ACCEPTED 24 November 2023
PUBLISHED 07 December 2023

CITATION
Hao L, Zhang B, Chen B, Wang H, Wu Y, Pan L and Huang Y (2023), Fracturing parameter optimization technology for highly deviated wells in complex lithologic reservoirs.
Front. Energy Res. 11:1303521.
doi: 10.3389/fenrg.2023.1303521

COPYRIGHT
© 2023 Hao, Zhang, Chen, Wang, Wu, Pan and Huang. This is an open-access article distributed under the terms of the Creative Commons Attribution License (CC BY). The use, distribution or reproduction in other forums is permitted, provided the original author(s) and the copyright owner(s) are credited and that the original publication in this journal is cited, in accordance with accepted academic practice. No use, distribution or reproduction is permitted which does not comply with these terms.

Fracturing parameter optimization technology for highly deviated wells in complex lithologic reservoirs

Lihua Hao[1], Binxin Zhang[2]*, Beibei Chen[1], Hongwei Wang[3], Yuankun Wu[4], Liyan Pan[1] and Yue Huang[5]

[1]Research Institute of Engineering Technology (Supervision Company), PetroChina Xinjiang Oilfield Company, Karamay, Xinjiang, China, [2]Key Laboratory of Tectonics and Petroleum Resources of Ministry of Education (China University of Geosciences), Wuhan, China, [3]Emergency Rescue Center, PetroChina Xinjiang Oilfield Company, Karamay, Xinjiang, China, [4]School of Geosciences, China University of Petroleum, Beijing, China, [5]YuanwangJingsheng Technology (Beijing) Co., Ltd., Beijing, China

Highly-deviated wells are the key technology to reduce the risk of drilling accidents and improve the utilization of reservoirs. However, for reservoirs with complex lithology, highly-deviated wells are faced with the problems of geomechanical transformation and fracturing parameter optimization. The research on fracturing parameter optimization technology of high-deviated wells in complex lithologic reservoirs is helpful to the research and application of geomechanics in deep unconventional reservoirs. This paper is based on geological mechanics laboratory experiments and logging interpretation, combined with regional geological background, to clarify the geological and mechanical characteristics of the Fengcheng Formation shale oil region in the Mabei Slope. On this basis, based on the current geostress field and natural fracture distribution pattern of the Mabei Slope, an integrated model of shale oil geological engineering in local well areas was established. Based on the finite element method, optimization design was carried out for the cluster spacing, construction fluid volume, displacement, and sand volume of highly deviated well fracturing, and three-dimensional simulation of fracturing fractures was completed. The research results indicate that: (1) The current dominant direction of the maximum principal stress in the Fengcheng Formation on the Mabei Slope is from northeast to southwest, with the maximum horizontal principal stress generally ranging from 90 to 120 MPa and the minimum horizontal principal stress generally ranging from 70 to 110 MPa. (2) The difference in stress between the two horizontal directions is relatively large, generally greater than 8 MPa. Two sets of natural fractures have developed in the research area, one with a northwest southeast trend and the other with a northeast southwest trend. The natural fracture density of the Fengcheng Formation shale reservoir in the Mabei Slope is 0.32–1.12/m, with an average of 0.58/m, indicating a moderate to high degree of fracture development. (3) The geological model and three-dimensional geo-mechanical model are established according to the actual drilling geological data, and different schemes are designed to carry out single parameter optimization. The optimization results show that the optimal cluster spacing of the subdividing cutting volume pressure of the highly deviated wells in the Fengcheng Formation of the Mabei Slope is 12 m, the optimal construction fluid volume is 1400–1600 m^3/section, the optimal construction displacement is 8 m^3/min, and the optimal

sanding strength is 2.5 m^3/m. At the same time, by comparing the fracturing implementation effect with the fracturing scheme design, it is proven that the artificial parameter optimization method for highly deviated wells based on the finite element method based on the regional stress background and the natural fracture development law proposed in this paper is feasible and can provide a scientific basis for the fracturing development of highly deviated wells in complex lithologic reservoirs. This research has been well applied in Mahu area of Xinjiang oilfield.

KEYWORDS

shale oil, lithologic reservoir, fracturing parameters, high-angle deviated hole, geomechanics

1 Introduction

With the deepening of oilfield exploration and development, oil and gas reservoirs represented by tight oil and shale oil and gas, with poor reservoir physical properties, bottom natural production capacity, and gradually increasing development difficulties, will be fractured and reformed to exploit the oil and gas wells more adequately (Liu et al., 2021; 2023a; Yang and Liu, 2021; Abdelaziz et al., 2023; Wang DB. et al., 2023). In the petroleum field, fracturing is a method of utilizing hydraulic forces to form fractures in oil or gas formations during oil or gas extraction, also known as hydraulic fracturing (Montgomery and Smith, 2010; Zoveidavianpoor and Gharibi, 2015; Osiptsov, 2017; Yao et al., 2021; Li et al., 2022; Xu et al., 2022; Shah and Shah, 2023). Fracturing artificially fractures the formation to improve the oil flow environment in the subsurface and increase well production, which can play an important role in improving wellbore flow conditions, slowing the interlayer and improving formation mobilization. Therefore, optimizing the fracturing parameters of reservoirs plays a very important role in increasing the production capacity of reservoirs (Warpinski et al., 2009; Shen et al., 2016; Chai and Yin, 2021; He et al., 2021; Dai et al., 2023; Hui et al., 2023).

The large-scale hydraulic fracturing of highly inclined Wells and horizontal Wells is the most effective means to efficiently develop low permeability sandstone and carbonate reservoirs, tight oil and gas reservoirs, and unconventional oil and gas reservoirs (shale gas, coalbed methane, shale oil) (Li et al., 2020; Ma et al., 2022; Wang H. et al., 2023). At present, the research on fracturing of high inclination well at home and abroad mainly focuses on fracture initiation and extension mechanism, fracturing technology of inclined well, laboratory simulation experiment and field test. However, the research focusing on Mahu area of Xinjiang oilfield is faced with practical problems. Usually, the investment in the construction of high-inclination Wells is 1.8 times that of conventional Wells, but the output reaches 3.2 times that of conventional Wells, increasing the demand for the goal of "less drilling, more oil production and improved oil recovery" (Soliman et al., 2008; Ouenes et al., 2016; Tang et al., 2021; Wang et al., 2021; Yang et al., 2021; Li et al., 2022; Liu et al., 2022; 2023b; Li et al., 2023). The large-slope wells may have problems such as fracture initiation and sand addition difficulties, so the establishment of a set of optimization methods for the fracturing parameters of large-slope wells is crucial for the development of shale reservoirs with complex lithologies.

The purpose of this paper is to establish an integrated geological and engineering model for shale oil based on the present ground stress field and natural fracture distribution law through the combination of reasonable geology and engineering and to carry out in-depth systematic research on the characteristics of artificial fracture initiation and expansion, optimal design of fracturing and reforming, and postpressure analysis and evaluation to realize geology by combining reasonable geology and engineering and to achieve the optimal configuration of engineering parameters and it has novelty. We will carry out in-depth and systematic research on artificial fracture initiation and expansion characteristics, optimized design of fracturing and reforming, and postcompression analysis and evaluation to achieve the optimal configuration of geological and engineering parameters, form an integrated geological and engineering research model for shale oil reservoir fracturing and reforming, and reduce the cost of development to realize the purpose of beneficial development.

2 Geological setting

2.1 Tectonic location and geologic structure

The study area North Slope of the Mahu Depression belt (later referred to as the Mahu North Slope) is located in Hebkeser Mongol Autonomous County, Xinjiang Uygur Autonomous Region, approximately 28.87 km east of the Urhe District of Kelamayi City, and tectonically situated in the Wuxia Fracture Zone of the western uplift of the Junggar Basin, next to the Central Depression of the Mahu Depression, with the surface of the Gobi and the ground surface being relatively flat, with an average ground surface elevation of approximately 400 m (Figure 1).

Exploration in the study area began in the 1980 s, and the Fengcheng Formation (P_1 *f) of the Marbei slope (Pf)* was located in the Xiazijie nosedive zone during both the Jurassic and Cretaceous orogenic periods, and present-day tectonics suggest that the area is still nosedive at present (Ma et al., 2022; Chen et al., 2022; Shi et al., 2022; Lu et al., 2023). The development of two large-scale retrograde fractures is the main through-origin fracture in this area, and the large-scale fractures are accompanied by microfractures around them (Xiao et al., 2021). Oil test in the well section of 4,831.0–4,886.0 m in the P_1f_1 layer of the Permian

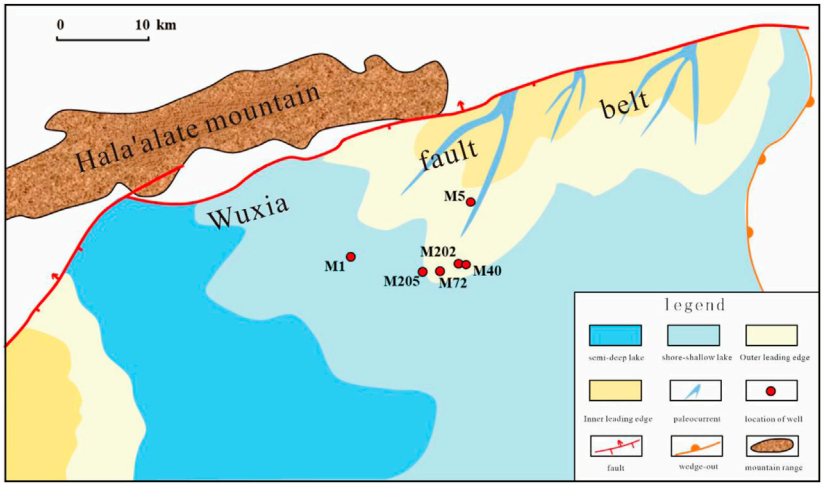


FIGURE 1
Geographic location map of the Fengcheng Formation reservoir in the northern slope of the Mahu Sag.

Fengcheng Formation yielded 3.65 t of oil per day from a 4 mm nozzle and 1.48 m^3 of water per day; oil test in the well section of 4,683.0–4,701.0 m in the P_1f_2 layer of the Permian Fengcheng Formation without fracturing yielded 0.54 t of oil per day from a 4 mm nozzle; oil test in the well section of 4,571.0–4,594.0 m in the P_1f_3 layer of the Permian Fengcheng Formation, stratigraphic test, obtained 1.13 t of oil per day. From the oil test, the natural production capacity of a single well is low, and fracturing and reforming are needed to increase the production.

2.2 Stratigraphy

The main stratigraphic strata drilled from top to bottom in the study area are the Cretaceous Tugulu Group, Jurassic Qigu Formation, Toutunhe Formation, Xishanyao Formation, Sanguohe Formation, Badawan Formation, Triassic Baikaitan Formation, Karamay Formation, Baikouquan Formation, Permian Upper Urho Formation, Lower Urho Formation, Xazijie Formation, Fencheng Formation, and Jiamuhe Formation. Among them, there is an unconformable contact between the Cretaceous and Jurassic, Jurassic and Triassic, Triassic and Permian, as well as the Permian Upper Urho Formation and the underlying strata (Zhu et al., 2021; Chen et al., 2022; Huang et al., 2022).

The Permian Fengcheng Formation in the Mabei slope area is a fan-delta-lake deposition accompanied by volcanism, and the scale of volcanic activity gradually decreases from bottom to top. The Fengcheng Formation is divided into the P_1f_1 layer, P_1f_2 layer, and P_1f_3 layer according to lithological, electrical, and depositional cyclic characteristics.

2.3 Sedimentary characteristics

The P_1f_1 layer of the Permian Fengcheng Formation on the Marbei Slope mainly features a set of rhyolitic fused conglomerates. Through the systematic analysis of the core, chip logging and petrographic analysis of the completed drilling wells, it is found that in the early Permian Fengcheng period (the P_1f_1 layer), the Marbei Slope was at the edge of the Junggar Plateau, and the stratigraphic environment of the slope was in the transition from the terrestrial rift volcano-building phase to the lake basin phase. The bottom stratigraphy of the Permian Fengcheng Formation of the Mabei Slope has both volcanic and lacustrine sedimentary stratigraphy, which is a set of longitudinal superpositions of volcanic clastic stratigraphy and sedimentary stratigraphy.

The P_1f_2 layer is a fan delta-lagoon deposition accompanied by volcanic activity, which is a mixed deposition of endogenous (mud crystal tuffs and mafic rocks formed by chemical deposition in the environment of the low-energy lagoon) and exogenous (input from the fan delta supplying terrestrial source of detrital materials and the air fall of volcanic dust supplying tuffaceous materials), which are inversely related to each other and thus form three types of reservoirs, namely, sandstone dominated by detrital materials, mafic rocks dominated by the environment of the alkali lagoon, and tuffaceous deposits under the domination of the volcano. The P_1f_2 layer has a large thickness, stable lateral spreading and is mainly interbedded with mudstone and muddy siltstone with high tuff content.

2.4 Reservoir characterization

Based on the oil test and logging data to determine the oil-water distribution relationship of the P_1f_1 layer reservoir, combined with the results of the M40 well oil test (3-layer combined test, oil and water in the same layer) analysis, the oil bottom height is taken as the bottom boundary of the upper shot hole layer section of the M40 well −4,437.0 m, and the bottom boundary of the oil out layer section of the test oil of the M202 well −4,432.0 m, which is 5 m higher than the height of the oil bottom. Combined with the production of the M202 well, the production time is 5,713 days. The production time is 5,713 days, the oil production is nearly 3.6×10^4 t, and no water is still observed. The analysis suggests that the oil-water interface should be lower than the oil bottom height, so the

TABLE 1 Results of whole-rock analysis and X-ray diffraction analysis of reservoirs in the Fengcheng Formation (4,808–4,810 m).

Mineral species and content (%)							Total clay minerals (%)
Sapphire	Potassium feldspar	Plagioclase (rock-forming mineral, type of feldspar)	Calcite (CaCO3 as rock-forming mineral)	Limonite	Ferric oxide Fe2O3	Barite (geology)	
59	17	15	3			2	4
Relative clay mineral content (%)						Mixed layer ratio (%S)	
S	I/S	I	K	C	C/S	I/S	C/S
		4			96		50

The layer oil layer of P_1f_1 is concentrated vertically without an interlayer in the middle, the upper part of the oil layer develops a nearly 30 m thick sandy mudstone septum, and the lower part develops a nearly 40 m thick sandy mudstone septum.

middle value of the top boundary of the layer section of the water out of the M202 well (−4,463.0 m) and the top boundary of the layer section of the oil out of the M40 well is taken as the oil-water interface, and the oil-water interface is −4,450.0 m. Overall, the reservoirs of the P_1f_1 layer are layered dorsal inclined tectonic rocky reservoirs with side water under the control of tectonics. According to the tectonic interpretation, oil test data and comprehensive geological study, the P_1f_2 reservoir is a shale oil reservoir.

The P_1f_1 layer of the Permian Fengcheng Formation on the slope of Ma Bei has a stable lateral distribution and vertical concentration, and the average thickness of the oil layer is approximately 20 m. The P_1f_2 layer of the oil layer has a stable lateral distribution and a vertical span of approximately 170 m, 5 sets of desert bodies have developed from the top to the bottom, and the thickness of the stacked layers ranges from 17.3 to 72.6 m, with an average of 51.0 m. The thickness of the stacked layers of the single desert body ranges from 4.4 to 22.6 m, with an average of 11.1 m P_1f_1 layer oil reservoir. The central part of the reservoir is at an elevation of −4,408 m, and the central part is buried at a depth of 4,810 m. The central part of the P_1f_2 layer reservoir is at an elevation of −4,298 m, and the central part is buried at a depth of 4,700 m, which belongs to a typical deep oil reservoir.

2.5 Regional stress characteristics

The regional tectonic background is the determining factor for the distribution of the present-day ground stress field. Mainland China is part of the Eurasian plate, sandwiched between the Indian, Philippine, Pacific and Siberian-Mongolian plates. Under the influence of the collision between the Indian plate and the Eurasian plate, the present-day horizontal maximum principal stresses in the western part of the oil and gas basin are in a north–north-east-south–south-west direction, while in the central part of China, under the influence of the two plates, the present-day maximum principal stresses are in a nearly north–north-east direction (Fan et al., 2012). The Junggar Basin is located in the western part of China, and the present-day horizontal maximum principal stresses in the region are in the north–northeast-south–south-west direction. The study area is located in the northwestern edge of the Junggar Basin, in front of the Hara Arat Mountains, the descending plate of the Wuxia Fracture Zone, the whole is in the remote effect of the collision between the Indian plate and the Eurasian plate, and the regional stress background of the Hashan retrograde thrusting and overturning folding, and it is predicted that the study area is in the NNE-SNSW extrusion and levitated torsional and torsional sliding stress field, and the direction of the stress has been deflected to some extent due to the influence of the local tectonics.

3 Geomechanical characteristics of the Fengcheng Formation reservoir

3.1 Reservoir lithology and physical characteristics

The results of whole rock analysis and X-ray diffraction analysis of P_1f_1 layer are shown in Table 1, and the overall content of clay minerals in the core is 4%. The clay minerals are dominated by the green montmorillonite layer, accounting for 96% of the clay minerals. Through the core stability experiment, first, the core at 4,808–4,810 m of the P_1f_1 layer of the M72 well was immersed in 2% KCl solution, and second, it was put into an 85°C water bath. After 30 h, if there was no swelling and loosening phenomenon of the core, the core had low water sensitivity.

The swelling height of the core of the M1 well in clear water in the study area is small, there is no obvious change in immersion, the potential water sensitivity of the reservoir is weak, and the water sensitivity of the P_1f_2 layer is weak. However, the matrix of the P_1f_2 layer contains silica-boron sodalite, and the presence of boron will cause the guanidinium gel fracturing fluid to have difficulty breaking the gel, and there is the possibility of residual gel injury.

The layer oil layer of P_1f_2 has a longitudinal span of approximately 170 m, is mainly interbedded mudstone and mud siltstone, and has a high tuff content. Five sets of dessert bodies are developed from top to bottom, and the thickness of the interlayer between each dessert body ranges from 0.8 to 30.2 m, with an average of 10.8 m. Single dessert body, 2-3 sets of interlayers are developed in the inner part of the formation, with thicknesses ranging from 0.85 to 8.83 m, with an average of 4.39 m. The oil layer is mainly composed of mudstone and mud siltstone interbedded with high tuff content.

The pore types of P_1f_1 layer are mainly primary pores of various sizes, accounting for 99%, and a small number of micro-cracks,

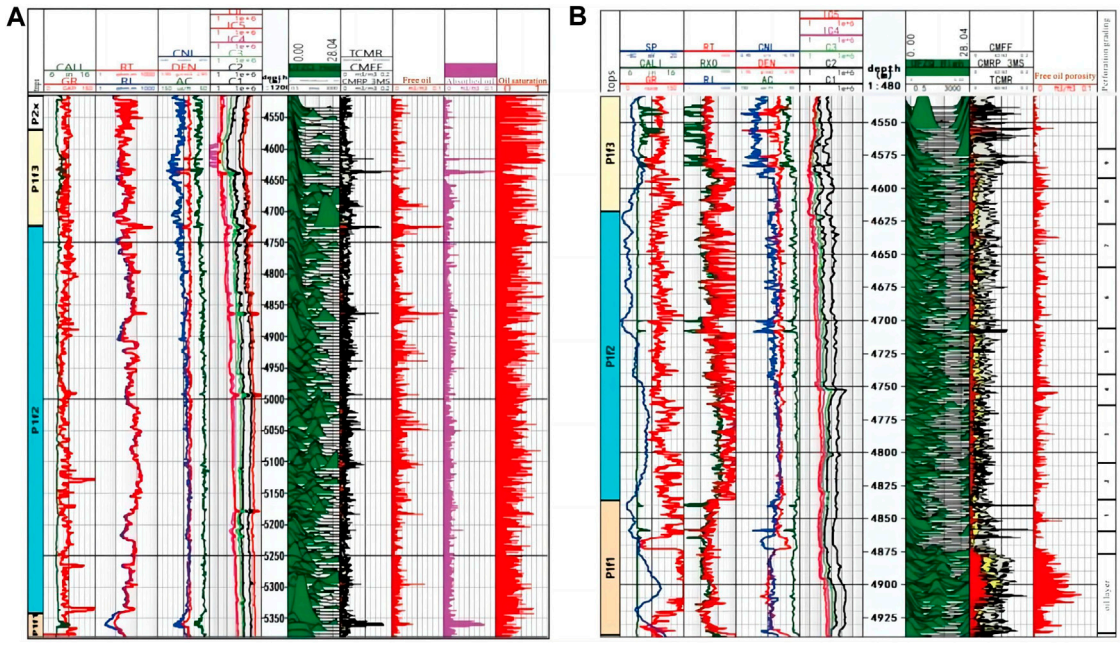


FIGURE 2
Comparison of reservoir quality evaluation of wells M205 and M1 Permian Fengcheng Formation P_1f. **(A)** The P_1f reservoir quality evaluation map of the Permian Fengcheng Formation in well M205 **(B)** The P1f reservoir quality evaluation map of the Permian Fengcheng Formation in well M1.

accounting for 1% (mainly playing a communication role). The shape of the pores is irregular, up to 20 mm. According to the size of the pores, the degree of development and the connection relationship, it has a very close relationship with the lithology (volcanic debris). The porosity of the oil reservoir is mainly distributed in 10.1%–30.1%, with an average of 15.87%; the permeability of the oil reservoir is mainly distributed in 0.01–7.82 mD, with an average of 0.187 mD, which belongs to the medium-low pore dense reservoir.

P_1f_2 The main reservoir space of the layer is matrix pores (drainages or dissolved pores of silica-boronatite and carbonate-calcite salt minerals within the matrix) and microfine fractures. The porosity of the sweet spot section ranges from 3.8% to 18.9%, with an average of 6.9%; the oil saturation ranges from 35.8% to 67.2%, with an average of 53.1%; and the permeability ranges from 0.02 to 0.67 mD, with an average of 0.09 mD, belonging to the extralow porosity and extralow permeability reservoir.

According to the 2D NMR special logging interpretation of the M205 well, the P_1f free oil porosity body averages approximately 0.72%, which is slightly better than that of the neighboring M1 wells. Combined with imaging logging for the overall evaluation study of well M205, P_1f natural fractures are very developed, mainly in medium and high angles, mostly high conductivity fractures, which is favorable for later reservoir modification (Figure 2A). Drawing on the research results of the M1 well reservoir classification and evaluation standard (Figure 2B), P_1f of the M205 well was evaluated for desserts, and 446.03 m of Class I desserts, 123.99 m of Class II desserts and 255.23 m of Class III desserts were interpreted, with the proportion of Class I and Class II desserts accounting for 69.07%.

3.2 Mechanical properties of reservoir rocks

Rock mechanical parameters are the basic data for solving many petroleum engineering technologies, which are of great significance for solving the drilling well wall stabilization, hydraulic fracture initiation and expansion laws. In this paper, we carried out indoor experiments to determine the mechanical parameters of rocks in the target formation, mainly including uniaxial compression mechanics experiments, triaxial compression mechanics experiments, and Brazilian splitting experiments, recorded the pictures of rocks before and after the experiments, outputted the axial and radial stress–strain curves of the rocks, and then calculated the modulus of elasticity, Poisson's ratio, and compressive strength of these rock mechanical parameters based on the data from the stress–strain curves (Table 2), among them, the confining pressure is determined by the minimum horizontal principal stress.

After the dynamic and static conversion of rock mechanical elasticity and rock mechanical strength parameters and the calculation of brittleness parameters, we obtained a series of logging interpretation data (Figure 3). These data are close to the actual situation of underground rock, which meets the needs of actual projects and can be utilized to establish a continuous single-well interpretation profile, which is of great practicality in actual applications. According to the logging interpretation results of the M5 wells, the Young's modulus of the M5 well area shows an overall trend of increasing and then decreasing, generally in the range of 30–60 GPa; the Poisson's ratio has little change overall, with an average value of approximately 0.2; the brittleness index of the P_1f_1 layer averages 57.3%, which is moderately brittle; the brittleness index of the P_1f_2 layer averages 70.0%, which is more brittle; and the brittleness index of the P_1f_3 layer averages 55.3%, which is slightly less brittle.

TABLE 2 Results of whole-rock analysis and X-ray diffraction analysis of the Fengcheng Formation reservoir.

Serial number	Test items	Pressurization (MPa)	Compressive strength (MPa)	Tensile strength (MPa)	Young's modulus (GPa)	Poisson's ratio
1	Brazilian splits	-	-	25.8	-	-
2	Brazilian splits	-	-	20.09	-	-
3	Uniaxial compression test	0	599.08	-	31.62	0.14
4	Triaxial compression test	46	315.11	--	35.67	0.15
5	Triaxial compression test	51	470.51	-	54.93	0.15
6	Triaxial compression test	51	574.03	-	48.06	0.13
7	Triaxial compression test	51	499.23	-	57.91	0.20
8	Triaxial compression test	51	432.55	-	49.84	0.17

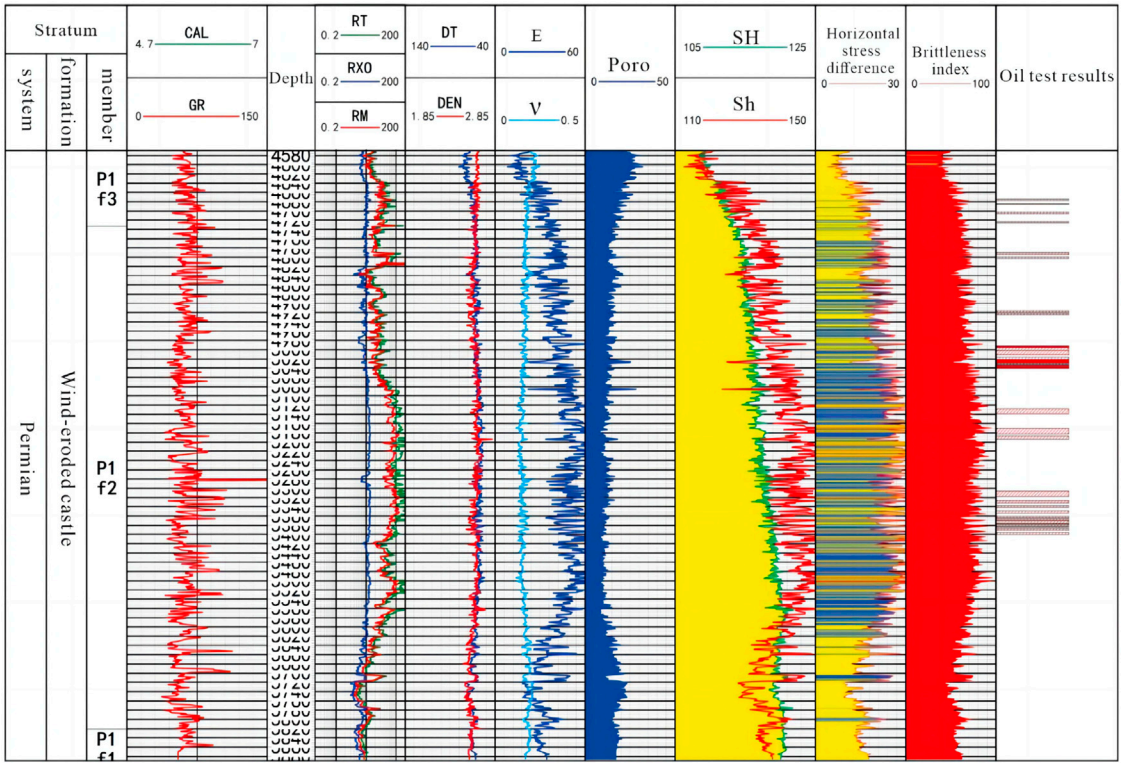


FIGURE 3
Synthesis histogram of the Fengcheng Formation in the Ma 51X well.

3.3 Present-day stress characteristics

3.3.1 Direction of present-day stress

In this study, the direction of current ground stress is determined mainly by using dipole acoustic wave logging fast transverse wave orientation and electric imaging logging drilling-induced fracture orientation. Dipole array acoustic logging data can be used to calculate the anisotropy of formation shear wave velocity, and the azimuth of fast shear wave is the direction of formation anisotropy. The anisotropy of the velocity is mainly caused by the imbalance of the ground stress in the undeveloped fracture formation, and the azimuth of the fast shear wave calculated at this time represents the direction of the maximum horizontal principal stress.

TABLE 3 Measured horizontal maximum principal stress direction statistics of drilling wells in the Fengcheng Formation, Mabei Slope.

Horizontal maximum principal stress orientation	Horizontal maximum principal stress interval (°)	Wells	Percentage	Total as a percentage
north-east–south-west	Less than 45	4	36.4	81.8
	45-90	5	45.5	
north-west–south-east	90-135	2	18.2	18.2

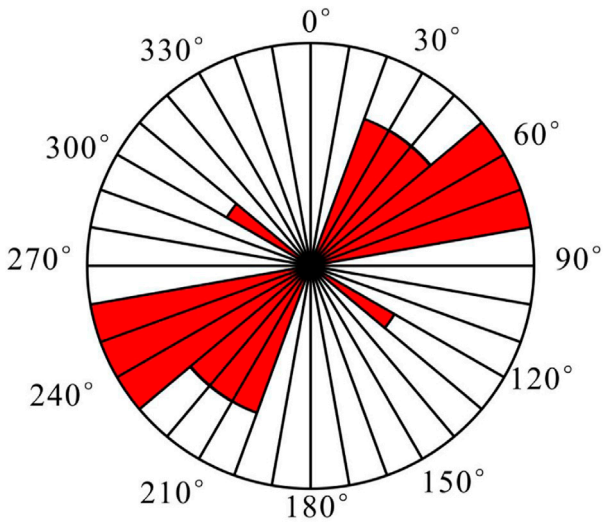


FIGURE 4
Schematic diagram of the maximum horizontal principal stress direction of the Fengcheng Formation oil reservoir in the northern slope of the Mahu Sag.

In the process of drilling, extrusion pressure is generated along the direction of maximum horizontal principal stress due to the joint action of drilling tool, ground stress and high pressure drilling fluid. When the extrusion pressure exceeds the fracture pressure of rock, the drilling induced crack is formed, and it is reflected in the electrical imaging (or acoustic imaging). Therefore, the orientation of the drilling induction joint can indicate the direction of the current maximum horizontal principal stress near the well area.

Statistical analysis of the present-day horizontal maximum principal stress orientation shown by dipole acoustic wave logging fast transverse wave orientation and electric imaging logging drilling-induced fracture orientation of 11 wells in the study area (Table 3), combined with the regional stress background, suggests that the present-day maximum principal stress dominant direction of shale oil in the Fengcheng Formation of the Mabei Slope is in the direction of north-east–south-west (Figure 4).

3.3.2 Present-day stress values

Geostress is spatially divided into vertical principal stress and maximum and minimum horizontal principal stresses. The vertical principal stress is caused by static rock pressure and can be obtained from density logging data. The two horizontal principal stresses, on the other hand, are caused by tectonic movement and are related to the pressure, tectonic stress and pore pressure of the overlying strata. The acoustic emission method is a method to determine the ground stress on the basis of the Kaiser effect, which is also called the Kaiser effect method (Lavrov, 2003; Meng et al., 2018). In practical applications, the correction between the logging interpretation value and the measured value is carried out to correct the dynamic and static geostress to obtain a more accurate geostress (Liu et al., 2021). In this study, the acoustic emission method combined with the logging interpretation method was used to obtain the stress values in the study area (Figure 3). The formula for calculating ground stress is as follows (Xu, 2019).

$$\begin{cases} S_H = \dfrac{\mu}{1-\mu}\left(\sigma_v - \alpha P_p\right) + \beta_2\left(\sigma_v - \alpha P_p\right) + \alpha P_p \\ S_h = \dfrac{\mu}{1-\mu}\left(\sigma_v - \alpha P_p\right) + \beta_2\left(\sigma_v - \alpha P_p\right) + \alpha P_p \\ S_V = \int_0^H \rho(h) g dh \end{cases} \quad (1)$$

In the formula, "S_H" is the maximum horizontal principal stress; "S_h" is the minimum horizontal principal stress; "S_V" is the vertical principal stress; "β_1" and "β_2" are horizontal structural stress coefficient, dimensionless; "α" is the Boit coefficient, dimensionless; "μ" is the poisson's ratio, dimensionless; "P_p" is the pore pressure, MPa; "H" is the depth, m; ρ (h) is the overburden density, g/cm^3; "g" is the acceleration of gravity, m/s^2. The horizontal structural stress coefficient and Boit coefficient in the model are obtained by correcting and inversely calculating the measured ground stress results.

Based on the acoustic emission experiments, the stress values of three samples in the study area were obtained, in which the maximum principal stress was 90.7 MPa, the minimum principal stress was 82.6 MPa, and the stress difference was 8.1 MPa, which provides data references for the logging calculations and the simulation of the stress field (Table 4). According to the logging interpretation results of the M5 well, the minimum horizontal principal stress of the M5 well area is more than 73 MPa, of which P_1f_1 is more than 120 MPa, the maximum horizontal principal stress is more than 82 MPa, P_1f_1 can be up to 130 MPa, the difference in the two-way stress in the middle horizontal of P_1f_2 can be more than 20 MPa, and the difference in the two-way stress in the horizontal of P_1f_1 and P_1f_3 is approximately 15 MPa. The maximum and minimum horizontal principal stresses generally increase, and the stress gradients are approximately 2.12 MPa/hm and 1.98 MPa/hm, respectively.

3.4 Characterization of natural fracture development

The Mabei Fengcheng Formation is located in the Wuxia Fracture Zone, which is characterized by strong tectonic activity, fault development, and overall development of natural fractures, with weak local development. The development of natural fractures is controlled by the influence of the activities of the Wuxia Fracture Zone (Feng et al., 2009; Jia et al., 2022). According to the analysis of

TABLE 4 The *in situ* stress test results of the Fengcheng Formation reservoir.

Serial number	Pressurization (MPa)	Compressive strength (MPa)	Modulus of elasticity (GPa)	Poisson's ratio	*In situ* stress
1	0	412.23	42.01	0.18	Maximum principal stress 90.7 MPa
2	0	174.65	40.06	0.16	Minimum principal stress 82.6 MPa
3	0	403.61	55.07	0.17	Horizontal stress difference of 8.1 MPa

TABLE 5 Statistical data on the development characteristics of natural fractures in fengcheng formation image logging.

Pound sign	Stratum (geology)	Type of fracture	Fracture strike dominant orientation (°)	Number of explanatory fractures (bars)	Fracture density (Article/m)	Number of high-lead seams (Article)	Percentage of high-conductivity seams (%)
M5	P f_{13}	High-angle fractures	North–North-East-South–South-West	107	0.36	42	39.3
	$P_1 f_2$	High-angle fractures	North–North-East-South–South-West North–North-West-South–South-East	633	0.64	307	48.5
M4	$P_1 f_3$	conformal solution fracture	North East East - South West West	155	1.03	138	89.0
	$P_1 f_2$	High-angle fractures	North East East - South West West	686	0.71	526	76.7
M205	$P_1 f_3$	Medium to high angle fractures	North-west–south-east	50	0.32	415	52.7
	P f_{12}	Medium to high angle fractures	North-west–south-east	690	1.12		
M203	$P_1 f_3$, P_1 f 1	conformal solution fracture	North–North-East-South–South-West	148	0.49	28	18.9
M208	$P_1 f_3$	High-angle fractures	North–North-East-South–South-West	32	0.13	1	0.7
	P_1 f 2	conformal solution fracture	North–North-West-South–South-East	59	0.09	18	30.5
Total				2,560	0.58	1,475	57.6

the spreading characteristics of the Wuxia fracture zone on the north-east-east–south-west strike, combined with the statistical law of natural fracture development interpreted by imaging logging, two groups of natural fractures are developed in the study area, one group on the north-west–south-east strike and one group on the north-east–south-west strike. The P_1 f natural fracture density of the Mabei slope is 0.32–1.12 fractures/m, with an average of 0.58 fractures/m, which is a medium-high degree of fracture development. The P_1f_2 layer has a fracture density of 0.64–1.12 fractures/m, with an average of 0.78 fractures/m, which is a higher degree of fracture development. P_1 f high conductivity fracture accounts for a high proportion of fractures, which reaches 57.6%, which indicates that the fracture filling degree is low, which is favorable for enhancing the seepage capacity of the reservoir and facilitating the fracturing process. and at the same time facilitates natural fracture opening and expansion during fracturing (Table 5). From the perspective of layers, except for well M4, the natural fracture development degree of the P_1f_2 layer is higher than that of the P_1f_3 layer in each well area. From the perspective of well area, the natural fracture development degree of the P_1f_3 layer and P_1f_2 is higher in the M4 well, followed by the M205 well and M5 well, and the fracture development degree of the M208 well is the lowest.

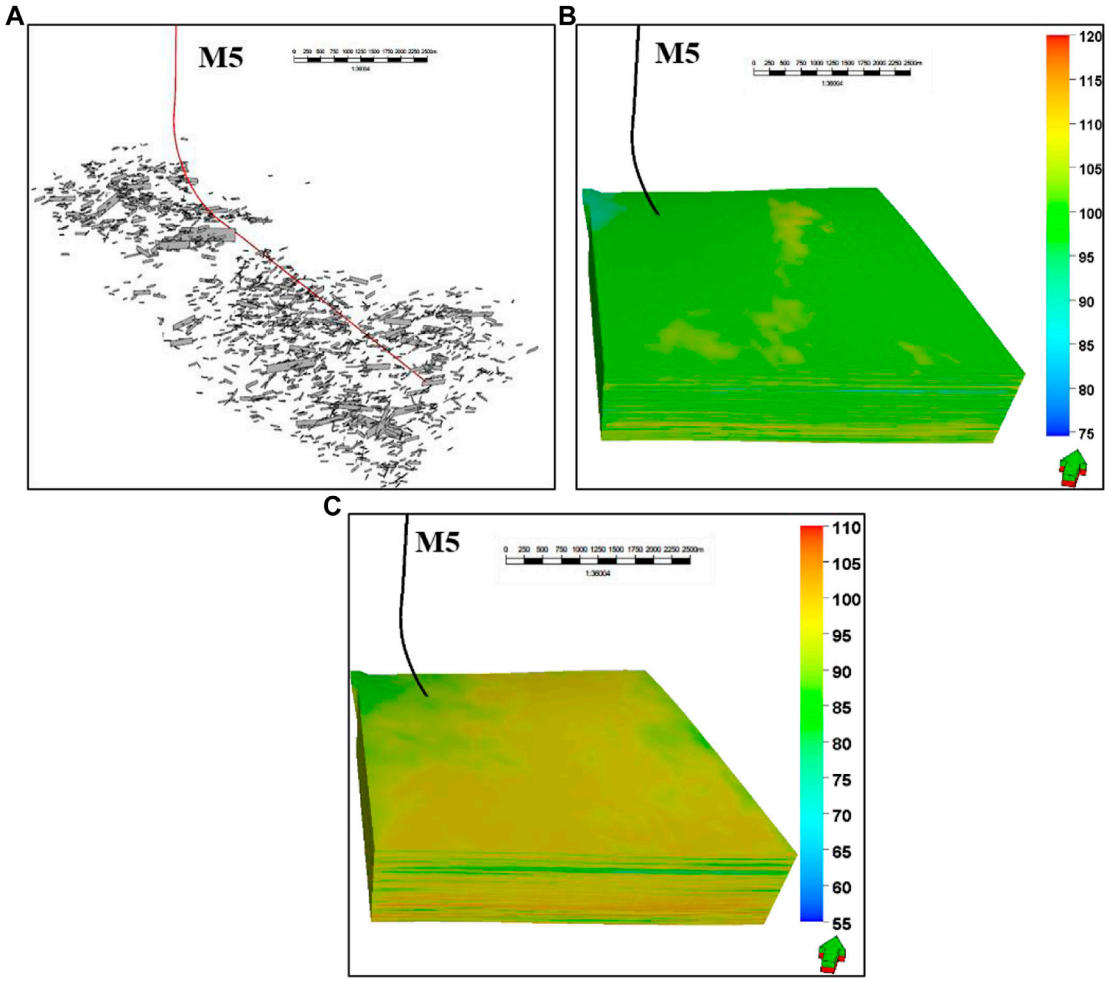


FIGURE 5
Three-dimensional model of the integration of natural fractures and present-day geostress in the M5 well zone. **(A)** Natural fracture model of the M5 well zone **(B)** Horizontal maximum principal stress model of the M5 well zone (MPa) **(C)** Horizontal minimum principal stress model of the M5 well zone (MPa).

4 optimization of fracturing parameters for large slope wells

4.1 Localized 3D geostress and natural fracture modeling in the context of regional stresses

Due to the production characteristics of shale reservoirs, such as small pore throats, poor matrix flow capacity, fast decreasing production, rapid energy depletion, and low degree of reserve utilization, the shale oil reservoirs in this area are considered to be complex in lithology with multilayer characteristics and are developed by using large inclined wells. Theoretical analysis and numerical simulation are combined to establish an integrated shale oil geoengineering model (Figure 5). Based on the present-day ground stress field and natural fracture distribution pattern of the Mabei slope, taking the M5 well as an example, and the modeling method is described in. From the results of the stress field simulation, the horizontal maximum principal stress in the M5 well area is 90–120 MPa, the horizontal minimum principal stress is 70–110 MPa, and the simulation results are basically consistent with the results of the well logging interpretation. Based on the finite unit method for the optimization design of cluster spacing, construction fluid volume, displacement, and sand volume for fracturing of large-slope wells, the three-dimensional simulation simulation of fracturing fracture is completed to achieve the purpose of the optimal design of fracturing modification and the effective assessment of fracturing after compression.

4.2 Optimization of artificial fracture parameters

4.2.1 Cluster spacing optimization

Based on the finite element method to carry out three-dimensional simulation of artificial fractures, three sets of different cluster spacing schemes (cluster spacings of 8 m, 10 m, and 12 m) were designed to optimize the cluster spacing of injection

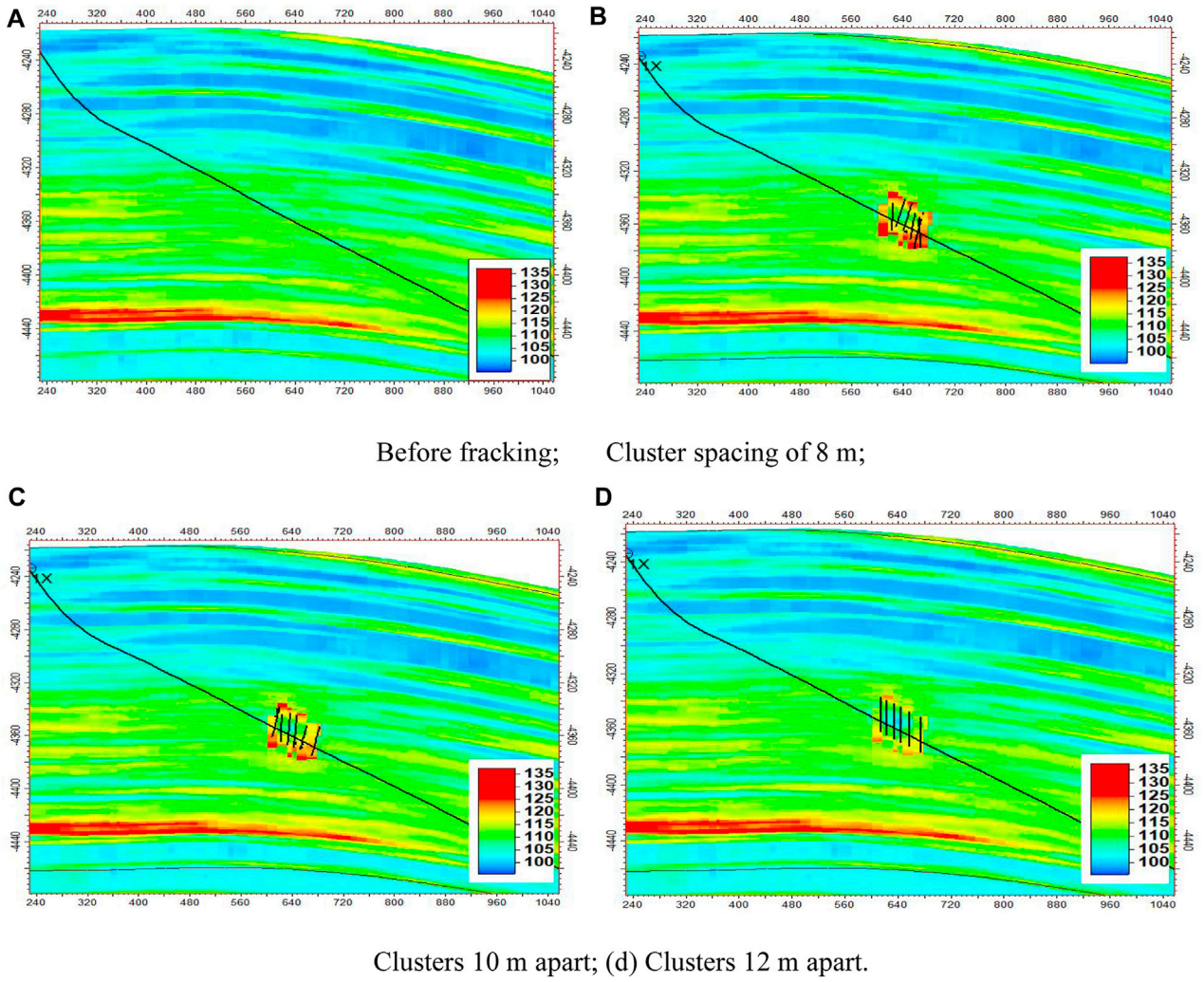


FIGURE 6
Simulation of artificial fracture extension under different cluster spacing conditions (vertical stress). **(A)** Before fracking; **(B)** Cluster spacing of 8 m; **(C)** Clusters 10 m apart; **(D)** Clusters 12 m apart.

holes, and the degree of stress interference between the postpressure slit networks was used as an evaluation index to select the appropriate cluster spacing. The simulation results show that (Figure 6), when the cluster spacing is less than or equal to 8 m, the interference between clusters is serious; there is interference between clusters between 10 m and 12 m; when the cluster spacing is greater than 12 m, the interference between clusters disappears. The optimal cluster spacing is recommended to be approximately 12 m, taking into consideration the adequacy of fracturing modification and minimizing the intercluster interference.

4.2.2 Optimization of construction fluid volume

Five sets of fracturing simulation schemes with different construction fluid volumes (1,000, 1,200, 1,400, 1,600, and 1800 m^3/section) were designed to optimize the construction fluid volume for each section, and the postfracturing seam network reforming volume was used as the evaluation index to select the appropriate fluid volume. The simulation results show that when the construction fluid volume is larger than 1,600 m^3/segment, the relationship curve between the reformed volume of the postfracturing seam network and the construction fluid volume shows an inflection point (Figure 7), and the increase slows down dramatically, so it is recommended that the construction fluid volume be 1,400–1,600 m^3/segment.

4.2.3 Construction displacement optimization

The design takes 12 m as the cluster spacing, and in the construction fluid volume of 1,600 m^3/section as the base condition, five sets of different construction displacements are designed for comparison (4, 6, 8, 10, and 12 m^3/min), and the same postfracturing slit-net reforming volume is used as the evaluation index to optimize the appropriate displacements. The simulation results show that when the construction displacement is larger than 8 m^3/min, the relationship curve between the modified volume of the postfracturing seam network and the construction displacement shows an inflection point (Figure 8), and the increase

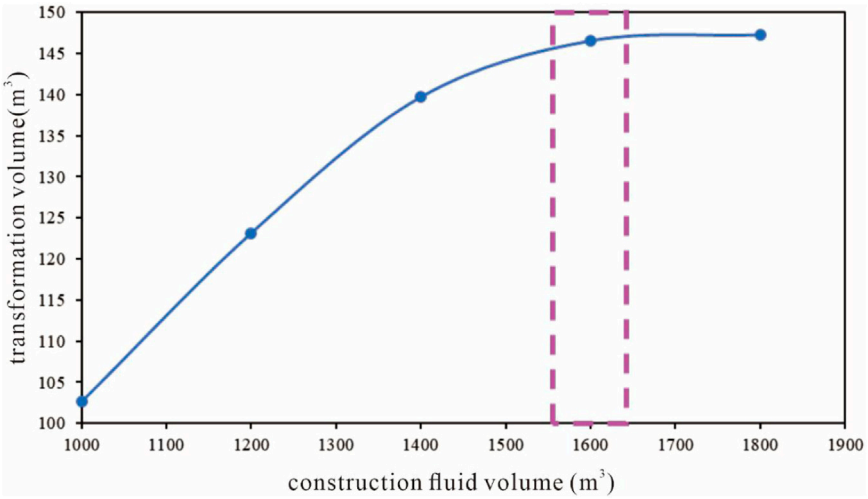


FIGURE 7
Relation curve between reconstruction volume of fracture network and construction fluid volume after fracturing.

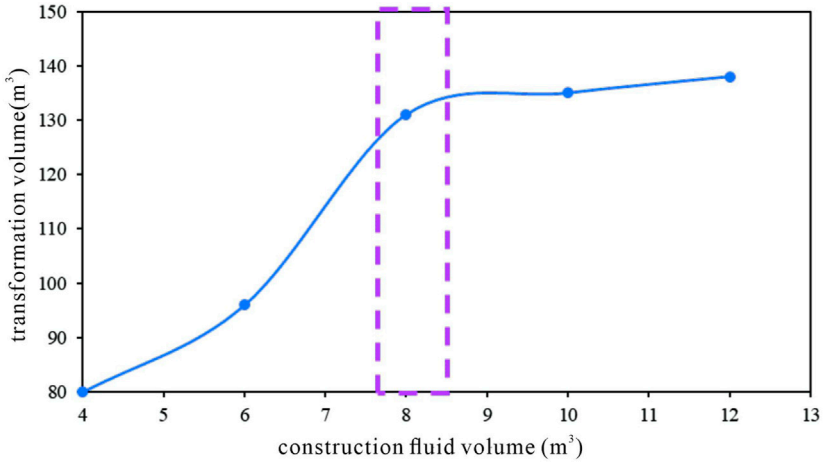


FIGURE 8
Relation curve between fracture pattern reconstruction volume and construction displacement after fracturing.

in the modified volume of the postfracturing seam network is slowed down, so the optimal construction displacement is suggested to be 8 m^3/min.

4.2.4 Optimization of sanding strength

The design takes 12 m as the cluster spacing, and in the construction fluid volume of 1,600 m^3/section and construction displacement of 8 m^3/min as the base condition, five different sets of sand addition intensity programs are compared (1.0, 1.5, 2.0, 2.5, and 3.0 m^3/m), and the postfracturing seam network permeability is used as the evaluation index to optimize the appropriate sand addition intensity. The simulation results show that when the construction sanding strength is greater than 2.5 m^3/m, the inflection point of the relationship curve between the permeability of the postfracturing seam network and the sanding strength occurs (Figure 9), and the increase in the permeability of the postfracturing seam network slows down, so it is suggested that the optimal sanding strength is 2.5 m^3/m.

4.2.5 Prediction of three-dimensional spatial spreading of artificial seams

Based on actual drilling geological data, a geological model and 3D geomechanical model were established, and based on the optimized design of artificial fractures, a 3D simulation of fracturing fractures was carried out for the whole well section. The designed cluster spacing is 12 m, the construction fluid volume is 1,600 m^3/section, the construction displacement is 8 m^3/min, and the strength of sand addition is 2.5 m^3/m as the basic conditions. Based on the natural fracture model, three-dimensional ground stress field, and the actual construction

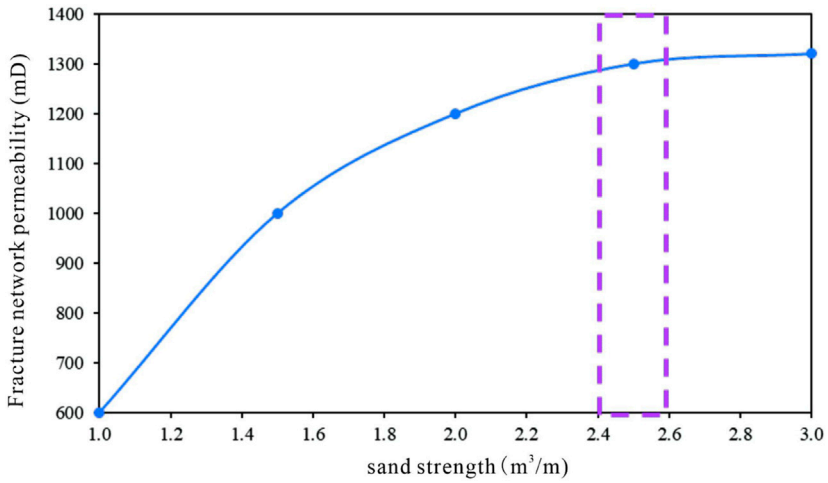


FIGURE 9
Relationship curve between the permeability of the fracture network and sanding strength after fracturing.

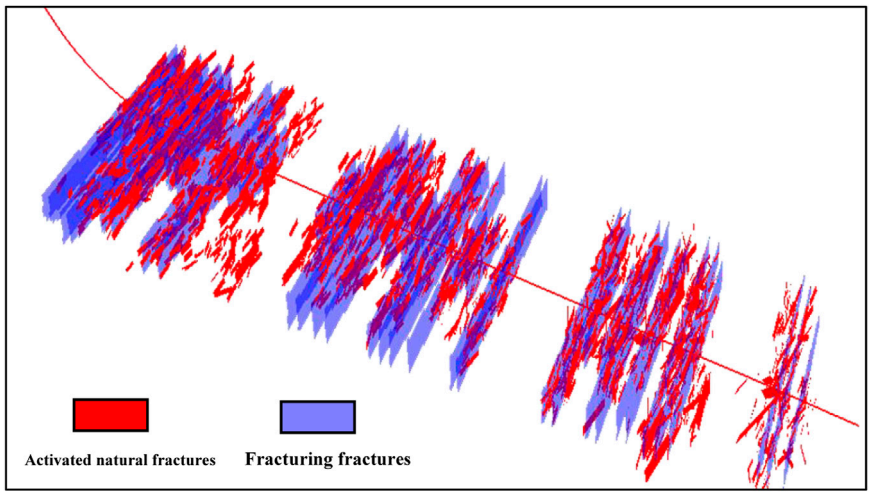


FIGURE 10
Three-dimensional simulation of fracturing fracture in Well M5.

design parameters of the M5 well, a three-dimensional model of fractured fracture in the M5 well is completed (Figure 10). The effect of fracturing simulation shows that the hydraulic main fracture extends along the direction of maximum horizontal stress, activates a small number of natural fractures and is vertically affected by the trajectory of the well with a large inclination, and the phenomenon of penetrating the layer is more common.

4.3 Evaluation of fracturing effectiveness

Comparison of fracturing construction data and fracturing design, combined with three-dimensional fine simulation of artificial fracture, postpressure fracture evaluation and assessment of modification effect were carried out. From the analysis of pressure construction data, the total designed fluid volume is 30,844 m^3, and the actual total fluid volume of fracturing is 31,285.4 m^3, with a compliance rate of 101.4%. The total designed sand volume is 1735 m^3, and the actual total sand volume is 1,621 m^3, with a compliance rate of 93.4%. For 24-stage fracturing, the compliance rate of adding sand is lower than 80%, except for the 10th, 12th, 14th, and 17th fracturing, for a total of 4-stage fracturing (Figure 11), which is analyzed because of the natural fracture. This is due to less activation of natural fractures, which leads to higher construction pressure and relative difficulty in adding sand. Overall, the program design requirements were basically met.

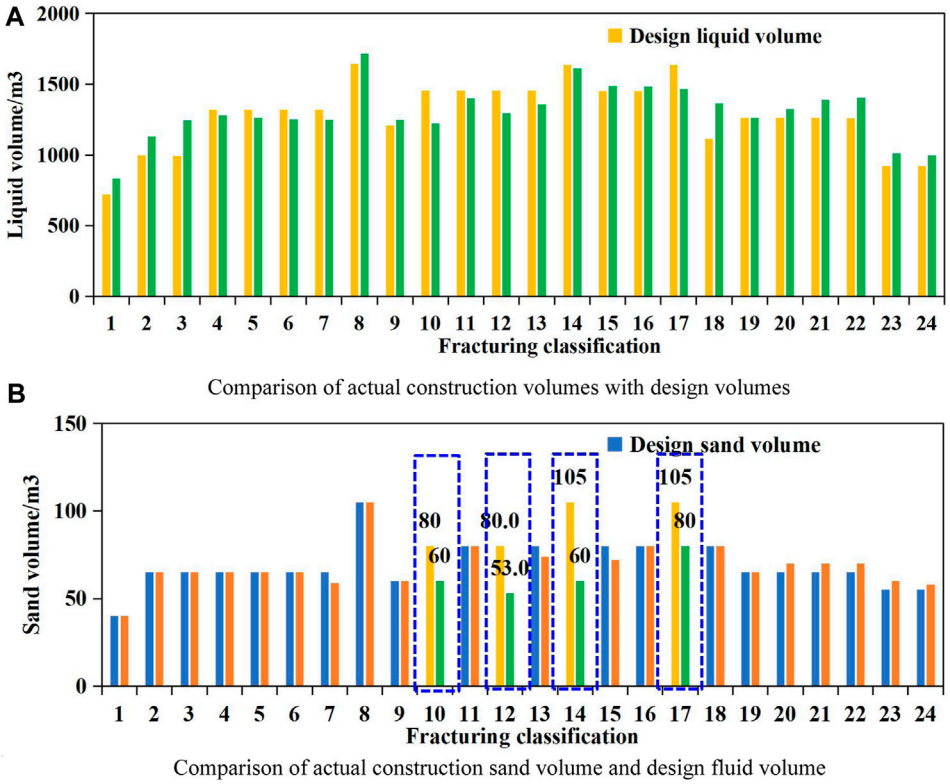


FIGURE 11
Comparison of fracture construction and design parameters for Well M5. **(A)** Comparison of actual construction volumes with design volumes. **(B)** Comparison of actual construction sand volume and design fluid volume.

5 Conclusion

(1) Based on geomechanical indoor experiments and logging interpretation, combined with the regional geological background, this paper clarifies the regional geomechanical characteristics of shale oil in the Mabei Slope Fengcheng Formation and concludes that the present maximum principal stress of the Mabei Slope Fengcheng Formation dominates the direction of the north-east–south-west trend, the horizontal maximum principal stress is generally in the range of 90–120 MPa, the horizontal minimum principal stress is generally in the range of 70–110 MPa, and the horizontal difference of the stress in both directions is generally larger than 8 MPa; two groups of natural fractures have developed in the study area. The horizontal stress difference between the two directions is large, generally greater than 8 MPa; two groups of natural fractures are developed in the study area, one group with a northwest–southeast orientation and one group with a northeast–southwest orientation. The density of natural fractures in the P_1f slope of Mabei is 0.32–1.12 fractures/m, with an average of 0.58 fractures/m, which belongs to the medium-high degree of fracture development.

(2) Based on actual drilling geological data, a geological model and three-dimensional geomechanical model are established, and different schemes are designed to carry out single-parameter optimization. The optimization results show that the optimal cluster spacing for subdividing the cutting volumetric pressure of large-slope wells in the Fengcheng Formation of the Mabei Slope is 12 m, the optimal construction fluid volume is 1,400–1,600 m^3/segment, the optimal construction displacement is 8 m^3/min, and the optimal strength of sand addition is 2.5 m^3/m.

(3) A comparison between the fracturing implementation effect and the fracturing scheme design proves that the artificial parameter optimization method for large inclined wells in shale oil with complex lithology proposed in this paper is feasible based on the finite element method in the basis of the regional stress background and the natural fracture development law.

(4) The advantages of this method are that it can solve the problems of geomechanical transformation and optimization of fracturing parameters faced by high inclination Wells in complex lithology reservoir environment. However, the disadvantages are that its application scope is Xinjiang oilfield area, and more data are needed to verify its wide application.

Data availability statement

The original contributions presented in the study are included in the article/Supplementary material, further inquiries can be directed to the corresponding author.

Author contributions

LH: Writing–original draft. BZ: Writing–review and editing. BC: Writing–review and editing. HW: Writing–review and editing. YW: Writing–review and editing. LP: Writing–review and editing. YH: Writing–review and editing.

Funding

The author(s) declare financial support was received for the research, authorship, and/or publication of this article. This study received funding from Science and Technology Project of Oil and Gas and New Energy Branch of petrochina Co., Ltd., "Risk Exploration Field and Target Research, Engineering Technology Research and Field Test in Junggar Basin." The funder was not involved in the study design, collection, analysis, interpretation of data, the writing of this article or the decision to submit it for publication.

Conflict of interest

Authors LH, BC, and LP were employed by Research Institute of Engineering Technology (Supervision Company), PetroChina Xinjiang Oilfield Company. Author HW was employed by Emergency Rescue Center, PetroChina Xinjiang Oilfield Company. Author YH was employed by YuanwangJingsheng Technology (Beijing) Co., Ltd.

The remaining authors declare that the research was conducted in the absence of any commercial or financial relationships that could be construed as a potential conflict of interest.

Publisher's note

All claims expressed in this article are solely those of the authors and do not necessarily represent those of their affiliated organizations, or those of the publisher, the editors and the reviewers. Any product that may be evaluated in this article, or claim that may be made by its manufacturer, is not guaranteed or endorsed by the publisher.

References

Abdelaziz, A., Ha, J., Li, M., Magsipoc, E., Sun, L., and Grasselli, G. (2023). Understanding hydraulic fracture mechanisms: from the laboratory to numerical modelling. *Adv. Geo-Energy Res.* 7 (1), 66–68. doi:10.46690/ager.2023.01.07

Chai, Y., and Yin, S. (2021). 3D displacement discontinuity analysis of in-situ stress perturbation near a weak faul. *Adv. Geo-Energy Res.* 5 (3), 286–296. doi:10.46690/ager.2021.03.05

Chen, H., Lv, Q., Gao, J., Yu, J., Pang, Y., Li, B., et al. (2022). The characteristics and controlling factors of glutenite reservoirs in the permian upper Urho Formation, southern zhongguai rise, Junggar Basin, NW China. *Geol. J.* 57 (1), 221–237. doi:10.1002/gj.4293

Dai, C., Huang, Y., Liu, C., Wu, Y., Zou, C., Yan, X., et al. (2023). Progress and prospect of fracturing fluid system for deep/ultra-deep reservoir reconstruction. *J. China Univ. Petroleum (Edition Nat. Sci).* 47 (4), 77–92.

He, W., Barzgar, E., Feng, W., and Huang, L. (2021). Reservoirs patterns and key controlling factors of the lenghu oil and gas field in the qaidam basin, northwestern China. *J. Earth Sci.* 32 (4), 1011–1021. doi:10.1007/s12583-020-1061-z

Huang, L., Wan, R., Zou, Y., Wan, M., Chang, Q., and Qian, Y. (2022). Accumulation characteristics of continuous sand conglomerates reservoirs of upper permian upper wuerhe formation on Manan slope area, Junggar Basin. *Petroleum Geol. Exp.* 44, 51–59. doi:10.11781/sysydz202201051

Hui, G., Chen, Z. X., Lei, Z. D., Song, Z. J., Zhang, L. Y., Yu, X. R., et al. (2023). A synthetical geoengineering approach to evaluate the largest hydraulic fracturing-induced earthquake in the East Shale Basin, Alberta. *Petroleum Sci.* 20 (1), 460–473. doi:10.1016/j.petsci.2023.01.006

Jia, Z., Peng, J., Lu, Q., Qiao, J., Wang, F., Zang, M., et al. (2022). Formation mechanism of ground fissures originated from the hanging wall of normal fault: a case in fen-wei basin, China. *J. Earth Sci.* 33 (2), 482–492. doi:10.1007/s12583-021-1508-x

Lavrov, A. (2003). The Kaiser effect in rocks: principles and stress estimation techniques. *Int. J. Rock Mech. Min. Sci.* 40 (2), 151–171. doi:10.1016/s1365-1609(02)00138-7

Li, L. G., He, H. Q., Fan, T. Z., Liu, H. N., Yang, T., Wan, L. K., et al. (2020). Oil and gas exploration progress and upstream development strategy of CNPC. *China Pet. Explor.* 25 (1), 1. doi:10.3969/j.issn.1672-7703.2020.01.001

Li, M. H., Zhou, F. J., and Huang, G. P. (2022). A finite element simulation method for multi-fracture propagation in horizontal wells based on fluid pipe element. *J. China Univ. Pet. Ed. Nat. Sci.* 46, 105–112.

Li, J., Yang, Z., Wang, Z., Tang, Y., Zhang, H., Jiang, W., et al. (2023). Quantitative characterization and main controlling factors of shale oil occurrence in permian Fengcheng Formation, Mahu sag, Junggar Basin. *Petroleum Geol. Exp.* 45 (4), 681–692. doi:10.11781/sysydz202304681

Liu, J., Ding, W., Yang, H., Dai, P., Wu, Z., and Zhang, G. (2023b). Natural fractures and rock mechanical stratigraphy evaluation in the huaqing area, ordos basin: a quantitative analysis based on numerical simulation. *Earth Sci.* 48 (7), 1–17.

Liu, J., Mei, L., Ding, W., Xu, K., Yang, H., and Liu, Y. (2023a). Asymmetric propagation mechanism of hydraulic fracture networks in continental reservoirs. *GSA Bull.* 135 (3-4), 678–688. doi:10.1130/b36358.1

Liu, J., Yang, H., Bai, J., Wu, K., Zhang, G., Liu, Y., et al. (2021). Numerical simulation to determine the fracture aperture in a typical basin of China. *Fuel* 283, 118952. doi:10.1016/j.fuel.2020.118952

Liu, J., Yang, H., Xu, K., Wang, Z., Liu, X., Cui, L., et al. (2022). Genetic mechanism of transfer zones in rift basins: insights from geomechanical models. *GSA Bull.* 134 (9-10), 2436–2452. doi:10.1130/b36151.1

Ma, T., Wang, H., Liu, Y., Shi, Y., and Ranjith, P. (2022). Fracture-initiation pressure model of inclined wells in transversely isotropic formation with anisotropic tensile strength. *Int. J. Rock Mech. Min. Sci.* 159, 105235. doi:10.1016/j.ijrmms.2022.105235

Meng, Q., Zhang, M., Han, L., Pu, H., and Chen, Y. (2018). Acoustic emission characteristics of red sandstone specimens under uniaxial cyclic loading and unloading compression. *Rock Mech. Rock Eng.* 51, 969–988. doi:10.1007/s00603-017-1389-6

Montgomery, C. T., and Smith, M. B. (2010). Hydraulic fracturing: history of an enduring technology. *J. Petroleum Technol.* 62 (12), 26–40. doi:10.2118/1210-0026-jpt

Osiptsov, A. A. (2017). Fluid mechanics of hydraulic fracturing: a review. *J. petroleum Sci. Eng.* 156, 513–535. doi:10.1016/j.petrol.2017.05.019

Ouenes, A., Umholtz, N. M., and Aimene, Y. E. (2016). Using geomechanical modeling to quantify the impact of natural fractures on well performance and microseismicity: application to the Wolfcamp, Permian Basin, Reagan County, Texas. *Interpretation* 4 (2), SE1–SE15. doi:10.1190/int-2015-0134.1

Peng, L. I., Xiong, J., Qi, Y., Zhu, Z., Liu, X., Wu, J., et al. (2022). Lithological influences to rock mechanical properties of permian Fengcheng Formation in Mahu sag, Junggar Basin. *Petroleum Geol. Exp.* 44 (4), 569–578. doi:10.11781/sysydz202204569

Shah, M. S., and Shah, S. N. (2023). Comparative assessment of mechanical and chemical fluid diversion techniques during hydraulic fracturing in horizontal wells. *Petroleum Sci.* doi:10.1016/j.petsci.2023.07.013

Shen, W., Xu, Y., Li, X., Huang, W., and Gu, J. (2016). Numerical simulation of gas and water flow mechanism in hydraulically fractured shale gas reservoirs. *J. Nat. Gas Sci. Eng.* 35, 726–735. doi:10.1016/j.jngse.2016.08.078

Soliman, M. Y., East, L., and Adams, D. (2008). Geomechanics aspects of multiple fracturing of horizontal and vertical wells. *SPE Drill. Complet.* 23 (03), 217–228. doi:10.2118/86992-pa

Tang, Y., Cao, J., He, W. J., Guo, X. G., Zhao, K. B., and Li, W. W. (2021). Discovery of shale oil in alkaline lacustrine basins: the late paleozoic Fengcheng Formation, Mahu sag, Junggar basin, China. *Petroleum Sci.* 18 (5), 1281–1293. doi:10.1016/j.petsci.2021.04.001

Wang, D. B., Qin, H., Wang, Y. L., Hu, J. Q., Sun, D. L., and Yu, B. (2023a). Experimental study of the temporary plugging capability of diverters to block hydraulic fractures in high-temperature geothermal reservoirs. *Petroleum Sci.* doi:10.1016/j.petsci.2023.07.002

Wang, H., Ma, T., Liu, Y., Wu, B., and Ranjith, P. (2023b). Numerical and experimental investigation of the anisotropic tensile behavior of layered rocks in 3D space under Brazilian test conditions. *Int. J. Rock Mech. Min. Sci.* 170, 105558. doi:10.1016/j.ijrmms.2023.105558

Wang, S., Wang, G., Huang, L., Song, L., Zhang, Y., Li, D., et al. (2021). Logging evaluation of lamina structure and reservoir quality in shale oil reservoir of Fengcheng Formation in Mahu Sag, China. *Mar. Petroleum Geol.* 133, 105299. doi:10.1016/j.marpetgeo.2021.105299

Warpinski, N. R., Mayerhofer, M. J., Vincent, M. C., Cipolla, C., and Lolon, E. (2009). Stimulating unconventional reservoirs: maximizing network growth while optimizing fracture conductivity. *J. Can. Petroleum Technol.* 48 (10), 39–51. doi:10.2118/114173-pa

Xiao, M., Wu, S., Yuan, X., and Xie, Z. (2021). Conglomerate reservoir pore evolution characteristics and favorable area prediction: a case study of the lower triassic baikouquan formation in the northwest margin of the Junggar Basin, China. *J. Earth Sci.* 32, 998–1010. doi:10.1007/s12583-020-1083-6

Xu, K. (2019). *Current in-situ stress of gaoshangpu reservoir, nanpu Sag, bohai bay basin, China*. East China: China University of Petroleum.

Xu, S. Q., Guo, J. C., Feng, Q. H., Ren, G., Li, Y., and Wang, S. (2022). Optimization of hydraulic fracturing treatment parameters to maximize economic benefit in tight oil. *Fuel* 329, 125329. doi:10.1016/j.fuel.2022.125329

Yang, C., and Liu, J. (2021). Petroleum rock mechanics: an area worthy of focus in geo-energy research. *Adv. Geo-Energy Res.* 5 (4), 351–352. doi:10.46690/ager.2021.04.01

Yang, Z. F., Tang, Y., Guo, X. G., Huang, L. L., Wang, Z. Q., and Zhao, X. M. (2021). Occurrence states and potential influencing factors of shale oil in the permian Fengcheng Formation of Mahu sag, Junggar Basin. *Petroleum Geol. Exp.* 43 (5), 784–796. doi:10.11781/sysydz202105784

Yao, J., Li, Z. H., LiuFan, L. J. W. P., Zhang, M., and Zhang, K. (2021). Optimization of fracturing parameters by modified variable-length particle-swarm optimization in shale-gas reservoir. *SPE J.* 26 (02), 1032–1049. doi:10.2118/205023-pa

Zhu, N., Cao, Y., Xi, K., Wu, S., Zhu, R., Yan, M., et al. (2021). Multisourced CO2 injection in fan delta conglomerates and its influence on reservoir quality: evidence from carbonate cements of the Baikouquan Formation of Mahu sag, Junggar Basin, northwestern China. *J. Earth Sci.* 32, 901–918. doi:10.1007/s12583-020-1360-4

Zoveidavianpoor, M., and Gharibi, A. (2015). Application of polymers for coating of proppant in hydraulic fracturing of subterraneous formations: a comprehensive review. *J. Nat. Gas Sci. Eng.* 24, 197–209. doi:10.1016/j.jngse.2015.03.024

frontiers | Frontiers in Energy Research

TYPE Review
PUBLISHED 29 December 2023
DOI 10.3389/fenrg.2023.1338715

Check for updates

OPEN ACCESS

EDITED BY
Peng Tan,
CNPC Engineering Technology R&D Company Limited, China

REVIEWED BY
Shuheng Tang,
China University of Geosciences, China
Suoliang Chang,
Taiyuan University of Technology, China
Longyi Shao,
China University of Mining and Technology, Beijing, China

*CORRESPONDENCE
Zhang Xiao,
zhangxiao@cup.edu.cn

RECEIVED 15 November 2023
ACCEPTED 12 December 2023
PUBLISHED 29 December 2023

CITATION
Guangbo Z, Suian Z, Wei J, Xiao Z, Yang Z, Haoyu L, Xiaohua L and Huili F (2023), Grouting solidification technology for fractured soft coal seams and its application in coalbed methane (coal mine gas) extraction.
Front. Energy Res. 11:1338715.
doi: 10.3389/fenrg.2023.1338715

COPYRIGHT
© 2023 Guangbo, Suian, Wei, Xiao, Yang, Haoyu, Xiaohua and Huili. This is an open-access article distributed under the terms of the Creative Commons Attribution License (CC BY). The use, distribution or reproduction in other forums is permitted, provided the original author(s) and the copyright owner(s) are credited and that the original publication in this journal is cited, in accordance with accepted academic practice. No use, distribution or reproduction is permitted which does not comply with these terms.

Grouting solidification technology for fractured soft coal seams and its application in coalbed methane (coal mine gas) extraction

Zhang Guangbo[1], Zhang Suian[2], Jia Wei[1], Zhang Xiao[2]*, Zhang Yang[1], Lian Haoyu[2], Lian Xiaohua[1] and Fang Huili[1]

[1]PetroChina North China Oilfield Engineering Technology Research Institute, Renqiu, Hebei, China, [2]China University of Petroleum, Beijing, China

This article presents an effective method for improving the structure and performance of coal rock masses, thereby facilitating coalbed methane extraction—the grouting solidification technique. A systematic review is conducted on grouting solidification materials, process methods, evaluation techniques, and other related aspects. In conclusion, it is emphasized that the grouting solidification technique requires further refinement in its system, and its continued significance in the dynamically evolving energy and coal industry is underscored. This is crucial for ensuring the efficient development and sustainable utilization of coal and coalbed methane resources.

KEYWORDS

grouting solidification, deep coal reservoir modification, coalbed methane extraction, grouting materials, grouting process

1 Introduction

Currently, coal resources are an indispensable and crucial component of China's energy structure (Teng et al., 2016). With the continuous exploitation of coal mining resources and the advancement of coalbed methane industrialization in China, the exploration and development of coal resources and coalbed methane are gradually advancing into deeper, structurally complex fractured soft coal seams. However, the unique mechanical properties of fractured soft coal seams, such as their friability, high Poisson's ratio, low Young's modulus, and strong plasticity, pose significant challenges to mining and extraction operations (Zhang et al., 2022). Grouting solidification technology is currently an effective approach to improving the structure and performance of coal-rock masses. This technology involves injecting grout uniformly into cracks or voids under the influence of hydraulic or pneumatic pressure. The grout permeates, fills, and fractures, expelling air and moisture from the fractures in the coal-rock mass. Once the grout solidifies, the originally loose rock mass or fractures consolidate into a cohesive, strong, waterproof, and chemically stable new rock mass (Xie, 2021).

Fractured soft coal seams are a type of coal seam characterized by unique geological features, with their cohesion coefficient (f-value) being less than 1. These coal seams typically undergo compression and kneading during geological tectonic movements, resulting in loose, soft, and friable coal bodies with a lower content of rock minerals. Consequently, they exhibit reduced mechanical strength, compressive resistance, and a propensity for expansion upon contact with water. The mechanical properties manifest as a higher Poisson's ratio and

lower Young's modulus, making them prone to deformation, collapse, susceptibility to external stress, and the potential occurrence of geological phenomena such as folding and sliding (Zhou et al., 2016). In coal mining, dealing with fractured soft coal seams requires specialized engineering techniques to ensure the stability and safety of the mine. Excavating and supporting these coal seams necessitate a comprehensive consideration of their unique properties. Additionally, fractured soft coal seams often contain coalbed methane, making them prone to sudden occurrences of coal and gas outbursts. This phenomenon, known as outburst, is particularly evident during construction, drilling, and other engineering operations in fractured soft coal seams. It can lead to phenomena such as wall contraction, wall collapse, and even the ejection of holes under gas pressure and dynamic excitations, resulting in engineering accidents such as stuck drilling and buried drilling (Guo et al., 2020). The unique properties of fractured soft coal seams require the adoption of innovative engineering methods and technologies to ensure the safety and feasibility of mines and underground projects. Grouting solidification technology plays a pivotal role in this field, providing a reliable solution for the safe development of coal seams and the extraction of coalbed methane. Its application can be extended and adapted based on the specific conditions of different coal mines (Li et al., 2021).

This article aims to delve into the principles, materials, construction methods, and practical applications of the principles of fragmented soft and deep coal seam grouting solidification technology. Through a comprehensive discussion of this critical technology, the intention is to provide a deeper understanding and practical guidance for addressing challenges in the development of coal seams. In the ever-changing energy and coal industry landscape, grouting solidification technology will continue to play a crucial role in ensuring the efficient development and sustainable utilization of coal and coalbed methane resources.

2 Current Research Status of grouting solidification agents

2.1 Requirements and classification of solidification agents

Grouting solidification agents are a crucial component in grouting technology, and the rational selection of these agents plays a key role in the grouting process and the subsequent reinforcement and modification effects. Grouting solidification agents are formulated liquids composed of main agents, solvents, and additives. Regardless of the specific formulation, each grouting agent has unique applications based on factors such as particle size, mechanical properties, chemical characteristics, construction processes, and cost-effectiveness, making it impractical to satisfy all grouting scenarios uniformly. The selection of grouting materials should be based on the characteristics of the crushed soft coal seam, the geological conditions of the actual construction target of the crushed soft coal seam, the expected goals after grouting, injection method requirements, density requirements, setting time and viscosity, cost, hydrogeological conditions, and environment. The comprehensive performance of the slurry material should be considered based on influencing factors, and different slurries should be selected to ensure the coal seam solidification effect.

Grouting solidification materials suitable for fractured soft coal seams should meet the following requirements:

1) The grout should have good flowability, low viscosity, and good injectability, capable of penetrating into fine cracks;
2) The grout's gelation time should be controllable through temperature, additives, and other methods;
3) The density of the grout should be similar to that of the fractured soft coal seam being reinforced and modified;
4) The grout should be of low toxicity or non-toxic, odorless, and environmentally non-polluting;
5) The grout should be easy to formulate, and the grouting process should be straightforward;
6) The grout should exhibit good stability, maintaining its basic properties for an extended period under normal temperature and pressure;
7) The grout should not corrode grouting equipment or the coal seam;
8) The consolidation formed by the injected grout into the coal seam should have sufficient strength and stability, allowing for extraction operations;
9) The grout should have a broad source, and its cost should be low.

According to the characteristics of grouting solidification agents, as shown in Figure 1, these agents are mainly divided into two major categories: inorganic grouting solidification agents and organic grouting solidification agents. Inorganic grouting solidification agents include clay-based, cement-based, water glass (sodium silicate) based, cement-clay hybrid, and cement-water glass hybrid agents. These agents are characterized by low cost and easy availability. However, they have a slow curing time, and the larger particle size of their grout reduces permeability, making it challenging for the grout to penetrate into minute pores. Additionally, the curing process is irreversible, causing significant harm to coal seams. Organic grouting solidification agents, including acrylamide-based, polyurethane-based, methyl methacrylate-based, epoxy resin-based, and lignin-based agents, exhibit better permeability, and their gelation time is adjustable. However, the materials used in these agents are relatively more expensive (Gen and g, 2019).

2.2 Inorganic grouting agents

2.2.1 Clay-based solidification slurry

The clay-based solidification slurry originally referred to a grouting material formed by mixing clay with water in certain proportions, representing the most primitive form of grouting solidification material. With the development of grouting solidification, engineers have modified clay slurry based on different grouting requirements. This involves incorporating additives such as water glass, cement, and solidification agents in varying proportions, giving rise to a category known as clay-based solidification slurry. Clay, with a composition that includes complex components such as silicate minerals, forms dispersed clay particles with negative charges when mixed with water. The edges of cracks in

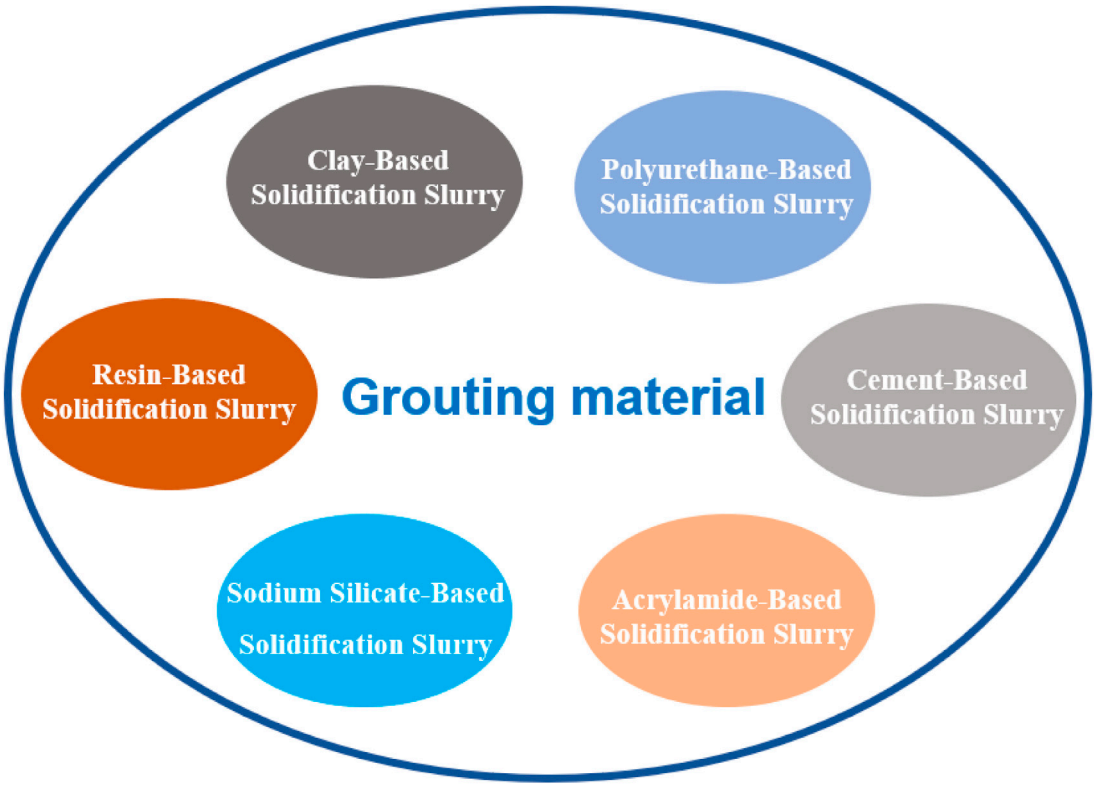


FIGURE 1
Classification of grouting solidification agents (Gen and g, 2019).

coal seams often carry a certain positive charge. When injected into underground fissures, these clay particles undergo electrostatic action, hydration reactions, and ion exchange, binding and solidifying the cracks. However, the initial viscosity of the clay-based slurry is relatively high, the injection range is limited, and the strength of the consolidation formed after solidification is low, making it less favorable for extraction operations (Zhang et al., 1995).

2.2.2 Cement-based solidification slurry

Cement-based solidification slurry refers to a grouting solidification material formed by mixing powdered rigid inorganic solidifying materials (main components) with other modifying materials (such as polyurethane, resins, styrene-butadiene latex, fly ash, water glass, carbon nanotubes, etc.) in a certain proportion with water. The silicate, aluminate, and ferric-aluminate components in cement undergo a hydration reaction with water, forming precipitates. These precipitates crystallize and fix the free water in the system, filling the fissures in the coal seam, ultimately forming a high-strength consolidated structure. Cement-based solidification slurry has advantages such as high strength of the consolidated structure, good deformation resistance, strong water plugging ability, environmental friendliness, cost-effectiveness, ease of construction, and wide applicability. Consequently, it is currently the most widely used and abundant grouting material. It can be used for water plugging and well consolidation in coal seams. However, the initial viscosity of cement-based solidification slurry is relatively high, making it challenging to inject into fine cracks in coal seams (Ruan, 2005).

2.2.3 Sodium silicate-based solidification slurry

Sodium silicate-based slurry consists primarily of a sodium silicate aqueous solution (water glass) as the main agent, with the addition of coagulants (such as calcium chloride, sodium aluminate, silicon tetrafluoride, and formaldehyde) to form a gel. Sodium silicate slurry is an inorganic grouting material that has been used relatively early in grouting technology. It is characterized by its low cost, good penetrability, ease of construction, and environmental friendliness. However, its mechanical strength is relatively low, and it can be modified by mixing with cement (Chao et al., 2016).

2.3 Organic-based solidification agents

2.3.1 Acrylamide-based solidification slurry

Acrylamide-based solidification slurry is generally composed of crosslinking agents such as N, N′-methylenebisacrylamide, initiators, reducers, retarding agents, and other components. Acrylamide-based solidification agents initiate the chain reaction by the initiator to form free radical active centers. Once the monomer free radicals are formed, they undergo polymerization with acrylamide monomers, leading to chain growth. Simultaneously, the amide groups of acrylamide form hydrogen

bonds with functional groups on the coal surface, such as hydroxyl groups, bonding the coal particles. This process aims to improve the mechanical properties of coal and rock. The initial viscosity of acrylamide-based solidification slurry is adjustable, facilitating pumping into formations with initially low permeability (KAROL, 1990). Acrylamide-based slurry offers adjustable gelation time, making it less susceptible to impurities' interference. The permeability of the slurry remains consistent during the grouting process. After solidification, the slurry becomes impermeable, demonstrating good durability and stability. The construction operation is straightforward, and the cost is low (Feng, 2007), Therefore, it is applied in the grouting reinforcement of tunnel support and coal mine excavation tunnels.

2.3.2 Polyurethane-based solidification slurry

Polyurethane-based solidification slurry is primarily composed of polyisocyanate prepolymers, polyether polyols, and other catalytic additives in specific proportions. Surfactants and other modifiers can be added to achieve lower viscosity, ensuring the slurry's uniform dispersion in water. Consequently, it exhibits good injectability and diffusion. Its strong bonding with coal makes it easily diffusible, effectively consolidating a large area. After solidification, it attains high compressive strength, demonstrating stable physical and chemical properties. It can incorporate flame retardants to prevent spontaneous combustion in coal bodies, ensuring safe use in tunnel reinforcement, underground safety reinforcement, roof reinforcement, and other safety-related production activities. However, polyisocyanates have inherent toxicity and corrosiveness, requiring careful handling and storage (Hou et al., 2022).

2.3.3 Epoxy resin-based solidification slurry

Epoxy resin-based grouting materials are typically composed of epoxy chloropropane, bisphenol A or polyols, curing agents, modifiers, fillers, diluents, and other components. The viscosity of epoxy resin is generally high, but it can be adjusted over a wide range by adding diluents. After curing, epoxy resin forms a highly cross-linked structure with low toughness and poor ductility, making it suitable for subsequent fracturing construction. The most commonly used type is bisphenol A epoxy resin, synthesized from propylene oxide and epichlorohydrin, with epoxy groups at both ends of the molecule. Common curing agents include amines and anhydrides. This type of grouting material is widely used in crack reinforcement and consolidation grouting of foundations and concrete structures. However, it has some limitations. For certain engineering applications, the bonding strength of such grouting materials is susceptible to external factors. Additionally, the raw materials are not widely available, mechanical properties need improvement, it is relatively expensive, and it possesses toxicity, all of which limit its application (Yang and Gao, 2000).

2.3.4 Melamine-formaldehyde resin-based solidification slurry

Melamine-formaldehyde resin-based solidification slurry is typically composed of urea, formaldehyde, a certain amount of curing agent (mainly acid and acidic salts), and other modifiers or a combination with other resins. It has a wide range of material sources, low cost, low viscosity, and forms a consolidated structure with high compressive strength after reaction. However, it tends to be brittle with low toughness, making it prone to cracking, which is advantageous for subsequent fracturing construction. On the downside, its resistance to permeation is relatively poor. The slurry contains a significant amount of formaldehyde, resulting in an irritating odor during construction. This can pose a certain carcinogenic risk to humans and lead to environmental and groundwater pollution. Moreover, the acidic nature of the curing agent can corrode grouting equipment and pipelines (Wang, 2011).

3 Current research status of grouting solidification processes

3.1 Injection theory

In the practical implementation of grouting solidification technology, the theory of grouting has undergone continuous development. However, the engineering design parameters of grouting solidification technology are often based on engineering experience, and theoretical development lags behind practice, making it challenging to provide guidance for the engineering design of grouting solidification technology. Grouting theory is a comprehensive application of interdisciplinary knowledge, involving fluid mechanics, polymer chemistry, rock mechanics, and other disciplines. Depending on the geological characteristics and objectives of the construction site, the selection of grouting parameters and materials may vary. Different grouting methods can lead to different grouting effects (Wang et al., 2017). There are three main injection theory models: Permeation Grouting Theory, Compaction Grouting Theory, and Fracture Grouting Theory as shown in Figure 2.

1) Permeation Grouting Theory

Assumptions of Permeation Grouting Theory: ①The injection and diffusion of the slurry will not alter the fractures in the grouted medium or affect the skeletal structure; ②The slurry is assumed to be a continuous point or linear entity; ③The construction medium is considered isotropic (Zhang, 2022). During the construction process, the injected slurry permeates the construction medium, filling internal voids or fractures without disrupting the internal structure of the construction medium. After solidification, this process effectively enhances the mechanical properties of the construction medium. In the theory of permeation grouting, the diffusion forms of the slurry mainly include spherical diffusion and columnar diffusion (LI et al., 2016).

As shown in Figure 3, spherical diffusion is the radial spread of grouting material from the injection point in all directions, forming a spherical zone of influence around the injection point. It provides relatively uniform coverage in all directions, effectively filling voids and cracks around the injection point. Spherical diffusion is suitable for applications that require a consistent and isotropic (equal in all directions) distribution of injected material. Columnar diffusion involves the axial spread of grouting material from injection points arranged in a columnar distribution into a cylindrical zone of influence within the construction media. This diffusion pattern directs the spread more prominently in a specific direction,

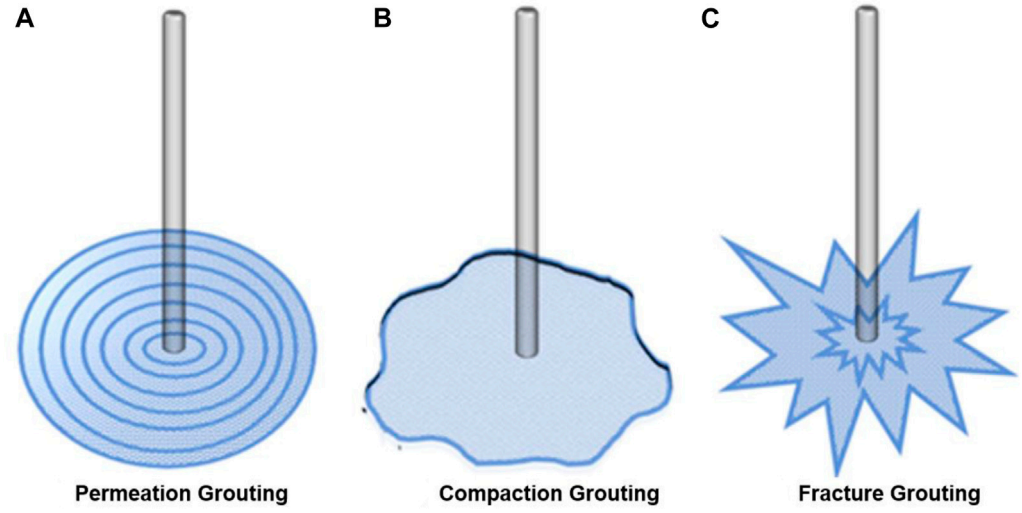


FIGURE 2
Different types of injection theory models (Wang, 2017). **(A)** Permeation Grouting **(B)** Compaction Grouting **(C)** Fracture Grouting.

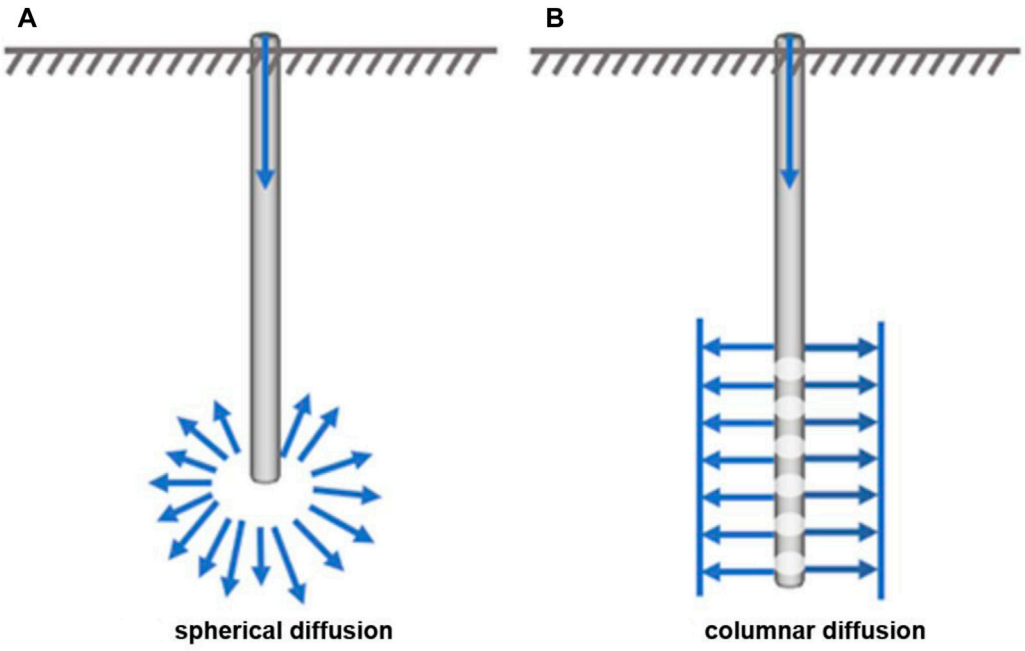


FIGURE 3
Schematic diagram of slurry infiltration and diffusion forms (LI et al., 2016). **(A)** Spherical diffusion **(B)** Columnar diffusion.

forming a cylindrical zone of influence. Columnar diffusion is advantageous when targeting specific planes or directions (e.g., along tunnels or pipelines). It is applicable in situations where material injection needs to be guided along a specific path, such as tunnel excavation or creating barriers along particular geological features (LI et al., 2016). The choice between spherical and columnar diffusion depends on the specific requirements of the project, including geological conditions, desired outcomes, and the need for uniformity or directed applications.

(2) Compaction Grouting Theory

Compaction grouting theory involves continuously injecting a large amount of grouting material with poor diffusivity into the construction medium by increasing the injection pressure within a certain range. As the grouting volume increases, the pressure exerted by the slurry on the grouting medium steadily rises, leading to compaction and consolidation without causing fracturing damage. This process aims to strengthen the

construction medium and improve its resistance to permeation (Zhan et al., 2010).

(3) Fracture Grouting Theory

Fracture grouting theory involves increasing the injection pressure after compaction grouting until the slurry fractures and creates cracks within the construction medium. This process aims to increase the grouting volume, thereby using fracturing technology to improve the actual range of grouting solidification. (Li et al., 2014).

3.2 Grouting technology

Grouting technology is a widely used geological engineering method in various fields such as underground engineering, construction, mining, and civil engineering. It involves injecting specific liquids or slurries into underground rocks or soils to improve their engineering properties, enhance geological stability, control water inflow, reinforce foundations or rock layers, and improve the mechanical properties of soils or rocks. Grouting technology allows for *in-situ* reinforcement or modification of the construction medium, enabling the construction medium within the grouting range to be connected with the grouting material to form a unified whole, achieving the purpose of reinforcement or modification (Hu et al., 2022). The history of grouting technology can be traced back to 1802 when French engineers first used the method of manual pounding to inject clay slurry into the walls of the port of Dieppe for reinforcement. Subsequently, grouting technology continued to evolve, introducing materials such as cement, water glass, polyurethane, and others, becoming crucial for reinforcement and waterproofing in fields like mining and construction. With the development of the chemical industry, the diversity of grouting materials increased, expanding the application scope of grouting technology and significantly improving its effectiveness (Xiao et al., 2021).

Currently, grouting technology is widely applied in various fields, including grouting in mine shafts, plugging water inrush points, restoring flooded mines, grouting in shafts to block water in aquifers or along water-bearing faults, curtain grouting for water cutoff, reducing mine water inflow, bottom grouting for solidification to prevent water inrush, and more (Chen, 2019). In these applications, grouting technology has achieved favorable results, providing reliable solutions for engineering safety and stability.

3.3 Construction process

Grouting process is an essential part of grouting consolidation technology, and it is matched with grouting materials to achieve optimal grouting effects. When grouting, the construction technology needs to be reasonably selected based on comprehensive considerations such as the geological structural conditions of the construction medium, the depth and scope of grouting, the goals expected to be achieved after grouting, environmental factors, and the project budget. Currently, the grouting consolidation technology includes the following processes: single-stage grouting consolidation process, multi-stage grouting consolidation process, layered and staged grouting consolidation process, and "concentric ring" grouting consolidation process (YANG et al., 2022).

The single-stage grouting consolidation process involves drilling holes into the construction medium to the required depth. Based on the needed volume of grout, the entire range of reinforcement and modification is achieved in one go by grouting through a single hole (Zhou et al., 2010).

The multiple-stage grouting consolidation process involves conducting additional grouting sessions immediately after the first grouting session if the expected results are not achieved. The second grouting session supplements the initial one, filling unreinforced cracks and expanding the grouting area. If the desired effect is still not achieved, a third grouting session can be performed (Xu, 2017).

The staged grouting consolidation process involves injecting grout in stages based on the permeation mechanism of the grouting consolidation process, particularly the theory of spherical diffusion. It includes grouting and consolidating the shallow areas of the boreholes first. After effectively reinforcing the soft conditions in the shallow area of the boreholes, additional boreholes are drilled, and the process is repeated in multiple stages to reinforce large areas of the construction medium (Zhang et al., 2018).

The "concentric ring" grouting consolidation process is designed for situations where some fragmented coal layers are challenging to support during drilling. Initially, a small-scale pre-consolidation is performed on the boreholes, and then larger-diameter boreholes are used for expanding and reinforcing specific sections. Finally, the reinforced boreholes are employed to inject grout and consolidate the construction medium (Zhang et al., 2019).

4 Methods for evaluating the grouting solidification effect

After the completion of grouting solidification, it is essential to conduct a comprehensive evaluation of the grouting effect. Currently, the primary evaluation methods include analytical methods, borehole inspection methods, and geophysical methods (Wang et al., 2019).

The analytical method involves systematically organizing construction information obtained during the grouting solidification process, including grouting pressure, grouting velocity, total grout volume, reinforcement volume, and water inflow before and after grouting. Through the analysis and comparison of these data with simulated numerical values, a rational evaluation of the grouting solidification effect is conducted (Pang, 2008).

The borehole inspection method involves drilling holes in the deep-seated zones of grouting solidification during and after the construction process. The evaluation is based on the difficulty of drilling, water and sand inflow in the detection hole, filling status of cracks in the borehole, and experimental measurements on samples extracted. This comprehensive assessment helps judge the effectiveness of grouting solidification (Shao, 2020).

The geophysical method involves measuring the resistivity and electromagnetic characteristics of the construction media before and

after grouting. Through comparative analysis, this method evaluates the effectiveness of grouting solidification (Liu et al., 2022).

5 Conclusion

The grouting solidification of fragmented coal seams holds significant importance for increasing production and ensuring safety in the exploitation of coal and coalbed methane resources. Currently, drawing insights from grouting technologies across various industries, substantial research achievements have been made in the grouting solidification techniques for fragmented coal seams. The rational selection of grouting materials and processes can be achieved by considering the specific geological conditions of individual coal seams. However, challenges persist in the current approach.

1) The classification of fragmented coal seams primarily relies on the coal's firmness coefficient. In the grouting solidification process, the target medium for injection is predominantly the fractures. Before undertaking grouting solidification for fragmented coal seams, it is imperative to thoroughly consider parameters such as coal-rock strength, joint parameters, coal body integrity, crack width and length, as these factors have a tangible impact on the actual effectiveness of grouting solidification. This consideration provides a theoretical basis for the selection of grouting solidification materials.
2) For grouting materials, a prolonged setting time and excellent stability are required. Currently, existing grouting materials that meet these requirements are characterized by high costs and the potential to induce groundwater contamination and trigger coal spontaneous combustion. Future grouting solutions should primarily focus on the development of novel grouting materials that are safe, environmentally friendly, and cost-effective, addressing the shortcomings associated with the current options.
3) For the grouting process, it is essential to tailor the grouting parameters to different crack widths. The selection of appropriate grouting techniques should be based on the actual conditions, gradually forming a comprehensive set of process standards.
4) The current evaluation of grouting effectiveness often relies on qualitative and subjective assessments, lacking standardized, quantitative, and easily operational criteria. In the future, the evaluation of grouting effectiveness should introduce personalized and quantitative standards, taking into account various factors such as the nature of the target medium, distinct mechanical and joint parameters within the same medium, and specific engineering requirements. This approach aims to provide a more accurate and systematic assessment of the grouting outcomes.

Author contributions

ZG: Writing–original draft. ZS: Methodology, Writing–review and editing. JW: Writing–review and editing, Investigation. Zi: Conceptualization, Writing–review and editing, Writing–original draft. ZY: Investigation, Writing–review and editing. LH: Investigation, Writing–original draft. LX: Investigation, Writing–review and editing. FH: Investigation, Writing–review and editing.

Funding

The author(s) declare financial support was received for the research, authorship, and/or publication of this article. This study received funding from: North China Oilfield Company by a North China Oilfield Company Collaborative Research Project "Efficient Transformation Technology Research and Application of Medium and High-Rank Coal Reservoirs" (2020-HB-XQ07); China National Petroleum Corporation by a China National Petroleum Corporation Forward-looking Foundational Project "Technological Research on Low-Damage and Efficient Development of Coalbed Methane: Supporting Engineering" (2021DJ2305); North China Oilfield Company by a North China Oilfield Company Research Project "Key Technology Research on Efficient Fracturing for Coalbed Methane Production" (2022-HB-M07). The funders were not involved in the study design, collection, analysis, interpretation of data, the writing of this article or the decision to submit it for publication.

Conflict of interest

Authors ZG, JW, ZY, LX, and FH were employed by PetroChina North China Oilfield Engineering Technology Research Institute.

The remaining authors declare that the research was conducted in the absence of any commercial or financial relationships that could be construed as a potential conflict of interest.

Publisher's note

All claims expressed in this article are solely those of the authors and do not necessarily represent those of their affiliated organizations, or those of the publisher, the editors and the reviewers. Any product that may be evaluated in this article, or claim that may be made by its manufacturer, is not guaranteed or endorsed by the publisher.

References

Chao, F., Xia, R., and Rong, C. (2016). Etc. Preparation and properties of PU/silicate organic-inorganic hybrid materials by *in situ* method. *China Plast. Ind.* 44 (07), 7–10.

Chen, Y. (2019). *Formation mechanism of the collapse column of 19109 working face in Jinggong No.1 Mine Evaluation of governance effects*.

Feng, Z. (2007). Material development and research of osmosis and diffusion on chemical grouting for extraordinary cracked coal and rockmass [D]. Doctoral thesis. Coal Science Research Institute.

Geng, G. (2019). Application research of grouting material in coal mining. *Shanxi Chem. Ind.* 39 (02), 122–124. doi:10.16525/j.cnki.cn14-1109/tq.2019.02.43

Guo, W., Ma, Z., and Bai, E. (2020). Current status and prospect of coal mining technology under buildings, water bodies and railways, and above confined water in China. *Coal Sci. Technol.* 48 (09), 16–26. doi:10.13199/j.cnki.cst.2020.09.002

Hou, K., Wang, S., and Yao, S. (2022). etc. Research progress on modification of polyurethane grouting materials in mines. *Coal Sci. Technol.* 50 (10), 28–34. doi:10.13199/j.cnki.cst.2021-0501

Hu, S., Liu, Q., and Li, S. (2022). etc. Advance and review on grouting critical problems in fractured rock mass. *Coal Sci. Technol.* 50 (01), 112–126. doi:10.13199/j.cnki.cst.2021-0103

Karol, R. H. (1990). *Chemical grouting[M]*. New York: Marcel Dekker, 465.

Li, J., Li, G., and Haijin, H. (2021). etc. Technology of across-goaf drainage of coalbed methane from a lower coal seam group and its primary application: taking Sihe mine field as an example. *Coalf. Geol. Explor.* 49 (04), 96–104. doi:10.3969/j.issn.1001-1986.2021.04.012

Li, S., Zhang, W., and Zhang, Q. (2014). etc. Research on advantage-fracture grouting mechanism and controlled grouting method in water-rich fault zone. *Rock Soil Mech.* 35 (03), 744–752. doi:10.16285/j.rsm.2014.03.030

Li, S., Liu, R., and Zhang, Q. (2016). etc. Protection against water or mud inrush in tunnels by grouting: a review. *J. Rock Mech. Geotechnical Eng.* 8 (5), 753–776. doi:10.1016/j.jrmge.2016.05.002

Liu, S., Chen, J., and Xu, Z. (2022). Study on the effect of karst grouting based on indoor geophysical model test. *Railw. Eng.* 62 (12), 158–161. doi:10.3969/j.issn.10031995.2022.12.31

Pang, T. (2008). Experimental study of whole process grouting used in tunnel passing through existing structures. *Rock Soil Mech.* 29 (12), 3451–3458. doi:10.16285/j.rsm.2008.12.008

Ruan, W. (2005). Research on diffusion of grouting and basic properties of grouts. *J. Geotechnical Eng.* (01), 69–73. doi:10.3321/j.issn:1000-4548.2005.01.011

Shao, H. (2020). Analysis and treatment of cracks in high roller compacted concrete arch dams. *Water conserv. Tech. Superv.* (05), 202–205. doi:10.3969/j.issn.1008-1305.2020.05.055

Teng, J., Qiao, Y., and Song, P. (2016). Analysis of exploration, potential reserves and high efficient utilization of coal in China. *Chin. J. Geophys.* 59 (12), 4633–4653. doi:10.6038/cjg20161224

Wang, D. (2011). Mechanism of hydrodynamically chemical grouting in porous media [D]. Doctoral thesis. China University of Mining and Technology.

Wang, L. (2017). *Study of grouting technology's mechanism and application in subgrade reinforcement [D]*. Master's thesis. Shan Dong University. doi:10.3969/j.issn.1671-1815.2017.23.020

Wang, X., Qin, Q., and Su, P. (2017). Etc. Research status and development tendency of fractured surrounding rock grunting reinforcement technology. *Sci. Technol. Eng.* 17 (23), 122–131.

Wang, X., Qin, Q., and Xiong, Z. (2019). Etc. Comprehensive evaluation for grouting effect of fractured surrounding rock in deep roadway. *Chin. J. Undergr. Space Eng.* 15 (02), 576–582.

Xiao, Z., Yang, Z., and Long, J. (2021). etc. The development trend and application of grouting support materials. *Industrial Minerals Process.* 50 (05), 38–41+8. doi:10.16283/j.cnki.hgkwyjg.2021.05.010

Xie, C. (2021). Experimental study on coal model reinforced by new polyurethane/water glass double liquid slurry grouting [D]. Master's thesis. Anhui University of Science and Technology. doi:10.26918/d.cnki.ghngc.2020.000289

Xu, J. (2017). Application of double liquid multiple splitting grouting reinforcement and rectification of soft soil foundation. *Constr. Technol.* 46 (S1), 145–149.

Yang, L., and Gao, B. (2000). Experiment study of concrete element remedy by chemical grouting. *Archit. Technol.* (06), 385–386. doi:10.3969/j.issn.1000-4726.2000.06.011

Yang, R. K., Zhang, S., and Tao, W. P. (2022). Etc. Application of sectional grouting by polymer material in sand reinforcement. *J. Munic. Technol.* 40 (05), 146–150. doi:10.19922/j.1009-7767.2022.05.146

Zhan, Y., Song, X., and Chen, M. (2010). Research progress on grouting theory in rock mass. *Roadbed Proj.* (02), 20–22. doi:10.3969/j.issn.1003-8825.2010.02.008

Zhang, C., Liang, J., and Yang, J. (2019). etc. Sealing mechanism of slurry materials considering temporal and spatial variation of viscosity. *Chin. J. Geotechnical Eng.* 41 (05), 974–980. doi:10.11779/CJGE201905022

Zhang, J., Li, S., and Zhang, X. (2018). etc. Model test on grouting diffusion in rock and soil layered medium. *J. Zhejiang Univ. Eng. Sci.* 52 (05), 914–924. doi:10.3785/j.issn.1008-973X.2018.05.011

Zhang, K., Zeng, X., and Zhang, L. (1995). Etc. Testing and study of water shut-off by solidifid clay mud. *Explor. Eng. Geotech. Drill. Eng.* (01), 18–20.5.

Zhang, Q., Li, Q., and Fan, X. (2022). etc. Current situation and development trend of theories and technologies for coal and CBM co-mining in China. *Nat. Gas. Ind.* 42 (06), 130–145. doi:10.3787/j.issn.1000-0976.2022.06.011

Zhang, Z. (2022). Study of mechanism and technology of high-pressure fracturing grouting in roadway in 1000m deep coalmine [D]. Doctoral thesis. China Coal Research Institute. doi:10.27222/d.cnki.gmkzy.2021.000012

Zhou, B., Jinwei, H., and Zhang, C. (2016). Analysis on borehole instability under coupled multiple stress and dynamic sealing technology in soft coal seam. *Coalf. Geol. Explor.* 44 (04), 161–166. doi:10.3969/j.issn.1001-1986.2016.04.031

Zhou, L., Liao, S., and Shi, N. (2010). Etc. *In-situ* test of grouting reinforcement for subway tunnel foundation in soft ground. *J. Chongqing Jiaot. Univ. Nat. Sci.* 29 (06), 880–884.

frontiers | Frontiers in Energy Research

TYPE Original Research
PUBLISHED 29 December 2023
DOI 10.3389/fenrg.2023.1328662

Check for updates

OPEN ACCESS

EDITED BY
Xiaojin Zheng,
Princeton University, United States

REVIEWED BY
Wang Song,
China University of Petroleum, China
Bo Yu,
Northeast Petroleum University, China

*CORRESPONDENCE
Li Dan,
lidan6@cnooc.com.cn

RECEIVED 27 October 2023
ACCEPTED 29 November 2023
PUBLISHED 29 December 2023

CITATION
Yu Q, Dan L, Shanshan Y and Qixin L (2023), Geophysical exploration methods on bauxite reservoirs in L gasfield, Ordos Basin.
Front. Energy Res. 11:1328662.
doi: 10.3389/fenrg.2023.1328662

COPYRIGHT
© 2023 Yu, Dan, Shanshan and Qixin. This is an open-access article distributed under the terms of the Creative Commons Attribution License (CC BY). The use, distribution or reproduction in other forums is permitted, provided the original author(s) and the copyright owner(s) are credited and that the original publication in this journal is cited, in accordance with accepted academic practice. No use, distribution or reproduction is permitted which does not comply with these terms.

Geophysical exploration methods on bauxite reservoirs in L gasfield, Ordos Basin

Qi Yu, Li Dan*, Yu Shanshan and Li Qixin

Cnooc Research Institute Ltd., Beijing, China

Introduction: The L gasfield on the eastern edge of the Ordos Basin mainly focuses on the exploration and development of coalbed methane and tight sandstone gas. As the overlying strata of Majiagou Formation of Lower Ordovician in Lower Paleozoic, bauxite has always been considered a regional cap rock and has not been widely followed with interest. The drilled wells has revealed that bauxite can be used as a unconventional reservoir with good reservoir properties. In the future, it will become a new natural gas exploration target in the L region. This article is dedicated to the comprehensive study of geophysical methods for the bauxite exploration in the L region.

Methods: Firstly, we use seismic data to restore paleo-geomorphology of the Lower Paleozoic. Secondly, we analyze the well log data of different paleo-geomorphic unit. Then, we establish a mineral model based on the logging data to calculate the lithological composition and porosity, and use imaging logging to evaluate the pore structure and fluid type.

Result and Discussion: Finally, we obtained favorable reservoir development zones for bauxite, guiding exploration and evaluation of bauxite.

KEYWORDS

bauxite reservoirs, paleo-geomorphology, well logging evaluation, imaging logging, unconventional reservoir

1 Introduction

The L region is an unconventional gas region of China National Offshore Oil Corporation. Mainly focused on the exploration and development of tight sandstone gas and deep coalbed methane in the Carboniferous and Permian. At present, exploration in these two fields has gradually come to an end (Zhu et al., 2022; FengRuyong, 2022; Li, 2023; Xu et al., 2023; Tang et al., 2022; Tang et al., 2023). In the L region, as the overlying strata of Ordovician in Lower Paleozoic, bauxite has always been considered a regional cap rock and has not been widely followed with interest (Nan et al., 2022; Pan et al., 2023; Yuan et al., 2016). After 2020, China National Petroleum Corporation Changqing Oilfield conducted research and production testing on bauxite reservoirs, obtaining high production. During this period, She, Du, and others conducted geophysical forward modeling research on the sedimentary structure of bauxite, and used waveform indication simulation technology and inversion to predict the reservoir of bauxite (She et al., 2022; Du et al., 2022). Liu Wenhui and others qualitatively evaluated bauxite reservoirs using conventional, Full Micro-Resistivity Imaging (FMI) and Nuclear Magnetic Resonance (NMR) logging (Liu et al., 2015; Liu et al., 2022a). Liu Die quantitatively explained the lithology and porosity of bauxite reservoirs through core experimental data, combined with conventional logging and imaging logging (Liu et al., 2022b). Fu Jinhua conducted a detailed

analysis of nearly a hundred rock samples from the bauxite formation, and concluded that the bauxite reservoir developed dissolution pores and was controlled by sedimentary paleo-environments and paleo-geomorphology. The conclusion was drawn that bauxite gas exploration has opened up new fields for basin exploration (Fu et al., 2021; Fu et al., 2023). Comprehensive research has revealed that bauxite has become a new unconventional reservoir, but the exploration techniques for bauxite in different regions vary, and it is still necessary to find suitable exploration techniques for us.

This article uses 3D seismic data and logging data from nearly 160 drilled wells to restore paleo-geomorphology using the impression method, and obtains a map of the Ordovician top interface paleo-geomorphology. We classified and analyzed the bauxite rock data under different karst backgrounds. Establish a quantitative evaluation method for logging in this region through existing core experiments, and analyze the pore structure in combination with ERMI and NMR logging. Conduct a detailed analysis of the drilling data from over a hundred existing wells in this area to guide the exploration and development of bauxite suitable for this region.

2 Regional overview

The region L is located in the eastern edge of the Ordos Basin. The main exploration targets are the Upper Paleozoic Carboniferous Benxi Formation, Permian Shihezi Formation, Shanxi Formation, and Taiyuan Formation. Among them, the 4 + 5$^{\#}$ and 8 + 9$^{\#}$ coal seams developed in the Benxi Formation and Taiyuan Formation are the main source rocks. The tight sandstone reservoirs of the Upper Paleozoic in this area belong to typical lithological gas reservoirs. Influenced by the Northern source and sedimentary environment, shallow marine delta or shallow lake delta sand bodies are mainly developed. Currently, the main exploration and development forces are still tight sandstone gas and deep coalbed methane.

The bauxite rock is developed at the bottom of the Benxi Formation and is a product of the weathering crust karst deposition of the Lower Paleozoic Ordovician. The Benxi Formation in the eastern part of the Ordos Basin is mainly composed of shallow sea continental shelves, lagoons, and tidal flats. A set of strata composed of iron aluminum layers, mudstones, sandstones, limestone, and coal seams was deposited. The lagoon facies developed gray black iron aluminum mudstone, bauxite, and tuffaceous sandstone and mudstone.

Bauxite rock is formed by weathering and leaching of aluminosilicate minerals in the original rock, forming aluminum containing colloids and high potassium clay. It is transported *in situ* or close proximity to karst depressions, lakes, bays, and lagoon basins, and is directly deposited or formed by terrestrial decomposition, directly covering the weathered crust, forming characteristic oolitic, bean and block structures.

3 Reservoir characteristics and exploration research methods of bauxite

The bauxite in China can be divided into four types: sedimentary type, accumulation type, laterite type, and magmatic type. The bauxite in this study belongs to the weathering crust sedimentary type. The underlying bedrock is Ordovician carbonate rock. Due to different weathering crust karst processes, the sedimentary thickness of bauxite varies greatly and is widely distributed. Under different sedimentary conditions, the thickness, mineral content, and porosity of bauxite varies. At present, bauxite rock settlement can be divided into three categories: monadnock, terraces, and trenches. By using paleo-geomorphic restoration techniques, these three types of sedimentary methods can be accurately classified.

The main mineral of bauxite is diaspore, which can be divided into bauxite mudstone (with a diaspore content of 25%–50%), argillaceous bauxite (with a diaspore content of 50%–75%), and bauxite (with a diaspore content exceeding 75%) based on its mineral content. Through X-Ray Diffraction (XRD) analysis, in addition to diaspore, bauxite contains terrigenous clastic rocks such as clay minerals and quartz, as well as heavy minerals such as pyrite, hematite, and anatase. The mineral composition is complex and diverse (Table 1). The highest content of diaspore is 94%, the highest content of heavy metals is 35%, and the clay minerals range from 3% to 10%, with a porosity range of 2.5%–10%.

The logging of bauxite have the characteristics, which are high neutron, high gamma, high density, low slowness and low resistivity. Under weathering and leaching, elements such as potassium and sodium are lost. During the Ordovician period, the Ordos Basin was at a high tide of marine invasion, and the crust continued to sink during the sedimentary period of the Benxi Formation, further expanding the scope of marine invasion. The abundance of carbonate solution increases the solubility of uranium in seawater, and elements such as uranium and thorium are transported and enriched after being fully analyzed. Bauxite rock have strong adsorption properties, resulting in the occurrence of high uranium, high thorium, and low potassium in the bauxite rock (Yang et al., 2006; Jiang and Wang, 2004). Enriched high radioactive elements such as uranium and thorium result in abnormally high natural gamma rays, with some layers having natural gamma values higher than 600API.Therefore, using gamma rays to determine the formation of bauxite has become the most commonly used logging method.

The exploration technology and methods for bauxite reservoirs, which detailed introduction in Figure 1, are mainly divided into the following three steps:1) Using a large amount of drilled data and 3D seismic data, the Paleo-geomorphology restoration of the Ordovician top interface was carried out using impression technology.2) Establish a quantitative logging interpretation model based on core experimental data (XRD, physical property analysis, thin sections, etc.). Calculate parameters such as lithology, minerals, porosity, permeability, and divide pore structure through imaging logging system.3) Divide favorable areas for bauxite exploration through sedimentary characteristics and quantitative interpretation of drilled holes, and guide the next step of work.

4 Paleo-geomorphology restoration technology

The characteristics of Paleo-geomorphology control the mode and intensity of karst. The sedimentary characteristics of bauxite vary under different karst Paleo-geomorphology. This study used the impression method to restore Paleo-geomorphologys in the region.

TABLE 1 Mineral content and logging response table for core experiments.

Well	Lithology	Mineral content					Well log data				
		Diaspore	Sand	Shale	Pyrite	Anatase	GRAPI	DT us/ft	DEN g/cm3	$\varnothing_{cnl}$%	RtΩ·m
L-A	Argillaceous bauxite	71	2	7	4	13	497.4	59.0	2.97	56.8	199.6
L-A	Bauxite	80	0	6	6	12	546.5	52.5	3.15	67.5	22.4
L-A	Argillaceous bauxite	63	0	16	10	26	462.5	52.1	3.16	64.1	33.8
L-A	bauxitic shale	48	0	22	13	35	437.9	49.4	3.09	53.9	21.3
L-B	Bauxite	94	0	3	1	2	547.2	52.6	2.92	71.5	21.4

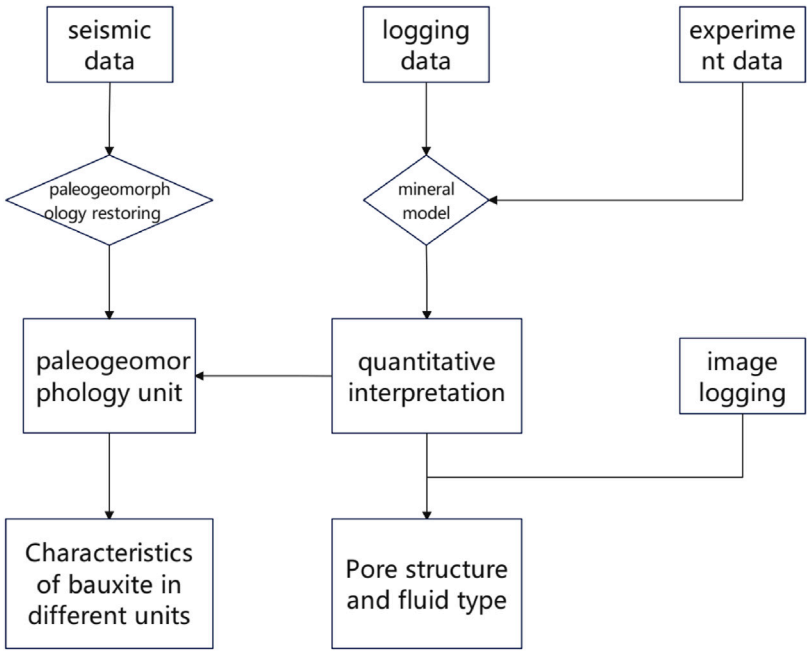


FIGURE 1
Flow chart of research on bauxite exploration methods.

The impression method utilizes the principle of sedimentary compensation to use the top boundary of the overlying strata as an isochronous reference plane, restoring the thickness between the top boundary of the erosion surface and the reference plane, and describing the paleo-geomorphology form through a mirror image relationship (Cao et al., 2020; Jia et al., 2023; Qiu et al., 2021). The top of the Benxi Formation is the 8# coal seam, which can be stably distributed and tracked throughout the entire area. The bottom of the Benxi Formation is the Ordovician erosion surface. By leveling the $8^{\#}$ coal seam, the bottom of the Benxi Formation is the pre-sedimentary Paleo-geomorphologys of Benxi.

4.1 Horizon interpretation

There is the stable coal seams in region at the top of Benxi formation, with a solid coal density of about 1.5 g/cm^3 and a sonic transit time of 120 us/ft, exhibiting low impedance and a strong amplitude trough in the seismic waveform, as shown in Figure 2. The bottom of Benxi is composed of bauxite and bauxite mudstone, and the underlying strata are Ordovician carbonate rocks. The density and velocity of bauxite vary with the content of diaspore. However, the underlying strata still exhibit high impedance, manifested as wave peaks, and the amplitude varies with the content of diaspore. The Benxi Formation is a transitional sedimentary facies of the sea route, with complex lithology, including various lithologies such as coal seams, sandstone, mudstone, limestone, bauxite.

As shown in Figure 3, according to more than 160 drilled wells in the region, the thickness of the Benxi Formation varies from 50 to 110 m. According to the thickness of the Benxi Formation, the Paleo-geomorphology units are further divided, as shown in Table 1. The lithology of the Benxi Formation includes coal and carbonaceous mudstone with low longitudinal impedance, mudstone with medium longitudinal

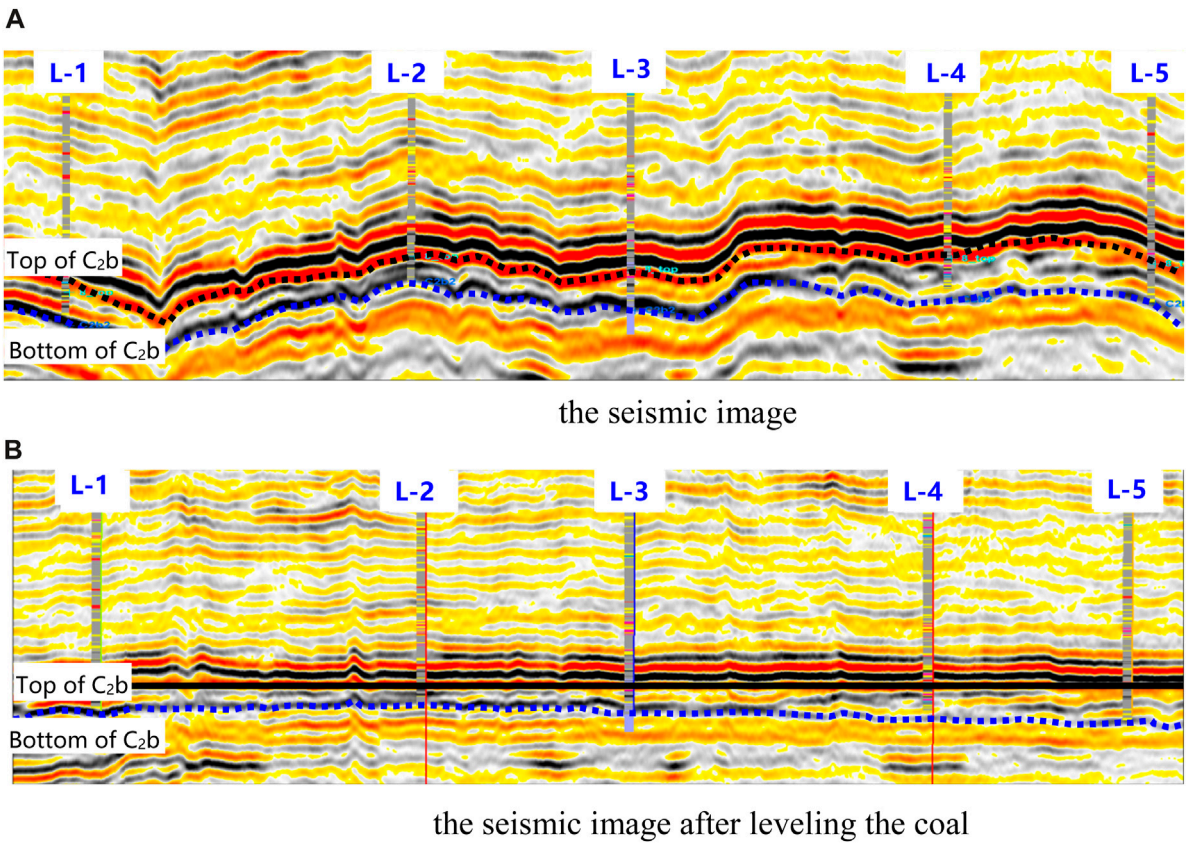


FIGURE 2
Impression method for paleo-geomorphology characterization. **(A)** the seismic image. **(B)** the seismic image after leveling the coal.

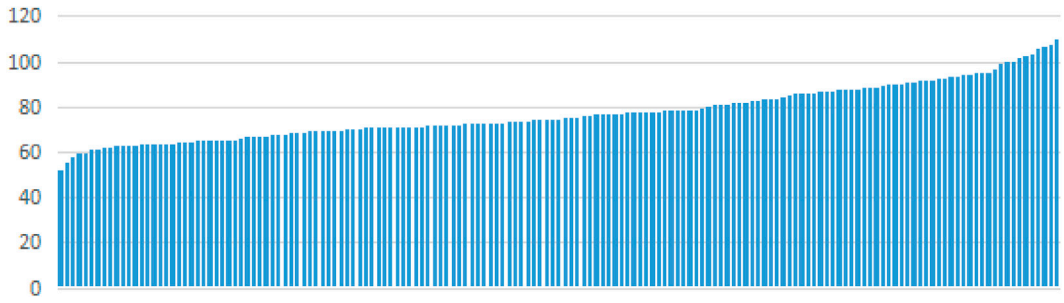


FIGURE 3
Thickness statistics of benxi formation for 162 Wells in L region.

impedance, gas-bearing sandstone, mudstone with medium to high longitudinal impedance, bauxite mudstone, dry sandstone, and limestone and bauxite with high longitudinal impedance. The complex and diverse lithology and wide range of thickness variation make it difficult to interpret the seismic horizons at the bottom of the Benxi Formation, This article verifies the correctness of the interpretation layers through forward modeling using different interpretation schemes.

4.2 Analysis of karst paleo-geomorphology classification

This region has been drilled and explained, with a depth range of 45–110 m in the Benxi Formation. As shown in Table 2, based on the thickness of the Benxi Formation and the classification of paleo-geomorphology, the secondary paleo-geomorphic units can be divided into karst slopes and karst

10.3389/fenrg.2023.1328662

TABLE 2 Division table of paleo-geomorphic units.

Secondary paleo-geomorphic unit	Tertiary paleo-geomorphic unit	The thickness of benxi formation	
karst slopes	monadnock	45–90 m	45–55 m
	slopes		55–65 m
	trench		65–90 m
karst basins	monadnock	60–110 m	60–75 m
	terraces		75–85 m
	trench		85–110 m

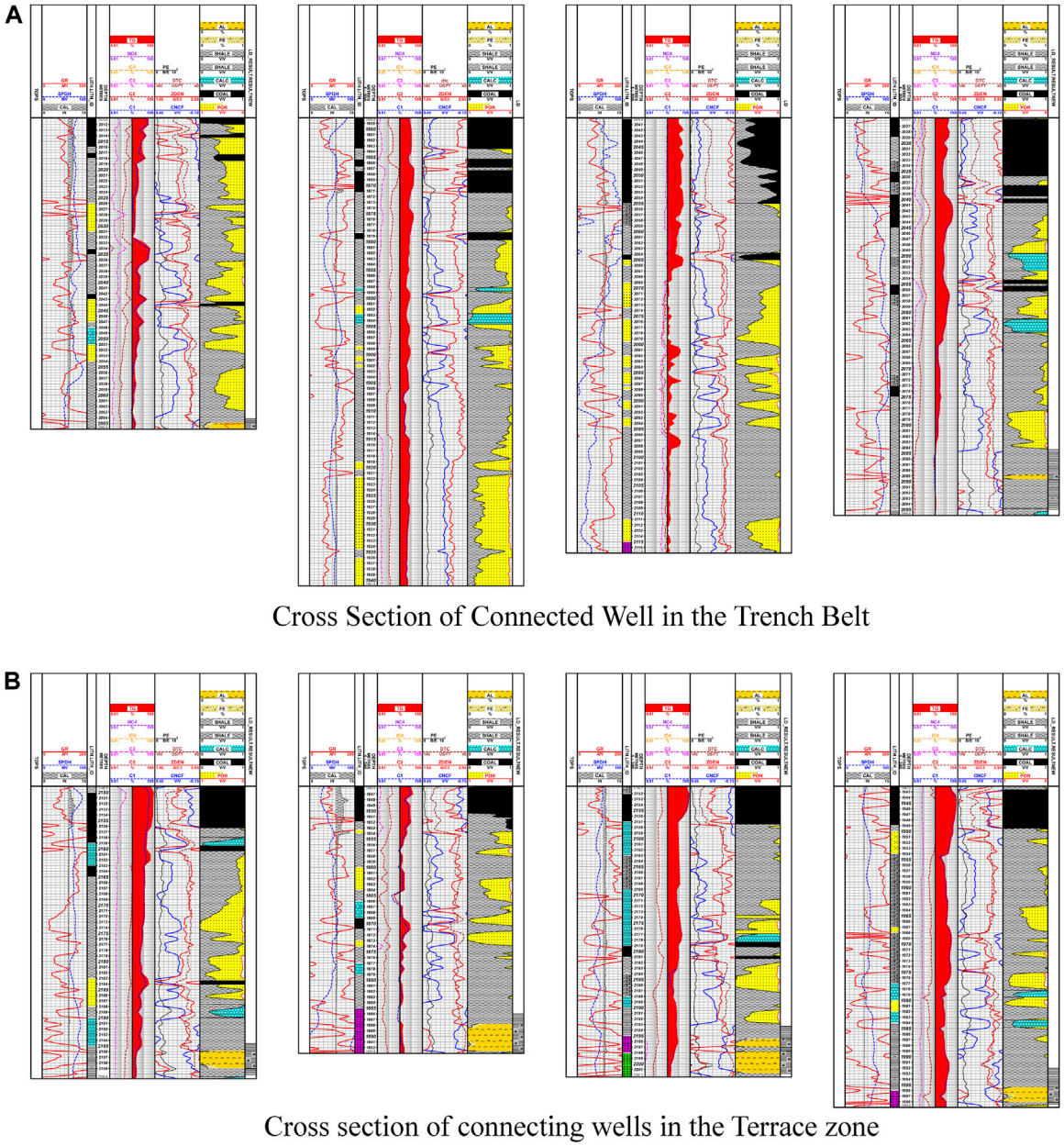
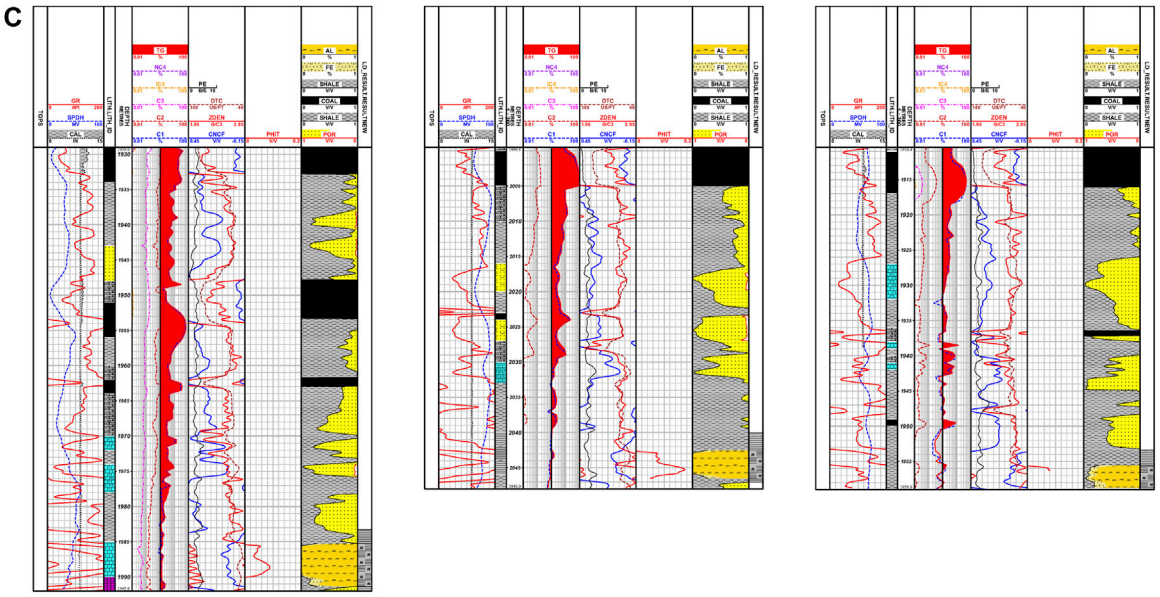
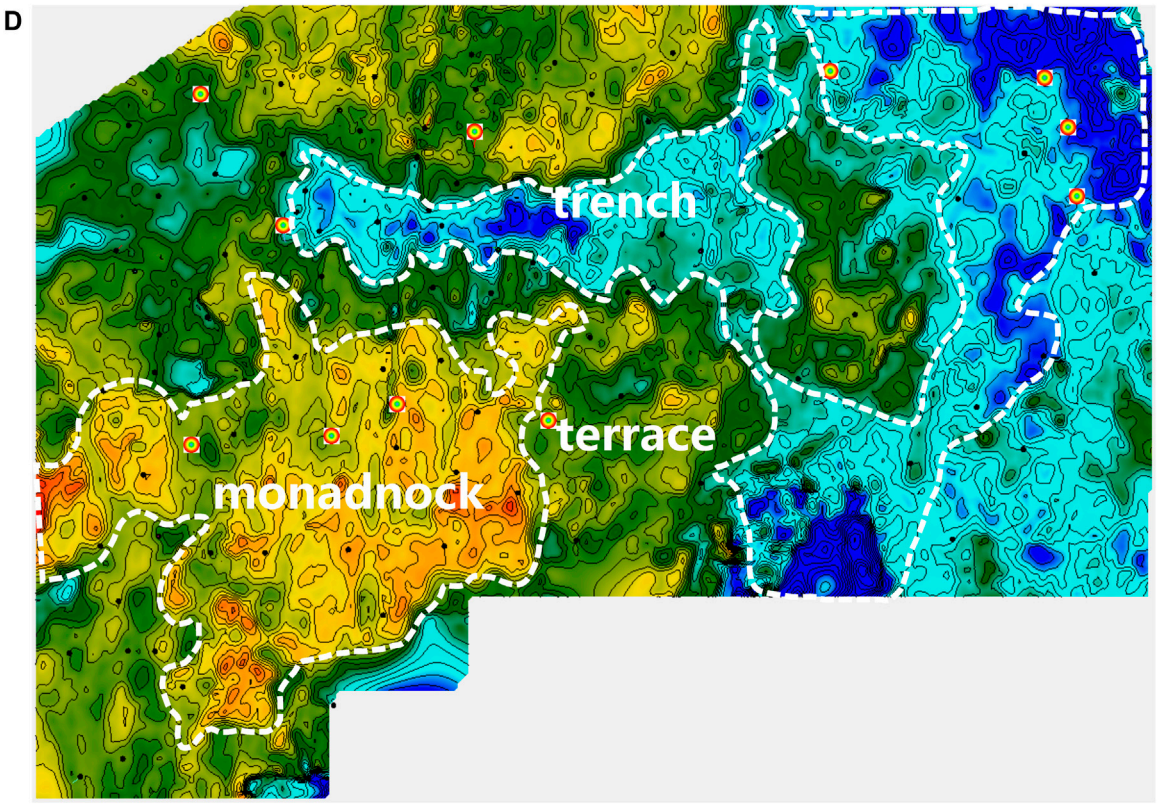


FIGURE 4
Analysis of logging interpretation and connected well profiles within different paleo-geomorphic units. **(A)** Cross section of connected well in the Trench Belt. **(B)** Cross section of connecting wells in the Terrace zone. **(C)** Cross section of connected wells in the in the sinkhole of monadnock. **(D)** Restoration map of paleo-geomorphology of benxi formation in region L Figure 4 Analysis of logging interpretation and connected well profiles within different paleo-geomorphic units.



Cross section of connected wells in the in the sinkhole of monadnock



Restoration Map of paleo-geomorphology of Benxi Formation in Region L

FIGURE 4
(Continued) Analysis of logging interpretation and connected well profiles within different paleo-geomorphic units. **(A)** Cross section of connected well in the Trench Belt. **(B)** Cross section of connecting wells in the Terrace zone. **(C)** Cross section of connected wells in the in the sinkhole of monadnock. **(D)** Restoration map of paleo-geomorphology of benxi formation in region.

basins, and each secondary unit can be further divided into three levels of units. Conduct well connection analysis on the trench, monadnock, and terraces (slopes) within the third level unit, and summarize the impact of paleo-geomorphology units on the sedimentary thickness and porosity of bauxite.

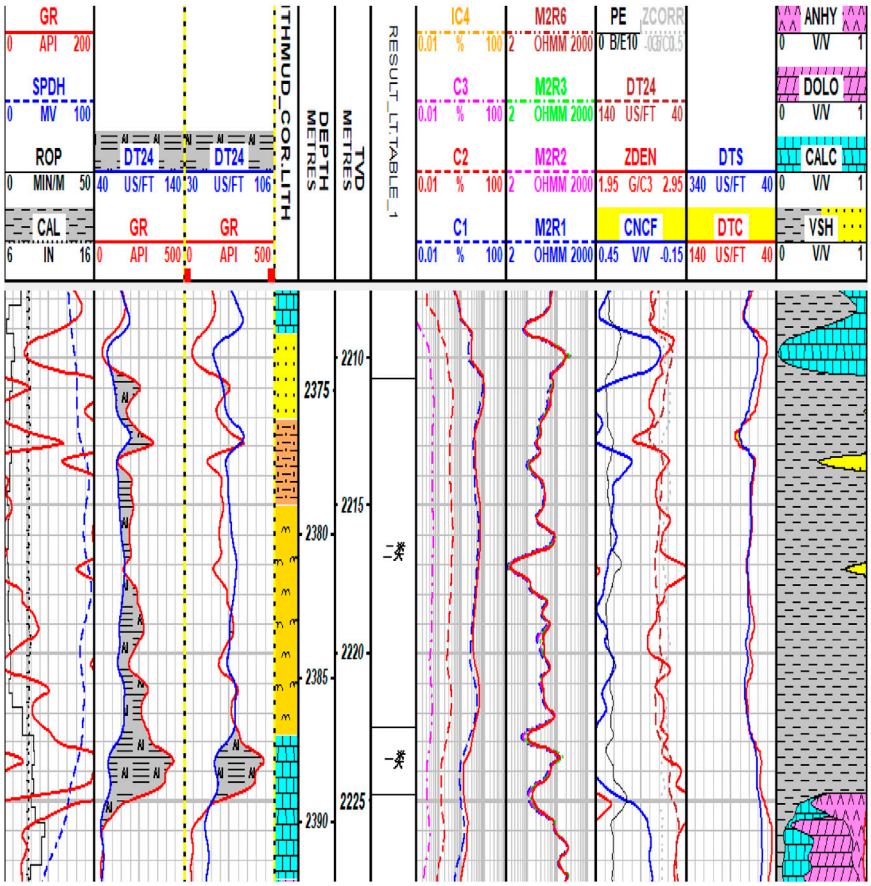


FIGURE 5
Qualitative analysis of logging interpretation.

Trench: As shown in Figure 4A, logging interpretation was performed on four wells within the trench, with a thickness range of 65–85 m for the Benxi Formation. Three wells are located in the trench zone of the basin, with bauxite rock thicknesses of 0, 0, and 0.7 m respectively; A well is located in a slope trench zone, with a thickness of 1.2 m of bauxite and an average thickness of about 0.5 m.

Slopes: As shown in Figure 4B, logging interpretation was performed on four wells within the slopes. The thickness range of the Benxi Formation for the four wells is 50.4–57 m, located in the slope zone. The thickness of the bauxite rock is 3.2, 4.8, 4.7, and 3 m, respectively, with an average thickness of 3.9 m.

Monadnock:As shown in Figure 4C, logging interpretation was performed on three wells with the sinkhole in the monadnock. The thickness range of the Benxi Formation in the three wells is 48.5–63 m, located in the sinkhole of the slope monadnock. The thickness of the bauxite rock is 6.3, 4, and 3.5 m, with an average thickness of 4.6 m.

As shown in Figure 4, by restoring the thickness of paleo-geomorphology, we divided different units, and the wells within each unit were statistically analyzed.Besides, the thickness of bauxite in the trench zone is thinner than that of slopes and monadnock, and there is basically no bauxite reservoirs in the trench. There is the thicker and more pure bauxite rocks in slopes and monadnock, with a thickness of 3–6.3 m. The total gas values of bauxite rocks in the slopes areas are higher than those in the sinkhole of monadnock, indicating better gas properties.

5 Well logging evaluation

The qualitative identification of bauxite rock lithology is relatively simple, as shown in Figure 5. The anomaly high value of Gamma Ray in bauxite formation is the standard for qualitative identification. In the early stage, the GR and DT curve in the logging series intersected (the second and third channels) to distinguish between bauxite mudstone and high-quality bauxite reservoir. This method can only provide qualitative conclusions and has a relatively large error, making it difficult to quantitatively evaluate the porosity of high-quality bauxite rocks.

5.1 Establishing a logging model

Based on core experimental data and logging curve information, we can establish the relationship between rock

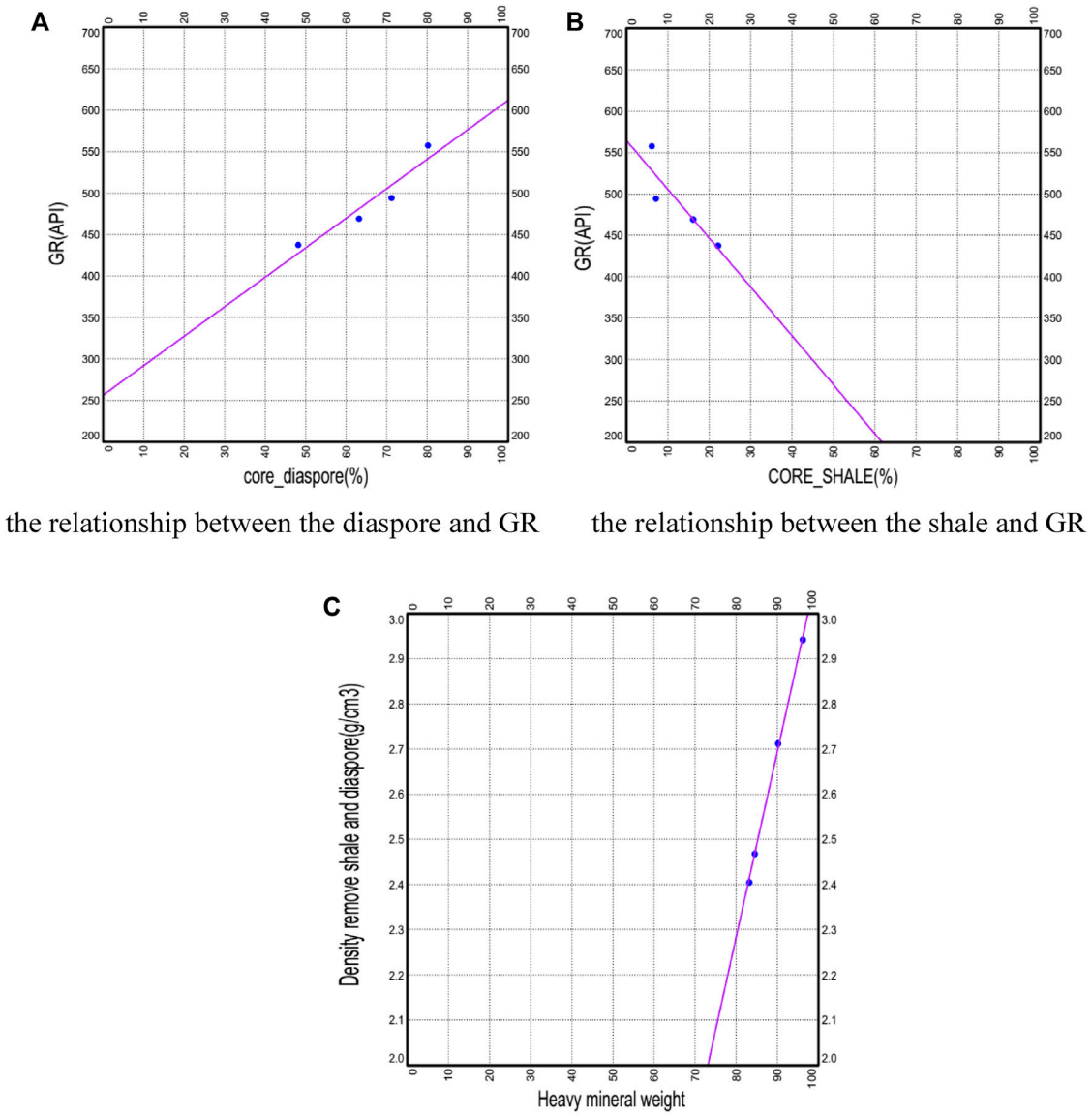


FIGURE 6
Relationship between mineral composition and logging response. **(A)** the relationship between the diaspore and GR. **(B)** the relationship between the shale and GR. **(C)** the relationship between the heavy mineral and density remove shale and diaspore.

mineral content and logging value, from formula 1–3. As shown in Figure 6, the R^2 is 0.996, 0.902, 0.998, respectively. And from these formulas we obtain a quantitative explanation of the lithological components. Based on the experience of neighboring areas, we establish the Wylle relationship between DT and porosity (equations 4; 5). And quantitatively explain the porosity of porosity and permeability through the pore permeability relationship.

$$V_{di} = 0.3717*GR - 114 \quad (1)$$

$$V_{py+an} = \frac{\rho + 1.0003 - 2.65*V_{sh} - 0.0411*V_{di}}{0.055485} \quad (2)$$

$$V_{sh} = -0.18823*GR + 104 \quad (3)$$

$$\Delta t_{ma} = 127.4V_{di} + 194V_{py+an} + 250V_{sh} \quad (4)$$

$$\varnothing = \frac{\Delta t - \Delta t_{ma}}{\Delta t_f - \Delta t_{ma}} - V_{sh}\frac{250 - \Delta t_{ma}}{\Delta t_f - \Delta t_{ma}} \quad (5)$$

5.2 Model validation

We verified the correctness of the quantitative lithology and porosity of the logging interpretation model through two wells, L-XX and L-XY. Among them, L-XX has core experimental data, and L-XY well has conducted NMR logging in the bauxite formation. Figure 7 is the log interpretation diagram of L-XX well. The logging traces from left to right in the figure are lithology logging traces, depth traces, total gas logging

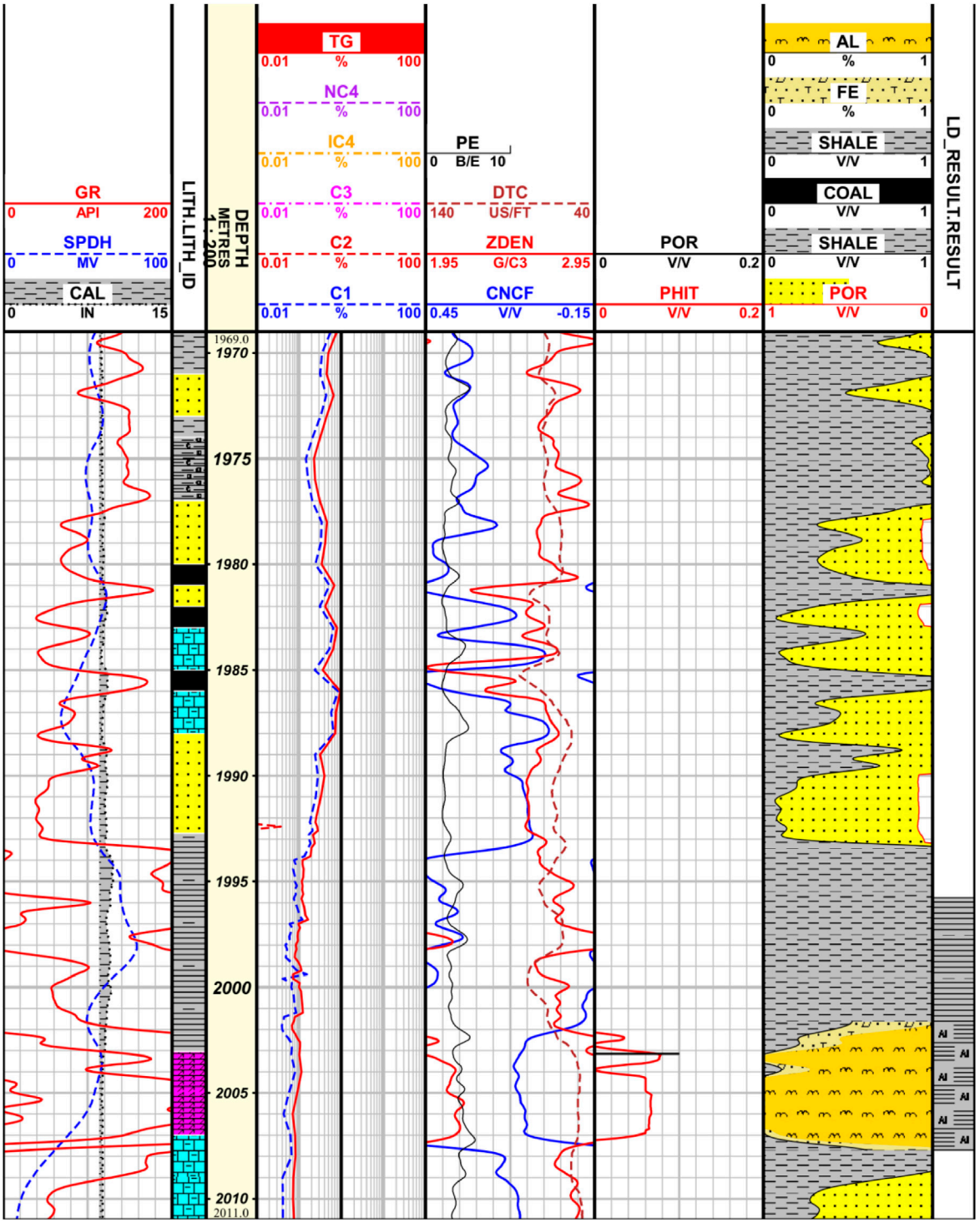


FIGURE 7
L-XX well logging interpretation and core experiment diagram.

traces, porosity logging traces, porosity traces, logging quantitative interpretation lithology traces, and logging interpretation conclusion traces. The content of diaspore, heavy mineral, and clay in the logging interpretation results of L-XX well is 94.5%, 1.1%, and 4.2%, respectively. Compared with the results of XRD diffraction analysis 94, 3, and 3, the relative errors are 0.5%, 1.9%, and 1.2%, respectively. Figure 8 is the log interpretation diagram of L-XY well. The porosity of the well was interpreted in sections ① and ②, which is consistent with the bimodal characteristics of the NMR T2 spectrum, verifying the rationality of quantitative interpretation of lithology and porosity.

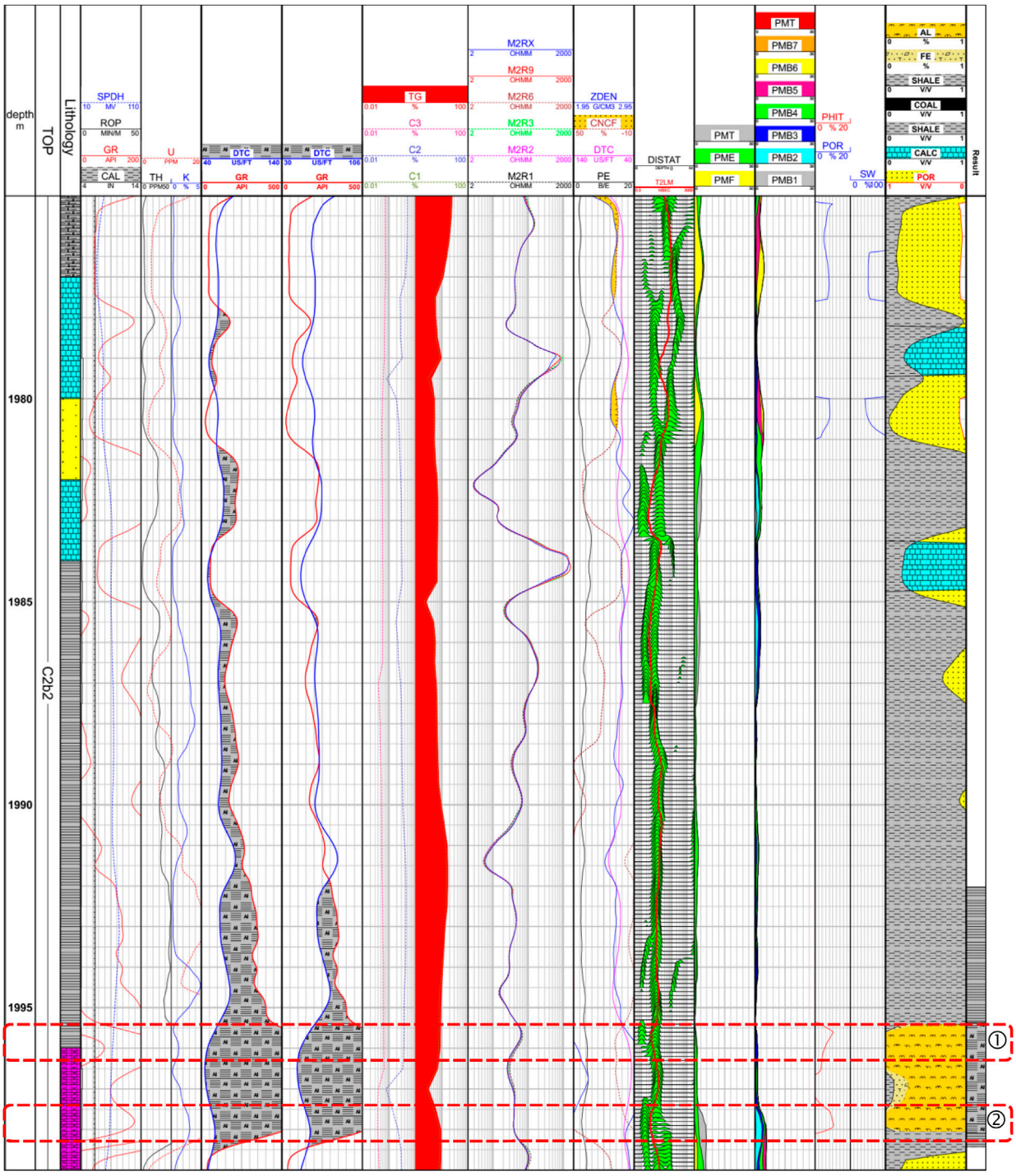


FIGURE 8
L-XY well logging interpretation of bauxite with NMR logging.

5.3 Imaging logging analysis

The imaging logging series includes various logging methods such as acoustic wave, resistivity, nuclear magnetic resonance, etc., (Wang et al., 2022; Wang et al., 2021; Dan et al., 2019). At present, the development of imaging logging has been able to quantitatively evaluate fractures, identify pore structures, and evaluate fluid properties (Wang et al., 2023; Li et al., 2021; Li et al., 2021; Ben et al., 2020; Yang et al., 2019). This study further analyzes the pore structure and fluid properties of bauxite strata through electrical imaging porosity spectrum, conductivity spectrum, and apparent formation water resistivity distribution spectrum. The 14th trace in

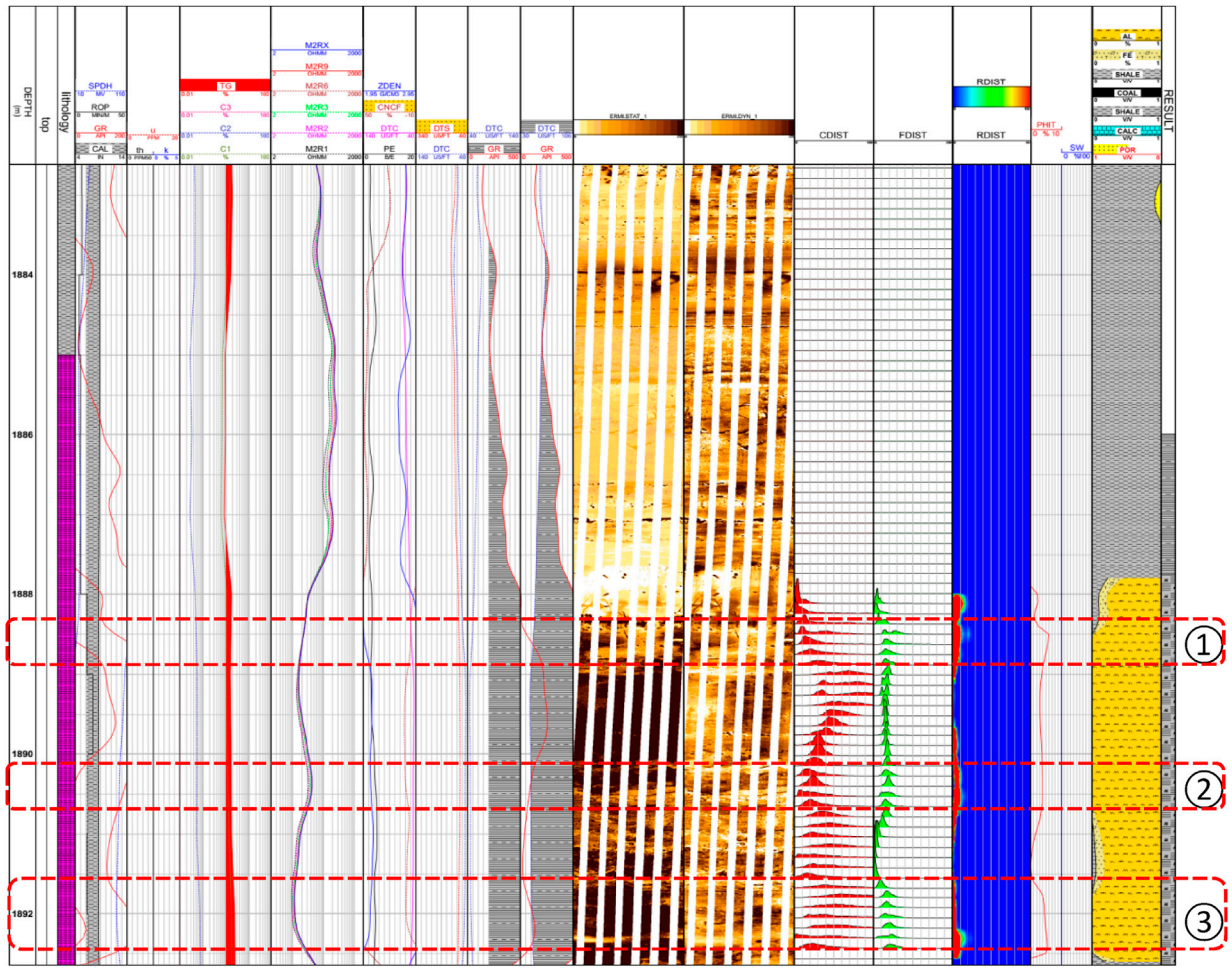


FIGURE 9
Analysis of electrical imaging logging spectrum.

Figure 9 shows the conductivity spectrum, which mainly reflects the difference in conductivity in the imaging logging image. In areas with high conductivity, the peak value shifts back as a whole. Both bauxite and argillaceous bauxite have high electrical conductivity. Conventional lithology analysis shows that some of the high electrical conductivity is influenced by heavy minerals and does not have good pores. The 15th trace in Figure 9 shows the porosity spectrum, which is similar to the T2 spectrum of NMR logging and can reflect the distribution of formation porosity and large and small pores. Compared with conventional lithology, it can be seen that bauxite with high content of diaspore has more developed pores. The developed porosity intervals in this well can be divided into three sections. There is a trailing phenomenon in the porosity spectrum, but the trailing is not obvious, indicating that the development degree of large pores is worse than that of ① and ③.The 16th trace in Figure 12 shows the distribution spectrum of apparent formation water resistivity, which can reflect the distribution of resistivity of fluids contained in the pores of the formation. The water layer has low resistivity and narrow spectral gaps. The gas layer has high resistivity and wide spectral peaks. The pore fluid in the bauxite rock of this well is mainly composed of water layers.

6 Conclusion

This article analyzes and processes seismic data and data from over 160 drilled wells, combined with core experimental data, to conduct a detailed analysis of bauxite reservoirs, and obtains the following understanding:

1) The bauxite strata in this region have been revealed through more than 160 drilled wells, and some of the wells have good reservoir properties and gas properties, making it a new type of unconventional reservoir. The average porosity of the drilled reservoirs in this favorable area is greater than 8%, which has certain exploration and development potential.
2) We completed the restoration of weathered crust paleo-geomorphology in the underlying strata of bauxite through the impression method. Based on the thickness of the drilled Benxi Formation, the second and third level units of paleo-geomorphology are divided. The thickness distribution of each third level unit of paleo-geomorphology is summarized, and the thickness of drilled bauxite is analyzed. It is believed that bauxite is distributed in sheet, strip, and point shapes in karst

monadnock, karst slopes or terraces, and karst trench, respectively. The lithology and porosity of bauxite rocks with different distributions are not the same.

3) The bauxite reservoir has special logging response characteristics, namely, high gamma, high density, high neutron, low resistance, and low difference time. It has a clastic structure and well-developed primary intergranular pore network. Through core experiments, a quantitative interpretation standard for bauxite rock was established for quantitative interpretation of lithology and porosity. The rationality of the interpretation was verified by combining imaging logging series, and further exploration was conducted on the pore structure and fluid properties of bauxite rock. The interpretation method of bauxite rock logging evaluation in this block was studied from scratch.

Data availability statement

The raw data supporting the conclusion of this article will be made available by the authors, without undue reservation.

Author contributions

QY: Writing–original draft, Writing–review and editing. LD: Writing–original draft, Writing–review and editing. YS: Writing–original draft, Writing–review and editing. LQ: Writing–original draft, Writing–review and editing.

Funding

The author(s) declare financial support was received for the research, authorship, and/or publication of this article. This research work has been supported by the technology project of China National Offshore Oil Corporation, titled “Reservoir Formation Conditions and Exploration Key Technologies for Bauxite and Ordovician in the Eastern Margin of the Ordos Basin” (No. KJZH-2023-2104).

Conflict of interest

Authors QY, LD, YS, and LQ were employed by Cnooc Research Institute Ltd.

The authors declare that this study received funding from China National Offshore Oil Corporation. The funder had the following involvement in the study: the study design, collection, analysis, interpretation of data, the writing of this article, and the decision to submit it for publication.

Publisher’s note

All claims expressed in this article are solely those of the authors and do not necessarily represent those of their affiliated organizations, or those of the publisher, the editors and the reviewers. Any product that may be evaluated in this article, or claim that may be made by its manufacturer, is not guaranteed or endorsed by the publisher.

References

Ben, J. L., Qiao, W. X., Che, X. H., Ju, X. D., Lu, J. Q., and Men, B. Y., Field validation of imaging an adjacent borehole using scattered P-waves. *Petroleum Sci.*, 2020, 17, 1272–1280. doi:10.1007/s12182-020-00475-5

Cao, H., Wu, H., Ren, X., et al. (2020). Karst paleogeomorphology and reservoir distribution pattern of Ordovician in the southeastern Ordos Basin. *China Pet. Explor.* 25 (3), 146–155. doi:10.3969/j.issn.1672-7703.2020.03.013

Chen, Li, Sun, L., and Sun Hansen, E. (2022). A method to evaluated gas content with coalbed methane reservoir based on adsorption theory and production analysis. *Geofluids* 2022, 3558643. doi:10.1155/2022/3558643

Dan, L. I., Qiao, W., Che, X., et al. (2019). Study on the response of dipole reflected acoustic imaging the near-borehole cave. *J. Appl. Acoust.* 38 (5), 767–773. doi:10.11684/j.issn.1000-310X.2019.05.002

Du, G., Li, M., Yu, bo, et al. (2022). *Seismic prediction technology and application of Taiyuan Formation bauxite reservoir in Longdong area*. Hainan, China: The Geophysical Exploration Technology Seminar of the Chinese Petroleum Society.

FengRuyong, A. (2022). Method to improve computational efficiency of productivity evaluation with rectangular coalbed methane reservoir. *Geofluids* 2022, 7341886. doi:10.1155/2022/7341886

Fu, J., Li, M., Zhang, L., et al. Breakthrough in the exploration of bauxite gas reservoir in Longdong area of the Ordos Basin and its petroleum geological implications. *Nat. Gas. Ind.*, Vol. 41, 11, p. 1–11. 2021. doi:10.3787/j.issn.1000-0976.2021.11.001

Fu, J., Zhao, H., Guodong, DONG, et al. (2023). Discovery and prospect of oil and gas exploration in new areas of Ordos Basin. *Nat. Gas. Geosci.* 34 (8), 1289–1304. doi:10.11764/j.issn.1672-1926.2023.06.004

Jia, L., Liu, H., Xue, Y., et al. Paleo-geomorphology and Gas-water distribution law in Shaan X block on the east side of Jingbian gas field. *Sci. Technol. Eng.*, 2023, 23(12), 5022–5032. doi:10.3969/j.issn.1671-1815.2023.12.011

Jiang, J., and Wang, B., Natural gas generation and reserve in taiyuan group of low permian in east of Ordos Basin, *Nat. Gas. Geosci.*, 2004, 15(5), 511–515. doi:10.3969/j.issn.1672-1926.2004.05.014

Li, D. (2023). A three-dimensional display technology of reflected acoustic logging and its application example. *Geofluids* 2023, 7979348. doi:10.1155/2023/7979348

Li, D., Qiao, W. X., Che, X. H., Ju, X., Yang, S., Lu, J., et al. Eliminating the azimuth ambiguity in reflected S-wave imaging logging based on the azimuthal receiver mode. *J. Petroleum Sci. Eng.*, 2021, 199: 108295. doi:10.1016/j.petrol.2020.108295

Liu, W., Pan, H., Li, J., et al. Well logging evaluation on bauxitic mudstone reservoirs in the Daniudi Gasfield, Ordos Basin. *Nat. Gas. Ind.*, 35(5),24–30. 2015. doi:10.3787/j.issn.1000-0976.2015.05.004

Liu, D., Zhang, H., Yang, X., et al. Well logging evaluation of bauxite reservoirs in Ordos Basin.*Xinjiang Pet. Geol.*, 43(3),2022b:P261–P270. doi:10.7657/XJPG20220302

Liu, K., Fu, X., Rong, W., et al. (2022a). Analysis of bauxite reservior in X area of Ordos Basin. *J. Xi`an Shiyou Univ. Sci. Ed.* 37 (2), P25–P31. doi:10.3969/j.issn.1673-064X.2022.02.004

Nan, J., Liu, Na, Wang, X., et al. (2022). Characteristics and formation mechanism of bauxite reservoir in Taiyuan Formation,longdong area,Ordos Basin. *Nat. Gas. Geosci.* 33 (2), 288–296. doi:10.11764/j.issn.1672-1926.2021.11.008

Pan, Bo, Zhao, W., Liu, D., et al. Geochemical characteristics of bauxite deposits of Benxi Formation in shenmu-mizhi area,Ordos Basin. *Nat. Gas. Geosci.*, 2023, 34(6): 1072–1089. doi:10.11764/j.issn.1672-1926.2023.01.009

Qiu, Yu, Li, A., Zhou, J., et al. (2021). Calibrating the bottom interface of granite weathering crust reservoir on the Songnan lift in the deep water areas of Qiongdongnan Basin. *Mar. Geol. Front.* 37 (7), 87–96. doi:10.16028/j.1009-2722.2021.087

She, Y., Fei, Li, Wang, Y., et al. (2022). *High resolution inversion technology and application of bauxite reservoir in Qingcheng area of Ordos Basin*. Hainan, China: The Geophysical Exploration Technology Seminar of the Chinese Petroleum Society.

Tang, L., Song, Y., Chen, X., Jiang, Z., Zhang, F., Li, Q., et al. (2023). Key parameters and the upper-lower limits of shale gas selection evaluation: case study from the Wufeng-Longmaxi Formation in the Sichuan Basin. *Nat. Gas. Geosci.* 34 (1), 153–168. doi:10.11764/j.issn.1672-1926.2022.09.011

Tang, L., Song, Y., Zhao, Z., et al. (2022). Origin and evolution of overpressure in shale gas reservoirs of the upper ordovician wufeng formation–lower silurian longmaxi Formation in the sichuan basin. *Nat. Gas. Ind.* 42 (10), 48–64. doi:10.3787/j.issn.1000-0976.2022.10.004

Wang, S., Wang, G., Huang, L., Song, L., Zhang, Y., et al. (2021). Logging evaluation of lamina structure and reservoir quality in shale oil reservoir of Fengcheng Formation in Mahu Sag, China. *Mar. Petroleum Geol.* 133, 105299. doi:10.1016/j.marpetgeo.2021.105299

Wang, S., Wang, G., Lai, J., Liu, S., Chen, X., et al. (2020). Logging identification and evaluation of vertical zonation of buried hill in Cambrian dolomite reservoir: a study of Yingmai-Yaha buried hill structural belt, northern Tarim basin. *J. Petroleum Sci. Eng.* 195, 107758. doi:10.1016/j.petrol.2020.107758

Wang, S., Wang, G., Li, D., Wu, X. N., Chen, X., Wang, Q. Q., et al. (2022). Comparison between double caliper, imaging logs, and array sonic log for determining the *in-situ* stress direction: a case study from the ultra-deep fractured tight sandstone reservoirs, the Cretaceous Bashijiqike Formation in Keshen8 region of Kuqa depression, Tarim Basin, China. *Petroleum Sci.* 19 (6), 2601–2617. doi:10.1016/j.petsci.2022.08.035

Xu, C., Lai, W., Zhang, X., et al. (2023). New progress and future exploration thinking of CNOOC oil and gas exploration.*China Offshore Oil Gas*, 35 (2), 1–12. doi:10.11935/j.issn.1673-1506.2023.02.001

Yang, H., Xi, S., Wei, X., et al. Evolution and natural gas enrichment of multicycle superimposed basinin Ordos Basin. *Pet. Geol.*, 2006, 1, 17–24.

Yang, S. B., Qiao, W. X., and Che, X. H., Numerical simulation of acoustic field in logging-while-drilling borehole generated by linear phased array acoustic transmitter . *Geophys. J. Int.*, 2019, 217(2): 1080–1088. doi:10.1093/gji/ggz071

Yuan, Z., Wu, F. U.-li, and Rong, FENG.The distribution rule and its geological significance of Bauxite in Yanchang gasfield of Ordos Basin.*J. Xi`an Univ. Sci. Technol.*, 36(6), 2016: P843–P848. doi:10.13800/j.cnki.xakjdxxb.2016.0614

Zhu, G., Li, B., Li, Z., et al. (2022). Practices and development trend of unconvertional natural gas exploration in eastern margin of Ordos Basin:Taking Linxing-Shenfu gas field as an example. *China offshore Oil Gas* 34 (4), 16–29. doi:10.11935/j.issn.1673-1506.2022.04.002

frontiers | Frontiers in Energy Research

TYPE Original Research
PUBLISHED 04 January 2024
DOI 10.3389/fenrg.2023.1321853

Check for updates

OPEN ACCESS

EDITED BY
Peng Tan,
CNPC Engineering Technology R&D Company Limited, China

REVIEWED BY
Chunxiao Li,
China University of Geosciences Wuhan, China
Yong Zheng,
Xi'an Shiyou University, China
Song Deng,
Changzhou University, China
Zizhen Wang,
China University of Petroleum (East China), China
Rui Liu,
Southwest Petroleum University, China
Chao Liu,
Aramco Services Company, United States

*CORRESPONDENCE
Mao Sheng,
shengmao@cup.edu.cn

RECEIVED 15 October 2023
ACCEPTED 13 December 2023
PUBLISHED 04 January 2024

CITATION
Cheng S, Sheng M and Deng C (2024), Identification of different lithofacies laminations in oil shale and their mechanical properties.
Front. Energy Res. 11:1321853.
doi: 10.3389/fenrg.2023.1321853

COPYRIGHT
© 2024 Cheng, Sheng and Deng. This is an open-access article distributed under the terms of the Creative Commons Attribution License (CC BY). The use, distribution or reproduction in other forums is permitted, provided the original author(s) and the copyright owner(s) are credited and that the original publication in this journal is cited, in accordance with accepted academic practice. No use, distribution or reproduction is permitted which does not comply with these terms.

Identification of different lithofacies laminations in oil shale and their mechanical properties

Shizhong Cheng, Mao Sheng* and Chao Deng

National Key Laboratory of Petroleum Resources and Engineering, China University of Petroleum (Beijing), Beijing, China

Lamination can greatly enhance the anisotropy and heterogeneity of shale and plays a significant role in influencing hydraulic fracturing. The structure and mechanical difference of different lithofacies lamination are the basis to reveal the fracture propagation mechanism. In this paper, research focused on three continental oil shale with different lithofacies in Qikou sag, Bohai Bay basin, including Quartz-Feldspar dominated shale, Carbonate dominated shale and mixed-mineral shale. Scanning electron microscopy and mineral analysis are used to identify quartz-feldspar lamination and mixture lamination in Quartz-Feldspar dominated shales, as well as carbonate lamination and mixture lamination in Carbonate dominated shales. The distinct laminations with different characteristics were precisely located using FIB, which served as the guiding tool for the indentation experiment. The micromechanical properties of laminations with different lithofacies in oil shale samples are examined using the nanoindentation technique, highlighting their distinct differences. The findings demonstrate that the micromechanical properties of quartz-feldspar lamination in Quartz-Feldspar dominated shales exhibit superior strength, while the mechanical difference between laminations in Quartz-Feldspar dominated shales are significantly larger. The quartz-feldspar lamination exhibits the highest resistance when subjected to indentation force. The mechanical properties of mixture lamination in Quartz-Feldspar dominated shales and Carbonate dominated shales are comparable due to their similar mineral composition. Moreover, in conjunction with macroscopic rock mechanics experiments, it has been verified that the lamination structure facilitates the initiation and propagation of macroscopic fractures under stress loading.

KEYWORDS

oil shale, micromechanics, lamination, lithofacies, nanoindentation

1 Introduction

With the extensive research on shale gas theory and the rapid advancements in exploration and development, laminated oil shale has garnered significant attention and recognition in recent years (Zhijun et al., 2021). Since the weak strength is distributed along the bedding planes, the direction of the bedding plane determines the failure mode. The special failure mode of laminated shale is different from that of isotropic formation, which is

Abbreviations: CL, Carbonate (calcite, dolomite) lamination; CS, Carbonate dominated shale; ML, Mixture lamination; MS, Mixed mineral shale; QFS, Quartz-Feldspar dominated shale; QFL, Quartz-Feldspar lamination.

controlled by bedding inclination and *in-situ* stress (Chenevert and Gatlin, 1965; Niandou et al., 1997). Due to its exceptional reservoir physical properties, laminated oil shale reservoir is more amenable to reformation, resulting in high production. Also, laminations have great influence on the mechanical properties of oil shale. The utilization of high-resolution testing methods to examine the mechanical properties of laminations in shale, thereby elucidating the fracture initiation mechanism, holds immense significance.

It has been proved that the lamination can significantly improve the anisotropy of shale (Vernik and Nur, 1992; Sayers, 2013; Li et al., 2017; Jin et al., 2018; Vernik and Nur, 1992) observed laminated black shale from Bakken formation. The scale of lamination is in the range of 0.2–3 mm through thin sections and up to 10–15 μm through back-scatter SEM (Scanning electron microscope). The gas-bearing shales of the Longmaxi Formation were analyzed by SHI et al. (2020) using thin section imaging and microscope observation, revealing two distinct lamination structures: muddy lamination with an average thickness of 76.54 μm and silty lamination with an average thickness of 54.14 μm (Mokhtari et al., 2014). observed calcite-filled discontinuities in Eagle Ford shale through thin-section and verified that tensile strength along lamination is always lower than that across lamination (Li et al., 2017). proposed a model to simulate the anisotropic mechanical behavior of shale with considering direction of laminations and elucidated directional dependence of tensile and compressive strengths. Subsequently, abundant research began to study the effect of lamination (Liu et al., 2020; Zhang et al., 2022) or heterogeneity (Huang et al., 2019; Huang et al., 2023) on fracture propagation through numerical simulation, macroscopic mechanics (Huang et al., 2020; Yang et al., 2021) and fracturing experiments (Lei et al., 2021; Yang et al., 2021) developed a novel constitutive model to investigate fracture evolution behavior in layered rock with considering the mechanical behavior of soft layers and hard layers as well as layer interfaces. Results demonstrated that bedding inclination angle greatly influenced finale fracture pattern of the layered rock (Tan et al., 2017; Tan et al., 2023). focused on initiation and vertical propagation of fractures in laminated shale formations through large-scale tri-axial experiments and concluded that lamination significantly influences the propagation of fracture height combined with numerical model (Tan et al., 2021).

Although the lamination or bedding of shale is widely acknowledged as a crucial geometrical factor that significantly influences the mechanical anisotropy and fracture propagation, there remains limited research on the mechanical characterization of lamination at the microscopic level. Nanoindentation technique has been successfully applied in the measurement of shale micromechanics (Li et al., 2019; Sheng et al., 2022; Ulm and Abousleiman, 2006; Ulm et al., 2007) developed grid-indentation and combined deconvolution approach to conduct statistical analysis on heterogeneous and anisotropic properties of shale (Cheng et al., 2021). have preliminarily identified the lamination in Longmaxi shale and carried out micromechanical tests to compare the micromechanical differences of lamination with different particle sizes. Therefore, further research on more detailed lamination characteristics, micromechanics and fracture mechanics is needed.

In this paper, three laminations with different lithofacies of oil shale in the Third Member of Shahejie Formation in Qikou sag, Bohai Bay basin were identified through SEM and mineral analysis. The distinct laminations with different characteristics were precisely identified using FIB (Focused ion beam), which served as the guiding tool for the indentation experiment. The nanoindentation approach was utilized to quantify the micro mechanical properties of three different laminations. The paper explores the mechanical variations among laminae in different lithofacies and demonstrates that the mechanical properties of laminae in Quartz-Feldspar dominated shales exhibit significant disparities, thereby facilitating interlamina fractures formation. Moreover, in conjunction with macroscopic rock mechanics experiments, it has been verified that the lamination structure facilitates the initiation and propagation of macroscopic fractures under stress loading.

2 Materials and methods

2.1 Material and specimen preparation

Three distinct shale samples were collected from the downhole cores at Shahejie Formation in Qikou sag, Bohai Bay basin. Qikou sag is located in the hinterland of Huanghua Depression. The effective exploration area of the paleogene in Qikou Sag is 5.28 × 103 km^2, and the main source rocks are from Sha-3 Member and Sha-1 Member (Xiugang et al., 2023). The samples are from Sha-3 Member and there measured depths are 4076, 4051 and 4000 m, respectively.

The mineral composition of three core samples was determined through XRD analysis according to the Standard SY/T 5163-2010, and the results are presented in Table 1. According to the chemical composition of the mineral, the mineral composition in the sample is divided into three types: Clay minerals, Quartz-Feldspar dominated minerals and Carbonate dominated minerals (Maowen et al., 2022). Other minerals were also quantitatively analyzed according to the standards. The lithofacies division is carried out based on the whole rock mineral composition, as shown in Figure 1. The lithofacies of three downhole samples are Quartz-Feldspar dominated shale (QFS), Mixed mineral shale (MS) and Carbonate dominated shale (CS).

The cubical specimen (10 mm length × 5 mm width × 2 mm height) were cut from the shale samples. Sample surfaces were firstly polished by using sanding paper meshing from 180# to 4000#. First mechanical polish is to achieve surface roughness of less than 0.5 micron. High energy argon ion beam was used in next polish step and continuously conducted for 2 h to achieve surface roughness less than 100 nm. The target surface for micromechanical testing was oriented perpendicular to the shale bedding planes, as depicted in Figure 1, allowing for the visualization of the laminated sedimentary structure.

2.2 Experimental methodology

SEM, EDS (Energy Dispersive Spectrometer) and FIB were conducted firstly to identify and locate different lithofacies laminations. Then, micromechanical properties of lamination could be quantified through nanoindentation tests. Uniaxial compression tests were carried out to verify the influence of laminations on macro fractures. The micromechanical and macroscopic mechanical samples were obtained from the downhole core of the same geological layer shown in Figure 1.

TABLE 1 Mineral composition of three distinct core samples.

Sample	Depth, m	Composition, wt%							Lithofacies
		Quartz	Feldspar	Calcite	Dolomite	Clay	Pyrite	Others	
1	4076.83	36.0	14.8	9.7	8.9	27.5	1.9	1.2	Quartz-Feldspar dominated shale (QFS)
2	4051.44	23.5	6.6	20.2	7.9	36.1	3.1	2.6	Mixed mineral shale (MS)
3	4000.7	13.3	3.4	24.6	28.7	26.0	2.6	1.4	Carbonate dominated shale (CS)

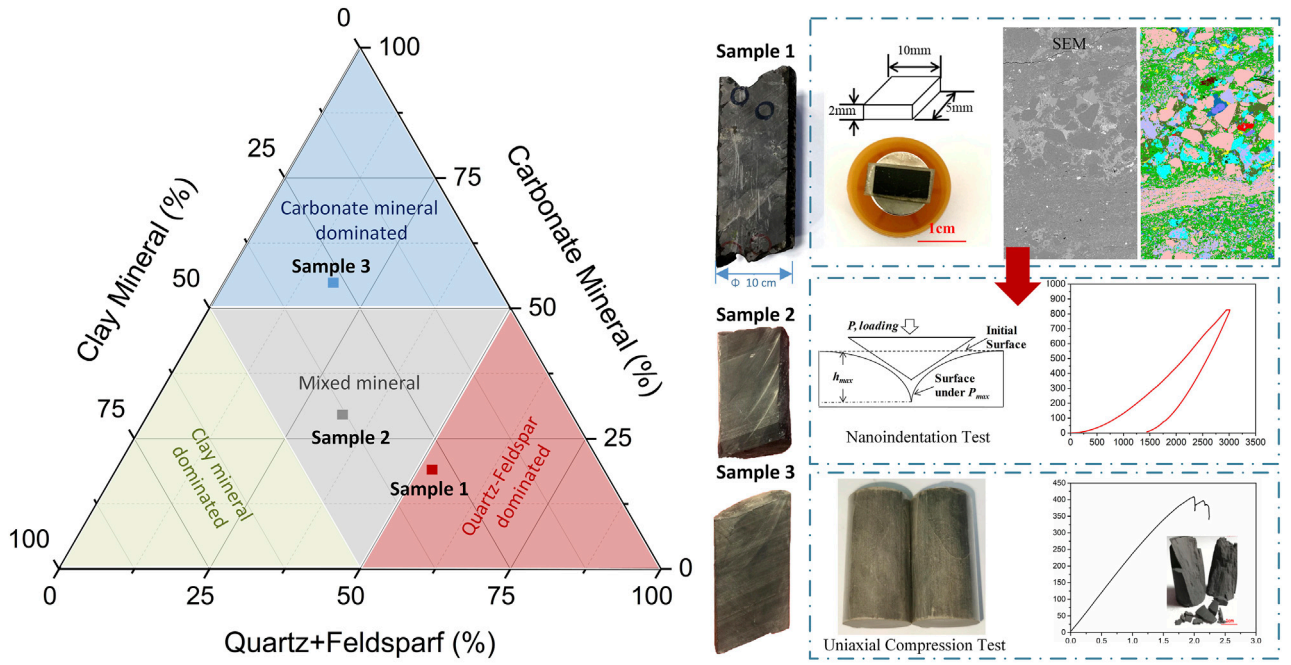


FIGURE 1
Lithofacies classification and experimental design scheme.

2.2.1 SEM

Different mineral laminations were observed firstly through SEM (ZEISS Merlin, ZEISS, Germany) and analyzed through EDS in three different lithofacies samples. Subsequently, FIB was employed to precisely locate distinct mineral laminations by utilizing a high current ion beam, ensuring the accurate identification of lamination features during optical microscope navigation in the nanoindentation device. Through micromechanical testing, the disparities in micromechanical properties among different lithologic laminations are ultimately elucidated. Then, FIB was performed to mark the beginning and end of the target lamination to ensure the correct position and angle of the lamination, as shown in Figure 2.

2.2.2 Nanoindentation

Nanoindentation (G200, Keysight, America) was conducted with continuous stiffness measurement (CSM) mode, which enables continuous measurement of mechanical properties over the indentation depth. The target lamination can be accurately located by recognizing FIB markers in optical microscope navigation in nanoindentation equipment. Furthermore, 1 × 10 points are arranged in each lamination, the point spacing is 100 microns, and the ultimate indent depth is 3,000 nm which could eliminate interaction between individual points and facilitate the measurement of minerals and mineral phases at multiple scales (Ulm and Abousleiman, 2006). In CSM mode, a harmonic oscillator is employed for the indenter, which can be considered as a cyclic loading process depicted in Figure 2D. For each load cycle, The elastic modulus and hardness at that depth are determined using the same computational approach as described below (Phani et al., 2020). The selection of a Berkovich diamond indenter in nanoindentation was based on its high spring constant range and ability for the measurement of composite materials with a wide range of elastic modulus.

The Young's modulus and hardness were determined by employing the following Eqs. (1–4) based on the load-displacement curve (Oliver and Pharr, 1992; Sheng et al., 2022):

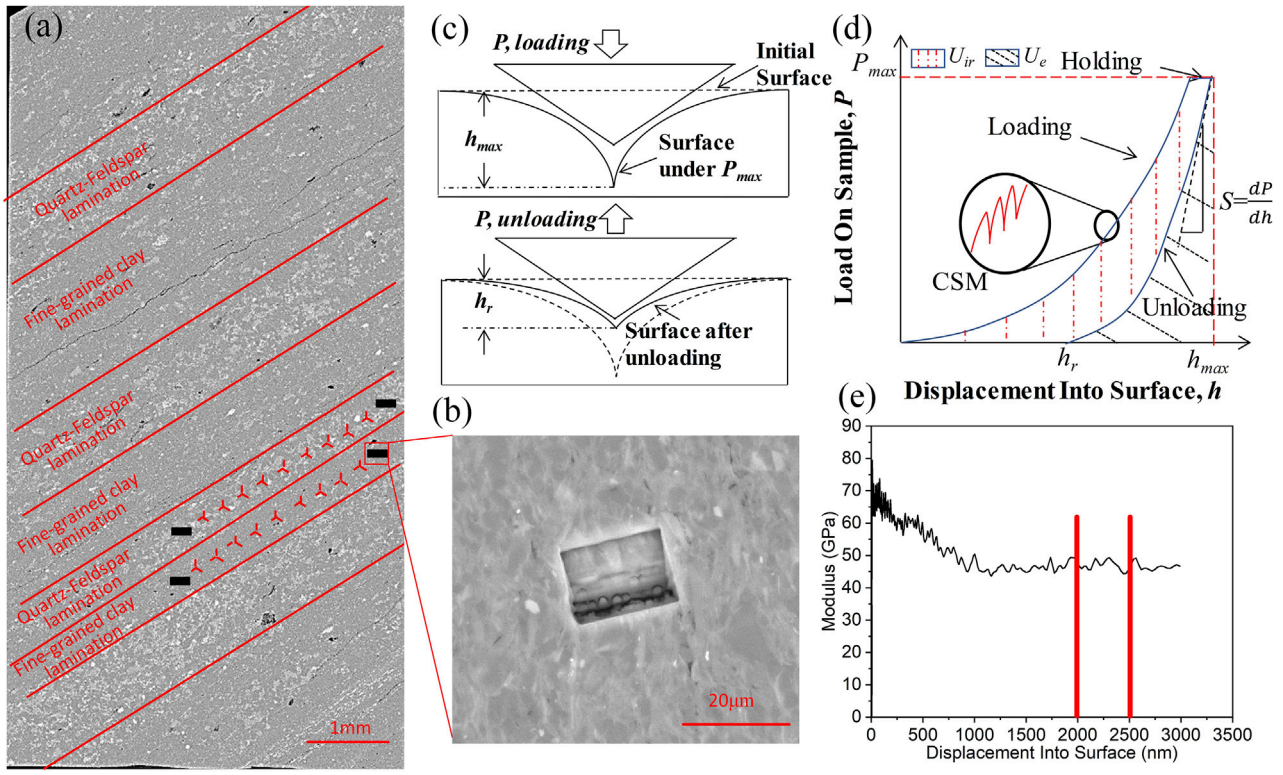


FIGURE 2
Nanoindentation schematic: **(A)** Grid indentations on laminations; **(B)** FIB marker; **(C)** Indentation scheme; **(D)** Nanoindentation load on sample-displacement into surface curve and continuous stiffness measurement (CSM) diagram; **(E)** CSM result example: Change of elastic modulus with indentation depth.

$$\frac{1}{E_{reduced}} = \frac{\left(1-\nu_{sample}\right)^2}{E_{sample}} + \frac{\left(1-\nu_{tip}\right)^2}{E_{tip}} \quad (1)$$

$$E_r = \frac{\sqrt{\pi}}{2}\frac{S}{\sqrt{A_c}} \quad (2)$$

$$H = \frac{P_{\max}}{A_c} \quad (3)$$

$$S = \frac{dP}{dh}\Big|_{h=h_{\max}} \quad (4)$$

Where, E_{reduced} is the reduced modulus; ν and E are Poisson's ratio and Young's modulus; $P_{\max}$ is the maximum load. S is the stiffness as shown in Figure 2D. A_c is the projected contact area. For Berkovich indenters, $A_c = 24.56h_c^2 + Ch_c$. C is a constant obtained in the calibration.

According to the indentation energy analysis method theory (Cheng et al., 2002; Liu et al., 2016; Zeng et al., 2017), the fracture toughness of indentation point could be calculated through Eqs (5–9):

$$U_{ir} = U_t - U_e \quad (5)$$

$$U_f = U_{ir} - U_{pp} \quad (6)$$

$$\frac{U_{pp}}{U_t} = 1 - \left[\frac{1-3\left(\frac{h_f}{h_{\max}}\right)^2 + 2\left(\frac{h_f}{h_{\max}}\right)^3}{1-\left(\frac{h_f}{h_{\max}}\right)^2}\right] \quad (7)$$

Where, U_{ir} is the irreversible energy, U_t is the total energy, U_e is the recoverable elastic energy, U_f is the fracture energy, and U_{pp} is the pure plastic energy. The relationship between critical energy release rate G_c and fracture energy U_f is as follows:

$$G_c = \frac{dU_f}{dA} = \frac{U_f}{A_{\max}} \quad (8)$$

The fracture toughness can be determined through the subsequent formula.

$$K_{ic} = \sqrt{G_c E_r} \quad (9)$$

2.2.3 Uniaxial compression test

The traditional uniaxial compression tests were conducted on the samples cut from the same part of the downhole core. The displacement-control mode was selected in the experiment. The loading rate was set at 0.04 mm/min, and a dual-channel acoustic emission system was incorporated during the experimental procedure. Stress-strain curves and AE counts were recorded. The sample's failure pattern was exhibited through photography.

3 Results and discussions

3.1 Identification of different lithological laminations

The lamination structure in different lithofacies shales was identified by SEM and mineral analysis (Vernik and Nur, 1992). observed laminated black shale from Bakken formation. The scale of lamination is in the range of 0.2–3 mm. And (SHI et al., 2020), using

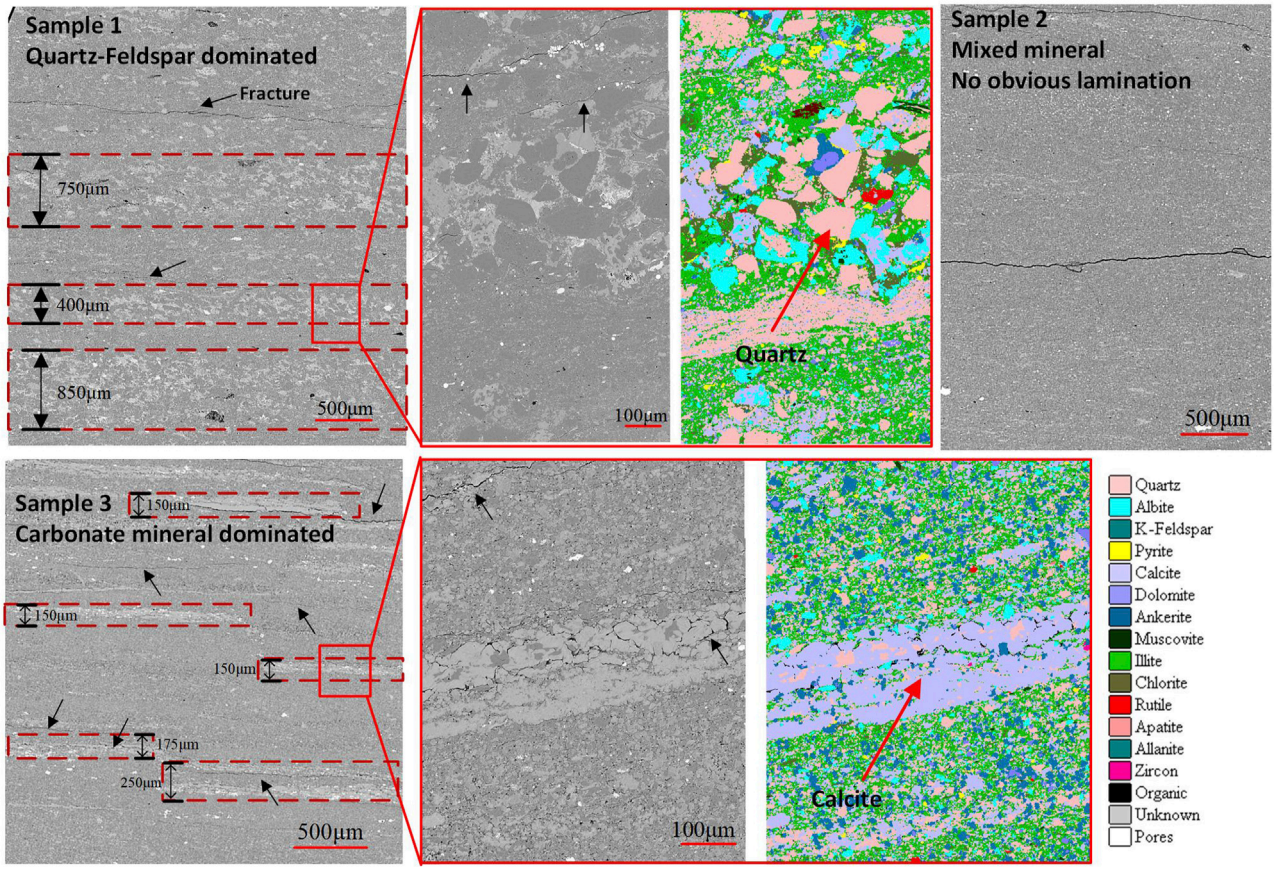


FIGURE 3
Typical laminations in different lithofacies samples. The developed laminations are enclosed by red rectangular. The black arrow points to the fractures.

TABLE 2 Shale lithofacies and their corresponding lamination component.

Shale lithofacies	Lamination component
QFS (Quartz-Feldspar dominated shale)	QFL (Quartz-Feldspar lamination)
	ML (Mixture lamination)
CS (Carbonate dominated shale)	CL (Carbonate lamination)
	ML (Mixture lamination)
MS (Mixed mineral shale)	No obvious laminations

thin section imaging and microscope observation, revealing two distinct lamination structures: muddy lamination with an average thickness of 76.54 μm and silty lamination with an average thickness of 54.14 μm. Previous studies identified shale bedding layers with various grain sizes (Cheng et al., 2021). However, it does not provide a detailed analysis of the specific components. In this study, the qualitative interpretation and quantitative analysis of different lithofacies laminations were carried out. Figure 3 shows the typical laminations in different lithofacies samples. The lamination characteristics observed in three lithofacies shale are shown in Table 2. In QFS, as shown in Sample 1, the lamination is characterized by alternating deposition of QFL and ML. QFL is composed of large grains (grain size>50 μm) of quartz and feldspar minerals, while ML is mainly composed of fine-grained clay mineral particles. In CS, as shown in Sample 3, the main laminations are CL and ML. However, in MS, lamination is not well developed, as shown in Sample 2. The mineral particles in the MS exhibit a more homogeneous dispersion pattern. The thickness of QFL in Sample 1 is relatively substantial, exceeding 400 μm on average. The observed carbonate laminations are consistently smaller than 300 μm.

Furthermore, the development of fractures can be discerned through the morphology observed in SEM. In MS, there are several primary fractures with relatively uncomplicated geometries. However, in QFS and CS, the development of lamination can induce a greater number of micro-fractures along the edges of mineral grains and enhance fracture complexity. These fractures predominantly occur at the junctions between lamination layers, indicating that these interfaces are inherently weak and susceptible to opening or communicate during fracturing.

3.2 Micromechanical differences of different lithological laminations

According to the different lithofacies lamination characteristics identified in Section 3.1, micron indentation experiments are carried

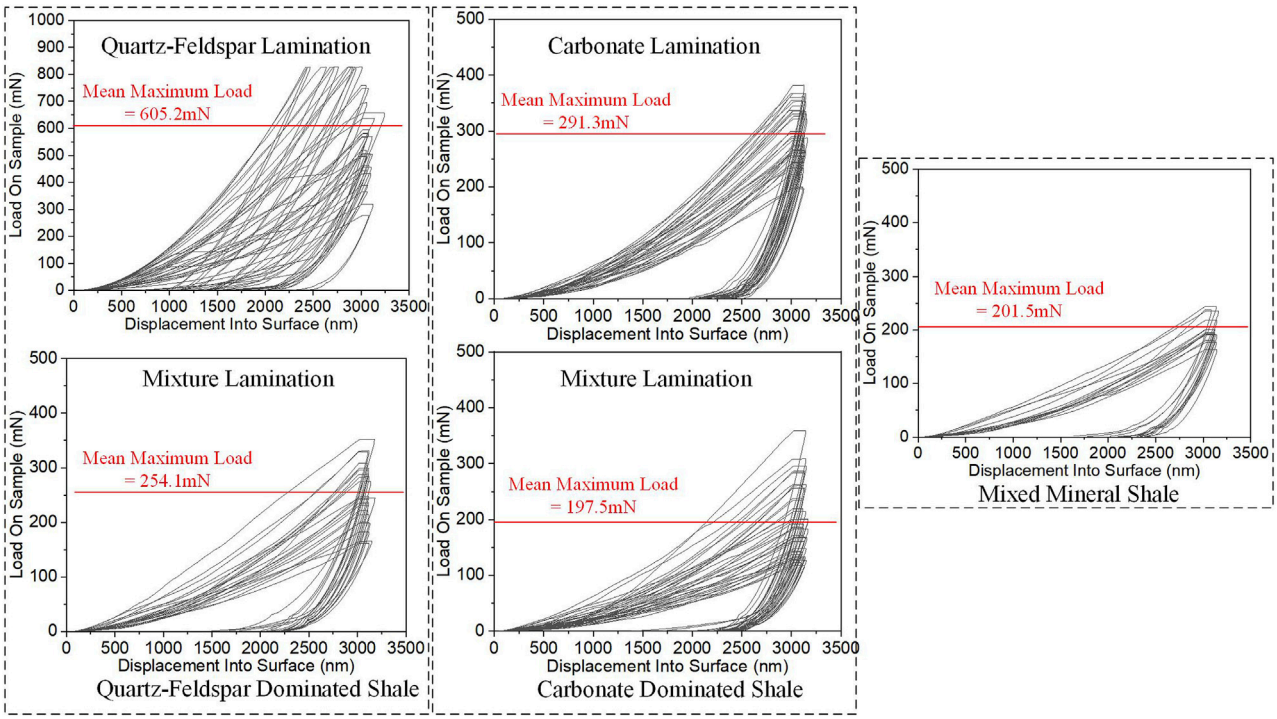


FIGURE 4
Displacement into Surface vs. Load on Sample curves at each indentation point.

out. In MS, no obvious lamination structure is observed, the mineral particles are uniformly distributed so that the micro indentation experiments were conducted randomly on the sample surface to avoid local effects. The load on sample vs. displacement into surface curves at each indentation point were shown in Figure 4. The mean maximum load in QFL was the highest, indicating that indenting QFL posed the greatest difficulty. This is due to the development of feldspar and quartz minerals in the QFL, which show a strong hardness. The mean maximum load in ML in QFS and CS are similar with that in MS because of the similar clay mineral composite. In particular, within the QFL, multiple curves demonstrate that when the displacement falls short of reaching the predetermined indentation depth of 3,000 nm, the load attains its maximum value. This further substantiates the high strength exhibited by QFL.

The characteristics of elastic modulus and hardness data of different lithological laminations were analyzed by interquartile range and variance, as shown in Figure 5. The elastic modulus and hardness of the quartz-feldspar lamination in QFS are the highest among the different lithofacies laminations. In QFS and CS, micro indentation experiments were conducted inside laminations. In QFS, the elastic modulus of QFL is 55% higher than that of ML, and the hardness is 232% higher. In CS, the elastic modulus and hardness of CL are 33% higher and 53% higher than that of ML. The elastic modulus and hardness of ML in QFS and CS are comparable to those observed in MS, as the composition of ML in both types of shales closely resembles that of MS, characterized by fine clay particles.

The fracture toughness of the indentation point was calculated from the displacement-load curves. The results unequivocally demonstrate the robust fracture toughness of QFL in Figure 6. The results show that the difference of fracture mechanics between the two types of lamination in QFS is the largest, while the difference of fracture mechanics between the two types of CS is small.

3.3 Effect of lamination structure on the formation and propagation of macroscopic cracks

Previous studies have confirmed that in the macroscopic rock mechanics and Brazilian tests considering the direction of bedding, cracks are prone to cracking along the bedding plains or laminations (Zhu et al., 2021). The lamination structure and mechanical difference among laminations facilitate the initiation of microcracks, which are prone to propagate into macro-cracks under loading conditions. Simulations have also verified that bedding or lamination structures greatly influence the mechanical properties and failure mode of shale rocks (Li et al., 2017). True tri-axial hydraulic fracturing experiments have been conducted to elucidated hydraulic fracture initiation and propagation was influenced by bedding plane (Tan et al., 2017). In this study, we have elucidated the distinct lithological lamination structure and micromechanical variations of laminations in shale, which serve as the microphysical and mechanical foundation for determining the initiation and propagation of macroscopic fractures.

Cylindrical samples were drilled from downhole core samples to carry out uniaxial compression experiments. Figure 7 illustrates the observed sample failure characteristics, stress-strain curve, and acoustic emission counting results from the experiment. Acoustic

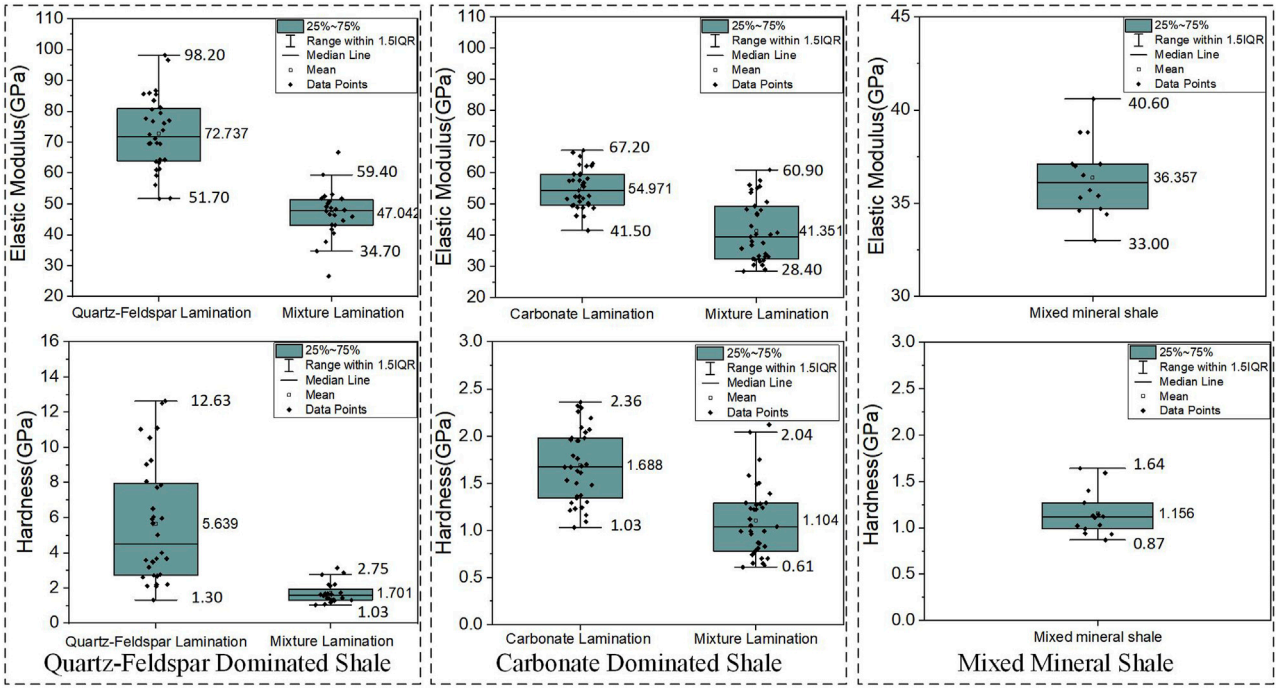


FIGURE 5
Micro indentation experiment results.

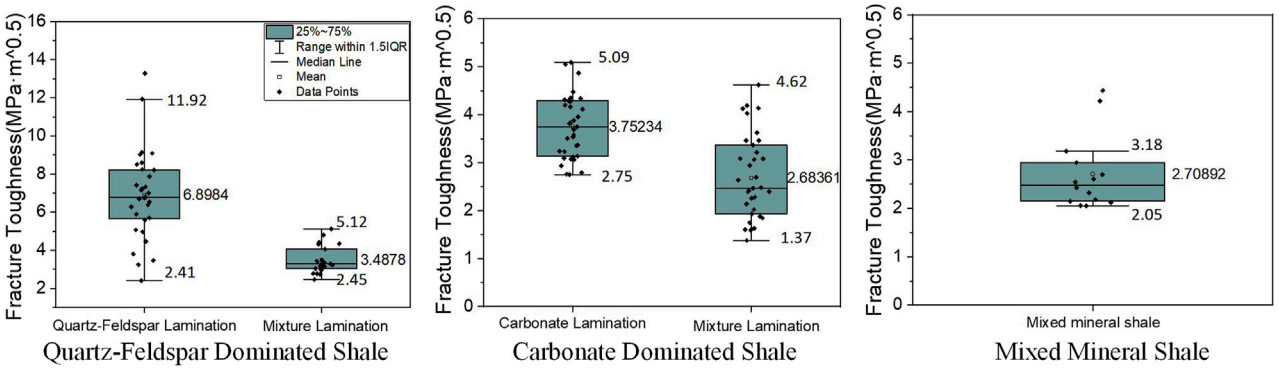


FIGURE 6
Fracture toughness of different laminations according to the Load-Displacement curves.

emission usually produces a large number of counts after sample failure because the sample continues to be compacted and cracked. The macroscopic cracks are mainly generated in the laminations and cracked along the lamination direction, as shown in Figure 7A. It can be observed that in these samples, the lamination is developed and the lamination thickness is small. Smaller lamination thickness exhibits lower total strength, resulting in more prone to cracking under stress. On the contrary, in Figure 7(a3), the lamination thickness is larger and the structure is more uniform. The mechanical test results show that its failure strength is high, the acoustic emission count is less and concentrated after the stress-strain peak, which confirms that fewer micro-cracks are generated during the loading process. Moreover, due to the multi-lamellar characteristics of the sample, the failure strength is relatively low, such as Sample No. (1, 2, 4, 5) in Figure 7A. Throughout the experiment, a substantial number of acoustic emission counts were recorded following the stress-strain peak, indicating that only a limited quantity of micro-cracks formed during the pre-peak loading stage. However, damage persisted after the peak as the weak surface of the lamination underwent progressive failure and compaction, ultimately resulting in complete sample failure. The lamination-developed samples eventually show the characteristics of macro fracture along the laminations.

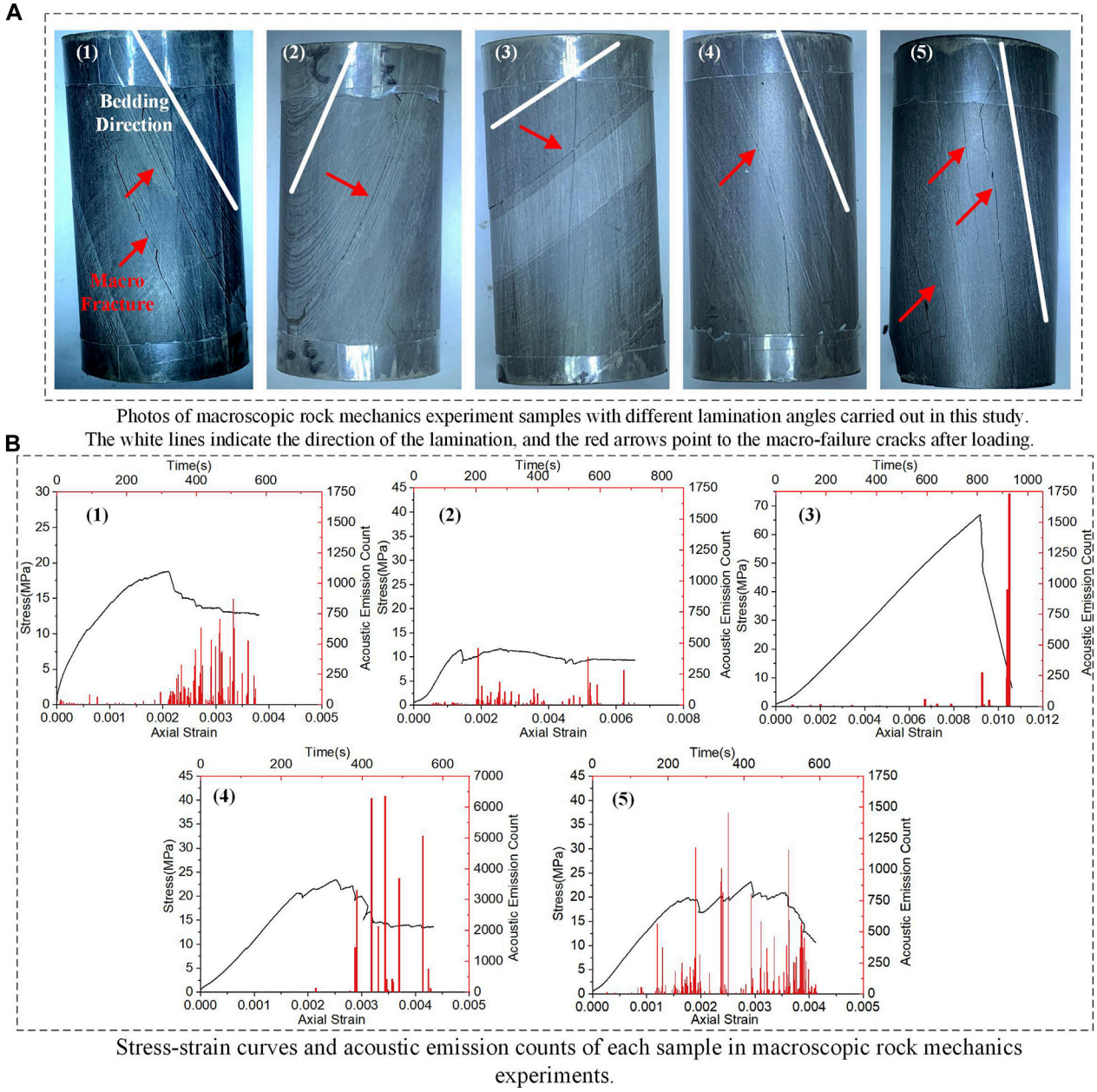


FIGURE 7
Macroscopic rock mechanics experiment results. **(A)** Photos of macroscopic rock mechanics experiment samples with different lamination angles carried out in this study. lie white lines indicate the direction of the lamination, and the red arrows point to the macro-failure cracks after loading. **(B)** Stress-strain curves and acoustic emission counts of each sample in macroscopic rock mechanics experiments.

4 Conclusion

Three laminations with different lithofacies of oil shale in the Third Member of Shahejie Formation in Qikou sag, Bohai Bay basin were identified through SEM and mineral analysis. The thickness of quartz-feldspar lamination commonly exceeds 400 μm on average because of its large grain size. The observed carbonate laminations are consistently smaller than 300 μm. The distinct laminations with different characteristics were precisely identified using FIB, which served as the navigation for the indentation experiment precisely. The micro mechanical properties of three distinct laminations were quantified using the nanoindentation method. This study investigates the mechanical differences between laminations in various lithofacies and reveals that Quartz-Feldspar dominated shales display significant variations in their mechanical characteristics, which ultimately promote the formation of fractures between different layers. Combined with macroscopic rock mechanics experiments, it is confirmed that distinct lithological lamination structure and micromechanical

variations of laminations in shale were microphysical and mechanical foundation for determining the initiation and propagation of macroscopic fractures. The micromechanical test results will be utilized in the subsequent step to establish a macroscopic mechanical model, aiming to investigate the correlation between lamination micromechanics and macroscopic rock mechanics.

Data availability statement

The raw data supporting the conclusions of this article will be made available by the authors, without undue reservation.

Author contributions

SC: Conceptualization, Data curation, Formal Analysis, Investigation, Methodology, Validation, Visualization, Writing–original draft. MS: Conceptualization, Data curation, Funding acquisition, Project administration, Validation, Writing–review and editing. CD: Formal Analysis, Investigation, Visualization, Writing–original draft.

Funding

The author(s) declare financial support was received for the research, authorship, and/or publication of this article. This research was funded by National Natural Science Foundation of China, grant number 52074315.

Conflict of interest

The authors declare that the research was conducted in the absence of any commercial or financial relationships that could be construed as a potential conflict of interest.

Publisher's note

All claims expressed in this article are solely those of the authors and do not necessarily represent those of their affiliated organizations, or those of the publisher, the editors and the reviewers. Any product that may be evaluated in this article, or claim that may be made by its manufacturer, is not guaranteed or endorsed by the publisher.

References

Chenevert, M. E., and Gatlin, C. (1965). Mechanical anisotropies of laminated sedimentary rocks. *Soc. Petroleum Eng. J.* 5, 67–77. doi:10.2118/890-PA

Cheng, S., Sheng, M., Chen, Z., Tian, S., and Li, G. (2021). "Identification of shale bedding layers from micromechanical evaluation," in Presented at SPE Annual Technical Conference and Exhibition 2021, ATCE 2021, Dubai, United arab emirates, September 21, 2021 - September 23, 2021, 2021 (Society of Petroleum Engineers SPE). doi:10.2118/206256-MS

Cheng, Y.-T., Li, Z., and Cheng, C.-M. (2002). Scaling relationships for indentation measurements. *Philos. Mag. A* 82, 1821–1829. doi:10.1080/01418610208235693

Huang, D., Li, B., Ma, W.-Z., Cen, D.-F., and Song, Y.-X. (2020). Effects of bedding planes on fracture behavior of sandstone under semi-circular bending test. *Theor. Appl. Fract. Mech.* 108, 102625. doi:10.1016/j.tafmec.2020.102625

Huang, L., Liu, J., Zhang, F., Dontsov, E., and Damjanac, B. (2019). Exploring the influence of rock inherent heterogeneity and grain size on hydraulic fracturing using discrete element modeling. *Int. J. Solids Struct.* 176-177, 207–220. doi:10.1016/j.ijsolstr.2019.06.018

Huang, L., Tan, J., Fu, H., Liu, J., Chen, X., Liao, X., et al. (2023). The non-plane initiation and propagation mechanism of multiple hydraulic fractures in tight reservoirs considering stress shadow effects. *Eng. Fract. Mech.* 292, 109570. doi:10.1016/j.engfracmech.2023.109570

Jin, Z., Li, W., Jin, C., Hambleton, J., and Cusatis, G. (2018). Anisotropic elastic, strength, and fracture properties of marcellus shale. *Int. J. Rock Mech. Min. Sci.* 109, 124–137. doi:10.1016/j.ijrmms.2018.06.009

Lei, B., Zuo, J., Liu, H., Wang, J., Xu, F., and Li, H. (2021). Experimental and numerical investigation on shale fracture behavior with different bedding properties. *Eng. Fract. Mech.* 247, 107639. doi:10.1016/j.engfracmech.2021.107639

Li, C., Ostadhassan, M., Kong, L., and Bubach, B. (2019). Multi-scale assessment of mechanical properties of organic-rich shales: a coupled nanoindentation, deconvolution analysis, and homogenization method. *J. Petroleum Sci. Eng.* 174, 80–91. doi:10.1016/j.petrol.2018.10.106

Li, W., Rezakhani, R., Jin, C., Zhou, X., and Cusatis, G. (2017). A multiscale framework for the simulation of the anisotropic mechanical behavior of shale. *Int. J. Numer. Anal. Methods Geomechanics* 41, 1494–1522. doi:10.1002/nag.2684

Liu, J., Liang, X., Xue, Y., Fu, Y., Yao, K., and Dou, F. (2020). Investigation on crack initiation and propagation in hydraulic fracturing of bedded shale by hybrid phase-field modeling. *Theor. Appl. Fract. Mech.* 108, 102651. doi:10.1016/j.tafmec.2020.102651

Liu, K., Ostadhassan, M., and Bubach, B. (2016). Applications of nano-indentation methods to estimate nanoscale mechanical properties of shale reservoir rocks. *J. Nat. Gas Sci. Eng.* 35, 1310–1319. doi:10.1016/j.jngse.2016.09.068

Maowen, L., Ma, X., Jin, Z., Li, Z., Jiang, Q., Wu, S., et al. (2022). Diversity in the lithofacies assemblages of marine and lacustrine shale strata and significance for unconventional petroleum exploration in China. *OIL GAS Geol.* 43, 1–25. doi:10.11743/ogg20220101

Mokhtari, M., Bui, B. T., and Tutuncu, A. N. (2014). "Tensile failure of shales: impacts of layering and natural fractures," in *Presented at SPE western north American and rocky mountain joint meeting*. SPE-169520-MS: All Days. doi:10.2118/169520-ms

Niandou, H., Shao, J. F., Henry, J. P., and Fourmaintraux, D. (1997). Laboratory investigation of the mechanical behaviour of tournemire shale. *Int. J. Rock Mech. Min. Sci.* 34, 3–16. doi:10.1016/S1365-1609(97)80029-9

Oliver, W., and Pharr, G. (1992). An improved technique for determining hardness and elastic modulus using load and displacement sensing indentation experiments. *J. Mater. Res.* 7, 1564–1583. doi:10.1557/JMR.1992.1564

Phani, P. S., Oliver, W. C., and Pharr, G. M. (2020). Understanding and modeling plasticity error during nanoindentation with continuous stiffness measurement. *Mater. Des.* 194, 108923. doi:10.1016/j.matdes.2020.108923

Sayers, C. M. (2013). The effect of anisotropy on the young's moduli and Poisson's ratios of shales. *Geophys. Prospect.* 61, 416–426. doi:10.1111/j.1365-2478.2012.01130.x

Sheng, M., Cheng, S.-Z., Lu, Z.-H., Zhang, Y., Tian, S.-C., and Li, G.-S. (2022). Influence of formation in-situ stress on mechanical heterogeneity of shale through grid nanoindentation. *Petroleum Sci.* 19, 211–219. doi:10.1016/j.petsci.2021.10.006

Shi, Z., Dong, D., Wang, H., Sun, S., and Wu, J. (2020). Reservoir characteristics and genetic mechanisms of gas-bearing shales with different laminae and laminae combinations: a case study of member 1 of the lower silurian longmaxi shale in sichuan basin, sw China. *PETROLEUM Explor. Dev.* 47, 888–900. doi:10.1016/s1876-3804(20)60104-5

Tan, P., Chen, Z., Fu, S., and Zhao, Q. (2023). Experimental investigation on fracture growth for integrated hydraulic fracturing in multiple gas bearing formations. *Geoenergy Sci. Eng.* 231, 212316. doi:10.1016/j.geoen.2023.212316

Tan, P., Jin, Y., Han, K., Hou, B., Chen, M., Guo, X., et al. (2017). Analysis of hydraulic fracture initiation and vertical propagation behavior in laminated shale formation. *Fuel* 206, 482–493. doi:10.1016/j.fuel.2017.05.033

Tan, P., Jin, Y., and Pang, H. (2021). Hydraulic fracture vertical propagation behavior in transversely isotropic layered shale formation with transition zone using xfem-based czm method. *Eng. Fract. Mech.* 248, 107707. doi:10.1016/j.engfracmech.2021.107707

Ulm, F.-J., and Abousleiman, Y. (2006). The nanogranular nature of shale. *Acta Geotech.* 1, 77–88. doi:10.1007/s11440-006-0009-5

Ulm, F.-J., Vandamme, M., Bobko, C., Alberto Ortega, J., Tai, K., and Ortiz, C. (2007). Statistical indentation techniques for hydrated nanocomposites: concrete, bone, and shale. *J. Am. Ceram. Soc.* 90, 2677–2692. doi:10.1111/j.1551-2916.2007.02012.x

Vernik, L., and Nur, A. (1992). Ultrasonic velocity and anisotropy of hydrocarbon source rocks. *Geophysics* 57, 727–735. doi:10.1190/1.1443286

Xiugang, P., Miaochao, M., Bincheng, G., Kejia, Z., Congsheng, B., Jianying, M., et al. (2023). Shale lithofacies characteristics and shale oil bearing differences in the es3^{s} of qibei subsag, oikou sag, bohai bay basin. *J. Northeast Petroleum Univ.* 47, 55–69. doi:10.3969/.issn.2095-4107.2023,02.005

Yang, L., Sharafisafa, M., and Shen, L. (2021). On the fracture mechanism of rock-like materials with interbedded hard-soft layers under brazilian tests. *Theor. Appl. Fract. Mech.* 116, 103102. doi:10.1016/j.tafmec.2021.103102

Zeng, Q., Feng, Y., and Xu, S. (2017). A discussion of "application of nano-indentation methods to estimate nanoscale mechanical properties of shale reservoir rocks" by k liu, m osatadhassan and b bubach. *J. Nat. Gas Sci. Eng.* 42, 187–189. doi:10.1016/j.jngse.2017.02.027

Zhang, Y., Liu, Z., Han, B., Zhu, S., and Zhang, X. (2022). Numerical study of hydraulic fracture propagation in inherently laminated rocks accounting for bedding plane properties. *J. Petroleum Sci. Eng.* 210, 109798. doi:10.1016/j.petrol.2021.109798

Zhijun, J., Rukai, Z., Xinping, L., and Yunqi, S. (2021). Several issues worthy of attention in current lacustrine shale oil exploration and development. *PETROLEUM Explor. Dev.* 48, 1276–1286. doi:10.11698/PED.2021.06.20

Zhu, Y., Liu, K., Zhong, X., Wang, Y., Chen, C., Zhang, H., et al. (2021). Experimental investigation on the anisotropic behaviors induced by bedding planes in mechanical properties of ma′quan oil shale. *Arabian J. Sci. Eng.* 47, 11385–11403. doi:10.1007/s13369-021-06027-2

frontiers | Frontiers in Energy Research

TYPE Original Research
PUBLISHED 05 January 2024
DOI 10.3389/fenrg.2023.1339895

Check for updates

OPEN ACCESS

EDITED BY
Liuke Huang,
Southwest Petroleum University, China

REVIEWED BY
Xiaohua Wang,
Tongji University, China
Yongxiang Zheng,
Shijiazhuang Tiedao University, China

*CORRESPONDENCE
Haoyong Huang,
huang_hy@petrochina.com.cn

RECEIVED 17 November 2023
ACCEPTED 13 December 2023
PUBLISHED 05 January 2024

CITATION
Wu J, Wu M, Guo Y, Huang H, Zhang Z, Zhong G, Gui J and Lu J (2024), Study on multi-cluster fracturing simulation of deep reservoir based on cohesive element modeling.
Front. Energy Res. 11:1339895.
doi: 10.3389/fenrg.2023.1339895

COPYRIGHT
© 2024 Wu, Wu, Guo, Huang, Zhang, Zhong, Gui and Lu. This is an open-access article distributed under the terms of the Creative Commons Attribution License (CC BY). The use, distribution or reproduction in other forums is permitted, provided the original author(s) and the copyright owner(s) are credited and that the original publication in this journal is cited, in accordance with accepted academic practice. No use, distribution or reproduction is permitted which does not comply with these terms.

Study on multi-cluster fracturing simulation of deep reservoir based on cohesive element modeling

Jianfa Wu[1], Mingyang Wu[2], Yintong Guo[2], Haoyong Huang[1]*, Zhen Zhang[1], Guanghai Zhong[1], Junchuan Gui[1] and Jun Lu[3]

[1]Shale Gas Research Institute of PetroChina Southwest Oil and Gas Field Company, Chengdu, Sichuan, China, [2]State Key Laboratory of Geomechanics and Geotechnical Engineering, Wuhan Institute of Rock and Soil Mechanics, Chinese Academy of Science, Wuhan, China, [3]Institute of Deep Earth Science and Green Energy, College of Civil and Transportation Engineering, Shenzhen University, Shenzhen, China

With the depletion of conventional reservoir development, reservoir fracturing under deep high geo-stress and high geo-stress difference conditions is receiving increasing attention. Deep reservoirs typically require multi-cluster fracturing to achieve efficient reservoir transformation and development. In this paper, considering the relevant geological parameters of a certain reservoir in the southwest, three-dimensional multi-cluster reservoir fracturing models were established based on cohesive element modeling. Then, the propagation law of artificial fractures in reservoirs under the influence of the different number of fracturing clusters, injection displacement, and Young's modulus in different regions of the 60 m fracturing well section is analyzed, and the quantitative law of parameters such as fracture length, maximum fracture width, injection point fracture width, fracture area, and tensile failure ratio during multi-cluster fracturing construction, as well as the propagation law of fracture morphology are revealed. The simulation results show that using multi-cluster fracturing can significantly improve the effectiveness of reservoir reconstruction, but as the number of fracturing clusters increases, it is also easy to form some small opening artificial fractures. These small opening artificial fractures may not be conducive to the transportation of proppants and fluids. During single cluster fracturing, the interface stiffness and rock Young's modulus have a significant impact on the propagation of artificial fractures in the reservoir. As the number of fracturing clusters increases, the competition between artificial main fractures expands significantly, which may reduce the impact of interface stiffness and rock Young's modulus. The fluid injection rate has a significant impact on reservoir fracturing, and in the same area, using high displacement injection can significantly increase the volume of reservoir reconstruction. This study can provide some reference for multi-cluster fracturing construction in deep reservoirs.

KEYWORDS

multi-cluster fracturing, deep shale, cohesive element modeling, high geo-stress, fracture propagation

1 Introduction

With the decrease of shallow structural oil and gas resources, the development and utilization of deep unconventional oil and gas resources have become very important (Ma, et al., 2023). The deep shale reservoir is an important source of unconventional oil and gas resources (Liu et al., 2018a; Moghadasi et al., 2019; Wu et al., 2020a; Huang, et al., 2021). Unfortunately, the *in-situ* stress of deep shale reservoirs is greater than that of shallow shale reservoirs. As a result, the current conventional fracture propagation research methods of shale reservoirs are no longer effective and cannot provide accurate guidance for fracturing operations in deep shale reservoirs (Britt, et al., 1994; Casas, et al., 2006; Zhao, et al., 2018). Then, construction methods such as liquid nitrogen fracturing (Li et al., 2023; Yang et al., 2023a) and multi-cluster fracturing (Liu et al., 2018b; Yuan et al., 2018) have been proposed one after another. Considering that multi-cluster fracturing is currently widely used, the impact mechanism in deep high-ground stress differential reservoirs is still unclear. Therefore, it is necessary to study the influence of different construction parameters on the propagation behaviour of compression fractures under deep high geo-stress and high geo-stress difference conditions.

The research methods of reservoir fracture propagation mainly include the laboratory test method, theoretical derivation method, numerical simulation method, and field test method (Wei et al., 2015; Liu, et al., 2018a; Wu et al., 2018b; Luo et al., 2022). The current research on true triaxial fracturing experiments can already consider the influence of natural bedding in reservoirs and the propagation of multiple clusters of fractures. However, the current size of cube specimens in the laboratory is usually 100 mm × 100 mm × 100 mm or 300 mm × 300 mm × 300 mm, with few experimental specimens reaching the meter level in size, far smaller than the actual reservoir modification area (Shang et al., 2018; Liu et al., 2021; Qiu et al., 2023). Therefore, there are still significant size limitations in the physical simulation research of multi-cluster fracturing based on indoor experiments (Wang, et al., 2022; Yang et al., 2023b). Meanwhile, it is worth mentioning that conducting physical simulation research on the fracturing of meter-scale experimental specimens is usually very expensive, making it difficult to conduct a comprehensive analysis. Therefore, numerical simulation technology, as a research method that can simulate the heterogeneous characteristics of reservoirs, has a certain reference value and is easy to conduct comprehensive analysis, has been increasingly widely used. After years of development, numerical simulation technology has become more and more mature, which can better analyze the complex fracture propagation in the fracturing process (Bai et al., 2023). Three kinds of numerical methods are commonly used to simulate hydraulic fractures (Xiang et al., 2009; Ju et al., 2016; Yan et al., 2018; Rougier et al., 2019): extended finite element, boundary element, and discrete element. The Extended finite element method (XFEM) (Salimzadeh and Khalili, 2015; Shi et al., 2022) is a numerical method for solving discontinuous mechanics problems (Zou, et al., 2020). The characteristic of XFEM is that it does not need to re-divide the mesh when simulating fracture propagation, which overcomes the difficulty of high-density mesh generation in high-stress and deformation concentration areas such as the fracture tip. The boundary element method (BEM) divides the elements on the boundary of the domain and approximates the boundary conditions with functions satisfying the governing equations. The discrete element method (DEM), which divides the material into separate rigid elements in a discrete manner, describes the motion and interaction of each rigid element through contact connection based on Newton's law of motion and allows fluid flow in the channel formed between discontinuous blocks or particles, which can well describe the expansion of hydraulic fractures (Huang et al., 2022). These methods can simulate the growth of complex fractures, but each has its advantages and disadvantages. For example, the discrete element method simulates fluid migration through the connected mesh between particles and the deformation and fracture characteristics of reservoir rocks through the contact fractures between particles (Huang et al., 2019; Huang et al., 2023). However, it is difficult to consider particle size and computational efficiency, so it is difficult to be used in reservoir fracturing research. The finite element discrete element method (FDEM), proposed by Dr. Munjiza (Munjiza, 2004), has been widely used in the simulation of ground stress, fluid migration, reservoir fracturing, *etc.*, and its applicability has been proved. In fact, the FDEM method can be implemented through globally embedded cohesive elements and can also be used for multi-cluster fracturing simulation research in deep heterogeneous reservoirs. However, when using globally embedded cohesive elements to describe the fractured interface of a reservoir, simulation calculations are very slow (Sharafisafa et al., 2023). Therefore, when the model size is large, the number of grids is large, and there are many grid nodes, the method of locally embedded cohesive elements (Wang et al., 2023) for numerical simulation research can quickly obtain large-scale fracturing simulation results. That is, using the cohesive element to conduct multi-cluster fracturing simulation research on a deep reservoir scale will more efficiently reveal the influencing factors of multi-cluster fracture propagation in deep shale reservoirs. Therefore, it is necessary to conduct three-dimensional multi-cluster fracturing simulation research on deep shale reservoirs under the influence of high ground stress and high ground stress difference based on the cohesive element modelling method.

In this paper, considering the relevant geological parameters of a certain reservoir in the southwest, three dimensional (3D) multi-cluster reservoir fracturing models based on cohesive element modeling are established, and the propagation law of artificial fractures in deep shale reservoir under the conditions of high ground stress and high ground stress difference is analyzed. The simulation method, modeling process, and benchmark model parameters are presented in Section 2, and the fracture propagation law under the influence of the different number of fracturing clusters, injection displacement, and Young's modulus are analyzed in Section 3. The conclusion is presented at the end.

2 Numerical model

To explore the influencing factors of deep shale multi-cluster fracturing construction process through numerical simulation research. The simulation methods related to fluid-solid coupling, cohesive element rupture, fluid flow, flow distribution, and other aspects of the cohesive element modeling used in this paper were

introduced. Then, a method for embedding cohesive elements and establishing simulation models based on the natural fracture characteristics of the target block reservoir was described. Finally, based on on-site investigation and experimental testing results, the simulation parameters used in this simulation were determined.

2.1 Simulation method

Hydraulic fracturing is a typical multi-physical field coupling process that involves fluid distribution, pore pressure, stress, displacement, and other changes under the influence of fluid injection. Therefore, the stress equilibrium process under the influence of fluid-structure coupling can be described by the following equation (Wu et al., 2018b)

$$\int_V (\bar{\sigma} - p_w \boldsymbol{I})\delta\boldsymbol{\varepsilon}\delta dV = \int_S \boldsymbol{t}\cdot\delta\boldsymbol{v}dS + \int_V \boldsymbol{f}\delta\boldsymbol{v}dV \tag{1}$$

where $\bar{\sigma}$ represented the effective stress matrix, MPa; p_w denoted the pore pressure, MPa; $\delta\boldsymbol{\varepsilon}/s^{-1}$ was the virtual strain rate matrix; $\boldsymbol{t}$ was the surface force matrix, N/m^2; $\delta_{\boldsymbol{v}}$ was the virtual velocity matrix, m/s and $\boldsymbol{f}$ was the physical force matrix, N/m^3.

During fracturing, the fluid pressure and flow rate in the reservoir are controlled by multiple factors such as fluid density and matrix porosity ratio. At this point, the fluid continuity equation can be described as (Dahi Taleghani et al., 2018)

$$\frac{d}{dt}\left(\int_V\left(\frac{\rho_w}{\rho_w^0}ndV\right)\right) + \int_S \frac{\rho_w}{\rho_w^0}n\boldsymbol{n}\cdot v_w dS = 0 \tag{2}$$

where J represented the volume change ratio of porous media, dimensionless; ρ_w was the fluid density, kg/m^3; n_w was the void ratio, dimensionless and v_w was the fluid seepage velocity, m/s.

During fracturing, there is seepage flow inside the rock in the reservoir, which conforms to Darcy's law (Li and Ghosh, 2006)

$$\boldsymbol{v}_w = -\frac{1}{n_w \boldsymbol{g}\rho_w}\boldsymbol{k}\cdot\left(\frac{\partial p_w}{\partial \boldsymbol{x}} - \rho_w \boldsymbol{g}\right) \tag{3}$$

where $\boldsymbol{k}$ represented a permeability matrix, m/s and $\boldsymbol{g}$ was the gravity acceleration vector, m/s^2.

During fracturing simulation, the deformation and failure of the cohesive element are used to simulate the initiation and opening of fractures. Before the fracture occurs, the stress-strain relationship of the Cohesive element satisfies the linear elastic relationship (Wu et al., 2019)

$$\begin{aligned}\boldsymbol{\sigma}_{coh} &= \begin{Bmatrix}\sigma_{coh_n}\\ \sigma_{coh_s}\\ \sigma_{coh_t}\end{Bmatrix} = \boldsymbol{K}_{coh}\boldsymbol{\varepsilon}_{coh}\\ &= \begin{bmatrix}K_{coh_nn} & K_{coh_ns} & K_{coh_nt}\\ K_{coh_ns} & K_{coh_ss} & K_{coh_st}\\ K_{coh_nt} & K_{coh_st} & K_{coh_tt}\end{bmatrix}\begin{Bmatrix}\varepsilon_{coh_n}\\ \varepsilon_{coh_s}\\ \varepsilon_{coh_t}\end{Bmatrix}\end{aligned} \tag{4}$$

where $\boldsymbol{\sigma}_{coh}$ denoted the stress vector of a cohesive element; $\boldsymbol{\sigma}_{coh-h}$, $\boldsymbol{\sigma}_{coh-s}$, $\boldsymbol{\sigma}_{coh-t}$ were the normal stress (perpendicular to the upper and lower surfaces of the cohesive element), the first tangent stress and the second tangent stress (non-existent in two-dimensional cases), respectively. Here, $\boldsymbol{K}_{coh}$ denoted the stiffness matrix of a cohesive element; $\boldsymbol{\varepsilon}_{coh}$ was the strain matrix of a cohesive element and $\boldsymbol{\varepsilon}_{coh-n}$, $\boldsymbol{\varepsilon}_{coh-s}$, $\boldsymbol{\varepsilon}_{coh-t}$ represented the normal strain, the first tangential strain and the second tangential strain of a cohesive element, respectively. They were defined as follows (Réthoré, et al., 2008; Wu et al., 2019):

$$\varepsilon_{coh_n} = \frac{d_n}{T_0}, \varepsilon_{coh_s} = \frac{d_s}{T_0}, \varepsilon_{coh_t} = \frac{d_t}{T_0} \tag{5}$$

where d_n, d_s, d_t represented the normal displacement, the first displacement and the second tangential displacement of a cohesive element, respectively. Here, T_0 was the constitutive thickness of the cohesive element.

When the stress and strain of the cohesive element used to simulate hydraulic fracture and the fracture propagation reach a certain level, the element will undergo damage and failure, resulting in further extension of the fracture and a decrease in fluid pressure inside the fracture. For the convenience of simulation, this article uses the maximum principal stress criterion to determine the failure situation of the cohesive element (Wang, 2019)

$$\left\{\frac{\langle\sigma_n\rangle}{\sigma_n^0}\right\}^2 + \left\{\frac{\sigma_s}{\sigma_s^0}\right\}^2 + \left\{\frac{\sigma_t}{\sigma_t^0}\right\}^2 = \lambda \tag{6}$$

where σ_n was the normal stress; σ_s, σ_t represented tangential stress (σ_t did not exist in two-dimensional cases), MPa; σ_s^0, σ_t^0 were the threshold stress of tangential damage, MPa; λ indicated that cohesive elements resist tension stress but not compression stress: $1 \le \lambda \le 1.05$.

After being damaged, the cohesive element still has a certain degree of deformation resistance, so a damage factor is introduced to describe the attenuation process of the stiffness of the damaged cohesive element. The relevant formulas can be described as (Xavier et al., 2014; Wu et al., 2018a; Wu et al., 2019)

$$E = (1-d)\times E^0 \tag{7}$$

where E_0, E were the initial elastic modulus (without damage) and the elastic modulus after damage, Pa, respectively. Here, d denoted a damage factor, dimensionless.

Damage factors could be calculated by

$$d = \frac{\delta_m^f\left(\delta_m^{\max} - \delta_m^0\right)}{\delta_m^{\max}\left(\delta_m^f - \delta_m^0\right)} \tag{8}$$

where δ_m^{max}, δ_m^f , δ_m^0 signify distinct displacements in the context of element behaviour under loading conditions. Specifically, δ_m^{max} refers to the maximum displacement experienced by the element during loading. On the other hand, δ_m^f denotes the displacement corresponding to the point of complete damage to the element. Lastly, δ_m^0 represents the displacement at the onset of initial damage to the element.

For multi-cluster fracturing (Figure 1), the total amount of injected fluid corresponds to the total flow rate of different clusters and perforations as follows.

$$Q = \sum_{i=1}^{N} Q_i \tag{9}$$

Correspondingly, the fluid pressure drop can be expressed as

$$p_0 = p_{pf,i} + p_{cf,i} + p_{wf,i} \tag{10}$$

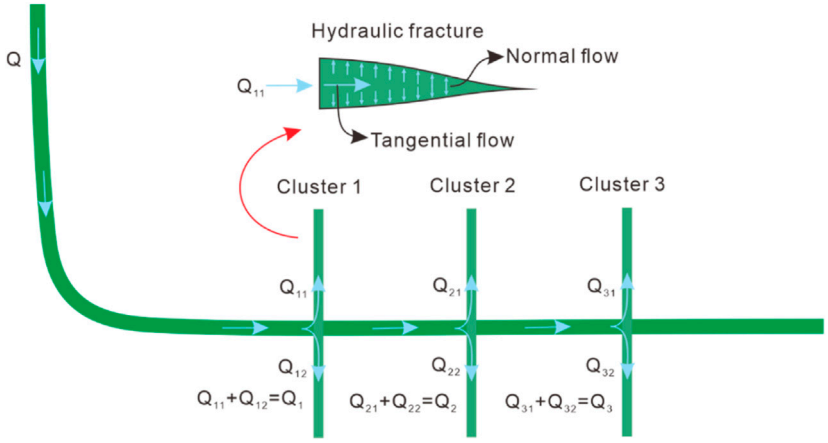


FIGURE 1
Schematic diagram of multi-cluster fracturing flow distribution.

TABLE 1 Main parameters used in simulation models.

Input parameters	Vaule
Young's modulus (GPa)	35
Poisson's ratio (dimensionless)	0.20
Permeability coefficient (m/s)	1e-7
Porosity (dimensionless)	0.04
Tensile strength of natural fractures (MPa)	2
Critical damage displacement (m)	0.001
Injection rate (m^3/min)	14–18
Fracturing fluid viscosity (mPa·s)	1
Pipe roughness (mm)	0.015×10^{-3}
Number of perforations	38
perforation diameter (m)	0.01

The roughness of a horizontal wellbore surface can induce pressure during fluid flow, and this pressure loss correlates with wellbore length. The relationship between frictional resistance and flow rate through the cluster can be accurately described by Bernoulli's equation. In this study, proppant erosion on the cluster node is disregarded, allowing the utilization of Bernoulli's equation for the perforation friction model.

$$\nabla p - \rho g \Delta Z = (C_L + K_i)\frac{\rho v^2}{2},$$
$$C_L = \frac{fL}{D_h},$$
$$f = 8\left[\left(\frac{8}{\mathrm{Re}}\right)^{12} + \frac{1}{(A+B)^{1.5}}\right]^{1/12}, \quad (11)$$
$$A = \left[-2.457\ln\left(\left(\frac{7}{\mathrm{Re}}\right)^{0.9} + 0.27\left(\frac{K_s}{D_h}\right)\right)\right]^{16},$$
$$B = \left(\frac{37350}{\mathrm{Re}}\right)^{16}$$

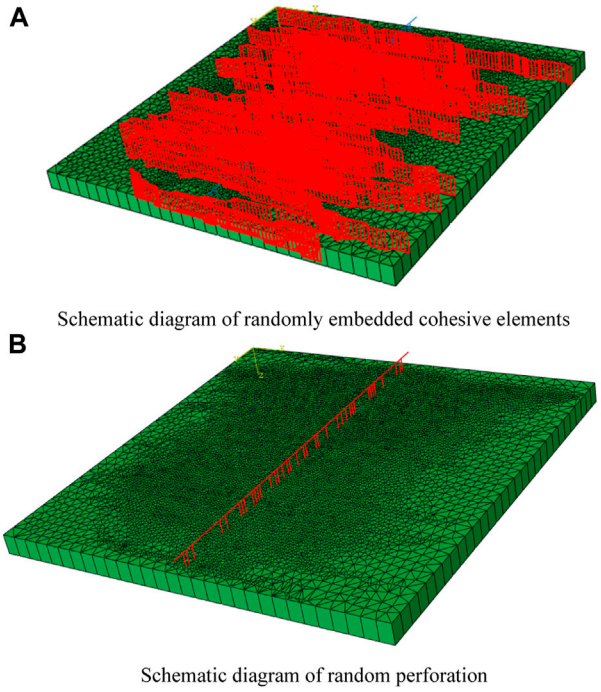


FIGURE 2
Schematic diagram of multi segment and multi-cluster fracturing model.

where ΔP is the pressure difference at the node of the cluster, ΔZ is the elevation difference of the node, v is the fluid velocity in horizontal wellbore, ρ is the fluid density, G is the acceleration of gravity, C_L is the loss coefficient, f is the friction force on the wellbore, L is the wellbore length, K_i is the loss term in fixed direction, K_s is the roughness of wellbore, D_h is the wellbore diameter, Re is the Reynolds number of the fluid in the wellbore.

In this study, the consideration of proppant erosion on the cluster node is omitted, enabling the utilization of the pressure drop

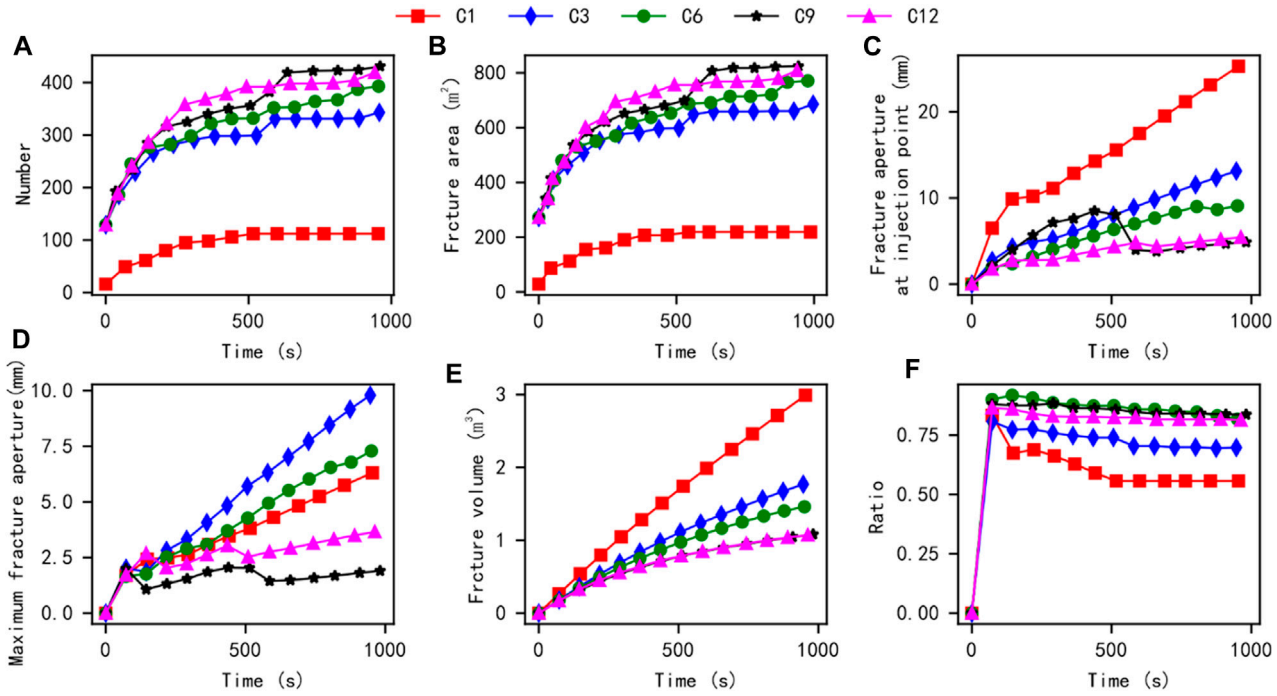


FIGURE 3
Comparison results of conventional quantization parameters under the influence of different clusters.

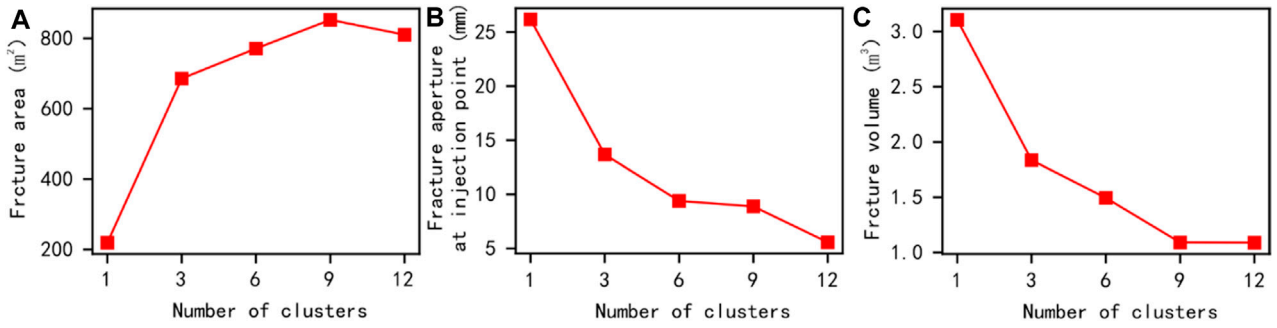


FIGURE 4
Comparison results of conventional quantization parameters under the influence of different clusters at 1000s.

model derived from Bernoulli's equation for modeling perforation friction. (Cramer et al., 2019).

$$p_f = 0.087249 \times \frac{\rho}{n^2 D_p^4 C^2} q_i^2 \tag{12}$$

where n is the number of perforations in each cluster, in this paper, the value is 16, D_p is the perforation diameter, C is the coefficient affecting perforation flow, generally 0.56–0.9 (Modeland et al., 2011; Zhang et al., 2023), in this paper, the value is 0.6.

The initiation and expansion of fractures, simulated using cohesive elements in fracturing simulations, result in the tangential and vertical flow of fracturing fluid along these elements. Assuming the fluid behaves as an incompressible Newtonian fluid for tangential flow, we define the volume flow vector per tangential unit length.

$$q = \frac{t^3}{12u} \nabla p \tag{13}$$

where q represented the volume flow vector per tangential unit length; t was the thickness of a cohesive element, m; μ was the viscous coefficient of fracturing fluid in a cohesive element; p was the fluid pressure in a cohesive element, MPa.

Examining the normal flow of hydraulic fracturing fluid within fractures reveals the intricate interaction between fluid in fractures and fluid in rock blocks. This interaction can be effectively characterized by the filtration rate of fracturing fluid

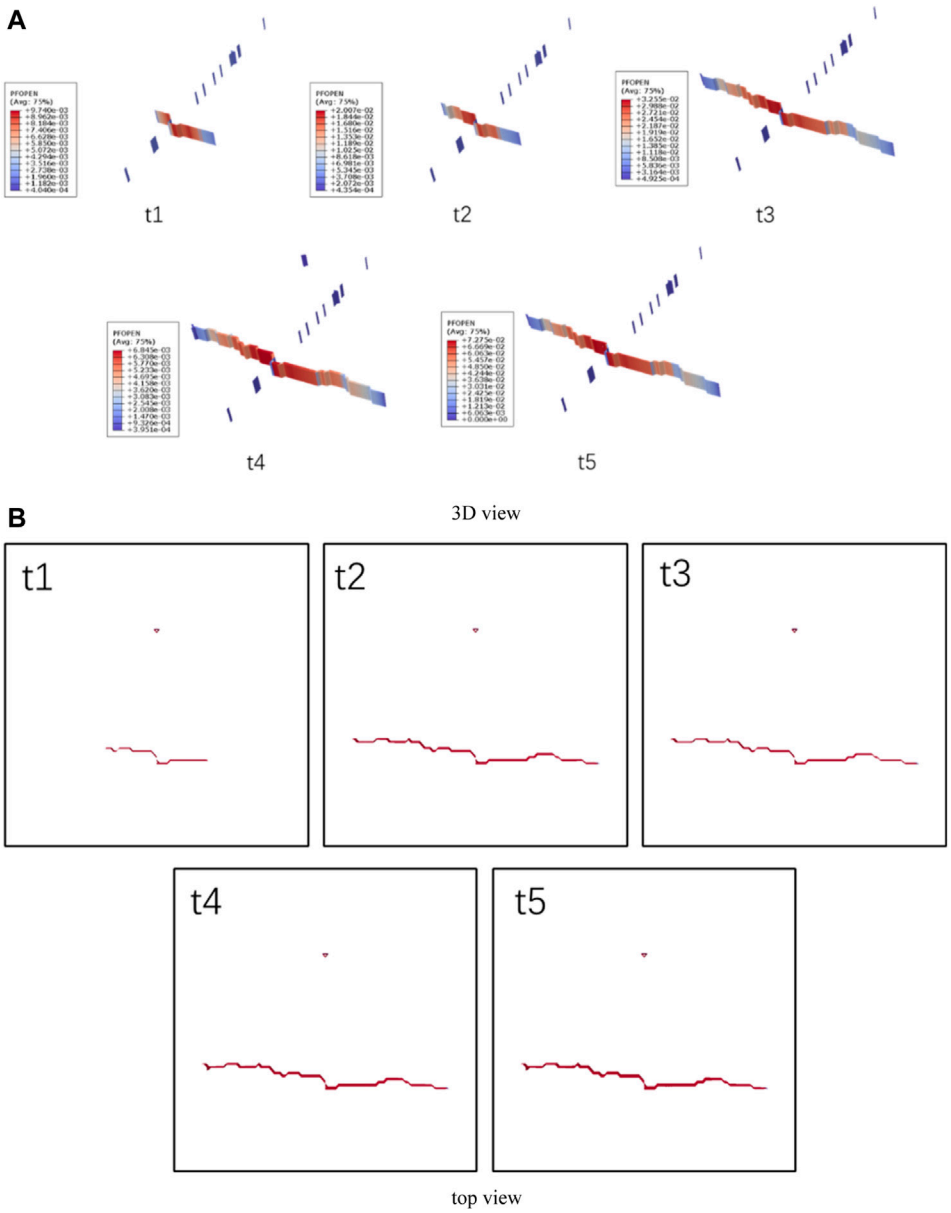


FIGURE 5
The process of fracture morphology changes during single cluster fracturing.

on both the upper and lower surfaces of the fractures. The methodology for calculating the filtration rate of fracturing fluid is

$$\begin{cases} q_t = c_t(p_i - p_t) \\ q_b = c_b(p_i - p_b) \end{cases} \tag{14}$$

where q_t, q_b represented the volumetric flow rate of the fluid flowing out of the upper and lower surfaces of a cohesive element. They also denoted the surface flow rate in a two-dimensional plane. The terms c_t, c_b were the filtration coefficient of the upper and lower surfaces, m/min$^{0.5}$; p_t, p_b were the pore pressure of the upper and lower surfaces, MPa and p_i was the fluid pressure of the middle surface of a cohesive element, MPa.

2.2 Model setup

To conduct numerical simulation research on multi-cluster fracturing for a well in Southwest China, detailed on-site data of a well in Southwest China was consulted. The relevant description for constructing a multi-cluster fracturing simulation model is as follows: ① The reservoir near the fracturing well is divided into multiple layers, mainly consisting of gray-black shale and black shale. According to core observation statistics, there are significant natural fracture development characteristics in some layers, with a linear density of about 1.56 pieces/m and a main inclination angle of 10°–30°. Based on this, it is assumed that the research area is 60 m × 60 m, with a thickness of 3 m. ② On-site testing shows that the triaxial

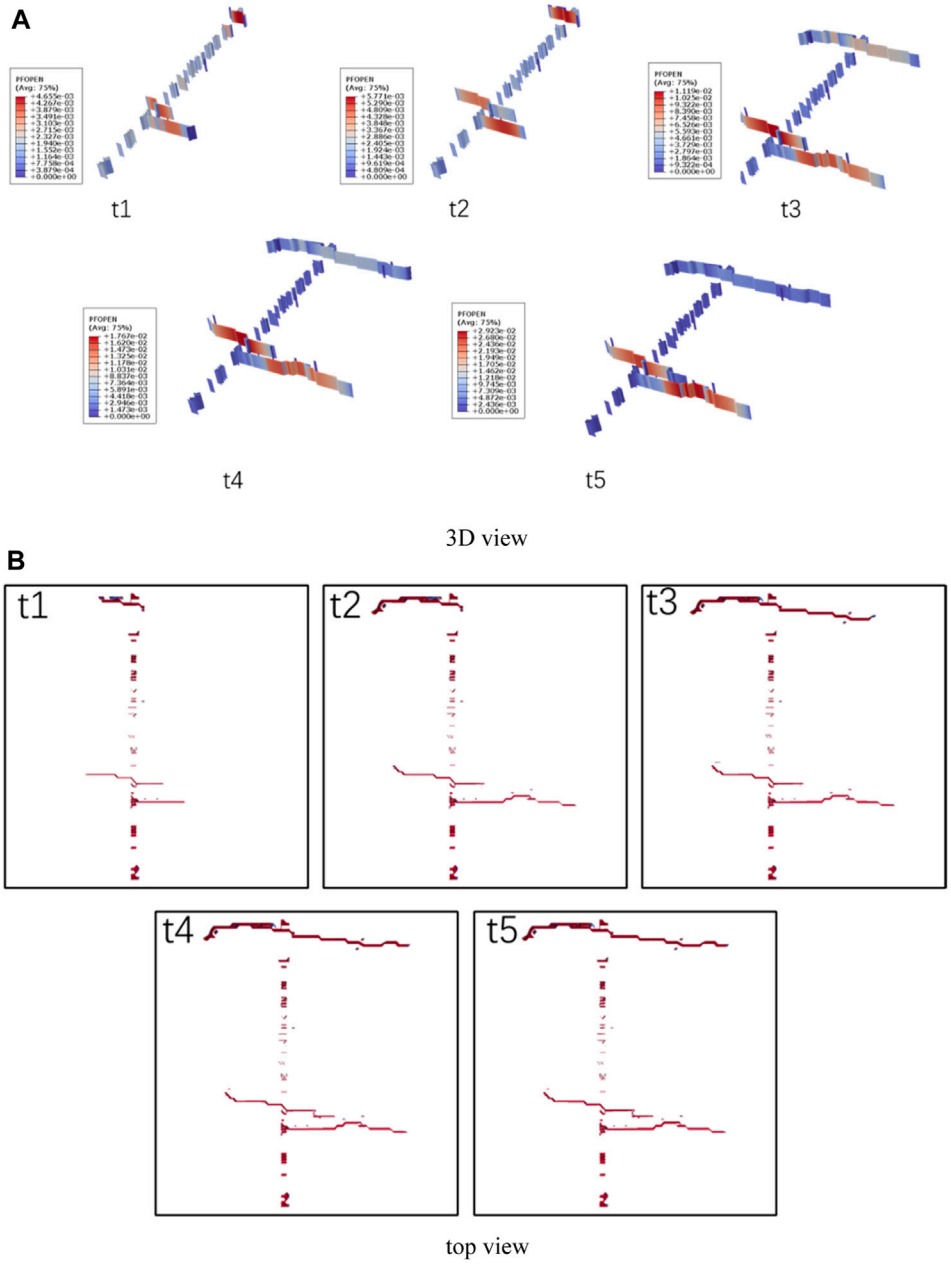


FIGURE 6
The process of fracture morphology changes during three cluster fracturing.

and triaxial principal stresses of the fractured well have a maximum horizontal stress value is about 96 MPa, a minimum horizontal stress value is about 86 MPa, and a vertical stress value is about 93 MPa. ③ According to the on-site data, triaxial compression tests were conducted. The main parameters include a temperature of 108°C, overlying rock pressure of 91.5 MPa, confining pressure of 77.8 MPa, and pore pressure of about 66.2 MPa. After experiments, the compressive strength of the fractured reservoir was obtained to be 435.3–570.71 MPa, with a Young's modulus of 28.79–40.67 GPa and a Poisson's ratio between 0.181 and 0.235. ④ In fact, the target block of this study is the well section that has undergone a fracturing transformation. The specific perforation segmentation is mainly as follows: during on-site construction, well sections with similar geological and engineering parameters are divided into the same fracturing section. The main length of the segmented section is designed to be 60 m, and the construction displacement is 14–18 m^3/min. Regarding the perforation concept, the main body adopts 6 clusters for perforation. Due to significant construction equipment and conditions, perforation and fracturing clusters cannot be strictly controlled. Therefore, the cluster spacing should be set at 9–10 m while maintaining consistent cluster spacing as much as possible.

Based on the above on-site data description, the model settings of the constructed simulation model are as follows:

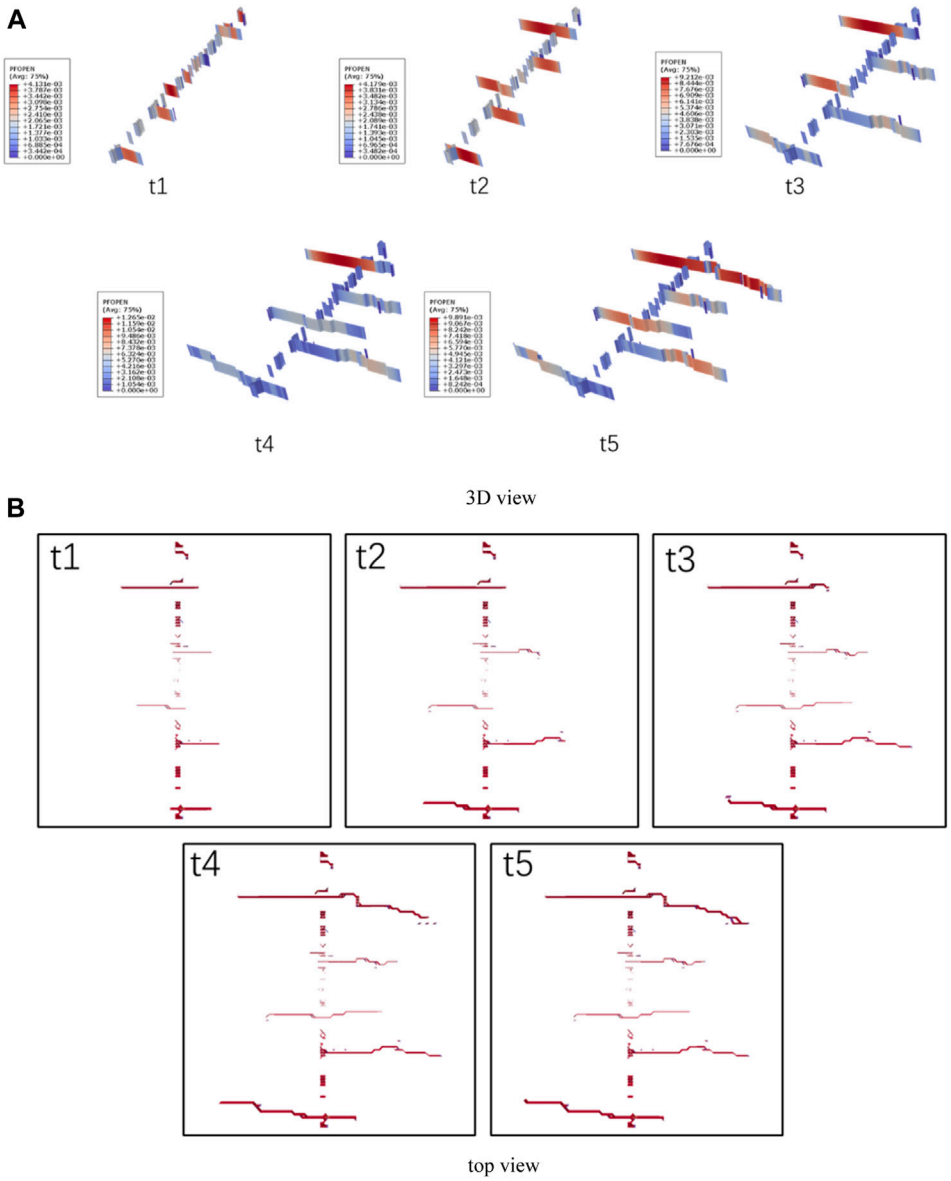


FIGURE 7
The process of fracture morphology changes during six cluster fracturing.

① The model size is 60 m × 60 m × 3 m, given the presence of random natural bedding in the target reservoir, and the fact that natural weakly cemented bedding is mainly present during shale reservoir fracturing. Considering that natural fractures in reservoirs usually have a certain degree of roughness, a rough discrete fracture network based on the rough discrete fracture network reconstruction method (Shi, et al., 2023) was established for natural fracture inclination angles between 10° and 30°. Subsequently, the rough discrete fracture network was imported into Abaqus software through Python scripts developed by us, and a fracturing simulation model containing a randomly distributed rough discrete fracture network was established. It is worth mentioning that on-site perforation is often limited by construction conditions and equipment, making it difficult to achieve uniform perforation. To simulate this randomness, the model directly constructed 38 perforation points based on a discrete fracture network (Table 1).

② The injected fluid flows into the reservoir after being diverted along the wellbore components. Therefore, the fp3d2 unit is used to set up a simulated wellbore located at the bottom of the reservoir area, and the fpc3d2 unit is used to simulate the friction before flowing into the reservoir. The interaction between fluid volume and fluid pressure in the simulation is achieved by binding the wellbore tip node and the reservoir interface unit node. Therefore, during single cluster fracturing, the injection point of the model is located at the endpoint of the wellbore. In addition, there is randomness in the actual on-site perforation spacing. To simulate perforation more realistically, the perforation of this model is randomly set, with a total of 38 perforation points (Figure 2B).

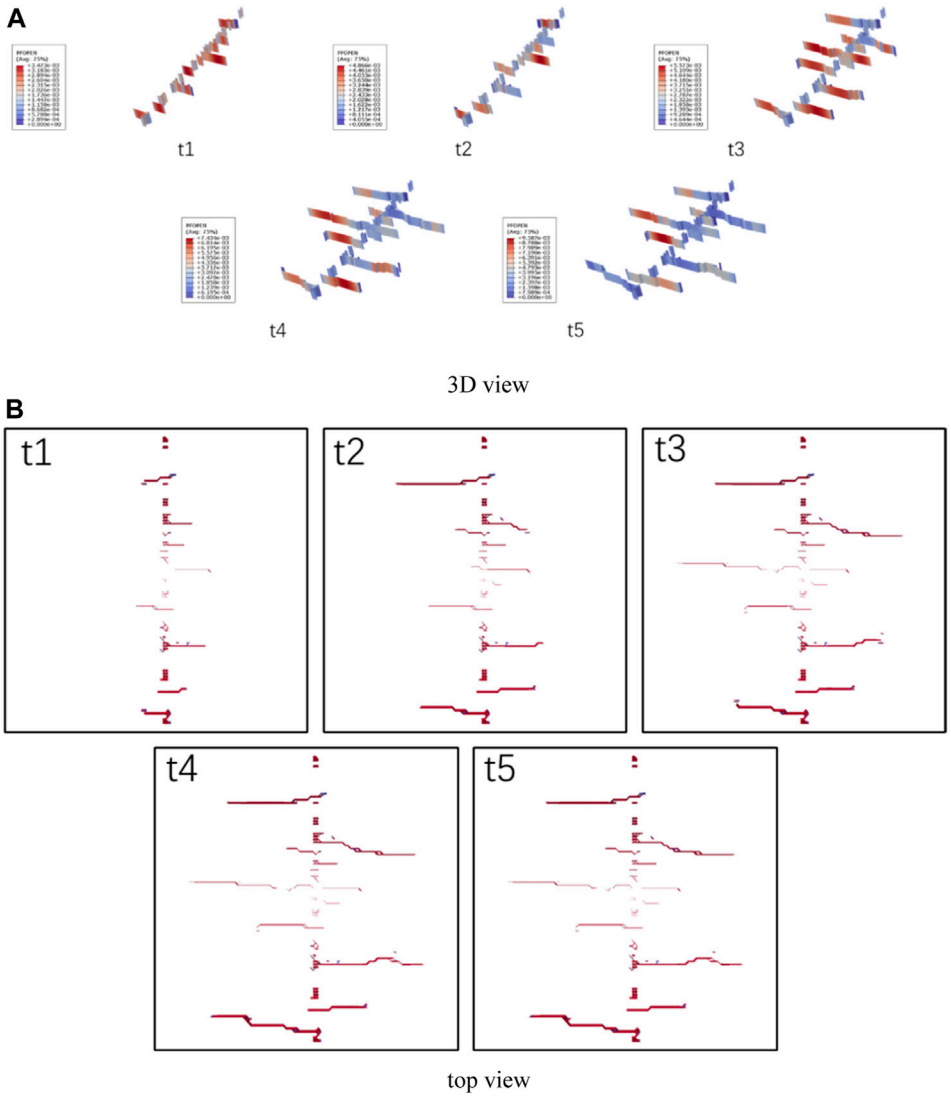


FIGURE 8
The process of fracture morphology changes during nine cluster fracturing.

③ The conventional interface element method with global embedding has phenomena such as long computational time and severe local shear collapse of fractures. Therefore, the use of random modelling to form a discrete nonplanar sequence fracture network facilitates the development of multi-cluster fracturing.

④ The x direction is assumed to be the maximum horizontal principal stress direction, the z direction is assumed to be the vertical principal stress direction and the y direction is assumed to be the minimum horizontal principal stress direction. The outer boundary of the model is a fixed displacement and impermeable boundary condition, with upper and lower boundaries constraining displacement in the z direction and left and right boundaries constraining displacement in the x and y directions.

⑤ To reduce computational complexity, larger grid seeds were used for grid generation. After grid generation, the total grid size of the reservoir components was 17,105, including 13,305 rock block elements, 3,800 interface elements, and a total of 28,632 nodes. The total number of simulated wellbore elements is 115, including 38 fpc3d2 elements, 77 fp3d2 elements, and a total of 116 nodes.

Based on the geological and mechanical conditions of the target reservoir, mechanical experimental results, and on-site construction settings, the corresponding model parameters are selected. The benchmark calculation example is based on single cluster fracturing, assuming a reservoir thickness of 3 m, an injection displacement of 14 m^3/min, and a total injection time of 3,600 s. Using a super hydrostatic pressure system for simulation, the stress boundary condition is effective stress. Meanwhile, the total geo-stress in the benchmark model is 96 MPa, 86 MPa, and 93 MPa, with a pore pressure of 66 MPa. Meanwhile, the constitutive parameters of cohesive units in the model refer to previous reservoir fracturing simulation studies that considered heterogeneity (Wu et al., 2022; Wu et al., 2023). In addition, the multi-cluster fracturing parameters are referenced from Zhang's research (Zhang et al., 2023). The detailed information is shown in Table 1. Afterwards, corresponding simulation results can be obtained based on Eqs 1–14.

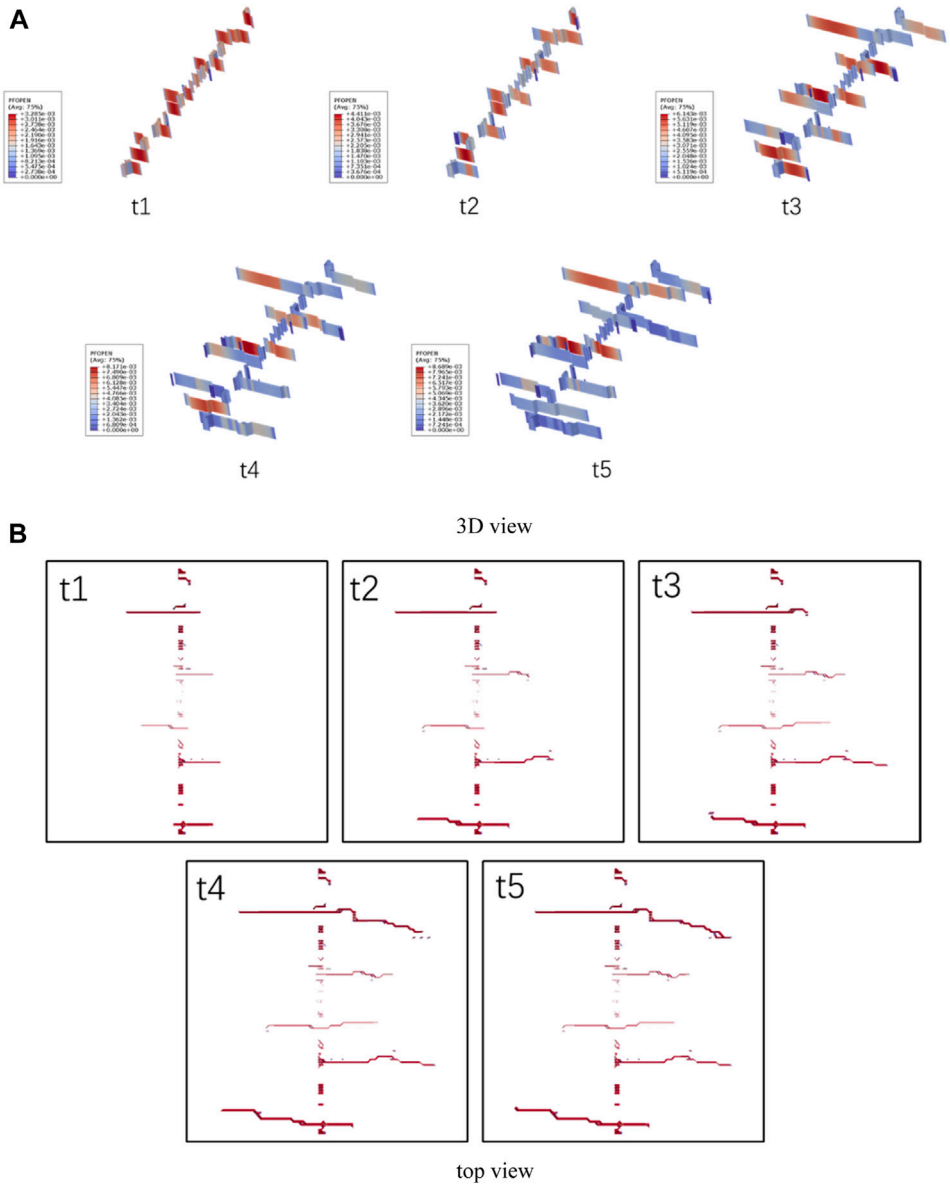


FIGURE 9
The process of fracture morphology changes during twelve cluster fracturing.

3 Results and analysis

Compared to conventional shallow reservoir mining, deep shale reservoirs have a larger depth and therefore exist in high-stress environments. Affected by mineral distribution, there is a certain range of fluctuations in the elastic modulus of rocks in the reservoir. In addition, when using multi-cluster fracturing construction, the construction design displacement and the number of fracturing clusters usually also affect the morphological expansion of artificial fractures in the reservoir. Therefore, this section delves into the hydraulic fracture propagation law of the target block reservoir under multi-cluster fracturing construction conditions, injection rate changes, and reservoir rock Young's modulus changes.

3.1 Effect of fracturing cluster number

Referring to the calculation methods of conventional quantitative parameters in previous studies (Wu et al., 2020b; Wu et al., 2022), The conventional fracture morphology parameters (fracture area, fracture aperture at the injection point, maximum fracture aperture, fracture volume) are calculated based on the damaged cohesive element morphology, and the tensile failure ratio is obtained through MMIXDME and MMIXDMI field variables. Then, by adjusting the number of fracturing clusters to 1, 3, 6, 9, and 12, the fracturing results under different cluster and cluster spacing conditions are shown in Figure 3. From this figure, as the cluster spacing increases, the number of fracture elements and total fracture area in the simulation model show an

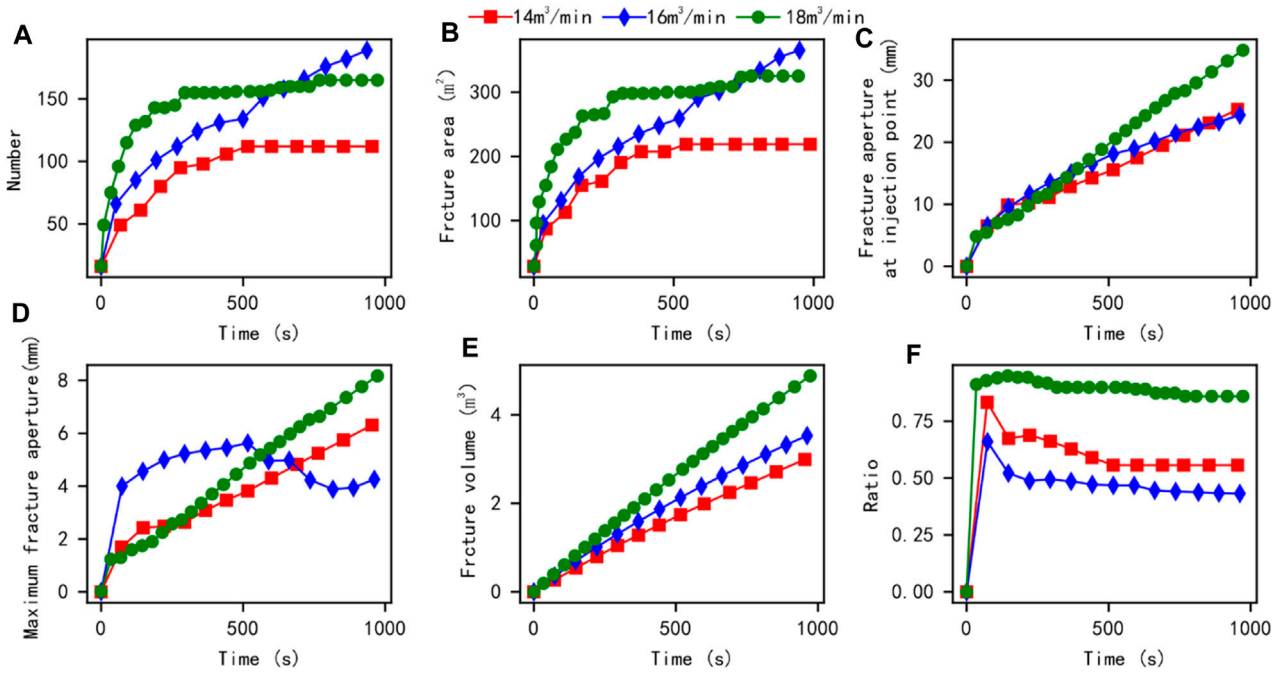


FIGURE 10
Comparison results of conventional quantitative parameters under different displacement effects during single cluster fracturing.

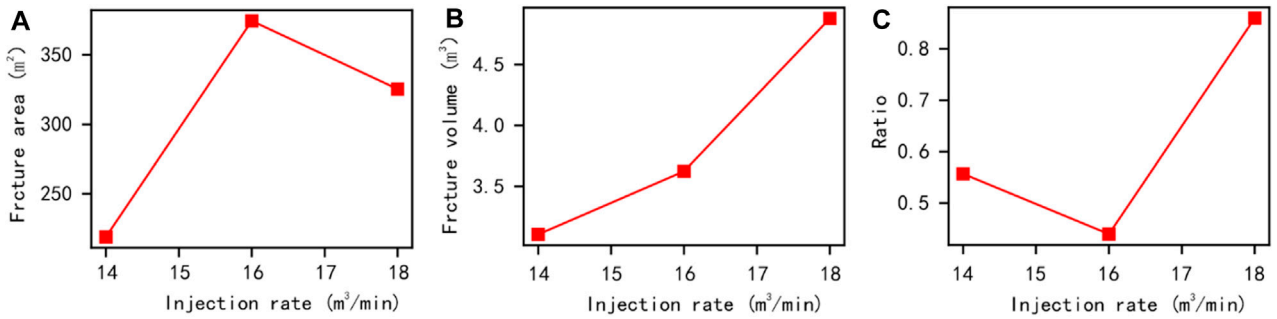


FIGURE 11
Comparison results of conventional quantitative parameters under different displacement effects (single cluster fracturing at 1000s).

increasing trend. It is worth mentioning that from 1 cluster fracturing to 3 clusters fracturing, the number of fracture elements and total fracture area increased significantly, followed by a smaller increase. Meanwhile, as the distance between clusters increases and the number of clusters increases, the volume of fractures in the model decreases, and the proportion of tensile failure significantly increases. This should be because single cluster fracturing is more difficult to form large-scale fractures, and the injected fluid is mainly used for fracture opening.

The statistics of the values of a certain stage in the simulation results are shown in Figure 4. In this model, as the number of clusters increases, the cluster spacing decreases. The total area of fracture fractures in the model increases, the width of injection point fractures decreases, and the total volume of visible fractures decreases. These phenomena indicate that in this simulation model, as the number of clusters increases and the spacing between clusters decreases, the model is more likely to form many fractures with small openings, resulting in an increase in the total area of fractures and a decrease in the visible fracture volume.

The morphological evolution process of artificial fractures during single cluster and three cluster fracturing is shown in Figure 5 and Figure 6. Please note that since the width of artificial fractures is much smaller than the reservoir scale, to highlight the results of artificial fracture morphology, a 10-fold deformation scaling factor was used in both the top view and the 3D view. Under the conditions set in this model, single cluster fracturing is mainly used to form a single main fracture, and the phenomenon of fracture initiation near the wellbore is not significant. As the number of clusters increased to 3, three main slots expanded in the model, and there were both single wing and double wing expansion

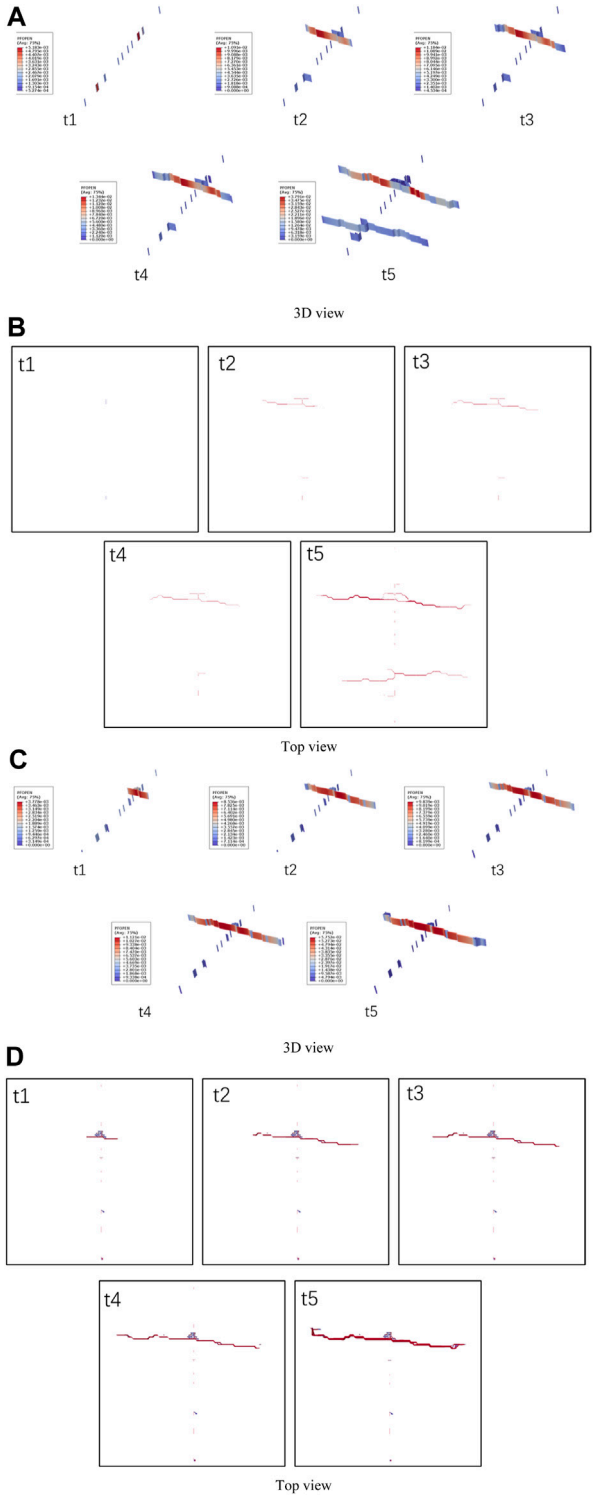


FIGURE 12
The results of fracture morphology under different displacement effects during single cluster fracturing (injection displacement of **(A,B)** is 16 m^3/min, and injection displacement of **(C,D)** d is 18 m^3/min).

phenomena in the main slots. This indicates that increasing the number of fracturing clusters may be beneficial for the initiation of fractures near the wellbore, as well as for the expansion of multiple main fractures.

The artificial fracture propagation process under six and nine-cluster fracturing construction conditions is shown in Figure 7 and Figure 8. When using the construction process of 6 cluster fracturing, multiple fractures appeared near the wellbore, and 5 main fractures developed simultaneously. When using the nine-cluster fracturing construction process, there is also a phenomenon of multiple fracture initiation near the wellbore, with nearly ten main fractures developed. It is worth mentioning that the fracture morphology in the simulation results has been magnified by ten times the deformation to ensure that most of the fractured fractures can be seen. However, when using six-cluster fracturing, the main fracture path of the artificial fracture is significant. When using nine-cluster fracturing construction, the main fracture path of some artificial fractures is not continuous, indicating that there are many locally small opening fractures in the main fractures of some artificial fractures. These small opening fractures are obviously not conducive to the transportation of proppant in the reservoir and therefore are not conducive to subsequent mining.

The result of the twelve-cluster fracturing is shown in Figure 9. Obviously, more than twelve artificial fractures sprouted near the wellbore in the early stage of the twelve -cluster fracturing model. As the fracturing continues, there is a competitive expansion of budding fractures within each cluster in the model, resulting in some budding fractures not further opening, while others further opening. Therefore, as the fracturing continues, the number of main extended fractures in the reservoir gradually decreases, ultimately leading to the phenomenon of ten main fractures expanding one after another. Unfortunately, we can observe the fracture morphology of almost all the main fractures in the 3D view, while only some of the main fractures can be observed in the top view (five main fractures appear in the top view). These results indicate that under the conditions set in this model, the number of main fractures that are beneficial for proppant transport and later development may not increase with the increase of cluster numbers. Therefore, in the evaluation process of fracture propagation results, not only the total area of artificial fractures needs to be considered, but also factors such as the number and area of effective support fractures under the influence of the proppant ceramic particle size should be further considered.

3.2 Effect of injection rate

During multi-group fracturing construction, the expansion of artificial fractures is not only affected by the setting of the compression fracture group but also by the injection rate. Given that the number of fracturing clusters has a significant impact on the simulation results, this section selected single cluster and 12 cluster fracturing simulation models and obtained corresponding numerical simulation results by setting the injection rate to 14–18 m^3/min.

The model parameter results under the influence of different injection rates during single cluster fracturing are shown in Figure 10. As the injection flow rate increases, the number of rupture elements in the model increases more rapidly, and the overall number of rupture elements and total rupture area in the model show an increasing trend. Meanwhile, the total volume of

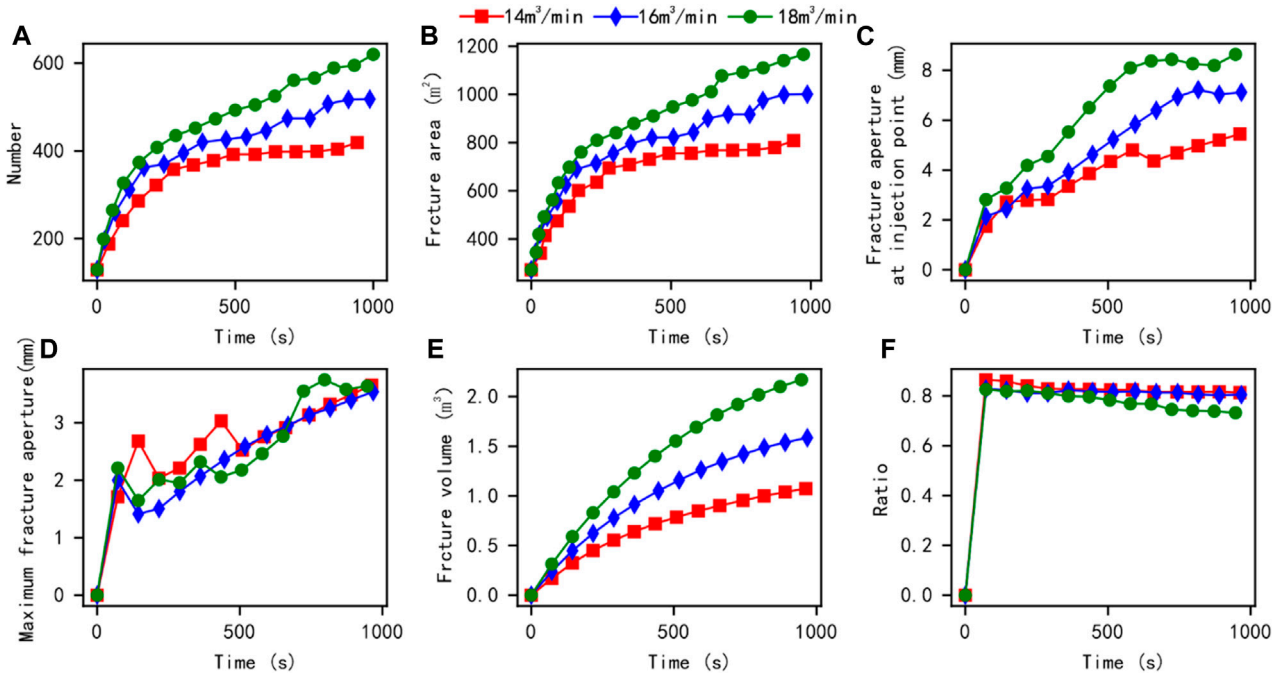


FIGURE 13
Comparison results of conventional quantitative parameters under the influence of different displacement during twelve-cluster fracturing.

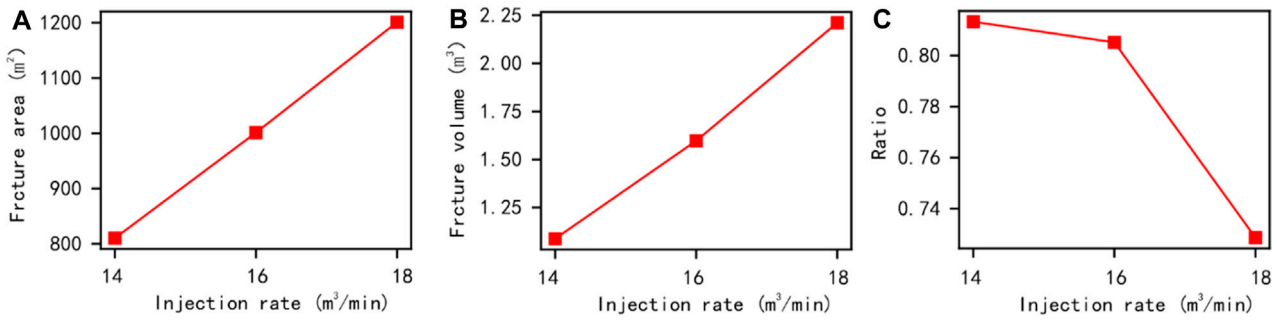


FIGURE 14
Comparison results of conventional quantitative parameters under the influence of different displacement during twelve-cluster fracturing (1000s).

fractures in the model decreases, while the proportion of tensile shear failure exhibits a certain degree of dispersion. Firstly, the decrease in the total volume of fractures indicates an increase in small opening fractures, so the total volume change cannot be calculated under the resolution of model data extraction. The discreteness of the tensile shear failure ratio in the model should be due to the comprehensive influence of factors such as natural interface paths and *in-situ* stress during the reservoir fracturing process (Zheng et al., 2022).

To analyse the influencing factors of the model, we further extracted the parameter results of the model at 1000s (Figure 11). Basically, as the displacement increases, the total area of fractures and the proportion of tensile failure in the model show a certain fluctuation, while the total volume of artificial fractures shows an increasing trend. Under the same reservoir conditions, increasing injection rate is beneficial for increasing the volume of artificial fractures. This may be to promote the expansion of the artificial main seam or to increase the opening of the main seam.

To further analyse the differences in fracture morphology in the model, Figure 12 shows the development process of artificial fractures at injection rates of 16 m^3/min and 18 m^3/min. Given the difficulty in observing the influence of artificial fracture width in 3D views, while the overall complexity of artificial fractures is difficult to observe in 2D top views. Therefore, both a 3D view and a 2D top view are drawn in the following figure. From the following figure, when the injection rate is 16 m^3/min, the fracture initiation phenomenon near the wellbore can be seen in the three-dimensional view, while it is difficult to see in the two-dimensional top view. This phenomenon indicates that under high injection fluid conditions, it may be easier to form small opening fractures, which makes it

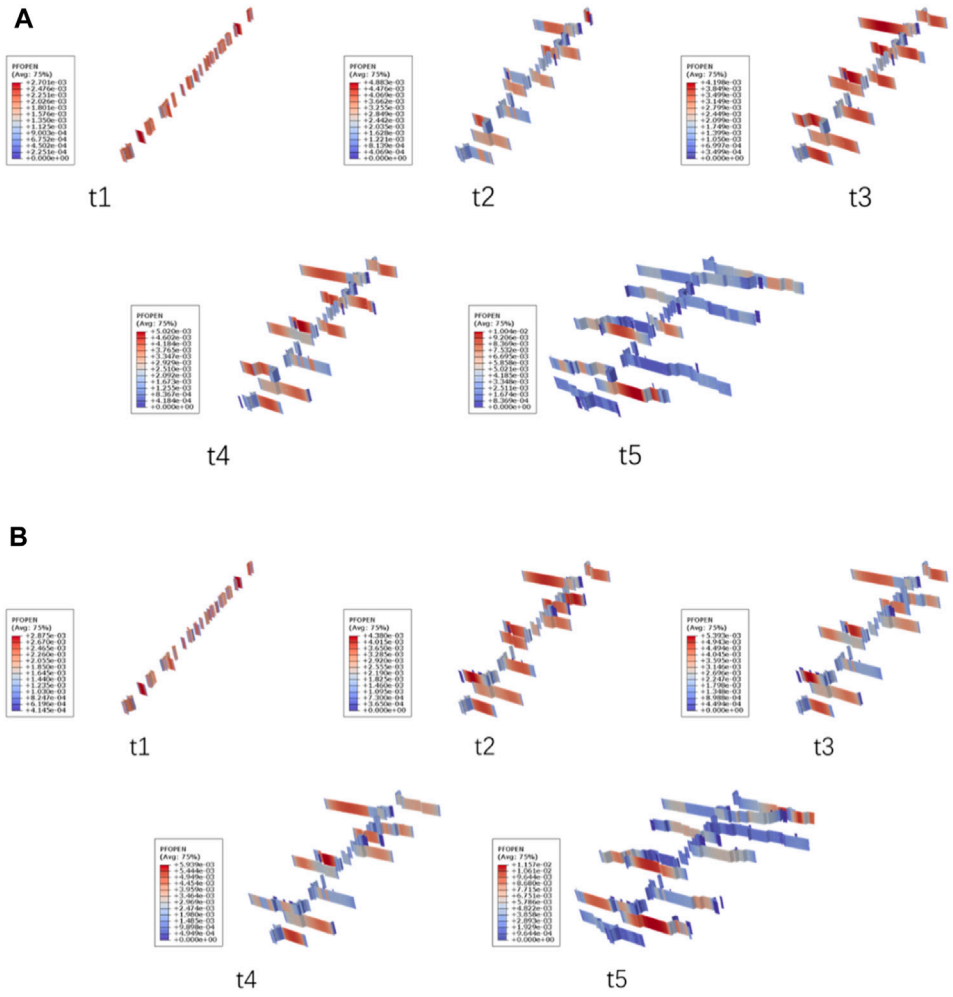


FIGURE 15
The results of fracture morphology under the influence of different displacement during twelve-cluster fracturing (injection displacement of a is 16 m^3/min, and injection displacement of b is 18 m^3/min).

difficult to predict the initiation of fractures near the wellbore area at the extracted resolution. Meanwhile, when the injection displacement is 16 m^3/min, a total of three main fractures were developed in the initial stage. As the fracturing continues, the expansion of the large main fracture is formed first, followed by the gradual expansion of the secondary main fracture, and finally, a total of two large and three small fracture expansion forms are formed, including two main fractures and three immature fractures with insufficient extension. Under this condition, using temporary plugging and repeated fracturing to further open the other three budding fractures will help further improve the effectiveness of reservoir reconstruction.

Like the simulation results when the injection rate is 16 m^3/min, the fracture initiation phenomenon near the wellbore can be seen in the 3D view, while it is difficult to see in the 2D top view. This phenomenon indicates that under high injection fluid conditions, it may be easier to form small opening fractures, which makes it difficult to predict the initiation of fractures near the wellbore area at the extracted resolution. At the same time, under the conditions of this model, when the injection rate is 18m3/min, one main fracture developed initially, and local collapse and fracture phenomenon occurred near the main fracture. As the fracturing continued, this one main fracture further extended, while no other initiation fractures were observed. This phenomenon indicates that during reservoir fracturing, if there is a dense rupture of micro seismic data near a certain perforation, it may be necessary to temporarily block the area near the perforation after the fracturing to fully fracture other areas and improve the effectiveness of reservoir reconstruction.

Further extraction of model parameter results under the influence of different injection displacement during twelve-clusters of fracturing was conducted to significantly compare the differences in the effects of different displacement, as shown in Figures 13, 14. From this figure, as the injection flow rate increases, the number of rupture elements in the model increases more rapidly, and the overall number of rupture elements and total rupture area in the model show an increasing trend. Meanwhile, the total volume of fractures in the model increases, while the proportion of tensile shear failure shows a decreasing trend. Compared to the simulation results of single cluster fracturing, the conventional quantitative

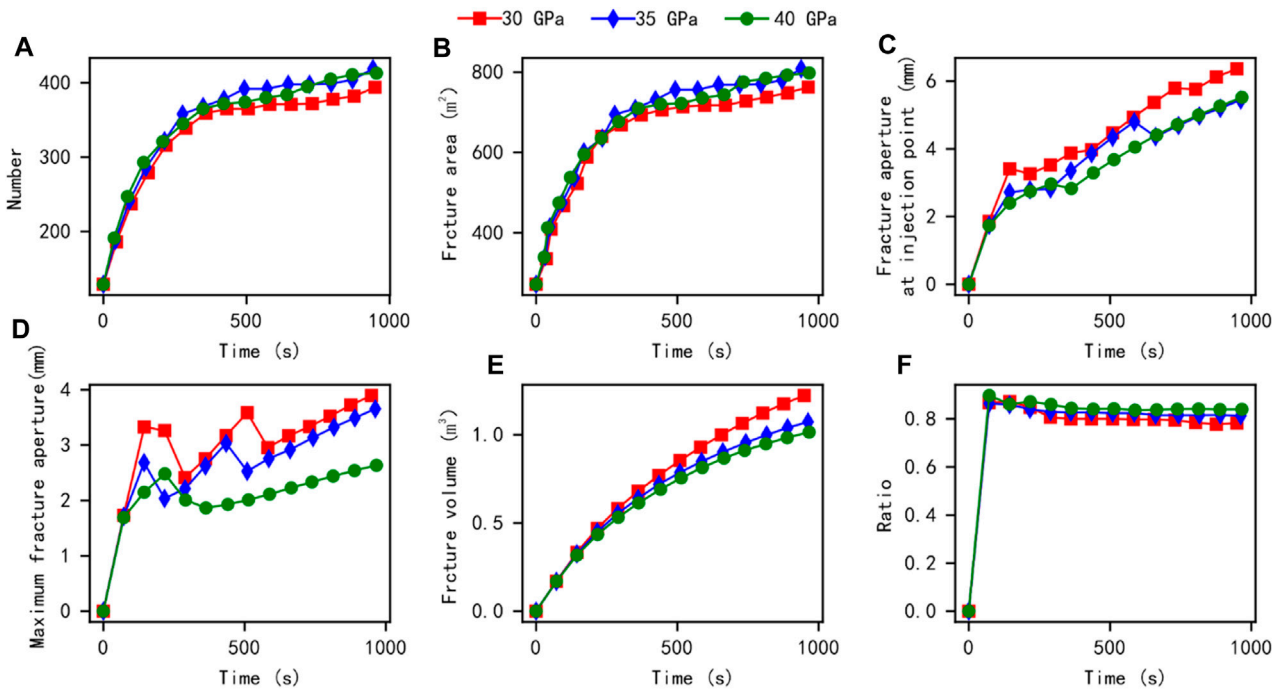


FIGURE 16
Comparison results of conventional quantitative parameters under different displacement effects during twelve cluster fracturing.

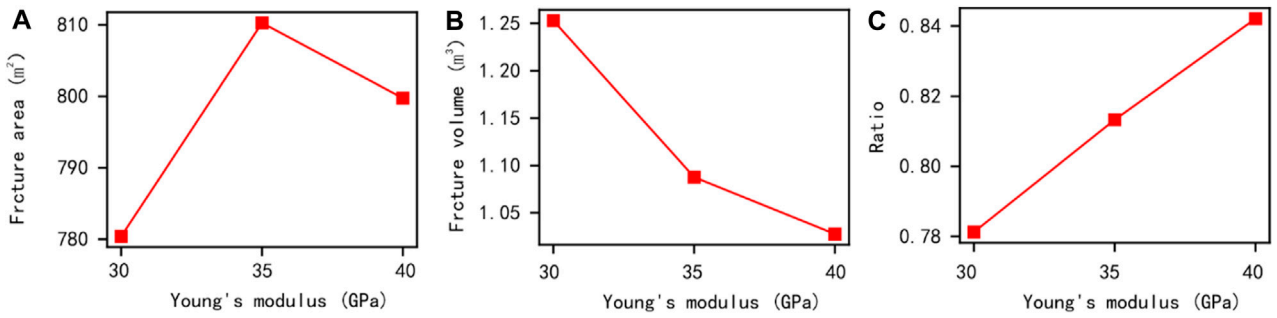


FIGURE 17
Comparison results of conventional quantitative parameters under different displacement effects during twelve cluster fracturing (1000s).

parameters in the model have more regularity. The above phenomenon can indicate that with the development of multi-cluster fracturing, the qualitative and quantitative trend of displacement for artificial fracture fracturing in reservoirs will be more regular.

Figure 15 shows the development process of artificial fractures under twelve-cluster fracturing conditions with injection rates of 16 m^3/min and 18 m^3/min. When the injection rate is 16 m^3/min, the 3D view shows the phenomenon of fracture initiation near the wellbore. Compared to the results of single cluster fracturing, the two-dimensional top view also more significantly shows the phenomenon of artificial fracture initiation near the wellbore of the reservoir. Meanwhile, when the injection displacement is 16 m^3/min, many budding fractures develop in the initial stage. As the fracturing continues, the expansion of the large main fracture is formed first, followed by the gradual expansion of the secondary main fracture, and finally ten main fractures are formed. As the fluid injection displacement increases, the number of main fractures in the model increases to eleven.

3.3 Effect of Young's modulus

Numerous studies have shown that Young's modulus of rocks significantly affects the effectiveness of reservoir fracturing (Wu et al., 2020a; Wu et al., 2022), and on-site testing shows that the elastic modulus of the reservoir is about 30–40 GPa. Therefore, to explore the differences in fracturing transformation effects in different Young's modulus areas of the target block using multi-cluster fracturing construction. By adjusting Young's modulus to 30,

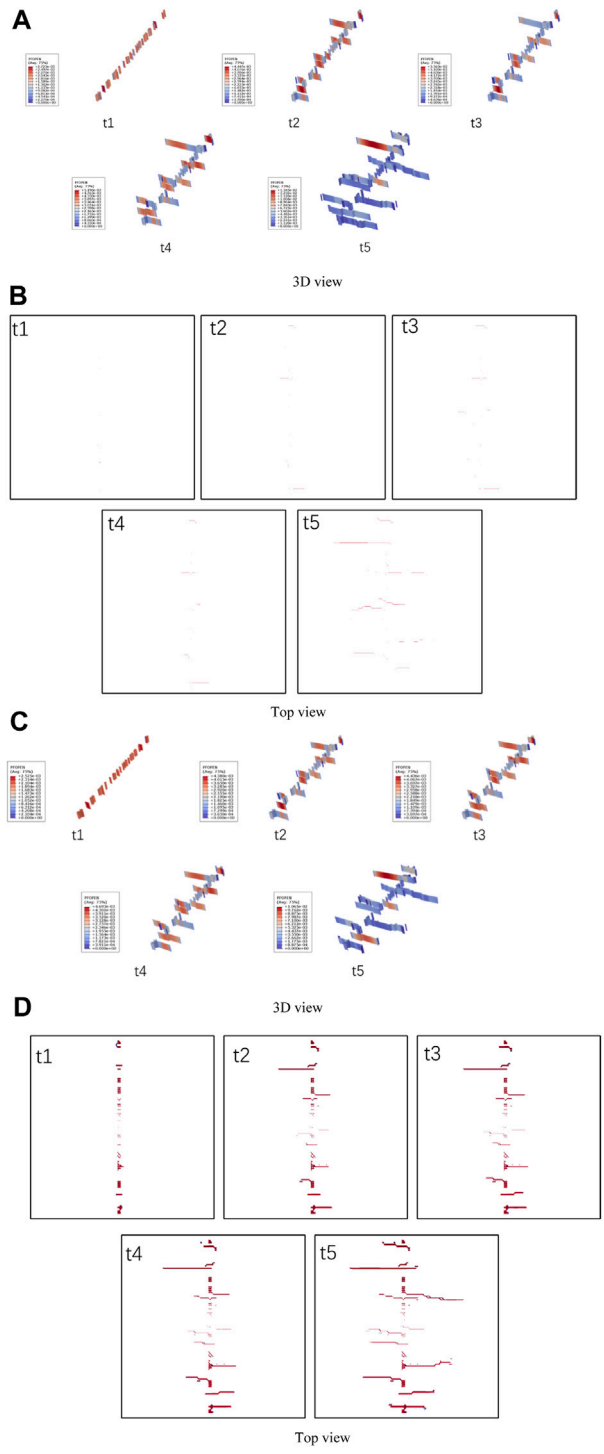


FIGURE 18
The results of fracture morphology under the influence of different Young's moduli during twelve-cluster fracturing (the Young's moduli of **(A,B)** are 30 GPa, and the Young's moduli of **(C,D)** are 40 GPa).

35, and 40 GPa, different simulation results of twelve cluster fracturing models were obtained, and the corresponding changes in conventional quantitative parameters are shown in Figure 16 and Figure 17. The number of interface unit fractures in the simulation model and the fracture area of artificial fractures in the reservoir show certain fluctuations under the influence of Young's modulus, and the difference in influence is limited. Meanwhile, when Young's modulus of reservoir rock decreases, the fracture width at the injection point in the centre of the model and the artificial fracture width generated by the overall model may show an increasing trend, while the total volume of the fracture may show a certain decreasing trend, resulting in a decrease in the proportion of artificial fractures caused by tensile failure. This phenomenon indicates that the change in Young's modulus in the area near the fracturing well affects the effectiveness of reservoir reconstruction but is not significantly affected by the constraints of the target area's geo-stress and multi-cluster fracturing construction.

The results of artificial fracture morphology changes when Young's modulus is 30GPa and 40 GPa are shown in Figure 18. Figures 18A–C show that as Young's modulus of reservoir rocks changes, the artificial fractures in the reservoir are still mainly extended by multiple clusters of main fractures due to the influence of high ground stress difference, and the extended main fractures are mainly in a single wing expansion mode. It is worth noting that under low Young's modulus conditions, the fracture morphology is not significant in the top view of the model (Figure 18B), while under high Young's modulus conditions, the artificial fracture morphology in the reservoir is more significant. This is because the width of the fractures formed in the reservoir is usually small, on the millimetres scale. Therefore, it is usually difficult to display relative to the reservoir. For this reason, the simulation results have magnified the deformation by ten times. Unfortunately, under low Young's modulus conditions, it is still difficult to observe obvious artificial fractures from the top view, while under high Young's modulus conditions, obvious artificial fractures can be observed from the top view. Therefore, fracturing in reservoirs with high Young's modulus of rocks may be more conducive to the formation of large opening fractures, which is beneficial for proppant support and subsequent mining.

4 Conclusion

Considering the relevant geological parameters of a certain reservoir in the southwest, this paper establishes a 3D multi-cluster reservoir fracturing model based on cohesive element modeling. Then, the propagation law of artificial fractures in reservoirs under the influence of the different number of fracturing clusters, injection displacement, and Young's modulus in different regions of the 60 m fracturing well section is analyzed, and the quantitative law of parameters such as fracture length, maximum fracture width, injection point fracture width, fracture area, and tensile failure ratio during multi-cluster fracturing construction, as well as the propagation law of fracture morphology are revealed.

(1) As the number of clusters increases, the distance between clusters decreases. The total area of fracture fractures in the model increases (nearly 4 times), the width of injection point fractures decreases, and the total volume of visible fractures decreases. These phenomena indicate that in this simulation model, as the number of clusters increases and the spacing between clusters decreases, the model is more likely to form

many fractures with small openings, resulting in an increase in the total area of fractures and a decrease in the visible fracture volume.

(2) During single cluster fracturing, as the injection flow rate increases, the number of fracture elements in both single cluster fracturing and multi-cluster fracturing models increases more rapidly, and the overall number of fracture elements and total fracture area in the model show an increasing trend ((nearly 1 time)). It is worth mentioning that the proportion of tensile shear failure in the single cluster model exhibits a certain degree of dispersion, while the conventional quantitative parameters in the multi-cluster fracturing model are more regular. The above phenomenon indicates that with the development of multi-cluster fracturing, the qualitative and quantitative trend of displacement for artificial fracture fracturing in reservoirs will be more regular.

(3) Under the influence of Young's modulus, the number of damaged cohesive elements in the simulation model and the fracture area of artificial fractures in the reservoir exhibit certain fluctuations, and the difference is limited under the comprehensive influence of *in-situ* stress and other factors. Meanwhile, when Young's modulus of reservoir rock decreases, the fracture width at the injection point in the center of the model and the artificial fracture width generated by the overall model may show an increasing trend, while the total volume of the fracture may show a certain decreasing trend, resulting in a decrease in the proportion of artificial fractures caused by tensile failure.

Data availability statement

The raw data supporting the conclusions of this article will be made available by the authors, without undue reservation.

Author contributions

JW: Conceptualization, Investigation, Project administration, Supervision, Writing–review and editing. MW: Investigation, Methodology, Writing–original draft. YG: Investigation, Project administration, Writing–review and editing. HH: Conceptualization, Data curation, Investigation, Project administration, Resources, Supervision, Writing–review and editing. ZZ: Investigation, Supervision, Writing–review and editing. GZ: Resources, Supervision, Writing–review and editing. JG: Resources, Supervision, Writing–review and editing. JL: Funding acquisition, Investigation, Writing–review and editing.

Funding

The author(s) declare financial support was received for the research, authorship, and/or publication of this article. The authors gratefully acknowledge the financial support given by Open Research Fund of State Key Laboratory of Geomechanics and Geotechnical Engineering, Institute of Rock and Soil Mechanics, Chinese Academy of Sciences, Grant NO SKLGME022020, and Hubei Provincial Natural Science Foundation (Grant No. 2022CFB400).

Conflict of interest

Authors JW, HH, ZZ, GZ, and JG were employed by Shale Gas Research Institute of PetroChina Southwest Oil and Gas Field Company.

The remaining authors declare that the research was conducted in the absence of any commercial or financial relationships that could be construed as a potential conflict of interest.

Publisher's note

All claims expressed in this article are solely those of the authors and do not necessarily represent those of their affiliated organizations, or those of the publisher, the editors and the reviewers. Any product that may be evaluated in this article, or claim that may be made by its manufacturer, is not guaranteed or endorsed by the publisher.

References

Bai, Y., Hu, Y., Liao, X., Tan, J., Zheng, Y., and Wang, W. (2023). Research on the influence of stress on the penetration behavior of hydraulic fracture: perspective from failure type of beddings. *Front. Earth Sci.* 11. doi:10.3389/feart.2023.1163295

Britt, L. K., Hager, C. J., and Thompson, J. W. (1994). "Hydraulic fracturing in a naturally fractured reservoir," in International Petroleum Conference and Exhibition of Mexico.

Casas, L., Miskimins, J. L., Black, A., and Green, S. (2006). "Laboratory hydraulic fracturing test on a rock with artificial discontinuities, " in Paper presented at the SPE Annual Technical Conference and Exhibition, San Antonio, TX, September 2006. doi:10.2118/103617-MS

Cramer, D., Friehauf, K., Roberts, G., and Whittaker, J. (2019). "Investigating near-wellbore diversion methods for refracturing horizontal wells," in SPE Hydraulic Fracturing Technology Conference and Exhibition D031S007R001.

Dahi Taleghani, A., Gonzalez-Chavez, M., Yu, H., and Asala, H. (2018). Numerical simulation of hydraulic fracture propagation in naturally fractured formations using the cohesive zone model. *J. Petroleum Sci. Eng.* 165, 42–57. doi:10.1016/j.petrol.2018.01.063

Huang, L., Dontsov, E., Fu, H., Lei, Y., Weng, D., and Zhang, F. (2022). Hydraulic fracture height growth in layered rocks: perspective from DEM simulation of different propagation regimes. *Int. J. Solids Struct.* 238, 111395. doi:10.1016/j.ijsolstr.2021.111395

Huang, L., Liu, J., Zhang, F., Dontsov, E., and Damjanac, B. (2019). Exploring the influence of rock inherent heterogeneity and grain size on hydraulic fracturing using discrete element modeling. *Int. J. Solids Struct.* 176-177, 207–220. doi:10.1016/j.ijsolstr.2019.06.018

Huang, L., Tan, J., Fu, H., Liu, J., Chen, X., Liao, X., et al. (2023). The non-plane initiation and propagation mechanism of multiple hydraulic fractures in tight reservoirs considering stress shadow effects. *Eng. Fract. Mech.* 292, 109570. doi:10.1016/j.engfracmech.2023.109570

Huang, N., Liu, R., Jiang, Y., and Cheng, Y. (2021). Development and application of three-dimensional discrete fracture network modeling approach for fluid flow in fractured rock masses. *J. Nat. Gas Sci. Eng.* 91, 103957. doi:10.1016/j.jngse.2021.103957

Ju, Y., Liu, P., Chen, J., Yang, Y., and Ranjith, P. G. (2016). CDEM-based analysis of the 3D initiation and propagation of hydrofracturing cracks in heterogeneous glutenites. *J. Nat. Gas Sci. Eng.* 35, 614–623. doi:10.1016/j.jngse.2016.09.011

Li, S., Fan, Y., He, T., Yang, J., Li, J., and Wang, X. (2023). Research and performance optimization of carbon dioxide foam fracturing fluid suitable for shale reservoir. *Front. Energy Res.* 11. doi:10.3389/fenrg.2023.1217467

Li, S., and Ghosh, S. (2006). Multiple cohesive crack growth in brittle materials by the extended Voronoi cell finite element model. *Int. J. Fract.* 141 (3-4), 373–393. doi:10.1007/s10704-006-9000-2

Liu, C., Jin, X., Shi, F., Lu, D., Liu, H., and Wu, H. (2018a). Numerical investigation on the critical factors in successfully creating fracture network in heterogeneous shale reservoirs. *J. Nat. Gas Sci. Eng.* 59, 427–439. doi:10.1016/j.jngse.2018.09.019

Liu, C., Zhang, D., Zhao, H., Li, M., and Song, Z. (2021). Experimental study on hydraulic fracturing properties of elliptical boreholes. *Bull. Eng. Geol. Environ.* 81 (1), 18. doi:10.1007/s10064-021-02531-9

Liu, Q., Sun, L., Liu, P., and Chen, L. (2018b). Modeling simultaneous multiple fracturing using the combined finite-discrete element method. *Geofluids*, 1–20. doi:10.1155/2018/4252904

Luo, H., Xie, J., Huang, L., Wu, J., Shi, X., Bai, Y., et al. (2022). Multiscale sensitivity analysis of hydraulic fracturing parameters based on dimensionless analysis method. *Lithosphere* 2022 (12), 9708300. doi:10.2113/2022/9708300

Ma, Y., Wang, D., and Zheng, Y. (2023). Influence of the bedding plane on the propagation of multiple hydraulic fractures. *Front. Earth Sci.* 10. doi:10.3389/feart.2022.1077652

Modeland, N., Buller, D., and Chong, K. K. (2011). "Statistical analysis of the effect of completion methodology on production in the haynesville shale," in North American Unconventional Gas Conference and Exhibition SPE-144120-MS.

Moghadasi, R., Rostami, A., and Hemmati-Sarapardeh, A. (2019). Application of nanofluids for treating fines migration during hydraulic fracturing: experimental study and mechanistic understanding. *Adv. Geo-Energy Res.* 3 (2), 198–206. doi:10.26804/ager.2019.02.09

Munjiza, A. A. (2004). *The combined finite-discrete element method*. John Wiley and Sons.

Qiu, G., Chang, X., Li, J., Guo, Y., Wang, L., Ma, H., et al. (2023). Study on rock brittleness characteristics of deep volcanic reservoir under different confining pressures. *J. Petroleum Explor. Prod. Technol.* doi:10.1007/s13202-023-01717-z

Réthoré, J., de Borst, R., and Abellan, M.-A. (2008). A two-scale model for fluid flow in an unsaturated porous medium with cohesive cracks. *Comput. Mech.* 42 (2), 227–238. doi:10.1007/s00466-007-0178-6

Rougier, E., Munjiza, A., Lei, Z., Chau, V. T., Knight, E. E., Hunter, A., et al. (2019). The combined plastic and discrete fracture deformation framework for finite-discrete element methods. *Int. J. Numer. Methods Eng.* 121, 1020–1035. doi:10.1002/nme.6255

Salimzadeh, S., and Khalili, N. (2015). A three-phase XFEM model for hydraulic fracturing with cohesive crack propagation. *Comput. Geotechnics* 69, 82–92. doi:10.1016/j.compgeo.2015.05.001

Shang, D., Yin, G., Zhao, Y., Deng, B., Liu, C., Kang, X., et al. (2018). Local asymmetric fracturing to construct complex fracture network in tight porous reservoirs during subsurface coal mining: an experimental study. *J. Nat. Gas Sci. Eng.* 59, 343–353. doi:10.1016/j.jngse.2018.09.005

Sharafisafa, M., Aliabadian, Z., Sato, A., and Shen, L. (2023). Combined finite-discrete element modelling of hydraulic fracturing in reservoirs with filled joints. *Geoenergy Sci. Eng.* 228, 212025. doi:10.1016/j.geoen.2023.212025

Shi, D., Li, L., Guo, Y., Liu, J., Tang, J., Chang, X., et al. (2023). Estimation of rough fracture network permeability using fractal and topology theories. *Gas Sci. Eng.* 116, 205043. doi:10.1016/j.jgsce.2023.205043

Shi, F., Wang, D., and Li, H. (2022). An XFEM-based approach for 3D hydraulic fracturing simulation considering crack front segmentation. *J. Petroleum Sci. Eng.* 214, 110518. doi:10.1016/j.petrol.2022.110518

Wang, H. (2019). Hydraulic fracture propagation in naturally fractured reservoirs: complex fracture or fracture networks. *J. Nat. Gas Sci. Eng.* 68, 102911. doi:10.1016/j.jngse.2019.102911

Wang, L., Zhou, J., Guo, Y., Song, X., and Guo, W. (2022). Laboratory investigation and evaluation of the hydraulic fracturing of marine shale considering multiple geological and engineering factors. *Front. Earth Sci.* 10. doi:10.3389/feart.2022.952655

Wang, W., Zhao, P., Liao, Y., Zhang, Y., Peng, J., Xian, H., et al. (2023). Investigating fracture initiation and propagation in deep buried shale due to thermal shock: a numerical approach. *Front. Energy Res.* 11. doi:10.3389/fenrg.2023.1231958

Wei, W., Cai, J. C., Hu, X. Y., and Han, Q. (2015). An electrical conductivity model for fractal porous media. *Geophys Res. Lett.* 42 (12), 4833–4840. doi:10.1002/2015gl064460

Wu, M., Gao, K., Liu, J., Song, Z., and Huang, X. (2022). Influence of rock heterogeneity on hydraulic fracturing: a parametric study using the combined finite-discrete element method. *Int. J. Solids Struct.* 234-235, 111293. doi:10.1016/j.ijsolstr.2021.111293

Wu, M., Jiang, C., Song, R., Liu, J., Li, M., Liu, B., et al. (2023). Comparative study on hydraulic fracturing using different discrete fracture network modeling: insight from homogeneous to heterogeneity reservoirs. *Eng. Fract. Mech.* 284, 109274. doi:10.1016/j.engfracmech.2023.109274

Wu, M., Liu, J., Lv, X., Shi, D., and Zhu, Z. (2018a). A study on homogenization equations of fractal porous media. *J. Geophys. Eng.* 15 (6), 2388–2398. doi:10.1088/1742-2140/aac4c1

Wu, M., Wang, W., Zhang, D., Deng, B., Liu, S., Lu, J., et al. (2020a). The pixel crack reconstruction method: from fracture image to crack geological model for fracture evolution simulation. *Constr. Build. Mater.*, 121733. doi:10.1016/j.conbuildmat.2020.121733

Wu, M. Y., Zhang, D. M., Wang, W. S., Li, M. H., Liu, S. M., Lu, J., et al. (2020b). Numerical simulation of hydraulic fracturing based on two-dimensional surface fracture morphology reconstruction and combined finite-discrete element method. *J. Nat. Gas Sci. Eng.* 82, 103479. doi:10.1016/j.jngse.2020.103479

Wu, Z., Sun, H., and Wong, L. N. Y. (2019). A cohesive element-based numerical manifold method for hydraulic fracturing modelling with voronoi grains. *Rock Mech. Rock Eng.* 52 (7), 2335–2359. doi:10.1007/s00603-018-1717-5

Wu, Z., Xu, X., Liu, Q., and Yang, Y. (2018b). A zero-thickness cohesive element-based numerical manifold method for rock mechanical behavior with micro-Voronoi grains. *Eng. Analysis Bound. Elem.* 96, 94–108. doi:10.1016/j.enganabound.2018.08.005

Xavier, J., Oliveira, M., Morais, J., and De Moura, M. (2014). Determining mode II cohesive law of *Pinus pinaster* by combining the end-notched flexure test with digital image correlation. *Constr. Build. Mater.* 71, 109–115. doi:10.1016/j.conbuildmat.2014.08.021

Xiang, J., Munjiza, A., Latham, J.-P., and Guises, R. (2009). On the validation of DEM and FEM/DEM models in 2D and 3D. *Eng. Comput.* 26 (6), 673–687. doi:10.1108/02644400910975469

Yan, C., Jiao, Y.-Y., and Zheng, H. (2018). A fully coupled three-dimensional hydro-mechanical finite discrete element approach with real porous seepage for simulating 3D hydraulic fracturing. *Comput. Geotechnics* 96, 73–89. doi:10.1016/j.compgeo.2017.10.008

Yang, H., Wang, L., Yang, C., Guo, W., Bi, Z., and Guo, Y. (2023a). Experimental investigation on different effects of fracturing fluids on mechanical properties and failure mechanism of continental shale. *Int. J. Rock Mech. Min.* 164, 105362. doi:10.1016/j.ijrmms.2023.105362

Yang, R., Wang, Y., Song, G., and Shi, Y. (2023b). Fracturing and thermal extraction optimization methods in enhanced geothermal systems. *Adv. Geo-Energy Res.* 9 (2), 136–140. doi:10.46690/ager.2023.08.07

Yuan, J., Jiang, R., and Zhang, W. (2018). The workflow to analyze hydraulic fracture effect on hydraulic fractured horizontal well production in composite formation system. *Adv. Geo-Energy Res.* 2 (3), 319–342. doi:10.26804/ager.2018.03.09

Zhang, H., Chen, J., Li, Z., Hu, H., and Mei, Y. (2023). Numerical simulation of multi-cluster fracturing using the triaxiality dependent cohesive zone model in a shale reservoir with mineral heterogeneity. *Rock Mech. Rock Eng.* doi:10.1007/s00603-023-03527-5

Zhao, L. H., Zhang, S. H., Huang, D. L., Zuo, S., and Li, D. J. (2018). Quantitative characterization of joint roughness based on semivariogram parameters. *Int. J. Rock Mech. Min.* 109, 1–8. doi:10.1016/j.ijrmms.2018.06.008

Zheng, Y., He, R., Huang, L., Bai, Y., Wang, C., Chen, W., et al. (2022). Exploring the effect of engineering parameters on the penetration of hydraulic fractures through bedding planes in different propagation regimes. *Comput. Geotechnics* 146, 104736. doi:10.1016/j.compgeo.2022.104736

Zou, J., Jiao, Y.-Y., Tang, Z., Ji, Y., Yan, C., and Wang, J. (2020). Effect of mechanical heterogeneity on hydraulic fracture propagation in unconventional gas reservoirs. *Comput. Geotechnics* 125, 103652. doi:10.1016/j.compgeo.2020.103652

frontiers | Frontiers in Energy Research

TYPE Original Research
PUBLISHED 08 January 2024
DOI 10.3389/fenrg.2023.1342254

Check for updates

OPEN ACCESS

EDITED BY
Liuke Huang,
Southwest Petroleum University, China

REVIEWED BY
Xiao Yan,
Tongji University, China
Wenjun Xu,
Yangtze University, China

*CORRESPONDENCE
Yuliang Su,
suyuliang@upc.edu.cn

RECEIVED 21 November 2023
ACCEPTED 13 December 2023
PUBLISHED 08 January 2024

CITATION
Zeng B, Wu M, Su Y, Guo Y, Feng J, Gui J and Lu J (2024), Study on the fracture propagation law of deep shale reservoir under the influence of different number of fracturing clusters.
Front. Energy Res. 11:1342254.
doi: 10.3389/fenrg.2023.1342254

COPYRIGHT
© 2024 Zeng, Wu, Su, Guo, Feng, Gui and Lu. This is an open-access article distributed under the terms of the Creative Commons Attribution License (CC BY). The use, distribution or reproduction in other forums is permitted, provided the original author(s) and the copyright owner(s) are credited and that the original publication in this journal is cited, in accordance with accepted academic practice. No use, distribution or reproduction is permitted which does not comply with these terms.

Study on the fracture propagation law of deep shale reservoir under the influence of different number of fracturing clusters

Bo Zeng[1,2], Mingyang Wu[3], Yuliang Su[1]*, Yintong Guo[3], Jiangrong Feng[2], Junchuan Gui[2] and Jun Lu[4]

[1]School of Petroleum Engineering, China University of Petroleum, Shandong, Qingdao, China, [2]Shale Gas Research Institute of PetroChina Southwest Oil & Gas Field Company, Chengdu, Chengdu, Sichuan, China, [3]State Key Laboratory of Geomechanics and Geotechnical Engineering, Wuhan Institute of Rock and Soil Mechanics, Chinese Academy of Science, Wuhan, China, [4]Institute of Deep Earth Science and Green Energy, College of Civil and Transportation Engineering, Shenzhen University, Shenzhen, China

Deep reservoirs have a large difference in geo-stress, and compared to shallow reservoirs, multiple clusters of fracturing are usually required to effectively improve the quality of reservoir reconstruction. In this paper, considering the relevant geological parameters of a certain reservoir in the southwest, multi-cluster reservoir fracturing models under three-dimensional conditions based on the cohesive element modelling method are established. Then, the quantitative rules of fluid pressure, fracture length, fracture aperture, fracture area, tensile failure rate, and the fractal dimension of fracture morphology under different fracturing cluster numbers were revealed. The results show that compared to conventional fracturing, multi-cluster fracturing can significantly increase the number of main fractures and improve the effectiveness of reservoir reconstruction. As the number of clusters increases, the number of main fractures in the reservoir increases, but it can also lead to the increase of small opening fractures, which may be unfavourable for the pumping of proppant and subsequent mining. Meanwhile, based on the fractal dimension results of fracture morphology, it was found that under this simulation condition, the number of fracturing clusters had a significant impact on the fractal dimension of fracturing fractures before the fracturing of six clusters, while after the fracturing of six clusters, the impact of the number of fracturing clusters on the fractal dimension of fracturing fractures decreased. Therefore, when considering factors such as the complexity of fractures, multi-cluster fracturing does not necessarily result in more fracturing clusters being better but should be comprehensively considered for optimization. This study has certain reference significance for selecting the spacing between multiple fracturing clusters.

KEYWORDS

deep shale, multi cluster fracturing, fracture morphology, fracture propagation, fractal dimension

1 Introduction

With the development of unconventional oil and gas, more and more attention has been paid to the exploration and development of deep shale (Song, et al., 2017). Because of the high in-situ stress in deep shale reservoirs (Guo, et al., 1993; Huang, et al., 2019; Jiang, et al., 2019; Moghadasi et al., 2019; Yang et al., 2023), it is difficult for hydraulic fractures to start

and expand, and hydraulic fractures are easy to close under high in-situ stress, so conventional methods of shale reservoir fracture growth cannot be used to study unconventional shale reservoirs (Wu, et al., 2020; Luo, et al., 2022). For deep shale reservoir reconstruction engineering, the way of stage fracturing is usually adopted, so it is necessary to study the law of multi-cluster fracture propagation in deep shale reservoirs.

Early fracturing research was achieved through theoretical derivation and indoor experiments. With the deepening of fracturing research, the assumption of homogeneous rocks in theoretical derivation has made it difficult to meet the current research needs. Meanwhile, although indoor experiments are an excellent method for fracturing research (Qiu, et al., 2023; Tan, et al., 2023), they are limited by sample size and cost, making it difficult to conduct more targeted on-site numerical simulation studies. As an accurate, efficient and convenient research method, numerical simulation can take into account some special factors in the actual reservoir, such as irregular natural fractures, random lithology mutants, and even complex ground stress states, and it is very suitable for studying the fracture propagation mechanism of deep shale reservoirs(Wei, et al., 2015; Liu, et al., 2018; Wu M. et al., 2018; Zheng, et al., 2022). At present, the numerical methods commonly used in hydraulic fracture propagation simulation (Xiang, et al., 2009; Ju, et al., 2016; Yan, et al., 2018; Rougier, et al., 2019) mainly include the unified pipe-interface element method (Yan, et al., 2021; Yan and Yu, 2022), peridynamics, cracking particles method, finite element method (FEM) (Xiang, et al., 2009; Lecampion and Desroches, 2015), extended finite element method (XFEM) (Wang, 2016; Zou, et al., 2020), displacement discontinuity method (DDM), discrete element method (DEM) (Huang, et al., 2022) and phase field method (PFM). The FEM, as a mature numerical calculation method, is widely used in hydraulic fracturing numerical simulation because of its flexibility in dealing with complex mechanical problems, such as rock heterogeneity. However, fractures can only expand along the grid boundary and grid reconstruction is required. Based on the conventional finite element continuous displacement field, the XFEM characterizes discontinuity of displacement by adding local enrichment function to the element containing fracture, allowing fracture to penetrate the grid without grid reconstruction. Compared with the finite element method, XFEM has obvious advantages and is widely used in the simulation of hydraulic fracture propagation. However, this method has some difficulties in dealing with complex fracture networks and multi-cluster fracture propagation. DDM as an indirect boundary element method, only needs to discrete the fracture, but does not need to discrete other areas outside the fracture. Therefore, compared with the finite element method, DDM is one of the most used numerical methods for the simulation of complex fracture networks.

However, due to the assumption of discontinuous displacement solutions, this method cannot be applied to non-homogeneous and non-linearly elastic media. The discrete element method (DEM) discrete the medium into blocks (or particles) and judges the fracture behavior by the contact state between the blocks (Huang, et al., 2019). Hydraulic fracturing is the process in which rock mass fractures occur, so the DEM method is gradually used to simulate the propagation of hydraulic fractures. The advantages of this method in dealing with discontinuity problems make it very suitable for simulating the complex fracture network propagation process in reservoirs with high natural fracture development, but its disadvantages are that it cannot deal with continuum problems well, and the calculation amount is too large, and the calculation efficiency is low. The phase field method equates the fracture to a material weakening zone, and the displacement is continuous. Under the framework of finite element calculation, the phase field variable is introduced to describe the fracture without additional tracking of the fracture geometry. Compared with the discrete model, the PFM has a unique advantage in calculating complex fracture propagation such as fracture intersection, bifurcation, and three-dimensional arbitrary tortuous propagation path. However, the model also has some shortcomings, such as requiring the finite element mesh in the fracture propagation area to be sufficiently fine and commutative. The finite element discrete element method (FDEM) (Munjiza, 2004; Wu, et al., 2023) is a hybrid simulation method, that can give full play to the advantages of the finite element method and discrete element method, and avoid the disadvantages of both, so it is suitable for hydraulic fracturing simulation test. Unfortunately, the previous numerical simulation studies mainly focused on the study of fracture propagation mechanism under low geo-stress environments, and it is difficult to provide direct references for fracturing operations in deep-tight sandstone reservoirs. Therefore, based on the FDEM method, it is very necessary to study the law of multi-cluster hydraulic fracture propagation under high-ground stress. Meanwhile, deep reservoirs usually use multi-cluster fracturing construction. Yuan et al. (Yuan et al., 2018) established a mathematical model for CFS multi-stage fracturing of horizontal wells. Considering the differences in limited hydraulic fracture conductivity, hydraulic fracture inclination, and the different shapes of multi-wing fractures at perforation points, this model can effectively analyze the production performance of different multistage fractured horizontal well types. A simple and fast well-testing method has been proposed by Meng et al. (Meng et al., 2020) for fracturing evaluation and parameter estimation of non-uniform fractured multi-fracture horizontal wells. Then, they found that there is a good relationship between the fracturing treatment parameters and the generated fracture properties, including fracture length and reservoir ratio (or fracture volume ratio). Qin et al.'s research (Qin et al., 2019) shows that the fractal dimension of rough fractures significantly affects the permeability characteristics of reservoirs. Given that the evaluation of the fractal dimension of fractures after fracturing is more likely to be presented simultaneously with the fracturing results, it is also necessary to further evaluate the complexity of complex fractures using the fractal dimension.

This paper investigates a specific reservoir in the southwest by considering relevant geological parameters. Three-dimensional (3D) multi-cluster reservoir fracturing models using cohesive element modeling were established, and the quantitative rules of fluid pressure, fracture length, fracture aperture, fracture area, tensile failure rate, and the fractal dimension of fracture morphology under different fracturing cluster numbers were revealed. The simulation method, modeling process, and parameters for the benchmark model are presented in Section 2, and the simulation results and corresponding analysis are presented in Section 3. Afterward, the results of comparing and analyzing the differences in conventional quantitative parameters and morphological fractal dimensions of

fracture propagation during different cluster fracturing processes are presented in Section 4, and some suggestions for the number of fracturing clusters in the fracturing block were provided. The conclusion is presented at the end.

2 Numerical model

Reservoir fracturing is a typical fluid-solid coupling process that involves stress deformation and rock fracture caused by fluid injection (Huang, et al., 2023). Therefore, the fracturing process needs to meet the equilibrium equation. During the fracturing process, the fluid first flows from the perforation into the reservoir, involving the distribution of pipe flow in multiple clusters of fracturing. Subsequently, the fluid flows into the reservoir through different clusters and gradually forms artificial fractures, involving simulation processes such as reservoir fracturing. Therefore, this study is based on cohesive element modeling to achieve reservoir fracture simulation, and corresponding equations were used to simulate fluid flow in pipes, fractures, and matrices. Of course, the fracturing process may also involve the migration of porous media in the reservoir matrix (Song, et al., 2022a; Song, et al., 2022b). Based on above analysis, the detailed simulation methods and model settings is described below.

2.1 Simulation method

During the entire fracturing process, reservoir deformation and fluid flow need to meet the following equilibrium equations (Wu Z. et al., 2018)

$$\int_V (\bar{\sigma} - p_w \boldsymbol{I})\delta\boldsymbol{\varepsilon} dV = \int_S \boldsymbol{t}\cdot\delta\boldsymbol{v} dS + \int_V \boldsymbol{f}\delta\boldsymbol{v} dV \tag{1}$$

where $\bar{\sigma}$ represented the effective stress matrix, MPa; p_w denoted the pore pressure, MPa; $\delta\boldsymbol{\varepsilon}/s^{-1}$ was the virtual strain rate matrix; $\boldsymbol{t}$ was the surface force matrix, N/m^2; δ_v was the virtual velocity matrix, m/s and $\boldsymbol{f}$ was the physical force matrix, N/m^3.

Fluid flow needs to satisfy the continuity equation (Dahi Taleghani, et al., 2018)

$$\frac{d}{dt}\left(\int_V \left(\frac{\rho_w}{\rho_w^0} n dV\right)\right) + \int_S \frac{\rho_w}{\rho_w^0} n\boldsymbol{n}\cdot v_w dS = 0 \tag{2}$$

where n is the outward normal to the surface S, v_w is the fluid velocity, m/s, ρ_w was the fluid density kg/m^3, n_w was the void ratio.

When fracturing a real reservoir, fluid is first injected from the wellbore and further flowed into the reservoir through wellbore perforation and diversion. There is a relationship between the total amount of injected fluid and the total amount of different perforated fluids flowing into the reservoir.

$$Q = \sum_{i=1}^{N} Q_i \tag{3}$$

Correspondingly, the fluid pressure drop equilibrium equation can be described as

$$p_0 = p_{pf,i} + p_{cf,i} + p_{wf,i} \tag{4}$$

where p_0 is the injection point fluid pressure, $p_{pf,i}$ is the fluid pressure at the cluster, $p_{cf,i}$ is the pressure drop through the cluster, $p_{sf,i}$ is the pressure resulting from friction between the fluid and the wellbore.

It is worth mentioning that when fluid flows in the wellbore, there will be a certain pressure loss due to the influence of wellbore roughness, which can be calculated using the following formulas (Modeland, et al., 2011; Zhang, et al., 2023).

$$\begin{aligned} \nabla p - \rho g\Delta Z &= (C_L + K_i)\frac{\rho v^2}{2},\\ C_L &= \frac{fL}{D_h},\\ f &= 8\left[\left(\frac{8}{\mathrm{Re}}\right)^{12} + \frac{1}{(A+B)^{1.5}}\right]^{1/12},\\ A &= \left[-2.457\mathrm{In}\left(\left(\frac{7}{\mathrm{Re}}\right)^{0.9} + 0.27\left(\frac{K_s}{D_h}\right)\right)\right]^{16},\\ B &= \left(\frac{37350}{\mathrm{Re}}\right)^{16} \end{aligned} \tag{5}$$

where ΔP is the pressure difference at the node of the cluster, ΔZ is the elevation difference of the node, v is the fluid velocity in horizontal wellbore, ρ is the fluid density, G is the acceleration of gravity, C_L is the loss coefficient, f is the friction force on the wellbore, L is the wellbore length, K_i is the loss term in fixed direction, K_s is the roughness of wellbore, D_h is the wellbore diameter, Re is the Reynolds number of the fluid in the wellbore.

Given the complexity of the perforation situation, there may also be some pressure loss at the perforation location (Cramer, et al., 2019)

$$p_f = 0.087249 \times \frac{\rho}{n^2 D_p^4 C^2} q_i^2 \tag{6}$$

where n is the number of perforations in each cluster, in this paper, the value is 16, D_p is the perforation diameter, C is the coefficient affecting perforation flow, generally 0.56–0.9 (Modeland, et al., 2011; Zhang, et al., 2023), in this paper, the value is 0.6.

After the fluid flows into the reservoir through the wellbore and perforation, it will promote the initiation of artificial fractures. At this time, the deformation behaviour of artificial fractures can be described by linear elastic equations (Wu, et al., 2019)

$$\begin{aligned} \boldsymbol{\sigma}_{coh} &= \begin{Bmatrix} \sigma_{coh_n} \\ \sigma_{coh_s} \\ \sigma_{coh_t} \end{Bmatrix} = \boldsymbol{K}_{coh}\boldsymbol{\varepsilon}_{coh}\\ &= \begin{bmatrix} K_{coh_nn} & K_{coh_ns} & K_{coh_nt} \\ K_{coh_ns} & K_{coh_ss} & K_{coh_st} \\ K_{coh_nt} & K_{coh_st} & K_{coh_tt} \end{bmatrix} \begin{Bmatrix} \varepsilon_{coh_n} \\ \varepsilon_{coh_s} \\ \varepsilon_{coh_t} \end{Bmatrix} \end{aligned} \tag{7}$$

where $\boldsymbol{\sigma}_{coh}$ denoted the stress vector of a cohesive element; $\boldsymbol{\sigma}_{coh-h}$, $\boldsymbol{\sigma}_{coh-s}$, $\boldsymbol{\sigma}_{coh-t}$ were the normal stress (perpendicular to the upper and lower surfaces of the cohesive element), the first tangent stress and the second tangent stress (non-existent in two-dimensional cases), respectively. Here, $\boldsymbol{K}_{coh}$ denoted the stiffness matrix of a cohesive element; $\boldsymbol{\varepsilon}_{coh}$ was the strain matrix of a cohesive element and $\boldsymbol{\varepsilon}_{coh-n}$, $\boldsymbol{\varepsilon}_{coh-s}$, $\boldsymbol{\varepsilon}_{coh-t}$ represented the normal strain, the first tangential strain and the second tangential strain of a cohesive element, respectively. They were defined as follows (Réthoré, et al., 2008; Wu, et al., 2019):

$$\varepsilon_{coh_n} = \frac{d_n}{T_0}, \varepsilon_{coh_s} = \frac{d_s}{T_0}, \varepsilon_{coh_t} = \frac{d_t}{T_0} \tag{8}$$

where d_n, d_s, d_t represented the normal displacement, the first displacement and the second tangential displacement of a cohesive element, respectively. Here, T_0 was the constitutive thickness of the cohesive element.

It is generally believed that rock is a brittle material, and when it fails, fractures will rapidly initiate, and its strength stress-strain curve shows a rapid downward trend. To simulate this failure behaviour, the Cohesive element used to simulate artificial fractures cannot deform infinitely and can be judged using the maximum principal stress criterion (Wang, 2019)

$$\left\{\frac{\langle\sigma_n\rangle}{\sigma_n^0}\right\}^2 + \left\{\frac{\sigma_s}{\sigma_s^0}\right\}^2 + \left\{\frac{\sigma_t}{\sigma_t^0}\right\}^2 = \lambda \tag{9}$$

where σ_n was the normal stress; σ_s, σ_t represented tangential stress (σ_t did not exist in two-dimensional cases), MPa; σ_s^0, σ_t^0 were the threshold stress of tangential damage, MPa; λ indicated that cohesive elements resist tension stress but not compression stress: $1 \le \lambda \le 1.05$.

After the failure of reservoir rocks, fractures rapidly develop, but their bearing capacity does not directly decrease to 0. The reservoir rock still has a certain degree of continuous attenuation of deformation resistance, which can be described using damage variables (Xavier, et al., 2014; Wu M. et al., 2018; Wu, et al., 2019)

$$E = (1 - d) \times E^0 \tag{10}$$

where E_0, E were the initial elastic modulus (without damage) and the elastic modulus after damage, Pa, respectively. Here, d denoted a damage factor, dimensionless.

Damage factors could be calculated by

$$d = \frac{\delta_m^f\left(\delta_m^{\max} - \delta_m^0\right)}{\delta_m^{\max}\left(\delta_m^f - \delta_m^0\right)} \tag{11}$$

where δ_m^{max}, δ_m^f , δ_m^0 signify distinct displacements in the context of element behaviour under loading conditions. Specifically, δ_m^{max} refers to the maximum displacement experienced by the element during loading. On the other hand, δ_m^f denotes the displacement corresponding to the point of complete damage to the element. Lastly, δ_m^0 represents the displacement at the onset of initial damage to the element.

It is worth mentioning that the process of artificial fracture initiation, opening, and extension is accompanied by fluid flow. After the artificial fracture initiation, the fluid flow inside it can be calculated by the following equation.

$$q = \frac{t^3}{12u}\nabla p \tag{12}$$

where q represented the volume flow vector per tangential element length; t was the thickness of a cohesive element, m; μ was the viscous coefficient of fracturing fluid in a cohesive element; p was the fluid pressure in a cohesive element, MPa.

The flow of fluid in fractures is not limited to the flow inside the fractures. Since the interface between the fluid and the reservoir matrix is rock, there is also a certain degree of fluid flow ability. Under this condition, there may be some filtration of fluid within the fracture, i.e., it flows out of the fracture into the reservoir. At this point, the fluid filtration at the upper and lower interfaces of the fracture can be defined by the filtration coefficient.

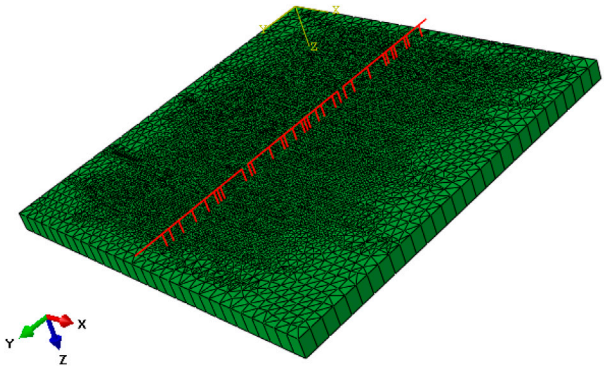


FIGURE 1
Schematic diagram of multi segment and multi-cluster fracturing model.

$$\begin{cases} q_t = c_t\left(p_i - p_t\right) \\ q_b = c_b\left(p_i - p_b\right) \end{cases} \tag{13}$$

where q_t, q_b represented the volumetric flow rate of the fluid flowing out of the upper and lower surfaces of a cohesive element. They also denoted the surface flow rate in a two-dimensional plane. The terms c_t, c_b were the filtration coefficient of the upper and lower surfaces, m/min$^{0.5}$; p_t, p_b were the pore pressure of the upper and lower surfaces, MPa and p_i was the fluid pressure of the middle surface of a cohesive element, MPa.

Finally, the fluid filtered into the reservoir from fractures and other locations will flow through Darcy flow to other areas of the reservoir, therefore, it can be described by Darcy flow (Li and Ghosh, 2006)

$$\boldsymbol{v}_w = -\frac{1}{n_w \boldsymbol{g} \rho_w}\boldsymbol{k} \cdot \left(\frac{\partial p_w}{\partial \boldsymbol{x}} - \rho_w \boldsymbol{g}\right) \tag{14}$$

where $\boldsymbol{k}$ represented a permeability matrix, m/s and $\boldsymbol{g}$ was the gravity acceleration vector, m/s^2.

2.2 Model setup

To conduct a targeted and in-depth analysis of the multi-cluster fracturing construction rules of a fracturing well in Southwest China, the on-site data of a fracturing well in Southwest China was first investigated. Subsequently, based on on-site data and existing researches (Wu, et al., 2022; Wu, et al., 2023), a multi-cluster fracturing simulation model for the reservoir was constructed, and the corresponding model settings are as follows.

① The fracturing well belongs to the well section that has completed the fracturing transformation, and the main construction process is the transformation mode of multiple clusters and large displacement within the section. The fracturing fluid is a low-viscosity and smooth water system. After comprehensive consideration, the range of segmented fracturing is 60 m ×

TABLE 1 Main parameters used in simulation models.

Input parameters	Value
Young's modulus (GPa)	43
Poisson's ratio (Dimensionless)	0.23
Permeability coefficient (m/s)	1e-7
Porosity (Dimensionless)	0.03
Tensile strength of natural fractures (MPa)	2
Critical damage displacement (m)	0.001
Injection rate (m^3/min)	18
Fracturing fluid viscosity (mPa·s)	1
Pipe roughness (mm)	0.015×10^{-3}
Number of perforations	32
perforation diameter (m)	0.01

60 m, mainly involving multiple layers, with the sum of thicknesses of the closest layer being about 3 m. Therefore, the simulation model study area size is set to 60 m × 60 m × 3 m. The fluid used in the simulation has a smooth water parameter of 0.001 Pa s.

② Observation and statistics of fractured well cores show the presence of natural bedding fractures, with linear density ranging from 0.5 to 30 per meter. Given that natural fractures are not the focus of this simulation, the model assumes that natural fractures are approximately 0.5 per meter. Meanwhile, the conventional interface element method with global embedding has phenomena such as long computational time and severe local shear collapse of fractures. Therefore, the use of random modelling to form a discrete nonplanar sequence fracture network (Shi, et al., 2023) facilitates the development of multi-cluster fracturing. Subsequently, based on the Python module developed by us; a corresponding grid model was formed as shown in Figure 1.

③ The injected fluid flows into the reservoir after being diverted along the wellbore components, and the pressure loss and fluid distribution in the wellbore can be simulated through the fluid pipe element (fp3d2 and fpc3d2) in Abaqus. Therefore, the fp3d2 element is used to set up a simulated wellbore located at the bottom of the reservoir area, and the fpc3d2 element is used to simulate the friction before flowing into the reservoir. The interaction between fluid volume and fluid pressure in the simulation is achieved by binding the wellbore tip node and the reservoir interface element node. Therefore, during single cluster fracturing, the injection point of the model is located at the endpoint of the wellbore. In addition, there is randomness in the actual on-site perforation spacing. To simulate perforation more realistically, the perforation of this model is randomly set, with a total of 32 perforation points.

④ The x direction is assumed to be the maximum horizontal principal stress direction, the z direction is assumed to be the vertical principal stress direction and the y direction is assumed to be the minimum horizontal principal stress direction. The outer boundary of the model is a fixed displacement and impermeable boundary condition, with upper and lower boundaries constraining displacement in the z direction and left and right boundaries constraining displacement in the *x* and *y* directions.

⑤ To reduce computational complexity, larger grid seeds were used for grid generation. After grid generation, the total grid size of the reservoir components was 16596, including 12710 rock block elements, 3885 interface elements, and a total of 28376 nodes.

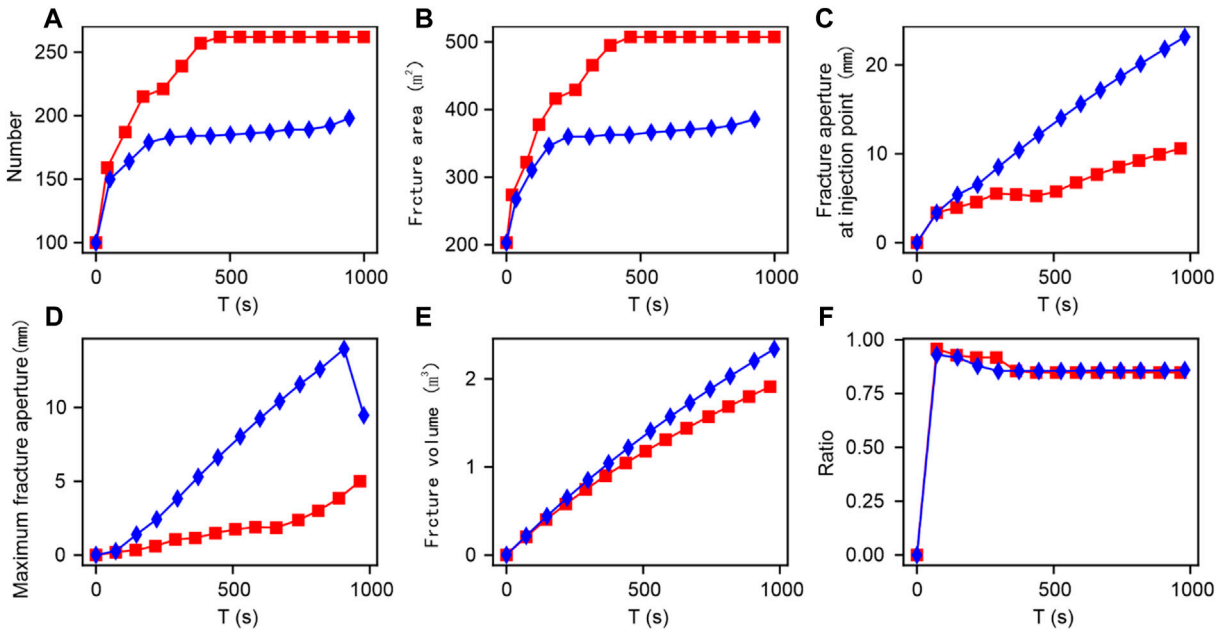


FIGURE 2
Comparison results of conventional quantitative parameters under the influence of interface element stiffness (Single cluster).

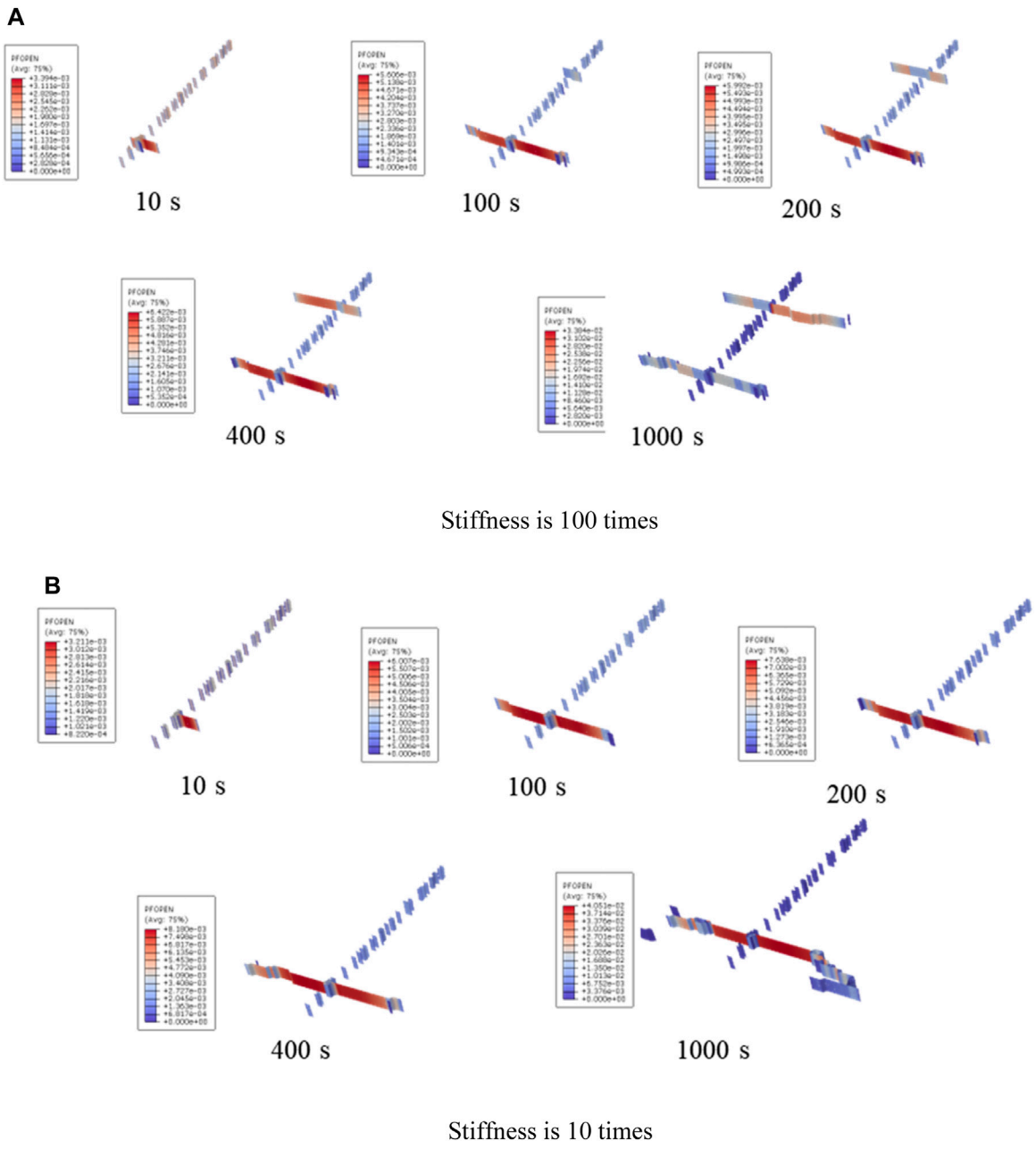


FIGURE 3
Comparison results of fracture morphology under the influence of interface element stiffness (3D view).

The total number of simulated wellbore elements is 95, including 32 fpc3d2 elements, 63 fp3d2 elements, and a total of 98 nodes.

⑥ On-site logging interpretation and triaxial compression tests show that the Poisson's ratio of the fractured rock is between 0.224 and 0.266, and Young's modulus is 40.16–48.58 GPa, the porosity ranges from 3.6% to 5.2%. Therefore, in the reservoir fracturing benchmark model, Young's modulus is taken as 43 GPa, Poisson's ratio is taken as 0.23, and porosity is taken as 0.03. At the same time, the maximum horizontal stress of the target section is about 110 MPa, the minimum horizontal stress is about 96 MPa, the vertical stress is about 106 MPa, and the pore pressure is about 66 MPa. During on-site construction, the displacement of the fracturing well is 18 m^3/min, and generally, fracturing takes 1–2 h. Therefore, the injection rate in the simulation model is set to 18 m^3/min, and the injection time is set to 3600 s. In addition to the above parameters, the simulation model also includes constitutive parameters of the cohesive element and fluid flow-related parameters of the simulated wellbore, all of which are referenced from previous studies (Wu, et al., 2022; Wu, et al., 2023; Zhang, et al., 2023). The main simulation parameters obtained are shown in Table 1. Then, the fracturing simulation results can be obtained based on Eqs 1–14.

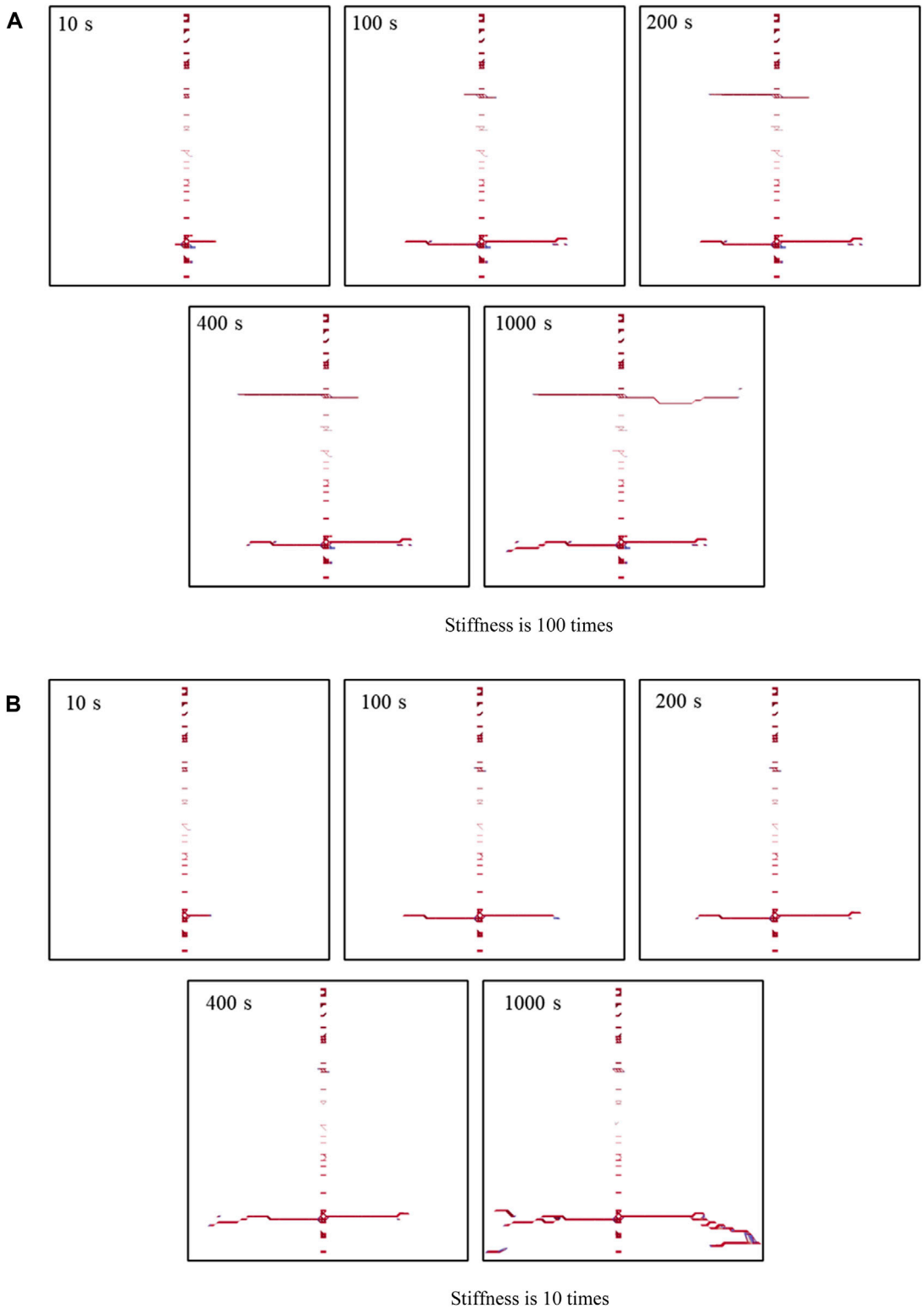


FIGURE 4
Artificial fracture development process during single cluster fracturing (top view).

3 Results and analysis

To explore the impact of fracturing cluster setting on the propagation of artificial fractures during fracturing construction in a certain block in southwestern China, this section conducted further numerical simulation research based on previous model settings, analysing the differences in the propagation of artificial fracture morphology from single cluster fracturing to twelve cluster

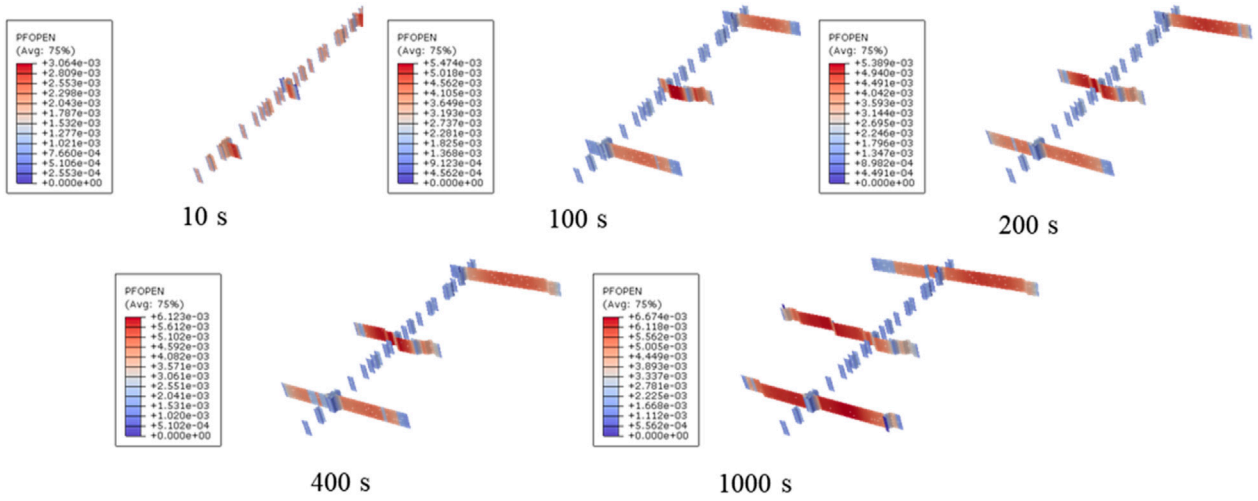


FIGURE 5
Artificial fracture development process during three clusters fracturing (3D view).

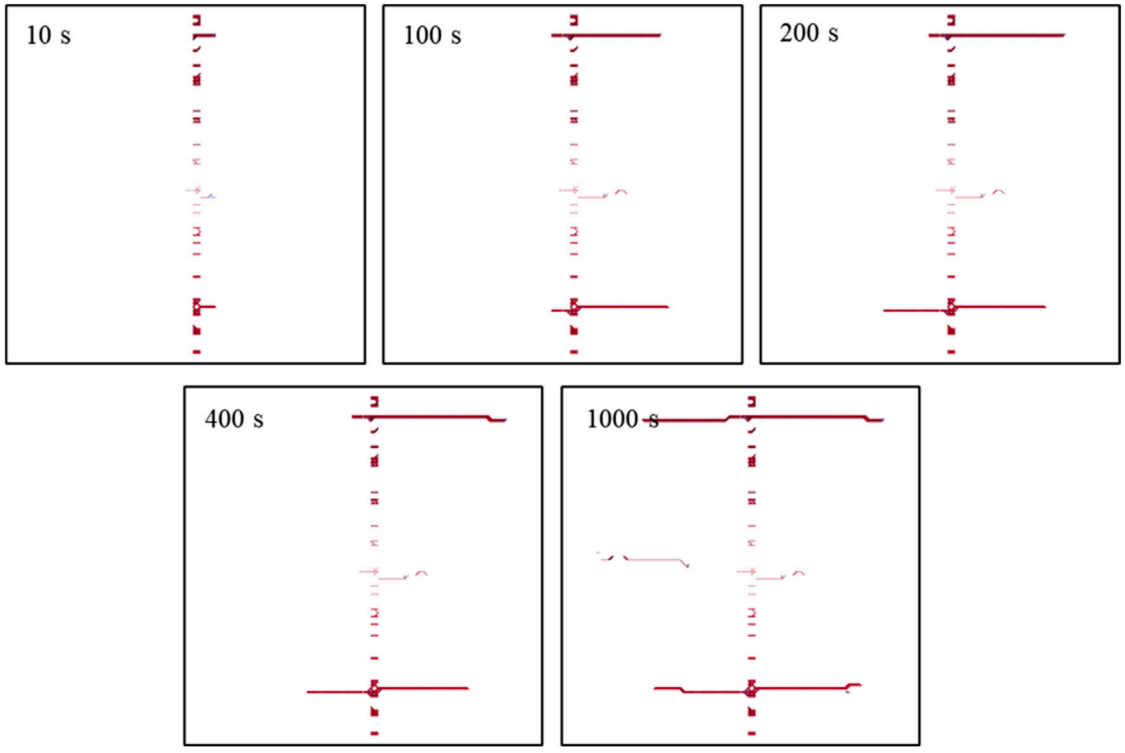


FIGURE 6
Artificial fracture development process during three clusters fracturing (top view).

fracturing construction conditions. To explore the impact of fracturing cluster setting on the propagation of artificial fractures during fracturing construction in a certain block in southwestern China, this section conducted further numerical simulation research based on previous model settings, analysing the differences in the propagation of artificial fracture morphology from single cluster fracturing to twelve clusters fracturing construction conditions.

3.1 Single cluster

After comprehensive consideration of the information collected earlier, a three-dimensional multi-cluster fracturing simulation model was created. To deeply analyze the fracture propagation characteristics under different fracturing cluster conditions, a single cluster fracturing analysis was first conducted. Considering

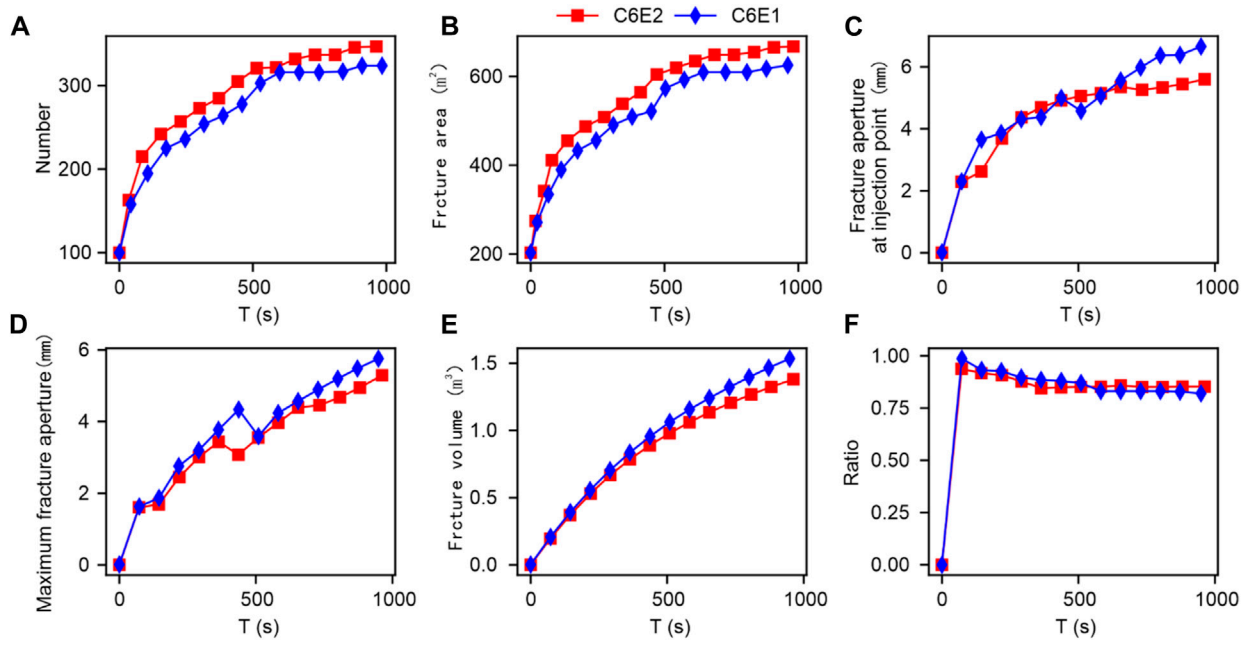


FIGURE 7
Comparison results of conventional quantitative parameters under the influence of interface element stiffness (Six clusters).

that the stiffness of interface elements has a certain impact on the simulation results during the simulation process, a comparison of stiffness was also considered in some single-cluster and multi-cluster simulations. In the subsequent simulation model, the cluster is represented by C, and the ratio of stiffness to rock modulus is represented by E. For example, C1 represents single cluster fracturing, and E1 and E2 represent the ratio of the stiffness of the interface element to the elastic modulus of the rock, which is 10 times and 100 times, respectively. Due to the limitations of model size, the propagation process of fracture morphology with the greatest variation in simulation mainly occurs between 0 and 1000s. Therefore, this simulation mainly extracted simulation result data between 0 and 1000s. Subsequently, conventional quantitative parameter results were extracted using extraction methods from existing researches (Wu, et al., 2022; Wu, et al., 2023) on the number of damaged cohesive elements, fracture length, fracture area, fracture aperture, and tensile failure ratio. The comparison results of conventional quantitative parameters under the influence of interface element stiffness are shown in Figure 2.

It can be seen from Figure 2 that when the stiffness value is large, the number of fracture elements and the total area of fractures are both large. This result indicates that the stiffness of interface elements has a certain impact on the morphology and development of rock mass compression fractures, with an area effect of up to twice. Meanwhile, when the stiffness is high, the fracture width at the injection point, the maximum fracture width, and the total volume of the fractures are relatively small, which may result in the formation of many local fractures with smaller openings and the interlocking phenomenon of remote fractures. The above results indicate that when the rock interface in the reservoir ruptures, under the same limit width conditions, the greater the stiffness, the more likely it is to generate small opening local fractures.

Figure 3 shows the comparison results of fracture morphology under the influence of interface element stiffness. Please note that the hydraulic fracture in Figure 3 is composed of multiple damaged cohesive elements. It can be seen from Figure 3 that when the stiffness is high, two artificial fractures are produced in a single cluster fracturing, and there is a phenomenon of bifurcation and propagation at the tip. When the stiffness is small, artificial fractures mainly propagate along the main fracture. Generally, the greater the stiffness of the interface element, the stronger the brittleness of the rock during fracture, and the easier it is to form some shear cracks under stress. Therefore, we speculate that the two clusters of fractures in Figure 3 may have developed from shear failure fractures during the early stages of fracturing. Correspondingly, the stronger the deformation resistance of the interface, the easier it is for the reservoir to form multiple clusters of fractures. The weaker the resistance to deformation, the more likely it is to form a main seam with a forked and bent tip (Figure 4).

3.2 Three clusters

Keeping the total injection flow constant and changing the model to three clusters, the obtained fracture morphology results are shown in Figure 5. From the figure, it can be observed that the initiation and propagation process of artificial fractures: ① Fracture initiation stage: in the early stage of fracturing, after the fluid flows into the wellbore, a large number of artificial fracture initiation phenomena first occur near the perforation position of the wellbore; ② Perforated fracture competition propagation stage: As the fluid is further injected, under the influence of multiple clusters of fracturing, fractures that have already sprouted between different clusters exhibit competition propagation phenomenon, gradually

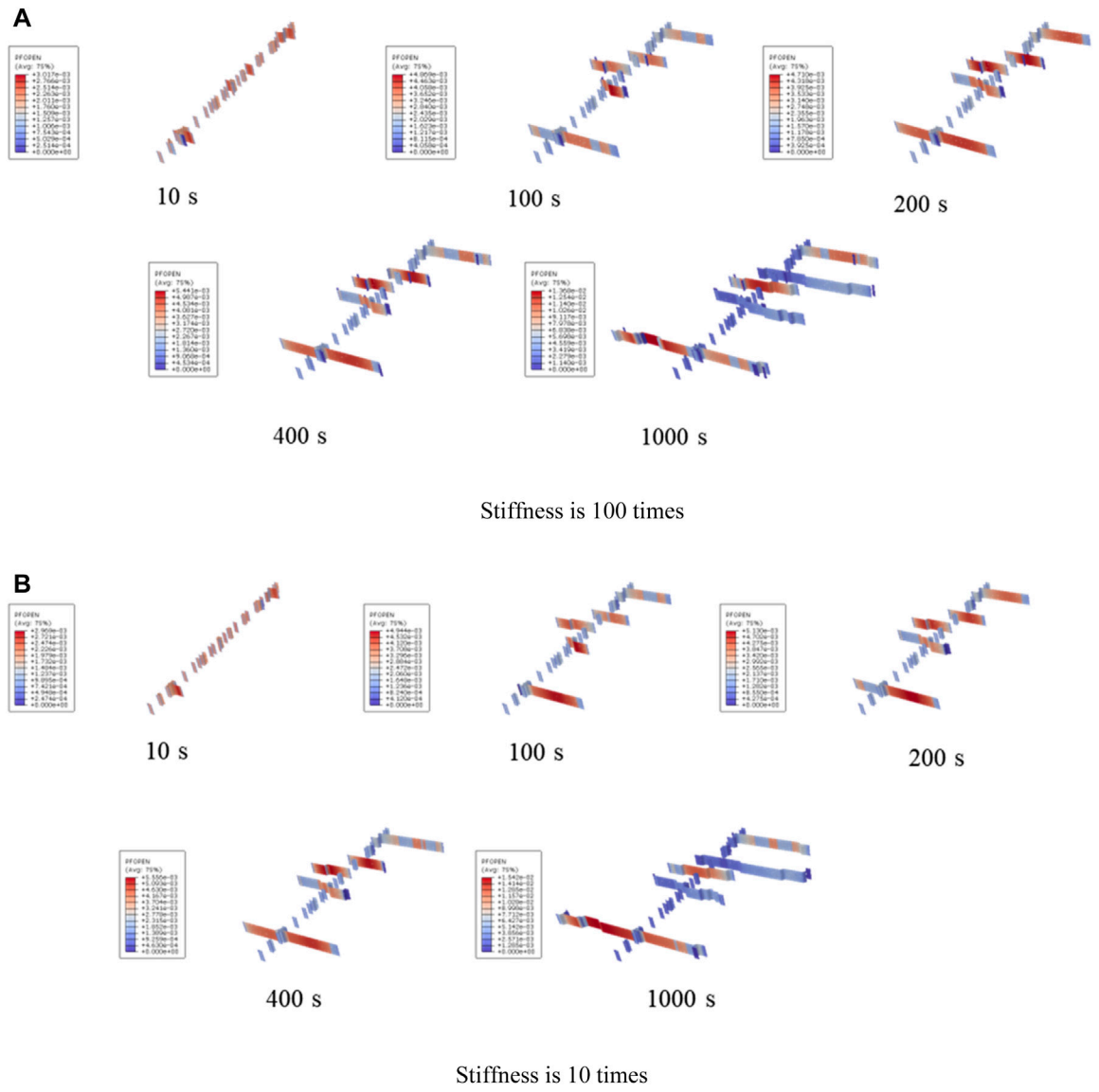


FIGURE 8
Comparison results of fracture morphology under the influence of interface element stiffness (3D View).

beginning to show the phenomenon of main fracture propagation within different clusters. It is worth noting that the artificial fractures formed during this period did not extend forward in a straight line. Affected by the stress and fluid distribution between different clusters, the first and third clusters in the three-cluster fracturing exhibit an approximate single-wing linear propagation pattern. However, the intermediate clusters may be affected by the development of fractures at both ends of the clusters, exhibiting significant non-planar propagation of a single wing; ③ The mutual influence and propagation stage of the main fractures within the cluster: When the fluid is further injected, the bending and propagation of the fractures lead to non-uniform distribution of ground stress, thereby inducing obstruction at the tip. It may cause a shift in the propagation path of the advantageous tip during the initiation of artificial fractures, leading to a transition from single-wing propagation to double-wing propagation of artificial fractures; ④ Main seam extension stage: After the artificial main seam is roughly formed, the artificial fracture will be more easily extended along the dominant main seam due to the comprehensive influence of stress difference and other conditions.

Figure 6 shows the development process of artificial fractures during three clusters of fracturing (top view). Compared to the above and below figures, the formation and development process and stages of artificial fractures during the three clusters of fracturing are basically consistent. It is worth noting that as the fracturing process continues, it can be seen from the following figure that there appeared artificial main fractures that did not seem to be connected between time t4 and t5, which was caused by the resolution setting during simulated data extraction. Due to the extremely small width of artificial fractures relative to reservoir size in the simulation results. Therefore, it is inevitable that some seemingly disconnected low-width artificial fractures will appear in the simulation

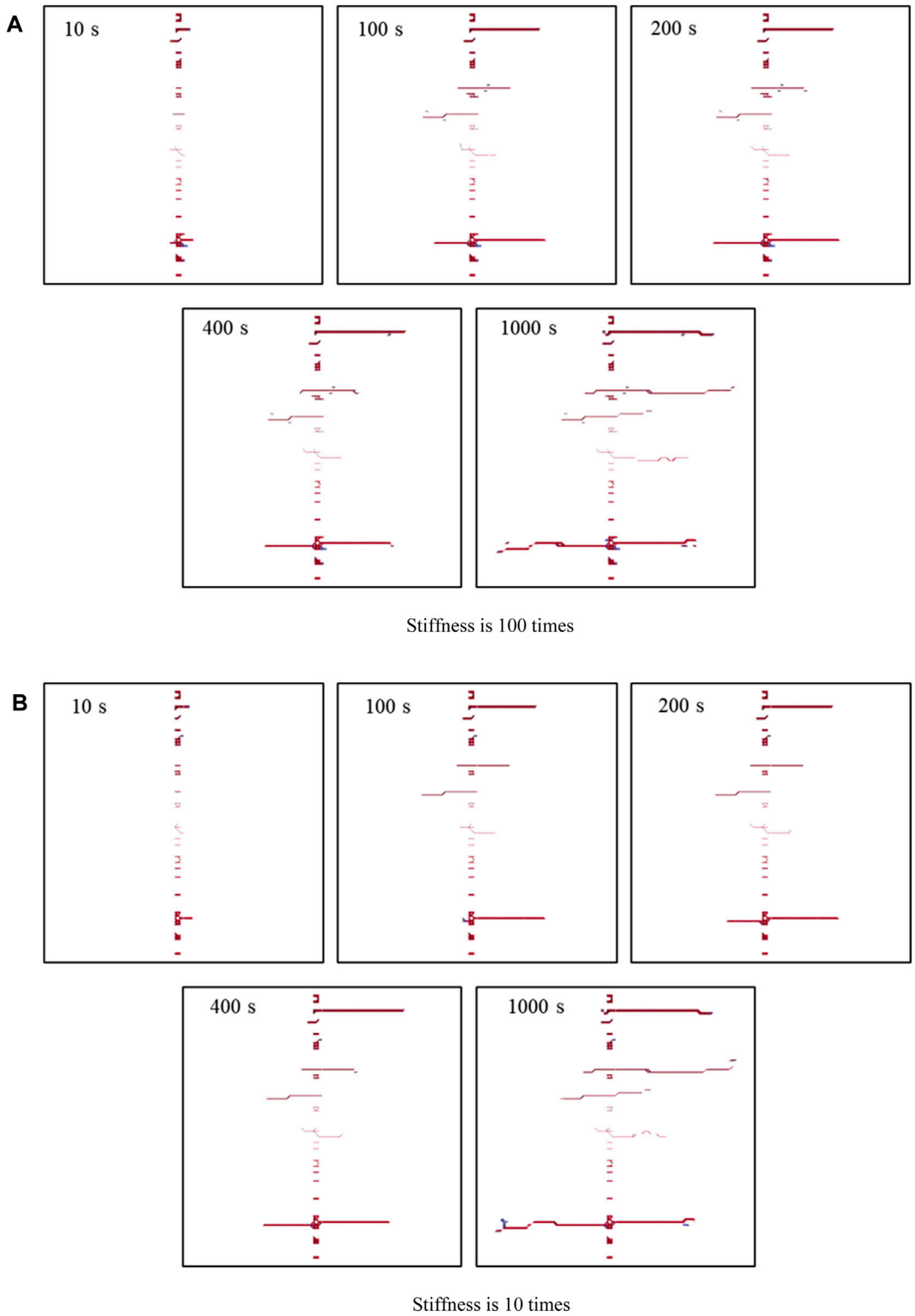


FIGURE 9
Artificial fracture development process during six clusters fracturing (top view).

results. These fractures are similar to the low-width fractures formed during the reservoir fracturing process, which may hinder the flow of proppants such as ceramides, and thus may lead to complex fracture networks detected by microseisms. However, proppants are difficult to flow into the supporting fractures, resulting in a phenomenon where the increase in production is not significant.

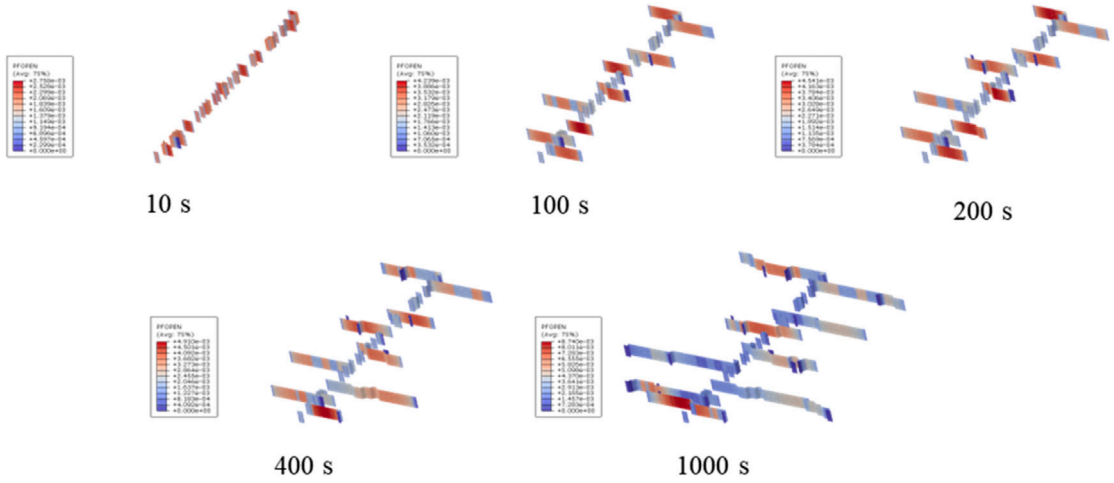


FIGURE 10
Artificial fracture development process during nine clusters of fracturing (3D view).

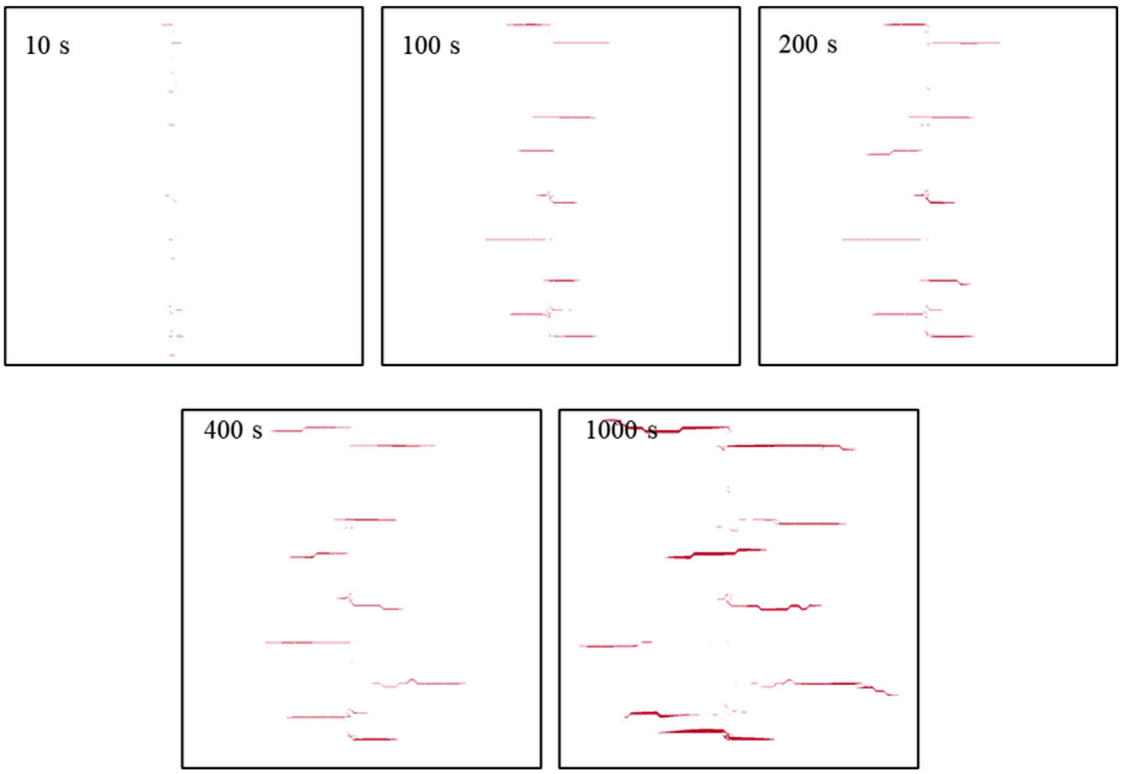


FIGURE 11
Artificial fracture development process during nine cluster fracturing (top view).

3.3 Six clusters

The simulation results under the influence of different interface stiffness during six clusters fracturing are shown in Figure 7. As the interface stiffness increases, the number of fracture elements increases, the total area of fractures increases, and the volume of fractures decreases. Meanwhile, comparing the results of single cluster fracturing, as the number of fracturing clusters increases, the model shows a significant decrease in the influence of rock interface stiffness.

Figures 8, 9 show that when using six clusters of fracturing, the shape of the artificial fracture network is less affected by the interface

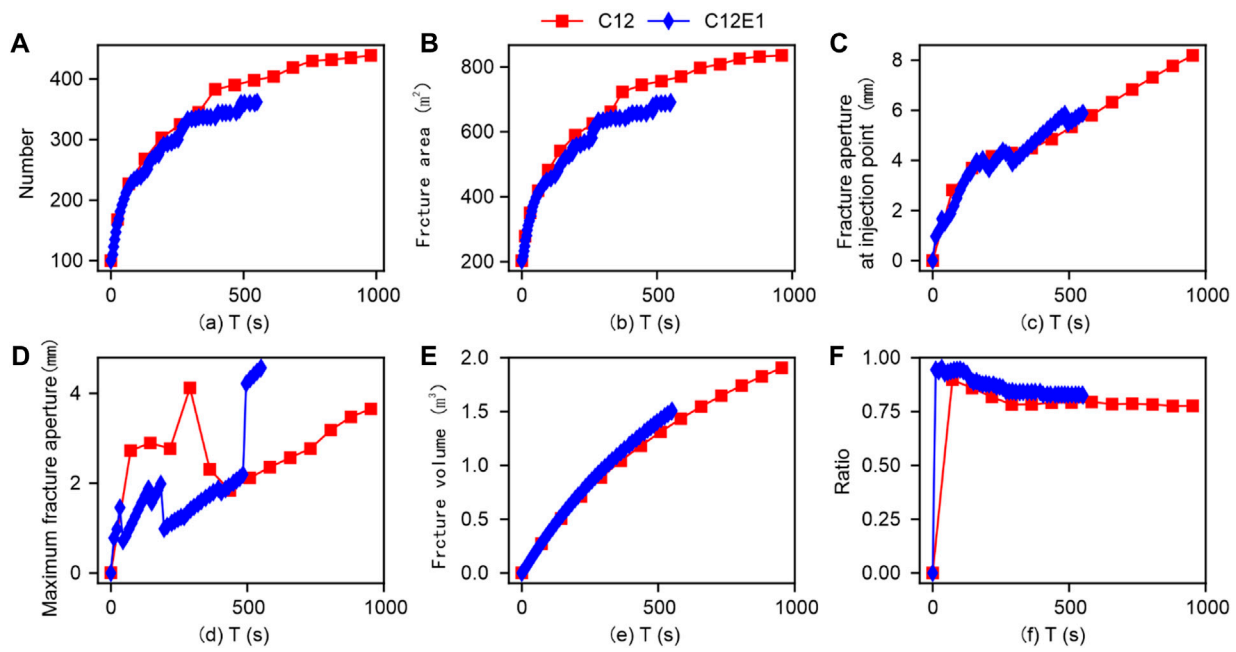


FIGURE 12
Comparison results of conventional quantitative parameters under the influence of interface element stiffness (Twelve clusters).

stiffness. This phenomenon indicates that in actual reservoir fracturing, the impact of reservoir fracture resistance on the effectiveness of reservoir reconstruction can be reduced by setting reasonable multi-cluster fracturing.

3.4 Nine clusters

Keeping the total injection flow constant and changing the model to nine cluster fracturing, the obtained fracture morphology results are shown in Figure 10. It can be observed from Figure 10 that the initiation and propagation process of artificial fractures is similar to the results of three cluster fracturing, which can be divided into the following four stages: ① fracture initiation stage; ② Stage of perforation gap competition propagation; ③ The mutual influence and propagation stage of the main fractures within the cluster; ④ Main seam extension stage. It is worth mentioning that compared to the three-cluster fracturing, there is no significant phenomenon of single-wing main fracture expanding to double-wing during the mutual influence stage of the main fractures within the cluster. This should be due to the more clusters, the more significant the phenomenon of artificial fracture competition and propagation. This should be due to the more clusters, the more significant the phenomenon of artificial fracture competition and propagation. In addition, the process of artificial fracture morphology change during nine clusters (top view) is shown in Figure 11. It can be seen from the figure that compared to the results of three clusters; more discontinuous main fractures appear in the artificial fractures. This phenomenon indicates that the more clusters, the more local wide fractures, and low-opening main fractures will be formed in artificial fractures.

3.5 Twelve clusters

Figure 12 shows the comparison results of conventional quantitative parameters under the influence of interface element stiffness during 12-cluster fracturing. From the above figure, as the interface stiffness increases, the number of fracture elements and total fracture area show an increasing trend, while the fracture volume shows a decreasing trend. Meanwhile, comparing the results of single cluster fracturing (Figure 2) and three cluster fracturing (Figure 7), as the number of fracturing clusters increases, the model shows a significant decrease in the influence of rock interface stiffness.

Figures 13 and 14 show that the artificial fracture development process during twelve cluster fracturing. Based on the comparison of the fracturing results between cluster 1 and cluster 6 in Sections 3.1 and 3.3, as the number of clusters increases, the impact of the interface stiffness within the reservoir, i.e., the reservoir's ability to resist fracture deformation, on the shape of the artificial fracture network in the reservoir shows a certain decreasing trend. This phenomenon indicates that in actual reservoir fracturing, the impact of reservoir fracture resistance on the effectiveness of reservoir reconstruction can be reduced by setting reasonable multi-cluster fracturing.

4 Discussions

The previous study analysed the results of fracture propagation under different cluster numbers, to further analyse the quantitative results of fracture propagation. This section further compares the variation process of conventional quantitative parameters of compression fractures under different clusters and the results at 1000s. Meanwhile, the complex characteristics of artificial fractures

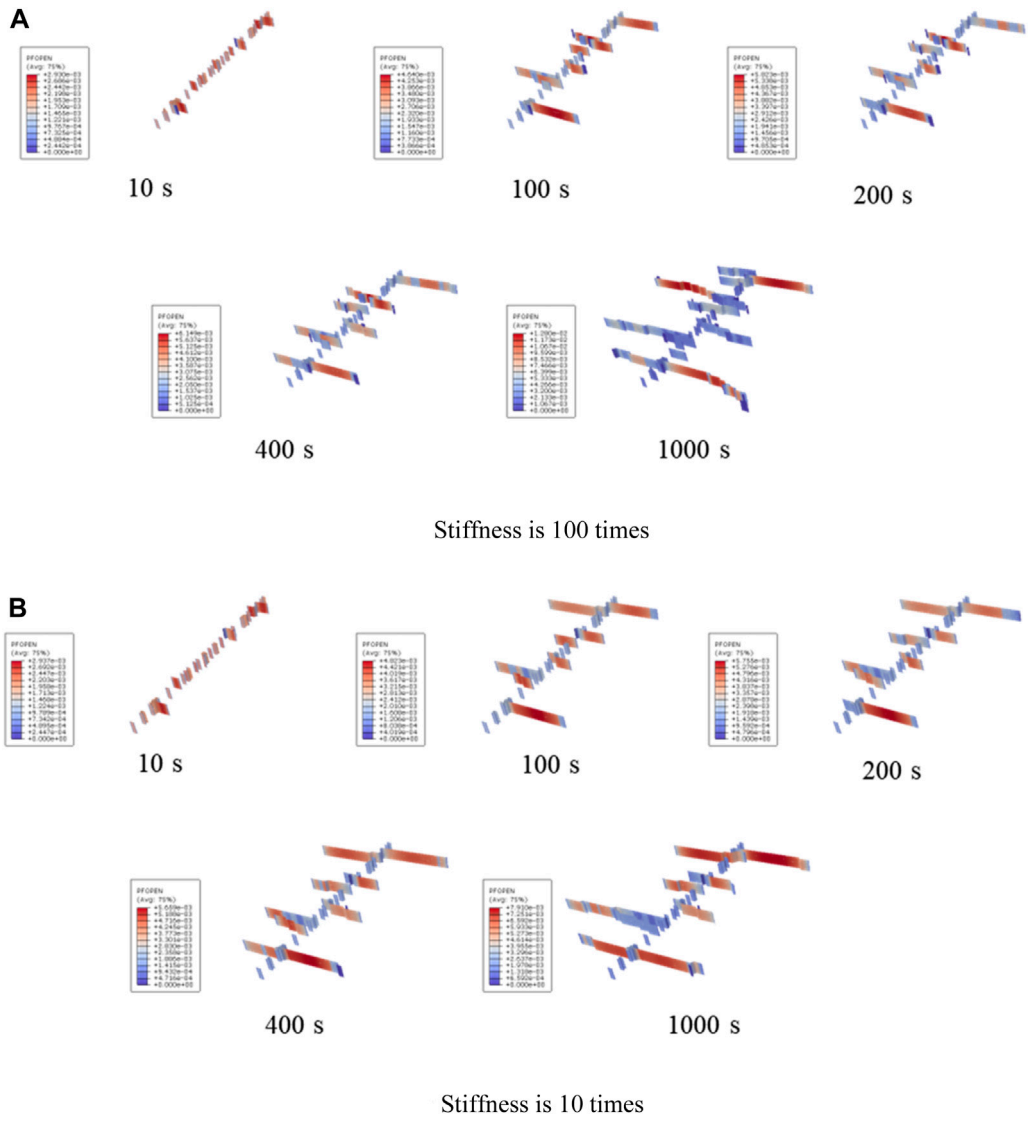


FIGURE 13
Comparison results of conventional quantitative parameters under the influence of interface element stiffness (3D view).

at the final 1000s were quantitatively analysed based on fractal dimension.

4.1 Comparison of conventional quantitative parameters

To further analyse the changes in parameters related to final fracture propagation during different cluster fracturing. Firstly, the conventional quantization parameter results of different clusters were comprehensively extracted, as shown in Figure 15. As the cluster spacing increases, the number of fracture elements and total fracture area in the simulation model show an increasing trend. Meanwhile, the final increase in cluster spacing from 1 cluster to six clusters and from six clusters to twelve clusters is relatively similar. The injection point fracture width and maximum fracture width exhibit significant randomness, making it difficult to use for direct quantitative analysis. The total volume of fractures shows a certain downward trend with the increase of cluster spacing. We speculate that this is due to the increase in the total extension area of the fractures, which makes it difficult for the same flow rate to support many large opening artificial fractures.

After extracting the final values, the morphological results shown in Figure 16 were obtained. Please note that the data results for the three fracturing clusters have not been fully calculated, and the corresponding results were not presented. By comprehensively comparing the fracture morphology of different clusters after fracturing, as the number of clusters increases, the multi-cluster phenomenon of artificial main fractures in the reservoir becomes more significant. When using the single cluster to twelve cluster fracturing, 2, 3, 5, 9, and 12 main fractures were formed respectively. Therefore, the fracture area has significantly increased. Meanwhile, as the number of clusters increases, the bending and branching of the formed fractures become more

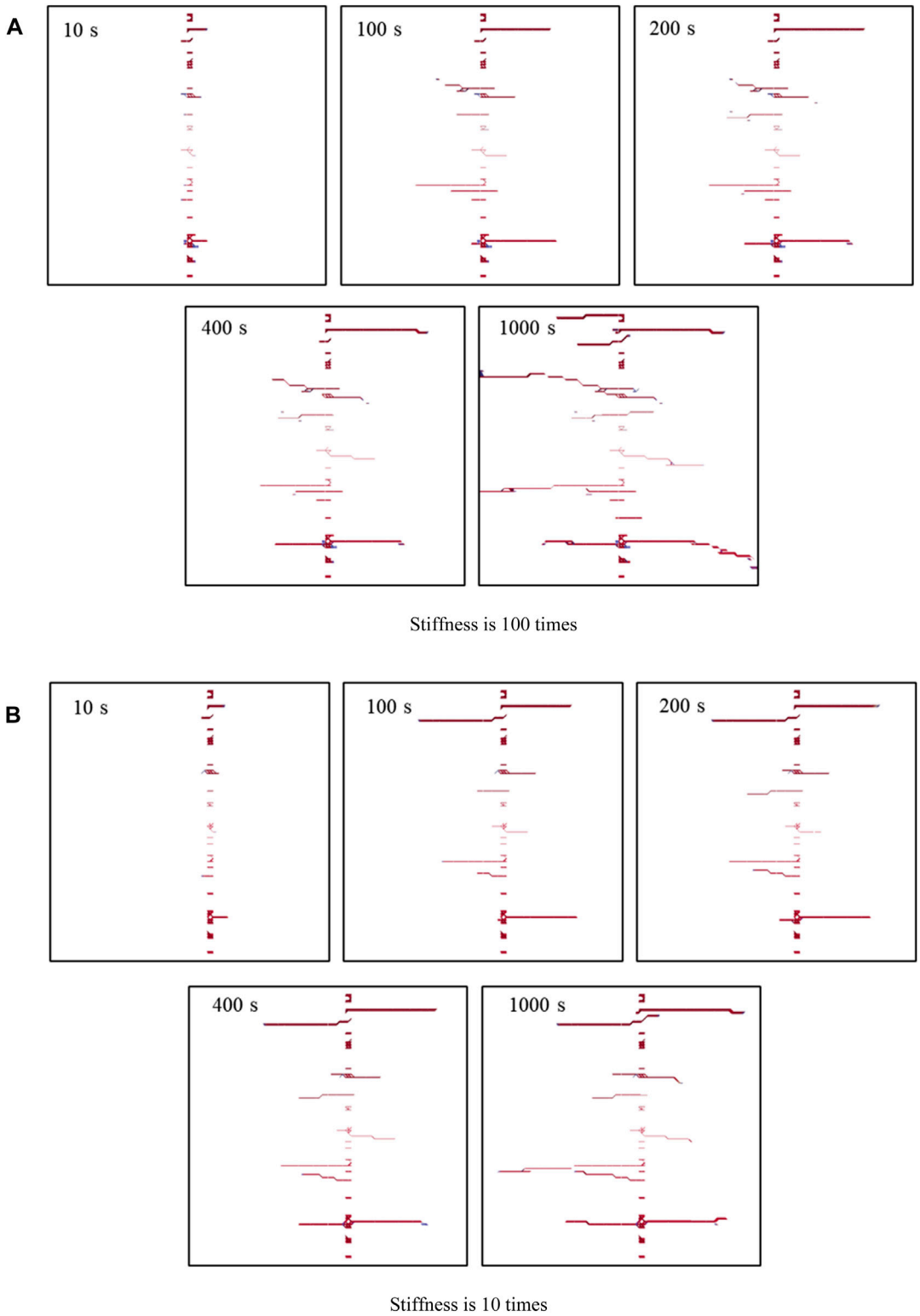


FIGURE 14
Artificial fracture development process during twelve cluster fracturing (top view).

significant, thus the proportion of hydraulic fractures formed by tensile failure decreases. It is worth mentioning that due to the extremely small opening of artificial cracks caused by shear failure, it is difficult to be counted in the total volume of cracks. Therefore, under the influence of shear stimulation, the volume of artificial cracks shows a decreasing trend. However, when the number of fracturing clusters reached twelve, there was a significant increase in the volume of artificial fractures. Combined with the fracture

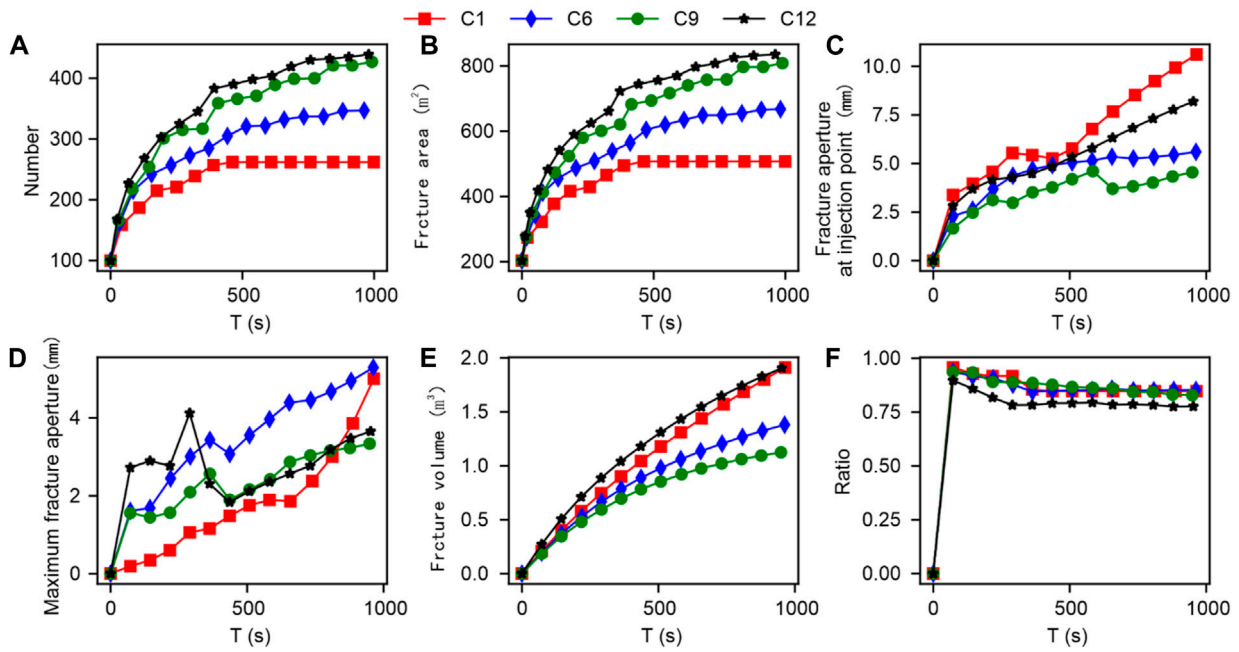


FIGURE 15
Comparison results of conventional quantization parameters under the influence of different clusters.

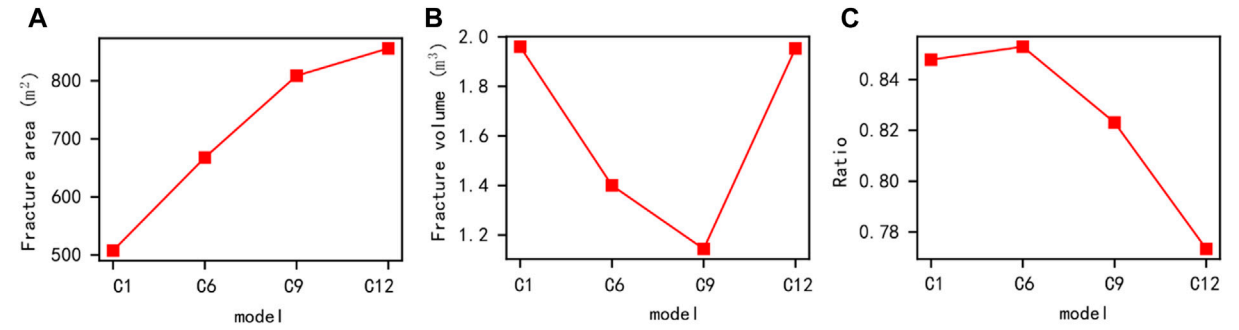


FIGURE 16
Comparison results of conventional quantitative parameters under the influence of different clusters (1000 s).

morphology results in Figure 14, we speculate that this may be due to insufficient growth in the length of multiple main fractures during the twelve-cluster fracturing, resulting in internal pressure suppression and an increase in the calculated fracture volume. Therefore, using multi-cluster fracturing with wellbore sealing can significantly improve the effectiveness of reservoir reconstruction. However, in actual construction, it may also be necessary to consider economic factors as a reference.

4.2 Comparison of fractal dimensions of multiple clusters of artificial fractures

The previous study compared in detail the conventional quantitative parameters and morphological results of artificial fractures under different stiffness and number of fracturing clusters. Unfortunately, many mining studies have shown that the efficiency of reservoir mining is not only affected by the length of fractures but also more significantly by the complexity of pores and fractures (Song, et al., 2020; Liu, et al., 2023). To this end, we first extracted the artificial fracture propagation results under different fracturing cluster conditions for 1000 s, as shown in Figure 17. It can be roughly inferred that as the number of fracturing clusters increases, the complexity of reservoir fractures shows an increasing trend. However, quantitative growth rates are difficult to obtain. It is worth mentioning that the complexity of artificial fractures can be characterized by fractal dimension (Costa, et al., 2007; Lai, et al., 2018), and the most used method is the box-counting dimension method. The specific calculation formula is as follows (Mandelbrot, 1982; Xie and Wang, 1999; Wu Z. et al., 2018).

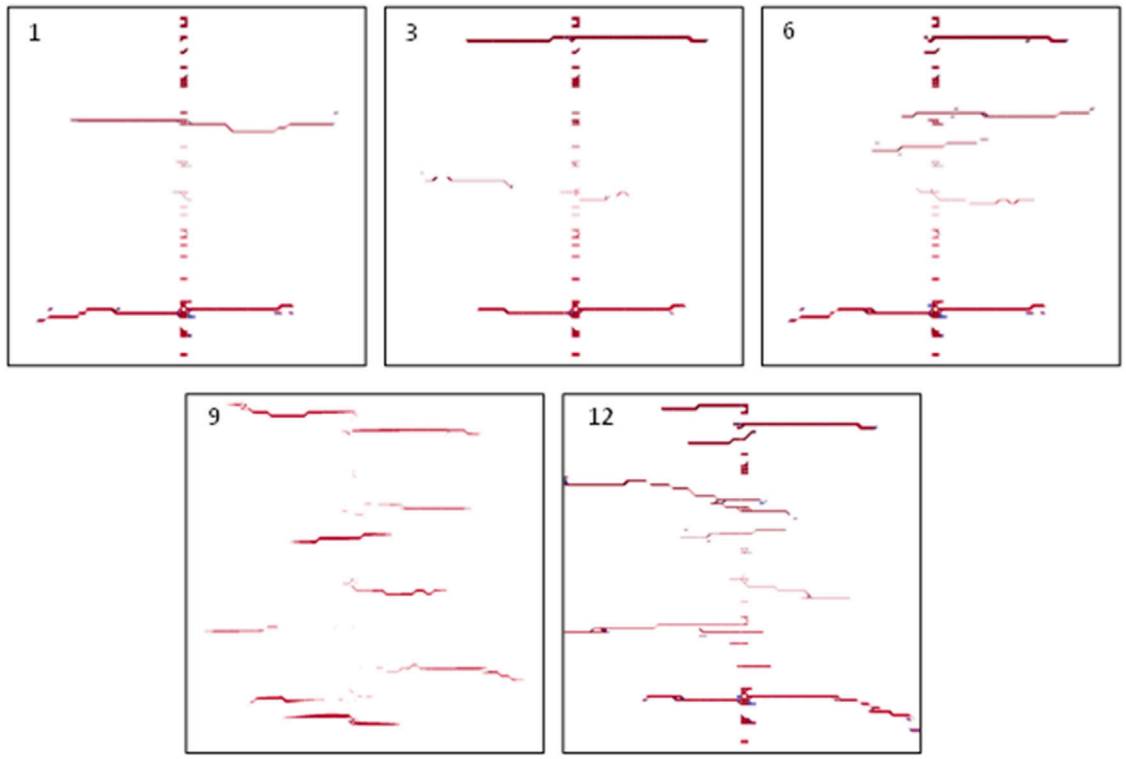


FIGURE 17
Comparison results of final fracture morphology under different cluster numbers (Top view).

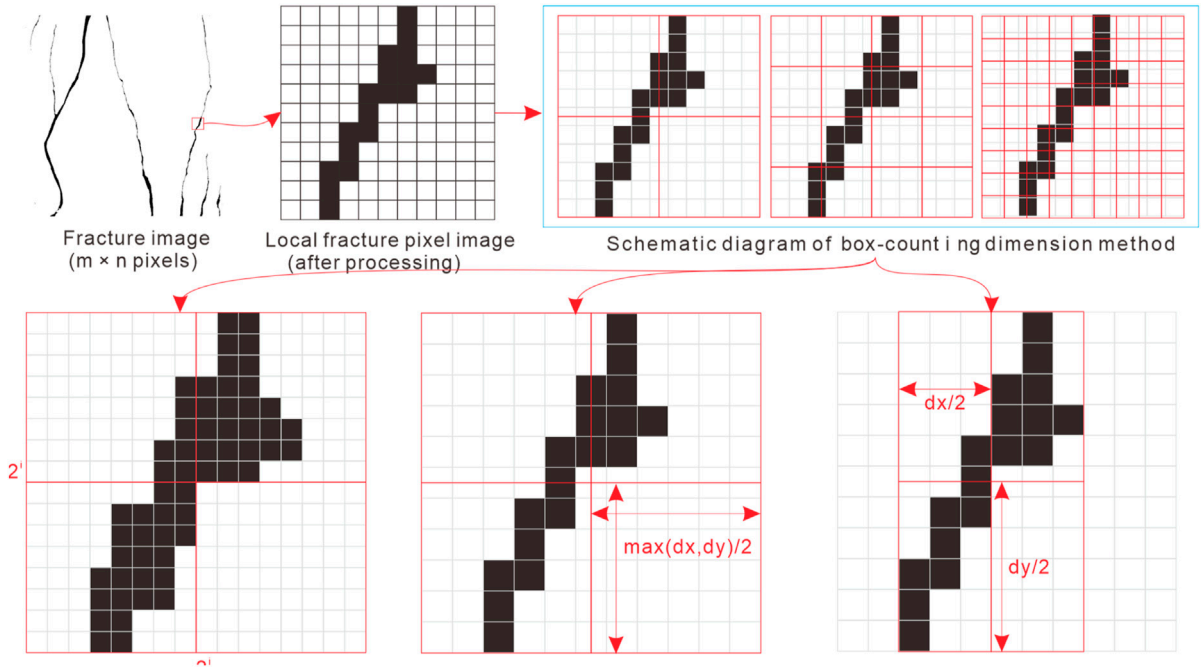


FIGURE 18
Schematic diagram of box calculation using improved box-counting method.

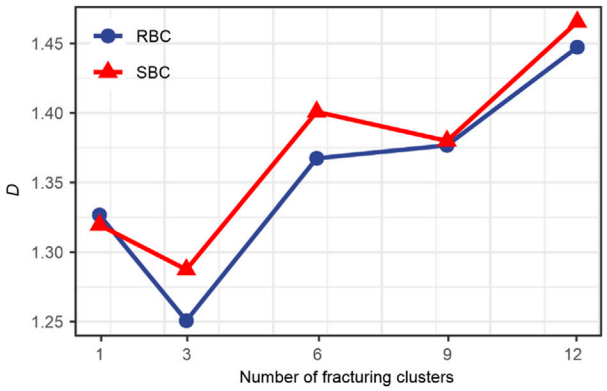


FIGURE 19
Fractal dimension results of artificial fracture morphology under different cluster conditions (1000 s).

$$D = -\lim_{r_i \to 0} \frac{\log N(r_i)}{\log r_i} \tag{15}$$

where i means the number of measurements, $r_i\,(r_i \to 0)$ is the scale, $N(r_i)$ represents the box number.

In previous studies (Lee, et al., 1990; Feng, et al., 2021; Wu, et al., 2021), the resolution of fracture images was usually processed to the nth power of 2, allowing for multiple equal divisions and obtaining the fractal dimension through the above equation. However, when processing actual fracture images, it is not possible to obtain fracture images that meet the conditions, and the processing process may cause distortion of the fracture images. Therefore, we have made improvements to our previous box calculation methods by proposing the square box method and the rectangular box method, respectively. As shown in Figure 18, The two improved box-counting dimensionality methods no longer need to process the resolution of the original fracture image. The square box method directly divides the values based on the maximum image resolution to determine the box occupied by the fracture and then obtains the fractal dimension result through Eq. 15. The rectangular box method directly takes equal values based on the resolution size, and its size is obtained by converting the square with equal area to determine the box occupied by the fracture. The fractal dimension result is obtained through Eq. 15.

Given that conventional morphological parameters such as fracture area and volume are often difficult to effectively evaluate the effectiveness of fracture network fracturing. Therefore, after pixel extraction of the final fracture morphology, the improved square and rectangular box methods were used to calculate the fractal dimension results of the final fracture morphology after different cluster fracturing. As shown in Figure 19 that the fractal dimension results of the final fracture during single cluster fracturing were 1.32672 and 1.31952, respectively. The fractal dimension results of the final fracture during three cluster fracturing were 1.25064 and 1.28741, respectively (please note that the three cluster fracturing results did not fully converge to the calculation, so the reference level is low), The fractal dimension results of the final fractures during six clusters fracturing were 1.36737 and 1.40083, respectively. The fractal dimension results of the final fractures during nine clusters fracturing were 1.37670 and 1.37988, respectively. The fractal dimension results of the final fractures during twelve clusters fracturing were 1.44731 and 1.46547, respectively. When using the square box dimension, the fractal dimension results as the number of clusters increases are 1.32672, 1.25064 (low reference level), 1.36737, 1.37670, and 1.44731, respectively. As the number of clusters increases, the fractal dimension of reservoir fractures significantly increases, indicating a significant increase in complexity. Therefore, when considering the fracturing situation of a square area reservoir, the more clusters, the better the fracturing effect. The rectangular box method is more sensitive to the rectangular space occupied by artificial sewing nets, thus better reflecting the local complexity of the formed sewing net structure. Therefore, the analysis of the rectangular box dimension results shows that the fractal dimension results as the number of clusters increases are 1.31952, 1.28741 (with low reference level), 1.40083, 1.37988, and 1.46547, respectively. From this result, it can be preliminarily determined that an increase of 5 clusters from single cluster fracturing to six clusters fracturing resulted in an increase of nearly 0.08 in fractal dimension. From six clusters to twelve clusters fracturing, an increase of six clusters resulted in an increase of nearly 0.06 in fractal dimension. At the same time, there is a decrease in fractal dimension results during the process from six clusters to nine clusters, indicating a possible downward trend in the complexity of fractures. Therefore, when considering the complexity of fracturing fractures characterized by the fractal dimension of cuboids, it is more inclined to choose six clusters of fracturing.

5 Conclusion

Considering the relevant geological parameters of a certain reservoir in the southwest, three-dimensional (3D) multi-cluster reservoir fracturing models using cohesive element modeling were established. Then, the quantitative rules of fluid pressure, fracture length, fracture aperture, fracture area, tensile failure rate, and the fractal dimension of fracture morphology under different fracturing cluster numbers were revealed. The following understandings are mainly drawn:

(1) There are several main stages of fracture propagation in multi cluster fracturing, including: ① fracture initiation stage; ② Stage of perforation gap competition propagation; ③ The mutual influence and propagation stage of the main fractures within the cluster; ④ Main seam extension stage. Meanwhile, as the number of fracturing clusters increases, the ability of the main fracture in the reservoir to expand from single wing to double wing decreases, and the phenomenon of single wing propagation intensifies.
(2) As the interface stiffness increases, the number of fracture elements increases, the total area of fractures increases, and the volume of fractures decreases. Meanwhile, comparing the results of single cluster fracturing, as the number of fracturing clusters increases, the model shows a significant decrease in the influence of rock interface stiffness. As the cluster spacing increases, the number of fracture elements and total fracture area in the simulation model show an increasing trend. Meanwhile, the final increase in cluster spacing from single

cluster to six clusters and from six clusters to twelve clusters is relatively similar. The injection point fracture width and maximum fracture width exhibit significant randomness, making it difficult to use for direct quantitative analysis. The total volume of fractures shows a certain downward trend with the increase of cluster spacing. From the fractal quantification results of fracture morphology, as the number of fracturing clusters increases, it is easier to form complex fractures within the reservoir research area.

(3) It is worth mentioning that when only considering the maximum cuboid calibration area of reservoir fractures for analysis, an increase of 5 clusters was achieved from single cluster fracturing to six clusters fracturing, achieving a fractal dimension increase of nearly 0.08. From six clusters to twelve clusters fracturing, an increase of six clusters was achieved, achieving a fractal dimension increase of nearly 0.06. This indicates that using fracturing clusters of about six clusters in this model reservoir may have higher economic efficiency.

Data availability statement

The raw data supporting the conclusion of this article will be made available by the authors, without undue reservation.

Author contributions

BZ: Conceptualization, Project administration, Resources, Supervision, Writing–original draft, Writing–review and editing. MW: Investigation, Methodology, Visualization, Writing–original draft. YS: Conceptualization, Investigation, Project administration, Resources, Supervision, Writing–review and editing. YG: Supervision, Writing–review and editing. JF: Investigation, Methodology, Supervision, Writing–review and editing. JG: Project administration, Validation, Writing–review and editing. JL: Investigation, Supervision, Writing–review and editing.

Funding

The author(s) declare financial support was received for the research, authorship, and/or publication of this article. The authors gratefully acknowledge the financial support given by Open Research Fund of State Key Laboratory of Geomechanics and Geotechnical Engineering, Institute of Rock and Soil Mechanics, Chinese Academy of Sciences, Grant No. SKLGME022020, and Hubei Provincial Natural Science Foundation (Grant No. 2022CFB400).

Conflict of interest

Authors BZ, JF, and JG were employed by Shale Gas Research Institute of PetroChina Southwest Oil and Gas Field Company.

The remaining authors declare that the research was conducted in the absence of any commercial or financial relationships that could be construed as a potential conflict of interest.

Publisher's note

All claims expressed in this article are solely those of the authors and do not necessarily represent those of their affiliated organizations, or those of the publisher, the editors and the reviewers. Any product that may be evaluated in this article, or claim that may be made by its manufacturer, is not guaranteed or endorsed by the publisher.

References

Costa, L. D., Rodrigues, F. A., Travieso, G., and Boas, P. R. V. (2007). Characterization of complex networks: a survey of measurements. *Adv. Phys.* 56 (1), 167–242. doi:10.1080/00018730601170527

Cramer, D., Friehauf, K., Roberts, G., and Whittaker, J. (2019). in SPE Hydraulic Fracturing Technology Conference and Exhibition D031S007R001.

Dahi Taleghani, A., Gonzalez-Chavez, M., Yu, H., and Asala, H. (2018). Numerical simulation of hydraulic fracture propagation in naturally fractured formations using the cohesive zone model. *J. Petroleum Sci. Eng.* 165, 42–57. doi:10.1016/j.petrol.2018.01.063

Feng, S., Wu, Y., Liu, Y., Li, X., Wang, X., and Chen, P. (2021). A fractal analysis of radon migration in discrete fracture network model. *Chemosphere* 266, 129010. doi:10.1016/j.chemosphere.2020.129010

Guo, F., Morgenstern, N. R., and Scott, J. D. (1993). Interpretation of hydraulic fracturing breakdown pressure. *Int. J. Rock Mech. Min. Sci. Geomechanics Abstr.* 30 (6), 617–626. doi:10.1016/0148-9062(93)91221-4

Huang, L., Dontsov, E., Fu, H., Lei, Y., Weng, D., and Zhang, F. (2022). Hydraulic fracture height growth in layered rocks: perspective from DEM simulation of different propagation regimes. *Int. J. Solids Struct.* 238, 111395. doi:10.1016/j.ijsolstr.2021.111395

Huang, L., Liu, J., Zhang, F., Dontsov, E., and Damjanac, B. (2019). Exploring the influence of rock inherent heterogeneity and grain size on hydraulic fracturing using discrete element modeling. *Int. J. Solids Struct.* 176-177, 207–220. doi:10.1016/j.ijsolstr.2019.06.018

Huang, L., Tan, J., Fu, H., Liu, J., Chen, X., Liao, X., et al. (2023). The non-plane initiation and propagation mechanism of multiple hydraulic fractures in tight reservoirs considering stress shadow effects. *Eng. Fract. Mech.* 2023, 109570. doi:10.1016/j.engfracmech.2023.109570

Jiang, C., Niu, B., Yin, G., Zhang, D., Yu, T., and Wang, P. (2019). CT-based 3D reconstruction of the geometry and propagation of hydraulic fracturing in shale. *J. Petroleum Sci. Eng.* 179, 899–911. doi:10.1016/j.petrol.2019.04.103

Ju, Y., Liu, P., Chen, J., Yang, Y., and Ranjith, P. G. (2016). CDEM-based analysis of the 3D initiation and propagation of hydrofracturing cracks in heterogeneous glutenites. *J. Nat. Gas Sci. Eng.* 35, 614–623. doi:10.1016/j.jngse.2016.09.011

Lai, J., Wang, G. W., Wang, Z. Y., Chen, J., Pang, X. J., Wang, S. C., et al. (2018). A review on pore structure characterization in tight sandstones. *Earth-Sci Rev.* 177, 436–457. doi:10.1016/j.earscirev.2017.12.003

Lecampion, B., and Desroches, J. (2015). Simultaneous initiation and growth of multiple radial hydraulic fractures from a horizontal wellbore. *J. Mech. Phys. Solids* 82, 235–258. doi:10.1016/j.jmps.2015.05.010

Lee, Y. H., Carr, J. R., Barr, D. J., and Haas, C. J. (1990). The fractal dimension as a measure of the roughness of rock discontinuity profiles. *Int. J. Rock Mech. Min.*, 27(6), 453–464. doi:10.1016/0148-9062(90)90998-H

Li, S., and Ghosh, S. (2006). Multiple cohesive crack growth in brittle materials by the extended Voronoi cell finite element model. *Int. J. Fract.* 141 (3-4), 373–393. doi:10.1007/s10704-006-9000-2

Liu, C., Jin, X., Shi, F., Lu, D., Liu, H., and Wu, H. (2018). Numerical investigation on the critical factors in successfully creating fracture network in heterogeneous shale reservoirs. *J. Nat. Gas Sci. Eng.* 59, 427–439. doi:10.1016/j.jngse.2018.09.019

Liu, Q., Li, J., Liang, B., Liu, J., Sun, W., He, J., et al. (2023). Complex wettability behavior triggering mechanism on imbibition: a model construction and comparative study based on analysis at multiple scales. *Energy* 275, 127434. doi:10.1016/j.energy.2023.127434

Luo, H., Xie, J., Huang, L., Wu, J.-f., Shi, X., Bai, Y., et al. (2022). Multiscale sensitivity analysis of hydraulic fracturing parameters based on dimensionless analysis method, *Lithosphere* 9708300. doi:10.2113/2022/9708300

Mandelbrot, B. B. (1982). *The fractal geometry of nature*. W. H. Freeman and Company.

Meng, M., Chen, Z., Liao, X., Wang, J., and Shi, L. (2020). A well-testing method for parameter evaluation of multiple fractured horizontal wells with non-uniform fractures in shale oil reservoirs. *Adv. Geo-Energy Res.* 4 (2), 187–198. doi:10.26804/ager.2020.02.07

Modeland, N., Buller, D., and Chong, K. K. (2011). in North American Unconventional Gas Conference and Exhibition SPE-144120-MS.

Moghadasi, R., Rostami, A., and Hemmati-Sarapardeh, A. (2019). Application of nanofluids for treating fines migration during hydraulic fracturing: experimental study and mechanistic understanding. *Adv. Geo-Energy Res.* 3 (2), 198–206. doi:10.26804/ager.2019.02.09

Munjiza, A. A. (2004). *The combined finite-discrete element method*. John Wiley & Sons.

Qin, X., Zhou, Y., and Sasmito, A. P. (2019). An effective thermal conductivity model for fractal porous media with rough surfaces. *Adv. Geo-Energy Res.* 3 (2), 149–155. doi:10.26804/ager.2019.02.04

Qiu, G., Chang, X., Li, J., Guo, Y., Wang, L., Ma, H., et al. (2023). Study on rock brittleness characteristics of deep volcanic reservoir under different confining pressures. *J. Petroleum Explor. Prod. Technol.* doi:10.1007/s13202-023-01717-z

Réthoré, J., de Borst, R., and Abellan, M.-A. (2008). A two-scale model for fluid flow in an unsaturated porous medium with cohesive cracks. *Comput. Mech.* 42 (2), 227–238. doi:10.1007/s00466-007-0178-6

Rougier, E., Munjiza, A., Lei, Z., Chau, V. T., Knight, E. E., Hunter, A., et al. (2019). The combined plastic and discrete fracture deformation framework for finite-discrete element methods. *Int. J. Numer. Methods Eng.* 121, 1020–1035. doi:10.1002/nme.6255

Shi, D., Li, L., Guo, Y., Liu, J., Tang, J., Chang, X., et al. (2023). Estimation of rough fracture network permeability using fractal and topology theories. *Gas Sci. Eng.* 116, 205043. doi:10.1016/j.jgsce.2023.205043

Song, R., Liu, J., and Cui, M. (2017). A new method to reconstruct structured mesh model from micro-computed tomography images of porous media and its application. *Int. J. Heat Mass Transf.* 109, 705–715. doi:10.1016/j.ijheatmasstransfer.2017.02.053

Song, R., Liu, J., Yang, C., and Sun, S. (2022a). Study on the multiphase heat and mass transfer mechanism in the dissociation of methane hydrate in reconstructed real-shape porous sediments. *Energy* 254, 124421. doi:10.1016/j.energy.2022.124421

Song, R., Wang, Y., Ishutov, S., Zambrano-Narvaez, G., Hodder, K. J., Chalaturnyk, R. J., et al. (2020). A comprehensive experimental study on mechanical behavior, microstructure and transport properties of 3D-printed rock analogs. *Rock Mech. Rock Eng.* 53 (12), 5745–5765. doi:10.1007/s00603-020-02239-4

Song, R., Wang, Y., Tang, Y., Jiajun, p., Liu, J., and Yang, C. (2022b). 3D Printing of natural sandstone at pore scale and comparative analysis on micro-structure and single/two-phase flow properties. *Energy* 261, 125226. doi:10.1016/j.energy.2022.125226

Tan, P., Chen, Z., Fu, S., and Zhao, Q. (2023). Experimental investigation on fracture growth for integrated hydraulic fracturing in multiple gas bearing formations. *Geoenergy Sci. Eng.* 231, 212316. doi:10.1016/j.geoen.2023.212316

Wang, H. (2016). Numerical investigation of fracture spacing and sequencing effects on multiple hydraulic fracture interference and coalescence in brittle and ductile reservoir rocks. *Eng. Fract. Mech.* 157, 107–124. doi:10.1016/j.engfracmech.2016.02.025

Wang, H. (2019). Hydraulic fracture propagation in naturally fractured reservoirs: complex fracture or fracture networks. *J. Nat. Gas Sci. Eng.* 68, 102911. doi:10.1016/j.jngse.2019.102911

Wei, W., Cai, J. C., Hu, X. Y., and Han, Q. (2015). An electrical conductivity model for fractal porous media. *Geophys Res. Lett.* 42 (12), 4833–4840. doi:10.1002/2015gl064460

Wu, M., Gao, K., Liu, J., Song, Z., and Huang, X. (2022). Influence of rock heterogeneity on hydraulic fracturing: a parametric study using the combined finite-discrete element method. *Int. J. Solids Struct.* 234-235, 111293. doi:10.1016/j.ijsolstr.2021.111293

Wu, M., Jiang, C., Song, R., Liu, J., Li, M., Liu, B., et al. (2023). Comparative study on hydraulic fracturing using different discrete fracture network modeling: insight from homogeneous to heterogeneity reservoirs. *Eng. Fract. Mech.* 284, 109274. doi:10.1016/j.engfracmech.2023.109274

Wu, M., Wang, W., Shi, D., Song, Z., Li, M., and Luo, Y. (2021). Improved box-counting methods to directly estimate the fractal dimension of a rough surface. *Measurement* 177, 109303. doi:10.1016/j.measurement.2021.109303

Wu, M., Wang, W., Zhang, D., Deng, B., Liu, S., Lu, J., et al. (2020). The pixel crack reconstruction method: from fracture image to crack geological model for fracture evolution simulation. *Constr. Build. Mater.* 273, 121733. doi:10.1016/j.conbuildmat.2020.121733

Wu, Z., Sun, H., and Wong, L. N. Y. (2019). A cohesive element-based numerical manifold method for hydraulic fracturing modelling with voronoi grains. *Rock Mech. Rock Eng.* 52 (7), 2335–2359. doi:10.1007/s00603-018-1717-5

WuM., Liu, J., Lv, X., Shi, D., and Zhu, Z. (2018). A study on homogenization equations of fractal porous media. *J. Geophys. Eng.* 15 (6), 2388–2398. doi:10.1088/1742-2140/aac4c1

WuZ., Xu, X., Liu, Q., and Yang, Y. (2018). A zero-thickness cohesive element-based numerical manifold method for rock mechanical behavior with micro-Voronoi grains. *Eng. Analysis Bound. Elem.* 96, 94–108. doi:10.1016/j.enganabound.2018.08.005

Xavier, J., Oliveira, M., Morais, J., and De Moura, M. (2014). Determining mode II cohesive law of *Pinus pinaster* by combining the end-notched flexure test with digital image correlation. *Constr. Build. Mater.* 71, 109–115. doi:10.1016/j.conbuildmat.2014.08.021

Xiang, J., Munjiza, A., Latham, J.-P., and Guises, R. (2009). On the validation of DEM and FEM/DEM models in 2D and 3D. *Eng. Comput.* 26 (6), 673–687. doi:10.1108/02644400910975469

Xie, H. P., and Wang, J. A. (1999). Direct fractal measurement of fracture surfaces. *Int. J. Solids Struct.*, 36(20), 3073–3084. doi:10.1016/S0020-7683(98)00141-3

Yan, C., Jiao, Y.-Y., and Zheng, H. (2018). A fully coupled three-dimensional hydro-mechanical finite discrete element approach with real porous seepage for simulating 3D hydraulic fracturing. *Comput. Geotechnics* 96, 73–89. doi:10.1016/j.compgeo.2017.10.008

Yan, X., Sun, Z., and Dong, Q. (2021). The unified pipe-interface element method for simulating the coupled hydro-mechanical grouting process in fractured rock with fracture propagation. *Eng. Fract. Mech.* 256, 107993. doi:10.1016/j.engfracmech.2021.107993

Yan, X., and Yu, H. (2022). Numerical simulation of hydraulic fracturing with consideration of the pore pressure distribution based on the unified pipe-interface element model. *Eng. Fract. Mech.* 275, 108836. doi:10.1016/j.engfracmech.2022.108836

Yang, R., Wang, Y., Song, G., and Shi, Y. (2023). Fracturing and thermal extraction optimization methods in enhanced geothermal systems. *Adv. Geo-Energy Res.* 8 (2), 136–140. doi:10.46690/ager.2023.08.07

Yuan, J., Jiang, R., and Zhang, W. (2018). The workflow to analyze hydraulic fracture effect on hydraulic fractured horizontal well production in composite formation system. *Adv. Geo-Energy Res.* 2 (3), 319–342. doi:10.26804/ager.2018.03.09

Zhang, H., Chen, J., Li, Z., Hu, H., and Mei, Y. (2023). Numerical simulation of multi-cluster fracturing using the triaxiality dependent cohesive zone model in a shale reservoir with mineral heterogeneity. *Rock Mech. Rock Eng.* doi:10.1007/s00603-023-03527-5

Zheng, Y., He, R., Huang, L., Bai, Y., Wang, C., Chen, W., et al. (2022). Exploring the effect of engineering parameters on the penetration of hydraulic fractures through bedding planes in different propagation regimes. *Comput. Geotechnics* 146, 104736. doi:10.1016/j.compgeo.2022.104736

Zou, J., Jiao, Y.-Y., Tang, Z., Ji, Y., Yan, C., and Wang, J. (2020). Effect of mechanical heterogeneity on hydraulic fracture propagation in unconventional gas reservoirs. *Comput. Geotechnics* 125, 103652. doi:10.1016/j.compgeo.2020.103652

frontiers | Frontiers in Energy Research

TYPE Original Research
PUBLISHED 12 January 2024
DOI 10.3389/fenrg.2024.1333016

Check for updates

OPEN ACCESS

EDITED BY
Liuke Huang,
Southwest Petroleum University, China

REVIEWED BY
Yongxiang Zheng,
Shijiazhuang Tiedao University, China
Yang Liu,
Southwest Petroleum University, China

*CORRESPONDENCE
Ning Xu,
xuning@stu.xust.edu.cn

RECEIVED 04 November 2023
ACCEPTED 03 January 2024
PUBLISHED 12 January 2024

CITATION
Yang S, Xu N, Liu H, Zhang X and Mei S (2024), Research and application of 'three zones' range within overlying strata in goaf of steep coal seam.
Front. Energy Res. 12:1333016.
doi: 10.3389/fenrg.2024.1333016

COPYRIGHT
© 2024 Yang, Xu, Liu, Zhang and Mei. This is an open-access article distributed under the terms of the Creative Commons Attribution License (CC BY). The use, distribution or reproduction in other forums is permitted, provided the original author(s) and the copyright owner(s) are credited and that the original publication in this journal is cited, in accordance with accepted academic practice. No use, distribution or reproduction is permitted which does not comply with these terms.

Research and application of 'three zones' range within overlying strata in goaf of steep coal seam

Shouguo Yang[1,2], Ning Xu[1]*, Haoxin Liu[3], Xiaofei Zhang[1] and Shuxin Mei[1]

[1]College of Safety Science and Engineering, Xi'an University of Science and Technology, Xi'an, China, [2]State Key Laboratory of Gas Disaster Detecting, Preventing and Emergency Controlling, Chongqing, China, [3]Shaanxi Yanchang Petroleum Yulin Kekegai Coal Industry Co Ltd., Yulin, China

The determination of the 'three zones' range within the overlying strata in goaf of paramount importance for effective gas extraction in the goaf and the prevention and control of gas levels exceeding limits in both the working face and the upper corner. Due to the influence of their dip angles, the existing formula used to calculate the breaking boundary angle of the overlying strata in the goaf of horizontal coal seams is no longer suitable for steep coal seams. In response to this issue, the movement law of the overlying strata during the mining of steep coal seams was analyzed and a formula for calculating the breaking boundary angle of the overlying strata in the goaf of steep coal seams was derived. The theoretical calculation formula was applied to the 3,103 fully mechanized mining face of a certain mine in southwest China, and compared and analyzed the results with numerical simulation and on-site measurement using microseismic monitoring technology. The research findings demonstrate that the formula effectively quantifies the 'three zones' range within the overlying strata in the goaf of steep coal seams. The 'three zones' range in steep coal seams is primarily influenced by factors such as the length of the filling area in the lower part of the goaf, changes in roof lithology, coal seam dip angle, length of the working face, and overburden load. The longer the length of the filling area, the larger the upper breaking boundary angle and the smaller the lower breaking boundary angle of the fracture zone. Based on the research results of three methods, the height of the caving zone in the 3,103 fully mechanized mining face is from 6.93 m to 7.7 m, the height of the fracture zone is from 28.91 m to 34.2 m, the lower breaking boundary angle of the fracture zone is from 40° to 44.5°, and the upper breaking boundary angle of the fracture zone is from 57.7° to 62°. The research results offer robust technical support and theoretical guidance for the determination of the 'three zones' range within the overlying strata during the future mining of steep coal seams.

KEYWORDS

steep coal seam, caving zone, fracture zone, breaking boundary angle, numerical simulation, microseismic monitoring

1 Introduction

The mining of coal seams is accompanied by the movement and deformation of surrounding rock formations and surface areas, which results in the formation of caving, fracture, and curved subsidence zones within the overlying strata. In the fracture zone, where fractures are well-developed and facilitate gas circulation (Ma et al., 2013; Wang et al.,

2015; Huang et al., 2018). The gas extraction boreholes in goaf are typically positioned at this location (Ye et al., 2017; Zhang Q. M. et al., 2022; Zhao et al., 2023). Therefore, it holds paramount significance to investigate the extent of the overlying strata's caving zone, fracture zone, and curved subsidence zone (collectively referred to as the 'three zones'), for efficient gas extraction in goaf areas, as well as for gas limit control in mining faces and upper corners. This research is instrumental in ensuring the safety of underground personnel and property.

Numerous scholars have conducted extensive and rich research on this issue. Wang et al. (Wang et al., 2022) established a prediction model for the height of horizontal coal seam fracture zone based on the quantitative relationship between the mining thickness of coal seams, the deformation amount of rock layers of caving zone and fracture zone, and the surface subsidence value. Xu et al. (Xu et al., 2023) established a relationship between the bearing strength of masonry beams and the height of the caving zone using methods such as UDEC numerical simulation and on-site 3D borehole television imaging, combined with the "S-R″ stability theory. Zhou et al. (Zhou and Yu, 2022) studied the height of the 'three zones' of overlying strata in the goaf of gently inclined and extremely thick coal seams through similar simulation experiments, numerical simulations, and on-site measurements. Liu et al. (Liu et al., 2019) proposed a method for predicting the height of the fracture zone based on multiple regression analysis and geographic information systems. Cheng et al. (Cheng et al., 2017) used microseismic monitoring technology to study the distribution patterns of microseismic events released from coal mine roof rock masses in both vertical and horizontal directions. Chen et al. (Chen et al., 2022) systematically studied the movement law and mining pressure of overlying strata on large-angle fully mechanized mining faces through theoretical analysis, similar material simulation, numerical calculation, and on-site monitoring methods. Lai et al. (Lai et al., 2021) used a research method that combines similarity simulation experiments, numerical simulations, and on-site monitoring to analyze the migration law of overlying strata and the distribution characteristics of fracture zone in coal seam mining under thick and loose layers. Yang et al. (Yang et al., 2021) derived a formula based on the thin plate theory for calculating the basic roof stress distribution in highly inclined coal seams. Xu et al. (Xu et al., 2018) derived a formula for calculating the fracture angle of the overlying strata in a horizontal coal seam goaf based on the theory of key layers, and verified the rationality and reliability of the formula through physical simulation experiments.

The research findings mentioned above have significantly advanced the study of the 'three zones' within the overlying strata in goaf, playing a pivotal role in both theoretical research and practical engineering applications. However, much of the existing research predominantly focuses on analyzing the height of the 'three zones', with limited attention directed toward the determination of the breaking boundary angle of the fracture zone. The breaking boundary angle of the fracture zone represents a crucial parameter for accurately defining the 'three zones' range within the overlying strata in the goaf and for planning the layout of gas extraction boreholes in the goaf (Cui et al., 2019a; Hu and Cai, 2020; Zhu et al., 2020). In the case of steep coal seams, rock blocks that collapse due to the influence of the coal seam's dip angle will slide downward along the inclined direction of the working face, filling the lower section of the goaf (Yao et al., 2017; Ye et al., 2018; Liu et al., 2020). Given the stabilizing influence of these rock blocks in the filling area on the roof, the conventional calculation formula for the breaking angle of the overlying strata in goaf based on the horizontal coal seams, is no longer suitable for steep coal seams. Consequently, it is particularly imperative to research the breaking boundary angle of the overlying strata in the goaf of steep coal seams.

Numerous studies have confirmed the effectiveness of numerical simulation methods in studying fracture evolution, such as reference (Huang et al., 2022; Luo et al., 2022; Zheng et al., 2022; Huang et al., 2023). In reference (Yang et al., 2023a), based on microseismic monitoring technology, the author studied the height of the fracture zone in the goaf of steep coal seams and compared with numerical simulation results. The obtained results are consistent, which presents a new technical approach for determining the height of the 'three zones' within overlying strata in the goaf of steep coal seams. On this basis, starting from the movement law of the overlying strata during the mining of steep coal seams, this article derives a formula for calculating the breaking boundary angle of the overlying strata in the goaf of steep coal seams. And in theory, the 'three zones' range of the overlying strata in the goaf of steep coal seams is quantified. Taking the 3,103 fully mechanized mining face of a certain mine in southwestern China as the background, a combination of theoretical calculation, numerical simulation, and on-site measurement via microseismic monitoring technology was used to study the 'three zones' range of overlying strata in the goaf of steep coal seams. The research outcomes supply robust technical support and theoretical guidance for the determination of the 'three zones' range within the overlying strata during future mining operations in steep coal seams.

2 Theoretical derivation of the 'three zones' range within the overlying strata in the goaf of steep coal seams

2.1 Movement law of overlying strata during mining of steep coal seams

During the mining of steep coal seams, the overlying strata are repeatedly disturbed and cause damage under their gravity load. As the mining face progresses, certain segments of the overlying strata at a particular height undergo collapse (Zhang et al., 2023). Owing to the influence of the seam's inclination angle, the collapsed rock blocks will slide toward the lower portion of the working face and subsequently fill the goaf. The lower filling area of the goaf plays a certain supporting role in the roof (Lai et al., 2020). After the completion of mining in the steep coal seam working face, it can be categorized into distinct sections, namely, the compacted filling area, the fully filling area, and the partial filling area, in a bottom-to-top arrangement along the direction of the working face inclination, as illustrated in Figure 1.

In the figure, θ_1 and θ_2 represent the lower and upper breaking boundary angles of the fracture zone, respectively; L represents the length of the inclined working face of the coal seam, m; x_1 and x_2 are

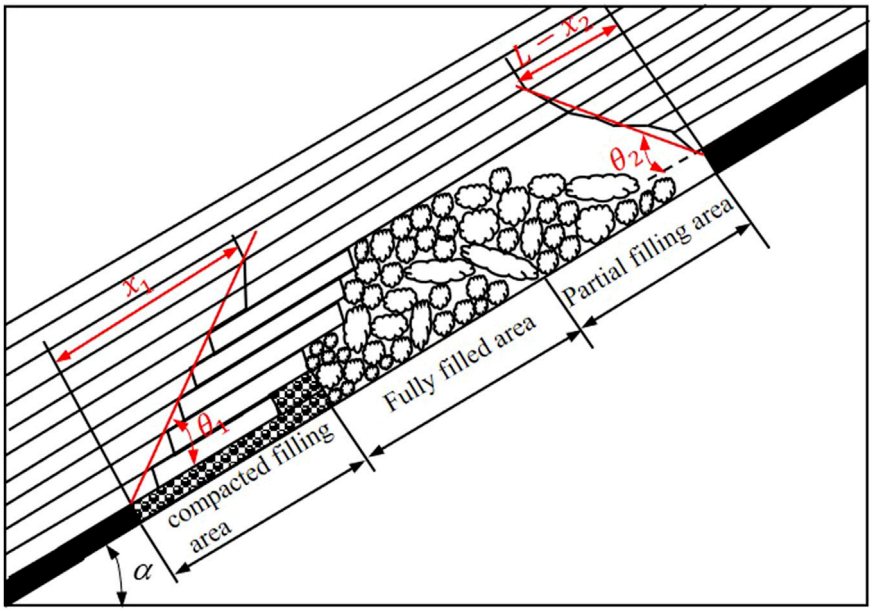


FIGURE 1
Schematic illustration of overlying strata movement during mining of steep coal seams.

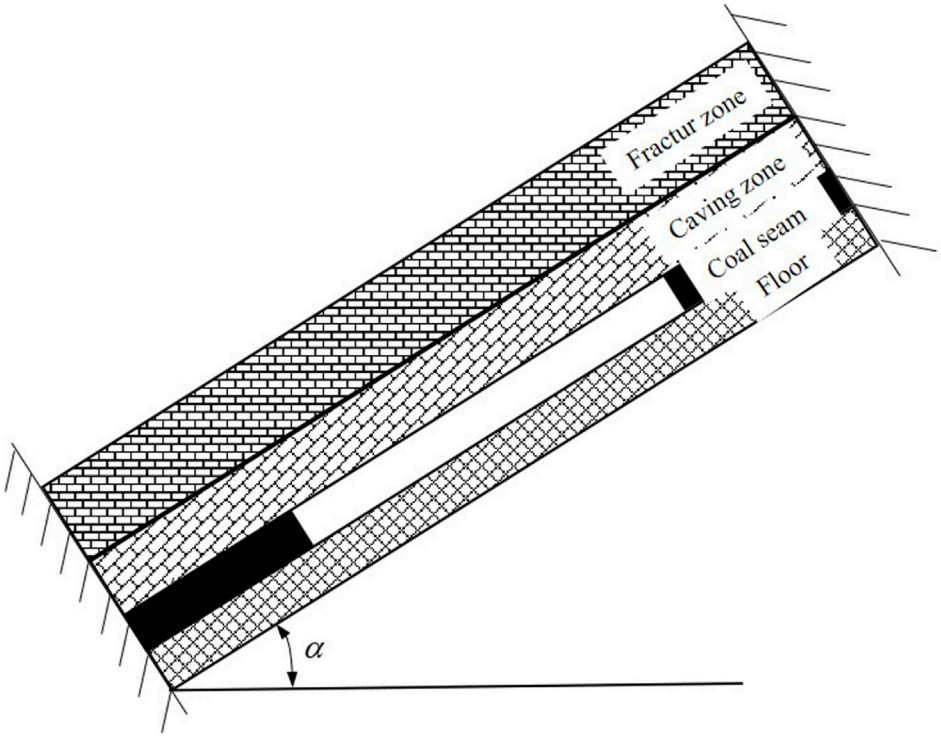


FIGURE 2
Analysis model for fracture characteristics of fracture zone.

the distances from the highest point of the fracture zone to the origin of the working face, respectively, m. The breaking boundary angles θ_1 and θ_2 of the fracture zone can be obtained by the following formula:

$$\tan\theta_1 = \frac{a}{x_1} \tag{1}$$

$$\tan\theta_2 = \frac{a}{L - x_2} \tag{2}$$

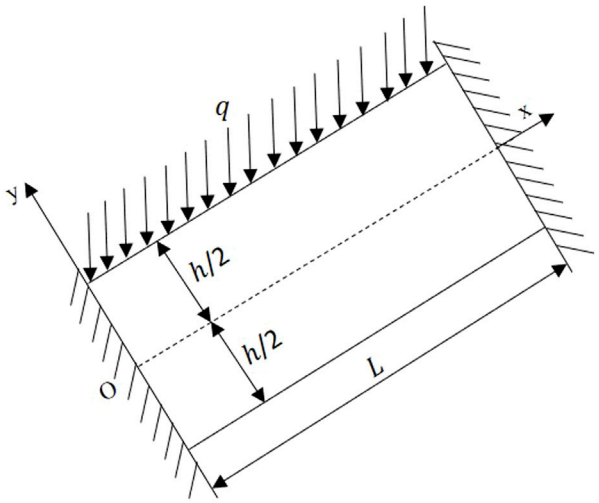


FIGURE 3
Stress analysis of rock beams in the caving zone.

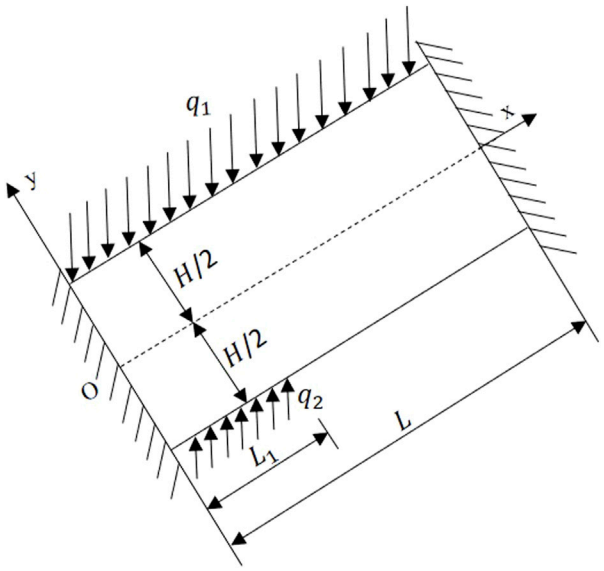


FIGURE 4
Stress analysis of rock beams in fracture zone.

Where a is the height of the fracture zone, m.

2.2 Mechanical derivation of breaking boundary angle for the fracture zone

When analyzing the fracture characteristics of the fracture zone, the overlying strata in the goaf can be simplified as a combination of two rock beams, namely, the caving zone and the fracture zone, as shown in Figure 2.

The disintegration of rock layers within the caving zone results in the filling of the goaf. It is important to note that the fully filled area offers less supporting ability to the roof in comparison to the compacted filling area. Consequently, the analysis of rock beams within the fracture zone focuses exclusively on the supporting ability by the compacted filling area for the rock beams. Reference (Wang et al., 2016) provides a calculation formula for the length of the compacted filling area in the goaf, as follows:

$$L_1 = \frac{hK_pL_T}{M} \tag{3}$$

Where L_1 is the length of the compaction area for filling in the goaf, m; h is the thickness of the rock beams for caving zone, m; K_p is the coefficient of collapse and expansion of the rock beams for caving zone; L_T is the ultimate span of the caving zone along the inclined direction, m; M is the thickness of the coal seam, m.

When calculating the ultimate span of the caving zone, the rock beam in the caving zone is considered a fixed beam structure. The load exerted by the overlying strata on the rock beam in the caving zone is simplified as a uniformly distributed load, as shown in Figure 3.

In the figure, q is the uniformly distributed load on the rock beam in the caving zone, MPa; h is the thickness of the rock beam in the caving zone, m; L is the length of the working face, m. The width of the rock beam in the caving zone is selected as a unit length of 1 m. According to the force analysis of the mechanical model of the rock beams of the caving zone in Figure 3, the maximum bending moment $M_{\max}$ and maximum tensile stress $\sigma_{\max}$ of the rock beam are obtained as follows:

$$M_{\max} = -\frac{1}{12}L^2q\cos\alpha \tag{4}$$

$$\sigma_{\max} = \frac{L^2q\cos\alpha}{2h^2} + q\sin\alpha \tag{5}$$

When the maximum tensile stress $\sigma_{\max}$ of the rock beam reaches the tensile strength limit σ_t, according to formula (5), the ultimate span of the rock beams for the caving zone can be calculated as:

$$L_T = h\sqrt{\frac{2\left(\sigma_t - q\sin\alpha\right)}{q\cos\alpha}} \tag{6}$$

Combining formulas (3) and (6), it can be obtained that the length L_1 of the compacted filling area in the goaf is:

$$L_1 = \frac{h^2K_p\sqrt{\frac{2\left(\sigma_t - q\sin\alpha\right)}{q\cos\alpha}}}{M} \tag{7}$$

The mechanical analysis of the rock beam in the fracture zone is carried out using a fixed support beam structure. The load of the overlying strata and the supporting force load of the compacted filling area are simplified as uniformly distributed loads acting on the rock beam in the fracture zone, as shown in Figure 4.

In the figure, q_1 represents the uniformly distributed load on the rock beam in the fracture zone, MPa; q_2 is the load of the support force at the bottom of the rock beam in the fracture zone, MPa; H is the thickness of the rock beam in the fracture zone, m. According to material mechanics, the bending moments q_1 and q_2 generated by M_{s1} and M_{s2} acting on the rock beam in the fracture zone are:

$$M_{s1} = -\frac{q_1\cos\alpha}{2}x^2 + \frac{Lq_1\cos\alpha}{2}x - \frac{L^2q_1\cos\alpha}{12} \tag{8}$$

$$\begin{cases} M_{s2}=\dfrac{L_1^2q_2\cos\alpha}{2L}x-\dfrac{L_1^2q_2\cos\alpha}{2}+\dfrac{L_1^2q_2\cos\alpha}{12L^2} \\ \left(6L^2-8LL_1+3L_1^2\right)\left(L_1\le x\le L\right) \\ M_{s2}=\dfrac{q_2\cos\alpha}{2}x^2-\left(q_2\cos\alpha L_1-\dfrac{q_2\cos\alpha L_1^2}{2L}\right)x+\dfrac{L_1^2q_2\cos\alpha}{12L^2} \\ \left(6L^2-8LL_1+3L_1^2\right)\left(0\le x\le L_1\right) \end{cases} \tag{9}$$

According to the principle of superposition of bending moments, the bending moment M_s at any point x on the rock beam in the fracture zone is:

$$\begin{cases} M_s=-\dfrac{q_1\cos\alpha}{2}x^2+\left(\dfrac{Lq_1\cos\alpha}{2}+\dfrac{L_1^2q_2\cos\alpha}{2L}\right)x \\ \quad -\dfrac{L^2q_1\cos\alpha+6L_1^2q_2\cos\alpha}{12} \\ \quad +\dfrac{L_1^2q_2\cos\alpha}{12L^2}\left(6L^2-8LL_1+3L_1^2\right)\ \left(L_1\le x\le L\right) \\ M_s=\left(\dfrac{q_2\cos\alpha-q_1\cos\alpha}{2}\right)x^2+\left(\dfrac{Lq_1\cos\alpha}{2}+\dfrac{L_1^2q_2\cos\alpha}{2L}-L_1q_2\cos\alpha\right)x \\ \quad -\dfrac{L^2q_1\cos\alpha}{12}+\dfrac{L_1^2q_2\cos\alpha}{12L^2}\left(6L^2-8LL_1+3L_1^2\right)\ \left(0\le x\le L_1\right) \end{cases} \tag{10}$$

According to formula (10), the tensile stress σ_x at any point x on the rock beam in the fracture zone can be obtained as:

$$\begin{cases} \sigma_x=\dfrac{3q_1\cos\alpha}{bH^2}x^2-\left(\dfrac{3Lq_1\cos\alpha}{bH^2}+\dfrac{3L_1^2q_2\cos\alpha}{bLH^2}\right)x \\ \quad +\dfrac{L^2q_1\cos\alpha+6L_1^2q_2\cos\alpha}{2H^2b} \\ \quad -\dfrac{L_1^2q_2\cos\alpha}{2L^2H^2b}\left(6L^2-8LL_1+3L_1^2\right)+\left(q_1-q_2\right)\sin\alpha\ \left(L_1\le x\le L\right) \\ \sigma_x=\dfrac{3q_1\cos\alpha-3q_2\cos\alpha}{bH^2}x^2-\dfrac{3L^2q_1\cos\alpha-6LL_1q_2\cos\alpha+3L_1^2q_2\cos\alpha}{bLH^2} \\ \quad +\dfrac{L^2q_1\cos\alpha}{2H^2b}-\dfrac{L_1^2q_2\cos\alpha}{2H^2L^2b}\left(6L^2-8LL_1+3L_1^2\right)+\left(q_1-q_2\right)\sin\alpha \\ \quad \left(0\le x\le L_1\right) \end{cases} \tag{11}$$

Where b is the ultimate span of the rock beam for the fracture zone in the strike direction, m. The calculation formula for b is:

$$b=\frac{H}{1-\mu^2}\sqrt{\frac{2\sigma_t}{q_1}\times\frac{1+\lambda^4}{1+\mu\lambda^2}} \tag{12}$$

Where H is the thickness of the rock beam in the fracture zone, m; μ is the Poisson's ratio of the rock layer, σ_t is the ultimate tensile strength of the rock layer, MPa; λ is the geometric shape coefficient of the goaf, $\lambda = b/L$.

When the tensile stress at x reaches the tensile strength limit σ_t of the rock beam for the fracture zone, the fracture failure positions x_1 and x_2 of the rock beam in the fracture zone are obtained by combining formulas (11) and (12). By incorporating it into formulas (1) and (2), the breaking boundary angles θ_1 and θ_2 of the fracture zone can be calculated. The range of fracture zone in the goaf of steep coal seams can be determined by the height a of the fracture zone and the breaking boundary angles θ_1 and θ_2 of the fracture zone.

3 Numerical simulation of the 'three zones' range within overlying strata in the goaf of steep coal seams

3.1 Model establishment and parameter settings

The discrete element method is a commonly used method for studying the 'three zones' range of overlying strata in goaf (Qin et al., 2023). 3DEC, as a numerical simulation software that uses the discrete element method to simulate the mechanical properties of discrete media, can effectively simulate the movement and fracture structure of overlying rock layers during coal mining. To verify the reliability of the theoretical formula of the fracture zone range within overlying strata in the goaf of steep coal seam, 3DEC software was used to simulate the fracture characteristics of overlying strata in steep coal seam mining. The geometric parameters and physical parameters of the model were selected from the K1 coal seam of 3,103 fully mechanized mining face in a mine in southwest China. The coal seam has a dip angle of 47° with an average thickness of 2.3 m. The inclined length of the working face is 135 m, the strike length of the working face is 1,190 m, and the buried depth of the coal seam is 550 m. To ensure calculation precision, the model was set to a length of 200 m along the strike direction of the working face and 200 m along the dip direction. Solid coal pillars, measuring 50 m in width, were retained on both sides of the working face's strike direction. The coal seam was excavated along the strike direction of the working face, covering an excavation length of 100 m. Among them, the X direction is the strike direction of the working face, and the Y direction is the tendency direction of the working face. The total size of the calculated model is: length × width × height is 200 m × 200 m × 270 m. According to the actual geological conditions of the coal seam and rock layer in the 3,103 working face, the model is divided into rock blocks of different thicknesses. At the same time, cut the rock blocks above the coal seam to form joints. After the formation of rock joints, the entire model is meshed using a tetrahedral mesh. The established model consists of 1,364,797 elements, as shown in Figure 5.

The overlying and underlying strata of the coal seams primarily consist of sandy mudstone, mudstone, limestone, and siltstone rock materials. In the graphical representation, the yellow area corresponds to sandy mudstone, the purple area to siltstone, the blue area to limestone, the gray area to mudstone, and the black area represents the coal seams. The Mohr-Coulomb model is selected for the constitutive model of the blocks in the numerical model, and the Coulomb slip model is selected for the constitutive model of the joints. Subsequently, the rock mechanics parameters of the unit grids were set. These parameters were determined based on both the actual geological conditions of the coal seam at the site and rock mechanics experiments measurements. The physical and mechanical properties of different coal rocks and joint mechanics properties are shown in Table 1 and Table 2.

Due to the height of the model not reaching the surface, the original rock stress load of 6.86 MPa was applied above the model through calculation. According to the lateral pressure coefficient of the coal seam being 1.2, the applied confining pressure was 8.4 MPa. The four sides of the model were fixed, the bottom was fixed, and the top was a free surface. Set the initial velocity of the plane at X = 0 m and X = 200m–0 m/s, the plane displacement at Y = 0 m and Y = 200 m–0m, and the plane displacement at Z = 0m–0 m.

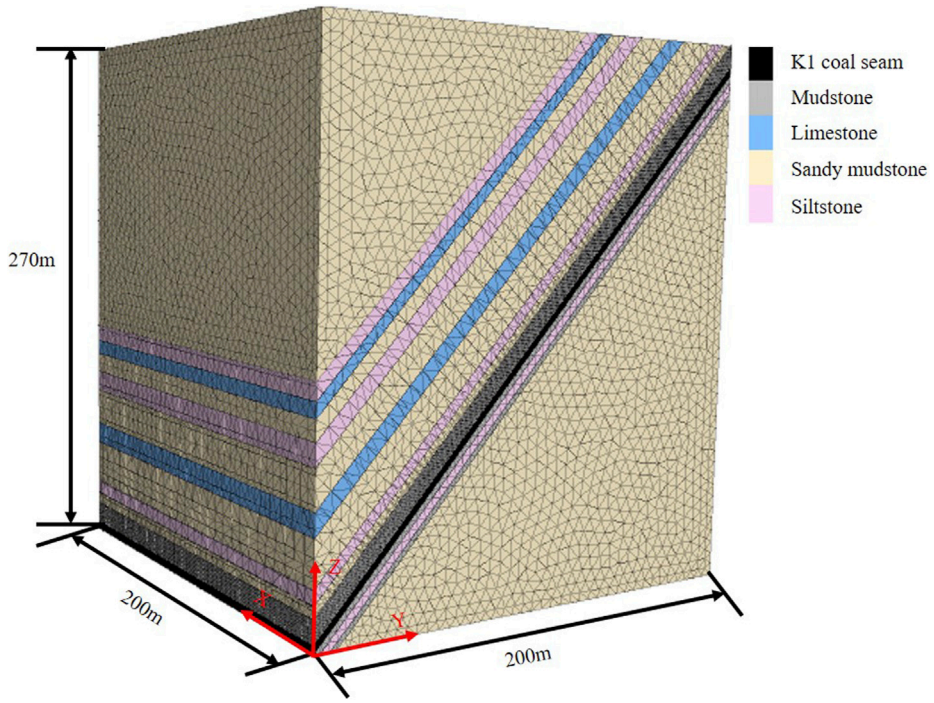


FIGURE 5
Schematic diagram of numerical model.

3.2 Analysis of numerical simulation results

After the coal seam is extracted, the overlying strata in goaf are affected by mining damage and stress disturbance of surrounding rocks, forming a certain range of caving zone and fracture zone (Tu et al., 2018; Zhang H. D. et al., 2022). Accurately predicting the range of fracture zone is great significance for the layout of gas extraction boreholes in the goaf. The structural characteristics of the 'three zones' of the overlying strata in the goaf, namely, the separation fissure above the fracture zone, are one of the methods for distinguishing the range of fracture zones. Meanwhile, due to the completion of coal seam mining, the overlying strata will exhibit varying degrees of displacement distribution in the vertical direction. By analyzing the range of different displacement zones, the range of the caving zone can be determined. Therefore, by analyzing the vertical displacement distribution of the model after excavation and combining it with the structural characteristics of the 'three zones' of the overlying strata, the range of the 'three zones' obtained from numerical simulation can be accurately determined. To facilitate the comparison of the 'three zones' range of the overlying strata in the goaf, the upper threshold in the displacement cloud map was set to 0m, and the lower threshold was set to 8 m. The parts with displacement exceeding 0 m in the cloud map are all blue, and the parts below 8 m are all red (Yang et al., 2023b). When the working face is excavated for 100m, the displacement cloud map along the inclined direction of the working face is shown in Figure 6.

From Figure 6, it can be seen that the overlying strata exhibit obvious 'three zones' structural features, namely, the caving zone, fracture zone, and the appearance of obvious separation fissure above the fracture zone. Based on this, it is determined that the green part in the figure is the caving zone, and the light blue part is the fracture zone. After analysis, the goaf caving zone is located in the mudstone above the K1 coal seam, with a height of 6.93 m. The fracture zone is located in the siltstone and sandy mudstone above the caving zone, with a height of 28.91 m. The lower breaking boundary angle of the fracture zone is 40°, and the upper breaking boundary angle is 61°. From the breaking boundary angle of the fracture zone, it can be seen that the lower breaking boundary angle is significantly smaller than the upper breaking boundary angle. This indicates that due to the influence of the dip angle, the collapsed rock blocks in the caving zone fill the lower area of the goaf. The supporting effect of the filling area causes the overall range of the fracture zone to move upwards, presenting an asymmetric feature. The numerical simulation results conform to the movement law of the overlying strata during the mining of steep coal seams.

4 On-site test of the 'three zones' range within overlying strata in goaf of steep coal seam based on microseismic monitoring

4.1 Microseismic monitoring technology for fracture of overlying strata in goaf

Coal rock is a stress medium, under the influence of coal seam mining, generates elastic waves when the overlying strata rupture (Cui et al., 2019b; Hou et al., 2020). These elastic waves propagate within the coal rock mass, constituting microseismic events. Based

TABLE 1 Physical and mechanical parameters of different coal rocks.

Rock name	Thickness (m)	Density (kg/m^3)	Elastic modulus (GPa)	Poisson's ratio	Cohesion (MPa)	Internal friction angle (°)	Tensile strength (MPa)
Sandy mudstone	—	2,570	11.5	0.23	2.4	40	2.6
Siltstone	4.88	2,770	33.5	0.21	3.3	42	1.2
Limestone	4.54	2,730	34	0.21	3.2	39	1.3
Sandy mudstone	5.45	2,570	11.5	0.23	2.4	40	2.6
Siltstone	6.47	2,770	33.5	0.21	3.3	42	1.2
Sandy mudstone	10.96	2,570	11.5	0.23	2.4	40	2.6
Limestone	6.37	2,730	34	0.21	3.2	39	1.3
Sandy mudstone	13.2	2,570	11.5	0.23	2.4	40	2.6
Siltstone	4.45	2,770	33.5	0.21	3.3	42	1.2
Sandy mudstone	3.37	2,570	11.5	0.23	2.4	40	2.6
Mudstone	6.65	2,470	9.7	0.26	1.5	30	0.5
K1 Coal seam	2.3	1,390	2.5	0.3	0.6	24	3.5
Mudstone	2.2	2,470	9.7	0.26	1.5	30	0.5
Siltstone	5.2	2,770	33.5	0.21	3.3	42	1.2
Mudstone	7.2	2,470	9.7	0.26	1.5	30	0.5
Sandy mudstone	—	2,570	11.5	0.23	2.4	40	2.6

TABLE 2 Mechanical parameters of different coal rock joints.

Joint type	Normal stiffness (GPa)	Tangential stiffness (GPa)	Cohesion (Mpa)	Internal friction angle (°)
Sandy mudstone	6.7	7.1	1	20
Siltstone	8.4	8.1	1.1	25
Mudstone	6.6	7.1	1.5	10
Limestone	9.8	7.7	6.72	35

on microseismic monitoring systems, these elastic waves can be identified, captured, and collected. Processing and analyzing elastic waves can locate the location of microseismic events in three-dimensional space. By using the P-wave (longitudinal wave) localization algorithm, the time, location, energy, and amplitude of microseismic events can be determined. Subsequently, based on the spatial distribution of microseismic events, the distribution status, evolution process, and trend of fractures can be analysed. Then the 'three zones' range of overlying strata in the goaf can be determined. The principle of microseismic monitoring is shown in Figure 7.

4.2 Arrangement of microseismic monitoring

The key components of a microseismic monitoring system include sensors, collectors, and hosts. Sensors can identify and capture the elastic waves generated by coal and rock mass fractures. The acquisition instrument can collect and record the captured microseismic signals. The host can view, analyze, and process the collected microseismic signals. To ensure the effectiveness of monitoring, a total of 4 collection instruments and 12 sensors are arranged in combination with the mine tunnel system. Two acquisition devices and six sensors are respectively arranged in the 3,103 haulage roadway and the 3,103 return air roadway, with each acquisition device equipped with three sensors. The position of the first arranged sensor is 50 m ahead of the working face, with a sensor spacing of 50m, as shown in Figure 8.

4.3 Analysis of microseismic monitoring results

After the completion of coal seam mining in the working face, microseismic data recorded by the four acquisition instruments is

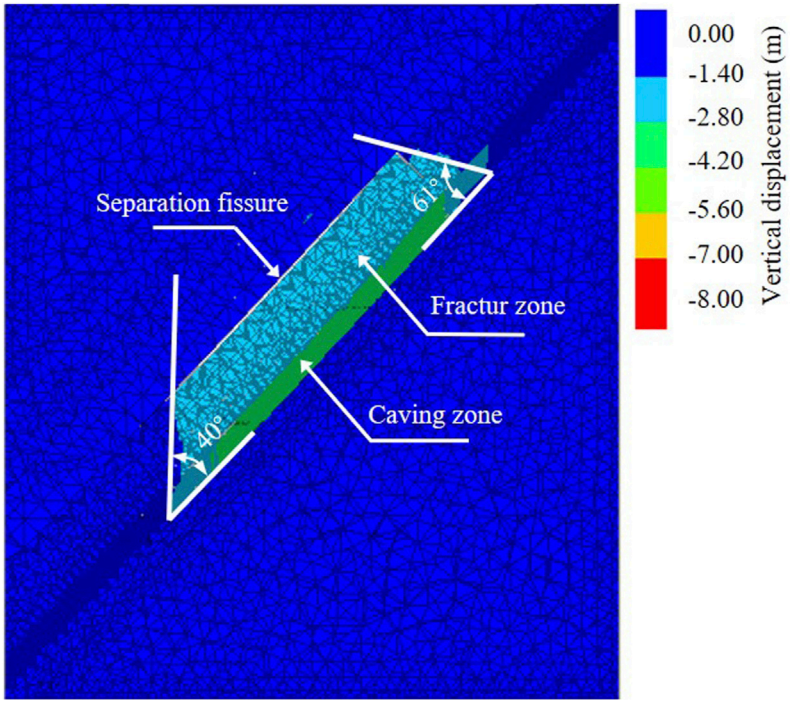


FIGURE 6
Displacement cloud map of the inclined direction during 100 m excavation of the working face.

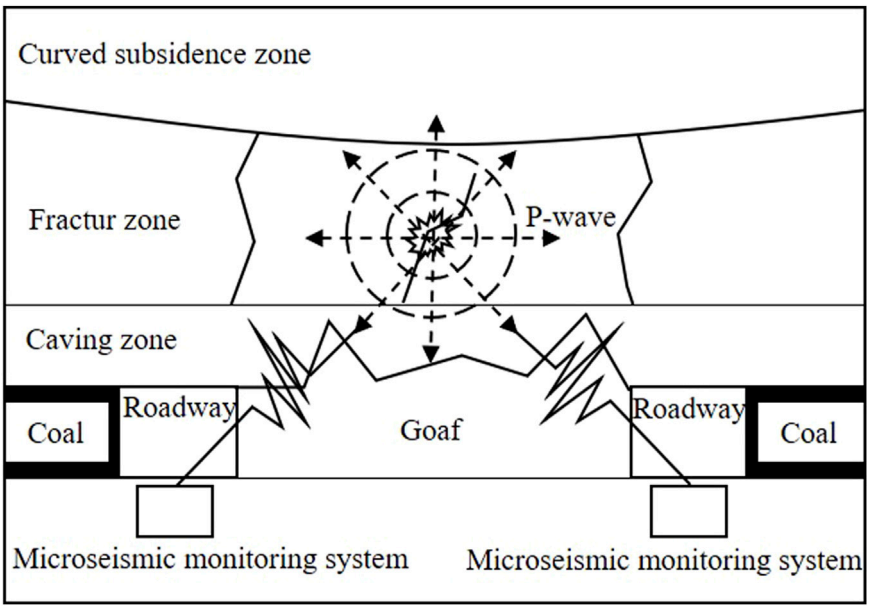


FIGURE 7
Schematic diagram of microseismic monitoring principle.

extracted. The specific acquisition instrument used is the YTZ-3 (B) type microseismic monitor. Since each acquisition instrument simultaneously records microseismic signals captured by three sensors, the microseismic signals from the same sensor are considerably dispersed. To facilitate the analysis and processing of microseismic data recorded by each sensor, dedicated YTZ-3 data decoding software is employed to decode this information. Throughout the coal seam mining process, various types of noise will be generated, leading the microseismic monitoring system to collect a considerable amount of invalid data. During practical

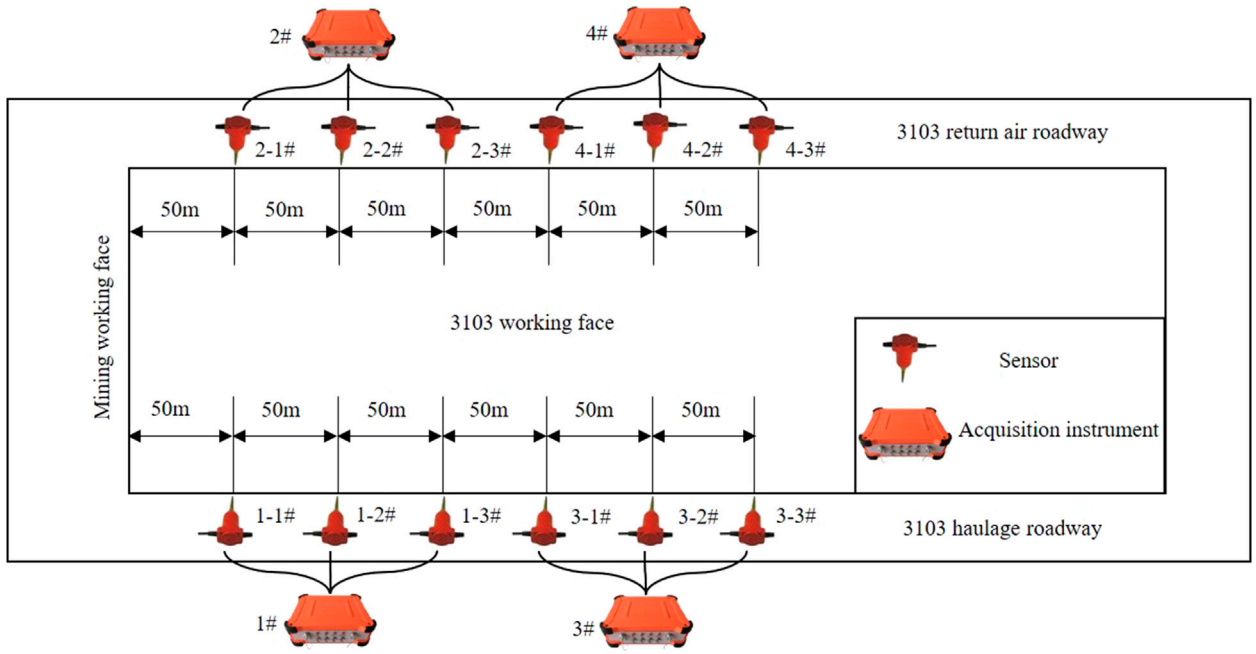


FIGURE 8
Layout of microseismic monitoring in the working face.

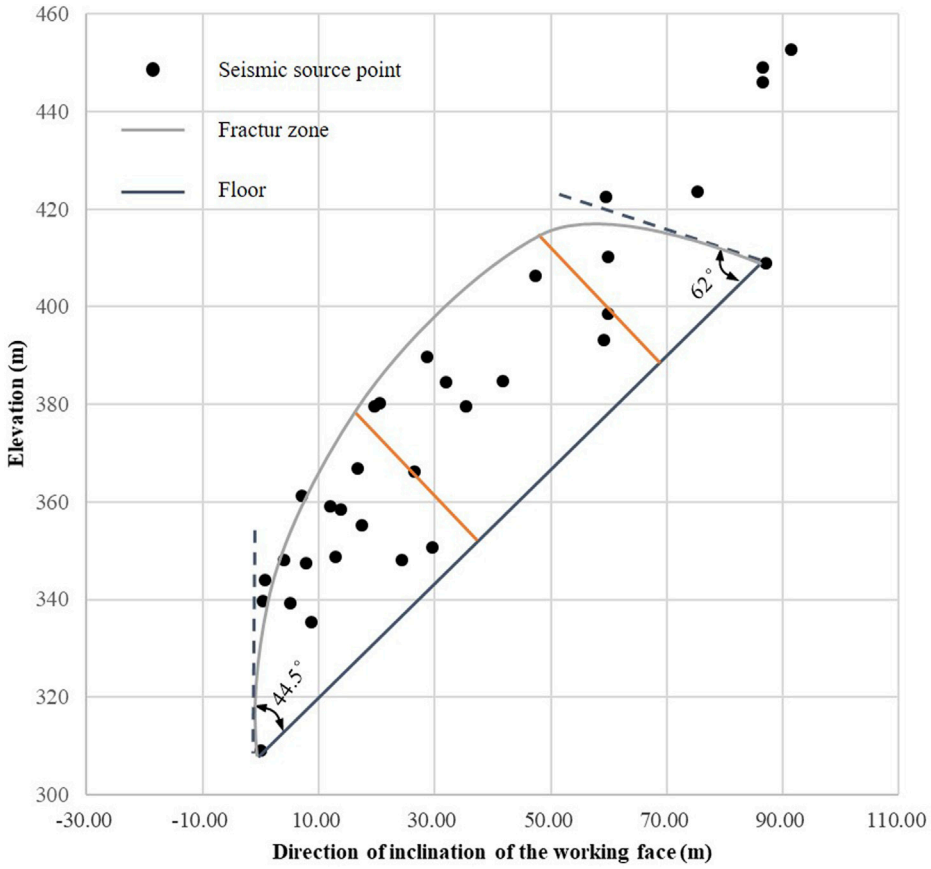


FIGURE 9
Seismic source distribution of microseisms in the inclined direction of coal seams.

TABLE 3 Calculation results of the 'three zones' range of different methods.

The "three zones " range	Numerical simulation	Theoretical calculation	Field measurement
Height of caving zone (m)	6.93	7.7	6.8
Height of fracture zone (m)	28.91	31.6	34.2
Lower breaking boundary angle of fracture zone (°)	40	42.7	44.5
Upper breaking boundary angle of fracture zone (°)	61	57.5	62

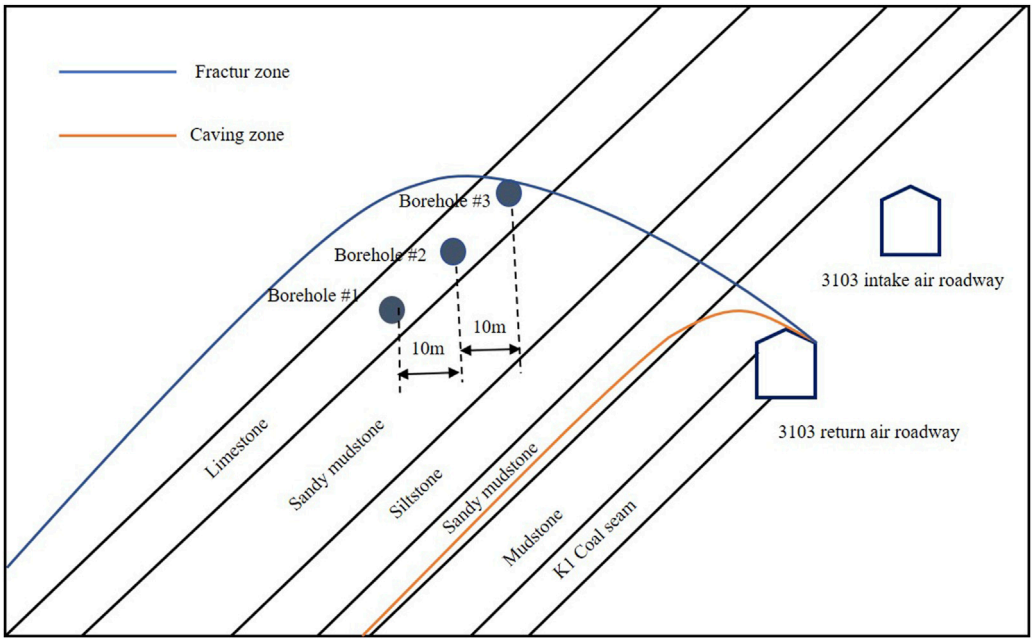


FIGURE 10
Section diagram of inclined direction of boreholes arrangement in the 3,103 working face.

testing, thousands of event data points were identified in each work shift. To obtain effective data more accurately, manual identification and selection of microseismic data captured by each sensor are carried out. Calculate the position coordinates and energy values of the seismic source using the YTZ-3 system software for manually identified and selected microseismic data. The vertical distance from the seismic source point to the coal seam and the projected coordinate on the inclined section can be calculated from the position coordinates of the seismic source, as shown in Figure 9.

From the figure, it can be seen that the maximum height of a typical microseismic event is 34.2m, the minimum height is 6.8m, and the average height is 23.6 m. Therefore, the height of the caving zone is 6.8m, and the height of the fracture zone is 34.2 m. After measurement, the lower breaking boundary angle of the fracture zone is 44.5°, and the upper breaking boundary angle is 62°.

5 Analysis and discussion

According to the coal and rock parameters of the 3,103 fully mechanized mining face, the height of the caving zone is calculated by empirical formula (13) to be 5.5–9.9m, with an average of 7.7 m. Formula (14) calculates that the height of the fracture zone is 26.0–37.2m, with an average of 31.6 m.

$$H_M = \frac{100\sum M}{4.7\sum M + 19} \pm 2.2 \tag{13}$$

$$H_L = \frac{100\sum M}{1.6\sum M + 3.6} \pm 5.6 \tag{14}$$

Where H_M is the height of the caving zone, m; H_L is the height of the fracture zone, m; $\sum M$ is the thickness of the coal seam, m.

From this, the fracture positions x_1 = 34.2 m and x_2 = 115 m of the rock beam in the fracture zone are obtained through formula (11). By incorporating it into formulas (1) and (2), the breaking boundary angles of the fracture zone are calculated to be θ_1 = 42.7° and θ_2 = 57.5°. Compare and analyze the calculation results of the three methods, as shown in Table 3.

From Table 3, it can be seen that the results of the 'three zones' range of the overlying strata in the goaf of the steep coal seam calculated by the three methods are in good agreement, and the differences are all within 5. This indicates that the theoretical calculation formula derived in this article can accurately calculate

the 'three zones' range of the overlying strata in the goaf of steep coal seams. From the research results of the three methods, it can be found that due to the influence of the coal seam dip angle, the lower breaking boundary angle of the fracture zone of the overlying strata in the goaf is smaller than the upper breaking boundary angle. Compared with the 'three zones' within overlying strata in the goaf of horizontal coal seams, the overall upward movement of the fracture zone in steep coal seams presents an asymmetric feature. The final determination is that the height of the caving zone in the 3,103 fully mechanized mining face was from 6.93 m to 7.7m, the height of the fracture zone was from 28.91 m to 34.2m, the lower breaking boundary angle of the fracture zone was from 40° to 44.5°, and the upper breaking boundary angle of the fracture zone was from 57.5° to 62°. According to this scope, three strike long boreholes were constructed in the 3,103 working face for gas extraction, as shown in Figure 10.

The borehole spacing is 10m, the aperture is 120 mm and they are all located above the 3,103 return air roadway. During the entire extraction process, the average gas extraction concentration was 53.55% and the average gas extraction amount was 5.37 m^3/min. After extraction, the gas concentration in the upper corner of the return air roadway was about 0.4%, and the gas concentration in the return air roadway was about 0.3%, which achieves a good gas prevention and control effect. The research methods and results can provide guidance and reference for the prediction of the 'three zones' range of overlying strata in goaf of similar coal seams.

On the other hand, the theoretical calculation of the upper breaking boundary angle of the fracture zone on the overlying strata of steep coal seam will be slightly lower than the numerical simulation and on-site measurement values. This is because in the theoretical derivation process, to simplify the calculation formula, only the support of the compacted filling area for the rock beam of the fracture zone was considered. In fact, the fully filled area also has a certain support for the rock beam of the fracture zone. From formula (11), it can be seen that the 'three zones' range of steep coal seams is mainly limited by various factors such as the length of the filling area in the lower part of the goaf, changes in roof lithology, coal seam dip angle, coal seam thickness, working face length, overburden load, etc. When all conditions remain unchanged and only increase the value of L_1, the upper breaking boundary angle of the fracture zone obtained will increase. In the future, it is possible to further refine theoretical calculation formulas.

6 Conclusion

To study the 'three zones' range within overlying strata in the goaf of steep coal seams, a formula for calculating the breaking boundary angle within overlying strata fracture zone in the goaf of steep coal seams was derived based on the movement law of overlying strata during mining. Taking the 3,103 fully mechanized mining face of a certain mine in southwestern China as the background, the 'three zones' range within overlying strata in the goaf was studied through three methods: theoretical calculation, numerical simulation, and on-site measurement based on microseismic monitoring technology. Draw the following conclusion:

(1) The derived formula for calculating the breaking boundary angle of the overlying rock strata in the goaf of steep coal seams can effectively quantify the 'three zones' range of the overlying rock strata in the goaf of steep coal seams.
(2) From the theoretical formula, it can be seen that the scope of the 'three zones' in steep coal seams is mainly limited by various factors such as the length of the filling area in the lower part of the goaf, changes in roof lithology, dip angle of the coal seam, thickness of the coal seam, length of the working face, and overburden load. Among them, the longer the filling area, the larger the upper breaking boundary angle of the fracture zone and the smaller the lower breaking boundary angle.
(3) Based on the research results of three methods, the height of the caving zone in the 3,103 fully mechanized mining face is from 6.93 m to 7.7m, the height of the fracture zone is from 28.91 m to 34.2m, the lower boundary of the fracture zone is from 40° to 44.5°, and the upper boundary of the fracture zone is from 57.7° to 62°. The research methods and results can provide guidance and reference for the prediction of the 'three zones' range of overlying strata in goaf of similar coal seams.

Data availability statement

The original contributions presented in the study are included in the article/Supplementary Material, further inquiries can be directed to the corresponding author.

Author contributions

SY: Conceptualization, Formal Analysis, Funding acquisition, Methodology, Project administration, Supervision, Validation, Writing–original draft, Writing–review and editing. NX: Formal Analysis, Investigation, Methodology, Validation, Visualization, Writing–original draft, Writing–review and editing. HL: Investigation, Writing–original draft. XZ: Formal Analysis, Writing–original draft. SM: Formal Analysis, Writing–original draft.

Funding

The author(s) declare financial support was received for the research, authorship, and/or publication of this article. This study was funded by the Open Fund of the State Key Laboratory of Gas Disaster Detecting, Preventing and Emergency Controlling, No. 2022SKLKF05.

Acknowledgments

First of all, we acknowledge the editors and reviewers for their valuable comments; secondly, we are grateful for the help of the fund from the State Key Laboratory of Gas Disaster Detecting, Preventing and Emergency Controlling; finally, we appreciate the authors of all references for their achievements that bring us new ideas.

Conflict of interest

Author HL was employed by Shaanxi Yanchang Petroleum Yulin Kekegai Coal Industry Co Ltd.

The remaining authors declare that the research was conducted in the absence of any commercial or financial relationships that could be construed as a potential conflict of interest.

Publisher's note

All claims expressed in this article are solely those of the authors and do not necessarily represent those of their affiliated organizations, or those of the publisher, the editors and the reviewers. Any product that may be evaluated in this article, or claim that may be made by its manufacturer, is not guaranteed or endorsed by the publisher.

References

Chen, Y., Wang, Z. W., Hui, Q. J., Zhu, Z. J., Sun, D. Q., Chen, Y., et al. (2022). Overlying rock movement and mining pressure in a fully mechanized caving face with a large dip angle. *Front. Earth Sci.* 10. doi:10.3389/feart.2022.963973

Cheng, G. W., Ma, T. H., Tang, C. A., Liu, H. Y., and Wang, S. J. (2017). A zoning model for coal mining - induced strata movement based on microseismic monitoring. *Int. J. Rock Mech. Min. Sci.* 94, 123–138. doi:10.1016/j.ijrmms.2017.03.001

Cui, F., Yang, Y. B., Lai, X. P., and Cao, J. T. (2019b). Similar material simulation experimental study on rockbursts induced by key stratum breaking based on microseismic monitoring. *Chin. J. Rock Mech. Eng.* 38 (04), 803–814. doi:10.13722/j.cnki.jrme.2018.1423

Cui, F., Zhang, T. H., Lai, X. P., Cao, J. T., and Shan, P. F. (2019a). Study on the evolution law of overburden breaking angle under repeated mining and the application of roof pressure relief. *Energies* 12 (23), 4513. doi:10.3390/en12234513

Hou, E. K., Fan, J. C., Xie, X. S., Long, T. W., Zhang, H. L., Wang, J. H., et al. (2020). Development characteristics of water-conducting fractured zone in deep coal seam based on microseismic monitoring. *Coal Geol. Explor.* 48 (05), 89–96. doi:10.3969/j.issn.1001-1986.2020.05.011

Hu, X. Y., and Cai, J. L. (2020). Research on the first breaking mechanism of the main roof of coal seam with high dip angle. *Adv. Civ. Eng.* 2020, 1–8. doi:10.1155/2020/8820625

Huang, L. K., Dontsov, E., Fu, H. F., Lei, Y., Weng, D. W., and Zhang, F. S. (2022). Hydraulic fracture height growth in layered rocks: perspective from DEM simulation of different propagation regimes. *Int. J. Solids Struct.* 238, 111395. doi:10.1016/j.ijsolstr.2021.111395

Huang, L. K., Tan, J., Fu, H. F., Liu, J. J., Chen, X. Y., Liao, X. C., et al. (2023). The non-plane initiation and propagation mechanism of multiple hydraulic fractures in tight reservoirs considering stress shadow effects. *Eng. Fract. Mech.* 2023, 109570. doi:10.1016/j.engfracmech.2023.109570

Huang, W. P., Li, C., Zhang, L. W., Yuan, Q., Zheng, Y. S., and Liu, Y. (2018). *In situ* identification of water-permeable fractured zone in overlying composite strata. *Int. J. Rock Mech. Min. Sci.* 105, 85–97. doi:10.1016/j.ijrmms.2018.03.013

Lai, X. P., Dai, J. J., and Li, C. (2020). Analysis on hazard characteristics of overburden structure in steeply inclined coal seam. *J. China Coal Soc.* 45 (01), 122–130. doi:10.13225/j.cnki.jccs.YG19.1405

Lai, X. P., Zhang, X. D., Shan, P. F., Cui, F., Liu, B. W., and Bai, R. (2021). Study on development law of water-conducting fractures in overlying strata of three soft coal seam mining under thick loose layers. *Chin. J. Rock Mech. Eng.* 40, 1739–1750. doi:10.13722/j.cnki.jrme.2021.0210

Liu, S., Yang, K., Tang, C. N., and Chi, X. L. (2020). Rupture and migration law of disturbed overburden during slicing mining of steeply dipping thick coal seam. *Adv. Civ. Eng.* 2020, 11. doi:10.1155/2020/8863547

Liu, Y., Yuan, S. C., Yang, B. B., Liu, J. W., and Ye, Z. Y. (2019). Predicting the height of the water-conducting fractured zone using multiple regression analysis and GIS. *Environ. Earth Sci.* 78 (14), 422. doi:10.1007/s12665-019-8429-3

Luo, H. R., Xie, J., Huang, L. K., Wu, J. F., Shi, X. W., Bai, Y. S., et al. (2022). Multiscale sensitivity analysis of hydraulic fracturing parameters based on dimensionless analysis method. *Lithosphere* 2022, 2022. doi:10.2113/2022/9708300

Ma, R., Lai, X. P., Cao, J. T., and Gao, J. Q. (2013). Similar simulation on strata movement of gob in shallow-contiguous seams. *J. Xi'an Univ. Sci. Technol.* 33 (03), 249–253. doi:10.13800/j.cnki.xakjdxxb.2013.03.021

Qin, S., Lin, H. F., Yang, S. G., and Wei, Z. Y. (2023). A mathematical model for parameter setting in discrete element numerical simulation. *Int. J. Coal Sci. Technol.* 10 (1), 87. doi:10.1007/s40789-023-00644-y

Tu, M., Cai, J. L., Zhang, H. L., and Rong, C. X. (2018). Safety mining technology of coal seams in weathered zone based on ground J-type pregrouting reinforcement. *Adv. Civ. Eng.* 2018, 1–10. doi:10.1155/2018/3210420

Wang, F. T., Zhang, C., Zhang, X. G., and Song, Q. (2015). Overlying strata movement rules and safety mining technology for the shallow depth seam proximity beneath a room mining goaf. *Int. J. Min. Sci. Technol.* 25 (1), 139–143. doi:10.1016/j.ijmst.2014.12.007

Wang, H. B., Zhang, Y., Pang, Y. H., and Jia, W. (2022). Prediction model of the height of fractured zone in abandoned goaf and its application. *Rock Soil Mech.* 43 (04), 1073–1082. doi:10.16285/j.rsm.2021.1183

Wang, H. W., Wu, Y. P., Xie, P. S., Li, Y. J., and Cao, P. P. (2016). The quantitative filling characteristics of the waste rock and roof movement mechanism in the steeply inclined working face. *J. China Univ. Min. Technol.* 45 (05), 886–892. doi:10.13247/j.cnki.jcumt.000561

Xu, B., Jiang, J. Q., Dai, J., and Zheng, P. Q. (2018). Mechanical derivation and experimental simulation of breaking angle of key strata in overlying strata. *J. China Coal Soc.* 43 (3), 599–606. doi:10.13225/j.cnki.jccs.2017.1346

Xu, Z. M., Han, Y. H., Chen, T. C., Chen, G., Huan, B. C., Zhao, R. Q., et al. (2023). Mining-induced overburden failure and height prediction in Jurassic weakly cemented roof. *J. Eng. Geol.* 31 (4), 1474–1485. doi:10.13544/j.cnki.jeg.2023-0239

Yang, K., Wei, Z., Chi, X. L., Gao, A. S., and Fu, Q. (2021). Fracture criterion of basic roof deformation in fully mechanized mining with large dip angle. *Energy Explor. Exploitation* 39 (3), 886–902. doi:10.1177/0144598720986628

Yang, S. G., Liu, H. X., Huang, R. M., and Li, J. L. (2023a). Investigation on the height of fracture zone in goaf of steep coal seam based on microseismic monitoring. *J. Phys. Conf. Ser.* 2562 (1), 012036. doi:10.1088/1742-6596/2562/1/012036

Yang, S. G., Xu, N., and Zhang, X. F. (2023b). Numerical simulation study on the evolution law of stress and crack in coal seam hydraulic fracturing. *Sustainability* 15 (14), 11351. doi:10.3390/su151411351

Yao, Q., Feng, T., and Liao, Z. (2017). Damage characteristics and movement of inclined strata with sublevel filling along the strike in the steep seam. *J. China Coal Soc.* 42 (12), 3096–3105. doi:10.13225/j.cnki.jccs.2017.0509

Ye, Q., Wang, G., Jia, Z. Z., Zheng, C. S., and Wang, W. J. (2018). Similarity simulation of mining-crack-evolution characteristics of overburden strata in deep coal mining with large dip. *J. Petroleum Sci. Eng.* 165, 477–487. doi:10.1016/j.petrol.2018.02.044

Ye, Q., Wang, W. J., Wang, G., and Jia, Z. Z. (2017). Numerical simulation on tendency mining fracture evolution characteristics of overlying strata and coal seams above working face with large inclination angle and mining depth. *Arabian J. geosciences* 10 (4), 82–15. doi:10.1007/s12517-017-2856-9

Zhang, H. D., Hu, G. Z., and Zhao, G. C. (2022b). Research on the movement law of roof structure in large-inclined coal seam working face: a case study in Liu.Pan.Shui. mining area. *Shock Vib.* 2022, 1–9. doi:10.1155/2022/6328851

Zhang, J., Li, X., Qin, Q., Wang, Y., and Gao, X. (2023). Study on overlying strata movement patterns and mechanisms in super-large mining height stopes. *Bull. Eng. Geol. Environ.* 82 (4), 142. doi:10.1007/s10064-023-03185-5

Zhang, Q. M., Wang, E. Y., Li, Z. H., Wang, H., and Xue, Z. Z. (2022a). Control of directional long borehole on gas drainage and optimal design: case study. *J. Nat. Gas Sci. Eng.* 107, 104766. doi:10.1016/j.jngse.2022.104766

Zhao, P. X., Chang, Z. C., Li, S. G., Zhuo, R. S., Lin, H. F., and Jin, S. K. (2023). Research and application of directional drilling sub area extraction in thick coal seam goaf. *China Saf. Sci. J.* 33 (1), 70. doi:10.16265/j.cnki.issn1003-3033.2023.01.0416

Zheng, Y. X., He, R., Huang, L. K., Bai, Y. S., Wang, C., Chen, W. H., et al. (2022). Exploring the effect of engineering parameters on the penetration of hydraulic fractures through bedding planes in different propagation regimes. *Comput. Geotechnics* 2022, 104736. doi:10.1016/j.compgeo.2022.104736

Zhou, Y., and Yu, X. Y. (2022). Study of the evolution of water-conducting fracture zones in overlying rock of a fully mechanized caving face in gently inclined extra-thick coal seams. *Appl. Sciences-Basel* 12 (18), 9057. doi:10.3390/app12189057

Zhu, H. Q., Fang, S. H., Huo, Y. J., Guo, J. L., Wu, Y., and Hu, L. T. (2020). Study of the dynamic development law of overburden breakage on mining faces. *Sci. Rep.* 10 (1), 6555. doi:10.1038/s41598-020-63526-2

frontiers | Frontiers in Energy Research

TYPE Original Research
PUBLISHED 12 January 2024
DOI 10.3389/fenrg.2023.1337069

Check for updates

OPEN ACCESS

EDITED BY
Peng Tan,
CNPC Engineering Technology R&D Company Limited, China

REVIEWED BY
Zaile Zhou,
Yangtze University, China
Dawei Zhou,
China University of Petroleum, Beijing, China

*CORRESPONDENCE
Yitao Huang,
huangyitao518@163.com

RECEIVED 12 November 2023
ACCEPTED 27 December 2023
PUBLISHED 12 January 2024

CITATION
Chen X, Huang Y, Li Y and Shen C (2024), Numerical simulation study on evolution law of three-dimensional fracture network in unconventional reservoirs.
Front. Energy Res. 11:1337069.
doi: 10.3389/fenrg.2023.1337069

COPYRIGHT
© 2024 Chen, Huang, Li and Shen. This is an open-access article distributed under the terms of the Creative Commons Attribution License (CC BY). The use, distribution or reproduction in other forums is permitted, provided the original author(s) and the copyright owner(s) are credited and that the original publication in this journal is cited, in accordance with accepted academic practice. No use, distribution or reproduction is permitted which does not comply with these terms.

Numerical simulation study on evolution law of three-dimensional fracture network in unconventional reservoirs

Xiyu Chen[1], Yitao Huang[1]*, Yongming Li[1] and Cheng Shen[2]

[1]State Key Laboratory of Oil and Gas Reservoir Geology and Development Engineering, Southwest Petroleum University, Chengdu, Sichuan, China, [2]PetroChina Southwest Oil and Gasfield Company, Chengdu, Sichuan, China

It has become a consensus that large-scale hydraulic fracturing is adopted to achieve the stimulation of unconventional oil and gas reservoir. The complex fracture network formed by fracturing is closely related to the effect of reservoir stimulation, which has extremely complicated evolution process. Therefore, it is necessary to study the evolution law of fracture network in large-scale hydraulic fracturing of unconventional reservoirs. In this article, the geological engineering parameters of horizontal well H in shale gas reservoir in southern Sichuan are taken as an example, a three-dimensional fracture network expansion model is established based on the boundary element method and finite volume method, and the simulation of the complex fracture network in a whole well section is carried out to analyze the evolution law of reservoir fracture network under different geological and engineering parameters. The results show that the horizontal stress field distribution has a significant effect on fracture geometric form. Hydraulic fractures in reservoirs with larger horizontal stress difference have stronger directivity, while the horizontal wellbore tends to obtain better reservoir stimulation results when it is parallel to the minimum horizontal principal stress setting. The conjugated natural fracture developed in the reservoir inhibits the hydraulic expansion fractures in both directions. Although it increases the complexity of the fractures, it is not necessarily conducive to improving the reservoir stimulation effectiveness. The lower the strength of natural fracture is, the more complex the fracture geometric form becomes, and the smaller the stimulated reservoir volume is. Correspondingly, the higher the strength of natural fracture is, the simpler the fracture geometric form becomes, and the larger the stimulated reservoir volume is. Suitable fracturing construction displacement can not only contribute to form a more complex fracture distribution, but also help to obtain a larger stimulated reservoir volume. The optimal construction displacement ranges from 10 to 14 m^3/min. Low viscosity fracturing fluids are suitable for the formation of long-narrow fractures and able to connect with the remote reservoir and form complex fracture networks. Lower viscosity fluids can be used to achieve better reservoir stimulation effectiveness when sand-carrying capacity is met.

KEYWORDS

unconventional reservoir, fracture network, numerical simulation, geological factors, engineering factors

1 Introduction

With the rapid development of global economy, the demand for oil and gas resources as the necessity of industry is increasing day by day (China Business Industry Research Institute, 2022). The shortage of conventional oil and gas resources highlights the rich reserves of unconventional oil and gas resources, which is worthy to explore and develop. Efficient development and utilization of oil and gas resources are of strategic significance to alleviate the imbalance between the supply and demand of global oil and gas (BP, 2014; Zou et al., 2014a; HARTENERGY, 2015; Wang et al., 2016). Unconventional oil and gas resources mainly include shale gas, shale oil, tight sandstone gas, coalbed methane and super heavy oil, etc (National Resources Canada; BIEWICK, 2014; KUUSKRAA et al., 2013-06; Wang et al., 2017; Develop, 2021; Fletcher et al., 2012). Among them, the amount of unconventional oil *in-situ* resources is about 720×10^8t, and the amount of available resources is about 210×10^8t, which is approximately equivalent to that of conventional oil resources. The amount of unconventional natural gas *in-situ* resources is about 320×10^{12}m^3, of which tight gas, coalbed methane and shale gas are three to four times the amount of available conventional natural gas resources. Till now, unconventional oil and gas resources have already become a new popular object in the territory of oil and gas exploration and development (The Unconventional Oil Subgroup of the Resources & Supply Task Group, 2011; JIA et al., 2012; COCCO and ERNANDEZ, 2013; Zou et al., 2014b).

Compared with conventional oil and gas reservoirs, the unconventional ones are characterized by low porosity (<10%) and low permeability (less than 0.1mD), and usually require large-scale hydraulic fracturing to produce industrial oil flow (Mayerhofer et al., 2008; East et al., 2011; Loucks et al., 2012; Valenza et al., 2013; Loucks et al., 2017; Chen et al., 2018). Previous studies have shown that the hydraulic fracturing of unconventional oil and gas reservoirs forms a complex fracture network different from conventional double plane fractures (Chen et al., 2017; Chen et al., 2019; Huang et al., 2020; Tan et al., 2020; Huang et al., 2023a; Huang et al., 2023b). In the process of stimulateing the fracturing unconventional reservoirs, hydraulic fractures contact with natural fractures in the reservoir, allowing them to reconnect with each other, and promoting the efficient flow of fluids from formation towards the wellbore (DETOURNAY, 2004; CHEN et al., 2017; Wang et al., 2018; Xie et al., 2020; Hou et al., 2021). Further research finds that the reservoir stimulation effectiveness is positively correlated with reservoir SRV (stimulated reservoir volume). How to form complex fracture network with high permeability and increase fracture-controlled volume through large-scale hydraulic fracturing has become the focus and the difficulty of current research. In order to explore the evolution process of complex fractures in unconventional reservoirs, some experts and scholars have carried out true triaxial hydraulic fracturing experiments by using outcrop rock samples or concrete preset rock samples. They conducted researches on fracture propagation law under the influence of different geological and engineering factors, and analyzed the influence of natural fractures on hydraulic fracture propagation during fracturing (Tan et al., 2023). However, physical experiments often fail to meet the economic, timeliness, and repeatability requirements of related research. Moreover, the size effect of rock samples can also affect the accuracy of research results. In this regard, scholars have built numerical models based on experimental research results. The most common methods for numerical models are FEM (Finite Element Method) (Hunsweck et al., 2013; Lecampion et al., 2017), XFEM (Extended Finite Element Method) (BELYTSCHKO, 1999; MOES and BELYTSCHKO, 1999), BEM (Boundary Element Method) (Chen et al., 2019), DDM (Displacement Discontinuous Method) (Yamamoto et al., 1999; Kresse and Weng), and DEM (Distinct Element Method) (Hamidi and Mortazavi, 2012; Huang et al., 2019; Huang et al., 2022; Huang et al., 2023c), etc, each with its own unique characteristics, sphere of application, advantages and disadvantages (as shown in Table 1). Existing numerical researches focus a lot on the mechanical mechanism of the interaction between hydraulic fractures and natural fractures, with few fully coupled fluid flow mechanism and proppant migration mechanisms studied, as well lack of field-scale simulation analysis and understanding.

This article selects the well H in southern Sichuan and, based on previous research results, establishes a three-dimensional fracture network expansion model according to BEM (Boundary Element Method) and FVM (Finite Volume Method). It conducts field scale simulation of complex fracture networks in the whole well section, analyzes the evolution patterns of reservoir fracture networks under different natural fracture settings, stress differences, different natural fracture strength and different pumping modes, and provides technical support for crystallizing unconventional reservoir development plans.

2 Numerical model

The numerical simulation of hydraulic fracture network evolution is a very complicated process, which involves the coupling of four key processes: reservoir rock deformation, dynamic fluid distribution in fractures, fluid flow in fractures, and stress interaction between fractures. The research model in this article is based on the following assumptions:

(1) The reservoir rocks are planar and isotropic;
(2) Fracture propagation follows the theory of linear elastic fracture mechanics;
(3) The fluid flow inside fracture is laminar flow;
(4) Fracture propagate in either mode I or mixed mode I/II;
(5) Thermal effect is ignored.

2.1 Governing equation

The governing equation controls fracture length, width, height, shear slip, proppant transport and fluid pressure. To simplify the equation form, the combination parameters of Eqs 1, 2, 3 are introduced:

$$E' = \frac{E}{1-\nu^2} \tag{1}$$

$$\mu' = 12\mu \tag{2}$$

$$K_{IC}^{'} = 4\left(\frac{2}{\pi}\right)^{1/2} K_{IC} \tag{3}$$

TABLE 1 Comparison of different numerical model methods for fracture propagation.

Numerical methods	Characteristics	Sphere of application	Advantages	Disadvantages
BEM (DDM)	Continuous medium, discrete interpolation in the mesh only at the boundary of defined domain	Two - and three-dimensional complex fracture models	To reduce the problem dimension and improve the computational efficiency	Difficult to handle heterogeneous and anisotropic problems, and difficult to couple with matrix pore fluid flow
FEM	Continuous medium, with preset fracture set between two rock matrix units, fracture propagation is controlled by traction separation criteria	Two - and three-dimensional fracture propagation models with fewer fractures	Effectively handling issues about reservoir heterogeneity and avoiding stress singularities at fracture tips	Fracture paths have to preset, fracture propagation arbitrariness is limited, and complex high-density fractures do not converge during cross propagation
XFEM	Continuous medium, fracture tip is described by shape function, with grid independence	Two - and three-dimensional fracture propagation models for low density fractures	Avoiding the difficulties caused by fine mesh division of finite element mesh tips	Difficult to deal with complex, high-density fracture intersections
DEM	Discontinuous medium, transmit load and estimate fracture propagation by contacting keys between particle units	Microscopic scale, complex fracture propagation	Easy to simulate complex fracture propagation and rock deformation behavior	Characterize macroscopic mechanical parameters indirectly, calibration is complex, with low calculation rate for mining scale issues
FDEM	Split the FEM element mesh into DEM domain and embed virtual elements to solve fracture propagation	Two - and three-dimensional complex fracture models	Solve problems such as FEM's inability to characterize the arbitrariness of fracture propagation and DEM's difficulty in simulating macroscopic fracturing	Certain parameters obtained without experiments or standards

Where E is Young modulus;$\upsilon$is Poisson's ratio;μ is fluid viscosity;K_{IC} is rock toughness.

The elastic equation can be shown as Eq. 4:

$$\begin{aligned} cp(a) - \sigma_c^n &= \sum_{m=1}^{M} [A_{nn} T(a,b) w(b)] + \sum_{m=1}^{M} [A_{ns} T(a,b) u(b)] \\ -\sigma_c^s &= \sum_{m=1}^{M} [A_{sn} T(a,b) w(b)] + \sum_{m=1}^{M} [A_{ss} T(a,b) u(b)] \end{aligned} \tag{4}$$

Where σ_c is horizontal far-field stress; s is shear direction components; n is normal direction components; m is fracture unit number; A_{nn}, A_{ns}, A_{sn} and A_{ss} are hypersingular Green's functions; T is 3-D influence coefficient; w is the fracture opening; u is fracture surface shear displacement; p is the fluid pressure; a is observation point; b is middle point of fracture line segment.

The elastic equation above is applicable to two-dimensional strain fracture. As for three-dimensional fractures, a threedimensional influence coefficient (Eq. 5) has to be introduced:

$$T = 1 - \frac{d^{\alpha}}{\left[d^2 + (H/\beta)^2\right]^{\alpha/2}} \tag{5}$$

Where d is distance between observation point with midpoint of line segment;H is fracture height;$\alpha$and $\beta$are empirical constants.

The viscous fluid flow in hydraulic fractures follows Poiseuille's law, and the fluid velocity in hydraulic fractures can be expressed as Eq. 4:

$$q = -\frac{w^3}{\mu'} \nabla p \tag{6}$$

Where q is fluid flow rate in fracture; ∇ is the gradient operator along the fracture path.

In the pseudo three-dimensional model, an extra consideration needs to be given to the height variation of each fracture unit. The average flow velocity inside fracture should be expressed as Eq. 7:

$$q = -\frac{w^3 H}{\mu' h} \nabla p \tag{7}$$

The mass balance equation for fracturing fluid flowing in hydraulic fractures is:

$$\frac{\partial w}{\partial t} + \nabla q = Q_i \delta \tag{8}$$

Where Q is fluid injection rate; δDirac delta function.

When the stress intensity factor reaches the fracture toughness of the rock, the fracture will expand forward, and the width of the fracture tip can be expressed as Eq. 9:

$$\lim_{r \longrightarrow 0} w = \left(\frac{K_{IC}'^3}{E'^3} r^{\frac{3}{2}} + 2 \cdot 3^{\frac{5}{2}} \frac{\mu' V r^2}{E'} \right)^{\frac{1}{3}} \tag{9}$$

Where V is propagation velocity.

Under stress interaction, hydraulic fractures are considered as I-II mixed mode fractures, and the local fracture propagation deflection angle is as Eq. 10:

$$\tan(\theta/2) = -\frac{2\kappa}{1 + \sqrt{1 + 8\kappa^2}} \tag{10}$$

The calculation method of k is shown in Eq. 11:

$$\kappa = \lim_{r \longrightarrow 0} \frac{u}{w} \tag{11}$$

Introducing the maximum circumferential stress criterion (Eq. 12) to reason:

$$\cos\frac{\theta}{2}\left(\cos^2\frac{\theta}{2} \lim_{r \longrightarrow 0} w - \frac{3}{2} \sin\theta \lim_{r \longrightarrow 0} v \right) = \left(\frac{K_{IC}'^3}{E'^3} r^{\frac{3}{2}} + 2 \cdot 3^{\frac{5}{2}} \frac{\mu' (r - r_o) r^2}{\Delta t E'} \right)^{\frac{1}{3}} \tag{12}$$

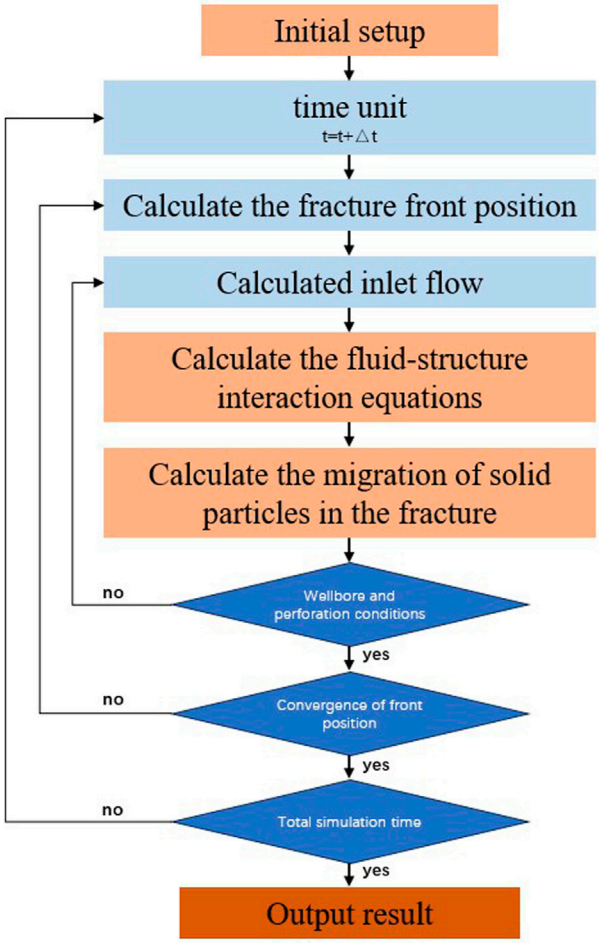


FIGURE 1
Numerical model calculation flow chart of complex hydraulic fracture propagation.

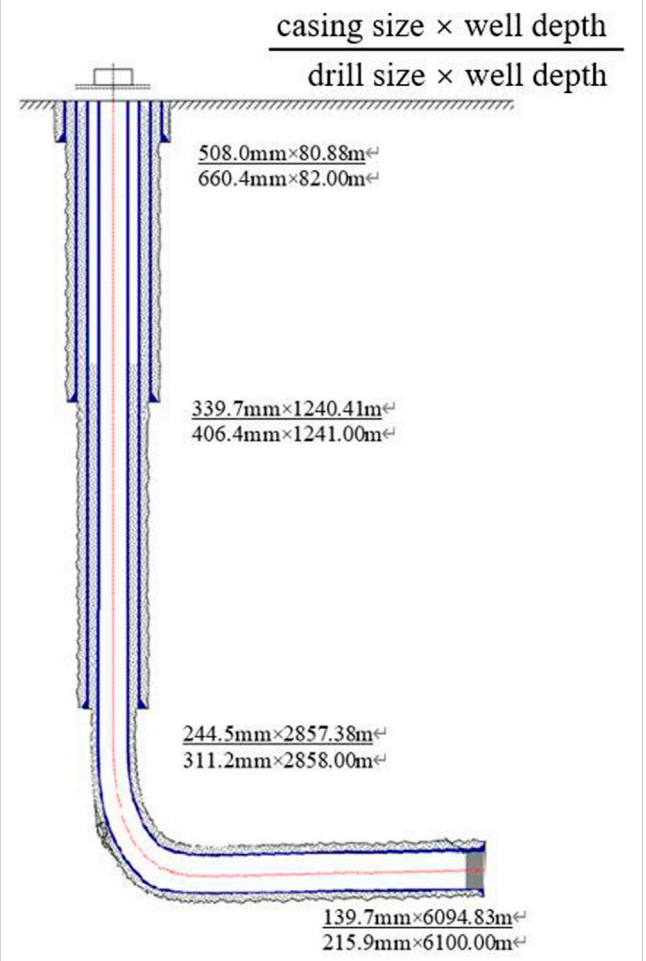


FIGURE 2
Schematic diagram of wellbore structure.

Considering the migration of proppant, the mass balance equation for the flow process of fracturing fluid and solid particles in fractures can be respectively established as follows:

$$\frac{\partial w}{\partial t} + \nabla q_f = Q\delta \tag{13}$$

$$\frac{\partial w\bar{\phi}}{\partial t} + \nabla q_p = Q\bar{\phi}_i\delta \tag{14}$$

Where $\theta$is local fracture deflection angle; $\kappa$is the ratio of Mode II stress intensity factor to mode I stress intensity factor; r and r_0 are the distances from the given point to the fracture tip, at the current and last time steps, respectively; t is time.

When considering the influence of solid particle migration in hydraulic fracture propagation models, the original fluid lubrication Eq. 8 should be replaced by Eqs 13, 14.

If natural fractures are widely developed in reservoir, when hydraulic fractures meet natural fractures, the relative energy release rate is calculated to identify the preferential extension path of the fracture. The capacity release rate along the angle ε can be expressed as Eq. 15:

$$G_\epsilon = \frac{1}{E'}\left(\overline{K_I}^2 + \overline{K_{II}}^2\right) \tag{15}$$

The calculation method of the modes I and II stress intensity factors are shown as Eqs 16, 17:

$$\overline{K_I} = \frac{1}{2}\cos\left(\frac{\epsilon}{2}\right)\left[K_I(1+\cos(\epsilon)) - 3K_{II}\sin(\epsilon)\right] \tag{16}$$

$$\overline{K_{II}} = \frac{1}{2}\cos\left(\frac{\epsilon}{2}\right)\left[K_I\sin(\epsilon) + K_{II}(3\cos(\epsilon) - 1)\right] \tag{17}$$

Where G is energy release rate; $K_I$and $K_{II}$are modes I and II stress intensity factors.

2.2 Boundary conditions

When multiple fractures propagate simultaneously, the sum of the injection amounts of fracturing fluid into each fracture is equal to the total injection amount, and the mass conservation equation can be expressed as Eq. 18:

$$Q = \sum_{i=1}^{N} Q_i \tag{18}$$

The continuity of fracture inlet pressure can be expressed as Eq. 19:

TABLE 2 The input parameters.

Parameter	Value	Parameter	Value
Young's modulus/Gpa	30	Wellbore diameter/m	0.1397
Poisson's ratio/dimensionless	0.25	Segment length/m	64
Rock fracture toughness/MPa·m$^{1/2}$	2	Cluster spacing/m	10
Natural fracture toughness/MPa·m$^{1/2}$	1	Perforated hole diameter/m	0.089
Average porosity/%	4.4	Holes number per cluster	8
Minimum horizontal principal stress/MPa	90	Fracturing fluid density/g/cm^3	1
Maximum horizontal principal stress/MPa	93	Fracturing fluid viscosity/mPa·s	3
Loss factor/m/min$^{1/2}$	0	Construction displacement/m^3/min	18
Fracture height/m	50		

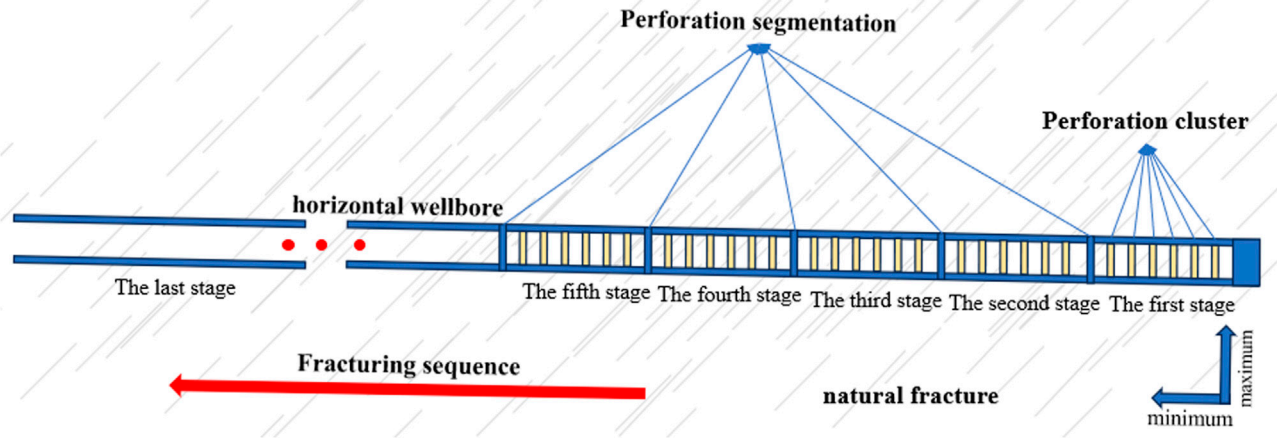


FIGURE 3
Schematic diagram of numerical model.

TABLE 3 Values of different influencing factors.

Influence factor	Range of value
Horizontal stress difference/MPa	0~10
Natural fracture strike angle/°	45,135,45+135 (conjugate fractures)
Fracture toughness/MPa·m$^{1/2}$	0.1~3
Fracturing construction displacement/ m^3·min^{-1}	6~20
Fracturing fluid viscosity/mPa·s	3~100

$$p_1^{\text{inlet}} = p_2^{\text{inlet}} = \ldots = p_N^{\text{inlet}} \tag{19}$$

In addition, assuming that the crack tip width and fluid flow are both 0, the mathematical expression is shown as Eq. 20, then:

$$\lim_{r \longrightarrow 0} w = 0 \tag{20}$$
$$\lim_{r \longrightarrow 0} q = 0$$

2.3 Model solving

In order to effectively simulate the propagation process of multiple hydraulic fractures in segmented multi cluster fracturing of horizontal wells, all components of the model need to be coupled for calculation, and the solution process is shown in Figure 1. The reliability of this model has been proved in previous article (Chen et al., 2019), and the numerical solution of the model is precisely consistent with corresponding accurate solution.

3 Geological situation and parameters

The target well has been drilled to a depth of over 6,000 m, with a vertical depth of nearly 4,000 m and a horizontal section length of 1,900 m. The wellbore structure is shown in Figure 2. The completed drilling horizon is located in the Longmaxi Formation, with main lithology of the target layer being grayish black and black shale. The

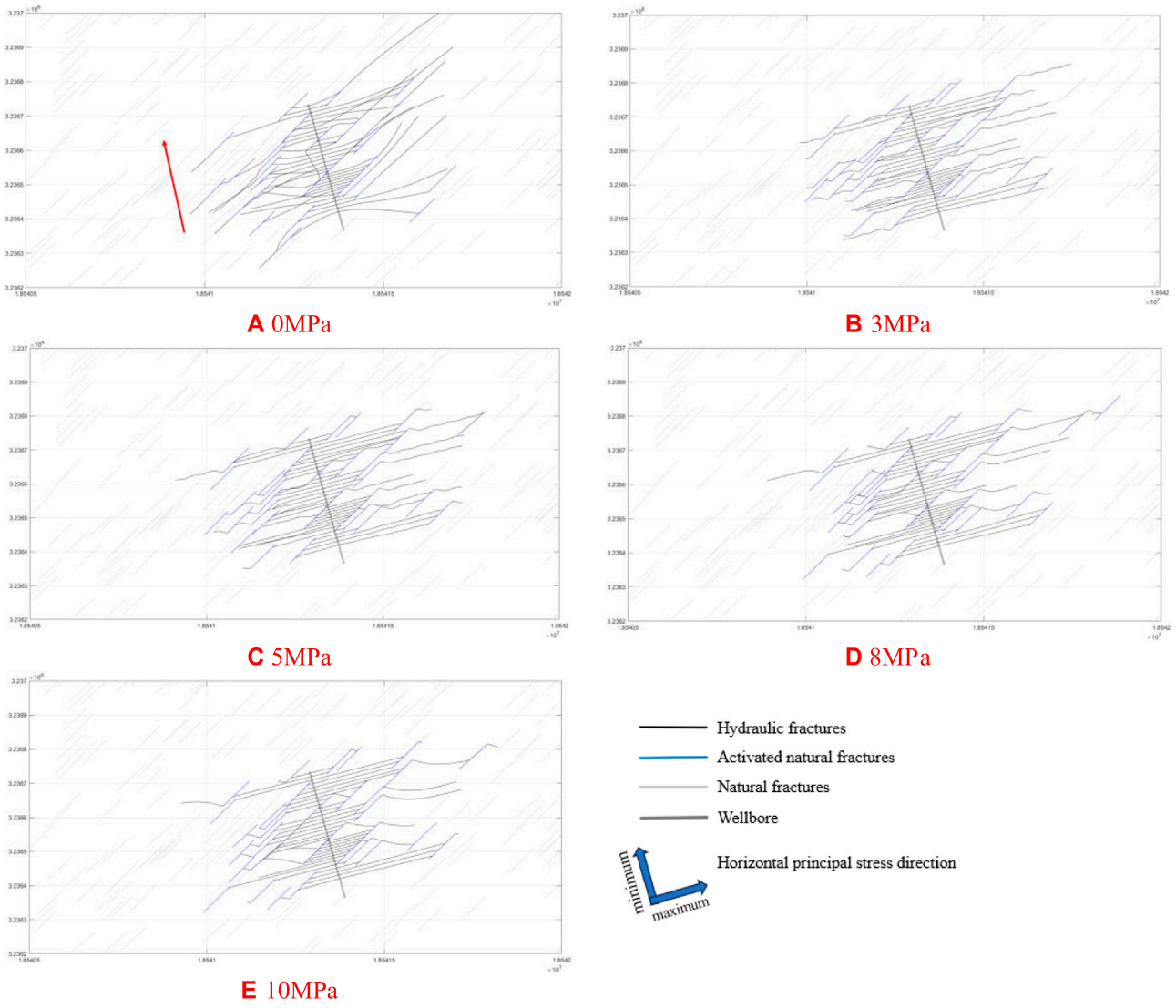


FIGURE 4
Fracture propagation under different horizontal stress differences.

reservoir has developed micro fractures, exhibits low porosity and permeability, and has a logging porosity of 2.2%–4.5%, with an average value of 3.3%. Both organic and inorganic pores are highly developed. Organic pores are mainly developed in mineral frameworks, variously sized from several nanometers to hundreds nanometers, and shaped like subcircular, elliptical, pitted, and honeycomb. Inorganic pores have larger sizes and complex, diverse pore morphology. The brittleness coefficient of the reservoir ranges from 50.6% to 94.1%, with an average value of 77.1%, which means it has good brittleness and compressibility and is conducive to the formation of natural fractures and the fracturing stimulation in later process. Segmented multi-cluster fracturing technology is adopted for the well, with high-strength and high-displacement construction. By forming complex network fractures in the reservoir, the stimulation volume can be increased largely, so that good reservoir stimulation effectiveness can be achieved.

Based on the geological conditions of the horizontal well H and the fracturing construction parameters of the well, the input parameters of the model are determined as shown in Table 2, and the final numerical model is established as shown in Figure 3.

4 Analysis of influencing factors

The natural fractures in reservoirs have a significant impact on the formation of complex fracture networks through hydraulic fracturing. When high-pressure fluids introduced by hydraulic fracturing operations activate natural fractures in rocks, these natural fractures can be expanded, extended, interconnected, and form complex fracture networks, which increases the reservoir fracture control volume and improve the effectiveness of reservoir stimulation. However, in the process of hydraulic fracturing, a lot of factors can influence the interaction between hydraulic fractures and natural fractures. Clarifying the evolution laws of three-dimensional fracture networks under different influencing factors plays a guiding role in making plans to develop unconventional reservoir. This article uses the single factor

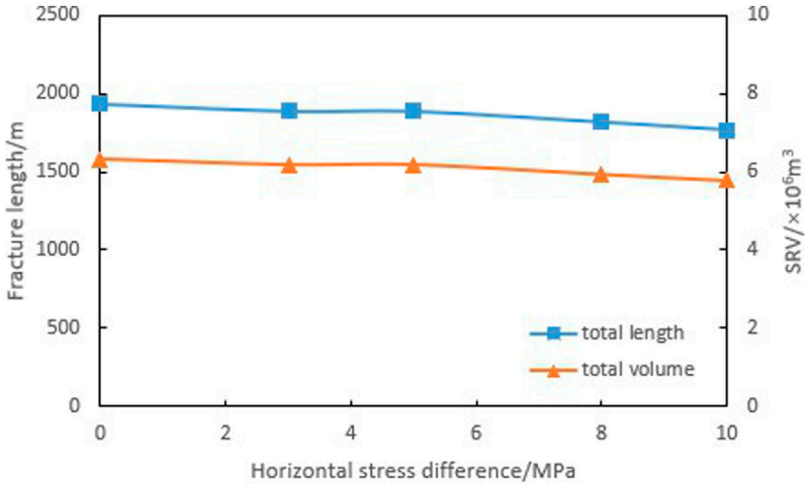


FIGURE 5
Fracture size under different horizontal stress differences.

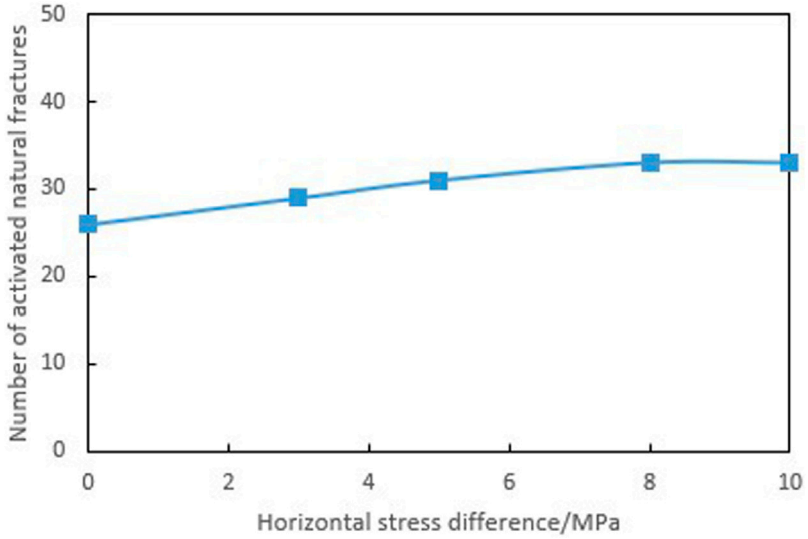


FIGURE 6
Number of activated natural fracture under different horizontal stress differences.

analysis method to simulate the first five stages of fracturing in H by controlling variables, and analyzes the hydraulic fracture propagation law under different geological parameters (horizontal stress difference, natural fracture strike angle: the Angle between the natural fracture and the horizontal, and natural fracture strength) and different engineering parameters (fracturing construction displacement and fracturing fluid viscosity). The values of each parameter are shown in Table 3.

4.1 Geological parameter

4.1.1 Horizontal stress difference

In general, crustal stress can be divided into stress components in three main directions: maximum horizontal principal stress, minimum horizontal principal stress and vertical stress. Horizontal stress difference refers to the difference between the maximum horizontal principal stress and the minimum horizontal principal stress. The horizontal stress difference has a significant effect on controlling fracture direction, fracture propagating speed, and fracture width. This article conducts research on the propagation law of hydraulic fractures under five stress difference levels of 0 MPa, 3 MPa, 5 MPa, 8 MPa, and 10 MPa.

Keeping the minimum principal stress invariable and increasing the maximum principal stress of the reservoir to simulate the fracture propagation under different horizontal stress differences (Figure 4). When five stages of fracturing are carried out in sequence following the red arrows in Figure 4A, the middle fractures in the same section will generate compressive stress on the both ends of the

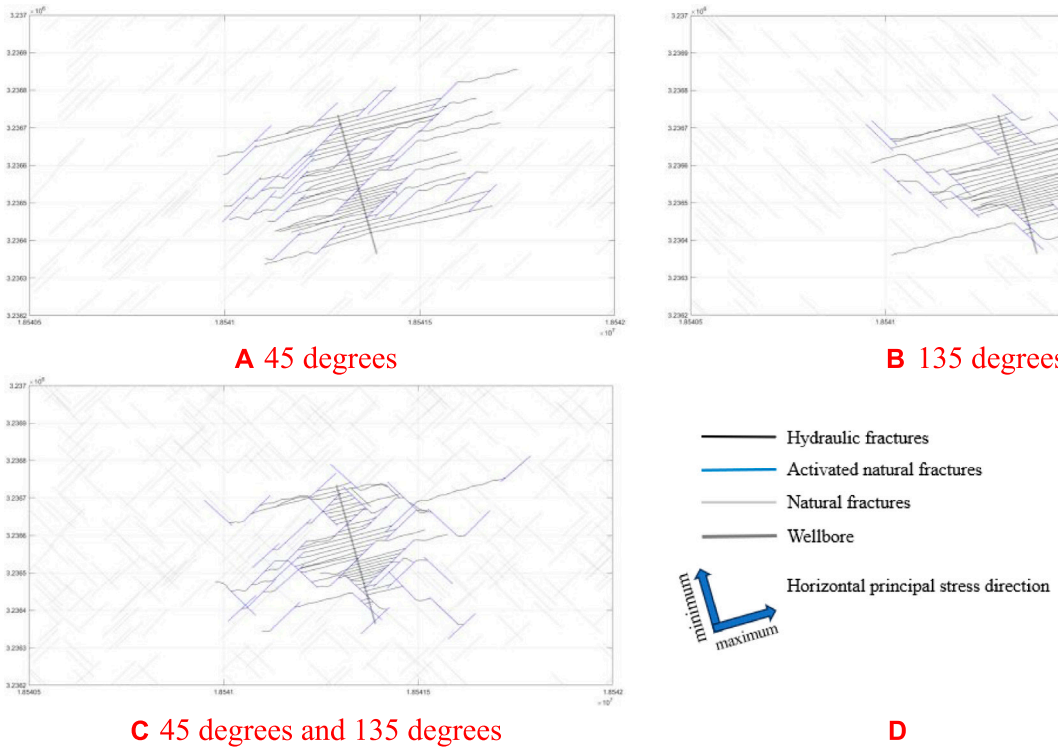


FIGURE 7
Fracture propagation under different natural fracture strike angles.

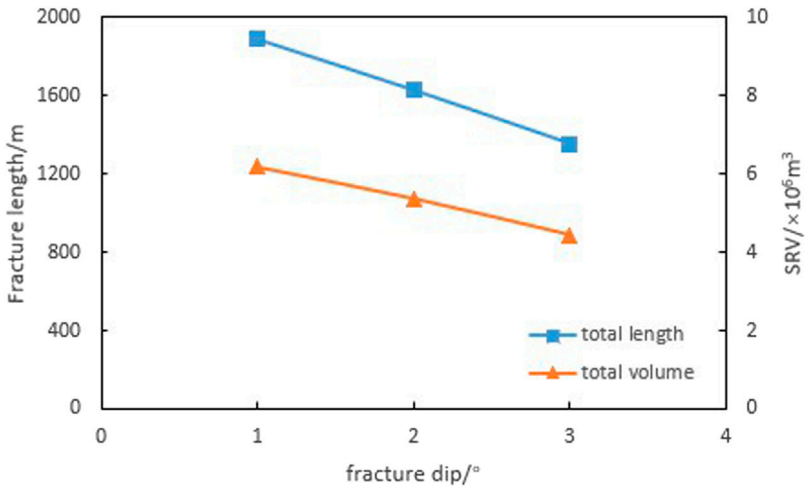


FIGURE 8
Fracture size under different natural fracture strike angles.

fracture, causing the toe fractures to bend towards the far wellbore direction while the heel fractures to bend towards the opposite direction, which exhibit a clear stress shadow phenomenon.

The extension direction of hydraulic fractures is not limited by crustal stress, and the fracture tip points have high degrees of freedom. When hydraulic fractures meet natural fractures, they turn along the natural fractures. As the horizontal stress difference increases, the propagation of hydraulic fracture is constrained, and the stress shadow phenomenon weakens. When there is a horizontal stress difference, the propagation direction of hydraulic fracture is significantly controlled by crustal stress, extending nearly parallel to the maximum principal stress direction. In a state of high stress difference, hydraulic fracture activates natural fracture, which rapidly deflects the direction after reaching the end, and then continuing to extend along the direction of maximum horizontal principal stress, and connecting natural

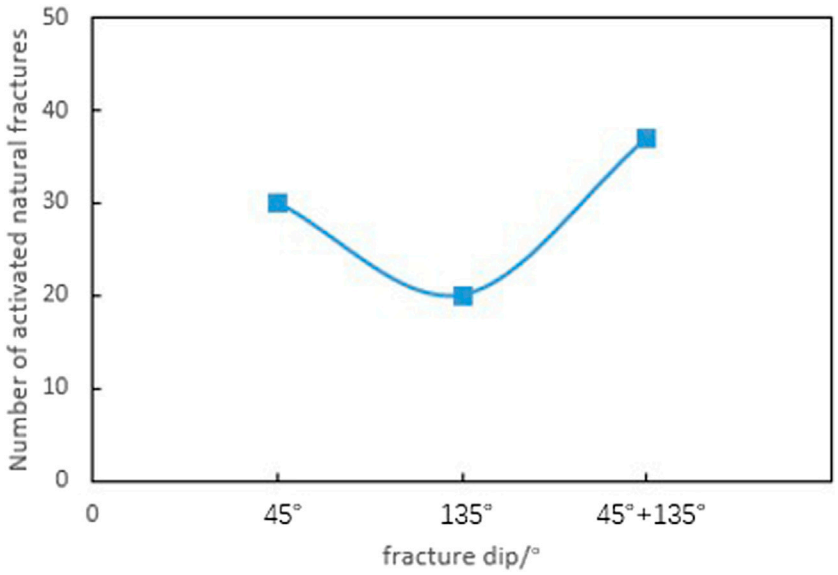


FIGURE 9
Number of activated and natural fractures under different strike angles of natural fractures.

fractures that are farther away in that direction. However, in all cases of horizontal stress difference, there is no hydraulic fracture crossing the natural fracture.

Figure 5 shows the variation of fracture size under different horizontal stress differences. As the horizontal stress difference increases, the extension of hydraulic fracture is constrained, and the extension in the direction of the minimum horizontal principal stress is limited, resulting in a slight decrease in the total length of fractures and total SRV. However, in the direction of the maximum principal stress, further extension of hydraulic fracture connects farther natural fractures, leads to the increase of number of activated natural fracture (Figure 6), and helps to connect target reservoirs in remote well areas. At the same time, the extension of hydraulic fractures is constrained by the maximum principal stress, which makes the directionality stronger and reduces the intersection of hydraulic fractures within and between segments. This is beneficial for improving the effectiveness of reservoir stimulation.

4.1.2 Natural fracture strike angle

Under different approach angles of hydraulic fractures and natural fractures, hydraulic fractures exhibit different propagation modes and final shapes. Hydraulic fractures tend to pass through natural fractures when the approach angle is large, and tend to turn along natural fractures while approach angle is small. When the approach angle is close to the middle value, the expansion behavior of hydraulic fractures after intersecting with natural fractures becomes more complex, and is usually accompanied by three modes: passing, opening, and branching. The target reservoir where well H is located has developed high dip angle (nearly vertical) conjugate fractures with strike angles of 45° and 135°. In this article, the study of hydraulic fracture propagation law under different natural fracture strike angles conditions is carried out by designing three different types of fractured reservoirs which develop natural fractures with strike angles of 45°, natural fractures with strike angles of 135°, and natural fractures with both strike angles of 45° and 135°.

Figure 7 shows the fracture propagation when a group of fractures and conjugate fractures exist simultaneously. When a reservoir develops a group of natural fractures, the fracture propagation patterns of the two types of natural fractures are basically the same. Hydraulic fractures mainly extend in the direction of the maximum horizontal principal stress. After the hydraulic fractures intersect with natural fractures, only a small portion of hydraulic fractures can continue to extend through natural fractures. Most hydraulic fractures activate natural fractures and continue to extend in the direction of maximum horizontal principal stress at the far end of the fractures. When two sets of conjugate fractures are developed in the reservoir, natural fractures constrain the extension of hydraulic fractures from two directions. Although natural fractures intersect with each other and increase the complexity of fractures, hydraulic fractures are difficult to effectively extend to the far wellbore area. As a result, it is difficult to obtain a larger fracture control volume.

Figure 8 indicates the changes in fracture size under different natural fracture conditions. When a group of natural fractures are developed in a reservoir, natural fractures with a strike angle of 135° have a stronger resistance to hydraulic fracture propagation than those with a strike angle of 45°. Under the same conditions, the total length of hydraulic fracture, the total SRV, and the number of activated natural fractures in reservoirs with fracture strike angle of 135° are all smaller than those in reservoirs with strike angle of 45°. When two sets of conjugated natural fractures are developed in the reservoir, the constraint of natural fractures on the expansion of hydraulic fractures increases, and comparing to only one set of natural fractures developed, there is a decrease in fracture length and SRV. Although conjugated natural fractures increase the probability of intersection between hydraulic fractures and natural fractures, also increase the number of activated natural fractures (Figure 9),

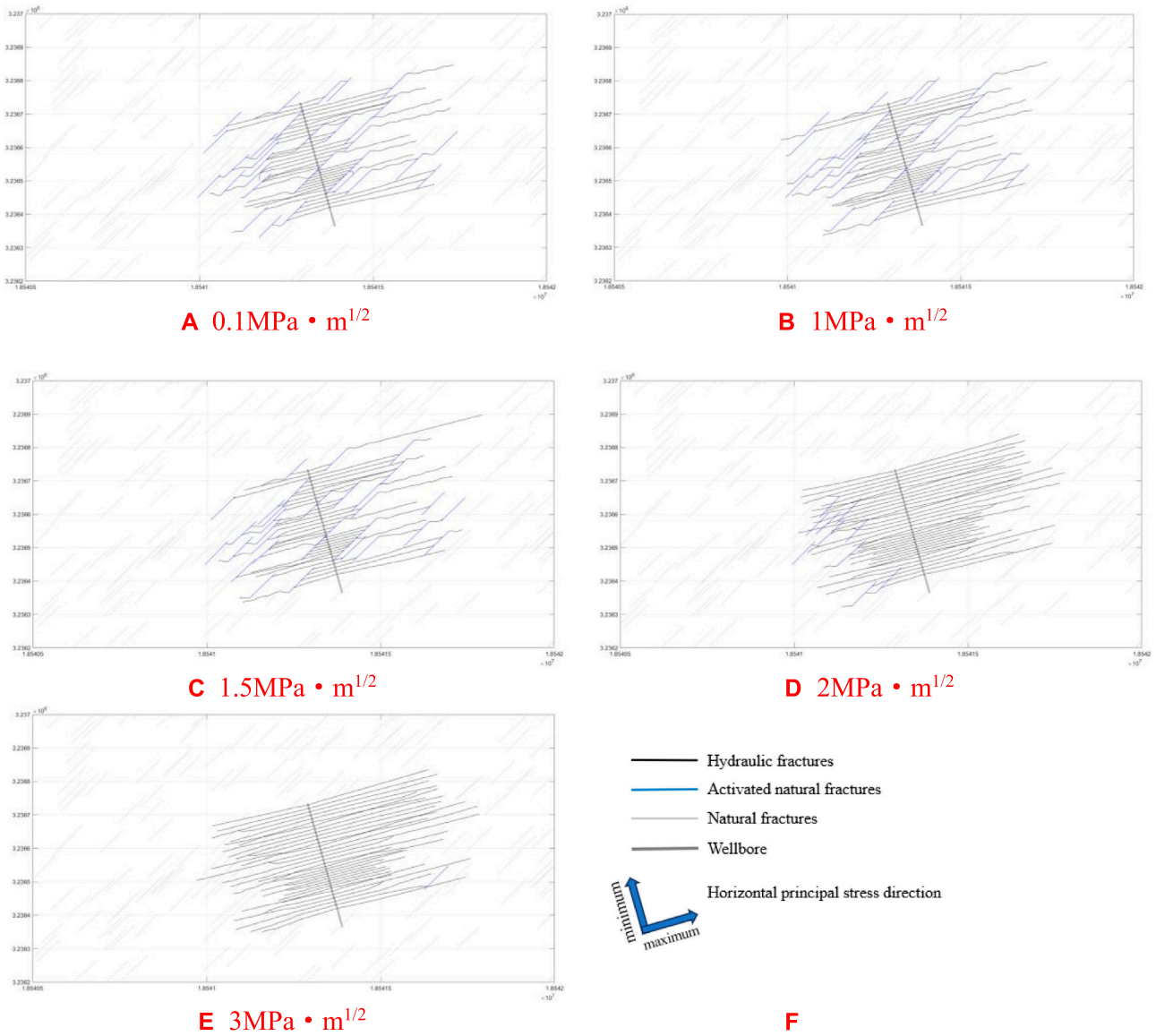


FIGURE 10
Fracture propagation under different natural fracture toughness conditions.

obtaining higher fracture complexity, most hydraulic fractures are limited to the near wellbore zone, which is actually not conducive to increasing the fracture controlled reserve.

4.1.3 Natural fracture strength

Fracture toughness characterizes the ability of a material to prevent fracture propagation and is a quantitative indicator of the toughness of a material. When the fracture size is fixed, the larger the fracture toughness value of the material is, the greater the critical stress required for the unstable propagation of the fracture will be. The fracture toughness of natural fracture cementitious mineral components determines the strength of natural fractures, as well as the propagation form of the intersection between hydraulic fractures and natural fractures, therefore it determines the final distribution form of three-dimensional fracture networks. Based on the distribution range of fracture toughness of the target reservoir, this article designed nine levels of natural fracture toughness, including 0.1 MP·$m^{1/2}$, 0.3 MPa·$m^{1/2}$, 0.5 MPa·$m^{1/2}$, 0.8 MPa·$m^{1/2}$, 1 MPa·$m^{1/2}$, 1.5 MPa·$m^{1/2}$, 2 MPa·$m^{1/2}$, 2.5 MPa·$m^{1/2}$, and 3 MPa·$m^{1/2}$, to study the propagation law of hydraulic fractures under different natural fracture strength conditions.

Figure 10 shows the fracture propagation under different natural fracture toughness conditions. When the toughness is low, the intersection of hydraulic fractures and natural fractures will activate the natural fractures, and the hydraulic fractures will extend to the end of the natural fractures and continue to expand along the direction of the maximum horizontal principal stress. When the fracture toughness of natural fractures is high, hydraulic fractures directly pass through natural fractures and continue to expand. As the fracture toughness increases, the difficulty of activating natural fractures by hydraulic fractures increases as well, while the number of activated natural fractures decreases, and the propagation of fractures changes from complex to simple. Under extremely high natural fracture toughness

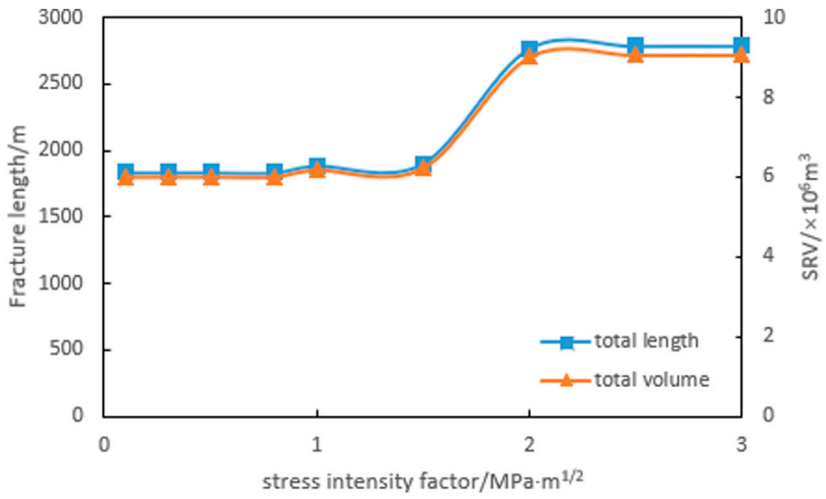


FIGURE 11
Fracture size under different natural fracture toughness conditions.

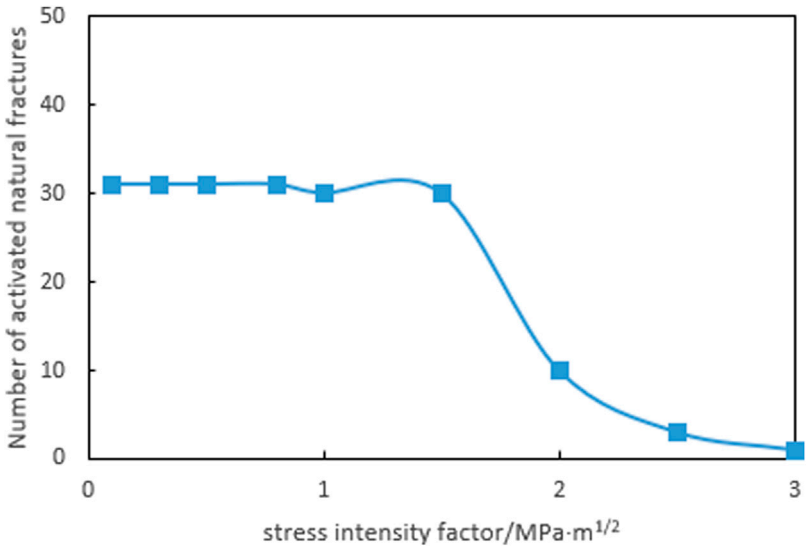


FIGURE 12
Number of activated natural fractures under different fracture toughness conditions.

conditions, the propagation of hydraulic fractures is almost unaffected by natural fractures, and only shows a slight deflection, presenting a nearly parallel state.

It can be seen from the fracture size under different natural fracture toughness conditions (Figure 11) that the activation of natural fractures is related to the comparative relationship between the fracture toughness of natural fractures and reservoir rocks. When the fracture toughness of natural fractures is less than 0.4 times that of rocks, the strength of natural fractures is at a lower level and can be activated indiscriminately by hydraulic fractures. As the fracture toughness of natural fractures increases, the difficulty of activating natural fractures increases as well, and the number of activated natural fractures decreases (Figure 12), so that the interference of natural fractures on the extension path of hydraulic fractures decreases, and the total length of fractures and total SRV increase. When the fracture toughness of natural fractures increases and exceeds the fracture toughness of reservoir rocks (2 MPa·m$^{1/2}$), hydraulic fracture propagation is almost not interfered by natural fractures. So the figure indicates that when the number of activated natural fractures approaches to 0, the total length of fractures and total SRV tend to stabilize.

4.2 Engineering parameters

4.2.1 Fracturing construction displacement

During the fracturing construction process, the selection of construction displacement is crucial for the effectiveness of

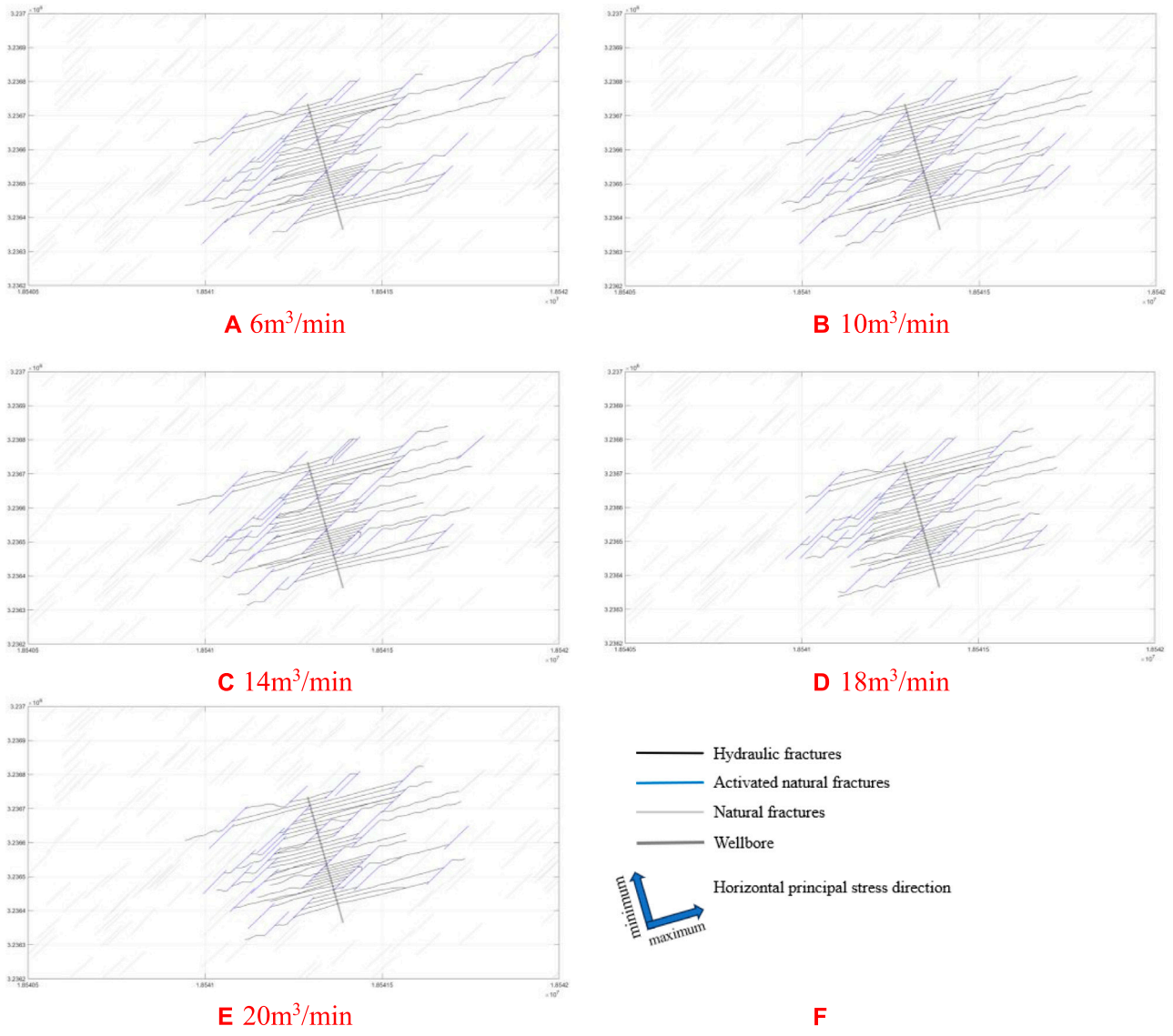


FIGURE 13
Fracture propagation under different fracturing construction displacement conditions.

hydraulic fracturing. When natural fractures develop, hydraulic fractures change direction and produce more natural fractures to form complex fracture networks. During this period, larger displacement, greater pump pressure and greater fluctuation of pump pressure are conducive to communicating more natural fractures and achieving better reservoir stimulation effectiveness. Based on the actual construction parameters on site, this article designed five levels of fracturing construction displacement: 6 m^3/min, 10 m^3/min, 14 m^3/min, 18 m^3/min, 20 m^3/min, and conducted research on the hydraulic fracture propagation law under different fracturing construction displacement conditions.

The fracture propagation results under different fracturing construction displacement are shown in Figure 13. The results demonstrate that as the fracturing construction displacement increases, the extension length of the fracture in the direction of the maximum horizontal principal stress decreases slightly.

Based on the fracture size and the number of activated natural fractures under different fracturing construction displacement conditions (Figures 14, 15), it can be seen that as the fracturing construction displacement increases, the total length of fractures, total SRV, and the number of activated natural fractures demonstrate a similar trend of increasing first and then decreasing. When the construction displacement is less than 10 m^3/min, all of the three curves rise as fracturing construction displacement increase. However, when the fracturing construction displacement continues increasing, they decline gradually, and when the construction displacement volume reaches 18 m^3/min, their values tend to be constant. Therefore, to achieve better reservoir stimulation results, the construction displacement range of the well should be 10–14 m^3/min.

4.2.2 Fracturing fluid viscosity

The rheological properties of fracturing fluid have a significant impact on the effectiveness of hydraulic fracturing construction.

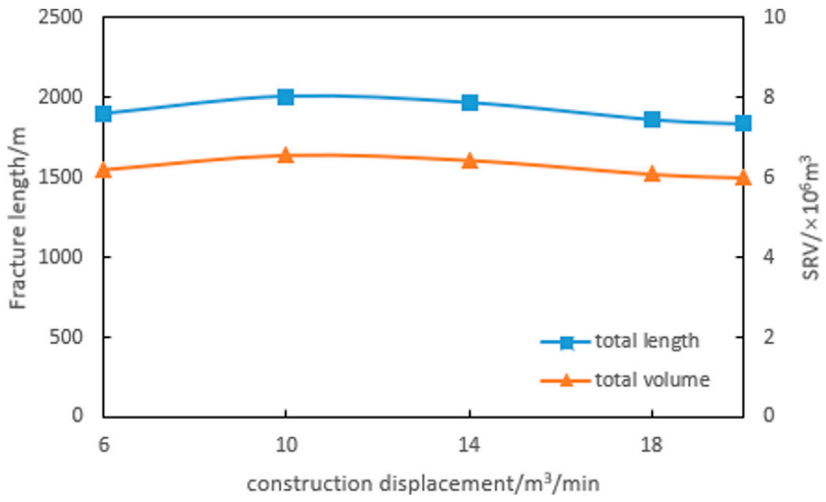


FIGURE 14
Fracture size under different fracturing construction displacement conditions.

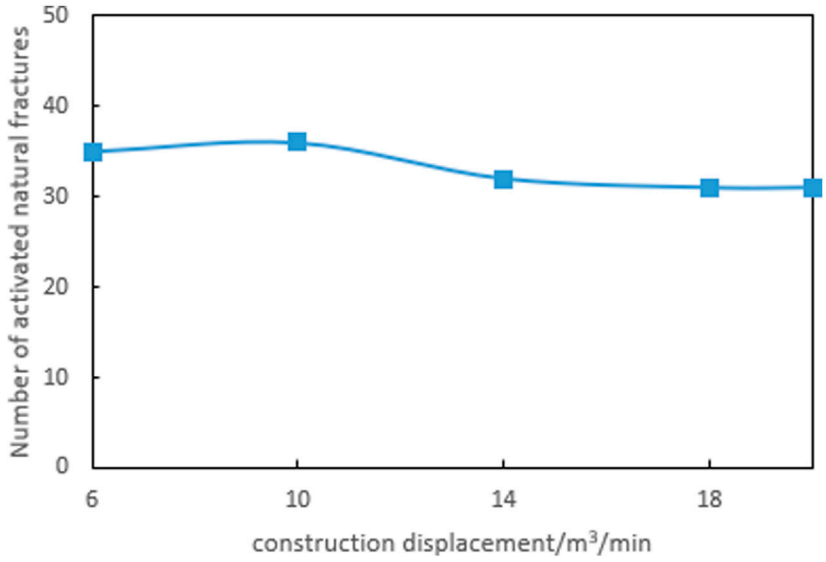


FIGURE 15
Number of natural fractures activated under different fracturing construction displacement conditions.

When other conditions are same, low viscosity fracturing fluid is suitable for creating long fractures and communicating more natural fractures, while high viscosity fracturing fluid is suitable for creating wide fractures and obtaining larger oil and gas seepage channels. Reasonable selection of fracturing fluid viscosity plays an important role in the final reservoir stimulation effectiveness. Based on the types and rheological parameters of fracturing fluids used in on-site construction, this article designs seven levels of fracturing fluid viscosity: 3 mPa·s, 5 mPa·s, 8 mPa·s, 10 mPa·s, 30 mPa·s, 60 mPa·s, and 100 mPa·s, and conducts a study on the hydraulic fracture propagation law under different fracturing fluid viscosity conditions.

Figure 16 indicates the results of fracture propagation under different fracturing fluid viscosity. It can be seen from the figure that the viscosity of the fracturing fluid significantly affects the fracture morphology as well. As the viscosity of the fracturing fluid increases, the extension length of hydraulic fractures, the distribution range of fractures, and the number of activated natural fractures decrease significantly. Low viscosity fracturing fluid reduces the resistance of the fluid inside the fracture, causing the fluid to spread further and form long-narrow fractures. Meanwhile, as the viscosity of the fracturing fluid increases, both the net pressure and induced compressive stress of the fracture increase, leading to the first segment of fracture bending towards the toe with larger amplitude. When the stress shadow phenomenon becomes obvious, the high viscosity fracturing fluid forms relative short and wide fractures.

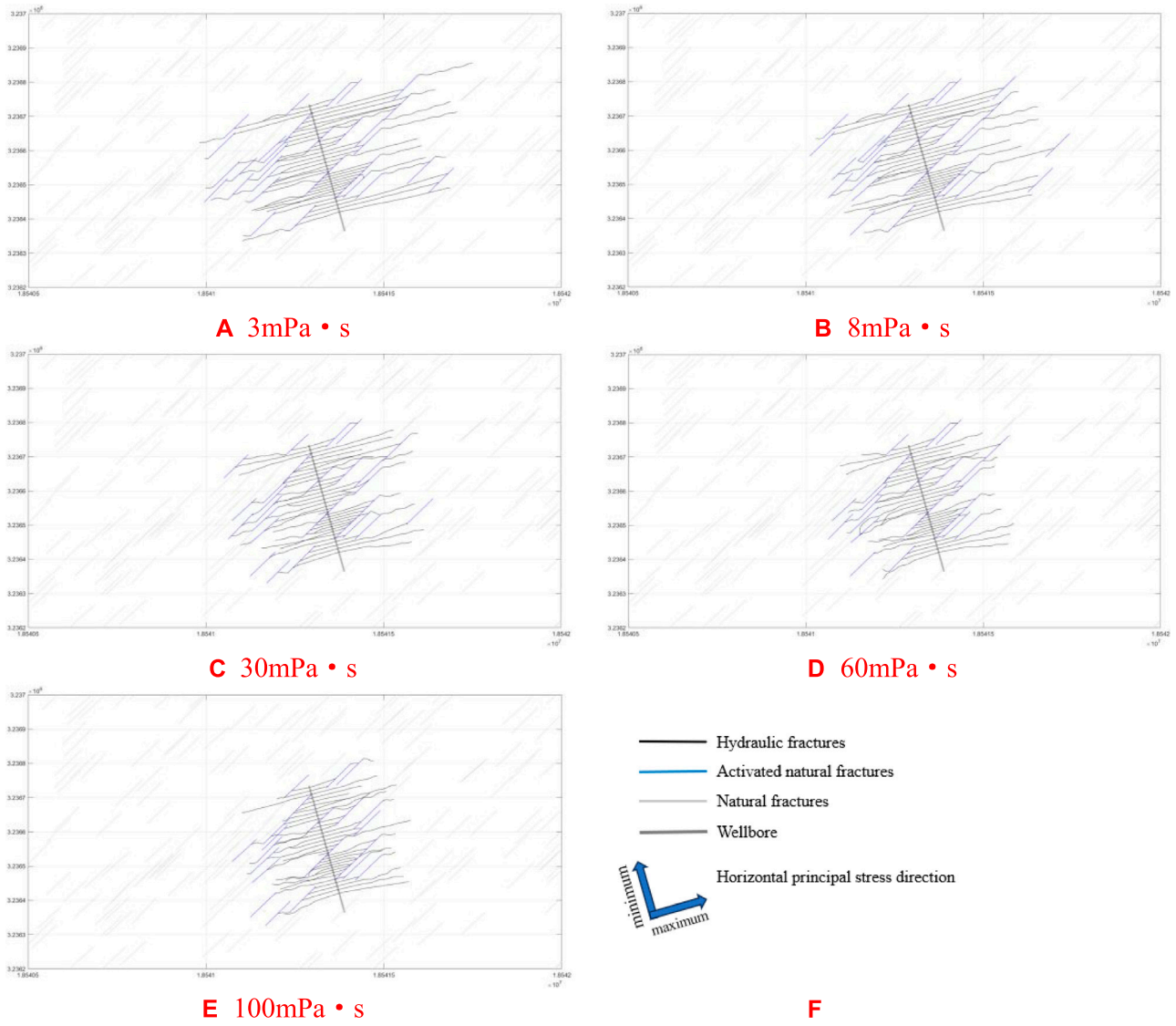


FIGURE 16
Fracture propagation under different fracturing fluid viscosity conditions.

According to Figures 17, 18, as the viscosity of the fracturing fluid increases, the total length of fractures, total SRV, and the number of activated natural fractures all tend to decrease. Minimizing the viscosity of the fracturing fluid while meeting the requirements of sand carrying design to connect the far end reservoir and activate more natural fractures can achieve better reservoir reconstruction effectiveness.

5 Conclusion

(1) The horizontal stress difference has relatively small effect on fracture size, showing a negative correlation with it. A large horizontal principal stress difference constrains the expansion of hydraulic fractures, strictly follows the phenomenon that expanding along the direction of maximum horizontal principal stress and weakening the stress shadow, makes the fractures have stronger directivity, reducing pressure channeling within and between segments. The well trajectory should be parallel to the minimum horizontal principal stress setting, which is conducive to improving the effectiveness of reservoir stimulation.

(2) In reservoirs which develop natural fractures, the natural fractures will hinder the expansion of hydraulic fractures, and the conjugate fractures will interfere with the expansion of hydraulic fractures from both directions. Although natural fractures are interlacing with each other and increase the complexity of fractures, the fractures are limited to the near-well zone, so that the fracture size will be smaller than that of a certain group of fractures developed separately, which is not conducive to improving the reservoir stimulation effectiveness.

(3) The fracture size is positively correlated with the strength of natural fractures. When the fracture toughness of natural

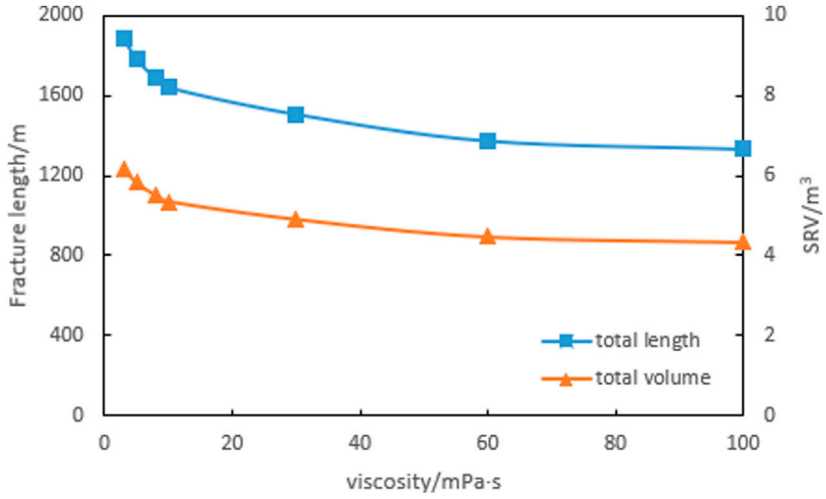


FIGURE 17
Fracture size under different fracturing fluid viscosity conditions.

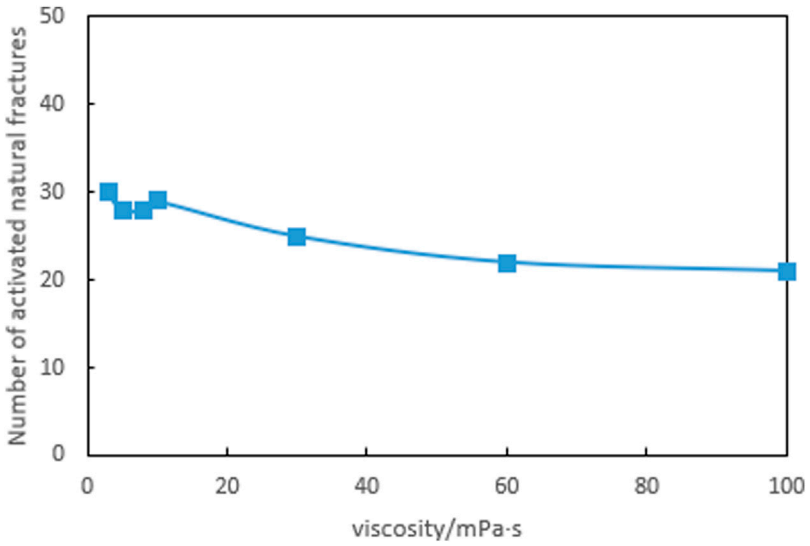


FIGURE 18
Number of natural fractures activated under different fracturing fluid viscosity conditions.

fractures is low, natural fractures are easily activated and the complexity of fractures is strong. When the stress intensity factor of natural fractures is large, natural fractures are easily penetrated directly and the distribution of fractures is simple. However, when the fracture toughness of natural fractures is excessively large, the fracture size is almost unaffected by the strength of natural fractures.

(4) As the fracturing construction displacement increases, the fracture size and the number of activated natural fractures show a pattern of increasing at first and then decreasing. A suitable construction displacement not only helps to break through the obstacles of natural fractures and form a more complex distribution of fractures, but also helps to obtain a larger reservoir stimulation volume. The optimal construction displacement for this well is 10–14 m^3/min.

(5) Low viscosity fracturing fluid is suitable for forming long and narrow fractures, while high viscosity fracturing fluid forms relatively short and wide fractures. To overcome the obstruction of natural fractures, connect with remote reservoir, form complex fracture networks and achieve better reservoir stimulation effectiveness, low viscosity fracturing fluid should be used as much as possible to meet the requirements of sand carrying design Kresse and Weng, 2017, National Resources Canada, 2016.

Data availability statement

The original contributions presented in the study are included in the article/supplementary material, further inquiries can be directed to the corresponding author.

Author contributions

XC: Software, Supervision, Writing–original draft. YH: Writing–original draft, Writing–review and editing. YL: Methodology, Validation, Writing–review and editing. CS: Software, Writing–review and editing.

Funding

The author(s) declare financial support was received for the research, authorship, and/or publication of this article. The research was supported by 1) the National Natural Science Foundation of China (Grant no. U19A2043), 2) Science and Technology Cooperation Project of the CNPC-SWPU Innovation Alliance, 3) Supported by Sichuan Science and Technology Program 2023NSFSC0933.

Conflict of interest

Author CS was employed by PetroChina Southwest Oil and Gasfield Company.

The remaining authors declare that the research was conducted in the absence of any commercial or financial relationships that could be construed as a potential conflict of interest.

Publisher's note

All claims expressed in this article are solely those of the authors and do not necessarily represent those of their affiliated organizations, or those of the publisher, the editors and the reviewers. Any product that may be evaluated in this article, or claim that may be made by its manufacturer, is not guaranteed or endorsed by the publisher.

References

Belytschko, T. (1999). Elastic crack growth in finite elements with minimal remeshing. *Int. J. Numer. Methods Eng.* 45 (5), 601–620. doi:10.1002/(sici)1097-0207(19990620)45:5<601::aid-nme598>3.0.co;2-s

Biewick, L. R. (2014). *Map of assessed coalbed-gas resources in the United States*. Washington, D: U.S. Department of the Interior.

Bp, (2014). BP energy outlook 2035. [2016-06-28] http://wwwbpcom/en/global/corporate/about-bp/energy-economics/energy-outlookhtml.

Chen, X., Li, Y., Zhao, J., Xu, W., and Fu, D. (2017a). Numerical investigation for simultaneous growth of hydraulic fractures in multiple horizontal wells. *J. Nat. Gas Sci. Eng.* 51, 44–52doi. doi:10.1016/j.jngse.2017.12.014

Chen, X., Zhao, J., Li, Y., Yan, W., and Zhang, X. (2019). Numerical simulation of simultaneous hydraulic fracture growth within a rock layer: implications for stimulation of low permeability reservoirs. *J. Geophys. Res. Solid Earthdoi* 124, 13227–13249. doi:10.1029/2019jb017942

Chen, X., Zhao, J., Yan, W., and Zhang, X. (2018). Numerical investigation into the simultaneous growth of two closely spaced fluid-driven fractures. *SPE Journaldoi* 24, 274–289. doi:10.2118/194188-pa

Chen, Z., Jeffrey, R. G., Zhang, Xi, and Kear, J. (2017b). Finite-element simulation of a hydraulic fracture interacting with a natural fracture. *SPE J.* 22 (1), 219–234. doi:10.2118/176970-pa

China Business Industry Research Institute (2022). TOP10 global energy consumers in 2022 https://m.163.com/dy/article/HBGTR4SU051481OF.htm1.

Cocco, M. J., and Ernandez, J. E. (2013). *Reservoir characterization of junin area, orinoco oil belt region*. Venezuela. SPE 171136-MS. Medellín, Colombia.

Detournay, E. (2004). Propagation regimes of fluid-driven fractures in impermeable rocks. *Int. J. Geomechanics* 4 (1), 35–45. doi:10.1061/(asce)1532-3641(2004)4:1(35)

East, L., Soliman, M. Y., and Augustine, J. (2011). Methods for enhancing far-field complexity in fracturing operations. *SPE Production8.Operations* 26 (3), 291–303. doi:10.2118/133380-pa

Fletcher, P., Cobos, S., Jaska, C., Forsyth, J., Crabtree, M., and Gaillard, N., (2012). *Improving heavy oil recovery using an enhanced polymer system*. Tulsa, Oklahoma, USA: Spe Improved Oil Recovery Symposium.

Hamidi, F., and Mortazavi, A. (2012). "Three dimensional modeling of hydraulic fracturing process in oil reservoirs," in *46th US rock mechanics/geomechanics symposium* (Chicago, Illinois),

Hartenergy, (2015). Unconventional oil & gas center. http://www.hartenergy.com/Midstream/Data-Services/.

Hou, B., Wu, A., and Chang, Z., (2021). Experimental study on vertical propagation of fractures of multi-sweet of spots shale oil reservoir. *Chin. J. Geotechnical Eng.* 43 (7), 1322–1330. doi:10.11779/CJGE202107018

Huang, L., Dontsov, E., Fu, H., Lei, Y., Weng, D., and Zhang, F. (2022). Hydraulic fracture height growth in layered rocks: perspective from DEM simulation of different propagation regimes. *Int. J. Solids Struct.* 238, 111395. doi:10.1016/j.ijsolstr.2021.111395

Huang, L., He, R., Yang, Z., Tan, P., Chen, W., Li, X., et al. (2023c). Exploring hydraulic fracture behavior in glutenite formation with strong heterogeneity and variable lithology based on DEM simulation. *Eng. Fract. Mech.* 278, 109020. doi:10.1016/j.engfracmech.2022.109020

Huang, L., Liu, J., Zhang, F., Donstov, E., and Damjanac, B. (2019). Exploring the influence of rock inherent heterogeneity and grain size on hydraulic fracturing using discrete element modeling. *Int. J. Solids Struct.* 176, 207–220. doi:10.1016/j.ijsolstr.2019.06.018

Huang, L., Liu, J., Zhang, F., Fu, H., Zhu, H., and Damjanac, B. (2020). 3D lattice modeling of hydraulic fracture initiation and near-wellbore propagation for different perforation models. *J. Pet. Sci. Eng.* 191, 107169. doi:10.1016/j.petrol.2020.107169

Huang, L., Tan, J., Fu, H., Liu, J., Chen, X., Liao, X., et al. (2023a). The non-plane initiation and propagation mechanism of multiple hydraulic fractures in tight reservoirs considering stress shadow effects. *Eng. Fract. Mech.* 292, 109570. doi:10.1016/j.engfracmech.2023.109570

Huang, L., Tan, J., Fu, H., Liu, J., Chen, X., Liao, X., et al. (2023b). The non-plane initiation and propagation mechanism of multiple hydraulic fractures in tight reservoirs considering stress shadow effects. *Eng. Fract. Mech.* 292, 109570. doi:10.1016/j.engfracmech.2023.109570

Hunsweck, M. J., Shen, Y., and Lew, A. J. (2013). A finite element approach to the simulation of hydraulic fractures with lag. *Int. J. Numer. Anal. Methods Geomechanics* 37 (9), 993–1015. doi:10.1002/nag.1131

Jia, C., Zou, C., Li, J., Li, D., Zheng, M., et al. (2012). Assessment criteria, main types, basic features and resource prospects of the tight oil in China. *Acta Pet. Sin.* 33 (3), 343–350. doi:10.7623/syxb201203001

Kresse, O., and Weng, X. W. (2017). Numerical modeling of 3D hydraulic fractures interaction in complex naturally fractured formations. *J . Rock Mech. Rock Eng.* 12, 3863–3881.

Kuuskraa, V., Stevens, S., and Moodhe, K. (2013). World shale gas and shale oil resources assessment. Available at: http://www.eia.gov/conference/2013/pdf/presentations/kuuskraa.pdf.

Lecampion, B., Bunger, A., and Zhang, X. (2017). Numerical methods for hydraulic fracture propagation: a review of recent trends. *J. Nat. Gas Sci. Eng.* 49, 66–83. doi:10.1016/jjngse.2017.10.012

Loucks, R. G., Reed, R. M., Ruppel, S. C., and Hammes, U. (2012). Spectrum of pore types and networks in mudrocks and a descriptive classification for matrix-related mudrock pores. *AAPGBulletin* 96 (6), 1071–1098. doi:10.1306/08171111061

Loucks, R. G., Ruppel, S. C., Wang, X., Ko, L., Peng, S., and Zhang, T., (2017). Pore types, pore-network analysis, and pore quantification of the lacustrine

shale-hydrocarbon system in the Late Triassic Yanchang Formation in the southeastern Ordos Basin, China. *China jl. Interpret.* 5 (2), SF63–SF79. doi:10.1190/int-2016-0094.1

Mayerhofer, M., Lolon, E., Warpinski, N., Cipolla, C., Walser, D., Rightmire, C., et al. (2008). What is stimulated rock volume. *SPE*, 12 119890. doi:10.2118/119890-MS

Moes, N., and Belytschko, T. (1999). A finite element method for crack growth withoutremeshing. *Int. J. Numer. Methods Eng.* 46, 131–150. doi:10.1002/(sici)1097-0207(19990910)46:1<131::aid-nme726>3.0.co;2-j

National Resources Canada (2016). North American tight oil. Available at: http://www.nrcan.gc.ca/energy/sources/crude/2114#oil1.

Tan, P., Fu, S. H., Chen, Z. W., and Zhao, Q. (2023). Experimental investigation on fracture growth for integrated hydraulic fracturing in multiple gas bearing formations. *Geoenergy Sci. Eng.* 231, 212316. doi:10.1016/j.geoen.2023.212316

Tan, P., Pang, H., Zhang, R., Jin, Y., Zhou, Y., and Kao, J., (2020). Experimental investigation into hydraulic fracture geometry and proppant migration characteristics for southeastern Sichuan deep shale reservoirs. *J. Pet. Sci. Eng.* 184, 106517. doi:10.1016/j.petrol.2019.106517

The Unconventional Oil Subgroup of the Resources & Supply Task Group (2011). *Potential of North American Unconventional Oil Resource*, Western Siberia, Russia.: The NPC North American Resource Development Study.

Valenza, J. J., Drenzek, N., Marques, F., Pagels, M., and Mastalerz, M. (2013). Geochemical controls on shale microstructure. *Geology* 41 (5), 611–614. doi:10.1130/g33639.1

Wang, H., Ma, F., Tong, X., Liu, Z., Zhang, X., Wu, Z., et al. (2016). Assessment of global unconventional oil and gas resources. *PETROLEUM Explor. Dev.* 43 (6), 925–940. doi:10.1016/s1876-3804(16)30111-2

Wang, L., Wang, S., Zhang, R., Wang, C., Xiong, Y., Zheng, X., et al. (2017). Review of multi-scale and multi-physical simulation technologies for shale and tight gas reservoirs. *J. Nat. Gas Sci. Eng.* 37 (37), 560–578. doi:10.1016/j.jngse.2016.11.051

Wang, R., Hu, Z., Liu, J., Wang, X., Gong, D., Tao, Y., et al. (2018). Comparative analysis of characteristics and controlling factors of fractures in marine and continental shales: a case study of the Lower Cambrian in Cengong area, northern Guizhou Province. *Oil Gas Geol.* 39 (4), 631–640.

Wang, Y. (2021). The exploration and development prospects of unconventional oil and gas resources in China are broad. *Petroleum Knowledge* 6, 14–15.

Xie, J., Tang, J., Rui, Y., Fan, Y., Zuo, L., Chen, X., et al. (2020). A 3-D hydraulic fracture propagation model applied for shale gas reservoirs with multiple bedding planes. *Eng. Fract. Mech.* 228, 106872. doi:10.1016/j.engfracmech.2020.106872

Yamamoto, K., Shimamoto, T., and Maezumi, S. (1999). *The SPE asia pacific oil and gas conference and exhibition jakarta*. Indonesia: SPE.Development of a true 3D hydraulic fracturing simulator

Zou, C., Tao, S., Hou, L., et al. (2014a). *Unconventional petroleum geology*. Beijing, China: Geological Publishing House.

Zou, C., Yang, Z., Zhang, G., Hou, L., Zhu, R., Tao, S., et al. (2014b). Conventional and unconventional oil "orderly accumulation": concept and practical significance. *Petroleum Explor. Dev.* 41 (1), 14–27. doi:10.1016/S1876-3804(14)60002-1

frontiers | Frontiers in Energy Research

TYPE Original Research
PUBLISHED 12 January 2024
DOI 10.3389/fenrg.2024.1309037

Check for updates

OPEN ACCESS

EDITED BY
Peng Tan,
CNPC Engineering Technology R & D Company Limited, China

REVIEWED BY
Hu Li,
Southwest Petroleum University, China
Zhipeng Huo,
Northeastern University at Qinhuangdao, China

*CORRESPONDENCE
Guanjie Zhang,
zgj199688@163.com

RECEIVED 07 October 2023
ACCEPTED 03 January 2024
PUBLISHED 12 January 2024

CITATION
Liu Z, Cheng Q, Liao X, Zhang L, Liu W and Zhang G (2024), Characteristics and controlling factors of tectonic fractures within the buried hill reservoirs from the Archaean metamorphic basement: a case study in the Bozhong 19–6 condensate gas field, Bohai Bay Basin. *Front. Energy Res.* 12:1309037. doi: 10.3389/fenrg.2024.1309037

COPYRIGHT
© 2024 Liu, Cheng, Liao, Zhang, Liu and Zhang. This is an open-access article distributed under the terms of the Creative Commons Attribution License (CC BY). The use, distribution or reproduction in other forums is permitted, provided the original author(s) and the copyright owner(s) are credited and that the original publication in this journal is cited, in accordance with accepted academic practice. No use, distribution or reproduction is permitted which does not comply with these terms.

Characteristics and controlling factors of tectonic fractures within the buried hill reservoirs from the Archaean metamorphic basement: a case study in the Bozhong 19–6 condensate gas field, Bohai Bay Basin

Zongbing Liu[1], Qi Cheng[1], Xinwu Liao[1], Lei Zhang[1], Wenchao Liu[1] and Guanjie Zhang[2]*

[1]Bohai Oilfield Research Institute, Tianjin Branch, CNOOC China Limited, Tianjin, China, [2]School of Earth Resources, China University of Geosciences, Wuhan, China

The Bozhong 19–6 Condensate gas field is the first giant gas field discovered in the Bohai Bay Basin in recent years. The gas field reservoir has diverse reservoir space and strong heterogeneity.In this paper, we systematically summarize tectonic fractures development patterns and explore the main factors controlling fractures development and clarify the influence of fractures on reservoir quality through core and microscopic thin section observations, physical property data, imaging logging data. The results show that the major types of tectonic fractures in study area are shear fractures, followed by tensile fractures. Study area mainly developed high-angle fractures and completely filled fractures, fractures are commonly filled with carbonate and clay cement. Four groups of tectonic fractures were found in the study area, which corresponds to the four fracture formation period. Tectonic movement controls the fractures development in study area, the multi-stage tectonic movement had caused a complex fractures network system. The faults control the development of associated fractures formation in the fractures zone, different faults control the fractures formation and orientations in the vicinity. Rock type and minrals content is the basis of forming different fractures, such as the high felsic content is the basis of developed fractures in metamorphic rocks, and rock layer thickness, reservoir porosity and permeability are important factors of the fractures development heterogeneity longitudinally.

KEYWORDS

tectonic fractures, deep metamorphic rock, buried hill, faulted basin, main controlling factors

1 Introduction

In recent years, a large condensate gas field has been found in the deep Archean metamorphic buried hill in the Bozhong 19–6 structural belt, southwestern Bozhong sag, which is the largest gas field discovered so far in the Bohai sea basin. (Wang et al., 2019; Ye et al., 2021; Wang et al., 2022). The permeability of such reservoirs is significantly improved by the tectonic fractures and their associated secondary pores (Lyu et al., 2019), it provides a effective pathways for oil and gas migration and reservoir space for oil and gas accumulation (Cui et al., 2013). In addition, tectonic fractures connect "geological sweet spots" and "engineering sweet spots" together (Wang et al., 2017; Gong et al., 2021), therefore, the study of tectonic fractures in metamorphic buried hill reservoirs should run through the whole exploration and development process.

In recent years, many scholars have studied the controlling factors of fracture development in metamorphic rock buried hill reservoirs. It is believed that tectonic movement, lithology, weathering intensity and thickness of layers are the main controlling factors of fractures development within the metamorphic rock buried hill reservoirs (Bazalgette et al., 2010; Eig and Bergh, 2011; Zeng et al., 2013; Wang et al., 2016; Yin et al., 2019; Li et al., 2020; Huang et al., 2022; Liu et al., 2023a; Liu et al., 2023b). The tectonic movement affects the structure fractures development indirectly by affecting the tectonic stress field distribution, which is the most important external factor controlling the development of reservoir fractures (Ezati et al., 2018; Maerten et al., 2018). Affected by the difference of fault spatial activity, the local stress distribution near the fault is obviously different, which affects the development mode of fracture near the fault (Aydin, 2000). In fault-related folds, faults and turning ends are the main controlling factors of fracture development. The fractures at the turning end of the fold are often more developed than those at the wing of the fold. The density of tectonic fractures decreases exponentially with the distance increasing from the fault (Ding et al., 2013; Lavenu et al., 2013). Under the same tectonic stress, rocks with smaller particles and rich in brittle minerals such as felsic are more likely to break and develop fractures (Ye et al., 2021). Weathering and eluviation can cause irregular fractures of different scales near the rocks surface, high rupture degree and well-development fractures were developed (Salah and Alsharhan, 1998; Liu et al., 2016; Yin et al., 2016). The stress concentration degree of fracture tip in different rock stratum thickness is different. Generally, the stress of thinner rock stratum is more concentrated at the fracture tip, and the development degree of the fracture is higher. However, when the thickness of the rock stratum reaches a certain critical value, the rock stratum thickness does not affect the fracture density, and the fracture density tends to be constant (Lianbo and Xiang-Yang, 2009; Fan et al., 2021).

Many scholars have studied the tectonic fractures of metamorphic buried hill reservoirs in Bozhong 19–6 gas field, Bohai Bay Basin (Yu and Koyi, 2016; Ye, Chen, et al., 2020; Wang et al., 2021; Zeng et al., 2022). However, the main research is the important role of fractures in the process of oil and gas migration and accumulation, there is still a lack of analysis and research on the comprehensive characterization of reservoir tectonic fractures and the influencing factors of reservoir fracture development in the area. Therefore, the observation and statistics of imaging logging, core and thin section tectonic fractures are carried out to quantitatively characterize the tectonic fractures of metamorphic buried hill reservoirs in Bozhong 19–6 gas field, combining with the whole rock mineral analysis, core porosity and permeability analysis, and clarify the control factors of structural fracture development in the study area. These results provide a guidance for the prediction of tectonic fractures in the study area, and provide reliable basic data for the further exploration and development of the Bozhong 19–6 gas field.

2 Geological setting

Bozhong 19–6 condensate gas field is located in the southwest of Bozhong sag, surrounded by Bozhong sag, Shanan sag and Huanghekou sag (Zhao et al., 2015a; Xu et al., 2019) (Figure 1A). From the top to the bottom, the stratum is Pingyuan Formation, Minghuazhen Formation, Guantao Formation, Dongying Formation, Shahejie Formation, Kongdian Formation, local Mesozoic stratum and Archean metamorphic rock basement (Xu et al., 2019; Feng et al., 2020) (Figure 1B). Mesozoic rock reservoirs are mainly developed in the Minghuazhen Formation, Guantao Formation and Kongdian Formation, the lithology is mainly glutenite and tuff (Li et al., 2012).

Archean is the main gas-bearing interval of Bozhong 19–6 condensate gas field, and it is buried more than 3,800 m (Wang et al., 2021). Its lithology is metamorphic granite, mainly including monzonitic gneiss, plagioclase gneiss, locally developed cataclastic mixed granite (Liu et al., 2023b). The rock components are mainly albite, quartz and potassium feldspar, followed by chlorite, calcite, illite, muscovite and dolomite (Ye et al., 2022). The core physical property test shows that the average porosity of Archean metamorphic rock buried hill reservoir is 5.22%, and the average permeability is 0.37 mD (Pei et al., 2022). The reservoir space is mainly intergranular pore and dissolution pore (Cao et al., 2015; Wang et al., 2018).

The Bozhong 19–6 condensate gas field has experienced multi-stage tectonic activities since Indosinian (Liu et al., 2022; Yi et al., 2022). During the Indosinian period, the South China plate subducted and collided with the North China plate, forming a regional compressive stress field from south to north. A series of south to north thrust faults were formed, and the fractures were mainly distributed in the near EW direction (Zhou et al., 2012). During the Yanshanian period, the study area was affected by the NW compressive stress, due to the NW subduction of the ancient Pacific Ocean. At the same time, the Tanlu Fault was left-laterally squeezed, forming a large number of NE strike-slip faults. The large-scale faults of the Indosinian period were reversed during the formation of the buried hill, and the original continuous Indosinian uplift zone was cut into a series of fragments of different sizes. At the same time, the internal part of the buried hill block was broken (Chen, 1998; Huang et al., 2003). The early formation of fractures in the study area was subjected to the north-northwest tensile stress of the Himalayanian period, while it was subjected to the superimposed modification of the right-lateral tensile action of the Tanlu Fault. The early NNW and N-E faults

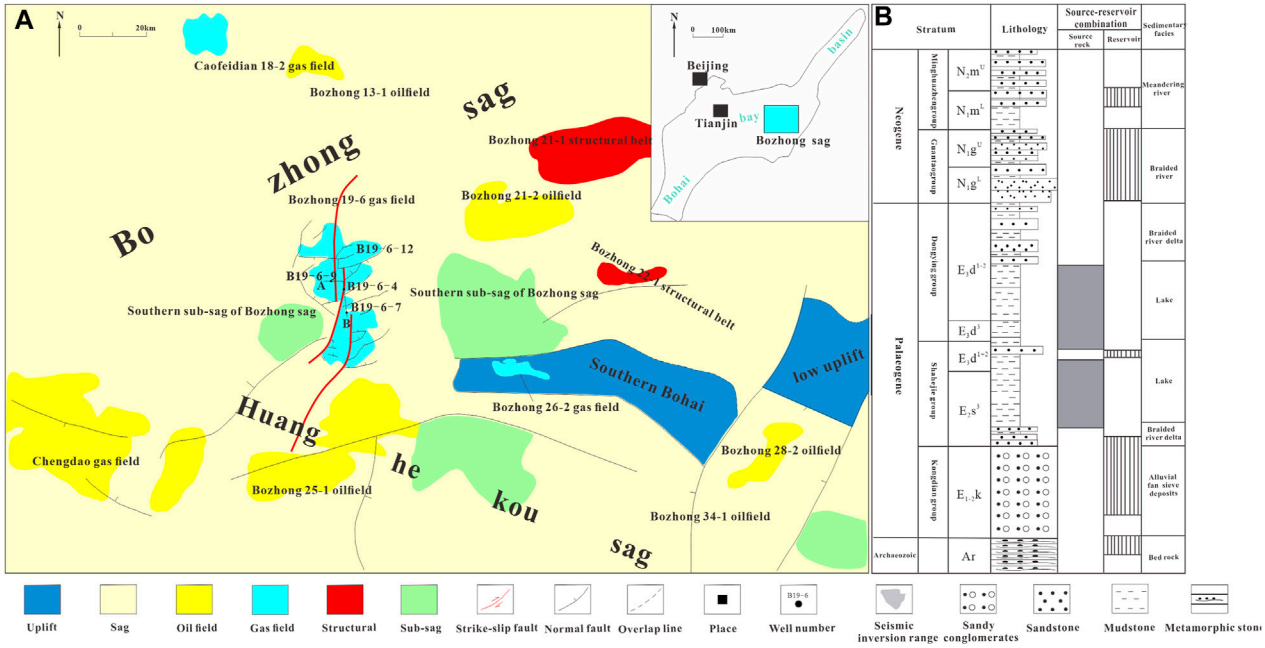


FIGURE 1
(A) Regional location of the BZ19-6 condensate gas field; **(B)** Comprehensive stratigraphic column of the BZ19–6 condensate gas field.

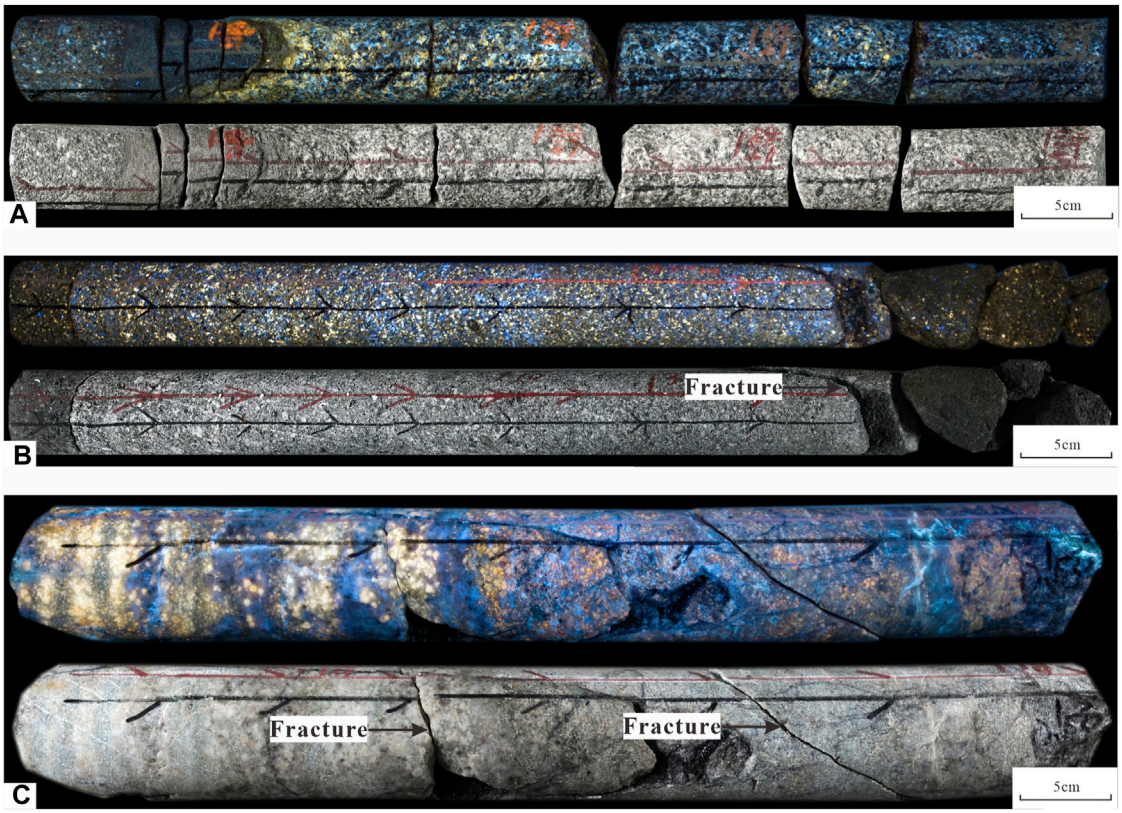


FIGURE 2
(A) Well BZ19-6-C, 4538.05–4538.90 m, exhibits numerous shear and tensile fractures with significant variations in orientations. The distribution forms a mesh-like intersection pattern, with many fractures being partly or completely filled. **(B)** Well BZ19-6-I, 4429.00–4429.90 m, displays a high-angle shear fracture and a weathered and dissolved fractured zone in the lower part. **(C)** Well BZ19-6-C, 4678.06–4678.59 m, shows multiple shear and tensile fractures. The filling minerals within the fractures have undergone dissolution.

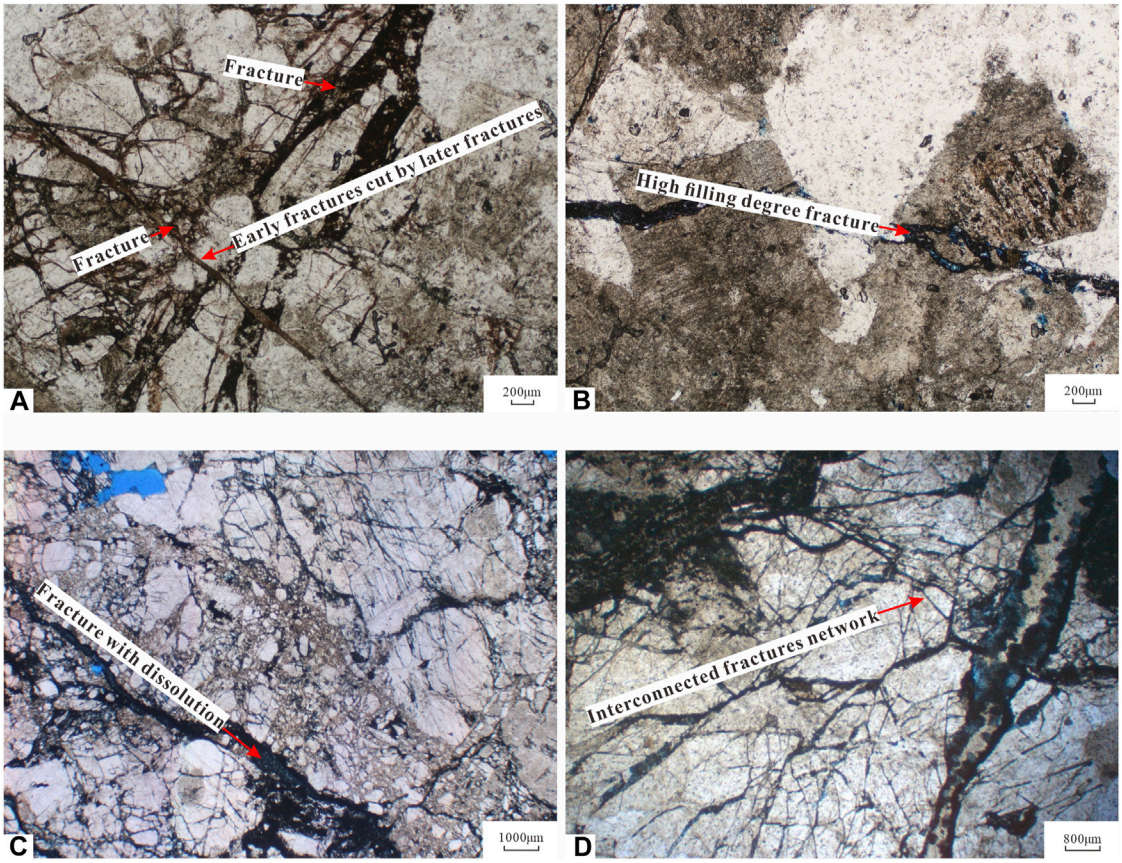


FIGURE 3
(A) Well BZ19-6-C, 4251.1 m, monzonal gneiss, single polarized light, exhibits two phases of fractures, with distinct early fractures being intersected by later fractures; **(B)** Well BZ19-6-K, 4343.5 m, plagioc gneiss, single polarized light, shows fractures filled with mud, siderite, and ankerite; **(C)** Well BZ19-6-H, 4349.0 m, broken porphyry, single polarized light, features dissolved pores at the edges of fractures; **(D)** Well BZ19-6-J, 4068.0 m, monzonal gneiss, single polarized light, displays an intersecting network of fractures forming a mesh-like fracture system.

were reactive, and the overall fracture subsided. Finally the tectonic appearance of the buried hill was shaped (Zhao et al., 2015a).

3 Data and methods

The data and samples of this study are derived from the metamorphic buried hill reservoir of Bozhong 19–6 condensate gas field. Nine wells (BZ19-6-A, BZ19-6-B, BZ19-6-C, BZ19-6-D, BZ19-6-E, BZ19-6-F, BZ19-6-G, BZ19-6-H and BZ19-6-I) with a total of 73.6 m cores and 288 wall cores were observed. The lithology and fracture types have been identified, and the development degree and filling degree of fractures also have been identified. A total of 359 casting sheets were collected to observe the development degree and filling degree of microfractures and dissolution along microfractures, A total of 112 samples of reservoir properties test results were collected, including porosity and permeability, and 25 samples of whole rock mineral analysis results, and the mineral content composition of different lithology was obtained.

Logging data, including conventional and imaging logging data from 11 wells, were obtained to interpret the fracture characteristics, including orientation, dip angle, scale, and fracture linear density (Liu et al., 2021). We define the total fractures number divided by the total length or the total fractures number per unit core length as fracture linear density (Ortega et al., 2006). The above data and samples were provided by CNOOC China Limited, Tianjin Branch.

4 Results

4.1 Fracture development characteristics

The tectonic fractures of metamorphic buried hill reservoir in Bozhong 19–6 condensate gas field are mainly shear fractures. High angle fractures ($45^\circ < \theta < 75^\circ$) and vertical fractures ($\theta > 75^\circ$) are mainly developed, and a small number of low angle fractures ($\theta < 45^\circ$) are locally developed (Figure 2A). The scratches on the shear fractures surface are obvious. The fractures length varies greatly (0–30 cm). The filling degree of fractures is high, and most of them are filled with mud (Figure 2B). The development of tensile fractures is less, which is mainly developed in granitic gneiss, and the fractures filling degree is high. It is mostly filled with clay, calcite and other minerals, accompanied by a small amount of mineral dissolution phenomenon (Figure 2C). According to the core fractures cutting relationship, combined with the regional stress evolution process. It is believed that there are at least four phases of

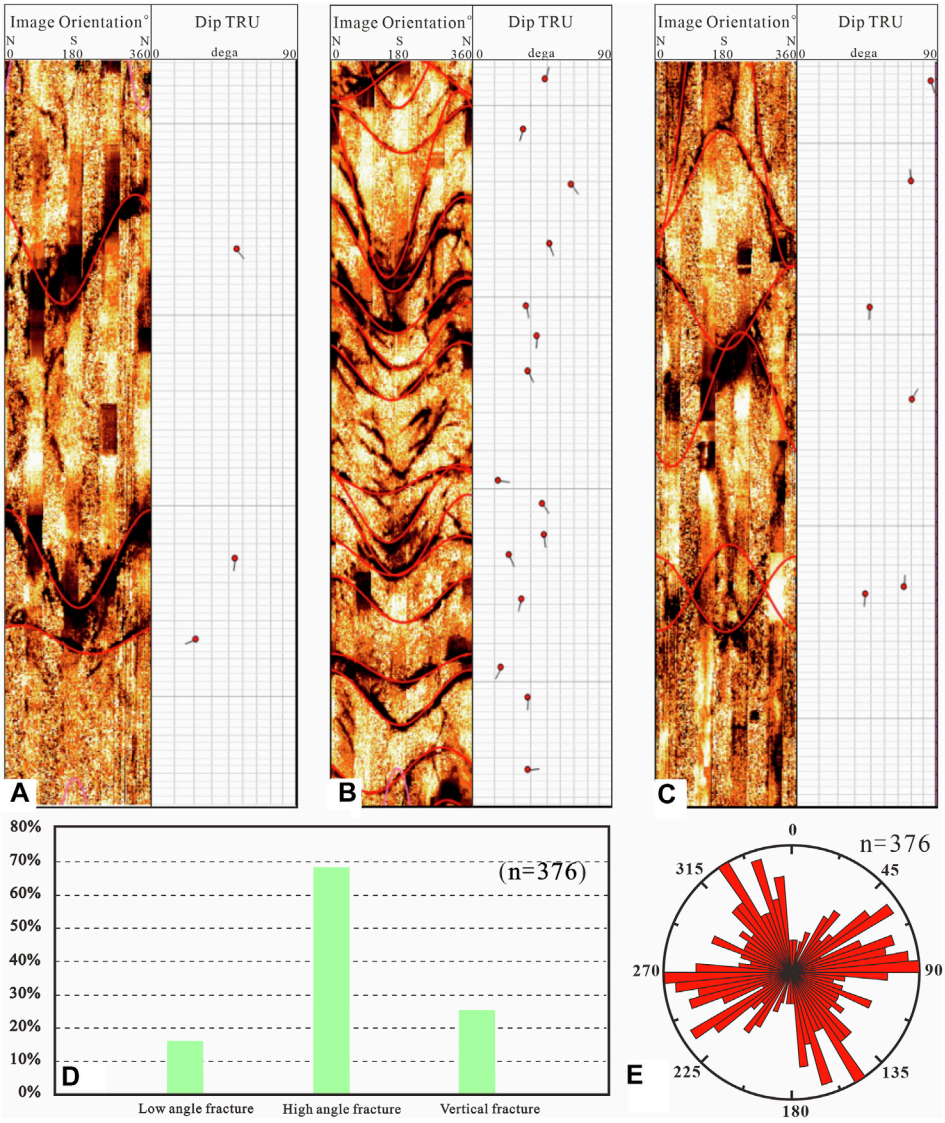


FIGURE 4
(A) Well BZ19-6-D, 4615.8–4617.9 m, exhibits grouped fissures; **(B)** Well BZ19-6-D, 4602.1–4604.5 m, features a network of fissures; **(C)** Well BZ19-6-D, 4607.2–4609.6 m, shows widened fissures due to dissolution along fractures; **(D)** Histogram of the tectonic fractures dip angle spread of metamorphic reservoir; **(E)** Rose diagram depicting the structural fracture orientations in the metamorphic reservoir.

tectonic fractures in the study area: the near EW tectonic fractures in the early Indosinian period, the NW tectonic fractures in the late Indosinian period, the NWW tectonic fractures in the Yanshanianian period, the NE tectonic fractures in the Himalayan period.

The microfractures of metamorphic rock buried hill reservoir in Bozhong 19–6 condensate gas field are developed. It can be observed that the early fractures are cut by the later fractures, and the later fractures development is restricted by the early fractures (Figure 3A). Shear fractures are mainly developed, and the fracture surface is relatively straight. The fracture aperture is between 2 and 7 mm and the fracture length is between 1 and 10 mm. The fracture filling degree is high, and the fractures are mainly filled with clay and carbonate minerals (Figure 3B). Fractures mostly cut through quartz, feldspar and other mineral particles, and are accompanied by dissolution, pores enlarged by dissolution are developed along microfractures (Figure 3C). In addition, the network fracture system intersected by fractures can also be observed (Figure 3D), it is significant for improving the storage and permeability properties of metamorphic rock reservoirs.

Interpreting the fracture characteristics from 11 imaging logging, including orientation, dip angle, scale, and fracture density, there are three kinds of combination patterns of tectonic fractures in the study area. It mainly includes parallel patterns fractures (Figure 4A), which refers to two or more fractures with similar orientations; network fractures (Figure 4B), multiple fractures are intertwined, and the orientations are irregular; conjugation fractures (Figure 4C). Two fractures have similar dip angles but opposite trends. High angle fractures ($45^\circ < \theta < 75^\circ$) and vertical fractures ($\theta > 75^\circ$) are mainly developed, and a small number of low angle fractures ($\theta < 45^\circ$) are locally developed (Figure 4E). Four groups of near EW, NE-SW, NW-SE and NNW-SSE tectonic

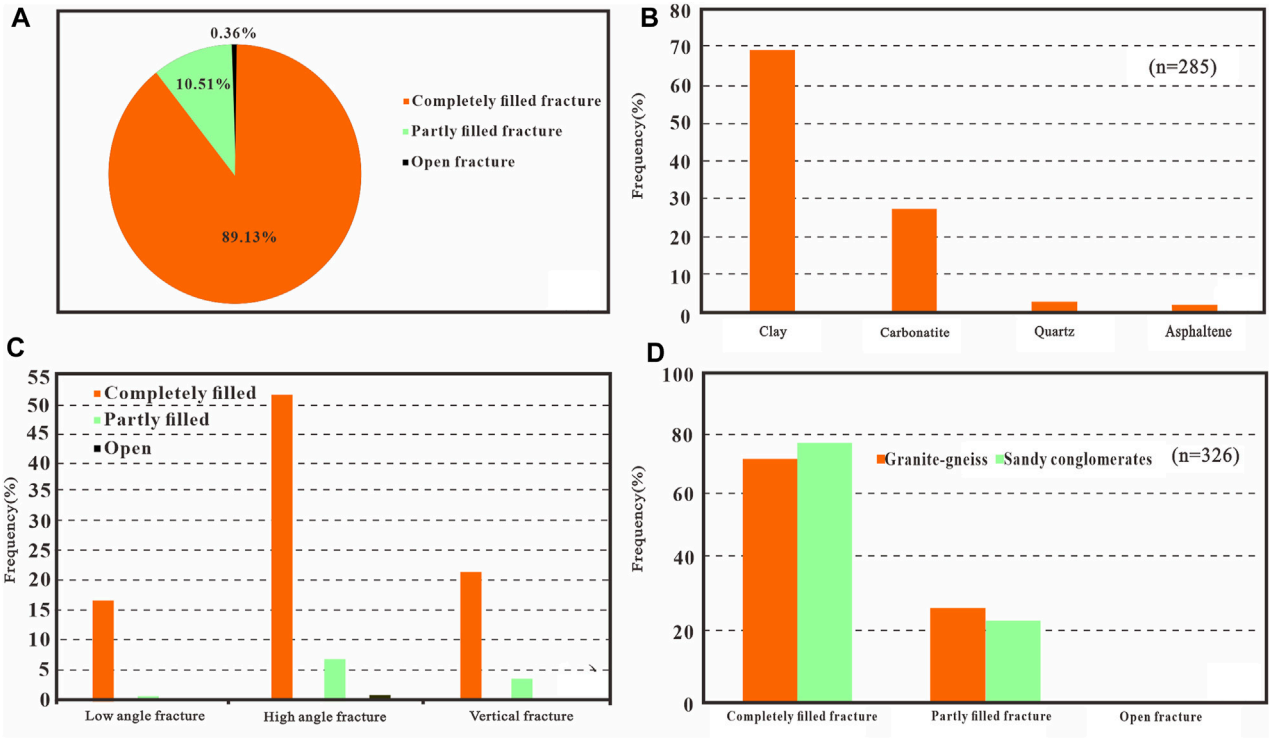


FIGURE 5
(A) Types of structural fracture filling; **(B)** Types of materials filling tectonic fractures; **(C)** Filling degree of tectonic fractures at different angles; **(D)** The Filling degree in tectonic fractures for different lithologies.

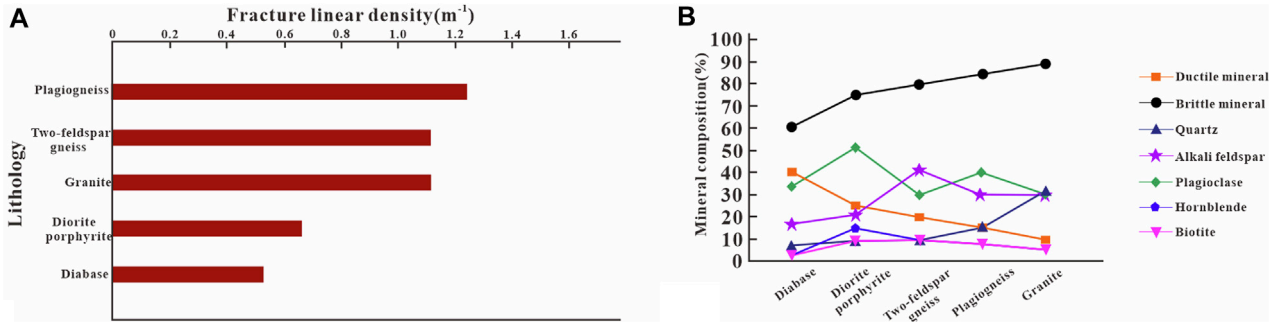


FIGURE 6
(A) Connection about density and lithology of structural fracture; **(B)** Distribution of mineral content in diverse lithologies.

fractures are identified, which indicates the formation period of four fractures.

The fracture filling degree of metamorphic buried hill reservoir in Bozhong 19–6 condensate gas field is high, it is mainly completely filled fractures, accounting for 89.13%, followed by partly filled fractures, accounting for 10.51%, open fractures only accounts for 0.36% (Figure 5A). The fractures are mainly filled with caly, followed by carbonate fillings, quartz fillings and asphaltene account for a small proportion of fractures (Figure 5B). The filling degree of low angle fractures is higher, and the filling degree of high angle fractures and vertical fractures is lower (Figure 5C). The fractures filling degree of glutenite is high, and the fractures effectiveness is low. A certain number of partly filled fractures are developed in granitic gneiss, and the fractures effectiveness is high (Figure 5D).

5 Discussion

5.1 Controlling factors of fractures in metamorphic hills

5.1.1 Lithology

The difference of rock mineral composition and rock fabric of different lithologies determines the difference of structural fracture

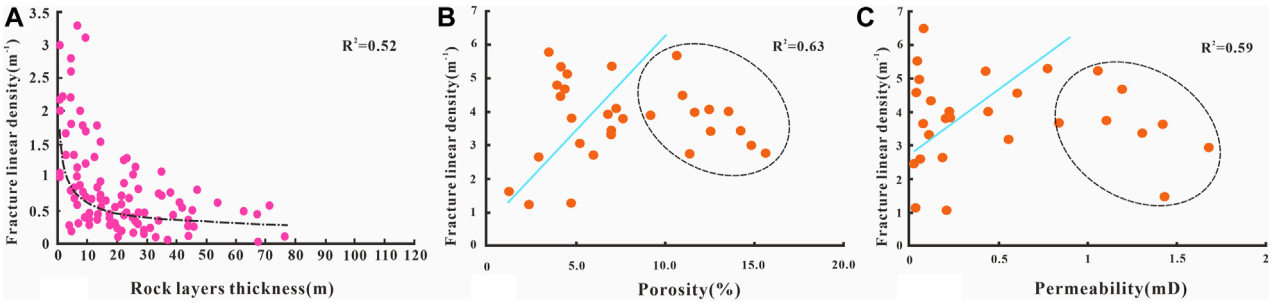


FIGURE 7
(A) Intersection diagram of structural fracture density and rock layer thickness; **(B)** intersection diagram of structural fracture density and reservoir porosity; **(C)** intersection diagram of structural fracture density and reservoir permeability.

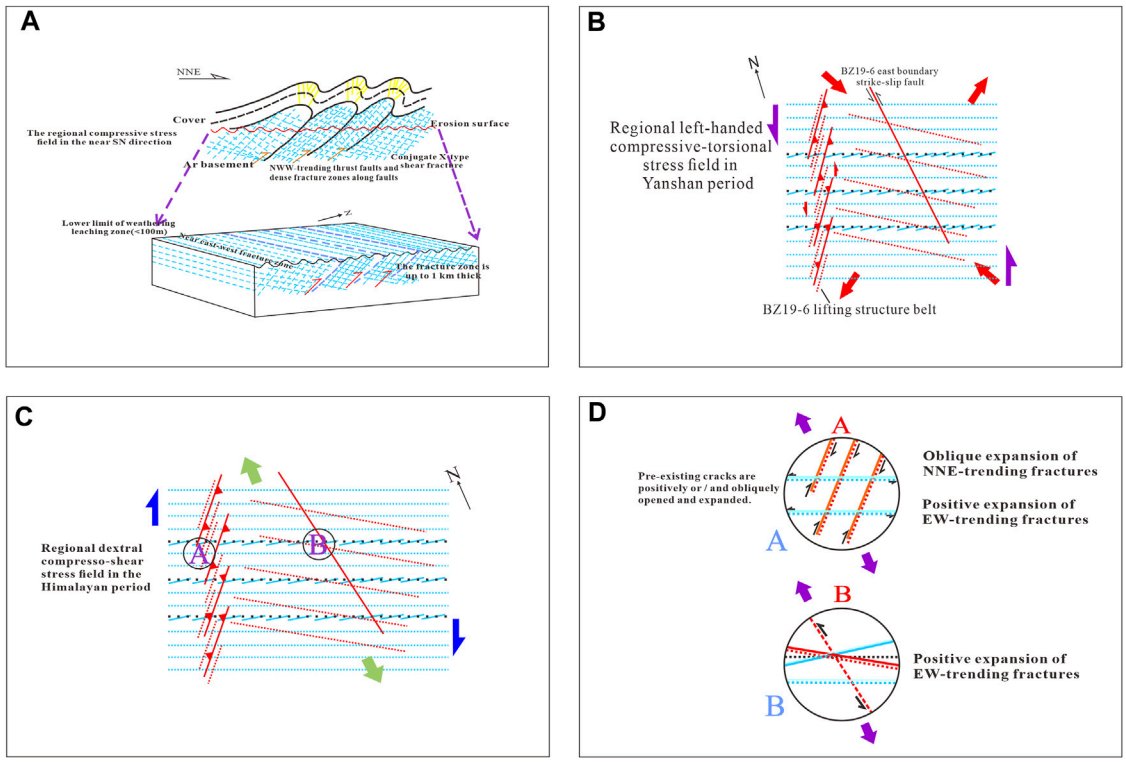


FIGURE 8
Structural fracture development patterns in different tectonic periods within BZ19-6 condensate gas field.

development, which is the internal factor determining the difference of fracture development (Ding et al., 2012; Ju and Sun, 2016). There are various types of metamorphic buried hill reservoir rocks in Bozhong 19–6 condensate gas field, and the main reservior rocks are metamorphic rocks and intrusive dikes. The tectonic fractures in the study area are mainly developed in plagioclase gneiss and monzonitic gneiss, which density is high, followed by fractures density in the granite, and the fracture density in diorite porphyrite and diabase is low (Figure 6A). The content of brittle minerals in plagioclase gneiss, monzonitic gneiss and granite is more than 80%, and diorite porphyry and diabase is less than 80% (Figure 6B). The rock of lower plastic minerasl content has a better brittleness. Under the action of tectonic stress, it is easy to development fractures, and the degree of fractures development is higher (Wang et al., 2023). It is common for plagioclase gneiss, monzonitic gneiss and granite to undergo migmatization (Lander and Laubach, 2015). Recrystallization makes the rock grains become larger from small, as the mineral grains increase, the particle size becomes longer (Maréchal et al., 2004). Under the same tectonic stress, the moment exerted on the same kind of mineral increases with larger grain size. Larger mineral grains are more likely to exceed the stress-bearing strength and generate fractures (Li et al., 2017).The observation results of core and thin section show that the rock with relatively high content of brittl minerals has a high

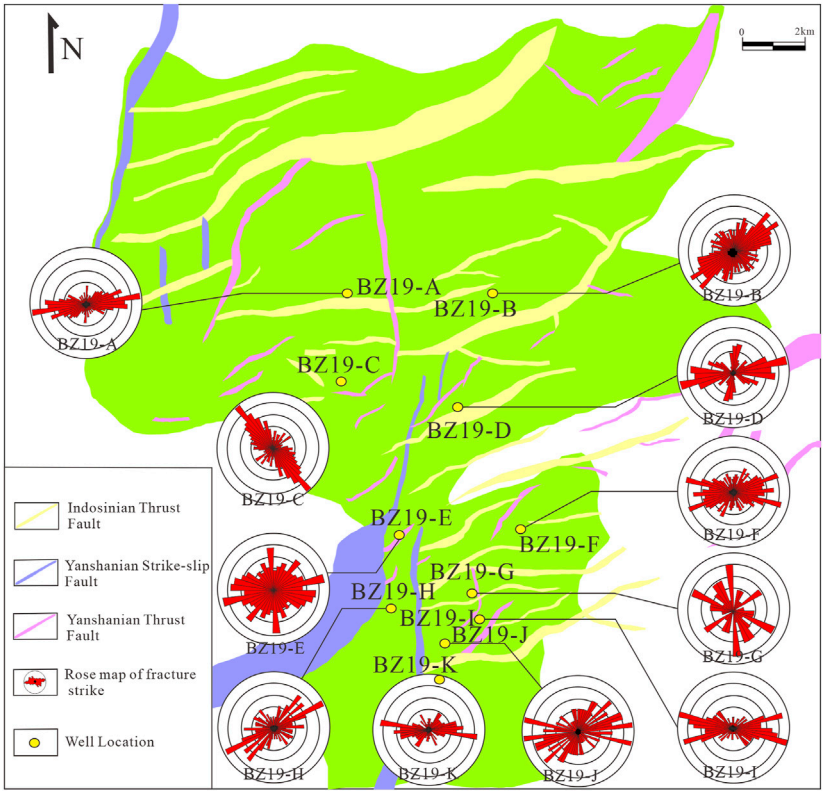


FIGURE 9
Major larger fault distribution map, modified from (Dai et al., 2021), the fracture orientations are obtained from the data of 11 wells.

degree of composition and structural heterogeneity. The rock contains minerals of various scales, components and shapes, and the transmission speed of each grain to force and its own deformation are different, which leads to the uneven distribution of stress field in the rock. Under the action of stress, it is more likely to development fractures due to the influence of rock composition and structural heterogeneity (Li et al., 2022). Therefore, rocks with a high degree of heterogeneity are more likely to development fractures.

5.1.2 Rock layers thickness

Under the action of tectonic stress, the fractures development degree of thinner rock thickness is higher (Nelson and Mold, 2000). The difference of rock layers thickness is an important factor causing the vertical heterogeneity of fractures development in the study area. The linear density of tectonic fractures decreases gradually with the increase of rock layers thickness (Figure 7A). The linear density of tectonic fractures decreases significantly when the thickness of the rock layer increases from 2 m to 15 m.When the thickness of the rock layer is greater than 15 m, the degree of fracture development is low, and the thickness of the rock layer has little effect on the linear density of the fractures.

5.1.3 Reservoir porosity and permeability

If the porosity and permeability of the reservoir are high, it shows that the rock is relatively loose, when the fracture extends and expands, it is easy to produce stress release in the matrix pores, and it is difficult to form large scale fractures. If the porosity and permeability of the reservoir are low, it shows that the rock is dense, its compressive strength and critical fracture pressure become larger, and the degree of tectonic fractures development will be lower when subjected to tectonic stress. Only when the porosity and permeability are in the suitable range, the rock compressive strength, critical fracture value and fracture extension ability can achieve the optimal combination. The relationship between fracture linear density and reservoir porosity and permeability has a two-stage relationship. When the reservoir porosity is less than 10%, the porosity is positively correlated with the development degree of tectonic fractures. When the matrix porosity is more than 10%, the porosity is negatively correlated with the development degree of tectonic fractures (Figure 7B). When the reservoir permeability is less than 1.1 mD, the permeability is positively correlated with the degree of structural fracture development. When the matrix permeability is greater than 1.1 mD, the permeability is negatively correlated with the development degree of tectonic fractures (Figure 7C).

5.1.4 Tectonic background

5.1.4.1 Tectonic movement

The thrust extrusion in the Indosinian period is the key factor for the reservoir fractures development in the study area. The metamorphic rock basement is subjected to strong compression and thrusting, forming a large number of large scale faults in the N-W oriented. Especially, the core of the extrusion is the stress

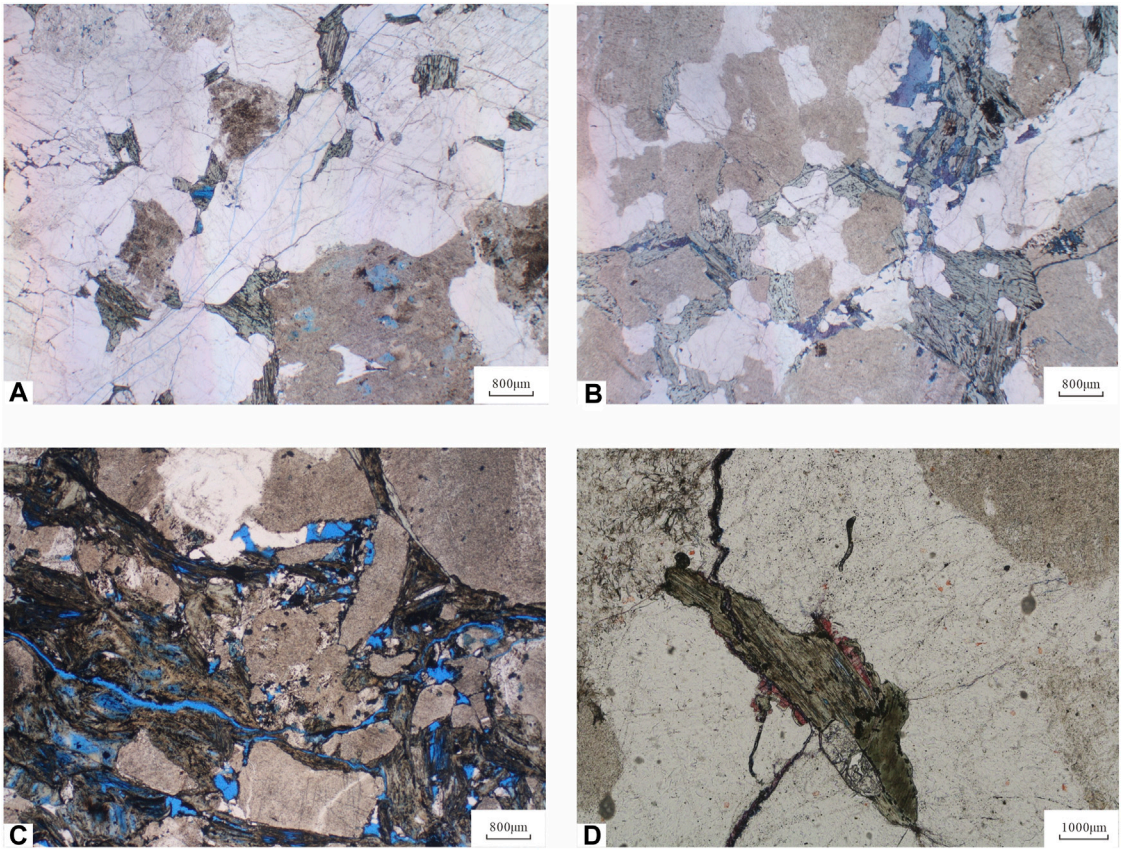


FIGURE 10
(A) Well BZ19-6-E, 4564.0 m, granular rock, single polarized light, dissolution intergranular pores and dissolution intragranular pores; **(B)** Well BZ19-6-E, 4630.0 m, plagioc gneiss, single polarized light, intragranular dissolution pores; **(C)** Well BZ19-6-E, 4515.0 m, plagioc gneiss, single polarized light, intergranular pores, intracrystalline dissolution pores, and unfilled fractures; **(D)** Well BZ19-6-C, 5190.0 m, plagioc gneiss, single polarized light, biotite intracrystalline dissolution pores and feldspar dissolution pores along cleavage.

concentration development area, and a large number of tectonic fractures are formed inside the buried hill (Cheng et al., 2018) (Figure 8A). At the same time, the N-E oriented thrust extrusion caused the study area to uplift sharply, forming an anticline uplift structure. The Archean metamorphic rock basement exposed the surface to weathering and leaching, and atmospheric water leached along the fault to the interior of the buried hill, forming a thick weathering crust. Due to the early formation time, these fractures experienced strong diagenesis in the later deep burial process, and most of the fractures were filled (Tong et al., 2012). During the Yanshanian period, it was mainly affected by the N-W trending low angle subduction of the Paleo Pacific Ocean. A large number of N-E oriented trending strike-slip faults were formed in the Bozhong sag, which retransformed the early fractures and further expanded the scale of fracture development (Huang et al., 2003) (Figure 8B). The influence of the Himalayan tectonic movement on the reservoir in the study area is mainly reflected in the reactivation of early fractures and the generation of new fractures. Most of the fractures formed in the Indosinian and Yanshanian periods are filled with argillaceous, iron and carbonate minerals (Wang et al., 2022). A large number of high angle fractures are formed inside or on the edge of the early filled fractures, and a small number of new fractures are generated. The Himalayan period is the main period for the formation of effective fractures in the reservoir of the study area. Although the ability of the Himalayan period to development new fractures is not as good as that of the Indosinian and Yanshanian periods, the Himalayan tectonic movement can re-activate the early fractures (Wang et al., 2018)(Figures 8C,D).

In general, The formation of buried hill reservoir fractures in the study area has experienced the initial formation of buried hill caused by strong extrusion in Indosinian period, the superimposed transformation and destruction of compression-torsion strike-slip in early Yanshanian period, the reformation of fault depression into mountains in middle Yanshanian period, and the multi-stage structural transformation and superimposed transformation process of reactivation of tension-torsion extension fractures in Himalayan period. The strong compressional tectonism in Indosinian period laid the reservoir foundation of buried hill, the sinistral strike slip in Yanshanian period further expanded the scale of fractures, and the dextral strike slip in Himalayan period reactivated the early fractures and formed a super large scale fractures system.

5.1.4.2 Control of faults on fractures

Studies have shown that although there are differences in the characteristics and formation mechanism of tectonic fractures in the

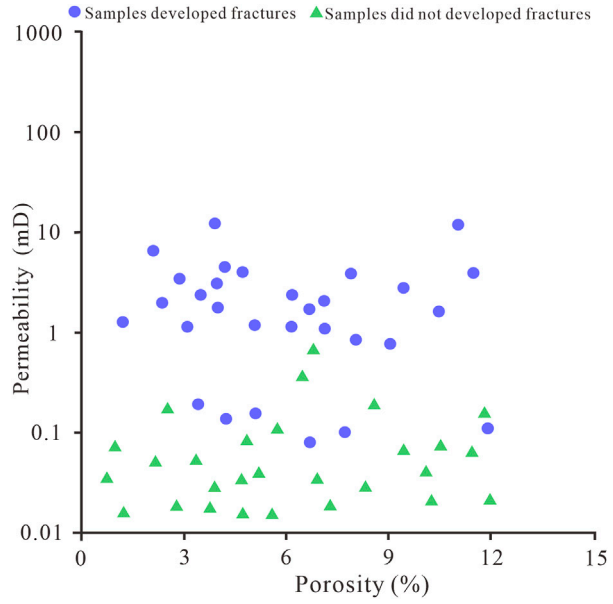


FIGURE 11
Relationship of permeability and porosity in metamorphic rock reservoirs. Analyzed by Physical Property Testing (N = 58).

fault zone under different mechanical properties, it is a common law that the farther the distance from the fault zone is, the less developed the tectonic fractures are (Lavenu et al., 2013). According to the rose diagram of fracture trends in 11 wells (Figure 9), it can be seen that the fractures orientation is parallel or nearly parallel to the orientation of adjacent faults, which indicates that faults play an important role in the development of tectonic fractures. In addition, near the fault or at the inflection point and intersection of the fault zone, the stress is concentrated, and the tectonic fractures are developed. BZ19-6-I, BZ19-6-J, and BZ19-6-K are located at the intersection of multiple different sequence faults, and the fracture density is high. In addition, the cataclastic zone in these three wells is extremely developed and has a certain direction, which is the result of the combined action of shear stress and tensile stress.

5.2 Contributions of fractures to reservoir quality

Previous studies have shown that weathering crust, as well as pore-fractures type reservoirs are the major types of the Paleozoic reservoirs in BZ19-6 condensate gas field (Luo et al., 2005). The study shows that the reservoir space of metamorphic buried hill reservoir in Bozhong 19–6 condensate gas field mainly includes intergranular pores, intragranular dissolution pores, fractures of cataclastic grains in sandy conglomerate and metamorphic buried hill, and dissolution expansion pores developed along microfractures (Figure 10). The study area has experienced multi-tectonic movement, and a large number of fractures are developed under the tectonic stress. The fractures are cut and connected with each other, which is an important reservoir space in the study area. In addition, these fractures effectively communicate intergranular pores and intragranular dissolved pores, which play a role in the formation of effective reservoirs. Based on the analysis of 58 samples of reservoir physical property test results collected, it is considered that there are obvious differences in permeability between samples from the same lithology, and the difference in permeability depends on whether the sample has microscopic effective fractures. The measured permeability of core samples without effective fractures is concentrated in 0.01–0.1 mD, while the measured permeability of core samples with effective fractures is 1–10 mD. Therefore, it is considered that the development of fractures increases the reservoir permeability by 1-2 orders of magnitude (Figure 11). This difference in permeability reflects that fractures are the key to improving the seepage capacity of deep reservoirs.

In general, metamorphic rocks must undergo fracture and dissolution before they can become favorable reservoirs (Guo et al., 2016). For dense metamorphic rocks, the depth of weathering and leaching during the exposure period of buried hills is limited, and it is difficult to effectively transform them. Therefore, in order to form an effective reservoir in the inner part of the buried hill, it is first necessary to form fractures by strong tectonic movement. Fractures can become a channel for weathering and leaching to expand to the bedrock, thus forming dissolution fractures (Chai and Yin, 2021). These results imply that the development degree of fractures determines the distribution of favourable reservoirs.

6 Conclusion

The tectonic fractures of metamorphic rock buried hill reservoir in Bozhong 19–6 condensate gas field mainly develop shear fractures, and the development of tensile fractures is less. The fracture filling degree is high, and the filling materials mainly include clay, carbonate, silicate and other minerals. The dip angle of fractures is mainly high angle fractures and vertical fractures. The strike of tectonic fractures is scattered. There are four groups of tectonic fractures in EW, NE-SW, NW-SE and NNW-SSE oriented.

Lithology is the internal factor that determines the difference of fracture development. In rocks with relatively high content of light minerals, the degree of fracture development increases with the increase of composition and structural heterogeneity. Under the same stress condition, the thinner the rock thickness is, the more developed the fractures are. The vertical difference of single rock thickness is an important factor to cause the vertical heterogeneity of fracture development degree in metamorphic rock reservoir. When the porosity and permeability of the reservoir are in a suitable combination, the mechanical properties of the rock and the extension ability of the fractures can achieve the optimal combination and promote the development of the fractures. Indosinian periods and Yanshanian periods are the main periods of fractures formation. The early tectonic fractures were reactivated in Himalayan epoch, and the multi-tectonic movements caused the complex fractures system.

Fractures in metamorphic rock reservoirs connect dispersed pores and improve the effectiveness of reservoirs. The existence of fractures increases the permeability of metamorphic rock reservoirs by 1–2 orders of magnitude, which is the key to improving the seepage capacity of metamorphic rock reservoirs. It provides effective space for the accumulation and migration of oil

and gas, and plays an important role in the formation of metamorphic rock reservoirs.

Data availability statement

The raw data supporting the conclusion of this article will be made available by the authors, without undue reservation.

Author contributions

ZL: Methodology, Writing–review and editing, Funding acquisition. QC: Funding acquisition, Writing–review and editing. XL: Data curation, Funding acquisition, Resources, Writing–review and editing. LZ: Writing–review and editing. WL: Project administration, Supervision, Writing–review and editing. GZ: Writing–original draft, Writing–review and editing.

Funding

The author(s) declare financial support was received for the research, authorship, and/or publication of this article. The major science and technology project of CNOOC (China) Co., Ltd. High-efficiency development technology of complex oil and gas reservoirs in the middle and deep layers of Bohai Sea (CNOOC-KJ 135 ZDXM 36 TJ 03 TJ-GD 2020-01); Tianjin branch of CNOOC (China) Co., Ltd. Unveiled the project Research on the main controlling factors of fracture development and favorable reservoir distribution of different types of buried hills in Bohai (ZZKY-2022-TJ-JG-02).

Conflict of interest

Authors ZL, QC, XL, LZ, and WL were employed by the CNOOC China Limited.

The remaining author declares that the research was conducted in the absence of any commercial or financial relationships that could be construed as a potential conflict of interest.

Publisher's note

All claims expressed in this article are solely those of the authors and do not necessarily represent those of their affiliated organizations, or those of the publisher, the editors and the reviewers. Any product that may be evaluated in this article, or claim that may be made by its manufacturer, is not guaranteed or endorsed by the publisher.

References

Aydin, A. (2000). Fractures, faults, and hydrocarbon entrapment, migration and flow. *Mar. Petroleum Geol.* 17 (7), 797–814. doi:10.1016/S0264-8172(00)00020-9

Bazalgette, L., Petit, J.-P., Amrhar, M., and Ouanaïmi, H. (2010). Aspects and origins of fractured dip-domain boundaries in folded carbonate rocks. *J. Struct. Geol.* 32 (4), 523–536. doi:10.1016/j.jsg.2010.03.002

Cao, X., Li, S., Xu, L., Guo, L., Liu, L., Zhao, S., et al. (2015). Mesozoic–Cenozoic evolution and mechanism of tectonic geomorphology in the central North China Block: constraint from apatite fission track thermochronology. *J. Asian Earth Sci.* 114, 41–53. doi:10.1016/j.jseaes.2015.03.041

Chai, Y., and Yin, S. (2021). 3D displacement discontinuity analysis of *in-situ* stress perturbation near a weak faul. *Adv. Geo-Energy Res.* 5 (3), 286–296. doi:10.46690/ager.2021.03.05

Chen, A. (1998). Geometric and kinematic evolution of basement-cored structures: intraplate orogenesis within the Yanshan Orogen, northern China. *Tectonophysics* 292 (1–2), 17–42. doi:10.1016/S0040-1951(98)00062-6

Cheng, Y., Wu, Z., Lu, S., Li, X., Lin, C., Huang, Z., et al. (2018). Mesozoic to cenozoic tectonic transition process in zhanhua sag, Bohai Bay Basin, east China. *Tectonophysics* 730, 11–28. doi:10.1016/j.tecto.2018.02.010

Cui, J., Zhang, J., and Zhang, H. (2013). Features of the carboniferous volcanic rocks fracture reservoirs in Hongshanzui oilfield, Junggar Basin. *J. Earth Sci.* 24 (6), 997–1007. doi:10.1007/s12583-013-0397-z

Dai, X., Tang, H., Li, H., Zhang, Y., Xu, P., Wang, P., et al. (2021). Characteristics and formation mechanism of the fractures in Archaean buried hill: a case study in the BZ19-6 Block, Bohai Bay Basin, China. *Geol. J.* 56 (4), 2240–2257. doi:10.1002/gj.4052

Ding, W., Li, C., Li, C., Xu, C., Jiu, K., Zeng, W., et al. (2012). Fracture development in shale and its relationship to gas accumulation. *Geosci. Front.* 3 (1), 97–105. doi:10.1016/j.gsf.2011.10.001

Ding, W., Zhu, D., Cai, J., Gong, M., and Chen, F. (2013). Analysis of the developmental characteristics and major regulating factors of fractures in marine–continental transitional shale-gas reservoirs: a case study of the Carboniferous–Permian strata in the southeastern Ordos Basin, central China. *Mar. Petroleum Geol.* 45, 121–133. doi:10.1016/j.marpetgeo.2013.04.022

Eig, K., and Bergh, S. G. (2011). Late Cretaceous–Cenozoic fracturing in Lofoten, North Norway: tectonic significance, fracture mechanisms and controlling factors. *Tectonophysics* 499 (1–4), 190–205. doi:10.1016/j.tecto.2010.12.002

Ezati, M., Azizzadeh, M., Riahi, M. A., Fattahpour, V., and Honarmand, J. (2018). Characterization of micro-fractures in carbonate Sarvak reservoir, using petrophysical and geological data, SW Iran. *J. Petroleum Sci. Eng.* 170, 675–695. doi:10.1016/j.petrol.2018.06.058

Fan, C., Xu, C., Li, C., Liu, A., Li, H., Hou, J., et al. (2021). Identification and prediction of allo-source overpressure caused by vertical transfer: example from an HTHP gas reservoir in the ledong slope in the yinggehai basin. *Geofluids* 2021, 1–20. doi:10.1155/2021/6657539

Feng, W., Wang, F., Jiang, T., Zhao, X., Guan, J., Ma, X., et al. (2020). Origin and accumulation of petroleum in deep precambrian reservoir in baxian sag, Bohai Bay Basin, China. *Mar. Petroleum Geol.* 120, 104541. doi:10.1016/j.marpetgeo.2020.104541

Gong, L., Gao, S., Liu, B., Yang, J., Fu, X., Xiao, F., et al. (2021). Quantitative prediction of natural fractures in shale oil reservoirs. *Geofluids* 2021, 1–15. doi:10.1155/2021/5571855

Guo, P., Yao, L., and Ren, D. (2016). Simulation of three-dimensional tectonic stress fields and quantitative prediction of tectonic fracture within the Damintun Depression, Liaohe Basin, northeast China. *J. Struct. Geol.* 86, 211–223. doi:10.1016/j.jsg.2016.03.007

Huang, C. H., Zhu, H. Y., Wang, J. D., Han, J., Zhou, G. Q., and &Tang, X. H. (2022). AFEM-DFN model for the interaction and propagation of multi-cluster fractures during variable fluid-viscosity injection in layered shale oil reservoir. *Petroleum Sci.* 19 (6), 2796–2809. doi:10.1016/j.petsci.2022.06.007

Huang, S., Li, L., Vleugels, J., Wang, P., and Van Der Biest, O. (2003). Thermodynamic prediction of the nonstoichiometric phase Zr1–zCezO2–x in the ZrO2–CeO1.5–CeO2 system. *J. Eur. Ceram. Soc.* 23 (1), 99–106. doi:10.1016/S0955-2219(02)00073-0

Ju, W., and Sun, W. (2016). Tectonic fractures in the lower cretaceous xiagou formation of qingxi oilfield, jiuxi basin, NW China part one: characteristics and controlling factors. *J. Petroleum Sci. Eng.* 146, 617–625. doi:10.1016/j.petrol.2016.07.042

Lander, R. H., and Laubach, S. E. (2015). Insights into rates of fracture growth and sealing from a model for quartz cementation in fractured sandstones. *Geol. Soc. Am. Bull.* 127 (3–4), 516–538. doi:10.1130/B31092.1

Lavenu, A. P. C., Lamarche, J., Gallois, A., and Gauthier, B. D. M. (2013). Tectonic versus diagenetic origin of fractures in a naturally fractured carbonate reservoir analog (Nerthe anticline, southeastern France). *AAPG Bull.* 97 (12), 2207–2232. doi:10.1306/04041312225

Li, A., Ding, W., Wang, R., He, J., Wang, X., Sun, Y., et al. (2017). Petrophysical characterization of shale reservoir based on nuclear magnetic resonance (NMR) experiment: a case study of Lower Cambrian Qiongzhusi Formation in eastern Yunnan Province, South China. *J. Nat. Gas Sci. Eng.* 37, 29–38. doi:10.1016/j.jngse.2016.11.034

Li, H., Qin, Q., Zhang, B., Ge, X., Hu, X., Fan, C., et al. (2020). Tectonic fracture Formation and distribution in ultradeep marine carbonate gas reservoirs: a case study of the maokou formation in the jiulongshan gas field, sichuan basin, southwest China. *Energy and Fuels* 34 (11), 14132–14146. doi:10.1021/acs.energyfuels.0c03327

Li, H., Yu, F., Wang, M., Wang, Y., and Liu, Y. (2022). Quantitative prediction of structural fractures in the Paleocene lower Wenchang formation reservoir of the Lufeng Depression. *Adv. Geo-Energy Res.* 6 (5), 375–387. doi:10.46690/ager.2022.05.03

Li, S., Zhao, G., Dai, L., Zhou, L., Liu, X., Suo, Y., et al. (2012). Cenozoic faulting of the Bohai Bay Basin and its bearing on the destruction of the eastern north China craton. *J. Asian Earth Sci.* 47, 80–93. doi:10.1016/j.jseaes.2011.06.011

Lianbo, Z., and Xiang-Yang, L. (2009). Fractures in sandstone reservoirs with ultra-low permeability: a case study of the upper triassic yanchang formation in the ordos basin, China. *AAPG Bull.* 93 (4), 461–477. doi:10.1306/09240808047

Liu, C., Xie, Q., Wang, G., Zhang, C., Wang, L., and Qi, K. (2016). Reservoir properties and controlling factors of contact metamorphic zones of the diabase in the northern slope of the Gaoyou Sag, Subei Basin, eastern China. *J. Nat. Gas Sci. Eng.* 35, 392–411. doi:10.1016/j.jngse.2016.08.070

Liu, J., Ding, W., Yang, H., Dai, P., Wu, Z., and Zhang, G. (2023b). Natural fracturesand rock mechanical stratigraphy evaluationin huaqing area, OrdosBasin: a quantitative analysis basedon numerical simulation. *EarthScience* 48 (7), 2572–2588. doi:10.3799/dqkx.2022.234

Liu, J., Ding, W., Yang, H., and Liu, Y. (2021). Quantitative multiparameter prediction of fractured tight sandstone reservoirs: a case study of the yanchang formation of the ordos basin, Central China. *SPE J.* 26 (05), 3342–3373. doi:10.2118/205495-PA

Liu, J., Mei, L., Ding, W., Xu, K., Yang, H., and Liu, Y. (2023a). Asymmetric propagation mechanism of hydraulic fracture networks in continental reservoirs. *GSA Bull.* 135 (3–4), 678–688. doi:10.1130/B36358.1

Liu, J., Yang, H., Xu, K., Wang, Z., Liu, X., Cui, L., et al. (2022). Genetic mechanism of transfer zones in rift basins: insights from geomechanical models. *GSA Bull.* 134 (9–10), 2436–2452. doi:10.1130/B36151.1

Luo, J., Morad, S., Liang, Z., and Zhu, Y. (2005). Controls on the quality of Archean metamorphic and Jurassic volcanic reservoir rocks from the Xinglongtai buried hill, western depression of Liaohe basin, China. *AAPG Bull.* 89 (10), 1319–1346. doi:10.1306/05230503113

Lyu, W., Zeng, L., Zhou, S., Du, X., Xia, D., Liu, G., et al. (2019). Natural fractures in tight-oil sandstones: a case study of the upper triassic yanchang formation in the southwestern ordos basin, China. *AAPG Bull.* 103 (10), 2343–2367. doi:10.1306/0130191608617115

Maerten, L., Maerten, F., and Lejri, M. (2018). Along fault friction and fluid pressure effects on the spatial distribution of fault-related fractures. *J. Struct. Geol.* 108, 198–212. doi:10.1016/j.jsg.2017.10.008

Maréchal, J. C., Dewandel, B., and Subrahmanyam, K. (2004). Use of hydraulic tests at different scales to characterize fracture network properties in the weathered-fractured layer of a hard rock aquifer: FRACTURE NETWORK PROPERTIES IN HARD ROCK. *Water Resour. Res.* 40 (11). doi:10.1029/2004WR003137

Nelson, R. A., and Mold, E. P. (2000). Production characteristics of the fractured reservoirs of the La Paz field. *Maracaibo basin, venezuela. AAPG Bull.* 84. doi:10.1306/8626C393-173B-11D7-8645000102C1865D

Ortega, O. J., Marrett, R. A., and Laubach, S. E. (2006). A scale-independent approach to fracture intensity and average spacing measurement. *AAPG Bull.* 90 (2), 193–208. doi:10.1306/08250505059

Pei, L., Wang, X., Wang, Q., Zhang, Q., Luo, H., and Liu, W. (2022). Origin, accumulation and secondary alteration of natural gas around Qingshui Sub-sag, Liaohe Depression, China: insights from molecular and isotopic composition. *Mar. Petroleum Geol.* 135, 105390. doi:10.1016/j.marpetgeo.2021.105390

Salah, M. G., and Alsharhan, A. S. (1998). The Precambrian basement: a major reservoir in the rifted basin, Gulf of Suez. *J. Petroleum Sci. Eng.* 19 (3–4), 201–222. doi:10.1016/S0920-4105(97)00024-7

Tong, K., Zhao, C., Lü, Z., Zhang, Y., Zheng, H., Xu, S., et al. (2012). Reservoir evaluation and fracture chracterization of the metamorphic buried hill reservoir in Bohai Bay Basin. *Petroleum Explor. Dev.* 39 (1), 62–69. doi:10.1016/S1876-3804(12)60015-9

Wang, G., Li, S., Wu, Z., Suo, Y., Guo, L., and Wang, P. (2019). Early paleogene strike-slip transition of the tan–Lu fault zone across the southeast Bohai Bay Basin: constraints from fault characteristics in its adjacent basins. *Geol. J.* 54 (2), 835–849. doi:10.1002/gj.3344

Wang, J., Xie, H.-P., Matthai, S. K., Hu, J.-J., and Li, C.-B. (2023). The role of natural fracture activation in hydraulic fracturing for deep unconventional geo-energy reservoir stimulation. *Petroleum Sci.* 20, 2141–2164. S1995822623000079. doi:10.1016/j.petsci.2023.01.007

Wang, N., Xu, Y.-H., Wang, F.-L., Liu, Y., Huang, Q., and Huang, X. (2022). Identification and geochemical significance of unusual C24 tetracyclic terpanes in Shahejie Formation source rocks in the Bozhong subbasin, Bohai Bay Basin. *Petroleum Sci.* 19 (5), 1993–2003. doi:10.1016/j.petsci.2022.03.025

Wang, Q., Hao, F., Niu, C., Zou, H., Miao, Q., Yin, J., et al. (2021). Origins and deep petroleum dynamic accumulation in the southwest part of the Bozhong depression, Bohai Bay Basin: insights from geochemical and geological evidences. *Mar. Petroleum Geol.* 134, 105347. doi:10.1016/j.marpetgeo.2021.105347

Wang, R., Ding, W., Zhang, Y., Wang, Z., Wang, X., He, J., et al. (2016). Analysis of developmental characteristics and dominant factors of fractures in Lower Cambrian marine shale reservoirs: a case study of Niutitang formation in Cen'gong block, southern China. *J. Petroleum Sci. Eng.* 138, 31–49. doi:10.1016/j.petrol.2015.12.004

Wang, W., Yi, J., Shan, X., Zhang, X., Liu, X., Liu, P., et al. (2022). Characteristics of fractures development and its controlling factors within the buried hill reservoirs from the Archaean metamorphic basement in the Bozhong Sag, Bohai Bay Basin, Eastern China. *Front. Earth Sci.* 10, 935508. doi:10.3389/feart.2022.935508

Wang, X., Wang, R., Ding, W., Yin, S., Sun, Y., Zhou, X., et al. (2017). Development characteristics and dominant factors of fractures and their significance for shale reservoirs: a case study from Є1b2 in the Cen'gong block, southern China. *J. Petroleum Sci. Eng.* 159, 988–999. doi:10.1016/j.petrol.2017.08.007

Wang, Y., Zhou, L., Liu, S., Li, J., and Yang, T. (2018). Post-cratonization deformation processes and tectonic evolution of the North China Craton. *Earth-Science Rev.* 177, 320–365. doi:10.1016/j.earscirev.2017.11.017

Wang, Z., Xiao, S., Wang, F., Tang, G., Zhu, L., and Zhao, Z. (2021). Phase behavior identification and formation mechanisms of the BZ19-6 condensate gas reservoir in the deep Bozhong sag, Bohai Bay Basin, eastern China. *Geofluids* 2021, 1–19. doi:10.1155/2021/6622795

Xu, C., Yu, H., Wang, J., and Liu, X. (2019). Formation conditions and accumulation characteristics of Bozhong 19-6 large condensate gas field in offshore Bohai Bay Basin. *Petroleum Explor. Dev.* 46 (1), 27–40. doi:10.1016/S1876-3804(19)30003-5

Xu, S., Hao, F., Xu, C., Zou, H., Zhang, X., Zong, Y., et al. (2019). Hydrocarbon migration and accumulation in the northwestern Bozhong subbasin, Bohai Bay Basin, China. *J. Petroleum Sci. Eng.* 172, 477–488. doi:10.1016/j.petrol.2018.09.084

Ye, T., Chen, A., Niu, C., Luo, J., and Hou, M. (2022). Effective fractures linked with tectonic reactivation and multiple genetic fluids in the ultradeep Paleozoic carbonate buried hills of the Bozhong sag, North China. *Mar. Petroleum Geol.* 140, 105642. doi:10.1016/j.marpetgeo.2022.105642

Ye, T., Chen, A., Niu, C., Wang, Q., and Guo, L. (2020). Characteristics and vertical zonation of large-scale granitic reservoirs, a case study from Penglai oil field in the Bohai Bay Basin, North China. *Geol. J.* 55 (12), 8109–8121. doi:10.1002/gj.3932

Ye, T., Chen, A., Niu, C., and Wang, Q. B. (2021). Structural, petrophysical and lithological characterization of crystalline bedrock buried-hill reservoirs: a case study of the southern jinzhou oilfield in offshore Bohai Bay Basin, north China. *J. Petroleum Sci. Eng.* 196, 107950. doi:10.1016/j.petrol.2020.107950

Yi, J., Li, H., Shan, X., Hao, G., Yang, H., Wang, Q., et al. (2022). Division and identification of vertical reservoir units in archaeozoic metamorphic buried hill of Bozhong sag, Bohai Bay Basin, east China. *Petroleum Explor. Dev.* 49 (6), 1282–1294. doi:10.1016/S1876-3804(23)60349-0

Yin, S., Ding, W., Zhou, W., Shan, Y., Wang, R., Liu, J., et al. (2016). Logging assessment of tight clastic rock reservoir fractures via the extraction of effective pore aspect ratios: a case study of lower Permian strata in the southern Qinshui Basin of eastern China. *J. Nat. Gas Sci. Eng.* 36, 597–616. doi:10.1016/j.jngse.2016.11.001

Yin, S., Han, C., Wu, Z., and Li, Q. (2019). Developmental characteristics, influencing factors and prediction of fractures for a tight gas sandstone in a gentle structural area of the Ordos Basin, China. *J. Nat. Gas Sci. Eng.* 72, 103032. doi:10.1016/j.jngse.2019.103032

Yu, F., and Koyi, H. (2016). Cenozoic tectonic model of the Bohai Bay Basin in China. *Geol. Mag.* 153 (5–6), 866–886. doi:10.1017/S0016756816000492

Zeng, L., Gong, L., Guan, C., Zhang, B., Wang, Q., Zeng, Q., et al. (2022). Natural fractures and their contribution to tight gas conglomerate reservoirs: a case study in the northwestern Sichuan Basin, China. *J. Petroleum Sci. Eng.* 210, 110028. doi:10.1016/j.petrol.2021.110028

Zeng, W., Zhang, J., Ding, W., Zhao, S., Zhang, Y., Liu, Z., et al. (2013). Fracture development in Paleozoic shale of Chongqing area (South China). Part one: fracture characteristics and comparative analysis of main controlling factors. *J. Asian Earth Sci.* 75, 251–266. doi:10.1016/j.jseaes.2013.07.014

Zhao, X., Jin, F., Wang, Q., and Bai, G. (2015a). Buried-hill play, Jizhong subbasin, Bohai Bay basin: a review and future propespectivity. *AAPG Bull.* 99 (01), 1–26. doi:10.1306/07171413176

Zhou, L., Fu, L., Lou, D., Lu, Y., Feng, J., Zhou, S., et al. (2012). Structural anatomy and dynamics of evolution of the qikou sag, Bohai Bay Basin: implications for the destruction of north China craton. *J. Asian Earth Sci.* 47, 94–106. doi:10.1016/j.jseaes.2011.06.004

frontiers | Frontiers in Energy Research

TYPE Original Research
PUBLISHED 15 January 2024
DOI 10.3389/fenrg.2023.1338428

Check for updates

OPEN ACCESS

EDITED BY
Peng Tan,
CNPC Engineering Technology R & D Company Limited, China

REVIEWED BY
Zhaoyi Liu,
Northeast Petroleum University, China
Yuedu Chen,
Taiyuan University of Technology, China

*CORRESPONDENCE
Yongxiang Zheng,
zhengyx@stdu.edu.cn
Wei Wang,
wangweiuuu@163.com

RECEIVED 14 November 2023
ACCEPTED 29 December 2023
PUBLISHED 15 January 2024

CITATION
Gao H, Jia B, Lei Y, Zheng Y, Shi B, Wei H, Zhang T, Wang W and Niu Q (2024), The propagation of hydraulic fracture in layered coal seam: a numerical simulation considering the interface thickness based on the distinct element method.
Front. Energy Res. 11:1338428.
doi: 10.3389/fenrg.2023.1338428

COPYRIGHT
© 2024 Gao, Jia, Lei, Zheng, Shi, Wei, Zhang, Wang and Niu. This is an open-access article distributed under the terms of the Creative Commons Attribution License (CC BY). The use, distribution or reproduction in other forums is permitted, provided the original author(s) and the copyright owner(s) are credited and that the original publication in this journal is cited, in accordance with accepted academic practice. No use, distribution or reproduction is permitted which does not comply with these terms.

The propagation of hydraulic fracture in layered coal seam: a numerical simulation considering the interface thickness based on the distinct element method

Hongye Gao[1,2,3], Baoshan Jia[1,2], Yun Lei[3], Yongxiang Zheng[4,5]*, Bin Shi[6], Haiyang Wei[4], Tongjing Zhang[4], Wei Wang[4,5]* and Qinghe Niu[4,5]

[1]College of Safety Science and Engineering, Liaoning Technical University, Fuxin, China, [2]Key Laboratory of Mine Thermodynamic Disasters and Control of Ministry of Education, Liaoning Technical University, Huludao, China, [3]State Key Laboratory of Coal Mine Safety Technology, Shenyang Research Institute China Coal Technology & Engineering Group Corp, Shenyang, China, [4]Key Laboratory of Roads and Railway Engineering Safety Control, Ministry of Education, Shijiazhuang Tiedao University, Shijiazhuang, China, [5]Hebei Technology and Innovation Center on Safe and Efficient Mining of Metal Mine, Shijiazhuang, China, [6]Downhole Operation Company, CNPC Xibu Drilling Engineering Co., Ltd., Karamay, China

The intercalated layer of coal seam plays an important role in the propagation of hydraulic fracturing. To understand the role of the intercalated layer, a composite coal seam model considering the thickness of the intercalated layer was established. Based on the block distinct element method, the effects of rock structure (thickness of the coal seam and intercalated layer), rock properties (elastic modulus), and construction parameters (injection rate and fluid viscosity) on the penetration behavior of hydraulic fractures were analyzed. The results show that the intercalated layers influence the fracture deflection and have a hindering effect on fracture propagation. The thickness of the intercalated layer affects the stress on the bedding plane and the front edge of the fractures. On the contrary, the thickness of the coal seam mainly affects the penetration ability of hydraulic fractures and the extent of hydraulic fracture propagation. In addition, the elastic modulus of the intercalated layers and coal seams affects the hindering effect of the intercalated layer. The high injection rates reduce the hindering effect of the intercalated layer. When fracturing with a high-viscosity fluid, fractures are more likely to enter the intercalated layer. However, excessively high viscosity can make it difficult for fractures to penetrate the intercalated layer. This study can provide theoretical guidance for the fracturing of composite coal seams.

KEYWORDS

hydraulic fracturing, layered coal seam, distinct element method, thickness, intercalated layer

1 Introduction

Hydraulic fracturing is widely used to improve the permeability in low-permeability reservoirs. Based on numerical simulations (Huang et al., 2020; Liu et al., 2022; Huang et al., 2023a; Han et al., 2023) and experiments (Tan et al., 2019; Tan et al., 2020; Tan et al., 2023), there is a systematic understanding of the initiation and propagation mechanism of

hydraulic fractures. The previous understanding of fracture propagation mainly focused on the homogeneous matrix. However, the real strata are heterogeneity and anisotropy since most reservoirs are hosted in sedimentary formations which have bedding planes or intercalated layers (Huang et al., 2019; Huang et al., 2023b). Hydraulic fractures show different behaviors when they encounter bedding planes or intercalated layers (Liu et al., 2022). Thus, the intercalated layer has an important influence on fracture propagation. This paper will address the propagation pattern of hydraulic fractures when they encounter the intercalated layers.

In recent years, the influence of the interface on hydraulic fracture propagation has gradually become a focus. Ju et al. (2018) analyzed the elastic modulus and Poisson's ratio of adjacent rock layers for the propagation pattern of fractures that encounter the interface and discussed the role of contact properties of the interface. Huang et al. (2022) combined the effects of fracture toughness and elastic modulus from the perspective of energy dissipation to reduce and simplify the parameters of sensitivity analysis. Hadei and Veiskarami (2020) carried out a physical experiment based on manual models of adjacent rock layers. They discussed the effect of fracture energy of soft and hard rock layers and the effect of the angle of the adjacent layers. Guo et al. (2017) focused on the effect of stress differences and tensile strength of adjacent layers. Zhuang et al. (2023) carried out numerical simulations on the effects of initial stress field, stiffness difference, and interface angle with the phase field method. Qin et al. (2021) discussed the effect of stiffness ratio and strength ratio on the propagation behavior of fractures after they encounter the interface using the peridynamic method. Zhu et al. (2023) analyzed the effect of Young's modulus, natural fractures, and plasticity on the penetration behavior of fractures through layers. Wang et al. (2021) presented a comprehensive summary of the key factors affecting fracture penetration behavior, including lithology, layer thickness, degree of natural fracture development, interface properties, and construction fracturing parameters. Zheng et al. (2019) analyzed the stress and deformation at the interface/bedding plane based on the block distinct element method and fracture mechanics theory. They think that the discontinuous deformation at the interface was the intrinsic cause of the height containment of the fracture. On this basis, the influence of construction parameters (Zheng et al., 2022) and interface properties (Bai et al., 2023) on fracture propagation was investigated separately. In summary, the importance of the propagation behavior of hydraulic fractures after encountering an interface is now well-recognized. The rock properties, interface characteristics, and construction parameters of the adjacent layers are the key parameters (Ji et al., 2015; Song et al., 2017; Song et al., 2020; Luo et al., 2022; Liu et al., 2023; Wu et al., 2023). However, the interface thickness between the intercalated layers was generally considered to be 0 in previous studies. In fact, the thickness of the interfaces also has an important influence on the fracture propagation considering some factors such as filling within the fracture. Therefore, a composite layered coal seam model considering the thickness of the intercalated layer was established based on the block distinct element method. Then, the influence of the elastic modulus and construction parameters on the penetration behavior of hydraulic fractures was studied.

This paper is organized as follows: first, a composite coal seam model considering the thickness of the intercalated layer was established. Then, the propagation pattern of hydraulic fractures was analyzed considering the thickness of the intercalated layer based on the established model. Next, the effect of the elastic modulus of the intercalated layer and coal seams on the penetration behavior of hydraulic fractures was analyzed. Finally, the effect of construction parameters including viscosity and injection rate on the penetration behavior of hydraulic fractures was analyzed. In our study, the propagation of hydraulic fracture in composite coal seams considering the thickness of the intercalated layer was systematically analyzed. It can provide theoretical guidance for fracturing in the composite coal seams.

2 Fracture propagation in the composite coal seams

2.1 Numerical model of composite coal seams

Considering the characteristics of the composite coal seam and the symmetry in numerical calculation, the numerical model containing the intercalated layer is established and shown in Figure 1A. It contains two intercalated layers and three coal seams. The size of the model is 6 m × 6 m × 6 m, where the thicknesses of the coal seam and the intercalated layer are set according to the experimental schemes. In the block distinct element method, the fracture needs to be preset. Therefore, a vertical preset joint was set along the center of the model. In addition, there was a horizontal bedding plane between the coal seam and the intercalated layer. As a result, this model contains four horizontal bedding planes and one vertical joint. The specific joint model is shown in Figure 1B. The injection point was set at the center of the model, and the flow boundary of the injection point was constant.

The composite coal seam consists of coal seams and intercalated layers. The combination of thicknesses affects the propagation of hydraulic fractures when encountering an intercalated layer, which in turn affects the fracture height (vertical characterization) and fracture length (horizontal characterization). In order to analyze the influence of the thickness of the intercalated layer and coal seam on the hydraulic fracture propagation, six schemes were designed, as shown in Table 1. When analyzing the influence of the thickness of the intercalated layer, the thickness of the coal seam is found to be 1 m. The thicknesses of the intercalated layers are 0.1–0.6 m in all six cases. When analyzing the influence of the thickness of the coal seam, the thickness of the intercalated layer is found to be 0.3 m, and the thicknesses of the coal seams are 0.6–1.1 m in a total of six cases.

Other parameters are set as follows: the injection rate is 0.001 m^3/s. The viscosity of the fracturing fluid is 1 cp, and the fracturing time is 3,600 s. The cohesion of the joints is 2 MPa, the friction angle is 20°, and the tensile strength is 2 MPa. The Young's modulus of the coal seam is 50 GPa, and that of the intercalated layer is 70 GPa. The Poisson's ratio of both the coal seam and the intercalated layer is 0.25.

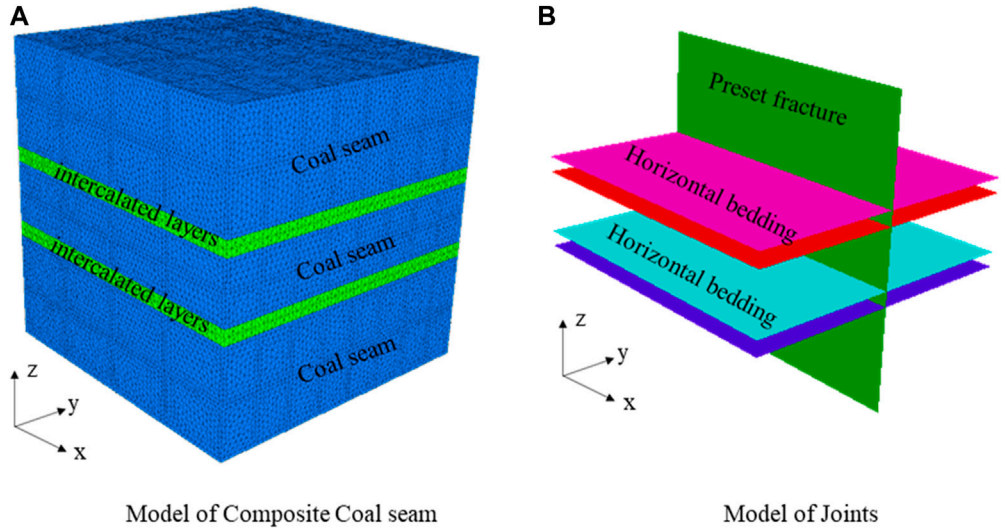


FIGURE 1
Numerical model of the composite coal seam.

TABLE 1 Table of simulation schemes.

Parameter	Influence of the intercalated layer						Influence of the coal seam					
Case number	J1	J2	J3	J4	J5	J6	M1	M2	M3	M4	M5	M6
Thickness of the intercalated layer/m	1	1	1	1	1	1	0.6	0.7	0.8	0.9	1.0	1.1
Thickness of the coal seam/m	0.1	0.2	0.3	0.4	0.5	0.6	0.3	0.3	0.3	0.3	0.3	0.3

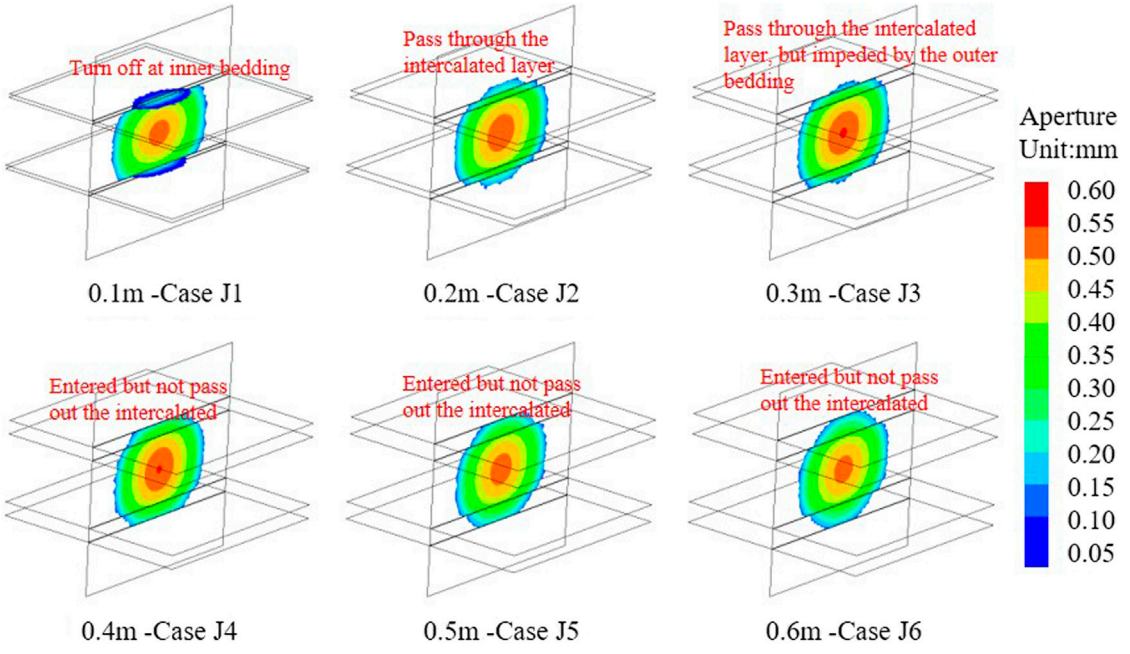


FIGURE 2
Fracture propagation with different thicknesses of the intercalated layer.

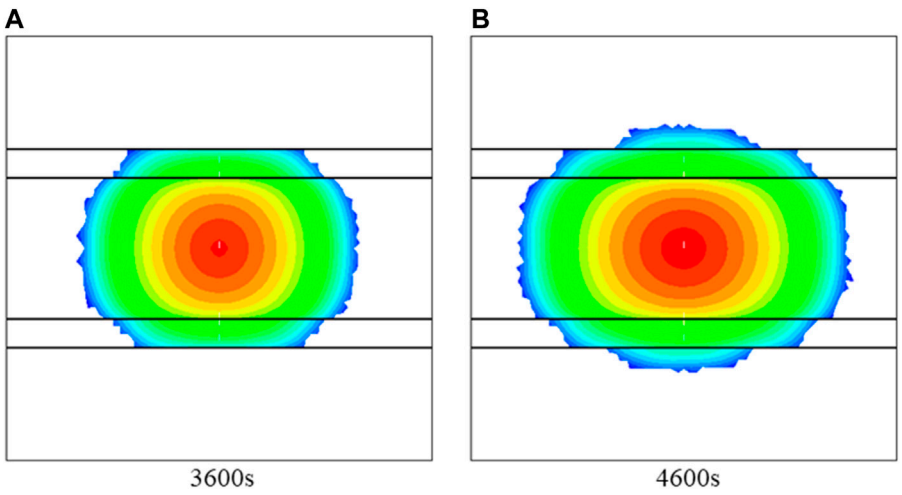


FIGURE 3
Fracture propagation at a different time of case J4.

2.2 Effect of the intercalated layers on fracture propagation

2.2.1 The fracture propagation with different intercalated layers

According to the scheme shown in Table 1, the fracture propagation of the intercalated layer with different thicknesses was calculated and is shown in Figure 2. According to the figure, when the thickness of the intercalated layer is 0.1 m, the hydraulic fracture fails to enter the intercalated layer after encountering the intercalated layer but turns to the bedding plane between the intercalated layer and the coal seam. When the intercalated layers are 0.2 and 0.3 m thick, the hydraulic fractures enter the bedding plane directly and penetrate out of the bedding plane. Although in both the cases the hydraulic fractures enter the intercalated layer, it should be noted that in some cases, the hydraulic fractures are impeded in penetrating the intercalated layer. As a result, the fracture length penetrating out the intercalated layer is less than the fracture length within the intercalated layer. In addition, the fracture height of the 0.3-m-thick interlayer was less than that of the 0.2-m-thick interlayer. When the thickness of the intercalated layer was 0.4 m or more, the hydraulic fractures enter the intercalated layer but fail to pass through it.

The intercalated layer affects the fracture propagation in the composite coal seam under the same fracturing conditions. In the formation with the thin intercalated layers, the fracture fails to enter the bedding plane and turns after encountering the bedding plane. As a result, the fracture height is less. Conversely, in the formation with the thick intercalated layer, the hydraulic fracture can enter the intercalated layer. Therefore, in the fracturing of composite coal seams containing thin intercalated layers, attention should be paid to the fracture deflection. The presence of thin intercalated layers results in insufficient fracture height. At this time, it is necessary to regulate the fracturing parameters to ensure that the hydraulic fracture can effectively penetrate the whole coal seam.

In addition, attention should be paid to the penetration behavior of hydraulic fractures. If the hydraulic fractures only enter but not pass through the intercalated layer, the hydraulic fractures still cannot connect the whole coal seam. In order to determine the obstruction of the intercalated layer to fracture penetration, the fracturing time of the J4 case is increased. As shown in Figure 3A, the fracture enters the intercalated layer but cannot pass through the intercalated layer. However, with the increase in fracturing time, the hydraulic fractures can break through the intercalated layer (Figure 3B). However, the propagation in the direction of its length (or horizontal direction) after fracture penetration is smaller than that of the center coal seam and intercalated layer. Therefore, the fracturing time should be prolonged appropriately for the hindering effect of the intercalated layer. At the same time, the discontinuity of fracture length due to the obstruction of the intercalated layer should be noted. If the existence of the intercalated layer is ignored, the fracturing efficiency may be lower than expected.

In summary, the influence of the intercalated layer on the fracture propagation includes the fracture deflection problem of encountering the thin intercalated layer and the hindering effect of the intercalated layer on fracture penetration. First, the hydraulic fracture turns after encountering the thin intercalated layer, and the height of the fracture is limited. In this case, it cannot effectively connect the whole coal seam. Second, the hindering effect of the intercalated layer prevents it from being passed through and subsequently affects the fracture height. The fractures penetrate the intercalated layer, but the fracture length was lower than that of the center coal seam.

2.2.2 The mechanisms of the intercalated layer thickness in propagation

The hindering effect of the intercalated layer on fracture penetration is related to the discontinuous displacement on both sides of the intercalated layer (Zheng et al., 2019; Zhu et al., 2023). Therefore, to analyze the effect of the intercalated layer thickness, the displacement around the intercalated layer should be analyzed first. Figure 4 shows the displacement in the YOZ plane. It shows the displacements around the injection point caused by fracturing. The injection time is 1,600 s,

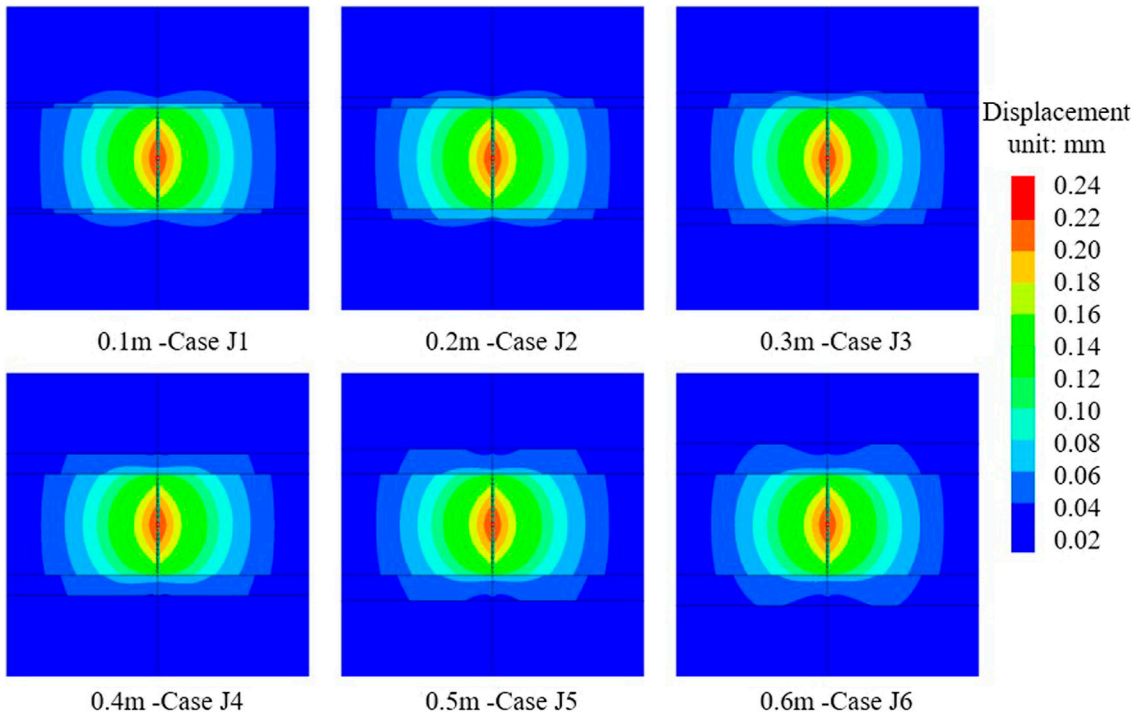


FIGURE 4
Formation displacement with different thicknesses of the intercalated layer.

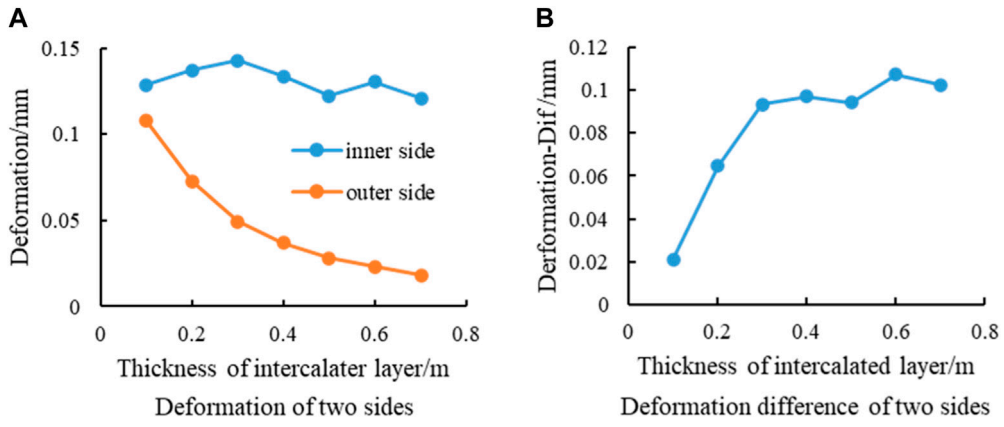


FIGURE 5
Deformation of bedding planes on both sides of the intercalated layer.

when the hydraulic fracture is about to meet the inner bedding plane of the intercalated layer. It is an important indication for analyzing the behavior of the hydraulic fracture through the layer. As shown in the figure, the displacements are discontinuous on both sides of the intercalated layer. When the thickness is 0.1 m, the displacement discontinuity on the upper and lower sides of the intercalated layer is obvious. The discontinuity of the displacement on both sides of the intercalated layer decreases as the thickness is increased. Combined with the fracture morphology shown in Figure 2, it can be hypothesized that the fracture deflection is related to discontinuous displacements caused by the thin intercalated layer.

Figure 5 shows the deformation of the bedding planes on both the inner and outer sides of the intercalated layer. The deformation of the inner and outer sides of the intercalated layer is analyzed. As shown in Figure 5A, the difference in deformation on the inner side of the intercalated layer is small because the inner side is mainly affected by hydraulic fracture propagation. The displacement on the outer side of the intercalated layer decreases with decreasing thickness. The decrease rate is fast for the thin intercalated layer and slows down for a thick intercalated layer. Figure 5B analyzes the deformation difference between the inner and outer sides of the intercalated layer with different thicknesses. When the thickness of

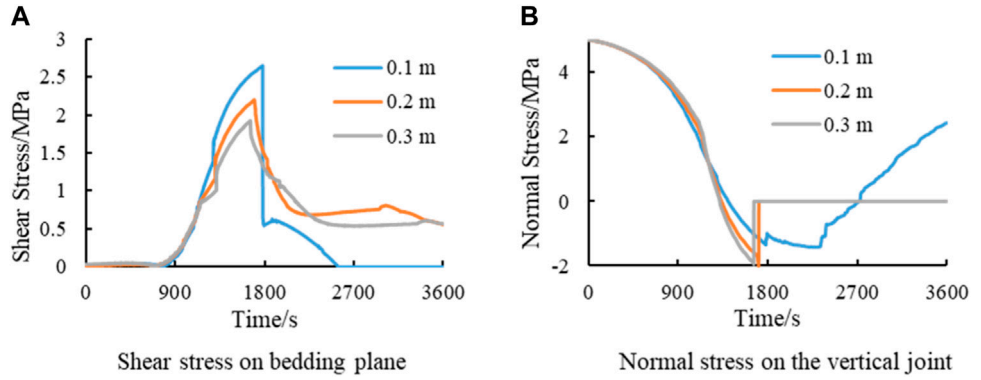


FIGURE 6
Stress curves at the intersection of the hydraulic fracture and intercalated layer.

the intercalated layer is less than 0.3 m, the deformations of the two sides of the intercalated layer are sensitive to the thickness change. When the thickness of the intercalated layer is greater than 0.3 m, the difference in deformation is gradually stabilized.

Combining the fracture propagation shown in Figure 2 and the deformation shown in Figure 5, it can be concluded that the effect of thin intercalated layers on the formation's deformation and fracture propagation is more obvious. Therefore, the focus should be on the mechanical behavior of thin intercalated layers. In this paper, an intercalated layer with thickness less than 0.3 m is considered thin intercalated layer. Figure 6 analyzes the stress at the point where the hydraulic fracture intersects with the inner bedding plane of the intercalated layer. The shear stress on the horizontal bedding plane at the intersection is shown in Figure 6A. The shear stress characterizes the shear damage of the bedding plane. The shear damage of the bedding plane provides conditions for hydraulic fractures to expand toward the horizon. Figure 6B shows the normal stress on the vertical joint surface at the intersection. The normal stress characterizes the tensile failure of the vertical joint surface and can provide conditions for fractures to enter the intercalated layer. As shown in Figure 6A, the thickness of the intercalated layer affects the evolution of shear stresses on the bedding plane. The maximum shear stress can reach 2.36 MPa at the intercalated layer thickness of 0.1 m. The maximum magnitude of shear stress decreases as the thickness of the intercalated layer increases, and the maximum shear stress is 1.89 MPa when the thickness of the intercalated layer is 0.3 m. The deflection of hydraulic fractures is related to shear damage on the bedding plane. In other words, the fracture deflection is controlled by shear stress. Therefore, the higher the shear stress is, the higher the probability of deflection. The results show that the thinner the intercalated layer is, the faster the shear stress increases and the higher the maximum shear stress. It provides the reason for easy deflection in thin intercalated layers in terms of mechanical mechanisms. Figure 6B shows that the variation of normal stresses on the vertical joint surface is also affected by the thickness of the intercalated layer. The thickness of the intercalated layer affects the rate of reduction of normal stress. The greater the thickness of the intercalated layer is, the greater the reduction rate of normal stress. Therefore, for the thicknesses of 0.2 m and 0.3 m, the normal stress decreases to the tensile strength of the joint (normal stress is positive by compression), and the hydraulic fracture passes through the bedding plane and enters the intercalated layer. Then, the shear stress on the horizontal bedding plane gradually decreases and finally maintains a low value. So the fracture does not deflect.

It is possible to summarize the mechanical effect of the thickness of the intercalated layer on the penetration of the hydraulic fracture. For thin intercalated layers, the smaller the thickness, the faster the increase rate of shear stress on the horizontal bedding plane and the higher the maximum magnitude, and the slower the decrease rate of normal stress on the vertical joint surface, which is favorable for hydraulic fracture deflection. On the contrary, the larger the thickness, the slower the shear stress increase rate on the horizontal bedding plane and the lower the maximum value, and the more the normal stress reduction rate on the vertical joint surface, which is favorable for hydraulic fractures to pass through the bedding plane to enter the bedding plane.

2.3 The effect of coal seam thickness on fracture propagation

According to the experimental scheme shown in Table 1, the influence of coal seam thickness on fracture propagation is analyzed. The calculation results are shown in Figure 7. Since the thickness of the intercalated layer in this study is 0.3 m in all cases, the fractures are able to penetrate into the intercalated layer during the propagation. The effect of seam thickness on fracture propagation is the penetration behavior. The hydraulic fractures can penetrate the intercalated layer in all the cases with the thicknesses of 0.6–1.0 m of the coal seam. When the seam thickness was 1.1 m, the hydraulic fracture fails to penetrate the intercalated layer. In addition, hydraulic fractures can penetrate the intercalated layer in coal seams less than 1 m thick, but the degree of penetration varies. In conclusion, the thinner the coal seam, the smaller the hindering effect. As the coal seam thickens, the range of penetration of hydraulic fractures is smaller.

The thickness of the coal seam affects the penetration ability. Then, it affects the extent range of hydraulic fracture propagation. Figure 8A categorizes hydraulic fractures into the main zone, intercalated layer zone, and outward zone according to their location. The thickness of the coal seam directly determines the height of the main fracture zone. Figure 8B summarizes the fracture propagation length and height for different coal seam thicknesses.

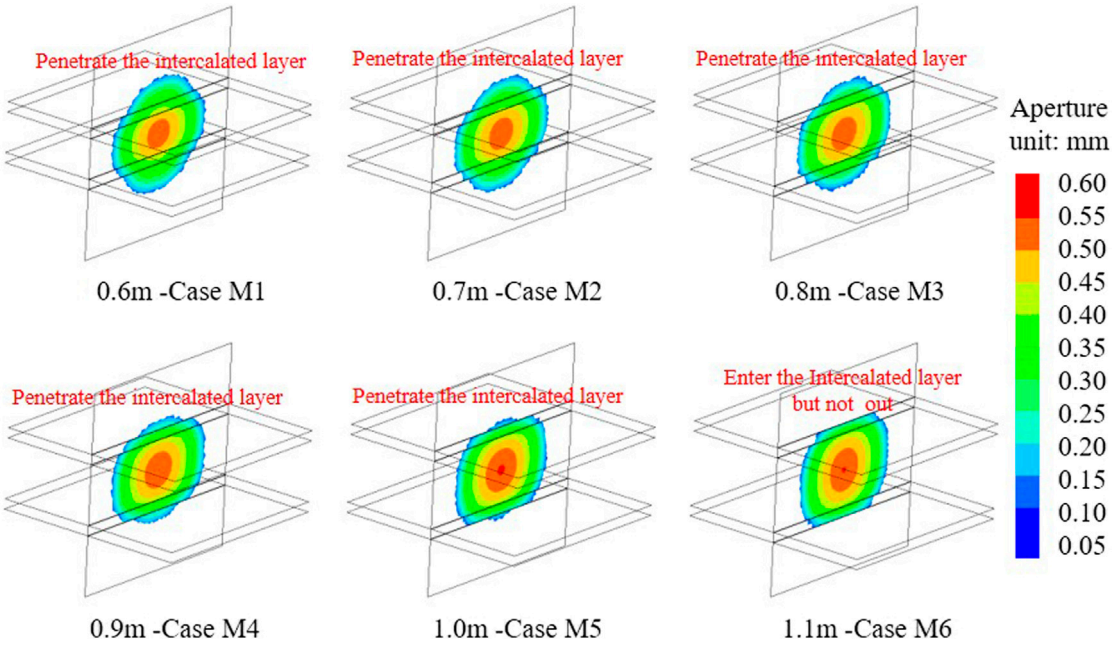


FIGURE 7
Fracture propagation pattern under different coal seam thicknesses.

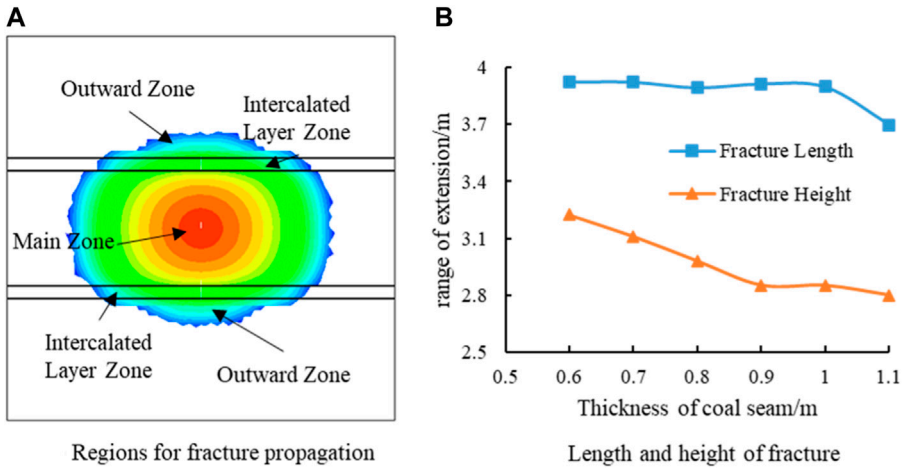


FIGURE 8
Propagation of fractures.

The results show that the length of hydraulic fractures remains generally consistent, but the height of hydraulic fractures is affected by the thickness of the coal seam. Hydraulic fracture height decreases gradually with the increase in the coal seam thickness. Low fracture height implies a reduction in the extent of fracturing.

In summary, the thickness of the coal seam mainly affects the ability of the hydraulic fracture to pass through the intercalated layer and the range of hydraulic fracture propagation. As the thickness of the seam increases in a composite seam, the hindering effect of the intercalated layer on the height of the fractures should be considered. When the coal seam is thin, the influence of the intercalated layer on the propagation of fractures is less. While the coal seam is thick, the influence of the intercalated layer on the vertical propagation of fractures is more, which should be emphasized in the design of fracturing.

3 Effect of elastic modulus on fracture propagation

3.1 The fracture propagation with different elastic moduli

The elastic modulus characterizes the deformability of rocks. Furthermore, the difference in the elastic modulus between the

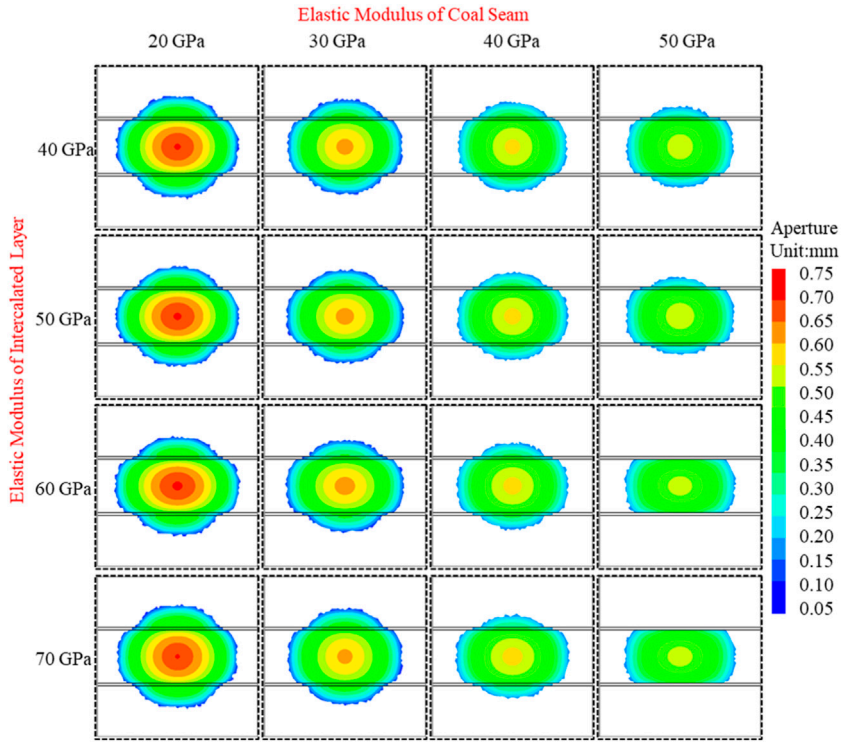


FIGURE 9
Fracture propagation under different elastic moduli.

intercalated layer and coal seams has a significant effect on the penetration behavior of fractures. In order to analyze the effect of the elastic modulus on fracture propagation, the elastic moduli of the coal seam (Ec) are taken to be 20 GPa, 30 GPa, 40 GPa, and 50 GPa, and the moduli of the intercalated layer (Ei) are taken to be 40 GPa, 50 GPa, 60 GPa, and 70 GPa. Combined simulations are carried out for various scenarios, and a total of 16 sets of simulation scenarios are designed. The fracture propagation under each case is summarized in Figure 9.

First, the effect of the Ec is analyzed. Moreover, the same row shown in Figure 9 has the same Ei, and the Ec varies. With a small Ec, hydraulic fractures can penetrate the intercalated layer. As the Ec increases, the hindering effect of the intercalated layer on the vertical propagation of the fractures is enhanced. Second, the effect of Ei is analyzed. The same column in the figure has the same Ec and different Ei. The effect of Ei on hydraulic fracture propagation has different patterns at high and low Ec. In the low Ec (left first column), the Ei has little effect on fracture propagation. In the high Ec (50 GPa), hydraulic fractures can penetrate the intercalated layer when the Ei is low (40 GPa and 50 GPa). When the Ei is high (60 GPa and 70 GPa), the hydraulic fractures turn after encountering the intercalated layer, and the intercalated layer hinders the vertical propagation of the hydraulic fractures.

In summary, the influence of Ec on fracture propagation can be summarized. The hindering effect of the intercalated layer on fracture propagation increases with the increase in Ec. Furthermore, the influence of the Ei on the behavior of fracture propagation can be summarized. In low elastic modulus coal seams, the influence of the Ei on fracture propagation is small. Conversely, in high elastic modulus coal seams, the hindering effect of the intercalated layer on hydraulic fractures increases with the increase in the Ei.

3.2 The effect of the elastic modulus of coal seams

According to Figure 9, as the Ec increases, it becomes more difficult for hydraulic fractures to pass through the intercalated layer. The elastic modulus characterizes the deformation. As shown in the figure, the hydraulic fracture with a small elastic modulus has a large aperture. Moreover, the aperture decreases with the increase in the Ec. The aperture determines the fracture volume. Furthermore, different fracture volumes under the same fluid injection volume determine the difference of pressure within the fracture. Different pressures ultimately cause differences in stress evolution. Figure 10 analyzes the stress evolution at the intersection of the hydraulic fracture and the intercalated layer for different Ec when the Ei is 70 GPa. The figure shows that the Ec affects the distribution of shear stresses on the bedding plane and normal stresses on the vertical joint.

First, the elastic modulus affects the change gradient in stress. As shown in Figures 10A, B, the stress curve for the coal seam with an elastic modulus of 20 GPa is on the leftmost side, which means that the stress change corresponding to this elastic modulus is earlier than that in the other cases. Whereas the stress evolution is related to fracture propagation, as the fracture approaches a certain point (numerical node), the stress profile at that point changes

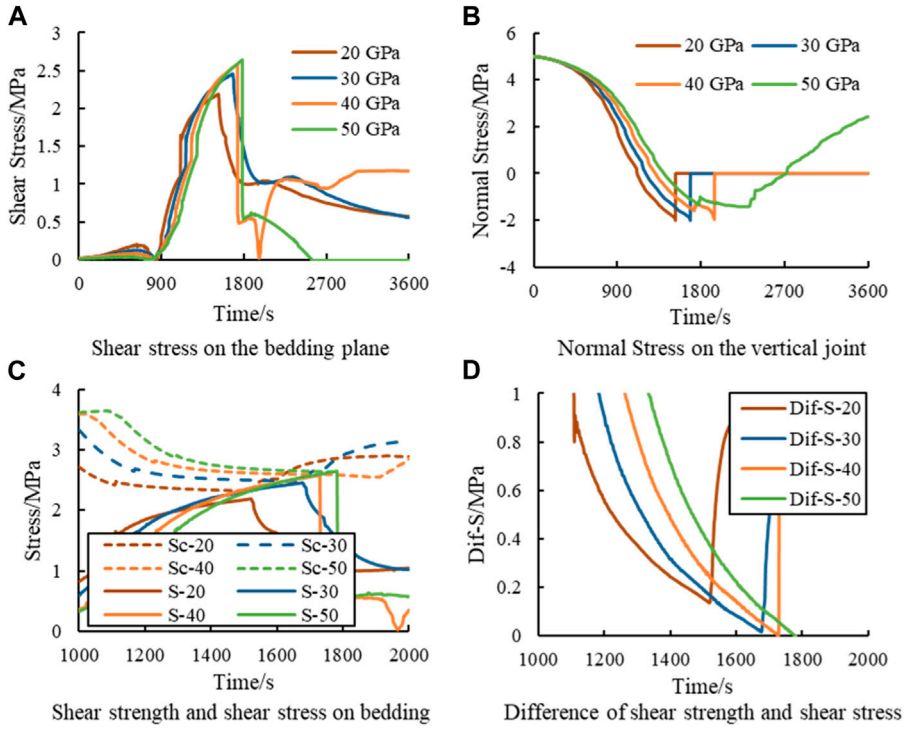


FIGURE 10
Stress curves with different Ec (Ei = 70 GPa).

significantly. In addition, the sequence of stress curve changes in the figure characterizes the rate of hydraulic fracture propagation. Therefore, it can be known that hydraulic fractures expand fast when the Ec is small and expand slow when the Ec is large.

As shown in Figure 10A, the maximum shear stress increases with the increase in the Ec. Shear stress causes shear damage of the bedding plane. The shear stress increases with Ec, which subsequently increases the tendency of hydraulic fractures to turn toward the bedding plane and increases the hindering effect of the intercalated layer. However, it is worth noting that as shown in Figure 10A, the shear stress increases fastest at low Ec (the slope of the curve is the largest), but its maximum shear stress is at the lowest Ec. The paradox of a fast increase in the shear stress but a low maximum value needs to be explained in terms of the change in normal stress. From Figure 10B, it can be seen that the normal stress on the vertical joint surface decreases with injection time. The fastest rate of stress reduction occurs when the Ec is 20 GPa. When the stress decreases to −2 MPa, reaching the tensile strength of the joint, the hydraulic fracture expands vertically through the bedding plane. Now, the shear stress on the horizontal bedding plane reaches its peak. Due to the rapid decrease in normal stress, the shear stress does not increase. As the Ec increases, fracture propagation slows down, thus requiring more time for normal stress to decrease to tensile strength. Finally, the maximum shear stress increases. When the Ec is 50 GPa, the normal stress does not reduce to the tensile strength, and the shear stress reaches the shear strength of the bedding plane. Now, the bedding plane shear damage occurs, and the hydraulic fractures turn to the bedding plane.

Figure 10C shows the corresponding shear strength and shear stress curves of the bedding plane at different Ec. In the figure, the *Sc* curve represents shear strength, and the *S* curve represents shear stress. The shear strength (*Sc*) of the bedding plane gradually decreases with injection, while the shear stress (*S*) gradually increases. Finally, the two are gradually close to each other. Figure 10D shows the difference between the shear strength and shear stress (*Dif-S*) curves. According to the figure, *Dif-S* is gradually decreasing before the damage occurs at the intersection point. The minimum value of *Dif-S* decreases with the increase in the Ec. Actually, this difference can reflect the tendency of the shear damage of the bedding plane.

In summary, the mechanism of the Ec on the hindering effect of the intercalated layer is as follows: the influence of the elastic modulus on the deformation determines the fracture propagation rate and the stress distribution characteristics. The fracture propagates fast under low elastic modulus. So the normal stress on the vertical joint decreases fast. Then, the fracture is preferred to extend vertically through the intercalated layer. Under high elastic modulus, the fracture propagates slowly. So the normal stress on the vertical joint decreases slowly. Then, the shear stress on the bedding plane is preferred to reach the shear strength, and the bedding plane undergoes shear damage. The minimum value of *Dif-S* can be used to characterize the hindering effect of the intercalated layer. The smaller the *Dif-S*, the stronger the hindering effect. Therefore, with the increase in the elastic modulus, the minimum *Dif-S* decreases and the hindering effect of the bedding plane increases.

3.3 The effect of the elastic modulus of the intercalated layer

From Figure 9, it can be seen that the effect of Ei on the hydraulic fracture propagation pattern needs to consider the Ec. When the Ec

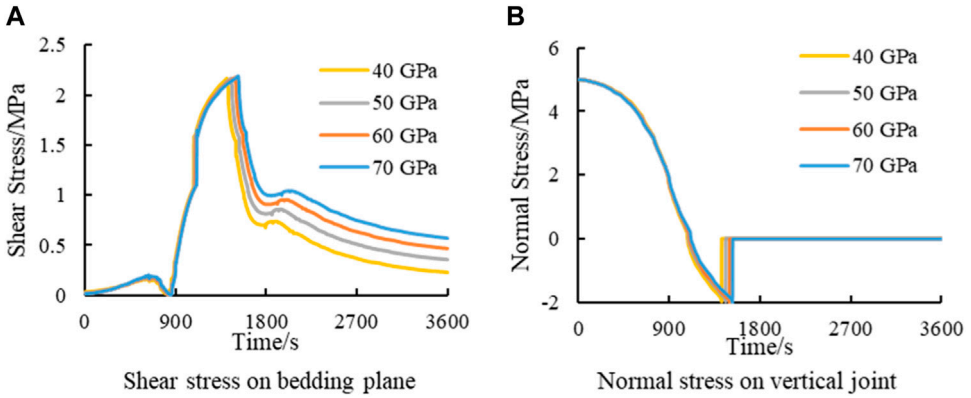


FIGURE 11
Stress curves with a small Ec (20 sGPa).

is small (such as 20 GPa), changes in Ei have little effect on hydraulic fracture penetration. When the Ec is large (such as 50 GPa), the effect of Ei on hydraulic fracture penetration is significant. As shown in the figure, the fracture pattern changes from passing through the intercalated layer to being hindered by the intercalated layer with increase in Ei. Therefore, the effect of the intercalated layer on fracture patterns should be discussed for the classification of different Ec values.

Figure 11 shows the stress evolution curve corresponding to the Ec of 20 GPa. Since the coal seams have the same elastic modulus, the curves overlap before encountering the intercalated layer. As the fracture approaches the intercalated layer, the stress curves begin to differ. At this stage, the stress curve corresponding to 40 GPa is more to the left, indicating that stress changes occur earlier. The curve corresponding to 70 GPa is most to the right, indicating that stress changes occur later. Therefore, the effect of Ei on the stress change is mainly manifested in the following ways. The lower the Ei is, the earlier and faster the stress response at the fracture approaching. Although the effect of Ei on the stress evolution has been analyzed above, the overall influence of the interacted layer on the maximum shear stress and the minimum normal stress is very small. The stress curves shows that the normal stress reaches the tensile strength of the vertical joint and the hydraulic fracture directly penetrates the intercalated layer. Furthermore, the shear stress has not reached the shear strength at this point, so hydraulic fractures do not turn. In seams with low elastic modulus, Ei has little effect on the penetration behavior of hydraulic fractures.

Figure 12 shows the stress variation curves for the elastic modulus of 50 GPa. Combining the analysis in Figures 12A, B, the normal stress is shown to decrease to reach the tensile strength and the hydraulic fracture penetrates the intercalated layer at the Ei of 40 GPa and 50 GPa. The normal stresses do not reach the tensile strength at the Ei of 60 GPa and 70 GPa, so the hydraulic fractures fail to penetrate the intercalated layer.

All the shear stress curves shown in Figure 12A undergo a sudden vertical decrease. Combining the results of Zheng et al. (2022) and Figure 10, it can be seen that the vertical decrease in the shear stresses indicates that shear damage has occurred at this time. Although shear damage occurs in all horizontal bedding planes, the propagation patterns of hydraulic fractures at different Ei are different. In order to analyze the effect of Ei, the two cases of Ei of 50 GPa and 60 GPa are taken as examples to analyze the stress evolution. Their stress curves are plotted in Figures 12C, D. From Figure 12C, it can be seen that when the Ei is 50 GPa, the horizontal bedding plane can still withstand a certain amount of shear stress after shear failure. Thus, stresses and strains can be transferred from one side to the other side of the bedding plane. Therefore, the normal stresses on the vertical joint surface can continue to decrease. Finally, the normal stress is reduced to the tensile strength of the vertical joint, and the hydraulic fractures extend vertically through the bedding plane. When the Ei is 60 GPa, the stress and strain transfer between the two sides of the bedding plane is poor after the shear damage. So the normal stress does not reduce. As a result, the hydraulic fracture cannot pass through the bedding plane. Then, the hydraulic fracture can only continue to be extended along the bedding plane. Eventually, the fracture at this point opens up and loses its shear capacity, and both sides of the bedding plane lose the transfer ability of stress and strain. In summary, the mechanism of the intercalated layer on the penetration behavior in the high elastic modulus coal seam is as follows: Ei affects the reduction of the normal stress on the vertical joint. When Ei is lower, the normal stress can continue to decrease and the hydraulic fractures can penetrate the bedding plane. When Ei is higher, the normal stress cannot continue to decrease, and then hydraulic fractures cannot pass through the bedding plane.

4 The effect of construction parameters on fracture propagation

The above has clarified the influence of rock structure (thickness) and rock properties (elastic modulus) on hydraulic fracture propagation. However, the rock structure and rock properties belong to the inherent properties of the stratum, and they are difficult to be changed artificially. During the fracturing operation, the fracturing parameters, including injection rate and fluid viscosity, can be controlled to manually intervene on the fracture penetration behavior. Therefore, revealing the influence of construction parameters on fracture propagation in composite coal seam fracturing has an important role for fracturing

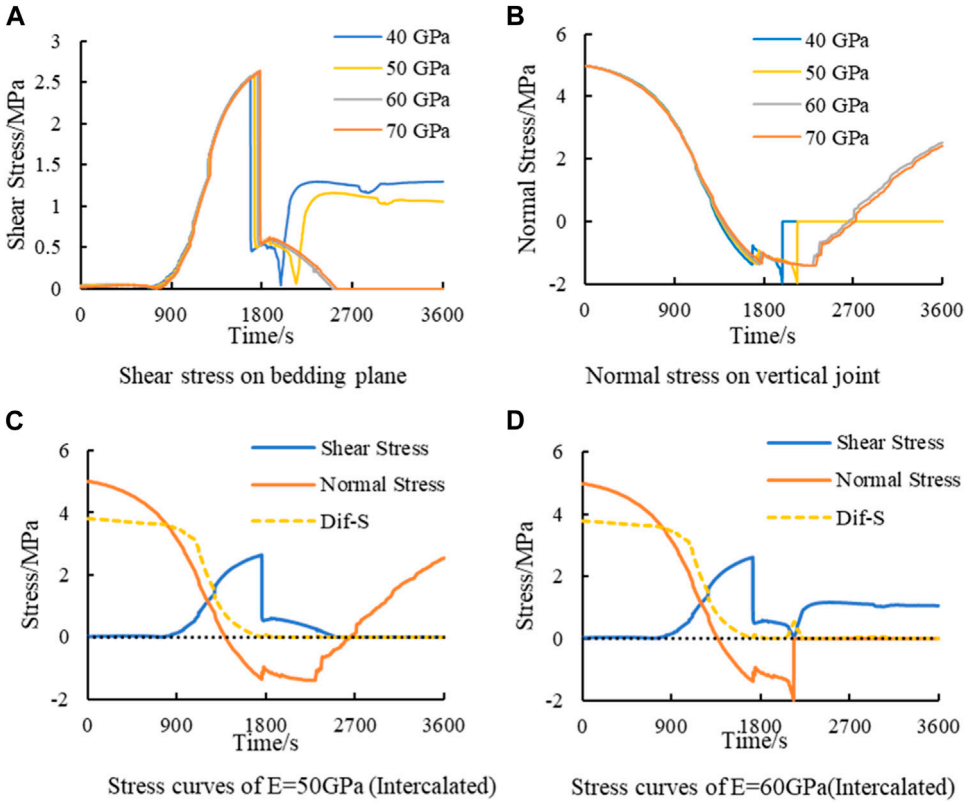


FIGURE 12
Stress curves at a high Ec (50 GPa).

construction. Based on this, the influence of the injection rate and fluid viscosity on fracture propagation is calculated and revealed.

4.1 The influence of the injection rate on fracture propagation

The injection rate is one of the key construction parameters that can be artificially controlled in fracturing construction. In order to analyze the effect of injection rate on fracture propagation, eight injection schemes are developed as shown in Figure 13. The viscosity in the scheme is 1 cp. In order to unify the evaluation criteria, the total injection volume is used as the evaluation criterion in the simulation. Figure 13 shows the fracture propagation under the same injection volume. It can be seen from the figure that when the injection rate is 0.0005 m^3/s (500 mL/s) and 0.001 m^3/s (1000 mL/s), the hydraulic fracture is hindered after encountering the bedding plane, and the hydraulic fracture fails to pass through the intercalated layer. When the injection rate is 0.0015 m^3/s, the hydraulic fracture passes through the intercalated layer. However, the hydraulic fractures on both sides of the intercalated layer are discontinuous. The intercalated layer has a strong hindering effect on the hydraulic fracture. With the increase in the injection rate, the hindering effect of the intercalated layer on the hydraulic fracture is reduced. Therefore, in the fracturing design, the injection rate should be designed according to the penetration behavior of the fracture, combined with the rock structure and rock property. The high injection rate is more conducive to the hydraulic fracture through the intercalated layer to ensure the fracture height. However, the high injection rate requires stronger power equipment, high injection pressure, and increased cost. Although the high injection rate is helpful for the fracture to penetrate the layer, the injection rate should be determined according to the actual situation of the reservoir.

Figure 14 shows the shear stress on the horizontal bedding plane and the normal stress on the vertical joint plane corresponding to the case shown in Figures 13A–D. Due to the different injection rates, the corresponding injection time is different at the same injection volume. In order to unify the evaluation criteria, the total injection volume is plotted along the x-axis in the figure. As shown in the figure, when the injection rate is low, the shear stress on the horizontal bedding increases slowly. With the increase in the injection rate, the shear stress rise rate increases (the curve moves to the left). When the injection rate is bigger than 0.0015 m^3/s, the shear stress curve basically coincides. It can be seen from Figure 14A that the shear stress curves all show a vertical decline, which indicates that shear failure occurs on the horizontal bedding plane. It can be seen from Figure 14B that the normal stress of 0.0015 and 0.0020 m^3/s can continue to decline after the shear failure of the horizontal bedding plane. As the normal stress decreases to the tensile strength, the vertical joint opens and the hydraulic fracture passes through the bedding plane. When the injection rate is low, the normal stress cannot continue to decrease, and the fractures can only expand along the bedding plane.

In summary, the influence of the injection rate on the penetration of hydraulic fractures is as follows. At a small

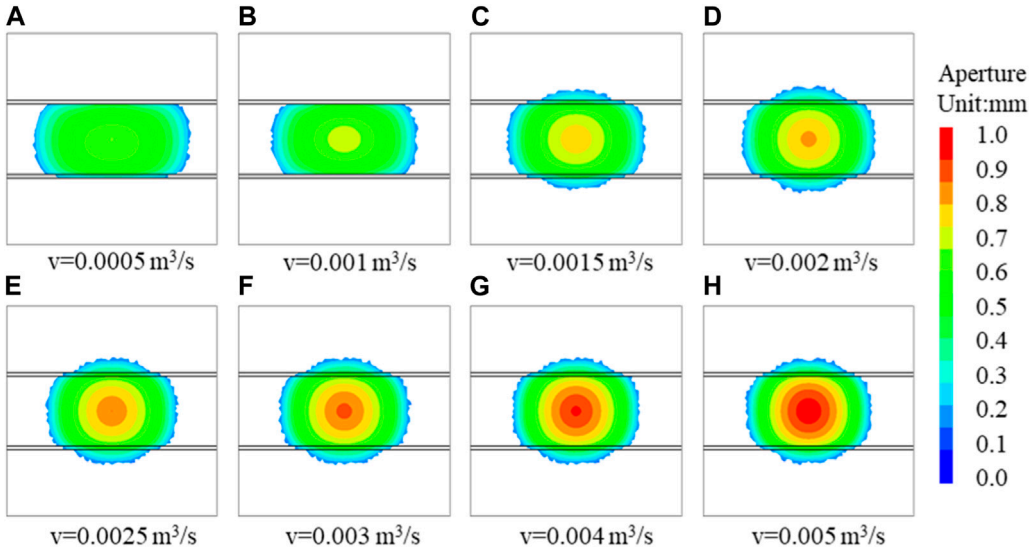


FIGURE 13
Fracture propagation morphology under different injection rates.

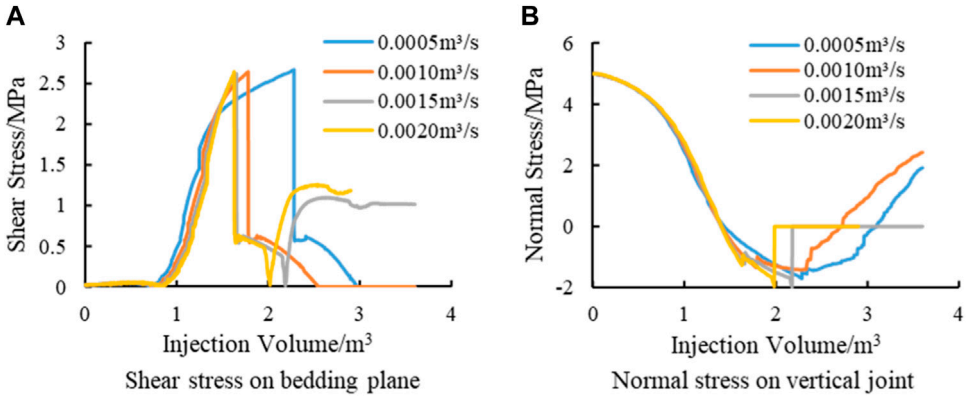


FIGURE 14
Stress changes under different injection rates.

injection rate, the normal stress on the vertical joint cannot reach its tensile strength, and the hydraulic fracture cannot expand vertically. Therefore, the hydraulic fractures tend to expand along the horizontal bedding plane. With the increase in the injection rate, the normal stress on the vertical joint can reach the tensile strength, and the hydraulic fracture can extend along the vertical direction, weakening the trend of extending along the horizontal bedding plane. As a result, the hindering effect of the intercalated layer fractures decreases, and hydraulic fractures tend to expand directly through the intercalated layer.

4.2 Effect of fluid viscosity on fracture propagation

The fluid viscosity is another key construction parameter that can be artificially controlled in fracturing construction. In order to analyze the influence of fluid viscosity on fracture propagation, eight viscosity schemes are designed as shown in Figure 15. In the scheme, the fixed injection rate is 0.001 m³/s. Figure 15 shows the fracture morphology under different viscosities.

As shown in the figure, the hydraulic fracture is hindered by the bedding plane with the viscosities of 50 cp and 100 cp. It means that the hindering effect of the intercalated layer on hydraulic fractures increases with the increase in fluid viscosity. This conclusion is inconsistent with the previous understanding of the influence of construction parameters on the penetration behavior (Zheng et al., 2022). In the previous studies, the research on the penetration behavior of the hydraulic fracture was mainly aimed at the weak plane of bedding, while we establish the actual intercalated layer considering the thickness. Different from the above simulation, the hydraulic fracture penetrated the internal bedding plane and entered the intercalated layer but failed to penetrate the external bedding plane. In order to analyze this process, the hydraulic fracture

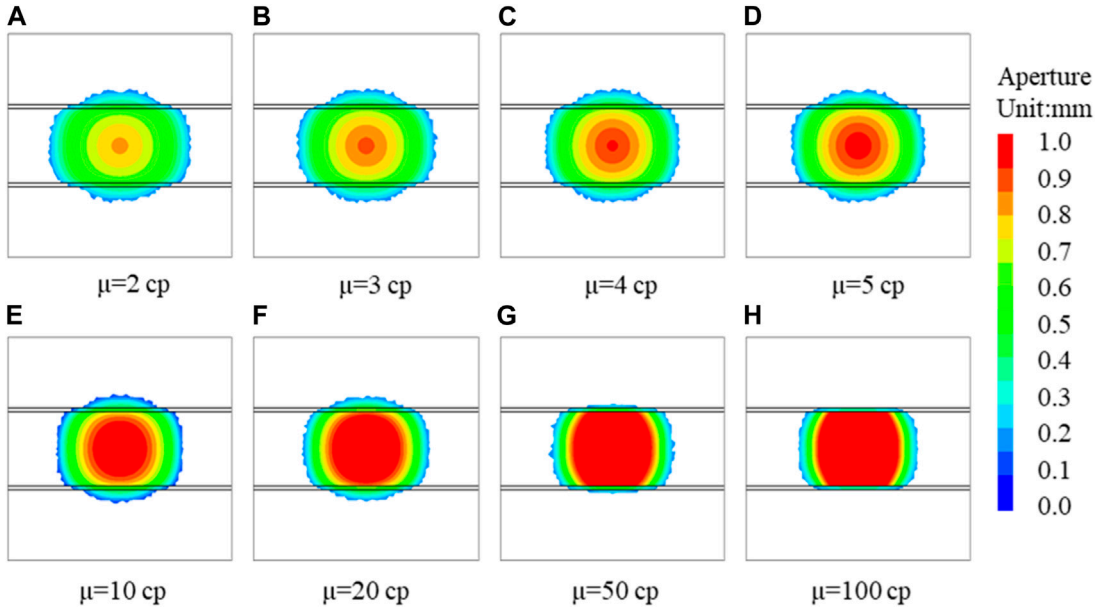


FIGURE 15
Fracture morphology under different viscosities.

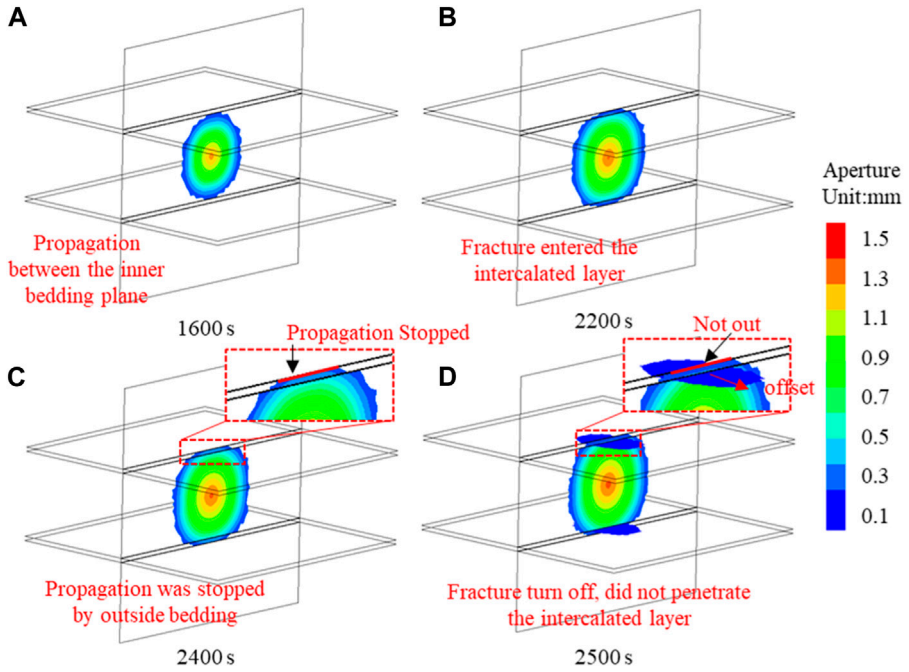


FIGURE 16
Fracture propagation process (100 cp).

propagation process with the injection viscosity of 100 cp is given in Figure 16. Before 1,600 s, the hydraulic fracture expands in the main zone, and the hydraulic fracture is penny-shaped. At 1,600 s, the hydraulic fracture reaches the inner bedding plane of the intercalated layer. Subsequently, hydraulic fractures can pass through the bedding plane into the intercalated layer (Figure 16B), which is consistent with the previous understanding of the influence of construction parameters on the fracture penetration behavior. However, this paper considers the thickness of the actual intercalated layer, so the intercalated layer is divided into two layers. Hydraulic fractures can enter the intercalated layer, but they are hindered by the outer bedding

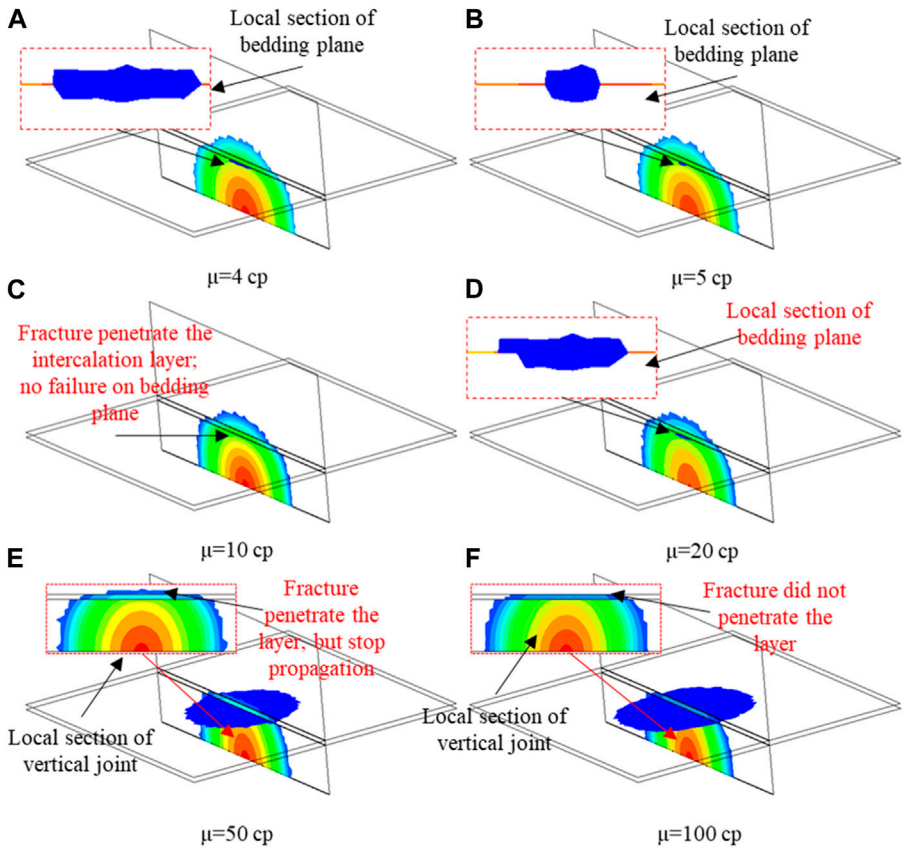


FIGURE 17
Fracture detail characteristics under different viscosities.

plane coming out of the intercalated layer (Figure 16C). Subsequently, the internal bedding plane reached the shear failure condition, and the hydraulic fracture turned to expand along the internal bedding plane (Figure 16D). The propagation process of fractures under high fluid viscosity is as follows: first, the hydraulic fractures pass through the bedding plane and enter the intercalated layer. Then, the hydraulic fractures are hindered when they pass through the intercalated layer. Finally, the hydraulic fractures turn to expand along the internal bedding plane. In this process, although the hydraulic fracture expands along the internal bedding plane, the fracture first passes through the bedding plane, but it turns to the bedding plane due to obstruction. This is different from the direct offset of hydraulic fractures after encountering bedding planes in the previous studies.

In summary, when considering the two bedding planes and the thickness of the intercalated layer, the viscosity of the fracturing fluid has a significant effect on the penetration of the hydraulic fracture through the intercalated layer. Figure 17 shows the details of fracture propagation under different viscosities for the analysis of the propagation characteristics of hydraulic fractures under different viscosities. For clarity, only the top half of the fractures is shown. As shown in the figure, although the hydraulic fracture passes through the intercalated layer, the shear failure occurs on the internal bedding plane when the viscosity is 4 cp and 5 cp. The shear failure range at low viscosity is greater than that at high viscosity. Furthermore, the shear range characterizes the hindrance of the bedding plane. The larger the shear failure range is, the greater the hindrance effect. It means that in this viscosity range, the hindering effect of the bedding plane decreases as the viscosity increases. When the viscosity is 10 cp, the hydraulic fracture passes through the intercalated layer, and no shear failure occurs on the bedding plane. When the viscosity is 20 cp, the hydraulic fracture passes through the intercalated layer, but the shear failure area appears on the horizontal bedding plane. When the viscosity is 50 cp, the hydraulic fracture can pass through the intercalated layer, but it fails to expand vertically after passing out. In addition, the hydraulic fracture expands along the horizontal bedding plane.

Figure 18 shows the stress evolution curve corresponding to Figure 17. In order to facilitate the marking, the shear stress on the horizontal bedding plane is represented by S-H, and the normal stress on the vertical joint plane is represented by N-V. The position of the intersection point between the internal bedding plane and the vertical joint plane is denoted by *in*. The position of the intersection point between the outer bedding plane and the vertical joint is denoted by *out*. As shown in the figure, when the viscosity is 4 cp and 5 cp, the horizontal bedding plane first undergoes shear failure. Then, the N-V can continue to decrease to the tensile strength, so the hydraulic fracture eventually expands vertically. When the viscosity is 10 cp, no shear failure occurs on the horizontal bedding plane. As the viscosity continues to increase, under the conditions of 20 cp, 50 cp, and 100 cp, the vertical joint first undergoes tensile failure. Then, the internal bedding surface undergoes shear failure.

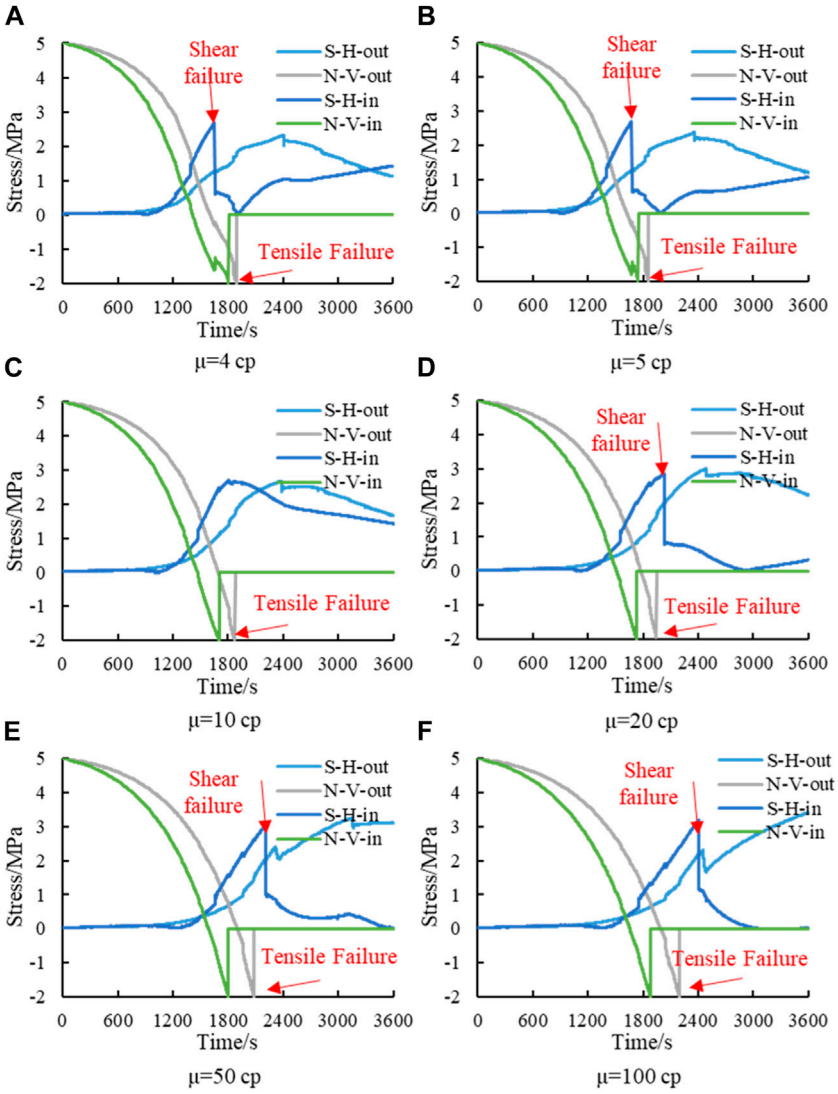


FIGURE 18
Stress evolution under different viscosities.

Therefore, the viscosity of the fracturing fluid affects the order of failure of the horizontal bedding plane. Under the condition of low viscosity, the shear failure of the horizontal bedding plane precedes the tensile failure of the vertical joint. In a word, the viscosity affects whether the hydraulic fracture can penetrate the intercalated layer by the shear failure of the horizontal bedding plane. At this time, the greater the viscosity, the easier it is for hydraulic fractures to enter the intercalated layer.

In summary, this study considers the thickness of the intercalated layer. High viscosity increases the tendency for fractures to enter the intercalated layer. Furthermore, the difficulty of passing out through the intercalated layer increases. This understanding is different from the existing understanding of the impact of construction parameters on the penetration behaviors. During fracturing operations, it is not advisable to blindly increase the viscosity of fracturing fluids, but rather to consider the increased difficulty of penetrating the interlayer caused by increased viscosity of fracturing fluids.

5 Conclusion

In this paper, a composite coal seam model considering the thickness of the intercalated layer is established. Based on the block distinct element method, the effect of rock structure (thickness of coal seam and intercalated layer), rock properties (elastic modulus), and construction parameters (injection rate and fluid viscosity) on the penetration behavior of hydraulic fractures is analyzed. The main conclusions are as follows:

(1) The influence of the intercalated layer on the fracture propagation of the composite coal seam includes the fracture deflection problem of the thin intercalated layer and the hindering effect of the intercalated layer on fracture penetration.
(2) The thin intercalation layer leads to a rapid increase in shear stress on the horizontal bedding plane, weakening the decrease in normal stress on the vertical joint plane.

Therefore, the thin intercalation layer is beneficial for the offset of hydraulic fracture. Conversely, the thick intercalation layer is beneficial for the hydraulic fracture to penetrate through the bedding plane into the intercalation.

(3) The thickness of the coal seam mainly affects the ability of the hydraulic fracture to penetrate the intercalated layer and the propagation range. When the coal seam is thin, the intercalated layer has little effect on the propagation of the fracture. When the coal seam is thick, the intercalated layer has a substantial influence on the vertical propagation range.

(4) The hindering effect of the intercalated layer on the fracture increases with the increase in the elastic modulus of the coal seam. In the low elastic modulus coal seam, the intercalated elastic modulus has little effect on the fracture propagation. In the coal seam with high elastic modulus, the hindering effect of the intercalated layer on the hydraulic fracture increases with the increase in the elastic modulus of the intercalated layer.

(5) With the increase in the injection rate, the hindering effect of the intercalated layer on fractures decreases, and hydraulic fractures tend to penetrate the intercalated layer. With the increase in fluid viscosity, the trend of hydraulic fractures entering the intercalated layer increases, but the difficulty of penetrating the intercalated layer also increases.

Data availability statement

The original contributions presented in the study are included in the article/Supplementary Material; further inquiries can be directed to the corresponding authors.

Author contributions

HG: writing–original draft and writing–review and editing. BJ: supervision and writing–review and editing. YL: funding acquisition, investigation, and writing–review and editing. YZ: conceptualization, funding acquisition, methodology, software, and writing–original draft. BS: writing–review and editing. HW: writing–review and editing. TZ: writing–review and editing. WW: writing–review and editing, funding acquisition, and supervision. QN: formal analysis, validation, and writing–review and editing.

Funding

The authors declare financial support was received for the research, authorship, and/or publication of this article. The authors acknowledge the support provided by the Natural Science Foundation of Hebei Province (E2021210036 and E2021210128).

Conflict of interest

Authors HG and YL were employed by Shenyang Research Institute China Coal Technology & Engineering Group Corp. Author BS was employed by Downhole Operation Company, CNPC Xibu Drilling Engineering Co., Ltd.

The remaining authors declare that the research was conducted in the absence of any commercial or financial relationships that could be construed as a potential conflict of interest.

Publisher's note

All claims expressed in this article are solely those of the authors and do not necessarily represent those of their affiliated organizations, or those of the publisher, the editors, and the reviewers. Any product that may be evaluated in this article, or claim that may be made by its manufacturer, is not guaranteed or endorsed by the publisher.

References

Bai, Y., Hu, Y., Liao, X., Tan, J., Zheng, Y., and Wang, W (2023). Research on the influence of stress on the penetration behavior of hydraulic fracture: perspective from failure type of beddings. *Front. Earth Sci.* 11, 11. doi:10.3389/feart.2023.1163295

Guo, J., Luo, B., Lu, C., Lai, J., and Ren, J (2017). Numerical investigation of hydraulic fracture propagation in a layered reservoir using the cohesive zone method. *Eng. Fract. Mech.* 186, 195–207. doi:10.1016/j.engfracmech.2017.10.013

Hadei, M. R., and Veiskarami, A. (2020). An experimental investigation of hydraulic fracturing of stratified rocks. *Bull. Eng. Geol. Environ.* 80 (1), 491–506. doi:10.1007/s10064-020-01938-0

Han, L., Xizhe, L., Liu, Z., Duan, G., Wan, Y., Guo, X., et al. (2023). Influencing factors and prevention measures of casing deformation in deep shale gas wells in Luzhou block, southern Sichuan Basin, SW China. *Petroleum Explor. Dev.* 50 (4), 979–988. doi:10.1016/s1876-3804(23)60443-4

Huang, L., Dontsov, E., Fu, H., Lei, Y., Weng, D., and Zhang, F (2022). Hydraulic fracture height growth in layered rocks: perspective from DEM simulation of different propagation regimes. *Int. J. Solids Struct.* 238, 111395. doi:10.1016/j.ijsolstr.2021.111395

Huang, L., He, R., Yang, Z., Tan, P., Chen, W., Li, X., et al. (2023a). Exploring hydraulic fracture behavior in glutenite formation with strong heterogeneity and variable lithology based on DEM simulation. *Eng. Fract. Mech.* 278, 109020. doi:10.1016/j.engfracmech.2022.109020

Huang, L., Liu, J., Zhang, F., Dontsov, E., and Damjanac, B (2019). Exploring the influence of rock inherent heterogeneity and grain size on hydraulic fracturing using discrete element modeling. *Int. J. Solids Struct.* 176-177, 207–220. doi:10.1016/j.ijsolstr.2019.06.018

Huang, L., Liu, J., Zhang, F., Fu, H., Zhu, H., and Damjanac, B (2020). 3D lattice modeling of hydraulic fracture initiation and near-wellbore propagation for different perforation models. *J. Petroleum Sci. Eng.* 191, 107169. doi:10.1016/j.petrol.2020.107169

Huang, L., Tan, J., Fu, H., Liu, J., Chen, X., Liao, X., et al. (2023b). The non-plane initiation and propagation mechanism of multiple hydraulic fractures in tight reservoirs considering stress shadow effects. *Eng. Fract. Mech.* 292, 109570. doi:10.1016/j.engfracmech.2023.109570

Ji, Y., Wang, J., and Huang, L. (2015). Analysis on inflowing of the injecting Water in faulted formation. *Adv. Mech. Eng.* 7, 1–10.

Ju, W., Wu, C., and Sun, W. (2018). Effects of mechanical layering on hydraulic fracturing in shale gas reservoirs based on numerical models. *Arabian J. Geosciences* 11 (12), 323. doi:10.1007/s12517-018-3693-1

Liu, Q., Li, J., Liang, B., Sun, W., He, J., et al. (2023). Complex wettability behavior triggering mechanism on imbibition: a model construction and comparative study based on analysis at multiple scales. *Energy* 275, 127434. doi:10.1016/j.energy.2023.127434

Liu, Z., Pan, Z., Li, S., Zhang, L., Wang, F., Han, L., et al. (2022). Study on the effect of cemented natural fractures on hydraulic fracture propagation in volcanic reservoirs. *Energy* 241, 122845. doi:10.1016/j.energy.2021.122845

Luo, H., Xie, J., Huang, L., Wu, J., Shi, X., Bai, Y., et al. (2022). Multiscale sensitivity analysis of hydraulic fracturing parameters based on dimensionless analysis method. *Lithosphere* 2022, 9708300. doi:10.2113/2022/9708300

Qin, M., Yang, D., Chen, W., et al. (2021). Hydraulic fracturing model of a layered rock mass based on peridynamics. *Eng. Fract. Mech.* 258, 108088. doi:10.1016/j.engfracmech.2021.108088

Song, R., Liu, J., and Cui, M. (2017). A new method to reconstruct structured mesh model from micro-computed tomography images of porous media and its application. *Int. J. Heat Mass Transf* 109, 705–715. doi:10.1016/j.ijheatmasstransfer.2017.02.053

Song, R., Wang, Y., Ishutov, S., Zambrano-Narvaez, G., Hodder, K. J., Chalaturnyk, R. J., et al. (2020). A comprehensive experimental study on mechanical behavior, microstructure and transport properties of 3D-printed rock analogs. *Rock Mech. Rock Eng* 53, 5745–5765. doi:10.1007/s00603-020-02239-4

Tan, P., Chen, Z., Fu, S., and Zhao, Q (2023). Experimental investigation on fracture growth for integrated hydraulic fracturing in multiple gas bearing formations. *Geoenergy Sci. Eng.* 231, 212316. doi:10.1016/j.geoen.2023.212316

Tan, P., Jin, Y., Yuan, L., Xiong, Z. Y., Hou, B., Chen, M., et al. (2019). Understanding hydraulic fracture propagation behavior in tight sandstone–coal interbedded formations: an experimental investigation. *Petroleum Sci.* 16 (1), 148–160. doi:10.1007/s12182-018-0297-z

Tan, P., Pang, H., Zhang, R., Jin, Y., Zhou, Y., Kao, J., et al. (2020). Experimental investigation into hydraulic fracture geometry and proppant migration characteristics for southeastern Sichuan deep shale reservoirs. *J. Petroleum Sci. Eng.* 184, 106517. doi:10.1016/j.petrol.2019.106517

Wang, Y., Hou, B., Wang, D., and Jia, Z (2021). Features of fracture height propagation in cross-layer fracturing of shale oil reservoirs. *Petroleum Explor. Dev.* 48 (2), 469–479. doi:10.1016/s1876-3804(21)60038-1

Wu, M., Jiang, C., Song, R., Liu, J., Li, M., Liu, B., et al. (2023). Comparative study on hydraulic fracturing using different discrete fracture network modeling: insight from homogeneous to heterogeneity reservoirs. *Eng. Fract. Mech.* 284, 109274. doi:10.1016/j.engfracmech.2023.109274

Zheng, Y., He, R., Huang, L., Bai, Y., Wang, C., Chen, W., et al. (2022). Exploring the effect of engineering parameters on the penetration of hydraulic fractures through bedding planes in different propagation regimes. *Comput. Geotechnics* 146 (146), 104736. doi:10.1016/j.compgeo.2022.104736

Zheng, Y., Liu, J., and Zhang, B. (2019). An investigation into the effects of weak interfaces on fracture height containment in hydraulic fracturing. *Energies* 12, 3245. doi:10.3390/en12173245

Zhu, D., Zhang, L., Song, X., Lian, H., and Niu, D (2023). Propagation mechanism of the hydraulic fracture in layered-fractured-plastic formations. *Int. J. Fract.* 241 (2), 189–210. doi:10.1007/s10704-023-00694-y

Zhuang, X., Li, X., and Zhou, S. (2023). Transverse penny-shaped hydraulic fracture propagation in naturally-layered rocks under stress boundaries: a 3D phase field modeling. *Comput. Geotechnics* 155, 105205. doi:10.1016/j.compgeo.2022.105205

frontiers | Frontiers in Energy Research

TYPE Methods
PUBLISHED 15 January 2024
DOI 10.3389/fenrg.2023.1333137

Check for updates

OPEN ACCESS

EDITED BY
Xiaojin Zheng,
Princeton University, United States

REVIEWED BY
He Xiang,
Wuhan Polytechnic University, China
Zuliang Shao,
University of South China, China
Muhammad Jawad Munawar,
University of the Punjab, Pakistan

*CORRESPONDENCE
Dahui Qin,
qindahui@qq.com

RECEIVED 04 November 2023
ACCEPTED 26 December 2023
PUBLISHED 15 January 2024

CITATION
Dong H, Jia H, Qin D and Hu D (2024), Research on micro/nano scale 3D reconstruction based on scanning electron microscope.
Front. Energy Res. 11:1333137.
doi: 10.3389/fenrg.2023.1333137

COPYRIGHT
© 2024 Dong, Jia, Qin and Hu. This is an open-access article distributed under the terms of the Creative Commons Attribution License (CC BY). The use, distribution or reproduction in other forums is permitted, provided the original author(s) and the copyright owner(s) are credited and that the original publication in this journal is cited, in accordance with accepted academic practice. No use, distribution or reproduction is permitted which does not comply with these terms.

Research on micro/nano scale 3D reconstruction based on scanning electron microscope

Huibao Dong[1,2], Hongliang Jia[1,2], Dahui Qin[1,2]* and Dawei Hu[2]

[1]State Key Laboratory of Geomechanics and Geotechnical Engineering, Wuhan, China, [2]School of Civil Engineering and Geomatics, Southwest Petroleum University, Chengdu, China

Scanning electron microscopy (SEM) has an important application in the petroleum field, which is often used to analyze the microstructure of reservoir rocks, etc. Most of these analyses are based on two-dimensional images. In fact, SEM can carry out micro-nano scale three-dimensional measurement, and three-dimensional models can provide more accurate information than two-dimensional images. Among the commonly used SEM 3D reconstruction methods, parallax depth mapping is the most commonly used method. Multiple SEM images can be obtained by continuously tilting the sample table at a certain Angle, and multiple point clouds can be generated according to the parallax depth mapping method, and a more complete point clouds recovery can be achieved by combining the point clouds registration. However, the root mean square error of the point clouds generated by this method is relatively large and unstable after participating in point clouds registration. Therefore, this paper proposes a new method for generating point clouds. Firstly, the sample stage is rotated by a certain angle to obtain two SEM images. This operation makes the rotation matrix a known quantity. Then, based on the imaging model, an equation system is constructed to estimate the unknown translation parameters, and finally, triangulation is used to obtain the point clouds. The method proposed in this paper was tested on a publicly available 3D SEM image set, and the results showed that compared to the disparity depth mapping method, the point clouds generated by our method showed a significant reduction in root mean square error and relative rotation error in point clouds registration.

KEYWORDS

scanning electron microscope, 3D reconstruction, parallel projection, camera calibration, point clouds registration

1 Introduction

One of the main drawbacks of optical microscopes is their limitations in resolving finer details. Scanning electron microscopes (SEM) use electron imaging, and the wavelength of electrons is much smaller than that of photons, easily achieving magnifications of tens or even hundreds of thousands of times. However, SEM can only obtain 2D images and cannot directly generate 3D shapes. Compared to 2D images, three-dimensional structures can provide more information for many micro research fields. For example, SEM has important applications in the petroleum field, (Zhu, 2013; Liu et al., 2023; Wu et al., 2023), used SEM in the analysis of the micro pore structure of reservoir rocks. Yao used SEM combined with deep learning based image processing to characterize the nanoscale pore structure of rock debris (Yao et al., 2022). Scholars have also used SEM to observe and analyze the microstructure of solid/oil well cement stone (Li et al., 2016; Zhang et al., 2013;

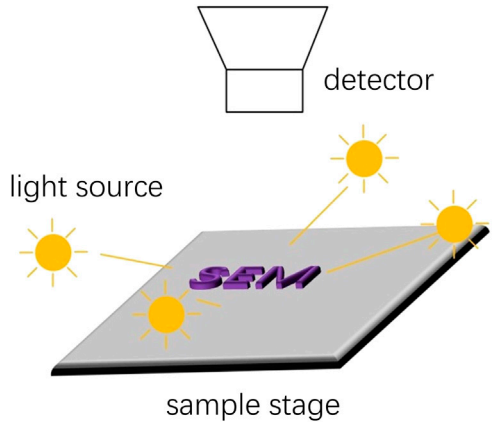


FIGURE 1
Photometric Stereo (PS) method.

Song et al., 2017; Song et al., 2020). Munawar used optical polarization microscopy in transmission mode to document the whole-rock mineralogy, diagenetic relationships, porosity characteristics and clay occurrences in the pores of these samples (Munawar et al., 2018a). Wang used focused ion beam scanning electron microscopy (FIB-SEM) to reconstruct the internal organic matter pores of shale using a three-dimensional-slicing-imaging reconstruction technology route, but its literature also indicated that FIB can cause damage to the sample during the slicing process, which is a destructive analysis method (Wang et al., 2019). Munawar mentions that micro-CT imaging has certainly some limitations concerning sample size and resolution (Munawar et al., 2018b). It is reliable to captures micron scale features, whereas it is not possible for micro-CT to capture nanometer scale features (Munawar et al., 2018b; Luo et al., 2022; Ji et al., 2015). There are scholars used X-ray CT to perform three-dimensional measurements on carbonate rock and sandstone sample (Munawar et al., 2021). A series of two-dimensional slices stack into a 3D image. Data are arranged in an array of pixels in the two-dimensional slice. A pixel in the third dimension makes it three-dimensional volume which is a voxel. This is, the distance between two consecutive slices is a voxel. The 3D model formed by stacking sliced images is a discrete model, but compared to FIBSEM, this is a reconstruction method for non-destructive samples. The resolution of the new scanning electron microscope can reach 1 nm. Based on SEM 3D reconstruction, nanoscale, spatially continuous 3D models can be obtained, which is helpful for calculating porosity. There are many scholars also use SEM equipment in petroleum energy research (Huang et al., 2023a; Huang et al., 2023b; Tan et al., 2023; Tan et al., 2020; Huang et al., 2020; Huang et al., 2022). SEM can provide high-resolution images without damaging the sample. If standard SEM machines can be used to restore the microscopic three-dimensional structure of samples such as rocks in the above research, it will provide more information for analyzing pore structure, material toughness, etc. without damage. In order to effectively measure and visualize the three-dimensional structure of microscopic samples, many scholars have been trying to convert scanning electron microscopy into microscopic three-dimensional measurement tools.

Currently, the commonly used 3D reconstruction algorithms under scanning electron microscopy include the Photometric Stereo (PS) method (Ikeuchi, 1981; Basri et al., 2007; Goldman et al., 2010). As shown in Figure 1, in the PS based method, the sample stage and detector of the scanning electron microscope remain stationary, providing illumination in different directions to the sample stage. From a single perspective, the detector captures a set of 2D images in different lighting directions and quickly calculates the 3D geometric shape of the SEM sample. However, since only one perspective is used, it is not possible to create a complete point clouds, and the PS method requires illumination from different directions on the sample stage, making it difficult to have such additional lighting conditions using standard scanning electron microscopy machines, which increases equipment costs and limitations.

(Wang et al., 2013) used SFS (shape from shading) technology to analyze the grayscale information of a single top view SEM image, and ultimately reconstructed the three-dimensional surface structure. However, due to the fixed perspective, a complete point clouds cannot be obtained.

(Ding et al., 2019) adopted a nanorobot system to automatically capture a set of scanning electron microscope images along a linear path with a fixed step size, and used light field theory to reconstruct the three-dimensional surface model of SEM samples. As shown in Figure 2A, the sample is fixed on the sample stage via either glue, tape or customized grippers according to sample properties. After assembling the nano-robotic manipulation system inside SEM, the linear positioner is utilized to move step by step along x-axis with a fixed step size, and one SEM image is taken after each step. Figure 2B shows the SEM images obtained at each step. However, not all SEM devices are equipped with nanorobot systems, and the step accuracy of nanorobot systems is limited, requiring a large number of images to be captured.

Tafti et al., 2015; Tafti et al., 2016 designed an optimized, parameter adaptive, and intelligent multi view method, 3DSEM++, for 3D surface reconstruction of SEM images. He also publicly and freely provided a 3D SEM image set, which is derived from Tafti's publicly available image set. Some scholars have studied the use of optical measurement software for three-dimensional reconstruction of SEM images (Eulitz and Reiss, 2015; Kareiva et al., 2015), but optical measurement software often does not consider the imaging characteristics of SEM itself, and generally requires images to contain EXIF information and camera model, which SEM images often do not have.

The parallax depth mapping method (Samak et al., 2007; Baghaie et al., 2017; Yi et al., 2019; Bian, 2020) is the simplest and fastest way to obtain the three-dimensional structure of SEM samples. As shown in Figure 3A, θ is the rotation angle, and the relationship between disparity d and depth h is given by a formula.

$$h = \frac{d}{2^{*} \sin \theta}$$

, by rotating the sample stage at a certain angle to obtain two SEM images, a point clouds can be created based on parallax. However, since parallax depth mapping can only use two images at once, it is also not possible to create a complete point clouds. In response to the

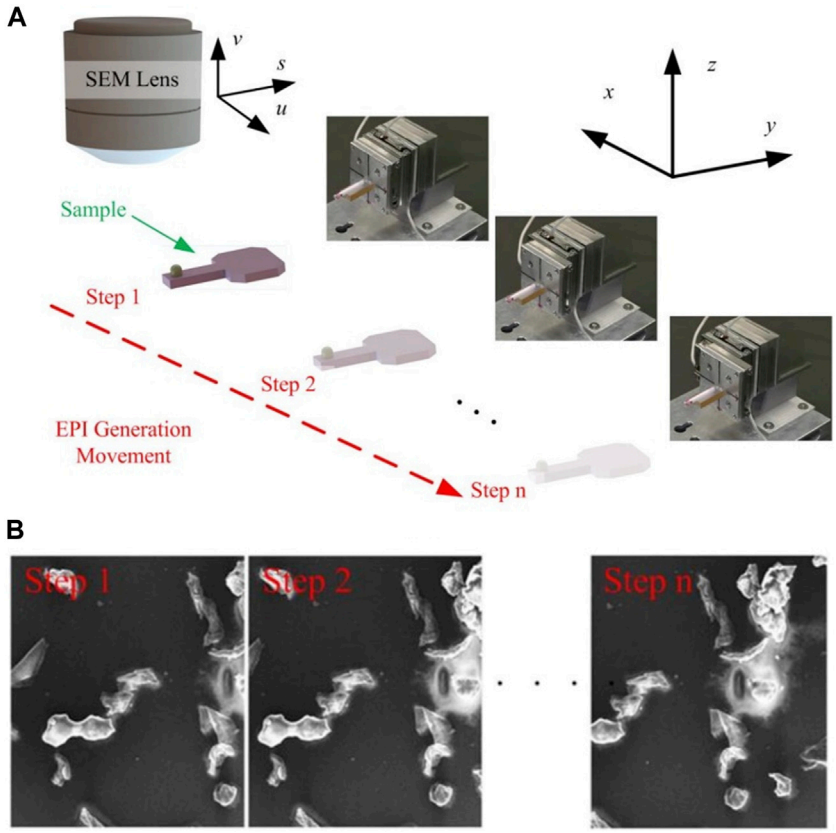


FIGURE 2
(A) The movement process of nanorobots **(B)** Image obtained step by step.

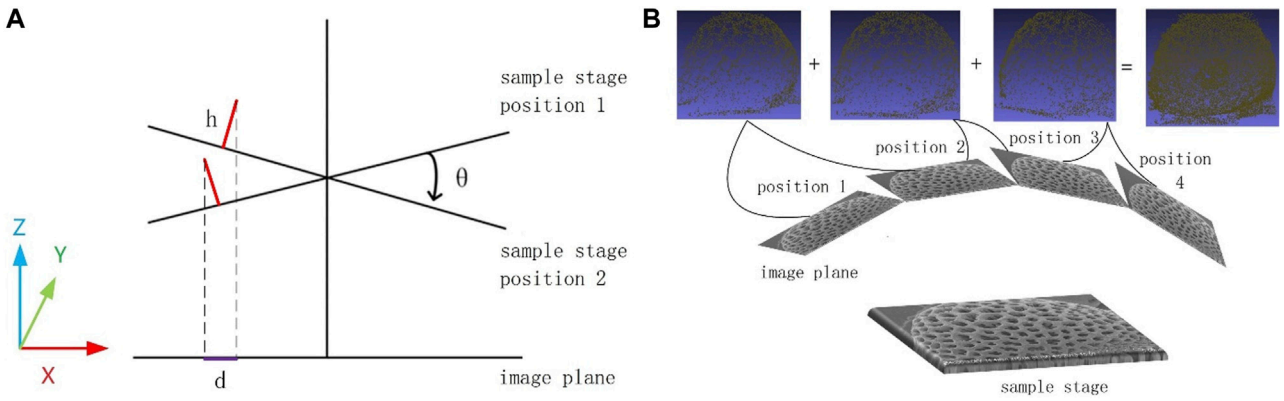


FIGURE 3
(A) The principle of disparity depth mapping and the rotation method of the sample stage **(B)** Parallax depth mapping to obtain multiple point clouds, and then point clouds registration.

insufficient integrity of the point clouds reconstructed by the disparity depth mapping method, Rehman used disparity depth mapping combined with point clouds registration to achieve multi view SEM 3D reconstruction [Rehman, 2018]. As shown in Figure 3B, multiple point clouds are obtained by using the parallax depth mapping multiple times, and then point clouds registration is performed

Liu used incremental motion recovery structure (SFM) to perform 3D reconstruction of the SEM image sequence of the *Drosophila* head, and successfully restored the point clouds (Liu, 2018). SFM uses singular value decomposition of the essential matrix to obtain initial rotation and translation parameters. Unfortunately, this method yields poor results on the image set presented in this paper.

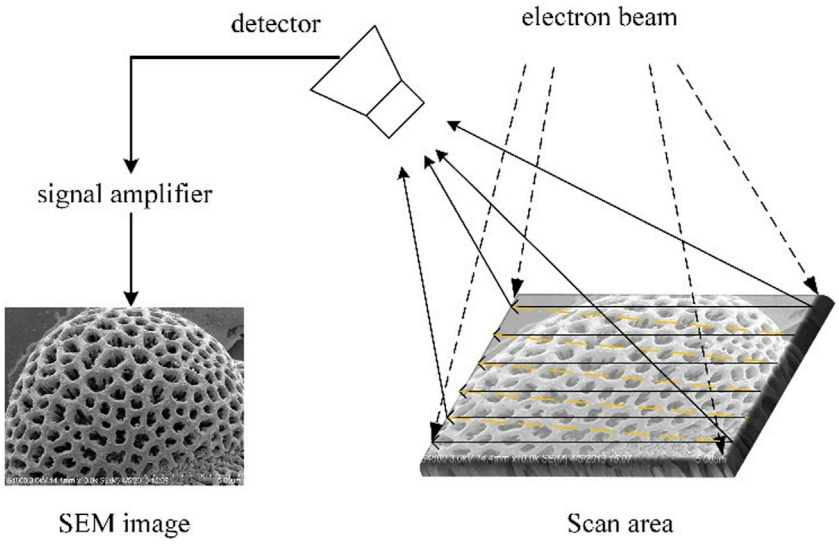


FIGURE 4
Schematic diagram of SEM imaging process.

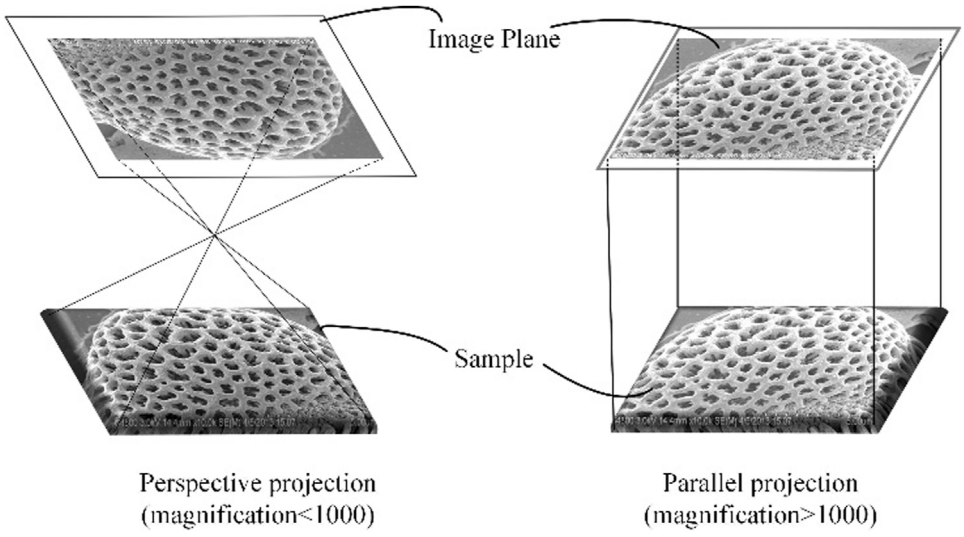


FIGURE 5
SEM imaging model under different magnification.

This article improves the shortcomings of the aforementioned SEM based 3D reconstruction methods, such as a single perspective, equipment cost limitations, lack of consideration for SEM imaging characteristics, and time consumption. It proposes a method for restoring the detector pose, which is different from traditional essential matrix singular value decomposition. It uses imaging equations of multiple image points to form a system of equations, analyzes the known internal and external parameters in the imaging model, and calculates the motion parameters of the position. Triangulation is used to generate point clouds of different parts of the microscopic sample, and then point clouds registration is combined to obtain a more complete point clouds. Thus, standard SEM machines can be used to achieve three-dimensional reconstruction of microscopic samples from multiple perspectives.

The content of this article is arranged as follows. The first section is an introduction, which introduces the commonly used methods and shortcomings of three-dimensional reconstruction of microscopic samples under SEM.

Section 2 will introduce the publicly available 3D SEM image set and point out that there are some known conditions in this image set that are beneficial for subsequent calibration work.

Section 3 will introduce the SEM three-dimensional measurement model. When the magnification of the SEM exceeds 1,000, the SEM imaging process is similar to a double telecentric lens. At

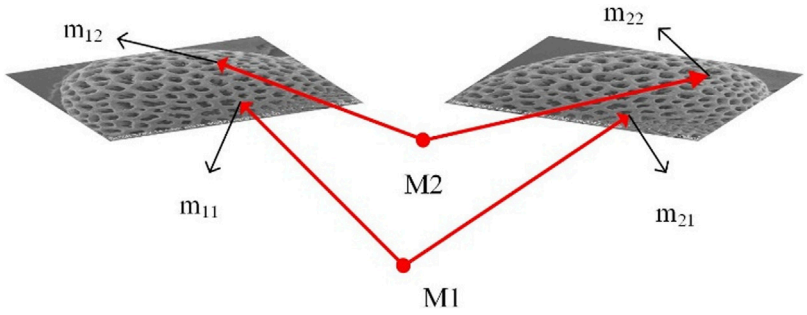


FIGURE 6
Simultaneous imaging equation of multiple image points.

this point, the parallel projection model is more suitable for the SEM imaging model. Then, based on the publicly available 3D SEM image set, a motion parameter estimate method between SEM image sequences suitable for this image set is derived.

Section 4 will present a more specific experimental process and results.

In Section 5, the evaluation indicators for point clouds registration, including root mean square error and relative rotation error, will be introduced. Due to the fact that the relative translation motion in relative transformation does not have a true value as a reference, relative translation error cannot be used as an evaluation indicator. Under these indicators, the registration results of our method will be compared and analyzed with those of the disparity depth mapping method.

Section 6 will provide the discussion and conclusion of this article.

2 3D SEM image set

The 3D SEM image set used in this article is from the publicly available SEM image set by Tafti, available at the website https://dataverse.harvard.edu/dataset.xhtml?persistentId=doi:10.7910/DVN/HVBW0Q#__sid=js0, the characteristic of this image set is that, as shown in Figure 3A, in the image sequence, the Y-axis of the sample stage itself is used as the rotation axis, and a fixed angle is rotated around that axis θ to obtain the next image, during the actual shooting process, this rotation operation will be continuously performed to obtain multiple SEM images. The rotation angle θ will serve as an important rotational motion parameter in the imaging model.

Although the actual operation process involves the sample stage rotating around its Y-axis while the imaging plane remains stationary, it can be seen that the sample stage remains stationary and the imaging plane rotates around the sample stage because the motion is relative. Figure 3B shows the equivalent shooting process of SEM images of " Pollen grain from Brassica rapa " in the image set.

This publicly available 3DSEM image set was obtained using standard SEM equipment, and its special motion method is to apply the disparity depth mapping method. Many scholars have also used this image set to conduct extensive research based on disparity depth mapping. Among them, Rehman added point clouds registration to it, enabling all SEM images to be used and obtaining a more complete point clouds (Rehman, 2018). However, the above studies are all based on disparity depth mapping. In fact, this image set can use calibration methods to estimate motion parameters, and then use triangulation to recover point clouds. Section 5 will compare these two methods.

3 SEM 3D measurement model

3.1 SEM imaging model

As shown in Figure 4, the SEM imaging process essentially involves hitting the surface of the sample with an electron beam, and then sampling by the detector to obtain the grayscale information of each sampling point. This process can be seen as a three-dimensional to two-dimensional mapping (Liu, 2018). Therefore, the SEM imaging process is also regarded by many scholars as a projection transformation. SEM expert Reimer once pointed out that the SEM imaging process can be approximated as a perspective projection process (Reimer, 1985), but in recent years, research has shown that the imaging model of electronic imaging systems is different under different magnifications: when the magnification is low, the field of view and angle of view are large, and the classical perspective projection model can be used to model the imaging system, when the magnification is large, the field of view and angle of view are both very small, and the imaging process is approximately parallel projection.

Due to the fact that the SEM imaging model depends on the size of the magnification, finding an appropriate critical value has become the key to studying two different projection models. (Sutton et al., 2007). conducted extensive research on the SEM projection model and obtained a widely recognized critical value, which is that when the magnification is higher than 1,000x, the projection model can be approximated as a parallel projection, When the magnification is below 1,000x, the projection model can be considered as a transmission projection. As shown in Figure 5.

The magnification of the 3D SEM image set used in this article exceeds 1,000x, so this article mainly studies 3D reconstruction

TABLE 1 Detailed parameters of the 3D SEM image set.

Image sets	Pollen grain from Brassica rapa	Diatom
a	337.3438	595.3125
θ(°)	3°	−15°
Dpi (pixel/Inch)	512	512
Scale (μm/pixel)	5/34	5/60
Image size	854*640	2,560*1920
Image number	4	3

under parallel projection models. The formula for the parallel projection imaging model is as follows:

The mathematical model of image points $[u\ v]$ and corresponding world points $[X\ Y\ Z]$ is as follows (Liu, 2018):

$$\begin{bmatrix} u \\ v \\ 1 \end{bmatrix} = \begin{bmatrix} a & 0 & 0 \\ 0 & a & 0 \\ 0 & 0 & 1 \end{bmatrix} \begin{bmatrix} 1 & 0 & 0 & 0 \\ 0 & 1 & 0 & 0 \\ 0 & 0 & 0 & 1 \end{bmatrix} \begin{bmatrix} r_{11} & r_{12} & r_{13} & t_x \\ r_{21} & r_{22} & r_{23} & t_y \\ r_{31} & r_{32} & r_{33} & t_z \\ 0 & 0 & 0 & 1 \end{bmatrix} \begin{bmatrix} X \\ Y \\ Z \\ 1 \end{bmatrix}, \tag{1}$$

The matrix where *a* is located in equation 1 is the SEM internal matrix. Due to the characteristics of parallel projection, the main point of the image in the internal matrix is 0, and *a* is the scale factor between pixel size and actual scale, it can be calculated from the dpi of the SEM image and the scale bar on the image. The dpi of the image represents the number of pixels per inch of length, and SEM images usually provide scale bar and other information at the bottom of the image, r_{ii} are the element within the rotation matrix, t_x, t_y, and t_z are the elements within the translation vector. The two together form the SEM external matrix. It can be observed that the third row of the rotation matrix r_{3i} and the third component of the translation vector t_z do not affect the imaging process, as they are multiplied by 0. Therefore, equation 1 is simplified as follows:

$$\begin{bmatrix} u \\ v \\ 1 \end{bmatrix} = \begin{bmatrix} a & 0 & 0 \\ 0 & a & 0 \\ 0 & 0 & 1 \end{bmatrix} \begin{bmatrix} r_{11} & r_{12} & r_{13} & t_x \\ r_{21} & r_{22} & r_{23} & t_y \\ 0 & 0 & 0 & 1 \end{bmatrix} \begin{bmatrix} X \\ Y \\ Z \\ 1 \end{bmatrix}, \tag{2}$$

3.2 Estimating relative translational motion

Generally speaking, SFM extrinsic parameter estimate is obtained by performing singular value decomposition on the essential matrix E to obtain four sets of R and t, and then selecting a suitable set of R and t based on the 3D point in front of the camera (Zhang, 1996). Unfortunately, this method did not achieve good results on the publicly available 3D SEM set. Therefore, after analyzing the known conditions that SEM image sequences can provide, this article adopts the imaging equations of multiple image points to form an equation system, and estimate the motion parameters by solving the equation system. In SFM, it is common to make the image coordinate system of the first images coincide with the world coordinate system. Therefore, the rotation matrix of the first SEM image is the third-order identity matrix, and the translation vector is the zero vector. Substituting into equation 2 yields the following

$$\begin{bmatrix} u \\ v \\ 1 \end{bmatrix} = a \begin{bmatrix} X \\ Y \\ 1 \end{bmatrix}, \tag{3}$$

From equation 3, it can be seen that for a SEM image, the X and Y components of the image point and the world point only differ by one magnification of a. If there are two SEM images, as shown in Figure 6.

The feature point m_{11} can be detected on the first SEM image, Set M_1 as m_{11} corresponding to the world point, the X and Y components of the world point M_1 can be calculated using equation 3, set as X_{M1} and Y_{M1}. Then, on the second SEM image, find the feature point m_{21} that matches m_{11}. The world point corresponding to m_{21} is M_1, and the equation for projecting the world point M_1 onto m_{21} is as follows

$$\begin{bmatrix} u_{m21} \\ v_{m21} \\ 1 \end{bmatrix} = \begin{bmatrix} a & 0 & 0 \\ 0 & a & 0 \\ 0 & 0 & 1 \end{bmatrix} \begin{bmatrix} r_{11} & r_{12} & r_{13} & t_x \\ r_{21} & r_{22} & r_{23} & t_y \\ 0 & 0 & 0 & 1 \end{bmatrix} \begin{bmatrix} X_{M1} \\ Y_{M1} \\ Z_{M1} \\ 1 \end{bmatrix}, \tag{4}$$

In equation (4), *a*, X_{M1}, Y_{M1} are known quantities. As already introduced in section 2, rotating a certain angle around the Y-axis of the sample stage itself to obtain the next image, θ it can be used to calculate the rotation parameter r_{ii}, so r_{ii} is a known quantity. Now, there are three unknown variables t_x, t_y, and Z_{M1} in Eq. (4), but there are only two equations. If a pair of identical image points m_{12} and m_{22} are added to two SEM images, there are world points M_2 corresponding to it. The X and Y components of M_2 are set to X_{M2} and Y_{M2}, and the equation for projecting the world point M_2 to the image point m_{22} is as follows:

$$\begin{bmatrix} u_{m22} \\ v_{m22} \\ 1 \end{bmatrix} = \begin{bmatrix} a & 0 & 0 \\ 0 & a & 0 \\ 0 & 0 & 1 \end{bmatrix} \begin{bmatrix} r_{11} & r_{12} & r_{13} & t_x \\ r_{21} & r_{22} & r_{23} & t_y \\ 0 & 0 & 0 & 1 \end{bmatrix} \begin{bmatrix} X_{M2} \\ Y_{M2} \\ Z_{M2} \\ 1 \end{bmatrix}, \tag{5}$$

In equation 5, there are three unknowns: t_x, t_y, and Z_{M2}. Observing Equations 4, 5, it can be seen that t_x and t_y are fixed unknowns. For each increase in world point, the unknowns increase by one, which is the Z component of the world point. However, the number of equations increases by two. Assuming that n pairs of identical image points are detected on two SEM images, there are 2 * n equations with n+2 unknowns. When 2 * n > n+2, which is $n \geq 2$, the equation is solvable. The above equation system can be simplified to the form of Ax = b. There are many methods to solve this type of equation, and experiment in this article uses the generalized inverse of the matrix to solve it. In this way, a series of three-dimensional coordinates of the world points are obtained, as well as the relative translational motion t_x and t_y between the two SEM images. At this point, the external motion parameters between the two SEM images are known.

3.3 Triangulation

Section 3.2 provides the solution process for the Z component of the world point, t_x and t_y. Combining the X and Y components described in Eq. (3), the three-dimensional coordinates of the world point can be formed. However, in a large number of matching image

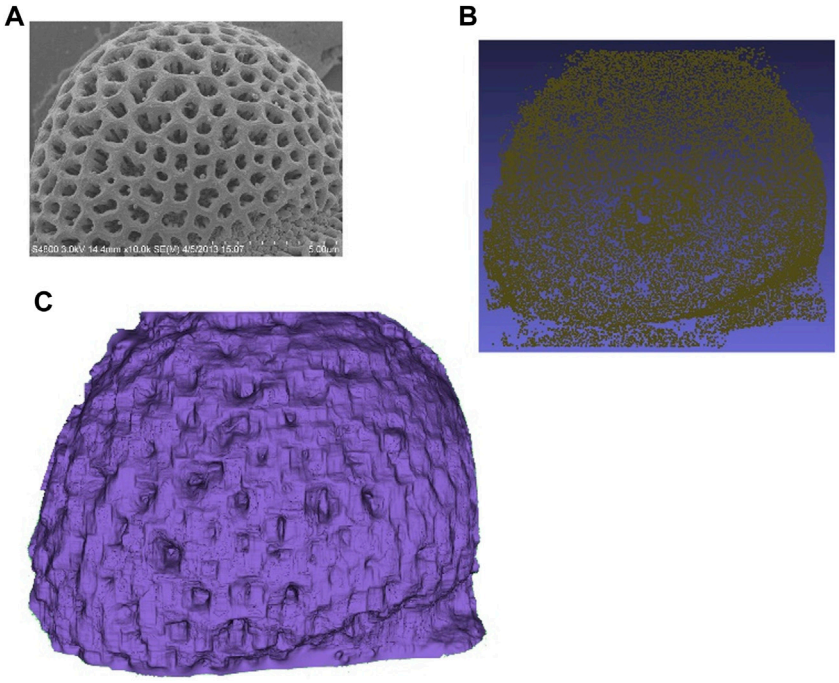


FIGURE 7
Example of Pollen reconstruction results. **(A)** SEM image, **(B)** Point clouds, **(C)** Surface mesh.

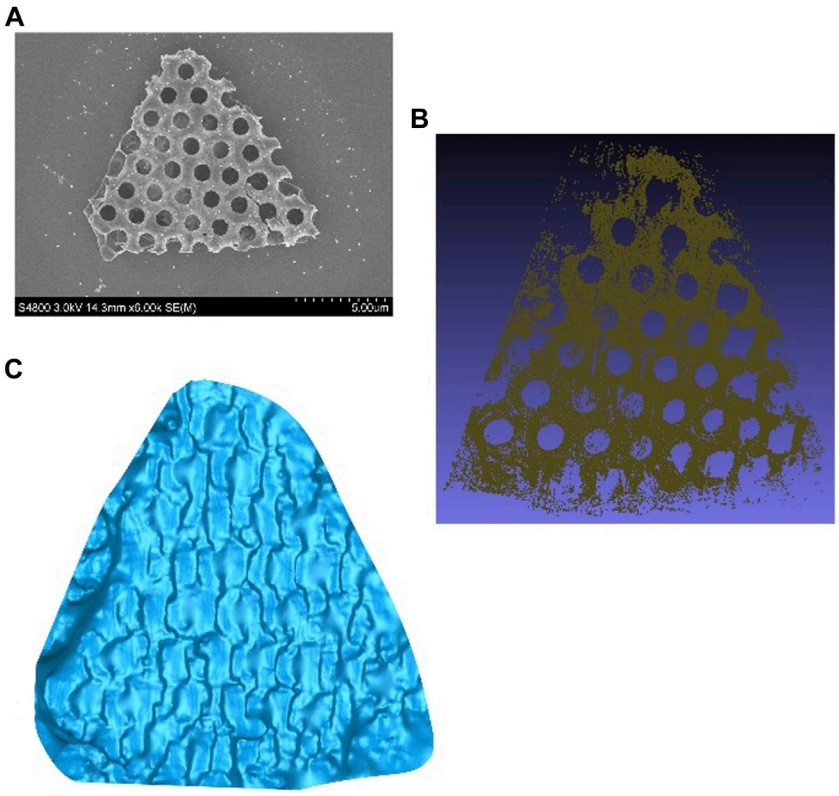


FIGURE 8
Example of Diatom reconstruction results. **(A)** SEM image, **(B)** Point clouds, **(C)** Surface mesh.

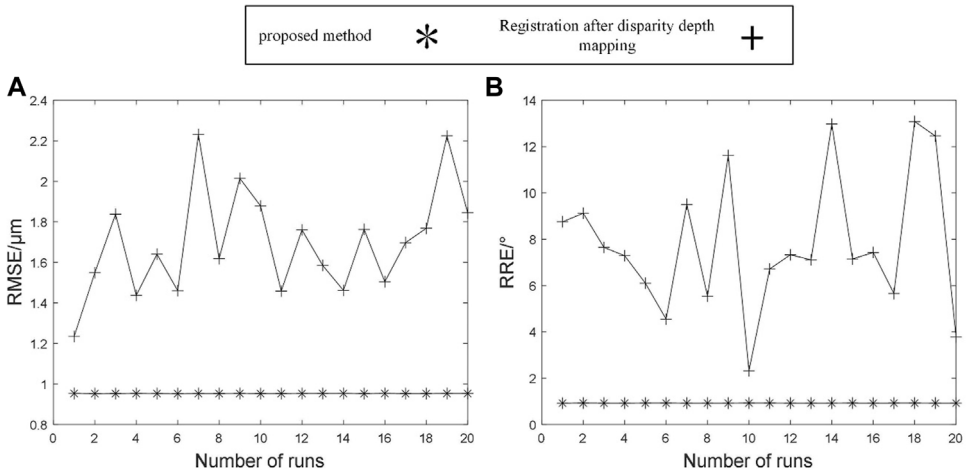


FIGURE 9
For example, pollen, RMSE **(A)** and RRE **(B)** curves after 20 runs.

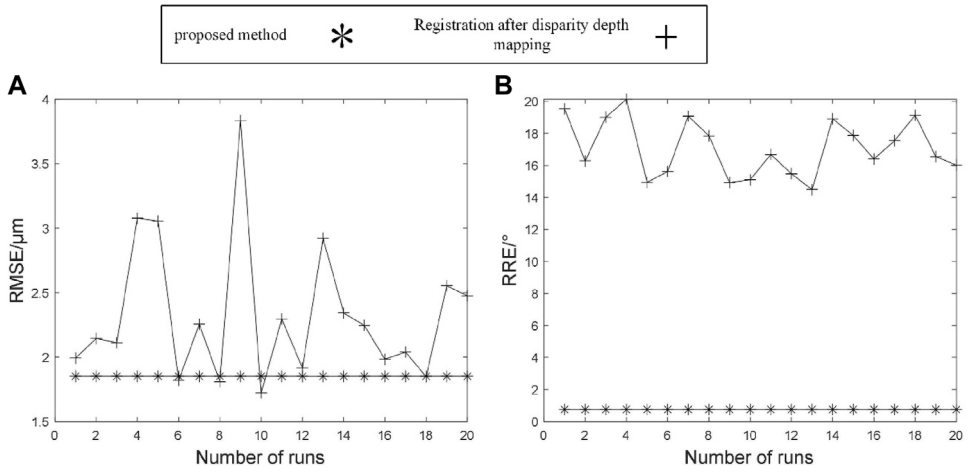


FIGURE 10
For example, diatom, RMSE **(A)** and RRE **(B)** curves after 20 runs.

points, there may be incorrect matches. If incorrect matches are included in the equation set, it will contaminate the equation set and affect the accuracy of solving other unknown quantities. Therefore, after estimating t_x and t_y, we still use triangulation to restore the point clouds, even if there are incorrect matches, it will not affect the solution of other points. After obtaining the internal and external motion parameters of two SEM images, the projection matrix can be calculated, and combined with a series of corresponding image points, the point clouds can be obtained through triangulation. The formula is as follows

$$\begin{bmatrix} u_i \\ v_i \\ 1 \end{bmatrix} = P \begin{bmatrix} X \\ Y \\ Z \\ 1 \end{bmatrix} with\, i = 1, 2, \tag{6}$$

In equation (6), P is the projection matrix, which is composed of the SEM internal and external parameter matrices in equation 5. For a set of identical image points, there are four equations, and the coordinates of the corresponding world point have three unknown quantities. The method for solving the equation system composed of equation 6 is already a mature theory and will not be repeated.

4 Experimental process and results

4.1 Experimental data and process

Table 1 shows the detailed data of the 3D SEM image set, *a* in Table 1 is obtained by dpi and scale.

This experiment was implemented on Matlab 2020a, where the point clouds registration used the pcregistericp function, the input parameters of this function are fixed asfollows pcregistericp (ptCloud2,ptCloud1,'MaxIterations',10,000,'Tolerance', [1e-5,1e-3]), and the specific process is as follows:

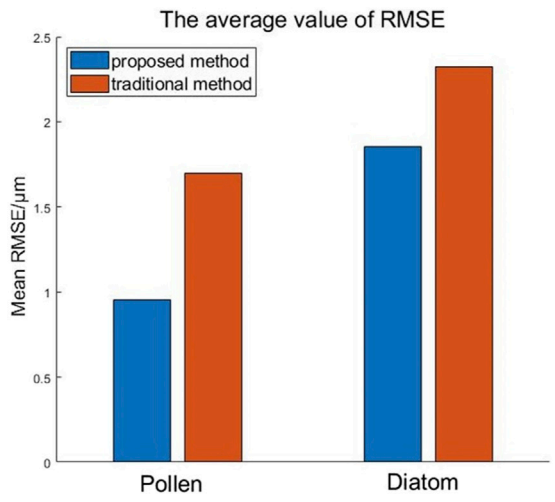


FIGURE 11
In two examples, the average value of the RMSE curve.

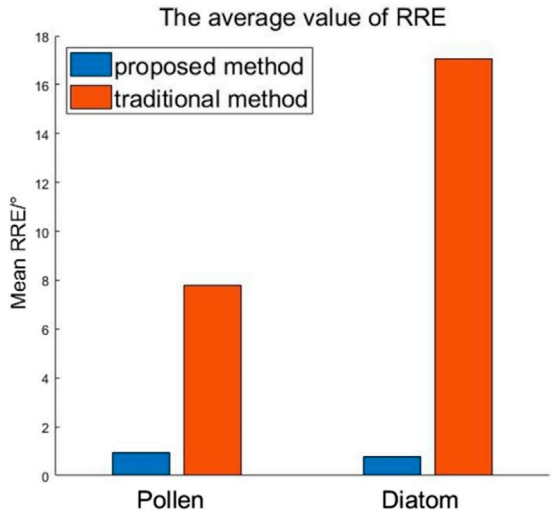


FIGURE 12
In two examples, the average value of the RRE curve.

1) The SEM sample stage rotates continuously around its Y-axis at a fixed angle to obtain a sequence of SEM images.
2) In the SEM image sequence, two adjacent images are grouped together, and feature detection and matching are performed on each group of images.
3) Within a set of images, according to equation 3, the X and Y components of the world point corresponding to the matching image points are calculated using the feature points detected on the previous image.
4) Within a set of images, according to the formula in section 3.2, the relative translation vector between the two images is estimated by imaging equation system of points on the latter image
5) For multiple sets of images, triangulation is performed to calculate the point clouds sequence. It should be noted that relative rotation and relative translation are used to calculate the projection matrix within the each set of images, resulting in a rotational motion difference between the point clouds sequences, which will provide a true rotation matrix for the evaluation criteria of relative rotation error in point clouds registration. In fact, for image sequences, if a global rotation matrix can be used, and the translation vector is still a relative translation vector, the estimated rotation transformation matrix between point clouds sequence is the third-order identity matrix.
6) Point clouds registration.

4.2 Experimental results

The implementation of our method for the two examples in Table 1 is shown in Figure 7 to Figure 8, which show the original SEM image a), the obtained point clouds b), and the meshed surface c).

5 Comparison and analysis

5.1 Point clouds registration evaluation criteria

5.1.1 Root mean square error

Root mean square error (RMSE) is the average Euclidean distance between the nearest neighboring points of two point clouds after registration. The smaller the error, the closer the two point clouds align. The RMSE calculation formula is shown in Eq. (7). For multiple point clouds registration, this article adopts multiple RMSEs to calculate the average.

$$RMSE = \sqrt{\frac{\sum_i^n d_i^2}{n}}$$
$$di = \sqrt{\left(x_p - x_q\right)^2 + \left(y_p - y_q\right)^2 + \left(z_p - z_q\right)^2}, \quad (7)$$

5.1.2 Relative rotation error

Relative rotation error (RRE) is a comparison between the rotation matrix obtained from registration results and the existing true rotation transformation matrix. The RRE calculation formula is shown in Eq. (8), where Re is the true rotation transformation matrix, and Rc^{-1} is the inverse of the relative rotation matrix obtained from point clouds registration. The closer the RRE is to 0, the closer the estimated rotation is to the true rotation. For multiple point clouds registration, this article adopts multiple RREs to calculate the average.

$$RRE = \arccos\left(\frac{trace\left(R_e R_c^{-1}\right) - 1}{2}\right) * \frac{180}{\pi}, \quad (8)$$

The method for the control experiment is the one proposed by (Rehman, 2018), which is also based on generating multiple point clouds from multiple adjacent image pairs and then registering them. The difference is that Rehman used disparity depth mapping

TABLE 2 Standard deviation of RMSE and RRE after 20 runs.

		The standard deviation of the RRE (°)	The standard deviation of the RMSEs (μm)	True size of the image frame (μm)
Pollen	Proposed	0.0013	0.0003	125*94
	Contrast	2.978	0.2596	
Diatom	Proposed	0.0004	4.549e-5	213*160
	Contrast	1.7659	0.5377	

to generate point clouds, while this article obtain multiple point clouds by estimating motion parameters then triangulates. In order to ensure the objectivity of the results, the point clouds size of the two experiments was scaled to the size of the real sample. The parameters of the point clouds registration function pcregistericp in both experiments, such as the number of iterations and step accuracy, were consistent. Then compare the root mean square error (RMSE) and relative rotation error (RRE) of point clouds registration. After running the program 20 times, the results are shown in Figure 9 to Figure 10. Figure 11 to Figure 12 show the mean values of RMSE and RRE after 20 runs, Table 2 shows the standard deviation of the result data.

By observing Figure 9 to Figure 10, it can be seen that compared to traditional disparity depth mapping methods, the RMSE of the point clouds sequence generated by our method after registration is reduced in both examples, and RRE is significantly reduced in the diatom example. Furthermore, by analyzing Figures 11, 12, in the pollen example, the average RMSE reduction and RRE reduction are 44% and 88% by of our method, in the diatom example, the average RMSE decreased by 20% and the average RRE decreased by 96%. By observing Figures 9, 10, it can be found that after 20 runs, the results curves of RMSE and RRE of our method are very close to straight lines. Furthermore, from the standard deviation of the above data in Table 2, it can be seen that the standard deviation of our method after multiple runs is lower than that of traditional methods by multiple orders of magnitude, proving that our method has significant advantages in stability.

6 Disscussion and clusions

Although parallax depth mapping and SFM can also be applied on standard SEM devices, the point clouds registration method after parallax depth mapping requires the sample stage to perform a special rotation motion as shown in Figure 3A multiple times in a row, which limits the shooting angle of the SEM device and the point clouds registration error is large and unstable. However, the method proposed in this paper only requires one special rotation motion as shown in Figure 3A to obtain the initial point clouds, the rotation and translation parameters of subsequent images can be estimated using the PnP algorithm, so the shooting angle of subsequent images is arbitrary and unrestricted. At the same time, the method proposed in this paper is based on point clouds obtained through triangulation, which can exclude some error points and noise points through the indicator of reprojection error, which is an indicator that disparity depth mapping does not have.

The difference between this method and SFM lies in the approach of obtaining initial three-dimensional points. SFM uses singular value decomposition of the essential matrix to estimate the initial rotation and translation parameters, thereby obtaining a projection matrix to solve the three-dimensional points. The rotation and translation parameters of subsequent images are also estimated using the PnP algorithm. SFM does not require SEM equipment to perform special movements on Figure 3A, Unfortunately, on publicly available 3D SEM datasets, the rotation parameters estimated through the essential matrix are far from the actual rotation parameters, making it impossible to obtain good initial point clouds. Fortunately, SEM equipment is an indoor device that can control rotation motion. Compared to SFM estimated rotation parameters, using known rotation parameters is more stable. Therefore, the method proposed in this article only requires one special motion as shown in Figure 3A, after obtaining the real rotation parameters, the translation parameters can be estimated by constructing an equation system through the imaging model, and then the initial point clouds can be obtained through triangulation. The rotation and translation parameters of subsequent images can also be estimated using the PnP algorithm. In fact, the method proposed in this article is a compromise between disparity depth mapping and SFM. We believe that the proposed method can replace the disparity depth mapping and SFM.

Data availability statement

The original contributions presented in the study are included in the article/Supplementary Material, further inquiries can be directed to the corresponding author.

Author contributions

HD: Investigation, Methodology, Writing–original draft. HJ: Writing–review and editing, Data curation, Supervision. DQ: Conceptualization, Project administration, Writing–review and editing. DH: Funding acquisition, Project administration, Writing–review and editing.

Funding

The author(s) declare financial support was received for the research, authorship, and/or publication of this article. Project of Research on 3D Reconstruction Method of Ultrafine Microstructure Based on Scanning Electron Microscope Imaging (Z020026). This Project was supported by State Key Laboratory of Geomechanics and Geotechnical engineering.

Conflict of interest

The authors declare that the research was conducted in the absence of any commercial or financial relationships that could be construed as a potential conflict of interest.

Publisher's note

All claims expressed in this article are solely those of the authors and do not necessarily represent those of their affiliated organizations, or those of the publisher, the editors and the reviewers. Any product that may be evaluated in this article, or claim that may be made by its manufacturer, is not guaranteed or endorsed by the publisher.

Supplementary material

The Supplementary Material for this article can be found online at: https://www.frontiersin.org/articles/10.3389/fenrg.2023.1333137/full#supplementary-material

References

Baghaie, A., Tafti, A. P., Owen, H. A., D'Souza, R. M., and Yu, Z. (2017). SD-SEM: sparse-dense correspondence for 3D reconstruction of microscopic samples. *MICRON* 97, 41–55. doi:10.1016/j.micron.2017.03.009

Basri, R., Jacobs, D. W., and Kemelmacher, I. (2007). Photometric stereo with general, unknown lighting. *Int. J. Comput. Vis.* 72 (3), 239–257. doi:10.1007/s11263-006-8815-7

Bian, W. G. (2020). *3D imaging of dual secondary electron detectors in SEM*. Suzhou: University of Suzhou of China, 43–56.

Ding, W., Zhang, Y., Lu, H., Wan, W., and Shen, Y. (2019). Automatic 3D reconstruction of SEM images based on Nano-robotic manipulation and epipolar plane images. *ULTRAMICROSCOPY* 200, 149–159. doi:10.1016/j.ultramic.2019.02.014

Eulitz, M., and Reiss, G. (2015). 3D reconstruction of SEM images by use of optical photogrammetry software. *J. Struct. Biol.* 191 (2), 190–196. doi:10.1016/j.jsb.2015.06.010

Goldman, D. B., Curless, B., Hertzmann, A., and Seitz, S. M. (2010). Shape and spatially-varying brdfs from photometric stereo. *IEEE Trans. Pattern Analysis Mach. Intell.* 32 (6), 1060–1071. doi:10.1109/tpami.2009.102

Huang, L., Dontsov, E., Fu, H., Lei, Y., Weng, D., and Zhang, F. (2022). Hydraulic fracture height growth in layered rocks: perspective from DEM simulation of different propagation regimes. *Int. J. Solids Struct.* 238, 111395. doi:10.1016/j.ijsolstr.2021.111395

Huang, L., He, R., Yang, Z., Tan, P., Chen, W., Li, X., et al. (2023b). Exploring hydraulic fracture behavior in glutenite formation with strong heterogeneity and variable lithology based on DEM simulation. *Eng. Fract. Mech.* 2023, 278, 109020.

Huang, L., Liu, J., Zhang, F., Fu, H., Zhu, H., and Damjanac, B. (2020). 3D lattice modeling of hydraulic fracture initiation and near-wellbore propagation for different perforation models. *J. Pet. Sci. Eng.* 191, 107169. doi:10.1016/j.petrol.2020.107169

Huang, L., Tan, J., Fu, H., Liu, J., Chen, X., Liao, X., et al. (2023a). The non-plane initiation and propagation mechanism of multiple hydraulic fractures in tight reservoirs considering stress shadow effects. *Eng. Fract. Mech.* 292, 109570. doi:10.1016/j.engfracmech.2023.109570

Ikeuchi, K. (1981). Determining surface orientations of specular surfaces by using the photometric stereo method. *IEEE Trans. Pattern Analysis Mach. Intell.* 3 (6), 661–669. doi:10.1109/tpami.1981.4767167

Ji, Y., Wang, J., and Huang, L. (2015). Analysis on inflowing of the injecting Water in faulted formation. *Adv. Mech. Eng.* 7, 1–10. doi:10.1177/1687814015590294

Kareiva, S., Selskis, A., Ivanauskas, F., Šakirzanovas, S., and Kareiva, A. (2015). Scanning electron microscopy: extrapolation of 3D data from SEM micrographs. *MATER SCI-MEDZG* 21 (4), 640–646. doi:10.5755/j01.ms.21.4.11101

Li, M., Deng, S., Yan, P., et al. (2016). Research on the toughening mechanism of fiber/Whisker on oil well cement stone. *J. Southwest Petroleum Univ. Sci. Technol. Ed.* 38 (05), 151–156.

Liu, Q., Li, J., Liang, B., et al. (2023). Complex wettability behavior triggering mechanism on imbibition: a model construction and comparative study based on analysis at multiple scales. *Energy*, 275, 127434. doi:10.1016/j.energy.2023.127434

Liu, X. J. (2018). *Visual computing based micro-nano scale 3D SEM topography measurement*. Wuhan: Huazhong University of Science and Technology of China, 77–81.

Luo, H., Xie, J., Huang, L., Wu, J., Shi, X., Bai, Y., et al. (2022). Multiscale sensitivity analysis of hydraulic fracturing parameters based on dimensionless analysis method. *Lithosphere* 2022, 9708300. doi:10.2113/2022/9708300

Munawar, M. J., Lin, C., Chunmei, D., Zhang, X., Zhao, H., Xiao, S., et al. (2018a). Architecture and reservoir quality of low-permeable Eocene lacustrine turbidite sandstone from the Dongying Depression, East China. *Open Geosci.* 10 (1), 87–112. doi:10.1515/geo-2018-0008

Munawar, M. J., Lin, C., Cnudde, V., Bultreys, T., Chunmei, D., Zhang, X., et al. (2018b). Petrographic characterization to build an accurate rock model using micro-CT: case study on low-permeable to tight turbidite sandstone from Eocene Shahejie Formation. *Micron* 109, 22–33. doi:10.1016/j.micron.2018.02.010

Munawar, M. J., Vega, S., Lin, C., Alsuwaidi, M., Ahsan, N., and Bhakta, R. R. (2021). Upscaling reservoir rock porosity by fractal dimension using three-dimensional micro-computed tomography and two-dimensional scanning electron microscope images. *J. Energy Resour. Technol.* 2021 (1), 143. doi:10.1115/1.4047589

Rehman, W. (2018). *3D SEM surface reconstruction from multi-view images*. Wisconsin: University of Wisconsin-Milwaukee of America. https://dc.uwm.edu/etd/1908.

Reimer, L. (1985). Scanning electron microscopy:physics of image formation and microanalysis. *Opt. Acta Int. J. Opt.* 31 (8), 848. doi:10.1080/713821585

Samak, D., Fischer, A., and Rittel, D. (2007). 3D reconstruction and visualization of microstructure surfaces from 2D images. *CIRP Ann. - Manuf. Technol.* 56 (1), 149–152. doi:10.1016/j.cirp.2007.05.036

Song, R., Liu, J., and Cui, M. (2017). A new method to reconstruct structured mesh model from micro-computed tomography images of porous media and its application. *Int. J. Heat Mass Transf.* 109, 705–715. doi:10.1016/j.ijheatmasstransfer.2017.02.053

Song, R., Wang, Y., Ishutov, S., Zambrano-Narvaez, G., Hodder, K. J., Chalaturnyk, R. J., et al. (2020). A comprehensive experimental study on mechanical behavior, microstructure and transport properties of 3D-printed rock analogs. *Rock Mech. Rock Eng.* 53, 5745–5765. doi:10.1007/s00603-020-02239-4

Sutton, M. A., Li, N., Garcia, D., Cornille, N., Orteu, J. J., McNeill, S. R., et al. (2007). Scanning electron microscopy for quantitative small and large deformation measurements Part II: experimental validation for magnifications from 200 to 10,000. *Exp. Mech.* 47 (6), 789–804. doi:10.1007/s11340-007-9041-0

Tafti, A. P., Holz, J. D., Baghaie, A., Owen, H. A., He, M. M., and Yu, Z. (2016). 3DSEM++: adaptive and intelligent 3D SEM surface reconstruction. *MICRON* 87, 33–45. doi:10.1016/j.micron.2016.05.004

Tafti, A. P., Kirkpatrick, A. B., Alavi, Z., Owen, H. A., and Yu, Z. (2015). Recent advances in 3D SEM surface reconstruction. *MICRON* 78, 54–66. doi:10.1016/j.micron.2015.07.005

Tan, P., Fu, S. H., Chen, Z. W., and Zhao, Q. (2023). Experimental investigation on fracture growth for integrated hydraulic fracturing in multiple gas bearing formations. *Geoenergy Sci. Eng.* 2023, 212316. doi:10.1016/j.geoen.2023.212316

Tan, P., Pang, H., Zhang, R., Jin, Y., Zhou, Y., Kao, J., et al. (2020). Experimental investigation into hydraulic fracture geometry and proppant migration characteristics for southeastern Sichuan deep shale reservoirs. *J. Pet. Sci. Eng.* 184, 106517. doi:10.1016/j.petrol.2019.106517

Wang, Q., Zhu, F., Sun, M., et al. (2013). Three-dimensional reconstruction techniques based on one single SEM image. *Nami Jishu yu Jingmi Gongcheng/Nanotechnology Precis. Eng.* 11 (6), 541–545.

Wang, X. Q., Jin, X., Li, J. M., et al. (2019). FIB-SEM applications in petroleum geology research. *J. Chin. Electron Microsc. Soc.* 38 (3), 303–319. doi:10.3969/j.issn.1000-6281.2019.03.015

Wu, M., Jiang, C., Song, R., et al. (2023). Comparative study on hydraulic fracturing using different discrete fracture network modeling: insight from homogeneous to heterogeneity reservoirs. *Eng. Fract. Mech.*, 284, 109274. doi:10.1016/j.engfracmech.2023.109274

Yao, S. X., Cheng, H. R., Xiong, Z., et al. (2022). Method characterizing shale oil reservoirs in Jimsar based on quantitative digital analysis of cuttings. *OIL Drill. Prod. Technol.* 44 (01), 117–122.

Yi, J., Ma, S. J., Zhong, K., et al. (2019). A locally efficient 3D measurement method under SEM. *Transducer Microsyst. Technol.* 38 (11), 133–135.

Zhang, C. M., Guo, X. Y., and Cheng, X. W. (2013). Study on the interface characteristics of N80 steels and silica matrix coatings and well cement. *J. Southwest Petroleum Univ. Sci. Technol. Ed.* 35 (01), 144–149. doi:10.3863/j.issn.1674-5086.2013.01.022

Zhang, Z. Y. (1996). *A new multistage approach to motion and structure estimation: from essential parameters to euclidean motion via fundamental matrix*. France: INRIA Sophia-Antipolist.

Zhu, Z. B. (2013). *Fractal features research on the microscopic pore structure of petroleum reservoir rocks*. Heilongjiang: Northeast Petroleum University of China, 11–18.

frontiers | Frontiers in Energy Research

TYPE Original Research
PUBLISHED 19 January 2024
DOI 10.3389/fenrg.2024.1333686

Check for updates

OPEN ACCESS

EDITED BY
Xiaojin Zheng,
Princeton University, United States

REVIEWED BY
Jianwei Cheng,
China University of Mining and Technology, China
Shixiang Tian,
Guizhou University, China

*CORRESPONDENCE
Yunpei Liang,
liangyunpei@126.com
Wanjie Sun,
sunwanjie@outlook.com

RECEIVED 05 November 2023
ACCEPTED 04 January 2024
PUBLISHED 19 January 2024

CITATION
Liang Y, Sun W, Wu Z, Mao S and Ran Q (2024), Effect of disturbed coal pore structure on gas adsorption characteristics: mercury intrusion porosimetry.
Front. Energy Res. 12:1333686.
doi: 10.3389/fenrg.2024.1333686

COPYRIGHT
© 2024 Liang, Sun, Wu, Mao and Ran. This is an open-access article distributed under the terms of the Creative Commons Attribution License (CC BY). The use, distribution or reproduction in other forums is permitted, provided the original author(s) and the copyright owner(s) are credited and that the original publication in this journal is cited, in accordance with accepted academic practice. No use, distribution or reproduction is permitted which does not comply with these terms.

Effect of disturbed coal pore structure on gas adsorption characteristics: mercury intrusion porosimetry

Yunpei Liang[1,2]*, Wanjie Sun[1,2]*, Zhaopeng Wu[1,2], Shuren Mao[1,2] and Qican Ran[1,2]

[1]State Key Laboratory of Coal Mine Disaster Dynamics and Control, Chongqing University, Chongqing, China, [2]School of Resources and Safety Engineering, Chongqing University, Chongqing, China

Studying pore structures of disturbed coal and their influences on adsorption characteristics is conducive to in-depth understanding of occurrence and migration of gas in reservoirs in areas prone to coal and gas outbursts. A mercury porosimeter and a high-pressure gas adsorption instrument were separately used to investigate pore structures and measure adsorption characteristics of disturbed coal and undisturbed coal in Ningtiaota Coal Mine and Xigu Coal Mine (Shaanxi Province, China). In addition, pore structures and gas adsorption characteristics of coal samples were studied. The Menger's sponge model was adopted to calculate fractal dimensions of coal samples, to estimate influences of pore structures and fractal features on the gas adsorption characteristics of disturbed and undisturbed coal. Results show that the pore volume of undisturbed coal is mainly contributed by micropores and transitional pores, while that of disturbed coal arises mainly from macropores and mesopores. Micropores and transitional pores account for large proportions of the specific surface area of pores in both disturbed and undisturbed coal. The adsorption isotherms of disturbed and undisturbed coal conform to the Langmuir equation and tectonism increases the limiting adsorption quantity of coal. The fractal dimensions D_1 of the four types of coal samples in the experiments are in the range of 2.7617–2.9961, while the fractal dimensions D_1 and D_2 of disturbed coal are both larger than those of undisturbed coal, indicating that disturbed coal is more likely to collapse under high pressure. The total pore volume, total specific surface area of pores, and fractal dimensions are positively correlated with the adsorption constant *a*, while they have U-shaped correlations with the adsorption constant *b* of coal samples. The adsorption constant *a* of disturbed coal is always greater than that of undisturbed coal, while no obvious trend is observed between the adsorption constant *b* and tectonism. The research results can provide theoretical basis for further study of gas occurrence in disturbed coal seams.

KEYWORDS

disturbed coal, coalbed methane, pore structures, mercury intrusion porosimetry, adsorption characteristics

1 Introduction

Coal reservoirs in China mainly occur at depth; because the geological and coal mining conditions are characterized by high crustal stress, high geothermal temperature, high gas content, and low permeability, gas accidents such as coal and gas outbursts occur frequently (Lu et al., 2015; Wang and Du, 2020; Zhao et al., 2023a; Zou et al., 2023a). The development of gas accidents is generally related to the complex geological structures of reservoirs, which directly or indirectly affect the burial depth, gas occurrence, and gas permeability of surrounding rocks of coal seams (Huang et a.,2023; Tan et al., 2021; Zhao et al., 2023b; Zou et al., 2023b). In fact, the majority of gas accidents happen in the deformation zone of geological structures, and geological structures are important in controlling such outbursts (Zhai et al., 2016; Zhang et al., 2020; Tan et al., 2023). A soft structural coal belt with a certain thickness is generally developed in areas prone to outbursts. After the long geotectonic evolution, the primary structures of coal experience different extents of embrittlement, fracture, deformation, and superimposed damage, and the resulting coal is porous, has a low strength and low permeability (Hou et al., 2012; Ran, Liang, Zou, and Hong et al., 2023; An and Cheng, 2014; Ye et al., 2023). The pore structure characteristics of such coal have become one of the important foci of research into techniques for the control of gas disasters in coal mines (Ran, Liang, Zou, and Zhang et al., 2023; Wang et al., 2019; Xu et al., 2019).

In recent years, numerous researchers have investigated the mechanism of formation (Jiang et al., 2010; Cao et al., 2020), reservoir property (Pan et al., 2012; Dong et al., 2018), pore structure (Li et al., 2015), and adsorption characteristic (Li et al., 2019; Sun et al., 2021; Yang et al., 2021) of disturbed coal. Based on mercury intrusion porosimetry, Qu et al. (2010) compared and studied the pore structures and compressibility of different types of disturbed coal and found that tectonism mainly increases the volume of pores with a diameter exceeding 100 nm. In addition, the more intense the tectonism, the larger the number of open pores and the stronger the connectivity of pore networks. The compressibility reduces with the increasing intensity of tectonism. The differences in porosity and pore compressibility are influenced by tectonism to a significant extent. Dong et al. (2020) calculated pore tortuosity of disturbed coal under different pressures. They found that the pore tortuosity increases with increasing pressure and the pore tortuosity of disturbed coal is always higher than that of undisturbed coal. Wang et al. confirmed that the gas adsorption capacity of disturbed coal is positively correlated with the metamorphic grade of the coal, and therefore believed that the extent of development of pore structures plays an important role. Zhao et al. (2020) studied the influences of the mass ratio of disturbed coal on the amount of gas adsorption of coal and the initial speed of gas diffusion and stated that the gas adsorption increases with the increasing proportion (by mass) of disturbed coal. During gas adsorption, the hardness (Sun et al., 2020; Ullah et al., 2022), structural classification (Li et al., 2015; Wang et al., 2020), metamorphic grade (Meng and Li, 2018; Ren et al., 2022), and water content (Liu et al., 2022) of coal all exert different influences on the gas adsorption.

Existing research approaches for pore structures in coal mainly include mercury intrusion porosimetry (Okolo et al., 2015; Yu et al., 2018), magnetic resonance imaging (Zhao et al., 2017), scanning electron microscopy (Kutchko et al., 2013), N_2/CO_2 adsorption (Nie et al., 2015; Chu et al., 2024), and transmission electron microscopy (Lee et al., 2006). Agbabiaka et al. (2013) studied the fractal features of spherical pores using scanning electron microscopy and a small-angle X-ray scattering method. Jia et al. (2022) and Lin et al. (2020) explored the porosity and pore size of coal at different metamorphic grades by conducting mercury injection and low-temperature liquid nitrogen adsorption experiments. By using scanning electron microscopy and low-pressure N_2/CO_2 adsorption, Mangi et al. (2020) systematically evaluated influences of pore size distribution and fractal dimension on gas adsorption and desorption quantities. Wang et al. (2021) conducted low-temperature liquid nitrogen adsorption experiments to explore adsorption characteristics of micropores in coal at low temperature and low pressure. In the study of coal pore structure, fractal dimension can represent the complexity or roughness of coal pore structure, so as to effectively represent pore characteristics. There are many calculation methods for fractal dimension, includes Menger (Fu et al., 2005; Zhao et al., 2023), Frenkel-Halsey-Hill (Yao et al., 2008; Huang L. K. et al., 2023; Huang L. et al., 2023), BET (Dormant and Adamson, 1972; Lin et al., 2023) and Langmuir (Rigby, 2005; Ji et al., 2023) fractal models, *etc.* Previous research results play a positive role in understanding pore structure characteristics of disturbed coal and studying the gas adsorption characteristics thereof; however, due to the complexity of disturbed coal, research into the influences of pore structures in disturbed coal on gas adsorption should be studied further. The pore structure in coal is an important index representing gas adsorption capacity and rate. Due to the low Protodyakonov coefficient, high initial speed of gas diffusion, and low permeability, disturbed coal seams are found to exhibit complex gas emission behaviors in the mining process and therefore are difficult to treat. Hence, it is necessary to study the difference of disturbed coal and undisturbed coal in pore structures and their influences on the gas adsorption characteristics. Disturbed coal and undisturbed coal in Ningtiaota Coal Mine and Xigu Coal Mine in Shaanxi Province, China were selected, for which mercury injection experiments and gas adsorption experiments were conducted to test microstructures of pores and gas adsorption characteristics. The microstructural characteristics of disturbed coal and their influences on gas adsorption characteristics were studied, to provide a theoretical basis for in-depth research on gas occurrence in disturbed coal seams.

2 Experimental instruments and methods

2.1 Sampling locations and basic parameters

Coal samples used in the experiments were separately obtained from the tectonic regions (faults) and non-tectonic regions of Ningtiaota Coal Mine and Xigu Coal Mine in Shaanxi Province, located in Ordos Basin and the folded zone on its margin. The sampling locations are shown in Figure 1. The disturbed coal is obtained near the structural zone by coring long drilling holes, and the undisturbed coa as a contrast is obtained



FIGURE 1
Sampling locations.

TABLE 1 Industrial analysis results of coal samples.

Sample	M_{ad}/wt%	A_d/wt%	V_{ad}/wt%	FC_{ad}/wt%	f
NT01	2.63	17.19	10.28	69.90	1.62
NT02	2.19	24.38	11.73	61.70	0.35
XG01	0.44	19.06	14.86	65.79	0.68
XG02	0.32	18.10	15.57	66.12	0.28

Notes: M_{ad}, moisture, air-drying basis; A_{ad}, ash yield, air-drying basis; V_{ad}, volatile, air-drying basis; FC_{ad}, fixed carbon content, air-drying basis; f, firmness coefficient.

from the intact coal wall without structure. The coal samples were drilled, then sealed, and taken to the laboratory. The undisturbed coal in Ningtiaota Coal Mine, disturbed coal in Ningtiaota Coal Mine, undisturbed coal in Xigu Coal Mine, and disturbed coal in Xigu Coal Mine were separately labelled NT01, NT02, XG01, and XG02.

Basic industrial parameters of coal samples were tested using a coal quality industrial analyzer (Table 1). The two types of coal samples both belonged to bitumite at a low metamorphic grade and contained a low water content (0.32%–2.63%). The firmness coefficient of the coal samples was tested. The firmness coefficients f of the two types of disturbed coal are obviously lower (by 78.39% and 26.82%) compared with those of the undisturbed coal, which indicates that coal subjected to tectonism softened, became more prone to fracture, and its strength decreased.

2.2 Pore tests

An Auto Pore IV 9510 mercury porosimeter was adopted to perform mercury injection experiments (Figure 2). The high pressure mercury intrusion porosimetry method is the most commonly used method to test the pore structure of coal and shale at present. This method mainly relies on the intrusion of mercury into the pores of coal body under high pressure. The pore diameter, pore specific surface area and porosity of coal body can be calculated by the curve of mercury content as the pressure changes. The range of test pressure and the measurement range of pore size of the instrument were 0–413 MPa and 3 nm to 370 μm, respectively. Coal specimens with particle sizes ranging from 2.8 to 4 mm were selected. After vacuum-drying in an oven at 80°C for 8 h, a coal sample of 5 g was placed in a dilatometer, which was then sealed and put in the low and high-pressure chambers successively to conduct

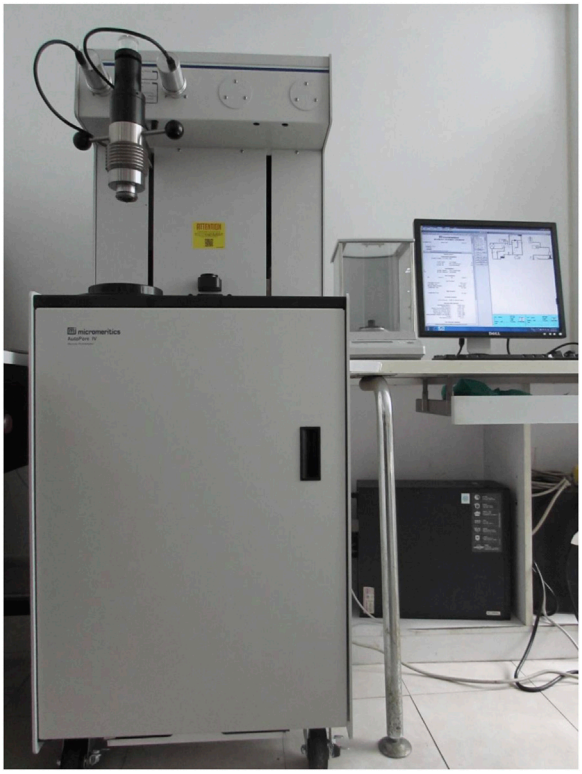


FIGURE 2
Auto Pore IV 9510 mercury porosimeter.

mercury injection experiments. The surface tension of mercury, contact angle of mercury with the sample, and density of the mercury were separately 0.485 N/m, 130°, and 13.5335 g/cm^3.

2.3 Adsorption tests

A self-built automatic high-pressure gas adsorption instrument was used to conduct methane adsorption experiments on coal. The test pressure and the highest test temperature of the instrument were separately 0–20 MPa and 200°C. With high precision, the instrument was able to monitor subtle changes in the adsorption achieved in the initial stage of adsorption (Figure 3). Four types of pulverized coal of 6–7 g with the particle size ranging from 0.18 to 0.25 mm could be prepared. Before experiments, the pulverized coal was degassed under vacuum for 6 h. Thereafter, isothermal adsorption experiments for methane were conducted under an initial adsorption pressure of 5 MPa and a temperature of 30°C, ambient temperature of (25 ± 2) °C, and relative humidity of 30%.

3 Test results and analysis

3.1 Mercury injection and ejection curves

Many experiments on the microstructure of coal reveal that the mercury injection and ejection curves of the coal samples are not overlapped but exhibit a certain hysteresis. The coal samples tested also exhibit differences in pore structure characteristics,

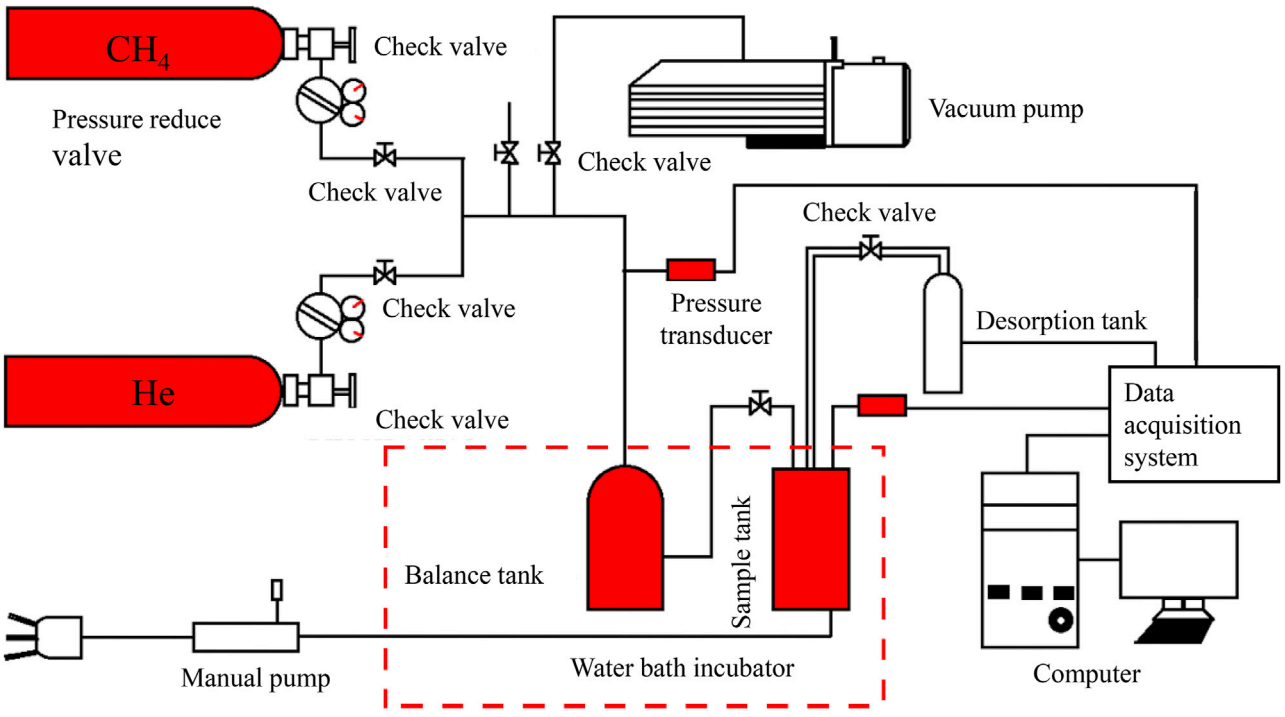


FIGURE 3
High-pressure gas adsorption instrument.

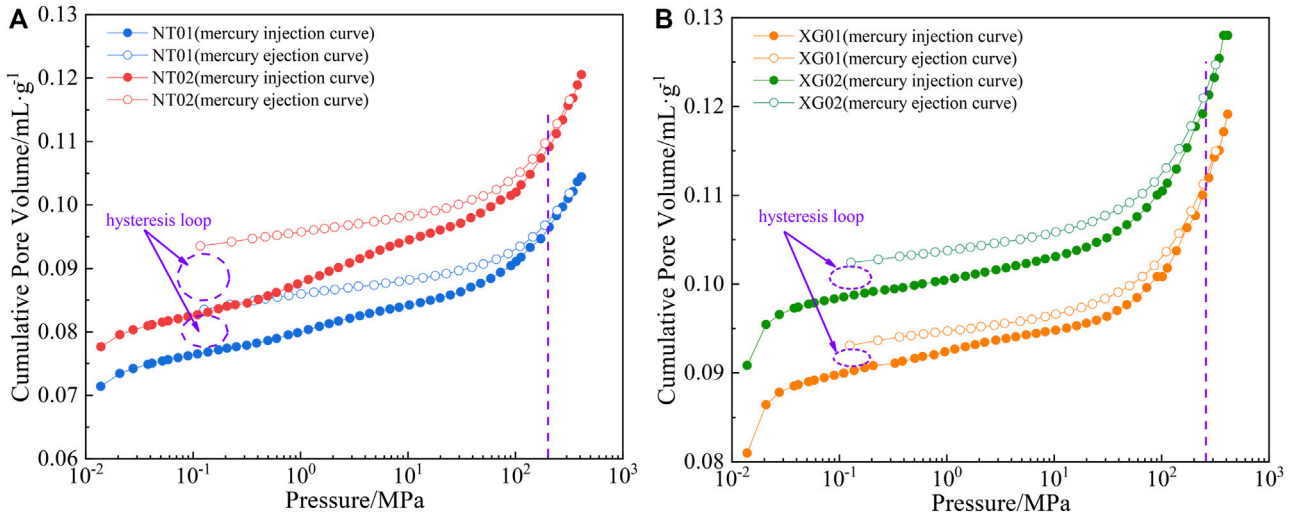


FIGURE 4
Mercury injection and ejection curves of coal samples. **(A)** NT01 and NT02; **(B)** XG01 and XG02.

therefore, the morphological characteristics of pores are commonly analyzed according to hysteresis loops of mercury injection and ejection curves.

According to mercury injection experimental data, mercury injection and ejection curves of each coal sample were drawn, as shown in Figure 4.

The mercury injection curves of coal samples NT01 and NT02 ascend in an inverted S-shape in the low-pressure mercury injection stage, while linearly descend in main sections of the high-pressure mercury ejection stage. The mercury ejection curves start from mercury withdrawal and pressure relief. The difference in pore volume at the same pressure gradually increases with decreasing pressure and the mercury ejection curves begin to depart from mercury injection curves and descend slowly when the pressure is decreased to 200–300 MPa. Under such conditions, the difference in pore volume increases significantly, indicative of a high proportion of open pores in coal samples. The mercury injection and ejection curves of coal samples XG01 and XG02 are both manifest as concave arcs. When the pressure is below 300 MPa, the hysteresis loops are enlarged, which suggests that pores in coal samples are mainly semi-closed and thin-necked, bottle-shaped pores, and there are a certain number of these present as open macropores. Disturbed coal samples taken from the same coal mine show similar forms of mercury injection and ejection curves compared with undisturbed coal, while the hysteresis loops of disturbed coal are larger than those of undisturbed coal. This indicates that pore connectivity of the coal subjected to tectonism is greatly enhanced, which increases the volume available to gas. The result suggests that gas is likely to diffuse during pressure relief in a disturbed coal seam, which explains why a large amount of gas is more likely to escape within a short time when mining disturbed coal seams from the perspective of pores. This is extremely likely to trigger coal and gas outburst accidents, so gas drainage with pressure relief should be mainly performed in the coal mining process.

3.2 Distribution characteristics of pore volume and specific surface area

When using the Mercury Intrusion Porosimetry to study pore structures, the pore classification method proposed by Hodot is generally used (Hodot, 1966). According to the pore diameter, pores can be classified into micropores (<10 nm), transitional pores (10–10^2 nm), mesopores (10^2–10^3 nm), macropores (10^3–10^5 nm), and visible holes and fractures (>10^5 nm).

The pore volume in unit mass of coal is a reference basis for gas storage capacity and extent and severity of failure therein. The distribution of pore volumes in different coal samples is shown in Table 2. The pore volume of undisturbed coal is mainly contributed by micropores and transitional pores: micropores and transitional pores separately account for 55.88% and 31.27% of the total pore volume in sample NT01, while macropores and mesopores are less well developed and separately account for 7.22% and 5.64% of the total volume. Micropores and transitional pores separately account for 34.54% and 53.27% of total pore volume in sample XG01, which also contains a small number of macropores (5.21%) and mesopores (6.98%). This indicates that undisturbed coal exhibits weak tectonic deformation and pores mainly include primary pores. The pore volume in disturbed coal is mainly contributed by macropores and mesopores. Due to brittle deformation of sample XG02, the pore structures change substantially: the volume of macropores and mesopores increases (with proportions of 35.29% and 34.58% separately) while that of micropores and transitional pores are decreased, which separately account for 15.26% and 14.88% of the total volume. Sample NT02 is deformed more than sample XG02 and the proportion of macropores (by volume) increases to a greater extent, accounting for 45.31% of the total pore volume; the proportion (by volume) of mesopores (36.84%) is similar to that in sample XG02, while the volume of micropores and transitional pores further decreases to proportions of 8.17% and 9.68%, respectively.

The distribution of pore volume of coal reveals that the total pore volume of undisturbed coal arises mainly in the form of

TABLE 2 Distribution of pore volume of coal samples.

Coal samples	Total pore volume /$cm^3 \cdot g^{-1}$	Pore volume/$cm^3 \cdot g^{-1}$				Proportion of pore volume/%			
		Macropores	Mesopores	Transitional pores	Micropores	Macropores	Mesopores	Transitional pores	Micropores
NT01	0.1045	0.0075	0.0059	0.0327	0.0584	7.22	5.63	31.27	55.88
NT02	0.1192	0.0540	0.0439	0.0115	0.0097	45.31	36.84	9.68	8.17
XG01	0.1144	0.0059	0.0080	0.0610	0.0395	5.20	6.97	53.28	34.55
XG02	0.1369	0.0483	0.0473	0.0204	0.0209	35.29	34.58	14.88	15.26

TABLE 3 Distribution of specific surface area of pores in coal samples.

Coal samples	Total specific surface area/ $cm^2 \cdot g^{-1}$	Specific surface area of pores/$cm^2 \cdot g^{-1}$				Proportion of specific surface area of pores/%			
		Macropores	Mesopores	Transitional pores	Micropores	Macropores	Mesopores	Transitional pores	Micropores
NT01	11.3462	0.0023	0.0238	1.2401	10.0799	0.02	0.21	10.93	88.84
NT02	15.3471	0.0010	0.2400	2.0219	13.0840	0.01	1.56	13.17	85.25
XG01	14.6394	0.0117	0.0176	1.6733	12.9368	0.08	0.12	11.43	88.37
XG02	15.6609	0.0016	0.0235	1.9686	13.6673	0.01	0.15	12.57	87.27

10.3389/fenrg.2024.1333686

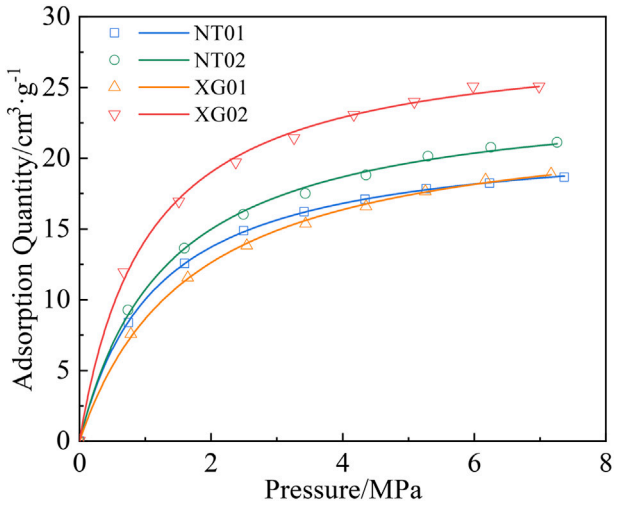


FIGURE 5
Isothermal adsorption curves of coal samples.

micropores and transitional pores, which indicates that undisturbed coal is slightly deformed and pores are mainly dominated by primary pores and a small number of metamorphic pores. In comparison, most pores in disturbed coal are macropores and mesopores. Sample NT02 is more significantly deformed than sample XG02, so the proportion of macropores increases more in sample NT02. This suggests that as the deformation of the coal increases, the proportions of macropores and mesopores also increases, especially macropores, which increase to an even greater extent. Macropores are generated along with fractures in coal, forming the principal channels for gas seepage, so the more numerous the macropores, the more permeable the coal seam.

The specific surface area of pores refers to the internal surface areas of all pores in unit mass of coal. The specific surface area of pores is influenced by the shape of pores, surface defects, and pore structures of coal, and is closely related to the degree of development of pores. The distribution of the specific surface areas of pores in various coal samples is summarized in Table 3. In terms of the total specific surface area of pores in coal samples, disturbed coal is akin to undisturbed coal: micropores and transitional pores account for large proportions by total volume. Therein, micropores account for the largest proportion of the specific surface area (88%), while the proportion of transitional pores is 12%; the proportions of specific surface areas of mesopores and macropores are relatively low, both being below 2%.

3.3 Results of adsorption experiments

Figure 5 illustrates the isothermal adsorption curves of coal samples. During low-pressure adsorption (<3 MPa), the gas adsorption by coal samples increases rapidly with increasing pressure. When the pressure exceeds 3 MPa, the adsorption quantity exhibits slow growth. The Langmuir equation (Eq. 1) (Ezzati, 2020) is used to fit the adsorption curves and the fitting results are summarized in Table 4. The degrees of fitting of adsorption curves of the four types of coal samples all exceed 0.99, which means that the adsorption curves of the four types of coal samples all conform to the Langmuir equation. Under the maximum pressure, the samples are listed in an ascending order as NT01, XG01, NT02, and XG02 according to the saturated adsorption quantities. The gas adsorption quantities of the two types of disturbed coal are both larger than those of their corresponding undisturbed coal samples.

$$Q = \frac{abP}{1 + bP} \tag{1}$$

where P represents pressure (MPa); Q denotes the adsorption quantity under pressure P (cm^3/g); a is an adsorption constant (cm^3/g); b is also an adsorption constant (MPa^{-1}).

The values of adsorption constants a and b physically represent the saturated gas adsorption quantity and adsorption rate of coal, respectively. Based on the PCT adsorption experimental data, the Langmuir equation was adopted to calculate the gas adsorption constants of each coal sample. Analysis results of isothermal adsorption experiments on coal samples were obtained (Table 4). Table 4 indicate that the adsorption constant a of the four types of coal samples is between 21.697 and 28.753. The coal samples are also listed in the same order as that according to the saturated adsorption quantities (also in ascending order) as NT01, XG01, NT02, and XG02. Samples XG02 and XG01 separately have the highest and lowest adsorption constant b, namely, 0.975 and 0.593.

4 Discussion

4.1 Fractal features of pores

The fractal dimension of pores in coal can be used as a measure of the irregularity and roughness of pore surfaces. Menger's model (Eq. 2) more suitable for mercury injection experiments was selected

TABLE 4 Measured adsorption characteristics of coal samples.

Coal samples	Adsorption constants		Fitting curves	R^2
	a	b		
NT01	21.697	0.858	$Q = 18.616P/1 + 0.858P$	0.999
NT02	24.812	0.761	$Q = 18.857P/1 + 0.761P$	0.998
XG01	23.249	0.593	$Q = 13.786P/1 + 0.593P$	0.999
XG02	28.753	0.975	$Q = 28.034P/1 + 0.975P$	0.997

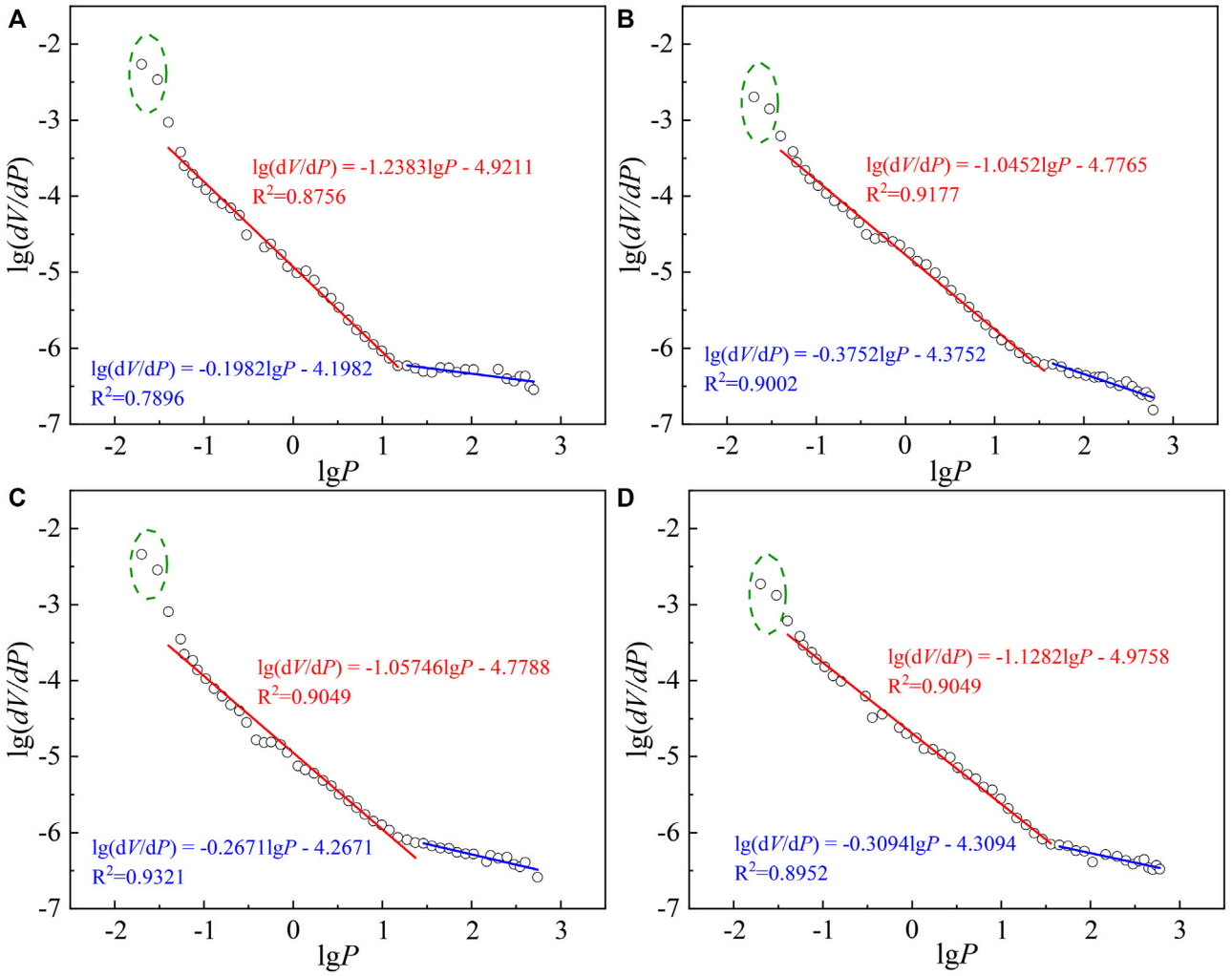


FIGURE 6
Fitted relationship between lg (d*V*/d*P*) and lg*P* of coal samples. **(A)** NT01; **(B)** NT02; **(C)** XG01; **(D)** XG02.

to analyze the experimental results (Han et al., 2020). The fractal dimension calculated following the principle of mercury injection experiments is called the volumetric fractal dimension. In the Menger, porous materials such as coal are assumed to be in the form of a regular cube, leading to:

$$\lg\left[\frac{\mathrm{d}V}{\mathrm{d}P}\right] = \mathrm{A}_2 \lg P \tag{2}$$

where V and P separately represent the mercury intake and pressure in mercury injection experiments; A_2 is the power exponent, which has a linear relationship with the fractal dimension D_2 and its value is the slope of the double logarithmic curves dV/dP and lg P; the fractal dimension is $D_2 = 4 + A_2$.

The pore volume V, applied pressure P, lg (dV/dP), and lg$P$ can be obtained according to experimental data of the four types of coal samples, and then the scatter plots are drawn, as shown in Figure 6, followed by linear fitting. The volumetric fractal dimension of pores can then be calculated according to the slope of the lines. The Fractal dimension fitting and calculation results are shown in Table 5. Combining these data with values of the fractal dimensions of coal specimens, the mercury injection experimental process of coal can be divided into three stages.

1) Pre-injection stage (green circles in Figure 6). Mercury influx first fills the space between coal particles while it does not enter the pores in the coal. The fractal dimension in the stage is generally less than 2. How obvious the stage is related to the particle size of the samples used in the experiments: the smaller the particle size the more obvious the curves in the stage. The coal samples used in the mercury injection experiments have the particle size of 2.8–4 mm, so only several points appear at the start of the curves in mercury injection experiments of the four types of coal samples in the stage, indicating that the stage is not obvious;
2) Injection stage (red fitted lines in Figure 6). Mercury influx fills the pores in the coal under the pressure applied by the instrument. The fractal dimension D_1 in the stage is between 2 and 3. This is a stage in which the fractal dimension can be most effectively and accurately calculated in mercury injection experiments. The larger the absolute

TABLE 5 Fractal dimensions of pores in coal samples.

Coal samples	Injection stage			Post-injection stage		
	Fitting equations	D_2	R^2	Fitting equations	D_3	R^2
NT01	lg (dV/dP) = −1.2383lg$P$–4.9211	2.7617	0.8756	lg (dV/dP) = −0.1982lg$P$–4.1982	3.62125	0.7896
NT02	lg (dV/dP) = −1.0452lg$P$–4.7765	2.9548	0.9177	lg (dV/dP) = −0.3752lg$P$–4.3752	3.71889	0.9002
XG01	lg (dV/dP) = −1.05746lg$P$–4.7788	2.8718	0.9049	lg (dV/dP) = −0.2671lg$P$–4.2671	3.67175	0.9321
XG02	lg (dV/dP) = −1.1282lg$P$–4.9758	2.9961	0.9049	lg (dV/dP) = −0.3094lg$P$–4.3094	3.69491	0.8952

value of the curve slope in the stage, the greater the corresponding volumetric fractal dimension and the more complex the pore structures present in the coal;

3) Post-injection stage (blue fitted lines in Figure 6). In the stage, the increase in the mercury intake is not only because mercury is filled in pores in coal, but also due to the compression effect of mercury on coal. The curves in the stage have a small slope and the calculated fractal dimension D_2 is generally larger than 3. Coal is a porous medium. Due to the compressibility of the coal matrix, when the mercury injection pressure is large, the pore structure of the coal body will be destroyed and collapsed, resulting in the fractal dimension of the high pressure section being greater than 3, and the pore measurement results also have greater errors. The larger the fractal dimension is in the stage, the more easily the coal used in the experiments is compressed. Therefore, the value of the fractal dimension in the stage can be employed to qualitatively describe the compressibility of coal. Among the four types of coal samples selected in the research, sample XG02 has the largest fractal dimension (3.71889), indicating that sample XG02 is most easily compressed.

Therefore, D_1 calculated in the injection stage is adopted as the volumetric fractal dimension to characterize the complexity of pores in coal. The fractal dimension D_2 of experimental coal samples is in the range of 2.7617–2.9961, very approximate to 3, suggesting high complexity of pores in the four types of coal. The fractal dimensions D_1 and D_2 of the two types of disturbed coal are both larger than those of the undisturbed coal. This finding implies that the complexity of pores in the coal subjected to tectonism is increased and the compressibility of pores is also enhanced, so that the coal is more likely to collapse under high pressure.

4.2 Influences of pore structure on adsorption constants

Pores in coal are places for adsorption and free flow of gas. Pore characteristics exert important influences on the gas adsorption and desorption properties of coal. The relationships between pore parameters and adsorption constants (a and b) of undisturbed coal and disturbed coal were estimated. The relationships between total pore volume and adsorption constants are shown in Figure 7; the relationships between the total specific surface area of pores and adsorption constants are illustrated in Figure 8; the relationships between fractal dimensions and adsorption constants are displayed in Figure 9.

Disturbed coal contains highly developed pores. The tectonic stress enhances the pore connectivity and improves the gas adsorption capacity of coal. The void content in coal affects the gas adsorption capacity of coal. As shown in Figure 8A, Figure 9A, the total pore volume and total specific surface area of pores are positively correlated with the adsorption constant a, and the adsorption constant a reflects the maximum amount of gas that can be adsorbed by the coal. The increase in the void content means that coal has a larger potential area over which adsorption can occur and more adsorption sites, so the total amount of gas that can be adsorbed by coal samples with a larger void content also increases. The adsorption constant a of disturbed coal is always greater than that of undisturbed coal, which indicates that tectonism enlarges the volume available to gas storage in disturbed coal specimens.

Figure 8B, Figure 9B show that the total pore volume and total specific surface area of pores of coal have U-shaped correlations with the adsorption constant b of the coal. The adsorption constant b is the pressure under which the coal samples reach the maximum adsorption (by volume). The lack of any significant linear trend in these parameters may arise because of the uncertain changes in pore morphologies due to tectonism. The adsorption constant b is not only related to the void content but also to the pore connectivity.

As illustrated in Figure 9A, the fractal dimensions of coal show strong positive correlations with the adsorption constant a of coal. Compared with undisturbed coal, disturbed coal is found to have a larger fractal dimension of pores, rough internal surfaces, and many pores, so the volume available to gas adsorption is larger and the adsorption thus enhanced. The result indicates that coal samples with different fractal dimensions differ in their gas adsorption capacity. Within a certain range, the larger the volumetric fractal dimension, the stronger the gas adsorption capacity of coal. Figure 9B shows that the fractal dimension of coal has a U-shaped relationship with the adsorption constant b of coal.

5 Conclusion

The pore structures were analyzed and the gas adsorption characteristics were measured for disturbed coal and undisturbed coal in Ningtiaota Coal Mine and Xigu Coal Mine. The pore structure and gas adsorption characteristics of coal samples were investigated, and the Menger sponge model was used to calculate the fractal dimensions of coal. Moreover, influences of pore structures and fractal features on gas adsorption characteristics of disturbed

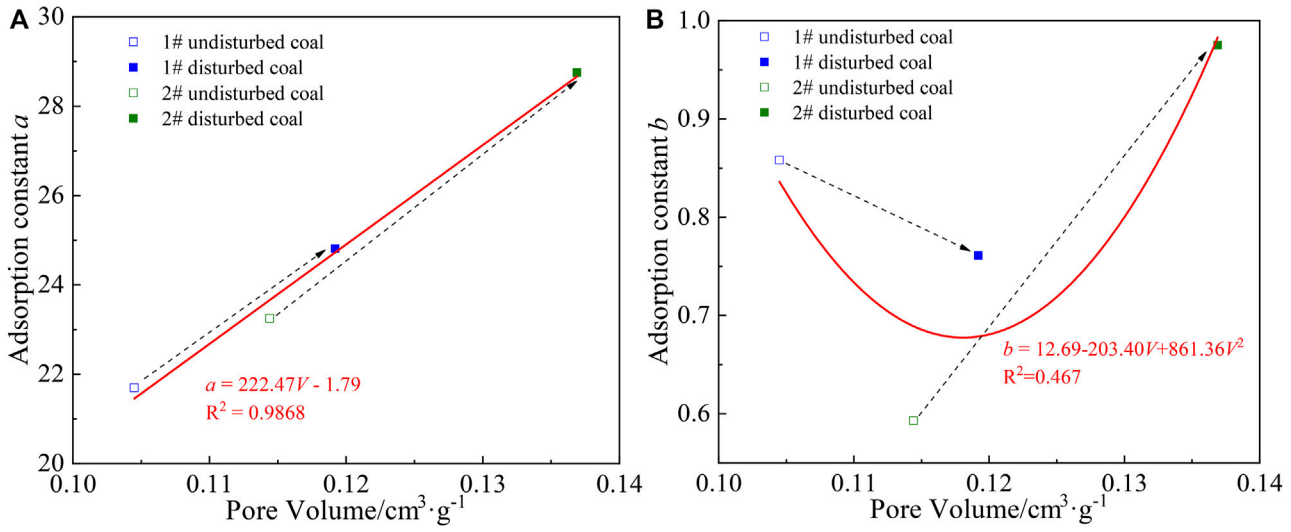


FIGURE 7
Relationships between the total pore volume and adsorption constants. **(A)** Adsorption constant *a*; **(B)** Adsorption constant *b*.

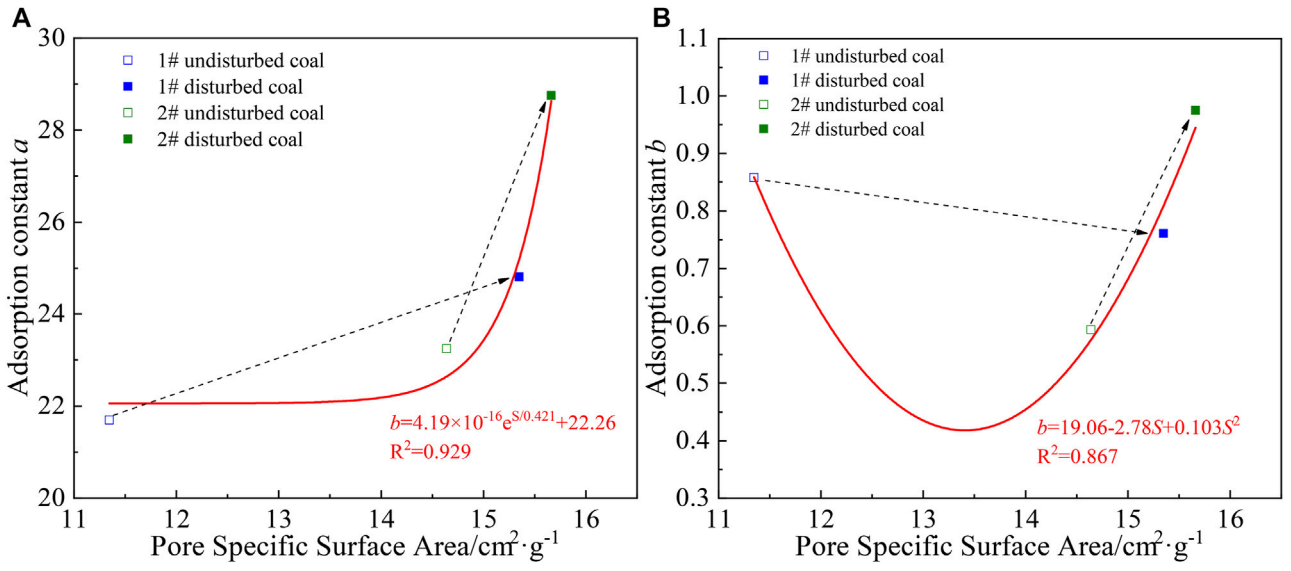


FIGURE 8
Relationships between the total specific surface area of pores and adsorption constants. **(A)** Adsorption constant *a*; **(B)** Adsorption constant *b*.

coal and undisturbed coal were investigated. The results showed that.

1) Mercury intrusion porosimetry was utilized to measure the pore structure characteristics of coal samples. The pore volume of undisturbed coal arises mainly in the forms of micropores and transitional pores, while that of disturbed coal is mainly accounted for by macropores and mesopores. Micropores and transitional pores account for high proportions in specific surface areas of both disturbed coal and undisturbed coal. The results suggest that undisturbed coal is slightly deformed, and pores are dominated by primary pores and a small number of metamorphic pores. After being subjected to structural deformation, the contents of macropores and mesopores increased (especially for macropores, which increase to an even greater extent);
2) The adsorption isotherms of disturbed coal and undisturbed coal conform to the Langmuir equation. The tectonism enhances the limit adsorption quantity of coal by increasing the void content and strengthening the pore connectivity in coal;
3) The mercury injection testing can be divided into the pre-injection, injection, and post-injection stages. The fractal phenomenon is not apparent in the pre-injection stage. The

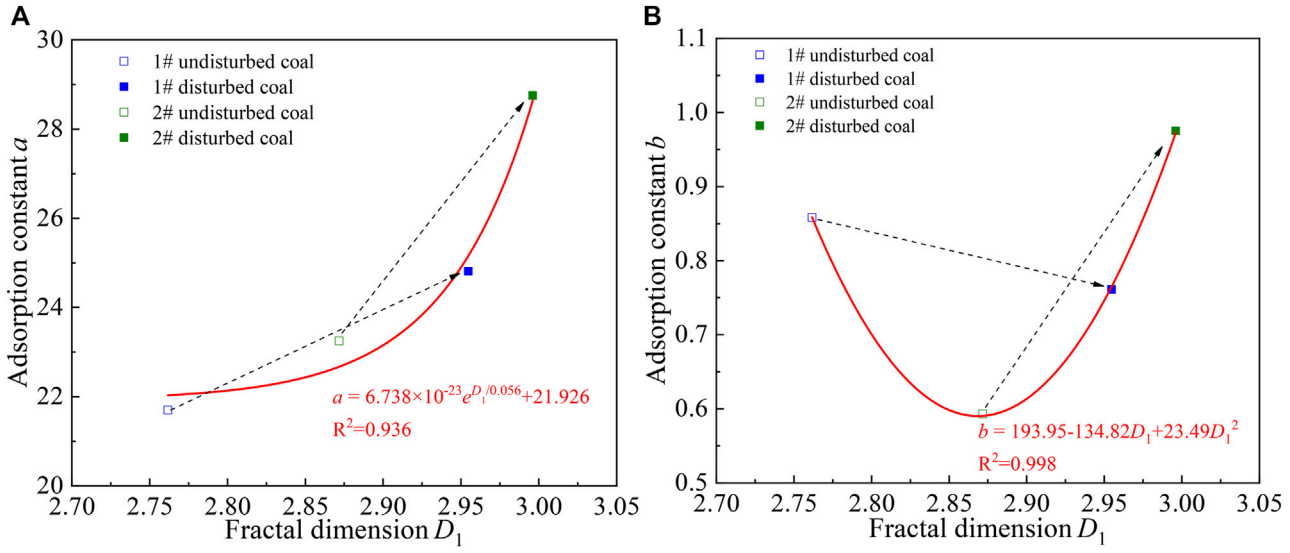


FIGURE 9
Relationships between the fractal dimensions and adsorption constants. **(A)** Adsorption constant *a*; **(B)** Adsorption constant *b*.

fractal dimensions D_1 of the four types of experimental coal samples calculated in the injection stage range between 2.7617 and 2.9961. The fractal dimension calculated in the post-injection stage is always greater than 3. The fractal dimensions D_1 and D_2 of disturbed coal are both greater than those of undisturbed coal. Pores in disturbed coal are more likely to collapse under high pressure;

4) The total pore volume, total specific surface area of pores, and fractal dimensions have positive correlations with the adsorption constant *a* and U-shaped correlations with the adsorption constant *b* of coal. The adsorption constant *a* of disturbed coal is always greater than that of undisturbed coal. This is because the increasing void content due to tectonism means that the coal has a larger potential area over which adsorption can occur and more numerous adsorption sites. As a result, the total gas content that can be adsorbed by disturbed coal also increases and at the same time, the adsorption constant *a* characterizing the adsorption capacity of coal also increases. The adsorption constant *b* exhibits no clear trend with tectonism, perhaps because changes in pore morphologies due to tectonism are also uncertain.

Data availability statement

The original contributions presented in the study are included in the article/Supplementary Material, further inquiries can be directed to the corresponding authors.

Author contributions

YL: Conceptualization, Writing–original draft, Writing–review and editing. WS: Conceptualization, Writing–original draft, Writing–review and editing. ZW: Conceptualization, Writing–original draft. SM: Writing–original draft. QR: Writing–original draft.

Funding

The author(s) declare financial support was received for the research, authorship, and/or publication of this article. This research was financially supported by the National Key R&D Program of China (Grant No. 2022YFC3004704) and the National Natural Science Foundation of China (Grant No. 52174166), which are gratefully acknowledged.

Conflict of interest

The authors declare that the research was conducted in the absence of any commercial or financial relationships that could be construed as a potential conflict of interest.

Publisher's note

All claims expressed in this article are solely those of the authors and do not necessarily represent those of their affiliated organizations, or those of the publisher, the editors and the reviewers. Any product that may be evaluated in this article, or claim that may be made by its manufacturer, is not guaranteed or endorsed by the publisher.

Supplementary material

The Supplementary Material for this article can be found online at: https://www.frontiersin.org/articles/10.3389/fenrg.2024.1333686/full#supplementary-material

References

Agbabiaka, A., Wiltfong, M., and Park, C. (2013). Small angle X-ray scattering technique for the particle size distribution of nonporous nanoparticles. *J. Nanoparticles* 2013, 1–11. doi:10.1155/2013/640436

An, F. H., and Cheng, Y. P. (2014). An explanation of large-scale coal and gas outbursts in underground coal mines: the effect of low-permeability zones on abnormally abundant gas. *Nat. Hazards Earth Syst. Sci.* 14 (8), 2125–2132. doi:10.5194/nhess-14-2125-2014

Cao, D., Wang, A., Ning, S., Li, H., Guo, A., Chen, L., et al. (2020). Coalfield structure and structural controls on coal in China. *Int. J. Coal Sci. Technol.* 7 (2), 220–239. doi:10.1007/s40789-020-00326-z

Chu, P., Xie, H. P., Gao, M. Z., Li, C. B., Shang, D. L., Liu, Q. Q., et al. (2024). Influence of desorption hysteresis effects on coalbed methane migration and production based on dual-porosity medium model incorporating hysteresis pressure. *Comput. Geotechnics* 165, 105893. doi:10.1016/j.compgeo.2023.105893

Dong, J., Cheng, Y., Hu, B., Hao, C., Tu, Q., and Liu, Z. (2018). Experimental study of the mechanical properties of intact and tectonic coal via compression of a single particle. *Powder Technol.* 325, 412–419. doi:10.1016/j.powtec.2017.11.029

Dong, J., Cheng, Y., Jiang, J., and Guo, P. (2020). Effects of tectonism on the pore characteristics and methane diffusion coefficient of coal. *Arabian J. Geosciences* 13 (12), 482. doi:10.1007/s12517-020-05475-8

Dormant, L. M., and Adamson, A. W. (1972). Application of the BET equation to heterogeneous surfaces. *J. Colloid Interface Sci.* 38 (1), 285–289. doi:10.1016/0021-9797(72)90244-5

Ezzati, R. (2020). Derivation of pseudo-first-order, pseudo-second-order and modified pseudo-first-order rate equations from Langmuir and freundlich isotherms for adsorption. *Chem. Eng. J.* 392, 123705. doi:10.1016/j.cej.2019.123705

Fu, X., Qin, Y., Zhang, W., Wei, C., and Zhou, R. (2005). Fractal classification and natural classification of coal pore structure based on migration of coal bed methane. *Chin. Sci. Bull.* 50 (S1), 66–71. doi:10.1007/BF03184085

Han, W., Zhou, G., Gao, D., Zhang, Z., Wei, Z., Wang, H., et al. (2020). Experimental analysis of the pore structure and fractal characteristics of different metamorphic coal based on mercury intrusion-nitrogen adsorption porosimetry. *Powder Technol.* 362, 386–398. doi:10.1016/j.powtec.2019.11.092

Hodot, B. B. (1966). *Outburst of coal and coalbed gas (Chinese Translation)*. Beijing: China Coal Industry Press, 318.

Hou, Q., Li, H., Fan, J., Ju, Y., Wang, T., Li, X., et al. (2012). Structure and coalbed methane occurrence in tectonically deformed coals. *Sci. China Earth Sci.* 55 (11), 1755–1763. doi:10.1007/s11430-012-4493-1

Huang, L., Tan, J., Fu, H., Liu, J., Chen, X., Liao, X., et al. (2023b). The non-plane initiation and propagation mechanism of multiple hydraulic fractures in tight reservoirs considering stress shadow effects. *Eng. Fract. Mech.* 292, 109570. doi:10.1016/j.engfracmech.2023.109570

Huang, L. K., He, R., Yang, Z. Z., Tan, P., Chen, W. H., Li, X. G., et al. (2023a). Exploring hydraulic fracture behavior in glutenite formation with strong heterogeneity and variable lithology based on DEM simulation. *Eng. Fract. Mech.* 278, 109020. doi:10.1016/j.engfracmech.2022.109020

Ji, P. F., Lin, H. F., Kong, X. G., Li, S. G., Cai, Y. C., Wang, R. Z., et al. (2023). Experimental study on enhanced coal seam gas extraction by uniform pressure/pulse pressure N2 injection. *Fuel* 351, 128988. doi:10.1016/j.fuel.2023.128988

Jia, T., Zhang, S., Tang, S., Wang, M., Xin, D., and Zhang, Q. (2022). Characteristics and evolution of low-rank coal pore structure around the first coalification jump: case study in southeastern junggar basin. *Nat. Resour. Res.* 31 (5), 2769–2786. doi:10.1007/s11053-022-10094-z

Jiang, B., Qu, Z., Wang, G. G. X., and Li, M. (2010). Effects of structural deformation on formation of coalbed methane reservoirs in Huaibei coalfield, China. *Int. J. Coal Geol.* 82 (3-4), 175–183. doi:10.1016/j.coal.2009.12.011

Kutchko, B. G., Goodman, A. L., Rosenbaum, E., Natesakhawat, S., and Wagner, K. (2013). Characterization of coal before and after supercritical CO 2 exposure via feature relocation using field-emission scanning electron microscopy. *Fuel* 107, 777–786. doi:10.1016/j.fuel.2013.02.008

Lee, G., Pyun, S., and Rhee, C. (2006). Characterisation of geometric and structural properties of pore surfaces of reactivated microporous carbons based upon image analysis and gas adsorption. *Microporous Mesoporous Mater.* 93 (1-3), 217–225. doi:10.1016/j.micromeso.2006.02.025

Li, W., Jiang, B., and Zhu, Y. (2019). Impact of tectonic deformation on coal methane adsorption capacity. *Adsorpt. Sci. Technol.* 37 (9-10), 698–708. doi:10.1177/0263617419878541

Li, W., Liu, H., and Song, X. (2015). Multifractal analysis of Hg pore size distributions of tectonically deformed coals. *Int. J. Coal Geol.* 144-145, 138–152. doi:10.1016/j.coal.2015.04.011

Lin, H., Bai, Y., Bu, J., Li, S., Yan, M., Zhao, P., et al. (2020). Comprehensive fractal model and pore structural features of medium- and low-rank coal from the zhunnan coalfield of xinjiang, China. *Energies* 13 (1), 7. doi:10.3390/en13010007

Lin, H., Ji, P., Kong, X., Li, S., Long, H., Xiao, T., et al. (2023). Experimental study on the influence of gas pressure on CH4 adsorption-desorption-seepage and deformation characteristics of coal in the whole process under triaxial stress. *Fuel* 333, 126513. doi:10.1016/j.fuel.2022.126513

Liu, L., Yang, M., Cao, Z., and Zhang, X. (2022). Nuclear magnetic resonance study on the law of methane adsorption in water-bearing medium rank lump coal. *Energy Sources. Part a, Recovery, Util. Environ. Eff.* 44 (2), 4411–4426. doi:10.1080/15567036.2022.2077861

Lu, Y., Yang, Z., Li, X., Han, J., and Ji, G. (2015). Problems and methods for optimization of hydraulic fracturing of deep coal beds in China. *Chem. Technol. Fuels Oils* 51 (1), 41–48. doi:10.1007/s10553-015-0573-1

Mangi, H. N., Detian, Y., Hameed, N., Ashraf, U., and Rajper, R. H. (2020). Pore structure characteristics and fractal dimension analysis of low rank coal in the Lower Indus Basin, SE Pakistan. *J. Nat. Gas Sci. Eng.* 77, 103231. doi:10.1016/j.jngse.2020.103231

Meng, Y., and Li, Z. (2018). Experimental comparisons of gas adsorption, sorption induced strain, diffusivity and permeability for low and high rank coals. *Fuel* 234, 914–923. doi:10.1016/j.fuel.2018.07.141

Nie, B., Liu, X., Yang, L., Meng, J., and Li, X. (2015). Pore structure characterization of different rank coals using gas adsorption and scanning electron microscopy. *Fuel* 158, 908–917. doi:10.1016/j.fuel.2015.06.050

Okolo, G. N., Everson, R. C., Neomagus, H. W. J. P., Roberts, M. J., and Sakurovs, R. (2015). Comparing the porosity and surface areas of coal as measured by gas adsorption, mercury intrusion and SAXS techniques. *Fuel* 141, 293–304. doi:10.1016/j.fuel.2014.10.046

Pan, J., Hou, Q., Ju, Y., Bai, H., and Zhao, Y. (2012). Coalbed methane sorption related to coal deformation structures at different temperatures and pressures. *Fuel* 102, 760–765. doi:10.1016/j.fuel.2012.07.023

Qu, Z., Wang, G. G. X., Jiang, B., Rudolph, V., Dou, X., and Li, M. (2010). Experimental study on the porous structure and compressibility of tectonized coals. *Energy and Fuels* 24 (5), 2964–2973. doi:10.1021/ef9015075

Ran, Q., Liang, Y., Zou, Q., Hong, Y., Zhang, B., Liu, H., et al. (2023a). Experimental investigation on mechanical characteristics of red sandstone under graded cyclic loading and its inspirations for stability of overlying strata. *Geomechanics Geophys. Geo-Energy Geo-Resources* 9 (1), 11. doi:10.1007/s40948-023-00555-x

Ran, Q., Liang, Y., Zou, Q., Zhang, B., Li, R., Chen, Z., et al. (2023b). Characteristics of mining-induced fractures under inclined coal seam group multiple mining and implications for gas migration. *Nat. Resour. Res.* 32 (3), 1481–1501. doi:10.1007/s11053-023-10199-z

Ren, J., Niu, Q., Wang, Z., Wang, W., Yuan, W., Weng, H., et al. (2022). CO2 adsorption/desorption, induced deformation behavior, and permeability characteristics of different rank coals: application for CO2 -enhanced coalbed methane recovery. *Energy and Fuels* 36 (11), 5709–5722. doi:10.1021/acs.energyfuels.2c00635

Rigby, S. P. (2005). Predicting surface diffusivities of molecules from equilibrium adsorption isotherms. *Colloids Surfaces a Physicochem. Eng. Aspects* 262 (1-3), 139–149. doi:10.1016/j.colsurfa.2005.04.021

Sun, W., Lin, H., Li, S., Kong, X., Long, H., Yan, M., et al. (2021). Experimental research on adsorption kinetic characteristics of CH4, CO2, and N2 in coal from junggar basin, China, at different temperatures. *Nat. Resour. Res.* 30 (3), 2255–2271. doi:10.1007/s11053-021-09812-w

Sun, Z., Li, L., Wang, F., and Zhou, G. (2020). Desorption characterization of soft and hard coal and its influence on outburst prediction index. *Energy Sources. Part a, Recovery, Util. Environ. Eff.* 42 (22), 2807–2821. doi:10.1080/15567036.2019.1618991

Tan, P., Fu, S. H., Chen, Z. W., and Zhao, Q. (2023). Experimental investigation on fracture growth for integrated hydraulic fracturing in multiple gas bearing formations. *Geoenergy Sci. Eng.* 231 (1), 212316. doi:10.1016/j.geoen.2023.212316

Tan, P., Jin, Y., and Pang, H. W. (2021). Hydraulic fracture vertical propagation behavior in transversely isotropic layered shale formation with transition zone using XFEM-based CZM method. *Eng. Fract. Mech.* 248, 107707. doi:10.1016/j.engfracmech.2021.107707

Ullah, B., Cheng, Y., Wang, L., Yang, W., Jiskani, I. M., and Hu, B. (2022). Experimental analysis of pore structure and fractal characteristics of soft and hard coals with same coalification. *Int. J. Coal Sci. Technol.* 9 (1), 58. doi:10.1007/s40789-022-00530-z

Wang, K., and Du, F. (2020). Coal-gas compound dynamic disasters in China: a review. *Process Saf. Environ. Prot.* 133, 1–17. doi:10.1016/j.psep.2019.10.006

Wang, X., Cheng, Y., Zhang, D., Liu, Z., Wang, Z., and Jiang, Z. (2021). Influence of tectonic evolution on pore structure and fractal characteristics of coal by low pressure gas adsorption. *J. Nat. Gas Sci. Eng.* 87, 103788. doi:10.1016/j.jngse.2020.103788

Wang, Z., Cheng, Y., Qi, Y., Wang, R., Wang, L., and Jiang, J. (2019). Experimental study of pore structure and fractal characteristics of pulverized intact coal and tectonic coal by low temperature nitrogen adsorption. *Powder Technol.* 350, 15–25. doi:10.1016/j.powtec.2019.03.030

Wang, Z., Cheng, Y., Wang, L., Zhou, H., He, X., Yi, M., et al. (2020). Characterization of pore structure and the gas diffusion properties of tectonic and intact coal: implications for lost gas calculation. *Process Saf. Environ. Prot.* 135, 12–21. doi:10.1016/j.psep.2019.12.020

Xu, X., Meng, Z., and Wang, Y. (2019). Experimental comparisons of multiscale pore structures between primary and disturbed coals and their effects on adsorption and seepage of coalbed methane. *J. Petroleum Sci. Eng.* 174, 704–715. doi:10.1016/j.petrol.2018.11.082

Yang, H., Bi, W., Zhang, Y., Yu, J., Yan, J., Lei, D., et al. (2021). Effect of tectonic coal structure on methane adsorption. *J. Environ. Chem. Eng.* 9 (6), 106294. doi:10.1016/j.jece.2021.106294

Yao, Y., Liu, D., Tang, D., Tang, S., and Huang, W. (2008). Fractal characterization of adsorption-pores of coals from North China: an investigation on CH4 adsorption capacity of coals. *Int. J. Coal Geol.* 73 (1), 27–42. doi:10.1016/j.coal.2007.07.003

Ye, C. F., Xie, H. P., Wu, F., and Li, C. B. (2023). Study on the nonlinear time-dependent deformation characteristics and viscoelastic-plastic model of shale under direct shear loading path. *Bull. Eng. Geol. Environ.* 82 (5), 189. doi:10.1007/s10064-023-03170-y

Yu, S., Bo, J., Pei, S., and Jiahao, W. (2018). Matrix compression and multifractal characterization for tectonically deformed coals by Hg porosimetry. *Fuel* 211, 661–675. doi:10.1016/j.fuel.2017.09.070

Zhai, C., Xiang, X., Xu, J., and Wu, S. (2016). The characteristics and main influencing factors affecting coal and gas outbursts in Chinese Pingdingshan mining region. *Nat. Hazards* 82 (1), 507–530. doi:10.1007/s11069-016-2195-2

Zhang, K., Wang, L., Cheng, Y., Li, W., Kan, J., Tu, Q., et al. (2020). Geological control of fold structure on gas occurrence and its implication for coalbed gas outburst: case study in the qinan coal mine, huaibei coalfield, China. *Nat. Resour. Res.* 29 (2), 1375–1395. doi:10.1007/s11053-019-09511-7

Zhao, J. J., Tian, S. X., Li, P., Xie, H. G., and Cai, J. J. (2023a). Molecular dynamics simulation and experimental research on the influence of SiO2-H2O nanofluids on wettability of low-rank coal. *Colloids Surfaces A Physicochem. Eng. Aspects* 679, 132580. doi:10.1016/j.colsurfa.2023.132580

Zhao, J. J., Tian, S. X., Xie, H. G., and Zhang, X. (2023b). Study of time-varying laws of stability and wettability of SiO2–H2O nanofluids with different particle sizes. *Industrial Eng. Chem. Res.* 62 (34), 13529–13540. doi:10.1021/acs.iecr.3c02110

Zhao, P., Liu, H., Li, S., Ho, C., Qin, L., Jia, Y., et al. (2020). Exploring the adsorption and diffusion characteristics of tectonic coal at different mass ratios based on the specific surface Gibbs function. *Powder Technol.* 376, 604–611. doi:10.1016/j.powtec.2020.06.067

Zhao, P., Zhuo, R., Li, S., Lin, H., Shu, C. M., Shuang, H., et al. (2023). Greenhouse gas protection and control based upon the evolution of overburden fractures under coal mining: a review of methods, influencing factors, and techniques. *Energy* 284, 129158. doi:10.1016/j.energy.2023.129158

Zhao, Y., Sun, Y., Liu, S., Wang, K., and Jiang, Y. (2017). Pore structure characterization of coal by NMR cryoporometry. *Fuel* 190, 359–369. doi:10.1016/j.fuel.2016.10.121

Zou, Q. L., Ning, Y. H., Zhang, B. C., Tian, S. X., Jiang, Z. B., and An, Y. Q. (2023a). Mechanical properties and failure characteristics of sandstone under ramp loading paths. *Geomechanics Geophys. Geo-Energy Geo-Resources* 9 (1), 39. doi:10.1007/s40948-023-00574-8

Zou, Q. L., Zhan, J. F., Wang, X., and Huang, Z. (2023b). Influence of nanosized magnesia on the hydration of borehole-sealing cements prepared using different methods. *Int. J. Coal Sci. Technol.* 10, 66. doi:10.1007/s40789-023-00605-5

frontiers | Frontiers in Energy Research

TYPE Original Research
PUBLISHED 22 January 2024
DOI 10.3389/fenrg.2023.1328236

Check for updates

OPEN ACCESS

EDITED BY
Xiaojin Zheng,
Princeton University, United States

REVIEWED BY
Jun Liu,
Sichuan University, China
Guangtan Huang,
Chinese Academy of Sciences (CAS), China
Guiyun Gao,
Ministry of Emergency Management, China

*CORRESPONDENCE
Chang Wang,
306001759@qq.com

RECEIVED 26 October 2023
ACCEPTED 22 December 2023
PUBLISHED 22 January 2024

CITATION
Wang C, Yin C, Shi X, Zhang D, Liao M and Zhang R (2024), Research on geophysical response analysis and prediction technology of geostress in the shale gas area of the southern Sichuan Basin.
Front. Energy Res. 11:1328236.
doi: 10.3389/fenrg.2023.1328236

COPYRIGHT
© 2024 Wang, Yin, Shi, Zhang, Liao and Zhang. This is an open-access article distributed under the terms of the Creative Commons Attribution License (CC BY). The use, distribution or reproduction in other forums is permitted, provided the original author(s) and the copyright owner(s) are credited and that the original publication in this journal is cited, in accordance with accepted academic practice. No use, distribution or reproduction is permitted which does not comply with these terms.

Research on geophysical response analysis and prediction technology of geostress in the shale gas area of the southern Sichuan Basin

Chang Wang[1,2,3]*, Cheng Yin[1], Xuewen Shi[2,3], Dongjun Zhang[2,3], Maojie Liao[2,3] and Ruhua Zhang[1,2,3]

[1]School of Geosciences and Technology, Southwest Petroleum University, Chengdu, China, [2]Shale Gas Research Institute, Petrochina Southwest Oil and Gasfield Company, Chengdu, China, [3]Shale Gas Evaluation and Exploitation Key Laboratory of Sichuan Province, Chengdu, China

The exploration and development potential of shale gas reservoirs in the Sichuan Basin is enormous; however, it also faces difficulties such as complex structures, strong heterogeneity, and unclear geophysical response characteristics. Fine prediction of geostress is an important part of shale gas exploration and development, which directly affects the implementation effect of reservoir evaluation, well trajectory design, and fracture reconstruction. The existing geostress prediction techniques lack high-precision seismic data constraints, making it difficult to accurately reflect the planar distribution characteristics of geostress in the block with rapid changes in complex tectonic zones. At the same time, the geophysical response characteristics of geostress in the Sichuan Basin are unknown, and the geostress seismic prediction technology lacks theoretical basis. This paper combines numerical simulation and physical experiments and defines the characteristics of the geophysical response of shale gas reservoirs in the Sichuan Basin changing with the stress field, and technical countermeasures for geostress seismic prediction have been established to provide technical means for accurate prediction of the geostress field in the shale gas block. Based on the geostress sensitive parameters obtained from prestack seismic inversion, the geostress field prediction of a shale gas work area in the Sichuan Basin is realized.

KEYWORDS

shale gas, geostress, geophysical response, seismic inversion, differential horizontal stress ratio

1 Introduction

For geostress, many theories, methods, and applications are still in the exploratory stage (Yang et al., 2013; Song et al., 2017; Song et al., 2020; Liu et al., 2023). Geostress is a key factor affecting shale hydraulic fracturing design (Huang et al., 2019; Zheng et al., 2022; Huang et al., 2023a; He et al., 2023; Tan et al., 2023). Meanwhile, understanding geostress is a prerequisite for successful development of shale gas (Tan et al., 2017; Luo et al., 2022; Zhang et al., 2022; Huang et al., 2023b). The predecessors have carried out in-depth research on geostress logging calculation, geostress numerical simulation, and geostress seismic prediction methods and obtained a series of achievements (Karadeniz, 2019; Wu et al.,

2023). However, due to various factors, it is difficult to make a major breakthrough in geophysical response characteristics and geostress seismic prediction methods under the condition of a natural fracture geostress-coupling medium.

First, the deep shale gas area in the southern Sichuan Basin is subject to multi-stage tectonic evolution, and the geostress changes rapidly (Craig, 2014; Huang et al., 2017). This study area mainly develops northeast structural groups, and small faults are developed in synclines between structures, with complex geological conditions. The geostress changes between different structural units are complex. The existing geostress prediction technology is mainly based on the theory of geomechanics and is obtained by finite element simulation using the calculation results of single-well geostress. This technology does not fully consider the lateral variation characteristics of the reservoir and lacks planar data constraints, resulting in low prediction accuracy between larger well spacing (Schoenball and Ellsworth, 2017; Wang et al., 2022). Seismic waves contain the stress and strain characteristics of reservoirs. Combining the advantages of seismic lateral resolution, starting from the constitutive equation of the reservoir, the geostress field seismic topological relationship is established to form a set of geostress prediction methods based on seismic data.

Second, the geophysical response of deep shale reservoirs in southern Sichuan to geostress is unclear. The underground structure and stress are key factors affecting the seismic anisotropy of shale reservoirs (Xu et al., 2019). Deep shale reservoirs have complex geological stresses, natural fractures are developed, and the geophysical response under the coupling conditions of geological stress field and natural fractures is unclear (Ji et al., 2015; Huang et al., 2018; Huang et al., 2022; Song et al., 2022). Therefore, it is considered to establish a deep shale reservoir structure stress equivalent model; explore the acoustic expression patterns of rock masses under different fault levels, fault properties, and stress conditions; clarify the seismic azimuth anisotropy response characteristics under natural fracture geostress coupling conditions; and provide theoretical support for geostress azimuth prediction.

Third, the seismic prediction technology of geostress in a deep shale reservoir is immature. The magnitude and orientation of geostress are the main factors for predicting the geostress field (Hayavi and Abdideh, 2016). The geostress azimuth prediction technology based on wide-azimuth seismic data is immature, and the seismic prediction technology for geostress size has not fully considered the reservoir heterogeneity, making the prediction accuracy low. Therefore, based on experimental research results, we will conduct research on seismic anisotropy characteristics based on wide-azimuth seismic data, clarify the dominant orientation of anisotropy, and achieve the prediction of geostress orientation. In terms of the magnitude of geostress, a rock physical model containing saturated fluid and fractured media is constructed based on linear sliding theory, and a prestack seismic inversion objective function based on anisotropy is constructed. By deriving the constitutive equation, the transformation from elastic waves to geostress magnitude is achieved.

Accurate prediction of geostress field is an internationally recognized problem in the industry today, but it is also an urgent problem in the field of shale gas exploration and development (Huang et al., 2020; Detournay et al., 2022; Dontsov, 2022; Zhang et al., 2023). This paper has confirmed the seismic wave response characteristics of deep shale reservoirs in southern Sichuan under the condition of natural fracture and geostress coupling, established the identification mode of deep shale reservoir geostress geophysical response, and integrated anisotropic petrophysical modeling, prestack seismic inversion, prestack seismic attribute, and other technical means to realize the seismic prediction technical method of deep shale reservoir geostress in southern Sichuan, which is of great significance to support the rapid and beneficial production of deep shale gas.

2 Physical model test of geophysical response to deep shale reservoir geostress

2.1 Preparation of core samples

The test pieces for rock mechanic parameter testing are obtained from surface outcrops and underground cores. According to the ISRM standard, each specimen is processed into a standard small cylinder with a diameter of 25 mm and a length of 50 mm, as shown in Figure 1, and the parallelism of the upper and lower end faces is controlled to be less than 0.01 mm.

Since shale often presents a certain degree of anisotropy under the compaction of perennial geological structures when it is formed, to have a more complete understanding of the mechanical properties of this batch of outcrops, with a bedding plane as a reference, we will drill cores from shales at different angles and test shale samples drilled from the same angle by applying different confining pressure values to observe the changes of shale strength of material parameters.

The test results of rock mechanics behavior in the outcrop are shown on the left side of Figure 2, and the rock cores are shown on the right side. There is less difference in the rock mechanics behavior between the rock sample of the proposed crop model specimen and the deep shale rock sample under different confining pressures, and the selected outcrop has good representativeness.

2.2 Preparation of shale models containing faults

For the geological body model containing faults, we used field shale as the basic material, cut at different angles, and used cement slurry materials with different lime sand ratios as the filling material for simulating faults. After being formed by casting and curing, we will reform physical model for geophysical testing, as shown in Figure 3. A fracturing physical model test plan was constructed under different stresses, fault dip angles, and filling materials, and the parameters of those model are shown as Table 1.

2.3 Experimental methods

Experimental schemes for P-wave anisotropy were constructed under different stresses, fault dip angles, and filling materials, as shown in Figure 4 and Figure 5. Active source probes and several



FIGURE 1
Field outcrop preparation core and underground core.

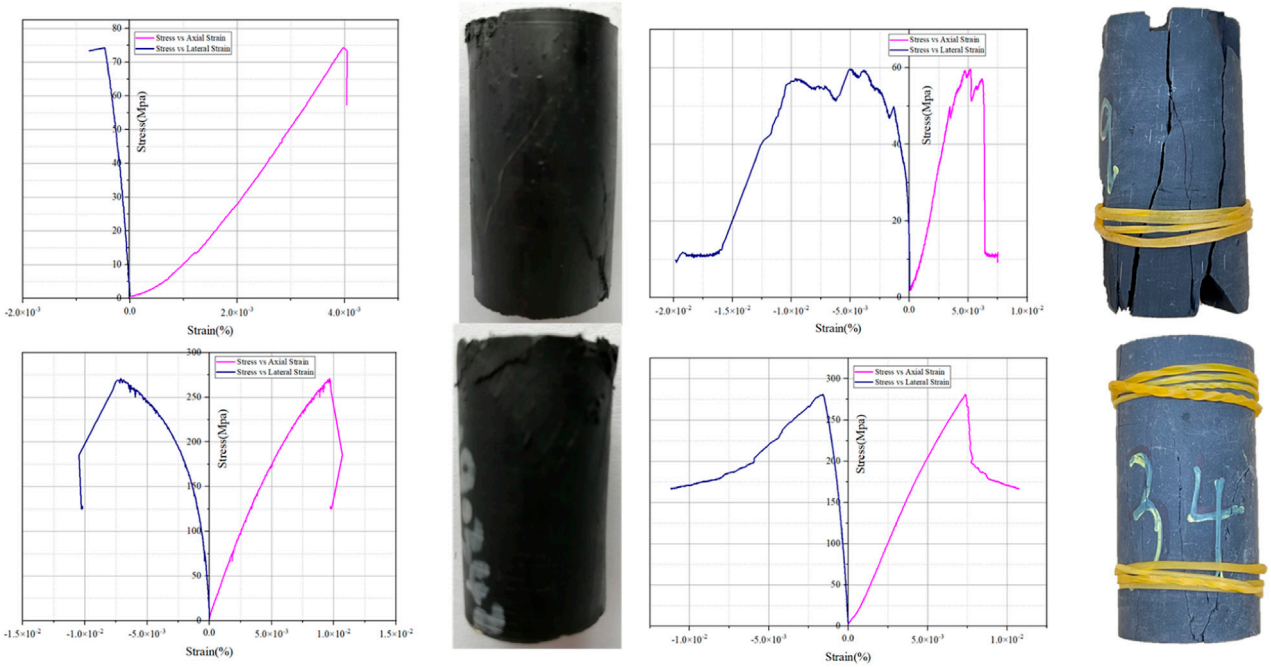


FIGURE 2
Stress–strain curve based on triaxial stress testing. Outdoor outcrop (left) and underground core (right).

passive acquisition probes are arranged on both sides of the cube specimen, when considering both sides of the fault. The receiving probes are arranged in a fixed grid array, and their positions are sequentially changed. The amplifier and acoustic acquisition system are connected, and the active source probe is activated to emit excitation waves. The acoustic response of the receiving acquisition probe at each position is observed.

The data collection scheme adopts a multi-point excitation, multi-point reception, and extraction scheme. In order to improve the coverage frequency, wide-azimuth transmission reception is adopted. After theoretical wavelet excitation, amplitude compensation and consistency processing are carried out on the collected data to ensure uniform energy of each receiving channel. Environmental noise and high-frequency random noise are suppressed, and the K-means algorithm is used to extract the first arrival of P-waves, as shown in Figure 6.

As observed from the experimental data, as the dip angle of the fault increases, the receiving velocity first decreases and then increases; as the



FIGURE 3
Production of shale rock samples containing filled faults after molding.

TABLE 1 Physical model test plans under different stresses, fault dip angles, and different filling materials.

Number	*Sigma1-2-3*/(MPa)	Fault dip angle/(°)	Fault filling ash: sand ratio
XF1	0-0-0	30°	0
XF2	0-0-0	45°	0
XF3	0-0-0	60°	0
XF4	0-0-0	0°	2:1
XF5	0-0-0	0°	3:1
XF6	0-0-0	0°	4:1
XF7	4-3-1	0°	0
XF8	7-6-4	0°	0
XF9	10-9-7	0°	0

density and stress of the filling material increase, the receiving speed increases, the detailed results of which are shown in Table 2.

After a series of AVAZ seismic data processing techniques such as bandpass filtering, channel equalization, and partial stacking, azimuth geophysical data are obtained. After extracting and analyzing the amplitude of the first arrival seismic wave data, the transmitted wave AVAZ response of the acoustic experiment under different stress states was obtained. The amplitude energy of the first arrival wave was extracted to obtain the projected wave AVAZ response, as shown in Figure 7. Subtracting the energy of isotropic transmitted waves (0 directional projected wave energy) yields the anisotropic transmitted energy, as shown in Figure 8. By comparison, it can be found that when the vertical principal stress is fixed, the AVAZ response of the transmitted wave gradually decreases with the increase in the geostress difference; with the decrease in the geostress difference, the transmitted wave AVAZ response gradually increases, indicating that the P-wave velocity exhibits anisotropic characteristics under different stress conditions, laying the foundation for subsequent research.

The geostress orientation is fixed, the transmission wave AVAZ feature detection of different strike fault models is carried out, and the influence of the geostress orientation on the seismic wave AVAZ feature is studied, as shown in Figure 9. By using the rose plot for transmitted wave amplitude, the AVAZ characteristics of transmitted waves have been found to have good consistency with the fault strike. When faults or fractures have already been formed, applying principal stress from other azimuths has a very little impact on seismic AVAZ, and it is difficult to observe the effect of stress orientation on seismic AVAZ through experiments. The rose plot direction is basically consistent with the fault orientation.

3 Numerical simulation of geophysical response to deep shale reservoir geostress

3.1 Analysis of the influence of geostress on the elastic parameters of shale reservoirs

For deep fractured shale, the *in situ* geological conditions of high temperature and pressure have put forward higher requirements for shale exploration and fracture development (Zhang et al., 2022). Therefore, after completing the establishment of the rock physical

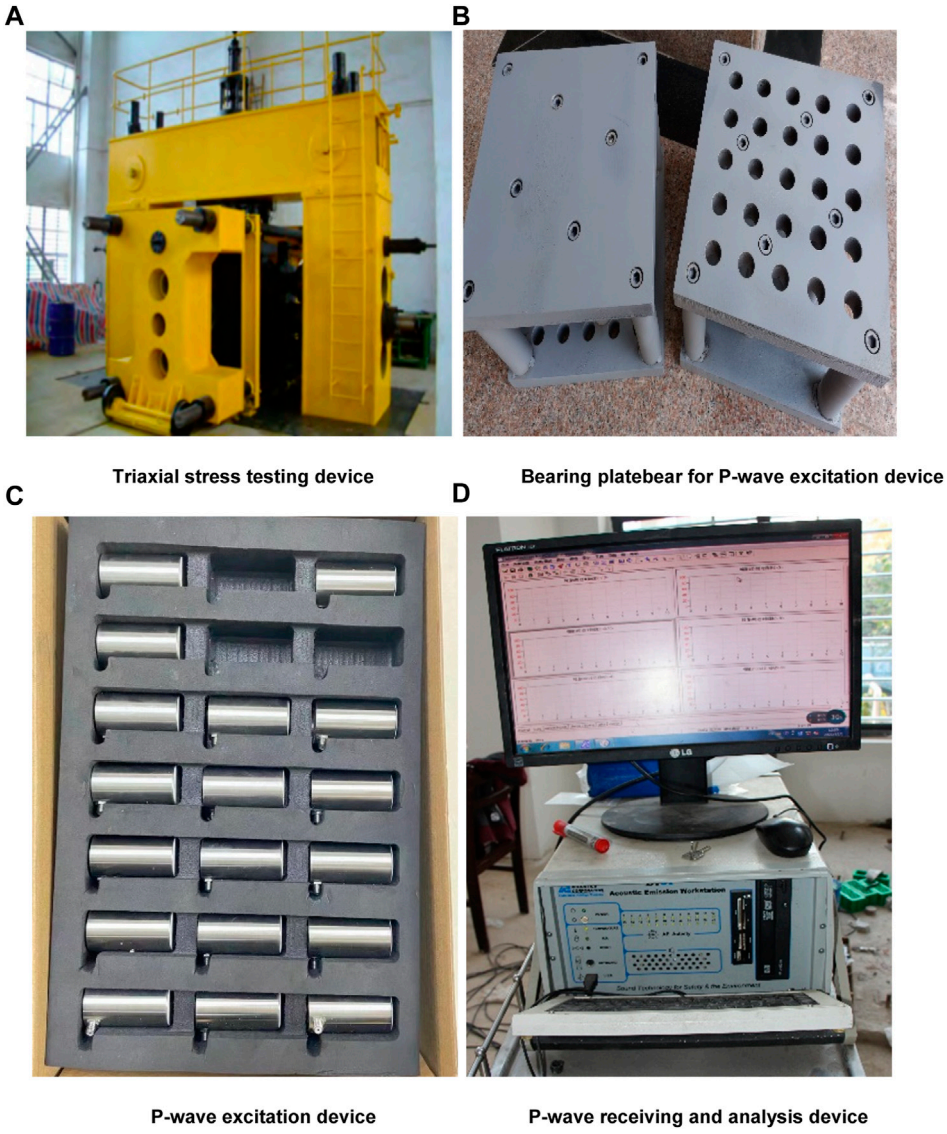


FIGURE 4
Comprehensive device for detecting the anisotropy of P-waves under three-dimensional stress **(A)** Triaxial stress testing device **(B)** Bearing platebear for P-wave excitation device **(C)** P-wave excitation device **(D)** P wave receiving and analysis device.

model of shale, it is necessary to consider the influence of pressure on elastic parameters and then study the influence of pressure on the geophysical response. David and Zimmerman proposed the DZ model in 2012 to study the variation of rock stiffness parameters with pressure. In rock media without fractures, the equivalent bulk modulus and equivalent shear modulus obey the following expressions:

$$\frac{1}{K_{eff}} = \frac{1}{K_{eff}^{\infty}} + \left(\frac{1}{K_{eff}^{0}} - \frac{1}{K_{eff}^{\infty}}\right)\exp\left(-\sigma_{11}/\tau_{K}\right),$$

$$\frac{1}{\mu_{eff}} = \frac{1}{\mu_{eff}^{\infty}} + \left(\frac{1}{\mu_{eff}^{0}} - \frac{1}{\mu_{eff}^{\infty}}\right)\exp\left(-\sigma_{11}/\tau_{\mu}\right),$$

where σ_{11} represents vertical principal stress, τ represents attenuation coefficient, and $(\cdot)^{0}$ and $(\cdot)^{\infty}$ represent the elastic parameters under no pressure and ultimate pressure, respectively. Daley and Schoenberg derived similar fracture flexibility parameters as a function of pressure:

$$Z_T = Z_T^{\infty} + \left(Z_T^{0} - Z_T^{\infty}\right)\exp\left(-\sigma_{11}/\tau_{Z_T}\right),$$

$$Z_N = Z_N^{\infty} + \left(Z_N^{0} - Z_N^{\infty}\right)\exp\left(-\sigma_{11}/\tau_{Z_N}\right).$$

Based on the linear sliding theory of Schoenberg and Sayers (1995), the equivalent flexibility tensor S of fractured reservoirs is approximately equivalent to the sum of the flexibility tensor of the background media without fractures and the fracture disturbance flexibility tensor as follows:

$$\mathbf{S} = \mathbf{S}_b + \mathbf{S}_f.$$

The variation of the flexibility coefficient of the background medium with pressure and the variation of the fracture flexibility coefficient with pressure can be calculated separately, ultimately obtaining the stiffness coefficient of fractured shale under different

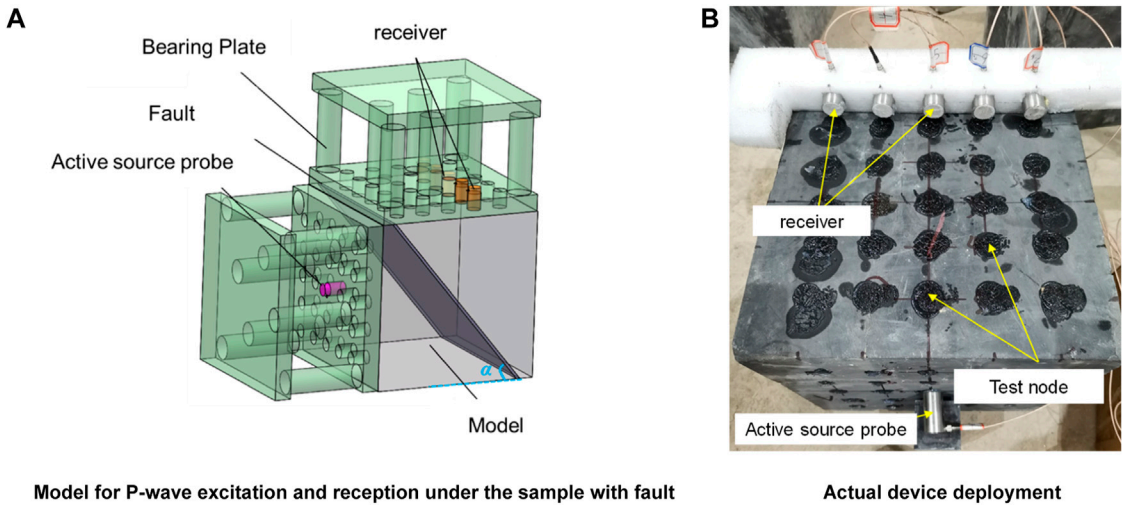


FIGURE 5
Acoustic testing model for rock samples containing faults.

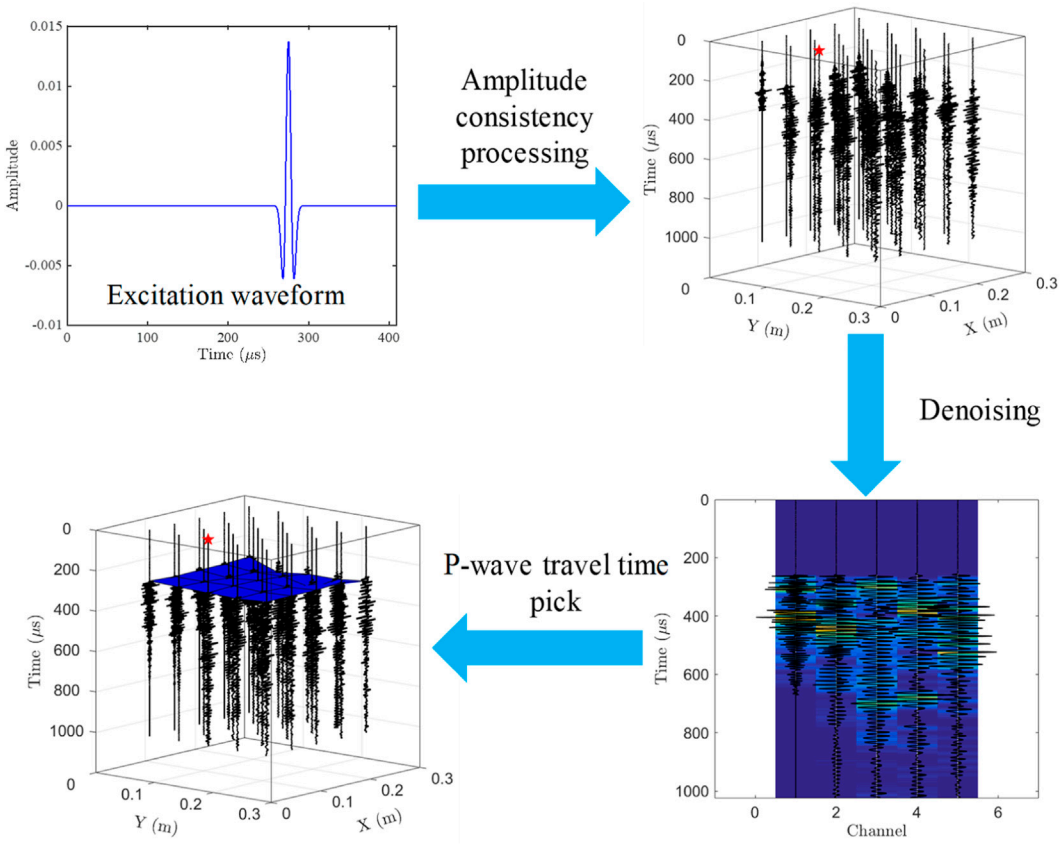


FIGURE 6
Method of P-wave travel time extraction.

pressures. Figure 7 shows the pressure-dependent curves of C33 and C55 parameters of the background medium obtained using the DZ model, where the stiffness coefficients C33 and C55 are important parameters in the VTI medium:

$$C_{33} = \rho v_p^2(0), C_{55} = \rho v_s^2(0), C_{11} = \rho v_p^2(90), C_{44} = \rho v_s^2(90),$$

where $v_p(0)$ and $v_p(90)$ represent the P-wave velocity in both vertical and horizontal directions, respectively. $v_s(0)$ and $v_s(90)$

TABLE 2 P-wave travel time extraction results under different stresses, fault dip angles, and filling materials.

Number	*Sigma1-2-3*/(MPa)	Fault dip angle/(°)	Fault filling ash: sand ratio	P-wave travel time (μs)	P-wave velocity (m/s)
XF1	0-0-0	30°	0	289.4560	3157.894737
XF2	0-0-0	45°	0	303.8880	2799.761087
XF3	0-0-0	60°	0	301.6080	2741.428467
XF4	0-0-0	0°	2:1	281.2560	3456.221198
XF5	0-0-0	0°	3:1	292.2080	3068.990916
XF6	0-0-0	0°	4:1	303.7840	2744.036294
XF7	4-3-1 (△σ = 3)	0°	0	315.5760	2476.882431
XF8	7-6-3 (△σ = 4)	0°	0	303.3280	2755.529429
XF9	10-9-5 (△σ = 5)	0°	0	296.3360	2944.640754

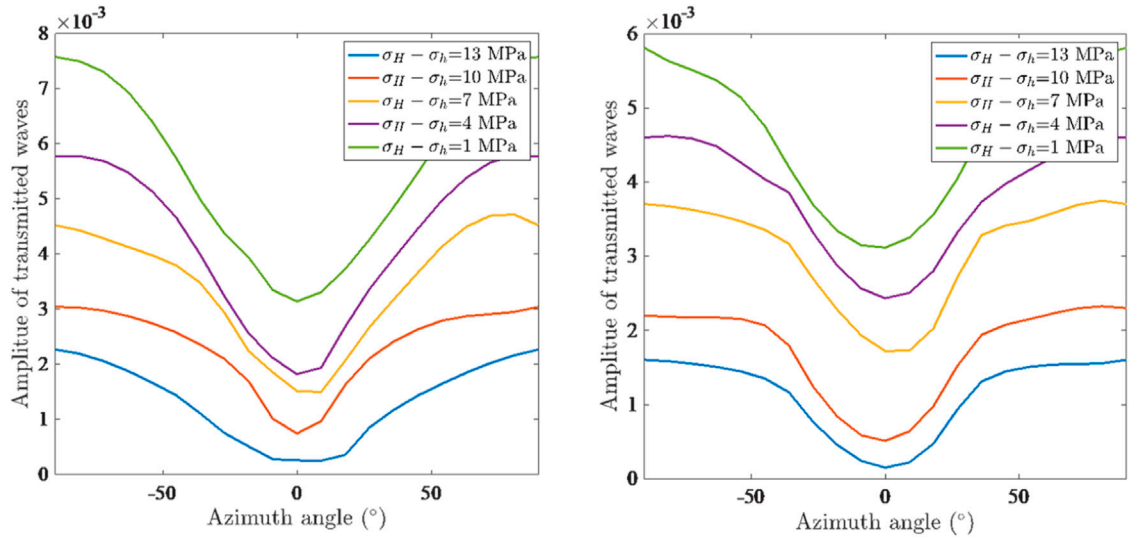


FIGURE 7
AVAZ response of the P-wave under different stresses.

represent the S-wave velocity in both vertical and horizontal directions, respectively.

We explore the variation law of the stiffness coefficient based on the influence of pressure on velocity anisotropy. C33 and C55 will continue to increase with increasing pressure. At the beginning of applying of stress, the stiffness coefficient will rapidly increase with the increase of pressure, and when the pressure increases to a certain threshold value, it will increase extremely slowly until the limit state, and the results are shown in Figure 10.

Similarly, the variation of fracture flexibility parameters with stress can be obtained. The fracture flexibility parameter represents the elastic parameter of the compressibility of the fracture, and the smaller its value, the smaller the transverse-to-longitudinal ratio of the fracture, which is close to the compacted state. From Figure 11, it can be observed that as the stress increases, Z_N and Z_T gradually decrease until the limit state.

By using the fracture flexibility parameter, we can convert the distribution of geostress and provide a guarantee for the application of stress in subsequent experiments. The relationship between the maximum horizontal principal stress and the minimum horizontal principal stress is shown in Figure 12, while ensuring that the rock maintains its current fracturing condition.

$$\sigma_h = \sigma_v \frac{\nu(1+\nu)}{1+EZ_N-\nu^2},$$
$$\sigma_H = \sigma_v \frac{\nu(1+EZ_N+\nu)}{1+EZ_N-\nu^2}.$$

Through calculation, it can be obtained that the maximum and minimum horizontal principal stresses will basically increase with the increase of stress, and the relationship is close to linear growth. The differential horizontal stress ratio (DHSR) obtained using geostress is an important brittleness index indicating fracturing, and its expression is as follows:

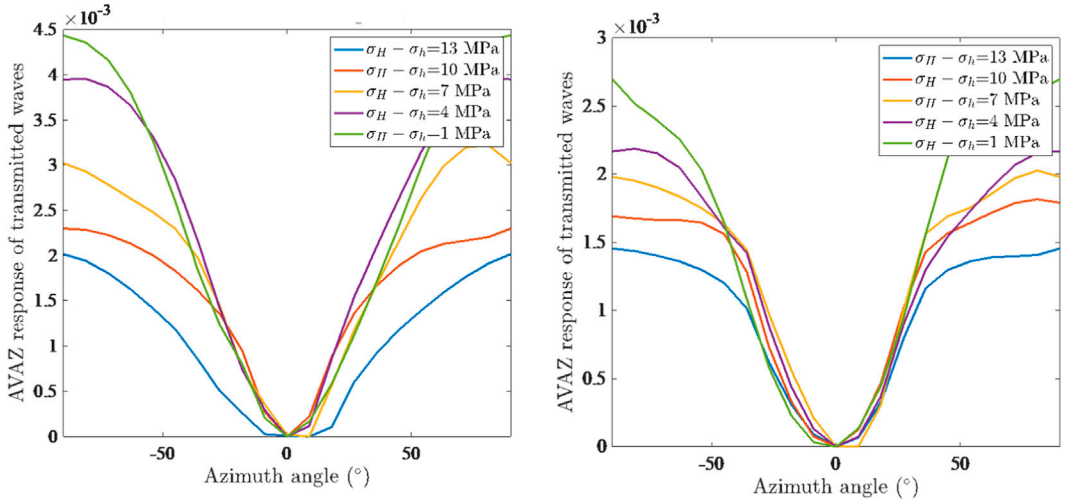


FIGURE 8
Anisotropic AVAZ response of the P-wave under different stresses.

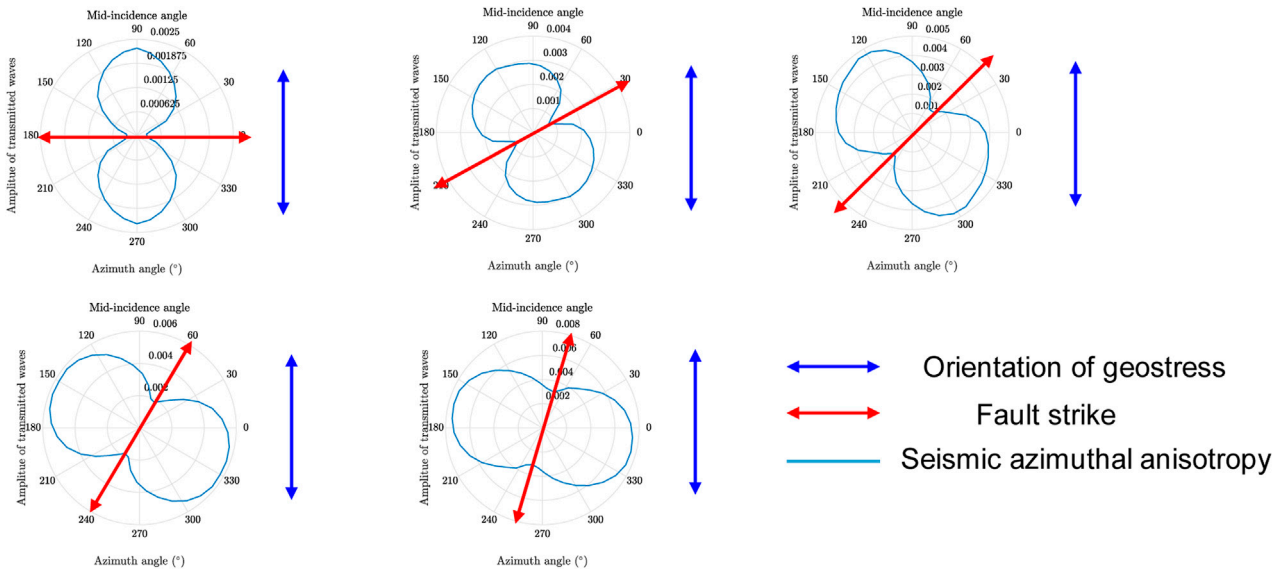


FIGURE 9
Rose plot of the relationship between seismic azimuth anisotropy and geostress orientation.

$$DHSR = \frac{\sigma_H - \sigma_h}{\sigma_H} = \frac{EZ_N}{1 + EZ_N + \nu}.$$

The DHSR is not related to σ_v, so it is not necessary to know the magnitude of overlying formation pressure in the DHSR calculation process. Usually, if the DHSR value is large, there are a large number of fractures parallel to the maximum horizontal stress direction in the formation. However, if the DHSR value is small, the area is more suitable for fracturing development and is prone to forming an orthogonal fracture network, which is conducive to the migration of oil and gas in the reservoir and the extraction of unconventional reservoirs.

Figure 13 shows the variation of DHSR parameters with pressure, and it can be observed that shale gradually increases the difficulty of fracturing with increasing pressure, mainly controlled by the compaction degree of the background medium. However, the presence of fractures can effectively improve the effectiveness of fracturing, so, theoretically, accurate prediction of fractures can provide a very good indicator for fracturing.

3.2 Geophysics response simulation of geostress in shale reservoirs

Based on the previous rock physics modeling, we can obtain the stiffness coefficient and density of the deep fractured shale rock

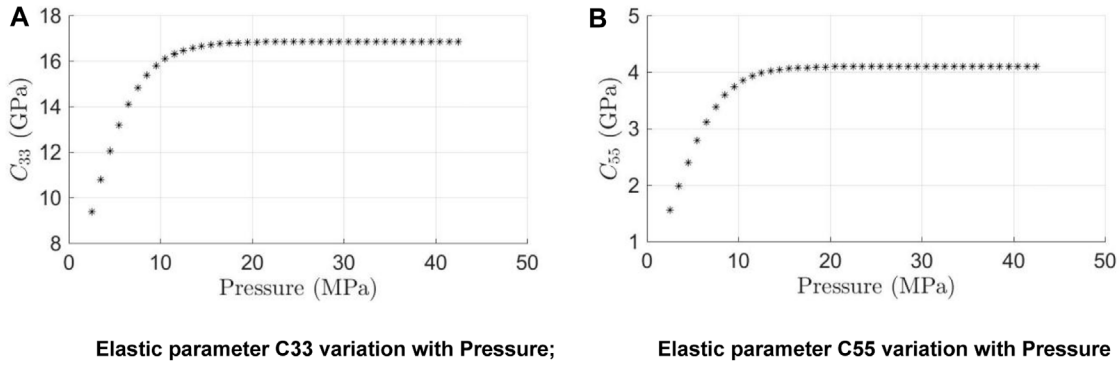


FIGURE 10
Elastic parameters of fractured shale background medium and their variation characteristics with pressure.

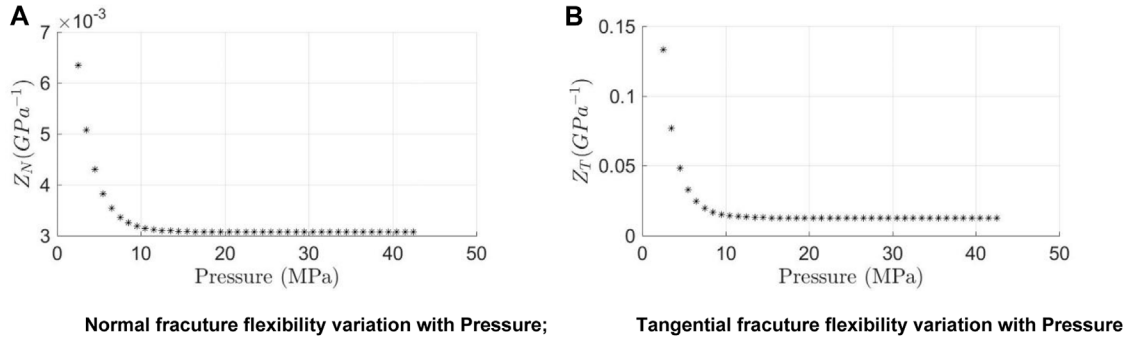


FIGURE 11
Variation characteristics of fracture flexibility with varying pressure.

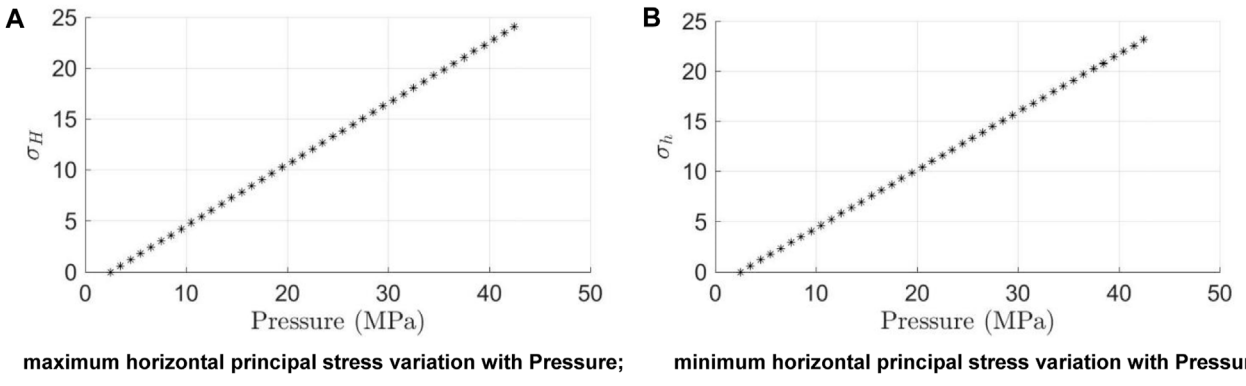


FIGURE 12
Variation characteristics of maximum and minimum horizontal principal stresses with varying pressure.

physics model. When we set this stratum as the underlying stratum, we can obtain the geophysics response of the reflection interface through the above formula by changing the different upper media. Here, we define the overlying strata as isotropic sandstone and non-fractured shale and discuss them separately.

3.2.1 The overlying strata are sandstone

According to the perturbation principle, seismic wave propagates in weakly anisotropic media, and the reflection coefficient can be expressed as an isotropic part and anisotropic perturbation part.

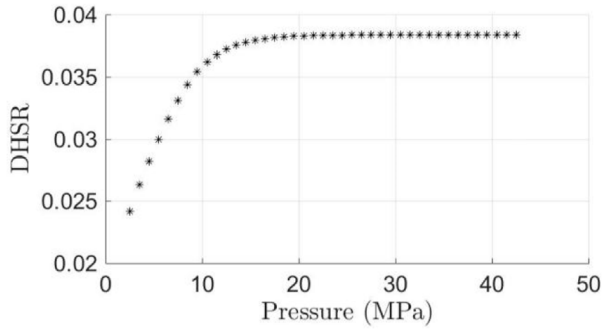


FIGURE 13
Characteristics of changes in the DHSR under pressure.

$$R_{pp} = R_{pp}^{iso} + R_{pp}^{ani}.$$

The isotropic part can be expressed using the Zoeppritz formula or Aki–Richard formula as follows:

$$R_{pp}^{iso} = \frac{1}{2}\sec^2\theta\frac{\Delta v_p}{v_p} - 4\zeta_b \sin^2\theta\frac{\Delta v_s}{v_s} + \frac{1}{2}\left(1 - 4\zeta_b \sin^2\theta\right)\frac{\Delta\rho}{\rho}.$$

The anisotropic part can be expressed as follows:

$$R_{pp}^{ani} = \frac{1}{4\rho_b^2\cos^2\theta}\left(\Delta\rho\xi + \sum_{I=1}^{6}\sum_{J=1}^{6}\Delta C_{IJ}\eta_{IJ}\right).$$

Among them, ΔC_{IJ} and $\Delta\rho$ represent the perturbation quantities of rigid parameters and density, respectively:

$$\eta = \frac{1}{\alpha_0^2}\begin{bmatrix}
\sin^4\theta\cos^4\phi & \sin^4\theta\sin^2\phi\cos^2\phi & \sin^2\theta\cos^2\theta\cos^2\phi & 2\sin^3\theta\cos\theta\sin\phi\cos^2\phi & -2\sin^3\theta\cos\theta\cos^3\phi & \sin^4\theta\sin\phi\cos^3\phi \\
\sin^4\theta\sin^2\phi\cos^2\phi & \sin^4\theta\sin^4\phi & \sin^2\theta\cos^2\theta\sin^2\phi & -2\sin^3\theta\cos\theta\sin^3\phi & -2\sin^3\theta\cos\theta\sin^2\phi\cos\phi & \sin^4\theta\sin^3\phi\cos\phi \\
\sin^2\theta\cos^2\theta\cos^2\phi & \sin^2\theta\cos^2\theta\sin^2\phi & \cos^4\theta & 2\sin\theta\cos^3\theta\sin\phi & -2\sin\theta\cos^3\theta\cos\phi & 2\sin^2\theta\cos^2\theta\sin\phi\cos\phi \\
-2\sin^3\theta\cos\theta\sin\phi\cos^2\phi & 2\sin^3\theta\cos\theta\sin^3\phi & -2\sin\theta\cos^3\theta\sin\phi & -4\sin^2\theta\cos^2\theta\sin^2\phi & -4\sin^2\theta\cos^2\theta\sin\phi\cos\phi & -4\sin^3\theta\cos\theta\sin^2\phi\cos\phi \\
2\sin^3\theta\cos\theta\cos^3\phi & 2\sin^3\theta\cos\theta\sin^2\phi\cos\phi & 2\sin\theta\cos^3\theta\cos\phi & -4\sin^2\theta\cos^2\theta\sin\phi\cos\phi & -4\sin^2\theta\cos^2\theta\cos^2\phi & -4\sin^3\theta\cos\theta\sin\phi\cos^2\phi \\
2\sin^4\theta\sin\phi\cos^3\phi & 2\sin^4\theta\sin^3\phi\cos\phi & 2\sin^2\theta\cos^2\theta\sin\phi\cos\phi & 4\sin^3\theta\cos\theta\sin^2\phi\cos\phi & 4\sin^3\theta\cos\theta\sin\phi\cos^2\phi & 4\sin^4\theta\sin^2\phi\cos^2\phi
\end{bmatrix}.$$

The influence of different fracture azimuth angles on AVAZ data is shown in Figure 14, in which the blue line represents the seismic AVAZ. It can be found that the AVAZ rose plot can be used to determine the orientation of faults and fractures.

3.2.2 The overlying strata are non-fractured shale

When the overlying strata are non-fractured shale, the reflection coefficient is expressed as follows:

$$R_{pp} = R_{pp}^{vti} + R_{pp}^{hti}.$$

The anisotropic part of VTI can be expressed using Graebner's exact formulation or Ruger's approximate formula:

$$R_{pp}^{vti} = \frac{1}{2}\sec^2\theta\frac{\Delta v_p}{v_p} - 4\zeta_b \sin^2\theta\frac{\Delta v_s}{v_s} + \frac{1}{2}\left(1 - 4\zeta_b \sin^2\theta\right)\frac{\Delta\rho}{\rho} + \frac{1}{2}\Delta\delta\sin^2\theta + \frac{1}{2}\Delta\varepsilon\sin^2\theta\tan^2\theta.$$

The anisotropic part can be expressed as follows:

$$R_{pp}^{ani} = \frac{1}{4\rho_b^2\cos^2\theta}\left(\Delta\rho\xi + \sum_{I=1}^{6}\sum_{J=1}^{6}\Delta C_{IJ}\eta_{IJ}\right).$$

Here, we assume that both the overlying and underlying strata are shale with consistent backgrounds, except for the development of fractures in the lower layer. Therefore, through formula

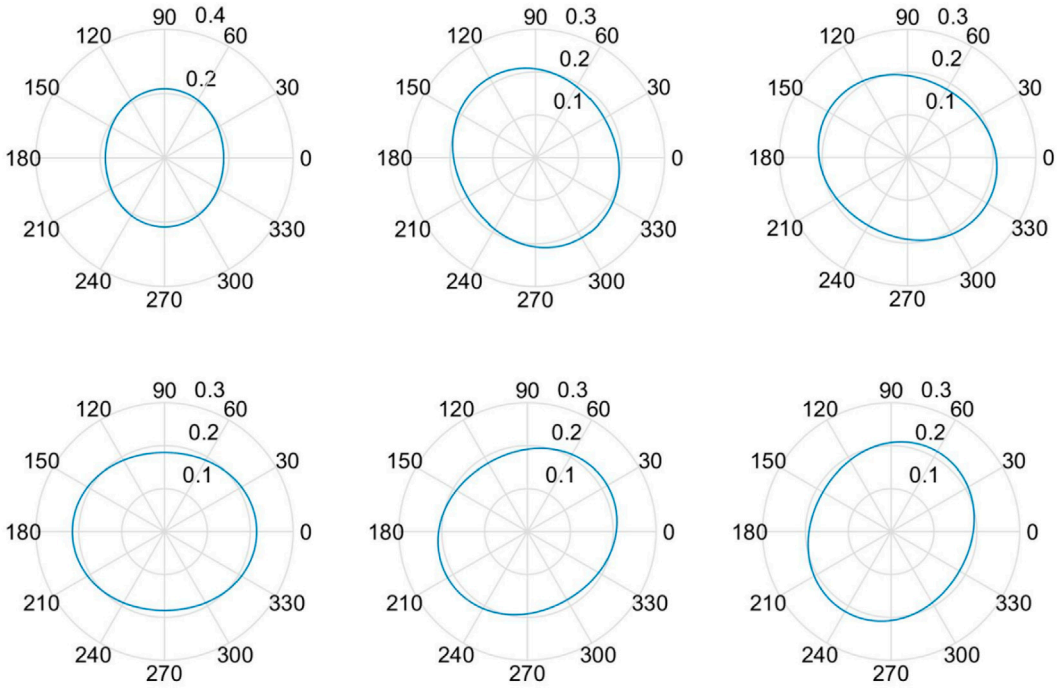


FIGURE 14
Influence of fracture azimuth on seismic AVAZ.

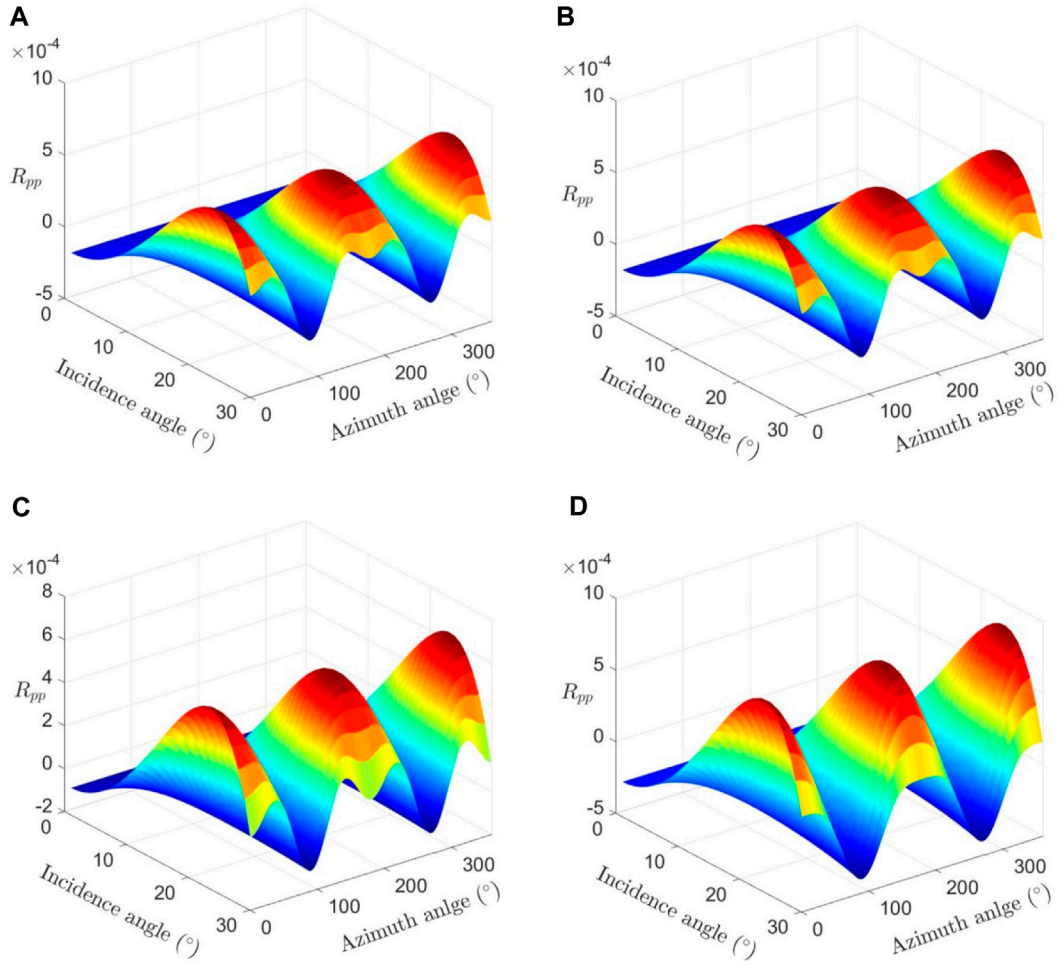


FIGURE 15
Variation of the seismic reflection coefficient with incident angle and azimuth under different stress conditions: **(A)** 0 MPa, **(B)** 10 MPa, **(C)** 20 MPa, and **(D)** 30 MPa.

derivation and numerical simulation, the variation of reflection coefficient Rpp with incident angle and azimuth angle can be obtained. Because the background is completely consistent, the difference is mainly reflected in the anisotropic perturbation part.

We compare the changes in reflection coefficients with incident angle and azimuth angle under different pressure states, as shown in Figure 15. Through comparison, it was found that fracture parameters can affect the variation of seismic amplitude with the incident angle and azimuth angle. Therefore, in conventional seismic exploration, directional anisotropy difference data can be used to extract fracture parameters, such as fracture strength and anisotropy parameters. Then, the obtained anisotropic parameters are brought into the conventional AVA/AVO inversion algorithm to obtain conventional linear elasticity parameters, such as Young's modulus and Poisson's ratio, to characterize the reservoir brittleness.

When the azimuth or incidence angle is fixed, the influence of seismic wave amplitude on the incidence angle and formation pressure can be studied, as shown in Figure 15. It can be observed that the reflection coefficient changes with changes in pressure. During the initial process of applying of pressure, the elastic parameters of the rock will undergo significant changes, resulting in significant changes in the geophysical response; when the pressure is applied to a certain extent, the changes of linear elasticity parameters reach a certain threshold value and are in a relatively balanced state.

Overall, the influence of stress on seismic reflection coefficients is relatively small, and the main contribution is reflected in the anisotropic part.

As observed from the numerical simulation results of step-by-step pressurization, the seismic reflection coefficient changes significantly when the stress difference is less than 20 MPa, and the seismic reflection coefficient is sensitive to the change of stress difference, which verifies the reliability and effectiveness of seismic prediction of geostress, as shown in Figure 16.

4 Research on prediction technology of geostress based on azimuth anisotropy inversion

Thomson (1986) proposed Thomson weak anisotropy parameters to obtain the seismic reflection coefficient in anisotropy media. Gary (2013) established the relationship between Thomson weak anisotropy

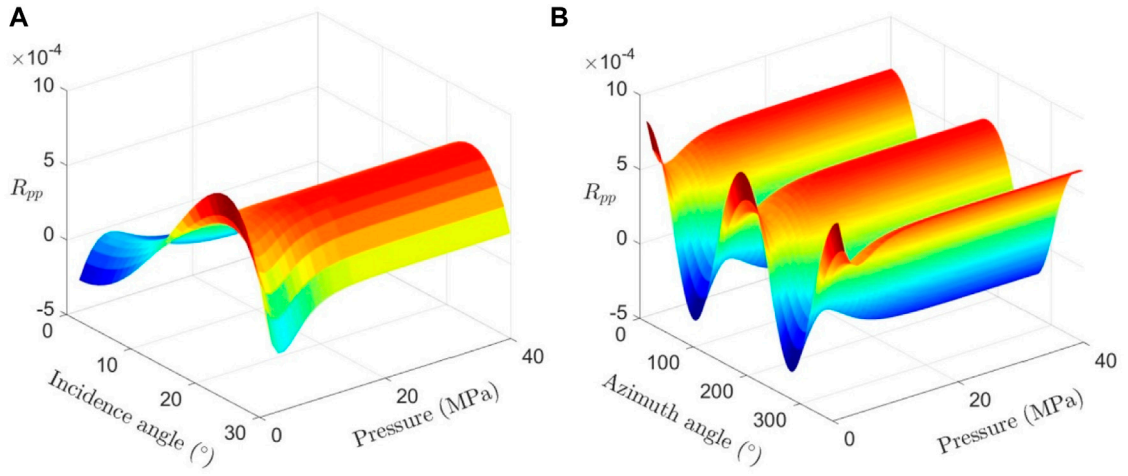


FIGURE 16
(A) Variation of the seismic reflection coefficient with stress and incident angle; **(B)** variation of the seismic reflection coefficient with stress and azimuth angles.

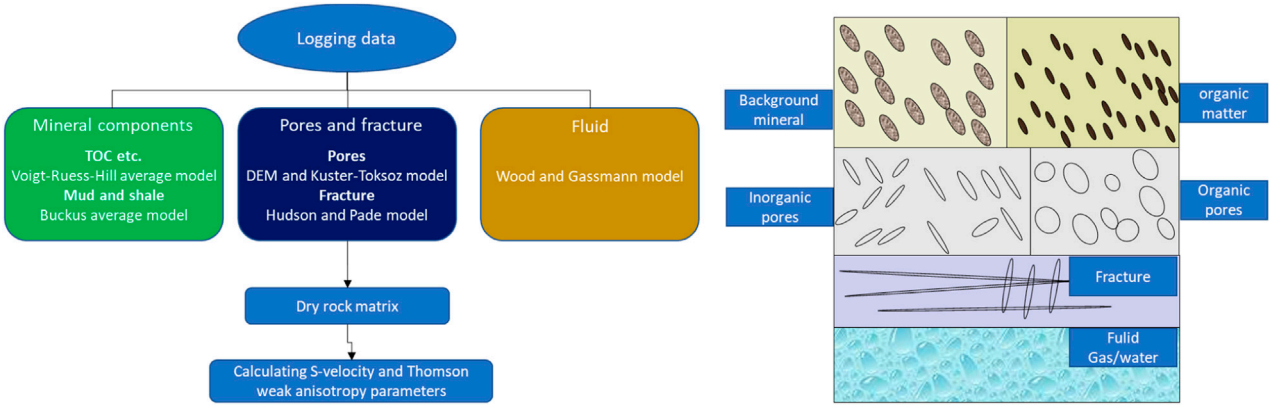


FIGURE 17
Rock physical modeling for Thomson weak anisotropy parameters.

parameters with the geostress sensitive parameter DHSR to describe the favorable areas for shale gas reservoir fracturing, as shown in Figure 17. Because the DHSR cannot be obtained by well logging directly, we consider the mineral components, pores and fracture, and fluid characteristics of shale gas reservoirs in the Sichuan Basin to establish the rock physical model to estimate the Thomson weak anisotropy parameter and the workflow of rock physical modeling.

Estimation of Thomson weak anisotropy parameters based on the rock physics model: the calculation results of longitudinal and shear waves are highly consistent with logging data, and the estimation of anisotropic parameters is reliable, as shown in Figure 18.

Ruger (1997) provided the reflection coefficient equation based on first-order perturbation theory, with the specific form as follows:

$$R_{pp}(\theta,\phi) = \frac{1}{2}\frac{\Delta Z}{\bar{Z}} + \frac{1}{2}\left\{\frac{\Delta a}{\bar{a}} - 4k^2\frac{\Delta G}{\bar{G}} + \left[\Delta\delta^{(V)} + 8k^2\Delta\gamma\right]\cos^2\phi\right\}\sin^2\theta + \frac{1}{2}\left\{\frac{\Delta\alpha}{\bar{\alpha}} + \Delta\varepsilon^{(V)}\cos^4\varphi + \Delta\delta^{(V)}\sin^2\varphi\cos^2\varphi\right\}\sin^2\theta\cos^2\theta,$$

where Z and ΔZ represent the mean value and difference of longitudinal wave impedance of upper and lower media, respectively; G and ΔG represent the mean value and difference of shear modulus of upper and lower media, respectively; α and $\Delta\alpha$ represent the mean value and difference of longitudinal wave velocity of upper and lower media, respectively; β represents the mean value of shear wave velocity of upper and lower media; $\Delta\delta^{(V)}\Delta\gamma\Delta\varepsilon^{(V)}$ represents the difference of anisotropy parameters of upper and lower media; θ represents the incidence angle; φ represents the azimuth angle, which refers to the included angle between the survey line direction and the fracture tendency.

According to Connolly (1999) and Martin (2001), the above equation is transformed into an azimuthal anisotropic elastic impedance form:

$$EI(\theta,\varphi) = (\alpha)^{a(\theta)}(\beta)^{b(\theta)}(\rho)^{c(\theta)}\exp\left(d(\theta,\varphi)\varepsilon^{(v)} + e(\theta,\varphi)\gamma + f(\theta,\varphi)\delta^{(v)}\right).$$

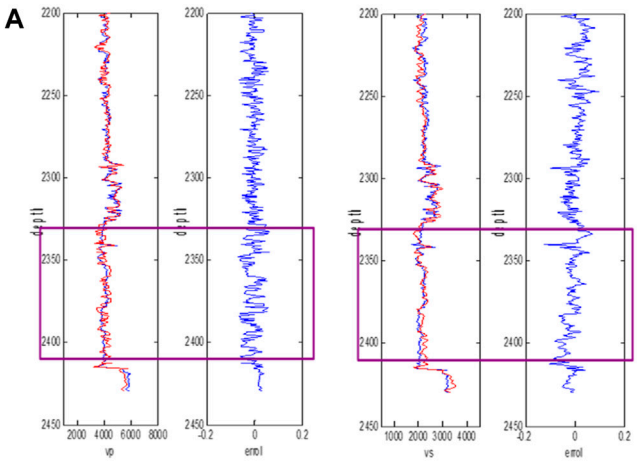


FIGURE 18
(A) Comparison between predicted Vp and Vs with actual well logging data; **(B)** calculation of Thomson weak anisotropy parameters by well logging data.

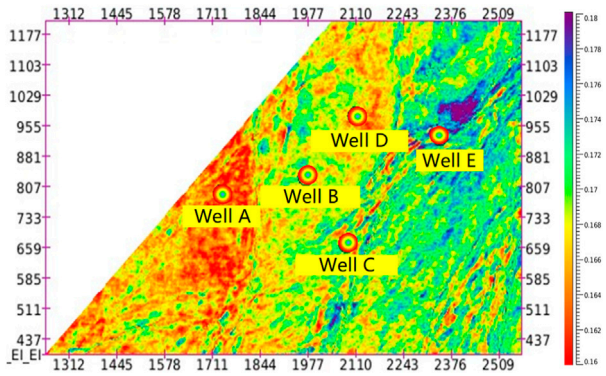


FIGURE 19
DHSR prediction plan of a shale gas work area in the Sichuan Basin.

In the above formula, the six coefficients that form a trigonometric functions relationship with azimuth and incident angles are expressed as follows:

$$a = \frac{1}{2}(1 + \tan^2\theta), \mathrm{b} = -4k^2\sin^2\theta, c = \frac{1}{2}(1 - 4\mathrm{k}^2\sin^2\theta), \mathrm{d} = \frac{1}{2}\sin^2\theta\cos^2\varphi(1 + \tan^2\theta\sin^2\varphi),$$

$$e = \frac{1}{2}\cos^4\varphi\sin^2\theta\tan^2\theta, f = 4k^2\sin^2\theta\cos^2\varphi.$$

By using the formula of azimuthal anisotropic elastic impedance for predicting geostress, the impedance value of azimuthal elastic impedance is shown to often decrease sharply with the change of the incident angle, which is not conducive to the analysis of geostress changes. Normalization of azimuthal anisotropic elastic impedance is performed to obtain the normalized elastic impedance form:

$$EI(\theta,\varphi) = \alpha_0\rho_0\left(\frac{\alpha}{\alpha_0}\right)^{a(\theta)}\left(\frac{\beta}{\beta_0}\right)^{b(\theta)}\left(\frac{\rho}{\rho_0}\right)^{c(\theta)}\exp(\mathrm{d}(\theta,\varphi)\varepsilon^{(\mathrm{v})} + \mathrm{e}(\theta,\varphi)\gamma + f(\theta,\varphi)\delta^{(\mathrm{v})}).$$

To obtain six anisotropic elastic parameters, six elastic resistance antibodies with different orientations and incidence angles are required. Substituting multiple azimuth and multiple incidence angles into the above equation, we obtain the following equation system:

$$\begin{bmatrix} \ln\left(\frac{EI(\theta_1,\varphi_1)}{EI_0}\right) \\ \ln\left(\frac{EI(\theta_2,\varphi_2)}{EI_0}\right) \\ \ln\left(\frac{EI(\theta_3,\varphi_3)}{EI_0}\right) \\ \ln\left(\frac{EI(\theta_4,\varphi_4)}{EI_0}\right) \\ \ln\left(\frac{EI(\theta_5,\varphi_5)}{EI_0}\right) \\ \ln\left(\frac{EI(\theta_6,\varphi_6)}{EI_0}\right) \end{bmatrix} = \begin{bmatrix} a(\theta_1) & \mathrm{b}(\theta_1) & c(\theta_1) & \mathrm{d}(\theta_1) & \mathrm{e}(\theta_1) & \mathrm{f}(\theta_1) \\ a(\theta_2) & \mathrm{b}(\theta_2) & c(\theta_2) & \mathrm{d}(\theta_2) & \mathrm{e}(\theta_2) & \mathrm{f}(\theta_2) \\ a(\theta_3) & \mathrm{b}(\theta_3) & c(\theta_3) & \mathrm{d}(\theta_3) & \mathrm{e}(\theta_3) & \mathrm{f}(\theta_3) \\ a(\theta_4) & \mathrm{b}(\theta_4) & c(\theta_4) & \mathrm{d}(\theta_4) & \mathrm{e}(\theta_4) & \mathrm{f}(\theta_4) \\ a(\theta_5) & \mathrm{b}(\theta_5) & c(\theta_5) & \mathrm{d}(\theta_5) & \mathrm{e}(\theta_5) & \mathrm{f}(\theta_5) \\ a(\theta_6) & \mathrm{b}(\theta_6) & c(\theta_6) & \mathrm{d}(\theta_6) & \mathrm{e}(\theta_6) & \mathrm{f}(\theta_6) \end{bmatrix} \times \begin{bmatrix} \ln(\alpha/\alpha_0) \\ \ln(\beta/\beta_0) \\ \ln(\rho/\rho_0) \\ \varepsilon^{(\mathrm{v})} \\ \gamma \\ \delta^{(\mathrm{v})} \end{bmatrix}.$$

Based on the regression calculation of the elastic impedance of the well bypass and logging data, the coefficient matrix is obtained. By multiplying the data for inverted elastic impedance from different angles at each sampling point by the inverse of the coefficient matrix, the anisotropic elastic parameters at each point can be obtained. According to the wide-azimuth seismic inversion technology, necessary parameters can be obtained, which can then be used to calculate the DHSR.

Figure 19 shows the DHSR prediction results of a shale gas work area in the Sichuan Basin. The prediction results are highly consistent with the core test results, verifying the effectiveness of the method. This achievement has been successfully applied to the shale gas well location deployment and fracturing scheme design in

the work area, realizing the fine evaluation of the "sweet spot" of the project.

5 Conclusion

Under the condition of horizontal two-way geostress clamping in a faultless geological body, the propagation speed of longitudinal wave velocity along the maximum horizontal principal stress direction is the highest. For a stress difference less than 20 MPa, the greater the stress difference, the more obvious the AVAZ characteristics of the longitudinal wave, laying a theoretical foundation for conducting geostress prediction based on prestack seismic inversion.

The geostress orientation inside the geological body is greatly affected by geostress shielding. When the geological body has a fault, the geostress orientation only shows a certain deflection at the end of the fault. The internal principal stress orientation is almost consistent with the geostress orientation. The prediction of the geostress orientation based on seismic anisotropy needs to be further carried out by comprehensively considering the geostress and structural characteristics.

The theory of seismic prediction technology for geostress difference is solid, and the technology is mature, which can be further applied.

Data availability statement

The data analyzed in this study are subject to the following licenses/restrictions: dataset will not be publicly available without PetroChina permission. Requests to access these datasets should be directed to Wang Cen, wangc2018@petrochina.com.cn.

Author contributions

CW: conceptualization, data curation, formal analysis, methodology, software, writing–original draft, and writing–review and editing. CY: supervision and writing–review and editing. XS: funding acquisition, resources, and writing–review and editing. DZ: project administration, validation, and writing–review and editing. ML: investigation and writing–review and editing. RZ: data curation and writing–review and editing.

Funding

The author(s) declare that no financial support was received for the research, authorship, and/or publication of this article.

Acknowledgments

The authors are grateful for the financial support from the following institutions: Scientific research project fund of PetroChina Southwest Oil and Gasfield Company, "20210304-02".

Conflict of interest

Authors CW, XS, DZ, ML, and RZ were employed by PetroChina Southwest Oil and Gasfield Company.

The remaining author declares that the research was conducted in the absence of any commercial or financial relationships that could be construed as a potential conflict of interest.

Publisher's note

All claims expressed in this article are solely those of the authors and do not necessarily represent those of their affiliated organizations, or those of the publisher, the editors, and the reviewers. Any product that may be evaluated in this article, or claim that may be made by its manufacturer, is not guaranteed or endorsed by the publisher.

References

Craig, D. P. (2014). "New type curve analysis removes limitations of conventional after-closure analysis of DFIT data. SPE 168988-MS," in Proceedings of the Paper presented at the SPE Unconventional Resources Conference, The Woodlands, TX, April 2014.

Detournay, C., Damjanac, B., Torres, M., Cundall, P., Ligocki, L., and Gil, I. (2022). Heat advection and forced convection in a lattice code–Implementation and geothermal applications. *Rock Mech. Bull.* 1 (1), 100004. doi:10.1016/j.rockmb.2022.100004

Dontsov, E. V. (2022). Analysis of a constant height hydraulic fracture driven by a power-law fluid. *Rock Mech. Bull.* 1 (1), 100003. doi:10.1016/j.rockmb.2022.100003

Hayavi, M. T., and Abdideh, M. (2016). Estimation of insitu horizontal stresses using the linear poroelastic model and minifrac test results in tectonically active area. *Russ. J. Earth Sci.* 16 (4), 1–9. doi:10.2205/2016es000576

He, R., Yang, J., Li, L., Yang, Z., Chen, W., Zeng, J., et al. (2023). Investigating the simultaneous fracture propagation from multiple perforation clusters in horizontal wells using 3D block discrete element method. *Front. Earth Sci.* 11, 1115054. doi:10.3389/feart.2023.1115054

Huang, J., Shahri, M. P., and Perez, O. (2017). "An integrated approach to constrain geostress field: comprehensive geomechanical analysis," in Proceedings of the Paper presented at the 51st US Rock Mechanics/Geomechanics Symposium held in San Francisco, California, USA, June 2017, 25–28.

Huang, L., Dontsov, E. V., Fu, H., Lei, Y., Weng, D., and Zhang, F. (2022). Hydraulic fracture height growth in layered rocks: perspective from DEM simulation of different propagation regimes. *Int. J. Solids Struct.* 238, 111395. doi:10.1016/j.ijsolstr.2021.111395

Huang, L., He, R., Yang, Z., Tan, P., Chen, W., Li, X., et al. (2023b). Exploring hydraulic fracture behavior in glutenite formation with strong heterogeneity and variable lithology based on DEM simulation. *Eng. Fract. Mech.* 278, 109020. doi:10.1016/j.engfracmech.2022.109020

Huang, L., Liu, J., Ji, Y., Gong, X., and Qin, L. (2018). A review of multiscale expansion of low permeability reservoir cracks. *Petroleum* 4, 115–125. doi:10.1016/j.petlm.2017.09.002

Huang, L., Liu, J., Zhang, F., Dontsov, E., and Damjanac, B. (2019). Exploring the influence of rock inherent heterogeneity and grain size on hydraulic fracturing using discrete element modeling. *Int. J. Solids Struct.* 176, 207–220. doi:10.1016/j.ijsolstr.2019.06.018

Huang, L., Liu, J., Zhang, F., Fu, H., Zhu, H., and Damjanac, B. (2020). 3D lattice modeling of hydraulic fracture initiation and near-wellbore propagation for different perforation models. *J. Petroleum Sci. Eng.* 191, 107169. doi:10.1016/j.petrol.2020.107169

Huang, L., Tan, J., Fu, H., Liu, J., Chen, X., Liao, X., et al. (2023a). The non-plane initiation and propagation mechanism of multiple hydraulic fractures in tight reservoirs considering stress shadow effects. *Eng. Fract. Mech.* 292, 109570. doi:10.1016/j.engfracmech.2023.109570

Ji, Y., Wang, J., and Huang, L. (2015). Analysis on inflowing of the injecting Water in faulted formation. *Adv. Mech. Eng.* 7, 1–10.

Karadeniz, K. E. (2019). *Geostress magnitude and orientation determination of Ankara Kazan district from FMI log*. Ankara, Türkiye: Middle East Technical University.

Liu, Q., Li, J., Liang, B., Liu, J., Sun, W., He, J., et al. (2023). Complex wettability behavior triggering mechanism on imbibition: a model construction and comparative study based on analysis at multiple scales. *Energy* 275, 127434. doi:10.1016/j.energy.2023.127434

Luo, H., Xie, J., Huang, L., Wu, J., Shi, X., Bai, Y., et al. (2022). Multiscale sensitivity analysis of hydraulic fracturing parameters based on dimensionless analysis method. *Lithosphere* 2022, 9708300. doi:10.2113/2022/9708300

Schoenball, M., and Ellsworth, W. L. (2017). A systematic assessment of the spatiotemporal evolution of fault activation through induced seismicity in Oklahoma and southern Kansas. *JGR Solid Earth* 122 (12), 10189–10206. doi:10.1002/2017jb014850

Song, R., Liu, J., and Cui, M. (2017). A new method to reconstruct structured mesh model from micro-computed tomography images of porous media and its application. *Int. J. Heat Mass Transf.* 109, 705–715. doi:10.1016/j.ijheatmasstransfer.2017.02.053

Song, R., Liu, J., Yang, C., and Sun, S. (2022). Study on the multiphase heat and mass transfer mechanism in the dissociation of methane hydrate in reconstructed real-shape porous sediments. *Energy* 254, 124421. doi:10.1016/j.energy.2022.124421

Song, R., Wang, Y., Ishutov, S., Zambrano-Narvaez, G., Hodder, K. J., Chalaturnyk, R. J., et al. (2020). A comprehensive experimental study on mechanical behavior, microstructure and transport properties of 3D-printed rock analogs. *Rock Mech. Rock Eng.* 53, 5745–5765. doi:10.1007/s00603-020-02239-4

Tan, P., Chen, Z., Fu, S., and Zhao, Q. (2023). Experimental investigation on fracture growth for integrated hydraulic fracturing in multiple gas bearing formations. *Geoenergy Sci. Eng.* 231, 212316. doi:10.1016/j.geoen.2023.212316

Tan, P., Jin, Y., Han, K., Hou, B., Chen, M., Guo, X., et al. (2017). Analysis of hydraulic fracture initiation and vertical propagation behavior in laminated shale formation. *Fuel* 206, 482–493. doi:10.1016/j.fuel.2017.05.033

Wang, C., Yin, C., Shi, X., Pan, S., Gou, Q., Zhang, D., et al. (2022). Direct prediction method of fracturing ability in shale formations based on pre-stack seismic inversion. *J. seismic Explor*.

Wu, M., Jiang, C., Song, R., Liu, J., Li, M., Liu, B., et al. (2023). Comparative study on hydraulic fracturing using different discrete fracture network modeling: insight from homogeneous to heterogeneity reservoirs. *Eng. Fract. Mech.* 284, 109274. doi:10.1016/j.engfracmech.2023.109274

Xu, S., Singh, A., and Zoback, M. D. (2019). "Variation of the least principal stress with depth and its effect on vertical hydraulic fracture propagationduring multi-stage hydraulic fracturing," in Proceedings of the Paper presented at the 53rd U.S. Rock Mechanics/Geomechanics Symposium, New York, New York, USA, June 2019.

Yang, M., Liu, X., Jiao, D., et al. (2013). "Hydraulic fracture design flaws- proppant selection. Presented at the SPE western regional and AAPG pacific section meeting," in Proceedings of the Paper presented at the SPE Western Regional and AAPG Pacific Section Meeting 2013 Joint Technical Conference, Monterey, California, USA, April 2013.

Zhang, F., Huang, L., Yang, L., Dontsov, E., Weng, D. W., Liang, H. B., et al. (2022). Numerical investigation on the effect of depletion-induced stress reorientation on infill well hydraulic fracture propagation. *Petroleum Sci.* 19 (1), 296–308. doi:10.1016/j.petsci.2021.09.014

Zhang, T., Luo, S., Zhou, H., Hu, H., Zhang, L., Zhao, Y., et al. (2023). Pore-scale modelling of water sorption in nanopore systems of shale. *Int. J. Coal Geol.* 273, 104266. doi:10.1016/j.coal.2023.104266

Zheng, Y., He, R., Huang, L., Bai, Y., Wang, C., Chen, W., et al. (2022). Exploring the effect of engineering parameters on the penetration of hydraulic fractures through bedding planes in different propagation regimes. *Comput. Geotechnics* 146, 104736. doi:10.1016/j.compgeo.2022.104736

frontiers | Frontiers in Energy Research

TYPE Original Research
PUBLISHED 23 January 2024
DOI 10.3389/fenrg.2023.1330550

Check for updates

OPEN ACCESS

EDITED BY
Liuke Huang,
Southwest Petroleum University, China

REVIEWED BY
You Zhang,
PetroChina Hangzhou Research Institute of Geology, China
Jiawei Li,
Schlumberger, United States
Song Hong-Wei,
Yangtze University, China

*CORRESPONDENCE
Bolong Zhu,
zblong1109@163.com

RECEIVED 31 October 2023
ACCEPTED 20 December 2023
PUBLISHED 23 January 2024

CITATION
Qi H, Li D, Zhao J, Ma H, Wang X, Wang X, Zhu B, Lin J and Zhao X (2024), The experimental and numerical analysis of elastic rock mechanical properties in tight conglomerate rock samples: a case study in Junggar Basin.
Front. Energy Res. 11:1330550.
doi: 10.3389/fenrg.2023.1330550

COPYRIGHT
© 2024 Qi, Li, Zhao, Ma, Wang, Wang, Zhu, Lin and Zhao. This is an open-access article distributed under the terms of the Creative Commons Attribution License (CC BY). The use, distribution or reproduction in other forums is permitted, provided the original author(s) and the copyright owner(s) are credited and that the original publication in this journal is cited, in accordance with accepted academic practice. No use, distribution or reproduction is permitted which does not comply with these terms.

The experimental and numerical analysis of elastic rock mechanical properties in tight conglomerate rock samples: a case study in Junggar Basin

Hongyan Qi[1], Danyang Li[1], Jun Zhao[1], Hailong Ma[1], Xueliang Wang[2], Xianhu Wang[2], Bolong Zhu[3,4]*, Jiaying Lin[3,4] and Xiangyun Zhao[3,4]

[1]Research Institute of Exploration and Development, PetroChina Xinjiang Oilfield Company, Karamay, China, [2]Xinjiang Branch, China National Logging Corporation, Karamay, China, [3]College of Petroleum Engineering, China University of Petroleum—Beijing at Karamay, Karamay, China, [4]College of Petroleum Engineering, China University of Petroleum (Beijing), Beijing, China

Tight conglomerate rocks consist of gravels and rock matrices. The existence of these stiff gravels leads to heterogeneity in conglomerates and makes it difficult to characterize rock mechanical properties, which then affects drilling and hydraulic fracturing operations in tight conglomerate hydrocarbon-bearing reservoirs. This case study introduces a series of experimental and numerical analyses for the better understanding of rock deformation and elastic wave propagation patterns in a tight conglomerate reservoir in Junggar Basin, China. Tri-axial compression tests, acoustic test, and finite element modeling of rock deformation and elastic wave propagation in conglomerate rocks are presented. Experimentally tested samples exhibit good brittleness and shearing failure patterns, while well correlated static-dynamic elastic moduli and P-S wave velocities are captured. Numerical results show that the existence of stiff gravels leads to strong direction-dependent stress and strain anisotropies. Stress concentrations are also induced by gravels radially and axially. In the elastic wave domain, stiff gravels facilitate the propagation of elastic waves. The gravel close to the wave source also induces stronger compressive/tensile states in the wave domain, indicating that the existence of gravels in conglomerates can alter waveforms. This integrated approach improves the quantitative understanding of stress, strain, and elastic wave responses in heterogeneous tight conglomerates. This case study also serves as a reference for the brittleness evaluation and geomechanical evaluation in the study area. The contribution of this work is primarily about the integrated experimental study, solid deformation modeling, and elastic wave modeling of tight conglomerate rocks.

KEYWORDS

tight rock, experimental study, numerical study, field study, deformation

1 Introduction

Tight conglomerate rocks are often characterized with heterogeneity and low permeability and porosity. They have attracted increasing attention as a significant source of hydrocarbon production in unconventional reservoirs (Zou et al., 2012; Ji et al., 2015). The exploitation of these complex reservoirs requires advanced experimental and simulation techniques to optimize engineering strategies and relevant parameters (Li, 2022). In this process, improving the understanding of the rock mechanical properties of reservoir rocks is critical as they directly affect the quality of drilling and fracturing operations. Typically, experimental and numerical techniques are often used for the characterization of rock mechanical properties.

Experimental strategies have evolved significantly over the past years to enhance the understanding of the rock physical and mechanical properties and behaviors of tight rocks under certain conditions. Core analysis is a widely used technique for determining the petrophysical properties of tight rocks (Ross and Bustin, 2009; Yin et al., 2020). Wang et al. (2016) investigated the impact of confining pressure on the permeability alteration of tight sandstone cores using a triaxial method. Their findings revealed the stress-dependent behavior of permeability, which provides valuable insights into the fluid flow characteristics of tight rocks under reservoir conditions. To analyze the structural and mechanical properties at multilevel, some advanced techniques such as micro-CT scanning and nanoindentation have been employed in several tests (Javadpour et al., 2007; He et al., 2021; Liang et al., 2007; Yao et al., 2023). In a sophisticated study, Qiao et al. (2021) employed micro-CT imaging and image analysis techniques to investigate the effect of rock fabric on the pore structure and permeability of tight sandstone. Their study highlighted the relationship between pore connectivity and permeability, contributing to a better understanding of fluid flow mechanisms in tight rocks. Moreover, experimental studies have focused on fluid flow behavior in tight rocks. Pulse-decay permeability measurements have been instrumental in understanding the complex fluid flow mechanisms in these low-permeability formations (Cui et al., 2009; Ju et al., 2023). Jia et al. (2017) employed pulse-decay permeability tests to investigate the impact of mineral composition and confining pressure on the permeability of tight carbonate reservoir rocks. Their study revealed the important role of mineralogy in determining the rock physical behaviors of tight rocks, providing valuable insights for reservoir characterization and production optimization. Tracer studies have also provided insights into the diffusion and adsorption behavior of hydrocarbons in tight rocks (Zhai et al., 2014; Yuan et al., 2014). Specifically, Zhang et al. (2014) utilized radioactive tracers to investigate the diffusion and sorption characteristics of natural gas in tight shale formations. Their study revealed the impact of organic matter content and clay mineralogy on the sorption behavior of methane, contributing to a better understanding of gas storage and transport in tight shale reservoirs. Furthermore, the use of advanced experimental techniques such as acoustic emission monitoring and rock deformation tests has enabled the characterization of the mechanical properties and deformation behaviors of tight rocks under stress conditions (Zhou et al., 2013; Lei et al., 2017; Zhang et al., 2019). These studies have provided insights into the mechanical response and formation stability of tight reservoirs. They help to optimize the design of hydraulic fracturing and wellbore stability analysis. In a combined study using both experimental and numerical methods, Chen et al. (2021a) proposed a methodology to quantify the complex and heterogeneous tight conglomerate reservoir rock behaviors under tri-axial compression. A numerical model was calibrated by parameters obtained in the rock mechanical tests. Then, the model was used to characterize the stress and strain within the cores, which could not be quantified solely by tri-axial tests.

Numerical simulation techniques have been proved to be useful in the understanding of physical and mechanical properties of tight rocks. Due to the low permeability and complex pore structure nature of tight reservoir rocks, simplified numerical models often struggle to accurately represent the complex flow mechanisms in tight rocks (Clarkson and Pedersen, 2010; Guo et al., 2016). Consequently, some specialized techniques have been developed to address these challenges. Dual-porosity and dual-permeability models have been widely employed to account for matrix-fracture interactions in tight rocks (Warren and Root, 1963; Li et al., 2020; Zhong et al., 2020; Song et al., 2023). Nasrollahzadeh et al. (2021) used a dual-porosity model to simulate gas production from fractured tight sandstone reservoirs. To better the understanding of rock mechanical behaviors, the study incorporated geomechanical effects such as stress-dependent permeability and porosity to improve the accuracy of production forecasting. Discrete fracture network (DFN) models are also used for the simulation of the complex fracture networks in tight rocks (Karimi-Fard et al., 2003; Li et al., 2019; Zhang et al., 2019). Li et al. (2019) employed a DFN model to study the effects of fracture network characteristics on the depletion behaviors of tight carbonate reservoirs. They quantified the influence of fracture density, orientation, and connectivity on reservoir responses, providing important insights for optimal well placement and production strategies. The quantitative relationship between non-planar fracture geometries and stress shadow is also a relevant factor (Huang et al., 2023). 3D lattice modeling has also been employed to understand the initiation of fracture and wellbore tortuosity effects (Huang et al., 2020). Bedding planes can be reliably quantified by the discrete element method considering fracture height growth (Luo et al., 2022; Zheng et al., 2022). Pore-scale models based on digital rock analysis are also regarded as valuable tools for understanding multiphase flow and transport processes and deformation processes in tight rocks (Andrade et al., 2013; Prodanović et al., 2015; Zhou et al., 2023). In addition to these techniques, recent advancements in computational methods have allowed for the development of coupled reservoir-geomechanical models to better understand the interaction between fluid flow, heat transfer, and solid rock deformation in tight reservoirs (Guo et al., 2018; Wang et al., 2018; Zhang et al., 2019). These models couple geomechanical effects such as stress-induced changes in rock properties with fluid flow processes. They enable a comprehensive assessment of reservoir behavior. As an example, in a series of studies, Sangnimnuan et al. (2018), Guo et al. (2021) and Guo et al. (2023) proposed a coupling strategy for the quantification of temporal and spatial evolution of pressure, stress, and temperature in hydrocarbon-bearing formation, where stress-dependent reservoir rock behaviors are comprehensively analyzed. The characterization of rock deformation and failure requires the use of accurate modeling techniques. For example, displacement

discontinuity methods in 2D and 3D and their combination with joint elements can help to improve the understanding of stress evolutions caused by fracturing (Li et al., 2022; Li and Wu, 2022).

Experimental and numerical methods have been widely used to measure and quantify rock mechanical properties in tight rocks. In this study, a case study is introduced where an integrated experimental and numerical workflow is proposed for the improved understanding of highly heterogeneous and tight conglomerate reservoir rocks in Mahu Sag, Junggar Basin, China. Tri-axial compression tests, P and S wave velocity measurements, and finite element modeling of the solid deformation process are involved in the methodology. This case study provides a reference for the quantification of rock mechanical properties in highly heterogeneous conglomerate rocks in tight hydrocarbon-bearing reservoirs. The observations in the study can be used in the determination of optimum well drilling and completion strategies.

2 Methodology

This study involves rock mechanical tests and numerical modeling. In the rock mechanical tests, tri-axial compression tests and acoustic testing are employed. In the numerical modeling, a finite element modeling technique is used to solve for the stress distributions in the heterogeneous rock samples.

2.1 Rock mechanical tests

In the experimental method, the tests are conducted using the GCTS high-temperature and high-pressure rock mechanics experimental platform, which enables triaxial compression tests and acoustic testing under high-temperature and high-pressure conditions. During the test, the rock sample is placed inside the triaxial compression testing machine and immersed in a container filled with silicone oil. By applying pressure to the silicone oil, confining pressure is applied to the rock sample. This method considers the principal stress conditions in hydrocarbon-bearing reservoirs. The static rock mechanical parameters, such as elastic modulus and Poisson's ratio, are determined based on the stress and strain results. In addition, by increasing the temperature of the silicone oil containing the sample, a more realistic subsurface temperature condition can be obtained. Thus, the test can be conducted at specific confining pressures and temperatures to improve the reliability.

The acoustic testing is also conducted. The purpose of this experiment is to measure the compressional and shear wave velocities (Vp and Vs) of the reservoir rock samples using the ultrasonic pulse transmission method in order to obtain dynamic elastic parameters. In the experiment, compressional and shear waves are emitted from the transducer placed at the top of the rock sample and received by the receiver placed at the bottom. The time required for the compressional and shear waves to propagate along the axial direction of the rock sample is calculated from the acoustic waveforms. The transit times of the compressional and shear waves through the reservoir rock sample can be calculated using the following formula, which provides the required compressional and shear wave velocity data:

$$t_P = t_P^{'} - t_{P0} \tag{1}$$

$$t_S = t_S^{'} - t_{S0} \tag{2}$$

In Eq. 1 and Eq. 2, where t_P and t_S are the transit times of the P and S waves through the sample; $t_P^{'}$ and $t_S^{'}$ are the transit times of the P and S waves measured between the transducer and the receiver; t_{P0} and t_{S0} are the transit times of P and S waves through the holders of the testing machine. Thus, the actual transit times through the rock can be calculated.

2.2 Numerical modeling

The previous section introduces the rock mechanical testing method where tri-axial compression tests and acoustic tests are employed. They can provide the stress, strain, and wave velocities of the entire rock sample. A limitation is that the rock deformation patterns within the rock cannot be directly characterized by the experimental results. To improve the methodology, numerical modeling is used so that the rock deformation patterns within the entire domain can be understood.

In this method, the assumptions of the quasi-static state and infinitesimal deformation are used (Chen B. et al., 2021). Based on these, the momentum balance can be described using the Cauchy stress tensor as:

$$\nabla \cdot \boldsymbol{\sigma} = 0 \tag{3}$$

In Eq. 3, where $\boldsymbol{\sigma}$ is the stress tensor. It describes the quasi-static momentum balance.

The constitutive relationship between the stress and strain for the description of rock deformation is given as:

$$\boldsymbol{\sigma}_{el} = \mathbf{C} : \boldsymbol{\varepsilon}_{el} \tag{4}$$

In Eq. 4, where $\mathbf{C}$ is the elasticity tensor; $\boldsymbol{\varepsilon}_{el}$ is the elastic strain. Also, the elastic strain $\boldsymbol{\varepsilon}_{el}$ and the inelastic $\boldsymbol{\varepsilon}_{inel}$ strain follow a relationship of $\boldsymbol{\varepsilon} = \boldsymbol{\varepsilon}_{el} + \boldsymbol{\varepsilon}_{inel}$. Note that the elasticity tensor can be written as Eq. 5:

$$\mathbf{C} = \mathbf{C}(E, \nu) \tag{5}$$

Based on the infinitesimal deformation theories and elastic derivations, the relationship between strain and displacement can be related as Eq. 6:

$$\boldsymbol{\varepsilon} = \frac{1}{2}\left[(\nabla \mathbf{u})^{\mathrm{T}} + (\nabla \mathbf{u})\right] \tag{6}$$

When the state of isotropy is considered, the elasticity can be expressed as Eq. 7:

$$\mathrm{D} = \frac{E}{(1+\nu)(1-2\nu)} \begin{bmatrix} 1-\nu & \nu & \nu & & & \\ \nu & 1-\nu & \nu & & & \\ \nu & \nu & 1-\nu & & & \\ & & & \frac{1-2\nu}{2} & & \\ & & & & \frac{1-2\nu}{2} & \\ & & & & & \frac{1-2\nu}{2} \end{bmatrix} \tag{7}$$

For this problem, several relevant boundary conditions can be used. The traction boundary conditions can be expressed by:

$$\boldsymbol{\sigma} \cdot \mathbf{n} = \boldsymbol{t} \tag{8}$$

$$\boldsymbol{t} = \boldsymbol{P} \cdot \mathbf{n} \tag{9}$$

$$\mathbf{u} = 0 \tag{10}$$

In Eq. 8, where $\mathbf{n}$ represents the normal vector; In Eq. 9, $\boldsymbol{P}$ represents the nominal stress or the pressure boundary; $\boldsymbol{t}$ represents the traction boundary. Eq. 10 is used to prescribe the fixed boundary where no displacement is allowed.

The equations above describe the rock deformation caused by the exertion of boundary loads on the studied domain. Then, the governing equations for the elastic wave propagation in the domain representing the rock sample are also provided. They can be used to quantify the wave propagation in the domain, which is especially meaningful for heterogeneous rock samples such as conglomerates.

In an elastic domain, the relationship between velocity and strain can be expressed as Eq. 11, Eq. 12 and Eq. 13:

$$\rho \frac{\partial \mathbf{v}}{\partial t} - \nabla \cdot \boldsymbol{\sigma} = \boldsymbol{b} \tag{11}$$

$$\frac{\partial \boldsymbol{\varepsilon}}{\partial t} - \frac{1}{2}\left[\nabla \mathbf{v} - (\nabla \mathbf{v})^{\mathrm{T}}\right] = 0 \tag{12}$$

$$\boldsymbol{\sigma} = \mathbf{C}\colon \boldsymbol{\varepsilon}\,(\text{elastic wave domain}) \tag{13}$$

where $\mathbf{v}$ is the velocity; ρ is the density of the rock; $\boldsymbol{b}$ is the body force possibly exerted on the entire domain. It governs the transient behaviors associated with elastic wave propagations.

3 Case study

This case study is based on tight conglomerated rock samples cored in Mahu Sag, Junggar Basin, China. Tight oil reservoirs in this region have been commercially developed (Wang et al., 2022a; Wang et al., 2022b). The implementation of horizontal well drilling and hydraulic fracturing has largely improved the productivity here (Chen et al., 2021b; Zhi et al., 2021). Unlike tight sand reservoirs or shale reservoirs, tight conglomerate reservoirs have strong heterogeneities caused by the existence of gravels. Conventional compression tests and acoustic tests only obtain the entire stress-strain behaviors and waveforms, and they do not always suit the case in tight conglomerate rock.

In the study area, tight conglomerate rocks are composed of matrix, cement, and gravels, exhibiting strong mechanical heterogeneity and anisotropy. The gravels are embedded in the rock matrix and conglomerates usually exhibit heterogeneous patterns. Thus, their response to loadings can be rather complex. As a result, the accuracy of interpreting elastic parameters such as elastic modulus and Poisson's ratio through acoustic logging is affected, thus increasing the uncertainty in brittleness evaluation and fracability assessment, consequently influencing the effectiveness of drilling and fracturing operations. In order to improve the accuracy of elastic parameter interpretation for tight conglomerate rocks, this study focuses on the lab measurements of tight conglomerate rock cores. By utilizing a high-temperature and high-pressure triaxial rock mechanics test and simultaneous testing of compressional and shear wave velocities, static elastic parameters, and waveforms, the study establishes the conversion relationship between the dynamic and static elastic properties of rock samples. The established conversion relationship between dynamic elastic properties (based on P and S wave velocity measurement) and static elastic properties (based on compression tests) can be a reference for acoustic logging interpretation as some acoustic logs provide P and S wave velocity data within continuous ranges of depth intervals.

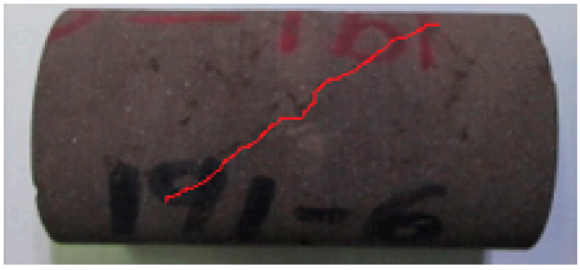


FIGURE 1
Failure plane caused by the tri-axial compression of the tight conglomerate rock sample.

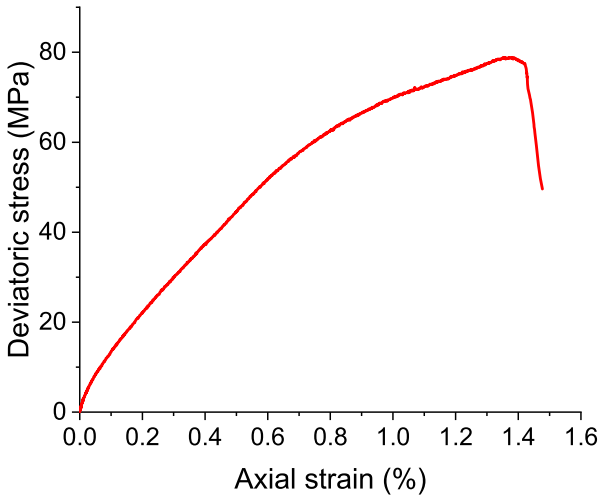


FIGURE 2
Stress and strain curve of the tight rock sample.

In this study, a tight rock sample is first examined by the tri-axial compression test and the acoustic test. Then, a 2D finite element model is established to analyze the rock deformation and elastic waves in the domain. Finally, a sensitivity analysis is established to study the effect of gravel properties on static deformation and wave propagation behaviors.

3.1 Rock mechanical testing results

3.1.1 Compression test for static rock mechanical parameters

The compression test is achieved in the GCTS RTR-1500 rock mechanical testing platform. Figure 1 shows the typical rock sample with a failure plane caused by the tri-axial compression

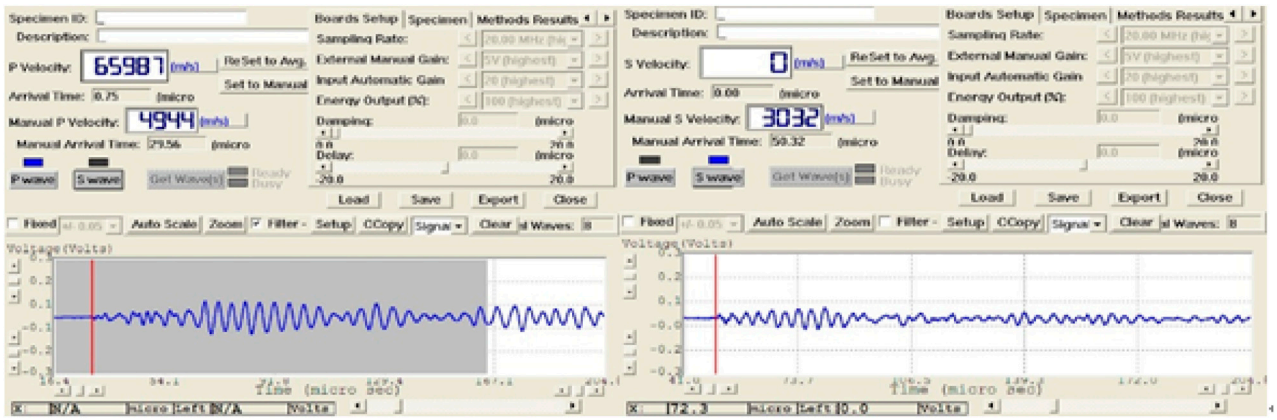


FIGURE 3
Recorded testing readings from the lab.

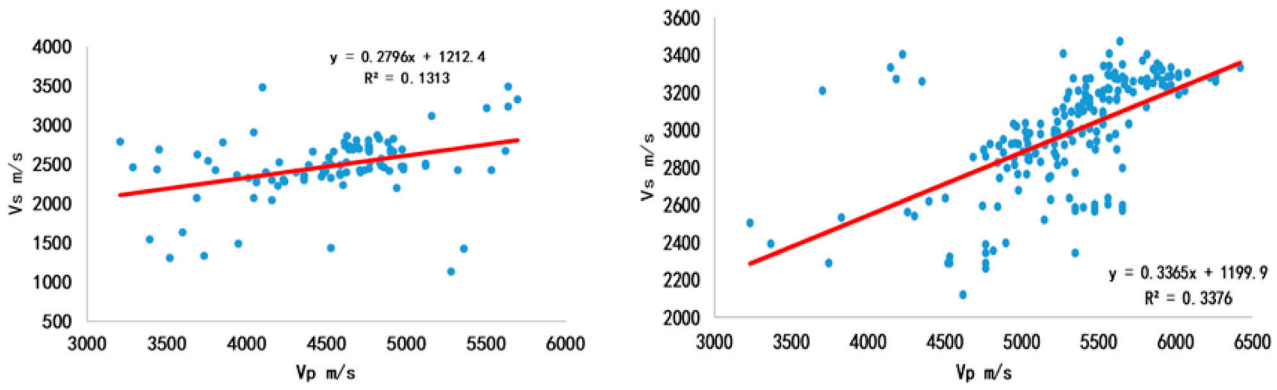


FIGURE 4
Correlations between primary and shear wave velocities.

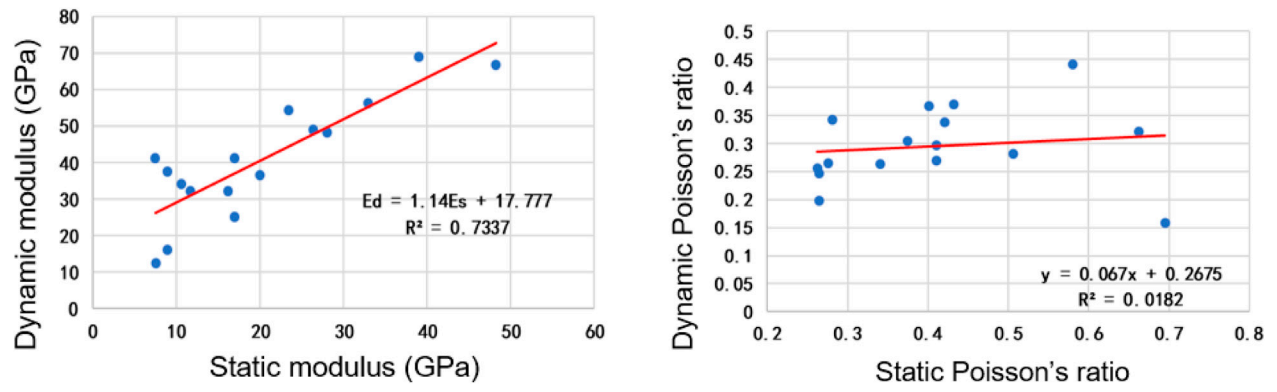


FIGURE 5
Correlations between static and dynamic properties for samples obtained from different wells.

test in this study. The shear failure plane can be clearly observed. Some gravels can be observed in the sample and they are embedded in the matrix, leading to a relatively complex structure. It can be also observed that the shear failure plane is not strictly even as the existence of gravels results in curvatures. This is primarily caused by the existence of gravels in the tight

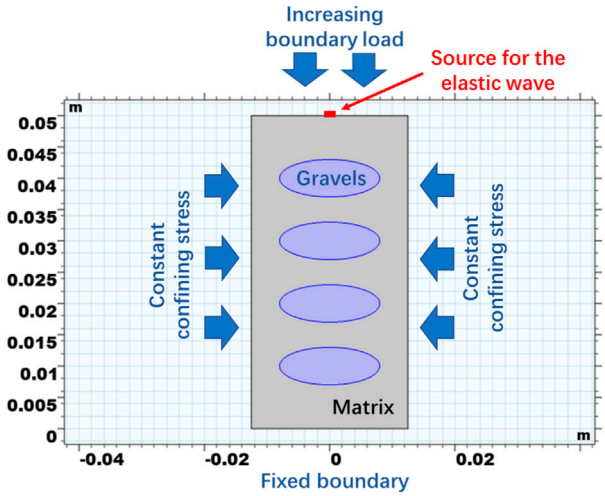


FIGURE 6
Correlations between static and dynamic properties for samples obtained from different wells.

rock sample, and the curved failure plane is associated with the boundaries and shapes of the embedded gravels.

Figure 2 shows the stress and strain curve obtained during the compression test. During the test, a constant confining pressure of 40 MPa is used. At the starting point, the axial stress is equal to the constant confining pressure. Then, the axial stress is gradually increased and the deviatoric stress becomes greater than 0. The deviatoric stress and axial strain result shows that the rock sample exhibits elastoplastic behaviors before the peak strength. When the axial strain is relatively small, nearly linear and inelastic behaviors are observed. After reaching the peak strength, the shear failure leads to a relative fast failure of the rock sample. Since the failure of the rock sample is achieved with a relatively low strain, the rock sample exhibits brittle deformation patterns in the compression test.

3.1.2 Acoustic test for dynamic rock mechanical parameters

In addition, acoustic testing is conducted for this rock sample. This test is based on the ULT-200 ultrasonic velocity measurement system.

In the testing, both raw data and processes data can be obtained. The raw data exhibits significant fluctuations, but through waveform analysis using the rock mechanics experimental platform, the processed and corrected waveform results are obtained. By employing the ultrasonic wave module for processing, the P-wave and S-wave waveforms are extracted, which improves the accuracy of compressional and shear wave velocity measurements. The fluctuations in the raw data can be attributed to various factors, including measurement noise, sample heterogeneity, and experimental conditions. To enhance the accuracy and reliability of the results, waveform analysis is performed, which involves filtering, time correction, and other processing techniques to extract the desired compressional and shear wave signals. As shown in Figure 3, the results present the processed and corrected waveform results obtained from the acoustic testing. The waveform analysis helps to remove noise and improve the clarity of the waveforms, enabling a more accurate determination of the compressional and shear wave velocities. The corrected waveforms provide valuable information about the wave propagation characteristics and elastic properties of the rock samples. The use of the ultrasonic wave module for waveform processing enhances the precision of compressional and shear wave velocity measurements. By accurately extracting the P-wave and S-wave waveforms, the acoustic testing results become more reliable and can be used to calculate dynamic elastic modulus, Poisson's ratio, and other elastic parameters important for reservoir characterization and rock mechanics analysis.

The obtaining and processing of signals are important in the determination of wave velocity values. The analog-to-digital converter helps to obtain the digital forms. Certain enhancement techniques are then employed. Here, filtering and amplification processes are carried out to remove unwanted noises and frequencies and to improve the signal strength. After theses processes, the time-of-flight data can be obtained by determining how long it takes to travel through the rock specimens. After the calculation, calibration and visualization are realized in the experimental platform.

3.1.3 Static and dynamic parameter correlations and observations

Based on the static elastic parameters obtained from the mechanical experiments and the dynamic elastic parameters calculated from the compressional and shear wave velocities,

TABLE 1 Simulation parameters in the base case.

Modeling parameter	Value
Domain size	25 mm by 50 mm
Gravel size	8 mm for the long semi-axis and 3 mm for the short semi-axis of the ellipse
Constant confining stress	40 MPa
Increasing boundary load	80 MPa
Rock matrix Young's modulus	30 GPa
Gravel Young's modulus	40 GPa
Rock matrix Poisson's ratio	0.25
Gravel Poisson's ratio	0.20

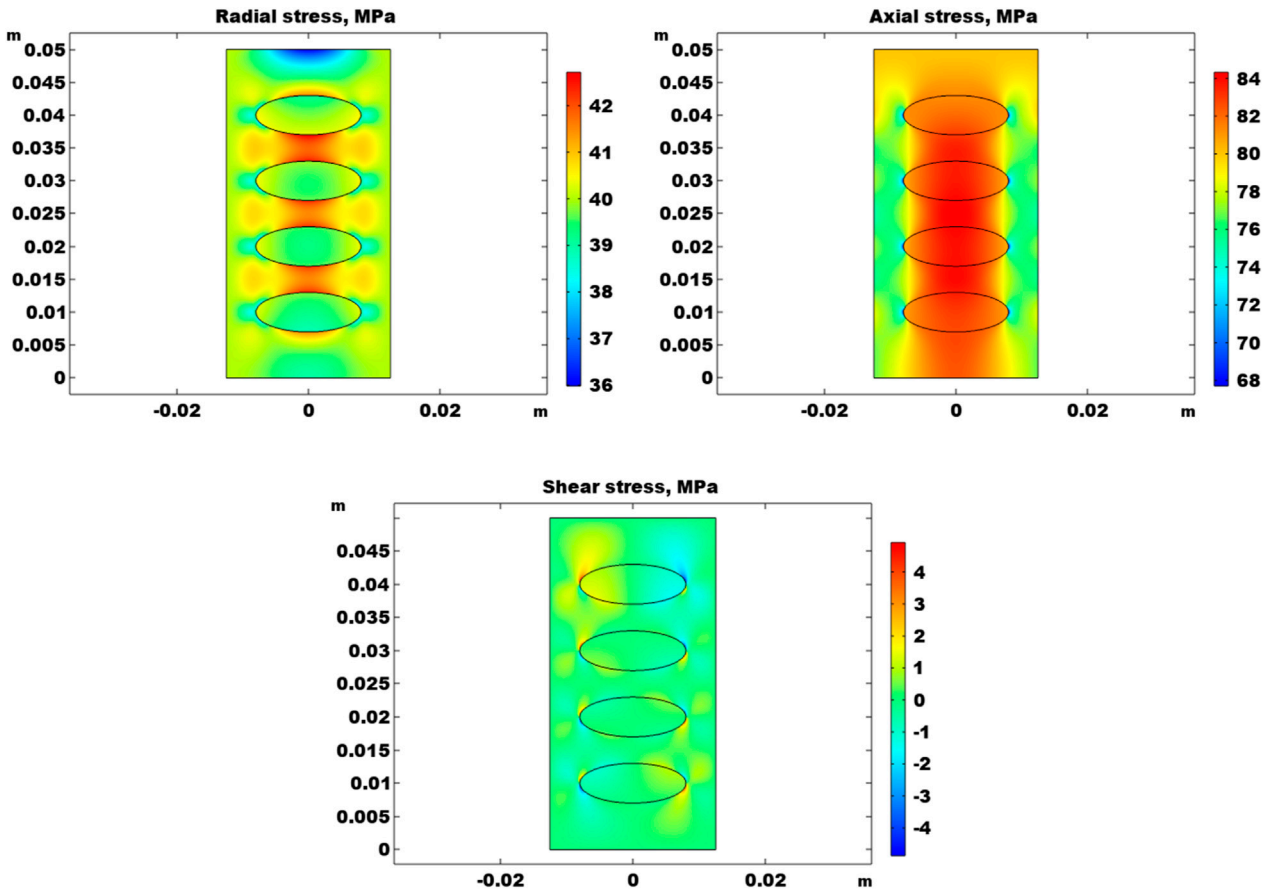


FIGURE 7
Stress distribution in gravels and in the rock matrix.

regression relationships for the compressional and shear wave velocities and the dynamic-static elastic parameter correlations can be established for the tight samples from the study area. The results show significant variations in the correlations of the compressional and shear wave velocity results across different well locations, while the correlations between the dynamic-static elastic parameters are stronger than those between the dynamic-static Poisson's ratios. The compressional wave velocities in the area range from 3,300 m/s to 6,500 m/s, while the shear wave velocities range from 1,200 m/s to 3,500 m/s. The dynamic elastic modulus ranges from 11 GPa to 70 GPa, and the dynamic Poisson's ratio ranges from 0.15 to 0.45 (Figures 4, 5). These regression relationships and parameter ranges provide valuable information for characterizing the elastic properties and wave velocities of the low-permeability conglomerate rocks in the study area in the Mahu Sag, Junggar Basin. Note that the outlier point with a Poisson's ratio of 0.45 indicates that this data point has significant radial deformation, which can be attributed to the nonuniform radial elongation caused by the axial compression.

The wide range of compressional and shear wave velocities indicates the heterogeneity of the rock formations in the area. The dynamic elastic modulus and Poisson's ratio ranges reflect the varying degrees of stiffness and deformability of the rocks, which are important factors for reservoir characterization and hydraulic fracturing design. Understanding the elastic properties and wave velocities of the conglomerate rocks is crucial for optimizing reservoir development strategies, assessing wellbore stability, and designing effective stimulation techniques in low-permeability reservoirs. The established regression relationships and parameter ranges contribute to a better understanding of the rock mechanics and provide a basis for accurate reservoir characterization and engineering applications in the Mahu Sag.

Based on the rock mechanical test results, it can be observed that the analyzed tight rock sample exhibits good brittleness as it totally fails with a strain less than 1.5%. Also, correlations between static and dynamic rock mechanical parameters are established. The correlation for Young's modulus is much better than the correlation for Poisson's ratio. This section provides an experimental understanding of the mechanical properties of the tight conglomerate rock sample. The experimental results can be used as a reference for the rock mechanics and geomechanics-related analysis in this field. From the correlations in Figures 4, 5, the variations in P and S wave velocities correspond to the tight nature of the reservoir rocks. How stiff the rock specimens are and how they react to applied stress can be quantified by the results as well. The data obtained here can help to improve the reservoir modeling accuracy and the efficacy of hydraulic fracturing design.

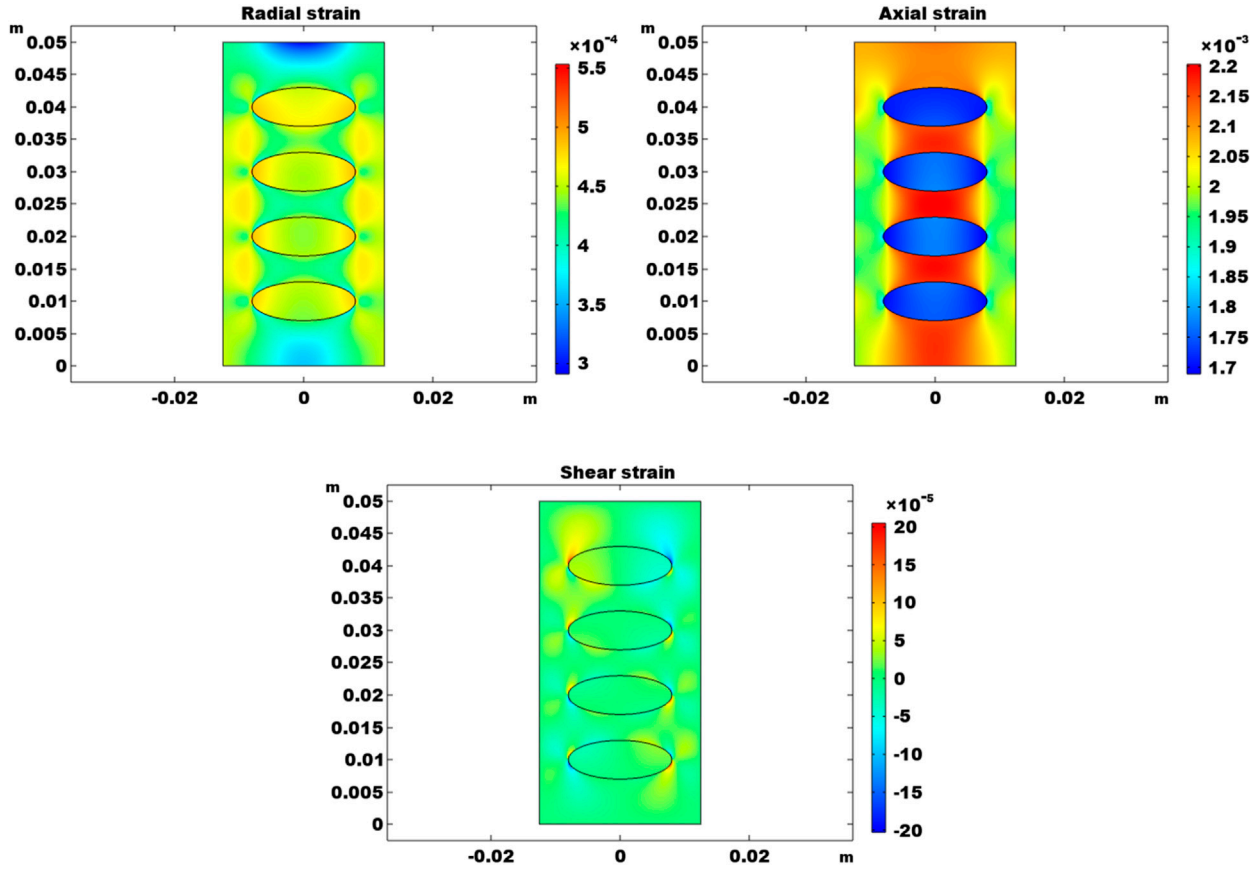


FIGURE 8
Strain distribution in gravels and in the rock matrix.

3.2 Numerical modeling results

After obtaining the lab observations and measurements of the reservoir rocks, some numerical analyses are then carried out for the understanding of the distribution and evolution of deformation-related parameters. In the previous section, the lab tests can provide overall measurements of the rock samples, while the deformation-related characteristic within the domain of the rock cannot be directly obtained or visualized. To address this limitation, the use of numerical modeling tools is employed as they can help to provide such observations. The numerical analysis in this section can provide quantified results that cannot be directly obtained in rock mechanical labs.

3.2.1 Base case

In the numerical analysis, a 2D model is established to simulate the rock deformation and the response to elastic waves in the heterogeneous rock. The domain size of the 2D model is 25 mm by 50 mm. In this domain, the stress, strain, and acoustic response are then simulated. As in Figure 6, the 2D domain has two constant confining stress boundaries on the left and on the right, ensuring the compression in the x-direction. There is also a stress boundary on the top where an increasing boundary load is exerted, which is used to obtain continuous changes in the stress and the strain fields. The red square on the top represents the source for the elastic wave in the domain. Four elliptical gravels are placed uniformly in the 2D domain, representing the heterogeneity in conglomerate rocks. The elliptical shape of gravels is used in the 2D model. This is a simplification based on the observation of the tight conglomerate samples where many gravels are nearly ellipsoids.

In the base case, the simulation papameters are shown in Table 1, where rock matrix has a Young's modulus of 30 GPa and a Poisson's ratio of 0.25. The gravels have a Young's modulus of 40 GPa and a Poisson's ratio of 0.20. This difference is related to the field observation that gravels contain more stiffer minerals such as quartz and calcite than the rock matrix. The ellipses have semi-axis lengths of 8 mm and 3 mm. In this model setup, relatively uniformly distributed gravels are used so that the deformation patterns can be quantified. A constant confining stress of 40 MPa is exerted on the left and the right boundaries. The increasing boundary load on the top is exerted as 80 MPa. This combination of stress boundaries is employed following the convention in the compression tests. They also follow the traction boundary conditions in Eqs 8, 9. A static equilibrium state for the momentum balance is achieved in the solution.

In Figures 7, 8, the rock deformation-related distribution of stress and strain results are plotted. Using the sign convention in geotechnical and rock mechanical communities, the compressive state is positive.

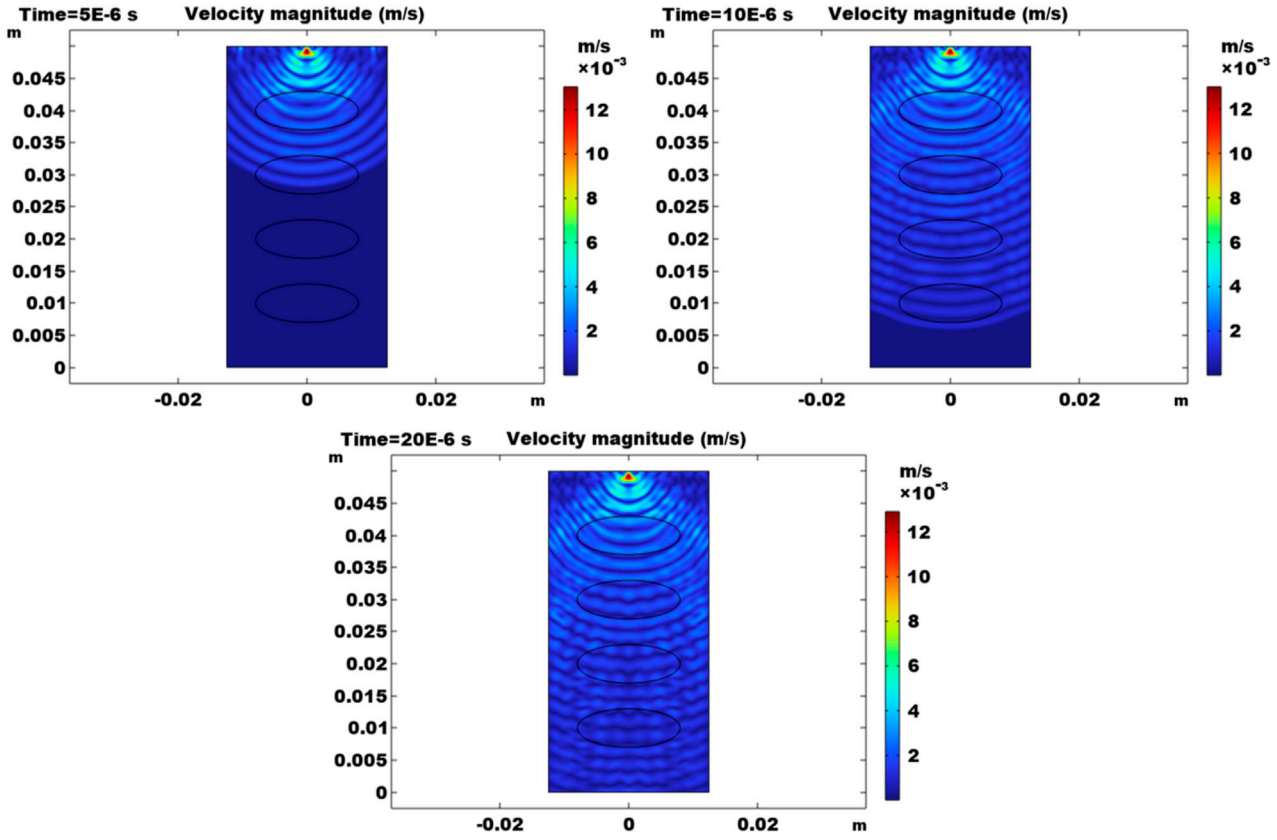


FIGURE 9
Velocity magnitudes at 5 ***μs***, 10 ***μs***, and 20 ***μs***. Velocities here are related to elastic wave-induced deformation in the elastic wave domain.

In Figure 7, the radial stress, the axial stress, and the shear stress are plotted. The radial and axial dimensions are corresponding to the convention used in tri-axial analysis of core samples. The radial dimension is identical to the x-direction and the axial dimension is identical to the y-direction. If the compression is in a homogeneous rock sample with no gravels, the radial stress is generally equal to the confining stress of 40 MPa and the axial stress is generally equal to the axial boundary load of 80 MPa. However, the existence of gravels introduces heterogeneities and the radial and axial stress results are largely altered and complicated. In the radial stress result, stress concentrations can be observed between neighboring gravels, where the radial stress magnitude is elevated by around 2 MPa. In gravels, radial stresses are not significantly altered. Decreases in radial stress can be observed at the top of the domain, at the bottom of the domain, and outside the longer semi-axes of gravels, leading to heterogeneous stress distributions. In contrast, radial stress increases are observed outside the shorter semi-axes of gravels. In the axial stress results, stress concentrations are observed along the vertical axis, where the axial stress magnitudes are greater than the axial load boundary of 80 MPa exerted at the top. Axial stresses outside the longer axes of gravels have lower stress magnitudes, while the lowest stress magnitudes are obtained at the tops of the gravels. The comparison between the radial and axial stress results indicate that the existence of stress concentrations is anisotropic: the stress concentration of radial stress is primarily in between gravels, while the stress concentration of axial stress is in both gravels and in between gravels. In addition to axial and radial stress results, Figure 7 also shows the distribution of shear stress. Shear stress magnitudes are generally below 5 MPa, which is caused by the existence of gravels. This is directly related to the heterogeneity introduced by gravels, indicating that gravels lead to shearing with in the conglomerate rock.

After the discussion of stress results, Figure 8 presents the radial strain, axial strain, and shear strain, and the strain results are indicative of compressive deformation. In the radial direction, the smallest deformations are observed at the centers of the top and the bottom regions. Tips of gravels and certain areas between tips of gravels have large radial deformations. In the axial direction, gravels exhibit strong stiffness and axial strains are low. Largest axial strains are obtained between gravels, which corresponds to the stress concentrations in stress results in Figure 7. Large shear strains are obtained near tips of gravels, indicating strong shearing effects near gravel tips.

Results in Figures 7, 8 shows that stiffer gravels lead to nonuniform deformation in the conglomerate, and this effect is highly direction-dependent. Due to the difference in stiffnesses of gravels and the rock matrix, relative deformation between gravels and the rock matrix is relatively significant. This leads to strong shearing effects, leading to shear strains and shear stresses especially at and near the contact areas between gravels and the matrix. This effect can only be captured by the consideration in this study, while traditional modeling using uniform and homogeneous assumptions cannot quantify this effect.

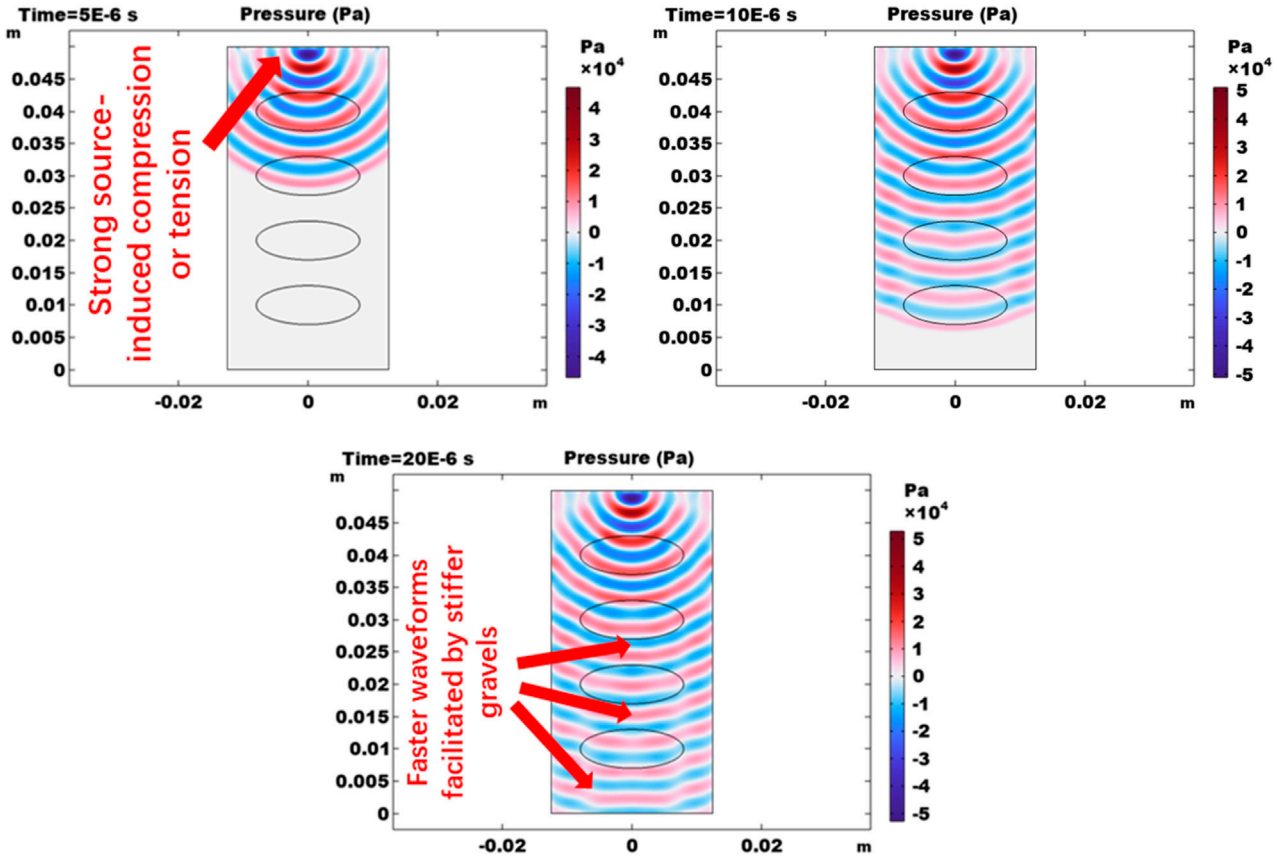


FIGURE 10
Pressure in the elastic wave domain at 5 ***μs***, 10 ***μs***, and 20 ***μs***. Pressure here denotes the magnitude of compression or tension caused by the waveforms in the elastic wave domain.

Previous studies demonstrate the stress and strain effects and their dependence on orientation. Then, elastic waves are also modeled in the conglomerate. The elastic wave generation source is located at the top center of the 2D domain, the length of the source is 0.2 mm. The wave generate follows the expression of: $\sigma_{source} = 0.1 \sin(2 \times 10^6 t)$. Here, the stress source is in MPa and a high frequency of the waveform is generated. Since the gravels have a higher stiffness, its corresponding wave velocities are greater than the matrix. The simulation time is 20 μs.

Figure 9 documents the velocity magnitudes generated at certain time steps of 5 μs, 10 μs, and 20 μs. This velocity term is related to the solid deformation and it is not related to the wave propagations. The evolution in the three time steps captures the propagation within the conglomerate domain. The velocity magnitude indicates the periodic deformation induced by the source. It can be noted that the existence of gravels makes the fronts move relatively faster. This effect is propagated in the system so that the oscillatory patterns can be observed at later time steps.

Figure 10 shows the induced stress propagations in the elastic wave domain, and the stress is described using the term pressure. The sign of this parameter indicates whether it is in a compression state. Strong compressive/tensile stress states are observed between the source and the first gravel near the top boundary. This is because the gravel is stiffer than the matrix, and the induced deformation is the most significant here. These results at three time steps show that the stiffer gravels help to advance the source-induced waveforms and the periodic elastic waves travel faster when they move through gravels than through the matrix.

Figure 11 shows the elastic wave-induced deformation in terms of displacement. At the first time step of 5 μs, the displacement profile travels through the second gravel from the top, while the rest of the domain has zero elastic-wave induced deformation. This is because the wave has not traveled far enough. For time steps of 10 μs and 20 μs, the front travels further and it finally reaches the bottom boundary. In these results, it is also observed that the waveforms presented by displacement magnitude are altered by the existence of gravels.

Based on the result in Figures 9–11, the heterogeneity caused by gravels alters the elastic wave propagation in the conglomerate. Stiffer gravels make the compressive or tensile states stronger between the source and the first gravel near the top boundary. They also make the elastic wave travels faster in gravels than in the rock matrix.

Figure 12 shows the velocity magnitude distributed along the axis in the rock specimen domain. Results at 4 steps of 0.5 μs, 5 μs, 10 μs, and 20 μs are plotted. In the result, the x-axis stands for the distance to the top of the rock sample where the waves are induced at the source. In the elastic wave domain, the velocity magnitude gradually decreases away from the source, indicating the change in energy. Similar to results in Figure 11, only the result at 20 μs indicates that the wave reaches the bottom (receiver).

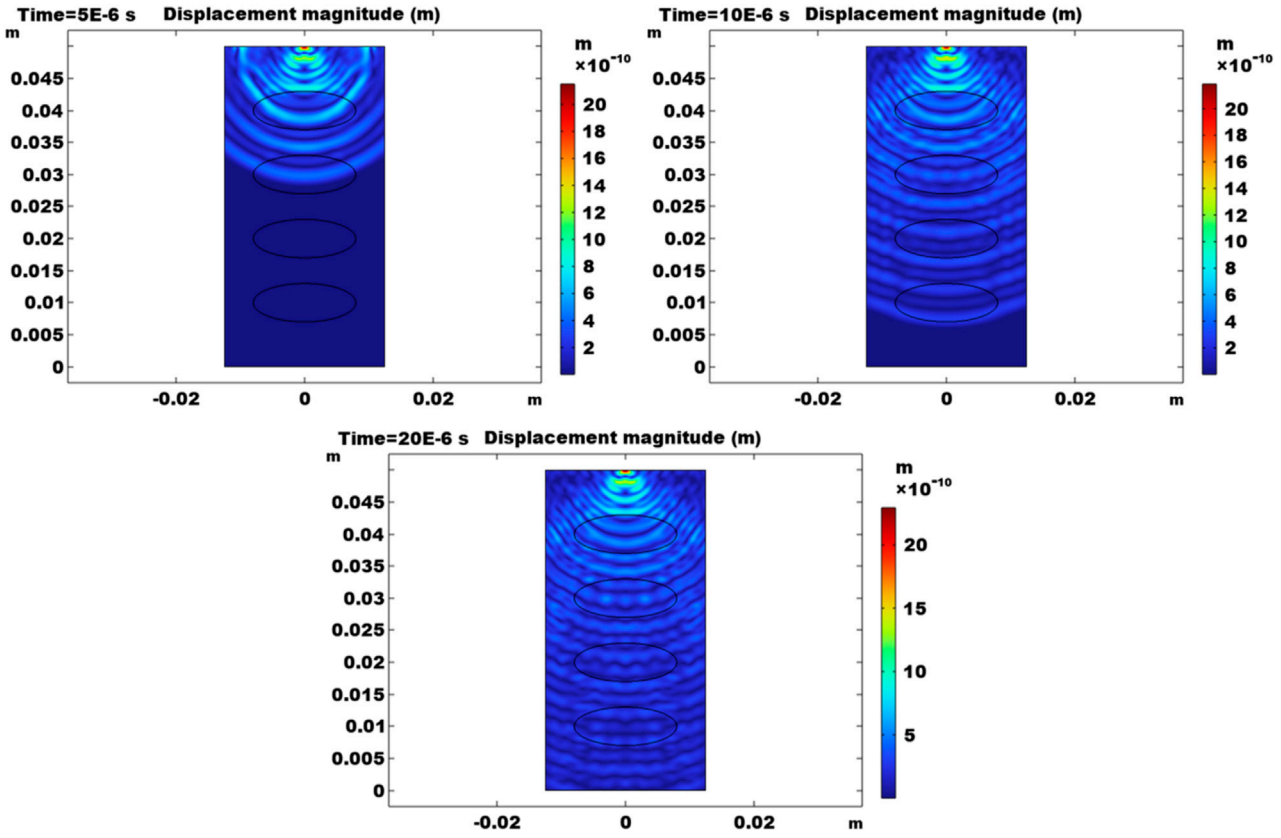


FIGURE 11
Displacement magnitudes at 5 ***μs***, 10 ***μs***, and 20 ***μs***. Displacement here represents the source-induced deformation in the elastic wave domain.

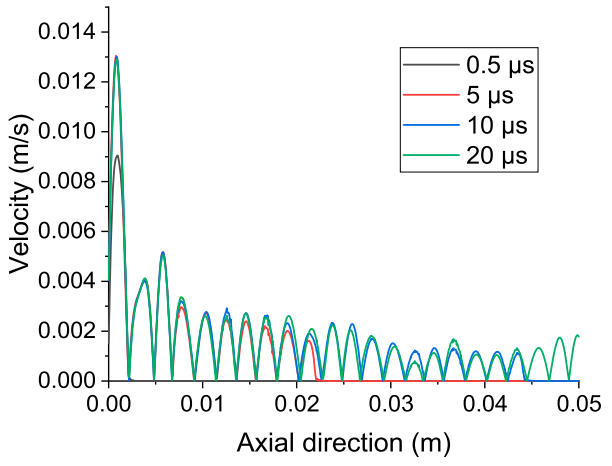


FIGURE 12
Velocity magnitude distribution in the axial direction at x = 0 m in the elastic wave domain at various time steps.

4 Conclusion

This case study introduces a series of experimental and numerical analyses of the deformation patterns in tight conglomerate samples. Correlations between static and dynamic elastic properties and P and S waves are established in the lab. The deformation patterns of the rock sample is also obtained in the experimental study. Additionally, finite element modeling is carried out to understand the effects of stiff gravels on solid deformation and elastic wave propagations in the conglomerate. The quantitative understanding in this case study serves as a reference for the brittleness and fracability evaluation in this field in Junggar Basin, China. The work also provides an integrated approach to the understanding of the elastic behaviors in tight conglomerate rock.

In conclusion:

(1) In the study area, the tested conglomerate rock is relatively brittle. Shearing failure is easily achieved when tri-axial compression is exerted in the lab. P and S wave velocities have relatively good correlations in this area, while the correlation between static and dynamic elastic moduli is much better than the correlation between static and dynamic Poisson's ratios.

(2) In the numerical modeling of solid rock deformation caused by tri-axial compression, the existence of gravels leads to strong direction-dependent and anisotropic stress and strain distributions. Stress concentrations are observed in and between stiff gravels. Compression-induced shearing is especially strong at and near tips of gravels, which can contribute to complex shearing failure types in conglomerate deformation.

(3) In the elastic wave domain, the existence of stiffer gravels alters the elastic wave propagation patterns and the compressive/tensile state magnitudes in and around gravels. Wave-induced compression/tension is greater between the source and the first gravel near the top boundary. Stiffer gravels also facilitate the traveling of elastic waves through them, and this effect is propagated further beyond gravels as time evolves.

(4) Lab and simulation results in the study demonstrate the tight and stiff nature of the rock specimens and the highly heterogeneous rock mechanical properties. In the design of fracture stage and cluster placement, the size and location of gravels should be considered as they affect the failure of tight conglomerate rocks.

Data availability statement

The original contributions presented in the study are included in the article/Supplementary material, further inquiries can be directed to the corresponding author.

Author contributions

HQ: Writing–original draft. DL: Investigation, Methodology, Writing–original draft. JZ: Methodology, Visualization, Writing–review and editing. HM: Investigation, Software, Writing–original draft. XuW: Methodology, Visualization, Writing–original draft. XiW: Methodology, Writing–review and editing. BZ: Investigation, Methodology, Writing–review and editing. JL: Visualization, Writing–review and editing. XZ: Visualization, Writing–review and editing.

Funding

The author(s) declare that no financial support was received for the research, authorship, and/or publication of this article.

Acknowledgments

The authors acknowledge the financial support from the CNPC Innovation Fund (2021DQ02-0502) and the National Natural Science Foundation of China (51991362; 51974338).

Conflict of interest

Authors HQ, DL, JZ, and HM were employed by PetroChina Xinjiang Oilfield Company. Authors XuW and XiW were employed by China National Logging Corporation.

The remaining authors declare that the research was conducted in the absence of any commercial or financial relationships that could be construed as a potential conflict of interest.

Publisher's note

All claims expressed in this article are solely those of the authors and do not necessarily represent those of their affiliated organizations, or those of the publisher, the editors and the reviewers. Any product that may be evaluated in this article, or claim that may be made by its manufacturer, is not guaranteed or endorsed by the publisher.

References

Andrade, J. E., and Tu, X. (2009). Multiscale framework for behavior prediction in granular media. *Mechanics of Materials* 41 (6), 652–669. doi:10.1016/j.mechmat.2008.12.005

Chen, A., Guo, X., Yu, H., Huang, L., Shi, S., and Cheng, N. (2021a). A parametric study of hydraulic fracturing interference between fracture clusters and stages based on numerical modeling. *Energy Explor. Exploitation* 39 (1), 65–85. doi:10.1177/0144598720953257

Chen, B., Ji, J., Lin, J., Chen, H., Wang, X., Guo, X., et al. (2021b). Experimental and numerical investigation of characteristics of highly heterogeneous rock mechanical responses in tight sandy conglomerate reservoir rock under tri-axial compression. *Front. Earth Sci.* 9, 735208. doi:10.3389/feart.2021.735208

Clarkson, C. R., and Pedersen, P. K. (2010). Tight Oil Production Analysis: Adaptation of Existing Rate-Transient Analysis Techniques," in Paper presented at the Canadian Unconventional Resources and International Petroleum Conference, Calgary, Alberta, Canada, October 2010. doi:10.2118/137352-MS

Cui, X., Bustin, A. M., and Bustin, R. (2009). Measurements of gas permeability and diffusivity of tight reservoir rocks: different approaches and their applications. *Geofluids* 9 (3), 208–223. doi:10.1111/j.1468-8123.2009.00244.x

Guo, X., Jin, Y., Zi, J., and Lin, B. (2021). Numerical investigation of the gas production efficiency and induced geomechanical responses in marine methane hydrate-bearing sediments exploited by depressurization through hydraulic fractures. *Energy and Fuels* 35 (22), 18441–18458. doi:10.1021/acs.energyfuels.1c02569

Guo, X., Jin, Y., Zi, J., Lin, J., and Zhu, B. (2023). A 3D modeling study of effects of heterogeneity on system responses in methane hydrate reservoirs with horizontal well depressurization. *Gas Sci. Eng.* 115, 205001. doi:10.1016/j.jgsce.2023.205001

Guo, X., Song, H., Killough, J., Du, L., and Sun, P. (2018). Numerical investigation of the efficiency of emission reduction and heat extraction in a sedimentary geothermal reservoir: a case study of the Daming geothermal field in China. *Environ. Sci. Pollut. Res.* 25, 4690–4706. doi:10.1007/s11356-017-0845-x

Guo, X., Wang, Y., and Killough, J. (2016). The application of static load balancers in parallel compositional reservoir simulation on distributed memory system. *J. Nat. Gas Sci. Eng.* 28, 447–460. doi:10.1016/j.jngse.2015.12.030

He, X., Liu, P., Xu, L., Hao, S., Qiu, X., and Shan, C. (2021). Pore structure representations based on nitrogen adsorption experiments and an FHH fractal model: Case study of the block Z shales in the Ordos Basin, China. *Journal of Petroleum Science and Engineering* 203, 108661. doi:10.1016/j.petrol.2021.108661

Huang, L., Liu, J., Zhang, F., Fu, H., Zhu, H., and Damjanac, B. (2020). 3D lattice modeling of hydraulic fracture initiation and near-wellbore propagation for different perforation models. *J. Petroleum Sci. Eng.* 191, 107169. doi:10.1016/j.petrol.2020.107169

Huang, L., Tan, J., Fu, H., Liu, J., Chen, X., Liao, X., et al. (2023). The non-plane initiation and propagation mechanism of multiple hydraulic fractures in tight reservoirs considering stress shadow effects. *Eng. Fract. Mech.* 292, 109570. doi:10.1016/j.engfracmech.2023.109570

Javadpour, F., Fisher, D., and Unsworth, M. (2007). Nanoscale gas flow in shale gas sediments. *J. Can. Petroleum Technol.* 46 (10), 55–61. doi:10.2118/07-10-06

Ji, Y., Wang, J., and Huang, L. (2015). Analysis on inflowing of the injecting Water in faulted formation. *Advances in Mechanical Engineering* 7 (6). doi:10.1177/1687814015590294

Ju, W., Huang, P., Zhong, Y., Hu, H., Liang, Y., and Liu, B. (2023). Experimental study of sandstone stress sensitivity under different fluids: Characteristics and mechanisms. *Geoenergy Science and Engineering* 223, 211537. doi:10.1016/j.geoen.2023.211537

Karimi-Fard, M., Durlofsky, L. J., and Aziz, K. (2003). An efficient discrete-fracture model applicable for general-purpose reservoir simulators. *SPE J.* 8 (2), 227–236. doi:10.2118/88812-pa

Li, H. (2022). Research progress on evaluation methods and factors influencing shale brittleness: a review. *Energy Rep.* 8, 4344–4358. doi:10.1016/j.egyr.2022.03.120

Li, J., Liu, Y., and Wu, K. (2022). A new higher order displacement discontinuity method based on the joint element for analysis of close-spacing planar fractures. *SPE J.* 27 (02), 1123–1139. doi:10.2118/208614-pa

Li, B., Zhou, F., Fan, W., Ren, D., Li, H., and Li, M. (2020). Experimental investigation and theoretical modeling of stress-dependent permeability in naturally fractured tight gas reservoir. *Journal of Petroleum Science and Engineering* 188, 106949. doi:10.1016/j.petrol.2020.106949

Li, J., and Wu, K. (2022). An efficient model for hydraulic fracture height growth considering the effect of bedding layers in unconventional shale formations. *SPE J.* 27 (06), 3740–3756. doi:10.2118/210572-pa

Lei, Q., Latham, J., and Tsang, C. (2017). The use of discrete fracture networks for modelling coupled geomechanical and hydrological behaviour of fractured rocks. *Computers and Geotechnics* 85, 151–176. doi:10.1016/j.compgeo.2016.12.024

Luo, H., Xie, J., Huang, L., Wu, J., Shi, X., Bai, Y., et al. (2022). Multiscale sensitivity analysis of hydraulic fracturing parameters based on dimensionless analysis method. *Lithosphere* 2022 (Special 12), 9708300. doi:10.2113/2022/9708300

Nasrollahzadeh, B., Amiri, H. A. A., and Ghabezloo, S. (2021). Field-scale fully coupled simulation of fluid flow and geomechanics: Gas storage/recovery process in a depleted sandstone reservoir. *Journal of Petroleum Science and Engineering* 200, 108423. doi:10.1016/j.petrol.2021.108423

Prodanović, M., Lindquist, W. B., and Seright, R. S. (2006). Porous structure and fluid partitioning in polyethylene cores from 3D X-ray microtomographic imaging. *Journal of Colloid and Interface Science* 298 (1), 282–297. doi:10.1016/j.jcis.2005.11.053

Qiao, J., Zeng, J., Chen, D., Cai, J., Jiang, S., and Xiao, E. (2021). Permeability estimation of tight sandstone from pore structure characterization. *Marine and Petroleum Geology* 135, 105382. doi:10.1016/j.marpetgeo.2021.105382

Ross, D. J., and Bustin, R. M. (2009). The importance of shale composition and pore structure upon gas storage potential of shale gas reservoirs. *Mar. Petroleum Geol.* 26 (6), 916–927. doi:10.1016/j.marpetgeo.2008.06.004

Sangnimnuan, A., Li, J., and Wu, K. (2018). Development of efficiently coupled fluid-flow/geomechanics model to predict stress evolution in unconventional reservoirs with complex-fracture geometry. *SPE J.* 23 (03), 640–660. doi:10.2118/189452-pa

Song, Y., Wang, Z., Wang, W., Yu, P., Chen, G., Lin, J., et al. (2023). Coupled thermal-hydraulic-mechanical modeling of near-well stress evolution in naturally fractured formations during drilling. *Processes* 11 (6), 1744. doi:10.3390/pr11061744

Wang, Y., Agostini, F., Skoczylas, F., Jeannin, L., and Portier, É. (2016). Experimental study of the gas permeability and bulk modulus of tight sandstone and changes in its pore structure. *International Journal of Rock Mechanics and Mining Sciences* 91, 203–209. doi:10.1016/j.ijrmms.2016.11.022

Wang, L., Li, Y., Xu, D., Gao, Y., Zhang, J., He, J., et al. (2022a). Evolution of near-well damage caused by fluid injection through perforations in wellbores in low-permeability reservoirs: a case study in a shale oil reservoir. *Lithosphere* 2022 (Special 12), 3824011. doi:10.2113/2022/3824011

Wang, Z., Guo, X., Zheng, G., Yu, P., Wang, W., Jin, Y., et al. (2022b). Effects of parent well spacing on the poroelastic behaviors in the infill zone in shale oil reservoirs: a case study in Jimsar Shale Oil, China. *Energy Sci. Eng.* 10 (4), 1043–1054. doi:10.1002/ese3.1059

Warren, J. E., and Root, P. J. (1963). The behavior of naturally fractured reservoirs. *Soc. Petroleum Eng. J.* 3 (03), 245–255. doi:10.2118/426-pa

Yao, C., Park, J., Chen, H., Datta-Gupta, A., Hennings, P., and Dommisse, R. (2023). "High Resolution Modeling of Pore Pressure Change, Fault Slip Potential and Induced Seismicity in the Fort Worth Basin. *In SPE Western Regional Meeting (p. D021S002R002). SPE.* doi:10.2118/212951-MS

Yin, S., Dong, L., Yang, X., and Wang, R. (2020). Experimental investigation of the petrophysical properties, minerals, elements and pore structures in tight sandstones. *Journal of Natural Gas Science and Engineering* 76, 103189. doi:10.1016/j.jngse.2020.103189

Yuan, W., Pan, Z., Li, X., Yang, Y., Zhao, C., Connell, L. D., and He, J. (2014). Experimental study and modelling of methane adsorption and diffusion in shale. *Fuel* 117, 509–519. doi:10.1016/j.fuel.2013.09.046

Zhai, Z., Wang, X., Jin, X., Sun, L., Li, J., and Cao, D. (2014). Adsorption and diffusion of shale gas reservoirs in modeled clay minerals at different geological depths. *Energy & Fuels* 28 (12), 7467–7473. doi:10.1021/ef5023434

Zhang, T., Xu, H., Zhang, Y., Jiang, Y., and Li, Y. (2019). Propagation behavior of hydraulic fracture across the coal-rock interface under different interfacial friction coefficients and a new prediction model. *J. Nat. Gas Sci. Eng.* 68, 102894. doi:10.1016/j.jngse.2019.05.007

Zheng, Y., He, R., Huang, L., Bai, Y., Wang, C., Chen, W., et al. (2022). Exploring the effect of engineering parameters on the penetration of hydraulic fractures through bedding planes in different propagation regimes. *Comput. Geotechnics* 146, 104736. doi:10.1016/j.compgeo.2022.104736

Zhi, D., Guo, X., Wang, W., Jin, Y., Liu, C., Chen, G., et al. (2021). Fracturing and production analysis of the efficacy of hydraulic fracture stage reduction in the improvement of cost-effectiveness in shale oil development: a case study of Jimsar shale oil, China. *Energy Sci. Eng.* 9 (9), 1337–1348. doi:10.1002/ese3.940

Zhou, T., Xiong, W., Zong, Z., and Chen, Z. (2013). Experimental study of mechanical properties of bedded salt rock under uniaxial compression. *Rock Mech. Rock Eng.* 46 (4), 777–787.

Zhou, X., Wei, J., Zhao, J., Li, X., Zhang, X., Fu, X., and Shamil, S. (2024). Study on pore structure and permeability sensitivity of tight oil reservoirs. *Energy* 288, 129632. doi:10.1016/j.energy.2023.129632

Zhong, X., Zhu, Y., Liu, L., Yang, H., Li, Y., Xie, Y., and Liu, L. (2020). The characteristics and influencing factors of permeability stress sensitivity of tight sandstone reservoirs. *Journal of Petroleum Science and Engineering* 191, 107221. doi:10.1016/j.petrol.2020.107221

Zou, C., Zhu, R., Wu, S., Yang, Z., Tao, S., Yuan, X., et al. (2012). Types, characteristics, genesis and prospects of conventional and unconventional hydrocarbon accumulations: Taking tight oil and tight gas in China as an instance. *Acta Petrolei Sinica* 33 (2), 173. doi:10.7623/syxb201202001

frontiers | Frontiers in Energy Research

TYPE Original Research
PUBLISHED 27 February 2024
DOI 10.3389/fenrg.2024.1361247

Check for updates

OPEN ACCESS

EDITED BY
Huiwen Pang,
China University of Petroleum, China

REVIEWED BY
Jingshou Liu,
China University of Geosciences Wuhan, China
Wei Ju,
China University of Mining and Technology, China

*CORRESPONDENCE
Ke Xu,
xukee0505@163.com

RECEIVED 25 December 2023
ACCEPTED 06 February 2024
PUBLISHED 27 February 2024

CITATION
Zhang Y, Xu K, Zhang H, Lai S, Liang J and Qian Z (2024), Numerical simulation and application of ground stress field in ultra-deep strike-slip faults—taking the FI12 fault zone in the Fuman Oilfield as an example.
Front. Energy Res. 12:1361247.
doi: 10.3389/fenrg.2024.1361247

COPYRIGHT
© 2024 Zhang, Xu, Zhang, Lai, Liang and Qian. This is an open-access article distributed under the terms of the Creative Commons Attribution License (CC BY). The use, distribution or reproduction in other forums is permitted, provided the original author(s) and the copyright owner(s) are credited and that the original publication in this journal is cited, in accordance with accepted academic practice. No use, distribution or reproduction is permitted which does not comply with these terms.

Numerical simulation and application of ground stress field in ultra-deep strike-slip faults—taking the FI12 fault zone in the Fuman Oilfield as an example

Yu Zhang[1,2,3,4], Ke Xu[1,2,3,4]*, Hui Zhang[1,2,3,4], Shujun Lai[1,2,3,4], Jingrui Liang[1,2,3,4] and Ziwei Qian[1,2,3,4]

[1]Research Institute of Exploration and Development, Tarim Oilfield Company, Korla, China, [2]R&D Center for Ultra Deep Complex Reservoir Exploration and Development, China National Petroleum Corporation (CNPC), Korla, China, [3]Engineering Research Center for Ultra-Deep Complex Reservoir Exploration and Development, Korla, China, [4]Xinjiang Key Laboratory of Ultra-Deep Oil and Gas, Korla, Xinjiang, China

This study carried out a research on the distribution characteristics of the geostress field of ultra-deep strike-slip faults, aiming to improve the exploration efficiency and development benefits of ultra-deep fault-controlled reservoirs. This study combines multiple geological information, drilling information, seismic data, and seismic attribute analysis. Taking the FI12 fault zone in the Fengman Oilfield as an example, it carried out numerical simulation of the geostress field, clarified the distribution pattern of geostress, analyzed the effectiveness of fracture mechanics, and proposed a reservoir quality evaluation method and production increase strategy based on geostress analysis. The study includes the following three aspects: 1) research on the heterogeneity of fault-controlled fractured carbonate reservoirs: Due to the existence of faults, fractures, and pores, carbonate reservoirs exhibit strong heterogeneity. These discontinuous structures lead to local stress field decreases to varying degrees. By analyzing the changes in geostress, it is possible to infer the development of faults, fractures, and pores. This provides important basis for predicting and evaluating reservoirs. 2) research on the distribution pattern of geostress: The geostress of fractured bodies exhibits a "shell-type" distribution pattern. Inside the fractured body, the geostress values are lower, indicating that this part is a favorable reservoir body. On the outside of the fractured body, the geostress exhibits high-value concentration, and this part has relatively poor permeability and can be regarded as an unfavorable drilling target. 3) research on the relationship between fault-fracture mechanical activity and reservoir quality and production capacity: Geostress and its influence on fault-fracture mechanical activity are directly related to the quality and production capacity of fault-controlled fractured carbonate reservoirs. When deploying well locations and optimizing well trajectories, geostress factors should be fully considered, and reservoir reformation efficiency should be taken into account to promote single well production increases and reservoir economic devel.

KEYWORDS

ultra-deep, strike-slip fault, fracture-controlled fracture-cave reservoir, geostress, geomechanics, reservoir quality

1 Introduction

Strike-slip faults are an important research area in structural geology. According to traditional views, large strike-slip faults are mainly developed on the margins of active continental plates, with long-distance extension and large slip distance. For example, the San Andreas Fault in the United States (Fossen, 2010) and the Altun Fault in China (Cui et al., 2002) are both typical examples.

However, with the improvement of seismic data acquisition technology, it has been discovered that there are also large strike slip faults within stable land blocks. Although these faults extend longer, their slip distance is relatively small, usually only a few hundred meters, and the maximum is only a few thousand meters. These faults are called intra cratonic strike slip faults and are mainly developed in tectonic stable areas, such as Siberia Basin (Gogonenkov and Timurziev, 2012), Sichuan Basin (Ma et al., 2018) and Tarim Basin (Wu et al., 2012; Yang et al., 2016; Han et al., 2017; Li et al., 2017; Lyu et al., 2017; Zheng et al., 2018; Wu et al., 2021).

Strike-slip faults within cratons play an important controlling role in the development of reservoirs and the formation of oil and gas reservoirs. In oil and gas exploration practice, these faults are often regarded as important exploration targets. Therefore, conducting research on strike-slip faults within cratons not only helps to deepen the understanding of the internal structural deformation and formation mechanisms of cratons, but also provides new ideas and directions for oil and gas exploration.

The study of strike-slip faults within cratons has important theoretical significance and production guidance value. By deeply studying the genetic mechanism, distribution pattern, and impact on reservoirs of strike-slip faults within cratons, more scientific and effective guidance can be provided for oil and gas exploration, promoting the development and utilization of oil and gas resources.

Research has shown that the control of strike-slip faults on the productivity of oil and gas wells is mainly reflected in the following aspects (Wang et al., 2018; Wang Y. et al., 2019; Li et al., 2021; Song X. et al., 2023; Wang Q. et al., 2023).

1. Formation of traps: Strike-slip faults can form various traps during tectonic movement, such as fault traps, fracture traps, and structural ridge traps. These traps can serve as spatial gather together spaces for oil and gas, affecting the productivity of oil and gas wells;
2. Control of the distribution of oil and gas reservoirs: Strike-slip faults can affect the migration and aggregation of oil and gas, making the oil and gas reservoirs exhibit directional distribution characteristics. This helps to predict the distribution of oil and gas reservoirs, guiding oil and gas exploration and development;
3. Regulation of the pressure system of oil and gas wells: Strike-slip faults can affect the pressure system of oil and gas wells, causing changes in wellbore pressure. When oil and gas wells are located near strike-slip faults, the wellbore pressure may be affected, thereby affecting the productivity of oil and gas wells;
4. Impact on the hydraulic characteristics of oil and gas wells: Strike-slip faults can alter the hydraulic characteristics of oil and gas wells, such as influencing the direction and velocity of groundwater flow. This may affect the extraction efficiency of oil and gas, further affecting the productivity of oil and gas wells;
5. Formation of preferential seepage channels: Strike-slip faults can form preferential seepage channels, enhancing the productivity of oil and gas wells. During the production process of oil and gas wells, fractures at strike-slip faults can serve as preferential seepage channels for oil and gas, making it easier for oil and gas to flow towards the wellbore, thereby increasing the productivity of oil and gas wells. Therefore, the control of strike-slip faults on the productivity of oil and gas wells is mainly reflected in the formation of traps, the distribution of oil and gas reservoirs, changes in wellbore pressure, regulation of hydraulic characteristics, and the formation of preferential seepage channels. In the process of oil and gas exploration and development, the impact of strike-slip faults needs to be fully considered to improve the productivity and extraction efficiency of oil and gas wells.

The FI12 fault zone is located in the eastern part of the Fuyuan II area (Jiao, 2017; Wang et al., 2021; Wang Qinghua et al., 2023). The overall structure of the roof of an Ordovician room in the area is gentle, and multiple sets of faults with different orientations are developed on the plane; The Paleozoic faults in the Fuyuan block are well-developed, and the fault system can be divided into two groups on the plane: northeast and northwest, both of which are strike slip faults. The activity periods can be divided into three periods. The first period is a northeast strike slip fault formed during the Middle Caledonian period, forming the fault pattern of this area. The plane is mainly characterized by linear and feathery structures, and the strike slip faults mostly have local compression and torsion properties, with a small fault distance of generally 10–20 m, Disconnect the layer from the basement to the bottom of the Ordovician Santam Formation; The second stage is the Late Caledonian period, based on the Middle Caledonian fault, the northeast trending fault in the middle of the block is further activated, and the fault layer extends from the basement to the Ordovician Santam Formation; The third stage is a northeast trending strike slip fault, only distributed in the northwest of the block. The fault style is mainly flower shaped, and on the plane, it only shows linear structures. The fault distance is relatively large, generally 10–40 m, and the fault layer is from the basement to the Permian. It can be seen that the FI12 fault zone is a “typical” fault zone of the ultra deep strike slip fault in the Tarim Basin, which is of great significance for the study of numerical simulation of the geostress field of the ultra deep strike slip fault. Moreover, the water injection flow law of the wells arranged in the fault zone is not clear from the water injection development stage, which affects the water injection development effect of the wells arranged in the fault zone (Song Xingguo et al., 2023).

Therefore, in order to improve the exploration efficiency and development benefits of carbonate reservoirs under the control of ultra-deep strike-slip faults, this article takes the FI12 fault zone in the Fuman Oilfield as an example to carry out numerical simulation of the *in-situ* stress field, clarify the distribution law of carbonate reservoirs under the control of strike-slip faults, clarify the correlation between factors related to *in-situ* stress and the quality of ultra-deep carbonate reservoirs, and provide suggestions and countermeasures based on the numerical

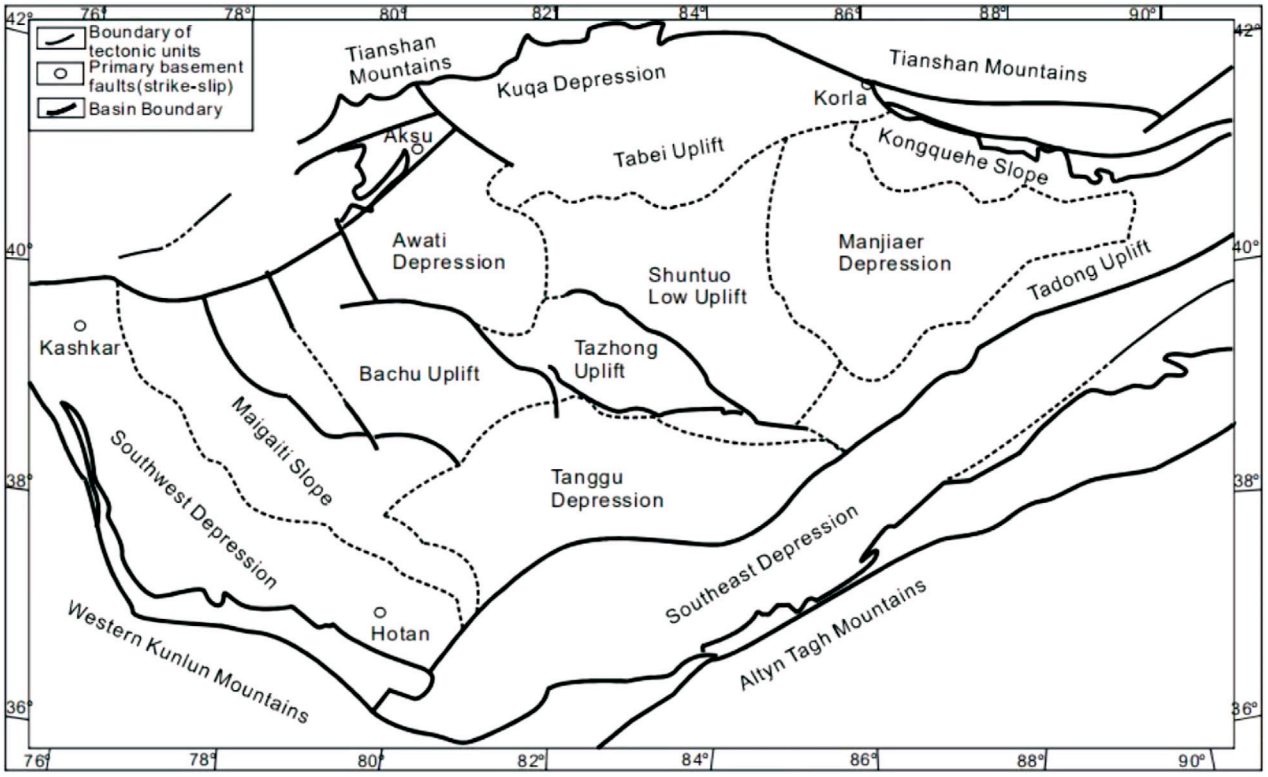


FIGURE 1
Main structural units of Tarim Basin (Mao et al., 2017).

simulation results of ultra-deep strike-slip faults, thus supporting efficient exploration and benefit development of ultra-deep carbonate reservoirs in Tarim Oilfield.

2 Geological setting

The Tarim Basin, a vast land of 560,000 square kilometers, is the largest inland basin in China and also a mysterious place with the least exploration. It is surrounded by the towering Tianshan Mountains, with majestic mountains to the north and the continuous Kunlun Mountains to the south. In the southeast of this basin, the Altyn Mountains stand tall and towering, as if they are a natural barrier to protect this land.Although its exploration level is relatively low, the abundant oil and natural gas resources here provide a solid support for China's energy development.

The Tarim Basin is rich in geological structure and geomorphic features. According to basement structure, primary basement fault and sediment distribution, the Tarim Basin is divided into more than 10 structural units, including 6 depressions and 4 uplifts. The distribution of these structural units, from north to south, is sequentially Kuche Depression, Tabei Uplift, Awati Depression, Manjia'er Depression, Tazhong Uplift, Bachu Uplift, Tadong Uplift, Tanggu Depression, Southwest Depression, and Southeast Depression. Among them, the Shuntuo low uplift is a relatively special structural unit. Compared with the northern and central uplift of the tower, the terrain of Shuntuo low uplift presents a moderately uplifted state. The Tabei Uplift and the Tazhong Uplift are located in their northern and southern parts, respectively, forming a relatively complete structural system (Figure 1).

The distribution of intracratonic strike-slip faults in the Tabei uplift, Shuntuo low uplift, and northern slope of the Tazhong uplift is an important area of geological research and is also the focus area of this study (Figure 2).

The Tarim Basin has experienced a complex multistage tectonic evolution, and the northern margin of the basin and the adjacent southern Tianshan orogenic belt have experienced multistage and complex basin range coupling and basin range conversion processes, forming a variety of types of basin range coupling and conversion modes (Mao et al., 2017).

About 750 million years ago, the Rodinian supercontinent began to disintegrate, forming some new continents and oceans. In this process, the basement of the Tarim Basin separated from the surrounding land, and gradually formed the shape of the basin we see today.

In the Early Paleozoic, the Tabei Block was under the background of extension, which led to the formation of the South Tianshan Ocean. During this period, due to the extension of the crust, the southern Tianshan region began to undergo rifting and formed a marine environment. The existence of this ocean had an important impact on the evolution of life at that time and laid the foundation for later tectonic evolution. The southern part of the Tarim Block developed a tectonic system called the Paleotethys Trench-Arc-Basin System. This tectonic system was formed during the closure of the Paleotethys Ocean and consists of tectonic units such as trenches, arcs, and basins (Li et al., 2020).

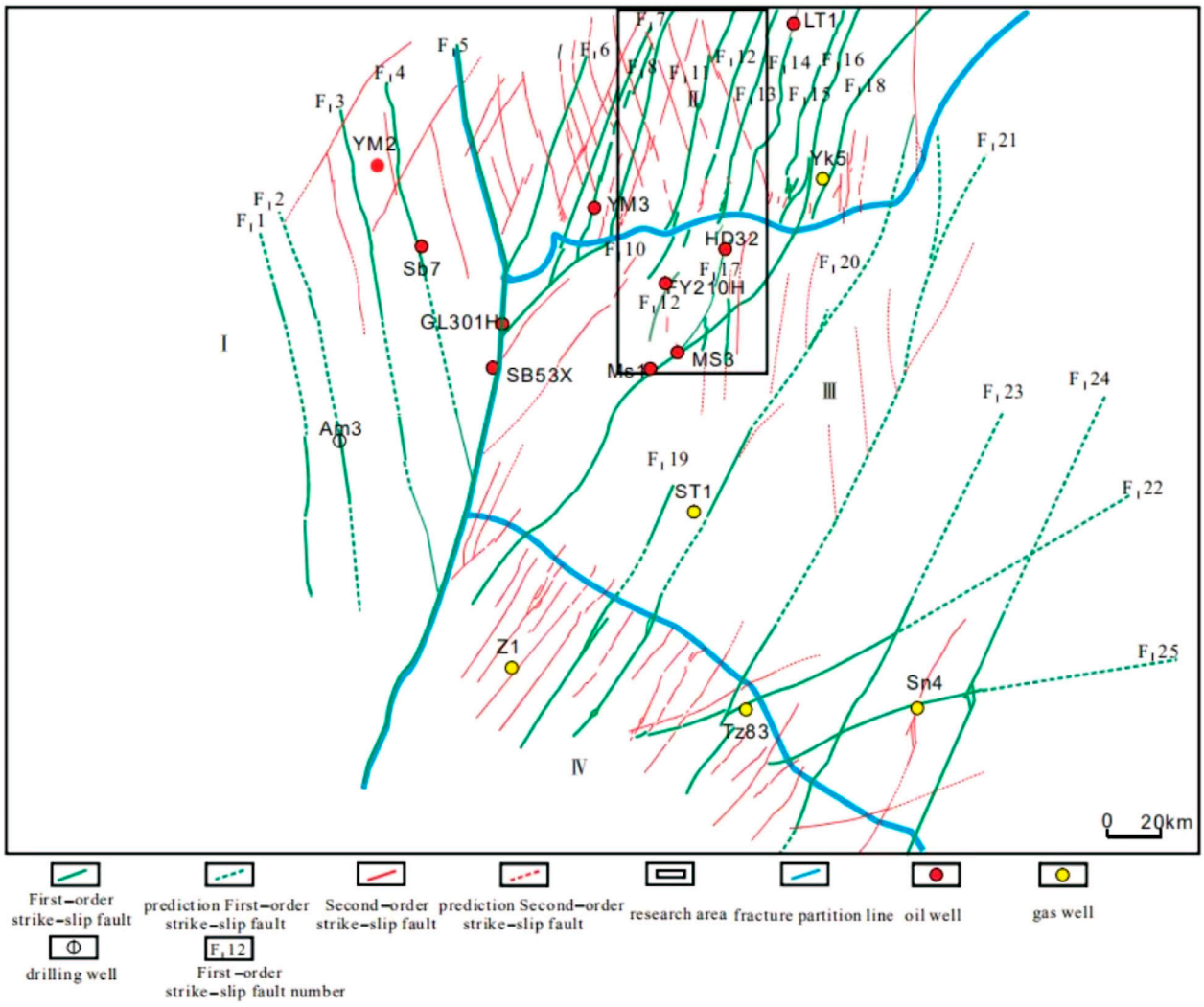


FIGURE 2
Distribution of strike slip faults in the central craton of Tarim Basin (Mao et al., 2017) (red).

Manjiaer Depression is an important tectonic unit in the Tarim Basin, and its formation and evolution are closely related to the surrounding geological environment and geodynamic process. In the Early Paleozoic, with the extension of the crust, the eastern part of the Tarim block began to appear rift, forming the embryonic form of Manjiar Depression.

Over time, the Manjiaer Depression has undergone multiple periods of tectonic movement and sedimentation. Under the influence of tectonic movement, the boundaries of the Manjiaer Depression have gradually expanded, and the internal structure has become more complex. At the same time, a large amount of sediment has accumulated within the depression, forming thick sedimentary layers (Figure 1).

The extensional environment underwent changes during the Middle Ordovician, and subduction began, leading to the closure of the Kudi Ocean in the southwest. Kudiyang is an ancient sea area in the Tarim Basin, which existed in the early Paleozoic era. In the Middle Ordovician, with the movement of the Earth's tectonic plates and the strengthening of their interactions, the two sides of the Kudi Ocean began to compress, forming reverse thrust structures and related high-pressure metamorphic rocks. This process marked the gradual closure of the Kudi Ocean, which had an important impact on the tectonic evolution of the Tarim Basin. On the one hand, the closure of the Kudi Ocean has led to adjustments and changes in the stress field within the basin, further affecting the tectonic movement and crustal deformation in the surrounding areas. On the other hand, the closure of the Kudi Ocean has also led to changes in sedimentation, affecting the distribution and characteristics of sedimentary rocks in the basin. At the same time, the closure of Kudiyang also provided conditions for the formation of oil and gas resources. During the closure of the Kudi Ocean, a large amount of organic matter is enriched in seabed sediments, providing a material basis for the generation of oil and gas. With the movement and tectonic evolution of the crust, these organic substances are transformed into oil and gas under appropriate conditions, forming the oil and gas reservoirs in the current Tarim Basin.

The tectonic environment of the Tarim Basin has undergone an evolutionary process from extension to compression.

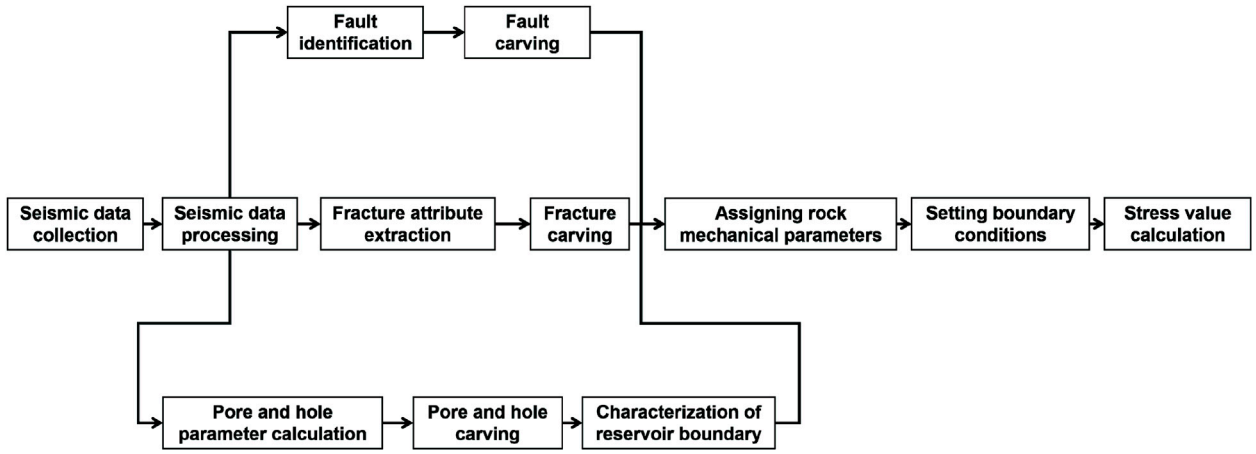


FIGURE 3
Flowchart of numerical simulation of *in-situ* stress field.

The evolution of this tectonic environment has had an important impact on the geological characteristics and resource distribution of the Tarim Basin. In an extensional environment, a large amount of sediment and organic matter were formed in the basin, which were buried and preserved in the subsequent compression environment, forming important oil and gas resources. During the interaction and movement of the Earth's tectonic plates, the newly formed marginal orogenic belt in the southwest gradually formed and developed. The formation of this type of orogenic belt is closely related to processes such as crustal compression, shortening, and magmatic activity. With the formation and evolution of the orogenic belt, the Tazhong Uplift and the Tabei Uplift gradually formed (Figure 1).

On the one hand, the newly formed active margin orogenic belt exerts a compressive force on the Tazhong uplift and the Tabei uplift. This compressive force causes the crust to deform and rise, forming structural features of uplift. At the same time, magmatic activity within the orogenic belt also provides a material basis for the formation of uplift. The upward migration and crystallization of magma into rock increases the material density of the crust, further promoting crustal uplift and uplift.

On the other hand, the newly formed active margin orogenic belt also affected the sedimentation and structural characteristics of the Tazhong uplift and the Tabei uplift. Under the influence of the orogenic belt, the depositional patterns and characteristics of sediments in the uplift areas changed, forming specific sedimentary layers and structural features.

At the end of the Late Ordovician, with the mutual collision of plates and the compression and shortening of the crust, the Kangxiwar East Kunlun Ocean and the Altun Ocean gradually closed, forming a strong orogeny. This orogeny led to the uplift and deformation of the crust in the south of the Tarim Basin, forming structural features such as thrust faults and folds. At the same time, the excavation of the crust caused the sediment to be stripped and transported, forming geomorphic features such as alluvial fans and canyons.

Thrusting has an important impact on the structural pattern and resource distribution in the southern Tarim Basin. On the one hand, the thrust action causes changes in the stress field of the crust, affecting the tectonic movement and crustal deformation in the surrounding areas. On the other hand, thrust also leads to the redistribution and metamorphism of sediments, affecting the distribution and characteristics of sedimentary rocks.

From the compressive stress field environment in the south to the formation and collision of the island arc in the middle Tianshan Mountains, to the opening and magmatic activity of the ancient Tethys Ocean, and the collision between the Eurasian plate and the Tarim block, a series of geological events together shape the present Tarim Basin (Wang Q. et al., 2019).

3 Numerical simulation method of *in-situ* stress field

The numerical simulation of the stress field of ultra-deep strike-slip faults is summarized in the following 10 steps (Figure 3).

1. Interpretation of faults in earthquake: First, collect relevant seismic data and perform necessary preprocessing on the raw data. Through analyzing the seismic data, identify and locate underground faults.
2. Loading fault: Based on known seismic data and interpretation results, establish a deterministic model. Load the identified fault information into this model.
3. Using Likelihood fracture prediction technology to calculate similarity: Extracting relevant attributes, such as likelihood attributes, based on seismic data to describe the similarity between acquisition points. By setting a certain threshold or criterion, information related to fracture development can be screened from the calculated similarity.
4. Extract attributes and characterize fractures using seismic data: Select seismic data related to fracture characterization, extract attributes that can describe fracture characteristics

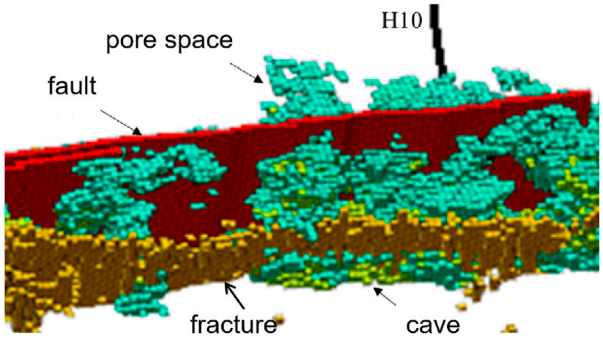


FIGURE 4
Characterization of faults, fractures, caves, and pores based on seismic data and attribute extraction analysis.

from the selected seismic data, and characterize or depict the location and morphology of fractures in the model based on the extracted attributes and previously predicted fracture probabilities. Integrate all processing and modeling results to form a complete geological model.

5. Classify and carve different types of storage bodies (Figure 4): Before carving the pores and holes, it is necessary to integrate and utilize the existing logging interpretation and geological data. Based on the structural description of the fault-controlled reservoir, the fractal dimension algorithm is used to construct the initial model. The microscopic characteristics of the model are controlled according to the changes in seismic amplitude, and by strengthening the seismic facies control factors, the spatial heterogeneity of the fault-controlled reservoir can be more accurately highlighted. According to the differences in logging porosity thresholds for different types of reservoirs, different types of reservoirs are carved according to their classification (Li et al., 2021).
6. Utilizing structural tensor attributes to characterize the boundary of fault-controlled reservoirs: Structural tensor attributes are a method for describing the texture characteristics of seismic data. By analyzing this attribute, the boundaries of fault-controlled reservoirs can be identified. Specifically, the boundaries of fault-controlled reservoirs exhibit unique and disordered texture characteristics on structural tensor attribute profiles.
7. Determine the threshold value of the structural tensor property through the calibration of the drilling time curve: By analyzing the changes in the drilling time curve, a threshold value for the structural tensor property can be calibrated.
8. Assign rock mechanical parameters directly to the model grid: The rock mechanical parameters obtained from seismic data are directly assigned to the model grid. In order to reduce the influence of boundary effects, the modeling range usually extends outside the fault zone to ensure that the internal model is closer to the actual situation. This can make the model more realistic and reflect the actual mechanical properties of underground rocks.
9. Setting model boundary conditions: determining the direction of *in-situ* stress based on regional structural analysis; determining the direction of *in-situ* stress based on drilling-induced fractures and wellbore collapse interpretation; constructing a single-well *in-situ* stress profile; through comprehensive analysis of these factors, the magnitude of *in-situ* stress can be constrained or limited, making the calculation results more accurate and reliable.
10. Automatic calculation of stress value: After setting the boundary conditions and entering relevant parameters, numerical simulation software can be used to automatically calculate the *in-situ* stress values. The compressive strength exceeds 100 MPa, which is equivalent to or even exceeds the mechanical parameters of reservoir rocks in the Kelasu tectonic belt with a depth of 7,000–8,000 m. The compressive strength of the reservoir in the Qiulitag tectonic belt with a depth of 6,000 m is only about 70–80 MPa. Construction data shows that the fracture pressure gradient of the Jurassic Ah Formation in the Dibei gas reservoir is about 2.4 MPa/100 m, and the construction pressure is about 95–100 MPa.

4 Calculation method and results of *in-situ* stress of single well

The calculation method of *in-situ* stress for single well is mainly divided into the following three steps.

4.1 Evaluation of the orientation of the main stress today

① Wellbore collapse method.

There are two methods to evaluate the current principal stress orientation using the drilling wellbore collapse method:

a) Using imaging data such as formation dip, resistivity, and sonic wave, a wellbore imaging map is obtained through processing. Looking for a symmetrical strip-shaped image with a certain width in the map indicates wellbore collapse. The orientation indicated in the image is the horizontal minimum principal stress orientation, and its vertical direction is the horizontal maximum principal stress orientation.

b) Extract the formation dip, well deviation in imaging data, wellbore azimuth, multi-arm caliper, No. 1 polar plate azimuth, and relative azimuth data. Use a rose diagram to statistically analyze the azimuth of the caliper expansion part. The resulting azimuth is the minimum horizontal principal stress azimuth, and its vertical direction is the maximum horizontal principal stress azimuth.

② Drilling induced fracture method.

Identifying fractures with characteristics of splay, symmetry, or straight, symmetrical features from the formation dip and acoustic and electrical imaging maps is the stress release-induced fracture in drilling. The directional angle value is read from the scale at the top of the figure, which is the maximum horizontal principal stress orientation.

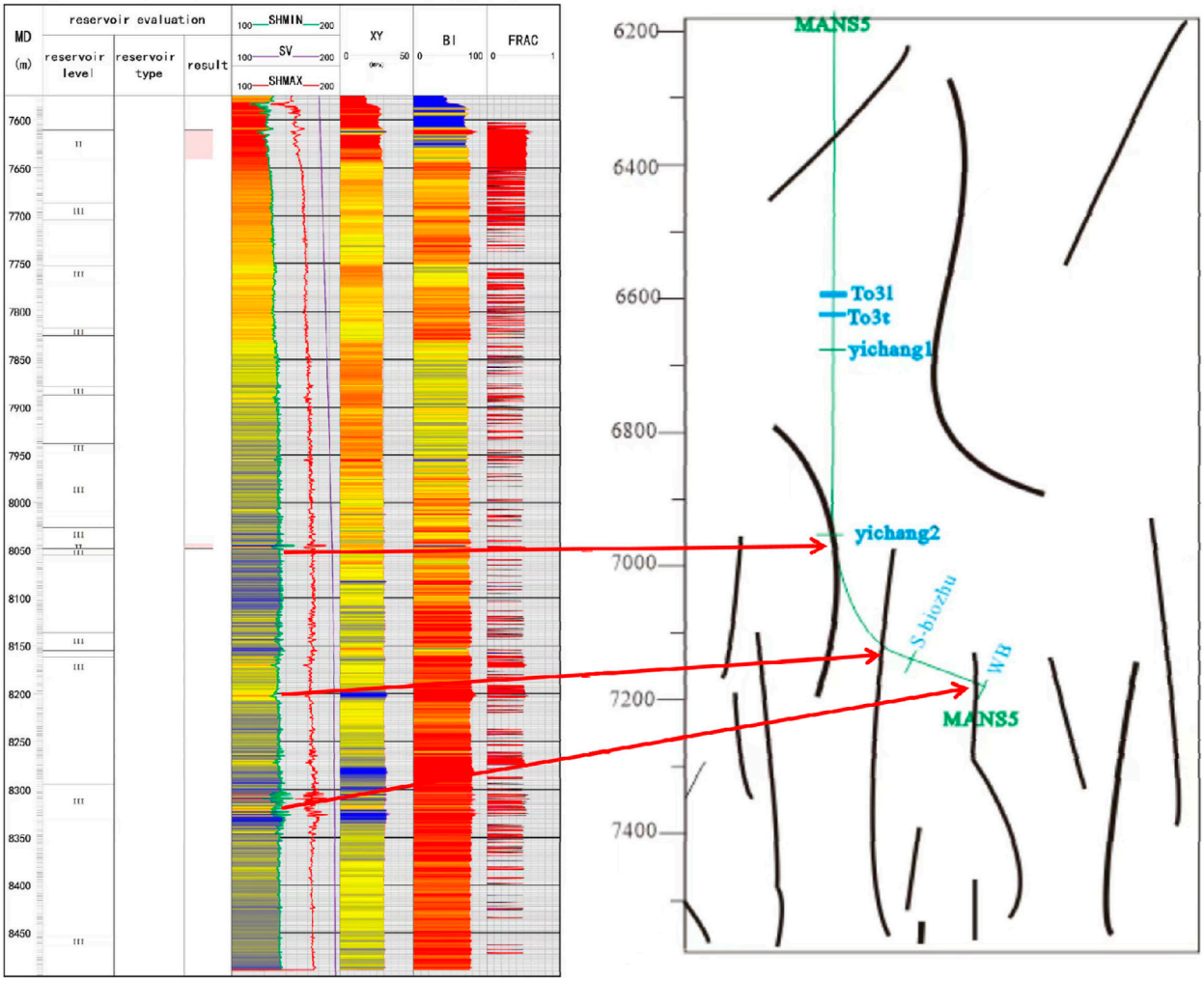


FIGURE 5
Correspondence between the *in-situ* stress and seismic profile interpretation of ManS 5 Well.

③ Fast transverse wave azimuth method.

The azimuth of the fast shear wave in the formation is obtained using the dipole array acoustic logging data processing, and the azimuth with the highest frequency is obtained using a rose diagram statistics, which is the maximum horizontal principal stress azimuth (Yang et al., 2008; Wang et al., 2009).

4.2 Evaluation of three-axis stress today calculation of vertical stress

$$\sigma_V = \int_{H_0}^{0} \rho_0(h) g dh + \int_{H}^{H_0} \rho(h) g dh$$

In the formula: σv-pressure of overlying strata, MPa;
ρ0—average density of the formation in the depth section without logging density value, g/cm3; ρ-density of the formation, g/cm3;
H0 - refers to the starting depth of density logging, m;
H - refers to the depth of the calculation point, m.

② Evaluation of horizontal principal stress.

The standard prioritizes the use of small-scale fracturing and formation leakage experimental methods to determine the horizontal minimum principal stress of the formation. When there is no data from small-scale fracturing and formation leakage experiments, the following calculation formula is used to obtain the horizontal principal stress using well logging data (Wang, 1993; Xu and Shen, 2005; Li and Liu, 2006).

$$\sigma_H = \frac{\mu}{1-\mu}\sigma_V + \frac{1-2\mu}{1-\mu}\alpha P_P + \frac{E}{1-\mu^2}\varepsilon_H + \frac{\mu E}{1-\mu^2}\varepsilon_h$$

$$\sigma_h = \frac{\mu}{1-\mu}\sigma_V + \frac{1-2\mu}{1-\mu}\alpha P_P + \frac{E}{1-\mu^2}\varepsilon_h + \frac{\mu E}{1-\mu^2}\varepsilon_H$$

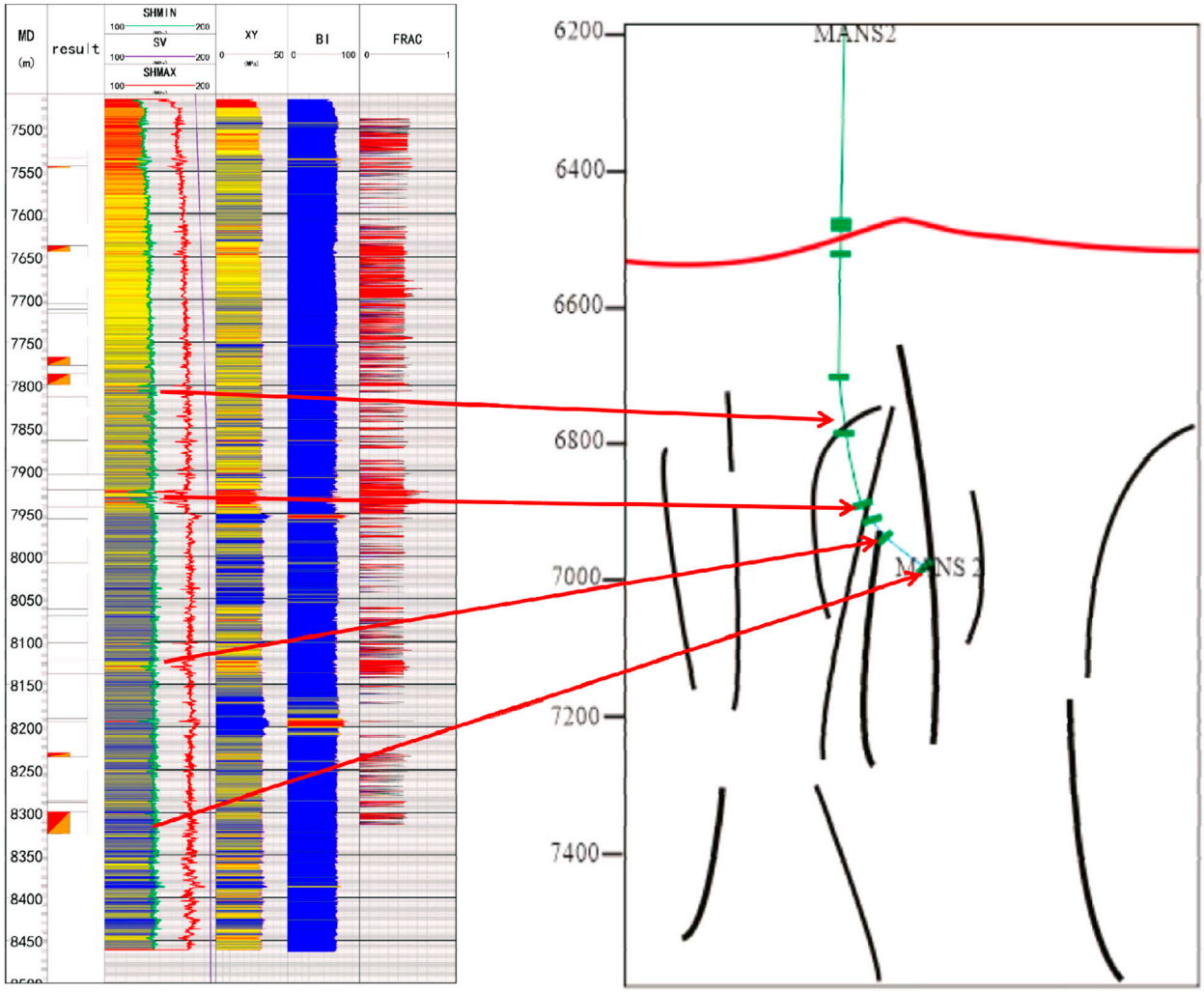


FIGURE 6
Correspondence between the *in-situ* stress and seismic profile interpretation of ManS 2 Well.

In the formula:
σH–maximum horizontal principal stress, MPa;
σh–horizontal minimum principal stress, MPa;
σv—pressure of overlying strata, MPa;
PP–formation pore pressure, MPa; μ–Poisson's ratio, dimensionless; α—Biot coefficient;
εh—strain in the direction of the minimum horizontal principal stress, mm;
εH—strain in the direction of the maximum horizontal principal stress, mm;
E – Young's modulus, GPa.

4.3 Evaluation of rock mechanical parameters

Through analysis of well logging data, especially acoustic logging data and density logging data, rock mechanical parameters such as Young's modulus and Poisson's ratio can be calculated.

From the single well *in-situ* stress calculation results (Figures 5, 6), it can be seen that the locations where the current *in-situ* stress values decrease are the ones with developed fractures, holes, and pores.

5 Numerical simulation results

Figure 7 shows the distribution of the minimum horizontal principal stress. Based on the information in the figure, the following observations can be made:

In the vertical direction (with the increase of depth):

- The ground stress gradually increases. In the horizontal direction (along the extension direction of the fault):
- There are differences in the magnitude of stress values, which are segmented. Overall characteristics:
- The *in-situ* stress values at fracture zones and fissures are low.
- The degree of stress reduction varies among different fracture-cave systems, indicating a strong heterogeneity.

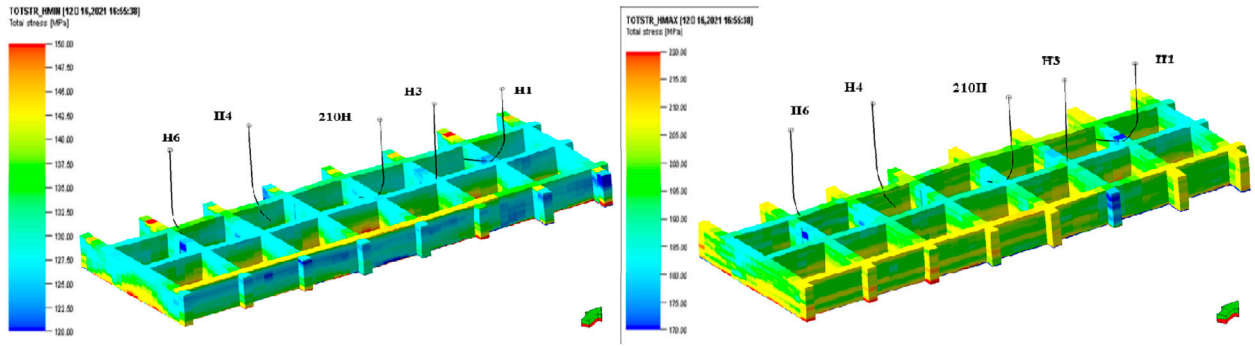


FIGURE 7
Simulation results of the maximum and minimum horizontal principal stress in the *in-situ* stress field of the FI12 fracture zone.

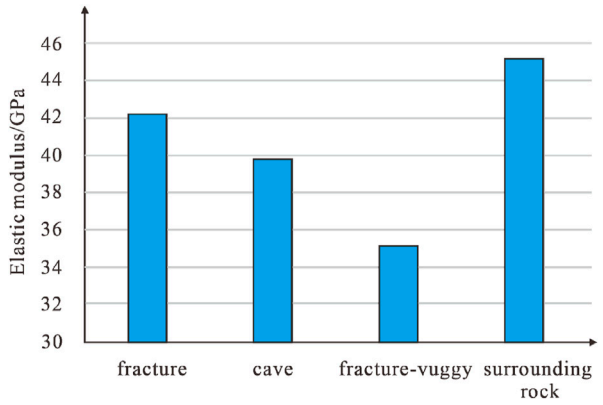


FIGURE 8
Statistical diagram of elastic modulus of different types of units in ManS 2 well.

- The heterogeneity at the bottom of the target layer slightly decreased.
- The magnitude of stress reduction in the fault zone weakens.

Summary: Figure 7 show the spatial distribution characteristics of the maximum and minimum horizontal principal stresses. This information is important for understanding the impact of faults and fractures on geostress, as well as for predicting the stability of geological structures and engineering projects.

Figure 8 combines the stress profile of a single well with seismic attribute profiles, providing insight into the variation of *in-situ* stress in different geological structures. Based on the information in the figure, the following conclusions can be drawn:

In the fracture-cave area, the elastic modulus decreases the most, reaching 22.25%. This indicates that in the fracture-cave area, the rigidity and strength of the rock significantly decrease, which may be due to dissolution and tectonic activity.

The *in-situ* stress in the cave area also decreased by 11.92%, indicating that the formation of caves has an impact on the stress state of surrounding rocks.

The *in-situ* stress in the fracture zone decreased by 6.40%. Compared to fracture-cave bodies and karst caves, the decrease in *in-situ* stress in the fracture zone was relatively small, but still showed a certain degree of stress reduction.

Summary: Figure 8 shows the influence of different geological structures on stress through the combination of single-well stress profiles and seismic attribute profiles. These data are of great significance for deepening our understanding of the stress state of underground rocks and the stability of geological structures, and provide a basis for geological engineering design and risk assessment.

6 Discussions

6.1 The distribution characteristics of crustal stress in the fracture-cave system

Figure 9 displays the stress distribution changes at karstic voids. Different degrees of stress reduction are observed at the void edges, and there is also a certain range of stress elevation at the void margins. This stress distribution suggests that a high-stress "shell" region exists around the voids. To further clarify the stress "shell" distribution of voids, a three-dimensional geological model of the fracture-cave system was established (Figure 10). By varying the elastic modulus of the karstic voids, the impact of voids on the current stress distribution can be analyzed.

Based on the above information, the following conclusions can be drawn: By analyzing the impact of voids on the current stress distribution, it can be found that different voids have different ranges of influence on stress. This difference may be related to factors such as the size, shape, location, and surrounding rock properties of the voids.

Summary: The information in Figure 10 suggests that the high-stress "shell" around voids is an important factor affecting stress distribution.

Given the stress background of the known FI12 fault, we can establish the following model rock mechanical property parameters and boundary mechanical conditions:

Sv gradient = 0.0256 MPa/m.
SH gradient = 0.0234 MPa/m.
Sh gradient = 0.0187 MPa/m.

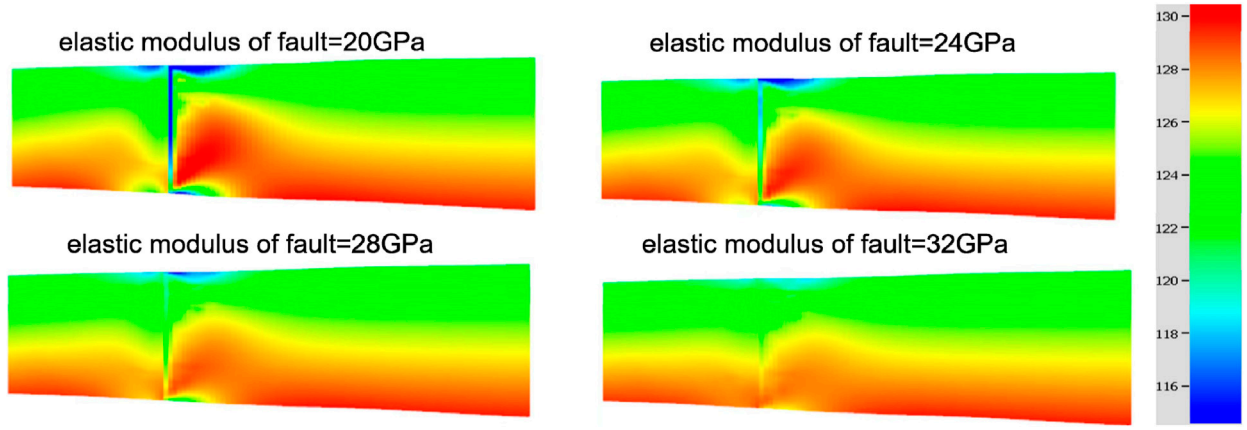


FIGURE 9
Analysis on the stress distribution characteristics of the FI12H well area.

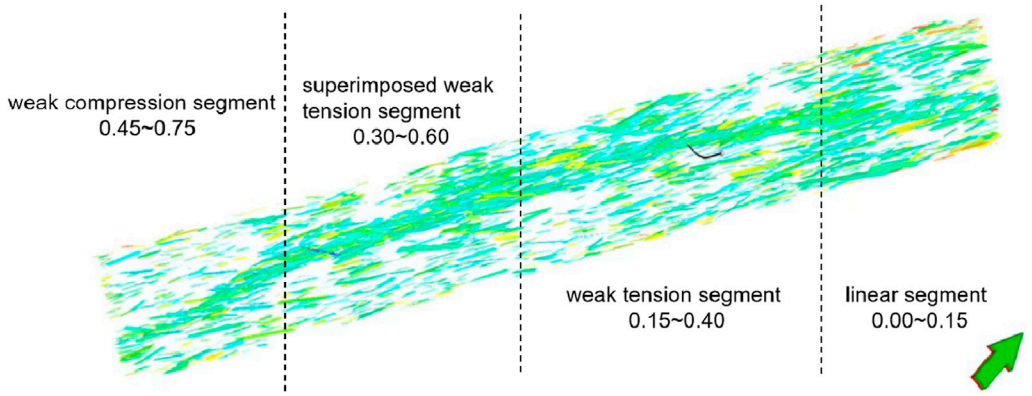


FIGURE 10
Analysis diagram of mechanical effectiveness of FI12 fault.

Mechanism of normal faulting.
SH direction = 59°N.

The simulation results indicate that the larger the difference in elastic modulus between the cave body and matrix, the more pronounced the decrease in *in-situ* stress within the void and the larger the influence range of the "shell" outside the void. This suggests that the "shell-type" stress distribution pattern of fracture-cave systems mainly depends on the difference in elastic modulus between the matrix and voids.

Therefore, to better understand and predict the stress distribution pattern, we need to further investigate the difference in elastic modulus between the matrix and voids, as well as how this difference affects stress distribution.

Based on the above analysis, we can draw the following conclusions: As the elastic modulus of voids increases, the current *in-situ* stress values also increase accordingly. This suggests that in underground rocks, if the elastic modulus of voids is relatively high, then the *in-situ* stress values will also increase accordingly. This relationship may be caused by the bearing and transmission effects of voids on *in-situ* stress.

Under conditions where vertical stress remains constant, the stress values are smallest for normal faulting mechanisms, largest for reverse faulting mechanisms, and intermediate for strike-slip mechanisms. This indicates that different faulting mechanisms have a significant impact on stress distribution. Normal faulting mechanisms typically result in a decrease in *in-situ* stress values, while reverse faulting mechanisms lead to an increase in *in-situ* stress values. Strike-slip mechanisms have relatively stable stress values that fall between normal and reverse faulting mechanisms.

Summary: These conclusions further confirm the important influence of voids and faulting mechanisms on stress distribution. Based on the above analysis, a further exploration of fracture-controlled stress distribution patterns and their impact on fluid flow in fracture-cave systems can be proposed. This model includes four scenarios:

a) The karstic void is completely filled with oil and gas: In this case, the stress distribution within the karstic void may be influenced by the supporting effect of oil and gas, resulting in a more uniform stress distribution and a decrease in *in-situ* stress values. The influence range of the high-stress "shell" outside the void may also be correspondingly reduced.
b) The karstic void is half filled with oil and gas and half filled with breccia: In this situation, the mixed filling of oil and gas with breccia may affect stress distribution. Due to the higher rigidity and strength of breccia, it may increase *in-situ* stress values within the void. At the same time, the combination of oil and gas with breccia may also reduce the influence range of the "shell" outside the void.
c) The oil and gas are filled within breccia pores: This situation is similar to scenario a). Oil and gas filling within breccia pores may affect stress distribution and decrease *in-situ* stress values. The influence range of the high-stress "shell" outside the void may also be correspondingly reduced.
d) The cave is filled with breccia cementation:In this case, the distribution of ground stress in the cave may be mainly controlled by the cementation of breccia. Due to the cementation of breccia, the rigidity and strength of the cave may be increased, thereby increasing the ground stress value. At the same time, due to the cementation of breccia, the influence range of the ground stress "shell" may also be correspondingly reduced.

Based on the above analysis, it can be concluded that as the difference between oil and gas and breccia inside the cave decreases, from a to d, the difference between inside and outside the cave decreases, and thus the degree of "shell-type" ground stress mode decreases. This indicates that the distribution pattern of ground stress is affected by the nature and distribution of the fillings inside the cave. Understanding this impact can help better predict the stability and potential risks of underground structures, and provide more accurate basis for geological engineering design and resource development.

6.2 Evaluation of fracture activity

Fracture activity is an important parameter used to characterize the sliding tendency of fracture surfaces and reflect the permeability and fluid transport effectiveness of fractures. Under the influence of regional stress fields, the stress on the fracture surface can be decomposed into an effective normal stress σne perpendicular to the fracture surface and a shear stress τ parallel to the fracture surface. The ratio of these two stresses can be used to indicate the sliding tendency of the fracture surface.

In addition, the physical properties (such as roughness) and mechanical properties of the fault zone itself can also affect its sliding tendency. Therefore, the sliding tolerance factor is an important indicator that comprehensively considers these factors.

The calculation method of fault activity is as follows:

Calculate the effective normal stress σne and shear stress τ perpendicular to the fracture surface.

Calculate the ratio of the two stresses, which is the slip tolerance factor. This ratio can be used to indicate the slip tendency of the fracture surface (Xu et al., 2023).

Considering the differences in physical and mechanical properties of the fault zone itself, the slip tolerance factor is corrected.

Based on the magnitude of the fault activity index, the sliding trend of the fault plane and the effectiveness of fluid transport are evaluated.

It should be noted that the calculation of fault activity requires consideration of multiple factors and requires comprehensive analysis and evaluation in conjunction with actual conditions.

Therefore, in practical applications, appropriate adjustments and modifications need to be made based on specific circumstances.

$$S = \frac{\tau}{\mu \cdot \sigma_{ne} + C}$$

Based on the above analysis, the mechanical effectiveness of the FI12 fault can be segmented (Figure 10). Overall, it can be divided into four segments:

Weak compression uplift section: The fault activity coefficient is between 0.45 and 0.75.

Stacking weak pull segmentation: The fault activity coefficient is between 0.30 and 0.60.

Weak pull segmentation: The fault activity coefficient is between 0.15 and 0.40.

Linear segment: The fault activity coefficient is 0–0.15.

In addition, the productivity of oil and gas wells on this fault zone is well correlated with the effectiveness of fracture mechanics. This indicates that the fracture-fracture system plays a key role in the development of oil and gas reservoirs controlled by faults. Therefore, segmented evaluation of the mechanical effectiveness of fracture-fracture systems can provide important evidence for the prediction of oil and gas well productivity and the development strategy formulation.

6.3 Application of *in-situ* stress research in oil and gas production

It is very important to fully consider geomechanical factors in optimizing the deployment of carbonate rock wells with controlled breakage. In order to optimize high-quality reservoirs and take into account the efficiency of reservoir reconstruction, as well as ensure the success rate of well placement, the following are some countermeasures and considerations based on geological stress:

When drilling into a cave, it is important to observe whether the drilling tools are empty and whether the drilling fluid is leaking. If there is active oil and gas display and no significant collapse of the wellbore, the evaluation result of *in-situ* stress is low, indicating that a favorable reservoir has been encountered. In this case, priority should be given to maintaining the current well location and taking appropriate measures to protect and utilize this favorable reservoir.

When the wellbore encounters the periphery of the cave, if there is a small amount of leakage, low oil and gas shows (total hydrocarbon values are generally below 0.5%), and imaging logging shows a small amount of collapse of the wellbore wall, indicating a small number of natural fractures, it indicates that the drilling has encountered the periphery of the favorable reservoir and there is a certain degree of stress concentration. In this case, large-scale sand fracturing can be used to communicate the reservoir to increase its permeability.

When the wellbore encounters the periphery of the cave, if there is no leakage or venting, no good oil and gas shows, and there is a serious stress-type wellbore collapse on the wall, it indicates that a strong stress shell outside the cave has been encountered. In this case, it is recommended to review the relationship between the wellbore, cave, fractures, and ground stress, and consider taking the approach of deepening or sidetracking to continue drilling towards favorable reservoirs (cave or fracture zones). This can avoid drilling inside the strong stress shell, improve drilling efficiency, and increase the chance of finding favorable reservoirs.

In general, *in-situ* stress is one of the key factors affecting the success of drilling in fault-controlled carbonate reservoirs. Therefore, when deploying well locations, it is necessary to fully consider geomechanical factors to maximize the opportunity to find favorable reservoirs and reduce drilling risks.

When drilling favorable reservoirs, there will be a significant decrease in stress on the stress profile. Well 212H and Well 216H have low stress zones within a certain depth range, and these low-stress zones are consistent with oil reservoir logging interpretation. This indicates that these two wells have successfully drilled favorable reservoirs and exhibit high oil production.

According to the analysis of the 3D geomechanical model, the mechanical activity of the fractures around the 216-H4 well is medium-to-poor. In particular, the opening pressure equivalent drilling fluid density of most fractures around the wellbore is high, while the opening pressure equivalent drilling fluid density of a fracture on the east side is low. This indicates that the opening pressure of fractures around the well is high, requiring high-pressure fluid to activate and communicate with the reservoir.

To effectively communicate with the reservoir, it is recommended to inject high-pressure liquid into Well 216-H4. Through calculation, the density of the injected liquid should be 1.05 g/cm^3, and the injection pressure should be approximately 30–47 MPa. After the transformation, the daily oil production of this well has significantly increased, exceeding 220 m^3.

In summary, by analyzing the *in-situ* stress profile and reservoir characteristics, we can better understand the distribution and properties of the reservoir, and provide important guidance for well placement and reservoir modification.

7 Conclusion

(1) Due to the strong heterogeneity of the fracture-controlled vuggy reservoir, faults, fractures, and vugs can lead to varying degrees of reduction in the local stress field. Therefore, the development and internal material composition of fractures and vugs can be inferred based on the degree of stress reduction. This inference method helps to better understand the characteristics and properties of the reservoir.

(2) The crustal stress field of the fracture-cave body presents a "shell-type" distribution pattern. In this pattern, the low-value region inside is a favorable reservoir body, while the outer strong stress shell is characterized by stress concentration and poor permeability. During drilling, if strong stress shells are encountered, wellbore collapse may occur, making these areas unfavorable drilling targets. To avoid this situation, it is recommended to adopt large-scale reconstruction, deepening, or sidetracking to avoid such areas.

(3) The *in-situ* stress and the mechanical activity of fractures and joints under its influence have an impact on the quality and productivity of fracture-controlled, fracture-cave reservoirs. Therefore, in the optimization process of well placement, the factor of *in-situ* stress should be fully considered. By optimizing high-quality reservoirs and taking into account reservoir reconstruction efficiency, the success rate of well placement can be guaranteed. 1) The heterogeneity of fault-controlled vuggy reservoirs is significant. Faults, fractures, and cavities cause varying degrees of stress reduction in the local stress field. Based on this, it is possible to deduce the development and internal composition of faults, fractures, and cavities by analyzing the extent of stress reduction.

Data availability statement

The original contributions presented in the study are included in the article/Supplementary material, further inquiries can be directed to the corresponding author.

Author contributions

YZ: Writing–original draft. KX: Conceptualization, Writing–original draft. HZ: Funding acquisition, Supervision, Writing–original draft. SL: Data curation, Software, Writing–original draft. JL: Data curation, Methodology, Writing–review and editing. ZQ: Formal Analysis, Resources, Visualization, Writing–review and editing.

Funding

The author(s) declare financial support was received for the research, authorship, and/or publication of this article. This study was supported by PetroChina Tarim Oilfield Company Science and Technology Project "Oil and Gas Field Geomechanics Technology Research and Application (II)" No. T202308.

Conflict of interest

Authors YZ, KX, HZ, SL, JL, and ZQ were employed by Tarim Oilfield Company. Authors YZ, KX, HZ, SL, JL, and ZQ were employed by China National Petroleum Corporation (CNPC).

Publisher's note

All claims expressed in this article are solely those of the authors and do not necessarily represent those of their affiliated organizations, or those of the publisher, the editors and the reviewers. Any product that may be evaluated in this article, or claim that may be made by its manufacturer, is not guaranteed or endorsed by the publisher.

References

Cui, J., Zhang, X., and Li, P. (2002). The Altun fault: its geometry, nature and mode of growth. *Acta Geosci. Sin.* 23 (6), 509–516.

Fossen, H. (2010). *Structural geology*. Cambridge, MA, USA: Cambridge University Press.

Gogonenkov, G. N., and Timurziev, A. I. (2012). Strike-slip faulting in the west siberian platform: insights from 3D seismic imagery. *Comptes Rendus Geosci.* 344 (3/4), 214–226. doi:10.1016/j.crte.2011.09.010

Han, X., Deng, S., Tang, L., and Cao, Z. (2017). Geometry, kinematics and displacement characteristics of strike-slip faults in the northern slope of Tazhong uplift in Tarim Basin: a study based on 3D seismic data. *Mar. Petroleum Geol.* 88, 410–427. doi:10.1016/j.marpetgeo.2017.08.033

Jiao, F. (2017). The significance of hydrocarbon exploration in the NE trending strike-slip fault belt in Shuntuoguole area, Tarim Basin. *Oil Gas Geol.* 38 (5), 831–839. doi:10.11743/ogg20170501

Li, Y., Wang, Q., and Ma, Y., (2020). Structural geometry and evolution of an intracratonic strike-slip fault zone: a case study from the north SB5 fault zone in the Tarim Basin, China. *J. Struct. Geol.* 146, 1–20.

Li, Y., Wang, Q., and Ma, Y., (2021). Modeling and application of crustal stress field in fault-controlled fractured-vuggy reservoirs of the Fuman oilfield. *J. Petroleum Sci. Eng.* 190, 108–124.2021

Li, Z., and Liu, J. (2006). Application of one-dimensional geomechanical model in dam engineering. *Water Power* 32 (6), 59–62.

Li, P., Chen, H., and Tang, D., (2017). Coupling relationship between NE strike-slip faults and hypogenic karstification in middle-lower Ordovician of Shunnan area, Tarim Basin, Northwest China. *Earth Sci.* 42 (1), 93–104.

Lyu, H., Zhang, S., and Ma, Q. (2017). Classification and formation mechanism of fault systems in the central and northern Tarim Basin. *Petroleum Geol. Exp.* 39 (4), 444–452.

Ma, D., Wang, Z., Duan, S., Gao, J., Jiang, Q., Jiang, H., et al. (2018). Strike-slip faults and their significance for hydrocarbon accumulation in Gaoshiti-Moxi area, Sichuan Basin, SW China. *Petroleum Explor. Dev.* 45 (5), 851–861. doi:10.1016/s1876-3804(18)30088-0

Mao, Y., Xue, L., and Chen, Y., (2017). Structural evolution of intracratonic strike-slip faults in the central Tarim Basin, NW China. *J. Struct. Geol.* 111 (1), 187–204.

Song, X., Chen, S., and Xie, Z., (2023a). Development characteristics of strike-slip faults in the east of Fuman oilfield and their hydrocarbon accumulation. *Oil Gas Geol.* 44 (2), 335–349.2023

Song, X., Shi, C., and Zhou, X., (2023b). Development characteristics of strike-slip faults in the east of Fuman oilfield, Tarim Basin and their hydrocarbon accumulation. *Oil Gas Geol.* 44 (02), 335–349.

Wang, Q., Li, Y., and Ma, Y., (2019b). Multiple thrust detachments and their implications for hydrocarbon accumulation in the northeastern Sichuan Basin, southwestern China. *J. Petroleum Sci. Eng.* 178, 385–398.

Wang, Q., Yang, H., Wang, R., Li, S., Deng, X., and Li, Y., (2021). Exploration discovery and technological innovation of large oil and gas fields controlled by strike-slip faults in ultra-deep layer of Tarim Basin. *China Pet. Explor.* 26 (4), 58–71. doi:10.3969/j.issn.1672-7703.2021.04.005

Wang, Q., Yang, H., and Zhang, Y., (2023a). Exploration and innovation of large oil and gas fields controlled by strike-slip faults in ultra-deep layer of Tarim Basin. *China Pet. Explor.* 28 (4), 58–71.2023

Wang, Q., Yang, H., Zhang, Y., Li, Y., Zhang, Y., and Yang, X., (2023b). Major discovery of Ordovician in Fudong 1 well in Fuman oilfield and its significance. *China Pet. Explor.* 28 (01), 47–58. doi:10.3969/j.issn.1672-7703.2023.01.005

Wang, S. (1993). Application of one-dimensional geomechanical model in geotechnical engineering. *J. Eng. Geol.* 1 (1), 1–8.

Wang, S., Wang, J., and Wang, C., (2009). Application of one-dimensional geomechanical modeling in tunnel engineering. *J. Eng. Geol.* 17 (4), 549–554.

Wang, Y., Hu, W., and Xu, X., (2018). Study on the control of strike-slip faults on oil and gas reservoirs - a case study of Nanpu depression. *Pet. Geophys.*, 5.2018

Wang, Y., Hu, W., and Xu, X., (2019a). Study on the control of strike-slip faults on oil and gas transportation and accumulation - a case study of Jiyang depression. *J. China Univ. Petroleum Nat. Sci. Ed.* 43 (6), 1–10.2019

Wu, G., Ma, B., Han, J., Guan, B., Chen, X., Yang, P., et al. (2021). Origin and growth mechanisms of strike-slip faults in the central Tarim Cratonic Basin, NW China. *Petroleum Explor. Dev.* 48 (3), 595–607. doi:10.1016/s1876-3804(21)60048-4

Wu, G., Yang, H., and Qu, T., (2012). The fault system characteristics and its controlling roles on marine carbonate hydrocarbon in the central uplift, Tarim Basin. *Acta Petrol. Sin.* 28 (3), 793–805.

Xu, K., Cai, Z., Zhang, H., Yin, G., Wang, Z., Fang, L., et al. (2023). Geomechanical modeling of ultradeep faultcontrolled carbonate reservoirs and its application, a case of the Fuman Oilfield in Tarim Basin. *Energy Sci. Eng.* 11, 3332–3343. doi:10.1002/ese3.1552

Xu, Z., and Shen, M. (2005). Study on discrete element method model for one-dimensional failure process analysis of rocks. *J. Rock Mech. Eng.* 24 (14), 2545–2551.

Yang, Q., Li, H., and Zhou, X. (2008). Application of one-dimensional geomechanical model in stability analysis of rock slope. *J. Rock Mech. Eng.* 27 (6), 1179–1186.

Yang, Y., Tang, L., and Guo, Y., (2016). Deformation characteristics and formation mechanism of NNE-trending strike-slip faults in Tazhong uplift. *Geol. China* 43 (5), 1569–1578.

Zheng, X., An, H., and Wang, Z., (2018). The segmentation features of strike-slip fault and its relation with the fault and reservoirs in Halahatang area, North Tarim Basin. *J. Zhejiang Univ. Sci. Ed.* 45 (2), 219–225.

frontiers | Frontiers in Energy Research

TYPE Original Research
PUBLISHED 07 March 2024
DOI 10.3389/fenrg.2024.1377400

Check for updates

OPEN ACCESS

EDITED BY
Liuke Huang,
Southwest Petroleum University, China

REVIEWED BY
Yuqiang Xu,
China University of Petroleum, China
Qiao Deng,
Yangtze University, China
Yanfang Gao,
Northwest University, China

*CORRESPONDENCE
Qinglin Shan,
shanqinglin2000@163.com

RECEIVED 27 January 2024
ACCEPTED 26 February 2024
PUBLISHED 07 March 2024

CITATION
Luan H, Liu M, Shan Q, Jiang Y, Li B, Wang C and Cheng X (2024), Numerical study of hydraulic fractures propagation in deep fracture-cavity reservoir based on continuous damage theory. *Front. Energy Res.* 12:1377400. doi: 10.3389/fenrg.2024.1377400

COPYRIGHT
© 2024 Luan, Liu, Shan, Jiang, Li, Wang and Cheng. This is an open-access article distributed under the terms of the Creative Commons Attribution License (CC BY). The use, distribution or reproduction in other forums is permitted, provided the original author(s) and the copyright owner(s) are credited and that the original publication in this journal is cited, in accordance with accepted academic practice. No use, distribution or reproduction is permitted which does not comply with these terms.

Numerical study of hydraulic fractures propagation in deep fracture-cavity reservoir based on continuous damage theory

Hengjie Luan[1], Mingkang Liu[1], Qinglin Shan[1]*, Yujing Jiang[1,2], Bo Li[3], Changsheng Wang[1] and Xianzhen Cheng[1]

[1]State Key Laboratory of Mining Disaster Prevention and Control Co-Founded by Shandong Province and the Ministry of Science and Technology, Shandong University of Science and Technology, Qingdao, China, [2]Graduate School of Engineering, Nagasaki University, Nagasaki, Japan, [3]College of Civil Engineering, Tongji University, Shanghai, China

Natural fractures and cavities are the primary spaces for oil and gas accumulation in fracture-cavity carbonate reservoirs. Establishing the connection between these spaces and the wellbore through hydraulic fracturing treatment is important for oil and gas extraction from such reservoirs. Due to the discontinuity and heterogeneity of the existing natural fracture-cavity system, anticipating the viability of hydraulic fracturing treatment is troublesome. A new method to simulate the hydraulic fracturing propagation in fracture-cavity reservoirs is proposed based on the continuous damage theory. The method considers the random spatial distribution of fractures and cavities and can simulate the arbitrary expansion of hydraulic fractures in the three-dimensional direction. Based on this method, the influence of different geological and engineering factors on the propagation patterns of hydraulic fractures in the fracture-cavity reservoirs is investigated. It is found that the increase of reservoir burial depth significantly limits the propagation ranges of hydraulic fractures. The propagation modes of hydraulic fractures encountering natural fractures change with increasing burial depth, undergoing a transition from "penetrate and deflect" to "defect" and then to "penetrate". The reduction of horizontal stress difference increases the complexity of hydraulic fractures, but it is not conducive for hydraulic fractures to connect more natural fractures and cavities. The increase in fracturing pump rate is significantly beneficial for hydraulic fractures to connect more natural fractures and cavities. The viscosity of fracturing fluid has a significant impact on the morphology of hydraulic fracture propagation, which undergoes a transition from simple to complex, and then to simple with the change of the fracturing fluid viscosity from low to high. either too high or too low viscosity of the fracturing fluid is not conducive to the connection of more natural fractures and cavities by hydraulic fractures. The obtained conclusions can provide a reference for the design of hydraulic fracturing treatment for fracture-cavity carbonate reservoirs.

KEYWORDS

fracture-cavity carbonate reservoir, hydraulic fracturing, fracture propagation, continuous damage theory, numerical simulation

1 Introduction

In recent years, It has been becoming increasingly important to explore and develop the fracture-cavity reservoirs, especially in deep basins worldwide (Tian et al., 2019; Wang et al., 2019). Fracture-cavity carbonate reservoirs with extreme internal heterogeneity and burial depth of more than 5,000 m are widely distributed in the Tahe oilfield in Xinjiang, China (Zhang et al., 2004; Mousavi et al., 2013; Xu et al., 2016; Jiao, 2019; Ren et al., 2020; Huang et al., 2022; Zhang et al., 2022; Huang et al., 2023a). In Tarim Basin, oil and gas reserves of the discovered fracture-cavity reservoirs could reach to 1 billion tons (Xiao et al., 2016; Zheng et al., 2019). Therefore, the efficient development of oil and gas in fracture-cavity reservoirs is of great significance. A typical carbonate fracture-cavity stratum is shown in Figure 1 (Qiao et al., 2022). As we can see, such stratum is randomly distributed with natural fractures and cavities of varying sizes. Compared with conventional reservoirs, fracture-cavity carbonate reservoirs have a dense matrix with pores compacted under high pressure, which basically do not have hydraulic connectivity and mobility (Kang et al., 2004; Chalikakis et al., 2011; Lv et al., 2011; Ji et al., 2015; Huang et al., 2018; Zhang et al., 2019; Tan et al., 2021; Zheng et al., 2022; Luo et al., 2022). Hydraulic fracturing treatment to enhance the connection between the wellbore and oil and gas enriched fracture-cavity system is one of the commonly used techniques to increase oil and gas production from fracture-cavity carbonate reservoirs (Rahm, 2011; Huang et al., 2020; Liu et al., 2020). Given the deep burial and the non-uniformly distributed natural fractures and cavities, there are still many uncertainties and room for improvement in understanding how the extreme heterogeneity influence the hydraulic fracture propagation and how to optimize the fracture-cavity reservoir stimulation treatment.

In past studies, a lot of research on the general behaviour of hydraulic fractures in heterogeneous reservoirs containing natural fractures has been carried out physically and numerically. Physical simulations can provide intuitive experimental results and are widely used to simulate the expansion of hydraulic fractures. Zhou experimentally investigated the influence of random natural fracture systems on the geometry and propagation behavior of hydraulic fractures, and found both random natural fractures and *in-situ* stress differences govern the hydraulic fracture geometry and propagation behavior (Zhou et al., 2010). Liu used true triaxial volumetric fracturing experiments to investigate the factors affecting the hydraulic fracture propagation, and found that the presence of random natural fractures around the wellbore, the size of the random natural fractures, the bulk density of the specimens, and the horizontal differential stresses all play a role in the process (Liu et al., 2018). Hou conducted a series of large-scale true triaxial experiments with acoustic emission monitoring, and found that low-viscosity fluid can activate discontinuities to form a complex fracture network, whereas a high-viscosity fluid is likely to produce large fractures under a high contrast in the horizontal stresses (Hou et al., 2018). Guo carried out physical simulations of triaxial hydraulic fracturing in tight sandstone and investigated the influences of natural fracture development degree, *in-situ* stress conditions, and fracture treatment parameters on fracture propagation, and found that natural fracture played an important factor on hydraulic fracture morphology in tight sandstone reservoirs (Guo et al., 2021). Tan carried out experiment tests on several groups of combination samples comprised of artificial rocks to study the effects of *in-situ* stress, injection rate, natural fracture and well type on fracture growth in coal measure strata, and found the behavior of the hydraulic fracture also varied significantly between vertical and horizontal wells (Tan et al., 2023). Numerical simulation methods can overcome the limitations of physical test specimen size and are widely used in the study of hydraulic fracture propagation. Chuprakov conducted a parameter sensitivity analysis of the fracturing interaction process using numerical simulation, and the numerical results showed the fracture interaction angle, *in-situ* stress parameters, the injection rate and viscosity of the fracturing fluid are important parameters controlling whether or not a hydraulic fracture can penetrate a natural fracture (Chuprakov et al., 2013). Zhang et al. (2017) developed a hybrid discrete-continuous numerical scheme to study the behavior of hydraulic fractures under the influence of natural fractures, and the simulation results showed different propagating paths under various stress ratios and roughness of the natural fracture surface and that the complexity of fracturing increases as the number and scale of natural fractures increase. Shan established a fracturing model based on the continuous damage theory and investigated the influences of three factors, namely, geostress difference, fracture fluid viscosity, and pump rate, on the hydraulic fracturing patterns in

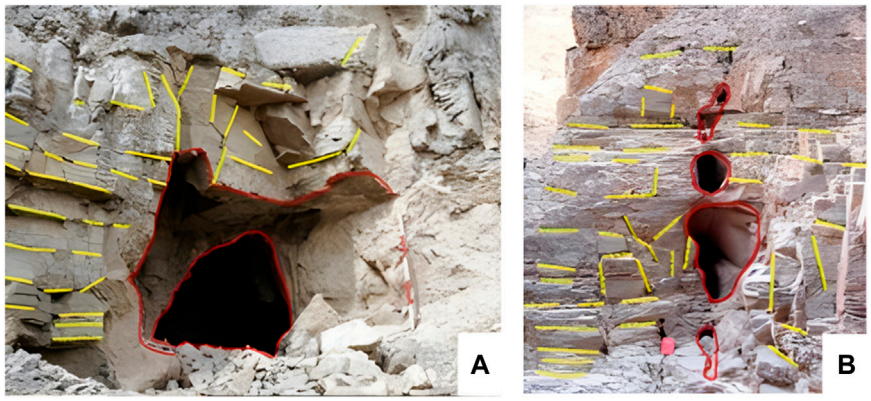


FIGURE 1
Typical carbonate fracture-cavity strata outcrops (Qiao et al., 2022). **(A)** Natural fractures and a single large cavity; **(B)** Natural fractures and a group of cavities.

TABLE 1 Summaries of research methods in published literature and future researching scope.

Methods in published literature	Limitations	Future researching scope
Indoor true tri-axial experiments on specimens with preset cavities and natural fractures	Size effect caused by limited specimen size	Numerical simulation of in- site scale considering the effect of randomly distributed fractures and cavities with diverse attitudes and scales in three-dimensional space
Numerical simulations of the effect of natural fractures and cavities on the propagation path of hydraulic fractures in the plane dimension	Ignoring the effect the random distribution of natural fractures and cavities in three-dimensional space	

laminated Shan et al. (2018). Wang (2019) presented a global cohesive zone model to study hydraulic propagation in naturally fractured reservoirs. Qiao et al. (2022) also showed that natural fractures have a great influence on the propagation of hydraulic fractures through the numerical simulation study of the hydraulic fracture propagation behavior of natural fractures under different influencing factors using the TOUGH-AiFrac simulator. There are still many other studies. Huang performed simulation to study the interaction between hydraulic fractures and gravels in glutenite formation based on 2D particle discrete element method, and results showed that the non-uniformly distributed stress field caused by the existence of glutenite maily affects the fracture propagating path (Huang et al., 2023b). Although the reservoir types studied are different and the methods used are also varied, these studies have reached similar conclusions regarding the expansion behavior of hydraulic fractures in fractured reservoirs (Song et al., 2017; Tan et al., 2017; Huang et al., 2019; Song et al., 2020; Tan et al., 2020; He et al., 2023; Liu et al., 2023; Wu et al., 2023). They all agreed the significant influence of reservoir heterogeneity and geostress states on the propagation path of hydraulic fractures, as well as the control effect of fracturing fluid flow rate and viscosity on the morphology of hydraulic fracture propagation.

Using similar methods as above, a few researches have been carried out on the propagation behaviour of hydraulic fractures in fracture-cavity carbonate reservoirs. Liu conducted a series of physical simulations of hydraulic fracturing under true triaxial stress states, to examine the influence of the cavity on the propagation of hydraulic fractures, and found that hydraulic fracturing turned to deflect by expanding around a cavity at low levels of stress difference (Liu et al., 2019). Cheng used the extended finite element method to simulate the interaction of hydraulic fracture with natural cavities and analyzed the influences of cavity location and horizontal stress difference on the interaction patterns of fractures and cavities (Cheng et al., 2019). Liu examined the connecting mechanisms between hydraulic fractures and cavities through experiments and numerical simulations, and found the importance of the connection of natural fractures by hydraulic fractures to enhance the oil/gas production from fracture-cavity reservoirs (Liu et al., 2020). Kao developed a solid-seepage-freeflow coupled fracturing model based on the discontinuous discrete fracture method to simulate the complex interaction behavior of fractures and cavities, and found the stress concentration around cavities is the main factor determining fracture propagation path (Kao et al., 2022). Zhu establishes a new coupled thermal-hydraulic-mechanical-chemical model to simulated acid fracturing in fracture-cavity reservoirs by treating natural fractures hierarchically, meanwhile different coupling methods were used for fractures of different scales (Zhu et al., 2023). In addition, Wang (Wang et al., 2018) and Luo (Luo et al., 2020) analyzed the intersection behavior of a single artificial fracture with a single cavity by numerical simulations, and the results showed that the presence of the cavities will disturb the fracture propagation path and make the fracture deflect.

Table 1 shows the summaries of research methods in published literature and future researching scope. At the present stage, most physical simulation experimental researches on the interaction between hydraulic fractures and cavities considering the effect of preset individual or limited numbers of cavities. What's more, the physical experiments on samples with relatively small size makes it difficult to quantitatively analyze the interaction law between hydraulic fractures and cavities. Also, most of the current numerical methods simulated interactions between hydraulic fractures and natural fracture-cavity systems on a two-dimension space, ignoring the effect of the objective conditions of the random spatial distribution of cavities in three-dimensional space, which is a significant gap with reality. Therefor, there is an urgent need to propose a new hydraulic fracture propagation model suitable for fracture-cavity reservoirs to meet the requirements of deep reservoir fracturing simulations.

Given the above analyses, a new method based on the continuous damage theory for hydraulic fracture simulation of fracture-cavity carbonate reservoirs is developed, which can consider the effect of randomly distributed fractures and cavities in three-dimensional space. Based on this model, the influences of different geologic and engineering factors on the propagation pattern of hydraulic fracture of the fracture-cavity reservoirs were investigated. The results of the study can provide guidance for the design of the fracture-cavity reservoir stimulation treatment.

2 Modeling theory and method

The continuous damage method has been proven to effectively simulate the dynamic expansion and complex morphology of hydraulic fractures, in which, the propagation direction of damage fractures are spontaneously determined by the material constitutive behavior (Busetti et al., 2012a; Busetti et al., 2012b). Previous research has proved that this method has advantages in simulating hydraulic fracture propagation in computational regions with geometric complexity and material heterogeneity (Shan et al., 2018; Shan et al., 2018). Therefore, in this paper we decides to use the continuous damage method to simulate hydraulic fracture propagation under the influence of heterogeneity in fracture-cavity reservoirs.

2.1 Coupled seepage-damage-stress model

Hydraulic fracturing is a complex seepage-damage-stress coupling problem. To accurately simulate hydraulic fracture propagation, it is necessary to take into account the pore seepage of the rock, the

deformation of the fractures, the fluid flow in the fractures, and the effect of natural fractures. The numerical method based on continuous damage theory is an important means to simulate hydraulic fracture propagation. The method uses the internal variable, damage factor, to describe the damage degree of an element, and associates the stiffness, strength, and seepage parameters of the element with the damage factor, so that the hydraulic fracture propagation process can be equated to damage evolution of the model. The main modeling theories are briefly introduced in the following.

The permeability of the carbonate reservoir matrix is extremely low. However, to simulate the propagation of hydraulic fracture by using the continuous seepage-damage-stress coupling theory, the matrix still needs to be assumed to be a porous elastic medium. The deformation of the matrix by external loads and the process of pore fluid seepage satisfy the differential equations of stress equilibrium and the equation of conservation of seepage mass (Detoumay and Cheng, 1993; Xu et al., 2010; Shan et al., 2018), which are denoted as:

$$\nabla(\boldsymbol{\sigma}' + \alpha p\mathbf{I}) + \boldsymbol{b} = 0 \tag{1}$$

$$\nabla\left(\frac{k}{\gamma_w}(\nabla p - \mathbf{b}_w)\right) + \mathbf{m}^T\dot{\boldsymbol{\varepsilon}} = 0 \tag{2}$$

Where $\boldsymbol{\sigma}'$ is the effectively stress tensor, tension is taken as positive; α is the Biot coefficient; p is the pore pressure; $\boldsymbol{b}$ is the body force vector of rock;k is the reservoir permeability; γ_w is element weight of water; $\mathbf{b}_w$ is the body force of water phase; $\dot{\boldsymbol{\varepsilon}}$ is the strain tensor, $\mathbf{I}$ is the Kronecker delta; $\mathbf{m} = [1, 1, 1, 0, 0, 0]$.

The process of hydraulic fracturing treatment involves continuously injecting fluid into the reservoir and holding up high pressure. When the pressure exceeds the strength limit of the rock, hydraulic fractures occur. Thus, a rock strength model for predicting hydraulic fracture initiation is needed, and here a hyperbolic Drucker-Prager plasticity model (Drucker and prager. 1952) is used as a criterion for fracture initiation, which can take into account the prediction of tensile and compressive shear failure of the rock (Hibbitt et al., 2016):

$$F = \sqrt{l^2 + q^2} - p\tan\theta - d = 0 \tag{3}$$

Where F is the yield function; q is the equivalent stress; p is the effectively mean stress; and θ are the friction angle and cohesion in $p \sim q$ space, related to the angle of internal friction; d is the intercept of the yield surface on the q-axis in the $p \sim q$ stress spaces. Figure 2 shows the comparison of the linear form and hyperbolic form of the Drucker-Prager criterion.

When the rock element reaches its strength limit under external loads, damage occurs. And macroscopic fracture occurs when the damage develops to a certain degree. The stiffness and strength of the rock at this stage can be expressed as a function of damage factor (Tang et al., 2002), For example, the stiffness and strength change with damage as:

$$\begin{cases} E = (1 - D)E_0 \\ \sigma_f = (1 - D)\sigma_{f0} \end{cases} \tag{4}$$

Where D is the damage factor; E_0 and σ_{f0} are the modulus of elasticity and strength of the rock before damage; E and σ_f are the modulus of elasticity and strength of the rock after damage.

The brittle behavior of rock is characterized by damage-displacement response, which could be used to define the energy

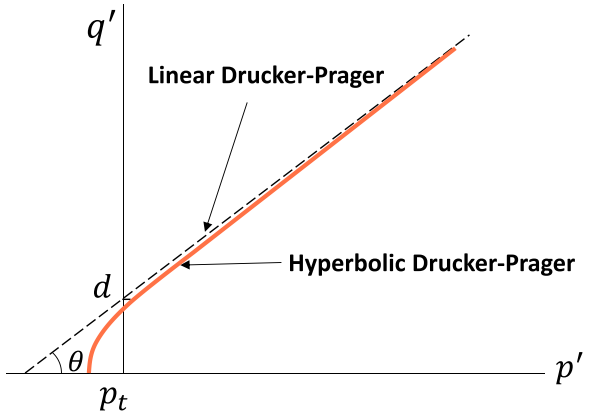


FIGURE 2
Comparison of the linear form and hyperbolic form of Drucker-Prager criterion in the $p \sim q$ plane.

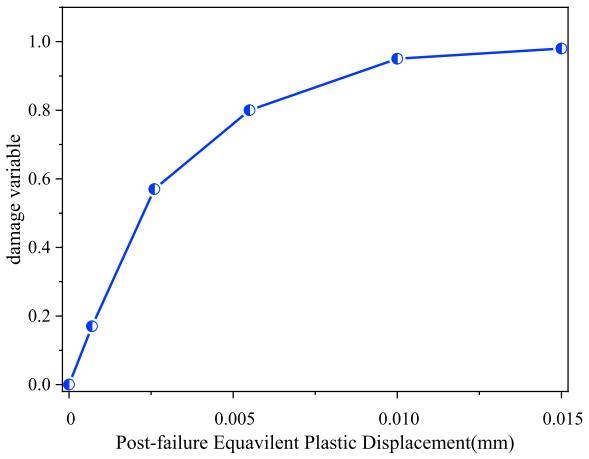


FIGURE 3
Relationship between D and $\bar{u}_{pm}$ post-failure equavilent plastic displacement.

required to open an element area of fracture (Hillerborg et al., 1976), as shown in Figure 3. When the rock element is deformed in an elastic phase, the damage factor is zero. It is generally accepted that damage occurs with plastic deformation and changes dramatically with increasing plastic deformation. The relationship between damage factor and plastic deformation can be fitted based on rock mechanical experimental parameters (Shan et al., 2018)

$$D = \frac{1}{e^{-1/a} - 1}e^{-\bar{u}_{pm}/a} - \frac{1}{e^{-1/a} - 1} \tag{5}$$

Where $\bar{u}_{pm}$ is the normalized equivalent plastic deformation, which is the ratio of the current plastic deformation to the ultimate plastic deformation; a is a material parameter that reflects the rate of evolution of the damage with plastic deformation.

When the rock is damaged under external load, the permeability of the rock is inevitably affected due to the formation of microfractures. Here, the permeability of damaged rocks is

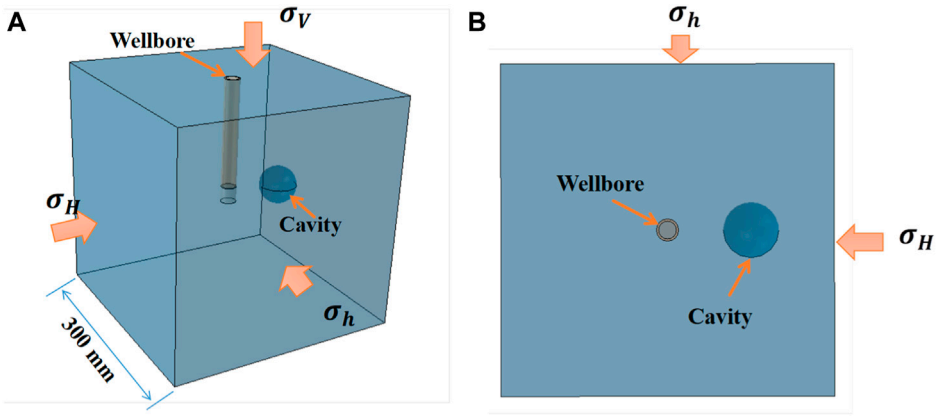


FIGURE 4
Model geometry of experimental scale and the loading direction, **(A)** 3D view; **(B)** vertical view.

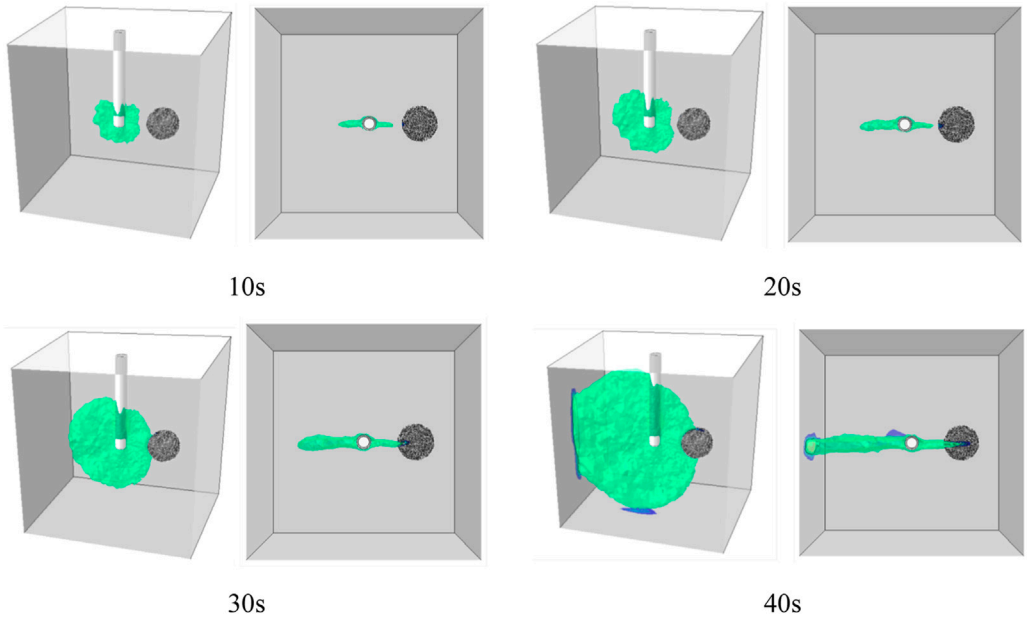


FIGURE 5
Hydraulic fracture propagation process of Case 1, displayed in 3D view and vertical view.

described in three stages based on the results of previous research (Zhou et al., 2010; Shan et al., 2018). For undamaged rock element, the permeability is a function of the mean stress; when the rock element is damaged but no macroscopic fractures occur, the permeability is considered to be mainly influenced by the mean stress and the degree of damage; after the formation of a macroscopic fractures, the permeability is defined using the cube law, which is expressed as:

$$k = \begin{cases} k_0 e^{-\eta(\sigma_m - \alpha p)} & D = 0 \\ \xi(D) k_0 e^{-\eta(\sigma_m - \alpha p)} & 0 < D < 1 \\ \frac{l}{l+b} \cdot \xi_u k_0 e^{-\eta(\sigma_m - \alpha p)} + \frac{b}{l+b} \cdot \frac{b^2}{12} & D = 1 \ and \ |\sigma_3| > \sigma_{t0} \end{cases} \quad (6)$$

where k_0 is the permeability of the undamaged rock; η is the coefficient of stress on rock permeability; σ_m is the effectively mean stress; l is the characteristic length of the element; b is the width of hydraulic fracture, which is approximated here as the tensile plastic deformation of the element. $\xi(D)$ denoted as the permeability damage multiplier as a function of the damage factor, which is assumed here to be linearly related to the damage variable D. ξ_u is the permeability damage multiplier when the element is fully damaged.

The above are the main theoretical equations to realize the simulation of hydraulic fracture propagation. There is an obvious coupling relationship between seepage, stress, and damage. During the hydraulic fracturing process, as the fracturing fluid is injected, the rock near the wellbore is damaged under hydraulic pressure. With the damaged area

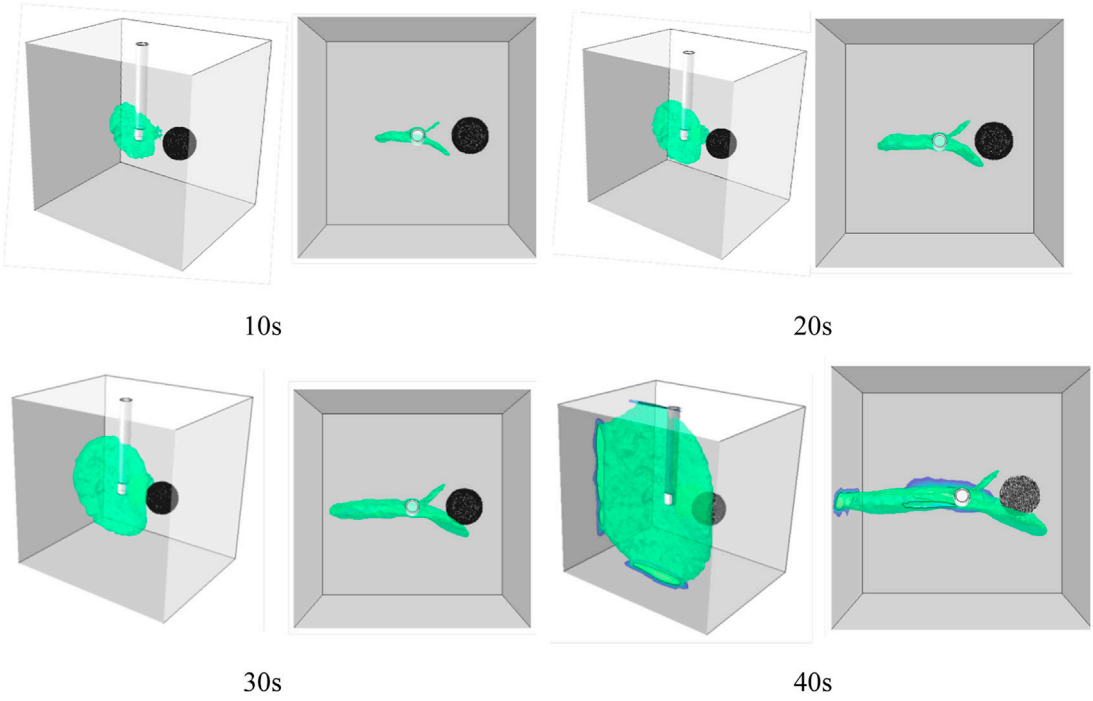


FIGURE 6
Hydraulic fracture propagation process of Case 2, displayed in 3D view and vertical view.

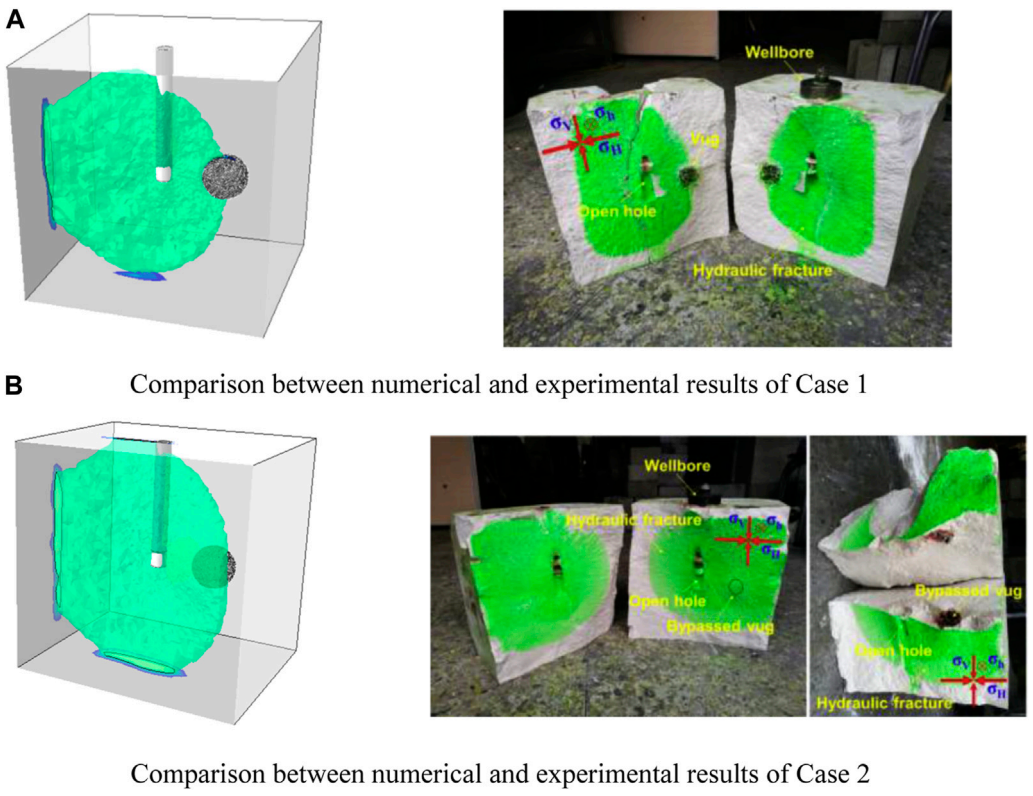


FIGURE 7
Comparison between numerical and experimental results (Liu et al., 2019). **(A)** Comparison between numerical and experimental results of Case 1. **(B)** Comparison between numerical and experimental results of Case 2.

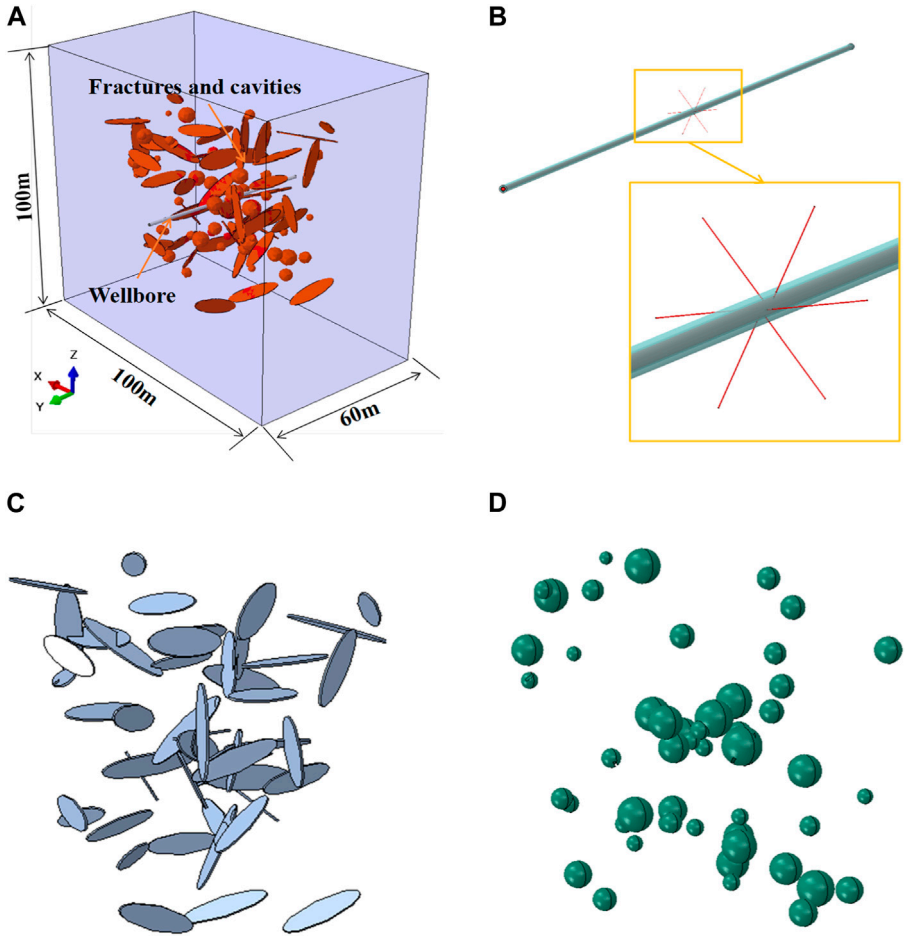


FIGURE 8
(A) Whole geometric model; **(B)** Set of wellbore and perforations; **(C)** Set of natural fractures; **(D)** Set of natural cavities.

TABLE 2 Geometric parameters of natural fractures and cavities.

Parameters	Value
Scale range of natural fractures	5 m~10 m
Dip angle range of natural fractures	20°~ 70°
Azimuth range of natural fractures	30° ~ 60°
Initial with of hydraulic fractures	2 mm
Size range of cavities	2 m ~6 m
Permeability	0.01 μDa

increased, the rock permeability is also increased, leading more fracturing fluid infiltration into the rock to further reduce the effectively stress, which promotes the formation of macroscopic fracture under the tensile stress. This process repeatedly occurs at the tip of hydraulic fractures, which promotes the forward propagation of the hydraulic fracture. The specific coupling process can be seen in Figure 6. Due to the large number of physical quantities involved and the nonlinear deformation characteristics, the finite element method is used here to solve the above equations.

2.2 Numerical modeling and parameter setting

To improve simulation efficiency, commercial software, ABAQUS, is used for building the model geometry and solving formulas, and we develop a user subroutine code to associate the rock element parameters with the damage variable to achieve the coupling of stress, seepage and damage (Hibbitt et al., 2016). The model geometric is discretized by linear tetrahedral elements. The Formula (1–6) are solved by principle of minimum potential energy using implicit method. Before applying this simulation method to fracture-cavity reservoirs, the effectiveness of the simulation method should be verified first.

Due to the fact that the ability of continuous damage methods in simulating the free propagation of hydraulic fractures in three-dimensional space and interaction between natural fractures and hydraulic fractures has been proved (Shan et al., 2018; Shan et al., 2018), here we only demonstrate the ability of the continuous damage method to simulate the influence of cavities on the direction of hydraulic fracture propagation. We will refer to existing physical simulation results (Liu et al., 2019) and compare them with the numerical simulation results calculated by our model to verify the effectiveness of the numerical method proposed in this

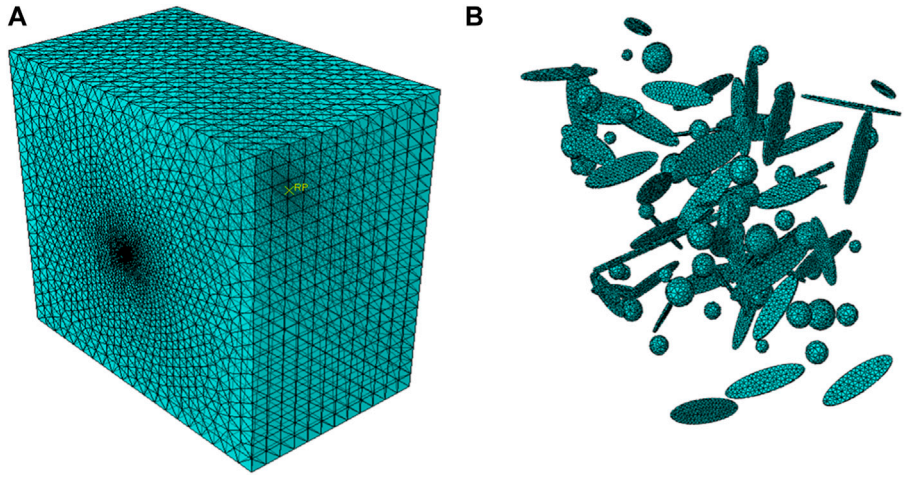


FIGURE 9
(A) Whole model meshed by tetrahedron grids; **(B)** Mesh encryption at key locations.

TABLE 3 Model reservoir rock material parameters.

Parameters	Value
Modulus of elasticity	45 GPa
Poisson's ratio	0.23
Tensile strength	8 MPa
Internal friction angle (Drafcker-Prager criterion)	58°
Shear expansion angle (Drafcker-Prager criterion)	50°
Permeability	0.01 μDa
Porosity ratio	0.016
Coefficient of stress on permeability, η	0.01 MPa^{-1}
Factor for the influence of damage on permeability, ξ_u	1×10^3
Rate of damage evolution a	0.15

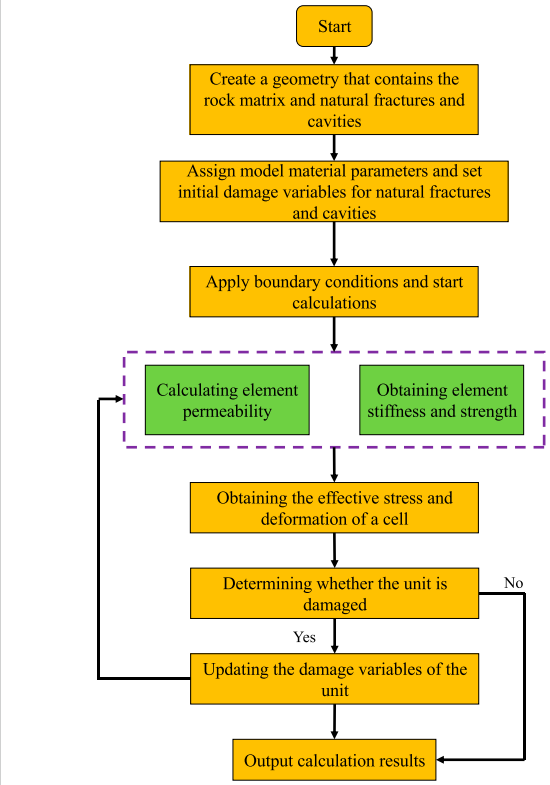


FIGURE 10
Numerical calculation flow.

study. In Liu's study, The experiments demonstrated the influence of cavities on the propagation path of hydraulic fractures under different conditions of geostress differences. Referring to his experimental process, we establish a geometric model of the same scale and assign the same material properties and boundary conditions. As shown in Figure 4 are the model geometry and the loading direction. It can been seen the cavity is pre-set on the potential expansion path of hydraulic fractures. Two loading schemes are designed to investigate the influence of geostress differences on fracture propagation paths refereeing Liu's study, where in Case 1, the $\sigma_V/\sigma_H./\sigma_h$ are set to 16/14/7 MPa with a horizontal stress difference of 7 MPa; while in Case 2, the $\sigma_V/\sigma_H./\sigma_h$ are set to 16/14/9 MPa with a horizontal stress difference of 5 MPa. The two cases use the same injection scheme with a pump rate of 20 mL/min.

Figures 5–7 show the numerical results and their comparison with experimental results. The green area in numerical simulations is the rock damage area, and its dynamic evolution can be equivalent to the path of hydraulic fractures. The numerical simulations obtained results consistent with the physical simulations. That is under high horizontal stress difference condition, it is easy for hydraulic fractures to connect the cavity that located in the direction of maximum horizontal stress (Figures 5, 7A). However, when the horizontal stress difference is low, the hydraulic fractures are prone to bypass the cavity (Figure 6; Figure 7B) due to the stress concentration around the cavity, as expressed in Cheng and Kao's work (Cheng et al., 2019;

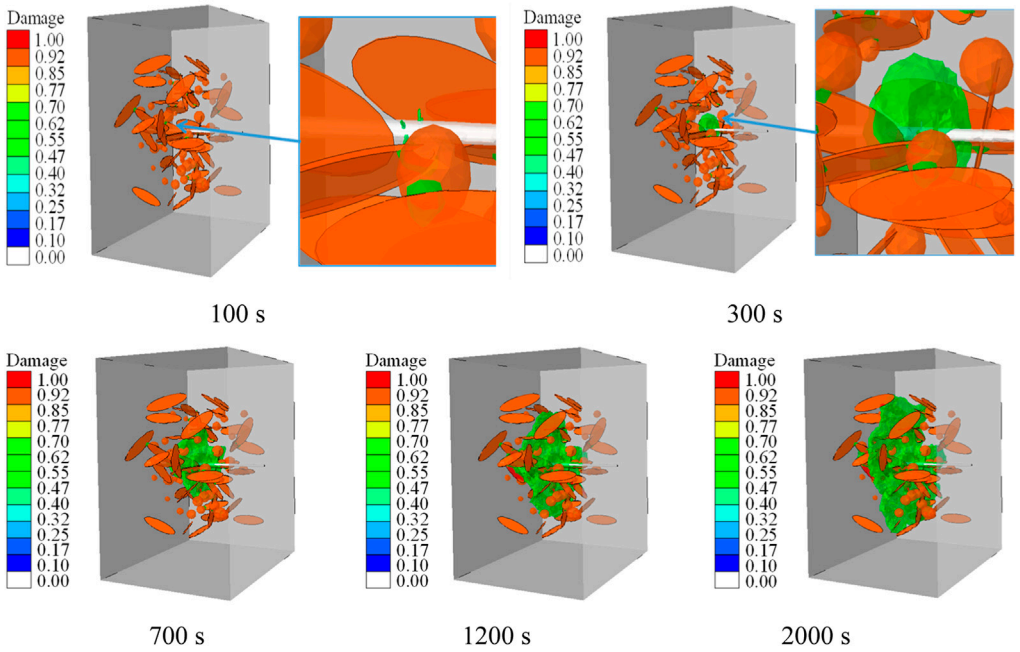


FIGURE 11
Propagation process of hydraulic fracture under the condition of reservoir.

Kao et al., 2022). It can be seen the numerical simulation method perfectly reproduces the experimental results. Therefore, the new simulation method proposed is effective and can be used for simulating hydraulic fracture propagation in fracture-cavity reservoirs.

According to the typical heterogeneity characteristics of fracture-cavity carbonate reservoirs, it is not suitable to use plane assumption, therefore, a three-dimensional model is established for the simulation. The scale of the model is 100 m × 100 m × 60 m (Figure 8A), and a cluster of perforations is set up in the center of the model with perforation phase of 60° and perforation number of 6 (Figure 8B). Referring to on-site seismic logging data and literature parameters (Kao et al., 2022), as shown in Table 2, randomly distributed natural fractures and cavities are generated in pre-processing stage (Figures 8C, D), assuming the natural fractures are elliptical and the cavities are spherical. To ensure the accuracy of the simulation results and computational efficiency, the geometric model is meshed using a tetrahedral mesh, and the grid is encrypted at the locations of the wellbore, perforation holes, natural fractures, and cavities (Figure 9).

Table 3 shows the reservoir rock material parameters, including the parameters related to the damage-permeability evolution of the reservoir rock. For material parameters of natural fractures and cavities, the nonzero initial damage variables are set for the natural fractures and cavities so that the natural fractures and cavities have lower initial strength and stiffness and higher initial permeability compared with the rock matrix. Here the initial damage variable for the natural fracture elements is set to be 0.9 and the initial damage variable value for the natural cavity elements is set to be 1 (i.e., complete damage with very low strength and very high permeability).

It is assumed that the wellbore is along the direction of the minimum horizontal stress, and the reservoir is in the state of positive fault geostress. The formation pressure gradient is set to 1.1 MPa/100 m, the vertical geostress gradient is taken as 2.2 MPa/100 m, and the maximum horizontal geostress gradient and the minimum horizontal geostress gradient are taken as 2.07 MPa/100 m and 1.8 MPa/100 m, respectively. The constant pore pressure boundary condition is applied in our model considering the model geometry is large enough to avoid the boundary effect on hydraulic fracture propagation. The viscosity and pump rate of the fracturing fluid is set concerning the range of values commonly used in field design.

The above-mentioned is the basic theory and key parameters of the model, and the overall computational flow is shown in Figure 10. The geometric model is first established containing different sets, such as the rock body matrix, natural fractures, and cavities. Then different model sets are respectively assigned with different material parameters and initial damage variables. Then the whole model is meshed and the boundary conditions are applied before calculation. During the calculation stage, the elements' damage state is updated in each analysis step to determine the elements' mechanics and permeability parameters, which are used to obtain the new stress and deformation field of the model. As the coupling calculation continues, the dynamic propagation process of hydraulic fracture characterized by damage can be simulated.

Figure 11 shows the hydraulic fracture propagation process of a simulation case with reservoir burial depth of 3,500 m. Due to the fact that this study only considers the case of one perforation cluster, the selected pump rate value is relatively small. Here, fracturing fluid pump rate of 2 m^3/min and viscosity of 3 mPa·s. It is worth noting that, although the legend in Figure 11 shows a damage range of 0~1, the hydraulic fracturing is only marked in green. That is because we selectively expose one damage isosurface, which is damage of 0.5 marked in green, to display

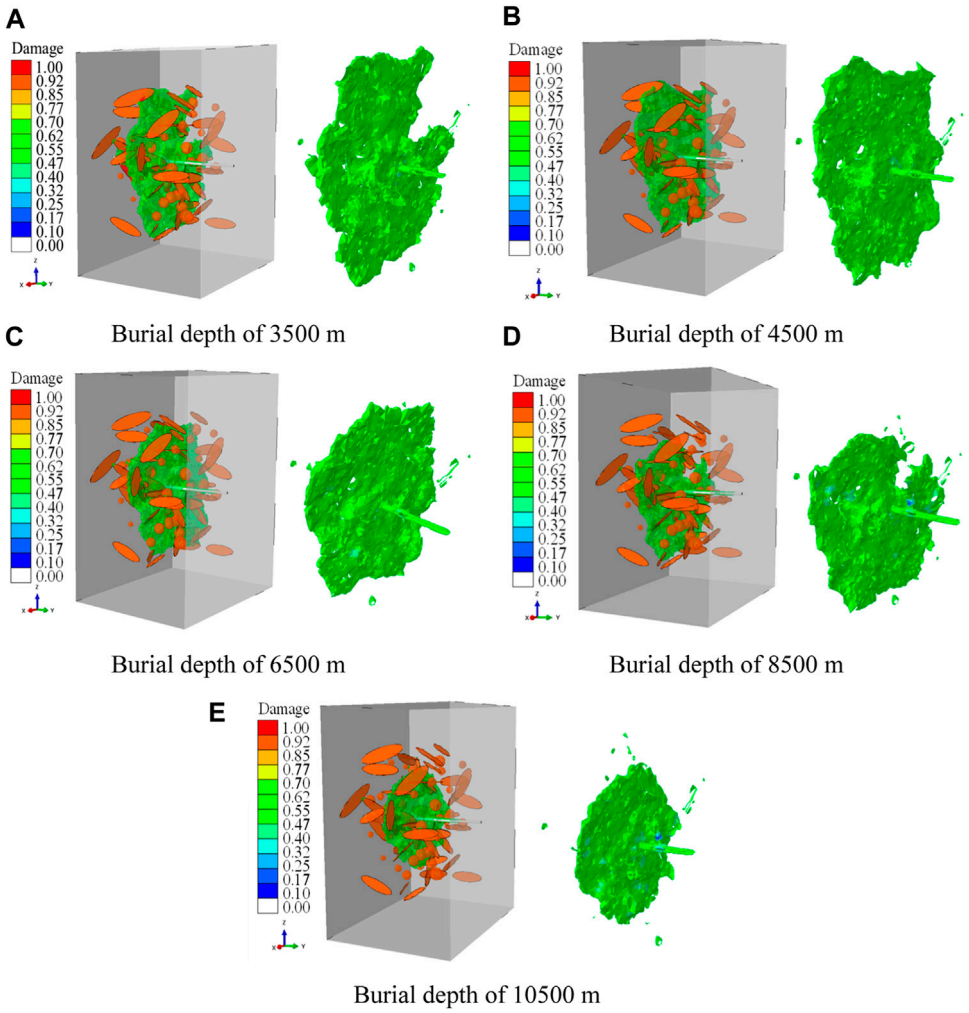


FIGURE 12
Influence of buried depth on the morphology of hydraulic fracture. **(A)** Burial depth of 3,500 m. **(B)** Burial depth of 4,500 m. **(C)** Burial depth of 6,500 m. **(D)** Burial depth of 8,500 m. **(E)** Burial depth of 10,500 m.

the three-dimensional morphology of hydraulic fractures more clearly. As we can see in Figure 11, at an injection time of 100 s, the hydraulic fracture starts from the injection hole location. When the injection time is 300 s, the hydraulic fractures initiated from each perforation converge to form a single fracture surface. With the continuous injection of fracturing fluid, the hydraulic fracture continued to propagate, connecting natural fractures and cavities.

3 Results and analysis

Given that fracture-cavity carbonate reservoirs to be developed are becoming deeper in burial depth, the influence of geological factors on hydraulic fracture propagation is becoming more and more significant. Based on the above modeling theory, this paper seeks to explore the influence and control mechanism of geological and engineering factors on the hydraulic fracture propagation of fracture-cavity carbonate reservoirs through factor analysis as follows:

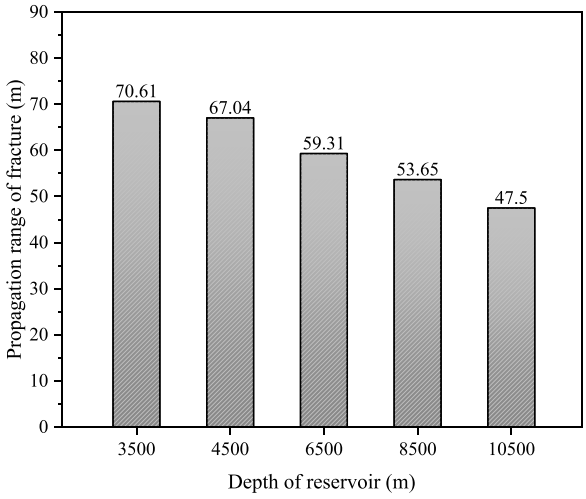


FIGURE 13
Variation of fracture propagation range with reservoir burial depth.

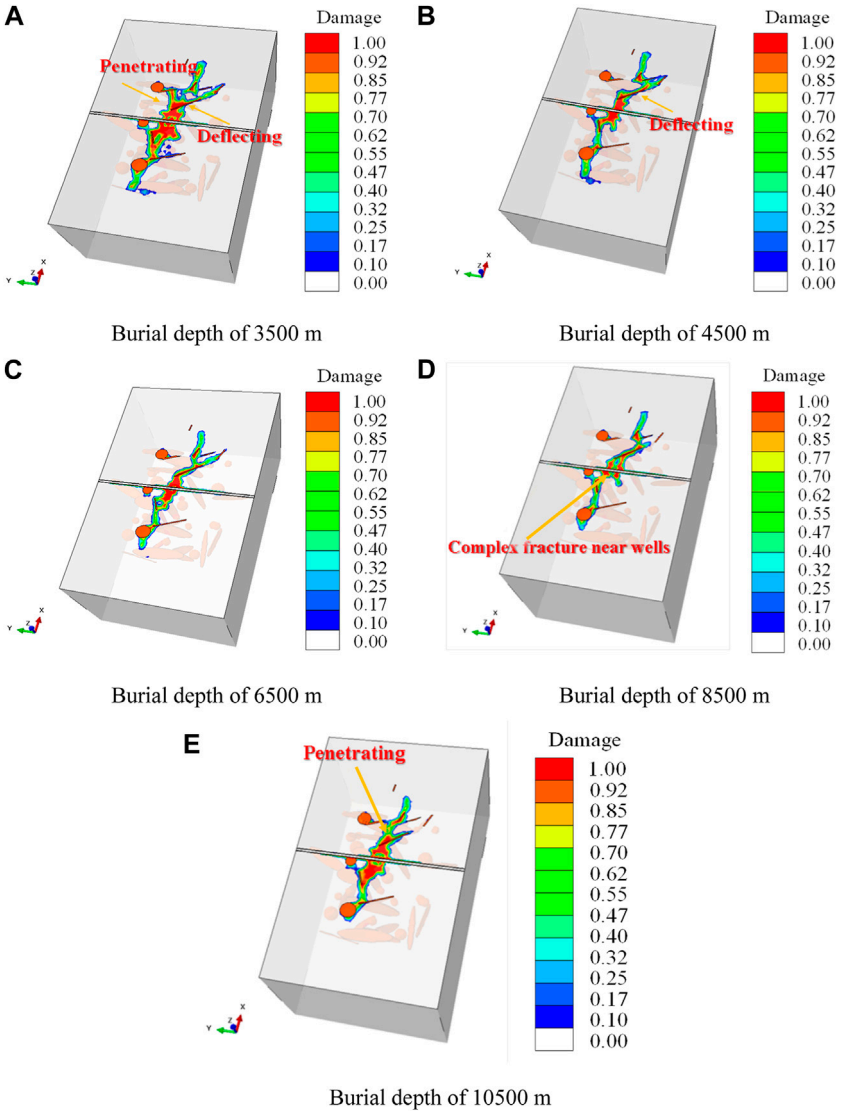


FIGURE 14
Influence of burial depth on hydraulic fracture propagation path. **(A)** Burial depth of 3,500 m. **(B)** Burial depth of 4,500 m. **(C)** Burial depth of 6,500 m. **(D)** Burial depth of 8,500 m. **(E)** Burial depth of 10,500 m.

3.1 Influence of burial depth

Keeping the geostress gradient and pore pressure gradient unchanged, five burial depths are taken, which are 3,500 m, 4,500 m, 6,500 m, 8,500 m, and 10500 m. The pump rate of the fracturing fluid is set to 2 m^3/min; the viscosity is 3 mPa·s; and the injection time is 2,000 s. Then the geostress parameters corresponding to different burial depths can be calculated by multiplying their respective gradients by depth and substituted into models for simulations, and the simulation results are compared afterward.

Figure 12 shows the influence of different burial depths on the propagation range of hydraulic fractures. To visually display the simulation results, part of the model surfaces are removed to observe the internal fracture morphology, and the hydraulic fractures are also extracted and displayed separately. It can be seen that under the influence of natural fractures and cavities, the hydraulic fractures show an obvious non-planar morphology and the propagation ranges decrease significantly with the increase of burial depth. The height of fracture propagation under each modeling condition is statistically presented in Figure 13, showing an approximate linear relationship with burial depth and decreasing by about 5% for every 1,000 m increased in reservoir burial depth.

To further examine the discrepancy of the influences of natural fractures and cavities on hydraulic fracture propagation under different burial depth conditions, a horizontal slice of each simulation result is displayed in Figure 14. By comparison, it is found that when the burial depth is relatively shallow (3,500 m, Figure 14A), the impact of geostress compression on fracture propagation is relatively small, and the hydraulic fracture expands sufficiently. The hydraulic fractures can both penetrate and deflect after meeting natural fractures, and then form a larger scale of complex fracture network. With the increase of burial

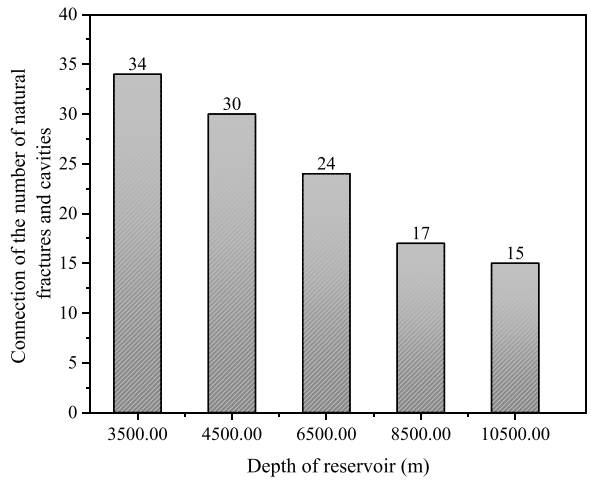


FIGURE 15
The number of natural fractures and cavities connected by hydraulic fractures under different reservoir burial depth.

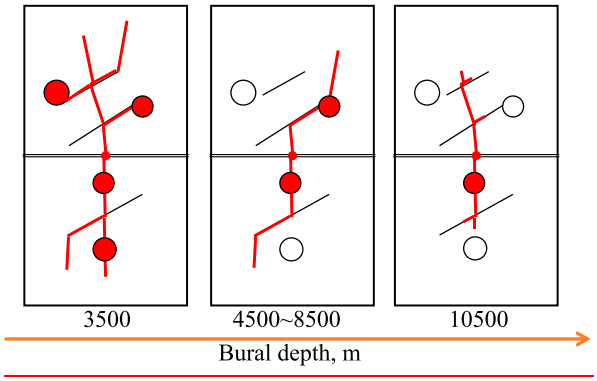


FIGURE 16
Typical features of influence of burial depth on hydraulic fracture morphology.

depth (4,500 m–8500 m, Figures 14B–D), the restraint effect of geostress on hydraulic fracture propagation is enhanced, increasing the rock matrix breakage difficulty. The hydraulic fractures tend to deflect and propagate along natural fractures. As the burial depth continues to increase (10500 m, Figure 14E), on the one hand, the increase of geostress limits the propagation range of hydraulic fractures, and Natural fractures are compacted tightly enough to prevent the filtration of low viscosity fracturing fluid into them. Therefore, The trend of hydraulic fractures deflecting when encountering natural fractures will weaken, and the hydraulic fractures tends to penetrate the natural fractures, and the morphology of the hydraulic fractures tend to be simple and short, which is not favorable for connecting more cavities. When the burial depth is 3,500 m, 4,500 m, 6,500 m, 8,500 m, and 10500 m, the number of natural fractures and cavities connected by hydraulic fractures is 34, 30, 24, 17, and 15, respectively, as shown in Figure 15, showing a more obvious decreasing tendency with the increase of burial depth.

We summarize the impact of burial depth on hydraulic fracture propagation in Figure 16. It can be concluded that there are two types of cavities that can be relatively easily communicated by hydraulic fractures: cavities located on the main hydraulic fracture propagation path, and cavities closer to the edge of natural fractures have the potential to be connected by hydraulic fractures. These two types of cavities can be further divided into two categories based on their distance from the wellbore. Therefore, each block in Figure 16 is illustrated with four circles representing four categories of cavities. For reservoirs with shallow burial depth (3,500 m), hydraulic fractures have a wide range of expansion and complex morphology, which can communicate with these four types of cavities. As the burial depth increases (4,500 m–8,500 m), the increase in geostress have a negative impact on the expansion of hydraulic fractures. Hydraulic fractures are prone to deflecting rather than penetrating when encountering natural fractures. Therefore, due to the inability to communicate enough natural fractures, or the expansion path being altered by natural fractures, hydraulic fractures cannot communicate with cavities far from the wellbore. When the burial depth increases to 10500 m, hydraulic fractures tend to be short and flat, only able to communicate with hydraulic fractures and cavities closer to the wellbore. Therefore, for deeply buried fracture-cavity reservoirs, adjusting the viscosity of fracturing fluid is no longer meaningful. It is possible to consider increasing the amount of acid to expand the communication range of hydraulic fractures.

3.2 Influence of horizontal stress difference

In this simulation case, the reservoir condition of 8,500 m burial depth is taken, and the pore pressure of 93.5 MPa, vertical geostress of 187 MPa, and maximum horizontal geostress of 176 MPa can be calculated correspondingly. Keeping the injection fracturing fluid pump rate of 2 m^3/min and viscosity of 3 mPa·s and the injection time unchanged, the minimum horizontal geostress are taken as 152 MPa, 158 MPa, 164 MPa, 170 MPa, and 176 MPa, to investigate the influence of different geostress differences on hydraulic fracture propagation. The simulation results are shown in Figure 17.

Figure 17 shows the influence of different horizontal stress differences on the hydraulic fracture propagation pattern, and it can be found that when the horizontal stress difference is large, the hydraulic fracture surface stays perpendicular to the direction of the wellbore (Figures 17A, B), and as the horizontal tress difference decreases, the hydraulic fracture surface no longer stays perpendicular to the wellbore during propagation (Figures 17C,D). When the horizontal stress difference is 0, it produces a fracture surface that propagates along the direction of the wellbore in addition to a fracture surface that propagates perpendicular to the wellbore (Figure 17E). Also, horizontal slices of simulation results are displayed to investigate the mechanism of effect of different stress differences, as shown in Figure 18. As can be seen from the figures, at a horizontal stress difference of 24 MPa, hydraulic fracture breaks the rock more easily due to the smaller minimum

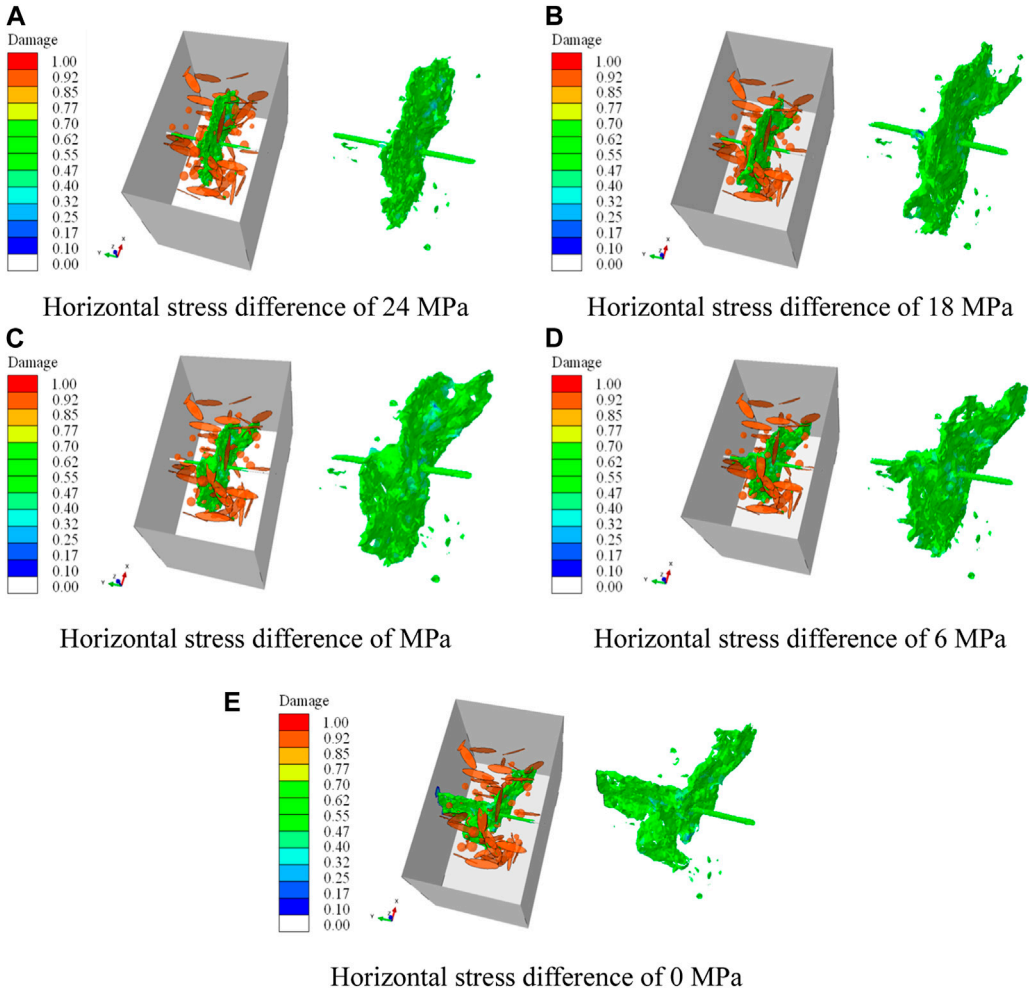


FIGURE 17
Influence of different horizontal stress differences on hydraulic fracture morphology. **(A)** Horizontal stress difference of 24 MPa, **(B)** Horizontal stress difference of 18 MPa, **(C)** Horizontal stress difference of MPa, **(D)** Horizontal stress difference of 6 MPa, **(E)** Horizontal stress difference of 0 MPa.

horizontal stress, and hydraulic fracture can easily penetrate the fracture without being induced by the natural fracture to deflect (Figure 18A). As the minimum horizontal stress increases and the horizontal stress difference decreases, it becomes more difficult to break the rock, and deflection occurs easily when natural fractures are encountered (Figures 13A–C). When natural fractures exist in the vicinity of the wellbore injection hole, it will induce hydraulic fractures to propagate along the wellbore direction, especially when the horizontal stress difference is 0, a complete fracture surface that propagates along the wellbore direction will be develop (Figure 17E; Figure 18E), increased the complexity of hydraulic fracture morphology. It can be seen from the simulation results that the influence of stress differences and natural fractures on the propagation path of hydraulic fractures is similar to that in fractured reservoirs such as shale (Zhou et al., 2010; Hou et al., 2018; Liu et al., 2018). This indirectly proves the effectiveness of the new method in simulating the influence of natural fractures and stress differences on the propagation morphology of hydraulic fractures.

Figure 19 shows the influence of different horizontal stress differences on the hydraulic fracture connecting natural fractures and cavities, and it can be seen that under certain conditions of fracturing fluid injection pump rate and viscosity, high stress differences are beneficial for hydraulic fractures to connect more natural fractures and cavities. The reason for that maybe high stress difference can promote the hydraulic fracture break through the natural fracture barrier, and then connect more natural fractures and cavities, while under conditions of low stress differences, hydraulic fractures are susceptible to natural fractures, and hydraulic energy is captured by natural fractures and cavities near the wellbore, causing limited reservoir stimulation. Another reason for this result may be that under low stress differential conditions, hydraulic fractures tend to bypass cavities, as presented by previous research findings (Cheng et al., 2019; Liu et al., 2019; Kao et al., 2022). Therefore, for fracture-cavity reservoirs, high stress differences are beneficial for improving hydraulic fracturing treatment effects, unlike shale fracturing which prefers low stress differences to increase fracture complexity.

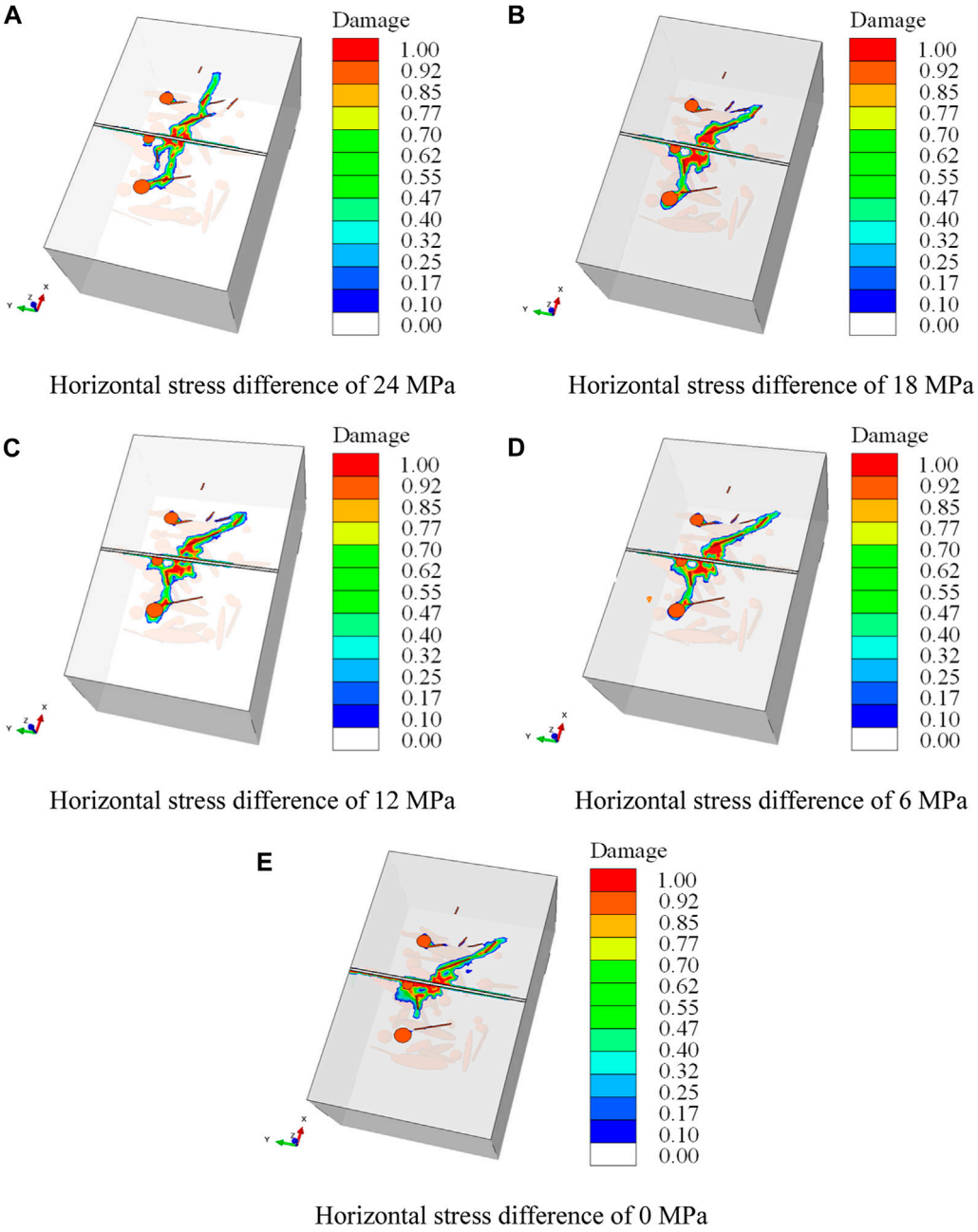


FIGURE 18
Influence of horizontal stress difference on hydraulic fracture propagation path. **(A)** Horizontal stress difference of 24 MPa, **(B)** Horizontal stress difference of 18 MPa, **(C)** Horizontal stress difference of MPa, **(D)** Horizontal stress difference of 6 MPa, **(E)** Horizontal stress difference of 0 MPa.

3.3 Influence of fracturing fluid pump rate

Create a new set of five models with the same geostress data. For each model, the reservoir burial depth is 8,500 m; the pore pressure is 93.5 MPa; the vertical stress is 187 MPa; the maximum horizontal stress is 176 MPa; the minimum horizontal stress is 164 MPa. To investigate the effect of pump rate on hydraulic fracture morphology, these five models take five different pump rates, 2, 4, 6, 8, and 10 m^3/min. And the viscosity of the fracturing fluid is set as 3 mPa·s for all five models.

Figure 20 and Figure 21 show the hydraulic fracture propagation patterns under different pump rates. It can be seen that when the pump rate is increased from 2 m^3/min to 4 m^3/min, the propagation range of hydraulic fracture increases more obviously, but the hydraulic energy is still insufficient for hydraulic fractures to penetrate the natural fractures

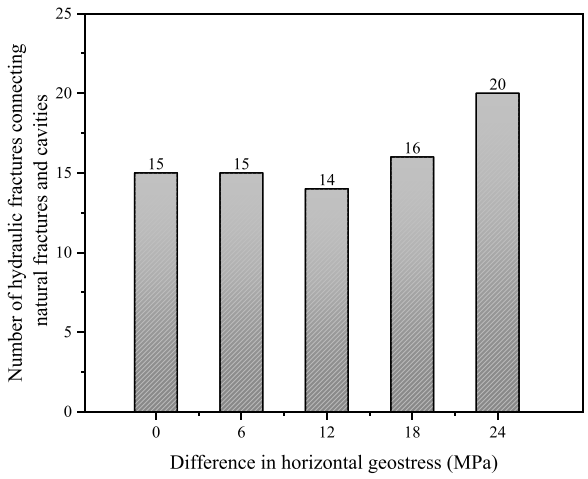


FIGURE 19
Influence of different geostress difference conditions on hydraulic fracture connecting natural fracture and natural cavity.

(Figure 21B). Thus the morphology of the hydraulic fracture does not change significantly (Figures 21A, B). When the pump rate is increased to 6 m^3/min or more, hydraulic fractures not only propagate along natural fractures, but also penetrate them, forming a multi-branched fracture morphology (Figures 21C–E). Typical features of the influence of pump rate on fracture morphology can be illustrated as shown in Figure 22. Figure 23 summarizes the number of natural fractures and cavities connected by hydraulic fractures under different pump rates. As can be seen in, the number of hydraulic fractures connecting natural fractures and cavities increases significantly when the discharge rate is increased from 4 m^3/min to 6 m^3/min. Whereas the pump rate increases to greater than 6 m^3/min, the increase in the number of hydraulic fractures connecting natural fractures and cavities is not obvious, which may be related to the scale of the model (Figure 23). In summary, under existing geological and engineering conditions set in this simulation case, in order to connect hydraulic fractures with as many natural fractures and cavities as possible, the fracturing fluid pump rate should be at least 6 m^3/min per cluster.

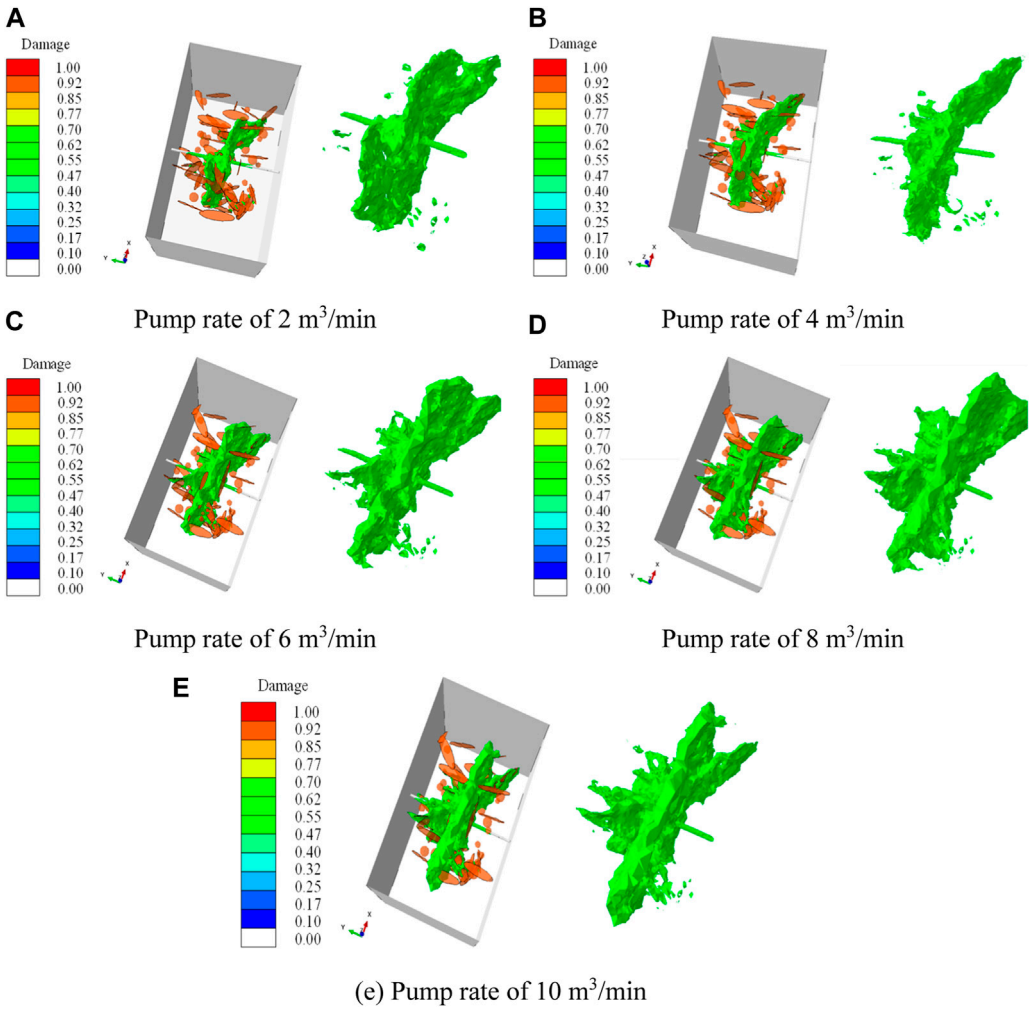


FIGURE 20
Morphology of hydraulic fracture under different fracturing fluid pump rates. **(A)** Pump rate of 2 m^3/min, **(B)** Pump rate of 4 m^3/min, **(C)** Pump rate of 6 m^3/min, **(D)** Pump rate of 8 m^3/min, **(E)** Pump rate of 10 m^3/min.

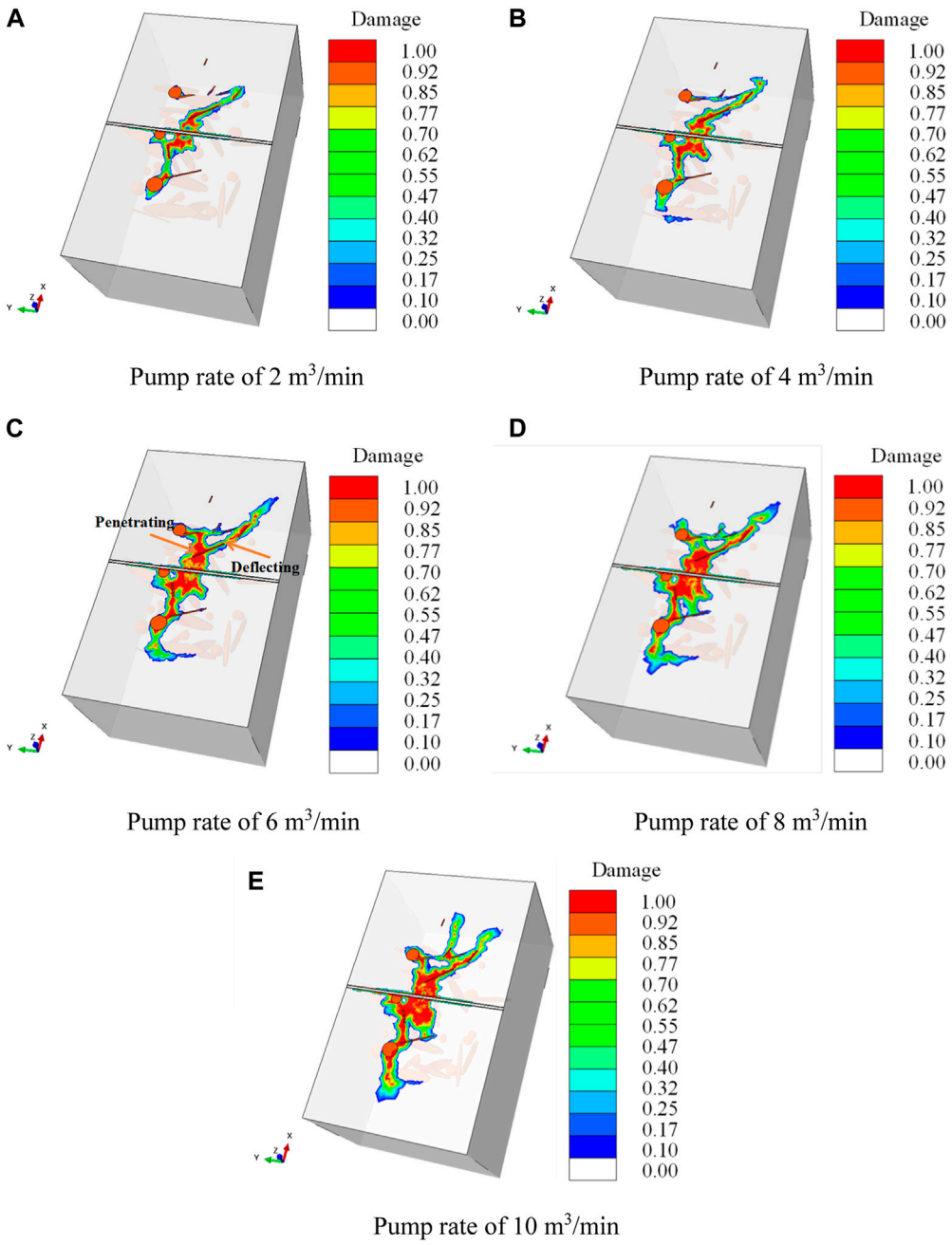


FIGURE 21
Influence of different fracturing fluid pump rates on the fracture propagation path. **(A)** Pump rate of 2 m^3/min, **(B)** Pump rate of 4 m^3/min, **(C)** Pump rate of 6 m^3/min, **(D)** Pump rate of 8 m^3/min, **(E)** Pump rate of 10 m^3/min.

3.4 Influence of fracturing fluid viscosity

In this simulation case, the burial depth is set as 8,500 m; pore pressure is 93.5 MPa; vertical stress is 187 MPa; maximum horizontal stress is 176 MPa; minimum horizontal stress is 164 MPa; the pump rate is 2 m^3/min. And five different viscosities of fracturing fluid for five models are taken to exam the influence of fracturing fluid viscosity on hydraulic fracture morphology, they are 3, 30, 100, 150, and 200 mPa·s.

Figure 24 and Figure 25 show the influence of fracturing fluid viscosity on the hydraulic fracture propagation pattern. It can be found that when the viscosity of the fracturing fluid is very low (3 mPa·s), the fracturing fluid is heavily lost into the natural fractures when the hydraulic fractures meet the natural fractures, inducing the hydraulic fractures to deflect and propagate along the natural fractures (Figure 25A). As the viscosity of the fracturing fluid increases, the seepage coefficient of the fracturing fluid in the natural fracture becomes lower, and the tendency of the hydraulic fracture

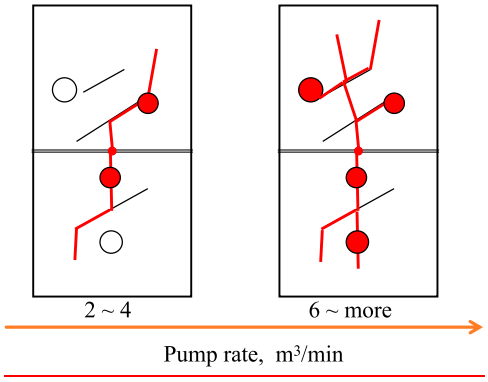


FIGURE 22
Typical features of the influence of pump rate on fracture morphology.

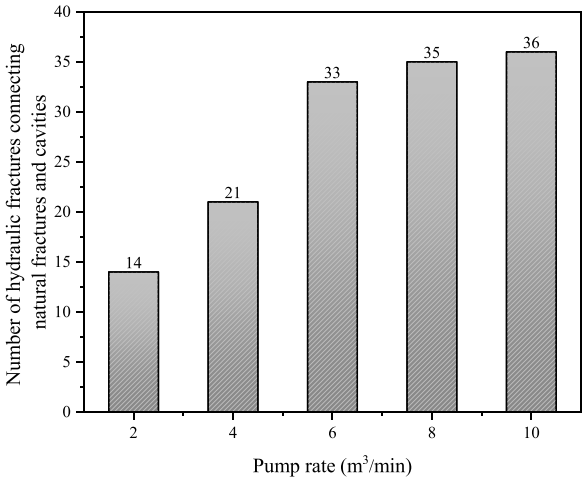


FIGURE 23
The number of natural fractures and cavities connected by hydraulic fractures under different pump rates.

to deflect along the natural fracture is weakened, which is conducive to hydraulic fractures penetrating natural fractures. Overall as the viscosity of the fracturing fluid increases, the hydraulic fracture morphology becomes more and more flat and perpendicular to the wellbore (Figure 24). Especially when the viscosity of the fracturing fluid exceeds 150 mPa·s, the hydraulic fracture meets the natural fracture and penetrates directly, and the influence of the hydraulic fracture on the propagation path of the natural fracture is already very small (Figures 25D, E). Typical features of the influence of fracture fluid viscosity on hydraulic fracture morphology is summarized in Figure 26, form which, it can be seen that the hydraulic fracture morphology undergoes a transition from simple to complex, and then to simple with the change the fracturing fluid viscosity from low to high. Also, It is worth noting that through the statistics of the number of natural fractures and cavities connected by hydraulic fracture under different fracturing fluid viscosities, either too high or too low viscosity of the fracturing fluid is not conducive to the connection of more natural fractures and cavities by hydraulic fractures. But there exists an optimum viscosity interval, where the viscosity of fracturing fluid is not too high to ensure the expansion of hydraulic fractures along natural fractures, nor too low to ensure that hydraulic fractures can penetrate natural fractures. In this simulation case, the optimal viscosity of the fracturing fluid is 30 mPa·s. Under this viscosity condition, the hydraulic fractures can not only propagate along the natural fractures, but also penetrate of the natural fractures (Figure 26), which is beneficial to connect more natural fractures and the cavities (Figure 27).

4 Discussion

From the above simulation results, it can be seen that the new simulation method proposed in this paper can break through the limitation of the physical simulation experiment size, and also overcome the limitations of the traditional numerical simulation methods with plane assumption. The simulation method based on continuous damage can better simulate the influence of natural fractures and cavities on hydraulic fractures under different conditions of geostress, fracturing fluid viscosity and pump rate, and is in good agreement with the results observed in previous physical simulation experiments. Based on the advantages of the simulation methodology in this paper, some relatively new or different results have been achieved compared to previous work in the following areas. Firstly, the new method overcomes the limitations of traditional numerical simulation methods that only study the influence of a single cavity on the hydraulic fracture propagation path. The discrete fracture modeling method is used to establish a model with randomly distributed natural fractures and cavities that is closer to the actual reservoir situation. Secondly, the influence of burial depth on the propagation range and morphology of fractures is investigated. Previous studies on the influence of geostress on the morphology of fractures were mostly confined to the influence of the geostress difference on the morphology of fractures at a certain burial depth, while actually the increase of the burial depth also has a significant influence on the morphology of fractures. Finally, evaluating the influence of geological and engineering factors on fracturing effectiveness by counting the number of hydraulic fractures connecting natural fractures and cavities in the simulation results, some meaningful conclusions can be quantitatively obtained.

Due to the assumptions and simplifications in the model in geologic modeling, such as the geometry, size, and distribution data of natural fractures and cavities, the model does not consider the real morphology of fractures and cavities, nor does it consider the variability of the mechanical and seepage properties of natural fractures and cavities during their formation, which differs greatly from the real situation. Thus, the conclusions obtained from the model in this paper can be used as a qualitative reference, and if the model is applied in the field practice, it needs to be combined with specific reservoir parameters to carry out more detailed modeling. This also provides a direction for the subsequent improvement work. That is, on the one hand, strive to obtain more accurate information on the real size and spatial distribution of the natural

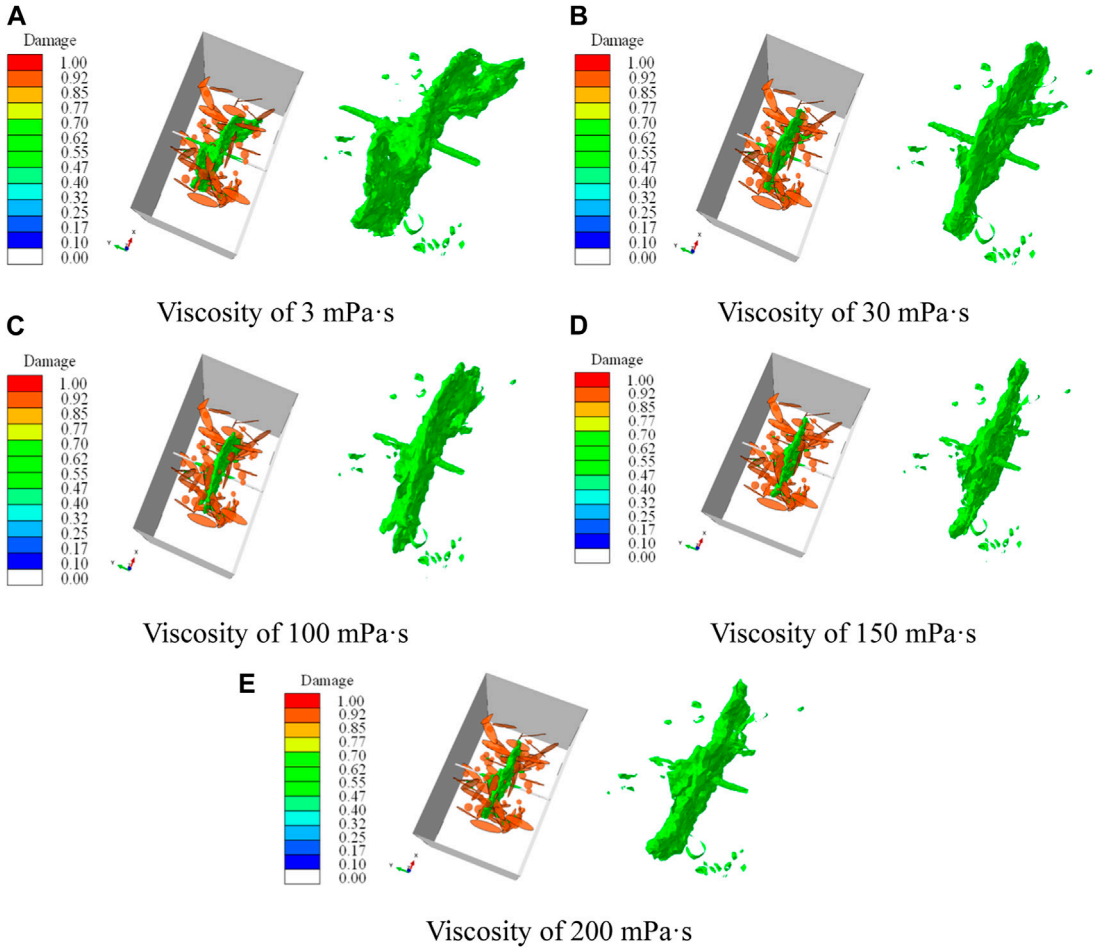


FIGURE 24
Influence of different fracturing fluid viscosities on hydraulic fracture morphology. **(A)** Viscosity of 3 mPa·s, **(B)** Viscosity of 30 mPa·s, **(C)** Viscosity of 100 mPa·s, **(D)** Viscosity of 150 mPa·s, **(E)** Viscosity of 200 mPa·s.

fractures and cavities; on the other hand, take into account the variation of the mechanical and seepage properties of the fractures and cavities, to make the simulation conditions more closer to the field.

5 Conclusion

In this paper, a finite element model for the propagation of hydraulic fracture propagation under the influence of natural fracture and cavity in a fracture-cavity carbonate reservoir was established based on the continuum damage theory. The model was validated against previous experimental results obtained by other researchers. Based on this model, the influences of burial depth, geostress difference, and fracturing fluid pump rate and viscosity on the hydraulic fracture propagation pattern were investigated, and the following conclusions were obtained:

(1) The burial depth of reservoir affects the ability of hydraulic fracture to penetrate natural fracture. When the burial depth is small (3,500 m), the hydraulic fractures can both penetrate and deflect after meeting natural fractures. With the increase of burial depth (4,500 m–8,500 m), the restraint effect of geostress on hydraulic fracture propagation is enhanced, hydraulic fractures tend to deflect and propagate along natural fractures. As the burial depth continues to increase (10500 m), natural fractures are compacted tightly enough to prevent the filtration of low viscosity fracturing fluid into them, the hydraulic fractures tends to penetrate the natural fractures, and the morphology of the hydraulic fractures tend to be simple and short.

(2) The horizontal stress difference has impact on the fracture morphology and the connection of hydraulic fractures with natural fractures and cavities. When the maximum horizontal stress is fixed, as the minimum horizontal stress increases and the horizontal stress difference decreases, it becomes more difficult for hydraulic fractures to break the rock, and the deflection occurs easily when natural fractures are encountered. What's more, high horizontal stress differences are beneficial for

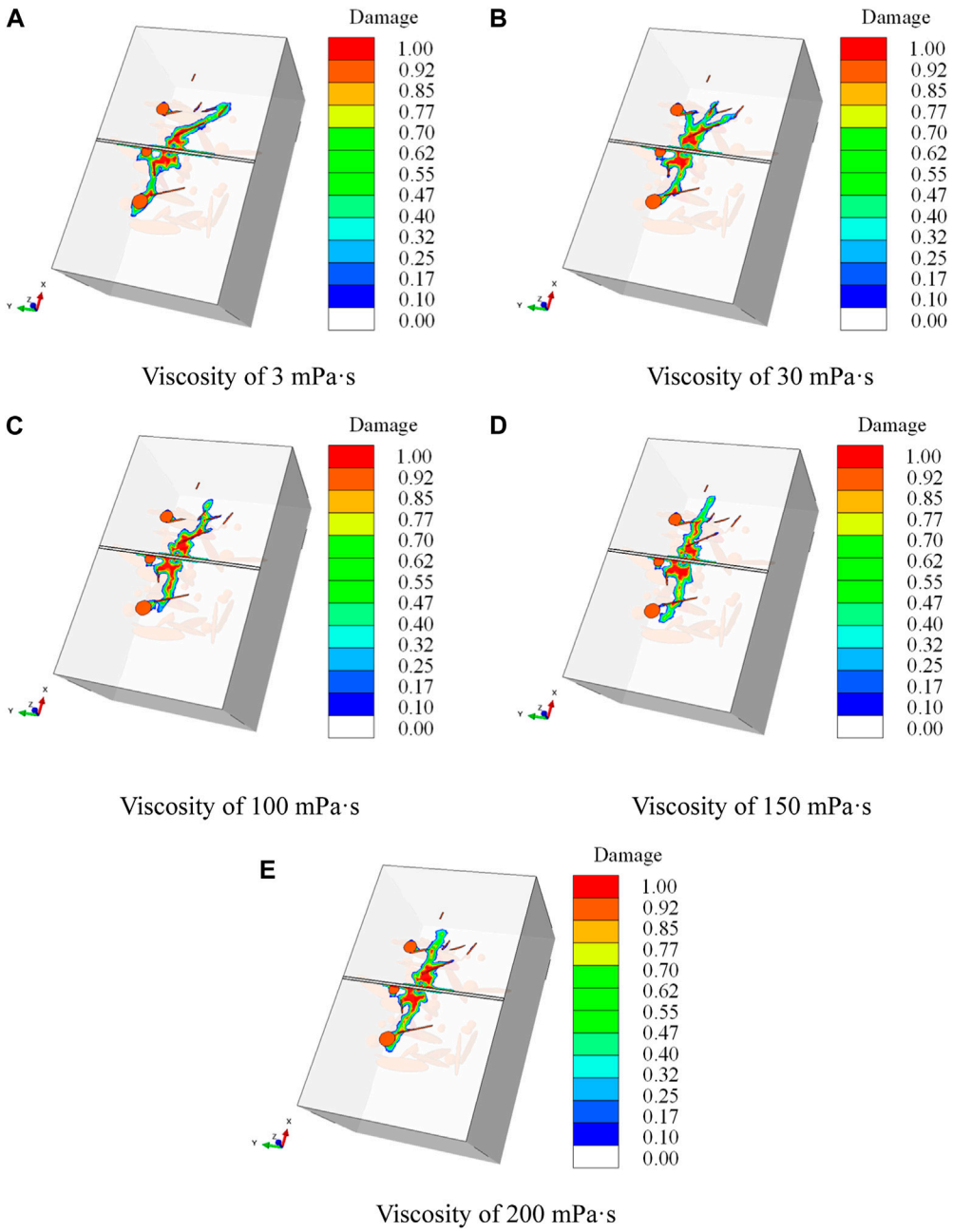


FIGURE 25
Influence of fracturing fluid viscosity on hydraulic fracture propagation paths. **(A)** Viscosity of 3 mPa·s, **(B)** Viscosity of 30 mPa·s, **(C)** Viscosity of 100 mPa·s, **(D)** Viscosity of 150 mPa·s, **(E)** Viscosity of 200 mPa·s.

hydraulic fractures to connect more natural fractures and cavities.

(3) The fracture fluid pump rate has significant effect on the connection of hydraulic fractures with natural fractures and cavities. With the increase of fracturing fluid pump rate, the ability of hydraulic fracture to penetrate the natural fractures is enhanced, also the propagation range and complexity of the hydraulic fractures are increased, promoting hydraulic fractures to connect more natural fractures and cavities.

(4) The fluid viscosity has significant influence on the hydraulic fracture morphology. The hydraulic fracture morphology can undergo a transition from simple to complex, and then to simple with the change of the fracturing fluid viscosity from low to high. However, either too high or too low viscosity of the fracturing fluid is not conducive to the connection of more natural fractures and cavities by hydraulic fractures. There exists an optimum viscosity interval, where the viscosity of fracturing fluid is not too high to ensure the expansion of hydraulic fractures along

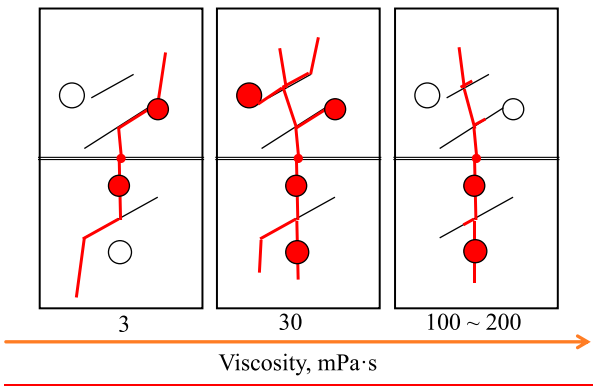


FIGURE 26
Typical features of the influence of fracture fluid viscosity on hydraulic fracture morphology.

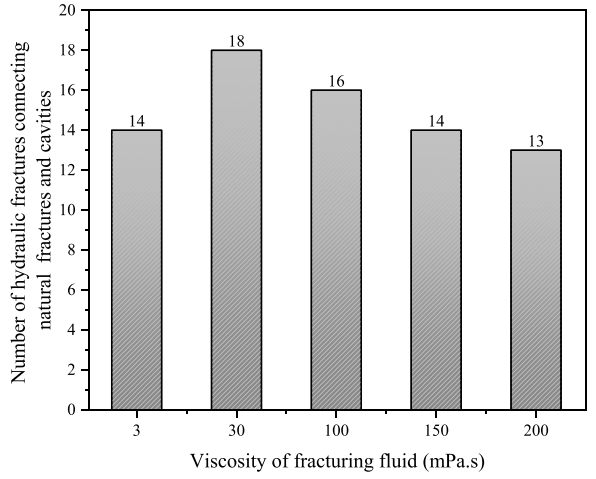


FIGURE 27
The number of hydraulic fractures connecting natural fractures and natural cavities under different fracturing fluid viscosity conditions.

natural fractures, nor too low to ensure that hydraulic fractures can penetrate natural fractures.

(5) The modelling method introduced in this article can examine the influence of reservoir heterogeneity caused by the presence of fractures and cavities, as well as different geological and engineering factors on the morphology of hydraulic fracture propagation. This method can be used for hydraulic fracturing design of treatment of fracture-cavity carbonate reservoirs.

Data availability statement

The original contributions presented in the study are included in the article/supplementary material, further inquiries can be directed to the corresponding author.

Author contributions

HL: Supervision, Writing–review and editing. ML: Investigation, Writing–original draft. QS: Funding acquisition, Methodology, Writing–original draft. YJ: Supervision, Writing–review and editing. BL: Investigation, Writing–review and editing. CW: Investigation, Writing–review and editing. XC: Investigation, Writing–review and editing.

Funding

The author(s) declare that financial support was received for the research, authorship, and/or publication of this article. This research was funded by the National Natural Science Foundation of China (No. 52204042) and the Shandong Provincial Natural Science Foundation, China (Nos. ZR2021QE154 and ZR2019ZD14).

Conflict of interest

The authors declare that the research was conducted in the absence of any commercial or financial relationships that could be construed as a potential conflict of interest.

Publisher's note

All claims expressed in this article are solely those of the authors and do not necessarily represent those of their affiliated organizations, or those of the publisher, the editors and the reviewers. Any product that may be evaluated in this article, or claim that may be made by its manufacturer, is not guaranteed or endorsed by the publisher.

References

Busetti, S., Mish, K., Hennings, P., et al. (2012b). Damage and plastic deformation of reservoir rocks; Part 1, Damage fracturing. *AAPG Bull.* 96 (9), 1687–1709. doi:10.1306/02011211011

Busetti, S., Mish, K., and Reches, Z. (2012a). Damage and plastic deformation of reservoir rocks; Part 1, Damage fracturing. *AAPG Bull.* 96 (9), 1687–1709. doi:10.1306/02011211010

Chalikakis, K., Plagnes, V., Guerin, R., Valois, R., and Bosch, F. P. (2011). Contribution of geophysical methods to karst-system exploration: an overview. *Hydrogeology J.* 19 (6), 1169–1180. doi:10.1007/s10040-011-0746-x

Cheng, L., Luo, Z. F., Yu, Y., Zhao, L., and Zhou, C. (2019). Study on the interaction mechanism between hydraulic fracture and natural karst cave with the extended finite element method. *Eng. Fract. Mech.* 222, 106680. doi:10.1016/j.engfracmech.2019.106680

Chuprakov, D., Melchaeva, O., and Prioul, R. (2013). Hydraulic fracture propagation across a weak discontinuity controlled by fluid injection. *ISRM Int. Conf. Eff. Sustain. hydraulic Fract. ISRM-ICHF-2013-2008.* doi:10.5772/55941

Detoumay, E., and Cheng, A. H. D. (1993). Fundamentals of poroelasticity. *Analysis Des. Methods* 2 (1), 113–171. doi:10.1016/B978-0-08-040615-2.50011-3

Drucke, D. C., and Prager, W. (1952). Soil mechanics and plastic analysis or limit design. *Q. Appl. Math.* 10 (2), 157–165. doi:10.1090/qam/48291

Guo, T. K., Tang, S. J., Liu, S., Liu, X., Xu, J., Qi, N., et al. (2021). Physical simulation of hydraulic fracturing of large-sized tight sandstone outcrops. *Spe J.* 26 (1), 372–393. doi:10.2118/204210-PA

He, R., Yang, J., Li, L., Yang, Z., Chen, W., Zeng, J., et al. (2023). Investigating the simultaneous fracture propagation from multiple perforation clusters in horizontal wells using 3D block discrete element method. *Front. Earth Sci.* 11, 1115054. doi:10.3389/feart.2023.1115054

Hibbitt, H. D., Karlsson, B. I., and Sorensen, E. P. (2016). *Abaqus/CAE user's guide*. Providence, RI: Dassault Systemes Simulia Corp. Available at: https://ceae-server.colorado.edu/v2016/books/usi/default.htm.

Hillerborg, A., Modeer, M., and Peterson, P. E. (1976). Analysis of crack formation and crack growth in concrete by means of fracture mechanics and finite elements. *Cem. Concr. Res.* 6 (6), 773–781. doi:10.1016/0008-8846(76)90007-7

Hou, B., Zhang, R. X., Tan, P., Song, Y., Fu, W., Chang, Z., et al. (2018). Characteristics of fracture propagation in compact limestone formation by hydraulic fracturing in central Sichuan, China. *J. Nat. Gas Sci. Eng.* 57, 122–134. doi:10.1016/j.jngse.2018.06.035

Huang, L., Dontsov, E., Fu, H., Lei, Y., Weng, D., and Zhang, F. (2022). Hydraulic fracture height growth in layered rocks: perspective from DEM simulation of different propagation regimes. *Int. J. Solids Struct.* 238, 111395. doi:10.1016/j.ijsolstr.2021.111395

Huang, L., He, R., Yang, Z., Tan, P., Chen, W., Li, X., et al. (2023b). Exploring hydraulic fracture behavior in glutenite formation with strong heterogeneity and variable lithology based on DEM simulation. *Eng. Fract. Mech.* 278, 109020. doi:10.1016/j.engfracmech.2022.109020

Huang, L., Liu, J., Ji, Y., Gong, X., and Qin, L. (2018). A review of multiscale expansion of low permeability reservoir cracks. *Petroleum* 4, 115–125. doi:10.1016/j.petlm.2017.09.002

Huang, L., Liu, J., Zhang, F., Dontsov, E., and Damjanac, B. (2019). Exploring the influence of rock inherent heterogeneity and grain size on hydraulic fracturing using discrete element modeling. *Int. J. Solids Struct.* 176, 207–220. doi:10.1016/j.ijsolstr.2019.06.018

Huang, L., Liu, J., Zhang, F., Fu, H., Zhu, H., and Damjanac, B. (2020). 3D lattice modeling of hydraulic fracture initiation and near-wellbore propagation for different perforation models. *J. Petroleum Sci. Eng.* 191, 107169. doi:10.1016/j.petrol.2020.107169

Huang, L., Tan, J., Fu, H., Liu, J., Chen, X., Liao, X., et al. (2023a). The non-plane initiation and propagation mechanism of multiple hydraulic fractures in tight reservoirs considering stress shadow effects. *Eng. Fract. Mech.* 292, 109570. doi:10.1016/j.engfracmech.2023.109570

Ji, Y., Wang, J., and Huang, L. (2015). Analysis on inflowing of the injecting Water in faulted formation. *Adv. Mech. Eng.* 7, 1–10. doi:10.1177/1687814015590294

Jiao, F. Z. (2019). Practice and knowledge of volumetric development of deep fractured-vuggy carbonate reservoirs in Tarim Basin, NW China. *Petroleum Explor. Dev.* 46 (3), 576–582. doi:10.1016/S1876-3804(19)60037-6

Kao, J. W., Wei, S. M., Wang, W. Z., and Jin, Y. (2022). Numerical analysis of the hydraulic fracture communication modes in fracture-cavity reservoirs. *Petroleum Sci.* 19 (5), 2227–2239. doi:10.1016/j.petsci.2022.05.011

Liu, B. H., Jin, Y., and Chen, M. (2019). Influence of vugs in fractured-vuggy carbonate reservoirs on hydraulic fracture propagation based on laboratory experiments. *J. Struct. Geol.* 124, 143–150. doi:10.1016/j.jsg.2019.04.007

Liu, Q., Li, J., Liang, B., Liu, J., Sun, W., He, J., et al. (2023). Complex wettability behavior triggering mechanism on imbibition: a model construction and comparative study based on analysis at multiple scales. *Energy* 275, 127434. doi:10.1016/j.energy.2023.127434

Liu, Z., Wang, S., Zhao, H., Wang, L., Li, W., Geng, Y., et al. (2018). Effect of random natural fractures on hydraulic fracture propagation geometry in fractured carbonate rocks. *Rock Mech. Rock Eng.* 51 (2), 491–511. doi:10.1007/s00603-017-1331-y

Liu, Z. Y., Tang, X. H., Tao, S., Zhang, G., and Chen, M. (2020). Mechanism of connecting natural caves and wells through hydraulic fracturing in fracture-cavity reservoirs. *Rock Mech. Rock Eng.* 53 (12), 5511–5530. doi:10.1007/s00603-020-02225-w

Luo, H., Xie, J., Huang, L., Wu, J., Shi, X., Bai, Y., et al. (2022). Multiscale sensitivity analysis of hydraulic fracturing parameters based on dimensionless analysis method. *Lithosphere* 2022, 9708300. doi:10.2113/2022/9708300

Luo, Z., Zhang, N., Zhao, L., Zeng, J., and Liu, P. (2020). Interaction of a hydraulic fracture with a hole in poroelasticity medium based on extended finite element method. *Eng. analysis Bound. Elem.* 115, 108–119. doi:10.1016/j.enganabound.2020.03.011

Lv, A., Yao, J., and Wang, W. (2011). Characteristics of oil-water relative permeability and influence mechanism in fractured-vuggy medium. *Procedia Eng.* 18, 175–183. doi:10.1016/j.proeng.2011.11.028

Mousavi, M., Prodanovic, M., and Jacobi, D. (2013). New classification of carbonate rocks for process-based pore-scale modeling. *Spe J.* 18 (2), 243–263. doi:10.2118/163073-PA

Qiao, J., Tang, X., Hu, M., Rutqvist, J., and Liu, Z. (2022). The hydraulic fracturing with multiple influencing factors in carbonate fracture-cavity reservoirs. *Comput. Geotechnics* 147, 104773. doi:10.1016/j.compgeo.2022.104773

Rahm, D. (2011). Regulating hydraulic fracturing in shale gas plays: the case of Texas. *Energy Policy* 39 (5), 2974–2981. doi:10.1016/j.enpol.2011.03.009

Ren, Q. Q., Jin, Q., Feng, J. W., and Du, H. (2020). Design and construction of the knowledge base system for geological outfield cavities classifications: an example of the fracture-cavity reservoir outfield in Tarim basin, NW China. *J. Petroleum Sci. Eng.* 194, 107509. doi:10.1016/j.petrol.2020.107509

Shan, Q. L., Jin, Y., Tan, P., and Zhang, R. (2018). Experimental and numerical investigations on the vertical propagation of hydraulic fractures in laminated shales. *J. Geophys. Eng.* 15 (4), 1729–1742. doi:10.1088/1742-2140/aac12f

Song, R., Liu, J., and Cui, M. (2017). A new method to reconstruct structured mesh model from micro-computed tomography images of porous media and its application. *Int. J. Heat Mass Transf.* 109, 705–715. doi:10.1016/j.ijheatmasstransfer.2017.02.053

Song, R., Wang, Y., Ishutov, S., Zambrano-Narvaez, G., Hodder, K. J., Chalaturnyk, R. J., et al. (2020). A comprehensive experimental study on mechanical behavior, microstructure and transport properties of 3D-printed rock analogs. *Rock Mech. Rock Eng.* 53, 5745–5765. doi:10.1007/s00603-020-02239-4

Tan, P., Fu, S., Chen, Z., and Zhao, Q. (2023). Experimental investigation on fracture growth for integrated hydraulic fracturing in multiple gas bearing formations. *Geoenergy Sci. Eng.* 231, 212316. doi:10.1016/j.geoen.2023.212316

Tan, P., Jin, Y., Han, K., Hou, B., Chen, M., Guo, X., et al. (2017). Analysis of hydraulic fracture initiation and vertical propagation behavior in laminated shale formation. *Fuel* 206, 482–493. doi:10.1016/j.fuel.2017.05.033

Tan, P., Jin, Y., and Pang, H. (2021). Hydraulic fracture vertical propagation behavior in transversely isotropic layered shale formation with transition zone using XFEM-based CZM method. *Eng. Fract. Mech.* 248, 107707. doi:10.1016/j.engfracmech.2021.107707

Tan, P., Pang, H., Zhang, R., Jin, Y., Zhou, Y., Kao, J., et al. (2020). Experimental investigation into hydraulic fracture geometry and proppant migration characteristics for southeastern Sichuan deep shale reservoirs. *J. Petroleum Sci. Eng.* 184, 106517. doi:10.1016/j.petrol.2019.106517

Tang, C. A., Tham, L. G., Lee, P. K. K., Yang, T., and Li, L. (2002). Coupled analysis of flow, stress and damage (FSD) in rock failure. *Int. J. Rock Mech. Min. Sci.* 39 (4), 477–489. doi:10.1016/S1365-1609(02)00023-0

Tian, F., Luo, X., and Zhang, W. (2019). Integrated geological-geophysical characterizations of deeply buried fractured-vuggy carbonate reservoirs in Ordovician strata, Tarim Basin. *Mar. Petroleum Geol.* 99, 292–309. doi:10.1016/j.marpetgeo.2018.10.028

Wang, B., Liu, X., Sima, L., et al. (2019). Grading evaluation and prediction of fracture-cavity reservoirs in cambrian longwangmiao formation of moxi area, sichuan basin, SW China. *Petrol. explor. Dev.* 46 (2), 301–313. doi:10.1016/S1876-3804(19)60010-8

Wang, H., Tang, X., Luo, Z., et al. (2018). *Investigation of the fracture propagation in fractured-vuggy reservoirs. ARMA US Rock Mechanics/Geomechanics Symposium*.

Wang, H. Y. (2019). Hydraulic fracture propagation in naturally fractured reservoirs: complex fracture or fracture networks. *J. Nat. Gas Sci. Eng.* 68, 102911. doi:10.1016/j.jngse.2019.102911

Wu, M., Jiang, C., Song, R., Liu, J., Li, M., Liu, B., et al. (2023). Comparative study on hydraulic fracturing using different discrete fracture network modeling: insight from homogeneous to heterogeneity reservoirs. *Eng. Fract. Mech.* 284, 109274. doi:10.1016/j.engfracmech.2023.109274

Xiao, Z., Li, M., Huang, S., Wang, T., Zhang, B., Fang, R., et al. (2016). Source, oil charging history and filling pathways of the Ordovician carbonate reservoir in the Halahatang Oilfield, Tarim Basin, NW China. *Mar. Petrol. Geol.* 73, 59–71. doi:10.1016/j.marpetgeo.2016.02.026

Xu, B., and Wong, R. C. K. (2010). A 3D finite element model for history matching hydraulic fracturing in unconsolidated sands formation. *J. Can. Petroleum Technol.* 49 (04), 58–66. doi:10.2118/2009-100

Xu, C., Di, B., and Wei, J. (2016). A physical modeling study of seismic features of karst cave reservoirs in the Tarim Basin, China. *Geophysics* 81 (1), B31–B41. doi:10.1190/geo2014-0548.1

Zhang, F., Damjanac, B., and Maxwell, S. (2019). Investigating hydraulic fracturing complexity in naturally fractured rock masses using fully coupled multiscale numerical modeling. *Rock Mech. Rock Eng.* 52, 5137–5160. doi:10.1007/s00603-019-01851-3

Zhang, F., Dontsov, E., and Mack, M. (2017). Fully coupled simulation of a hydraulic fracture interacting with natural fractures with a hybrid discrete-continuum method. *Int. J. Numer. Anal. Methods Geomechanics* 41 (13), 1430–1452. doi:10.1002/nag.2682

Zhang, F., Huang, L., Yang, L., Dontsov, E., Weng, D. W., Liang, H. B., et al. (2022). Numerical investigation on the effect of depletion-induced stress reorientation on infill well hydraulic fracture propagation. *Petroleum Sci.* 19 (1), 296–308. doi:10.1016/j.petsci.2021.09.014

Zhang, K., and Wang, D. (2004). Types of karst-fractured and porous reservoirs in China's carbonates and the nature of the Tahe oilfield in the Tarim Basin. *Acta Geol. Sinica-English Ed.* 78 (3), 866–872. doi:10.1111/j.1755-6724.2004.tb00208.x

Zheng, S., Min, Y., Kang, Z., Liu, Z., Long, X., Liu, K., et al. (2019). Controlling factors of remaining oil distribution after water flooding and enhanced oil recovery methods for fracturecavity carbonate reservoirs in Tahe Oilfield. *Petroleum Explor. Dev.* 46 (4), 786–795. doi:10.1016/s1876-3804(19)60236-3

Zheng, Y., He, R., Huang, L., Bai, Y., Wang, C., Chen, W., et al. (2022). Exploring the effect of engineering parameters on the penetration of hydraulic fractures through bedding planes in different propagation regimes. *Comput. Geotechnics* 146, 104736. doi:10.1016/j.compgeo.2022.104736

Zhou, J., Jin, Y., and Chen, M. (2010). Experimental investigation of hydraulic fracturing in random naturally fractured blocks. *Int. J. Rock Mech. Min. Sci.* 47 (7), 1193–1199. doi:10.1016/j.ijrmms.2010.07.005

Zhu, T., Wei, X., and Zhang, Z. (2023). Numerical simulation of hydraulic-mechanical-chemical field coupled acid fracturing in complex carbonate reservoir. *Comput. Geotechnics* 156, 105277. doi:10.1016/j.compgeo.2023.105277

frontiers | Frontiers in Energy Research

TYPE Original Research
PUBLISHED 22 April 2024
DOI 10.3389/fenrg.2024.1389877

Check for updates

OPEN ACCESS

EDITED BY
Peng Tan,
CNPC Engineering Technology R&D Company Limited, China

REVIEWED BY
Jianbin Liu,
Xi'an Shiyou University, China
Hao Chen,
China University of Petroleum, China

*CORRESPONDENCE
Li Wang,
wli-111@petrochina.com.cn

RECEIVED 22 February 2024
ACCEPTED 22 March 2024
PUBLISHED 22 April 2024

CITATION
Cai C, Wang L, Zhang R, Kang Q, Zhang Q, Zhao D, Guo J, Chen M, Chen H, Lei L, Wang K and He J (2024), Two-dimensional spectrum characteristics and oil movability study of the shale oil reservoir.
Front. Energy Res. 12:1389877.
doi: 10.3389/fenrg.2024.1389877

COPYRIGHT
© 2024 Cai, Wang, Zhang, Kang, Zhang, Zhao, Guo, Chen, Chen, Lei, Wang and He. This is an open-access article distributed under the terms of the Creative Commons Attribution License (CC BY). The use, distribution or reproduction in other forums is permitted, provided the original author(s) and the copyright owner(s) are credited and that the original publication in this journal is cited, in accordance with accepted academic practice. No use, distribution or reproduction is permitted which does not comply with these terms.

Two-dimensional spectrum characteristics and oil movability study of the shale oil reservoir

Changhong Cai[1,2], Li Wang[1,2]*, Rui Zhang[1], Qiang Kang[1,2], Qingxiu Zhang[1,2], Dan Zhao[1,2], Jingsu Guo[1,2], Manfei Chen[1,2], Hongbin Chen[1], Lei Lei[3], Ke Wang[1,2] and Jiahuan He[1,2]

[1]Exploration and Development Research Institute of PetroChina Southwest Oil and Gas Field Company, Chengdu, China, [2]Shale Gas Evaluation and Exploitation Key Laboratory of Sichuan Province, Chengdu, China, [3]Development Department of PetroChina Southwest Oil and Gas Field Company, Chengdu, China

Shale oil is mainly stored in the nano–micro-pores of shale in the form of adsorption or in a free state. Among them, only free-state oil is the main contributor to shale oil production under natural elastic energy. Therefore, it is crucial to evaluate the movability of crude oil effectively. In this paper, focusing on the Jurassic shale oil reservoir core in the middle-eastern Sichuan region of China, low-field nuclear magnetic resonance (NMR) technology is used to analyze the basic characteristics of shale oil core samples. Experiments on the low-field NMR one-dimensional and two-dimensional spectrum characteristics of the original core, heat-treated core, and thermogravimetric-treated shale core are carried out. The effects of the TG-MS method, T_2 method, and the volatilization of light oil components on the movability of shale oil reservoirs are analyzed, and the movability characteristics of shale oil reservoirs in the middle-eastern Sichuan region are preliminarily clarified. The results show that under thermal treatment, the distribution range of the two-dimensional spectrum of the core oil occurrence area is significantly reduced, and the T_1 and T_2 distribution ranges are reduced by 10.9% and 60.7%, respectively. According to the TG-MS method, the mobile oil, bound oil, and adsorbed oil account for 74.7%, 8.1%, and 17.2%, respectively. The quantitative calculation of movable oil saturation by NMR combined with heat treatment is 65.6%, which is lower than that calculated using the thermogravimetric method. In order to calculate the movability more accurately, the scale effect between different samples should be considered. This study could provide a theoretical basis for the subsequent shale oil development program.

KEYWORDS

shale oil, low-field nuclear magnetic resonance, moveable oil, two-dimensional spectrum, thermal gravity

1 Introduction

Shale oil is an emerging unconventional reservoir resource with huge potential reserves, which has important economic value and strategic significance (Liu et al., 2022; Tan et al., 2023; Feng et al., 2020; Wang et al., 2022; Li et al., 2021). However, due to its special reservoir characteristics and complex distribution status, it is very difficult to evaluate the shale oil stratum selection, find its "geological sweet spot" and "engineering sweet spot," and carry out the movability evaluation of the target reservoir (Jiang et al., 2018; Jin et al., 2022; Wang et al., 2021). The traditional movability characterization of shale oil mainly studies the occurrence state and oil-bearing characteristics of shale oil in shale oil reservoirs on the

basis of mastering the characteristics of mineral rock and pore structure, simulates the flow process of shale oil in the reservoir (Huang et al., 2023; Jiang et al., 2020; Tian et al., 2022; Enze et al., 2022; Tan et al., 2021), analyzes the mobilization parameters such as mobilization conditions, mobilization law, and mobilization amount of shale oil, and studies the influencing factors of shale oil movability (Liu et al., 2022; Liu et al., 2022; Wang et al., 2022). However, due to the restriction of experimental conditions, irreversible damage will be caused to the core, resulting in a large gap between the experimental results and the actual field conditions (Dong et al., 2019; Ge et al., 2021; Guo et al., 2021; Huang et al., 2023; Huang et al., 2020). Low-field nuclear magnetic resonance (NMR) is an efficient and non-destructive fluid detection technology for porous media, which is suitable for laboratory core analysis and downhole measurement. It can provide reservoir parameters such as porosity, permeability, and confined water saturation, as well as observe the fluid distribution state. It is one of the important methods for complex reservoir evaluation (Liu et al., 2023; Ma et al., 2023; Sun et al., 2022).

The study of the original oil and water distribution of shale oil has a great research prospect (Zhu et al., 2019). At present, some progress has been made in the study of fluid distribution and movability of shale reservoirs using low-field NMR technology. Studies have shown that the T_1–T_2 relaxation spectrum can obtain information about the interaction between fluid molecules and pore surfaces, thus effectively characterizing porous medium pores and their fluid distribution (Rui et al., 2022; Bao et al., 2021). Zou et al. (2014) pointed out that the movability characterization of shale oil is the movability characterization of free oil in shale oil. When the oil saturation index reaches 100 mg/g or more, the free oil in shale can flow. Using the results of NMR experiments and constant speed mercury intrusion experiments (Zou et al., 2014), Bi et al. (2021) pointed out that there is a good correspondence between the NMR T_2 spectrum and capillary pressure curve. The radius of the pore throat is smaller than the T_2 cutoff value of the movable fluid, and the fluid in the pore encounters flow difficulty (Bi et al., 2021). Wang et al. (2014) used the nuclear magnetic resonance T_2 spectrum and centrifuge experiments to master the T_2 spectrum distribution of shale reservoirs in the initial state, water saturated state, and oil content conditions and obtained the utilization law of shale oil (Wang et al., 2014). At present, the evaluation methods for shale oil movability are not mature (Yu et al., 2019; Wen et al., 2023), and the relevant influencing factors of movability are not clear. Targeted experimental methods and research techniques also need to be further mastered.

Therefore, in this paper, focusing on the Jurassic shale oil reservoir core in the middle-eastern Sichuan region of China, first, low-field nuclear magnetic resonance technology is used to analyze the basic characteristics of shale oil reservoirs. Experiments on the low-field nuclear magnetic resonance one-dimensional spectrum and two-dimensional spectrum characteristics of the original core, core heat treatment, and thermal gravity treatment of the shale core are carried out. The effects of the thermal gravity mass method, T_2 method, and light component volatilization of crude oil on the movability of shale oil reservoirs are analyzed. The movability characteristics of shale oil reservoirs in the middle-eastern Sichuan region are preliminarily clarified, providing a theoretical basis for the subsequent adjustment of shale oil development programs.

2 Materials and methods

2.1 Experimental materials and instruments

(1) Experimental core: The shale core and natural sandstone core were drilled on site, and the basic physical parameters are shown in Table 1.
(2) Experimental oil: The crude oil was acquired from the targeted tight oil well, with a density of 0.89 g/cm^3 and viscosity of 4.21 mPa s (60°C).
(3) Liquid of Soxhlet extraction: Toluene:ethanol:petroleum ether—2:1:1.
(4) Experimental instruments: Porosimeter, pulse decay permeameter, Soxhlet oil extraction instrument, high-pressure core saturation device, and low-field nuclear magnetic resonance online analysis system (MacroMR12-150H-I).

2.2 Experimental method

The basic flowchart of this study is shown in Figure 1. The detail experiment procedures are as followes.

(1) Core-saturated formation crude oil experiment: First, the core is oil washed using the Soxhlet oil extraction instrument. Then, the formation oil is saturated at a pressure of 20 MPa using the high-pressure saturation device.
(2) Saturated oil core T_1–T_2 spectrum test: The experimental core is placed in the holder of the low-field NMR device, the experimental temperature is stabilized for 30 min, and the T_1–T_2 and T_2 spectra of the core samples are tested using the IR-CPMG pulse sequence and CPMG pulse sequence, respectively. The two pulse sequence parameter settings are shown in Table 2.
(3) Oil occurrence characteristic experiment of shale oil: Part of the shale core of saturated crude oil is prepared into a diameter of approximately 3 mm, and a thermogravimetric curve of 110°C is determined using a synchronous thermal analyzer. The same core is taken by heating at 110°C for 20 min, the T_1–T_2 and T_2 spectra of the heated core sample are measured using the low-field NMR device, and then the above steps are repeated to determine the core T_1–T_2 and T_2 spectra after 20, 40, and 60 min of treatment and the characteristics of the specific thermogravimetric change and T_1–T_2 and T_2 spectra.
(4) The test temperature is set to 60°C, and the fluorinated liquid is circulated for 60 min until the temperature is stabilized. The oil sample is transferred from the crude oil bottle to a beaker, the temperature is set to 60°C, and the T_2 spectrum of the 60-C environment is measured using the CPMG pulse sequence. The T_2 spectrum of the original sample is measured at 60°C using the CPMG pulse sequence. The above process is repeated at different time intervals for sampling.

3 Results and discussion

3.1 Basic characteristics of the core and fluid

On the one hand, the distribution and movability of shale reservoir fluid are influenced by the structure of the rock pore

TABLE 1 Basic parameters of core samples.

Core number	Length/cm	Diameter/cm	Porosity/%	Permeability/10^{-6}μm^2
1	4.93	2.52	1.91	5.52
2	4.98	2.52	2.27	13.32

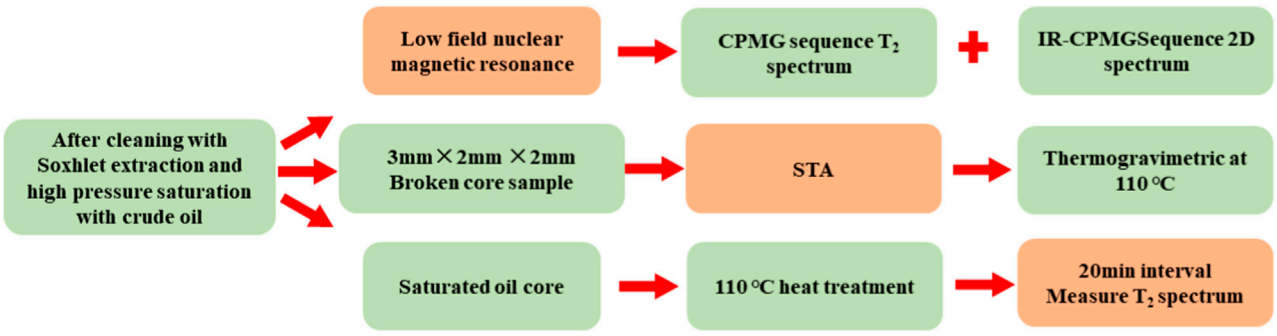


FIGURE 1
Experimental flowchart.

TABLE 2 Nuclear magnetic pulse sequence.

Parameter	RFD/ms	RG1/db	TW/ms	NS	DL2/ms	TE/ms	NECH
IR-CPMG	0.08	20	5,000	32	0.15	-	7,500
CPMG	0.10	20	1,000	64	-	0.30	12,000

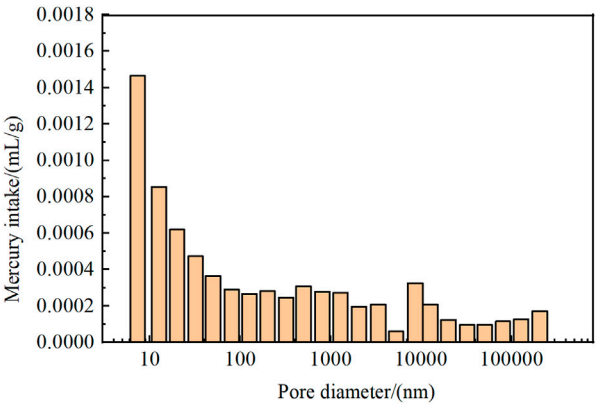


FIGURE 2
Pore size distribution of the core sample.

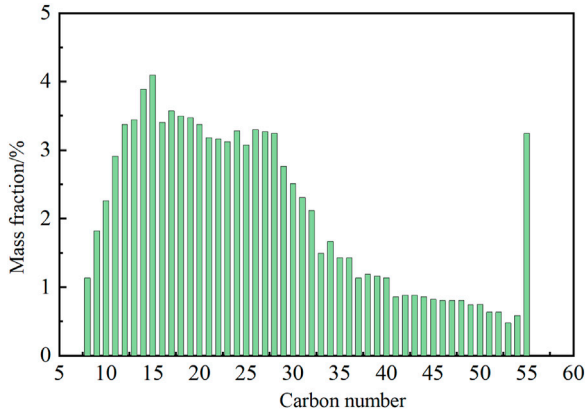


FIGURE 3
Distribution of the crude oil carbon number in the TD well.

throat. On the other hand, they are also related to the nature of the fluid itself. The more complex the pore throat structure, the worse the fluid flow capacity and the movability. The fluid composition determines its properties, and the more vulnerable it is to environmental changes, the more likely its flow capacity is to change, thus affecting the distribution and movability. In this section, the aperture distribution characteristics of cores are obtained through a high-pressure mercury experiment. Crude oil carbon number analysis is conducted to clarify the composition of crude oil. The experimental results are shown in Figures 2–5.

Figure 2 shows that the aperture distribution range of the core is 7.35–205,600 nm. The large distribution range of the pore size

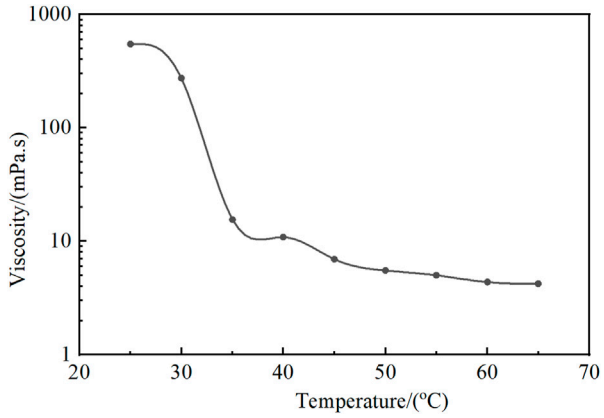


FIGURE 4
Crude oil viscosity vs temperature of the TD well.

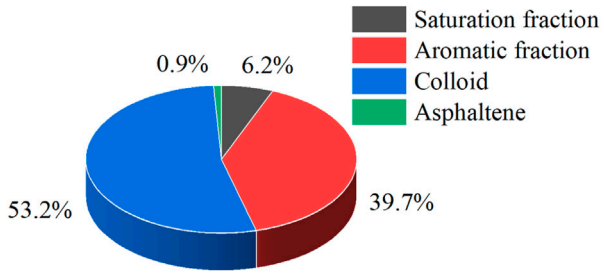


FIGURE 5
Component of crude oil from the TD well.

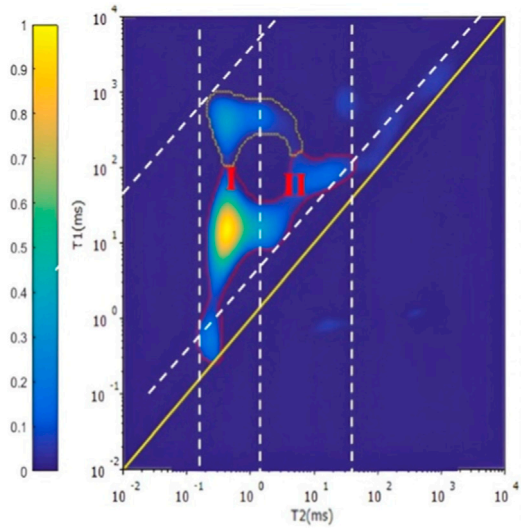


FIGURE 6
2D spectrum in the core saturated with crude oil.

further indicates that the pore throat structure of the shale core is highly heterogeneous, and the existence of large pore size, which shows that the shale texture is brittle and sensitive due to stress change, is easy to produce microcracks, thus Figure 2 existing the pore size of 10^6 nm scale. The results also show that the main pore size of the shale core ranges from 7.35 to 5,290 nm, accounting for 83.1% of the total pores. It shows that shale nano–micro pores are highly developed and are the main storage and transportation space of shale. The pore size of 8.61~205.60 μm accounted for 16.9%, which is mainly microfracture development.

TD well crude oil is mainly C10~C32, accounting for 72.6%, and the aromatic and colloid account for 92.9%. It does not flow at room temperature; however, the viscosity is reduced by 97.2% at 35°C, which improves the fluidity significantly. Attention should be made to the produced crude oil on site to heat and insulate, to strengthen the oil flow capacity.

3.2 Two-dimensional spectrum characteristics of the core saturated with crude oil

The distribution status of crude oil in the reservoir reveals different crude oil advantage areas, which is an important reference factor in the development process of improving EOR, and divides the application boundary for improving crude oil recovery techniques at different pore scales. Therefore, in order to explore the occurrence characteristics of crude oil in the pores of the shale reservoir, the MacroMR12-150H-I NMR online analysis system is used to measure the two-dimensional spectrum distribution of crude oil cores under saturated crude oil so as to clarify the occurrence of crude oil in shale pores of different sizes to facilitate the subsequent exploration of crude oil utilization at different pore boundaries. The results are shown in Figure 6.

After oil is saturated at high pressure, the area I crystalline water zone is within T_1, 0.21~1,018.3 ms and T_2, 0.19~4.4 ms; the main occurrence area of oil in a nanometer-sized pore is within T_1, 31.3.3~913.3 ms and T_2, 4.4~1,018.3 ms. That is, the occurrence status of crude oil can be more intuitively observed through the two-dimensional spectrum.

3.3 Two-dimensional spectrum characteristics of shale cores with heat treatment

High-pressure-saturated oil core pores are full of crude oil, but under the influence of the thermal effect, the crude oil gradually volatilized from the pores. To explore the volatilization of crude oil, the movability of shale oil can be explored; therefore, different heating time cores are taken, and the MacroMR12-150H-I MRI online analysis system is used to measure the 2D spectrum distribution of the crude oil core under different heating times. The results are shown in Figure 7:

With the extension of the heating time, the distribution pattern of the core changes. Region I is mainly crystallized water with treatment at 110°C. The use of crystallized water was not significant. the distribution of region I is largely unchanged, still remaining within the range of T_1: 0.21~1,018.3 ms, T_2: 0.14~2.3 ms, and T_1/T_2: 1.0~6,019.1. The main area is crude oil; with the increasing heating

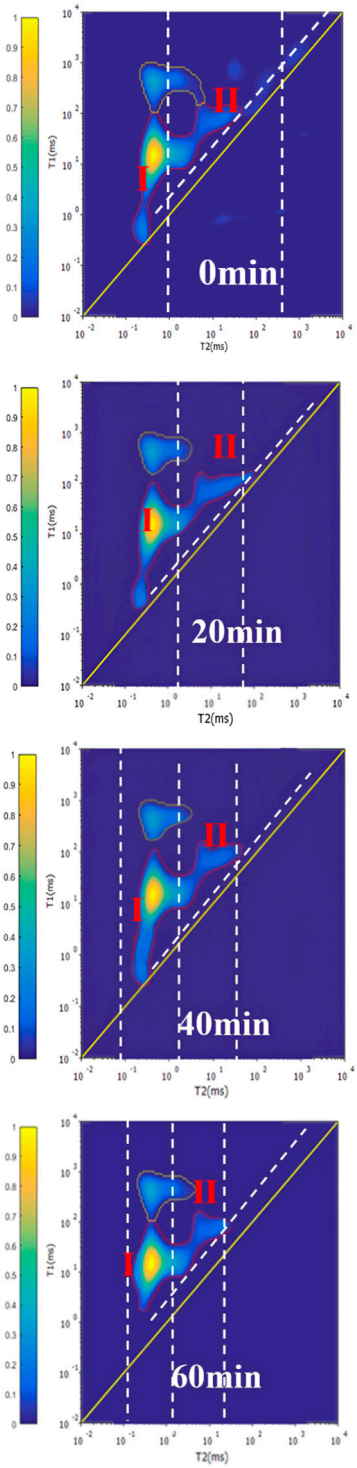


FIGURE 7
2D spectrum of the core during heat treatment at different times.

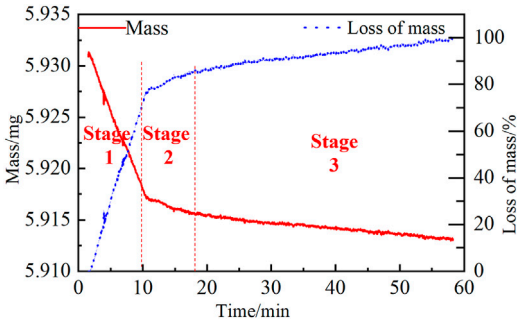


FIGURE 8
Mass change in the shale sample during thermogravimetric treatment.

time, the regional distribution range was significantly reduced, the T_1 distribution range decreased by 10.9% (from 5.5 to 103.7 ms to 5.5 to 93.0 ms), and the T_2 distribution range was reduced by 60.7% (from 1.9 to 43.4 ms to 1.9 to 18.2 ms). In other words, under high temperature, the crude oil in the nanometer-sized pore of the core volatilized gradually, which reduces the regional distribution range in the two-dimensional spectrum, and then, the dynamic oil amount of shale can be explored through thermogravimetric treatment.

3.4 Movable oil analysis of shale oil rock samples

3.4.1 Movable oil by thermogravimetric treatment

Thermogravimetric analysis of saturated oil shale records the change in the sample quality in real time to analyze the volatile amount of shale oil at different times. The volatile amount of shale oil (i.e., the loss of oil) increases with the increase in heating time. The volatile rate of shale oil in different samples is different. The volatile rate of shale oil depends on the pore structure of shale. The better the pore structure, the higher the volatilization rate of shale oil. According to different volatile rates, the content of movable oil, free oil, and bound oil at different stages can be determined, and then, the movable oil content of the shale core can be obtained under the fragmentation scale. The mass change in shale cores at different heat treatment times is shown in Figure 8.

The mass of shale samples at 110°C varies with time, consisting of three linear segments, and the slope gradually decreases with the heating time. The volatilization slope of shale oil type can be identified in different time periods of the shale oil volatilization process. The larger slope indicates a faster volatilization rate of shale oil and better movability. Therefore, the slope from large to small represents the movable oil, bound oil, and adsorbed oil, respectively. Phase I is the movable oil volatilization stage, lasting for 10.3 min, where the volatile oil amount is 0.013 mg; in the bound oil volatilization stage, the shortest time is 4.9 min, and the oil loss is 0.0014 mg; the adsorption oil volatilization stage is 42.9 min, and the oil loss is 0.0030 mg. The proportion of movable oil, bound oil, and adsorbed oil was 74.7%, 8.1%, and 17.2%, respectively.

3.4.2 Movable oil by the T_2 spectrum of the NMR method

The NMR T_2 spectrum of hydrogen fluid in the core pore saturation, high-pressure saturated oil after measuring the shale core T_2 spectrum, the core-saturated crude oil, total oil content T_2 signal for pore signal and shale itself, heating stability of the shale core T_2 spectrum, the core is still untreated completely bound oil, T_2 signal for pore bound oil signal and shale itself, drying oil after measuring the shale core T_2 spectrum, the core

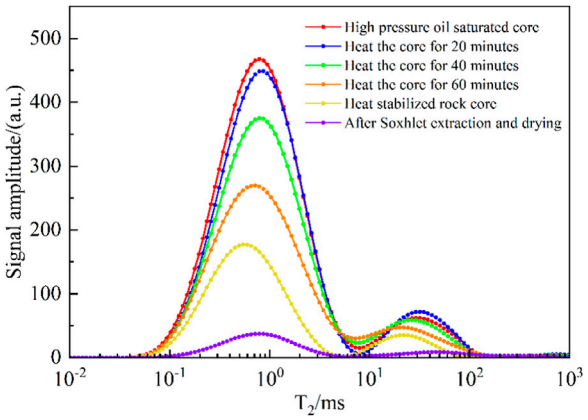


FIGURE 9
Dynamic T_2 spectrum of the core under high-temperature treatment.

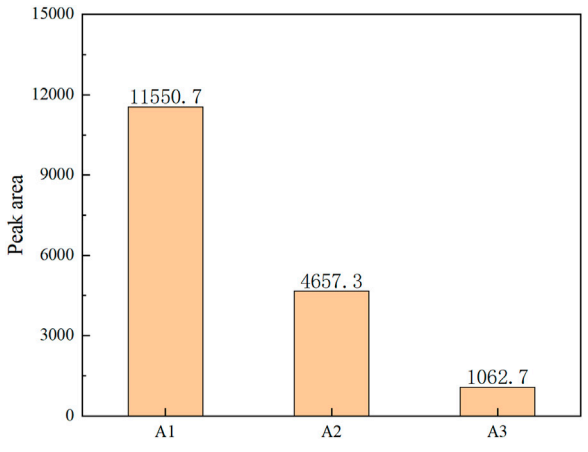


FIGURE 10
T_2 spectrum area of the core under high-temperature treatment.

is no fluid, T_2 signal for shale organic matter signal. Through the analysis of the NMR T_2 spectrum of the core sample during different heating times, the movable oil content at the core scale can be obtained at different heating times. The T_2 spectrum changes in shale cores at different heat treatment times are shown in Figure 9.

The peak area of the NMR T_2 spectrum can quantitatively represent the content of hydrogen fluid in the core pore, so the nuclear oil core can be used to quantitatively calculate the movable oil saturation for the saturated oil core:

$$S = (A1 - A2)/(A1 - A3), \quad (1)$$

where

S is the movable oil saturation, %;

A1 is the high-pressure-saturated oil core peak area;

A2 is the core T_2 spectrum area after heating and stabilizing; and

A3 is the core T_2 spectrum after Soxhlet extraction and drying.

The carbon and component analysis of crude oil are shown in Figures 4 and 5. Three states of oil occurrence in the shale sample are

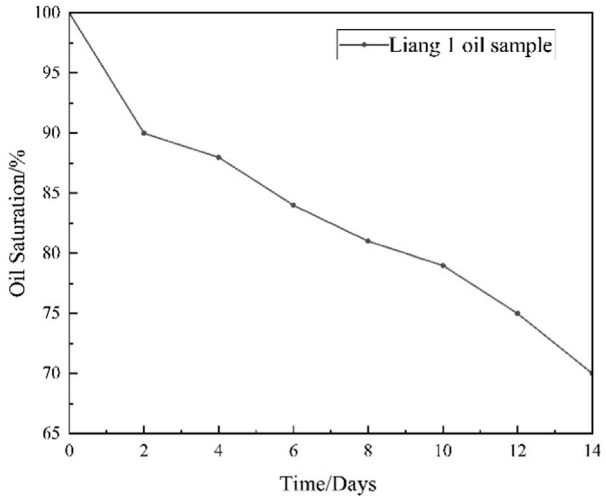


FIGURE 11
Light component evaporation of crude oil under heat treatment.

illustrated in Figure 10. The T_2 spectrum of the high-pressure-saturated oil core can represent all crude oil and shale organic matter, and the T_2 spectrum area is 11,550.7 a.u.. After heat treatment, the adsorbed oil adheres to the shale pore surface, while the movable oil is used to overcome the capillary force under the action of heat. The T_2 spectrum area is 4,675.3 a.u.; after washing the oil and drying the core, the T_2 spectrum represents the organic matter signal of shale itself, and the T_2 spectrum area is 1,062.7 a.u.. The movable oil saturation is calculated as follows:

$$S = (11550.7 - 4675.3)/(11550.7 - 1062.7) \times 100\% = 65.6\%.$$

3.4.3 Light component evaporation in crude oil under heat treatment

The T_2 spectrum of crude oil shows a single-peak distribution. The T_2 peak area is shown in Figure 11. With the increase in evaporation time, the peak gradually decreases, indicating that the light hydrocarbon components in crude oil escape gradually, resulting in the decrease in light component and the corresponding peak area of the T_2 spectrum.

4 Discussion

The evaporation experiment of the light component of crude oil heat treatment showed that the light hydrocarbon component in crude oil gradually escapes, resulting in the decrease in the crude oil hydrogen content and the corresponding peak area of the T_2 spectrum. Corresponding to the crude oil in the core pores of different scales, the crude oil gradually escapes from the pore under the thermal action, and the cores of different sizes have different evaporation resistances.

Samples for thermogravimetric analysis were 3 mm in diameter and approximately 2 mm in length, and samples for nuclear magnetic analysis were 49 mm in length and 25 mm in diameter. The two-to-scale difference led to the final thermal and nuclear magnetic movability. The movability calculated from the

thermogravimetric analysis was 74.7% *versus* 65.6% from the NMR T_2 spectrum. Thermogravimetric movability acquired with the broken sample is higher than that with the plug sample under the NMR method. For smaller-sized samples, under the thermal treatment, oil in pores is easier to overcome flow resistance. This indicates that for the same core sample, under the same temperature, the oil movability in the smaller-sized sample is higher than that in the large ones. Therefore, for a more accurate measurement of oil movability, the scale effect should be considered between different samples.

5 Conclusion

(1) From the thermogravimetric method, the volatile slope of shale oil over different time periods serves as an indicator for identifying shale oil types. A steeper slope implies a faster volatilization rate and enhanced movability of the shale oil. For the shale sample in this study, the movable oil, bound oil, and adsorbed oil account for 74.7%, 8.1%, and 17.2%, respectively.

(2) From the NMR T_2 spectrum of the Jurassic section of central and eastern Sichuan shale samples, laboratory-scale experiments yielded a movable oil saturation of 65.6%.

(3) The two-dimensional spectrum provides a comprehensive analysis of the occurrence of crude oil. In particular, under thermal conditions, the T_1 and T_2 distribution ranges of crude oil were reduced by 10.9% and 60.7%, respectively. This suggests that crude oil volatilizes gradually from the nanometer-sized pore under high temperatures.

(4) Upon exposure to heat, light hydrocarbon components in crude oil evaporate progressively. The movable oil in the broken sample exposed to the thermogravimetric method surpasses that of the core plug sample, as observed using the NMR method. Smaller samples exhibit higher movable oil saturation under thermal conditions. Scale effects should be considered across different sized samples.

Data availability statement

The original contributions presented in the study are included in the article/Supplementary Material; further inquiries can be directed to the corresponding author.

Author contributions

CC: writing–original draft and writing–review and editing. LW: investigation and writing–review and editing. RZ: writing–review and editing. QK: writing–review and editing. QZ: writing–review and editing. DZ: writing–review and editing. JG: writing–review and editing. MC: writing–review and editing. HC: writing–review and editing. LL: writing–review and editing. KW: writing–review and editing. JH: writing–review and editing.

Funding

The author(s) declare that financial support was received for the research, authorship, and/or publication of this article. This research was funded by PetroChina Southwest Oil and Gas Field Company (grant number 20220303-04). The funder was not involved in the study design, collection, analysis, interpretation of data, the writing of this article, or the decision to submit it for publication.

Acknowledgments

The authors acknowledge the PetroChina Southwest Oil and Gas Field Company. The authors thank the reviewers and editors for their careful review of this manuscript.

Conflict of interest

Authors CC, LW, RZ, QK, QZ, DZ, JG, MC, HC, KW, and JH were employed by the Exploration and Development Research Institute of PetroChina Southwest Oil and Gas Field Company. Author LL was employed by the Development Department of PetroChina Southwest Oil and Gas Field Company.

Publisher's note

All claims expressed in this article are solely those of the authors and do not necessarily represent those of their affiliated organizations, or those of the publisher, the editors, and the reviewers. Any product that may be evaluated in this article, or claim that may be made by its manufacturer, is not guaranteed or endorsed by the publisher.

References

Bao, W. C. (2021). *NMR study of shale oil mobility*. East China: China University of Petroleum.

Bi, B. (2021). *Experimental study on fluid mobility evaluation of tight oil reservoirs in Jinghe Oilfield*. China University of Petroleum, (Beijing, China).

Dong, M. Z., li, Y. J., Sang, X., Li, S., Li, M., and Sun, Y. L. (2019). Reservoir conditions and mechanism of shale oil flow. *petroleum Nat. gas Geol.* 40, 03.

Feng, Q. H., Xu, S. Q., and Xin, X. D. (2020). Advances and challenges in shale oil development: a critical review. *Adv. Geo-Energy Res.* 4, 04.

Ge, H. K., Chen, Y. K., Teng, W. W., Shen, Y. H., Liu, H. X., and Zhang, J. L. (2021). Discussion on micro production mechanism and EOR method of jimusar shale oil. *Xinjiang Petroleum Nat. gas* 17, 03.

Guo, Q. L., Wang, J., Chen, X. M., Chen, N. S., and Wu, X. Z. (2021). Evaluation method and application of shale oil original volume and movable oil volume. *petroleum Nat. gas Geol.* 42, 06.

Huang, F. Y. H., Zhang, J. Y., Zhang, S. C., He, K., Zhang, B., and Tian, H. (2023a). Characteristics of shale oil in different occurrence states of Cretaceous Qingshankou Formation in northern Songliao Basin. *Acta Geol. Sin.* 97, 02.

Huang, L. K., He, R., Yang, Z. Z., Tan, P., Chen, W. H., Li, X. G., et al. (2023b). Exploring hydraulic fracture behavior in glutenite formation with strong heterogeneity and variable lithology based on DEM simulation. *Eng. Fract. Mech.* 278, 109020. doi:10.1016/j.engfracmech.2022.109020

Huang, Z. K., Hao, Y. 1, and Li, S. (2020). Evaluation of hydrocarbon potential and shale oil mobility of shale series in Chang 7 member of Ordos Basin -- Taking well h317 as an example. *Geol. China* 47, 01.

Jiang, Q. G., Li, M. W., Ma, Y. Y., Cao, T. T., Liu, P., Qian, M. H., et al. (2018). Molecular geochemical evaluation method of shale oil mobility: a case study of shale oil in Jiyang depression. *Pet. Exp. Geol.* 40, 06.

Jiang, Z. X., Li, T. W., Gong, H. J., Jiang, T., Chang, J. Q., Ning, C. X., et al. (2020). Characteristics of low mature shale reservoir in Zhanhua sag and its influence on shale oil mobility. *Acta petrol. Sin.* 41, 12.

Jin, Z. J., Liang, X. P., Wang, X. J., Zhu, R. K., Zhang, Y. Y., Liu, G. P., et al. (2022). Shale oil enrichment mechanism and sweet spot optimization of Fengcheng Formation in Mahu depression. *Xinjiang Pet. Geol.* 43, 06.

Li, J. R., Yang, Z., and Wu, S. T. (2021). Key issues and development direction of petroleum geology research on source rock strata in China. *Adv. Geo-Energy Res.* 5, 02.

Liu, H. M. (2022a). Exploration practice and Prospect of shale oil in Jiyang depression. *PetroChina Explor.* 27, 01.

Liu, H. M., Bao, Y. S., Zhang, S. C., Li, Z., Li, J. L., Wang, X. J., et al. (2023). Structural characteristics and shale oil mobility of continental carbonate rich shale: a case study of Paleogene Shahejie Formation shale in Jiyang depression. *petroleum Explor. Dev.* 50, 06.

Liu, Q. Y., Li, P., Jin, Z. J., Sun, Y. W., Hu, G., Zhu, Y. D., et al. (2022). Organic matter rich formation and hydrocarbon enrichment of lacustrine shale series: a case study of Chang 7. *Chin. Sci. Geosciences* 52, 02.

Liu, Z. Y. (2022b). *Occurrence and mobility evaluation of continental shale oil in Jurassic Daanzhai member of central Sichuan*. Beijing, China: China University of Petroleum.

Ma, B. (2023). *Study on the mobility of continental shale oil based on various methods – a case study of the second member of the Kongdong shale in Cangdong depression*.

Rui, S., Wei, X., Hang, Y., Zeng, X., Wang, G., and Shao, G. (2022). Study on fluid mobility in sandwich-type shale oil reservoir using two-dimensional nuclear magnetic resonance approaches. *Energy Sources, Part A Recovery, Util. Environ. Eff.* 44 (3), 5951–5967. doi:10.1080/15567036.2022.2094503

Sun, Z. L., Li, Z. J., Shen, B. J., Zhu, Q. M., and Li, C. X. (2022). Application of nuclear magnetic resonance technology in shale oil and gas reservoir evaluation. *Pet. Exp. Geol.* 44, 05.

Tan, P., Fu, S. H., Chen, Z. W., and Zhao, Q. (2023). Experimental investigation on fracture growth for integrated hydraulic fracturing in multiple gas bearing formations. *Geoenergy Sci. Eng.* 231, 212316. doi:10.1016/j.geoen.2023.212316

Tan, P., Jin, Y., and Pang, H. W. (2021). Hydraulic fracture vertical propagation behavior in transversely isotropic layered shale formation with transition zone using XFEM-based CZM method. *Eng. Fract. Mech.* 248, 107707. doi:10.1016/j.engfracmech.2021.107707

Tian, S. S. (2022). Microscopic characteristics of shale reservoir pores and evaluation of shale oil occurrence and mobility. *China Univ. Petroleum (East China)*.

Wang, E., Li, C. R., Feng, Y., Song, Y. C., Guo, T. L., Li, M. W., et al. (2022b). Novel method for determining the oil moveable threshold and an innovative model for evaluating the oil content in shales. *Energy* 239, 121848. doi:10.1016/j.energy.2021.121848

Wang, J. M. (2021). *Geological sweet spot evaluation of shale oil layer series of Lucaogou Formation in jimusar sag*. East China: China University of Petroleum.

Wang, R. F., Qi, H. X., and Lv, X. H. (2014). Occurrence characteristics and control factors of mobile fluids in deep high pressure and low permeability sandstone reservoirs. *Petroleum Geol. Exp.* 36, 01.

Wang, X. N., Li, J. R., and Zhang, H. (2022a). Characteristics, current exploration practices, and prospects of continental shale oil in China. *Adv. Geo-Energy Res.* 6, 06.

Wang, Z. Q., Ge, H. K., Guo, H. Y., Zhou, H., and Zhang, Y. K. (2022c). Experimental study on mobility of jimusar shale oil under different temperature and pressure CO2 huff and puff in Junggar Basin. *Pet. Exp. Geol.* 44, 06.

Wen, J. C., Hu, Q. H., and Yang, S. Y. (2023). Shale reservoir characteristics and shale oil mobility evaluation of the second member of Kongdong formation in Cangdong sag, Bohai Bay Basin. *special oil gas Reserv.* 30, 04.

Yu, Z. Y., Zhang, X. W., and Tan, J. J. (2019). Study on the occurrence characteristics and mobility of shale oil in Biyang depression. *petroleum Geol. Eng.* 33, 01.

Zhu, X. M., Zhu, W. B., Cao, J., Song, Y., Zhang, D. M., Hu, S. Z., et al. (2019). Research Progress on shale oil mobility characterization methods. *Xinjiang Pet. Geol.* 40, 06.

Zou, C. N., Yang, Z., Zhang, G. S., Hou, L., Zhu, R., Tao, S., et al. (2014). Conventional and unconventional petroleum "orderly accumulation": concept and practical significance. *Petroleum Explor. Dev.* 41, 14–30. doi:10.1016/s1876-3804(14)60002-1

frontiers | Frontiers in Built Environment

TYPE Original Research
PUBLISHED 18 June 2024
DOI 10.3389/fbuil.2024.1395464

Check for updates

OPEN ACCESS

EDITED BY
Peng Tan,
CNPC Engineering Technology R & D Company Limited, China

REVIEWED BY
Chen Xiaobin,
Central South University, China
Shubin Xu,
Chongqing Research Institute of China Coal Technology and Engineering Group, China

*CORRESPONDENCE
Zhilin Li,
lizl_ccde@cnpc.com.cn

RECEIVED 04 March 2024
ACCEPTED 30 April 2024
PUBLISHED 18 June 2024

CITATION
Fan L, Li Z and Luo Y (2024), Parametrical design and optimization of a reverse circulation drill bit for dust control.
Front. Built Environ. 10:1395464.
doi: 10.3389/fbuil.2024.1395464

COPYRIGHT
© 2024 Fan, Li and Luo. This is an open-access article distributed under the terms of the Creative Commons Attribution License (CC BY). The use, distribution or reproduction in other forums is permitted, provided the original author(s) and the copyright owner(s) are credited and that the original publication in this journal is cited, in accordance with accepted academic practice. No use, distribution or reproduction is permitted which does not comply with these terms.

Parametrical design and optimization of a reverse circulation drill bit for dust control

Liming Fan[1], Zhilin Li[1]* and Yongjiang Luo[2]

[1]CCDC Drilling and Production Engineering Technology Research Institute, PetroChina, Deyang, China, [2]State Key Laboratory of Coal Mine Disaster Dynamics and Control, Chongqing University, Chongqing, China

The reverse circulation down-the-hole air hammer drilling (RC-DTH) method is renowned for its efficiency in hard rock formations and exceptional dust control performance. It presents opportunities for cost-saving, efficiency improvement, energy conservation, and environmental protection. Reverse circulation drill bits are critical components of this method. This study focused on the air reverse circulation regime, investigating various geometric parameters of the RC drill bits through computational and experimental methods to enhance its dust control performance. Results indicate that increasing the layers of suction nozzles, enlarging the diameters of the suction and mixing nozzles, and optimizing the input airflow rate can effectively channel airflow toward the central passage of the drill tool. Consequently, this optimization significantly improves the dust control performance of the RC drill bits. Conversely, increases in the flushing nozzle diameter and alterations in the suction nozzle location have detrimental effects on the dust control capability of the RC drill bits. Field tests were conducted at the Yuan Jiacun iron mine, affiliated with Taiyuan Iron and Steel (Group) CO., LTD. The field tests demonstrate that the optimized RC drill bit exhibits excellent dust performance.

KEYWORDS

orthogonal design, reverse circulation, DTH air hammer, drill bit, dust control, unconventional oil and gas reservoir

1 Introduction

Down-the-hole (DTH) air hammer drilling stands out as a premier method for hard rock drilling (Lyons et al., 2009). Its widespread adoption in various industries like mining, oil and gas, geothermal exploitation, and other drilling applications attests to its efficacy (Han et al., 2005; Deng et al., 2024). This technique offers several advantages, such as producing straighter boreholes, penetration without any drilling fluid, and lower bottom-hole pressure. Additionally, it finds utility in underbalanced drilling scenarios and proves beneficial in water-sensitive formations (Zhang et al., 2017). However, the prevalent use of DTH air hammer drilling tools presents a significant challenge in the form of respirable dust emissions (Organiscak and Page, 1995). Of particular concern is silica dust, classified as a carcinogen, with numerous studies underscoring the perils associated with prolonged exposure to it (Tavakol et al., 2016). Researchers have established a link between inhaling silica particles present in mining dust and the subsequent development of various respiratory ailments, including chronic obstructive pulmonary disease (COPD), emphysema, chronic bronchitis, and non-reversible asthma (Li et al., 2016). Overexposure to respirable silica can lead to severe health complications like lung

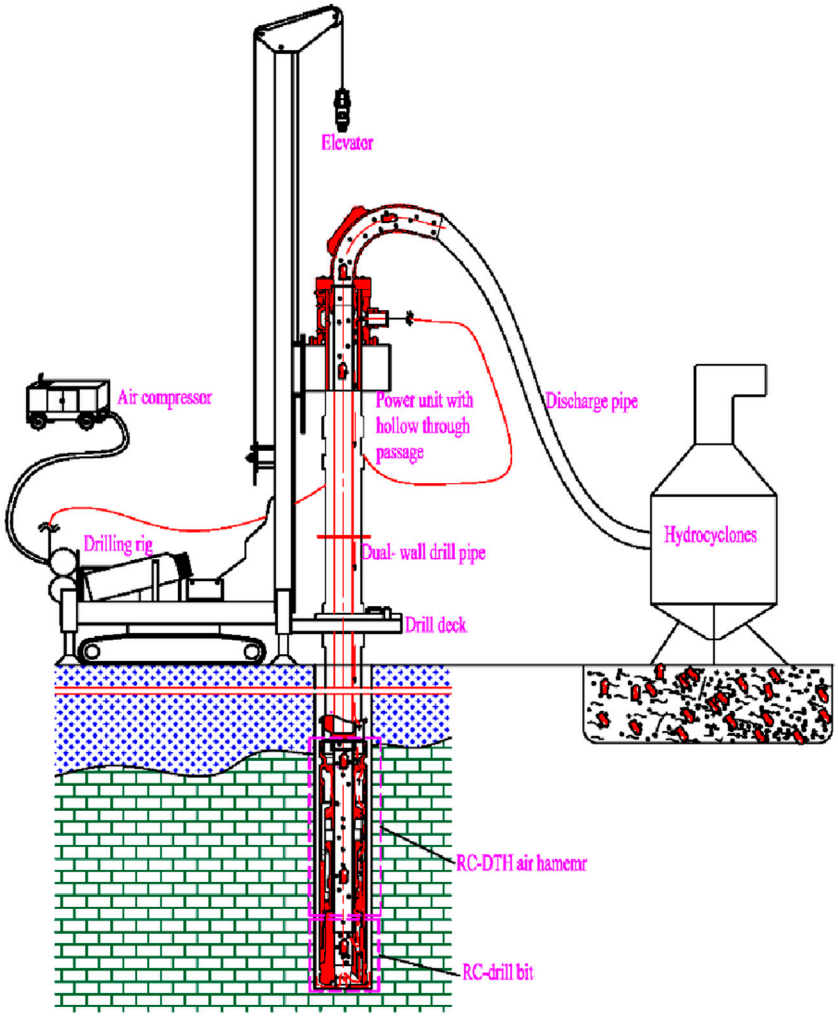


FIGURE 1
Schematic representation of the hollow-through DTH air hammer drilling system.

cancer, silicosis, or other silica-related diseases, characterized by the formation of lesions on lung tissue, which impairs oxygen absorption (Cooper et al., 2012). Recognizing the hazards posed by silica dust, regulatory bodies like the Occupational Safety and Health Administration (OSHA) have instituted guidelines to safeguard workers, particularly in concrete-related industries, from silica dust exposure (Mixon and Nain, 2013). These regulations mandate mine owners to implement measures for monitoring silica dust levels, controlling dust dispersion on job sites, and shielding workers from airborne silica exposure. Given the critical imperative to mitigate dust production during drilling operations, proactive measures are paramount to ensure the safety and wellbeing of workers in these environments.

Several studies have investigated methods to reduce dust production during the drilling process using the DTH air hammer drilling method. Cecala et al. (2003) developed an enclosed cab with retrofitted filtration and pressurization systems to protect the drill operators from the drilling dust. However, while this system offers shelter to the workers inside the cab, personnel in the vicinity of the drilling operations and machinery remain exposed to dusty environments. Studies by Li et al. (2016) indicate that controlling drilling by adjusting the penetration and rotational rates can reduce respirable dust. However, sacrificing the penetration rate for dust reduction is not a practical solution. Wet drilling technology is widely regarded as the most effective method for dust control, boasting efficiencies of up to 96% (USBM, 1987). To effectively control dust, the amount of water injected must be adjusted based on the drill type, geology, and the original moisture level of the formation being drilled (Cecala et al., 2012). However, maintaining appropriate water injection levels poses the following challenges: too little water reduces dust control efficiency, while excessive water can lead to operational issues such as drill bit plugging and rotation binding due to agglomeration of drill cuttings (USBM, 1987). Additionally, wet drilling accelerates bit wear and shortens its lifespan by over 50% (Hustrulid, 1982; Page, 1991; Sundae et al., 1995). In dry drilling operations, the dust collection systems installed on the drill deck typically consist of hydro-cyclones with exhaust fans and filters. However, these systems often suffer from poor maintenance, resulting in damaged, non-functional, or missing dust collector filters, leading

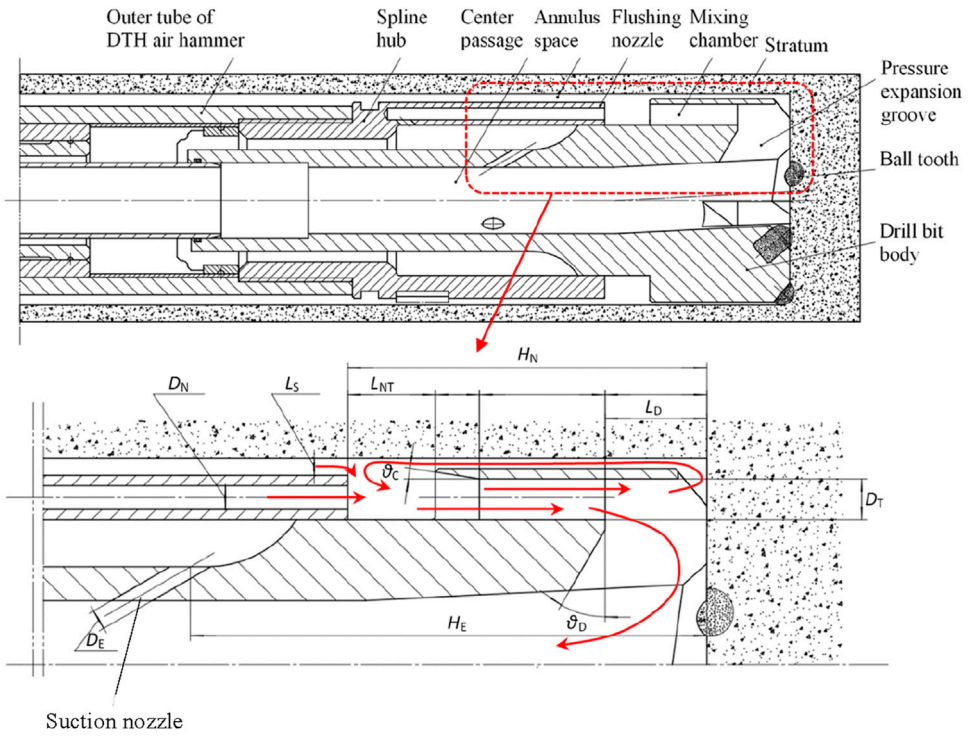


FIGURE 2
Schematic representation of the RC drill bit.

TABLE 1 Levels for each parameter employed by the numerical simulation.

Factor	Q_v/(m^3/min)		D_N/mm	L_{NT}/mm	D_T/mm	θ_C/degree	L_D/mm	L_S/mm	D_E/mm	H_E/mm	m/layer	θ_D/degree
Level	1	1	4	0	8	0	5	2	4	10	1	0
	2	5	5	10	10	15	10	3	5	85	2	15
	3	9	6	20	12	30	15	4	6	160	3	30

TABLE 2 Levels for each parameter employed by the experiments.

Factor		L_S/mm	m/layer	D_E/mm	D_N/mm	D_T/mm	L_{NT}/mm	Q_V/m^3/min
Levels	1	2	1	4	4	8	0	2
	2	4	2	5	5	10	10	4
	3		3	6	6	12	20	6

to dusty exhaust air emissions (Maksimovic and Page, 1985; Zimmer and Lueck, 1986; Zimmer et al., 1987). Other sources of emissions in the collection system can be attributed to damaged or worn enclosure components or operational conditions, hindering the containment and capture of dust.

Since the 1980s, the RC-DTH air hammer drill method has been developed to mitigate drill dust and enhance the penetration rates in fractured formations (Liu and Yin, 2012). The RC-DTH air hammer drill tool typically comprises a dual-passage faucet, dual-wall drill pipes, an RC-DTH air hammer, and an RC drill bit, as illustrated in Figure 1. A notable distinction between traditional rotary drilling and RC-DTH air hammer drilling methods lies in the circulation of discharged drill cuttings. In RC-DTH air hammer drilling, compressed air is injected into the annulus of dual-wall pipes, propelling the RC-DTH air hammer to deliver high-frequency blows to an RC drill bit, thereby forming reverse circulation. The exhaust air carrying drill cuttings returns to the surface through the central passage of dual-wall drill pipes instead of the annulus space between the drill pipes and the borehole wall. This drilling system effectively controls dust without water injection or additional

10.3389/fbuil.2024.1395464

TABLE 3 Orthogonal experimental design L_{27} (3^{13}) and results for the numerical simulation.

	Q_V	D_N	L_{NT}	D_T	θ_C	L_D	L_S	D_E	H_E	m	θ_D	$M_{annulus}$/kg/s
1	1	1	1	1	1	1	1	1	1	1	1	0.002493
2	1	1	1	1	2	2	2	2	2	2	2	0.006405
3	1	1	1	1	3	3	3	3	3	3	3	0.004503
4	1	2	2	2	1	1	1	2	2	2	3	0.0013
5	1	2	2	2	2	2	2	3	3	3	1	0.000419
6	1	2	2	2	3	3	3	1	1	1	2	−0.004346
7	1	3	3	3	1	1	1	3	3	3	2	−0.00116
8	1	3	3	3	2	2	2	1	1	1	3	−0.005496
9	1	3	3	3	3	3	3	2	2	2	1	−0.00282
10	2	1	2	3	1	2	3	1	2	3	1	0.027491
11	2	1	2	3	2	3	1	2	3	1	2	0.016585
12	2	1	2	3	3	1	2	3	1	2	3	0.033007
13	2	2	3	1	1	2	3	2	3	1	3	−0.012926
14	2	2	3	1	2	3	1	3	1	2	1	0.0097
15	2	2	3	1	3	1	2	1	2	3	2	0.004653
16	2	3	1	2	1	2	3	3	1	2	2	−0.0092
17	2	3	1	2	2	3	1	1	2	3	3	−0.01533
18	2	3	1	2	3	1	2	2	3	1	1	−0.027232
19	3	1	3	2	1	3	2	1	3	2	1	−0.00378
20	3	1	3	2	2	1	3	2	1	3	2	0.029851
21	3	1	3	2	3	2	1	3	2	1	3	0.006602
22	3	2	1	3	1	3	2	2	1	3	3	0.006529
23	3	2	1	3	2	1	3	3	2	1	1	−0.0253
24	3	2	1	3	3	2	1	1	3	2	2	−0.027281
25	3	3	2	1	1	3	2	3	2	1	2	−0.047896
26	3	3	2	1	2	1	3	1	3	2	3	−0.059197
27	3	3	2	1	3	2	1	2	1	3	1	−0.0235
y_{j1} (x10^{-3})	1.3	123.2	−84	−115.8	−37.2	−41.6	−30.6	−81	39.1	−97.6	−42.6	
y_{j2} (X10^{-3})	26.8	−47	−56	−21.7	−42	−37.5	−33.4	−6	−44.9	−51.8	−32.4	
y_{j3} (X10^{-3})	−144	−192	24.6	21.5	−36.4	−36.8	−52	−29	−110	33.4	−41	
$\overline{y_{j1}}$ (X10^{-3})	0.4	41.1	−28	−38.6	−12.3	−13.9	−10.2	−27	13	−32.5	−14.2	
$\overline{y_{j2}}$ (X10^{-3})	8.9	−16	−19	−7.2	−14.1	−12.5	−11.1	−2	−15	−17.3	−10.8	
$\overline{y_{j3}}$ (X10^{-3})	−48	−64	8	7.2	−12.1	−12.3	−17.3	−10	−36.7	11.2	−13.7	
R_j (X10^{-3})	57	105	36	45.7	1.999	1.59	7.14	25	49.71	43.7	3.39	
Order	D_N, Q_V, H_E, D_T, m, L_{NT}, D_E, L_S, θ_D, θc, L_D											

borehole entrance attachments, presenting an environmentally friendly and cost-effective drilling technique. Although extensive studies on the dust control performance of RC drill bits have been documented in the literature, with reported dust control efficiencies of up to 99%, dust emissions may still occur during the initial drilling phase due to lower annular back pressure and inadequate reverse circulation capacity without proper design. Furthermore, air loss in fractured formations can exacerbate the dust control performance of

TABLE 4 Orthogonal experimental design L_{18} (2×3^7) and results for the experiments.

	L_S	m	D_E	D_N	D_T	L_{NT}	Q_V	Error	$Q_{v\text{-}annulus}$
1	1	1	1	1	1	1	1	1	2
2	1	1	2	2	2	2	2	2	−2.8
3	1	1	3	3	3	3	3	3	−4.5
4	1	2	1	1	2	2	3	3	2.2
5	1	2	2	2	3	3	1	1	0.5
6	1	2	3	3	1	1	2	2	−3.2
7	1	3	1	2	1	3	2	3	−1
8	1	3	2	3	2	1	3	1	−5.3
9	1	3	3	1	3	2	1	2	8.6
10	2	1	1	3	3	2	2	1	−5.5
11	2	1	2	1	1	3	3	2	4.6
12	2	1	3	2	2	1	1	3	2
13	2	2	1	2	3	1	3	2	−2.2
14	2	2	2	3	1	2	1	3	−2.8
15	2	2	3	1	2	3	2	1	10
16	2	3	1	3	2	3	1	2	−2
17	2	3	2	1	3	1	2	3	7.8
18	2	3	3	2	1	2	3	1	3.2
y_{j1}	−3.5	−4.2	−6.5	35.2	2.8	1.1	8.3	4.9	
y_{j2}	15.1	4.5	2	−0.3	4.1	2.9	5.3	3	
y_{j3}		11.3	16.1	−23.3	4.7	7.6	−2	3.7	
$\overline{y_{j1}}$	−0.3889	−0.7	−1.0833	5.8667	0.4667	0.1833	1.3833	0.8167	
$\overline{y_{j2}}$	1.6778	0.75	0.3333	−0.05	0.6833	0.4833	0.8833	0.5	
$\overline{y_{j3}}$		1.8833	2.6833	−3.883	0.7833	1.2667	−0.333	0.6167	
R_j	2.0667	2.5833	3.7667	9.75	0.3167	1.0833	1.7167	0.3167	
Order	D_N, D_E, m, L_S, Q_V, L_{NT}, D_T								

this drilling system. To further enhance the dust control performance of RC drill bits and meet engineering requirements, the effects of the geometric parameters on the performance of a newly developed RC drill bit were investigated, and a field trial was conducted to validate its feasibility.

2 Structure of the drill bit

Figure 2 depicts the schematic representation of the RC drill bit. Following the operation of the DTH air hammer, compressed air exits through two passages: the suction nozzles positioned on the drill bit body and the flushing nozzles oriented perpendicular to the borehole bottom face. As compressed air flows through the suction nozzles, it forms jets at their outlets, creating a negative pressure zone nearby. The pressure differential between the borehole bottom and this negative pressure zone within the center passage generates a lifting force on the air, carrying drill cuttings. Furthermore, air entering the flushing nozzles serves to cool the bit inserts and direct the drill cuttings into the center passage. This synergistic process facilitates the formation of air reverse circulation without the need for any sealing elements. The dust control capability of the RC drill bit hinges on the mass flow rate of air drawn from the annulus between the drill pipes and the borehole. Greater air suction from the annular space into the center passage correlates with enhanced dust control performance and augmented reverse circulation capacity.

3 Orthogonal design

Orthogonal design was employed to optimize the dust control performance of the RC drill bit. The study investigated the effects of the geometric parameters, including the suction nozzle layer (m), diameter (D_E), and its location (H_E); the flushing nozzle diameter

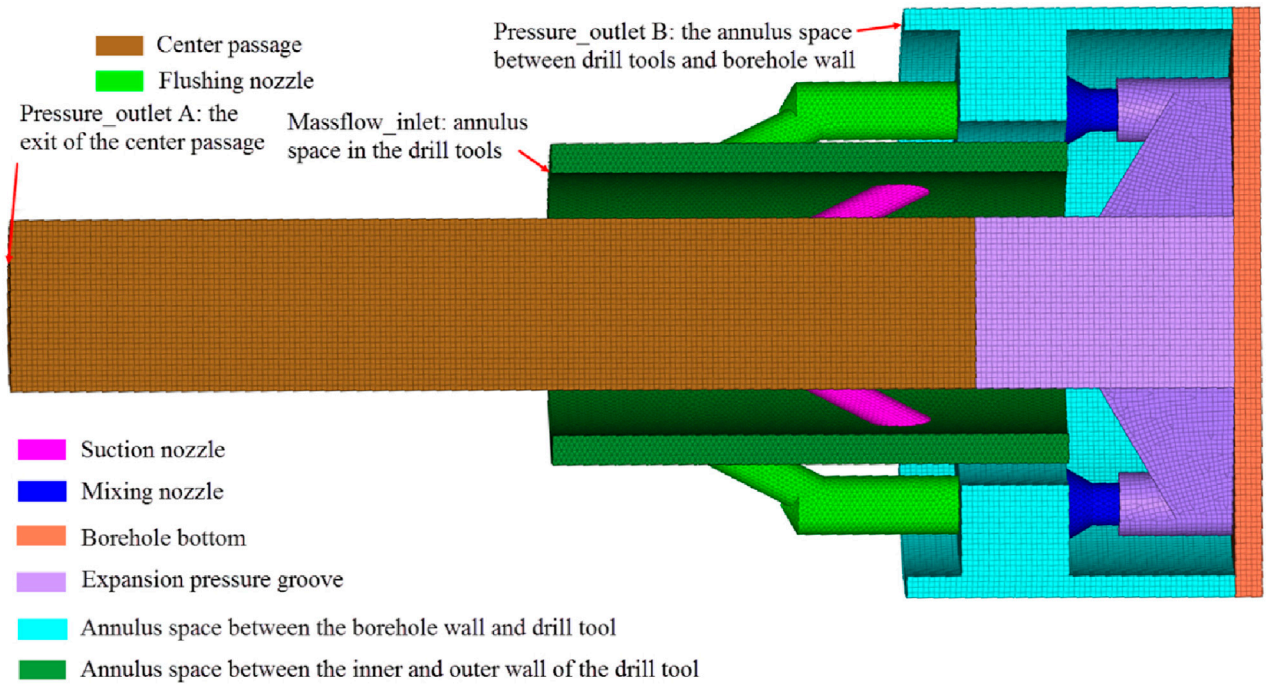


FIGURE 3
Typical meshed computational domain (the other half was masked).

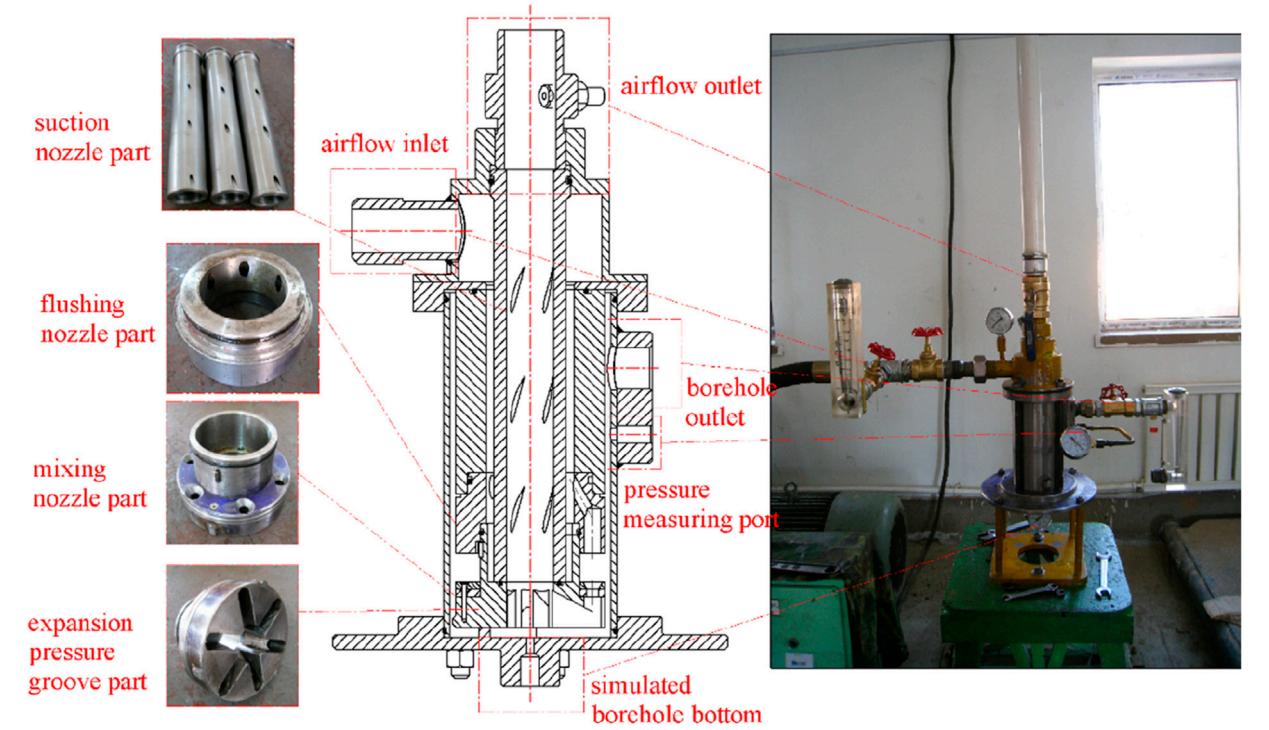


FIGURE 4
Apparatus for laboratory experiments.

(D_N); the mixing nozzle diameter (D_T); the size of the annulus between the drill bit and borehole wall (L_S); the distance between the flushing nozzle and mixing nozzle (L_{NT}); the throat angle of the mixing nozzle (θ_c); and the elevation angle (θ_D) and depth (L_D) of the expansion pressure groove on the dust control capacity of the RC drill bit. Additionally, the effect of the operational parameter, the

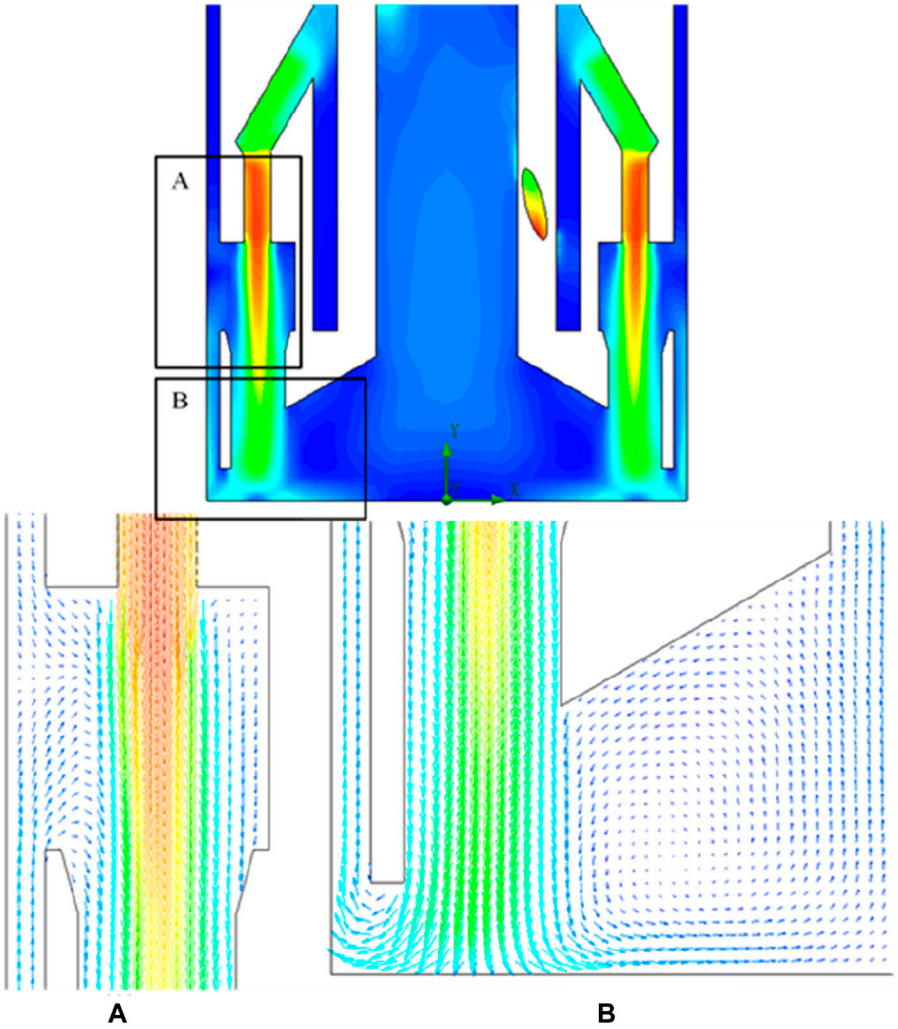


FIGURE 5
Typical velocity flow field in the drill bit. **(A)** Enlarged flow field view of annulus space, flushing nozzle section and mixing nozzle section. **(B)** Enlarged flow field view of annulus space, mixing nozzle section and expansion pressure section.

input air volume flow rate (Q_v), on the dust control capacity of the RC drill bit was investigated. The mass flow rate of the annulus between the drill bit and the borehole wall ($M_{annulus}$) served as the assessment index for simulation, while its volume flow rate ($Q_{v\text{-}annulus}$) was used as the assessment index for experiments. The drill bit, with an outer diameter of 92 mm and designed for the GQ-89 series RC-DTH air hammers, was intended for drilling boreholes with a minimum diameter of 96 mm. The central passage diameter of the drill bit measured was 33 mm, with a distance of 4 mm between the drill bit front face and the borehole bottom. For simulation and experiments, the orthogonal tables L_{27} (3^{13}) and L_{18} (2×3^7) were employed, respectively, with three levels designated for each parameter. Further details are presented in Tables 1–4.

4 CFD and experimental approaches

Computational domains were constructed using SolidWorks software and meshed with HyperMesh software. Figure 3 illustrates a typical computational domain with 2,571,513 grids, which are divided into eight parts. The regular parts were meshed with a structured grid, while the irregular parts utilized a tetrahedral grid. Pyramid grids were employed to ensure connectivity across all parts. The inlet face, situated in the annulus space of dual-wall drill tools, was designated as a mass-flow-inlet boundary, with the input mass flow rate adjusted based on the air compressor parameters. Outlet faces, located in the center passage and the annulus between the drill tool and borehole wall, were defined as pressure-outlet boundaries set to atmospheric pressure. No-slip stationary wall boundary conditions were applied to the remaining boundaries. The 3D continuity, momentum, and energy conservation equations governing compressible flow within the drill bit were solved using Ansys Fluent software. The k-ε turbulence model was employed to simulate turbulent flow, with second-order upwind discretization utilized for convective terms, turbulent kinetic energy function, and turbulent dissipation rate function. The coupling between velocity and pressure was managed using the SIMPLE (semi-implicit method for pressure-linked equations) algorithm.

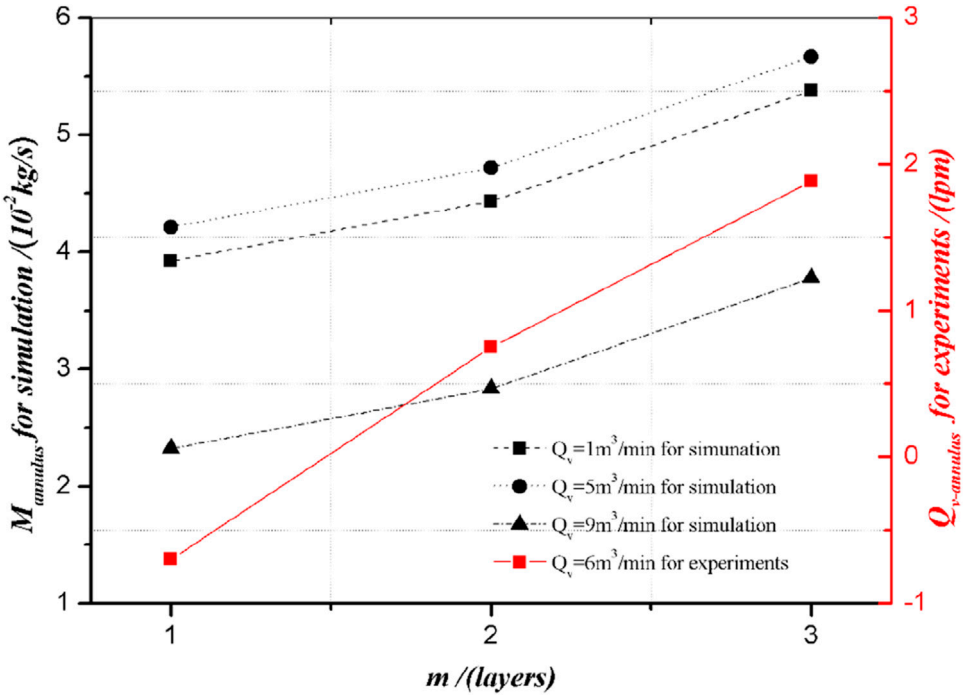


FIGURE 6
Influence of *m* on the dust control capacity.

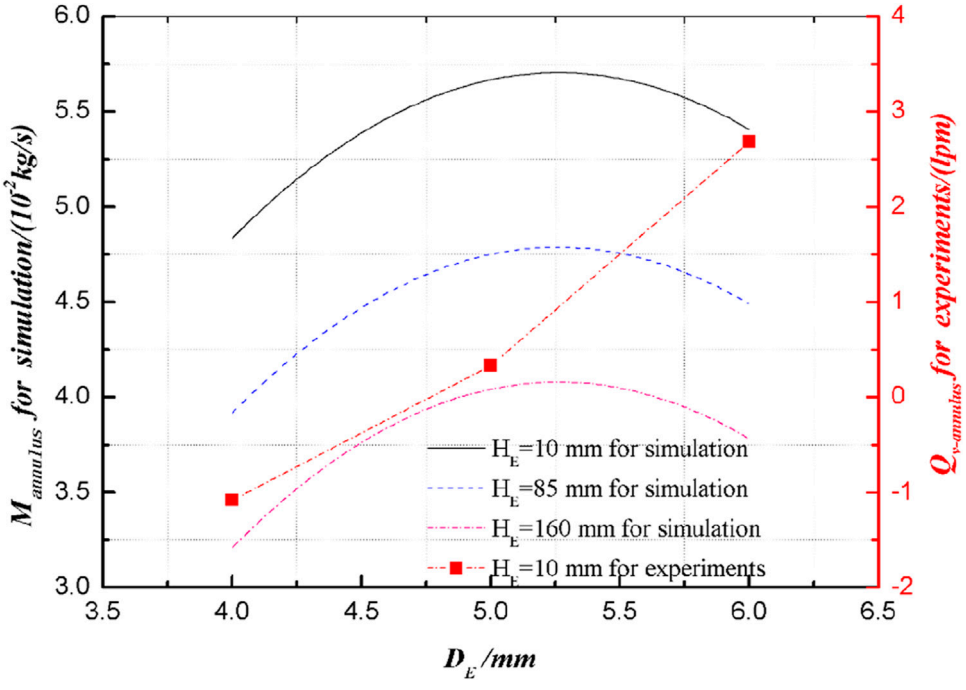


FIGURE 7
Influence of D_E on the dust control capacity.

A series of experiments were undertaken to validate the numerical simulation outcomes utilizing a specially designed experimental setup, as depicted in Figure 4. This apparatus was modularly designed to facilitate parameter adjustments according to the orthogonal design. The drill bit was segmented into four parts: the suction nozzle section, the flushing nozzle section, the mixing nozzle section, and the

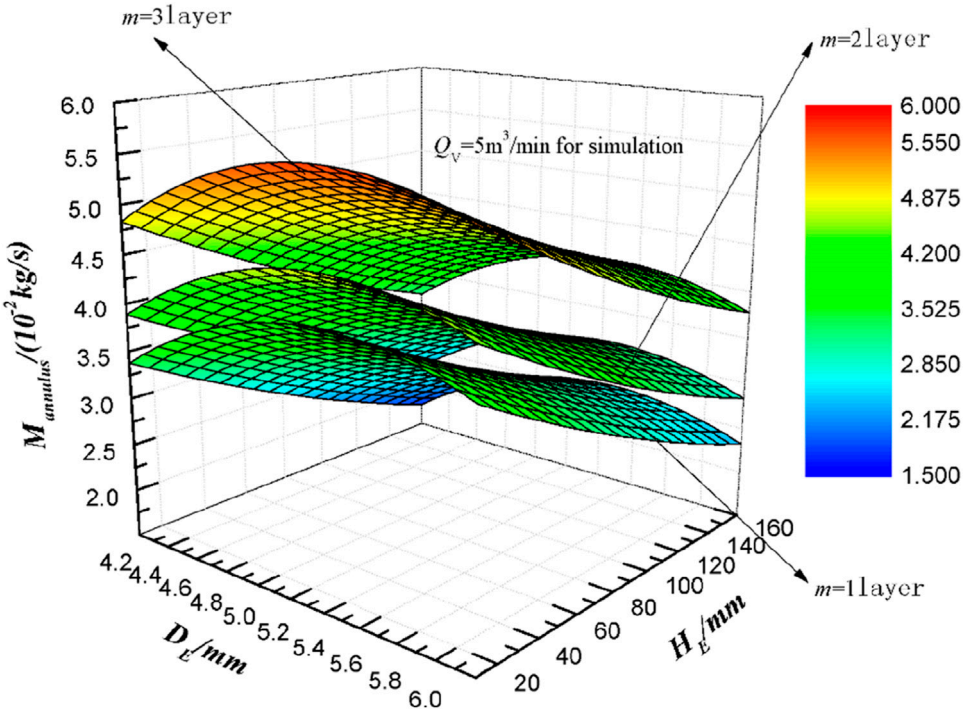


FIGURE 8
Synthetic influence of D_E & H_E on the dust control capacity.

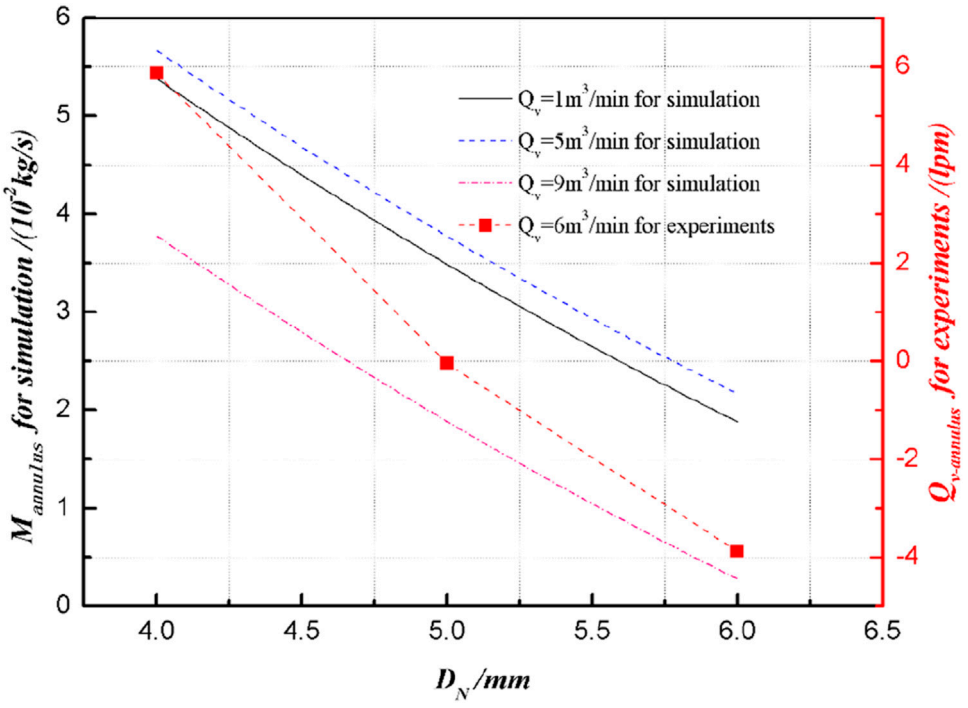


FIGURE 9
Influence of D_N on the dust control capacity.

expansion pressure groove section. To monitor the system parameters, two flowmeters and three pressure gauges were incorporated to measure the volume flow rate and pressure, respectively. The experiments employed a piston air compressor with a nominal volume flow of 6 m³/min and a nominal pressure of 0.8 MPa. In total, 18 experiments were conducted.

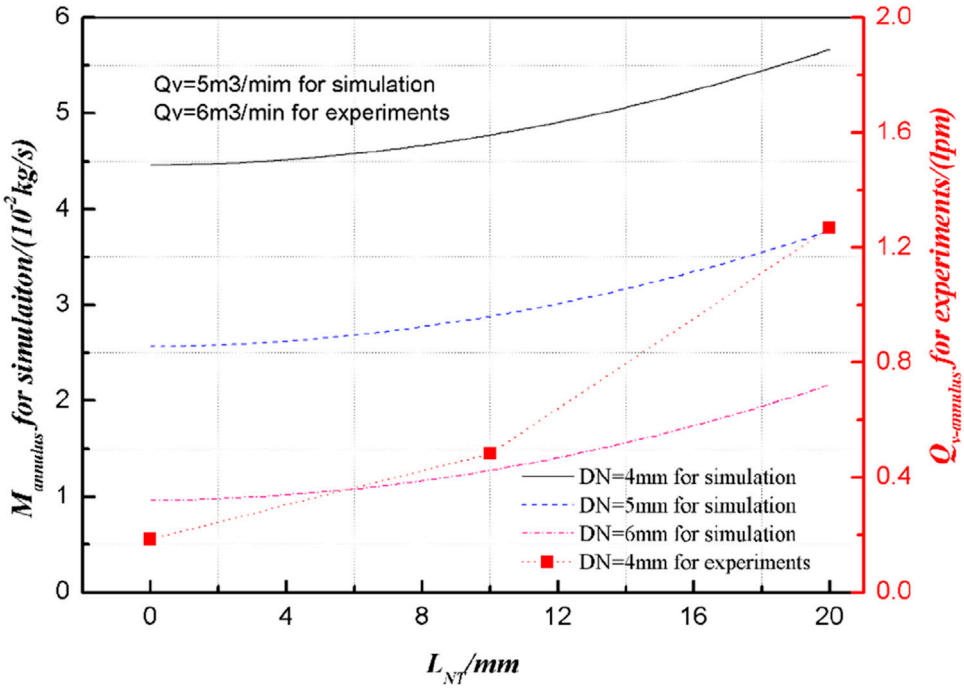


FIGURE 10
Influence of L_{NT} on the dust control capacity.

5 Results and discussion

A total of 27 computational models and 18 experiments were conducted based on an orthogonal design. The range analysis results yielded the order of each parameter. Among these parameters, the flushing nozzle diameter (D_N) exhibited the most significant effect on the dust control capacity of the drill bit, followed by the input air volume rate (Q_v), suction nozzle location (H_E), mixing nozzle diameter (D_T), distance between the flushing nozzle and mixing nozzle (L_{NT}), suction nozzle layers (m), suction nozzle diameter (D_E), the size of the annulus between the drill bit and borehole wall (L_S), and the elevation angle of the expansion pressure groove. Differences were observed between the simulation and experimental results for both drill bit structures. These disparities could be attributed to machine errors and leaks in the experimental apparatus, which are unavoidable in laboratory settings. Additionally, despite the use of a surge tank to mitigate fluctuations, the input volume flow rate remained variable during experimentation. Conversely, these factors were disregarded in the simulation process. Figure 5 illustrates the typical flow field in an RC drill bit. Following discharge from the flushing nozzles, compressed air entrains the nearby fluid into the mixing nozzles, effectively directing the drill cuttings toward the central passage with the aid of the lifting force generated by the pressure differential caused by the air jets from the suction nozzles.

5.1 Influence of m on the dust control capacity

Figure 6 illustrates the impact of the suction nozzle layers on the dust control capacity of the drill bit. It demonstrates that augmenting the suction nozzle layers can enhance the dust control performance of the RC drill bit. The cross-sectional area of the flow experiences a significant rise with each added suction nozzle layer, consequently amplifying the airflow from the suction nozzles while maintaining a constant input air volume. This augmentation proves advantageous in enlarging the pressure difference within the central passage, thereby bolstering its suction capacity. However, the increased airflow unavoidably leads to a reduction in airflow from the flushing nozzles, thereby diminishing the energy consumption resulting from the airflow collision at the borehole bottom. Within the range of input air volume flow rates from 1 to 9 m^3/min, there exists a critical input air volume flow rate. Initially, the sucked air flow rate increases with the rise in the input air volume flow rate. However, after the input air volume flow rate surpasses 3.8 m^3/min, there is a notable decline in the sucked air volume flow rate despite further increases in the input air volume flow rate.

5.2 Influence of D_E and H_E on the dust control capacity

A quadratic relationship is exhibited between the suction nozzle diameter and the suction of air flow rate, as shown in Figure 7. The suction of air flow rate reaches its maximum value when the suction nozzle diameter ranges from 5 to 5.5 mm. As for the effects of the suction nozzle layers, changing the suction nozzle diameter can change the allocation proportion of air flow rate from the suction and flushing nozzles. Enlarging the suction nozzle diameter before its critical value can maintain the air flow jet velocity while increasing the air flow rate, thus causing the improvement in the suction airflow. However, the airflow jet velocity would decrease

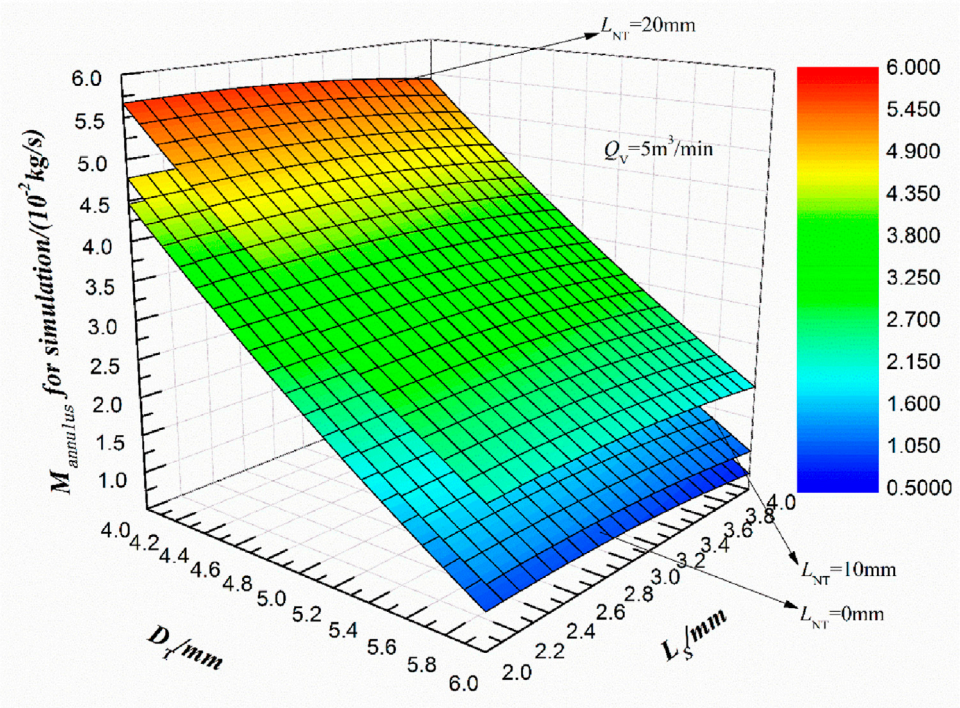


FIGURE 11
Influence of D_T & L_S on the dust control capacity.

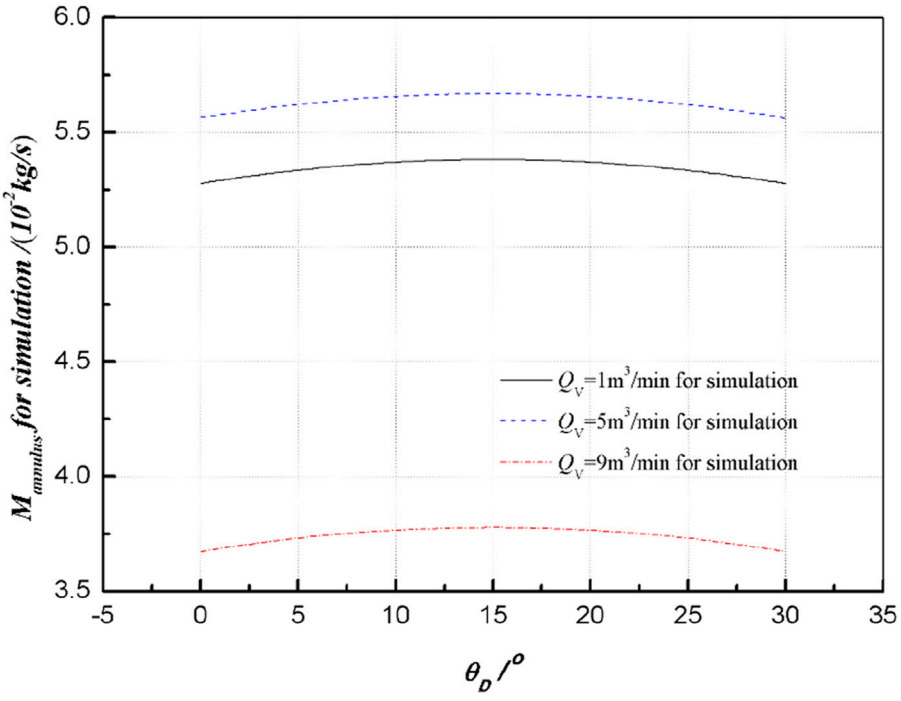


FIGURE 12
Influence of θ_D on the dust control capacity.

remarkably when the suction nozzle diameter was greater than the critical value. Therefore, there is an optimal total flow sectional area for the suction nozzles. Both changing the suction nozzle layers and the diameter under the condition of keeping its optimal total flow sectional area can ensure the optimum dust control capacity.

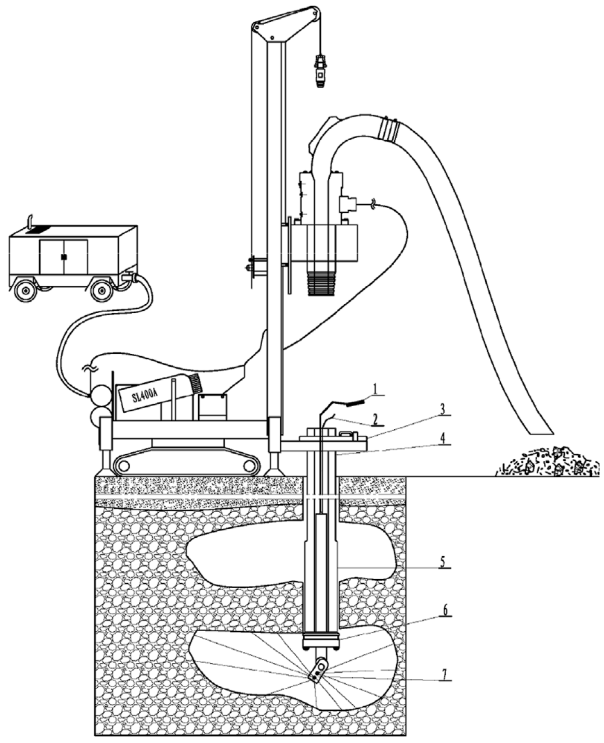


FIGURE 13
Schematic representation of the scanning process. 1: guide rod; 2: cable; 3: fork; 4: drill deck; 5: RC-DTH air hammer; 6: drill bit; 7: scanning unit.

Figure 8 depicts a negative correlation between the suction nozzle location and the accommodated airflow rate. The positioning of the negative pressure zone generated by the suction nozzle is determined by its placement. As illustrated, a distant suction nozzle location detrimentally affects the dust control capacity of the drill bit because the negative pressure area fails to cover the borehole bottom adequately. Hence, it is preferable to position the suction nozzle in close proximity to the borehole bottom.

5.3 Influence of D_N on the dust control capacity

The diameter of the flushing nozzle significantly impacts the dust control capacity of the RC drill bit. As depicted in Figure 9, the accommodated airflow rate noticeably decreases with the enlargement of the flushing nozzle diameter, all while maintaining a constant input air volume flow rate. As mentioned earlier, the input airflow can exit the drill tool through two passages: the suction nozzles and the flushing nozzles. When other parameters remain constant, increasing the flushing nozzle diameter indirectly reduces the suction nozzle size. As illustrated in Figure 5, airflow from the flushing nozzles can either enter the annulus between the drill tools and the borehole wall or flow into the center passage. The heightened airflow from the flushing nozzles due to diameter enlargement increases the airflow escaping into the annulus between the drill tools and the borehole wall, consequently resulting in poorer dust control performance.

The input air volume flow rate also significantly influences the dust control capacity of the drill bit when the flushing nozzle diameter is fixed. Initially, the accommodated airflow increases with the rise in the input airflow volume, but it subsequently decreases as the input airflow volume continues to increase. This suggests the presence of a critical input air volume flow rate for the given drill bit parameters.

5.4 Influence of L_{NT} on the dust control capacity

The distance between the flushing and mixing nozzles must not be too small; a distance of 20 mm appears to be optimal for L_{NT}, as indicated in Figure 10. A smaller distance would constrain its air-suction capability. Maintaining the flushing nozzles with a robust air-suction capacity allows them to capture a portion of the escaping airflow. As previously discussed, when the RC drill bit lacks flushing nozzles, all input airflow can only exit the drill tools via the suction nozzles, indirectly improving the airflow rate from the suction nozzles. However, efficiently carrying out drill cuttings becomes challenging without the assistance of flushing nozzles to clear them away. Additionally, the drill bit's teeth require cooling during the drilling process, making the flushing nozzles an essential component of the drill bit.

5.5 Influence of D_T and L_S on the dust control capacity

Figure 11 illustrates the impact of the mixing nozzle diameter on the dust control performance of the drill bit. It indicates that enlarging the mixing nozzle diameter is advantageous for enhancing its dust control capacity. As the airflow exits the flushing nozzle, it draws air from the annulus region into the mixing nozzle. Mixing nozzles with a larger diameter guarantee adequate energy and mass exchange between the air jet and the drawn airflow. Furthermore, a larger diameter decreases the flow velocity of the mixing flows, consequently reducing the escaped airflow.

Flow resistance plays a pivotal role in determining the airflow direction, and increasing the flow resistance proves to be an effective method for preventing airflow escape into the annulus between the drill tools and the borehole wall. Consequently, restricting the L_S with a drill bit featuring smaller blades can enhance the dust control performance of the RC drill bit, as depicted in Figure 11.

5.6 Influence of L_D and θ_D on the dust control capacity

According to the results of the range analysis, L_D has little influence on the dust control performance of the RC drill bit, with L_D = 15 mm being optimal for the current drill bit structure.



FIGURE 14
Field test of the RC-DTH air hammer. **(A)** Dusty drilling site with the conventional DTH air hammer drilling method. **(B)** Clean drilling site with the RC-DTH air hammer drilling method. **(C)** Discharged drill cuttings. **(D)** Preparation to place the scanning unit into the cavity through the center passage of the drill tools. **(E)** Cavity auto-scanning laser unit. **(F)** Conducting the cavity scanning process.

Although θ_D has minimal effect on its dust control performance, there is a discernible trend for θ_D, demonstrating a parabolic relationship, as shown in Figure 12. A very small θ_D results in a right-angle turn at the inlet of the mixing nozzle, leading to significant local loss. Conversely, a very large θ_D induces a sudden turn, creating a whirlpool effect and increasing energy consumption.

6 Field test

The RC drill bit (150 mm in diameter) with optimized parameters and its matched DTH air hammer GQ-142 were manufactured. They were employed to detect multilayer cavities with the assistance of a cavity auto-scanning laser system in Yuan Jiacun iron ore, which is affiliated with the Taiyuan Iron and Steel (Group) CO., LTD., and is located in Lanxian county of Shanxi province in the northwest of China. Figure 13 illustrates the schematic representation of this technique. During the drilling process, the system operates normally until the drill bit penetrates the roof of the cavity. At this point, the air hammer and the drill bit descend a segment due to gravity, limited by semi-circle clips, and the RC-DTH air hammer ceases operation immediately due to a valve mechanism failure. In the detection process, the lower drill pipes are secured on the drill deck to prevent the drill tools from falling into the cavity. Initially, the upper drill pipe above the ground is removed; then, the detection system is inserted into the cavity through the center passage of the drilling tool to obtain dimension information of the cavity. Finally, after completing the detection, the detection system is removed, and additional joints are added to continue the drilling process to detect the cavity below the upper one. The through-hole of the drill bit measures 55 mm, allowing the scanning unit with a diameter of 50 mm to cross it. Figure 14 depicts the field test drilling site employing the RC-DTH air hammer drilling method for detecting the goaf cavity. Compared with the conventional DTH air hammer employed nearby the test drilling site, the drill dust emission has been completely controlled. The field test verified that the modified drill bit effectively reduces dust emission.

7 Conclusion

The structure parameters of the RC-DTH air hammer drilling method were optimized using an orthogonal design via fluid computational and experimental methods to enhance its dust control performance. Although some disparities exist between the simulation and experimental results, the effective trends for all the parameters align consistently. The findings indicate that increasing the suction nozzle layers, enlarging both the suction and mixing nozzle diameters, and optimizing the input airflow within a certain range are conducive to improving the dust control performance of the RC drill bit. Conversely, enlarging the flushing nozzle diameter and adjusting the suction nozzle location negatively impact the dust control capacity. Based on the optimized parameters, a 150-mm outer diameter RC drill bit was

manufactured along with matching drill tools, including the DTH air hammer GQ-142. The field test results demonstrate the excellent dust control performance of the optimized RC drill bit. The DTH air hammer plays a critical role in reverse circulation drilling, and the parameters discussed in this paper can be applied to boreholes of any size. Enhanced dust control capability reduces well leakage.

As wells delve deeper and the initial spud-in drilling diameters increase, conventional drilling methods face challenges in circulating cuttings out of the wellbore, particularly in cases of circulation loss. Although conventional gas drilling can address circulation loss, it often requires substantial quantities of compressed air, numerous air supply units, occupies significant drilling site space, and incurs high costs, especially in large-diameter well drilling. These drawbacks limit the effectiveness of conventional gas drilling. However, dual-wall reverse circulation (RC) gas drilling technology has proven effective in addressing these challenges. This technology has shown no wellbore erosion due to high-speed returned air, minimal damage to low-pressure and permeability reservoirs, suitability for formation water applications, lower air consumption, and reduced drilling costs. It is widely utilized in geological prospecting, foundation engineering, hydrological well drilling, and other fields. Although RC gas drilling technology is relatively new in oil and gas exploration, it offers long-term benefits in cost-saving, efficiency improvement, energy conservation, and environmental protection. It holds promise for successful application in shallow gas, shale gas, coalbed methane (CBM), and other unconventional oil and gas reservoir exploration in the future.

Data availability statement

The original contributions presented in the study are included in the article/supplementary material; further inquiries can be directed to the corresponding authors.

Author contributions

LF: investigation, methodology, and writing–original draft. ZL: methodology, project administration, and writing–review and editing. YL: resources, supervision, and writing–review and editing.

Funding

The author(s) declare that financial support was received for the research, authorship, and/or publication of this article. This study received financial support from the Scientific Research and Technological Development Project of China Petroleum Group Oilfield Technology Services Co., Ltd., under the title “Development and Application of Supporting Tools for Deep and Ultra-Deep Drilling, Completion, and Testing in Ten Thousand Meters” (No. 2024T-001-002).

Acknowledgments

The authors extend sincere appreciation for the valuable suggestions provided by the editor and reviewers.

Conflict of interest

Author LF and ZL were employed by PetroChina.

The remaining author declares that the research was conducted in the absence of any commercial or financial relationships that could be construed as a potential conflict of interest.

The authors declare that this study received funding from China Petroleum Group Oilfield Technology Services Co. Ltd. The funder had the following involvement in the study: data collection and analysis, decision to publish.

Publisher’s note

All claims expressed in this article are solely those of the authors and do not necessarily represent those of their affiliated organizations, or those of the publisher, the editors, and the reviewers. Any product that may be evaluated in this article, or claim that may be made by its manufacturer, is not guaranteed or endorsed by the publisher.

References

Cecala, A. B., O’Brien, A. D., Schall, J., Colinet, J. F., Franta, R. J., Schultz, M. J., et al. (2012) *Dust control handbook for industrial minerals mining and processing*. United States: National Institute for Occupational Safety & Health. Report of Investigations 9689.

Cecala, A. B., Organiscak, J. A., Zimmer, J. A., Heitbrink, W. A., Moyer, E. S., Schmitz, M., et al. (2003). Reducing enclosed cab drill operator’s respirable dust explosure at surface coal operation with a retrofitted filtration and pressurization system. *Sme Trans.* 314, 31–36.

Cooper, M. R., Susi, P., and Rempel, D. (2012). Case study: evaluation and control of respirable silica exposure during lateral drilling of concrete. *J. Occup. Environ. Hyg.* 9 (2), D35–D41. doi:10.1080/15459624.2011.640303

Deng, H., Fan, L., and Xu, Q. (2024). Development and prospects of multi-type reverse circulation drilling technology. *J. Drill. Prod. Technol.* 47 (1), 60–72. doi:10.3969/J.ISSN.1006-768X.2024.01.08

Han, G., Bruno, M., and Dusseault, M. (2005) *Dynamically modelling rock failure in percussion drilling. The 40th U.S. Symposium on rock mechanics (USRMS): rock mechanics for energy, mineral and infrastructure*. Anchorage, Alaska: Development in the Northern Regions. ARMA/USRMS 05-819.

Hustrulid, W. A. (1982) *Underground mining methods handbook*. United State: Socioty.

Li, M., Luo, Y., and Jiang, H. (2016). Effects of proper drilling control to reduce respirable dust during roof bolting operations. *Int. J. Coal Sci. Technol.* 3 (4), 370–378. doi:10.1007/s40789-016-0154-x

Liu, J., and Yin, K. (2012). Development of SGQ-320 type reverse circulation DTH hammer used in gas drilling. *Pet. Drill. Tech.* 40 (1), 114–118. doi:10.3969/j.issn.1001-0890.2012.01.023

Lyons, W. C., Guo, B., and Hawley, G. D. (2009) *Air and gas drilling manual*. Third Edition. USA: Elsevier.

Maksimovic, S. D., and Page, S. J. (1985) *Quartz dust sources during overburden drilling at surface coal mines. Information Circular/1985*. Pittsburgh, PA (USA): Bureau of Mines. PB-86-169141/XA Pittsburgh Research Center.

Mixon, B., and Nain, J. (2013). Complying with occupational safety and health administration regulations: a guide for compounding pharmacists. *Int. J. Pharm. Compd.* 17 (3), 182–190.

Organiscak, J. A., and Page, S. J. (1995) *Assessment of airborne dust generated from small truck-mounted rock drills*. Pittsburgh Pa: U.s.department of the Interior Bureau of Mines Ri. Report of Investigations 9616.

Page, S. J. (1991). Respirable dust control on overburden drills at surface mines. *Proc. 1991 Am. Min. Congr. Coal Convention* 4, 523–539.

Sundae, L. S. (1995) *The reduction of airborne dust generated by roof bolt drill bits through the use of water*. United States: United States Department of the Interior. Report of Investigations 9594.

Tavakol, E., Azari, M., Zendehdel, R., Salehpour, S., Khodakrim, S., Nikoo, S., et al. (2016). Risk evaluation of construction workers' exposure to respirable crystalline silica and respirable dust. *J. Saf. Promot Inj. Prev.* 3 (4), 263–270.

USBM (1987) *Optimizing dust control on surface coal mine drills*. United States: By Page SJ. U.S. Department of the Interior. Bureau of Mines Technology News 286.

Zhang, D., Zhu, T., Lv, Y., Hou, J., and He, Y. (2017) *Research on fault diagnosis for air drilling based on an improved PSO for optimization of fuzzy neural network*. Singapore: Springer Singapore.

Zimmer, R., Lueck, S., and Page, S. (1987). Optimization of overburden drill dust control systems on surface coal mines. *Int. J. Surf. Min. Reclam. Environ.* 1 (2), 155–157. doi:10.1080/09208118708944113

Zimmer, R. A., and Lueck, S. R. (1986) *Investigation of quartz dust sources and control mechanisms on surface-coal-mine operations*. United States: Volume 1. Results, analysis, and conclusions. Open File Report, June 1984 March 1086.

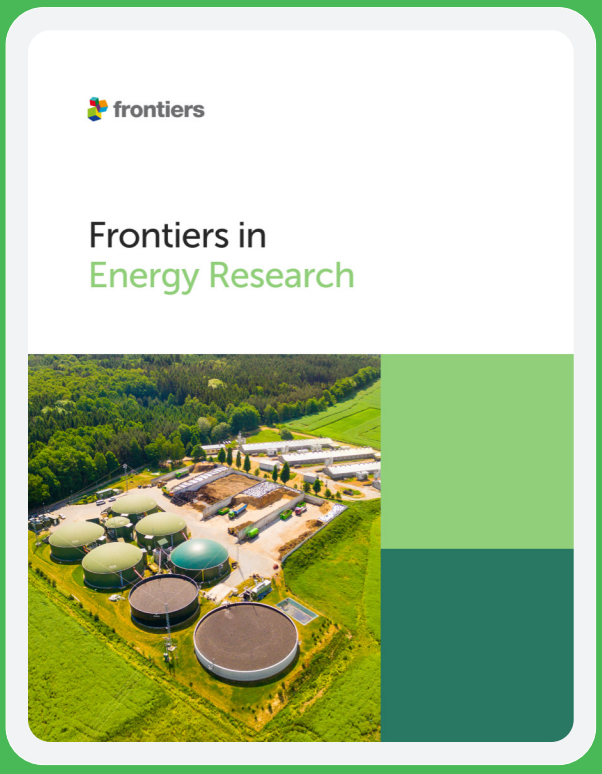
Frontiers in Energy Research

Advances and innovation in sustainable, reliable and affordable energy

Explores sustainable and environmental developments in energy. It focuses on technological advances supporting Sustainable Development Goal 7: access to affordable, reliable, sustainable and modern energy for all.

Discover the latest Research Topics

See more →



Frontiers

Avenue du Tribunal-Fédéral 34
1005 Lausanne, Switzerland
frontiersin.org

Contact us

+41 (0)21 510 17 00
frontiersin.org/about/contact